

A Novel Knowledge-aided Approach for Training Data Selection

Su-Dan Han, Chong-Yi Fan, Xiao-Tao Huang, and Zhi-Min Zhou

School of Electronic Science and Engineering, National University of Defense Technology, China

Abstract— This paper proposes a novel knowledge-aided approach for selecting training data in space-time adaptive processing (STAP) whose performance suffers from a severe degradation in heterogeneous interference environment. The proposed approach exploits distances between interference covariance matrices of training data and tested data as the measurements of interference statistical similarities, which helps us gain a deeper insight into the statistics from the point of geometry. Three distances including Euclidean distance, Riemannian distance and a physical distance are combined to distinguish various heterogeneous phenomena. A prior knowledge is employed in estimating the interference covariance matrices of both training data and tested data. Simulation results illustrate the effectiveness of the proposed approach.

1. INTRODUCTION

Space-time adaptive processing (STAP) is an important technique for suppressing strong clutter in airborne radar systems which designs an adaptive filter by learning the statistical characteristics of the interference environment [1]. Traditional STAP implementation employs training data near the range under test to estimate interference covariance matrix and generate the optimal weight vector under the assumption that they are independent and identically distributed with the tested data [2]. However, realistic interference environments usually appear heterogeneous, thereby violating the assumption, leading to covariance estimation errors, adaptive weight vector mismatch and consequently, degradation in STAP performance [3]. One useful approach to mitigate the effect of heterogeneity is screening the training data before covariance estimation.

Lots of screening methods have been proposed, such as power-selected training (PST) [4], the combination of phase and power-selected training [5] and the nonhomogeneity detector (NHD) [6]. PST selects the most powerful range cells to generate a deep clutter null for avoiding clutter residues, and phase and power-selected training attempts to remove those chosen powerful range cells which may potentially include target-like signals. Both of these two techniques make the assumption that the interference heterogeneity only lies in the power. NHD, however, takes the interference statistical properties into consideration instead of power, hence is a better criterion in theory. But the performance of NHD method depends upon a reliable selection metric [7]. Performance loss may occur when the metric is estimated using training data due to its heterogeneity.

Recently, distances between interference covariance matrices of the training data and tested data are put forward as one of the means to measure the statistical similarities within them, which provides a method of judging the interference heterogeneity from the perspective of geometry [8]. The interference covariance matrix of tested data is usually estimated using sample covariance matrix whose performance may degrade significantly when sample covariance matrix contains heterogeneous range cells. A knowledge-aided interference covariance matrix estimation based on clutter model is employed in this paper to estimate the statistical characteristic of tested data, which mitigates the heterogeneity from the root since it exploits no information of training data. In addition, a prior knowledge of noise spectral density is used to construct a positive-definite interference covariance matrix of training data which is necessary in calculating distances. Three different distances containing Euclidean distance, Riemannian distance and a physical distance are combined to separate all kinds of interference heterogeneities mentioned above. Simulation results illustrate the effectiveness.

2. STAP SIGNAL MODEL

Consider a uniform linear array radar system with N antenna elements. The radar transmits M pulses in a coherent processing interval (CPI), and there are K fast-time samples for each returned pulse. STAP is inherently a two-dimensional filtering process in space and slow-time plane which adaptively designs a weight vector $\mathbf{w}_k \in C^{MN \times 1}$ for the space and slow-time data snapshot $\mathbf{x}_k \in C^{MN \times 1}$ in the k th range cell. According to the usual linearly-constrained minimum-variance (LCMV) principle, the optimal weight vector for the k th range cell can be expressed as follows [1]

$$\mathbf{w}_{opt} = \mu \mathbf{R}_k^{-1} \mathbf{v} \quad (1)$$

where $\mu = 1/(\mathbf{v}^H \mathbf{R}_k^{-1} \mathbf{v})$ is a constant, \mathbf{R}_k is the interference covariance matrix in the k th range cell and \mathbf{v} is the space-time steering vector for a moving target with a given radial velocity and the direction of arrival.

However, the interference covariance matrix is usually unknown in reality, thereby should be estimated from measurement observations or other prior knowledge. The interference includes clutter, noise and jammer. Conventionally, the interference covariance is estimated from multiple space-time data snapshots of range cells nearby to the range under test (RUT) [1], defined as sample covariance matrix

$$\hat{\mathbf{R}} = \frac{1}{N_s} \sum_{i=1}^{N_s} \mathbf{x}_i \mathbf{x}_i^H \quad (2)$$

where $\mathbf{x}_i \in C^{MN \times 1}$ is the i th training data, N_s is the number of training data, and the superscript H denotes conjugate transpose.

Under ideal homogenous interference environment, if $2MN$ independent and identically distributed (IID) training data are available, the performance of this technique denoted as SMI can approach the ideal, known-covariance case to within 3 dB [2]. Unfortunately, interference environments of real data appear heterogeneous or non-IID, which deviates from the assumptions, thereby leading to covariance matrix estimation errors, adaptive filter mismatch, and consequently, degradation in performance of SMI. To mitigate the effect of heterogeneity, training data should be screened before covariance matrix estimation to select range cells which share similar statistical characteristics with the range under test.

3. TRAINING DATA SELECTION METRIC

The goal of training data selection metric is to measure the interference statistical similarity between training data and tested data. The best criterion is possibly the interference probability density function which completely represents the statistical characteristics. However, the probability density function is hardly to obtain accurately in practical applications. Instead, interference covariance matrix, as an important mathematical characteristic, gains a lot of attention and is widely used. In the angle of geometry, the similarity between two covariance matrices can be measured by the distance between them.

The most common distance is Euclidean distance which calculates the Frobenius norm of difference between the interference covariance matrix of training data denoted as \mathbf{R}_1 and the interference covariance matrix of tested data denoted as \mathbf{R}_0

$$d_1^2 = \|\mathbf{R}_1 - \mathbf{R}_0\|_F^2 \quad (3)$$

Clearly, Euclidean distance only cares about the power difference between two covariance matrices, and doesn't make use of the covariance structure.

Another kind of distance is Riemannian distance which is defined as

$$d_2^2 = \left\| \log \left(\mathbf{R}_0^{-1/2} \mathbf{R}_1 \mathbf{R}_0^{-1/2} \right) \right\|_F^2 \quad (4)$$

where \mathbf{R}_0 and \mathbf{R}_1 are constrained to positive-definite matrices. Riemannian distance is the foundation of information geometry and is theoretically more effective than Euclidean distance to measure the statistical similarity since covariance structure information is considered.

In addition, a physical distance is defined in [8] by

$$d_3^2 = \left\| \mathbf{R}_0^{-1/2} \mathbf{R}_1 \mathbf{R}_0^{-1/2} - \mathbf{I} \right\|_F^2 \quad (5)$$

where \mathbf{I} is the identity matrix. Under ideal conditions, this physical distance is a first order Taylor approximation of Riemannian distance. Its effectiveness has been verified in [8] using measured data.

4. KNOWLEDGE-AIDED COVARIANCE MATRIX ESTIMATION

The key point in the calculation of aforementioned distances is the interference covariance matrix estimations of both training data and tested data since they are unknown. Traditionally, the interference covariance matrix of tested data is estimated by sample covariance matrix according

to Equation (2). However, it suffers from errors when training data is heterogeneous. An alternative way to the estimation is based on the clutter model [1] whose structure is given by (jammer is not considered for simplicity)

$$\hat{\mathbf{R}} = \mathbf{R}_c + \mathbf{R}_n = \sum_{p=1}^{N_c} |\alpha_p|^2 \mathbf{v}_p \mathbf{v}_p^H \circ \mathbf{T}_p + \sigma_n^2 \mathbf{I} \quad (6)$$

where \mathbf{R}_c and \mathbf{R}_n are the covariance matrix of clutter and noise, respectively, N_c is the number of independent clutter patches in tested data, α_p and \mathbf{v}_p are the complex amplitude and space-time steering vector, respectively, for the p th ground clutter patch, \circ is the Hadamard matrix product, \mathbf{T}_p is a covariance matrix taper (CMT) that allows for incorporation of subspace leakage effects such as internal clutter motion (ICM) and channel error, σ_n^2 is the average noise power per measurement. Covariance matrix constructed in this way only takes statistics of the range under test into consideration. As a result, it can mitigate fundamentally the effect of heterogeneity brought by training data.

For a clutter patch with azimuth angle θ and depression angle φ measured from the reference of platform moving direction, its space-time steering vector can be expressed as

$$\mathbf{v} = \mathbf{v}_t \otimes \mathbf{v}_s \quad (7)$$

$$\mathbf{v}_t = [1, \exp(jw_d), \dots, \exp(j(M-1)w_d)]^T, \quad \mathbf{v}_s = [1, \exp(jw_s), \dots, \exp(j(N-1)w_s)]^T \quad (8)$$

$$w_d = \frac{4\pi v}{\lambda f_r} \cos(\theta + \alpha) \cos \varphi, \quad w_s = \frac{2\pi d}{\lambda} \cos \theta \cos \varphi \quad (9)$$

where M is the number of pulses transmitted in a CPI, N is the number of antenna elements, d is the distance between adjacent antenna elements, f_r and λ are pulse repetition frequency and wavelength of the transmitted signal, respectively, v is the velocity of airborne radar platform and α is the crab angle, \otimes is Kronecker product, \mathbf{v}_t and \mathbf{v}_s are time and space steering vector whereas w_d and w_s are normalized Doppler frequency and spatial frequency, respectively. If parameters of radar system, antenna platform are known as a prior or can be measured conveniently, the space-time steering vector of each clutter patch can be obtained according to their locations. The amplitude of each clutter patch α_p can be estimated directly from a prior knowledge such as SAR images [9] or indirectly from measured data [10]. CMT \mathbf{T}_p can be similarly determined indirectly from measured data [10] under some proper models or directly from a prior knowledge. For example, a widely accepted Gaussian model for ICM only requires the specification of wavelength λ , pulse repetition frequency f_r and variance of the clutter spectral spread [10]. The power of the noise σ_n^2 can be accurately estimated through calibration procedures in practice.

The interference covariance matrix estimation of training data is generally a function of training data, and a possible choice could be the sample covariance matrix, namely $\mathbf{R}_i = \mathbf{x}_i \mathbf{x}_i^H$. However, it can't meet the requirement of positive-definiteness which is necessary to calculate the Riemannian distance, hence a technique proposed in [11] is exploited here to generate a modified positive-definite sample covariance matrix

$$\hat{\mathbf{R}}_i = \mathbf{U}_i \mathbf{\Lambda}_i \mathbf{U}_i^H \quad (10)$$

where $\mathbf{\Lambda}_i = \text{diag}([\lambda_i, \sigma_n^2, \dots, \sigma_n^2])$, with $\lambda_i = \max(\sigma_n^2, \|\mathbf{x}_i\|^2)$ and σ_n^2 being the average noise power, \mathbf{U}_i is a unitary matrix consisting of the eigenvectors of $\mathbf{x}_i \mathbf{x}_i^H$ whose first eigenvector corresponds to the eigenvalue $\|\mathbf{x}_i\|^2$.

5. SIMULATIONS

The simulation parameters are as follows. Radar is flying at an altitude of 885 m and the distance between the radar and the center range is 10150 m. The radar platform moves at the velocity of 140 m/s. The pulse-repetition frequency of the transmitted signal f_r is 2800 Hz and the wavelength λ is 0.2 m. The number of pulses in a CPI M is 10 and the number of antenna receive elements N is 12. The distance between adjacent receive elements d equals to half of the wavelength. There are 151 range cells in total and the target is placed in the 76th range cell. Without loss of generality, the noise power level is assumed to be 0 dB, and the target power is set to be 10 dB.

The interference statistical characteristics of each range cell are listed in Table 1. All kinds of heterogeneities consisting of power differences, target-like signals, clutter discretions and spectral

dissimilarities are taken into consideration. And the spectral dissimilarities are modeled using a well-known CMT model which is regularly used to describe channel error

$$\mathbf{T} = \mathbf{I}_{M \times M} \otimes \left(\sin c \left(\frac{(m-n)\Delta}{\pi} \right) \right) \quad m, n = 1, 2, \dots, N \quad (11)$$

where Δ is assumed to be a uniformly distributed random value among 0 and 0.1 in range cells from 121 to 151 and 0 in other range cells. In addition, we assume that each target-like signal has the same azimuth angle and velocity and so as the clutter discretizes.

Table 1: Interference statistical characteristics of each range cell.

Range cell	Interference statistical characteristics
1–30, 61–151	$\sigma_c^2 = 30$ dB
31–60	$\sigma_c^2 = 35$ dB
50, 60, 70, 80, 90	Target-like signals, $\sigma_t^2 = 20$ dB
45, 55, 65, 75, 85	Target-like signals, $\sigma_t^2 = 35$ dB
40, 90, 100, 110, 120	Clutter discretizes, $\sigma_d^2 = 40$ dB
35, 85, 95, 105, 115	Clutter discretizes, $\sigma_d^2 = 45$ dB
121–151	CMT is considered

Three kinds of distances for each range cell except the 76th one are calculated using the sample covariance matrix and knowledge-aided covariance matrix estimation respectively. Figure 1 shows the results under the assumption that knowledge is accurate. The blue solid line denotes distances using knowledge-aid covariance matrix estimation while the red dashed one denotes distances using sample covariance matrix estimation. The result of Euclidean distance shows that both of the covariance matrix estimation work well, yet only power difference can be detected, weak target-like signals and spectral dissimilarities is hardly to be found. Moreover, it is impossible to distinguish between target-like signals and clutter discretizes. The results of Riemannian distance and physical distance, however, show that knowledge-aided covariance estimation performs better than sample covariance estimation which fails to detect power differences, target-like signals and clutter discretizes. Both of the knowledge-aided Riemannian distance and physical distance can well find the target-like signals even when their power is 10 dB lower than clutter and they can detect strong clutter discretizes. Knowledge-aided Riemannian distance fails to detect weak clutter discretizes, and it is interesting that the knowledge-aided Riemannian distances of clutter discretizes are lower than ideal values while those of target-like signals are higher than ideal values. In addition, if target-like signals and clutter discretizes exist simultaneously in one range cell, the statistical properties of target-like signals occupy the dominant position. Spectral dissimilarities are obvious comparing these three distances, and those range cells should be removed.

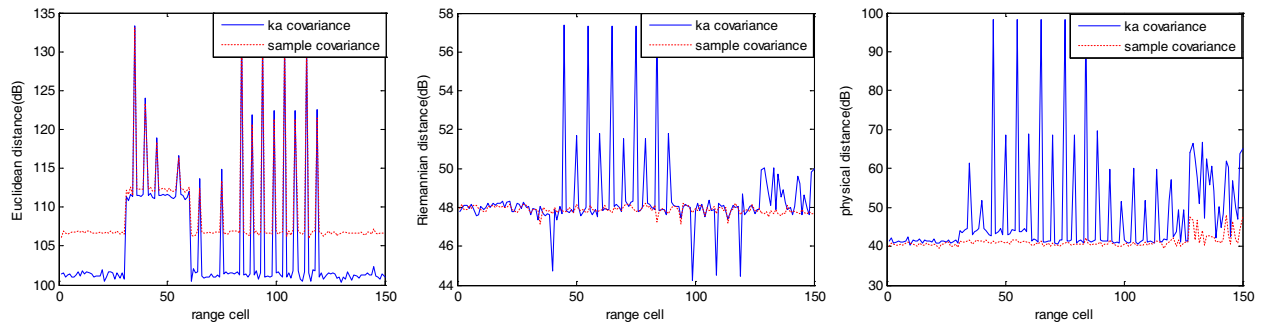


Figure 1: Three distances (Euclidean, Riemannian, physical) using sample covariance matrix and knowledge-aided covariance matrix under the assumption that knowledge is accurate.

However, knowledge of clutter parameters is not always accurate in practice, and power error is one of the most common situations. Figure 2 shows the condition that the clutter power is overestimated by 10 dB while Figure 3 displays the results that the clutter power is underestimated by 10 dB. Both of the figures testify the effectiveness of knowledge-aided distances although there

is a 10 dB clutter power error. Actually, the error enhances the performance slightly in detecting clutter discretely for knowledge-aided Riemannian distance either in power overestimation or underestimation condition while it only improves the performance of knowledge-aided physical distance in power underestimation condition and reduces the performance moderately in power overestimation condition.

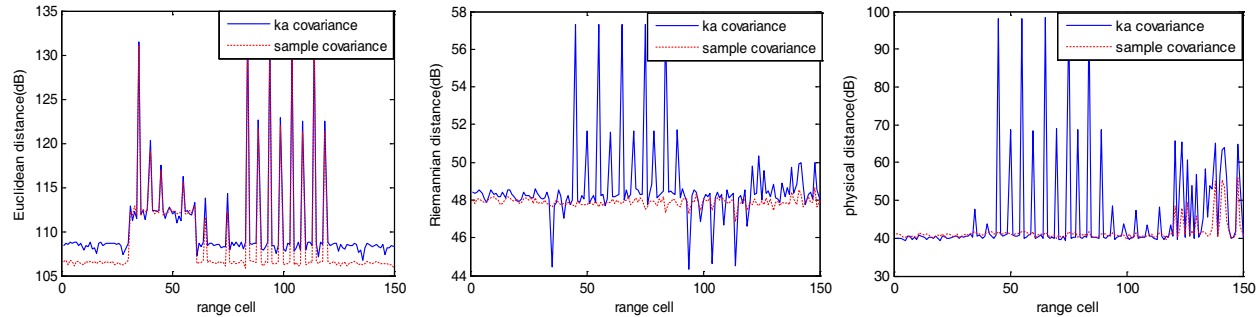


Figure 2: Three distances (Euclidean, Riemannian, physical) under the condition that the clutter power is 10 dB higher than actual value.

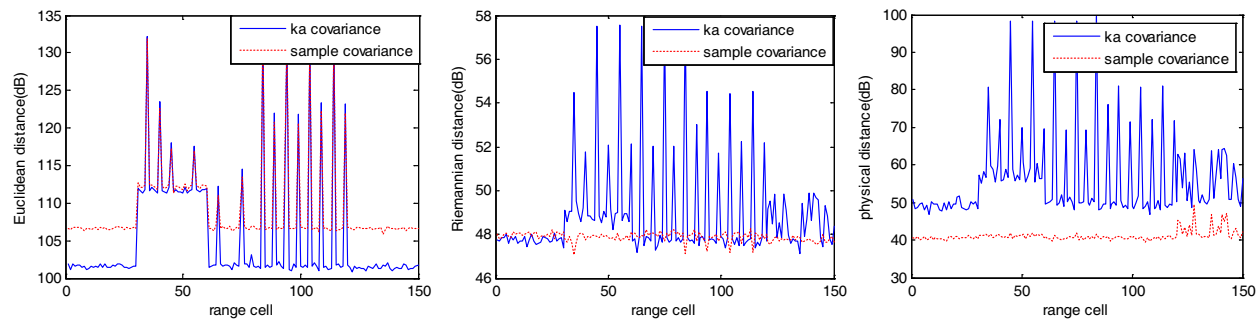


Figure 3: Three distances (Euclidean, Riemannian, physical) under the condition that the clutter power is 10 dB lower than actual value.

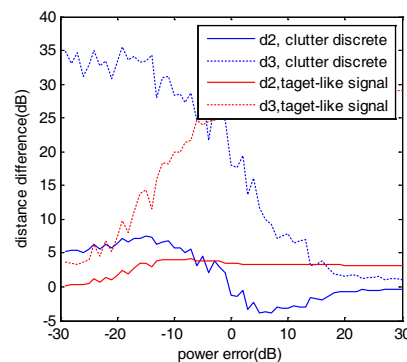


Figure 4: Riemannian and physical distance of clutter discrete and target-like signal compared with the ideal values under different clutter power estimations.

Next, based on the aforementioned results, the knowledge-aided Riemannian and physical distances of clutter discrete and target-like signal compared with ideal values under different clutter power estimations are discussed. Assume the power of clutter discrete and target-like signal are 45 dB and 20 dB, respectively. Figure 4 shows that the Riemannian distance of clutter discrete is higher than the ideal value at first and then lower than the ideal value with the change of clutter power estimation, yet that of target-like signal is always higher than ideal values and approximately invariant when the clutter power is overestimated. Besides, the difference between physical distance of clutter discrete and ideal value presents a tendency of descent while that of target-like signal

presents an opposite ascendant tendency. Both of the properties can be used to distinguish clutter discrete and target-like signal, which is very useful since range cells containing target-like signals should be removed to avoid target elimination, nevertheless range cells containing clutter discretos sometimes should be exploited to drive a deep null.

6. CONCLUSIONS AND FUTURE WORK

In this paper, we measure the statistical similarities of data in different range cells from the perspective of geometry. Distances between interference covariance matrices of different range cells containing Euclidean distance, Riemannian distance and a physical distance are selected as the training data selection metrics. With regard to the interference covariance matrix estimation, two methods including sample covariance matrix estimation and a knowledge-aided covariance matrix estimation based on clutter model are compared. Simulation results show that different heterogeneous phenomenon consisting of power differences, target-like signals, clutter discretos and spectral dissimilarities can be detected and separated with the combination of three distances. With this guidance, training data can be well selected.

Significant future research is still required. Knowledge error except clutter power error should be considered and their impacts should be studied. In addition, our proposed approach should be testified using measured data rather than simulated data, and improvement of our approach should be investigated according to the effects analyzed from the measured data.

REFERENCES

1. Ward, J., *Space-time Adaptive Processing for Airborne Radar*, MIT Lincoln Laboratory, 1994.
2. Reed, I. S., J. D. Mallett, and L. E. Brennan, "Rapid convergence rate in adaptive arrays," *IEEE Transactions on Aerospace and Electronic Systems*, Vol. 10, No. 6, 853–863, 1974.
3. Melvin, W. L., "Space-time adaptive radar performance in heterogeneous clutter," *IEEE Transactions on Aerospace and Electronic Systems*, Vol. 36, No. 2, 621–633, 2000.
4. Rabideau, D. J. and A. O. Steinhardt, "Improved adaptive clutter cancellation through data-adaptive training," *IEEE Transactions on Aerospace and Electronic Systems*, Vol. 35, No. 3, 879–891, 1999.
5. Kogon, S. M., "Adaptive weight training for post-doppler STAP algorithms in non-homogeneous clutter," *IEE Radar, Sonar and Navigation*, Series 14, IEE Press, UK, 2004.
6. Melvin, W. L., M. C. Wicks, and R. D. Brown, "Assessment of multichannel airborne radar measurements for analysis and design of space-time processing architectures and algorithms," *Proceedings of the 1996 IEEE National Radar Conference*, 130–135, 1996.
7. Melvin, W. L. and J. R. Guerci, "Knowledge-aided signal processing: A new paradigm for radar and other advanced sensors," *IEEE Transactions on Aerospace and Electronic Systems*, Vol. 42, No. 3, 983–996, 2006.
8. Degurse, J.-F., L. Savy, J.-P. Molinie, and S. Marcos, "A Riemannian approach for training data selection in space-time adaptive processing applications," *Proceedings of the 2013 IEEE International Radar Symposium*, June 2013.
9. Gurram, P. R. and A. Goodman, "Spectral-domain covariance estimation with a prior knowledge," *IEEE Transactions on Aerospace and Electronic Systems*, Vol. 42, No. 3, 1010–1020, 2006.
10. Melvin, W. L. and G. A. Showman, "An approach to knowledge-aided covariance estimation," *IEEE Transactions on Aerospace and Electronic Systems*, Vol. 42, No. 3, 1021–1042, 2006.
11. Aubry, A., A. D. Maio, L. Pallotta, and A. Farina, "Covariance matrix estimation via geometric barycenters and its application to radar training data selection," *IEE Radar, Sonar and Navigation*, in press.

Novel Design and Implementation of Ultra-wideband Pulse Generator Based on Avalanche Transistor

Y. Guo and G. Zhu

School of Electronic Science and Engineering
National University of Defense Technology, Changsha, China

Abstract— Based on the avalanche multiplication effect of the avalanche transistor, a novel ultra-wideband (UWB) pulse generator has been designed. The UWB pulse technologies are described, and then different approaches for UWB pulse are analyzed and compared. The considered pulse generation technologies are based on logic gates, Step-Recovery Diodes (SRD), and avalanche transistors. The basis of the proposed generator is a precision oscillator, an avalanche transistor, and an unique pulse-shaping circuit composed of the SRD and Schottky diode, which is used to reduce the pulse width and maintain the pulse amplitude high. Every component in the UWB pulse generator should be picked out, and the radio-frequency (RF) characteristics of the circuit must be considered. Finally, the UWB pulse generator with pulse duration of 356 ps, pulse amplitude of 3.1 V and ringing level of -15.9 dB has been simulated and fabricated. The measured result agrees with the simulation. Besides, the measured result is analyzed and the expectation is presented. With the features such as simple structure, stable performance and low cost, the proposed design is ideal for the UWB wireless communication system.

1. INTRODUCTION

After the American Federal Communications Commission (FCC) announced the ruling for ultra-wideband (UWB) systems, the UWB technology has increasingly gained interest by many researchers and several applications of such systems have been developed. Notable applications are those in communications, through-wall radar and ground penetrating radar (GPR). To generate an impulse-based UWB signal for these applications, the UWB pulse generator circuit is critically needed.

In recent years, there are mainly three kinds of narrow pulse generation methods: logic gate pulse generator [1, 2], SRD pulse generator [3, 4] and avalanche transistor pulse generator [5, 6]. Choosing a suitable method is very important to complete the corresponding application [7].

Logic gate pulse generator is based on a fast logic component (an inverter and a NAND or XOR gate). The pulse width is determined by the inverter propagation delay, whereas, the pulse edge depends on the rise/fall time of the output stage. The pulse generated in this method is very narrow and the jitter is very weak. However, the pulse width is limited by the logic component, and the pulse amplitude is less than 1 V.

SRD pulse generator is based on the transition time of the minority carrier. Two important characteristics affecting the performance of the SRD pulse generator need to be identified. One is the transition time of the SRD that determines the minimum achievable pulse's transition time. The other is the minority carrier lifetime (MCLT) of the SRD, which affects the storage time under reverse-bias conditions. The pulse generated in this method is narrower than that in the logic gate method. However, the pulse amplitude is too small.

Avalanche transistor pulse generator is based on the multiplication effect of the avalanche transistor. This method is a traditional method to produce nanosecond pulses, which can be synchronous and have great voltage, so it is very suitable for the UWB wireless communication system. However, it requires a relatively high power supply, the pulse width is a little wide, and the pulse jitter is a little strong.

The pulse generated in the above method is too wide, or the pulse amplitude is too small, so it also can't meet the UWB pulse for the wireless communication system. This paper presents a novel UWB pulse generator composed of a precision oscillator, an avalanche transistor, SRDs and a Schottky diode, and it has been simulated and fabricated on an FR-4 glass epoxy substrate. The result is that the pulse width is greatly narrowed and the pulse amplitude is kept at a high level. The innovation of this paper is to design the edge sharpener and the pulse-shaping network, combine it well with the avalanche circuit, and avoid the strict demand for the input signal. Besides, the tunable pulse repetition frequency (PRF) is helpful to the different applications. The proposed design is clear and simple, so it is ideal to be used for the UWB wireless communication system.

2. DESIGN AND SIMULATION

In the UWB wireless communication system, the penetrability and resolution of the UWB pulse are a pair of contrary factors. The longer the wavelength is, which weakens the resolution of the UWB pulse, the better the penetrability will be. On the other hand, the shorter the wavelength is, which enhances the resolution of the UWB pulse, the more the attenuation will be, that is, the worse the penetrability is. The research shows that the signal has good resolution and penetration performance at about 1 gigahertz [8]. The approximate pulse width can be determined as $\tau \cong 350/B$ (ps), where B is the bandwidth (in gigahertz) [9].

So the UWB pulse signal will be spread well, if the pulse width is about 350 ps. With the attenuation of the spreading, the higher UWB pulse amplitude is, the farther the pulse spreads.

In order to design and implement a UWB pulse generator producing high-voltage and narrow pulses, we need to introduce a multi-stage circuit. For the amplitude of the UWB pulse is relatively high, the basic avalanche circuit is used to generate a high-amplitude pulse. Considering that the pulse width should be about 350 ps, it is necessary for the pulse-shaping network to narrow the pulse width of the avalanche pulse and maintain a high voltage. Besides, an internal signal source is important to drive the avalanche circuit, which has important role in defining the prominent characteristics of the UWB pulse, such as the PRF. However the rise time of the square pulse from the CMOS component is always long, the edge sharpener is very essential.

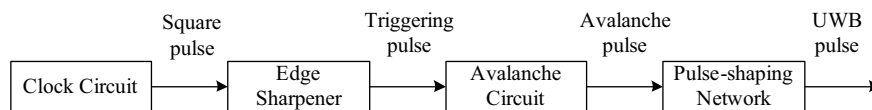


Figure 1: Block diagram of designed UWB pulse generator.

As can be seen from Figure 1, the square pulse from the clock circuit is converted to the triggering pulse after the edge sharpener, which can trigger the avalanche circuit for obtaining high-amplitude avalanche pulse, and then the pulse-shaping network will shape this pulse. Thus the UWB pulse circuit is composed of four parts: the clock circuit, the edge sharpener, the avalanche circuit and the pulse-shaping network, as shown in Figure 2.

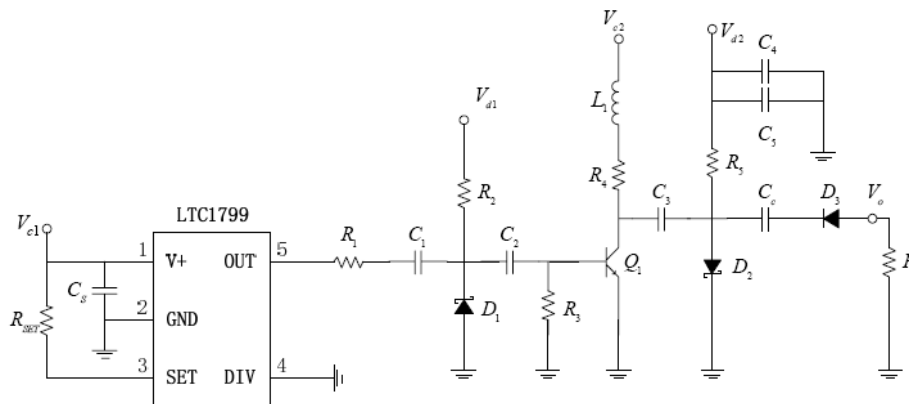


Figure 2: Circuit of designed UWB pulse generator.

The clock circuit is used to generate the square pulse, which can define the PRF of the UWB pulse. Because of the advantage of wide frequency range, low frequency error and low cost, the precision oscillator LTC1799 (Linear Technology) is picked out, which is easy to use and occupies very little PC board space. The oscillator frequency is programmed by a single external resistor (R_{SET}), and the frequency-setting resistor can vary from 3.32 k Ω to 1 M Ω to select a master oscillator frequency between 100 kHz and 30 MHz. If the supply V_{c1} is 5 V and C_S is 0.1 μ F, the relationship between R_{SET} and frequency can be described in following formula:

$$f_{OSC} = 10 \text{ MHz} \cdot (10k/R_{SET})$$

From the formula, it can be seen that the DIV PIN should set as GND and R_{SET} is 100 k Ω for PRF = 1 MHz, which is the ideal for lower power and better accuracy [10].

The edge sharpener is designed to sharp the rise time of the square pulse. The supply voltage V_{d1} and bias resistor R_2 forward bias the SRD D_1 and store a charge in the depletion region of the diode. As the rise edge of the square pulse appears, it tends to reverse bias the diode and deplete it of stored charge. During this charge depletion phase, the SRD continues to behave as a low impedance, shunting the rising input pulse to ground. When all the stored charge on the SRD is depleted, the diode snaps into its high impedance state, allowing the square pulse to return to ground through the resistor R_3 . This switching action can occur in as little as 100 ps, forming a triggering pulse with high speed rise edge.

The avalanche circuit is used to generate an avalanche pulse with high amplitude. The supply voltage V_{c1} and bias resistor R_4 make the transistor Q_1 in a critical avalanche state. V_{c1} is used to charge up C_3 until the avalanche transistor is in the conduction state, and the time constant of charging process is $\tau = R_4 C_3$. It is noted that this time constant is less than the pulse repetition frequency $PRT = 1/PRF$, that is, $\tau \leq 1/PRF$. In addition, the bias resistor should be suitable for the avalanche transistor, because the power consumption will be big if R_4 is too small, and the rise time will get long if R_4 is too big. The edge shaped triggering pulse can make the avalanche transistor generate a high speed down edge avalanche pulse.

The pulse-shaping network is designed to narrow the pulse width and suppress the pulse ringing. Due to the particular characteristics of the SRD D_2 , the forward bias SRD allows the positive current to the ground, storing a charge in the depletion region of the diode, and the reverse bias SRD depletes the stored charge, sharpening the negative avalanche pulse edge. The Schottky diode D_3 functions as a switch to suppress the overshoot of the pulse. Besides, the coupling capacitance C_3 and the load R_L form the high-pass filter naturally. Furthermore, the bypass capacitor C_4 and C_5 are used to filter out the noise of the power.

The circuit simulation was conducted using the Advanced System Design (ADS) platform, which is an accuracy simulation tool for RF and microwave circuits. The SRD used for shaping is MMD0840 manufactured by the Metelics Company, and the Schottky diode used for switching is MSS60,148-B10B manufactured by the Metelics Company. The simulation result of the designed UWB pulse generator is shown in Figure 3.

As can be seen from Figure 3, the UWB pulse has the pulse duration of 356 ps, the pulse amplitude of 3.2 V, and the ringing level of -25.8 dB. Clearly, the pulse width meets the designed requirement. Compared to [11] and [12], the pulse width has improved largely, while the pulse amplitude has also been kept at a high level. However there are still some small overshoot, which is mainly caused by the limited state transition between the breaking and opening of the Schottky diode.

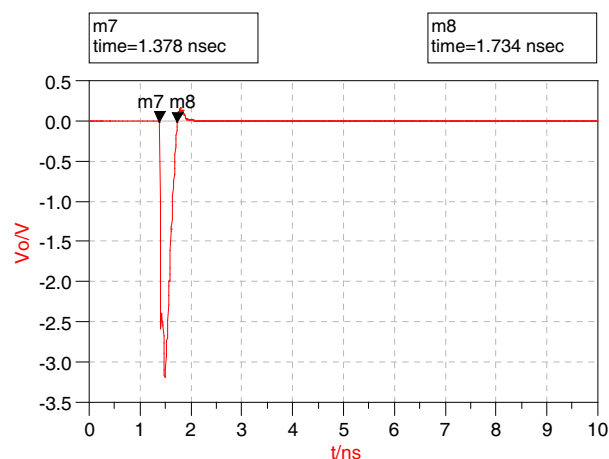


Figure 3: Simulation of designed UWB pulse generator.

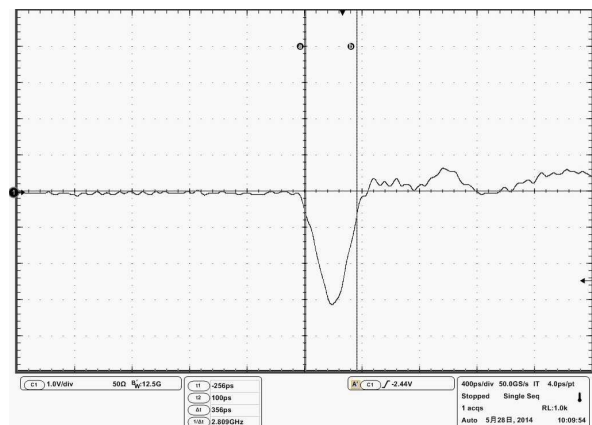


Figure 4: Measurement of designed UWB pulse generator.

3. FABRICATION AND MEASUREMENT

The novel UWB pulse generator has been fabricated on FR4 printed circuit board having a relative dielectric constant of 9.6, a thickness of 1.6 mm. The effect of the high frequency should be considered in the fabrication for avoiding the tail and the shock. The power supply used is

a MOTTECH LPS-305 (Linear Power Supply). For this pulse with 356-ps pulse width, the most sampling interval is 36 ps if it needs to sample at least ten points within the scope of the pulse width [10]. In other words, the sampling point frequency is at least 28 GS/s. As a result, we can use a Tektronix DPO-71254 (Digital Phosphor Oscilloscope) as the waveform testing instrument, because the sampling point frequency of this instrument reaches 50 GS/s.

As can be seen from Figure 4, a narrow pulse with the amplitude of 3.1 V and the pulse width of 356 ps is obtained. In other words, the measurement results agree with the theory analysis. At the same time, it is noted that the ringing level is below -15.9 dB, which may be caused by the high frequency crosstalk. From Table 1, the pulse generated in CMOS and SRD mode is narrower, but the pulse amplitude is very small, compared to the BJT mode. On the other hand, the pulse amplitude of the pulse in BJT mode is larger, meanwhile the pulse is wider. The pulse generated in this work has high amplitude, at the same time, the pulse width agrees with the design. The balance between the resolution and penetration performance is achieved.

Table 1: Comparison between this work and other proposed ones.

Ref.	PRF (MHz)	Supply (V)	Pulse width (ps)	Pulse Amplitude (V)	Technology
[1]	--	1.2	142	0.5	CMOS
[4]	10	> 7	400	0.2	SRD
[11]	2.5	25	2071	9.08	BJT
[12]	1–8	5	1900	2.16	BJT&SRD
This work	1 (tunable)	15	356	3.1	BJT&SRD

4. CONCLUSION

A novel UWB pulse generator has been simulated on the RF software ADS and fabricated on FR4 printed circuit board. This pulse generator uses an avalanche transistor, SRDs and a Schottky diode to produce UWB pulses with the pulse width of 356 ps, the pulse amplitude of 3.1 V and the ringing level of -15.9 dB. Good agreement between the measured and simulation results is achieved. As a result, the proposed UWB pulse has good resolution and penetration performance. So this kind of simple and high-performance UWB pulse generator is very suitable for the design of UWB wireless communication system, pulse radar and so on. The ringing and jitter will be suppressed at a lower level in the future. Besides, the PRF of the UWB pulse is tunable by means of varying the external resistance of the precision oscillator.

ACKNOWLEDGMENT

The author, Y. Guo, would like to express my deepest sense of gratitude and humble regards to Mr. Zhu for giving insightful suggestions and invariable support to carry out this work and all the brothers and sisters of the Ultra-wideband laboratory for their great help and encouragement.

REFERENCES

1. Arafat, M. A. and A. B. M. Harun-ur-Rashid, "A novel 7 Gbps low-power CMOS ultra-wideband pulse generator," *IET Circuits Devices Syst.*, Vol. 6, No. 6, 406–412, 2012.
2. Sim, S., D. Kim, and S. Hong, "A CMOS UWB pulse generator for 6–10 GHz applications," *IEEE Microwave Wireless Components Letters*, Vol. 19, No. 2, 83–85, 2009.
3. Ye, S., J. Chen, L. Liu, C. Zhang, and G. Fang, "A novel compact UWB ground penetrating radar system," *Proceedings of International Conference on Ground Penetrating Radar (GPR)*, 71–75, Shanghai, China, Jun. 2012.
4. Han, J., C. Huynh, and C. Nguyen, "Tunable monocycle pulse generator using switch controlled delay line and tunable RC network for UWB systems," *IEEE Antennas and Propagation Society International Symposium*, 1–4, Toronto, Canada, Jul. 2010.
5. Krishnaswamy, P., A. K. Thomas, P. T. Vernier, and M. A. Gundersen, "Compact subnanosecond pulse generator using avalanche transistors for cell electroperturbation studies," *IEEE Transactions on Dielectrics and Electrical Insulation*, Vol. 14, No. 4, 871–877, 2007.
6. Zou, A., H. Wang, and Y. Wang, "Nanosecond pulser based on serial connection of avalanche transistors," *Proceedings of International Conference on Measuring Technology and Mechatronics Automation*, 752–755, Changsha, China, Mar. 2010.

7. Alessio, D. A., D. Marco, G. Riccardo, and C. Paolo, “Experimental comparison of low-cost sub-nanosecond pulse generators,” *IEEE Transactions on Instrumentation and Measurement*, Vol. 60, No. 1, 310–318, 2011.
8. Fang, Z., *Application of Impulse Ultra-wideband Signals in Through-wall Radar*, Nanjing University of Science and Technology, Nanjing, 2009 (in Chinese).
9. Lee, J. S. and C. Nguyen, “A low-cost uniplanar sampling down-converter with internal local oscillator, pulse generator, and IF amplifier,” *IEEE Transactions on Microwave Theory and Techniques*, Vol. 49, No. 2, 390–392, 2001.
10. Fei, Y., *Ultra Wideband Radar Theory and Technology*, National Defense Industry Press, Beijing, 2010 (in Chinese).
11. Wang, Q., X. Tian, Y. Liu, B. Li, and B. Gao, “Design of an ultra-wideband pulse generator based on avalanche transistor,” *Proceedings of International Conference on Wireless Communications, Networking and Mobile Computing*, 1–4, Dalian, China, Oct. 2008.
12. Pongsoon, P., K. Bunnjaweht, and D. Kaemarungsi, “Edge-triggered driver circuit for ultra-wideband pulse generator with cascode impulse shaping,” *Proceedings of International Conference on Electrical Engineering/Electronics, Computer, Telecommunications and Information Technology (ECTI-CON)*, 1–4, Phetchaburi, Thailand, May 2012.

An Efficient Algorithm for the Calculation of Quantum Radar Cross Section of Flat Objects

Yun Lin, Liangshuai Guo, and Kun Cai

Science and Technology on Electromagnetic Scattering Laboratory, China

Abstract— In this paper, an efficient algorithm for simulating the quantum radar cross section of arbitrary shaped flat objects is proposed. Compared with previous studies on the simulation of quantum radar cross section the proposed algorithm used an alternative formula. Thus the proposed algorithm is more computationally efficient, and more favorable for large quantum system simulations.

1. INTRODUCTION

Quantum information science experienced dramatic developments in recent years. Those progresses have led to the advances in the field of quantum sensing and detection. The idea of using entangled photon pairs in a radar system to harness detection can be considered as the beginning of the quantum radar [1]. The quantum radar has been proposed as a candidate of new generation detection technologies [2]. Compared with classical radar, quantum radar features with anti-jamming capability [3], high resolution [4], low power consumption, and low delectability.

Similar as the radar cross section [5], the quantum radar cross section is a measurement of the ability of an object scattering the quantized electromagnetic waves in given directions. It is a crucial input parameter for designing a quantum radar system. However, only a few studies have been done on how to obtain quantum radar cross section [6–8]. Marco Lanzagorta defined the quantum radar cross section quantitatively [6, 7], and he proposed an algorithm for numerical simulating the quantum radar cross section. Marco gave the simulated quantum radar cross section of rectangular plates with different sizes. Unfortunately, the simulation is very time consuming. As presented in [6], even for a simple quantum system with one incident photon and 10,000 atoms, the simulation time is around 4 hours on a Intel 1.6 GHz desktop computer. In multiple incident photons cases, the problem becomes even worse, because the computational complexity increases exponentially with the increase of the number of incident photons. It is not feasible to simulate large quantum systems using Marco’s method. In this work, we derived a different formulation, and implemented a more efficient algorithm based on the new formulation for quantum radar cross section simulation. Furthermore, the propose algorithm is able to deal with arbitrary shaped flat objects. Several numerical examples are given to demonstrate the efficiency of the proposed method. The proposed algorithm is an excellent candidate for quantum radar cross section simulation.

This paper is organized as follows. In the Section 2, an alternative formulation of quantum radar cross section are presented. In the Section 3, numerical examples of quantum radar cross section of flat objects are given with discussions, followed by the conclusions in the Section 4.

2. THEORY AND FORMULATION

Analog to classical radar cross section, the quantum radar cross section is defined as,

$$\sigma_Q = \lim_{R \rightarrow \infty} 4\pi R^2 \frac{\langle I_s(\mathbf{r}_s, \mathbf{r}_d, t) \rangle}{\langle I_i(\mathbf{r}_s, \mathbf{r}_d, t) \rangle} \quad (1)$$

where the R is the distance between radar and object. $\mathbf{r}_s, \mathbf{r}_d$ denote the location of the scatters and location of detector. $\langle I_i \rangle, \langle I_s \rangle$ are the incident and scattered field intensity, respectively [6]. Assuming the incident wave is homogeneous distributed on the target which is consist by N atoms, the incident wave on the target surface can be expressed as,

$$\langle I_i(\mathbf{r}_s, \mathbf{r}_d, t) \rangle = \frac{\frac{1}{N} \sum_{i=1}^N \left| \Psi_\gamma^{(i), \text{INC}}(\Delta r_{si}, t) \right|^2}{S} \quad (2)$$

where $\Psi_\gamma^{(i), \text{INC}}$ denotes the incident photon wave function, which can be represented by,

$$\Psi_\gamma^{(i), \text{INC}}(\Delta r_{si}, t) = \frac{E_0}{r_{si}} \Theta(t - r_{si}/c) e^{-(i\omega + \Gamma/2)(t - r/c)} \quad (3)$$

where $\Theta(t - r_{si}/c)$ denotes a step function. If the absorption effect is ignored, all the incident energy on the target is scattered away, the intensity of the scattered field can be expressed as,

$$\langle I_s(\mathbf{r}_s, \mathbf{r}_t, t) \rangle = \frac{S_{\perp}}{r_{si}^2} \frac{1}{N} \left| \sum_{i=1}^N \Psi_{\gamma}^{(i),\text{SCT}}(\Delta r, t) \right|^2 \quad (4)$$

where $\Psi_{\gamma}^{(i),\text{SCT}}(\Delta r, t)$ denotes the incident photon wave function, which can be represented by,

$$\Psi_{\gamma}^{(i),\text{SCT}}(\Delta r_{id}, t) = \frac{E_0}{r_{id}} \Theta(t - r_{si}/c) e^{-i(\omega + \Gamma/2)(t - \Delta R/c)} \quad (5)$$

Then the quantum radar cross section can be expressed as,

$$\begin{aligned} \sigma_Q &= \lim_{R \rightarrow \infty} 4\pi R^2 \frac{\langle I_s(\mathbf{r}_s, \mathbf{r}_d, t) \rangle}{\langle I_i(\mathbf{r}_s, \mathbf{r}_d, t) \rangle} = \lim_{R \rightarrow \infty} 4\pi R^2 \frac{\frac{S_{\perp}}{N} \left| \sum_{i=1}^N \Psi_{\gamma}^{(i),\text{SCT}}(\Delta r, t) \right|^2}{\frac{1}{NS} \sum_{i=1}^N \left| \Psi_{\gamma}^{(i),\text{INC}}(\Delta r_{si}, t) \right|^2}}{\sum_{i=1}^N \left| \frac{E_0}{r_{si}} e^{-i(\omega + \Gamma/2)(t - \Delta R_i/c)} \right|^2} \\ &= \lim_{R \rightarrow \infty} 4\pi R^2 \frac{SS_{\perp} \frac{1}{r_{si}^2} \left| \sum_{i=1}^N \frac{E_0}{r_{id}} e^{-i(\omega + \Gamma/2)(t - \Delta R_i/c)} \right|^2}{\sum_{i=1}^N \left| \frac{E_0}{r_{si}} e^{-i(\omega + \Gamma/2)(t - r_i/c)} \right|^2} \end{aligned} \quad (6)$$

we use far field approximation $r_{si} \approx r_{id} \approx R$, Equation (6) can be simplified as,

$$\sigma_Q \approx 4\pi \lim_{R \rightarrow \infty} \frac{SS_{\perp} \left| \sum_{i=1}^N e^{-i(\omega + \Gamma/2)(t - \Delta R_i/c)} \right|^2}{\sum_{i=1}^N \left| e^{-i(\omega + \Gamma/2)(t - r_i/c)} \right|^2} \quad (7)$$

Then we further assume $\Gamma = 0$, Equation (7) can be simplified as,

$$\sigma_Q \approx 4\pi \lim_{R \rightarrow \infty} \frac{SS_{\perp} \left| \sum_{i=1}^N e^{-i\omega(\Delta R_i/c)} \right|^2}{\sum_{i=1}^N \left| e^{-i\omega(r_i/c)} \right|^2} \quad (8)$$

Compared with the formulation proposed in [6], as shown in Equation (9),

$$\sigma_Q \approx 2\pi S_{\perp} \lim_{R \rightarrow \infty} \frac{\left| \sum_{i=1}^N e^{-i\omega(\Delta R_i/c)} \right|^2}{\int_0^{2\pi} \int_0^{\pi} \left| \sum_{i=1}^N e^{-i\omega(r'_i/c)} \right|^2 \sin\theta' d\theta' d\phi'} \quad (9)$$

the new Equation (8) avoids the evaluation of the integration of a rapid changing pattern on a spherical surface as shown in the denominator of Equation (9), which requires a large number of integration points to be evaluated accurately. Therefore the proposed algorithm is much more efficient than the one based on Equation (9). For the multiple incident photons circumstances, this work follow the exact procedure used in [6]. In the next section, numerical examples are given to demonstrate the advantages of the proposed algorithm.

3. NUMERICAL EXAMPLES

In this section, we will use several numerical examples to demonstrate the correctness and efficiency of the proposed algorithm.

3.1. Rectangular Perfect Electrical Conductor (PEC) Plate

The first example is a rectangular PEC plate which can be found in [6]. The PEC plate is 2.5λ (λ is the wave length) in length and 4λ in width. The plate is placed in XOY plane. The mono-static quantum radar cross section in the XOZ plane ($\phi = 0^\circ$) is calculated. The simulated mono-static quantum radar cross section is shown in the Figure 1.

This example is simulated on a laptop computer with Intel 2.4 GHz CPU. The total simulation time for 181 incident angles is 7.5 seconds, i.e., 0.04 second per incident angle. Simulated results agree well with results presented in [7] as shown in the Figure 1. As discussed in Section 2, since

a different formulation is used, the simulation time is reduced from around 4 hours [7] to less than 10 second on a laptop computer.

Next, the same rectangular PEC plate is used to study the effect of the atom lattice structure on the simulated quantum radar cross section results. Two different atom lattices are used to represent the same rectangular PEC plate. The first lattice is a uniform square lattice, and the second lattice is a triangular lattice. Furthermore, the location of the atom in the triangular lattice can have a small random perturbation in the XOY plane. The maximum offset of the atom is five percent of the rectangular PEC plate length. The number of the atoms keeps the same for the two different lattices. The calculated quantum radar cross section of the rectangular PEC plate using different lattice structures are shown in Figure 2. In this figure, it is shown the type of the lattice structure does not have a noticeable effect on the simulation quantum radar cross section results of a rectangular PEC plate.

The same rectangular PEC plate is used to study the effect of the number of atoms on the simulation of the quantum radar cross section. The quantum radar cross section obtained by using a lattice with a large number of atoms is used as the reference results to calculate the relative error of the simulated quantum radar cross section using different number of atoms, as shown in the Figure 3. From the Figure 3, we conclude that if a relative accuracy less than 1% is required, an atom number larger than 30 per wavelength is needed.

3.2. Elliptical PEC Plate

The second example is an elliptical PEC disk, which is used to demonstrate the capability of the algorithm to deal with arbitrary shaped flat objects. The length of the major semi-axes of the disk

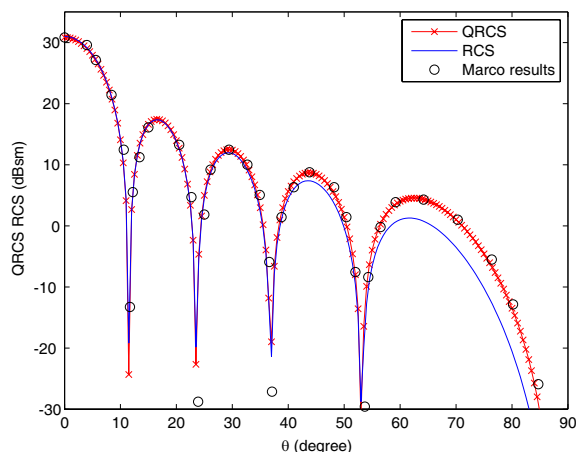


Figure 1: The simulated quantum radar cross section of a rectangular PEC plate.

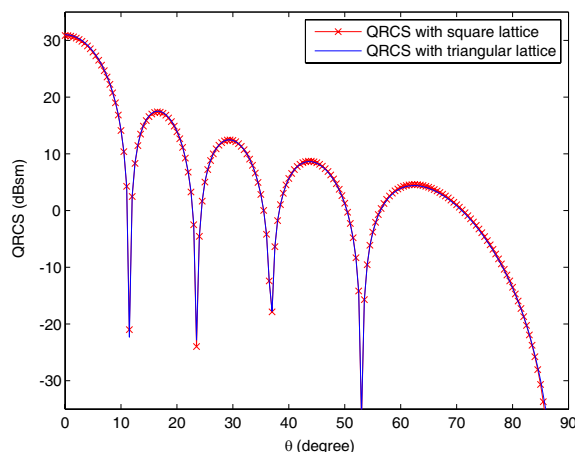


Figure 2: The simulated quantum radar cross section simulation using different atom structures.

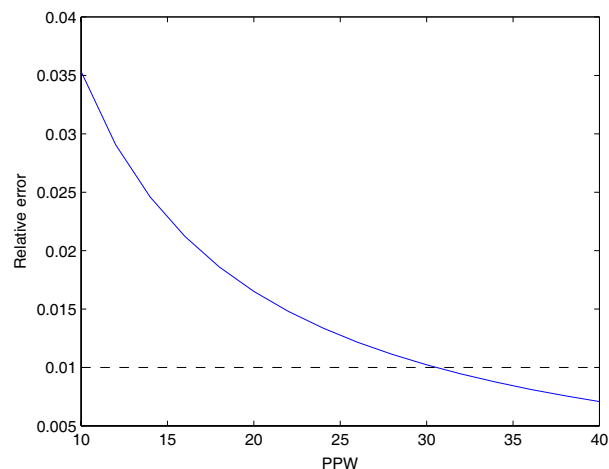


Figure 3: The relative error of simulated quantum radar cross section using different number of atoms.

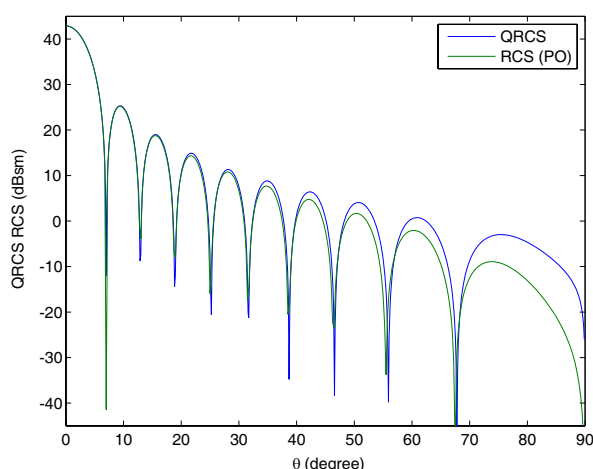


Figure 4: The simulated quantum radar cross section of a PEC elliptical disk.

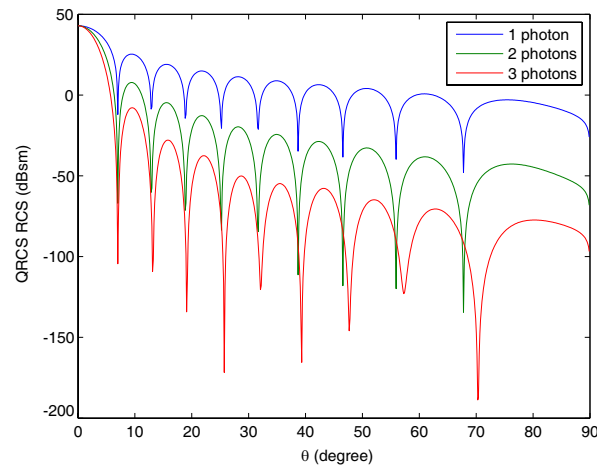


Figure 5: The simulated quantum radar cross section of a PEC elliptical disk with multiple incident photons.

is 5λ , and the length of the minor semi-axes of the disk is 2.5λ . The elliptical PEC disk is placed in XOY plane, the mono-static quantum radar cross section in XOZ plane ($\phi = 0^\circ$) is calculated. The simulated quantum radar cross section is shown in the Figure 4, with physical optics results as reference.

Using the same object, the effect of multiple incident photons is studied. The simulated quantum radar cross section results for multiple incident photons are shown in Figure 5. From the simulated results in Figure 5, we notice the quantum radar cross section in multiple incident photons case is very different from single incident photon case. The main lobe in multiple incident case is narrower than single incident case, which implies using multiple photons can increase the spatial resolution of the quantum radar [9]. Another interesting phenomenon can be observed in Figure 5 is that the peak value of the main lobe keeps unchanged for all cases.

4. CONCLUSIONS

In summary, an efficient algorithm based on an alternative formula for the quantum radar cross section simulation is proposed. The new algorithm is able to simulate the quantum radar cross section of arbitrary shaped flat objects. The accuracy and efficiency of the proposed method is demonstrated by numerical examples. The effects of the atoms lattice structure and the number of the atoms on the simulated quantum radar cross section are studied. The efficiency of the algorithm can be further improved by parallelization, which can be implemented straight forward. The proposed algorithm is very suitable for simulating large photon-quantum systems.

ACKNOWLEDGMENT

The authors would like to thank Xiaobing Wang for the inspiring on this topic, and Zichang Liang for the fruitful discussion.

REFERENCES

1. Allen, E. H. and M. Karageorgis, "Radar systems and methods using entangled quantum particles," US Patent 7375802, 2008.
2. Tan, H. and Z. Dai, "Key technology research in the quantum radar," *Journal of Huazhong Normal University*, Vol. 46, No. 3, 2012.
3. Malik, M., H. Shin, P. Zerom, and R. W. Boyd, "Quantum ghost image discrimination with single photon pair," *Proceedings of the Conference on Lasers and Electro-Optics/International Quantum Electronics Conference*, Optical Society of America, 2009.
4. Giovannetti, V., S. Lloyd, and L. Maccone, "Quantum-enhanced measurements: Beating the standard quantum limit," *Science*, 306, 2004.
5. Knott, E. F., J. F. Shaeffer, and M. T. Tuley, *Radar Cross Section*, SciTech Publishing, Herndon, 2004.
6. Lanzagorta, M., *Quantum Radar*, 1st Edition, Morgan & Claypool Publishers, 2012.
7. Lanzagorta, M., "Quantum radar cross section," *Proceedings of the Quantum Optics Conference, SPIE Photonics Europe*, 2010.

8. Liu, K., H.-T. Xiao, and H.-Q. Fan, “Analysis and simulation of quantum radar cross section,” *Chinese Physics Letter*, Vol. 31, No. 3, 2014.
9. Guha, S. and J. H. Shapiro, “Enhanced standoff sensing resolution using quantum illumination,” arXiv:1012.2548v1, 2010.

A Real Time 3D Multi Target Data Fusion for Multistatic Radar Network Tracking

El-Sayed Abdoul Moaty El-Badawy, Tarek Reda Abd-ElShahid, and Alaa El-Din Sayed Hafez
Faculty of Engineering, Alexandria University, Egypt

Abstract— The paper is devoted to propose a data fusion algorithms into multistatic radar network to improve its tracking capability. The proposed data fusion algorithm is based on using common measurement architecture gives state estimates with relatively low and medium uncertainty followed by cumulative measurement fusion (CMF) or cumulative state vector fusion (CSVF) algorithm which is very simple, easy to implement and can be used in real time. Extended Kalman Filter (EKF) is used as a non-linear tracking and predictor algorithm. The system is simulated using Matlab program to compare the performance of the estimation routines of both fusion algorithms and the targets scenario is simulated using Monte Carlo simulation. Simulation results have shown that these cumulative fusion algorithms improve the multistatic radar network tracking capability and produce a significant reduction in the root sum square error (RSSE), absolute error, and root sum square variance (RSSV) than achieved from monostatic radar.

1. INTRODUCTION

In a multistatic-multi-target environment, where each radar processes its own observations and sends the resulting tracks to a data fusion center, the first step is to determine whether or not two or more tracks, coming from different radar systems with different accuracies, represent the same target (track-to-track association). The next step is to combine the radar tracks when it is determined that they indeed represent the same target (track fusion). Both problems arise when several radars carry out surveillance over a common volume (overlapping sensor coverage). A survey of the current research in this area has been presented in [1–8]. Furthermore, the goal of data fusion is to operate on a combination of radar sensor measurements, features, track states, and object type and identification likelihoods to produce a single integrated air picture of the air space to a high degree of accuracy. Technologies that enable this synergistic fusion and interpretation of data at several levels from disparate, distributed radars and other sensors should enhance system acquisition, tracking and discrimination of threat objects in a cluttered environment and provide enhanced battle space awareness. There are two approaches for fusion of multiple radar data: measurement fusion and state vector fusion. In the first approach, the radar measurements are combined and an optimal estimate of the target state vector is obtained. State vector fusion is preferable for implementation in a variety of practical systems. In this approach, each radar employs an estimator to extract a target track state vector and its associated covariance matrix from its respective sensor measurement, that are then transmitted over a data link to a fusion center. At the fusion center, track-to-track correlation and state vector fusion are performed to obtain a composite target state vector [9].

The proposed method uses current radars data for track-to-track association using cumulative measurement fusion, and cumulative state vector fusion in order to produce an accurate target estimation and prediction with the multistatic radar network. Results based on Monte Carlo simulations are presented. The proposed method is able to perform track correlation and fusion with low root sum square error (RSSE), absolute error, and root sum square variance (RSSV) than achieved from monostatic radar. The remainder of this paper is organized as follows. Section 2 describes the target tracking algorithms and the extended Kalman filter. Section 3 presents a brief overview of data association and fusion methods in the tracking systems. In Section 4 present the proposed cumulative track-to-track association and track fusion. Simulation results and discussion are presented in Section 5. Finally, Section 6 concludes the paper.

2. THEORITICAL DESCRIPTION OF EKF

A general motion model used in discrete extended Kalman filter for target tracking is [10].

$$x(k) = FX(k-1) + Gw(k-1) \quad (1)$$

$$z(k) = h(X(k)) + v(k) \quad (2)$$

where $X(k)$ is the state vector, F is the state transition matrix and G is the process noise gain matrix. The process noise $w(k)$ and the measurement noise $v(k)$ are zero-mean, mutually independent, white, Gaussian with covariance Q and R respectively. $z(k)$ is the measurement vector at time k and $h(X(k))$ is a nonlinear function of the states computed at time k .

3. FUSION ALGORITHMS

3.1. Measurement Fusion (MF)

In this architecture (Fig. 1), the measurement vector consists of fused azimuth, fused elevation and range. Similarly, the measurement covariances for azimuth and elevation measurement noise covariance for range is taken from radars. Instead of fusing the measurement in the use of EKF, the measurements from radars are merged into an augmented measurement vector and measurement noise variances from radars also concatenated to produce the same results [13, 14].

State Prediction: (Eq. (4)).

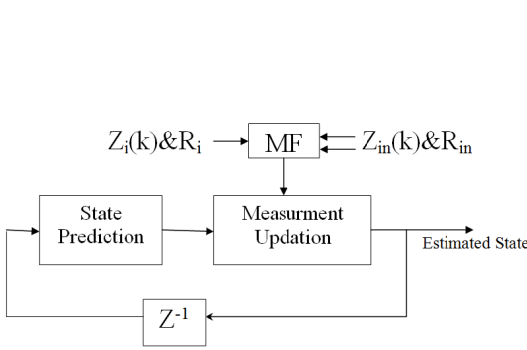


Figure 1: Information flow diagram of CMF algorithm.

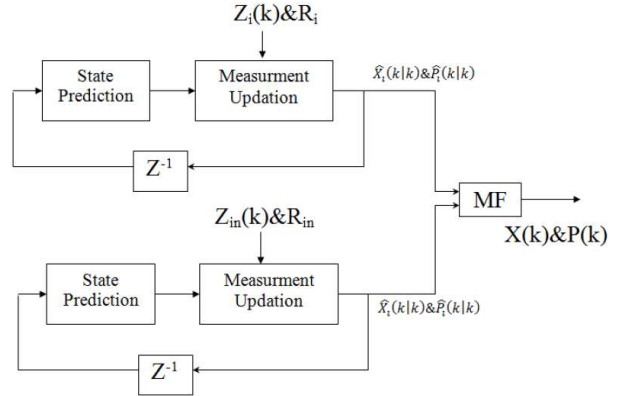


Figure 2: Information flow diagram of CSVF algorithm.

Fusion:

$$Z_d(k) = [\theta_{ri} \quad \varphi_{ri} \quad r_{ri}]^T \quad (3)$$

$$R_d(k) = \begin{bmatrix} \sigma_{r\theta} & 0 & 0 \\ 0 & \sigma_{r\varphi} & 0 \\ 0 & 0 & \sigma_{rr} \end{bmatrix} \quad (4)$$

$$Z_f = Z_i(k) + Z_i(k) [R_i + R_{i+1}]^{-1} (Z_{i+1}(k) - Z_i(k)) \quad (5)$$

$$R_f = R_i + R_i [R_i + R_{i+1}]^{-1} R_i \quad (6)$$

3.2. State Vector Fusion (SVF)

In this architecture (Fig. 2), tracks are found by radars measurements separately and the resultant state vectors (tracks) are fused to get final target state estimations. Similarly, the state error covariances of the individual tracks are fused to get the final state error covariance matrix.

$$\tilde{X}_i(k|k-1) = F \hat{X}_i(k-1|k-1) \quad (7)$$

$$\tilde{P}_i(k|k-1) = F \hat{P}_i(k-1|k-1) F^T + G Q G^T \quad (8)$$

Measurement updation:

$$H_i = h(\tilde{X}_i(k|k-1)) \quad (9)$$

$$e_i = z_i - \tilde{z}_i(k|k-1) \quad (10)$$

$$S_i = H_i P_i(k|k-1) H_i^T + R_i \quad (11)$$

$$K_i = \tilde{P}_i(k|k-1) H_i^T + S_i^{-1} \quad (12)$$

$$\hat{X}_i(k|k) = \tilde{X}_i(k|k-1) + K_i e_i \quad (13)$$

$$\hat{P}_i(k|k) = [I - K_i H_i] \tilde{P}_i(k|k-1) \quad (14)$$

Fusion:

$$\hat{X}_f(k|k) = \hat{X}_i(k|k) + \hat{P}_i(k|k) \left[\hat{P}_{i+1}(k|k) + \hat{P}_i(k|k) \right]^{-1} \left(\hat{X}_{i+1}(k|k) - \hat{X}_i(k|k) \right) \quad (15)$$

$$\hat{P}_f(k|k) = \hat{P}_i(k|k) + \hat{P}_i(k|k) \left[\hat{P}_{i+1}(k|k) + \hat{P}_i(k|k) \right]^{-1} \hat{P}_i^T(k|k) \quad (16)$$

4. SIMULATION RESULTS

The 3DOF kinematic model, with position, velocity and acceleration components in each of the three Cartesian coordinates x , y and z has the following transition and process noise gain matrices.

$$F = \text{diag} [\varphi \quad \varphi \quad \varphi] \quad (17)$$

$$G = \text{diag} [\eta \quad \eta \quad \eta] \quad (18)$$

where φ is

$$\varphi = \begin{bmatrix} 1 & T & T^2/2 \\ 0 & 1 & T \\ 0 & 0 & 1 \end{bmatrix} \quad (19)$$

$$\eta = [T^3/6 \quad T^2/2 \quad T] \quad (20)$$

where T is the sampling interval, F is the state transition matrix and G is the process noise gain matrix.

The percentage fit error (PFE) in x , y and z positions:

$$\text{PFEx} = 100 * \frac{\text{norm}(x - \hat{x})}{\text{norm}(x)} \quad (21)$$

similarly for y and z positions.

Root mean square error in position:

$$\text{RMSPE} = \sqrt{\frac{1}{N} \sum_{i=1}^N \frac{(x_i - \hat{x}_i)^2 + (y_i - \hat{y}_i)^2 + (z_i - \hat{z}_i)^2}{3}} \quad (22)$$

Root sum square error in position:

$$\text{RSSPE} = \sqrt{(x - \hat{x})^2 + (y - \hat{y})^2 + (z - \hat{z})^2} \quad (23)$$

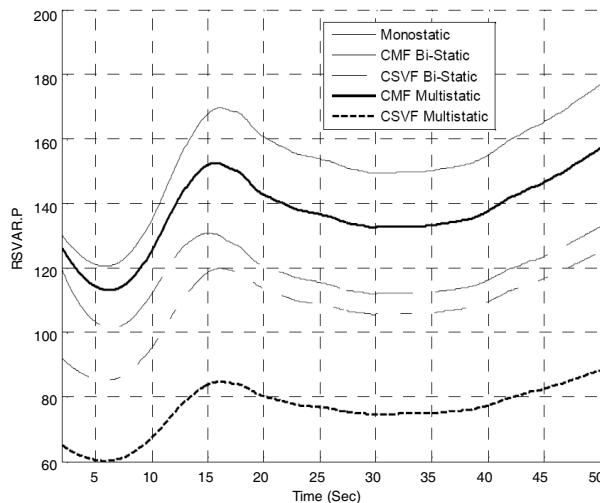


Figure 3: Root sum variance in position.

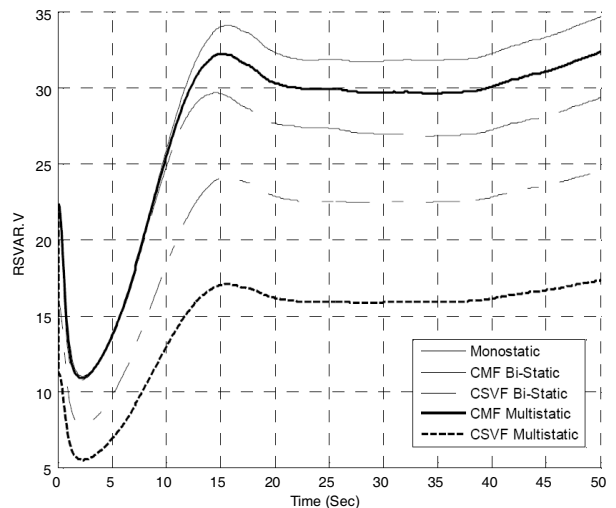


Figure 4: Root sum variance in velocity.

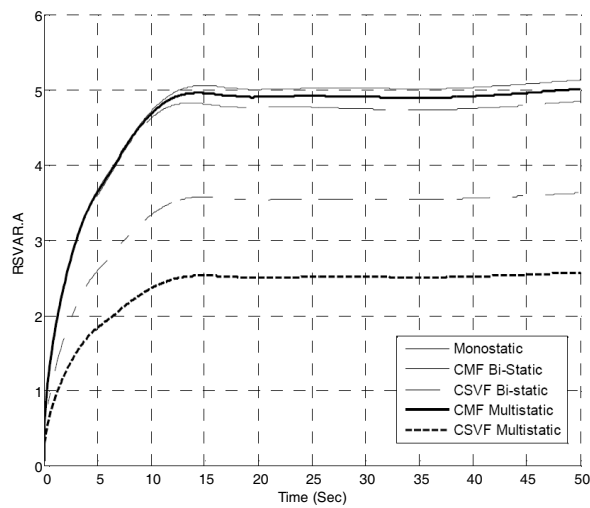


Figure 5: Root sum variance in acceleration.

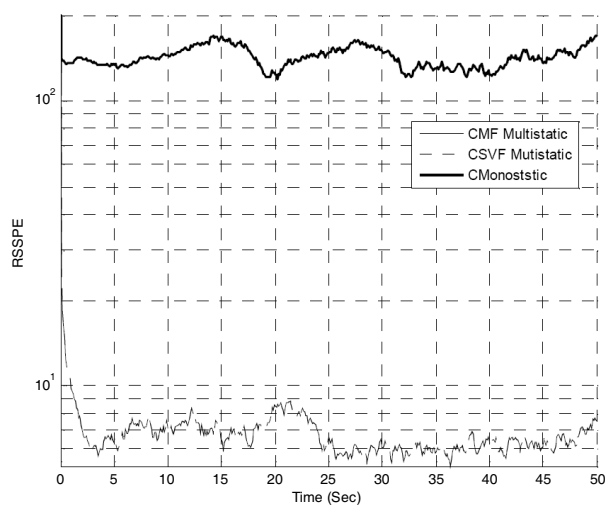


Figure 6: Root sum square error in position.

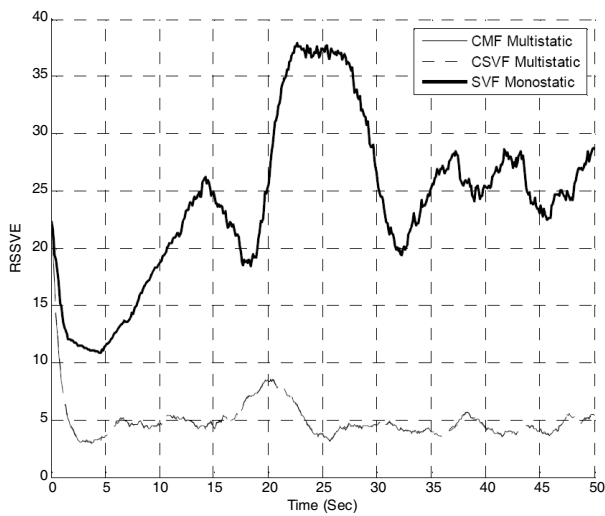


Figure 7: Root sum square error in velocity.

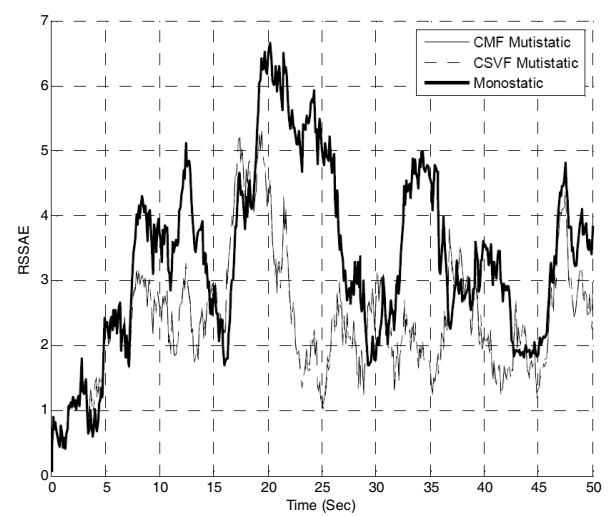


Figure 8: Root sum square error in acceleration.

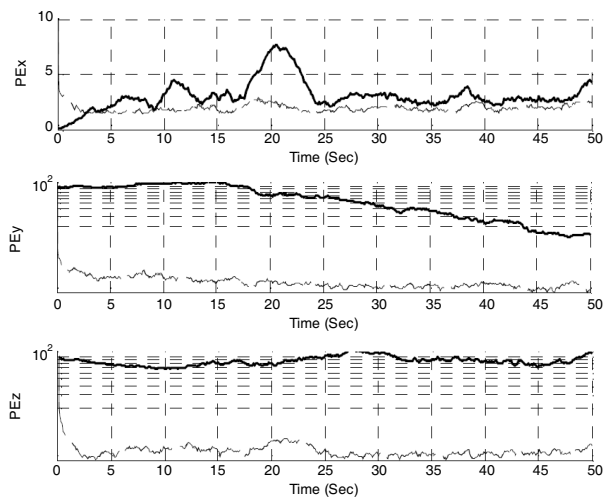


Figure 9: Absolute error in positions.

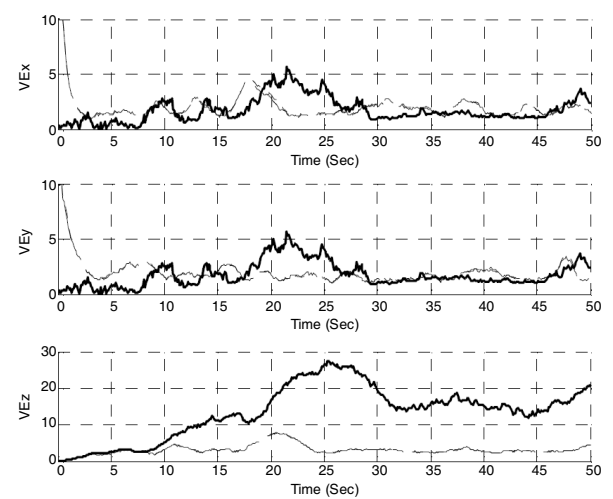


Figure 10: Absolute error in velocities.

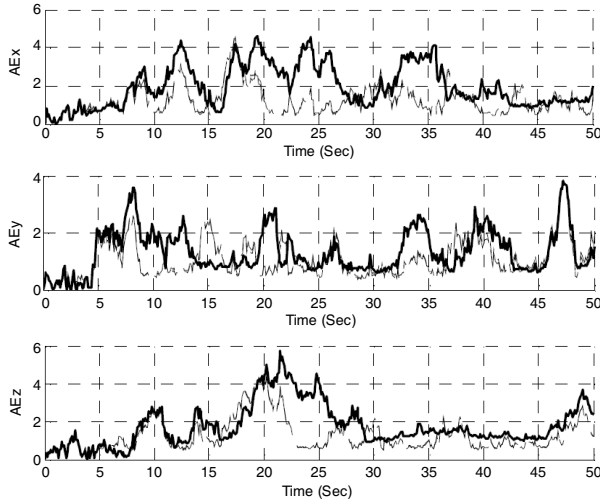


Figure 11: Absolute error in accelerations.

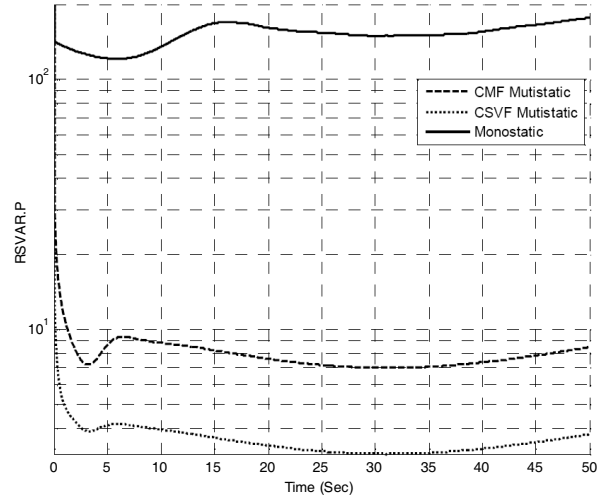


Figure 12: Root sum variance in position.

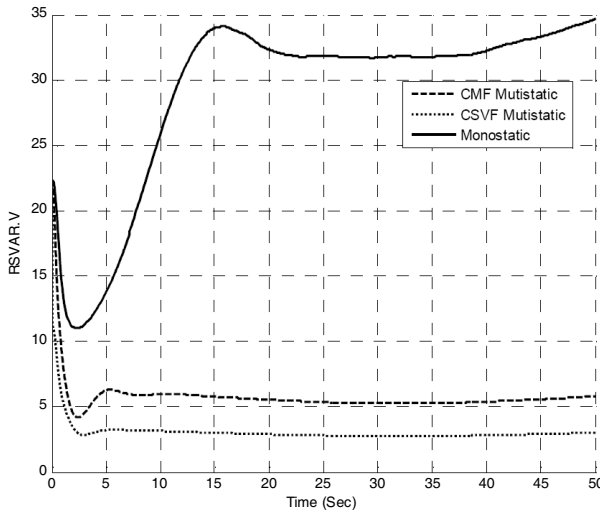


Figure 13: Root sum variance in velocity.

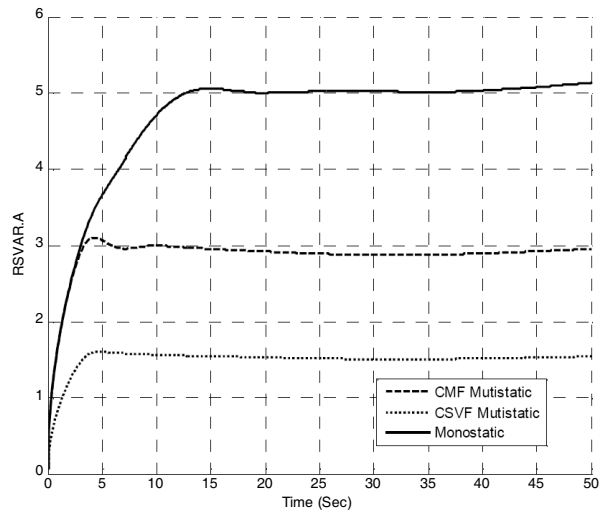


Figure 14: Root sum variance in acceleration.

Absolute error in (AE) x , y and z positions

$$AE_x(i) = |x(i) - \hat{x}(i)| \quad i = 1, 2, 3, \dots, N, \quad (24)$$

similarly for y and z positions.

The simulation taken first with two cases; the first Bistatic radar with the assumption of identical noise covariance matrix for the two radar information; the second multistatic radar also with identical noise covariance matrix for the four radar information. The two cases compared with monostatic radar information with CMF and CSVF algorithms. Figs. 3–5 show a comparison of root sum variance of the position, velocity, and acceleration with the two test cases with respect to monostatic radar. It is clear that multistatic radar with CSVF improves significantly the root sum variance of the position, velocity, and acceleration respectively. Figs. 6–8 demonstrate the root sum square error in position, velocity, and acceleration respectively for the multistatic radar compared with monostatic radar with both CMF and CSVF. These figures conclude the significant degradation in the RSSE for both fusion algorithms which reflects the great enhancement of the fusion algorithms with the multistatic radar network. The absolute errors in position, velocity, and acceleration are improved also with multistatic radar as shown in Figs. 9–11. The root sum variance comparison illustrated in Figs. 12–14, and clarify the strength of the fusion algorithms with the multistatic radar network.

5. CONCLUSION

The paper proposes a data fusion algorithms into multistatic radar network to improve its tracking capability. It uses current radars data for track-to-track association using cumulative measurement fusion, and cumulative state vector fusion in order to produce an accurate target estimation and prediction with the multistatic radar network. The system is simulated using Matlab program to compare the performance of the estimation routines of both fusion algorithms and the targets scenario is simulated using Monte Carlo simulation. Simulation results have shown that these cumulative fusion algorithms improve the multistatic radar network tracking capability and produce a significant reduction in the root sum square error (RSSE), absolute error, and root sum variance (RSSV) than achieved from monostatic radar.

REFERENCES

1. Blackman, S. S., *Multiple Target Tracking with Radar application*, Artech House, Norwood, MA, 1986.
2. Hall, D. L., *Mathematical Techniques in Multisensor Data Fusion*, Artech House, Norwood, MA, 1992.
3. Bar-Shalom, Y., *Tracking and Data Association*, Academic Press, 1988.
4. Bar-Shalom, Y., *Multitarget-Multisensor Tracking Applications and Advances*, Vol. I, Artech House, Norwood, MA, 1990.
5. Anwar, A. and A. Sultan, "An intelligent technique to multi sensor data fusion in target tracking," *Journal of Theoretical and Applied Information Technology*, Vol. 30, No. 2, 2005.
6. Singh, J. P., "Evolution of the radar target tracking algorithms: a move towards knowledge based multi-sensor adaptive processing," *2005 1st IEEE International Workshop on Computational Advances in Multi-Sensor Adaptive Processing*, Dehradun, India, Dec. 13–15, 2005.
7. Shams, S., "Neural network optimization for multi-target multi sensor passive tracking," *Proceedings of the IEEE*, Oct. 1996.
8. Godsill, S., A. Doucet, and M. West, "Maximum a posteriori sequence estimation using monte carlo particles filters," *Ann. Inst. Stat. Math*, 53, 2001.
9. Hall, D. L. and J. Llinas, *Hand Book of Multi-sensor Data Fusion*, CRC Press, 2001.
10. Skolnik, M. I., *Introduction to Radar Systems*, 2nd Edition, Tata Mcgraw Hill, New Delhi, 1999.
11. Brown, G. R., *Introduction to Random Signal Analysis and Kalman Filtering*, John Wiley & Sons, 1992.
12. Nadu, V., "Fusion architectures for 3D target tracking usingIRST and radar measurments," *Journal of Aerospace Sciences & Technology*, Vol. 62, No. 3, 2010.
13. Bar-Shalom, Y. and X. R. Li, *Estimation and Tracking: Principles, Techniques, and Software*, Artech House, Boston, London, 1993.
14. Hou, Z. and C. Han, "A target tracking system based on radar and image fusion," *International Conference on Information Fusion*, 1426–1432, Australia, 2003.

A New FPGA Prototype for Synchro to Digital Converter Using CORDIC Algorithm

Mohamed Rizk, Ahmed Hossin, and Alaa El-Din Sayed Hafez
Faculty of Engineering, Alexandria University, Alexandria, Egypt

Abstract— This paper introduce a new approach to FPGA implementation of synchro to digital converter using Co-ordinate Rotation Digital Computer CORDIC algorithm. This algorithm was the best replacement of analog conversion system by the high resolution digital. CORDIC algorithm used for the fast calculation of elementary functions like multiplication, division, trigonometric functions. The approach is based on receiving the synchro signals S_1 , S_2 , and S_3 from the synchro motor, and converts them to two perpendicular signals sin signal and cosine signal using solid state Scott-t transformer. Then the a CORDIC circuit receive this signals after converting them to digital and produce the azimuth angle in digital format. This prototype of hardware implementation of CORDIC algorithm used Spartan-III series FPGA, with constraint to area efficiency and throughput architecture. The prototype results show that the conversion time is less than $1\ \mu\text{s}$ which is suitable for real time applications in radar and missile control applications.

1. INTRODUCTION

CORDIC is the abbreviation of Co-ordinate Rotation Digital Computer. The first description for iterative approach of this algorithm is firstly provided by Jack E. Volder in 1959 [1]. CORDIC algorithm provides an efficient way of rotating the vectors in a plane by simple shift add operation to estimate the basic elementary functions like trigonometric operations, multiplication, division and some other operations like logarithmic functions, square roots and exponential functions. Most of the applications either in wireless communication or in digital signal processing are based on microprocessors which make use of a single instruction and a bunch of addressing modes for their working. As these processors are costs efficient and offer extreme flexibility but yet are not suited for some of these applications. During the last 50 years the CORDIC algorithm has emerged in a wide variety of applications. The CORDIC algorithm has received increased attention after a unified approach is proposed for its implementation [2].

The CORDIC arithmetic processor chip is designed and implemented to perform various functions possible in rotation and vectoring mode of circular, linear, and hyperbolic coordinate systems [3]. Since then, CORDIC technique has been used in many applications [4], such as single chip CORDIC processor for DSP applications [5, 6]. Recently several researches applied CORDIC algorithm in radar pulse compression, rotary encoders, and waveform generation [7–12]. This paper implement CORDIC S/D converter to convert synchro signals into high resolution digital azimuth angle. This achieves a high precision S/D conversion with low propagation delay compared with that implemented using microcontroller or analog processing.

2. CORDIC ALGORITHM

The CORDIC algorithm involves rotation of a vector v on the XY -plane in circular, linear and hyperbolic coordinate systems depending on the function to be evaluated. The CORDIC algorithm performs a planar rotation. Graphically, planar rotation means transforming a vector (X_i, Y_i) into a new vector (X_j, Y_j) [13, 14].

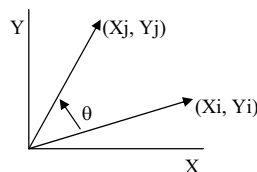


Figure 1: Rotating the vector.

Using a matrix form, a planar rotation for a vector of (X_i, Y_i) is defined as

$$\begin{bmatrix} X_j \\ Y_j \end{bmatrix} = \begin{bmatrix} \cos \theta & -\sin \theta \\ \sin \theta & \cos \theta \end{bmatrix} \begin{bmatrix} X_i \\ Y_i \end{bmatrix} \quad (1)$$

The θ angle rotation can be executed in several steps, using an iterative process. Each step completes a small part of the rotation. Many steps will compose one planar rotation. A single step is defined by the following equation:

$$\begin{bmatrix} X_{n+1} \\ Y_{n+1} \end{bmatrix} = \begin{bmatrix} \cos \theta_n & -\sin \theta_n \\ \sin \theta_n & \cos \theta_n \end{bmatrix} \begin{bmatrix} X_n \\ Y_n \end{bmatrix} \quad (2)$$

Equation (2) can be modified by eliminating the $\cos \theta_n$ factor.

$$\begin{bmatrix} X_{n+1} \\ Y_{n+1} \end{bmatrix} = \cos \theta_n \begin{bmatrix} 1 & -\tan \theta_n \\ \tan \theta_n & 1 \end{bmatrix} \begin{bmatrix} X_n \\ Y_n \end{bmatrix} \quad (3)$$

Equation (3) requires three multiplies, compared to the four needed in Equation (2). Additional multipliers can be eliminated by selecting the angle steps such that the tangent of a step is a power of 2. Multiplying or dividing by a power of 2 can be implemented using a simple shift operation. The angle for each step is given by

$$\theta_n = \arctan \left(\frac{1}{2^n} \right) \quad (4)$$

All iteration-angles summed must equal the rotation angle θ .

$$\sum_{n=0}^{\infty} S_n \theta_n = \theta \quad (5)$$

where

$$S_n = \{-1; +1\} \quad (6)$$

This results in the following equation for $\tan \theta_n$

$$\tan \theta_n = S_n 2^{-n} \quad (7)$$

Combining Equations (3) and (7) results in

$$\begin{bmatrix} X_{n+1} \\ Y_{n+1} \end{bmatrix} = \cos \theta_n \begin{bmatrix} 1 & -S_n 2^{-n} \\ S_n 2^{-n} & 1 \end{bmatrix} \begin{bmatrix} X_n \\ Y_n \end{bmatrix} \quad (8)$$

Besides for the $\cos \theta_n$ coefficient, the algorithm has been reduced to a few simple shifts and additions. The coefficient can be eliminated by pre-computing the final result. The first step is to rewrite the coefficient.

$$\cos \theta_n = \cos \left(\arctan \left(\frac{1}{2^n} \right) \right) \quad (9)$$

The second step is to compute Equation (9) for all values of 'n' and multiplying the results, which we will refer to as K .

$$K = \frac{1}{P} = \prod_{n=0}^{\infty} \cos \left(\arctan \left(\frac{1}{2^n} \right) \right) \approx 0.607253 \quad (10)$$

K is constant for all initial vectors and for all values of the rotation angle, it is normally referred to as the congruence constant. The derivative P (approx. 1.64676) is defined here because it is also commonly used. We can now formulate the exact calculation the CORDIC performs.

$$\begin{cases} X_j = K (X_i \cos \theta - Y_i \sin \theta) \\ Y_j = K (Y_i \cos \theta + X_i \sin \theta) \end{cases} \quad (11)$$

Because the coefficient K is pre-computed and taken into account at a later stage, Equation (8) may be written as

$$\begin{bmatrix} X_{n+1} \\ Y_{n+1} \end{bmatrix} = \begin{bmatrix} 1 & -S_n 2^{-n} \\ S_n 2^{-n} & 1 \end{bmatrix} \begin{bmatrix} X_n \\ Y_n \end{bmatrix} \quad (12)$$

or as

$$\begin{cases} X_{n+1} = X_n - S_n 2^{-2n} Y_n \\ Y_{n+1} = Y_n + S_n 2^{-2n} X_n \end{cases} \quad (13)$$

At this point a new variable called ‘ Z ’ is introduced. Z represents the part of the angle θ which has not been rotated yet.

$$Z_{n+1} = \theta - \sum_{i=0}^n \theta_i \quad (14)$$

For every step of the rotation S_n is computed as a sign of Z_n .

$$S_n = \begin{cases} -1 & \text{if } Z_n < 0 \\ +1 & \text{if } Z_n \geq 0 \end{cases} \quad (15)$$

Combining Equations (5) and (15) results in a system which reduces the not rotated part of angle θ to zero.

Or in a program-like style:

```

For  $n = 0$  to [inf]
  If ( $Z(n) \geq 0$ ) then
     $Z(n+1) := Z(n) - \text{atan}(1/2^n)$ ;
  Else
     $Z(n+1) := Z(n) + \text{atan}(1/2^n)$ ;
  End if;
End for;

```

The $\text{atan}(1/2^i)$ is pre-calculated and stored in a table. [inf] is replaced with the required number of iterations, which is about 1 iteration per bit (16 iterations yield a 16bit result).

If we add the computation for X and Y we get the program-like style for the CORDIC core.

```

For  $n = 0$  to [inf]
  If ( $Z(n) \geq 0$ ) then
     $X(n+1) := X(n) - (Yn/2^n)$ ;
     $Y(n+1) := Y(n) + (Xn/2^n)$ ;
     $Z(n+1) := Z(n) - \text{atan}(1/2^n)$ ;
  Else
     $X(n+1) := X(n) + (Yn/2^n)$ ;
     $Y(n+1) := Y(n) - (Xn/2^n)$ ;
     $Z(n+1) := Z(n) + \text{atan}(1/2^n)$ ;
  End if;
End for;

```

This algorithm is commonly referred to as driving Z to zero. The CORDIC core computes:

$$[X_j, Y_j, Z_j] = [P(X_i \cos(Z_i) - Y_i \sin(Z_i)), P(Y_i \cos(Z_i) + X_i \sin(Z_i)), 0].$$

There’s a special case for driving Z to zero:

$$\begin{aligned} X_i &= \frac{1}{P} = K \approx 0.60725 \\ Y_i &= 0 \\ Z_i &= \theta \\ [X_j, Y_j, Z_j] &= [\cos \theta, \sin \theta, 0] \end{aligned}$$

Another scheme which is possible is driving Y to zero. The CORDIC core then computes:

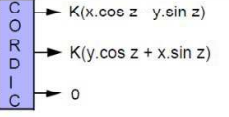
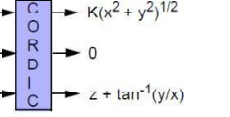
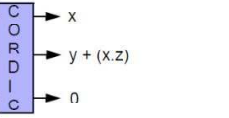
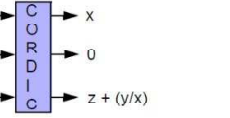
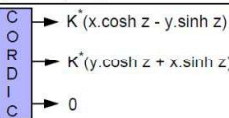
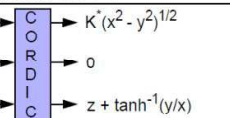
$$[X_j, Y_j, Z_j] = \left[P\sqrt{X_i^2 + Y_i^2}, 0, Z_i + \arctan\left(\frac{Y_i}{X_i}\right) \right]$$

For this scheme there are two special cases:

$$\begin{aligned}
 &1) \quad X_i = X \\
 &\quad Y_i = Y \\
 &\quad Z_i = 0 \\
 &[X_j, Y_j, Z_j] = \left[P\sqrt{X_i^2 + Y_i^2}, 0, \arctan\left(\frac{Y_i}{X_i}\right) \right] \\
 &2) \quad X_i = 1 \\
 &\quad Y_i = a \\
 &\quad Z_i = 0 \\
 &[X_j, Y_j, Z_j] = \left[P\sqrt{1 + a^2}, 0, \arctan(a) \right]
 \end{aligned}$$

As a Summary of CORDIC Functions is illustrated in Table 1.

Table 1: Summary of CORDIC algorithm.

	Rotation Mode: $d_i = \text{sign}(z^{(i)}); z^{(i)} \rightarrow 0$	Vectoring Mode: $d_i = -\text{sign}(x^{(i)}y^{(i)}); y^{(i)} \rightarrow 0$
Circular $\mu = 1$ $e^{(i)} = \tan^{-1}2^{-i}$	 <p> $x \rightarrow K(x \cdot \cos z - y \cdot \sin z)$ $y \rightarrow K(y \cdot \cos z + x \cdot \sin z)$ $z \rightarrow 0$ </p> <p>For $\cos z$ & $\sin z$, set $x = 1/K, y = 0$</p>	 <p> $x \rightarrow K(x^2 + y^2)^{1/2}$ $y \rightarrow 0$ $z \rightarrow z + \tan^{-1}(y/x)$ </p> <p>For $\tan^{-1} y$, set $x = 1, z = 0$</p>
Linear $\mu = 0$ $e^{(i)} = 2^{-i}$	 <p> $x \rightarrow x$ $y \rightarrow y + (x \cdot z)$ $z \rightarrow 0$ </p> <p>For multiplication, set $y = 0$</p>	 <p> $x \rightarrow x$ $y \rightarrow 0$ $z \rightarrow z + (y/x)$ </p> <p>For division, set $z = 0$</p>
Hyperbolic $\mu = -1$ $e^{(i)} = \tanh^{-1}2^{-i}$	 <p> $x \rightarrow K^*(x \cdot \cosh z - y \cdot \sinh z)$ $y \rightarrow K^*(y \cdot \cosh z + x \cdot \sinh z)$ $z \rightarrow 0$ </p> <p>For $\cosh z$ & $\sinh z$, set $x = 1/K^*, y = 0$</p>	 <p> $x \rightarrow K^*(x^2 - y^2)^{1/2}$ $y \rightarrow 0$ $z \rightarrow z + \tanh^{-1}(y/x)$ </p> <p>For $\tanh^{-1} y$, set $x = 1, z = 0$</p>

3. THE PROPOSED ARCHITECTURE

The resolver is an electromagnetic rotational device that detects angular displacement; an equivalent electrical representation and diagram of typical output signal formats a resolver are shown in Fig. 2. An ac excitation signal applied to the primary is inductive coupled to the secondary. The transformation ratios are amplitude modulated by the sin and cosine of the angle of the rotor relative to the stator.

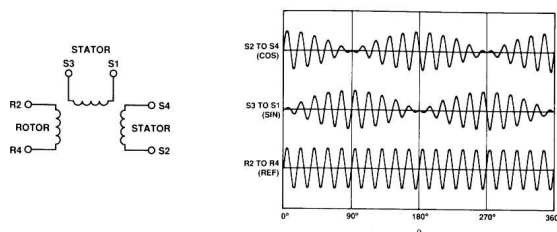


Figure 2: Electrical representation and typical resolver signals.

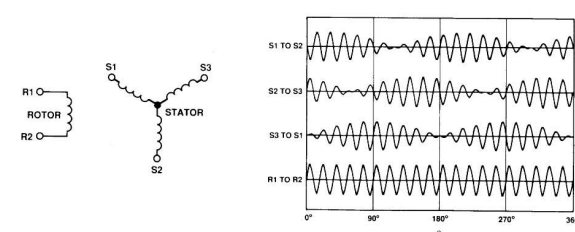


Figure 3: Electrical representation and typical synchro signals.

The operation of the synchro shown in Fig. 3 is very similar to that of the resolver. The fundamental difference is that the stator windings of the synchro are connected in a “Y” configuration, spaced 120 degrees apart, while the resolver has two isolated windings separated by 90 degrees.

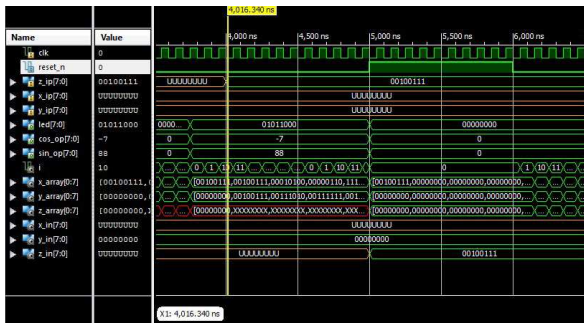


Figure 4: VHDL simulation of the CORDIC.

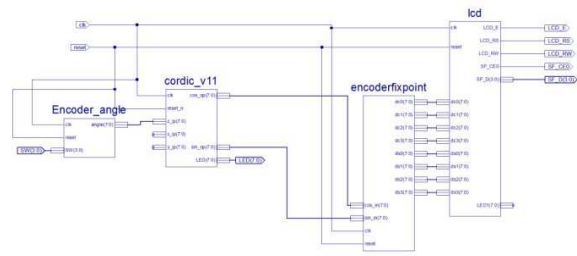


Figure 5: CORDIC Block diagram.



Figure 6: CORDIC FPGA Implementation.

The solid state Scott-T circuit uses two operational amplifiers to transform a synchro format signal into a resolver format. The envelop detector extract the synchro signals envelop and suppresses the references signal. The produced synchro signals are converted into digital format in order to be suitable for use with the FPGA. The CORDIC algorithm is implemented into the FPGA to produce the azimuth angle in digital format. The VHDL simulation is demonstrated in Fig. 4. The CORDIC block diagram is shown in Fig. 5.

4. CONCLUSION

This paper implement CORDIC S/D converter to convert synchro signals into high resolution digital azimuth angle. This achieves a high precision S/D conversion with low propagation delay compared with that implemented using microcontroller or analog processing. This prototype of hardware implementation of CORDIC algorithm used Spartan-III series FPGA, with constraint to area efficiency and throughput architecture. The prototype results show that the conversion time is less than $1 \mu\text{s}$ which is suitable for real time applications in radar and missile control applications.

REFERENCES

1. Volder, J. E., "The CORDIC trigonometric computing technique," *IRE Trans. Electron Computers*, Vol. 8, 330–334, Sept. 1959.
2. Walther, J. S., "A unified algorithm for elementary functions," *Proceedings of the AFIPS Spring Joint Computer Conference*, May 1971.
3. Haviland, G. L. and A. A. Tuszynski, "A CORDIC arithmetic processor chip," *IEEE Journal of Solid-State Circuits*, Vol. 15, No. 1, 4–15, 1980.
4. Hu, Y. H., "CORDIC-based VLSI architectures for digital signal processing," *IEEE Signal Processing Magazine*, Vol. 9, No. 3, 1992.
5. De Lange, A. A. J., A. J. van der Hoeven, E. F. Deprettere, and J. Bu, "Optimal floating-point pipeline CMOS CORDIC processor," *Proceedings of the IEEE International Symposium on Circuits and Systems (ISCAS '88)*, Vol. 3, 2043–2047, Jun. 1988.
6. De Lange, A. A. J. and E. F. Deprettere, "Design and implementation of a floating-point quasi-systolic general purpose CORDIC rotator for high-rate parallel data and signal processing," *Proceedings of the 10th IEEE Symposium on Computer Arithmetic*, 272–281, Jun. 1991.

7. Yu, J.-Y., D. Huang, N. Pei, S. Zhao, J. Guo, and Y. Xu, "CORDIC-based design of matched filter weighted algorithm for pulse compression system" *2012 IEEE 11th International Conference on Signal Processing (ICSP)*, Beijing, China, Oct. 2012
8. Misans, P., U. Derums, and V. Kanders, "FPGA implementation of elementary generalized unitary rotation with CORDIC based architecture," *NORCHIP*, Nov. 2012.
9. Causo, M., "Parallel scaling-free and area-time efficient CORDIC algorithm," *2012 19th IEEE International Conference on Electronics, Circuits and Systems (ICECS)*, Paris, France, Dec. 2012.
10. Zheng, D., S. Zhang, Y. Zhang, and F. Chen, "Application of CORDIC in capacitive rotary encoder signal demodulation," *2012 8th IEEE International Symposium on Instrumentation and Control Technology (ISICT)*, Jul. 2012.
11. Aggarwal, S. and K. Khare, "Efficient window-architecture design using completely scaling-free CORDIC pipeline," *2013 26th International Conference on VLSI Design and 2013 12th International Conference on Embedded Systems (VLSID)*, Jan. 2013.
12. Aggarwal, S., P. K. Meher, and K. Khare, "Scale-free hyperbolic CORDIC processor and its application to waveform generation," *IEEE Transactions on Circuits and Systems I*, Vol. 60, No. 2, Feb. 2013.
13. Lakshmi, B. and A. S. Dhar, "CORDIC architectures: A survey," *Hindawi Publishing Corporation VLSI Design*, Article ID 79489, 2010.
14. Arora, Er. M., Er. R. S. Chauhan, and Er. L. Bagga, "FPGA prototyping of hardware implementation of CORDIC algorithm," *International Journal of Scientific & Engineering Research*, Vol. 3, No. 1, Jan. 2012.

Improved Design of Ku Band High Power Rectangular Waveguide Directional Coupler

Chao Wang, Gaofeng Guo, and En Li

University of Electronic Science and Technology of China, Chengdu, China

Abstract— This paper demonstrates an effective designing method of the high power rectangular waveguide directional coupler. The coupler designed using this method has wide band, high directivity, flat coupling, low voltage standing ratio and manufacturing accuracy. According to the required technology parameter, and the engineering design method based on the modified Bethe aperture coupling theory, the relevant parameters of equally spaced waveguide directional coupler are preliminarily designed. On the basis of this, using simulation software HFSS to do the simulation and optimization of the space between three outside coupling holes of the head end and the tail end, the performance of isolation is improved. A directional coupler at Ku waveband is designed in this paper, the error between the simulation value of coupling and the required value -10 dB is less than 0.6 dB, and after optimization, the isolation is less than -47 dB in the whole operating frequency band.

1. INTRODUCTION

Directional couplers play an important role in almost every microwave application for measuring the power levels of signals in microwave systems, it was widely used in measurement, communication, radar and other electronic equipment. The traditional design method is based on the Bethe aperture coupling theory. In order to adapt the different needs of the development of electronic equipment, the directional coupler from the single hole coupling to porous coupling, from the waveguide narrow side coupled to the broadside coupled, to satisfy the different requirements of narrowband, broadband, strong coupling and weak coupling [1]. As a result of the directional coupler has stable performance, it is index were not affected by ambient temperature, so there is a method for the high power microwave measurement as shown in Figure 1. According to the coupling degree and direction of directional coupler to convert and calculate the power of signal source.

The physical properties of the transmission lines and their coupling method dictates the coupling properties of the coupler [2], so different kinds of couplers have their advantages and disadvantages. Microstrip and stripline directional couplers have attractive broad-band characteristics, but they are affected by their significant losses and low power-handling capabilities when high power handling is required; coaxial directional couplers are the traditional high-power solution when bandwidth are not critical [3]; waveguide Bethe hole couplers are usually used in high-power applications, unfortunately they have a relatively bandwidth, at least in terms of its directivity. But if the couplers are designed with as eries of coupling holes, the extra degrees of freedom can be used to increase this bandwidth. The principle of operation and design of such a multihole waveguide coupler is very similar to that of the multisection matching transform. After the basic aperture coupling theory which is proposed by Bethe and Cohn [4], scholars from many countries do further research on it in order to meet the various needs.

In this paper, an effective designing method of the directional coupler with wide frequency band and high directivity is proposed, and using this method, a directional coupler is designed with the aid of simulation software HFSS (High Frequency structure Simulator). So first, we design an equally spaced waveguide directional coupler according to there quired parameter and the modified Bethe aperture coupling theory; then we optimize the space between the coupling holes and reduce the size of some coupling holes of the head end and the tail end to get a valuable coupler with flatter coupling coefficient and higher directivity. A directional coupler at Ku waveband ($12.4 \sim 18$ GHz) is designed in this paper, the error between the simulation value and the required value is less than 0.6 dB and the directivity is more than 37 dB. Meanwhile, it reduces the requirement of the manufacturing accuracy as far as possible in consideration of the influence of manufacturing errors.

2. THE PERFORMANCE INDEX OF THE DIRECTIONAL COUPLER

As shown in Figure 1. The directional coupler is a network with four ports. They are the input port, through port, coupling port and isolation port. Describes the performance index of the directional coupler are coupling, isolation, direction, bandwidth.

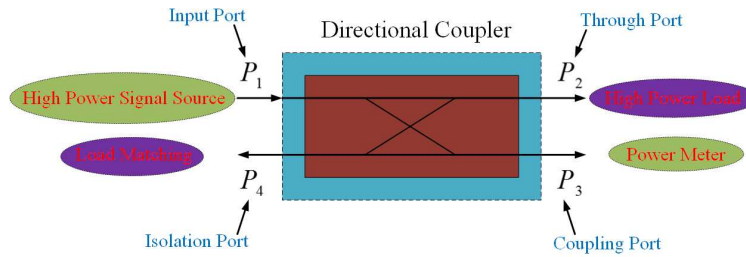


Figure 1: Structure of high power microwave through directional coupler.

(1) Coupling

$$C = 10 \cdot \lg \frac{P_3}{P_1} = 20 \cdot \lg |S_{31}| \quad (\text{dB}) \quad (1)$$

(2) Isolation

$$I = 10 \cdot \lg \frac{P_4}{P_1} = 20 \cdot \lg |S_{41}| \quad (\text{dB}) \quad (2)$$

(3) Direction

$$D = 10 \cdot \lg \frac{P_4}{P_3} = 20 \cdot \lg |S_{43}| \quad (\text{dB}) \quad (3)$$

(4) Bandwidth

Bandwidth refers to the frequency range design index of directional coupler are meet the requirements.

3. DESIGN AND OPTIMIZATION OF DIRECTIONAL COUPLER

3.1. The Design Requirements

The design of a bandwidth of 12.4 ~ 18 GHz, the coupling degree of C is -10 dB, directional D is greater than 37 dB.

3.2. Theoretical Basis

Aperture coupling theory was first proposed by Bethe, then large aperture coupling Cohn and McDonald on the finite thickness of the improved [5]. Bethe directional coupler is signal through a single hole in two waveguide broadside on the public from a waveguide coupled to another waveguide. The directional characteristics of directional coupler is through the use of two separate wave or wave component in the coupling port is added, and the isolation port phase cancellation and produce.

3.3. Design Procedure

Chebyshev response, Binomial response and equivalent aperture response are generally used in waveguide coupling. A Chebyshev coupler has a broader-band performance than the corresponding coupler designed with the binomial response, while the Chebyshev coupler requires higher manufacturing accuracy. As we all known, errors of the coupling apertures are inevitable in the manufacturing process, the higher manufacturing accuracy, the greater errors it brings, then it will lead to unsatisfactory results. To minimize manufacturing accuracy, we choose equivalent aperture response and optimize the aperture spacing and the radius of some apertures, which not only reduces errors but also improves coupling coefficient and directivity.

(1) Aperture array distribution

Figure 2 shows the structure of the coupling wall between the two waveguides proposed in this paper. It consists of two rows that have a distance of s between the center of circles and the edge of the waveguide, and ten columns that have different spacing. The coupling hole heart distance waveguide edge distance is S , aperture spacing are d , d_1 and d_2 , aperture radius are r , r_1 and r_2 .

(2) Aperture spacing

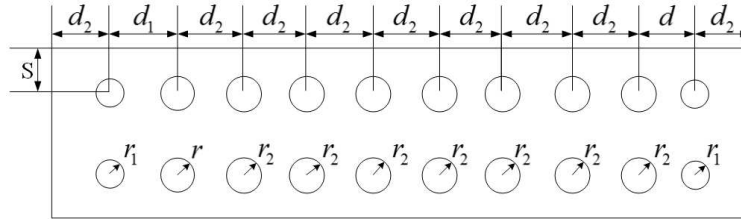


Figure 2: Aperture array distribution of Ku band directional coupler.

According to the principle of phase superposition, the spacing between the apertures should be kept constant and equal to a quarter wavelength of the center frequency of the band.

$$d = \frac{1}{4} \lambda_{g_0} = \frac{1}{4} \frac{2\lambda_{g_1}\lambda_{g_2}}{\lambda_{g_1} + \lambda_{g_2}} \quad (4)$$

where λ_{g_0} is the guide wavelength, λ_{g_1} is the minimum guide wavelength and λ_{g_2} is the maximum guide wavelength. d has a significant influence on coupling coefficient and directivity, thus we can adjust it to achieve flatter C and better D . According to the result of optimization, we choose $d = 5.8$ mm, $d_1 = 6.35$ mm and $d_2 = 6.3$ mm.

(3) Aperture radius

K_f and K_b are constants for the forward and backward coupling coefficients. The coupling and directivity can be calculated as

$$C = -20 \lg |K_f| - 20 \lg \sum_{n=0}^N r_n^3 \quad (5)$$

$$D = -C - 20 \lg |K_b| - 20 \lg \left| \frac{\sum_{n=0}^N r_n^3 e^{-2j\beta nd}}{\sum_{n=0}^N F_n} \right| \quad (6)$$

We can easily obtain r_n and N . The bigger aperture is, the more coupling it will be. We finally choose $N = 7$ mm, $r = 2.55$ mm, $r_1 = 2.15$ mm and $r_2 = 2.7$ mm in consideration of manufacturing accuracy.

(4) Aperture thickness h

The coupling coefficient increases in the straight line within crease of aperture thickness. If h increases, the attenuation will also increase when the coupling wave passes through the coupling hole, thus the coupling coefficient will increase. Therefore, we can change h to adjust the coupling coefficient of the directional coupler according to the requirements. However, what we should pay attention to in the engineering design is that the increase of h will also increase the directional coupler's dimensions in the space. Coupling value for different aperture thickness h versus frequency is shown in Figure 3, and finally we choose $h = 0.5$ mm for the consideration of flatter coupling value.

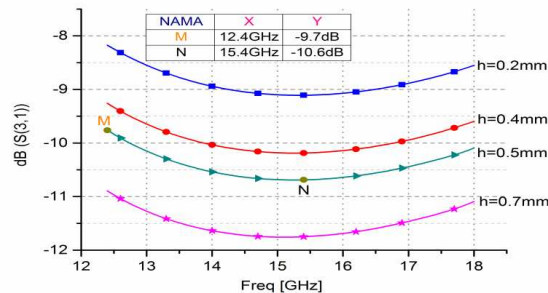


Figure 3: Coupling value for different aperture thickness h .

(5) The aperture offset from the sidewall of the guide

The distance between the center of circles and the sidewall of the guide is denoted as s , which has a huge influence on coupling coefficient especially for the low-frequency section. With the increase of s , the coupling coefficient decreases largely in the low frequency section and small in the high frequency section. Taking many factors into consideration, we choose $s = 3.1$ mm ultimately.

4. SIMULATION RESULTS

The proposed structure has been applied to realize abroad band coupler with coupling coefficient about -10 dB and directivity bigger than 37 dB in the frequency band between 12.4 to 18 GHz. The directional coupler is simulated with the aid of Ansoft HFSS and simulation results are reported in Figure 4 and Figure 5. It can be seen that directivity varies from -37.2 to 57.9 dB over the band and the isolation is less than -47 dB in the whole operating frequency band. The directional coupler uses waveguide structure, so the voltage standing wave ratio (VSWR) is generally ideal. Figure 5 gives input VSWR versus the working frequency, and we can see that the VSWR is less than 1.009 .

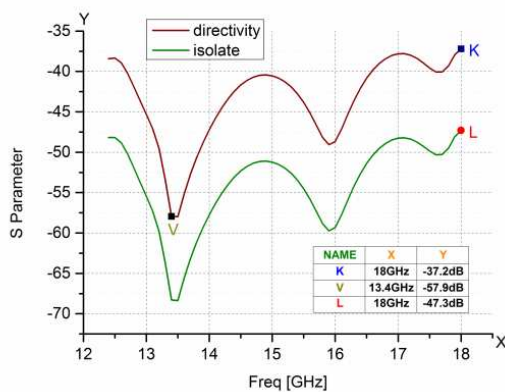


Figure 4: The cure of the S_{14} and directivity.

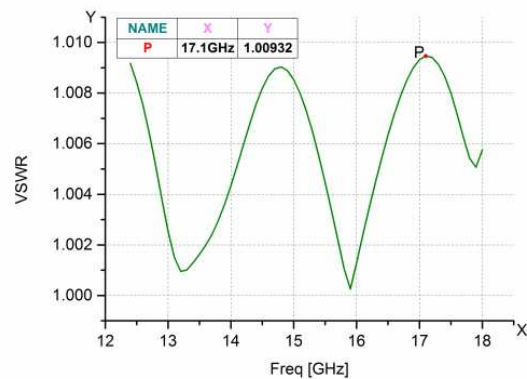


Figure 5: The cure of input VSWR.

5. CONCLUSION

A novel method has been proposed and analyzed for designing directional couplers in this paper. This method represents a significant improvement for high-power measurement systems since they have flat coupling coefficient, good directivity, low VSWR, high power handling capacity etc., and can be fabricated at low cost with smaller manufacturing errors. A Ku band rectangular waveguide directional coupler has been designed and simulated using the HFSS software. Because of little manufacturing accuracy, this method will have many applications in microwave wireless communication measurement systems.

REFERENCES

1. Xing, Z. N., "Optimal design of Ka waveband directional coupler," *Electronic Test*, Vol. 6, 53–56, 2010.
2. Hamidreza, M., A. Nasr-Azadani, and R. Safian, "A novel broadband high power coaxial-to-CPW directional coupler," 1152–1155, 2009.
3. Liao, W., L. Tong, Y. Tian, et al., "S band high power rectangular waveguide directional coupler's design," *Electronin Measurement Technology*, Vol. 34, No. 4, 50–52, 2011.
4. Bethe, H. A., "Theory of diffraction by small holes," *Phys. Rev.*, Vol. 66, 163–182, 1944.
5. McDonald, N. A., "Electric and magnetic coupling through smallapertures in shield wall of any thickness," *IEEE Trans. Microw. Theory Tech.*, Vol. 20, 689–695, 1972.

Magnetic Field Controlled Diffraction Grating

Guojing Huang, Henghe Jiang, Bin Zhou, and Zhuo Chen

Centre for Optical and Electromagnetic Research, South China Academy of Advanced Optoelectronics
South China Normal University, Guangzhou 510631, China

Abstract— A novel magnetically tunable diffraction grating based on V-shaped and magnetic nanoparticles is proposed and demonstrated experimentally. The grating’s period we made was $10\ \mu\text{m}$, and the grooves and the convex groove were both $5\ \mu\text{m}$. The refraction index of the ferrofluid is sensitive to surrounding magnetic field. We’ve demonstrated the magnetically tenability of this grating by measuring the changing of the diffraction angle of the high order diffraction light. The diffracted light was received by CCD and the movement of the laser spot, i.e., the small change of the diffraction angel was recorded. This approach is a good candidate for the following applications: magnetic sensors, magnetic controlled optical switches, modulator and so on.

1. INTRODUCTION

Diffraction gratings with periodic structures are very important optical spectral elements in optical system. The diffraction gratings are usually fabricated on the surface of planar substrate. Since the diffraction gratings is fixed and it is difficult to change the period. However in some cases, the diffraction property, i.e., the diffraction angle of a light beam with particular wavelength, is required to be adjustable. There’s one device called acousto-optic modulator [1] is developed to fulfill this requirement. In this paper we have proposed another novel tunable diffraction grating with the help of the ferrofluid. Ferrofluid is a kind of stable colloidal suspension of ferromagnetic nanoparticles in a liquid carrier. These ferromagnetic colloids are usually dispersed by different kinds of surfactant [2]. This material can be applied to various modern technology fields, e.g., optical transmission [3], magneto-optical [4], optical switches [5] and thermo-optical [6, 7]. One of the most fascinating application of ferrofluid used as optical device should be MF tunable optical grating [8] and shows an increasingly important role in wide range of potential applications. Up to date, there are few reports on the magnetic field sensor based on tunable optical grating. Such research done by Shengli Pu et al. [9], they developed a MF grating with photoresist and ferromagnetic interphase and found that the transfer of the energy of the 0th-order diffracted light to that of the higher-order is apparent. Hongzhu Ji et al. [10] also investigated direction of the emergent light after the V-shaped groove filled with magnetic fluid which is related to the strength of the externally applied magnetic field.

In this paper, we have developed another tunable diffraction grating based on V-shaped groove filled with ferrofluid. When the strength of the around it changes we could clearly observe the change of the diffraction angle and the movement of diffraction light beams.

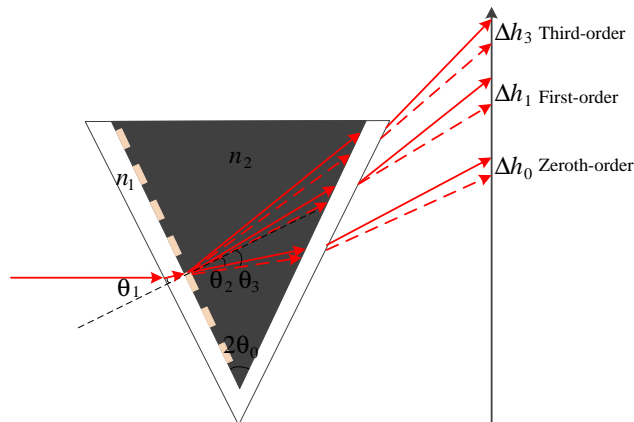


Figure 1: Schematic diagram.

2. THEORETICAL ANALYSIS

When the visible light incidence the diffraction grating, the light has the diffraction. It appears different order light. When they reach the ferrofluid's interface, they refract into the ferrofluid, for the different refraction index between glass and ferrofluid. As a result, there are diverse order lights, i.e., the zeroth-order, the first-order and the third-order and so on, displaying on the screen, as show solid line in Fig. 1. When we apply the external magnetic field, the refraction index of the ferrofluid changes consequently. The refraction angle transform θ_2 to θ_3 , as showed in Fig. 1. The light path also changes from the solid line to the dotted line as showed in Fig. 1. They reach another position, and the distances are Δh_0 , Δh_1 , Δh_3 , ..., etc. which are the expression of the refraction angle change of different order light.

3. THE EXPERIMENT AND THE RESULTS

The grating is fabricated on a glass substrate which can transmit light well. In order to have better hydrophobicity, hexamethyldisilazane (HMDS) should be sprayed on the surface of the glass substrate. The photoresist used in this experiment is AZ5214e which is interchangeable from positive to negative sides. After being daubed on the glass substrate, with a speed of 2000 rounds per second, photoresist would be evenly distributed. Heated to be solid and covered with a mask plate, photoresist will then be explored to UV light whose period is $10\ \mu\text{m}$, after which, it would be etched in solution and turn into a thin grating with $1\ \mu\text{m}$ depth as shown in Fig. 2(a) and a $10\ \mu\text{m}$ cycle as shown in Fig. 2(b).

The ferrofluid we use in the experiment is EMG 900 produced by the Ferrotec (USA) Corporation. This ferrofluid is oil-based magnetic fluid whose average particle size is 10 nm, viscosity is 60 cP at 27°C , volume concentration of magnetite is 9%, density is 1.74 g/ml at 25°C and saturation Magnetization (Ms) is 990 Gauss [11]. The refractive index of EMG 900 is estimated to be around 1.65 ± 0.02 [12].

The system setup is shown in Fig. 3. A semiconductor laser diode whose wavelength is 650 nm is applied as the light source in this experiment. The laser light goes through a small hole and becomes

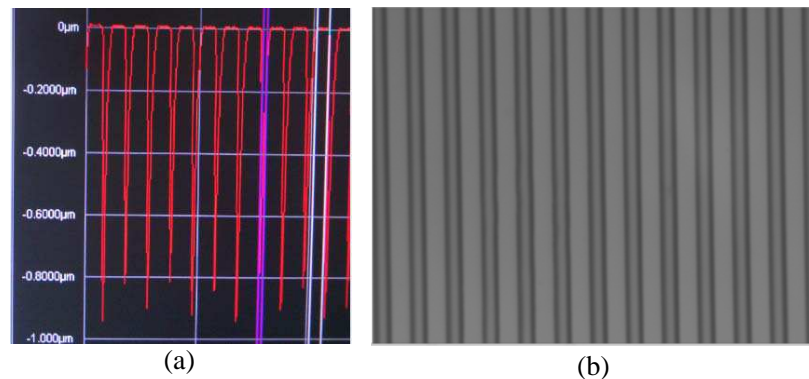


Figure 2: The measured drawing of the diffraction grating. (a) The depth of the diffraction grating is about $1\ \mu\text{m}$. (b) The period of the diffraction grating is about $10\ \mu\text{m}$.

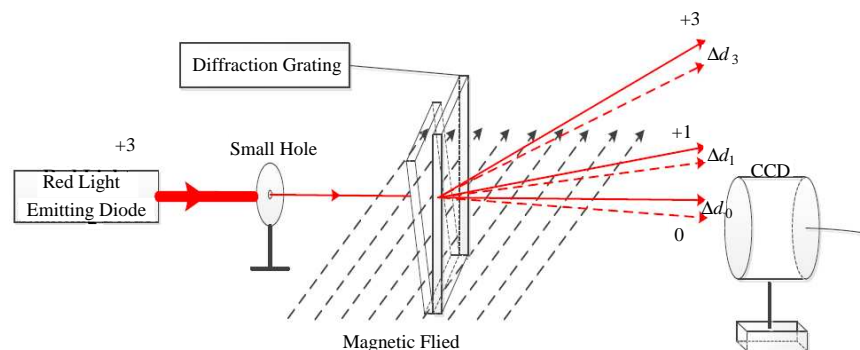


Figure 3: The experimental setup.

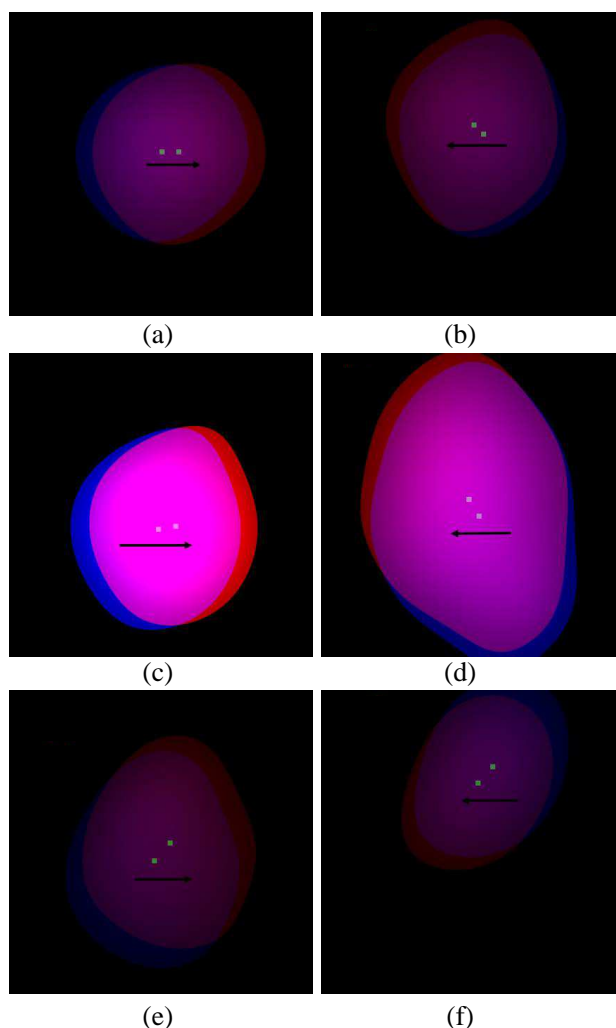


Figure 4: (a) and (b) is the experimental phenomenology of zeroth-order light, (c) and (d) is the experimental phenomenology of first-order light, (e) and (f) is the experimental phenomenology of third-order light.

thin and small. The thinner light will be perpendicular to the electrical field and the diffraction grating on the right. It diffracts in the diffraction grating, reflecting into the filling ferrofluid in the V-shaped grating. With an external magnetic field, the refractive index of ferrofluid will change, and the diffracting angle would be also varied accordingly. Consequently, the position recorded by the CCD shifts. The distance between CCD and grating sample is about 1 m. No matter the strength of magnetic increases or decreases, the diffracting angle will change so that the light spot also keeps alternative.

Without applying the external magnetic field, the position of the zeroth-order light was recorded in the blue spot as showed in Fig. 4(a). However, the spot moves toward the right side to the position of the red one shown in Fig. 4(a) when placing an 1000 Oe external magnetic field. The green spot is the midpoint of the blue and red ones. It is obvious that the green spot moves to the right after applying the external magnetic field. In addition, when the external of the magnetic field decreased from 1000 Oe to 0 Oe, the light spot moves back to the left as showed in Fig. 4(b). Similarly, with the same method and the same process the positions of the first-order and the third-order light spots are showed as Fig. 4(c), Fig. 4(d), Fig. 4(e), Fig. 4(f). The shift distance (the variety of the angle) is a little longer from the zeroth-order light to the third-order light. The changes of distance that the light spots move i.e., the shifts of reflecting angle is becoming lager and lager from the zeroth to third one. Furthermore, the first degree light owns the greatest diffraction efficiency, so we cannot make use of the higher degree light infinitely.

4. CONCLUSIONS

In summary, the diffraction grating with V-shaped groove based on ferrofluid has been analyzed theoretically and experimentally. It is the tunable diffraction grating by the strength of the external

magnetic field, which characteristics is studied experimentally. This approach is a good candidate for the following applications: magnetic sensors, magnetic controlled optical switches, modulator and so on. This is a new method to fabricate the magnetically tunable diffraction grating. Compared with some other present diffraction grating, the proposed magnetically tunable diffraction grating has simple configuration and is easier to be produced. The period of this magnetically diffraction grating can be tuned to adapt to the different application by adjusting the strength of the external magnetic field. All of these are in favor of its practical applications.

ACKNOWLEDGMENT

This work was supported in part by the National Natural Science Foundation of China under Grant 61307053 & 61177077, in part by the China Post-Doctoral Science Foundation under Grant 2-013M531866, and in part by the Guangdong Innovative Research Team Program under Grant 2010-01D0104799318.

REFERENCES

1. Corey, R., A. Schmidt, and P. Saulnier, "Using a moving diffraction grating to simulate the function of an acousto-optic modulator," *American Journal of Physics*, Vol. 64, No. 5, 614–617, 1996.
2. Rosensweig, R. E., *Ferrohydrodynamics*, Courier Dover Publications, 2013.
3. Yang, S., Y. Chiu, B. Jeang, et al., "Origin of field-dependent optical transmission of magnetic fluid films," *Applied Physics Letters*, Vol. 79, No. 15, 2372–2374, 2001.
4. Du, T. and W. Luo, "Dynamic interference patterns from ferrofluids," *Modern Physics Letters B*, Vol. 9, No. 25, 1643–1647, 1995.
5. Gu, Y., G. Valentino, and E. Mongeau, "Ferrofluid-based reconfigurable optofluidic switches for integrated sensing and digital data storage," *Applied Optics*, Vol. 53, No. 4, 537–543, 2014.
6. Du, T. and W. Luo, "Nonlinear optical effects in ferrofluids induced by temperature and concentration cross coupling," *Applied Physics Letters*, Vol. 72, No. 3, 272–274, 1998.
7. Pu, S., X. Chen, W. Liao, et al., "Laser self-induced thermo-optical effects in a magnetic fluid," *Journal of Applied Physics*, Vol. 96, No. 10, 5930–5932, 2004.
8. Hong, C.-Y., H. Horng, I. Jang, et al., "Magneto-chromatic effects of tunable magnetic fluid grating," *Journal of Applied Physics*, Vol. 83, No. 11, 6771–6773, 1998.
9. Pu, S., X. Chen, L. Chen, et al., "Tunable magnetic fluid grating by applying a magnetic field," *Applied Physics Letters*, Vol. 87, No. 2, 021901, 2005.
10. Ji, H., S. Pu, X. Wang, et al., "Magnetic field sensing based on V-shaped groove filled with magnetic fluids," *Applied Optics*, Vol. 51, No. 8, 1010–1020, 2012.
11. Arce-Diego, J. L., R. López-Ruisánchez, J. M. López-Higuera, et al., "Fiber Bragg grating as an optical filter tuned by a magnetic field," *Optics Letters*, Vol. 2, No. 9, 603–605, 1997.
12. Konstantaki, M., A. Candiani, and S. Pissadakis, "Optical fibre long period grating spectral actuators utilizing ferrofluids as outcladding overlayers," *Journal of the European Optical Society — Rapid Publications*, Vol. 6, 2011.

Analysis of Immunity by RF Wireless Communication Signals

Hongsik Keum¹, Jungyu Yang², and Heung-Gyoon Ryu³

¹EletroMagneticwave Technology Institute, RAPA, South Korea

²Department of Radio Environment Safety, Radio Research Agency, South Korea

³Department of Electronic Engineering, Chungbuk National University, South Korea

Abstract— Despite of widespread use of new digital wireless communications, the radiated immunity test based on IEC 61000-4-3 only has been performed with using amplitude modulation (AM) signal. In this study, we have analyzed the radiated immunity test method that is going on recent standardization activity to investigate close proximity fields from radio frequency (RF) wireless communications and have investigated the impact of digitally modulated signals. The results show that the devices were influenced much more by digital modulation signal than by AM or pulse modulation (PM) signal. Also it shows that we need to investigate the depth research on radiated immunity testing for the environment of modern communication technology.

1. INTRODUCTION

Recently, portable wireless communication devices as wireless phone, smart phone and wireless local area network (WLAN) have come into widespread use and acceptance. Along with the increase of intentional radiated RF by those devices the everyday electromagnetic environment has greatly changed. New technology has continued to advance making mobile phones smaller and smaller. The newer and smaller mobile phones can be placed virtually anywhere in our living place and are often being placed in close proximity to electronic equipment, giving rise to potential interference and compatibility issues.

The achievement of adequate immunity of electrical or electronic equipment is a basic provision to ensure electromagnetic compatibility (EMC) in these circumstance. Such immunity has reflect the expected electromagnetic disturbance at the intended location of operation as well as the characteristics of the equipment. The corresponding immunity levels are determined taking into account for a probabilistic aspects of a disturbance and an economical aspects of immunity test. Such a process is currently being performed by a working group of IEC TC 77 [1].

Because the new technologies, such as long term evolution (LTE) and WLAN, use a very large range of the frequency spectrum it is necessary to use different test methods which consider the physical behavior of magnetic coupling in the lower frequency range and the more electrical based characteristic in the higher frequency range. Immunity testing according to existing standards, such as IEC 61000-4-3, may not be suitable to assess compatibility with the complex electric and magnetic fields generated by RF emitters located in close proximity. There are two kinds of new standardization work being performed in SC77B WG10. One is IEC 61000-4-31 to test broadband conducted disturbance immunity and the other is IEC 61000-4-39 to test radiated fields immunity in close proximity [2]. The revision of IEC 60601-1-2, immunity standard for medical equipment and systems, has also recently been done in IEC TC62/SC62A and has including immunity to proximity fields from RF wireless communication equipment [3].

Recent wireless communications use a digital modulation technology. In these standards, the AM signal is mainly used to reference source signal to test the radiated immunity. But, the wireless communication signal is being simulated simply into a PM signal. According to recent research results, it has known that an equipment were influenced by digital modulation signal more than by AM or PM signal [4].

In this study, we have investigated by reviewing an immunity standards in close proximity which is recently being standardized in IEC. We have then analyzed the characteristics of the reference source signal for a radiated immunity test in those standards and compared with those of mobile communication signal. We have verified the influence of digital modulation signal through the FTP throughput test has performed in Gigahertz Transverse Electromagnetic cell (GTEM). Finally, we have proposed that it should be consider to use a digital modulation signal during standardizing of new radiated immunity test.

2. STANDARDIZATION ACTIVITIES OF CLOSE PROXIMITY IMMUNITY

2.1. IEC 61000-4-39

The use of portable wireless devices has increased sharply due to the widespread diffusion of portable wireless communication services such as mobile communication and WLAN, which in turn increased the possibility of such devices affecting other devices due to the intentional electromagnetic interference of portable wireless devices.

To reflect those conditions, IEC TC77 decided to create a new standard for the close proximity immunity test, beyond the existing IEC 61000-4-3 radiated immunity standard. The standardization work is performed by SC77B/WG10, with the active participation of experts.

This standard defines immunity test procedures and specifications with regard to the reference source signal, test level, and test method for the close proximity immunity test. The following areas are currently standardized:

- Test levels related with the magnetic field immunity and radiated RF field immunity.
- Test equipment.
- Test setup including test facility and arrangement of equipment.
- Test conditions, detailed test procedure, and verification method.
- Evaluation of test results and test report.

The electromagnetic disturbances specified in this standard are limited to continuous narrow-band signals (which may be pulse- or amplitude modulated by up to 1 kHz) but do not include disturbance signals that are basically transient or impulsive in nature. The frequencies or frequency bands to be selected for testing are limited to those where mobile radio telephones or other intentional RF emitting devices actually operate. Testing shall not be applied continuously over the entire frequency range covered by this standard.

Several test levels are defined for inhomogeneous fields in the frequency range of 9 kHz to 30 MHz and for RF fields in the frequency range of 400 MHz to 6 GHz. The test level applied during testing should be selected in accordance with the expected maximum output power of the portable transmitting device and the likely, or specified, separation distance between its transmitting antenna and the equipment subject to the disturbance created by the transmitting device.

For testing of equipment the carrier signal is modulated using pulse modulation. The pulse modulation shall adhere to the following parameters:

- Duty Cycle: 50%.
- Modulation frequency: 2 Hz, 217 Hz or 1 kHz.

2.2. IEC 60601-1-2

The medical equipment EMC standard, which has recently been revised, added the immunity test in the proximity field of wireless communications. The revised standard defined the immunity test specifications for the test frequency, modulation signal, and test level related with the latest representative wireless communication service.

Table 1 shows the test specifications for the proximity immunity of medical equipment, which specifies that the immunity test should be performed at the center frequency or three frequencies of the band, considering the bands of wireless communication services. The specification also defines that the additional test can be run at another frequency.

It is also defined that the test level should be determined after considering the minimum separation distance and maximum output of the wireless communication devices. Minimum separation distances for higher IMMUNITY TEST LEVELS shall be calculated using the following equation:

$$E = \frac{6}{d} \sqrt{P}$$

where P is the maximum power in W , d is the minimum separation distance in m , and E is the IMMUNITY TEST LEVEL in V/m .

Most of the standards define the reference immunity signal as a PM signal, in order to simulate the latest wireless communication signal.

This simplified modeling of the reference signal is based on an opinion that it is impossible to configure the cost-effective test conditions and set up all wireless communication services in the world using the real modulation signal, even though modulation makes a major contribution to causing electromagnetic interference in equipment.

Table 1: Test specifications for proximity immunity of medical equipment to RF wireless communications equipment.

Service	Band (MHz)	Test frequency (MHz)	Modulation	Test level (V/m) at 0.3 m distance
TETRA 400	380–390	385	PM 18 Hz	27
GMRS 460, FRS 460	430–470	450	FM ± 5 kHz deviation 1 kHz sine	28
LTE Band 13, 17	704–787	710, 745, 780	PM 217 Hz	9
GSM 800/900, TETRA 800, iDEN 820, CDMA 850, LTE Band 5	800–960	810, 870, 930	PM 18 Hz	28
GSM 1800; CDMA 1900; GSM 1900; DECT; LTE Band 1, 3, 4, 25; UMTS	1700 –1990	1720, 1845, 1970	PM 217 Hz	28
Bluetooth, WLAN 802.11 b/g/n, RFID 2450, LTE Band 7	2400–2570	2450	PM 217 Hz	28
WLAN 802.11 a/n	5100–5800	5240, 5500, 5785	PM 217 Hz	9

3. ANALYSIS OF THE CHARACTERISTICS OF THE SIMULATED PULSE MODULATION SIGNAL

The radiated immunity standard uses the PM signal to simulate the latest mobile communication signal because it is cost effective and easy to implement.

The modulation frequency simulated in the standard refers to the frequency that is selected to simulate the frame transmission cycle of the time division multiple access (TDMA), which sends a signal to a particular time slot only, into the pulse signal. The entire TDMA frame rate can be mapped to the pulse signal frequency, and the time slot rate can be mapped to the duty cycle of the pulse signal. In the global system for mobile (GSM), a frame with time duration of 4.61 ms is divided into 8 slots of each 0.577 ms, which is the basic transmission unit. PM 217 Hz simulates GSM's transmission cycle, RF frame length, and 4.61 ms.

LTE, the latest mobile communication standard, uses orthogonal frequency division multiple access (OFDMA) as a modulation method. As OFDMA uses different time slots for the frequency and time domain, LTE can also simulate the multi-access time frame using pulse signals. The radio frame of LTE has time duration of 10 ms in the time domain. A frame is divided into 20 slots of each 0.5 ms. However, the simulated pulse frequency is slightly different from the LTE frame in the standard. Table 2 shows the characteristics of each communication signal and the frequency of

Table 2: Characteristics of each communication signals and simulated PM.

	GSM	LTE	WLAN
Frame rate	4.61 ms, 480 ms (at discontinuous transmission mode)	10 ms	1 ms
Time slot length (Duty cycle)	0.577 ms (1/8)	1 ms (1/10)	96 μ s
Fundamental frequency of frame	217 Hz, 2.08 Hz	100 Hz	1 kHz
Simulated PM frequency on Std.	217 Hz, 2 Hz	217 Hz	217 Hz, 1 kHz

each simulated reference immunity signal.

The PM signal includes wide spurious due to the characteristics of the spectrum, which acts as an obstructive factor that causes interference to the audio system [5]. Figure 1 shows the PM frequency spectra defined by the new close proximity immunity standard IEC 61000-4-39. As the spectra exist within 2 kHz, which is the audible frequency band, it can cause a sound effect similar to 1 kHz AM (the standard analog immunity signal). Therefore, the PM simulation is valid as a reference signal to test the sound interference effect.

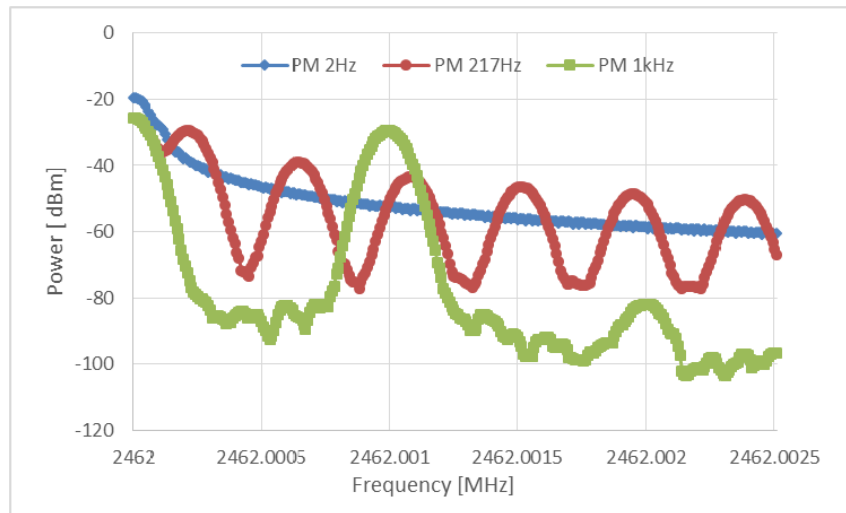


Figure 1: PM spectra simulated in IEC 61000-4-39.

4. CHARACTERISTICS ANALYSIS OF THE DIGITAL MODULATION SIGNAL

The latest mobile communication mainly uses the OFDM modulation method for high-speed transmission. Although the OFDM modulation increases spectral efficiency using the orthogonal frequencies, phase shift keying (PSK) modulation scheme is used as a basic data modulation method. The characteristics of the PSK modulation signal are fundamentally different from the PM signal that simulates mobile communication signal in the immunity standard.

The PM signal theoretically has a sector in which no signal exists in the time domain, and spectral discontinuity in the frequency domain depending on the duty cycle. On the other hand, the PSK signal has the modulation characteristic that the data and phase are mapped. Therefore, there is no sector in the PSK signal in which the signal is disconnected in the time domain, and

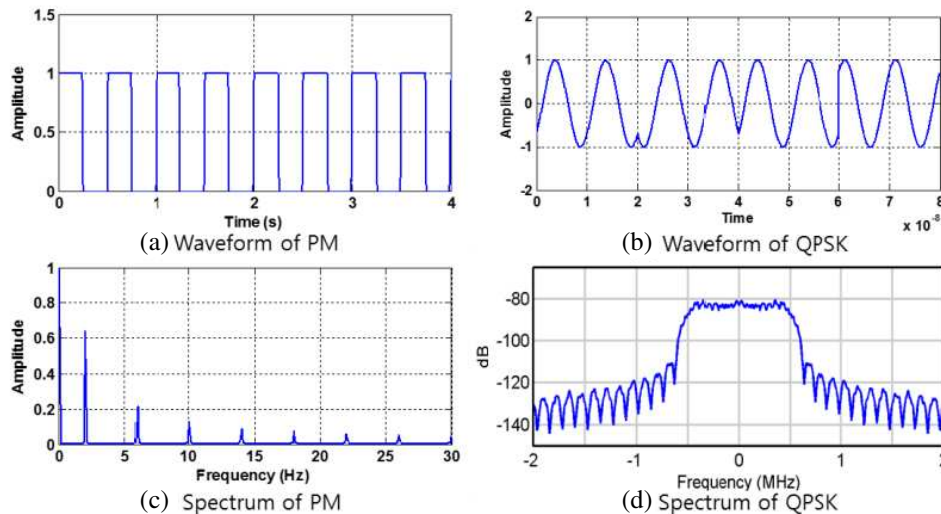


Figure 2: Comparison of the time domain signal and frequency domain spectrum for PM and PSK.

has the continuous spectrum in the frequency domain. Figure 2 shows the comparison of the time domain waveform and frequency domain spectrum.

Furthermore, the digital modulation signal used in the latest wireless communication has a broader bandwidth than the PM signal. The latest mobile communication or WLAN generally uses 10 MHz BW, and BW is expanding more and more for faster communication.

Due to this characteristic difference, the immunity test found that equipment was more influenced by digital modulation signal than by AM or PM signal.

We know the EMC's theoretical background is that the peak power of the reference test signal is the most dominant factor among the factors that affect the immunity test. In addition, based on this information, we can understand that the occupied bandwidth of the signal and the occupied energy on the time scale are also important factors.

We have tested the throughput difference by the reference signal of radiated immunity test in GTEM cell, to prove that the above hypothesis is valid in digital communication devices. For the test, a WLAN AP and a laptop were placed inside the GTEM, and a laptop connected to the WLAN AP was placed outside of the GTEM. The throughput was measured by sending files between two laptops using the FTP. The interference signal was provided through the GTEM, by adjusting the input signals in such a way that the signals have the same peak power according to the reference signal type. The WLAN communication was configured with the CH2 (2.417 GHz), 20 MHz bandwidth, and IEEE 802.11n mode. The interference signal was sent to 2.462 GHz so that it was not overlapped with the communication band. Table 3 shows the test result. It shows that the degradation of throughput by WCDMA is biggest than others. Through the simple WLAN test, the same trend of the interference effect as in the previous test result can be checked.

Table 3: Comparison of WLAN throughput according to reference signals used by radiated immunity test in GTEM Cell.

Status	Normal	Radiated immunity test				
Reference signal	None	AM 1 kHz	PM 2 Hz	PM 217 Hz	PM 1 kHz	WCDMA
WLAN throughput (kB/s)	6095.27	5752.58	5930.59	5806.19	6004.52	5593.35
Degradation of throughput (%)	0	5.6	2.7	4.7	1.5	8.2

5. CONCLUSION

As more and more portable mobile communication devices such as mobile communication and WLAN are used, international standards are being created to assess the impact of the intentional electromagnetic waves emitted by these portable wireless devices.

The close proximity immunity standard, which is standardized by the IEC, simulates the digital communication signal used by the latest wireless communication as a PM signal. The PM signal, as a reference signal of the radiated immunity test, can affect a wider frequency band than the AM signal, and has the strength of interfering in the audio system like AM. However, the latest digital modulation signals like LTE and WLAN have the broadband characteristics than PM in the frequency domain, and more occupied energy on the time scale. Due to these reasons, the digital modulation signal affects more than the PM signal, and this was verified by the WLAN throughput test. More studies are needed to take the effect of digital modulation signals into account during standardization activities in the future.

ACKNOWLEDGMENT

This research was supported by the ICT Standardization program of MSIP (Ministry of Science, ICT and Future Planning). Also the author would like to thank convener, John Mass, and other very active members of WG10 of IEC TC77/SC77B.

REFERENCES

1. Jaekel, B. W., "Electromagnetic environments — Phenomena, classification, compatibility and immunity levels," *IEEE EUROCON'09*, 1498–1502, 2009.
2. WG10_A0338-Draft CD 61000-4-39, IEC TC77/SC77B/WG10, 2014.
3. IEC 60601-1-2, "Medical electrical equipment — Part 1–2: General requirements for basic safety and essential performance — Collateral standard: Electromagnetic disturbances — Requirements and tests," IEC 62A/916/FDIS, 2013.

4. Keum, H., W. S. Cho, J. Yang, H. G. Ryu, and S. Choi, “Analysis upon the effect of the immunity of electronic devices by the emitted digital modulated signals,” *2012 International Symposium on IEEE Electromagnetic Compatibility (EMC EUROPE)*, 1–5, 2012.
5. Choi, S. and S. Park, “Analysis of interference signal from LTE phone on sound systems,” *IEEE ICT Convergence (ICTC)*, 826–830, Oct. 2013.
6. Jeon, S., Y.-C. Chung, C.-H. Jun, S.-T. Kwun, J. H. Yun, and S. Choi, “Evaluation of interference between microwave oven noise and IEEE802.11b using a GTEM cell,” *PIERS Online*, Vol. 5, No. 6, 571–575, 2009.

Resonant Properties of HE₁₁₁ Mode of a Complicated Microwave Cavity for a New Type of Rubidium Clock

Xiao Xiao Li, Shang Lin Hou, Yanjun Liu, and Jing Li Lei
School of Science, Lanzhou University of Technology, Gansu, China

Abstract— Resonant properties of HE₁₁₁ mode of a complicated microwave cavity with ceramic material, used in rubidium clock, are studied by mode matching method. The microwave cavity works at a certain frequency such as 6835 GHz by accommodating a glass bubble containing rubidium vapor. To make electromagnetism focus on the centre of the cavity for energy exchange and further miniaturize the cavity to a large extent, a ceramic dielectric ring is installed in the inner layer of the glass bubble. In order to study main factors influencing resonant characteristics, resonant frequencies of HE₁₁₁ mode are calculated through eigen equation and compared with simulated results. The results show that theoretical computations are in good agreement with finite element simulations. In addition, the effects of loaded dielectric and rubidium vapor on resonant frequency are also analyzed. This work is of great significance for the miniaturizing of the cavity and theory perfection in atomic clock.

1. INTRODUCTION

Rubidium frequency standard is widely used in global positioning system (GPS) [1], communication, navigation, positioning and running survey system for its good properties such as small volume, strong environment adaptability and good frequency flexibility [2, 3]. One of the most important microwave components in it is microwave cavity, which directly plays an impact on the properties of atom frequency standard [4, 5]. Placing a glass bubble filled with rubidium gas in the microwave cavity, microwave radiation field provided by microwave cavity can interact with rubidium gas inside the glass bubble and make rubidium atomic level transition occur [1, 6]. For some applications, it is desirable that microwave radiation field changes with the energy of rubidium gas at a certain frequency such as 6.835 GHz [7]. Generally, the resonant frequency is related to material property and rubidium gas parameters. So it is extremely critical for rubidium frequency standard design because of the effect of material property and rubidium gas parameters on resonant frequency.

The eigen value problem of microwave cavity filled with complicated materials belongs to the complex boundary value problem of electric and magnetic fields. And many methods, such as variation method, difference method, finite element method and mode matching method, etc. [8–13], are employed to study this problem. Though most researchers have studied boundary value problem of electric and magnetic fields, few papers published were paid more attention on theoretical analysis of complicated microwave cavity filled with rubidium gas [14, 15].

In this paper, the resonant frequency of HE₁₁₁ mode of the microwave cavity filled with ceramic material and rubidium gas is studied by mode matching method. In addition, the effects of the ceramic material and rubidium gas on the resonant frequency of the HE₁₁₁ mode are also analyzed. In addition, this work will propose a theoretical basis for the miniaturization of the microwave cavity.

2. THEORETICAL ANALYSIS

The basic structure of complicated microwave cavity which is used to exchange energy between gaseous rubidium and electromagnetic fields in rubidium frequency standard is modeled in Fig. 1. It is divided into three radial regions: p , q and t . Among these regions, region 2 will be filled with gaseous rubidium, regions 1, 3, 5, 7 and 9 are enclosed glass bubble, and region 6 is filled with ceramics. The microwave cavity and the outmost circuit are joined by regions 4, 8 and 10. The medium parameters in these regions are characterized by μ_{ri} and ε_{ri} ($i = 1, 2, 3, 4, 5, 6, 7, 8, 9, 10$), respectively, where μ_{ri} is the relative permeability of part i and ε_{ri} is the relative permittivity. All the loaded dielectrics are isotropic and $\mu_{r1} = \mu_{r2} = \mu_{r3} = \mu_{r4} = \mu_{r5} = \mu_{r6} = \mu_{r7} = \mu_{r8} = 1$.

In cylindrical coordinates, the longitudinal electric field components H_z of TE₀₁₁ mode in region

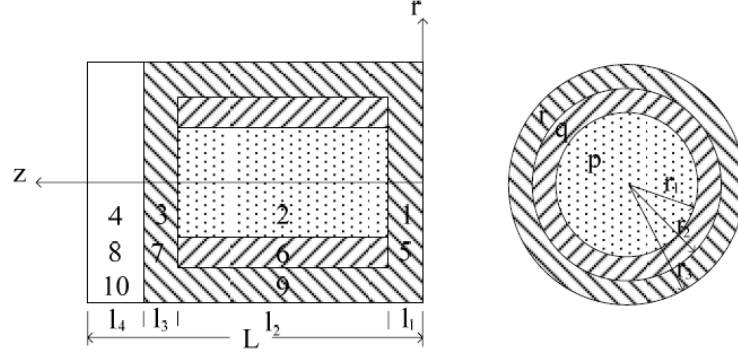


Figure 1: Basic structure of microwave cavity.

p are expressed as

$$H_{zp} = \sum_{m=1}^p A_m^p J_1(k_m^p r) \Phi_m^p(z) \quad (\text{region } p), \quad (1)$$

$$H_{zq} = \sum_{m=1}^{\infty} [A_m^q J_1(k_m^q r) + B_m^q N_1(k_m^q r)] \Phi_m^q(z) \quad (\text{region } q), \quad (2)$$

Considering the boundary condition of vanishing normal magnetic fields on the metallic wall surface, the magnetic field along the z axis in region t is

$$H_{zt} = \sum_{m=1}^{\infty} A_m^t \left[J_1(k_m^t r) + \frac{J_1(k_m^t r_3)}{N_1'(k_m^t r_3)} N_1(k_m^t r) \right] \Phi_m^t(z) \quad (\text{region } t), \quad (3)$$

where $J_1(k_m r)$ and $N_1(k_m r)$ are the first order Bessel function and zero order Neuman function, respectively. k_m^p , k_m^q and k_m^t represent the transverse propagation constants of region p , q and t , respectively. They are related to the resonant wave number k_0 and propagation constant β_{mi} in the following manner

$$\begin{aligned} (k_m^p)^2 &= k_0^2 \varepsilon_{ri} - \beta_{mi}^2 \quad (i = 1, 2, 3, 4), & (k_m^q)^2 &= k_0^2 \varepsilon_{ri} - \beta_{mi}^2 \quad (i = 5, 6, 7, 8), \\ (k_m^t)^2 &= k_0^2 \varepsilon_{ri} - \beta_{mi}^2 \quad (i = 9, 10). \end{aligned} \quad (4)$$

In region p , $H_z|_{z=0,L} = 0$. Enforcing field continuity condition of E_φ and H_r at the interface between the dielectric layers, the following Eigen equation comes into existence

$$\begin{aligned} & \frac{\tan \beta_{m2} l_2}{\beta_{m2}} + \frac{\tan \beta_{m1} l_1}{\beta_{m1}} + \frac{\tan \beta_{m3} l_3}{\beta_{m3}} + \frac{\tan \beta_{m4} l_4}{\beta_{m4}} - \frac{\beta_{m3}}{\beta_{m2} \beta_{m4}} \tan \beta_{m2} l_2 \tan \beta_{m3} l_3 \tan \beta_{m4} l_4 \\ & - \frac{\beta_{m3}}{\beta_{m1} \beta_{m4}} \tan \beta_{m1} l_1 \tan \beta_{m3} l_3 \tan \beta_{m4} l_4 - \frac{\beta_{m2}}{\beta_{m1} \beta_{m3}} \tan \beta_{m1} l_1 \tan \beta_{m2} l_2 \tan \beta_{m3} l_3 \\ & - \frac{\beta_{m2}}{\beta_{m1} \beta_{m4}} \tan \beta_{m1} l_1 \tan \beta_{m2} l_2 \tan \beta_{m4} l_4 = 0 \end{aligned} \quad (5)$$

Substituting (4) into (5), an equation about k_{mp} and k_0 is obtained.

In the same way, considering boundary condition $H_z|_{z=0,L} = 0$ and continuity condition of E_φ

and H_r lead to the following Eigen equation in region q and t

$$\begin{aligned} & \frac{\tan \beta_{m6} l_2}{\beta_{m6}} + \frac{\tan \beta_{m5} l_1}{\beta_{m5}} + \frac{\tan \beta_{m7} l_3}{\beta_{m7}} + \frac{\tan \beta_{m8} l_4}{\beta_{m8}} - \frac{\beta_{m7}}{\beta_{m6} \beta_{m8}} \tan \beta_{m6} l_2 \tan \beta_{m7} l_3 \tan \beta_{m8} l_4 \\ & - \frac{\beta_{m7}}{\beta_{m5} \beta_{m8}} \tan \beta_{m5} l_1 \tan \beta_{m7} l_3 \tan \beta_{m8} l_4 - \frac{\beta_{m6}}{\beta_{m5} \beta_{m7}} \tan \beta_{m5} l_1 \tan \beta_{m6} l_2 \tan \beta_{m7} l_3 \\ & - \frac{\beta_{m6}}{\beta_{m5} \beta_{m8}} \tan \beta_{m5} l_1 \tan \beta_{m6} l_2 \tan \beta_{m8} l_4 = 0, \end{aligned} \quad (6)$$

$$\frac{\tan \beta_{m7} (l_1 + l_2 + l_3)}{\beta_{m7}} + \frac{\tan \beta_{m8} l_4}{\beta_{m8}} = 0 \quad (7)$$

By matching the tangential field components at $r = r_1$ and $r = r_2$ and using the orthogonality of trigonometric function, a linear homogeneous system of equations is obtained as follows

$$\begin{pmatrix} X_1 & X_2 \\ X_3 & X_4 \end{pmatrix} \begin{pmatrix} A \\ B \end{pmatrix} = 0, \quad (8)$$

The special condition for the solution to these equations is that the determinant of the system matrix is equal to zero, i.e.,

$$\begin{vmatrix} X_1 & X_2 \\ X_3 & X_4 \end{vmatrix} = 0. \quad (9)$$

where $A = [A_1^q, A_2^q, \dots, A_m^q, \dots]'$, $B = [B_1^q, B_2^q, \dots, B_m^q, \dots]'$, X_1 , X_2 , X_3 and X_4 are partitioned matrix, respectively. The elements of this matrix are

$$\begin{aligned} x_{1im} &= \int_0^L \Phi_m^q(z) \Phi_i^p(z) dz \left[\frac{J_1(k_m^q r_1)}{J_1(k_i^q r_1)} - \frac{J_1'(k_m^q r_1) k_i^p}{J_1'(k_i^p r_1) k_m^q} \right], \\ x_{1im} &= \int_0^L \Phi_m^q(z) \Phi_i^p(z) dz \left[\frac{N_1(k_m^q r_1)}{J_1(k_i^p r_1)} - \frac{N_1'(k_m^q r_1) k_i^p}{J_1'(k_i^p r_1) k_m^q} \right], \\ x_{3im} &= \int_0^L \Phi_m^q(z) \Phi_i^t(z) dz \left[\frac{J_1(k_m^q r_2)}{J_1(k_i^t r_2) - \frac{J_1'(k_i^t r_3)}{N_1'(k_i^t r_3)} N_1(k_i^t r_2)} - \frac{J_1'(k_m^q r_2) k_i^r}{k_m^q \left[J_1'(k_i^t r_2) - \frac{J_1'(k_i^t r_3)}{N_1'(k_i^t r_3)} N_1'(k_i^t r_2) \right]} \right], \\ x_{4im} &= \int_0^L \Phi_m^q(z) \Phi_i^t(z) dz \left[\frac{N_1(k_m^q r_2)}{J_1(k_i^t r_2) - \frac{J_1'(k_i^t r_3)}{N_1'(k_i^t r_3)} N_1(k_i^t r_2)} - \frac{N_1'(k_m^q r_2) k_i^r}{k_m^q \left[J_1'(k_i^t r_2) - \frac{J_1'(k_i^t r_3)}{N_1'(k_i^t r_3)} N_1'(k_i^t r_2) \right]} \right]. \end{aligned}$$

Resonant frequencies of TE₀₁₁ mode of the complicated cavity can be calculated from (5), (6), (7) and (9).

3. CALCULATED RESULTS

In the microwave cavity, higher order modes have little influence on field distribution. In other words, the resonant properties are mainly determined by the low order modes. To make computation more convenient, (9) can be simplified to an identity by reserving the lowest mode.

Table 1 shows the frequencies of HE₁₁₁ mode of the complicated microwave cavity with different medium permittivity, assuming dimensions of $l_1 = 2$ mm, $l_2 = 28$ mm, $l_3 = 2$ mm, $l_4 = 10$ mm, $r_1 = 28$ mm, $r_2 = 30$ mm, $r_3 = 32$ mm. f_1 and f_2 denote the computed results and simulated results, respectively, and the unit of frequency is GHz. Rubidium vapor can be seen as some kind of dielectric and its relative permittivity is about determined by the equation $\varepsilon_r \approx 1 + \frac{N}{\varepsilon_0} \frac{\mu_0^2}{3kT}$, $N = 10^5$, $T = 300$ K. So the relative permittivity of the rubidium vapor is about 1.0005. It is clearly seen that the computed results excellently agree with the simulated results.

Figure 2 shows the curves of resonant frequency varying with rubidium molecular number inside the cavity with the parameters of $l_1 = 2$ mm, $l_2 = 28$ mm, $l_3 = 2$ mm, $r_1 = 28$ mm, $r_2 = 30$, $r_3 = 32$ mm, $\varepsilon_{r1} = \varepsilon_{r3} = \varepsilon_{r4} = \varepsilon_{r5} = \varepsilon_{r8} = \varepsilon_{r9} = 2.8$ and $\varepsilon_{r4} = \varepsilon_{r8} = \varepsilon_{r10} = 1$. Parameter L denotes the total cavity length. For the complicated microwave cavity, the temperature of rubidium gas is 300 K. The results show that the resonant frequency of the complicated microwave

Table 1: The comparison between computed results and simulated results.

ε_{r1}	ε_{r2}	ε_{r3}	ε_{r4}	ε_{r5}	ε_{r6}	ε_{r7}	ε_{r8}	ε_{r9}	ε_{r10}	f_1	f_2
1.0000	1.0000	1.0000	1.0000	1.0000	1.0000	1.0000	1.0000	1.0000	1.0000	4.5060	4.4980
1.0000	1.0005	1.0000	1.0000	1.0000	1.0000	1.0000	1.0000	1.0000	1.0000	4.5050	4.4970
2.8000	1.0005	2.8000	1.0000	2.8000	9.8000	1.0000	2.8000	1.0000	1.0000	4.0860	3.9940
3.3000	1.0005	3.3000	1.0000	3.3000	9.8000	3.3000	1.0000	3.3000	1.0000	4.0720	3.9330
1.0000	1.0005	1.0000	1.0000	1.0000	9.8000	1.0000	1.0000	1.0000	1.0000	4.3690	4.2950

cavity gradually decreases with the increasing of rubidium molecules number. When the rubidium molecules number increases, the rubidium gas polarization enhances and the equivalent permittivity of the rubidium gas increases, which directly leads to slightly decrease of the resonant frequency. Besides, the length of the cavity may be another factor that might contributes to the resonant frequency variation.

Figure 3 indicates how the resonant frequency varies with the glass radius r_3 . The parameters are set to be $l_1 = 2$ mm, $l_2 = 28$ mm, $l_3 = 2$ mm, $r_1 = 28$ mm, $r_2 = 30$, $\varepsilon_{r1} = \varepsilon_{r3} = \varepsilon_{r5} = \varepsilon_{r7} = \varepsilon_{r9} = 2.2$ and $\varepsilon_{r4} = \varepsilon_{r8} = \varepsilon_{r10} = 1$. As shown in Fig. 3, resonant frequency exhibits slightly decrease when the out radius r_3 increases. This phenomenon can be explained by dielectric perturbation theory [16]. As the outer radius increases, the perturbation body becomes larger, which directly causes the decrease of the frequency.

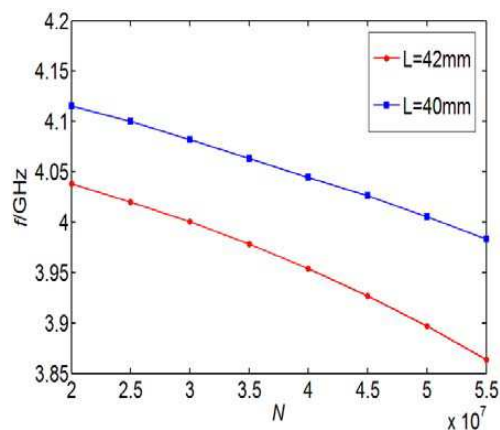
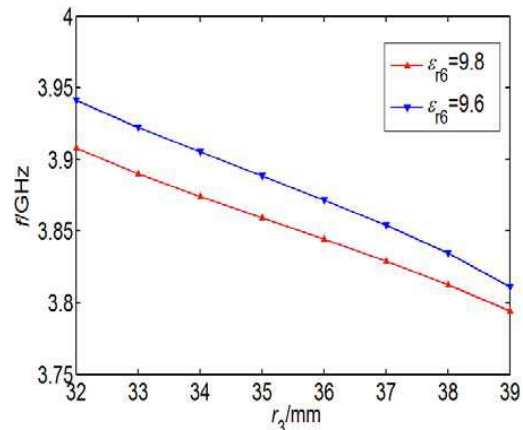


Figure 2: Variation of resonant frequency with molecule number.

Figure 3: Variation of resonant frequency with r_3 .

4. CONCLUSIONS

Resonant properties of a microwave cavity with ceramic material for a new type of rubidium clock are studied quantitatively by mode matching method. Resonant frequency of HE_{111} mode is then calculated by considering dielectric permittivity and rubidium gas parameters. The results show that decrease of the outer radius and the number of rubidium molecular number are all benefit for the increase of resonant frequency of the complicated microwave cavity with ceramic layer. These results play an important role in miniaturization and optimization of the microwave cavity for a new type of rubidium clock that has drawn considerably attention because of its potential application for communications.

ACKNOWLEDGMENT

This work was financially supported by the National Natural Science Foundation of China (Grant Nos. 61167005 and 61367007) and the Natural Science Foundation of Gansu province of China (Grant No. 1310RJYA021).

REFERENCES

1. Bandi, T., C. Affolderabch, and G. Mileti, "Laser-pumped paraffin-coated cell rubidium frequency standard," *Journal of Applied Physics*, Vol. 111, No. 124906, 1–8, 2012.

2. Huang, B. Y., *New Generation Atomic Clocks*, Wuhan University Press, Wuhan, 2006.
3. Vanier, J. and C. Mandache, “The passive optically pumped RB frequency standard: The laser approach,” *Appl. Phys. B*, Vol. 87, No. 4, 565–593, 2007.
4. Yi, L. and X. Z. Chen, “Research and progress of atomic clocks,” *Science*, Vol. 57, No. 5, 8–10, 2005.
5. Ning, X. L., S. B. Kang, F. Zhao, et al., “Laser pumped rubidium atomic frequency standard: An experimental study,” *Chinese J. Magn. Reson.*, Vol. 28, No. 3, 109–114, 2011.
6. Yang, S. Y., J. H. Tu, H. Feng, et al., “Experimental improvement investigation on microwave power frequency shift in rubidium atomic frequency standards,” *Atomic Energy Science and Technology*, Vol. 46, No. 6, 764–768, 2012.
7. Stefanucci, C., T. Bandi, F. Mwerli, et al., “Compact microwave cavity for high performance rubidium frequency standards,” *Review of Scientific Instruments*, Vol. 83, No. 104706, 1–8, 2012.
8. He, C. M., X. Y. Zhang, S. D. Run, et al., “Design of a digital temperature control circuit for rubidium atomic frequency standard,” *Chinese J. Magn. Reson.*, Vol. 26, No. 3, 175–384, 2009.
9. Liu, H. and W. M. Song, “The EM research of cylindrical cavity loaded with dielectric slabs,” *Journal of Microwaves*, Vol. 10, No. 1, 8–15, 1994.
10. Hu, C., H. S. Yang, and Z. Z. Lu, “Dyadic Green’s functions for dielectric loaded cylindrical cavity,” *Journal of Microwaves*, Vol. 12, No. 2, 212–225, 1996.
11. Cheng, R. T., “A method for computing resonant frequencies of cylindrical dielectric resonator mounted on a spacer,” *Journal of Microwaves*, Vol. 14, No. 3, 278–282, 1998.
12. John, G. H. and E. T. S. Michael, “Design of a microwave TE₀₁₁ mode cavity for a spacer borne H-maser,” *IEEE Transactions on Ultrasonics, Ferroelectrics, and Frequency Control*, Vol. 10, No. 52, 1638–1643, 2005.
13. Zhou, D. X., X. P. Chen, G. H. Huang, and S. P. Gong, “RMM analysis of TM₀ modes in a dielectric-loaded cylindrical resonant cavity,” *Chinese Journal of Radio Science*, Vol. 18, No. 4, 404–407, 2003.
14. Peng, Z. Q., J. H. Tu, H. Zhai, et al., “Simulation and experiments for the TE₁₁₁ microwave cavity of rubidium frequency standard,” *Journal of Astronautic Metrology and Measurement*, Vol. 28, No. 3, 26–30, 2008.
15. Cao, B. Z., S. X. Li, Q. Huang, et al., “Resonant characteristics of the mode HE₁₁₁ in microwave cavity for rubidium frequency standard,” *Journal of Lanzhou University (Natural Science)*, Vol. 46, No. 1, 124–128, 2010.

Dielectric Properties of Rice Husk/Carbon Nanotubes Composites in Ku-band

Y. S. Lee¹, F. Malek², E. M. Cheng³, Wei-Wen Liu⁴, F. H. Wee¹, M. N. Iqbal¹, L. Zahid¹,
M. S. Mezan², F. S. Abdullah², and M. Othman²

¹School of Computer and Communication Engineering, Universiti Malaysia Perlis (UniMAP)
Pauh Putra Campus, Arau, Perlis 02600, Malaysia

²School of Electrical Systems Engineering, Universiti Malaysia Perlis (UniMAP)
Pauh Putra Campus, Arau, Perlis 02600, Malaysia

³School of Mechatronic Engineering, Universiti Malaysia Perlis (UniMAP)
Pauh Putra Campus, Arau, Perlis 02600, Malaysia

⁴Institute of Nano Electronic Engineering (INEE), Universiti Malaysia Perlis (UniMAP)
Kangar, Perlis 01000, Malaysia

Abstract— This paper presents the dielectric properties of rice husk and carbon nanotubes (RHCNTs) composites materials. The RHCNTs composites materials prepared with various weight ratios of rice husk with CNTs 0–10 wt%. The length, width, and thickness of each RHCNTs composite sample are 15.799 mm, 7.899 mm, and 5 mm was fabricated. The rectangular waveguide technique was used to measure the complex relative permittivity of the RHCNTs composites materials. The conversion of s -parameters to complex relative permittivity parameter is computed by using 85071E Agilent technology software which using a transmission line technique consists of a network analyzer to perform the conversion to complex relative permittivity, ϵ_r . The complex relative permittivity is represented in terms of both the real and imaginary parts of permittivity in Ku-band frequency. The conductivity of RHCNTs shows increasing when the ratio of CNTs mixture increases. The materials, their dielectrics properties measurement result over 12.4–18 GHz frequency range are discussed.

1. INTRODUCTION

In recent years, rice husk (RH) is an agriculture waste material which potential used as microwave absorber been reported [1, 2]. Due to their complex permittivity, RH can design in pyramidal or flat microwave absorber [3–5]. Complex permittivity of a material is important parameter for microwave absorber application. The objective of this paper is to increase/enhance the complex permittivity of RH material by composites the RH with carbon nanotubes (CNTs). Recent years, CNT composites have potential applied in electronic, mechanical, and microwave application due to their unique properties [6, 7]. To form the composites, raw RH and CNTs were mixed with polyester and methyl-ketone-polymer. The RH was composite with difference amount of CNTs from 0% to 10% of weight ratio. The complex relative permittivity ($\epsilon_r = \epsilon'_r - j\epsilon''_r$) of rice husk and carbon nanotubes composites (RHCNTs) is measured and investigated in Ku-band. The real part of complex permittivity is the ability of a material to store electromagnetic wave, whereas the imaginary part of the complex permittivity is the ability of the material convert the electromagnetic wave into heat and dissipated. Furthermore, the alternative current (AC) conductivity can calculate by using Equation (1) [8]:

$$\sigma_{ac} = \omega\epsilon_0\epsilon''_r \quad (1)$$

where, σ_{ac} is the conductivity due to the alternating field (S/m), ω is the angular frequency (rad/s), ϵ_0 is the permittivity in free space, ϵ''_r is the imaginary part of relative complex permittivity (loss factor).

2. PREPARATION OF SAMPLES

First, the rice husk and CNTs were mix with polyester resin and methyl ethyl ketone peroxide (MEKP) harden agent. The RHCNTs composites were stir for 1 hour shown in Figure 1. After the composition, the RHCNTs composite were filled into waveguide sample holder to fabricate the rectangular shape sample for WR-62 waveguide. The RHCNTs samples were fabricated by using WR-62 sample holder mould shown in Figure 2. The RHCNTs samples were prepared in rectangular shapes, which fit into WR-62 waveguide sample holders.



Figure 1: RHCNTs after stir with polyester and MEKP.

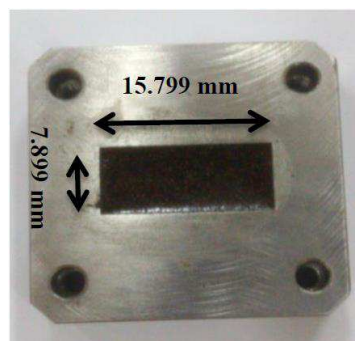


Figure 2: Ku-Band sample holder fit with RHCNTs sample.

3. EXPERIMENTAL

Before conduct to the measurement, calibration technique TRL (through-reflect-line) of waveguide flanges must be applied. The calibration technique is to minimize the residual errors of the measurements. The Dielectric properties were measured using rectangular waveguide transmission line technique. A pair of coaxial cable was connected to Agilent E8362B performance network analyzer and the two waveguide adaptors were connected with coaxial cables. The sample holder was place between the two waveguide adaptors. The 85071E software is originally developed by NRW to calculate the permittivity from transmission and reflection coefficient [9]. Figure 2 shows the dielectric measurement setup.

4. RESULTS AND DISCUSSION

The complex relative permittivity of samples versus frequency was shown in Figures 3(a) and (b). The complex relative permittivity of real part (dielectric constant, ϵ_r') and imaginary part (loss factor, ϵ_r'') of the composites increased over the measured frequency region with increasing the quantity percentage of CNTs. For rice husk, the average values of ϵ_r' and ϵ_r'' were 2.982 and 0.283 respectively. The RH-CNTs2%, RH-CNTs4%, and RH-CNTs10% samples has the average values of ϵ_r' was 5.448, 6.443, and 14.972 respectively. The average values of ϵ_r'' was increases from 0.283 (rice husk) to 8.492 (RH-CNTs10%). By increasing the quantity of CNTs in RHCNTs composites can enhance complex relative permittivity of the composites materials.

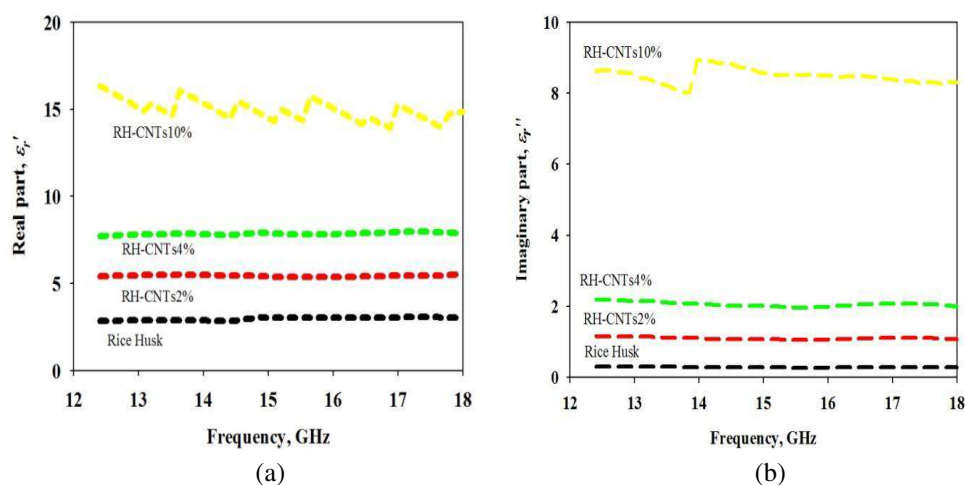


Figure 3: (a) Real part and (b) imaginary part of complex relative permittivity of samples.

Figure 4 shows the conductivity of samples. From the graph, RH-CNTs10% sample has the highest conductivity (580–800) S/cm than rice husk, RH-CNTs2%, and RH-CNTs4%. The conductivity of the RHCNTs composites is increasing when the content of CNTs increases in the RHCNTs composition. Refer to the Equation (1), the conductivity is proportional to the imaginary of complex

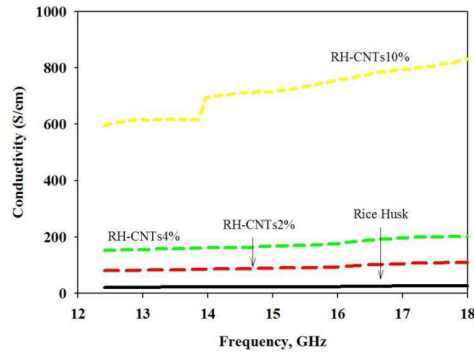


Figure 4: Conductivity of RHCNTs samples.

relative permittivity and frequency. Therefore, increase the quantity of CNTs in the RHCNTs composites, ϵ_r'' increased and the conductivity of the RHCNTs composites also increased. The average values conductivity of rice husk, RH-CNTs2%, RH-CNTs4%, and RH-CNTs10% samples were 24, 93, 174, and 717 S/cm respectively. The average values of dielectric constant, ϵ_r' , loss factor, ϵ_r'' , and conductivity, σ_{ac} are shown in Table 1.

Table 1: Average values of ϵ_r' , ϵ_r'' , and σ_{ac} .

Sample	Average values		
	Dielectric constant, ϵ_r'	Loss factor, ϵ_r''	Conductivity, (S/cm)
RH	2.982	0.283	24
RH-CNT2%	5.448	1.100	93
RH-CNT4%	6.443	1.584	174
RH-CNT10%	14.972	8.492	717

5. CONCLUSIONS

The complex relative permittivity of rice husk successful enhanced with composites rice husk with carbon nanotubes. The RHCNTs was increased up to 14.972 of dielectric constant and 8.492 of loss factor with composites with 10% CNTs. The conductivity of RHCNTs also increased from 24 S/cm (rice husk) up to 717 S/cm (RH-CNTs10%) over 12.4–18 GHz frequency range. Hence, the RHCNTs samples are suitable to apply in dielectric microwave absorber and shielding materials due to their complex permittivity and conductivity performance.

ACKNOWLEDGMENT

The authors acknowledge the University Malaysia Perlis and the Malaysian Ministry of Higher Education for providing the Fundamental Research Grant Scheme (FRGS Grant No. 9011-00011), which enabled the publication of this article.

REFERENCES

1. Nornikman, H., M. F. B. A. Malek, M. Ahmed, F. H. Wee, P. J. Soh, A. A. A.-H. Azremi, S. A. Ghani, A. Hasnain, and M. N. Taib, "Setup and results of pyramidal microwave absorbers using rice husks," *Progress In Electromagnetics Research*, Vol. 111, 141–161, 2011.
2. Nornikman, H., M. F. B. A. Malek, P. J. Soh, A. A. A.-H. Azremi, F. H. Wee, and A. Hasnain, "Parametric study of pyramidal microwave absorber using rice husk," *Progress In Electromagnetics Research*, Vol. 104, 145–166, 2010.
3. Malek, H. N. and F. O. Nadiyah, "Pyramidal microwave absorber design from waste material using rice husk and rubber tire dust," *Journal of Telecommunication, Electronic and Computer Engineering*, Vol. 4, No. 1, 2012.
4. Iqbal, M. N., M. F. B. A. Malek, S. H. Ronald, M. S. Bin Mezan, K. M. Juni, and R. Chat, "A study of the emc performance of a graded-impedance, microwave, rice-husk absorber," *Progress In Electromagnetics Research*, Vol. 131, 19–44, 2012.

5. Iqbal, M. N., et al., “A study of the anechoic performance of rice husk-based, geometrically tapered, hollow absorbers,” *International Journal of Antennas and Propagation*, Vol. 2014, 2014.
6. Logakis, E., et al., “Highly conducting poly (methyl methacrylate)/carbon nanotubes composites: Investigation on their thermal, dynamic-mechanical, electrical and dielectric properties,” *Composites Science and Technology*, Vol. 71, 854–862, 2011.
7. Spitalsky, Z., et al., “Carbon nanotube–polymer composites: Chemistry, processing, mechanical and electrical properties,” *Progress in Polymer Science*, Vol. 35, 357–401, 2010.
8. Al-Saleh, M. H., et al., “EMI shielding effectiveness of carbon based nanostructured polymeric materials: A comparative study,” *Carbon*, Vol. 60, 146–156, 2013.
9. Agilent_Technical_Overview, “Agilent technical overview. Agilent 85071E materials measurement software,” *Agilent Literature Number 5988-9472EN.*, 2012.

Contribution of Evanescent Waves to Vortex Vector Field with Inhomogeneous Polarization in Near Field

Yin-Long Feng¹ and Rui-Pin Chen^{1,2}

¹School of Sciences, Zhejiang A & F University, Lin'an, Zhejiang 311300, China

²Department of Physics, Zhejiang Sci-Tech University, Hangzhou 310018, China

Abstract— We study the evanescent wave of a vortex vector optical field with inhomogeneous states of polarization in the cross section of the field. The TE and TM terms of the evanescent wave and the propagating wave of a cylindrical vortex vector optical field with inhomogeneous states of polarization in the cross section of the field are derived by the vector angular spectrum method. The vector structure of the evanescent wave and propagating wave components of the cylindrical vector field is demonstrated. The ratio of the evanescent wave and the propagating wave of a cylindrical vector optical field with different states of polarization with different vortex charges n and polarization charges m as a function of propagation distance in near field is described. Comparison between the contribution of TE and TM terms of both the propagating and the evanescent waves of the cylindrical vortex vector field in free space is demonstrated. The intensity (squared modulus) distributions of the TE and TM terms of the propagating and evanescent waves are described to compare the contributions of the propagating and the evanescent waves associated with the cylindrical vector field with inhomogeneous states of polarization in the cross section of the field. These results, therefore, provide useful information on how to spatially manipulate the evanescent waves of a vortex vector cylindrical optical field in near field by choosing appropriate vortex charges n and states of polarization in the cross-section of the field.

Recently, the vector optical field with the different states of polarization in the cross-section of the field has attracted much interest in linear and nonlinear optics realms due to its novel properties and potential application [1, 2]. In the Cartesian coordinate system, the z -axis is taken to be the propagation axis. A cylindrical optical vector field is expressed as [1, 2]

$$E(r, \theta) = A(r, \theta)[\cos(m\theta + \theta_0)e_x + \exp(i\Delta\theta) \sin(m\theta + \theta_0)e_y], \quad (1)$$

where $r = \sqrt{x^2 + y^2}$ and $\theta = \arctan(y/x)$ are the polar radius and azimuthal angle in the polar coordinate system, respectively. m is the topological charge, and θ_0 is the initial phase. e_x and e_y are the unit vectors in x and y -direction, respectively. m is the topological charge, and θ_0 is the initial phase. e_x , e_y and e_z are the unit vectors in x , y and z -direction, respectively. When $m = 1$ with $\theta_0 = 0$ and $\pi/2$, the vector fields describe the radially and azimuthally polarized vector fields, respectively. When $m = 0$, Eq. (1) degenerate to the linearly-polarized fields. $A(r)$ represents the amplitude distribution in the cross-section of the cylindrical vector field. For the case with $\Delta\theta \neq 0$ (Eq. (1)), however, the x - and y -components have different phase, indicating a hybrid-polarized vector field with the linear, circular and elliptical polarization states located at different position in the field cross-section.

For the Gaussian distribution with the n -th vortex and an arbitrary polarized electromagnetic field (see Eq. (1)) in the source plane $z = 0$, $A(r, \theta) = \exp(-r^2/w^2) \exp(in\theta)$ where w is beam-width. By using the Fourier transform, the angular spectrum is

$$\begin{aligned} A(\rho \cos \phi, \rho \sin \phi) = & Q \{ P \exp[i(m\phi + n\phi + \theta_0)](e_x - i \exp(i\Delta\theta)e_y) \\ & + T \exp[-i(m\phi - n\phi + \theta_0)](e_x + i \exp(i\Delta\theta)e_y) \\ & - [P \exp[i(m\phi + n\phi + \theta_0)](\cos \phi - i \exp(i\Delta\theta) \sin \phi) \\ & + T \exp[-i(m\phi - n\phi + \theta_0)](\cos \phi + i \exp(i\Delta\theta) \sin \phi)] \rho / \gamma e_z \} \quad (2) \end{aligned}$$

with

$$\begin{aligned} P &= I_{(m+n-1)/2}(k^2 w^2 \rho^2 / 8) - I_{(m+n+1)/2}(k^2 w^2 \rho^2 / 8) \\ T &= I_{(m-n-1)/2}(k^2 w^2 \rho^2 / 8) - I_{(m-n+1)/2}(k^2 w^2 \rho^2 / 8) \\ Q &= \pi i^{m+n} \left(\frac{k}{2\pi} \right)^2 \frac{\sqrt{\pi} k w^3 \rho}{8} \exp(-k^2 w^2 \rho^2 / 8) \end{aligned}$$

where k is the wavenumber $I(\cdot)$ are the Bessel functions of the second kind and e_z is the unit vector in z direction. The electric field component of the vector cylindrical optical field in z plane can be represented as

$$\begin{aligned}
E(r) = & (-1)^{m+n} \frac{k^3 w^3 \sqrt{\pi}}{16} \int_0^\infty e^{-\frac{k^2 w^2 \rho^2}{s}} \{ P J_{m+n}(-kr\rho) \exp[i(m\theta + n\theta + \theta_0)] (e_x - i \exp(i\Delta\theta) e_y) \\
& + T J_{m-n}(-kr\rho) \exp[-i(m\theta - n\theta + \theta_0)] (e_x + i \exp(i\Delta\theta) e_y) \\
& + [P J_{m+n+1}(-kr\rho) \exp[i(m\theta + n\theta + \theta + \theta_0)] (1 - \exp(i\Delta\theta)) \\
& + P J_{m+n-1}(-kr\rho) \exp[i(m\theta + n\theta - \theta + \theta_0)] (1 + \exp(i\Delta\theta))] \\
& + T J_{m-n-1}(-kr\rho) \exp[-i(m\theta - n\theta - \theta + \theta_0)] (1 + \exp(i\Delta\theta)) \\
& + T J_{m-n+1}(-kr\rho) \exp[-i(m\theta - n\theta + \theta + \theta_0)] (1 - \exp(i\Delta\theta)) \} i\rho/2\gamma e_z \} \times \exp(ik\gamma z) \rho^2 d\rho \quad (3)
\end{aligned}$$

In order to compare the contributions of the propagating and the evanescent waves associated with the cylindrical vector field, the integrated intensity (squared modulus) of the propagating and evanescent fields, I_{pr} and I_{ev} , are calculated respectively [3, 4]:

$$I_{pr} = \iint |E_{pr}|^2 dx dy = \int_0^1 \int_0^{2\pi} [|a|^2 + |b|^2] \rho d\rho d\phi, \quad (4)$$

$$I_{ev} = \iint |E_{ev}|^2 dx dy = \int_1^\infty \int_0^{2\pi} [|a|^2 + |b_{ev}|^2] \exp(-2kz\sqrt{\rho^2 - 1}) \rho d\rho d\phi, \quad (5)$$

with

$$a = A(\rho, \phi) \cdot e_1 \quad b = A(\rho, \phi) \cdot e_2 \quad b_{ev} = A(\rho, \phi) \cdot e_{ev},$$

For $m = 1$,

$$I_{pr} = 2\pi \int_0^1 |Q|^2 [(P^2 + T^2)(2 - \rho^2) + 2\rho^2 PT \cos^2(\Delta\theta/2) \cos(2\theta_0)] / (1 - \rho^2) \rho d\rho \quad (6)$$

$$\begin{aligned}
I_{ev} = & 2\pi \int_1^\infty |Q|^2 [(P^2 + T^2)(2 - 3\rho^2 + 2\rho^4) + 2(3\rho^2 - 2\rho^4) PT \cos^2(\Delta\theta/2) \cos(2\theta_0)] \\
& \frac{\exp(-2kz\sqrt{\rho^2 - 1}) \rho}{1 - 3\rho^2 + 2\rho^4} d\rho \quad (7)
\end{aligned}$$

For $m > 1$,

$$I_{pr} = 2\pi \int_0^1 |Q|^2 [(P^2 + T^2)(2 - \rho^2)] / (1 - \rho^2) \rho d\rho \quad (8)$$

$$I_{ev} = 2\pi \int_1^\infty |Q|^2 (P^2 + T^2) \frac{(2 - 3\rho^2 + 2\rho^4) \exp(-2kz\sqrt{\rho^2 - 1})}{1 - 3\rho^2 + 2\rho^4} \rho d\rho \quad (9)$$

The substitution of Eqs. (4)–(7) into Eqs. (8) and (9), and performing integration over θ from zero to 2π yield a single integration of ρ . Then, the corresponding results can be obtained by performing numerical integration over ρ . The ratio $\delta = (I_{pr} - I_{ev})/I_{pr}$ provides direct information about the propagating and evanescent components of the field.

The ratio $\delta = (I_{pr} - I_{ev})/I_{pr}$ for $w = 0.1\lambda$ (highly non-paraxial case) and $w = 0.5\lambda$ cases as a function of different distances z from the initial plane $z = 0$ are shown in the Fig. 1. The evanescent field dominates near the source plane and the relative weight of I_{ev} would drastically decrease with the increasing propagation distance. Thus it can be negligible in the propagation distance $z = 0.5\lambda$ as shown in Fig. 1. Comparing Figs. 1(a) with (b), one can recognize that the relative weight of I_{ev} would reduce when the waist size w increases. i.e., the relative weight of the evanescent wave component is increasing with increasing non-paraxial as the waist size w decreases. The relative weight of I_{ev} would increase with the increasing topological charge. It can be explained that the field distribution will increasingly diverge and extend from the center of beam with the increasing topological charge. As a result, the relative weight of I_{ev} would increase with the increasing topological charge under the same conditions and beam parameters.

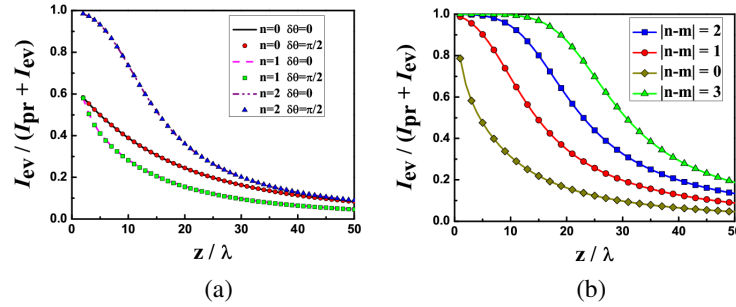


Figure 1: Ratio of the propagating and evanescent components of the field as a function of the propagation distances with (a) $m = 1$; (b) $m = 2, 3$.

The calculation results indicate that the evanescent wave component with different initial phase θ_0 for any topological charge (except $m = 1$) is same as shown in Fig. 1. For $m = 1$ case with different initial phase θ_0 , the relative weight of I_{ev} of the azimuthal polarization ($m = 1, \theta = \pi/2$) is maximum and the relative weight of I_{ev} of the radial polarization ($m = 1, \theta = 0$) is minimum as shown in Fig. 1. The physical explanation for the exception $m = 1$ is that the values of z -components of either propagation wave or evanescent wave are different with the different initial phase θ_0 , the values of z -components of either propagation wave or evanescent wave are maximum for $\theta_0 = \pi/2$ (i.e., radial polarization) whereas the z -components of either propagation wave or evanescent wave are zero for $\theta_0 = 0$ (i.e., azimuthal polarization).

REFERENCES

1. Zhan, Q. W., "Cylindrical vector beams: From mathematical concepts to applications," *Adv. Opt. Photon.*, Vol. 1, 1–57, 2009.
2. Wang, X. L., Y. N. Li, J. Chen, C. S. Guo, J. P. Ding, and H. T. Wang, "A new type of vector fields with hybrid states of polarization," *Opt. Express*, Vol. 18, 10786–10795, 2010.
3. Martínez-Herrero, R., P. M. Mejías, S. Bosch, and A. Carnicer, "Vectorial structure of non-paraxial electromagnetic beams," *J. Opt. Soc. Am. A*, Vol. 18, 1678–1680, 2001.
4. Chen, R. P. and G. Li, "The evanescent wavefield part of a cylindrical vector beam," *Opt. Express*, Vol. 21, 22246–22254, 2013.

VEMC Computing System for Electromagnetic Compatibility of Integrated Circuits

Boyuan Zhu¹, Hengxu Li¹, Junwei Lu¹, Haiyan Sun², Ling Sun², and Lingling Yang²

¹School of Engineering, Griffith University, Brisbane, Australia

²College of Electrical Engineering, Nantong University, Nantong, China

Abstract— This paper introduces a newly developed virtual electromagnetic compatibility (VEMC) computing system and related techniques for electromagnetic compatibility (EMC) computer modelling, simulation and optimisation in integrated circuit (IC). The system is a high performance computation and collaborative visualisation platform which provides researchers and engineers with an integrated and flexible computation environment in modeling, simulation and optimisation of IC EMC issues. It meets various computation needs and increases machine usage and computation efficiency of computation resources. A case study presents computational models of interested issues in IC-level EMC modelled, simulated and optimised by the developed system.

1. INTRODUCTION

In modern IC-level EMC, computational electromagnetic (CEM) modelling and visualisation techniques become most significant considerations [1–3]. They are now an integral part of design in engineering practice and implemented to solve real life EMC problems which is proved extremely important for this high EMC risks industry. Traditional “build then test” procedure for EMC was proved time consumed and very expensive in terms of cost. CEM modelling and visualisation allows designer to investigate, monitor and modify the interested area of the design at an early stage, which makes it play an important role in scientific research and industry applications of IC.

Visualisation and high performance computation are closely related that utilizes visualisation techniques to deal with the complicated dynamic electromagnetic problems. Due to the variety and complexity of different IC EMC problems, it always requires engineers from different disciplines work collaboratively to analyse and optimise the solution together. Using interactive and collaborative visualisation techniques [4] provide an alternative solution to achieve best performance and efficiency of teamwork. However, current CEM products and systems are still dominated by single user oriented designs.

The virtual electromagnetic compatibility (VEMC) computing system is a high performance distributed and parallel computation and visualisation system designed for requirements of high-load EMC modelling, simulation and optimisation tasks. Parallel and distributed computation is supported. It integrates a full electromagnetic modelling and simulation environment with various pre-defined model libraries and templates. The system uses cloud computing concept to offer users a remote working environment on the modelling and simulation. With this system, users do not need to install huge amount of professional software. The cost of entire system is well controlled comparing to professional supercomputing cluster structure due to its generic business computer based.

2. VEMC COMPUTING SYSTEM

2.1. System Architecture

The VEMC computing system uses a distributed computing architecture. It is a structure that involves multi-computers collaborating remotely from each other. Every computer under this architecture will be assigned a role in the computation or data processing. As shown in Figure 1, the cloud controller (CLC) is the main server of system which is used to provide multi-functions of access authority, load balance, license management, gate way and firewall. The user information and database are stored in the database (DB). A web service manager (WSM) is connected with CLC to provide system GUI. The cloud storage pool (SP) contains a pre-defined model library, virtual machine OS image file and other software image. Computation nodes are scalable in the system according to user’s demand.

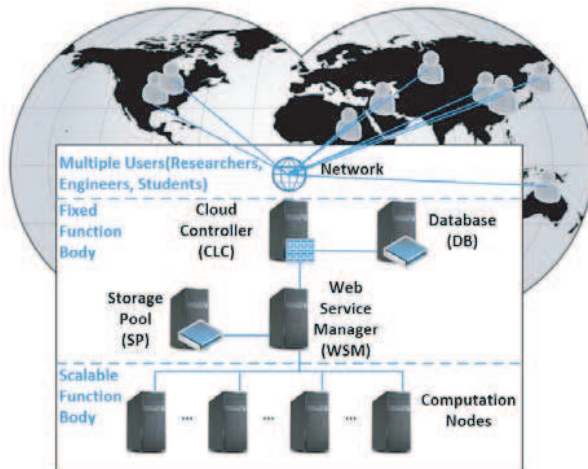


Figure 1: VEMC computing system structure.

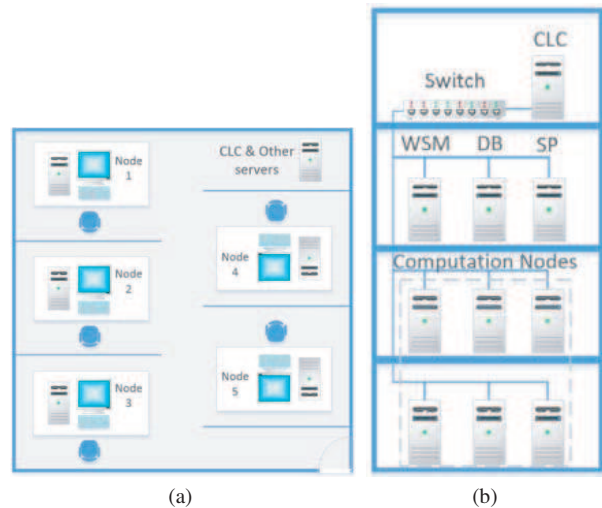


Figure 2: (a) Distributed structure and (b) assembly structure of VEMC computing system structure.

2.2. System Features

2.2.1. Cost Effective and Scalability

The VEMC computing system is built up with generic desktops which is found much cost effective and flexible. Computation using supercomputer can provide user with extreme performance but the system itself is high cost, hard to maintain and has an unfriendly interface. As compared in [5], it is surprised to find that the generic business desktop has the lowest cost per megaflop/s comparing to other supercomputing platforms. The cost of system is directly against the number of physical machines.

The architecture of VEMC computing system is very flexible, as shown in Figure 2. It can be setup and implemented according to the teaching demand. For any organizations, even old computers can also be assigned as computing nodes and added into the system. All computer nodes in the system are able to be added and removed as required, which means the system is of a strong scalability to satisfy the demand of students scale. It is also power efficient as the administrator can decide how many nodes to be turned on and off at any time.

2.2.2. Cloud Computation and Advanced Control

As a cloud computing based computation system, it enables a convenient, on-demand network access to a shared pool of configurable computing resources [6]. The user just needs to connect with the cloud and then can work anywhere anytime. The computer hardware resources, such as CPU core number, memory size, and disk space can be allocated within seconds by the request of end-user. The user can setup a new working environment by importing the pre-configured image file from the cloud storage server in a few minutes.

VEMC computing system automatically controls and optimises resource by a newly developed load balance control system. Resource usage can be monitored, controlled and reported by both service provider and user. Also, the system supports real-time process migration that secures user process and avoids data loss from system corruption.

2.2.3. Collaborative Visualisation

The system allows multiple users to access same project simultaneously under a secured channel across different platforms using collaborative visualisation techniques, as shown in Figure 3. Thus, it offers great convenience for multiple users, for example, a group of students, to discuss and collaborate on one modelling or simulation project. The template is used to format your paper and style the text. All margins, column widths, line spaces, and text fonts are prescribed; please do not alter them. You may note peculiarities. For example, the head margin in this template measures proportionately more than is customary. This measurement and others are deliberate, using specifications that anticipate your paper as one part of the entire proceedings, and not as an independent document. Please do not revise any of the current designations.



Figure 3: Collaborative visualisation across different platforms.

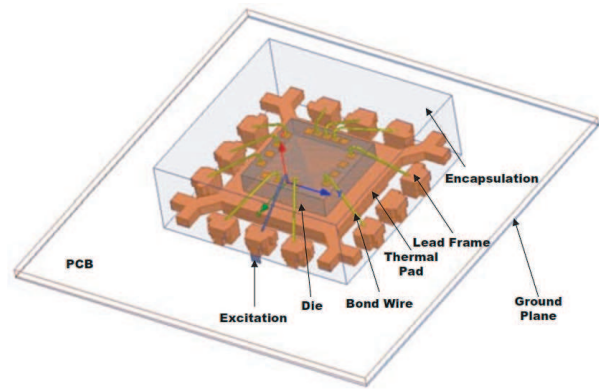


Figure 4: Simulation model of MMIC.

3. COLLABORATIVE SIMULATION OF A MONOLITHIC MICROWAVE INTEGRATED CIRCUIT (MMIC)

EMC of IC cannot be neglected in the modern electronic system due to the constant speed of growth in semiconductor technology. Therefore, IC-level EMC has taken an important position in the modern IC design. Comparing to traditional procedure of IC design, it requires more collaborative work when considering IC-level EMC. There is one prototype VEMC computing system available at Nathan campus, Griffith University, which conducts following modelling, simulation and optimisation in IC EMC.

3.1. MMIC Simulation Model

The MMIC operates at 24GHz in a small and high frequency device. The chip is packaged in a quad-flat no-leads (QFN) package with 12 pins. The size of the QFN package of the MMIC is 2 mm (length) \times 2 mm (width) \times 0.75 mm (height). The QFN package technology mounts the IC directly onto the surface of the PCB with no through-holes. The internal connections between the die and lead frame are bond wires. The simulation model is as shown in Figure 4. The excitation is set up at a lead, which is functioning as the only microwave port in the physical model. Some critical size parameters of the model are shown in Figure 5.

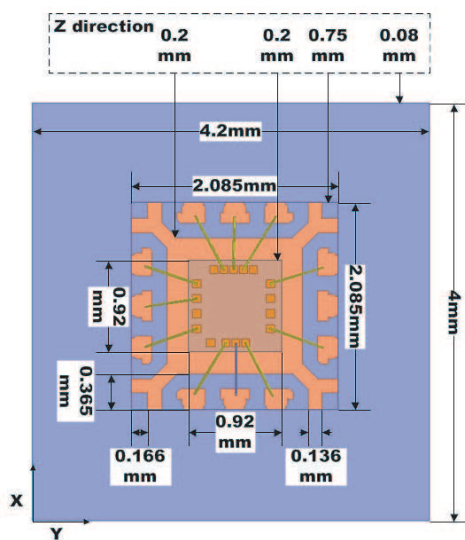


Figure 5: Size of simulation model of MMIC.

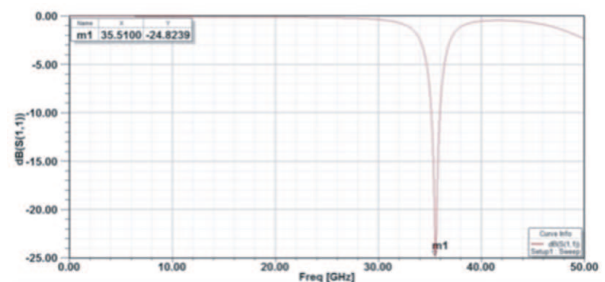


Figure 6: Reflection coefficient of the simulation model from 0 to 50 GHz.

The radiation boundary condition is used as a box shape surrounding the model. The materials assignment of the simulation model is described in Table 1.

Table 1: Materials assignment of the simulation model.

Name	Materials	Permittivity	Conductivity (Siemens/m)
Ground Plane	Copper	1	5.8×10^7
PCB	FR4 epoxy	4.4	0
Die	GaAs	12.9	0
Encapsulation	EME-G770HCD	4.2	0
Thermal Pad	Copper	1	5.8×10^7
Lead Frame	Copper	1	5.8×10^7
Bond Wire	Copper	1	5.8×10^7

3.2. Full-wave Techniques in the Frequency Domain

A full-wave electromagnetic solution, which solves electromagnetic problems with Maxwell's equations, is of great importance to high performance VLSI design in computational electromagnetics. With numerous fast numerical algorithms developed, the finite element method (FEM) is relatively efficient in finding approximate solutions of partial differential equations (PDE). The frequency domain vector wave equation for E field can be derived as:

$$\nabla \times \frac{1}{\mu} \nabla \times \vec{E} + \sigma_e \omega \vec{E} + \omega^2 \epsilon \vec{E} = -j\omega \vec{J} \quad (1)$$

where ω is the angular frequency, J is the source current density, σ_e is the effective conductivity, and μ and ϵ are the permeability and permittivity of the problem space respectively.

Simulations in the followed discussion are applied by a full-wave frequency domain solution with variable sized meshes. Frequency is set up to sweep in a specific range to determine the expectant resonant frequency. However, determining the correct frequency range is important for simulation results. Computational errors may be introduced if the frequency range of the solution is mismatched.

3.3. Simulation Results

Simulation is conducted under an excitation with the frequency swept from 0 to 50 GHz. The reflection coefficient plot shows there is a resonant frequency occurring at 35.51 GHz with -24.8239 dB as shown in Figure 6.

An E field plot of die surface at 36.01 GHz is produced in Figure 7. It is found that the electric field intensity is highest in the centre position at 1.5998×10^3 V/m.

As presented in Figure 8, the simulation result shows radiation power emitted vertically along the $+Z$ axis. The power radiating underneath the model is very weak.

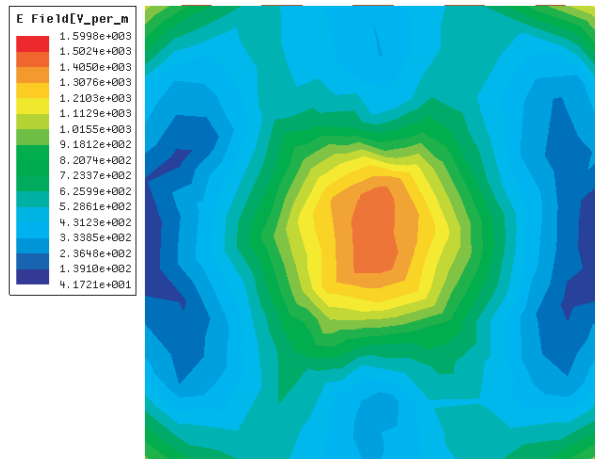
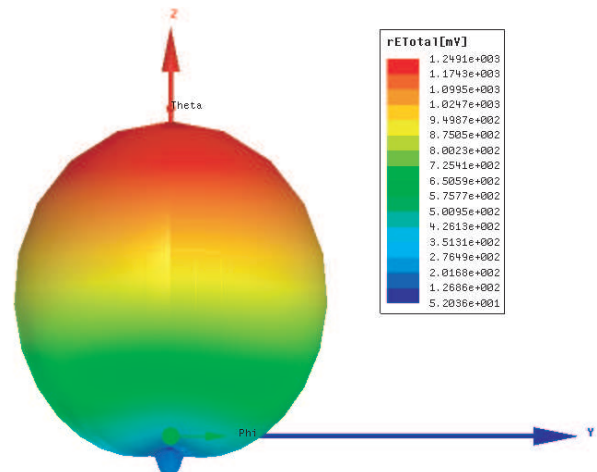

 Figure 7: E field simulation plot of die surface.


Figure 8: Far-field 3-D plot of the simulation model at 36.01 GHz.

4. PARALLEL OPTIMISATION OF MULTI-LAYER INTERCONNECTS

Parallel computation is another key attribution needed for IC EMC, especially in optimisation. For instance, optimisation of coupling issue regarding to multi-layer interconnects of IC requires a high load of computation resource.

4.1. Structure Modelling for MultilayerInterconnects of IC

As shown in Figure 9, it is an advanced multilayer structure for interconnects of IC. There are five levels of conductors inside two isolated layers upon a silicon substrate. Each layer is isolated by a low permittivity material. The population $G(t)$ for optimisation is the matrix of $[X1, X2, \dots, X8, Y9, Y10]$, as shown in Figure 10. With different combination of conductor positions, it varies the total ground capacitance and the total coupling capacitance of interconnects. The aim of this optimisation is to find out the best allocation of conductors which contributes to the lowest value for the trade- off between total ground capacitance and total coupling capacitance of interconnects.

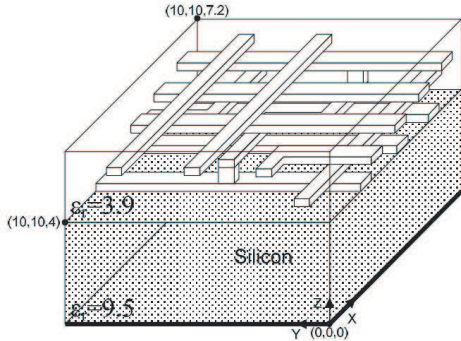


Figure 9: 3D multi-layer interconnects for optimization.

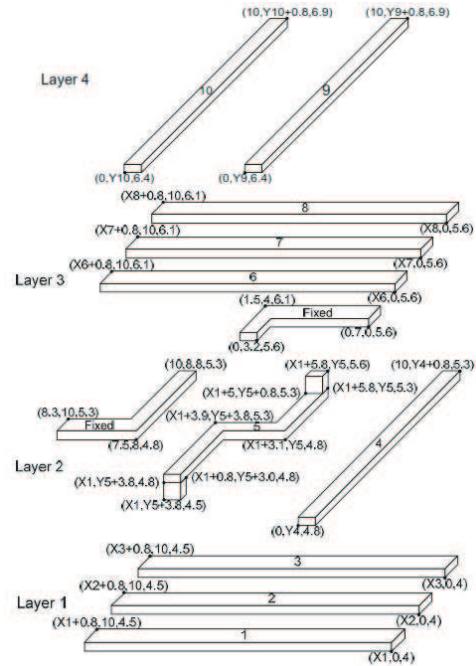


Figure 10: Dimension details of 3D multi-layer interconnects.

4.2. Capacitance Calculation Methodology

An accurate and fast method of capacitance calculation is to apply the principle of energy conservation using electrical field energy stored in the volume V . The electrostatic energy of a linear N electrode (the N th is ground) system is:

$$W = \frac{1}{2} \sum_{i=1}^N C_{ii}^g V_i^2 + \frac{1}{2} \sum_{i=1, j=1, i \neq j}^N C_{ij}^g V_i V_j \quad (2)$$

where, W is electrostatic energy; V_i or V_j is the potential of i th electrode with respect to the ground; C_{ii}^g is the self-ground capacitance of i th electrode and C_{ij}^g ($i \neq j$) is the mutual ground capacitance between electrodes. By applying appropriate voltages on electrodes, the coefficients of the ground capacitance can be calculated from the stored static energy.

4.3. Optimisation Method Applied via VEMC System

The selected optimisation method is the improved version of non-dominated sorting genetic algorithm (NSGA), NSGA-II [7]. It performs a fast multi-objective evolution in terms of finding a diverse set of solutions and in converging near the true Pareto-optimal set. The first step initialized the population (size N) based on the defined problem range and constraints. Then the non-dominated sorting is applied on initialized population, which is sorted based on non-domination

into each front. The first front is completely non-dominant set in the current population and the second front is dominated by the individuals in the first front only, and the front goes so on. After non-dominated sorting is done, the crowding distance is calculated and assigned for all individuals in the population. Based on the rank and crowding distance, parents are selected for evaluation manipulation which generates the offspring population. The current population and generated offspring will be combined again based on the non-domination. Only the best N individuals are selected for new population and others are truncated. Thus, iterations continue until stop criterion is achieved.

With Matlab and Java script, the parallelism used the structure as shown in Figure 11. The master node executes NSGA-II code and assigns parallel tasks to slave nodes. The slave nodes perform FEM simulation and calculate capacitances of assigned structure. The results will be collected by master node and process repeats. The entire procedure of optimisation involves 100 groups of generation.

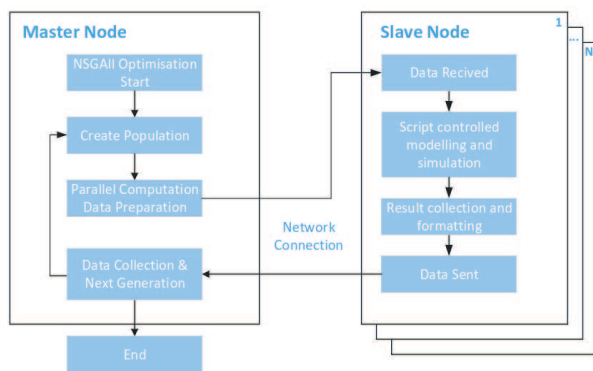


Figure 11: Parallel computing for NSGA-II.

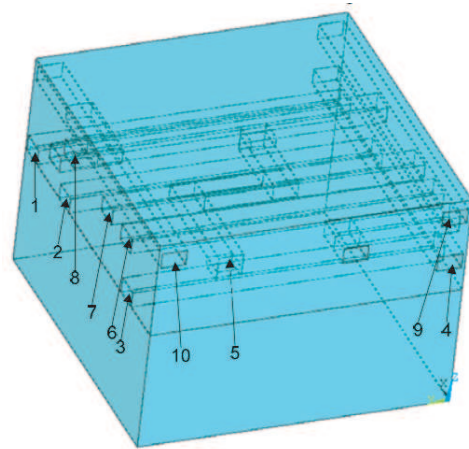


Figure 12: Optimized Structure of 3D multi-layer interconnects.

4.4. Optimisation Result

One of final optimized 3D structure is plotted in Figure 12. According to the figure, all parallel interconnects are separated widely to avoid coupling capacitance between each other. In addition, the structural width of interconnects 9 and 10 minimized overlapping coupling capacitance compared with interconnect 5 and two other fixed “L” shape interconnects.

When optimisation is implemented in one single physical machine, the maximum CPU usage is only 20% and maximum memory usage is 63.7%. The total runtime of entire procedure is 52.60 hours. In VEMC computing system, computer resources can be used more efficiently under the support of virtualisation technology. When then optimisation is paralleled in three virtual computing nodes, the maximum CPU usage and maximum memory usage are increased up to 100% while the total runtime is significantly reduced to 19.32 hours which is roughly 1/3 of runtime in one single physical machine.

5. CONCLUSIONS

This paper introduced a VEMC computing system which was designed and developed with high performance computation and collaboration visualisation capabilities in order to fulfil the requirement of IC EMC in modelling, simulation and optimisation. In addition, the system can be easily applied with existing computer hardware in any computer facilities which greatly increases machine usage and efficiency while relief provider from the financial pressure of setting up a supercomputing environment. Collaborative simulation and parallel optimisation played critical roles in IC EMC. Two case studies demonstrated the performance of VEMC computing system applied in IC-level EMC. Case one demonstrated a collaboration simulation of a MMIC. Case two analysed the performance of VEMC computing system in a parallel optimisation of multi-layer interconnects of IC.

ACKNOWLEDGMENT

The development of VEMC computing system is supported and funded by Griffith Enterprise, Griffith University, Australia. The model of MMIC in the QFN package is financially supported by the National Natural Science Foundation of China (No. 61040032 and No. 61306134).

REFERENCES

1. Lu, J., “High performance computation and interactive visualization of electromagnetics for engineering education programs,” *IEEE Transactions on Magnetics*, Vol. 48, No. 2, 299–302, Feb. 2012.
2. Lu, J. and D. Thiel, “Computational and visual electromagnetics for undergraduate engineering courses,” *IEEE Transactions on Magnetics*, Vol. 36, No. 4, 1000–1003, Jul. 2000.
3. Lu, J., D. Thiel, and S. Saario, “High performance numeric computation and visualization of electromagnetics using MATLAB,” *The Seventh Biennial IEEE Conference on Electromagnetic Field Computation, IEEE CEFC’96*, 275, Jun. 1996.
4. Wood, J., H. Wright, and K. Brodlie, “Collaborative visualization,” *Proc. IEEE Visualizat.*, 253–259, 1997.
5. Dan, O., “SUPERCOMPUTER vs your computer in bang-for-buck battle,” Mar. 8, 2012, http://www.theregister.co.uk/2012/03/08/supercomputing_vs_home_usa.
6. Mell, P. and T. Grance, “Cloud computing and storage optimization,” 2, SunGard Availability Service LP, 2009.
7. Deb, K., A. Pratap, S. Agarwal, and T. Meyarivan, “A fast and elitist multiobjective genetic algorithm: NSGA-II,” *IEEE Transactions on Evolutionary Computation*, Vol. 6, No. 2, 182–197, Apr. 2002.

Wide-angle Polarization-independent Planar Magnetic Metamaterials Based on Dielectric Resonators

Jiafu Wang¹, Shaobo Qu^{1,2}, Zhuo Xu², Hua Ma¹,
Hongliang Du¹, Jun Wang¹, and Hongya Chen¹

¹College of Science, Air Force Engineering University, Xi'an, Shaanxi 710051, China

²Electronic Materials Research Laboratory, Key Laboratory of the Ministry of Education
Xi'an Jiaotong University, Xi'an, Shaanxi 710049, China

Abstract— Based on dielectric resonators, the theory, design and implementation of planar magnetic metamaterials made of dielectric blocks were investigated. By etching simple metallic patterns on surface of the dielectric blocks, field distributions of the desired resonance modes can be enhanced while those of the undesired suppressed. In this way, the resonance frequency of the desired mode can be tuned down to lower frequency range. A wide-angle polarization-independent planar magnetic metamaterial based on short cylindrical dielectric resonators was proposed and analyzed. Due to its polarization-independence, wide incident angle, the magnetic metamaterial is ready to be used in various microwave components, such as antenna radomes, microwave filters and frequency selective surfaces.

1. INTRODUCTION

Metamaterials with negative permeability and/or negative permittivity have been attracting great attentions since the seminal work of Pendry and Smith [1, 2]. Due to unique electromagnetic properties, metamaterials have great potential application values in many fields. A great variety of metamaterials have been envisioned and fabricated. Similar to the working principle of SRR/Wire metamaterial, dielectric-metallic metamaterial unit cells, like S-shaped [3], Ω -shaped [4], coplanar magnetic/electric resonators [5], have been proposed. Nevertheless, there is an annoying problem for the above unit cells. Incident waves must be paralleled to the substrate plane, which make it quite troublesome to be fabricated and used. With an aim to overcome this problem, planar metamaterials, which allow the incident waves to be perpendicular to the substrate plane, were proposed and fabricated [6–11]. Typical planar metamaterials are the fishnet structures proposed by Soukoulis et al. [9].

Recently, many researchers are focusing on all-dielectric realization of metamaterials [12–18]. Many all-dielectric metamaterial unit cells, such as binary spherical [12], cubic [13] and disk-like unit cells [14], were proposed. These unit cells are based on different resonance modes in the unit cells which behave like dielectric resonators. Under a certain resonance mode, the effective permeability or/and permittivity are negative. The key to realizing all-dielectric metamaterials is to get the proper resonance modes. High-dielectric ceramics with good temperature stability and low dielectric loss are required to guarantee the long-wavelength condition. However, to date, dielectric constants of microwave ceramic materials, such as $\text{Ba}_2\text{Ti}_9\text{O}_{20}$, BaTi_4O_9 , $\text{BaO-PbO-Nd}_2\text{O}_3\text{-TiO}_2$, are mostly between 30 ~ 100, much less than some all-dielectric unit cells require [16, 17]. For many all-dielectric unit cells, their first resonance frequencies are so high that the long-wavelength condition cannot be met, so effective medium theory cannot be used to characterize them. As a result, it is desirable to design unit cells whose resonance modes can be tuned to lower frequencies.

In this paper, planar magnetic metamaterials based on practically-used dielectric resonators were proposed. As a typical example, magnetic metamaterials based on short cylindrical dielectric resonators were investigated. By etching a circular metallic ring on each end face of the dielectric resonator, the first resonance can be tuned significantly to lower frequency range so as to meet the long-wavelength condition. Thus, the magnetic metamaterial can be described by effective medium theory. Since the cross section of the dielectric resonator as well as the metallic ring are all circular, the magnetic metamaterial is independent of the polarization of incident waves. Under a wide incident angle range, the magnetic response keeps almost the same. Practical implementation of the proposed magnetic metamaterials was given. The proposed planar magnetic metamaterials owe its advantages to wide-angle incidence and polarization independence.

2. THEORY AND DESIGN

Only recently, materials having a dielectric constant between 30 and 100 with good temperature stability and low dielectric losses have become available. This greatly facilitate the design of practical all-dielectric metamaterials, but the dielectric constant of commercially available ceramic materials are still not so high as that required in some unit cells [16, 17]. This leads to a comparatively high resonance frequency. Thus, long-wavelength condition can not be satisfied and the corresponding metamaterials cannot be characterized by the effective medium theory. As a result, it is necessary to tune the desired resonance mode down to lower frequency ranges. All-dielectric metamaterials are always made of high-dielectric ceramic materials, no matter what shapes of the unit cells. A high-dielectric block can be regarded as a dielectric resonator, so we can design and tune the all-dielectric metamaterials by the same methods used in designing dielectric resonators.

For an isolated short cylindrical dielectric resonator shown in Fig. 1(a), the resonance mode with the lowest resonance frequency is the $TE_{0l\delta}$ mode. According to the electric and magnetic field distribution shown in Figs. 1(b) and (c), the resonators behaves like a magnetic dipole in $TE_{0l\delta}$ mode. Since the electric and magnetic dipole moments can be envisioned as the alphabet for making metamaterials [14], the resonator is expected to be a magnetic metamaterial in the $TE_{0l\delta}$ mode. Although the geometrical form of a dielectric resonator is extremely simple, an exact solution of the Maxwell equations is considerably more difficult than for hollow metal cavities. For this reason, the exact resonant frequency of a certain resonant mode, such as $TE_{0l\delta}$ mode, can only be computed by rather complicated numerical procedures. For an approximate estimation of the resonant frequency of the isolated dielectric resonator, the following simple formula [19] can be used

$$f_{\text{GHz}} = \frac{34}{r_{\text{mm}}\sqrt{\varepsilon_r}} \left(\frac{r}{h} + 3.45 \right) \quad (1)$$

The radius of the resonator is denoted by r and its height by h . The lengths are expressed in millimeters, and the frequency in gigahertz. The relative dielectric constant of the material is ε_r . The above formula is accurate to about 2% in the range

$$0.5 < r/h < 2 \quad \text{and} \quad 30 < \varepsilon_r < 50 \quad (2)$$

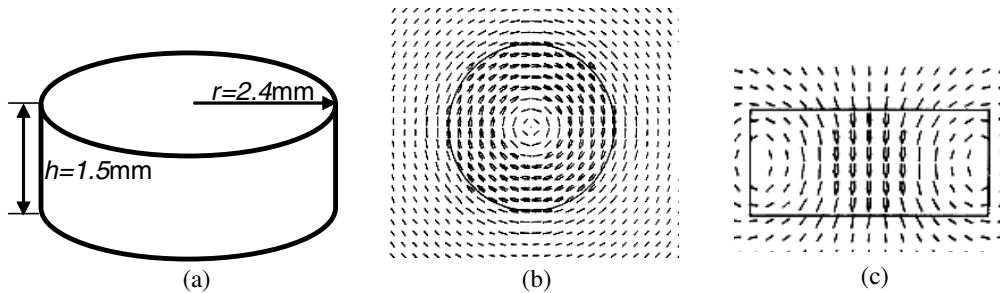


Figure 1: (a) An isolated short cylindrical dielectric resonator and (b) its electric field distribution in equatorial plane, (c) magnetic field distribution in meridian plane for $TE_{0l\delta}$ mode.

The dielectric resonator we consider in this paper as an example is made of $BaTi_4O_9$ whose dielectric constant $\varepsilon_r = 39.2$, loss angle tangent $\tan \delta = 0.0001$ and temperature coefficient $T_f = +4 \text{ ppm}/^\circ\text{C}$. The radius and height of the resonator are $r = 2.4 \text{ mm}$ and $h = 1.5 \text{ mm}$, respectively. By using (1) to estimate the first resonance frequency, we obtain

$$f_{\text{GHz}} = \frac{34}{1.5 \times \sqrt{39.2}} \left(\frac{2.4}{1.5} + 3.45 \right) \approx 18.3 \text{ GHz}$$

At 18.3 GHz, the wave-length in free space is about 16.4 mm, less than four times the diameter of the resonator, so the unit cell cannot be described by effective medium theory. The resonance frequency of the $TE_{0l\delta}$ mode has to be tuned down.

Figure 2 shows the unit cell of the magnetic metamaterial. The unit cell is put into a $5 \text{ mm} \times 5 \text{ mm} \times 3 \text{ mm}$ lattice. Compared with the dielectric resonator shown in Fig. 1(a), there are two thin

circular copper rings on each end face of the dielectric resonator. The outer radius of the copper ring, the width and thickness of the copper strip are: $r_0 = 2.2$ mm, $w = 0.2$ mm, $t = 0.050$ mm, respectively. From the electric and magnetic field distributions shown in Figs. 1(b) and (c), we can find that the electric field is stronger on the outer part of the end faces while the magnetic field is strongest in the center part around the axis. The copper ring is such that it is polarized along the electric field lines while perpendicular to the magnetic field lines. Thus, electric field on the end face and magnetic field pass through the copper ring all contribute to the enhancement of the magnetic resonance, so the copper ring can excite the $TE_{0l\delta}$ mode selectively. In contrast to the fact that the orientation of copper ring is along the direction of the electric field of $TE_{01\delta}$ mode, it is completely different from that of other higher order modes. As a result, the resonant frequency of $TE_{01\delta}$ mode will decrease significantly, whereas those of other modes will keep high.

3. SIMULATION RESULTS AND ANALYSIS

Numerical simulations were carried out using the commercial FDTD solver CST Microwave Studio. As shown in Fig. 2, the four lateral boundaries along x and y axes are Periodic Boundaries while the two boundaries along z axis are Open Boundaries. Plane waves are incident onto the unit cell with an incident angle θ with respect to the $-z$ direction.

Consider a normally incident plane wave onto the unit cell. Since the lateral boundaries are Periodic Boundaries, the structure is actually one layer of infinite magnetic metamaterial slab made of the unit cell shown in Fig. 2. Because the cross section of the dielectric resonator and the copper ring are all circular, the polarization of the incident plane wave has no influence on its magnetic response. Fig. 3 shows the simulated transmission spectra of one layer of the proposed magnetic metamaterial. As shown in Fig. 3, there is a transmission dip around 5 GHz. At 5 GHz, the wavelength in free space is about 60 mm, more than ten times larger the size of the unit cell, so effective medium theory can be employed. This means that we can use effective permeability and permittivity to describe the electromagnetic properties of the infinite magnetic metamaterial slab.

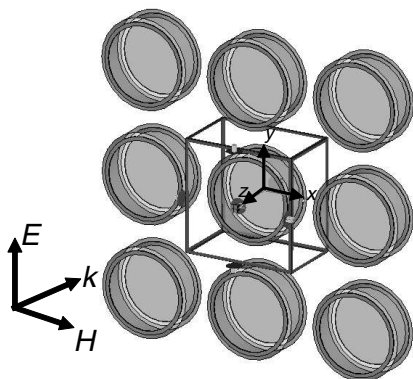


Figure 2: Unit cell of the planar magnetic metamaterial.

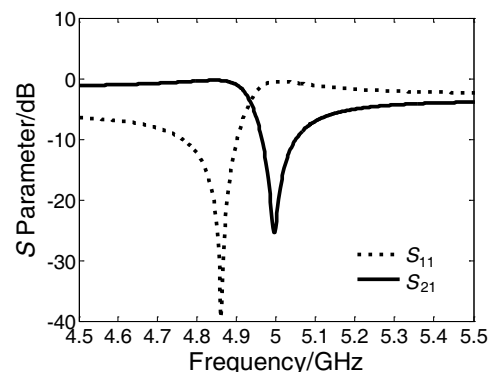


Figure 3: Transmission spectra under normal incidence.

The effective permeability and permittivity can be retrieved from S parameters obtained by simulations or experiments [20, 21]. Figs. 4(a) and (b) give the retrieved permeability and permittivity, respectively. Fig. 4(a) shows that the real part of effective permeability is negative from 4.95 GHz to 5.25 GHz. At the resonance frequency 4.95 GHz, there is a peak for the imaginary part of the effective permeability. In 4.95 ~ 5.05 GHz, the imaginary part is negative while in 5.03 ~ 5.25 GHz, the imaginary part is nearly zero. Since magnitude of the imaginary part is related to the magnetic loss, the magnetic loss is nearly zero in 5.05 ~ 5.25 GHz. As to the effective permittivity, there is a corresponding anti-resonance [22] in 4.95 ~ 5.25 GHz, as shown in Fig. 4(b).

For oblique incidences, we must consider two cases: incident TE plane waves and incident TM plane waves. In order to investigate the influence of the incidence angle, we can compare the transmission spectra under oblique incidences with that under normal incidence shown in Fig. 3. Since the transmission dip indicates a magnetic resonance, what we need to do is to see whether the dip varies greatly under different incidence angles. Figs. 5(a) and (b) show the transmission spectra under incident TE plane waves and incident TM plane waves, respectively. The incidence

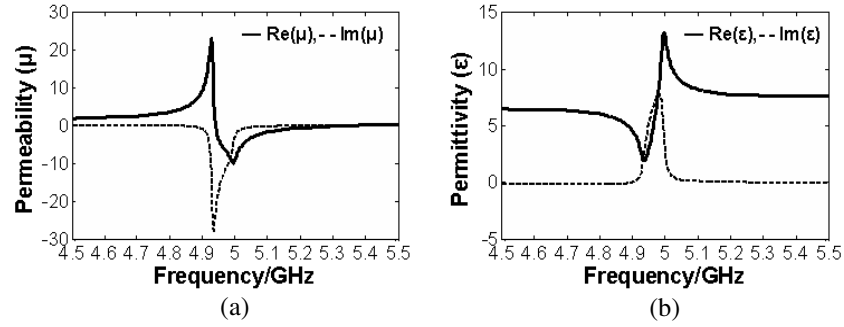


Figure 4: Retrieved constitutive parameters: (a) effective permeability and (b) effective permittivity for one layer of the proposed magnetic metamaterial.

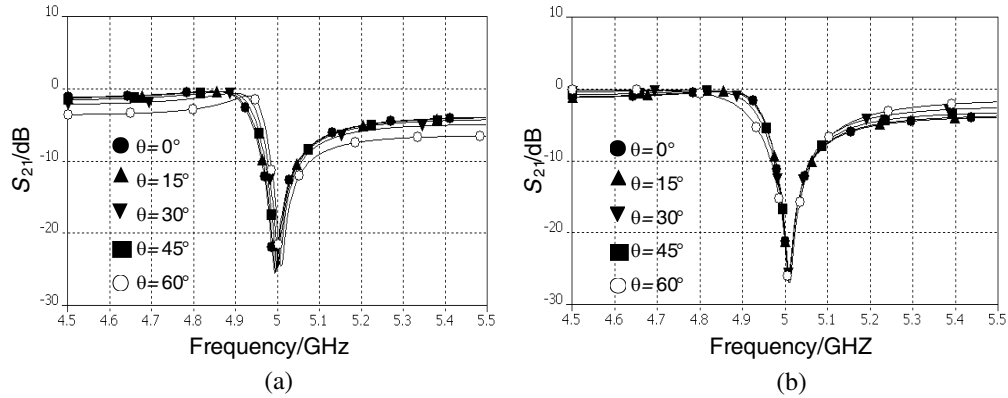


Figure 5: Transmission spectra for (a) TE waves and (b) TM waves with incident angles between $0 \sim 60^\circ$.

angles for the two cases vary from 0 to 60° . It is shown in Figs. 5(a) and (b) that the influence of incidence angles for both the TE and TM cases with incidence angles varying from 0 to 60° is so minor that the transmission dip almost keeps the same as that in normal incidence case. Thus, the magnetic resonance frequency keeps the same for varying incidence angles. Because negative effective permeability arises from the magnetic resonance, the frequency at which negative effective permeability starts is thus unchanged. Moreover, as the incidence angle increases, for the TE case, the upper part of the S_{21} curves bend lower than in the normal incidence case while for the TM case, the upper part of the S_{21} curves stand higher than in the normal incidence case. Since lower magnitude of S_{21} means lower transmission and thus wider bandwidth of negative permeability, as the incidence angle increases, the bandwidth of negative permeability in the TE cases becomes a bit wider than in the normal incidence case while in the TM case it becomes a bit narrower. However, the change of bandwidth with incidence angle is quite minor that we can approximately think that the bandwidth is the same as in the normal incidence case. From the above analysis, it can be concluded that the magnetic response of the proposed magnetic metamaterial keeps the same under a wide range of incidence angles.

3.1. Influences of Geometrical Parameters

For the proposed unit cell shown in Fig. 2, we use the copper ring to tune down the resonance frequency of $TE_{0l\delta}$ mode to realize negative permeability at much lower frequency range. Since the field intensity is different on different part of the dielectric resonator, the influence of copper ring is different when its geometrical parameters are changed. Thus, it is necessary to investigate the influence of its geometrical parameters. There are two main geometrical parameters for the copper ring: the outer radius and the strip width, so the influences of the two geometrical parameters were investigated.

Figures 6(a) and (b) show the transmission spectra under different outer radii and strip widths, respectively. As shown in Fig. 6(a), as the outer radius decreases, the transmission dip shifts to higher frequencies. This means that the resonance frequency of $TE_{0l\delta}$ mode increases as the outer radius decreases. This can be explained by the electric field distribution shown in Fig. 1(b). The electric field intensity is stronger on the outer part of the end face while weaker on the inner part.

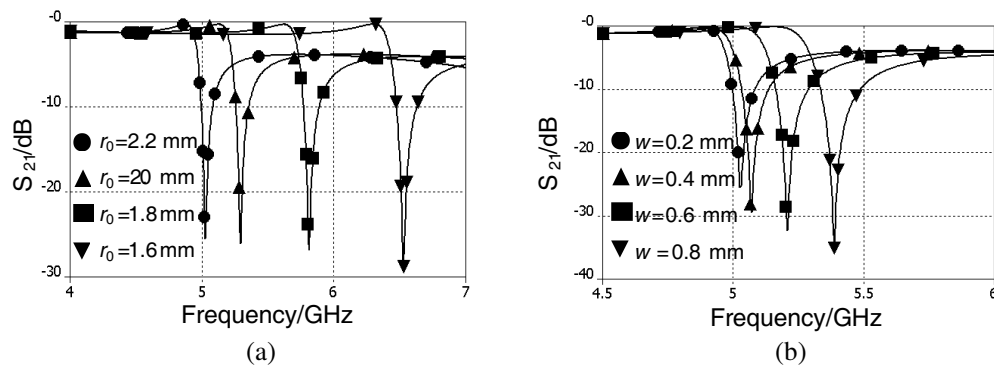


Figure 6: Influences of (a) the outer radius of copper ring and (b) the width of copper strip.

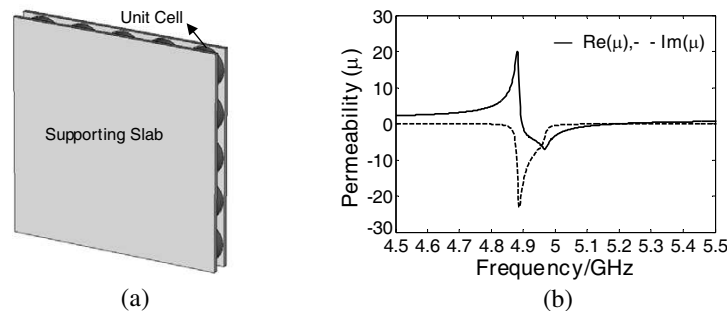


Figure 7: Practical implementation of the proposed magnetic metamaterials: (a) fixing the unit cells by two supporting slab; (b) retrieved effective permeability of the structure.

When the outer radius of the copper ring reduces, the electric field coupling to the copper ring becomes weaker. Thus, higher frequency is needed to excite the $TE_{0l\delta}$ mode resonance. Fig. 6(b) shows that as the strip-width increases, the transmission dip blue-shifts, which means that the magnetic resonance frequency increases with the strip-width. As the strip-width increases, the coupling between the copper ring and the electric field of the dielectric resonator increases, which increases the electric energy while reduces the magnetic energy. Thus, the magnetic field is reduced as the strip-width increases. Again, higher frequency is needed to excite the $TE_{0l\delta}$ mode resonance.

4. PRACTICAL IMPLEMENTATION OF THE MAGNETIC METAMATERIAL

In practice, the unit cells have to be fixed. Some authors chose the method of embedding the high-dielectric blocks into low-dielectric matrix [12–14]. This method is demanding for the fabrication techniques and thus is difficult to use. To avoid such a difficulty, the planar magnetic metamaterial can be realized in practice by two supporting slabs, as shown in Fig. 7(a). In order to reduce the influence of the two supporting slabs, materials of supporting slabs must be with low dielectric loss and low dielectric constant. Teflon (PTFE) with a dielectric constant 2.08 and loss angle tangent 0.0004 is chosen to be the material of supporting slabs. Besides its low dielectric loss and low dielectric constant, the flexibility of Teflon is quite good, so the planar magnetic metamaterial can be bent freely, which makes it convenient to apply the planar magnetic metamaterial.

The influence of the two Teflon supporting slabs on the negative permeability was also investigated. For one layer of magnetic metamaterial slabs shown in Fig. 7(a), the effective permeability is shown in Fig. 7(b). Compared with the effective permeability without supporting slabs shown in Fig. 4(a), the frequency range of negative real part of effective permeability, which has a red-shift, is now 4.9 ~ 5.2 GHz. In 4.9 ~ 5.0 GHz, the imaginary part is negative while in 5.0 ~ 5.2 GHz it is zero. The bandwidth without magnetic loss is 0.2 GHz, the same as the case without supporting slabs.

5. CONCLUSIONS

According to the field distributions of different resonance modes of the dielectric resonator, metallic patterns can be etched on some special positions on the surface dielectric resonators to adjust the field distributions. Thus, the desired resonance mode can be enhanced while the undesired

suppressed. As a result, resonance frequency of the desired modes will be reduced so as to meet the long wave-length condition. Metamaterials with negative permeability and/or negative permittivity can be realized by the desired resonance modes. Since there is a great many resonance modes for a given dielectric resonator, a great diversity of metamaterial can be designed based on different resonance modes. As a good example, a planar magnetic metamaterial based on short cylindrical dielectric resonators was designed and analyzed. The proposed planar magnetic metamaterial meets strictly the long wave-length condition and has almost the same electromagnetic response under a wide range of incidence angles. Because of its high flexibility, wide incidence angle range and polarization independence, the magnetic metamaterial is ready to be used in various microwave components, such as antenna radomes, microwave filters and frequency selective surfaces.

ACKNOWLEDGMENT

The authors are grateful to the supports from the National Natural Science Foundation of China under Grants Nos. 61331005, 11204378, 11274389, 11304393, 61302023, the National Science Foundation for Post-doctoral Scientists of China under Grant Nos. 2013M532131, 2013M532221, the Natural Science Foundation of Shaanxi Province under Grant Nos. 2011JQ8031, 2013JM6005, and the Aviation Science Foundation of China under Grant Nos. 20132796018 and 20123196015.

REFERENCES

1. Pendry, J. B., A. J. Holden, D. J. Robbins, and W. J. Stewart, *IEEE Trans. Microwave Theory Tech.*, Vol. 47, 2075, 1999.
2. Smith, D. R., W. J. Padilla, D. C. Vier, S. C. Nemat-Nasser, and S. Schultz, *Phys. Rev. Lett.*, Vol. 84, 4184, 2000.
3. Chen, H. S., L. X. Ran, J. T. Huangfu, X. M. Zhang, K. S. Chen, T. M. Grzegorzczuk, and J. A. Kong, *Phys. Rev. E*, Vol. 70, 057605, 2004.
4. Ran, L., J. Huangfu, H. Chen, Y. Li, X. Zhang, K. Chen, and J. A. Kong, *Phys. Rev. B*, Vol. 70, 073102, 2004.
5. Wang, J. F., S. B. Qu, Z. Xu, J. Q. Zhang, Y. M. Yang, H. Ma, and C. Gu, *Photon. Nanostruct.: Fundam. Appl.*, Vol. 6, 183, 2008.
6. Zhou, J. F., L. Zhang, G. Tuttle, T. Koschny, and C. M. Soukoulis, *Phys. Rev. B*, Vol. 73, 041101, 2006.
7. Zhou, J. F., E. N. Economou, T. Koschny, and C. M. Soukoulis, *Opt. Lett.*, Vol. 31, 3620, 2006.
8. Alici, K. B. and E. Ozbay, *Photonics Nanostruct.: Fundam. Appl.*, Vol. 6, 102, 2008.
9. Kafesaki, M., I. Tsiapa, N. Katsarakis, T. Koschny, C. M. Soukoulis, and E. N. Economou, *Phys. Rev. B*, Vol. 75, 235114, 2007.
10. Guven, K., A. O. Cakmak, M. D. Caliskan, T. F. Gundogdu, M. Kafesaki, C. M. Soukoulis, and E. Ozbay, *J. Opt. A: Pure Appl. Opt.*, Vol. 9, 361, 2007.
11. Zhou, J. F., T. Koschny, L. Zhang, G. Tuttle, and C. M. Soukoulis, *Appl. Phys. Lett.*, Vol. 88, 221103, 2006.
12. Holloway, C. L., E. F. Kuester, J. Baker-Jarvis, and P. Kabos, *IEEE Trans. Antennas Propagat.*, Vol. 51, 2596, 2003.
13. Kim, J. and A. Gopinath, *Phys. Rev. B*, Vol. 76, 115126, 2007.
14. Ahmadi, A. and H. Mosallaei, *Phys. Rev. B*, Vol. 77, 045104, 2008.
15. Popa, B.-I. and S. A. Cummer, *Phys. Rev. Lett.*, Vol. 100, 207401, 2008.
16. Peng, L., L. X. Ran, H. S. Chen, H. F. Zhang, J. A. Kong, and T. M. Grzegorzczuk, *Phys. Rev. Lett.*, Vol. 98, 157403, 2007.
17. Lepetit, T. and E. Akmansoy, *Microwave Opt. Tech. Lett.*, Vol. 50, 909, 2008.
18. Jylhä, L., I. Kolmakov, S. Maslovski, and S. Tretyakova, *J. Appl. Phys.*, Vol. 99, 043102, 2006.
19. Kajfez, D. and P. Guillon, 2nd Edition, Noble Publishing Corporation, Georgia, 1998.
20. Chen, X. D., T. M. Grzegorzczuk, B.-I. Wu, J. Pacheco, Jr., and J. A. Kong, *Phys. Rev. E*, Vol. 70, 016608, 2004.
21. Smith, D. R., D. C. Vier, T. Koschny, and C. M. Soukoulis, *Phys. Rev. E*, Vol. 71, 036617, 2005.
22. Koschny, T., P. Markos, D. R. Smith, and C. M. Soukoulis, *Phys. Rev. E*, Vol. 68, 065602(R), 2003.

High-efficiency Anomalous Reflection Characteristics of an Ultra-thin Gradient Meta-surface Based on SRRs

Hong Ya Chen, Jia Fu Wang, Hua Ma, Shao Bo Qu,
Jie Qiu Zhang, Yong Feng Li, Ming Bao Yan, and Yong Qiang Pang
College of Science, Air Force Engineering University, Xi'an, Shaanxi 710051, China

Abstract— In this paper, we proposed to redirect the reflected wave to the desired direction based reflective Gradient metasurfaces (GMs). An ultra-thin GM is designed using the square-ring resonators and further demonstrated both numerically and experimentally. The theory and design method of reflective GMs are presented. Both simulated and experimental results demonstrate that a finely designed gradient meta-surface supports high-efficiency anomalous reflections at the designed frequency, which agree quite well with theoretical predictions.

1. INTRODUCTION

Gradient metasurfaces (GMs) have evoked enormous interest recently [1–7]. By delicately design the phase gradient on GMs, the additional parallel wave vector is predefined on the GMs, which can not only redirect the reflection and refraction to the desired directions [3–7], but also convert incident EM waves to surface waves [1, 2]. Hence, GMs can realize anomalous reflection and refraction, negative reflection and refraction, surface wave conversion, and so on. Although intriguing properties of GMs are so attractive, the realization of high efficient GM is not easy. Equal amplitudes and strictly gradient phase changes of scattered waves must be satisfied simultaneously. However, it is comparatively easier to design a reflective GM since equal amplitudes can be realized by a metallic ground plane. In this way, the design of reflective GMs is reduced to the design of phase gradients.

In this letter, we propose to realize high efficient anomalous reflection based on reflective GMs. The theory and design method is presented. Moreover, we designed a sample based on square-ring resonators (SRRs). The GM is composed of an array of 12 SRRs with a phase change step $\pi/6$ per unit cell on the dielectric substrate. Both the simulation and experiment results show that high efficient anomalous reflection can be achieved under normal incidences around the designed frequency, which are good agreement with those predicted by generalized laws of reflection. Our study may pave the way applications such as high directivity antenna, flat focusing etc..

2. THEORY AND DESIGN METHOD

Suppose plane waves are obliquely incident onto a GM with a phase gradient $\xi = d\Phi/dy$ along the interface, and the incidence angle is θ_i . Because of the reflection phase gradient along the metasurface, the parallel wave vector of the reflected beam must be $k_y = \xi + k_0 \sin \theta_i$, where $k_0 = 2\pi/\lambda_0$ (λ_0 is the wavelength in free space). Particularly, the parallel wave vector of the reflected beam is completely equal to the phase gradient ξ under normal incidence, that is $k_y = \xi$. It has been demonstrated by the mode-expansion theory that the normal incident plane waves will be anti-reflected if the condition $\xi < k_0$ is satisfied, and the reflection angle meet generalized laws of reflection, that is $\theta_r = \arcsin(\xi/k_0)$ [4]. This phase gradient at the interface can also be understood as an additional momentum contribution; hence, for the sake of momentum conservation, the reflected wave direction has to change accordingly. It is obvious that the phase gradient ξ is the crucial parameter to determine reflection angle and direction under the normal incidence case.

Since the phase gradient ξ is often discrete in practice, we can using an array of resonant unit cells with constant phase change step but the same periodicity to approximately cover the 2π of phase range along the interface. Therefore, the phase change per each unit cell should be $\Delta\Phi = 2\pi/n$, where n is the number of unit cells in an array. Hence, each n unit cells form a super cell with periodicity $L = np$, where p is the single unit cell periodicity along the phase gradient direction. In this way, we get the phase gradient $\xi \approx \Delta\Phi/p = 2\pi/np = 2\pi/L$. Therefore, once the phase gradient ξ is determined by the super cell periodicity L and the condition $\xi < k_0$ is satisfied, anomalous reflection can be generated and the anomalous reflection angle is also determined. That means we can make the reflected waves to arbitrary direction by varying the periodicity of super cell.

3. SIMULATION RESULTS

As an example, we choose the square-ring resonators (SRRs) as the elementary component for GM, as shown in Figure 1(a). The unit cell consists of a SRR and a metallic sheet separated by a FR4 substrate (with a relative dielectric constant 4.3 and the loss tangent 0.025). We set the thickness of the substrate $h = 1.0$ mm. Suppose the GM is illuminated by a transverse-electric (TE) plane wave with y -polarized direction. A magnetic resonance effect can be generated due to the coupling between the SRR and the back metallic sheets, leading to a reflection phase change. By changing the dimension of the SRR, different reflection phases can be yielded. We fix periodicity of the metasurface unit cell $p = 6.53$ mm in the design, but let the length of square ring a and ring width w vary inside a super cell to realize the phase gradient. We choose 12 unit cells to construct a super cell with $(a, w) = (5.1$ mm, 1.3 mm), (5.2 mm, 0.5 mm), (5.9 mm, 1.9 mm), (5.8 mm, 1.4 mm), (6.1 mm, 2.3 mm), (5.8 mm, 1.2 mm), (6.1 mm, 1.9 mm), (6.2 mm, 2.2 mm), (6.1 mm, 1.6 mm), (6.1 mm, 1.4 mm), (5.9 mm, 0.7 mm), (6.2 mm, 0.3 mm), respectively. Since the 12 unit cells lies one by one with a constant phase change step along y -axis, we only need to consider relative phase change to achieve phase gradient under the same simulation shown in Figure 1(b). In this way, the super cell can discrete the phase gradient with $\Delta\Phi = \pi/6$ at designed frequency 8.0 GHz, as shown in Figures 1(b) and (c). Thus, we get the phase gradient $\xi \approx 0.481k_0 < k_0$.

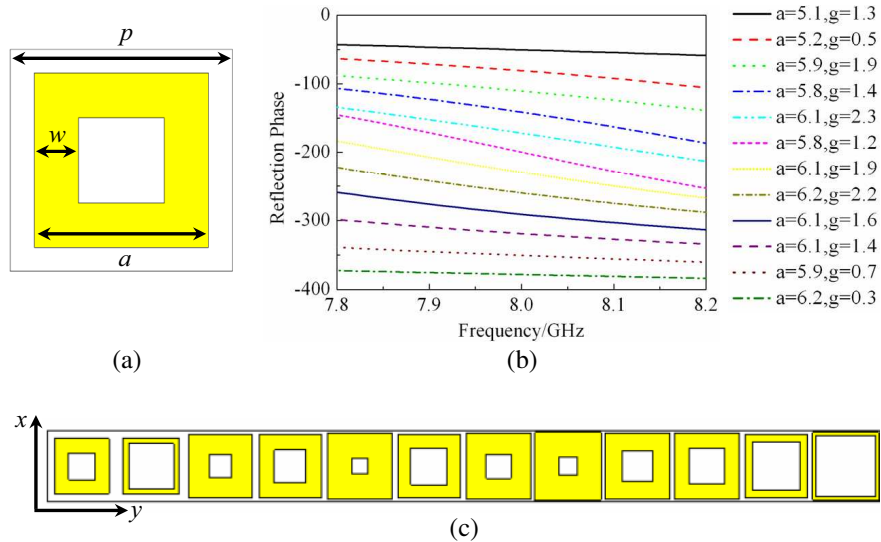


Figure 1: Design of GM composed of SRR super cell: (a) the SRR structure; (b) a reflection phase gradient realized enabled by 12 SRRs; (c) a single super cell composed of twelve SRRs.

In order to verify the design, we simulated a finite-size GM 65 mm \times 1560 mm normally illuminated by a TE plane wave with y -polarization at the middle of metasurface. Figure 2(a) plots the simulated normal reflection versus frequency for the finite-size GM. It is shown that the normal reflection is drastically reduced by 20 dB at the frequency 8.0 GHz.

To determine whether the reduced normal reflectivity is resulted from anomalous reflection, the field profiles on y - z plane are monitored. Figures 2(b) and (c) give the snapshots of E_y and H_x on y - z plane, respectively. It can be found that anomalous reflection is generated based on GM and the reflected direction is at the angle 29° , which is in good agreement with the predicted angles calculated by $\arcsin(\xi/k_0) = 29^\circ$. Anomalous reflection characteristics is also can be seen from power flow distributions as shown in Figure 2(d). Since we use 12 SRRs to approximately achieve the phase gradient along the interface in practice, this discreteness implies that there are also regularly reflected waves which follow conventional laws of reflection.

4. EXPERIMENTAL RESULTS

To further verify the design, we fabricated a 390 mm \times 390 mm square GM composed of the super cell and measured its normal reflection spectrum and reflection angle. Figure 3(a) shows the prototype of the fabricated GM sample. Figure 3(b) shows the measured reflection varying with frequency for the GM sample under normal incidence. It shows that the reflection curve shape is in good agreement with the simulated finite-size case. Further more, the reflection angle is also measured

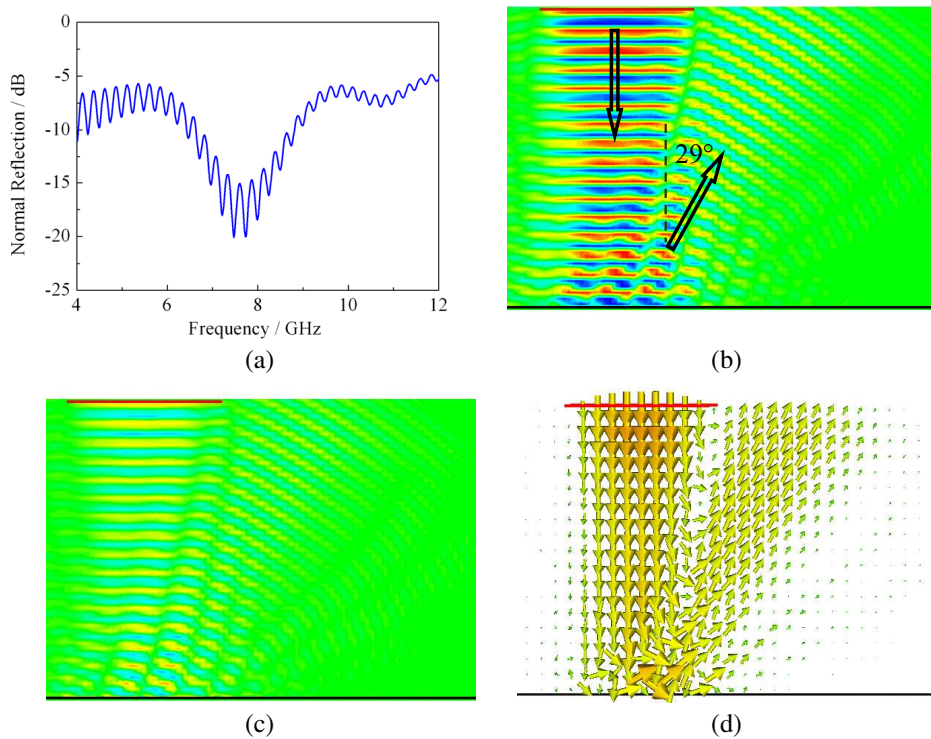


Figure 2: Simulation results of a finite GM composed of the 12-SRR super cells: (a) normal reflection of the finite GM under normal incidence; (b) E_y , (c) H_x , (d) power flow on $y-z$ plane at 8.0 GHz, respectively.

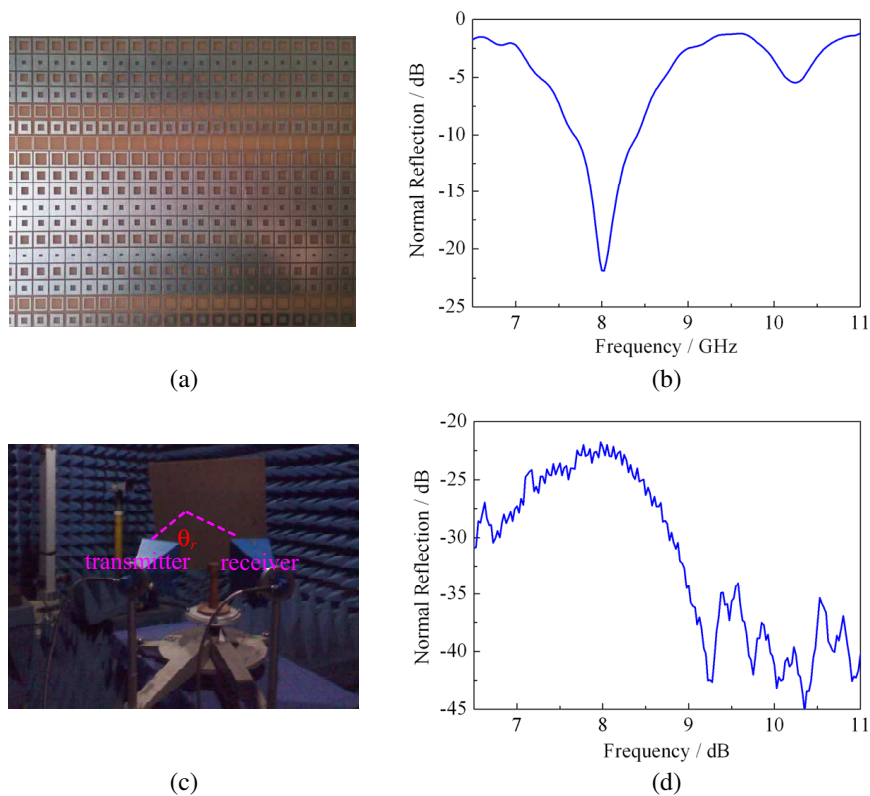


Figure 3: The fabricated GM sample and measured reflection results: (a) the GM sample (390 mm \times 390 mm); (b) measured normal reflection versus frequency under normal incidence; (c) the measuring setup of reflection angle; (d) measured reflection versus frequency under normal incidence at 30° between the two horns.

and the measuring setup is shown in Figure 3(c). We used two horn antenna connected to the same vector network analyzer. Let the left horn fixed as the emitter and illuminate normally on the sample. The right horn can orbit around the sample and acts as the receiver. We found that the reflection reaches the peak around 8.0 GHz when the angle between the two horns is 30 degree, as shown in Figure 3(d). This indicates that the anomalous reflection occurs at 30 degree, in good agreement with simulation and calculation results.

5. CONCLUSION

We demonstrate the anomalous reflection characteristics at microwave frequencies using GMs by simulation and experiment. By adjusting the dimensions of the SRR, it is possible to obtain GMs composed of array of SRR with a constant phase change to approximately cover 2π range. Both the simulation and experiment convincingly demonstrate that the anomalous reflection can achieve high efficiency around the designed frequency. Additionally, the anomalous reflection angle and direction is in excellent agree with those predicted by the generalized laws of reflection. Because of the freedom in manipulation of EM wave reflections, reflective GMs may pave the way towards high directivity antenna, flat focusing, etc..

ACKNOWLEDGMENT

The authors are grateful to the supports from the National Natural Science Foundation of China under Grant Nos. 61331005, 11204378, 11274389, 11304393, 61302023, the Aviation Science Foundation of China under Grant Nos. 20132796018, 20123196015, the National Science Foundation for Post-doctoral Scientists of China under Grant Nos. 2013M532131, 2013M532221, the Natural Science Foundation of Shaanxi Province under Grant No. 2013JM6005, and the Special Funds for Authors of Annual Excellent Doctoral Degree Dissertations of China under Grant No. 201242.

REFERENCES

1. Sun, S. L., Q. He, S. Y. Xiao, Q. Xu, X. Li, and L. Zhou, "Gradient-index meta-surfaces as a bridge linking propagating waves and surface waves," *Nat. Mater.*, Vol. 11, 426–431, 2012.
2. Wang, J. F., S. B. Qu, H. Ma, Z. Xu, A. X. Zhang, H. Zhou, H. Y. Chen, and Y. F. Li, "High-efficiency spoof plasmon polariton coupler mediated by gradient metasurfaces," *Appl. Phys. Lett.*, Vol. 101, 201104, 2012.
3. Sun, S. L., K. Y. Yang, C. M. Wang, T. K. Juan, W. T. Chen, C. Y. Liao, Q. He, S. Y. Xiao, W. T. Kung, G. Y. Guo, L. Zhou, and T. D. Ping, "High-efficiency broadband anomalous reflection by gradient meta-surfaces," *Nano Lett.*, Vol. 12, 6223–6229, 2012.
4. Yu, N. F., P. Genevet, M. A. Kats, F. Aieta, J. P. Tetienne, F. Capasso, and Z. Gaburro, "Light propagation with phase discontinuities: Generalized laws of reflection and refraction," *Science*, Vol. 334, 333–337, 2011.
5. Francesco, A., P. Genevet, N. F. Yu, M. A. Kats, Z. Gaburro, and F. Capasso, "Out-of-plane reflection and refraction of light by anisotropic optical antenna metasurfaces with phase discontinuities," *Nano Lett.*, Vol. 12, 1702–1706, 2012.
6. Bansal, R., "Bending Snell's laws," *IEEE Antenn. Propag. Mag.*, Vol. 53, 146–147, 2011.
7. Ni, X. J., N. K. Emani, A. V. Kildishev, A. Boltasseva, and V. M. Shalaev, "Broadband light bending with plasmonic nanoantennas," *Science*, Vol. 335, 427, 2012.

Study on Permittivity and Optimal Design of Metamaterial

Zihao Fu¹, Yanfang Li², and Guizhen Lu¹

¹Information School, Communication University of China, Beijing, China

²Materials and Machinery School, Jiangxi Science & Technology Normal University, Nanchang, China

Abstract— Artificial electromagnetic materials in the recent years develop rapidly, both in the military aspects about stealth technology and in daily life to absorb harmful electromagnetic waves in nature. As the environmental impact of electromagnetic radiation become terrible. The importance of artificial electromagnetic materials becomes more prominent. Artificial electromagnetic materials have great potential in the antenna and microwave devices and other research fields, because Metamaterials can be produced by the restructure of traditional materials in nature. We use new technology to prepare artificial electromagnetic materials. Therefore, for the study of Metamaterials has become very urgent. This paper analyses the characteristics of the Metamaterials. By the homogenization method we can effectively deal with the periodic structure situation, therefore, faced a similar problems, we can generally use the method of homogenization to solve. Firstly, considering the scope of its application, a frequency selective surface structure was verified. For the homogenization method, scattering parameters results were obtained to compare with the original structure. Target structure uses S -parameter inversion to obtain equivalent electromagnetic parameters. The paper analyses the absorbing properties of the structure, it also pays attention to the energy dissipation. On this basis, using the honeycomb structure instead of the original structure, better absorbing effect can be obtained. As is known, honeycomb structure not only has absorbing effect but also with good mechanical properties. The absorbing materials can effectively absorb the incident electromagnetic wave and make it decay. Cause electromagnetic loss so that electromagnetic energy is converted into thermal energy or other energy forms. Finally, this paper proposes a kind of absorbing structure with better performance.

1. INTRODUCTION

The electromagnetic absorbing materials related to the electromagnetic field and wave theory and the preparation of materials, and many other disciplines. Containing reflection, refraction, is the intersection of many disciplines. Absorbing material not only has special strategic position into the military, but also becoming increasingly widespread in the civil. Therefore, countries are scrambling to invest a lot of manpower and material resources to carry out extensive research [1–4]. Frequency selective surface is formed by a large number of passive elements are arranged in a distributed manner that in accordance with a particular cycle of the quasi-planar layered structure. FSS has good selectivity in transmission and reflection of electromagnetic waves. Application of the frequency selective surface can reach terahertz. Italy Agostino Monorchio and Filippo Costa et al. make depth analysis in frequency selective surface [5–11].

This paper using homogenization method to analyzes the frequency selective surface with high impedance. Homogenization method is a commonly used method [12, 13], is often used to obtain characteristics and parameters of the artificial electromagnetic materials for analysis, methods are required for the given type of structure, and to consider the scope of the methods used. In this paper, we analysis a particular type of absorbing material, first obtain the equivalent electromagnetic parameters, and the effective dielectric constant of the original model for analysis. Then further explore its energy is dissipated in the absorbing material, on this basis, we improved the existing structure, using a honeycomb structure with a better performance on the mechanics and electromagnetism to replace the original structure. At last, better band absorbing properties of absorbing material could be obtained.

2. ELECTROMAGNETIC PARAMETERS OBTAINED BY INVERSION

Think about the Nicholson-Ross-Weir conversion process [14]. Through the S -parameter analysis of the original structure, the reflection coefficient Γ can be calculated, and then further transmission coefficient T . It should be noted that the absolute value of the reflection coefficient could not be greater than 1 to ensure that the result is correct. Then you can calculate the anti performances μ and ε results based on these data.

By the following two formulas:

$$S_{11} = \frac{\Gamma(1 - T^2)}{(1 - \Gamma^2 T^2)} \quad (1)$$

$$S_{21} = \frac{T(1 - \Gamma^2)}{1 - \Gamma^2 T^2} \quad (2)$$

The simulation results can be scattered to the parameters. From the above two formulas we can get the reflection coefficient.

$$\Gamma = X \pm \sqrt{X^2 - 1} \quad (3)$$

It should be noted that the absolute value of the reflection coefficient is less than 1.

The expressions of permeability:

$$\mu_r = \frac{1 + \Gamma}{\Lambda(1 - \Gamma)\sqrt{\frac{1}{\lambda_0^2} - \frac{1}{\lambda_c^2}}} \quad (4)$$

And we can get the formula:

$$\frac{1}{\Lambda^2} = \left(\frac{\varepsilon_r * \mu_r}{\lambda_0^2} - \frac{1}{\lambda_c^2} \right) = - \left(\frac{1}{2\pi L} \ln \left(\frac{1}{T} \right) \right)^2 \quad (5)$$

In conclusion, we can get the formula about the dielectric constant:

$$\varepsilon_r = \frac{\lambda_0^2}{\mu_r} \left(\frac{1}{\lambda_c^2} - \left(\frac{1}{2\pi L} \ln \left(\frac{1}{T} \right) \right)^2 \right) \quad (6)$$

We can get the permittivity and magnetic permeability through the above formula.

Assuming a homogeneous medium model size of 10 mm * 10 mm * 4 mm, its permittivity is 4 and the permeability is 1, External air cavity is 10 mm * 10 mm * 80 mm, as shown in Fig. 1.

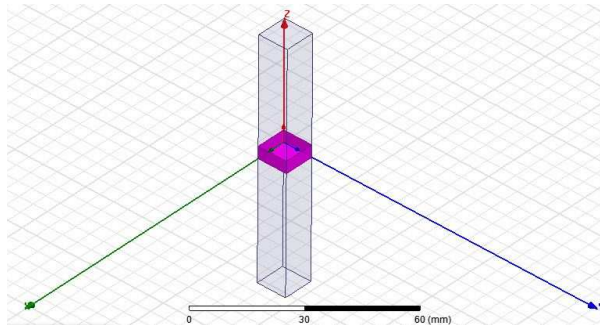


Figure 1: A unit structure.

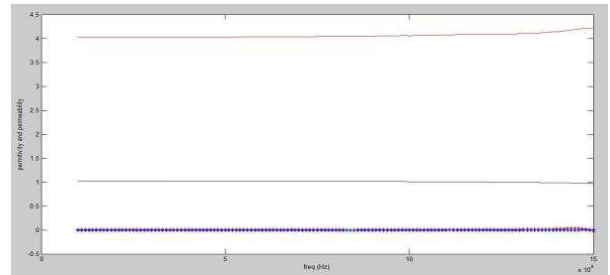


Figure 2: Equivalent permittivity and permeability.

In this situation, the incident wave from the Z direction. This method can get the S -parameter by simulation, then using MATLAB to deal with the data to can get the equivalent permittivity and permeability as shown in Fig. 2.

In the Fig. 2 the red lines are stand for the permittivity and the blue lines stand for permeability, the solid line representatives the real part and the dotted line representatives the imaginary part. The results are in line with our assuming. So we can get the conclusion that this method could be adopted in the range of 1 GHz to 10 GHz.

3. ANALYSIS OF DOUBLE FREQUENCY SELECTIVE SURFACE

In this model, we set the size as 10 mm * 10 mm * 4 mm, and dielectric constant is 3.5 [15]. There are two frequency selective surfaces. From the Z direction, the surfaces height is 2.4 mm and 3.1 mm from the bottom. The surface resistance value is 50 ohms. Shown in the Fig. 3.

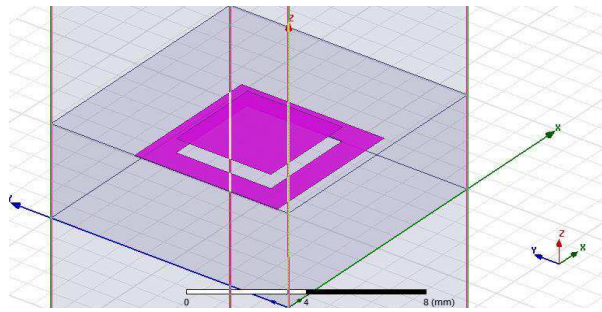


Figure 3: The model of the double frequency selective surface.

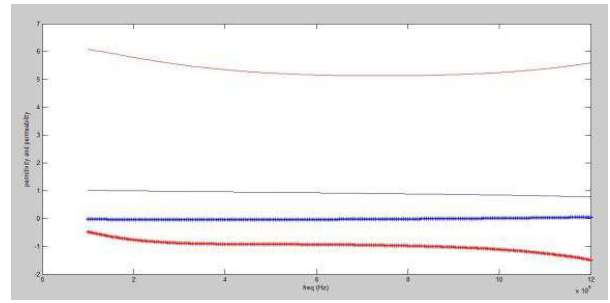


Figure 4: The equivalent permittivity and permeability.

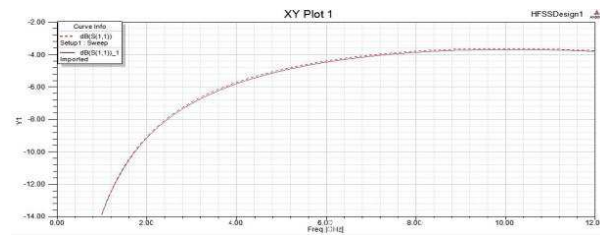


Figure 5: The S_{11} .

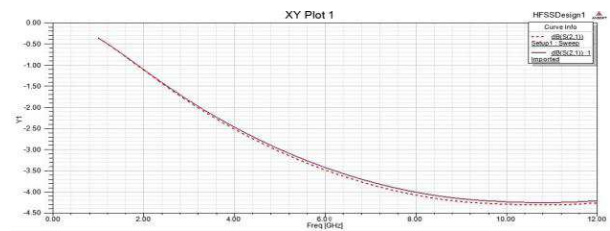


Figure 6: The S_{21} .

Using the formula mentioned earlier, we can get the equivalent permittivity and magnetic permeability of the model. Handled with the scattering parameters, we can draw the equivalent permittivity and permeability. Shown in the Fig. 4.

And similar to the above, the red lines stand for the permittivity and the blue lines stand for permeability, the solid line representatives the real part and the dotted line representatives the imaginary part. Then, we can compare the original data with the equivalent data to discover the difference.

The solid line stands for original structure and the dotted line stands for the homogenization structure.

The solid line stands for original structure and the dotted line stands for the homogenization structure. From the comparison, we can see in the extent applicable, the curves of scattering parameters match. So the method is effective.

It was found that the return loss caused by the impedance boundary, that leads to the absorber with complex permeability and complex permittivity. Attenuation of electromagnetic energy is mainly due to the impedance boundary layer, obtaining absorbing effect. The absorbing materials effectively absorb the incident electromagnetic wave, then the attenuation of electromagnetic waves to produce electromagnetic loss, electromagnetic energy changes to thermal energy or other forms of energy. Conductivity controlled within a certain range in order to achieve better performance absorbing effect. The absorption ability of medium for electromagnetic wave generally expressed as dielectric loss tangent and Magnetic loss tangent such as $\tan \delta_e = \frac{\varepsilon_i}{\varepsilon_r}$ and $\tan \delta_e = \frac{\mu_i}{\mu_r}$, the greater the value, the stronger the ability of absorbing. Where i is the imaginary part and r is the real part. Therefore, the imaginary part is relatively bigger, the better the absorbing effect.

The solid line stands for original structure and the dotted line stands for the homogenization structure. We can be found within the application range, return loss less than negative 10 dB, in line with our requirements

$$R = 20 \log \left(\frac{\sqrt{\frac{\mu_0}{\varepsilon_0}} \cdot \sqrt{\frac{\mu}{\varepsilon}} \cdot \tanh \left(\frac{i \cdot 2\pi f d}{c} \sqrt{\mu \varepsilon} \right) - \sqrt{\frac{\mu_0}{\varepsilon_0}}}{\sqrt{\frac{\mu_0}{\varepsilon_0}} \cdot \sqrt{\frac{\mu}{\varepsilon}} \cdot \tanh \left(\frac{i \cdot 2\pi f d}{c} \sqrt{\mu \varepsilon} \right) + \sqrt{\frac{\mu_0}{\varepsilon_0}}} \right) \quad (7)$$

where R is the return Loss [16], and d is the thickness of the medium, effective electromagnetic parameters are ε and μ , the frequency is set to f . If we want to achieve the desired result of R , we could set R to zero, so we should meet the condition that $\varepsilon = \mu$. So when the case is the value of ε close to μ , the best results can be achieved for absorbing materials. To achieve this purpose,

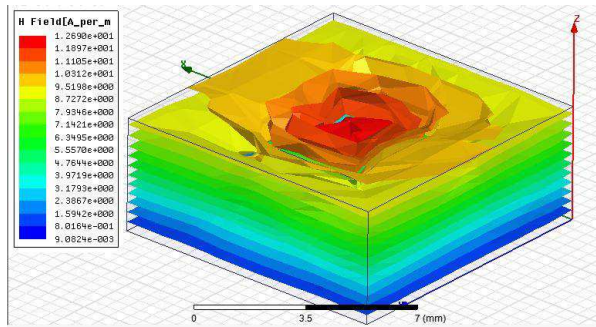
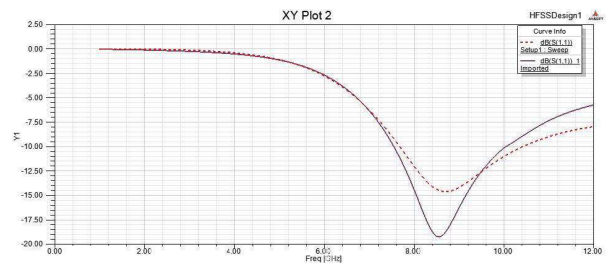


Figure 7: Internal magnetic field.

Figure 8: The S_{11} in the condition that bottom has the perfect electric boundary conditions.

we have to match ϵ and μ as much as possible. Because with a substantial change in frequency, its permittivity and permeability will also change, so we can only match the permittivity and permeability to the extent possible, permittivity and permeability's variation changes its absorption. After the data processing from the literature [17] the frequency selective surface can be drawn as a thin resistive impedance boundary patch. The size, patch square resistance and the thickness of the dielectric material changes all will affect the results. After simulation analysis we can decide the size of the model, and the resistance value is turn out to be 50 ohms.

4. HONEYCOMB STRUCTURE IMPROVEMENTS

The arrangement of the original changes from rectangular to hexagonal, such as shown in the Fig. 9. The return loss of the two results are compared in Fig. 10.

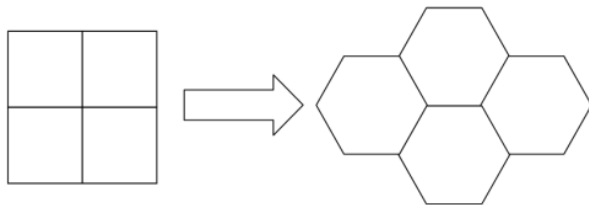


Figure 9: From rectangular to hexagonal.

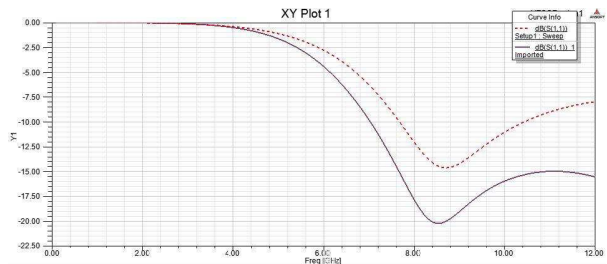


Figure 10: Compare the return loss in original structure and the honeycomb structure.

From the figure, we can clearly see that in the frequency range corresponding to the return loss of the honeycomb structure could reach -15 dB, and the original structure only reach -10 dB. As we know, the honeycomb structure also has a variety of excellent properties and stable in mechanical. Thus, this improvement is effective attempt.

5. CONCLUSION

Traditional absorbing materials mainly to the strength of the absorption capacity, new absorbing materials are required to meet more requirements, such as thin, light, wide, and other characteristics. The Insufficient about absorbing properties lead to the limit on the research and application of radar absorbing materials. This paper adapts the resistive losses in absorbing structure. Its attenuation of electromagnetic energy in the material is resistive, the main attenuation of electromagnetic energy on chip resistor, we can change its impedance to control the conductivity value variation. Using electric loss tangent to represents the attenuation ability of electromagnetic waves. First this article verifies the method for homogenizing, and then base on these, we use the honeycomb structure instead of the original structure to improve the absorbing effect. Not only the electromagnetic parameters were optimized but also the structure were been adjusted. It is believed that with the development of preparation techniques, absorbing structures have better results will also appear as soon as possible.

REFERENCES

1. Cheng, T., T. Li, S. Li, T. Zhao, Y. Cheng, and C. Hou, "Research progress on stealth materials," *Materials Review*, Vol. 25, No. 15, 2011.
2. Li, B., C. Wang, and W. Wang, "Progress of electromagnetic wave absorbing materials based on carbon," *Materials Review*, Vol. 26, No. 7, 2012.
3. Zhao, J., Y. Lin, R.-Z. Xu, C.-B. Liu, Y.-Y. Kuang, and Y. Yang, "Research in chiral absorbing materials," *Journal of Functional Materials*, Vol. 44, No. z1, 2013.
4. Tao, Z., X. Fan, Q. Wang, and Y. Shu, "Performance and applications of ferrite electromagnetic wave absorbers," *Journal of Magnetic Materials and Devices*, Vol. 38, No. 5, 2007.
5. Manara, G., A. Monorchio, and R. Mittra, "Frequency selective surface design based on genetic algorithm," *Electronics Letters*, 1400–1401, 1999.
6. Kern, D. J., D. H. Werner, A. Monorchio, L. Lanuzza, and M. J. Wilhelm, "The design synthesis of multiband artificial magnetic conductors using high impedance frequency selective surfaces," *IEEE Antennas and Propagation*, 8–17, 2005.
7. Costa, F., S. Genovesi, and A. Monorchio, "On the bandwidth of high-impedance frequency selective surfaces," *IEEE Antennas and Wireless Propagation Letters*, 1341–1344, 2009.
8. Costa, F., A. Monorchio, and G. Manara, "Ultra-thin absorbers by using high impedance surfaces with resistive frequency selective surfaces," *IEEE Antennas and Propagation Society International Symposium*, 861–864, 2007.
9. Costa, F., A. Monorchio, and G. Manara, "Analysis and design of ultra thin electromagnetic absorbers comprising resistively loaded high impedance surfaces," *IEEE Antennas and Propagation*, 1551–1558, 2010.
10. Genovesi, S., F. Costa, and A. Monorchio, "Low-profile array with reduced radar cross section by using hybrid frequency selective surfaces," *IEEE Antennas and Propagation*, 2327–2335, 2012.
11. Costa, F., A. Monorchio, and G. Manara, "Efficient analysis of frequency-selective surfaces by a simple equivalent-circuit model," *IEEE Antennas and Propagation Magazine*, 35–48, 2012.
12. Ouchetto, O., "Modeling of 3-D periodic multiphase composites by homogenization," *IEEE MTT*, Vol. 54, No. 6, 2615, 2006.
13. Ouchetto, O., "Homogenization of 3-D periodic bianisotropic metamaterials," *IEEE MTT*, Vol. 54, No. 11, 3893, 2006.
14. "Measurement of dielectric material properties application note," 19–20.
15. Lee, W. J., "Microwave absorbing structure with conducting polymer FSS coating," *Sixteenth International Conference on Composite Materials (ICCM-16)*, Vol. 1, 2007.
16. Rozanow, K. N., "Ultimate thickness to bandwidth ratio of radar absorber," *IEEE Trans. on Antennas and Propagation*, Vol. 48, No. 8, 1230, 2000.
17. Chen, L., B. Xu, S. Zhang, and L. Deng, "Absorbing performance of frequency selective surface with resistance patch," *Chinese Journal of Radio Science*, Vol. 21, No. 4, 548–552, 2006.

A Side Information Free PTS-PAPR Reduction in Coherent Optical OFDM Systems Using Superimposed Training

Changjian Guo, Haipeng Liu, and Han Zhang
South China Normal University, Guangzhou 510006, China

Abstract— In this paper, we report a side information free partial transmit sequence (PTS) technique to reduce the peak-to-average power ratio (PAPR) for coherent optical OFDM systems using superimposed training. Simulation results show that this scheme can reduce PAPR effectively, and have a slight BER performance improvement compared with the conventional superimposed training coherent optical OFDM systems.

1. INTRODUCTION

Coherent Optical Orthogonal Frequency-Division Multiplexing (CO-OFDM) [1] is a promising technology for optical long-haul systems because of its high spectral efficiency, high flexibility and its nature combination with digital signal processing (DSP). However, there is a common belief that OFDM has inferior tolerance to fiber nonlinearities because of its high peak-to-average-power ratio (PAPR). Therefore, several PAPR reduction techniques have been proposed [2–5] to reduce this nonlinear impairment. Among these methods, one promising scheme is the partial transmit sequence (PTS) [2, 6]. In traditional PTS schemes (T-PTS) [7], input data symbols are divided into disjointed sub-blocks which are separately phase-rotated by individually selected phase factors during PAPR optimization process. In order to detect the data symbols properly at the receiver, the phase factors are also transmitted as side information (SI) when data symbols are sent, resulting in a loss of data rate.

In this paper, an efficient SI free PTS-PAPR reduction scheme is presented, which combines the channel estimation and T-PTS method to reduce the PAPR of OFDM signals, called as the ST-PTS method. Its key idea is that the side information of PTS is considered as a part of channel frequency response which can be estimated within each interleaved PTS sub-block based on superimposed training (ST). Thus, the original OFDM signals could be directly recovered via superimposed training channel estimation [8] without any knowledge of the SI at the receiver. Furthermore, to enhance the performance of BER, a side information recovery is performed across the interleaved ST-PTS sub-blocks at receiver to achieve an accurate channel estimation over the whole sub-blocks. Simulation results demonstrate that the proposed method can reduce PAPR effectively and have slightly BER performance improvement compared with the conventional superimposed training coherent optical OFDM systems.

2. TRADITIONAL PTS SCHEME

For an OFDM system with N subcarriers, the transmitted signal in the time domain is given by

$$x(n) = \frac{1}{\sqrt{N}} \sum_{k=0}^{N-1} X(k) e^{j2\pi kn/N}, \quad 0 \leq n < N \quad (1)$$

where $X = [X(0), X(1), \dots, X(N-1)]$ is the input data block with N independent modulated data symbols $X(k)$ ($0 \leq k \leq N-1$). In general, the PAPR of the OFDM signal $x(n)$ is defined as

$$PAPR = \frac{\max_{0 \leq n \leq N-1} |x(n)|^2}{E[|x(n)|^2]} \quad (2)$$

where $E[\cdot]$ represents the expectation.

In T-PTS schemes [2], the input data vector X is firstly partitioned into M disjointed sub-blocks ($N = MG$), which are represented by the vectors $\{X^{(m)}, m = 0, 1, \dots, M-1\}$. Therefore, we can get

$$X = \sum_{m=0}^{M-1} X^{(m)}, \quad 0 \leq m \leq M-1 \quad (3)$$

where $X^{(m)} = [X_0^{(m)}, X_1^{(m)}, \dots, X_{G-1}^{(m)}]$ is the m th sub-block. Then each sub-block is rotated by a phase factor set $b_m = e^{j\phi_m}$, i.e., $X^{(m)} \cdot b_m$. In general, the phase factor set is limited with a finite number of elements to reduce the complexity. In this paper, we chose $\phi \in \{0, \pi\}$, this means $b_m \in \{\pm 1\}$. Taking Inverse Fast Fourier Transform of $X^{(m)} \cdot b_m$, we obtain $x^{(m)} = [x_0^{(m)}, x_1^{(m)}, \dots, x_{G-1}^{(m)}], 0 \leq m \leq M-1$. The sub-blocks are combined to find the optimal set of b_m with respect to minimize the PAPR of the transmitted OFDM signals. At the receiver, for the T-PTS method, when no bits are reserved to protect SI, the SI should be sent to the receiver with $(M-1) \log_2 Q$ bits, where Q is the number of the allowed phase factors, resulting in a decrease in the data rate.

3. ST BASED SI FREE PTS SCHEME

In ST based method [8], after the complex training sequence is superimposed to the complex data in frequency domain, the resulted signal is given by:

$$X_k = S_k + P_k \quad (4)$$

where S_k and P_k denote the complex data symbols and the pilot sequence respectively, $k = 0, 1, \dots, N-1$ is the sub-carrier index, and N is the number of sub-carriers. The data symbols S_k is assumed to have a zero mean. The interleaved T-PTS algorithm [2] is then followed to reduce the PAPR of OFDM signal according to the system model described above. Therefore, we can get the OFDM signal equipped with a phase factor b_m , i.e.,

$$X = \sum_{m=0}^{M-1} X^{(m)} = \sum_{m=0}^{M-1} b_m X_k, \quad k = Mg + m \quad (5)$$

where M is the number of sub-blocks, m is the sub-block index, and $g = 0, 1, \dots, G-1$ is the element-index of the sub-blocks.

The optical fiber channel is assumed to have a discrete-time channel impulse response (CIR), i.e., $h = [h_0, h_1, \dots, h_{L-1}]$, where L is the channel length. The corresponding channel frequency response (CFR) is $H = [H_0, H_1, \dots, H_{N-1}]$.

3.1. Joint Channel and Phase Factor Estimation: Initial Estimation

At the receiver, after taking the DFT operation, the received signal in the frequency domain can be written as

$$Y_k = X_k H_k + W_k, \quad 0 \leq k \leq N-1 \quad (6)$$

where H_k is the channel frequency response (CFR), and W_k is the frequency domain additive white Gaussian noise with zero mean. Using the PTS, the received signal Y_k is partitioned into M interleaved sub-blocks $Y_g^{(m)}$ ($0 \leq g \leq G-1, N = MG$), where the type of the disjoint sub-blocks is the same as that of the transmitter. As a result, the m th sub-block is

$$Y_g^{(m)} = b_m X^{(m)} H^{(m)} + W^{(m)} \quad (7)$$

where $X^{(m)} = X_k, k = Mg + m$ and $H^{(m)} = H_k, k = Mg + m$ denote the data and CFR of the m th sub-block, respectively.

Denote

$$\hat{H}^{(m)} = b_m H^{(m)} \quad (8)$$

as the virtual frequency channel response, which is the combination of the traditional channel frequency response and the phase rotation factors used in the PTS method.

Substituting Eq. (4) and Eq. (8) into Eq. (7), we have

$$\begin{aligned} E\left(Y^{(m)}\right) &= E\left(X^{(m)} \hat{H}^{(m)} + W^{(m)}\right) = E\left(S^{(m)} \hat{H}^{(m)} + P^{(m)} \hat{H}^{(m)} + W^{(m)}\right) \\ &= E\left(S^{(m)} \hat{H}^{(m)}\right) + E\left(P^{(m)} \hat{H}^{(m)}\right) + E\left(W^{(m)}\right) \end{aligned} \quad (9)$$

where $S^{(m)}$ and $P^{(m)}$ denote the complex data symbols and the pilot sequence of the m th sub-block respectively. In Eq. (9), the first and third expectations are zero since $S^{(m)}$ and $W^{(m)}$ are zero

mean, and clearly, the second expectation operator can be removed to give

$$E\left(Y^{(m)}\right) = P^{(m)}\hat{H}^{(m)} \quad (10)$$

Therefore, we have CFR of the m th sub-block, i.e.,

$$\hat{H}^{(m)} = E\left(Y^{(m)}\right) / P^{(m)} \quad (11)$$

Hence, data symbols within each interleaved sub-block can be directly recovered without SI by

$$\hat{X}^{(m)} = Y^{(m)} / \hat{H}^{(m)} - P^{(m)} \quad (12)$$

3.2. Estimation Enhancement: Phase Equalization Across Sub-blocks

Generally, the performance of PTS-PAPR reduction is directly proportional to the number of sub-blocks M . However, for a given ST power, a large M results in worse BER performance since the channel is estimated within each sub-block. To enable an efficient PAPR reduction without degrading the BER performance, an improved channel estimation with phase equalization across disjoint PTS sub-blocks can be adopted [6].

Note that, typically, in a CO-OFDM system, CFR H_k can be considered as time-invariant within the whole sub-blocks. The Phase factor set used at the transmitter can be recovered as follows.

$$\hat{b}_m = \frac{b_m H^{(m)}}{b_1 H^{(1)}} = \frac{\hat{H}^{(m)}}{\hat{H}^{(1)}}, \quad 0 \leq m \leq M-1 \quad (13)$$

where m is the sub-block index and b_m is the phase factor of the m th sub-block. After the decision of \hat{b}_m , the phase difference of the ST aided data sequence of each PTS sub-block is compensated by $\hat{Y}^{(m)} = Y^{(m)} / \hat{b}_m$. Hence, the estimation of CFR can be re-performed over the whole sub-blocks as

$$H_k = E(Y_k) / P_k, \quad 0 \leq k \leq N-1 \quad (14)$$

where $Y_k = \sum_{m=0}^{M-1} \hat{Y}^{(m)}$ is the ST aided data sequence with no phase difference. Finally, data symbols over the whole sub-blocks can be recovered using Eq. (12). To further improve the performance of channel estimation and thus yields a better BER performance, a decision feedback method [8, 9] can be adopted at receiver, where the recovered data symbols based on the channel estimation of the previous iteration by Eq. (12) are combined with the ST symbols to obtain a better channel estimate. After only a few iterations, the quality of the detected data symbols is substantially improved. For more details may refer to the ST based method [8, 9].

4. ST-PTS CO-OFDM SYSTEM ARCHITECTURE

The block diagram of ST-PTS CO-OFDM system is shown in Fig. 1. At the CO-OFDM transmitter, a pseudo random binary sequence (PRBS) is firstly modulated by using 4-QAM. After serial to parallel conversion, periodic training sequences are arithmetically added on to the data streams in frequency domain. To minimize the PAPR of the ST aided data streams, the T-PTS scheme is performed for each OFDM symbol. Next, IDFT and cyclic prefix (CP) insertion are followed to generate the time-domain OFDM signal which is then parallel/serial converted and D/A converted by two DACs operating at a sample rate of 32 GHz with 5-bit resolution. Finally, the optical domain OFDM signal generated via external modulation MZM is transmitted to the fiber link which consist of multiple spans of standard single mode fiber (SSMF), and each span have 80-km of the fiber with a span loss of 16 dB, an EDFA with a noise figure of 6 dB, and a 50-GHz optical band-pass filter.

At the CO-OFDM receiver, coherent detection with polarization diversity receiver is used for signal reception. After converting the signal from optical to electrical domain by using photo-detectors, the electrical signal is firstly resampled to 2 samples/sample and the resolution of the ADC is assumed to be 5 bits. To constrain the residual channel memory length to the one that can be detected by a training sequence with a short period, CD is compensated using a frequency domain equalizer [10], which is not shown in Fig. 1. After serial to parallel conversion, sub-block channel estimation is performed based on ST channel estimation method using Eq. (11). The phase

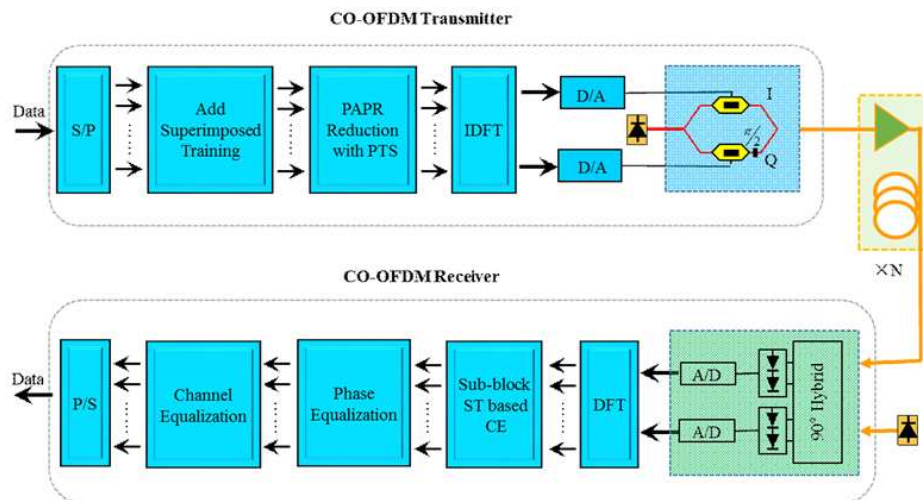


Figure 1: Simulation setup of the ST-PTS CO-OFDM system.

factor estimation is then carried out with the decision of the result of Eq. (13). Next, an accurate channel estimation is achieved over the whole sub-blocks on the condition that the phase difference of the ST aided data sequence of each PTS sub-block is equalized. Finally, the inverse of the estimated channel frequency response is applied to the received signal for the frequency domain equalization.

5. SIMULATION RESULTS AND DISCUSSION

The performance of the ST-PTS based SI free PAPR reduction scheme is evaluated through simulation on a coherent optical OFDM transmission system with the comparison of the traditional ST based channel estimation scheme. For each run, 16 OFDM symbols are used, each with 4096 point IFFT ($N_{\text{IFFT}} = 4096$) and oversampling ratio is 4 in all the simulations. Meanwhile, QPSK is used for mapping. The signal-to-pilot power ratio of the superimposed training is set to 12 dB. For simplicity, the set of phase rotation factors is $b_m \in \{1, -1\}$ and the number of the sub-blocks is 4 or 8.

Figure 2(a) shows the measured complementary cumulative distribution function (CCDF) curves of the PAPR in ST-PTS-OFDM, ST-OFDM and conventional OFDM (Conv-OFDM) transmission systems, respectively. As seen from Fig. 2(a), the PAPR performance of ST-OFDM scheme is very close to that of the conventional OFDM scheme. Compared with ST-OFDM method, the ST-PTS-OFDM offers about 1.7 dB and 2.8 dB of the PAPR reduction at $CCDF = 10^{-2}$ when $M = 4$ and $M = 8$, respectively.

Figure 2(b) shows the back-to-back (B2B) performance of the ST-PTS-OFDM and ST-OFDM methods when $M = 8$, respectively. For both schemes, one iteration feedback is used. It can be seen

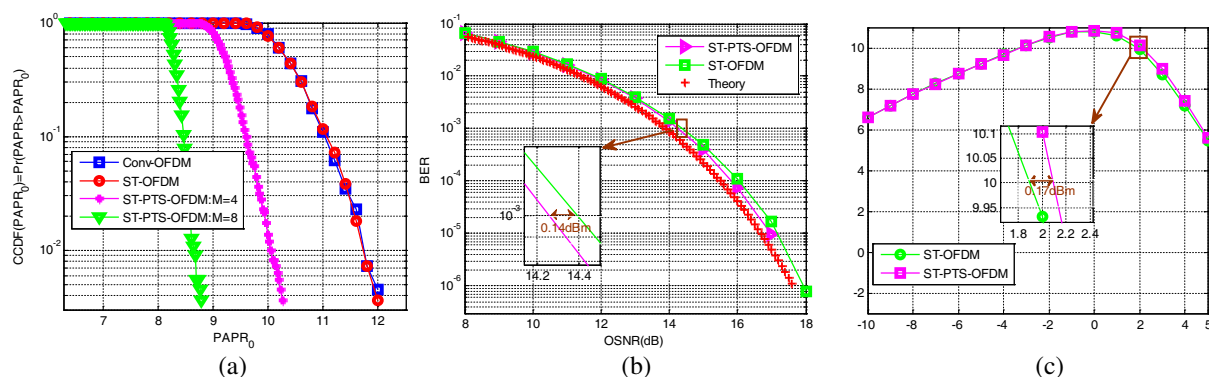


Figure 2: (a) CCDF comparison between the ST-PTS and ST methods, (b) back-to-back performances with different OSNR values, (c) comparison of 1600 km fiber performance.

that the BER performance of the ST-PTS-OFDM method is better than that of the ST-OFDM scheme with about 0.14 dB improvement at $\text{BER} = 1\text{E-}3$.

We also considered the nonlinear tolerance of the ST-PTS-OFDM approach after fiber transmission, which is shown in Fig. 2(c). A transmission link of 20 spans of SSMF is used. And the CD coefficient is 16 ps/ns/km while the fiber nonlinear refractive index is $2.6\text{e-}20\text{ m}^2/\text{W}$. An Erbium-doped fiber amplifier (EDFA) with a noise Figure $NF = 6$ dB is placed at the end of each fiber span. The results show that at Q -factor = 10, about 0.17 dBm launch-power penalty is achieved compared with the traditional ST based optical OFDM system. Therefore, the ST-PTS-OFDM method enables PAPR reduction of the traditional OFDM scheme based on [8, 11], and has a slight BER performance improvement.

6. CONCLUSION

The concept of the ST based SI free PTS-PAPR reduction for coherent optical OFDM transmission systems was introduced. The side information of PTS is considered as a part of channel frequency response which can be estimated using ST based channel estimation. With the aid of ST, an accurate channel estimation can be obtained followed by phase equalization across each interleaved PTS sub-block. Compared with the traditional ST-OFDM scheme without PAPR reduction, ST-PTS-OFDM method can get an OSNR improvement about 0.15 dB in both B2B and 1600 km fiber link coherent optical transmission systems.

ACKNOWLEDGMENT

This work is supported by the China Postdoctoral Science Foundation (No. 2013M531868), Guangdong Innovative Research Team Program (No. 201001D0104799318), 863 project (Ministry of Science and Technology of China, No. 2012AA012201), and the National Nature Science Foundation of China (No. 61107020).

REFERENCES

1. Shieh, W. and C. Athaudage, "Coherent optical orthogonal frequency division multiplexing," *Electron. Lett.*, Vol. 42, No. 10, 587–589, 2006.
2. Le Khoa, D., N. Tu, N. Thu, and N. Phuong, "Scramble PAPR reduction algorithms for fiber nonlinearity mitigation in long haul coherent optical OFDM systems," *IJCST. Org*, Vol. 3, No. 12, 8–13, 2012.
3. Tang, Y., W. Shieh, and B. S. Krongold, "DFT-spread OFDM for fiber nonlinearity mitigation," *IEEE Photonics Technol. Lett.*, Vol. 22, No. 16, 1250–1252, Aug. 2010.
4. Han, S. and J. Lee, "PAPR reduction of OFDM signals using a reduced complexity PTS technique," *IEEE Signal Process. Lett.*, Vol. 7, 2733–2740, Apr. 2004.
5. Liang, X., W. Li, W. Ma, and K. Wang, "A simple peak-to-average power ratio reduction scheme for all optical orthogonal frequency division multiplexing systems with intensity modulation and direct detection," *Opt. Express*, Vol. 17, No. 18, 15614–15622, Aug. 2009.
6. Tan, G., Z. Li, J. Su, and H. Zhang, "Superimposed training for PTS-PAPR reduction in OFDM: A side information free data recovery scheme," *Commun. Netw.*, 2013.
7. Jiang, T. and Y. Wu, "An overview: Peak-to-average power ratio reduction techniques for OFDM signals," *IEEE Trans. Broadcast.*, Vol. 54, No. 2, 257–268, Jun. 2008.
8. Guo, C., Z. Han, and L. Huang, "Channel estimation using superimposed training for coherent optical OFDM systems," *Asia Commun. Photonics Conf. 2013*, No. 3, AF2F.77, 2013.
9. Orozco-Lugo, A. G., M. M. Lara, and D. C. McLernon, "Channel estimation using implicit training," *IEEE Trans. Signal Process.*, Vol. 52, No. 1, 240–254, Jan. 2004.
10. Kudo, R., T. Kobayashi, K. Ishihara, Y. Takatori, A. Sano, and Y. Miyamoto, "Coherent optical single carrier transmission using overlap frequency domain equalization for long-haul optical systems," *J. Light. Technol.*, Vol. 27, 2009.
11. Huang, Z., J. Li, S. Zhang, F. Zhang, and Z. Chen, "Investigations of SPM suppression by PAPR reduction in coherent optical OFDM systems," *Asia Commun. Photonics Conf. Exhib.*, ThO5, 2009.

Dual-polarized FSS with Wide Frequency Tunability and Simple Bias Network

Hang Zhou¹, Xinhua Wang¹, Shaobo Qu¹, Lin Zheng¹, Hangying Yuan¹,
Mingbao Yan¹, Yongfeng Li¹, Jiafu Wang¹, Hua Ma¹, and Zhuo Xu²

¹College of Science, Air Force Engineering University, Xi'an 710051, China

²Electronic Materials Research Laboratory, Key Laboratory of the Ministry of Education
Xi'an Jiaotong University, Xi'an 710049, China

Abstract— In this paper, a dual-polarized frequency selective surface (FSS) with wide frequency tunability and simple bias network is presented. The FSS is composed of two-layered metallic structures. The top layer is etched with Jerusalem crosses and metallic grids. Varactor diodes are positioned between the grids and the Jerusalem crosses. The bottom layer is etched with crossed metallic lines. The two-layered structures are connected to each other with an array of plated vias. Based on this configuration, a DC path is created for biasing the varactors with the grids and crossed metallic lines. The FSS exhibits dual polarized performances using such a simple bias network. Numerical results obtained by full wave simulation method show that by altering the capacitance of the varactors from 0.2 to 1.0 pF, wide frequency tunability from 6.85 GHz to 3.7 GHz can be achieved. Design procedure and results of the FSS are presented and discussed.

1. INTRODUCTION

Frequency selective surfaces (FSSs) are usually planar periodic structures that function as spatial filters for electromagnetic (EM) waves [1, 2]. A classical application of FSS is to design the hybrid-radome for radar cross-section (RCS) controlling [3–5]. When the FSS radome is equipped in aircrafts, by properly designing the FSS filtering properties, the radar signal is not affected in the passband while the other signals out of the FSS passband can be reflected in the bi-static directions because of the radome's shape. In this case, a very weak signal will be left in the backscattering direction and make the radar stealthy out of band. However, in the passband such a FSS radome will be not effective for RCS reduction. To our knowledge, most of the radars have a wide frequency range. If we use a tunable FSS, the narrow passband of the FSS keeps synchronal with the aircraft radar narrow sweeping signal band, the exposed passband of the radar will be greatly reduced. Thus, the tunable FSS radome is an effective method of improving the radar stealth performance. In this situation, a tunable FSS with wide frequency tunability is required.

Early researchers have studied ferrite or liquid substrates in order to realize tunable FSS [6–9]. Literatures in [10, 11] use micro electromechanical system (MEMS) technology to build capacitors or switches to design tunable FSS. K. ElMahgoub et al. propose skewed grid method to achieve tunable FSS. A methodology for tunable FSS using Genetic Algorithms was presented in [12]. Varactor diode is an effective method of obtaining tunable FSS and has been investigated for about 30 years [13–21]. The key problem in designing tunable FSS is to realize a bias network [15, 17–19] because dynamic frequency behavior requires the reactive characteristics of the FSS to change with a tuning voltage or current.

In this paper, we design a frequency selective surface (FSS) with wide frequency tunability and simple bias network. A DC path is created for biasing the varactors with the grids and crossed metallic lines. The FSS exhibits dual polarized performances using such a simple bias network. In addition, by altering the capacitance of the varactors from 0.2 to 1.0 pF, wide frequency tunability from 6.85 GHz to 3.70 GHz can be achieved. Section 2 describes the process of designing the tunable FSS with a simple bias network. Moreover, Section 2 gives the analysis of the bandpass response of the FSS. Section 3 analyses different variable parameters' influences on the FSS performance. Finally, Section 4 documents the wide frequency tunability of such a tunable FSS structure.

2. DESIGN AND ANALYSIS

Figure 1 illustrates the configuration of the tunable FSS structure. The FSS is composed of two-layered metallic structures. The top layer is printed with Jerusalem crosses and metallic grids. Varactor diodes join the grids and the Jerusalem crosses. The bottom layer is printed with crossed metallic lines. Besides, the two-layered structures are connected to each other with an array of

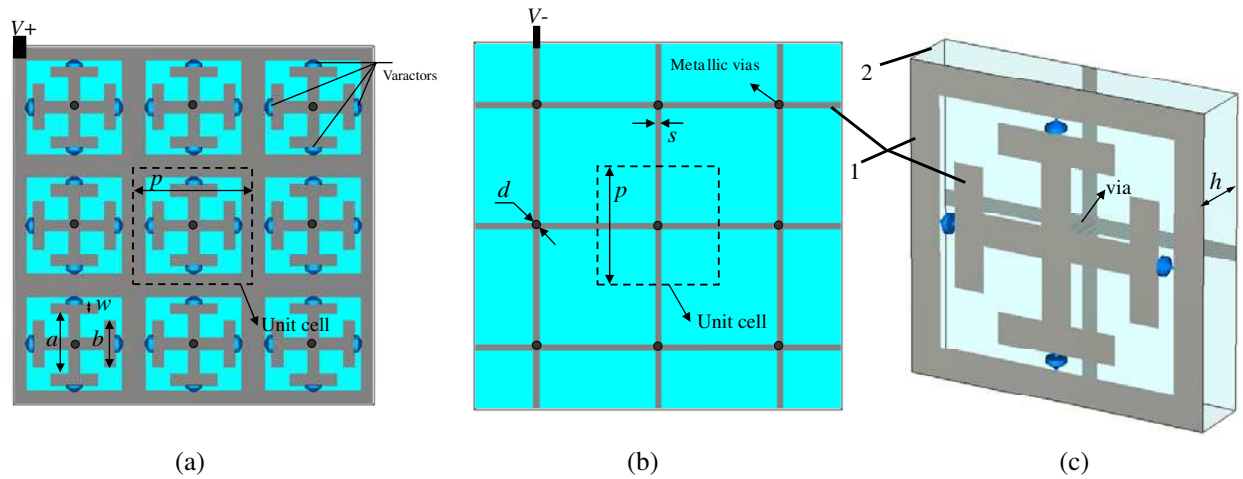


Figure 1: FSS structure. (a) Top view, (b) back view of the FSS and (c) three-dimensional view of the FSS unit cell. The FSS is a two-layered structure and connected by an array of plate vias. $p = 10.0$ mm, $a = 5.0$ mm, $b = 4.0$ mm, $s = 0.2$ mm, $d = 0.2$ mm, 1. PEC. 2. F4B-2 substrate, whose permittivity is 2.65, loss tangent is 0.001 and thickness is $h = 0.2$ mm.

plated vias. Using such a configuration, when the two-layered metallic structures are, respectively, loaded with positive and negative voltage, the varactor dipoles are excited. Thus, the capacitor values will be changed as the voltage changes.

CST Microwave Studio based on Finite Integration Method is used to calculate the transmission response. The FSS is assumed to be an infinite periodic structure. The FSS unit cell is excited by incident plane waves with different polarizations and various incident angles. The four sides of the unit cell are set to be periodic boundary conditions (PBC). Geometrical values of the structure are $p = 10.0$ mm, $a = 5.0$ mm, $b = 4.0$ mm, $s = 0.2$ mm, $d = 0.2$ mm. The substrate of the FSS is F4B-2, whose permittivity is 2.65, loss tangent 0.001 and thickness $h = 0.2$ mm. Transmission responses under different incidence angles and polarizations with varactor value $C = 0.4$ pF is shown in Fig. 2. For normal incidence, we can see that a resonance passband occurs at about 5.36 GHz and a transmission null appears at 6.36 GHz.

This phenomenon is usually generated by surface wave on the FSS. However, in all, such an unexpected resonance does not affect the transmission passband. Its equivalent circuit model can be shown in Fig. 3. In this model, L_1 and L_2 represent the top metallic grid and the bottom metallic lines, respectively. When the FSS is excited with TE or TM polarized electromagnetic waves, only two tunable varactors are effective. So the varactors can be expressed by C_v in the

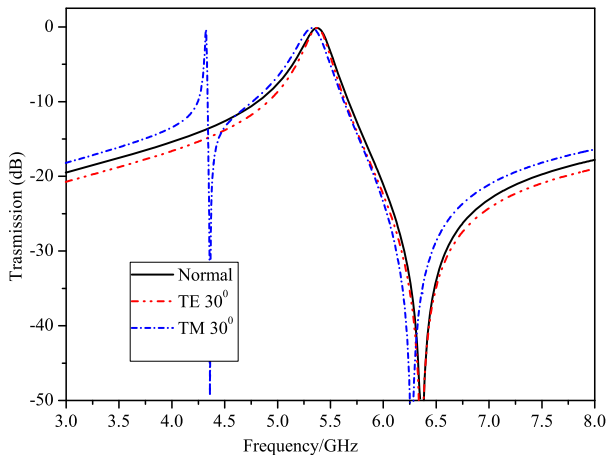


Figure 2: Transmission responses under different incidence angles and polarizations. The varactor value is $C = 0.4$ pF.

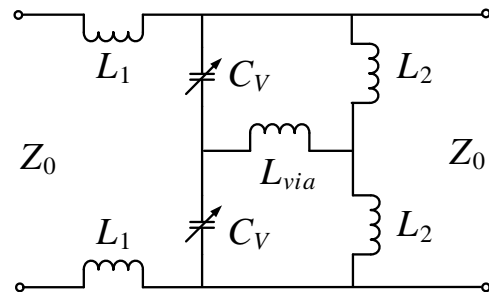


Figure 3: Circuit model of the FSS.

circuit. Besides, Z_0 represents the wave impedance in the vacuum, which is equivalent to 377Ω .

Stable performance of FSS under different incidence angles and polarizations is important for practical applications. From Fig. 2, we can find that for TE polarization and 30 degree incident angles, resonance of the passband is almost the same as the normal one except that bandwidth of the passband becomes a little narrower. For TM polarization and 30 degree incident angles, resonance of the passband shifts to a little lower frequency and an unexpected resonance occurs at about 3.27 GHz.

3. FREQUENCY TENABILITY

The varactors dipoles are excited by the bias network which is shown in Fig. 1. When the voltage is changed the capacitor values of the varactors will be changed. Limited by experimental equipment conditions, we cannot implement the experiment. Instead, we investigate the frequency tunability of the FSS when the capacitor value of the varactors is changed. Fig. 4 gives the transmission responses when capacitance of the varactors C ranges from 0.2 pF/mm to 1.0 pF. As shown in Fig. 4, by altering the capacitance of the varactors from 0.2 to 1.0 pF, a wide frequency tunability from 6.85 to 3.7 GHz can be achieved. Fractional bandwidth of the frequency tenability is about 60%. Such frequency tenability can also be illustrated by Fig. 5, which shows the reflection spectra versus the capacitance of the varactors. The reflection is about -15 dB and doesn't change evidently as the capacitance of the varactors increase. Consequently, such a tunable FSS possesses wide frequency tunability, simple bias network and good transmission response. It is a good candidate for designing aircraft FSS radar radomes.

4. CONCLUSION

A tunable frequency selective surface (FSS) with wide frequency tunability and simple bias network is presented. Numerical results obtained by full wave simulation method show that by altering the capacitance of the varactors from 0.2 to 1.0 pF, wide frequency tenability from 6.85 to 3.7 GHz can be achieved. The profile is only 0.2 mm and far less than the operating wavelength. By virtue of these advantages, such a FSS provides practical applications to FSS radomes for radar stealth.

ACKNOWLEDGMENT

This work was supported Project supported by the National Natural Science Foundation of China (Grant Nos. 61302023, 11274389, 11204378).

REFERENCES

1. Munk, B. A., *Frequency Selective Surfaces: Theory and Design*, Wiley, New York, 2000.
2. Wu, T. K., *Frequency Selective Surfaces and Grid Arrays*, Wiley, New York, 1995.
3. Pelton, E. L. and B. A. Munk, "A streamlined metallic radome," *IEEE Trans. Antennas Propag.*, Vol. 22, No. 6, 799–803, 1974.
4. Zhou, H., S. Qu, B. Lin, J. Wang, H. Ma, and Z. Xu, "Filter-antenna consisting of conical FSS radome and monopole antenna," *IEEE Trans. Antennas Propag.*, Vol. 60, No. 6, 3040–3045, 2012.
5. Yang, Y., H. Zhou, X.-H. Wang, and Y. Mi, "Low-pass frequency selective surface with wide-band high-stop response for shipboard radar," *Journal of Electromagnetic Waves and Applications*, Vol. 27, No. 1, 117–122, 2013.
6. Chang, T. K., R. J. Langley, and E. A. Parker, "Frequency selective surfaces on biased ferrite substrates," *Electron. Lett.*, Vol. 30, No. 15, 1193–1194, 1994.
7. Liu, Y., C. G. Christodoulou, and N. E. Buris, "Fullwave analysis method for frequency selective surfaces on ferrite substrates," *Journal of Electromagnetic Waves and Applications*, Vol. 11, No. 5, 593–607, 1997.
8. Lima, A. C., E. A. Parker, and R. J. Langley, "Tunable frequency selective surface using liquid substrates," *Electron. Lett.*, Vol. 30, No. 4, 281–282, 1994.
9. Li, M., B. Yu, and N. Behdad, "Liquid-tunable frequency selective surfaces," *IEEE Microw. Wireless. Comp. Lett.*, Vol. 20, No. 8, 423–425,
10. Schoenlinner, B., A. Abbaspour-Tamijani, L. C. Kempel, and G. M. Rebeiz, "Switchable low-loss RF MEMS Ka-band frequency-selective surface," *IEEE Trans. Microw. Theory Tech.*, Vol. 52, 2474–2481, 2004.

11. Coutts, G. M., R. R. Mansour, and S. K. Chaudhuri, “Microelectromechanical systems tunable frequency-selective surfaces and electromagnetic-bandgap structures on rigid-flex substrates,” *IEEE Trans. Microw. Theory Tech.*, Vol. 56, No. 7, 1737–1746, 2008.
12. Bossard, J. A., D. H. Werner, T. S. Mayer, and R. P. Drupp, “A novel design methodology for reconfigurable frequency selective surfaces using genetic algorithms,” *IEEE Trans. Antennas Propag.*, Vol. 53, No. 4, 1390–1400, 2005.
13. Hunter, I. C. and J. D. Rhodes, “Electronically tunable microwave bandpass filters,” *IEEE Trans. Microw. Theory Tech.*, Vol. 30, No. 9, 1354–1360, 1982.
14. Chang, T. K., R. J. Langley, and E. A. Parker, “Active frequency-selective surfaces,” *Proc. IEEE Microwaves, Antennas Propag.*, Vol. 143, 62–66, 1996.
15. Mias, C., “Varactor-tunable frequency selective surface with resistive lumped-element biasing grids,” *IEEE Microw. Wireless Compon. Lett.*, Vol. 15, No. 9, 2005.
16. Bayatpur, F. and K. Sarabandi, “A tunable metamaterial frequency-selective surface with variable modes of operation,” *IEEE Trans. Microw. Theory Tech.*, Vol. 57, No. 6, 1433–1438, Jun. 2009.
17. Sanz-Izquierdo, B., E. A. Parker, and J. C. Batchelor, “Dual-band tunable screen using complementary split ring resonators,” *IEEE Trans. Antennas Propag.*, Vol. 58, No. 11, 2010.
18. Bayatpur, F. and K. Sarabandi, “Design and analysis of a tunable miniaturized-element frequency-selective surface without bias network,” *IEEE Trans. Antennas Propag.*, Vol. 58, No. 4, 12414–1219, 2010.
19. Sanz-Izquierdo, B., E. A. Parker, J.-B. Robertson, and J. C. Batchelor, “Tuning patch-form FSS,” *Electron. Lett.*, Vol. 46, No. 5, 329–330, 2010.
20. Sanz-Izquierdo, B., E. A. Parker, and J. C. Batchelor, “Switchable frequency selective slot arrays,” *IEEE Trans. Antennas Propag.*, Vol. 59, No. 7, 2728–2731, 2011.
21. Martinez-Lopez, R., J. Rodriguez-Cuevas, A. E. Martynyuk, and J. I. Martinez Lopez, “An active ring slot with RF MEMS switchable radial stubs for reconfigurable frequency selective surface applications,” *Progress In Electromagnetics Research*, Vol. 128, 419–440, 2012.

Study and Design of the Novel Shunt Liner Active Power Filter for a Superconducting Magnet Power Supply

Jinglin Wu and Xiaoning Liu

University of Science and Technology of China, Hefei, Anhui, China

Abstract— The superconducting outsert of the 40 T hybrid-magnet in High Magnetic Field Laboratory (HFML) of Chinese Academy of Sciences (CAS) requires a highly stabilized low-voltage high-current power supply. One of the design is a switching power supply with active DC power filter. As the current flowing through a Shunt Active Power Filter (SAPF) is only the ripple current, the power loss caused by the filter can be very low, so SAPF is more and more applied in high-current devices. Usually, a shunt PWM converter can be used to generate current which is equal but oppositely phased to the ripple current. However, EMI noises caused by PWM have great influence on the circuit and the speed of response is limited by the switching frequency. Meanwhile, the load voltage variation makes it very difficult to design parameters of the filter. In this paper, a novel shunt liner active power filter (SLAPF) is designed to overcome the disadvantages of existing dc active filter schemes. Structurally, SLAPF can be divided into two components, one is the current compensator, and the other is the auxiliary power supply. The current compensator is composed of a power supply with fixed output voltage and two parallel branches, each of which consists an adjusting transistor. The auxiliary power supply is used to ensure the voltage across the adjusting transistors keep in a proper range, so the transistors can always operate in the saturation region. Based on the on-resistance variability of adjusting transistors, just as the series linear regulator, the output current of the current compensator can accurately track the oppositely phased out ripple current of main circuit, which leads to a good filter effect. In the paper, the detail structure and working principle of SLAPF are presented at first, then the design flow is described, which includes the control method of the current compensator, the analysis of topology chosen for auxiliary power supply. At last, the experimental results show that the filtering effect of SLAPF is good enough to make the power supply meet the technical requirements.

1. INTRODUCTION

One of the schemes of the power supply for the superconducting outsert in High Magnetic Field Laboratory (HFML) is the switching power supply. The magnet requires highly stabilized current, however, it is hard to depress the low frequency ripple caused by three-phase uncontrolled rectifier which is the input of the switching converter. In order to reduce the output ripple, the passive filter, if used alone, requires much larger output inductance and capacitance, which will increase the cost and volume of the device and exacerbate the dynamic characteristics. Moreover, the low-frequency output ripple cannot be depressed effectively. Accordingly, we consider to add an active DC power filter to the output of the switching power supply [1]. As the current flowing through a Shunt Active Power Filter (SAPF) is only the ripple current, the power loss caused by the filter can be very low, so SAPF is more and more applied in high-current devices [2]. Usually, a shunt PWM converter can be used to generate current which is equal but oppositely phased to the ripple current. However, EMI noises caused by PWM have great influence on the circuit and the speed of response is limited by the switching frequency. Meanwhile, the load voltage variation makes it very difficult to design parameters of the filter [3]. In this paper, a novel shunt liner active power filter (SLAPF) is designed to overcome the disadvantages of existing dc active filter schemes.

2. BASIC STRUCTURE OF SLAPF

Figure 1 shows the basic structure of SLAPF. In this figure, L_f represents the filter inductance, M_1 and M_2 represent series adjusting transistors which consist of multiple MOSFETs connected in parallel in actual design, i_b represents the current of the branch of filter capacitor C_f , i_c represents the current which flows through C_f , $-i_{Ah}$ represents the output current of SLAPF, APFS1 and APFS2 represent the auxiliary power supply while the voltage across APFS2 is V_{apf} and the voltage across APFS1 is $V_{apf+} - V_{apf} = V_{apfs1}$, R_o represents the load resistance, L_o represents the load inductance, V_o represents the output voltage, I_o represents the output current.

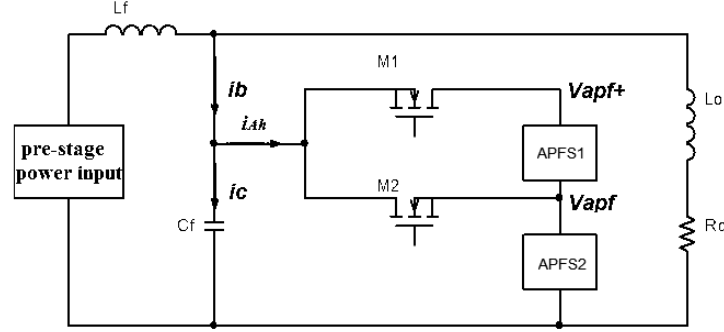


Figure 1: Structure of SLAPF.

According to Figure 1:

$$i_c = i_b - i_{Ah} \quad (1)$$

$$u_o = i_c \cdot Z_{cf} \quad (2)$$

where Z_{cf} is the impedance of C_f , u_o is the ripple of output voltage.

According to Equation (1) and Equation (2), if i_{Ah} can track i_b well, i_c will approach to 0, then the ripple of i_o will approach to 0 too. When $i_b > 0$, let M_2 be turned on while M_1 be turned off, and V_{apf} be set to be lower than V_o , then the positive half-cycle of i_b will flow through M_1 into APFS2. When $i_b < 0$, let M_1 be turned on while M_2 be turned off, and V_{apf+} be set to be higher than V_o , then the APFS1 and APFS2 will output compensating current which will flow through M_2 into the original circuit.

The variable on-resistance of MOSFET is used to realize current tracking. When the MOSFET works in the saturation region, its gate-source voltage can adjust the drain current with strongest ability, so V_{apf} need to be kept with a proper value to ensure a proper gate-source voltage so that the MOSFET can always work in the saturation region.

Structurally, SLAPF can be divided into two components, one is the current compensator composed by M_1 , M_2 APFS1 and a proper V_{apf} , the other is the auxiliary power supply APFS2.

3. ACTUAL STRUCTURE OF SLAPF

The actual structure of SLAPF is shown as Figure 2, where C_3 is an energy-storage capacitor [4].

The two adjusting transistor T_1 and T_2 could be considered as a bidirectional push-pull controlled current source. The voltage across C_3 will fluctuate when the current flows through the transistors to inject into or sink from C_3 . In the ideal situation, the average voltage across C_3 (U_{apf}) remain unchanged, however, the leakage current of C_3 and the irregular harmonic current can lead U_{apf} to be outside of the normal operating range.

When U_{apf} is lower than the lower bound of normal operating range, the constant current charging power supply HP-FS should charge C_3 to make U_{C3} raise back into the normal range. When U_{C3} is higher than the high bound of normal range, we can use a couple of resistors to release the stored energy of C_3 to make U_{C3} fall back into the normal range. Different value of resistance should be connected into the circuit under different U_{C3} to limit the discharge current. Synthesizes the above analysis, HP-FS, energy-removal resistor network, and C_3 make up the auxiliary power supply APFS2 in the basic structure.

In some cases, the V_{apf} should be negative to make certain the voltage across the transistor be higher than the ripple voltage. The adjustable DC power supply APFS3 can offer this negative voltage if the switch sk is turned on.

4. CALCULATION OF THE NORMAL OPERATING RANGE OF U_{APF}

Assume the drop collector-to-emitter voltage of T_1 is V_{ce1} , the drop collector-to-emitter voltage of T_2 is V_{ce2} , and the minimal drop collector-to-emitter voltage of the IGBT transistor is V_{ce_min} to ensure the transistor can always work in the saturation region. Obviously, $V_{ce1} \geq V_{ce_min}$, $V_{ce2} \geq V_{ce_min}$.

When T_1 is turned on while T_2 is turned off:

$$V_o - V_{ce2} = V_{apf} \quad (3)$$

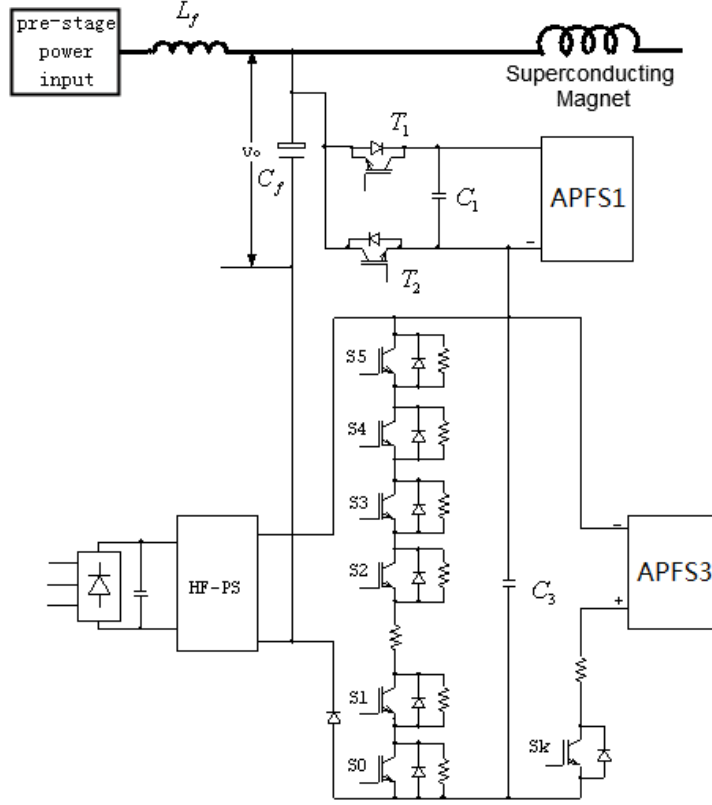


Figure 2: Actual structure of SLAPF.

When T_2 is turned on while T_1 is turned off:

$$V_{apf} + V_{apfs1} - V_{ce1} = V_o \quad (4)$$

According to Equations (3) and (4), we obtain:

$$V_o - V_{ce2} + V_{apf} + V_{apfs1} - V_{ce1} = V_{apf} + V_o \quad (5)$$

Thus,

$$V_{apfs1} = V_{ce1} + V_{ce2} \geq 2V_{ce_min} \quad (6)$$

According to Equation (3), we obtain:

$$V_{ce2} = V_o - V_{apf} \geq V_{ce_min} \Rightarrow V_o - V_{ce_min} \geq V_{apf} \geq U_{apf} - \Delta V \Rightarrow U_{apf} \leq V_o - V_{ce_min} + \Delta V \quad (7)$$

According to Equation (4), we obtain:

$$\begin{aligned} V_{ce1} &= V_{apf} + V_{apfs1} - V_o \geq V_{ce_min} \Rightarrow V_o + V_{ce_min} - V_{apfs1} \leq V_{apf} \leq U_{apf} + \Delta V \\ &\Rightarrow U_{apf} \geq V_o + V_{ce_min} - V_{apfs1} - \Delta V \end{aligned} \quad (8)$$

According to Equations (6) and (8), we obtain:

$$V_o + V_{ce_min} - V_{apfs1} - \Delta V \leq U_{apf} \leq V_o - V_{ce_min} + \Delta V \quad (9)$$

where $V_{apfs1} \geq 2V_{ce_min}$.

APFS1 is a DC power supply with adjustable output voltage in practice. On one hand, we can use Equation (9) to calculate the normal operating range of U_{apf} if V_{apfs1} is set to a fixed value, on the other hand, according to Equation (6), we obtain:

$$V_o + V_{ce_min} - V_{apfs1} - \Delta V \leq V_o + V_{ce_min} - 2V_{ce_min} - \Delta V = V_o - V_{ce_min} - \Delta V \quad (10)$$

According to Equations (8) and (10), if U_{apf} satisfies the flowing equation:

$$U_{apf} \geq V_o - V_{ce_min} - \Delta V \quad (11)$$

Then V_{apf1} satisfies Equation (8) certainly, which means if the normal operating range of U_{apf} is:

$$V_o - V_{ce_min} - \Delta V \leq U_{apf} \leq V_o - V_{ce_min} + \Delta V \quad (12)$$

Then the adjusting transistor can always work in the saturation region.

5. STRUCTURE OF HFPS

As shown in Figure 3, HF-PS is composed of a pair of ZVS switching converter with full bridge rectifier, the first windings of transformers is connected in parallel so that the current stress of the switch tubes can be less, the second windings of transformers is connected in series so that the voltage stress of the diodes can be less.

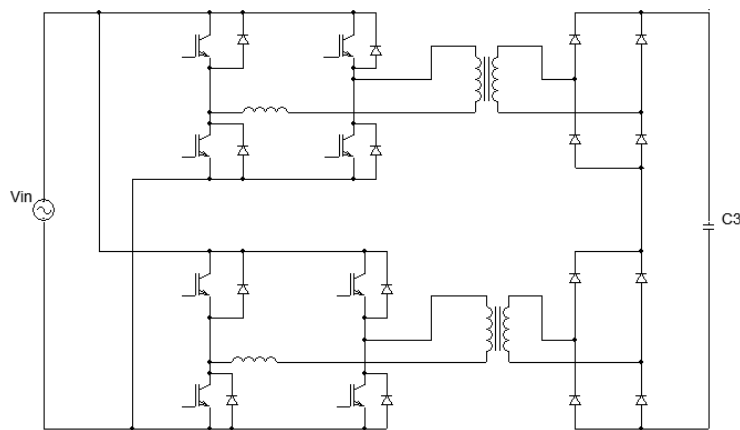


Figure 3: Structure of HF-PS.

6. EXPERIMENTAL VERIFICATION

In order to verify the filtering effect of SLAPF, a 10 V/1 kA prototype with $C_f = 50$ mF, $R_o = 10$ m Ω and $L_o \approx 5$ μ H is designed. The input of the switching converter is a 380 V/50 Hz three-phase uncontrolled rectifier. The current measurement is based on the high precision DCCT. In the prototype, a ZVS-CV converter is used to take the place of HP-FS and energy-removal resistor network [5].

The wave of output ripple without SLAPF comparing to that with SLAPF are shown in Figure 4 and Figure 5.

According to the Figure 4 and Figure 5, the ripple factor of output voltage without SLAPF is about 120 mV/10 V = 1.2%, and the ripple factor of output voltage with SLAPF is about 10 mV/10 V = 0.1% which is smaller than the maximum voltage ripple coefficient (1%).

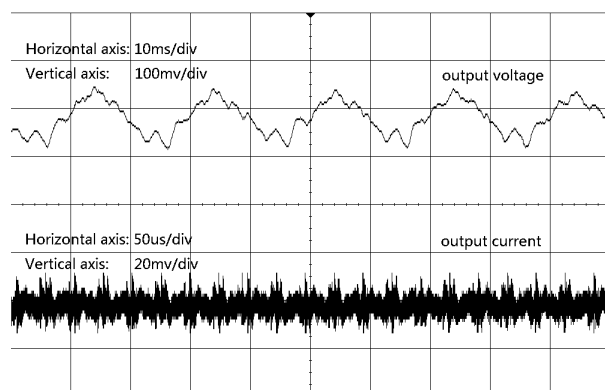


Figure 4: Output waveforms without SLAPF.

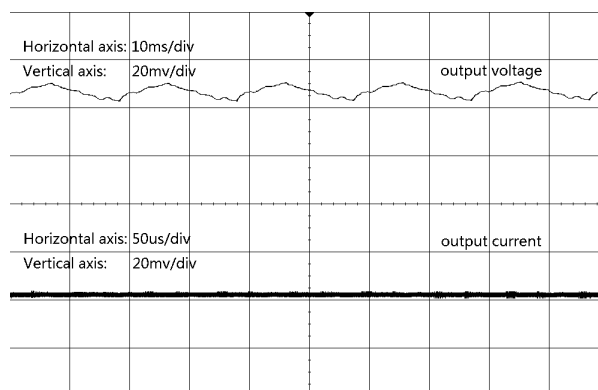


Figure 5: Output waveforms with SLAPF.

The peak-peak ripple of output current without SLAPF is about 3 A (0.03×100) while the ripple factor is $3/1000 = 0.3\%$, and the peak-peak ripple of output current with SLAPF is about 0.4 A (0.004×100) while the ripple factor is $0.4/1000 = 0.04\%$ which is smaller than the maximum current ripple coefficient (0.1%). The results show that the output current and voltage ripple are reduced by SLAPF dramatically.

ACKNOWLEDGMENT

The authors wish to thank the High Magnetic Field Laboratory of Chinese Academy of Sciences and the financial support for this research from the National Natural Science Foundation of China (No. 50977086).

REFERENCES

1. Kido, G., et al., "Development of active filter with MOS-FET for 15 MW dc power source," *Journal of Physics: Conference Series*, Vol. 51, No. 1, 580, 2006.
2. Murat, K. and E. Ozdemir, "An adaptive hysteresis band current controller for shunt active power filter," *Electric Power Systems Research*, Vol. 73, No. 2, 113–119, 2005.
3. Peng, F.-Z., H. Akagi, and A. Nabae, "A study of active power filters using quad-series voltage-source PWM converters for harmonic compensation," *IEEE Transactions on Power Electronics*, Vol. 5, No. 1, 9–15, 1990.
4. Long, J., J. Wu, X. Liu, and S. Chen, "Simulation and design of fast charging and discharging of bi-directional DC-DC converter for the active power filter," *High Voltage Engineering*, Vol. 39, No. 7, 1792–1797, 2013.
5. Chen, Z.-J. and X.-N. Liu, "Soft-switching DC/DC converter for intensive magnet field power supply," *Power Electronics*, Vol. 42, No. 2, 1618, 2008.

Design of Ku-band Dielectric Resonator Filter for Satellite Applications

Seyi Stephen Olokede, Nor Muzlifah Mahyuddin, Majid Rafiee, and Enoch Adama Jiya

School of Electrical & Electronic Engineering
Universiti Sains Malaysia, Nibong Tebal, Penang 14300, Malaysia

Abstract— Presented is the design of Ku-Band dielectric resonator filter for satellite applications. The uniqueness of this design is based on the simple feeding arrangement that utilizes a microstrip transmission line section but segmented piecewisely into four stubs, where each stub is offset from the preceding with a distance equal to the diameter of the DRs. Each DR couples electromagnetic energy from the input port via the first to another, and so until, until the final output port. The response of the design is assessed by comparing the simulated and experimental results. The simulated S -parameter results were compared with those obtained experimentally. The simulated and experimental reflection magnitude $|S_{11}|$ is within -6 dB across the band, whereas the transmission magnitude $|S_{12}|$ is -1.66 dB up to 17.5 GHz.

1. INTRODUCTION

Advances in technologies and continued growth of wireless devices has continue to challenge the community to design and produce new alternative but smaller and more multifunctional filters that are suitable and relevant to the current technology. It is evident that the traditional filter such as waveguide filter is no longer attractive, efficient, nor adequate for today's technology that demands small, compact, easy integration and cheap solution to almost every electronic device. Although until recently, alternative filter solutions employing microstrip technology where such filter design consist of only a few rows of parallel-coupled transmission lines has been ground breaking and remarkable. However, such filter becomes unrealizable as the frequency of the filter increases. The gap between the two neighbouring microstrip lines becomes narrower resulting to a very tight coupling. The strait spacing between the rows of parallel-coupled transmission lines complicates the fabrication processes of the filter as the printing machine only supports etch limitation up to a minimum trace and gap of about 0.3 mm.

To overcome this serious challenge therefore, it is contingent to investigate the possibility of an alternative novel-fed dielectric resonator filter for Ku-band applications. Dielectric resonators (DRs) offer more flexibility in filter design. The proposed design is such that three identical cylindrical DRs are excited by four microstrip lines of certain dimensions. The dimensions are multiples of quarter wavelengths of the centre frequency of which the filter operates, and are calculated to coincide with maximum radiation of the transmission lines based on the standing wave ratio formation of the voltage allocation on shorted microstrip transmission line. Besides, these stubs and the DRs were configured in such a way that the DRs were positioned in a manner that their various resonances overlap constructively [1]. In effect, wideband impedance bandwidth was achieved. Instead of the conventional direct side proximity-coupled microstrip feed line common among series feed array, the proposed utilizes the same principle, but rather with broken or piecewise segmented transmission stubs such that each stub is of a dimension of odd multiple of quarter wavelength. The widths are determined by their characteristic impedance equivalency. Not only was the transmission line broken into stubs, the stubs were also offset from each other by the diameter of the cylindrical DRs. By this arrangement, it is therefore evident that each DR is placed in between two transmission lines, and as such, the first DR coupled electromagnetic energy from the input port to the next transmission stub, and so on until the output port. Essentially, the proposed feed will mitigate the effect of unnecessary reflection, and thus deliver a better match, good reflection coefficient, improved bandwidth and performance as it is expected that a good impedance match will naturally improve the filter efficiency. In effect, the proposed will efficiently couple the signal energy from one microstrip to the other while providing a good performance and low insertion loss.

2. THE DESIGN

For a filter circuit to pass a certain frequency and rejects or attenuates all the other unwanted component of the signal, two frequencies f_1 and f_2 must be defined as the lower and upper cut-off frequencies respectively. The differential Δf between these two frequencies where ($\Delta f = f_2 - f_1$)

is referred to as the bandwidth. The magnitude of this differential determine whether the filter is a narrowband ($\Delta f < 500$ MHz), and wideband otherwise. One of the serious challenges militating against the DRs in spite of its many attractiveness is the narrow bandwidth limitations. Consequently, a new vista of challenges on bandwidth enhancement became serious issue of concern. Attempt to solve this limitation deepens, and several novel alternative solutions have been reported but with different performance penalties. According to Rezaei et al. [2], there are three broad techniques that can be used to enhance the bandwidth of the DR by either lowering the inherent Q -factor of the resonator or using external matching networks or combine multiple dielectric resonators. Matching networks, such as matching stubs can be used to increase the bandwidth of a DR by transforming its input impedance to better match than that of the coupling circuit. In this study, we have decided to employ the second approach, using a novel feed. This is because using additional DRs can also result in generating extra resonant frequency which can contribute to the wideband DR. In multiple DRs, dielectric resonator can be arranged either in stacked configuration or parasitic co-planar configuration [3]. The idea is that, the merged frequency band can achieve wideband provided that

$$f_1 + \frac{\Delta f_1}{2} \geq f_2 - \frac{\Delta f_2}{2} \quad (1)$$

where Δf is the 3-dB bandwidth of S_{11} curve, f_1 and f_2 is the resonant frequency from the two segments with $f_1 < f_2$ [2–4]. Whereas, if the resonant frequencies are spaced further apart, then a dual band operation instead of wide band will result. Two half rectangular DRs, due to their different size with the same permittivity, resonated in two different adjacent frequency merged together to produce wideband DR [1, 3].

In [5], Ain et al. uses three DRs in an arrangement depicted in Figure 1(b). Therefore, the filter performance was consequent on the geometry and the locations of the resonators on the feed line, where all the DRs have the same permittivity and dimensions. Each dielectric resonator resonates at the same mode but at different frequency, thus combines together the DRs respective frequencies to form a wide-bandwidth provided that Equation (1) is satisfied. Authors in [6] employed this technique with certain but significant modifications as shown in Figure 1(b). In his method, the effect of reflections due to coupling mismatch with attendant poor voltage standing wave ratio (VSWR) common to the conventional direct-coupled microstrip transmission line as employed by

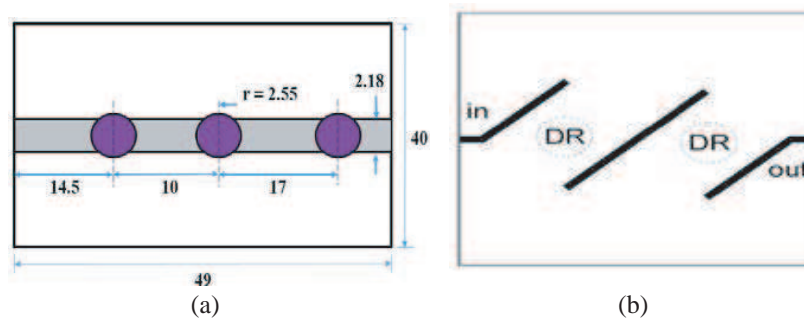


Figure 1: Existing similar works.

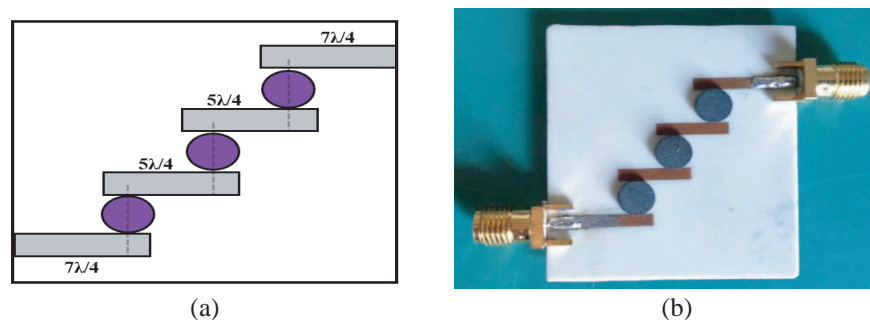


Figure 2: The proposed design. (a) Schematic. (b) Prototype.

Ain et al. was eliminated. Our proposed design is similar to that reported in [6] but differ in terms of the number of DRs and the geometry of the microstrip line. Instead, the microstrip feed stubs are configured as shown in Figure 2. The first (input port) and last (output port) stubs were set at $7\lambda/4$, whereas the two intermediate stubs were set at $5\lambda/4$ where λ is the guided wavelength. The width of each stub is calculated to be 1.9 mm in order to approximate to the characteristic impedance of the microstrip line. All the three DRs are identical, and are made of $\text{CaCu}_3\text{Ti}_4\text{O}_{12}$ (CCTO), each with a radius of 2.75 mm, a dielectric permittivity (ϵ_r) of 36, and a thickness (h) of 1 mm.

In this design, the signal is coupled to the DRs using a few procedure of parallel coupled transmission stub excitation as earlier said. Each resonator couples electromagnetic energy over $n\lambda/4$ stubs to the neighbouring resonator, thereby forming a staggered line. The DRs are then placed between each line, such that the coupling gap between each DR and the transmission line is 0.2 mm. The value of a quarter-wavelength is calculated to be 2.509 mm at the centre frequency, which is twice smaller than the diameter of each DR of 5.5 mm. Consequently, the length of the transmission line was adjusted to odd multiple integers of the guided wavelength in order to catch the antinodes radiation of the voltage allocation on a short-ended microstrip transmission line.

The proposed design was modeled using finite integration technique (FIT) full-wave CST commercial solver, and the resulting design is fabricated on the Duroid RO4003C microwave laminate board of permittivity (ϵ_s) of 3.38, with a substrate thickness (h_s) of 0.813 mm, $\tan(\delta)$ of 0.0027, and a metal thickness (t) of 0.035 mm. Subsequently, the fabricated design was measured, and the measured and simulated results were plotted to determine the degree of agreement.

3. RESULTS AND DISCUSSIONS

The TM_{01} resonant mode was excited, and the simulated resonance frequency occurred at 17.1 GHz which is within the Ku-Band of (12 to 18 GHz) as shown in Figure 3. The physical dimensions of the dielectric cylinder were optimized to satisfy the excitation mode resonance. The simulated $|S_{21}|$, $|S_{11}|$, and the bandwidth are -1.66 dB, -15 dB, and 366 MHz respectively as shown in the figure. The measured S -parameter results are shown in Figure 4. The measured $|S_{21}|$, $|S_{11}|$, and the bandwidth are -23.12 dB, -17.66 dB, and 550 MHz respectively.

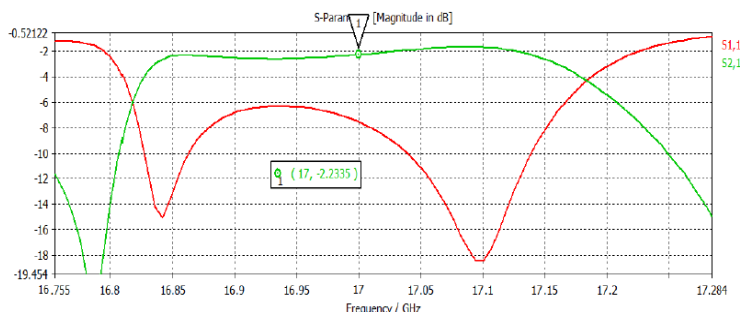


Figure 3: The simulated S -parameters of the proposed design.

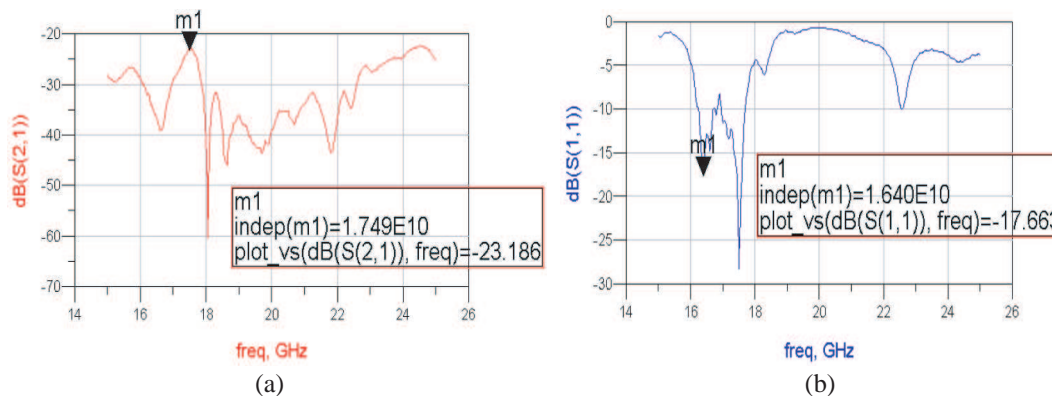


Figure 4: The measured S -parameters of the proposed design. (a) The $|S_{21}|$. (b) The $|S_{11}|$.

Table 1: Simulated and measured results comparison.

Parameters	Simulation	Measurement
$ S_{21} $ dB	-1.66	-23.12
$ S_{11} $ dB	-15.02	-17.66
Bandwidth (MHz)	366	550
f_0 (GHz)	17	17.5

The result obtained from testing the fabricated filter greatly differs from the simulated result. This is seen especially in the measured insertion loss value. The filter shows high insertion loss of -23.186 dB as compared to the simulation of -1.663 dB. The simulated result shows a good, almost 0 dB insertion value but the loss during measurements was significant. The high insertion loss value shows that a large unnecessary portion of the signal power is lost at the input port, resulting to a meagre transmitted signal energy through to the output port. In this case, the filter is therefore not efficient for real life use. Besides, the measured filter response shows a slight shift in the frequency. The operating frequency of the simulated result shows that the filter has a centre frequency of 17 GHz while the measured result shows resonance at 17.49 GHz. This suggests that the operating frequency of the filter shifted for a rough amount of 490 MHz. This situation is a bit difficult to totally avoid as it is pretty difficult to appropriate place all the DRs at exact coordinate as simulated. Alternatively therefore, the electromagnetic waves are not totally confined in the device. For high frequency RF devices, even a millimeter change will greatly affect the response of the device.

Further optimization was done where it was discovered that the measured loss at this point was approximately -3.249 dB. To compensate for the transmission line losses, the measured transmission line loss was subtracted from the measured insertion loss of the filter. Subsequently, issue of inefficient coupling due to relatively large coupling spacing between the DRs and feed line, which however could lead to tangible energy loss was addressed. Eventually, a better and efficient results were obtained as shown in Figure 5 and Table 2.

The insertion loss is better than the early design where the $|S_{21}|$ shows a good flat line that approached 0 dB. The 2 pole filter also exhibits a good return loss of over -15 dB. However the filter operates at a frequency of 15.75 GHz which is different from the previous un-optimized result. The measured result showed improvement in terms of $|S_{21}|$. Comparing this with the previous un-optimized filter, the insertion loss of the final design improves significantly to -6.363 dB. However, the operating frequency deviates from the simulation result. This dissimilarity is due to the inability to accurately position the DRs at the actual coordinate during, thus leading to a change in frequency and bandwidth. The simulated result and the measured result is compared in Table 2.

Moderately, the use of the three DRs is proven to produce a wide bandwidth bandpass filter.

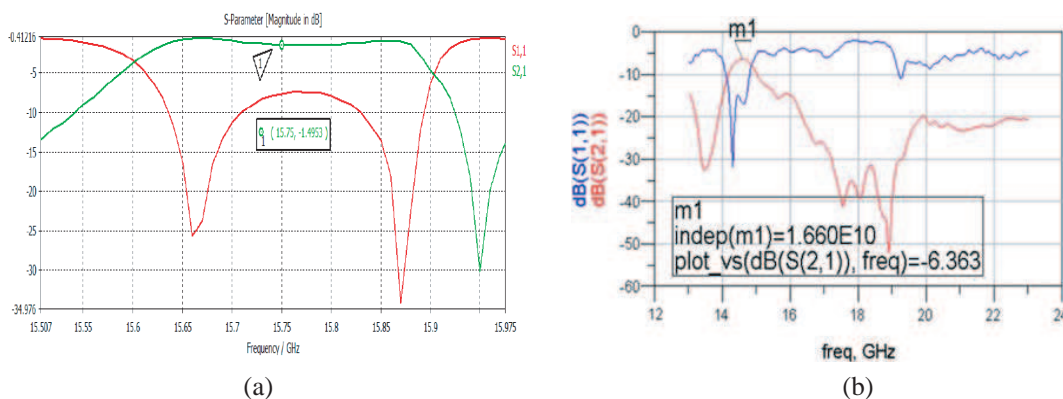

 Figure 5: The optimized S -parameters of the proposed design. (a) Simulated. (b) Measured.

Table 2: Optimized simulated and measured results comparison.

Parameters	Simulation	Measurement
$ S_{21} _{\text{dB}}$	-0.60	-6.36
$ S_{11} _{\text{dB}}$	-25.68	-17.0
Bandwidth (MHz)	299	800
f_0 (GHz)	15.75	14.59

The result shows that each dielectric resonator resonates with different frequency but in the same mode that the combination of all frequency will produce a wider response that could increase the overall bandwidth of the filter.

4. CONCLUSIONS

In this paper, the design of Ku-Band bandpass filter for satellite applications has been investigated. The parametric effect of the feed with respect to the coupling spacing, as well as the efficiency of the coupled energy bearing in mind the decomposed nature of the proposed feed. It was evident that the combination of all the DRs responses lead to a final bandwidth of 800 MHz, which is larger than each DR individual bandwidth. This therefore verify this theory that if there are DRs labelled as DR₁, DR₂ and DR₃, with their discrete resonant frequencies of f_1 , f_2 and f_3 , and bandwidth of BW₁, BW₂ and BW₃ respectively, then the combination of their composite resonances is a wideband provided a certain inter-element spacing is satisfied.

ACKNOWLEDGMENT

The authors gratefully acknowledge the part financial support of the Universiti Sains Malaysia through the USM Research University (RU) Grant under project No. 1001/PELECT/814206.

REFERENCES

- Petosa, A., *Dielectric Resonator Antenna Handbook*, Artech House Inc., 685 Canton Street, Norwood, MA 02062, 2007.
- Rezaei, P., M. Hakkak, and K. Forooghi, "Dielectric resonator antenna for wireless LAN applications," *IEEE Antennas and Propagation Society International Symposium*, 1005–1008, California, Jul. 12–15, 2006.
- Fan, Z., Y. M. M. Antar, A. Ittipiboon, and A. Petosa, "Parasitic coplanar three-element dielectric resonator antenna subarray," *Electronics Letters*, Vol. 32, No. 9, 789–790, 1996.
- Rezaei, P., M. Hakkak, and K. Forooghi, "Design of wide-band dielectric resonator antenna with a two-segment structure," *Progress In Electromagnetics Research*, Vol. 66, 111–124, 2006.
- Ain, M. F., Z. A. Ahmad, et al., "X-band dielectric resonator bandpass filter," *International Conference on Computer Applications and Industrial Electronics (ICCAIE-2010)*, 406–410, 2010.
- Ioachim, A., M. G. Banciu, L. Nedelcu, and C. A. Dutu, "Band-pass filters with (Zr_{0.8}, Sn_{0.2}) TiO₄ dielectric resonators," *Journal of Optoelectronics and Advanced Materials*, Vol. 8, No. 3, 941–943, 2006.

Deriving the Geometry of Frequency Selective Surfaces (FSS) and Metamaterials (MTM) Elements from Transmission Lines by Using Surrogate Meta-modeling Techniques

Fabrizia Ghezzi, Loris Serafino, Chunlin Ji, Xigeng Miao, and Ruopeng Liu

Kuang-Chi Institute of Advanced Technology

Gaoxin Zhong 1st Road, High-Tech Industrial Park, Shenzhen 518057, China

Abstract— In this work we have implemented a multi response model based on the Kriging surrogate modeling techniques to determine the correspondence between the resistance, capacitance, inductance, and admittance (RCLG) of a generalized transmission line and the dimensions of the geometrical features of a specific frequency selective surface (FSS) or metamaterial (MTM) structure - expressed in parametric form — operating in predefined frequency ranges. Specifically, this study was conducted considering the model for the application of FSS and MTM in the microwave frequency range. To demonstrate the potentiality of the newly developed model, an example of design of a metamaterial structure in a simplified case of perpendicular incidence and single layer configuration is analyzed and the preliminary results obtained are discussed.

1. INTRODUCTION

Frequency selective surfaces (FSS) and metamaterials (MTM) consist of surfaces made of periodically distributed elements whose size is much smaller than the wavelength [1]. These conductive elements are engineered in order to enhance the electromagnetic performance of the host material. In fact, while each individual element behavior cannot be perceived by the propagating wave, these elements collective behavior can considerably change the overall electromagnetic response of the medium. The behavior of a material with integrated sub-wavelength conductive resonant structures can be considered equivalent to a homogeneous material with effective relative permittivity and permeability. FSS have been used for decades in order to enhance the performance of the materials of many microwave devices. Areas where FSS have been applied since the 1970s [2] include antenna components for modern communications systems, frequency separation in beam splitters, transparent windows also known as radomes, artificial dielectrics, reflectors, absorbers, phase screens for beam steering and beam width equalization [3].

Very well known FSS elements can be identified with conductive open lines, solid patches, center connected lines and their combinations. Metamaterials are also periodic conductive elements of sub-wavelength size that differently from FSS can allow a medium to achieve properties that cannot be found in Nature. Materials with simultaneously negative permittivity and permeability also known as left handed materials or negative index materials, where theoretically presented by Victor Veselago in 1968 [4]. Negative index materials give rise to completely new electromagnetic phenomena. A part from the possibilities presented by Veselago, Pendry [5] was the first to propose the use of artificial materials, opening a new area of research. To practically realize these structures and achieve the desired performance it is necessary to first simulate their behavior. The computational effort that goes into the design of these elements is quite fundamental and accounts for most of the work to be completed to achieve the desired result and performance. Most of the structures studied in the literature, both in the case of FSS and metamaterials are generally derived by changing some of the geometrical features of resonant elements already studied in the literature. By doing so a new structure is found. After this step, a series of simulations need to be carried out to characterize its behavior at the varying frequency. This step is time consuming and computationally expensive. Varying the size and the shape of these elements brings the most diverse range of results and behaviors in a large frequency spectrum. It appears therefore necessary to develop some design tool in order to help the designer to select the right element geometry according to the requirements saving a lot of computational time. Many works in the literature are currently trying to solve the barrier imposed by the complexity of this design problem. For instance, genetic algorithms (GA) [6] are one of these proposed solutions. The disadvantage of the GA method consists on the large computational time required for obtaining the solution and also on the need of adding some selection criteria for filtering the results. Some of the structures found by simulations are often not practical and not feasible from the point of view of the fabrication.

Transmission line theory has also been used for the design and analysis of microwave networks [7]. Circuit models for metallic meshes and capacitive metallic plates in filter design have been intensively studied by TL which is seen as a quite promising tool for the design of these elements. Recently, several efforts have been also presented in metamaterials area [8–10]. The application of TL to metamaterials design is not straightforward. Moreover, if the circuit is representing a multilayer structure it will remain the same only if no interaction occurs between the layers [11] otherwise the interaction between these artificial atoms must be taken into account since it influences heavily the final material’s performance. Currently, when a new FSS or metamaterial structure is designed, it is possible to calculate the capacitance and inductance of the circuit of very simple models otherwise the calculation can be extremely difficult due to the complexity of the element’s geometry. The progress on the study of FSS and metamaterials by using TL theory seems to be limited by the complexity of the geometry of the individual elements. To fully utilize the potential of this field it seems necessary to develop a method which allows to obtain the structure with the desired transmission and reflection properties in a more general and efficient way. In this work we attempted to link a specific TL model to a FSS or metamaterial structure in the most general case of arbitrary angles of incidence and polarization by using a meta-modeling technique. Specifically, the method consists on the application of the Kriging surrogate modeling technique.

2. KRIGING SURROGATE MODEL

In material science optimization problems, often no analytical formula exists for accurately evaluating the following functional response $f : H \rightarrow \mathfrak{R}$ where H represents the space of the input variable, also called *design space*. In these cases the response to be optimized is accessible only as discrete sets of pairs of input and output from a simulation or from an experiment. Therefore, given a set of input (from a given sample space) $x = (x_1, \dots, x_n)^T$ and a response $y = (y_1, \dots, y_n)^T$ such that $y_i = f(x_i)$ with $i = 1, \dots, n$ the primary goal of meta-modeling is to predict the response $f(x_{new})$ at a new point by constructing an approximate (also called *surrogate*) model of the true functional response.

Surrogate models are convenient, computationally light to run and most importantly — for the case here studied — they can also yield to insights about the functional relationship between a set of input parameters and a target response. In general, meta-modeling consists of two steps: a) the design of experiment (DOE) and b) the meta-modeling procedure. The purpose of DOE techniques is to generate a suitable training set $\{(x_i, y_i) : y_i = f(x_i), i = 1, \dots, n\}$ that will be used for the construction and validation of the surrogate model. For the purpose of this work, we adopted the Latin hypercube sampling (LHS) space-filling strategy. The rationale behind LHS is to subdivide the design space into n intervals along each dimension. The samples are then chosen randomly such that each interval contains exactly one point [12]. Many meta-modeling procedures are available in the literature [13, 14]. The Kriging meta-modeling is particularly suitable when the functional response to be studied is deterministic and highly nonlinear [15]. A technical in-depth discussion of the Kriging techniques can be found in the works [16, 17]. Kriging techniques can be successfully extended to multiple response functional relation, characteristic aspect of the type of design required in this work. The DACE Matlab toolbox was used in this work to construct the Kriging surrogate model. *Pros* and *cons* of the Kriging approach with respect to other meta-modeling procedures are reported in the literature [18]. The Maximum Likelihood Estimators used to estimate the required parameters involves a constrained maximization step. This results in a number of complicated calculations including matrices inversion. The correlation matrix can become singular when the training points are too close to each other. Such problems may eventually overweight the approximation benefits. Nonetheless Kriging (together with LHD experimental design) resulted well suited for the simulation of the model here considered especially for the possibility of modeling a multivariate functional response. In this work we focus on the solution of the problem of linking a specific TL model with a FSS or metamaterial structure in the most general cases of oblique incidence and arbitrary polarization angles. The main idea of this work was to generate a functional model capable of describing the relation between the TL circuit parameters (RCLG values) and the parameters describing the geometry of the structure under consideration using one of the surrogate modeling techniques.

3. PRELIMINARY RESULTS

In the model, the design procedure is carried out in the following way. The geometry of the FSS or MTM element of interest is selected and expressed in a suitable parametric form characterized

by a specific number of geometrical parameters. These parameters include all the dimensions that are necessary to describe the element, i.e., the geometry of the structure including the size of the unit cell and the characteristics of the propagation of the wave (angle of incidence and polarization). An initial data set, determined by applying the Latin hypercube DoE, is solved by running full wave simulations in CST Microwave Studio software. The MatLab code developed for the Kriging runs automatically the simulations in CSTMW Studio and stores the results for subsequent analysis. Once the solutions in terms of transmission and reflection characteristics (S -parameters) are found for an established range of frequencies, the algorithm extracts the RCLG equivalent circuit characteristics from the S -parameters. The procedure for the extraction of the circuit characteristic values is different for the case of right-hand and left-hand media [19] and this is a key aspect that requires future work and investigations in order to include into the model's design abilities more complex cases. This step builds the correspondence between the RCLG circuit characteristics and the geometrical parameters of the physical model. Once the training of the Kriging model is completed, the code is ready for the inverse procedure. In a second phase in fact, by assigning the desired values of RCLG of a transmission line the model generates as an output the values of the geometrical parameters of the structure. It is necessary to point out that, currently, the model is limited to finding the correspondence of the generalized TL model in the case of arbitrary wave incidence and polarization angles with a pre-selected FSS or metamaterial element.

The model was validated by comparing the results obtained for the case presented in Fig. 1, also known as the Jerusalem Cross (JC). Figs. 2(a) and 2(b) show the transmission and phase characteristics of the JC element whose dimensions were found by applying the Kriging meta-model after specific values of RCLG were assigned. The RCLG values assigned to the model were the same calculated *a priori* after solving the specific case — the reference case — (with defined values of the geometrical parameters) in CST Studio. In other words, the JC reference case was

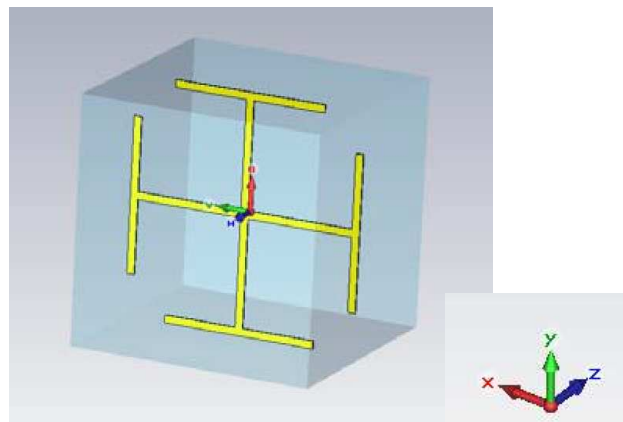


Figure 1: Jerusalem cross (JC) CST Microwave Studio model. The wave is propagating along the z -axis with the electric field component oriented along the y -axis and the magnetic component along the x -axis.

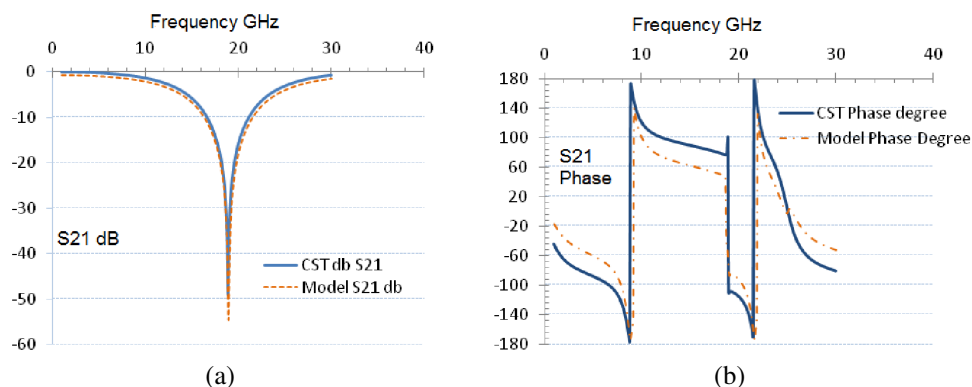


Figure 2: (a) Model's transmission characteristics S_{21} and (b) phase behavior compared with the results obtained by using CST Microwave studio.

modeled and firstly solved by using CST Microwave Studio in the frequency range [0, 40] GHz. The reason for the wide frequency spectrum is simply due to the interest of analyzing the behavior of the element in this entire frequency range. The resulting transmission behavior of the structure as obtained from the numerical simulation is presented by the blue curves. Secondly, the transmission and reflection characteristics were determined via application of the meta-model. For its successful application, the model was first trained on a data set (a number of cases where the dimensions of the structure varied) consisting of 100 samples. The results of the model are presented by the dash-orange lines in Figs. 2(a) and 2(b).

4. CONCLUSIONS

In this work we implemented a model based on the Kriging technique to generate the correspondence between the characteristic values of a generalized transmission line model (RCLG) extracted from assigned or desired S -parameter curves and the dimensions of a specific frequency selective surface (FSS) or metamaterial (MTM) element. Although this work focused on the application of the model for a simple case of perpendicular incidence on a well known metamaterial based FSS element, the model is built in a way that cases of arbitrary incidence and polarization angles can be solved. This part is currently under validation. Progress in this study can be remarkably helpful for the solution of several problems in metamaterials and frequency-selective surfaces design by using transmission lines or simply starting from given trends of the S -parameters. Its future generalization can be useful for the design and optimization of microwave devices based on FSS and metamaterials structures derived by simply assigning the desired S -parameters responses. The efficiency of the model depends on the ability of describing parametrically the geometry of the structure in the most general way. Besides the encouraging results obtained so far, further analysis is in progress to complete and verify the limits for the application of this methodology, especially for the case of left-hand media.

ACKNOWLEDGMENT

This research was financially supported by the Guangdong High-End Electronic Information Special in Strategic Emerging Industry (No. 2012556019); the Shenzhen Key Laboratory of Ultrahigh Refractive Structural Material (No. CXB201105100093A) and the Shenzhen Innovative R&D Team Program (Peacock Plan) (No. KQE201106020031A).

REFERENCES

1. Kozakoff, D. J., *Analysis of Radome-enclosed Antennas*, 2nd Edition, Artech House, Norwood, 2010.
2. Anderson, I., "On the theory of self-resonant grids," *The Bell System Technical Journal*, Vol. 54, No. 10, December 1975.
3. Munk, B. A., *Frequency Selective Surfaces: Theory and Design*, Jon Wiley & Son, New York, 2000.
4. Veselago, V. G., "The electrodynamics of substances with simultaneously negative values of ϵ and μ ," *Soviet Physics UspekHI*, Vol. 10, 509–514, English Translation, 1968.
5. Pendry, J. B., A. J. Holden, D. J. Robbins, and W. J. Stewart, "Magnetism from conductors and enhanced non linear phenomena," *IEEE Transaction on Microwave Theory and Techniques*, Vol. 47, No. 11, 2075–2084, November 1999.
6. Mitchell, M., *An Introduction to Genetic Algorithms*, MIT Press, Cambridge, MA, 1998.
7. Miano, G. and A. Maffucci, *Transmission Lines and Lumped Circuits*, Academic Press, 2001.
8. Gil, M., J. Bonache, J. Selga, J. Garcia-Garcia, and F. Martin, "Broadband resonant type metamaterial transmission lines," *IEEE Microwave and Wireless Components Letters*, Vol. 17, No. 2, February 2007.
9. Eleftheriades, G. V., A. K. Iyer, and P. C. Kremer, "Planar negative refractive index media using periodically L-C loaded transmission lines," *IEEE Transactions on Microwave Theory and Techniques*, Vol. 50, No. 12, 2702–12, 2865–73, December 2002.
10. Yasar-Orten, P., E. Ekmekci, and G. Turhan-Sayan, "Equivalent circuit models for split ring resonator arrays," *PIERS Proceedings*, 534–537, Cambridge USA, July 5–8, 2010.
11. Simovsky, C. R., "Bloch material parameter of magneto-dielectric metamaterials and the concept of Bloch lattices," *Metamaterials*, Vol. 1, No. 2, 62–80, 2007.
12. Park, J. S., "Optimal Latin-hypercube designs for computer experiments," *J. Stat Plan Inference*, Vol. 39, 95–111, 1994.

13. Sacks, J., W. J. Welch, T. J. Mitchell, and H. P. Wynn “Design and analysis of computer experiments,” *Statistical Science*, Vol. 4, No. 4, 409–435, 1989.
14. Sudjianto, A. K. T. Fang, and R. Li, *Design and Modeling for Computer Experiments (Computer Science & Data Analysis)*, Chapman & Hall/CRC, 2005.
15. Jones, D. R., M. Schonlau, and W. J. Welch, “Efficient global optimization of expensive black-box functions,” *Global Optimization*, Vol. 13, 455–492, 1998.
16. T. W. Simpson, T. M. Mauery, J. J. Korte, and F. Mistree, “Kriging models for global approximation in simulation-based multidisciplinary design optimization,” *AIAA Journal*, Vol. 39, No. 12, 2233–2241, 2001.
17. Kleijnen, J. P. C. and E. Mehdad, “Kriging in multi-response simulation, including a Monte Carlo laboratory,” CentER Discussion Papers Series No. 2012-039, May 16, 2012, Available at SSRN: <http://ssrn.com/abstract=2060891> or <http://dx.doi.org/10.2139/ssrn.2060891>.
18. Simpson, T. W., J. D. Peplinski, P. N. Koch, and J. K. Allen, “Metamodels for computer-based engineering design: Survey and recommendations,” *Engineering with Computers*, Vol. 17, 129–150, 2001.
19. Caloz, C. and T. Itoh, *Electromagnetic Metamaterials: Transmission Lines Theory and Microwave Applications*, J. Wiley & Sons, New Jersey, 2006.

Analysis and Design of Ku Band Coaxial-waveguide Transition

Chao Wang¹, Gaofeng Guo¹, Junhu Wang², and En Li¹

¹University of Electronic Science and Technology of China, Chengdu 611731, China

²Aerospace Research Institute of Materials and Processing Technology, Beijing 100076, China

Abstract— Coaxial-waveguide transition plays an important role in microwave system. Based on the influence of waveguide ladder exerted on transmission performance of electromagnetic wave in guided wave system, this paper demonstrates the situations of this structure applied in Ku band coaxial-waveguide converter designation. The reflected wave and insertion loss have been reduced by using a multi-steps structure with the coaxial probe excitation. The effectiveness of impedance matching is well-improved, and the transmission performance of coaxial-waveguide converter is highly-advanced. Simulation results proved the effectiveness of waveguide ladder in designing coaxial-waveguide converters. The VSWR of coaxial-waveguide transition designed in this paper is less than 1.04 in the 12.4–18 GHz octave bandwidth, and the high modulus produced is very small.

1. INTRODUCTION

Coaxial-waveguide transitions play an important role in microwave system which are very necessary and critical passive microwave components in Radar equipment, precision guidance and microwave testing circuit. Design of transitions from coaxial to waveguide applicable to commercial and military microwave system is of valuable importance. In the dielectric material permittivity test system, the performance of components is critical to the accuracy of the test result. Main aim for the designers is to achieve low levels of return loss during transformation of TEM mode in coaxial to TE-mode in waveguide in operating frequency band. The VSWR of coaxial-waveguide transition designed in this paper is less than 1.04 (return loss less than 34 dB) in the 12.4–18 GHz octave bandwidth, and the high modulus produced is very small. This paper introduces a standard 50 ohm coaxial cable which outer radius is 1 mm, inner radius is 0.435 mm and the dielectric constant is 2.08.

2. THE BASIC THEORY AND ANALYSIS

In this paper, the design of mode converter is based on the utilization of a rectangular cavity and a cylinder probe with conical part, a 4-step Chebyshev-response impedance transformer was designed using the combination construction with single ridge waveguide and reduced size rectangular waveguide. Design formulas resulting in an equal ripple or Chebyshev-type response were given by Cohn, Collin [1], and Riblet, and were experimentally verified.

Figure 1 shows the proposed structure of the transition. The transition consists of stepped impedance transformer and mode converter. It is well known that, the characteristic impedance of rectangular waveguide is a function of frequency rather than a constant value. Therefore a multi-step matching transformer is essentially for such extreme high impedance ratio together with wide fractional bandwidth. The first step for this approach was selection of the waveguide cross section,

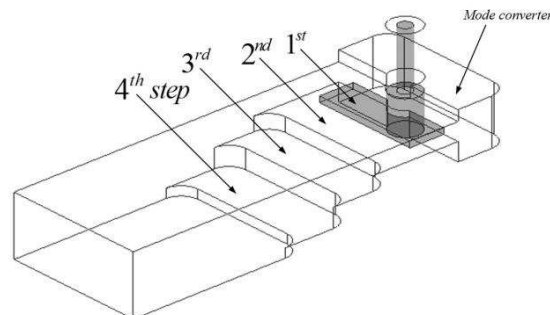


Figure 1: Structure of the proposed transitio.

with its resulting characteristic impedance and guided wavelength. The combination construction with single-ridge waveguide (the first-step) and reduced size waveguide (the second-, third- and fourth-step) was employed to frame a 4-section Chebyshev response quarter-wave transformer [2]. Single-ridge waveguide portion has been used due to its compatibility with both conventional circular coaxial and rectangular waveguide. The characteristic impedance of each step has been calculated [3]. Calculation by HFSS, we can know wave impedance is $Z = 298 \text{ Ohm}$ which correspond the center frequency is $f_0 = 15.2 \text{ GHz}$. The length l of each section in terms of the guide wavelengths in that section is defined by:

$$\begin{aligned}\Gamma(\theta) &= 2e^{-jN\theta} [\Gamma_0 \cos N\theta + \Gamma_1 \cos(N-2)\theta + \dots + \Gamma_n \cos(N-2n)\theta + \dots] \\ &= Ae^{-jN\theta} T_N(\sec \theta_m \cos \theta)\end{aligned}\quad (1)$$

As we know, $N = 4$. So we can obtain

$$\Gamma(\theta) = 2e^{-j4\theta} \left[\Gamma_0 \cos 4\theta + \Gamma_1 \cos 2\theta + \frac{1}{2}\Gamma_2 \right] = Ae^{-j4\theta} T_4(\sec \theta_m \cos \theta)\quad (2)$$

As $A = \Gamma_m = 0.05$ and

$$\sec \theta_m = \cosh \left[\frac{1}{N} \operatorname{ar} \cosh \left(\frac{\ln Z_L/Z_0}{2\Gamma_m} \right) \right] = \cosh \left[\frac{1}{4} \operatorname{ar} \cosh \left(\frac{\ln 298/50}{2 \times 0.05} \right) \right] = 1.4251\quad (3)$$

We can obtain

$$\begin{aligned}2 \left[\Gamma_0 \cos 4\theta + \Gamma_1 \cos 2\theta + \frac{1}{2}\Gamma_2 \right] &= A [\sec^4 \theta_m (\cos 4\theta + 4 \cos 2\theta + 3) - 4 \sec^2 \theta_m (\cos 2\theta + 1) + 1] \\ &= A \sec^4 \theta_m \cdot \cos 4\theta + (4A \sec^4 \theta_m - 4A \sec^2 \theta_m) \cdot \cos 2\theta + (3A \sec^4 \theta_m - 4A \sec^2 \theta_m + A)\end{aligned}\quad (4)$$

The corresponding coefficient equation can be obtained

$$\begin{aligned}2\Gamma_0 &= A \sec^4 \theta_m \Rightarrow \Gamma_0 = \Gamma_4 = 0.1031 \\ 2\Gamma_1 &= 4A \sec^4 \theta_m - 4A \sec^2 \theta_m \Rightarrow \Gamma_1 = \Gamma_3 = 0.2094 \\ \Gamma_2 &= 3A \sec^4 \theta_m - 4A \sec^2 \theta_m + A \Rightarrow \Gamma_2 = 0.2625\end{aligned}\quad (5)$$

So when $n = 0$, we can obtain

$$\begin{aligned}\ln Z_1 &= \ln Z_0 + 2\Gamma_0 = \ln 50 + 2 \times 0.1031 = 4.1182 \Rightarrow Z_1 = 61.4485 HFSS \Rightarrow l_1 = 1.63 \text{ mm} \\ n = 1, \ln Z_2 &= \ln Z_1 + 2\Gamma_1 = 4.537 \Rightarrow Z_2 = 93.4101 \Rightarrow l_2 = 2.48 \text{ mm} \\ n = 2, \ln Z_3 &= \ln Z_2 + 2\Gamma_2 = 5.062 \Rightarrow Z_3 = 157.906 \Rightarrow l_3 = 4.19 \text{ mm} \\ n = 3, \ln Z_4 &= \ln Z_3 + 2\Gamma_3 = 5.4808 \Rightarrow Z_4 = 240.038 \Rightarrow l_4 = 6.38 \text{ mm}\end{aligned}\quad (6)$$

where Γ is the reflection coefficient, and we can roughly calculate the length of each section with formulas (1) to (6).

It has been observed that by reconstruction the coaxial waveguide junction portion, a considerable decrease in VSWR can be achieved. A majority of the field in this section is concentrated in the TEM mode between the cylinder probe and the up wall of the ridged waveguide, and then radiated into the multistep impedance transformer, with just a few energy being propagated into the short-circuited waveguide cavity (shown in Fig. 2). This probably occurs because the equivalent reactance from the rectangular waveguide cavity stub may be sufficiently high to be neglected in an approximate treatment [4]. The hybrid section does, in fact, support multi-modes of propagation, whereas most of the energy has been transformed into TE₁₀ mode while pass through the mode converter. The advantage of this rectangular waveguide-coaxial portion is the ability to redistribute the electromagnetic field as it propagates from a coaxial waveguide through the single-ridge waveguide.

3. OPTIMIZATION AND RESULTS

The proposed structure has been applied to realize a broadband coaxial-waveguide transition with return loss less than -34 dB in the frequency band between 12.4 to 18 GHz. The transition has

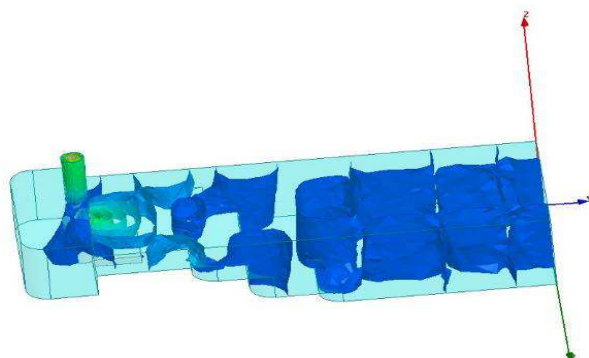


Figure 2: Field overlays of the transition.

been designed using the high frequency structure simulator Agilent HFSS based on finite-element field solver and simulation results are reported in Figure 3 and Figure 4. The design was optimized for use with a waveguide dielectric material test system for the operating frequency band from 12.4 GHz to 18 GHz. None but dominate mode wave can propagate in the rectangular waveguide in this frequency range. The length of the impedance transformer section has been calculated with formulas (1) to (6) and the shorted circular waveguide cavity is made equal to a quarter of the free-space wavelength at the mid-band frequency. Through simulation and optimization, we can get high of $l_1 = 1\text{st} = 4\text{ mm}$, $l_2 = 2\text{nd} = 4.1\text{ mm}$, $l_3 = 3\text{rd} = 4.7\text{ mm}$, $l_4 = 4\text{th} = 5.7\text{ mm}$. Those parameters are calculated on the base of wide-band impedance match theory, which is appropriate for the homogeneous case.

It can be seen that there reflection coefficient of the original model is below -22 dB (shown in Fig. 4). However, the model based on computed data for the homogeneous case might provide initial design parameters of the transition [5]. Those parameters are valuable reference for subsequent modification to a more nearly optimum performance. And several attempts have been made to modify the lengths of stepped impedance transformer sections to compensate for the shunt capacitances introduced by the step discontinuities. The design was optimized through several iterations and the results are presented in Fig. 4. Better than -34 dB return loss was obtained in the whole operating frequency band from 12.4 GHz to 18 GHz. Fig. 3 shows the input VSWR versus change with the working frequency, and we can see that the VSWR is less than 1.04 reflection coefficients less than -34 dB in Fig. 4. The real coaxial-waveguide transition used for testing is shown in Fig. 5 and the test results compared with the simulation results are almost the same.

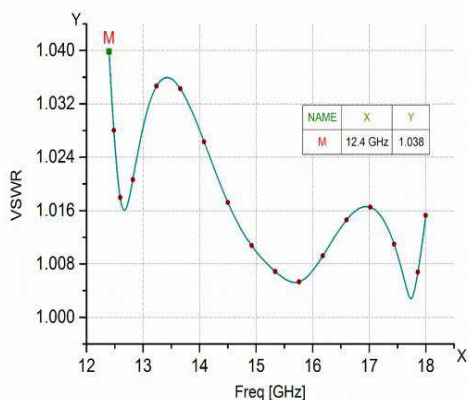


Figure 3: The cure of input VSWR for coaxial-waveguide transition.

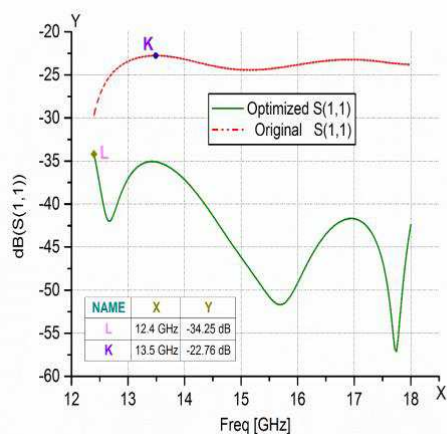


Figure 4: Comparison of the original and optimized reflection coefficient for the coax-to-rectangular waveguide transition.



Figure 5: The real coaxial-waveguide transition.

4. CONCLUSION

In this paper, we study on some the wave transformation from the coaxial line to rectangular waveguide. Coaxial-waveguide transition has been widely used in various microwave systems. So a novel transition from coaxial line to rectangular waveguide is proposed in this paper. Feasible way to optimize performance of the transition is analyzed and verified. Very good broadband performance of this transformer is described through rigorous simulation result. The prototype of this transition achieves return loss less than -34 dB, possible applications include high accuracy microwave material test and broadband horn antenna feeds. And we will research coaxial-waveguide transition which can be applied in widerband.

REFERENCES

1. Collin, R. E., *Field Theory of Guided Wave*, 323–332, McGraw-Hill, New York, 1961.
2. Wang, Y., “An X-band coaxial-to-rectangular waveguide transition,” *Microwave Technology and Computational Electromagnetics*, 129–131, 2011.
3. Collin, R. E., “Theory and design of wide-band multisession quarter-wave transformers,” *Proc. IRE Trans. on Microwave Theory and Techniques*, Vol. 3, 16–21, Apr. 1955.
4. Bialkowski, M. E., “Analysis of a coaxial-to-waveguide adaptor including a discended probe and a tuning post,” *IEEE MTT*, Vol. 43, 344–349, Feb. 1995.
5. Cohn, S. B., “Optimum design of stepped transmission-line transformer,” *IRE Trans. on Microwave Theory and Techniques*, Vol. 3, 16–21, Apr. 1955.

A Novel Monopulse Microstrip Antenna Array with Compound Feed Network

Feng-Wei Yao, Xiao-Qing Tian, Li-Li Zhu, Yuan-Bo Shang, and Xing-Zuo Dai
Shanghai Key Laboratory of Electromagnetic Environment Effects for Aerospace Vehicle
Shanghai 200438, China

Abstract— In this paper, a novel feed network design is presented, with which every microstrip line array of antenna is fed at the edge side with the middle of the row shorted and in E -plane the adjacent subarrays are fed with 180 degrees phase difference. This proposed feed network can suppress the near coupling problem in traditional monopulse microstrip antenna array design. Furthermore in order to minish the loss of substrate and microstrip feed line, a waveguide one-plane feed network and waveguide comparator are used, which is connected with every line array by SMA-waveguide connector. The simulated results have demonstrated that the -19 dB side-lobe level for the sum pattern and 32 dB null depth for the difference pattern have achieved.

1. INTRODUCTION

Microstrip structure has been developed for pulse antenna in monopulse radar system due to its lightweight low cost and convenient manufacture comparing with waveguide slot and Cassegrain parabolic antenna [1, 3].

The important function of monopulse antenna is to generate sum and difference beam, so the whole array plane is divided into four parts by two perpendicular symmetry axes every sub-array has own feed network in E and H -plane. For most monopulse microstrip antenna array in one layer, every line array is fed at the center side and E -plane feed network is placed between adjacent two patches of two sub-arrays [4], which may bring the significant near coupling between feed lines and sub-arrays, leading to deteriorate the side lobe and lower the efficiency of antenna to 20%. Pozar [5] mentioned that the sidelobe level and efficiency would be limited when the feed network and antenna elements were printed on eliminate the same substrate. Furthmore, the loss of substrate and microstrip feed line is unavoidable, which will significant reduce the gain especially in high frequency antenna with large aperture.

In this letter, a novel compound feed network of monopulse microstrip array is presented, in which the microstrip series line array is fed at the edge side with the middle of the row shorted in E -plane and the adjacent subarrays are fed with 180 degrees phase difference in H -plane. In order to minish the loss, a waveguide feed network in H -plane and waveguide comparator are all used, which connect with microstrip series line array by coaxial to waveguide adapter. The structure and simulated results of proposed array are presented as follow.

2. CONFIGURATION

The X-band monopulse microstrip antenna array as shown in Fig. 1 includes (1) microstrip radiator array divided into four sub-arrays; (2) the waveguide H -plane feed network, which is connected with every microstrip line array by coaxial to waveguide adapter respectively; (3) the waveguide comparator with four inputs connected to every sub-array and four outputs connected to the sum, H -plane difference, E -plane difference and matching load respectively. As shown in Fig. 1, in E -plane the adjacent subarrays are fed with 180 degrees phase difference. This proposed feed method can suppress higher order modes and decrease cross-polarization.

Every series line array is fed at the edge side with the middle of the row shorted as shown in Fig. 2. Due to the introduction of a shorted pin, there is a branch added to achieve good impedance match, the length and width of the branch are all important parameters in controlling the achievable bandwidth.

The distance between the shorted point and the adjacent patch is $\lambda_g/4$. The space between adjacent two patch which is designed to λ_g at center frequency, which will cause a discrepancy in gain between the higher and lower frequency.

The comparator is formed by using four 3 dB hybrid junctions which uses waveguide structure below the substrate in order to overcome the poor efficiency of microstrip line in high frequency.

The coaxial to waveguide adapter is shown in Fig. 3, the upside of the coaxial connector is connected with every line array, the underside of it is inside the waveguide below, which can be adjusted to be $100\ \Omega$ through changing the length of probe inside the waveguide.

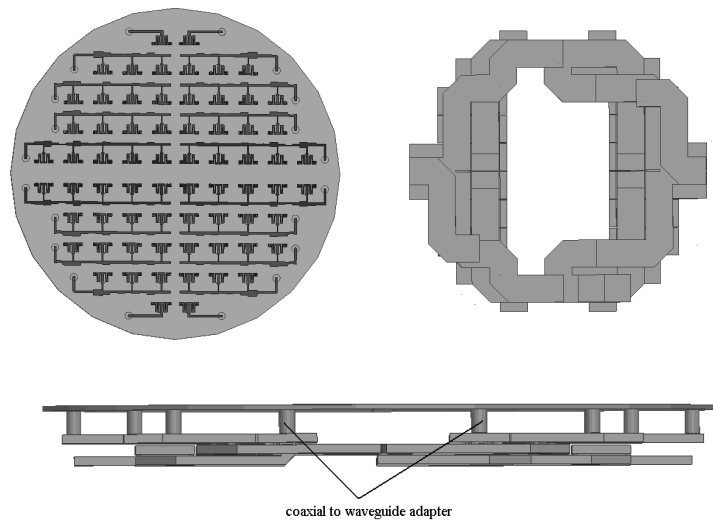


Figure 1: Structure of side feed monopulse antenna array.

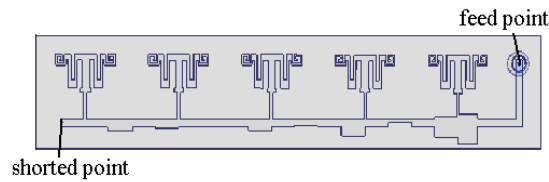


Figure 2: Structure of microstrip line array.

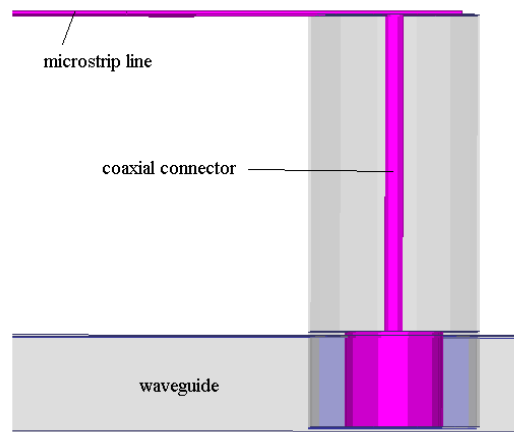


Figure 3: Coaxial to waveguide adapter.

3. SIMULATED RESULTS

In order to reduce the loss of substrate and microstrip line, the H -plane feed network use waveguide structure, which can accurate control the aperture excitation amplitude through changing the inclined angle of slots into the broad wall of waveguide.

The simulated amplitude distribution of H -plane feed network keeps constant basically during the operating band as shown in Fig. 4, which ensures the sidelobe levels of sum pattern stable between low frequency and high frequency.

The simulated vswr of comparator is less than 1.4 : 1 during the operating band as shown in Fig. 5.

The simulated maximum gain at center frequency is 23 dB as shown in Fig. 6, both for the

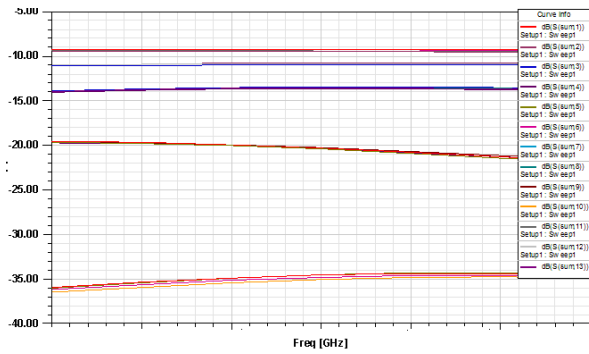


Figure 4: Simulated amplitude distribution of H -plane feed network.

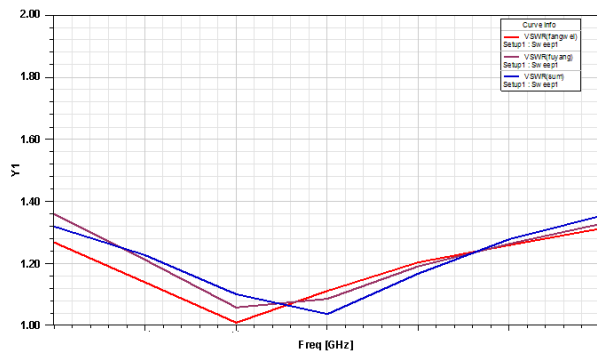


Figure 5: Simulated vswr curve of comparator.

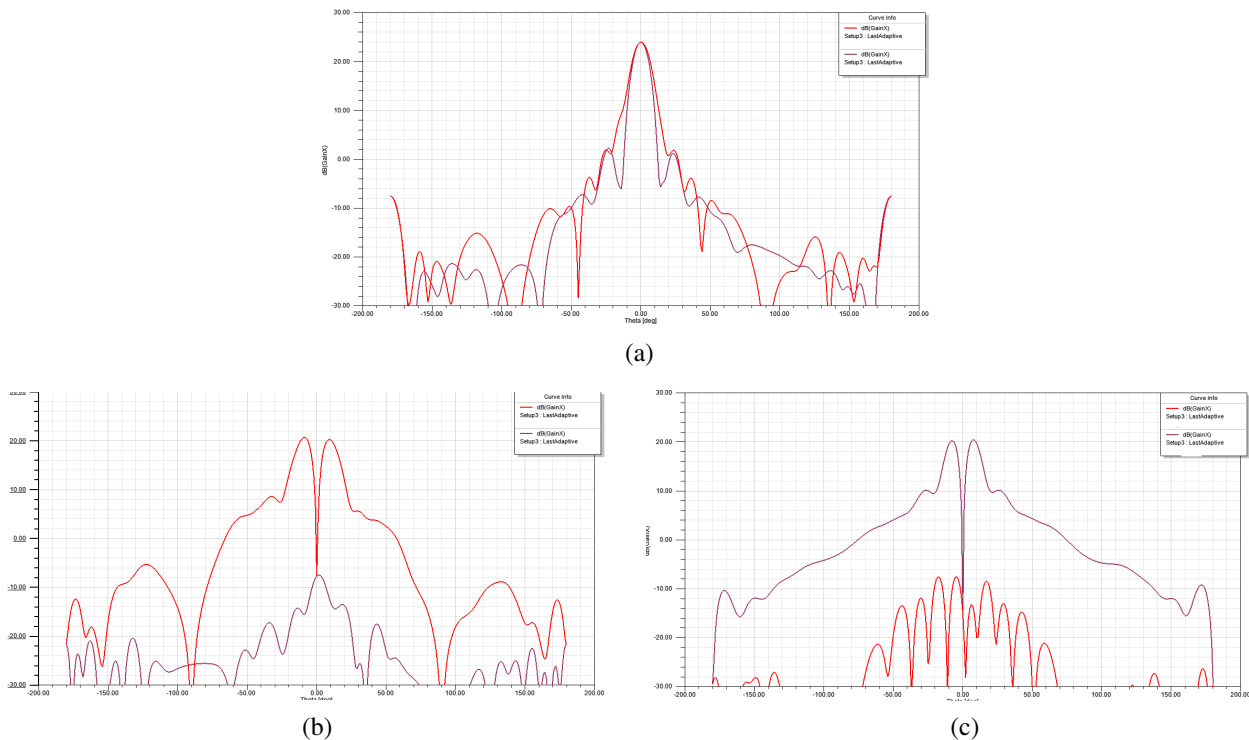


Figure 6: Simulated sum and difference patterns at center frequency. (a) Simulated sum patterns. (b) Simulated difference patterns in E -plane. (c) Simulated difference in patterns H -plane.

E -plane and for the H -plane the sidelobe levels of sum pattern are less than -19 dB. The null depth of difference pattern are all below -32 dB. The efficiency of the array is 40%, which is almost similar with that of the conventional Cassegrain parabolic antennas antenna.

There will be about 2 dB deterioration between the simulated and measured sidelobe levels. The discrepancy is due to the introduction of coaxial to waveguide adapter which inducts about 15 degree phase unbalance among microstrip line arrays in H -plane.

4. CONCLUSION

A novel compound feed network design is presented, which can solve the near coupling problem in traditional monopulse microstrip antenna array design and minish the loss of substrate and microstrip line. The SMA-waveguide adapter is used to connect the microstrip line array with waveguide one-plane feed network and waveguide comparator. With this new compound feed network, a monopulse microstrip array has been designed in this paper. The -19 dB side-lobe level for the sum pattern and -32 dB null depth for the difference pattern have achieved in the simulation at center frequency.

ACKNOWLEDGMENT

This work is supported by the national Nature Science Fund of China under Grant No. 61201116.

REFERENCES

1. Laheurte, J.-M., “Uniplanar monopulse antenna based on odd/even mode excitation of coplanar line,” *Electron Letter*, Vol. 37, No. 6, 338–340, Mar. 2001.
2. Zhong, S.-S., *Microstrip Antenna Theory and Applications*, Xidian University Press, Xian, China, 1991.
3. Kim, S. G. and K. Chang, “Low-cost monopulse antenna using bi-directionally-fed microstrip patch array,” *Electronics Letters*, Vol. 39, No. 20, 1428–1429, 2003.
4. Wang, H. and D. Fang, “A compact single layer monopulse microstrip antenna array,” *IEEE Transactions on Antennas and Propagation*, Vol. 54, No. 2, 503–509, 2006.
5. Pozar, D. M. and B. Kaufman, “Design consideration for low sidelobe microstrip arrays,” *IEEE Transactions on Antennas and Propagation*, Vol. 38, No. 8, 1176–1185, Aug. 1990.

Design of Signal Source without External Reference for Fiber Optical Comb System

Changqi Yang

School of Science, Xi'an Shiyou University, Xi'an 710065, China

Abstract— Femtosecond frequency comb is a great invention in the field of metrology at the end of the last century. It can simply and effectively synchronize the phases for optical signals of different wavelengths or RF signals. Erbium doped fiber optical comb has many advantages. The National Time Service Center of Chinese Academy of Sciences has launched a project on the new type erbium-doped fiber femtosecond optical comb research. This paper introduces the signal source which is designed for this project. DDS chip AD9854 is used as the signal source. The signal source output has a wideband from 1–80 MHz. Test result for the signal source is discussed.

1. INTRODUCTION

Femtosecond frequency comb is a great invention in the field of metrology at the end of the last century [1, 2]. It can simply and effectively synchronize the phases for optical signals of different wavelengths or RF signals. Direct synchronous frequency difference can be up to 100,000 times or more. It solves the problems of comparison between different optical frequency signals [3, 4]. There are many kinds of femtosecond frequency comb. The spectrum center of erbium doped fiber optical comb is located at 1.55 μm communication wavelength. Accordingly, erbium doped fiber optical comb has more advantages in component selection, price, and application. This makes the erbium doped fiber optical comb has many characteristics, such as high stability, small volume, low power consumption, flexible operation, and good robustness. In addition, by using the commercial nonlinear fiber crystal, it can be more convenient to extend the operation wavelength of erbium doped optical comb to that of several other optical combs.

A lot of time frequency laboratory are carrying on the research about doped femtosecond comb technology. At present, the National Time Service Center of Chinese Academy of Sciences has launched a project on the new type erbium-doped fiber femtosecond optical comb research. This paper introduces the signal source which is designed for this project.

Nearly almost all of the electric control system needs signal source. Many methods can be used to generate the signal. In the field of low frequency, it can be achieved with single-chip, and in the field of high frequency, it can be achieved by FPGA or DDS chip. Because of the stability of the DDS chip, usually in the RF and microwave bands, it is a good design by using DDS chip as the signal source [5]. In the next part, the authors will introduce the signal source that designed for this optical fiber frequency comb system. In the third part, the test results of the signal source will be introduced.

2. DESIGN OF SIGNAL SOURCE

The system's signal source use a DDS chip AD9854. When without an external reference source, sine wave, square wave and triangular wave of arbitrary frequency from 1 to 80 MHz can be generated by this signal source. DDS is a new kind of method of frequency synthesis. The reference clock is directly sampled, digitalized, and then use the digital computing technology to generate a frequency. The AD9854 is a type of high performance DDS chip produced by AD Company. The operation principle diagram of AD9854 is shown in Figure 1. It integrates 48-bit frequency accumulator, 48-bit phase accumulator, sine and cosine waveform table, 12-bit orthogonal digital-to-analog converter, and modulation and control circuit.

Its operating voltage is 3.3 V. The highest working frequency is 300 MHz. The output frequency ranges from 0 to 120 MHz. It can export FSK, PSK, BPSK, AM, and CHIRP signal. AD9854 has five kinds of work mode: Single-tone, Unramped FSK, Ramped FSK, Chirp, and BPSK. In the above five modes, Single-tone is one of the most flexible model. This model can be used to set the output signal's frequency, amplitude and phase characteristics.

In the design, we use AVR ATMEGA32 MCU to control the AD9854. Usually, the serial RS232 is used to communicate with MCU. The use of USB communication is a technology direction in recent years. This design uses the USB to serial RS232 chip CH340G. As to the system software

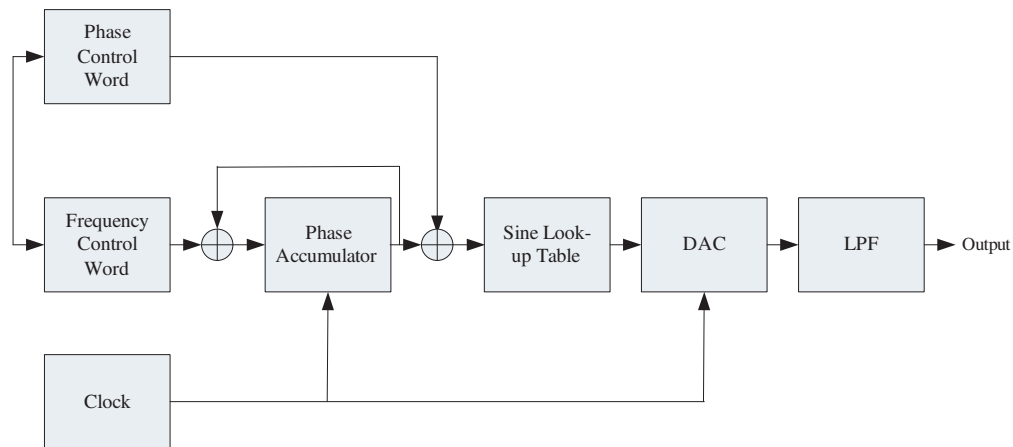


Figure 1: Operation principle of AD9854.

control part, first of all, set up the I/O update signal of AD9854. Whether the control signal is correct decides whether the AD9854 works correctly. Next, the internal 40 registers of AD9854 are set up. The control registers that have addresses from 1D-20 are 32 bits. They control the working mode, the comparator, the output amplitude, the system clock. After we have set up the control register, we set up the frequency registers amplitude registers, and phase registers. A chip has two frequency registers and two phase registers. Phase Adjust registers are used to control the waveform phase. Their addresses are 00 and 01. They are 14-bit registers. So the waveform phase generated has a 14-bit precision. Frequency tuning word register is used to control the waveform frequency. Their addresses are 04 and 09. They have a 48-bit precision. Output Shape Key I and Output Shape Key Q are amplitude registers. Their addresses are 21 and 24. They are 12-bit registers.

Figure 2 is the signal source software control interface that we design.

Figure 3 is the hardware circuit of signal source.

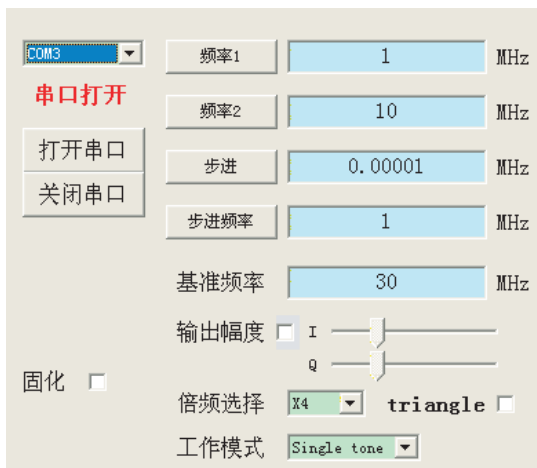


Figure 2: Signal source software control interface.

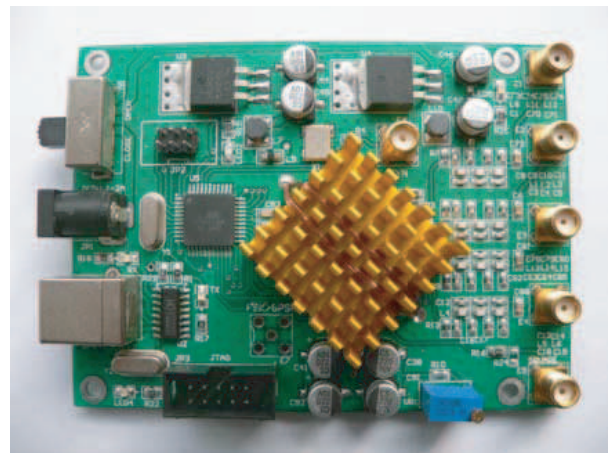


Figure 3: Hardware circuit of signal source.

We test the properties of the signal source. Test results are shown in Figure 4.

In Figure 4, a signal is generated by the circuit that we designed. Its frequency is 10 MHz. It is displayed by the oscilloscope. Signal with frequency from 1–80 MHz can be easily generated by the signal source.

3. DISCUSSIONS

From Figure 4, we can fully realize the circuit with expected function. AD9854 can be used to accurately generate different frequency sine wave and square wave. This paper is related to the issue that there is no outer reference input source. As to the next step research we will develop

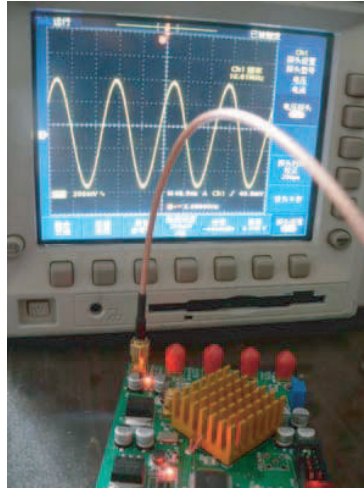


Figure 4: Test results of the signal source.

signal source with external reference input. Usually some high-frequency microwave signal is used as external reference input.

ACKNOWLEDGMENT

This research is sponsored by the funded projects of Xi'an Shiyou University research training program for University students.

REFERENCES

1. Diddams, S. A., et al., "Direct link between microwave and optical frequencies with a 300 THz femtosecond laser comb," *Phys. Rev. Lett.*, Vol. 84, 5102, 2000.
2. Udem, T., et al., "Accurate measurement of large optical frequency differences with a mode-locked laser," *Opt. Lett.*, Vol. 24, 881–883, 1999.
3. Touahri, D., et al., "frequency-synthesis chain — Results and improvement for the near future," *LPTF94&CPM 94*, Boulder, CO, Jun. 1994.
4. Schnatz, H., et al., "First phase-coherent frequency measurement of visible radiation," *Phys. Rev. Lett.*, Vol. 76, 18, 1996.
5. Cui, S. and X. Jia, "Application of DDS in primary reference clock design," *Radio Engineering*, Vol. 36, 49–51, 2006.

RF Shielded Hat for Protecting Cameraman from EMF Exposure

N. Hisham¹, H. A. Rahim¹, F. Malek², M. Jusoh¹,
F. A. A. Fuad¹, F. S. Abdullah², and M. S. Mezan²

¹Embedded, Networks and Advanced Computing Research Cluster (ENAC)

School of Computer and Communication Engineering, Universiti Malaysia Perlis, Perlis, Malaysia

²School of Electrical System Engineering, Universiti Malaysia Perlis, Perlis, Malaysia

Abstract— This paper presents a new layer of absorber for RF Shielded Hat. The objective of this studied is to create and develop a new layer of absorber for RF Shielded Hat made from Microwave Absorbing Sheet that can protect the cameraman from electromagnetic field (EMF). The Microwave Absorbing Sheet is used because of super light weight, good microwave shielding, high absorption and no problem for skin contact. Three different types of protective hat are chosen: back of the hat with no protection to allow adjustment of size, rear hat that covers the neck and hat that covers head and thyroid region. All hats are sewn with microwave absorber sheet. The investigation was aimed to study whether the types of hat worn reduce the electromagnetic exposure to human head. The measurement campaign was carried out in the anechoic chamber to completely absorb reflections of either sound or electromagnetic waves. The wireless video camera operated in frequency of 1.9 GHz to 2.7 GHz. The position of the wireless video camera was fixed on the right of the cameraman shoulder where this position is much closer to our heads. The experiment will be investigated in two different situations, while being exposed in the sham condition and also 2.45 GHz signal. Both of the measurement will be undertaken during the pre, during and after the experiments.

1. INTRODUCTION

Recently, people always exposed to electromagnetic field (EMF) in their everyday life. The electromagnetic field (EMF) are present everywhere in our environment but are invisible to the human eye [1]. Both electric and magnetic fields are present around appliances and power lines. However, electric fields are easily shielded and weakened by walls and other objects, where as magnetic fields can pass through buildings, humans and most other materials [2]. The use of ever-rising cellular phones whether private or business communication has determined an increased concern for possible adverse health effects deriving from exposure to the electromagnetic field radiated by such devices [3–5]. When the cellular phone is working, the transmitting antenna is place very close to the user head, arise the question whether people using it could be exposed to hazardous levels of electromagnetic radiation [5]. However, protecting the health of workers has been one of the problems to be handled wisely. Therefore, the international association such as IEEE Standards Association (IEEE-SA) and independent scientific organizations both have developed international guidelines and issuing limits for a safe exposure with the scientific rationale for these guidelines [6, 7].

In particular, one of the jobs in which wireless technology has been deployed is cameraman. In fact, the requirement of mobility not only for external shots but also for studio programmes demanding quick and dynamic changes in the view point, has pushed towards the introduction of wireless cameras. This trend, accompanied by the transition from analogue to digital transmission, has made the use of wireless video-cameras become more important [4].

Because this research has not been done yet and there was a complaint from a cameraman on the symptoms of dizziness, headaches and fatigue that occurs when using a wireless video camera that may be caused by low levels of exposure to EMF in the workplace, therefore this research is taken. Thus our project is to help the cameraman from exposed to this symptoms is to create and develop a new layer of absorber for RF Shielded Hat made from Microwave Absorbing Sheet.

2. MATERIAL SELECTION

In this study, microwave absorbing sheet is the main material that will be used. Microwave absorbing sheet is from LessEMF Inc with main material from carbon. Carbon is conductive in some forms, and a very good microwave absorber using non-woven nearly-pure carbon fibers, to achieve good microwave shielding and high absorption. Microwave absorbing sheet is super light weight and better durability with estimated weight of 34 g/m², thickness of 0.445 mm, resistivity of ~ 3 Ohms per square and tensile of 47 N/15 mm. Fig. 1 and Fig. 2 show the microwave absorbing sheet and a shielding performance of this material according to the manufacture [8].



Figure 1: Microwave absorbing sheet.



Figure 2: Shielding performance.

To measure absorption of the material using S parameter,

$$A = 1 - S_{11}^2 - S_{21}^2, \quad (1)$$

where

$$\begin{aligned} A &= \text{absorption} \\ S_{11}^2 &= \text{reflection} \\ S_{21}^2 &= \text{transmission} \end{aligned}$$

3. METHODOLOGY

3.1. Wireless Video Camera

The standard wireless video camera used for this experiment. The position of the wireless camera was fixed on the right of the cameraman's shoulder. The wireless video camera operated in frequency of 1.9 GHz to 2.7 GHz.

3.2. RF Shielded Hat

This project is focusing on three types of protective hat. The hat was functioning for protecting cameraman from EMF exposure. Fig. 1 shows the types of hats that will be used when doing a research.



Figure 3: Types of hats (a) the back of the hat with no protection to allow adjustment of size, (b) rear hat that covers the neck (c) hat that covers head and thyroid region.

4. MEASUREMENT SETUP

The experiment was carried out in an RF Shielded room at Electromagnetic Hyper Sensitivity (EHS) Laboratory to eliminate multipath reflections from surrounding environment. Measurement was performed on a cameraman. Research will be done on the subject with the position of the camera is placed on the right shoulders by using three different kinds of hats: Back of the hat with

no protection to allow adjustment of size, rear hat that covers the neck and hat that covers head and thyroid region. The antenna on the video camera connected to a Rohde & Schwarz SMBV100A with frequency range 9 kHz to 3.2 GHz. 4 meter Huber + Suhner Multiflex 141 flexible and low loss coaxial cable were used in the measurement campaign. The cable were wrapped with Eccosorb Flexible Broadband Urethane Absorber model: FGM-U-20-SA microwave absorbing foams to minimize the spurious radiation from and coupling between the coaxial cable. The measurement setup for cameraman shows in Fig. 4.

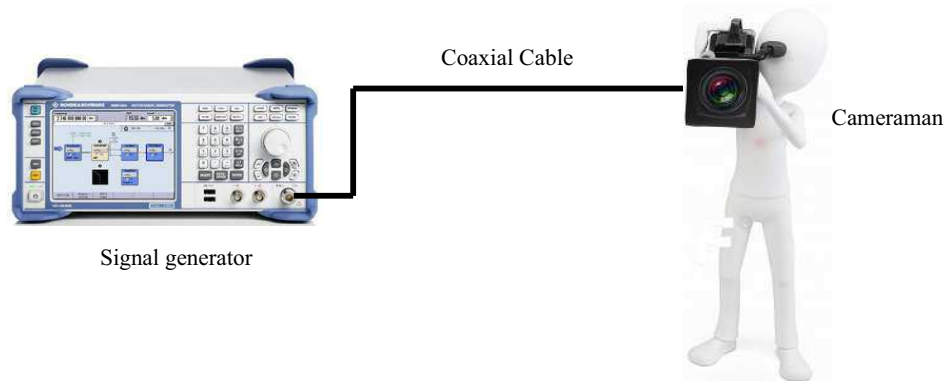


Figure 4: Cameraman measurement setup.

5. CONCLUSION

A light weight, good microwave shielding, high absorption and no problem for skin contact hats made from Microwave Absorbing Sheet that can protect the cameraman from electromagnetic field (EMF) is presented and discussed in this paper. Three different types of protective hat are chosen: back of the hat with no protection to allow adjustment of size, rear hat that covers the neck and hat that covers head and thyroid region. By using this shielded hat it will show a better performance to prevent the cameraman from symptoms of dizziness, headaches and fatigue.

REFERENCES

1. World Health Organization (WHO), "Electromagnetic field (EMF)," 2013, <http://www.who.int/peh-emf/about/WhatisEMF/en/>.
2. National Cancer Institute, "Magnetic field exposure and cancer," Apr. 21, 2005, <http://www.cancer.gov/cancertopics/factsheet/Risk/magnetic-fields>.
3. Bernardi, P., M. Cavagnaro, S. Pisa, and E. Piuzzi, "Specific absorption rate and temperature increases in the head of a cellular-phone user," *IEEE Transactions on Microwave Theory and Techniques*, Vol. 48, No. 7, 1118–1126, 2000.
4. Bernardi, P., M. Cavagnaro, M. La Rosa, S. Pisa, and E. Piuzzi, "Power absorption in the body of a cameraman exposed to the electromagnetic field emitted from a digital radio-camera," *Proceedings of the 39th European Microwave Conference*, 882–885, Rome, 2009.
5. Bernardi, P., M. Cavagnaro, and S. Pisa, "Evaluation of the SAR distribution in the human head for cellular phones used in a partially closed environment," *IEEE Transactions on Electromagnetic Compatibility*, Vol. 38, No. 3, 357–366, 1996.
6. IEEE Std C95.1-2005, "IEEE standard for safety levels with respect to human exposure to radio frequency electromagnetic fields 3 kHz to 300 GHz," New York, USA, 2006.
7. ICNIRP, "Guidelines for limiting exposure to time-varying electric, magnetic, and electromagnetic fields (up to 300 GHz)," *Health Physics*, Vol. 74, No. 4, 494–522, 1998.
8. LessEMF.com, "EMF shielding & conductive fabrics," 2013, <http://www.lessemf.com/fabric.html>.

Reflection Loss Performance and Performance Assessment of Pyramidal Microwave Absorber Using Agriculture Waste

M. S. Mezan¹, M. F. A. Malek², M. S. Jusoh¹, F. S. Abdullah², and N. A. M. Affendi²

¹School of Business Innovation and Technopreneurship, Universiti Malaysia Perlis
Jalan Kangar-Alor Setar, Kangar, Perlis 01000, Malaysia

²School of Electrical System Engineering, Universiti Malaysia Perlis
Pauh Putra Campus, Arau, Perlis 02600, Malaysia

Abstract— Agricultural product is one of the major revenue incomes for Malaysia. The large scale production of agricultural product lead to a new by product which is known as agricultural waste. Agricultural wastes materials can be applied for many applications. This research highlighted microwave absorber application as the output using proposed agricultural wastes. Microwave absorber is the most important element in anechoic chamber to deny signals reflection. Its performance is analyzed in term of reflection loss performance using the free space measurement technique. To answer the measurement goodness in this research, Rasch measurement model is applied.

1. INTRODUCTION

This research considered the alternatives way to utilize the agricultural waste and take the advantage from the pile up of the availability of wastes. The increase production of agricultural waste raise the loses of resources and produced the environmental damage. The utilization of agricultural waste may reduce the dumping of waste and become a substitute material for commercially available microwave absorber which use 100% chemical based of plastic foamed-based materials like polystyrene or polyurethane [1]. The proposed product from the waste is microwave absorber. Microwave absorber is used as the important element in anechoic chamber which is covered on the chamber wall. The microwave absorber will act as the absorbent material to absorb the scattered incident energy. For diversification in the material for microwave absorber, several agricultural residues are used in this research which is rice husk, mixture of rice husk and rubber tire dust, sugarcane bagasse and banana leaf.

2. MICROWAVE ABSORBER FABRICATION

The grinded material of agricultural wastes is fabricated into the shape of pyramid. Besides of the material's effect in microwave absorber, the shapes of the microwave absorber will also play the important characteristics and sensitive factor which can affect the reflectivity performance of the microwave absorber [1]. Pyramidal shapes absorber are usually applied for the frequency range between 1 GHz to 40 GHz and the square based pyramidal-shaped absorbers are commonly used for frequencies below than 1 GHz [2]. The material for microwave absorber is a mixed material of agricultural wastes and chemicals. The chemicals used are polyester which functioned as the resin and methyl ethyl ketone peroxide (MEKP) which reacts as a hardener agent for the materials to be moulded into pyramid. These polyester resins are used in adhesive, finishes and moulded objects. The characteristics are including low water absorption, volume resistance, heat distortion temperature, high tensile strength and elongation at break. For each materials of agricultural waste, nine pieces of pyramidal microwave absorber is made and compiled in 3×3 arrays, making the base dimension become 15 cm width \times 15 cm length. Figure 1 shows four different materials moulded and compiled into 3×3 arrays.

3. SAMPLE MEASUREMENT TECHNIQUES

The objective is to characterize the performance of its reflectivity for the different material microwave absorber. Every result from the measurement will demonstrate the actual performance of the microwave absorber that had been fabricated for the measurement. The measurement technique will involve two factors which were the microwave absorber electromagnetic properties and free space measurement to measure the reflectivity performances [3].

The measurement of dielectric properties is to characterize the different materials used and to define the physical and chemical properties, related to storage and loss of energy [4, 5]. For the



Figure 1: 3×3 array pyramidal microwave absorber. (a) Rice husk-rubber tire dust. (b) Sugarcane bagasse. (c) Rice husk. (d) Banana leaf.

dielectric constant measurement, open-ended coaxial probe technique was used to measure each materials of microwave absorber. The largest dielectric constant value shows by the material of rice husk rubber tire dust with $\epsilon' = 3.28$. For banana leaves, it shows the lowest value of dielectric constant with the value $\epsilon' = 2.33$. Dielectric constant for rice husk material is $\epsilon' = 3.00$. From the result in Table 1, each material gives a different value of dielectric constant (ϵ') and loss tangent ($\tan \delta$). Rice husk material gives a higher value compared to sugarcane bagasse and banana leaves. A material with a high density will lead to a higher dielectric constant thus explains the lower value for sugarcane bagasse and banana leaves [6]. The presence of rubber tire dust will increase the dielectric constant value. The different values of dielectric constant for different materials affects the velocity of microwave signals when propagate through material of MUT (Material Under Test). A high dielectric constant cause the microwave signal travel slower and velocity of microwave signal decrease.

Table 1: Average dielectric properties (dielectric constant, ϵ' ; tangent loss, $\tan \delta$).

Material	Dielectric Properties	
	ϵ'	$\tan \delta$
Rice Husk	2.99295	0.20614
Rice Husk Rubber Tire Dust	3.27711	0.14224
Sugarcane Bagasse	2.39184	0.14772
Banana Leaves	2.32908	0.10091

To measure reflection loss performance, a technique call free space measurement is implemented. RCS technique is used in this paper to measure reflection loss. RCS can be define as the area that can be perfectly detected back when electromagnetic waves were transmitted from its source to its target place. Result from the RCS measurement shows a good reflection loss performance as it gives an average value better than -10 dB. The highest reflection loss performance is -46.55 dB at frequency point of 7.6 GHz. The lowest reflection loss value is -28.10 dB for the frequency at 6.0 GHz. From the result, the reflection loss gets better when the frequency increased. The average value of reflection loss for rice husk rubber tire dust microwave absorber is -41.45 dB, slightly better than rice husk microwave absorber. This is due to the presence of small percentages of rubber tire dust with the ratio of 75 : 25; rice husk: rubber tire dust. The reflection loss performance for rice husk rubber tire dust gets better if the presence of rubber tire dust increased in the mix ratio between both materials [6].

Banana leaves give an average value of -37.40 dB for its reflection loss performances. The value indicates a good performance in term of reflection loss as it is better than -10 dB. The highest value of reflection loss gives by banana leaves material is -43.13 dB at 6.6 GHz while the least value is -33.97 dB at frequency point of 7.4 GHz. The value of decibel is varies through the range of frequencies. Although there are fluctuations in the reflection loss values, it can be considered to give a higher value as the frequency increased.

Sugarcane bagasse as material in microwave absorber fabrication shows the worst result of reflection loss. Although the result shown is -32.33 dB comply the reflection loss as a good value, still, it is the worst if compared with the other materials used in this paper. The worst reflection loss value is -28.10 at 6.0 GHz and the best value is -38.33 dB at 8.2 GHz for banana leaves material. As previous measurement, the reflection loss is varies through range of frequency and gives a better result for the increased frequencies. Figure 2 shows the comparison of the reflection losses among

the materials for fabricated microwave absorber.

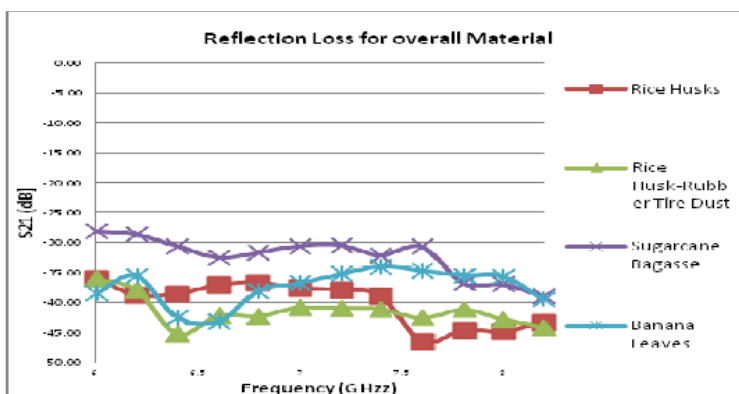


Figure 2: Reflection loss performance for the overall materials.

4. RASCH MEASUREMENT ANALYSIS

Rasch measurement model may determine the three major criteria for evaluating good measurement which are validity, reliability and significance of the RCS measurement technique. The Rasch model is a mathematical formula that specifies the form of the relationship between persons and the items that operationalize one trait [7]. Rasch measurement model is mostly used in social science educational measurement or psychometrics measurement [8–10]. Furthermore, Barrett (2003) indicates that there is suitability of Rasch measurement model in metrology measurement where it includes all theoretical and practical aspects of measurement [11]. The input from the analysis covers 12 Persons and 4 Items. Person and Item represented as 12 frequency points and four different types of materials respectively. Based on Table 2, Cronbach's alpha (KR-20) value is at 0.64 which is considered acceptable reliability at 0.64 of confidence level. Cronbach's alpha value of 0.64 is considerably higher than the acceptance level of 0.60 as agreed by Garson (1998), Gliem and Gliem (2003) and Leedy and Ormrod (2004) [12–14]. The measured value for Cronbach's alpha of 0.64 in this paper can be accepted as exploratory research while 0.80 for basic research and 0.90 for very critical issues research [9]. Material reliability of 0.52 shows the measurement technique sufficiency for number of items (materials) to measure the supposed output. It is still acceptable although the supposed reliability value is 0.60. In this Rasch measurement analysis, it is further supported by the value of z-standard = -1.4 which very near to 1 and 0 respectively. This value indicated, the assessment technique is considered as reliable in measuring the dimension exists by the materials.

Table 2: Overall summary statistics figure.

Material Reliability	0.52
Cronbach's Alpha (KR-20)	0.64
Z-Standard	-1.4

5. CONCLUSIONS

A proposed product has been successfully developed and fabricated into a microwave absorber. A low cost and environment friendly product was produced by a variety of agricultural waste materials which use a small percentage of chemicals. The microwave absorber is able to perform in the frequency range of 6.0 GHz to 8.2 GHz. This is due to the reflection loss performance's results which is better than -10 dB for each material and gives a value more than -30.0 dB.

Rice husk as microwave absorber's material gives a better result if compared to sugarcane bagasse and banana leaves. While for rice husk rubber tire dust microwave absorber is slightly better than rice husk with -1.362 dB significant. The proposed technique of measurement; RCS technique, was able to give different value of reflection loss. Based on most research, the technique of RCS measurement in free space technique is mostly used to gain the reflection loss performance

and it is valid and reliable based on the Rasch measurement model; Cronbach's $\alpha = 0.64$. This microwave absorber product can be marketed with a much lower cost and price compared to the commercial microwave absorber because the raw materials is agricultural wastes.

REFERENCES

1. Nornikman, H., P. J. Soh, A. A. H. Azremi, F. H. Wee, and M. F. Malek, "Investigation of an agricultural waste as an alternative material for microwave absorbers," *PIERS Proceedings*, 1287–1291, Moscow, Russia, Aug. 18–21, 2009.
2. Nornikman, H., F. Malek, M. Ahmed, F. H. Wee, P. J. Soh, A. A. H. Azremi, et al., "Setup and results of pyramidal microwave absorbers using rice husks," *Progress In Electromagnetics Research*, Vol. 111, 141–161, 2011.
3. Pitman, K. C., M. W. Lindley, D. Simkin, and J. F. Cooper, "Radar absorbers: Better by design," *IEEE Proceedings-F*, Vol. 138, No. 3, 223–228, 1991.
4. Wee, F. H., P. J. Soh, H. Nornikman, and A. A. M. Ezanuddin, "Free space measurement technique on dielectric properties of agricultural residues at microwave frequencies," *Microwave and Optoelectronics Conference (IMOC)*, 183–187, 2009.
5. Liyana, Z., F. Malek, H. Nornikman, N. A. M. Affendi, A. Ali, N. Hussin, et al., "Development of pyramidal microwave absorber using sugar cane bagasse (SCB)," *Progress In Electromagnetics Research*, Vol. 137, 687–702, 2013.
6. Malek, F., E. M. Cheng, O. Nadiyah, H. Nornikman, M. Ahmed, M. Z. A. A. Aziz, et al., "Rubber tire dust-rice husk pyramidal microwave absorber," *Progress In Electromagnetics Research*, Vol. 117, 449–477, 2011.
7. Green, K. E. and C. G. Frantom, "Survey development and validation with the rasch model," *International Conference on Questionnaire Development*, 2002.
8. Saidfudin, M. M. and A. A. Azrilah, "Rasch model: Scale construct and measurement structure," Workshop booklet Universiti Teknologi MARA (UiTM), Kangar, 2009.
9. Shahar, J. M., Z. Y. Rushami, A. Zakaria, A. A. Azrilah, M. M. Saidfudin, and B. Trevor, "Conformance and non-conformance cost of quality effects on quality management principles study: A rasch measurement approach," *7th Pacific Rim Objective Measurement Symposium (PROMS)*, paper ID015, Singapore, Jul. 2011.
10. Shahar, J. M., Z. Y. Rushami, A. Zakaria, A. A. Azrilah, M. M. Saidfudin, T. Bond, A. K. Noor Lide, and M. Akhir, "Rethinking correlation measure: Rasch analysis on-quality management principles," *7th Pacific Rim Objective Measurement Symposium (PROMS)*, paper ID043, Singapore, Jul. 2011.
11. Barrett, P., "Beyond psychometrics: Measurement, non-quantitative structure and applied numerics," *Managerial Psychology*, Vol. 18, No. 5, 421–439, 2003.
12. Garson, G. D., *Neural Networks: An Introductory Guide for Social Scientists*, SAGE, 1998.
13. Gliem, J. A. and R. R. Gliem, "Calculating, interpreting, and reporting Cronbach's alpha reliability coefficient for Likert-type scales," *Midwest Research to Practice Conference in Adult, Continuing, and Community Education*, Columbus, OH, 2011.
14. Leedy, P. D. and J. E. Ormrod, *Practical Research: Planning and Design*, 8th Edition, Macmillan, 2004.

An Effective Optimization of Reliability of Co-phase Power Supply Device

H. Xu, S.-F. Xie, and W.-L. Zhao

School of Electrical Engineering, Southwest Jiaotong University
Chengdu, Sichuan 610031, China

Abstract— In this paper, the structure and principle of a kind of co-phase power supply system is proposed. The co-phase power supply devices based on two-level quadruple modular topology structure and three-level duplicate topology structure are studied and the former one is chosen as a computational example. According to the analysis of high power electronic elements in power system, a $k/n(G)$ reliability model of the co-phase power supply device, based on two-level quadruple modular topology structure, is established. Then, the reliability of the co-phase power supply device is calculated. With the failure rate and Mean Time To Failures (MTTF) presented, the reliability of the co-phase power supply device is quantificationally evaluated. In order to promote the reliability of the device, two optimized schemes, which include increasing internal components of converter cells and increasing the standby branches of the device, are presented. Compared with the original scheme, the optimized schemes show the promotion of the reliability. Finally, to demonstrate, the computational method is adopted. The results agree well with the proposed schemes.

1. INTRODUCTION

There are many power quality problems existing in the traditional traction power supply system, such as unbalance, reactive power and harmonics to three-phase industrial grid [1, 2]. In [3, 4], the authors presented an advanced co-phase traction power supply system which can solve these power quality problems and improve the power quality greatly. [6] demonstrated the application of the back-to-back converter in active power compensation. The co-phase power supply device plays the key role of negative sequence compensation and harmonic suppression in the co-phase power supply system. As the core part of the system, its reliability index will directly affect the normal operation and application of the whole system. However, few studies have been done on the reliability of the co-phase power supply device or the whole system.

In this paper, the structure and principle of a kind of co-phase power supply system is proposed. A $k/n(G)$ reliability model of the co-phase power supply device, based on two-level quadruple modular topology structure, is established. Then, the reliability of the co-phase power supply device is calculated. In order to promote the reliability of the device, two optimized schemes, which include increasing internal components of converter cells and increasing the standby branches of the device, are presented.

2. CO-PHASE POWER SUPPLY SYSTEM

Figure 1 shows the main structure of the co-phase power supply system. There are two co-phase power supply devices in this scheme and the capacity of each device is 5 MVA. When the traction load is under the traction condition, the port β of the traction transformer only output active power, which will flow into the contact line through the PFC1# and PFC2#, to supply power for the running electric train. The quantity of the active power output by port β is equal to half of the total traction load under the substation's power supply range. Meanwhile, in both co-phase power supply devices, the converters connected to the traction load will output reactive power to the load, which will make the power factor achieve the desired value. Then, the power needed in the hole feeding section of the traction substation will be supplied by port α , and the partition of the electrical phases in the traction substation exports can be canceled; As port α and port β only output active power equally, the high-voltage side of the traction transformer will be three-phase symmetrical, and the negative phase sequence current will be completely compensated. When the traction load is under the regenerative braking condition, the active power flows to the opposite direction, and the power fluxion of the other parts is similar to the traction condition.

3. CO-PHASE POWER SUPPLY DEVICE

Figure 2(a) shows the inner structure of the co-phase power supply device based on two-level quadruple modular topology structure. This kind of device consists of four back-to-back converter

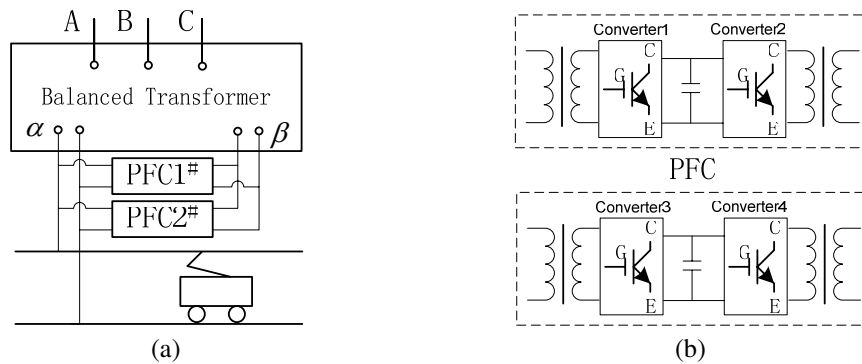


Figure 1: (a) Co-phase power supply system. (b) Co-phase power supply device.

branches which are connected to each other in parallel. Meanwhile, there are four converter cells in every back-to-back unit, and each converter cell consists of three single phase H bridges that are connected with each other in parallel. As the capacity of the whole device is 5 M·VA, every back-to-back converter branch's capacity will be 1.25 MV·A, and every converter's topology structure is shown in Figure 2(b).

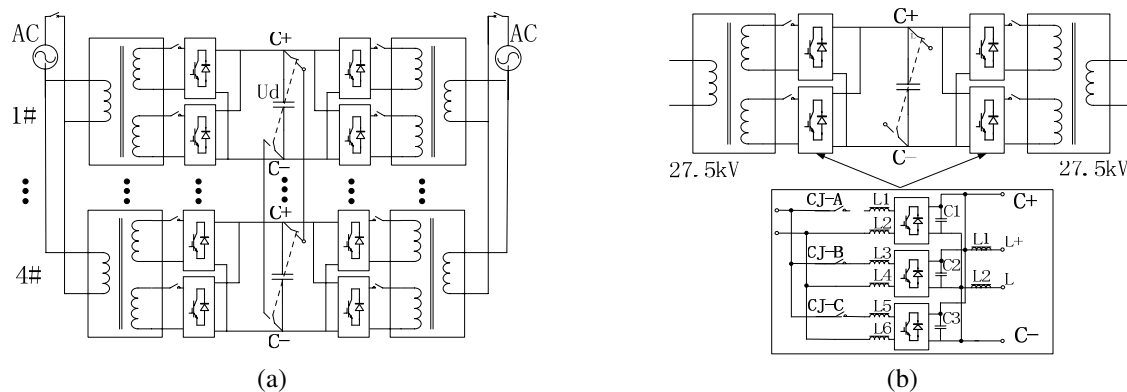


Figure 2: Co-phase power supply device based on two-level quadruple modular topology structure.

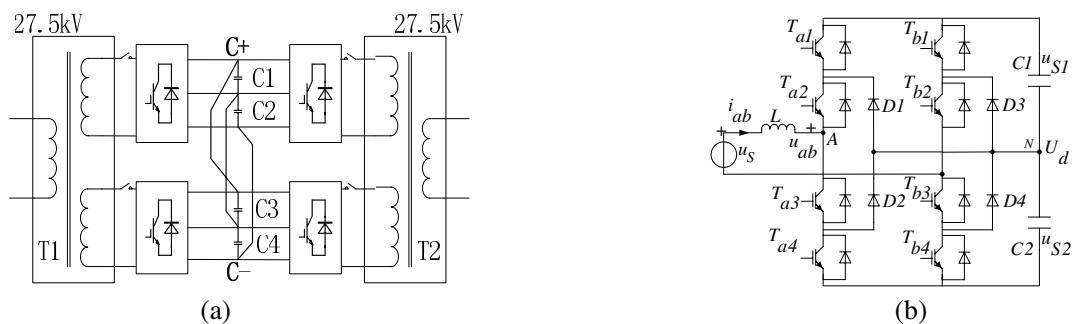


Figure 3: Co-phase power supply device based on three-level duplicate modular topology structure.

The co-phase power supply device based on three-level duplicate topology structure is shown in Figure 3(a). In this scheme, there are two converter units and the capacity of each unit is 2.5 MV·A. Figure 3(b) shows the inner structure of each converter units.

4. RELIABILITY OF THE ORIGINAL SCHEME

The co-phase power supply device consists of many high power electronic elements, such as Insulated Gate Bipolar Transistor (IGBT), Freewheel Diode (D), The Secondary Filter Unit (LC), and Dc-link Capacity (C). According to the American military standard "MIL-HDBK-217F" and the Chinese military standard "GJB/Z 299C-2006", the failure rates and reliability of the high power electronic elements are estimated and their exact values are

$$\begin{cases} \lambda_{IGBT} = 187 \text{ Fit} \\ \lambda_D = 128 \text{ Fit} \\ \lambda_C = 295 \text{ Fit} \\ \lambda_{LC} = 96 \text{ Fit} \end{cases} \Rightarrow \begin{cases} R_{IGBT} = e^{-\lambda t} = e^{-187t} \\ R_D = e^{-\lambda t} = e^{-128t} \\ R_C = e^{-\lambda t} = e^{-295t} \\ R_{LC} = e^{-\lambda t} = e^{-96t} \end{cases} \quad (1)$$

Since many restricted factors such as engineering practice, capacity requirements and economic reasons exist, the IGBT's nominal parameter should be 3300 V/1600A, and the freewheel diode's nominal voltage should be 3000 V. As it is not allowed to make the reverse voltage of IGBT higher than the half of its nominal voltage, choose $U_d = 1800$ V as the DC side voltage and $U_{N2} = 970$ V as the low voltage winding nominal voltage. Then, the low voltage winding nominal current I_{N2} , the IGBT's maximum value current and the number of IGBT modules can be figured out:

$$I_{N2} = \frac{S_1}{U_{N2}} = \frac{1250}{0.97} = 1289A \quad I_1 = \frac{1600}{3} \approx 533A \quad I_{CJ} = \frac{1250}{U_d} = 694.4A \quad I_1 < I_{CJ} < 2I_1 \quad (2)$$

According to Figure 3 and the analysis above, the number of normal work IGBTs mustn't less than two in every three. Then, the 2/3(G) reliability model and the k/n(G) reliability model of the co-phase power supply device is built in Figure 4.



Figure 4: (a) 2/3(G) reliability model. (b) k/n(G) reliability model of the co-phase power supply device.

The reliability and MTTF of a converter unit are

$$R_1(2, 3) = C_3^2 e^{-2\lambda t} (1 - e^{-\lambda t}) + C_3^3 e^{-3\lambda t} \quad T_{\text{MTTF}_1} = \int_0^{\infty} R_1(t) dt \quad (3)$$

As Figure 4(b) shows, the four branches stand for the four converter branches, and every branch consists of four converter units and a DC capacitor.

The reliability and MTTF of a converter branch are

$$R_2 = \left[3e^{-2\lambda t} (1 - e^{-\lambda t}) + e^{-3\lambda t} \right]^4 \cdot e^{-\lambda_c t} \quad T_{\text{MTTF}_2} = \int_0^{\infty} R_2(t) dt \quad (4)$$

The reliability and MTTF of the device are

$$R_3 = \left[3e^{-2\lambda t} (1 - e^{-\lambda t}) + e^{-3\lambda t} \right]^{16} \cdot e^{-4\lambda_c t} \quad T_{\text{MTTF}_3} = \int_0^{\infty} R_3(t) dt \quad (5)$$

5. RELIABILITY OF THE OPTIMIZED SCHEMES

Figure 5(a) shows the first optimized scheme based on increasing internal components of converter cells. Different with Figure 2(b), there are four converter cells in each converter unit, and the reliability model should be a 2/4(G) reliability model:

$$R_{11}(2, 4) = C_4^2 e^{-2\lambda t} (1 - e^{-\lambda t})^2 + C_4^3 e^{-3\lambda t} (1 - e^{-\lambda t}) + C_4^4 e^{-4\lambda t} \quad (6)$$

$$R_{31} = \left[6e^{-2\lambda t} (1 - e^{-\lambda t})^2 + 4e^{-3\lambda t} (1 - e^{-\lambda t}) + e^{-4\lambda t} \right]^{16} \cdot e^{-4\lambda_c t} \quad T_{\text{MTTF}_{31}} = \int_0^{\infty} R_{31}(t) dt \quad (7)$$

Meanwhile, Figure 5(b) shows the second optimized scheme which is based on increasing the standby branches of the device. Compared with the original scheme shown in Figure 2(a), there are

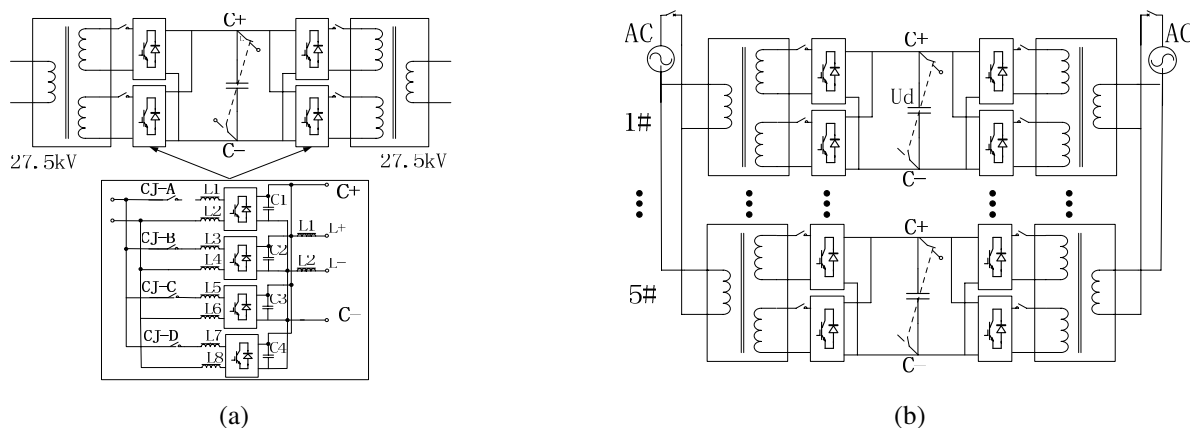


Figure 5: (a) The optimized scheme which is based on increasing internal components of converter cells. (b) The optimized scheme based on increasing the standby branches of the device.

five converter branches in the device. According to Eq. (4) the following equations can be achieved as

$$R_{32}(4, 5) = C_5^4 R_2^4 (1 - R_2) + C_5^5 R_2^5 \quad (8)$$

$$R_{32}(4, 5) = 5 \left[3e^{-2\lambda t} (1 - e^{-\lambda t}) + e^{-3\lambda t} \right]^{16} \cdot e^{-4\lambda c t} - 4 \left[3e^{-2\lambda t} (1 - e^{-\lambda t}) + e^{-3\lambda t} \right]^{20} \cdot e^{-5\lambda c t} \quad (9)$$

Substituting Eq. (1) into Eq. (5), Eq. (7) and Eq. (9), the MTTF of the devices with optimized schemes and the device with original scheme can be achieved. Table 1 shows the comparison of the MTTF between the three schemes and the comparison of the reliability curves is given in Figure 6.

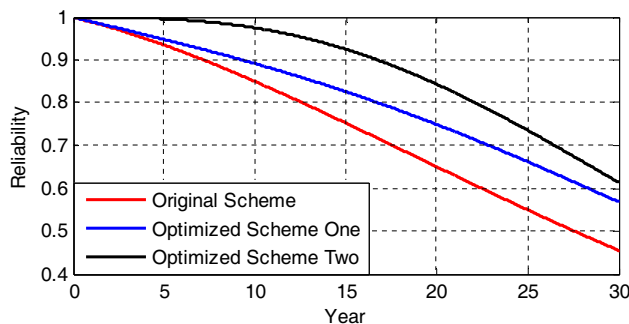


Figure 6: Reliability curves of three schemes.

Table 1: The MTTFs of different schemes.

Scheme	Original Scheme	The first Optimized Schemes	The second Optimized Scheme
MTTF/Year	23.8790	41.2477	36.6070

6. CONCLUSION

In this paper, the structure and principle of a kind of co-phase power supply system is proposed. Then, a $k/n(G)$ reliability model of the co-phase power supply device, based on two-level quadruple modular topology structure, is established. Furthermore, two optimized schemes are proposed to promote the reliability of the device. Finally, the computational results are adopted to demonstrate the validity of the proposed optimized schemes.

ACKNOWLEDGMENT

This work is supported by the key Project supported by the Joint Funds of the National Natural Science Foundation of China (Grant No. U1134205), and the National Natural Science Foundation

of China (Grant No. 51307143).

REFERENCES

1. Chen, T.-H., W.-C. Yang, and Y.-F. Hsu, "A systematic approach to evaluate the overall impact of the electric traction demands of a high-speed railroad on a power system," *IEEE Transactions on Vehicular Technology*, Vol. 47, No. 4, 1378–1384, 1998.
2. Chen, S.-L., R.-J. Li, and P.-H. Hsi, "Traction system unbalance problem-analysis methodologies," *IEEE Transactions on Power Delivery*, Vol. 19, No. 4, 1877–1883, 2004.
3. Shu, Z., S. Xie, K. Lu, Y. Zhao, X. Nan, D. Qiu, F. Zhou, S. Gao, and Q. Li, "Digital detection, control, and distribution system for co-phase traction power supply application," *IEEE Transactions on Industrial Electronics*, Vol. 60, No. 5, 1831–1839, 2013.
4. Shu, Z., S. Xie, and Q. Li, "Development and implementation of a prototype for co-phase traction power supply system," *The Asia-Pacific Power and Energy Engineering Conference (APPEEC)*, 1–4, 2010.
5. Wu, C., A. Luo, J. Shen, F. J. Ma, and S. Peng, "A negative sequence compensation method based on a two-phase three-wire converter for a high-speed railway traction power supply system," *IEEE Transactions on Power Electronics*, Vol. 27, No. 2, 706–717, 2012.
6. Shu, Z., S. Xie, and Q. Li, "Single-phase back-to-back converter for active power balancing, reactive power compensation, and harmonic filtering in traction power system," *IEEE Transactions on Power Electronics*, Vol. 26, No. 2, 334–343, 2011.
7. Tsao, T.-F. and H.-C. Chang, "Composite reliability evaluation model for different types of distribution systems," *IEEE Transaction on Power Syst.*, Vol. 18, 924–930, May 2003.
8. Battistelli, L., M. Pagano, and D. Proto, " 2×25 -kv 50 hz high-speed traction power system: Short-circuit modeling," *IEEE Transactions on Power Delivery*, Vol. 26, No. 3, 1459–1466, 2011.
9. Wu, C., A. Luo, J. Shen, F. J. Ma, and S. Peng, "A negative sequence compensation method based on a two-phase three wire converter for a high-speed railway traction power supply system," *IEEE Transactions on Power Electronics*, Vol. 27, No. 2, 706–717, 2012.

Criss-Cross Metamaterial Based Radiating Structures for C-band Applications

Kirti Inamdar¹, Y. P. Kosta², and S. Patnaik³

¹ECED, SVNIT, Surat, Gujarat, India

²MEFGI, Rajkot, Gujarat, India

³St. Xavier's Institute of Engineering, Mumbai, India

Abstract— In this paper, we present the design of a metamaterial based microstrip patch antenna, optimized for bandwidth and multiple frequency operations. A Criss-Cross structure has been proposed, this shape has been inspired from the famous Jerusalem Cross. The theory and design formulas to calculate various parameters of the proposed antenna have been presented. Design starts with the analysis of the proposed unit cell structure, and validating the response using software — HFSS Version 13, for obtaining negative response of ϵ and μ — metamaterial. Following this, a metamaterial-based-microstrip-patch-antenna is designed. A detailed comparative study is conducted exploring the response of the designed patch made of metamaterial and that of the conventional patch. The unique shape proposed in this paper gives improvement in bandwidth without reducing the gain of the antenna. The C-band of the frequency spectrum has been chosen for all the above mentioned exercise as it is the most popular band for commercial, satellite and radar applications. The proposed metamaterial based antenna can be utilized for higher gain and bandwidth requirements in any of these applications.

1. INTRODUCTION

Low gain and narrow bandwidth are the limitations of conventional microstrip antennas (MSA). The urge of having a compact antenna configuration further deteriorates these two parameters as gain and bandwidth both are directly related to the size of the antenna. Therefore, the most recent design consideration for most of the practical wireless communication applications is size reduction together with gain and bandwidth enhancement. In order to increase the gain, techniques like loading of high permittivity dielectric substrate [1], inclusion of an amplifier type active circuitry [2] and stacked configuration [3] are used. Bandwidth improves if the substrate thickness is increased or the dielectric constant is reduced, use of thick substrates with the help of air or foam along with impedance matching technique [4]. Use of metamaterials (MM) for further improving the performance of MSA has been the recent trend in this field. Majid et al. [5] has proved that the gain and bandwidth of MSA can be increased by placing an array of left-handed metamaterials (LHM) in front of patch. This paper lends its contribution for bandwidth enhancement using a unique MM of Criss-Cross shape. The use of this shape for miniaturisation has been reported in [6].

2. DESIGNING OF CRISS-CROSS SHAPE METAMATERIAL

2.1. Mechanical and Material Aspects

In the Criss-Cross shape [7], there are two cross shapes stacked over each other but electrically separated from each other by 45° as shown in Figure 1(a). The dimension of the unit cell is 6.35×6.35 mm with each of its strip with a width of 1.016 mm made of Copper with a thickness of 0.017 mm. The substrate used is Dupont with $\epsilon_r = 7.8$.

2.2. Simulations and Response

Figure 1(b) shows the results obtained in HFSS. The analysis of the unit cell when made on different substrate material and when its array was designed is presented well in [7]. The proposed signature structure exhibits negative μ & ϵ in the frequency band of 5 to 9 GHz. As per the thumb rule, the unit cell size less than quarter wavelength behaves like MM therefore, at higher frequency, its behaviour as MM is not effective. Therefore, band 5 to 7 GHz is considered to be the effective negative medium band. The negative parameter bandwidth obtained is thus 33%.

3. DESIGNING OF A CRISS-CROSS METAMATERIAL EMBEDDED MICROSTRIP PATCH ANTENNA

We now present the design aspects related to designing of rectangular microstrip patch antenna embodied on a host substrate — metamaterial (signature criss-cross), this is depicted in Figure 3(a).

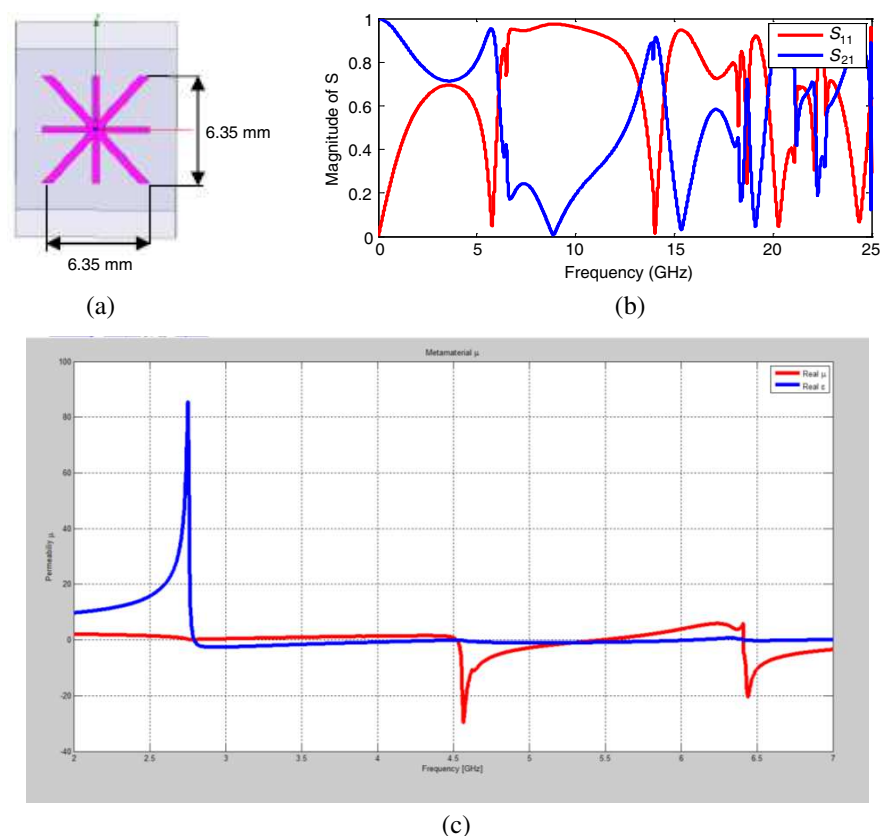


Figure 1: (a) A Criss-Cross shape unit cell with stacked X on both sides of substrate. (b) The S_{11} response of the Criss-Cross unit cell. (c) The extracted parameters of Criss-Cross shape unit cell when made on the substrate of Dupont ($\epsilon_r = 7.8$).

Comparison of the same is done with the conventional patch antenna that was designed to resonate at 6 GHz, shown in Figure 2(a). The length of the patch is 16.3 mm and its width is 19.8 mm. The substrate dimensions are $l = 22.4$ mm and $w = 25.9$ mm with a thickness of 1.016 mm with $\epsilon_r = 2.2$. The feed position is $(x, y) = (4, 4)$. The feed position was optimized in an attempt to obtain multi-band response covering a larger frequency bandwidth with a view that the negative medium band after inclusion of MM can be covered by the device. Figure 2(b) shows the return loss response for the conventional patch antenna for $f_0 = 6$ GHz.

In the next step, an array of Criss-Cross metamaterial inclusions was done in the substrate as shown in Figure 3(a). The frequency response of the above patch is changed as shown in

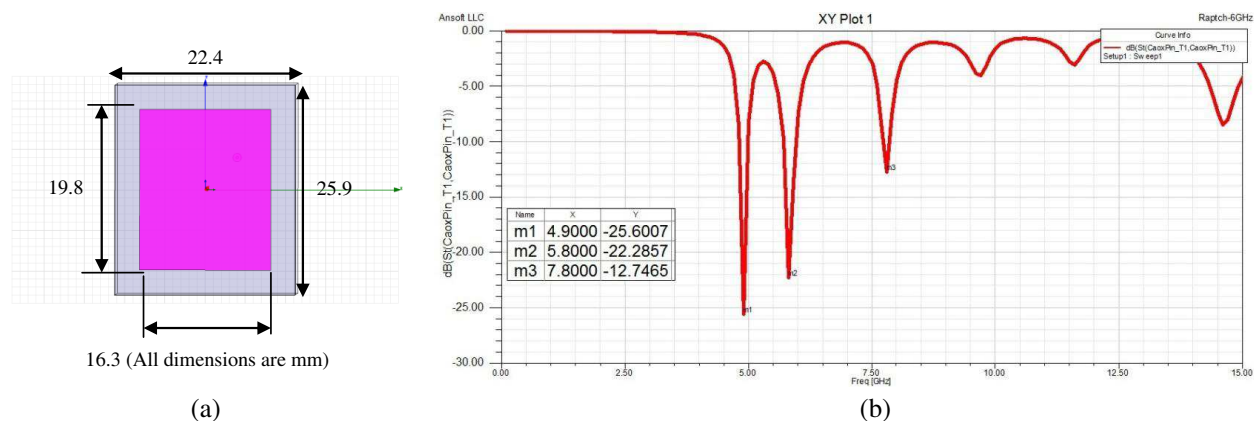


Figure 2: (a) Design for a conventional patch antenna for $f_0 = 6$ GHz. (b) S_{11} response for the conventional patch antenna.

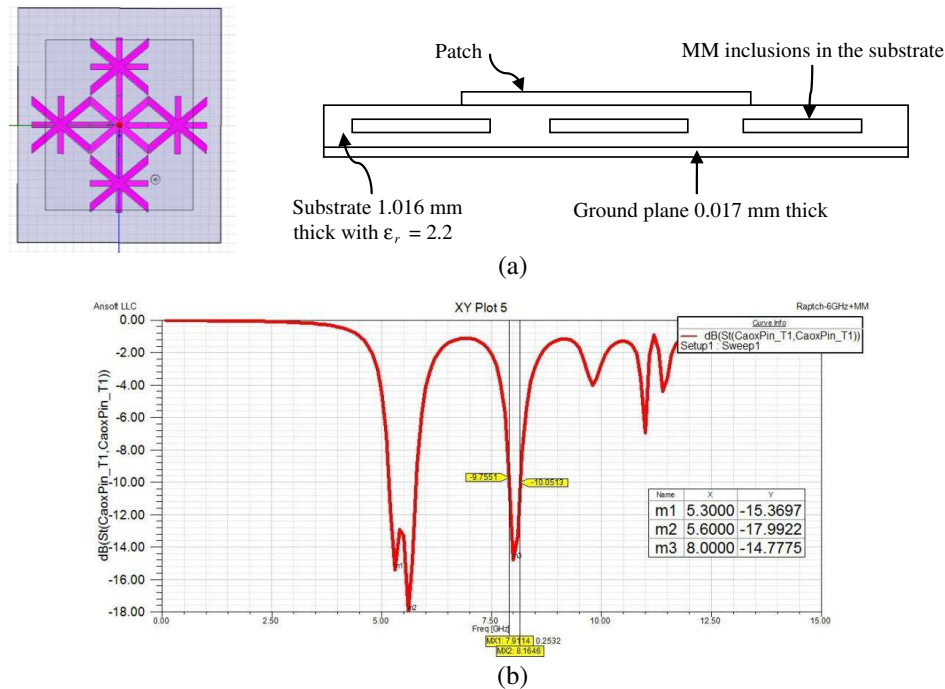


Figure 3: (a) Design of Criss-Cross metamaterial embedded patch antenna (top & front view). (b) S_{11} response for the Criss-Cross metamaterial embedded patch antenna.

Figure 3(b). The left shift in frequency is due to change in the effective impedance of the medium due to metamaterial inclusions. The bandwidth of this antenna configuration is 610 MHz. The bandwidth for simple patch was 300 MHz, so an enhancement of 310 MHz is thus achieved with a gain of 4.45 dB. The metamaterials work on the principle of effective medium theory. The variation in the size of unit cell, no of array elements, arrangement or distribution of unit cells along the structure, material used etc. can generate paths for further improvement in the performance of any model.

4. CONCLUSION

This paper presents the simulation results for a new signature — Criss-Cross shaped metamaterial structure. It has been shown that the proposed structure exhibits negative values of μ and ϵ in the region of design-interest. The negative parameter bandwidth obtained for this signature shape (criss-cross) is 33.33% which is distinctively higher as compared to Square SRR structure (17–18%) [8] and other reported cross structures (31%) [9]. Our proposed signature — criss-cross metamaterial structure when utilized to design a rectangular microstrip patch antenna multiple band operation was observed with an improvement of bandwidth within the multiple bands along with appreciable improvements in the gain as well, compared to the conventional patch antenna. Thus, inspired from the Jerusalem cross, this novel signature — Criss-Cross shaped metamaterial antenna can be strategically utilized to realized microstrip based radiating antennas.

REFERENCES

1. Habib Ullah, M., M. T. Islam, et al., "A parametric study of high dielectric material substrate for small antenna design," *Int. Jour. of App. EM and Mechanics*, Vol. 41, 2, 2013.
2. Robert, B., T. Razban, and A. Papiernik, "Compact amplifier integration in square patch antenna," *Electronics Letters*, Vol. 28, 1808–1810, Sep. 1992.
3. Lee, R. Q. and K. F. Lee, "Experimental study of the two-layer electromagnetically coupled rectangular patch antenna," *IEEE Trans. Antennas and Propagation*, Vol. 38, 1298–1302, Aug. 1990.
4. Huynh, T. and K. F. Lee, "Single layer single patch wideband microstrip patch antenna," *Electronics Letters*, Vol. 31, 1310–1311, Aug. 1995.

5. Majid, H. A., M. K. Abd Rahim, and T. Masri, “Microstrip antenna’s gain enhancement using left-handed metamaterial structure,” *Progress In Electromagnetics Research M*, Vol. 8, 235–247, 2009.
6. Inamdar, K., Y. P. Kosta, and S. Patnaik, “A Criss-Cross metamaterial based electrically small antenna,” *IJERA*, Vol. 3, No. 3, May–Jun. 2013.
7. Inamdar, K., Y. P. Kosta, and S. Patnaik, “A novel Criss-Cross shaped metamaterial,” *IJEAT*, Vol. 2, No. 3, Feb. 2013.
8. Smith, D. R., et al., “Electromagnetic parameter retrieval from inhomogeneous metamaterials,” *Physical Review E*, Vol. 71, 036617, 2005.
9. Katko, A. R., “Artificial negative permeability based on a fractal Jerusalem Cross,” Undergraduate Honors Thesis, 2009.

Microstrip Patch Antenna Design with Criss-Cross Metamaterial Based Radome Cover

Kirti Inamdar¹, Y. P. Kosta², and S. Patnaik³

¹ECED, SVNIT, Surat, Gujarat, India

²MEFGI, Rajkot, Gujarat, India

³St. Xavier's Institute of Engineering, Mumbai, India

Abstract— A high gain microstrip patch antenna with a metamaterial cover over it has been proposed in this paper. A new design namely Criss-Cross metamaterial is being used here. The Criss-Cross unit cell comprises of a cross printed on one face of dielectric substrate and the same cross rotated by 45° is being printed on the other face of the same substrate. The DNG behavior, i.e., both ϵ and μ are simultaneously negative for this metamaterial is obtained at 6 GHz; the patch also operates on the same frequency. The radome cover is constructed by stacking three layers made up of a 3×3 Criss-Cross metamaterial array. A 3×3 array of Criss-Cross metamaterial unit cell is printed on Duroid substrate. This arrangement of radome cover increases the gain of a simple patch antenna up to 3.66 dB. The radome cover over the antenna is used to protect the structure from environmental hazards. However due to use of conventional dielectric materials as radome, the performance of the antenna degrades. When a metamaterial is printed on such dielectric material, its properties and behavior changes. This leads to improvement of performance of patch antenna along with its physical protection. The directivity of the proposed patch antenna also improves due to the lens behavior of the radome cover over the patch. A conventional radome cover will scatter the EM radiations emitted by the patch antenna. But the metamaterial cover acts as a lens which focuses the EM radiations. This action is once again due to the unusual properties of the metamaterials.

1. INTRODUCTION

Patch antenna consists of a patch of metallization on a grounded substrate. These antennas are low-profile, lightweight and most suitable for aerospace and mobile applications. However, patch antennas also have some limitations such as lower gain, lower efficiency and narrow bandwidth. There has been a lot of study published on the improvement in the performances of patch antennas. Most of the solutions proposed were to use an array of several antennas. The particular disadvantage of this method comes from the feeding of each antenna and also from the coupling between each element. Other solutions have been suggested to make use of a substrate of either high permittivity or permeability [1]. However, this result in big loss of the material and high cost. In the past few years, left-handed metamaterials (LHMs) composed of split-ring resonators (SRRs) and wires have attracted considerable attention because of their unusual electromagnetic properties and can be applied to antennas reflectors, filters, perfect lens and so on [2–4]. Burokur et al. [5] numerically studied the influence of LHMs on the performances of the antenna and found the performance of the antenna can be improved using the focusing effect in the LHMs. Enoch et al. [6] investigated the properties of metallic composite metamaterials and demonstrated that monopole's directivity can be improved greatly using a very low refractive index of metamaterials. Chen et al. [7] theoretically investigated the controllable LHMs based on a varactor-loaded S-shaped resonator structure which can realise continuous scanning capability. In this paper, we study numerically the performances of a patch antenna when Double negative (DNG) is placed above.

2. DESIGNING OF DNG COVER USING CRISS-CROSS METAMATERIA

The design of a metamaterial-radome for a patch antenna operating in a specific frequency band requires the entire determination of its electromagnetic characteristics around the operating frequency with well defined properties. The composed multi-layered media should have an effective index of refraction near zero with low losses to not modify the antenna performances. In this study, the metamaterial radome is made by aligning the layers of the Criss-Cross resonators alternately with layers of air. Since the metamaterial radome is a 3D periodic structure of Criss-Cross, the effective permittivity and permeability of a metamaterial-slab are computed with Ansoft-HFSS software by using both the perfect electric conductor (PEC) and perfect magnetic conductor (PMC) boundaries. This method allows the microwave characterization of a semi-infinite effective homogeneous

slab with an infinite periodic array structure. For a plane wave incident normally on the homogeneous slab of thickness d , we compute the effective permeability from the reflection (S_{11}) and the transmission (S_{21}) coefficients of the simulated structure.

Here we study the effect of a DNG MM cover over a patch antenna. The MM cover was made of a 3×3 array of Criss-Cross MM [8]. The Criss-Cross structure gives negative ϵ and μ in the frequency band of 5–7 GHz. Thus a 6 GHz patch antenna was designed in order to match the resonating frequency. The functioning of a MM cover over the patch is explained in Fig. 1 where the scattered radiations from the patch are focused due to the MM cover over it. This action helps

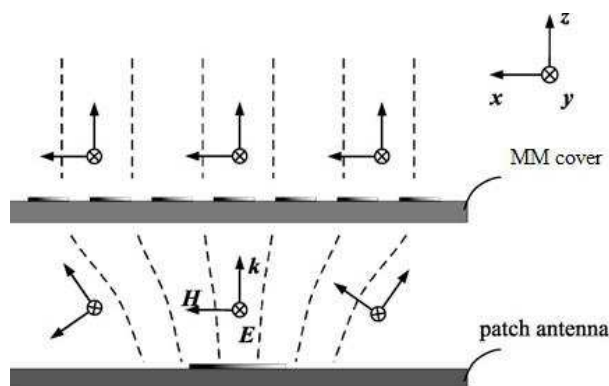


Figure 1: Lensing phenomenon by radome cover using MM over the patch antenna.

Table 1: Summary of different trials applied for radome cover.

TYPE	FREQ (GHz)	S_{11} (dB)	GAIN (dB)	DIRECTIVITY (dB)
Single layer				
i) ag = 10 mm	5.5	-15.49	2.51	3.48
ii) ag = 15 mm	5.8	-15.82	3.21	3.55
iii) ag = 20 mm	6.4	-16.12	4.61	4.68
iv) ag = 25 mm	6.6	-16.19	4.64	4.74
Double layer				
i) ag1 = 25 mm ag2 = 6.25 mm	5.5	-37.97	4.65	4.75
ii) ag1 = 25 mm ag2 = 10.25	6.2	-15.82	2.55	3.26
Triple layer				
(ag1 = 25 & ag2 = 6.25)				
i) ag3 = 6.25	6.3	-15.38	3.69	3.66
ii) ag3 = 10.25	6.4	-16.08	3.66	3.66

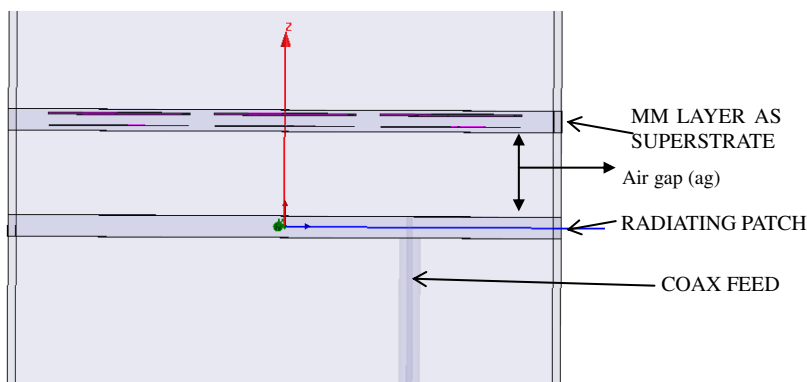


Figure 2: Criss-Cross MM based radome cover made up of single layer over the patch.

in improving gain and directivity of the patch antenna.

Figure 2 shows a single layer radome structure above the 6 GHz radiating patch. The dimensions of the radome optimized with the Ansoft-HFSS software. In order to form the radome cover, a layer consisting of 3×3 array of Criss-Cross MM being printed over Duroid substrate with $\epsilon_r = 2.2$ was used. The thickness of the substrate is 1 mm. The dimensions of Criss-Cross unit cell are same as in [8]. The distance between the patch and the cover is defined as ‘ag’. ‘ag’ has been varied in steps so as to see its effect on results.

Table 1 summarizes the different optimization trials applied to the radome structure. It has been noticed that the gain and directivity improved as the number of MM layers in the radome structure are increased.

3. CONCLUSION

Use of a conventional dielectric radome cover adds losses and disturbance to the radiation pattern of the patch antenna. But the use of MM for radome cover improves the gain and the directivity of the patch. The results show that under proper conditions the energy radiated by the MM cover antenna is concentrated, and a more directional and higher gain antenna is obtained. MM has the merits of simple structure, compact size, prepared convenience and the most important is that it can improve the performances of the patch antenna greatly. Furthermore, MM cover can also be used to the other antennas such as monopoles, dipole antennas, leak-wave antennas and aperture antennas.

REFERENCES

1. Jackson, D. R. and N. G. Alexopoulos, “Gain enhancement methods for printed circuit antenna,” *IEEE Trans. Antennas Propag.*, Vol. 33, No. 9, 976–987, 1985.
2. Veselago, V. G., “The electrodynamics of substances with simultaneously negative values of permittivity and permeability,” *Sov. Phys. Usp.*, Vol. 10, No. 4, 50–514, 1968.
3. Pendry, J. B., A. J. Holden, and W. J. Stewart, “Extremely low frequency plasmons in metallic meso structures,” *Phys. Rev. Lett.*, Vol. 76, No. 25, 4773–4776, 1996.
4. Pendry, J. B., A. J. Holden, D. J. Robbins, and W. J. Stewart, “Magnetism from conductors and enhanced nonlinear phenomena,” *IEEE Trans. Microw. Theor. Tech.*, Vol. 47, No. 11, 2075–2084, 1999.
5. Burokur, S. N., M. Latrach, and S. Toutain, “Theoretical investigation of a circular patch antenna in the presence of a left-handed medium,” *IEEE Antennas Wirel. Propag. Lett.*, Vol. 4, 183–186, 2005.
6. Enoch, S., G. Tayeb, P. Sabouroux, N. Guérin, and P. Vincent, “A metamaterial for directive emission,” *Phys. Rev. Lett.*, Vol. 89, No. 21, 213902-1–213902-3, 2002.
7. Chen, H., B. I. Wu, L. Ran, T. M. Grzegorzcyk, and J. A. Kong, “Controllable left-handed metamaterial and its application to a steerable antenna,” *Appl. Phys. Lett.*, Vol. 89, 053509–053509-3, 2006.
8. Inamdar, K., Y. P. Kosta, and S. Patnaik, “A novel Criss-Cross shaped metamaterial,” *IJEAT*, Vol. 2, No. 3, Feb. 2013.

A Multi-channel Digital Temperature Acquisition System Based on SOPC

W. He, Q.-Y. Feng, and D.-H. Jia

School of Information Science and Technology
Southwest Jiaotong University, Chengdu, Sichuan 610031, China

Abstract— In this paper, a multi-channel digital temperature acquisition system is proposed. Based on System on a Programmable Chip (SOPC) and 1-wire bus technologies, the temperature acquisition node is designed. The data acquired is transferred to the host computer through RS232 serial interface. The software on the computer analyzes and processes the received data to achieve the real-time monitoring and display of the temperature through the User Interface (UI). Programmable resolution 1-wire digital thermometer DS18B20 is adopted in this design. The acquisition node is configured by NIOS soft core CPU using Verilog HDL and C language, meanwhile, the UI on the PC is designed in Visual Basic language. The temperature sensor has an operating temperature range of -55° to 125° . The resolution of the acquisition is 0.0625° and the display resolution is 0.01° . All simulations in the design are done in Quartus and Modelsim tools. Finally, the operation of the temperature acquisition system is validated on an Altera Cyclone II series FPGA chip. The measure results are displayed on both the local LCD module of the acquisition node and the UI of the host computer. The system can also give out alarm signals when the temperature acquired exceeds the threshold set through software. Due to the use of SOPC technology, the system is of high integration, high design flexibility, small volume and low power consumption. The system can be widely used in areas such as intelligent greenhouses, temperature monitoring systems inside storehouses, equipments, or machinery, and process control systems.

1. INTRODUCTION

The temperature is one of the basic physical parameters, and the temperature acquisition is one of the most continually technology used in agriculture, industry and daily life. Temperature acquisition systems are widely applied in areas such as intelligent greenhouses, storehouses, equipments, machinery, and medicine, etc.. The traditional temperature acquisition systems usually use microprocessors as the central processing units. With the development of SOPC technology and the miniaturization of the electronic equipments, data acquisition systems start to introduce FPGA as the core of the systems.

In this paper, a multi-channel digital temperature acquisition system based on SOPC is proposed. The acquisition node is configured by NIOS soft core CPU using Verilog HDL and C language. The temperature sensors DS18B20 convert the temperature to digital word and the FPGA chip store it in the FIFO memory. Finally, the value of the temperature is displayed on the LCD module controlled by the NIOS soft core CPU and sent to the PC end through UART (Universal Asynchronous Receiver/Transmitter) for display. On the UI of the PC end, we can observe the real-time temperature and set the upper limit temperature. When the temperature acquired exceed the limit the UI will give out alarm signal. The integration and speed of the acquisition system are upgraded because of the introduction of the SOPC technology.

2. SYSTEM ARCHITECTURE OVERVIEW

The proposed temperature acquisition system is shown in Fig. 1. The system mainly consists of five parts, four DS18B20 temperature sensors, an Altera cyclone II FPGA board, a LCD12864 display module, a MAX232 UART module and a host computer.

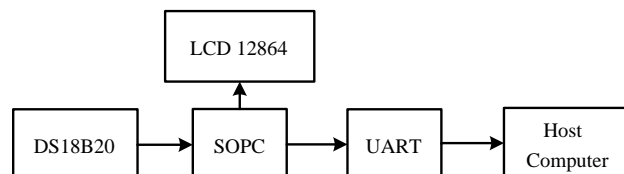


Figure 1: Functional block diagram of the temperature acquisition system.

- 1) The temperature sensors module includes four digital temperature sensors DS18B20. Under the control of the SOPC module, the sensors acquire the temperatures of the four channels and convert them into digits.
- 2) The SOPC module receives the digits sent by DS18B20 and stores them in the FIFO memory, and translates them into real values of the temperatures. After the translation, the SOPC send the data to the LCD12864 and UART module for display.
- 3) The LCD12864 display module consists of a liquid crystal display panel. The temperatures of the four channels are displayed on the module, so the user can observe the values of the temperature at the field even if there is no host computer.
- 4) The UART module implements the conversion between TTL/CMOS levels and TIA/EIA-232-F levels. Thus enable the SOPC to send data to the host computer.
- 5) The host computer receives the data sent by SOPC and displays the temperatures on the user interface (UI). We can also set the temperature thresholds on the UI. If the temperatures exceed the thresholds we set, the UI will give out alarm information to remind us the over temperature events.

3. HARDWARE DESIGN

In this section, the hardware design of the temperature sensors circuit, LCD display circuit, UART levels conversion circuit, and FPGA/SOPC system is described.

3.1. DS18B20 Temperature Sensors Circuit Design

DS18B20 is a 1-Wire Digital Thermometer, so that only one wire (and ground) needs to be connected from the FPGA to a DS18B20. The Data In/Out pin (pin 2) is pulled up to VCC through a 4.7k Ω resistor, in order to provide power for reading, writing, and performing temperature conversions by the data line itself. The four sensors use the same circuits as above and parallel acquisition is adopted to improve the conversion speed.

3.2. UART Circuit Design

The UART circuit realizes the conversion between TTL/CMOS levels and TIA/EIA-232-F levels. So the acquisition system can communicate with the host computer through serial port. The circuit of this part is shown in Fig. 3.

3.3. LCD12864 Display Circuit Design

In the acquisition system, a LCD12864 module is adopted as the temperatures display device. The controller/driver of the LCD12864 is ST7920 which has a wide operating voltage (2.7 V to 5.5 V) and low power consumption. The display module has a display definition of 128 \times 64 and works in parallel bus mode. The circuit is as Fig. 4 shows.

3.4. Hardware Design of SOPC System

The SOPC system is mainly comprised of the NIOS processor, the user-defined components and some peripheral. The structure of system is shown in Fig. 5. The system is created in Verilog hardware description language (HDL).

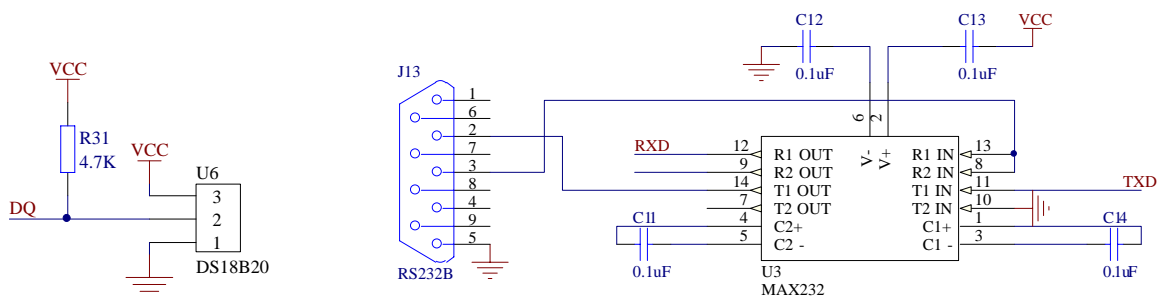


Figure 2: The schematic of temperature sensor.

Figure 3: The schematic of the UART circuit.

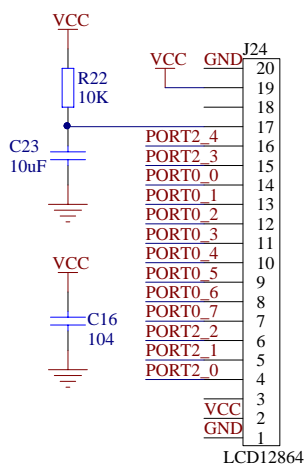


Figure 4: The schematic of the LCD12864 circuit.

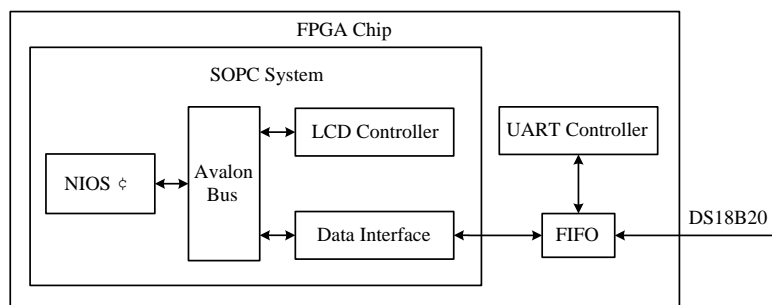


Figure 5: The structure diagram of the SOPC system.

4. SOFTWARE DESIGN BASED ON NIOS II

The software is designed in C language in the NIOS II IDE environment. In this system, the software mainly implements the control of the LCD display of the four channels' temperatures. When the temperature sensors DS18B20 finish the conversion, the system will call the display function and display the four temperatures on the LCD. The software flow chart is shown in Fig. 6. The control of the conversion of sensors and UART are finished by modules described in Verilog HDL.

The data sent to the serial port is made up of five bytes. The first byte is the channel label, so the UI on the host computer can recognize the corresponding temperatures of the four channels and display them on the interface correctly. The second to the fourth bytes of the data are the tens, units, tenths and hundredths of the temperature to be displayed respectively.

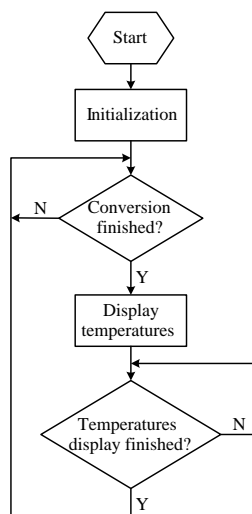


Figure 6: The flow chart of the program.

5. SYSTEM VERIFICATION

In order to verify the operation of the system, this paper utilizes Altera Cyclone II FPGA chip EP2C5Q208C8 to realize the system. The photo of the system is shown in Fig 7. The system mainly contains three circuit boards, a FPGA board, a LCD12864 display board and a DS18B20 temperature sensors board.

A UI on the host computer is designed in Visual Basic, the temperatures of the four channels can be displayed on the interface and temperature thresholds can be set through it. The operation

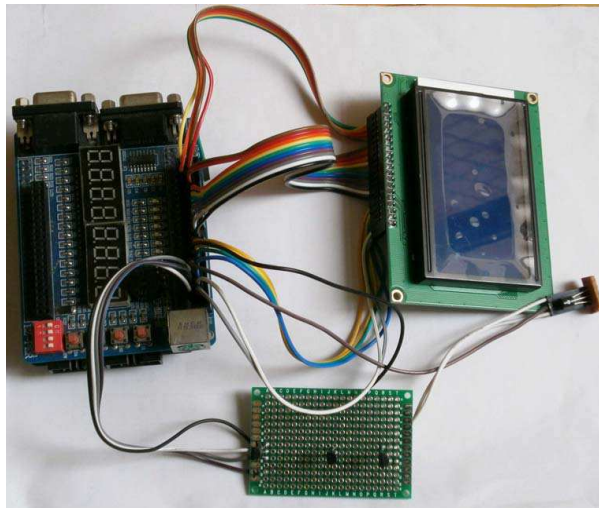


Figure 7: The photo of the system.

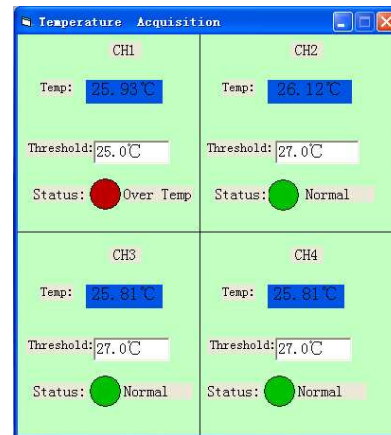


Figure 8: The operation of the User Interface (UI).

photo of the UI is shown in Fig. 8.

The temperature threshold of channel 1 is set to 25°, thresholds of channel 2–4 are set to 27°. The temperature acquired by channel 1 is 25.93° which has exceeded the threshold. So the status turns to “Over Temp” from “Normal” to report the fault.

6. CONCLUSION

In this paper, a multi-channel digital temperature acquisition system based on SOPC is designed. The integration of the system is improved due to the use of the SOPC technology. The operation of the system is verified on the Altera EP2C5Q208C8 FPGA chip and the host computer. The system can be widely used in areas such as intelligent greenhouses, temperature monitoring systems inside storehouses, equipments, or machinery, and process control systems.

ACKNOWLEDGMENT

This work is supported by the National Natural Science Foundation of China (NNSF) under Grant 61271090, and the National 863 Project of China under Grant 2012AA012305.

REFERENCES

1. Dong, H., et al., “A SOPC design for intelligent pressure sensor,” *Proceedings of 2009 International Conference on Information, Electronic and Computer Science*, Vols. I and II, 327–330, 2009.
2. Xiong, G. H., et al., “Design of minimum SOPC system board,” *2008 International Conference on Intelligent Computation Technology and Automation (ICICTA)*, Vol. 2, 20–24, 2008.
3. Jurgen, R. K., *Sensors and Transducers*, Society of Automotive Engineers, Warrendale, PA, 1997; Wiley-IEEE Computer Society, 1999.
4. Elrabaa, M. E. S., “A new FIFO design enabling fully-synchronous on-chip data communication network,” *2011 Saudi International Electronics, Communications and Photonics Conference (SIEPCP)*, 2011.
5. IEEE Standard Hardware Description Language Based on the Verilog(R) Hardware Description Language, IEEE Std 1364-1995, 1996.
6. Ciletti, M. D., *Advanced Digital Design With the Verilog HDL*, 2nd Edition, Prentice Hall, 2010.

A High Precision and Externally Synchronous CMOS Relaxation Oscillator

Y.-Y. Deng, Q.-Y. Feng, and D.-H. Jia

School of Information Science and Technology
Southwest Jiaotong University, Chengdu, Sichuan 610031, China

Abstract— A high precision and externally synchronous relaxation oscillator with simple structure is proposed in this paper. The oscillator consists of the current circuits, a capacitor, two comparators, a RS flip-flop and other components. In the current circuits positive and negative temperature coefficient currents are obtained. With the current temperature compensation, a low temperature current is used to charge and discharge the capacity. By optimizing the delay of the comparators the oscillator has a good ability of control linearity. In this method a high precision oscillator is obtained. Based on $0.5\ \mu\text{m}$ OKI technology library, HSPICE and Cadence software is used to circuit simulation the simulation results show that the oscillator has stable output frequency and external synchronization. Under the environment of typical applications in the chip system, the frequency of the oscillation is 500.1 kHz, With the power supply temperature changing from -40°C to 125°C , the frequency migration ranges from -0.3% to $+1.3\%$.

1. INTRODUCTION

With the advantages of light weight, small size and high efficiency, switching power supply is being widely used in almost all electronic devices. It has become an indispensable part in the development of the information industry. As a member of switching power supply with PWM circuit, the clock generation of DC/DC convertor plays a key role, its main types are: relaxation oscillator, ring oscillator and LC oscillator. Especially, the relaxation oscillator is used in capacitive sensors and monolithic power integrated circuits. A well-designed relaxation oscillator should have following features: good stability, wide frequency range and good control linearity. In this paper with the current temperature compensation, a low temperature current is used to charge and discharge the capacity, and a high-precision clock signal can then be obtained. By optimizing the delay of the comparators, the oscillator gets a good ability of control linearity. Meanwhile, in order to make the system with an oscillator works synchronously, this relaxation oscillator has a function of synchronized by external sync clock signal.

2. ARCHITECTURE OF RELAXATION OSCILLATOR

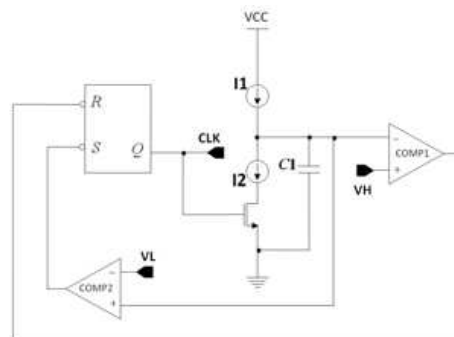


Figure 1: Layout of the tunable dual-band bandpass filter.

By taking advantage of the bi-stable characteristic of switching elements such as the flip-flop and comparator, the current circuits take turns to charge or discharge the clock capacitor. With the voltage waveform of the capacitor rising or falling, the node R and S are triggered and the state of the circuit is changed periodically. In Fig. 1, COMP1 and COMP2 are window comparators, their flipping threshold are V_H and V_L respectively.

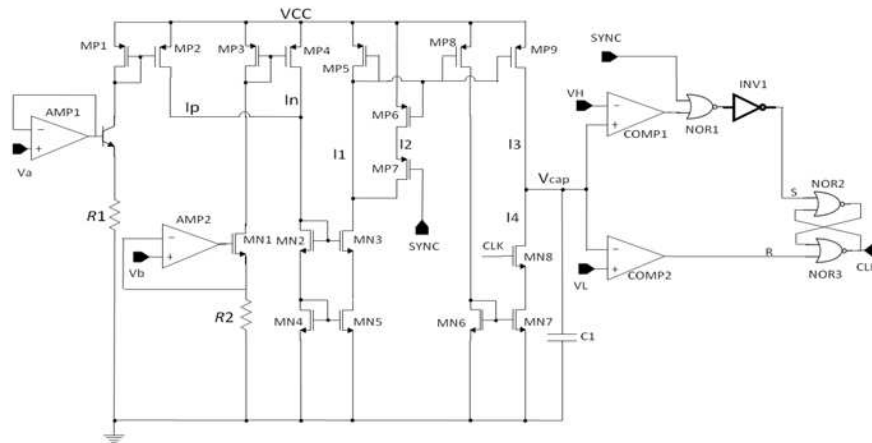


Figure 2: Layout of the tunable dual-band bandpass filter.

2.1. The Design of Relaxation Oscillator

The design of the relaxation oscillator is shown in Fig. 2, through two current circuits a temperature-compensated current is obtained. With the help of current mirror, the discharged current I_4 is greater than the charged current I_3 , the capacitor voltage is toothed with frequency stability, CLK is the clock signal.

The high level V_H of the amplitude control circuit is detected by the comparator COMP1, the low level is detected by the comparator COMP2. The generation of clock is shown in Fig. 3, $tp1$ and $tp2$ are the delays produced by the two comparators. In order to reduce the frequency distortion in frequency modulator caused by non-linearity, the delay should be as small as possible. How to reduce the delay will be described in next part.

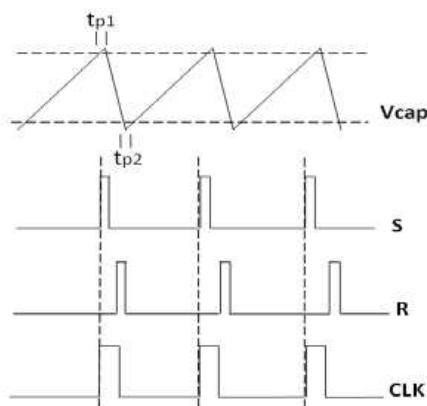


Figure 3: Sawtooth wave and generation of clock signal.

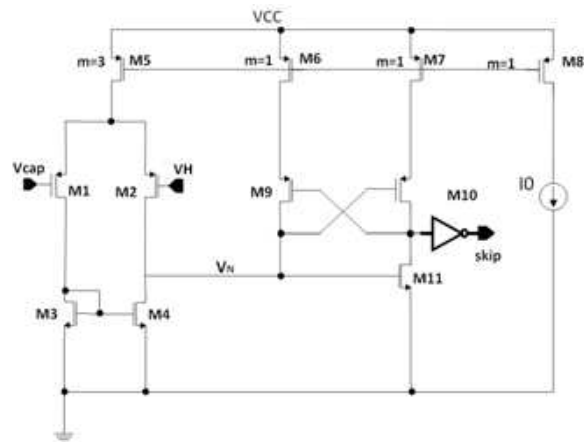


Figure 4: The comparator circuit.

The current I_p and I_n are obtained by the follower (AMP1, AMP2) tracking the reference voltage V_a and V_b respectively, which can be expressed as:

$$I_p = \frac{V_a - V_{be}}{R1} \times \frac{MP2}{MP1} \quad (1)$$

$$I_n = \frac{V_b}{R2} \times \frac{MP4}{MP3} \quad (2)$$

where $MP1$, $MP2$, $MP3$, $MP4$ mean the number of the devices in parallel respectively. With increasing temperature V_{be} decreases. However $R1$ and $R2$ are resistances with positive temperature coefficient. It can be derived that I_p is the current with positive temperature coefficient and I_n on the contrary is the current with negative temperature coefficient. The two currents gather

to charge and discharge the clock capacitor. Through temperature compensation a high-precision clock is obtained.

2.2. The Design of the Comparator

As the RS flip-flop is triggered by the rising edge, we should reduce the delay $tp1$. The comparator circuit is designed shown as Fig. 4.

When skip signal is high and V_{cap} is higher than V_H , M9 is on and M10 is off. The drain current of M6 (I_{D6}) and that of M2 (I_{D2}) flow in M4 together. It can be derived that the drain current of M4 is larger than that of M3 and V_N is then larger than threshold voltage of M11 to keep the skip signal high. Drain current of M4 (I_{D4}) can be given by

$$I_{D4} = I_{D2} + I_{D6} \quad (3)$$

While V_{cap} increase (V_H fixed), I_{D2} and I_{D3} decreases, V_N rises and

$$I_{D4} \geq I_{D3} \quad (4)$$

So the threshold of skip signal rising is achieved when I_{D4} equals to I_{D3} . As M1 and M2 work in saturation area, I_{D3} and I_{D2} can be expressed by

$$I_{D3} = I_{D1} = \frac{1}{2}\mu_p C_{ox} \frac{W}{L} (V_P - V_{cap} - |V_{TP}|)^2 \quad (5)$$

$$I_{D2} = \frac{1}{2}\mu_p C_{ox} \frac{W}{L} (V_P - V_H - |V_{TP}|)^2 \quad (6)$$

Where μ_p , C_{ox} , V_{TP} and W/L stand for effective channel mobility, gate oxide capacitance per unit area, threshold voltage and wide to length ratio of PMOS. From (3), (4), (5), the condition of rising threshold can be expressed by

$$I_{D1} = I_{D2} + I_{D6} \quad (7)$$

In Fig. 4, other current of transistors can be expressed as follow:

$$I_{D1} + I_{D2} = I_{D5} \quad (8)$$

$$I_{D5} = 3I_{D8} = 3I_0 \quad (9)$$

$$I_{D6} = I_{D8} = I_0 \quad (10)$$

where I_0 is current bias. From (7), (8), (9) and (10), I_{D1} and I_{D2} can be expressed by

$$I_{D1} = \frac{1}{2}(I_{D5} + I_{D6}) = 2I_0 \quad (11)$$

$$I_{D2} = \frac{1}{2}(I_{D5} - I_{D6}) = I_0 \quad (12)$$

From (5) and (11), (6) and (12), V_C and V_P can be expressed by

$$V_P = V_{cap} + |V_{TP}| + \sqrt{\frac{2I_0}{\mu_p C_{ox} W/L}} \quad (13)$$

$$V_P = V_H + |V_{TP}| + 2\sqrt{\frac{I_0}{\mu_p C_{ox} W/L}} \quad (14)$$

From (13) and (14), the threshold voltage of skip signal rising can be given by

$$V_{cap} = V_H + (\sqrt{2} - 2) \sqrt{\frac{I_0}{\mu_p C_{ox} W/L}} \quad (15)$$

From (15), it is clear that the rising threshold voltage is lower than V_H and in this way $tp1$ can be reduced.

3. EXTERNAL SYNCHRONIZATION APPLICATION

In order to make the whole system works in unified clock synchronously, the oscillator is with externally synchronous function. The external clock signal often has an unfixed duty cycle. Such waveform is generally not conducive to an edge-triggered RS flip-flop to flip quickly, so a shaping circuit is usually needed, it may adjust the duty cycle of the external clock signal to less than 10%. This circuit is simple and is not included in our paper. When the external synchronizing signal SYNC arrives the MP7 of Fig. 2 works, and I_2 takes parts of current I_1 , thus the charge-discharge current can be reduced in whole clock period. As V_{cap} is always lower than the voltage V_H , COMP1 will not overturn. The synchronous signal SYNC can be introduced through the logic gate NOR1, in this way the oscillator can work with the outside synchronous clock frequency.

4. SIMULATION RESULT

The relaxation oscillator has been implemented with a standard $0.5\ \mu\text{m}$ OKI process. Our design has been simulated in a temperature ranging from -40°C to 125°C on HSPICE. The results show that the oscillator is in high precision. Table 1 summarizes the simulation result of the oscillator in different temperature.

$T/^\circ\text{C}$	f_{osc}/MHz	offset/%
-40	506.5 kHz	+1.3
25	500.1 kHz	+0.02
40	504 kHz	+0.8
60	506.3 kHz	+1.26
85	499.3 kHz	-0.15
125	501.9 kHz	+0.38

Table 1: Frequency vs temperature.

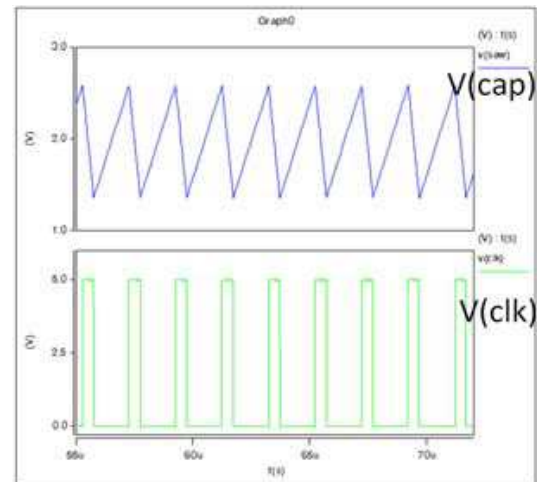


Figure 5: Simulation results of V_{cap} and OSC.

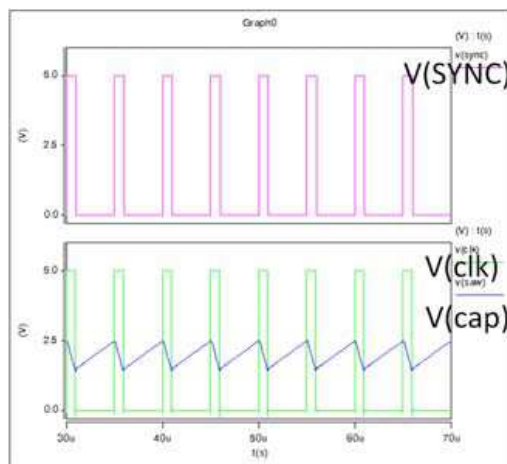


Figure 6: External synchronization with 200 kHz.

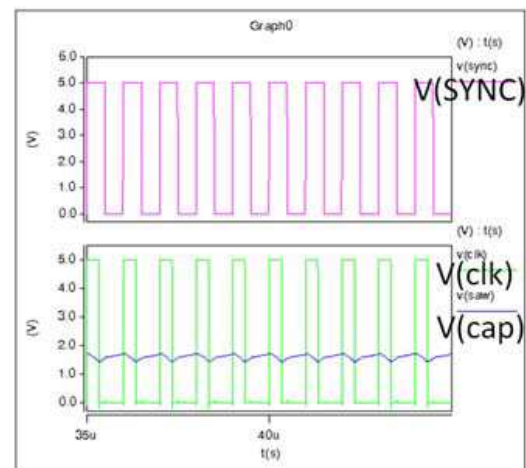


Figure 7: External synchronization with 1 MHz.

5. CONCLUSION

A high precision and externally synchronous relaxation oscillator is proposed. With the current temperature compensation, a low temperature current is used to charge and discharge the capacity.

The relaxation oscillator has been implemented with a standard 0.5 μm OKI process. This oscillator has been simulated in the temperature range of ($-40^{\circ}\text{C} \sim 125^{\circ}\text{C}$) on HSPICE. The results show that the oscillator is of stable frequency, high precision, and external synchronization ranging from 200 kHz to 1 MHz.

ACKNOWLEDGMENT

This work is supported by the National Natural Science Foundation of China (NNSF) under Grant 61271090, and the National 863 Project of China under Grant 2012AA012305.

REFERENCES

1. Allen, P. E. and D. Holberg, *CMOS Analog Circuit Design*, Oxford University Press, New York, 2002.
2. Shyu, Y.-S. and J.-C. Wu, "A process and temperature compensated ring oscillator," *Proc. Asia Pacific Conf. ASICs*, 283–286, Aug. 1999.
3. Barranco, B. L., A. R. Vazquez, E. S. Sinencio, and J. L. Huertas, "Frequency tuning loop for VCOs," *Proc. IEEE Int. Symp. Circuits Syst. (ISCAS)*, 2617–2620, Jun. 1991.
4. Sundaresan, K., P. E. Allen, and F. Ayazi, "Process and temperature compensation in a 7-MHz CMOS clock oscillator," *IEEE J Solid State Circuit*, Vol. 41, 433–442, 2006.
5. Fiori, F. and P. S. Crovetto, "A new compact temperature compensated CMOS current reference," *IEEE Trans Circuits and Systems*, Vol. 52, 724–728, 2005.
6. Kumar, R. and V. Kursun, "Voltage optimization for temperature variation insensitive CMOS circuits," *IEEE International Midwest Symposium Circuits and Systems*, Vol. 1, 476–479, 2005.

A Novel Algorithm of Landmine Detection

Xin-Yun Wang, Qian Song, Han-Hua Zhang, and Zhi-Min Zhou

College of Electronic Science and Engineering

National University of Defense Technology, Changsha, Hunan 410073, China,

Abstract— A novel algorithm which exploits aspectual invariance and local contrast to discriminate landmines from other man-made targets and natural clutter in Synthetic Aperture Radar (SAR) image is proposed in this paper. Firstly, Azimuth Scattering Entropy (ASE), which measures the characteristic of aspectual invariance, is extracted as a detection feature. The detection threshold is then acquired from the histogram of the ASE image with an auto-adaptation method. The ultimate detection result is obtained by fusing results from aspectual invariance detection and Constant False Alarm Rate (CFAR) detection of the full aperture image. The algorithm concerns with the use of prior information of the to-be-detected targets and provides new thinking for detection scheme in SAR image. The results of experimental data demonstrate the effectiveness and practicability of the proposed algorithm.

1. INTRODUCTION

Landmines left after war are difficult to clear, which threatens humans life and hinders the development of social economy. Landmine clearance is a task which brooks no delay. However, landmine detection is a worldwide problem [1], primarily due to: 1) landmines are usually of small size, which demands high resolution in imaging and detection and complicates the implementation of radar system. 2) Landmines have small Radar Cross Section (RCS) and low signal-to-clutter ratio (SCR) in SAR image. As a result, landmine detection is a typical weak and dim target detection problem in complex environments.

Recently, many detection techniques have been investigated. The Lincoln Laboratory Automatic Target Recognition (ATR) algorithm [2] is a typical procedure of ATR in SAR image due to its clear thinking and reasonable structure. The subsequent improved algorithms mainly improve on each stage (prescreening, discrimination and classification) of the Lincoln Laboratory ATR algorithm. In these methods, target characteristics are usually used in the discrimination stage, other than the prescreening stage, i.e., the detection stage. Assume that we bring forward target's prior information. That is to say, target characteristics, which might be used in the discrimination and classification stage, are included in the prescreening stage. Thus, the prescreening becomes more specific and its accuracy increases. Although new detection features involved in the prescreening stage increase the calculation amount of prescreening, the false alarm of the extracted Region of Interest (ROI) decreases, and this will eventually decrease the calculation amount of the discrimination and classification stage. In consequence, the calculation amount of the whole ATR scheme decreases.

This paper takes the background of detecting metal anti-tank mines with Airship Mounted Ultra-wide Band SAR (AMUSAR) [3], and is organized as follows. Section 2 gives full introduction to the fusion detection algorithm, and experimental result is given in Section 3 followed by conclusion in Section 4.

2. FUSION DETECTION ALGORITHM

2.1. Basics of Fusion Detection Algorithm

Common landmine detection features involve scattering intensity, double-hump [4], morphological feature, etc.. These features perform well in landmine detection, but operators usually ignore the aspect-frequency dependence of targets in the discrimination and classification stage. Landmine is a typical body-of-revolution (BOR) target [5] and aspectual invariance is the most significant and the most robust characteristic, while most man-made targets and natural clutter show inconspicuous aspectual invariance. Therefore, aspectual invariance is a promising discrimination feature of BOR targets and non-rotary body targets.

Fusion detection takes full advantage of multiple features of targets, which can efficiently increase detection rate and decrease false alarm rate. From the abstract level, fusion can be divided into: pixel-level fusion, feature-level fusion and decision-level fusion. As can be seen from the analysis above, detection based on aspectual scattering characteristic can distinguish BOR target and non-rotary body target effectively, but is not able to eliminate clutters with high aspectual invariance.

CFAR detection can detect strong scattering targets, but cannot distinguish BOR target and strong scattering clutters. If we fuse the detection results based on the two features, clutters with strong aspectual invariance and scattering can be eliminated effectively, which will decrease the false alarm rate of landmine detection.

2.2. Azimuth Scattering Entropy

In order to use aspectual invariance to detect landmines, appropriate measurement is needed. Assume that $I_{i,j}^n$ ($n = 1, \dots, N$) is the amplitude of pixel (i, j) corresponding to aspect angle θ_n , where N denotes the number of sub-apertures and i, j represents the pixel index along the range and azimuth directions, respectively. Let $p_{i,j}^n$ denotes the proportion of $I_{i,j}^n$.

$$p_{i,j}^n = I_{i,j}^n / \sum_{n=1}^N I_{i,j}^n, \quad n = 1, \dots, N \quad (1)$$

Azimuth scattering entropy, the measurement of aspectual invariance is given as

$$E_{i,j} = - \sum_{n=1}^N p_{i,j}^n \ln(p_{i,j}^n) \quad (2)$$

In order to enhance the distinguish degree of measurement, (2) is modified as (3) through nonlinear transform.

$$E_{i,j} = 1 / \left[\ln(N) + \sum_{n=1}^N p_{i,j}^n \ln(p_{i,j}^n) \right] \quad (3)$$

2.3. ASE Detector and Determination of Threshold

The detector is defined by the rule

$$\begin{cases} E_{i,j} > T_{ASE} & \text{presence of a target pixel} \\ E_{i,j} < T_{ASE} & \text{presence of a clutter pixel} \end{cases} \quad (4)$$

where $E_{i,j}$ is the azimuth scattering entropy of pixel (i, j) and T_{ASE} is the global threshold of ASE.

In general conditions, BOR targets have much bigger ASE than non-rotary body targets and clutters, so we can use an empirical value as the global threshold according to typical ASE values of different targets. However, the descent of SCR will reduce the estimation accuracy of ASE [6], and the calculated ASE of BOR targets is usually smaller than typical values. False alarms will emerge if empirical value by simulation data is used as the global threshold. To solve that problem, we determine global threshold with adaptive method. BOR targets are usually with bigger ASE, and the pixels of BOR targets stay in the tailing part of the histogram of ASE image.

Assume that random variable E denotes ASE of corresponding pixel. Given that the confidence coefficient of BOR target pixel is $1 - \varphi$, global threshold T_{ASE} is then determined by

$$P\{E > T_{ASE}\} = 1 - \varphi \quad (5)$$

where P denotes probability distribution of ASE histogram, and $\varphi \in [0, 1]$ is empirical value which is referred to as the proportion of non-rotary body target in the whole ASE image. If the cumulative distribution function (CDF) of ASE image is F , (5) is rewrite as

$$1 - F(T_{ASE}) = 1 - \varphi \quad (6)$$

2.4. Fusion Detection Algorithm

The scheme of our fusion detection algorithm is shown as Fig. 1. The local judgment of each part is ‘hard judgment’, and the fusion rule in decision fusion centre is ‘and’, which decreases false alarm, but demands 100% detection rate in each local detection. Low threshold is set in each local detection to guarantee high local detection rate.

As can be seen from the scheme, the introduction of new detection feature increases the calculation amount. However, the extra calculation amount won’t add up the whole runtime of landmine detection, primarily due to: 1) parallel fusion algorithm, 2) utilization of ‘multi-GPU and multi-CPU’ real-time processing framework [7] in engineering application. The primary added runtime stays on the decision fusion stage, and it is negligible to the reduced runtime in the subsequent discrimination stage due to the decrease of false alarm.

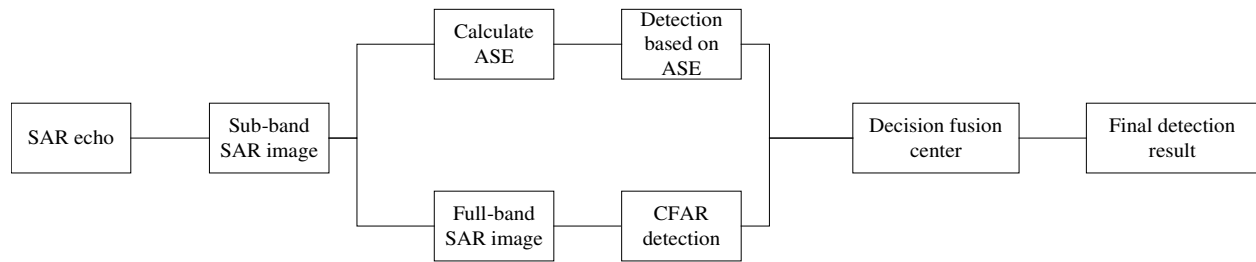


Figure 1: Framework of fusion detection algorithm.

3. EXPERIMENTAL RESULTS

Data used in this paper is collected by AMUSAR system, which adopts step frequency signal system and achieves resolution of 0.1 meter in range and azimuth directions. The system adopts Archimedean Spiral Antenna and has main beam angle wider than 60 degrees.

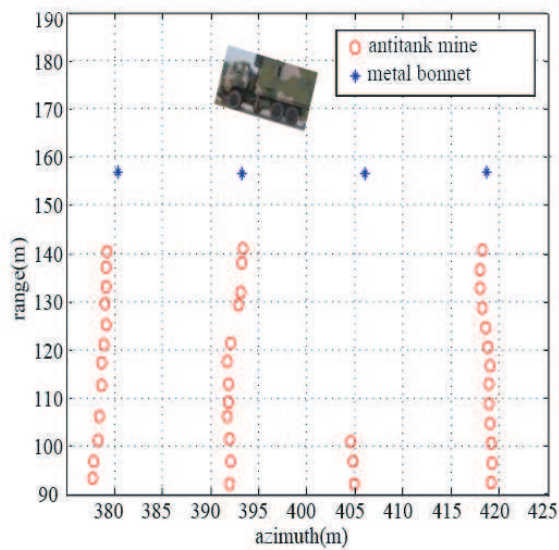


Figure 2: Sketch map of minefield.

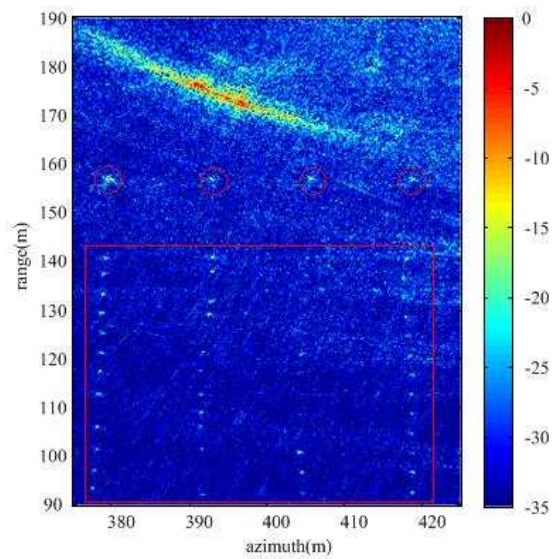


Figure 3: Full aperture SAR image.

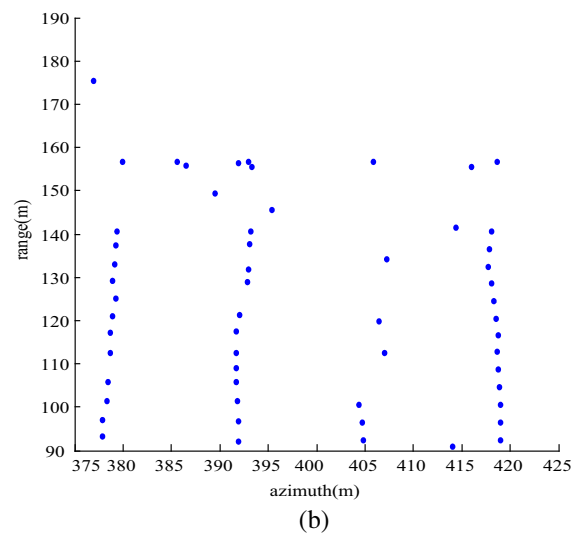
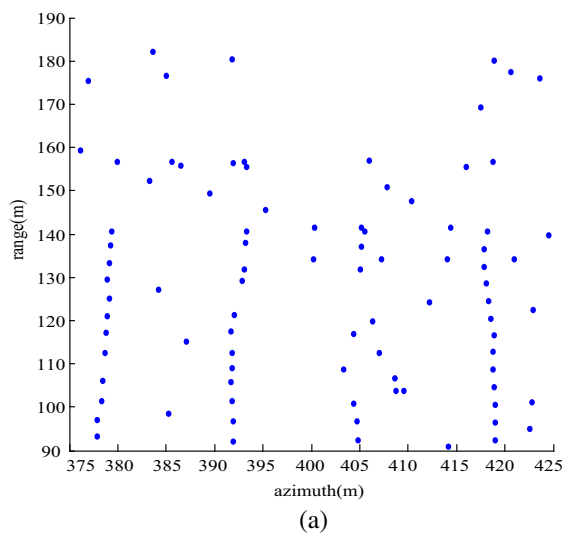


Figure 4: Detection result when the parameter of false alarm rate in CFAR detector is 0.005. (a) The CFAR detection result. (b) The fusion detection result.

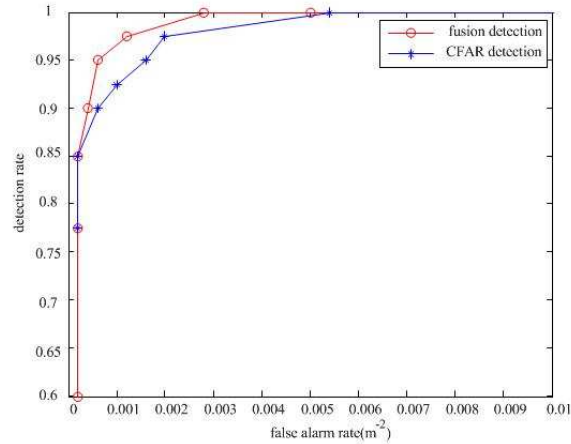


Figure 5: ROC curves.

The experimental layout is shown as in Fig. 2. The soil moisture in our experimental site is between 5% and 10%. There are 40 anti-tank mines with diameter of 30 cm and a truck in the minefield. Four metal bonnets with diameter of 30 cm and height of 30 cm are also placed as calibration objects.

Figure 3 is the full aperture SAR image obtained by BP imaging algorithm, in which the rectangular box and the circle represent the minefield and metal bonnet, respectively. CFAR detection result and fusion detection result are shown in Fig. 4. It can be seen that there are fewer false alarms in fusion detection. In order to acquire more accurate conclusion, the receiver operator characteristic (ROC) is adopted, as is shown in Fig. 5. Compared with single feature detection, fusion detection decreases false alarm rate while guaranteeing high detection rate.

4. CONCLUSION

In this paper, a fusion detection algorithm based on aspectual scattering characteristic and local contrast is proposed. Compared with traditional methods, this method takes full advantage of aspectual invariance of BOR targets and achieves lower false alarm rate and higher detection rate. Further research could include the utilization of sub-band information. And it would be of interest to see how well two-dimension prior information (sub-band and sub-aperture information) performs in landmine detection.

REFERENCES

- Schreiner, K., "Landmine detection research pushes forward, despite challenges," *IEEE Intelligent Systems*, Vol. 17, No. 2, 4–7, 2002.
- Novak, L. M., S. D. Halversen, G. J. Owirka, and M. Hiett, "Effects of polarization and resolution on SAR ATR," *IEEE Transactions on Aerospace and Electronic Systems*, Vol. 33, No. 1, 102–116, 1997.
- Song, Q., H. Zhang, F. Liang, and Z. Zhou, "Results from an airship-mounted ultra-wideband Synthetic Aperture Radar for penetrating surveillance," *APSAR 2011*, 194–197, Seoul, Korea, Sep. 2011.
- Jin, T. and Z. Zhou, "The double-peak characteristic enhancement algorithm for metallic landmine detection with UWB SAR," *Journal of Electronics & Information Technology*, Vol. 30, No. 9, 2077–2080, 2008.
- Ratto, C. R., P. A. Torrione, and L. M. Collins, "Exploiting ground-penetrating radar phenomenology in a context-dependent framework for landmine detection and discrimination," *IEEE Transactions on Geoscience and Remote Sensing*, Vol. 49, No. 5, 1689–1699, 2011.
- Liang, F., Q. Song, Y. Wang, and Z. Zhou, "Body-of-revolution target enhanced imaging algorithm based on aspect scattering entropy," *Journal of Electronics & Information Technology*, Vol. 35, No. 6, 7–14, 2013.
- Liang, F.-L., "Research on enhanced imaging techniques of low-altitude UAV-mounted UWB SAR," National University of Defense Technology, Changsha, 2013.

TDLAS Based Early-stage Forest Fire Detection System

Jiawei Zhang¹, Mingbao Li², Wei Li³, and Hongli Zhang¹

¹College of Mechanical and Electrical Engineering, Northeast Forestry University, China

²College of Civil Engineering, Northeast Forestry University, China

³Traffic College, Northeast Forestry University, China

Abstract—The commonly used forest fire detection methods are insufficient to detect the early-stage forest fire. In order to solve this problem, this paper presents a novel method to detect early-stage forest fire using TDLAS (Tunable Diode Laser Absorption Spectroscopy) technique. With the high sensitivity and rapid response, TDLAS is used to detect trace gas CO concentration sourcing from the early-stage forest fire. The TDLAS system is composed of a White-type multi-pass cell, combined with wavelength modulation and harmonic detection. The analysis of second-harmonic spectrum and the lab tests to different CO concentrations show that the relationship between CO concentration and spectrum intensity abide by linearity relations, and the system has high accuracy. It can be concluded that it is feasible to detect early-stage forest fire by measuring CO concentration and it interests to improve the system performance in the forest fire detection field.

1. INTRODUCTION

Forest fire will bring the most devastating consequences to the forest and the human life [1]. In our country, ground patrol and protect, watchtower monitoring [2], air patrol and protect and remote sensing satellites [3] are commonly used to detect forest fire. But all the above methods cannot detect the early fire effectively. The wireless temperature sensing technology [4] was proposed to improve the imperfections, but to no avail.

In order to improve the performance and sensitivity of forest fire detection system, this paper adopts a gas detection method with high detection sensitivity, which is the early detection of forest fire.

2. CHARACTERISTIC GAS IN EARLY FOREST FIRE

The forest fire has the specific physical and chemical characteristics process, which are outputted respectively in early stage, smoldering stage, heating stage and flame attenuation stage [5–7]. Gasses are mainly the product of the imperfect combustion in the early stage. In view of the produced gasses is earlier than temperature and flame, the early detection system detect gasses should be enough sensitive and rapid, then more easily to discovery the early detection of forest fire. So extracting characteristic signals of gasses in early forest fire has broad prospect [8].

The burning process will inevitably produce CO and CO₂. CO₂ is a kind of common gas with a certain concentration in atmospheric environment, but its concentration would rise sharply if the fire broke out. Usually it occurs in minute amounts for CO in the atmosphere and it is produced earlier than the CO₂ in the forest fire. CO is lighter than air and can rise and spread fast with little heat or without any heat, so it can be easily detected [9–11]. In a word, CO can be viewed as characteristic gas to detect is a rapid and accurate way in early forest fire.

So far, commonly used detection methods of gas concentration are mainly classified as chemical method, gas chromatography and spectral absorption method, but all methods are not ideal to detect trace gas detection. In recent years, due to it detects trace gas is rapid, real-time and highly sensitive, tunable diode laser absorption spectroscopy (TDLAS) has been widely applied in environmental, biomedical and industrial fields.

3. THE PRINCIPAL OF TDALS

In fact, TDLAS is a kind of absorption spectrum technology, using laser characteristics of narrow line width and wavelength tuning to scan the single absorption peak of the gas. It can obtain gas concentration by analyzing the spectral selective absorption. Beer-Lambert law is the theoretical basis of TDLAS [12, 13] technology. According to the law, the intensity of light beam will can be attenuated after gas molecules absorption to be

$$I_t(v) = I_0(v) \exp[-\alpha(v)CL] \quad (1)$$

whereas, $I_0(v)$ is incident light intensity, $I_t(v)$ is transmission light intensity after gas absorption, $\alpha(v)$ is absorption coefficient for unit concentration and unit length at frequency v , C is volume fraction, L is light path length.

4. SELECTION OF CO SPECTRAL ABSORPTION

The gas absorption spectrum can be obtained from HITRAN (2008) spectral database. The Absorption spectral line selection should consider both laser interference and background gas. It is shown from Figure 1 that CO has larger absorption spectrum strength at wavelength of about $1.58 \mu\text{m}$. Around $1.58 \mu\text{m}$, CO has higher spectral intensity than other gases and narrower wavelength than other domains, which is more suitable for TDLAS detection, as shown in Figure 2.

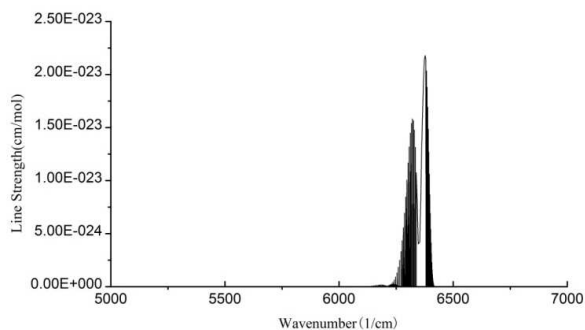


Figure 1: CO absorption spectral lines around $1.43 \mu\text{m} \sim 2.0 \mu\text{m}$.

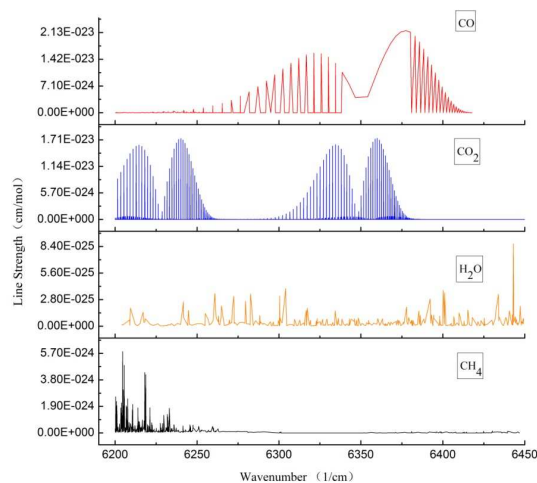


Figure 2: Absorption lines of common gases around $1.55 \mu\text{m} \sim 1.61 \mu\text{m}$.

5. BLOCK DIAGRAM OF THE DETECTION SYSTEM

For TDLAS based early forest fire detection system, its core part is the laser. Laser selection should consider several points: 1, the central frequency of the laser should match with the characteristics of gas absorption spectrum; 2, the price should be relatively cheap and suitable for extensive application. In addition, due to Beer-Lambert law demands strictly monochromatic light, the light source should be selected distribution feedback (DFB) laser with the central wavelength distribution around $1.58 \mu\text{m}$, narrow band width and high effective optical power, which helps to improve the system sensitivity.

The block diagram of TDLAS system is shown in Figure 3. The American Thorlabs ITC5000 controller is used to make the laser wavelength scan through the whole absorption lines by adjusting the injection laser current and temperature of the laser. The current is modulated by the external input modulation signal, and the modulation signal sent to the phase-locked amplifier as the reference signal. Laser driver drives the laser beam through the long optical path cell filled with gas. The light reaches the photoelectric detector after multiple reflections. After the weak light signal is multiplied and integrated by phase-locked amplifier and suppress noise, the useful harmonic signal is obtained. The harmonic signal is collected by the data acquisition card (DAQ card) sent to computer processes and operates data, and then gas concentration is got.

This system adopts the structure of White absorption pool [14, 15]. The basic structure of the pool is shown in Figure 4(a). The absorption pool is mainly composed of three pieces of spherical mirrors; including primary mirror A , secondary mirror B and B' . All the mirrors have the same radius of curvature. Primary mirror is placed at one end of the absorption pool, and its center of curvature is in the middle of the secondary B and B' . The secondary B and B' is placed at the other side of the pool, and its curvature center is located on the primary mirror. Its entity structure is shown in Figure 4(b).

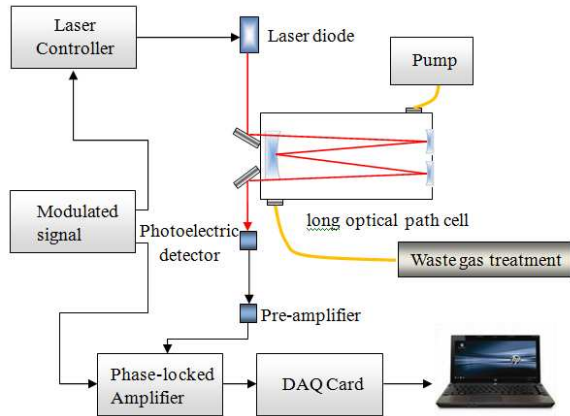


Figure 3: Block diagram of TDLAS system.

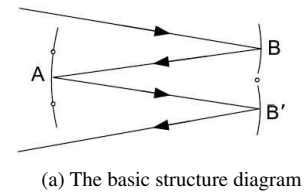


Figure 4: The structure diagram and entity structure of the absorption pool spectrum.

6. RESULTS AND DISCUSSION

Due to the interference of the background gas, the direct absorption measurement technique and harmonic detection which have better measurement sensitivity and accuracy is adopted to measure of weak signal. With the increase of harmonics, the harmonic signal amplitude will decrease, so in the practical application first or second harmonic detection is generally chosen. It can be seen from Figure 5 that, in the line center, the second harmonic has relative high amplitude and the first harmonic is close to zero. Therefore, this paper uses the second harmonic peak to achieve concentration detection.

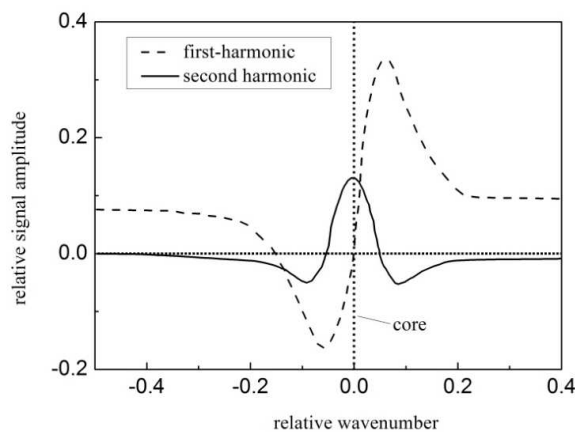


Figure 5: Second harmonic spectrum and first harmonic.



Figure 6: The picture of TDLAS detection system for early forest fire.

Referred to the existing literature [16–19] about TDLAS technology and the research progress of gas detection technology, the early forest fire CO gas detection system is designed and the picture is shown in Figure 6.

The laser frequency is adopted at 5 kHz for modulating the wavelength and the frequency is selected at 20 hz for scanning gas absorption peak. Selecting nitrogen as balance gas, CO gas was prepared with the volume fraction of 20 ppmv to 165 ppmv. The measurement result is shown in Figure 7. It can be seen that the second harmonic intensity changes with the concentration. From the linear fitting results shown in Figure 8, it can be demonstrated that the concentration of CO is in linear relation with the second harmonic intensity and the fitting result is $Y = 0.0251 + 0.00451X$.

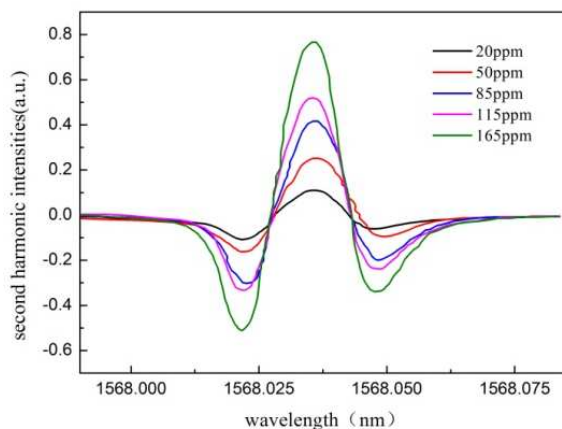


Figure 7: Second-harmonic spectrum for different CO concentrations.

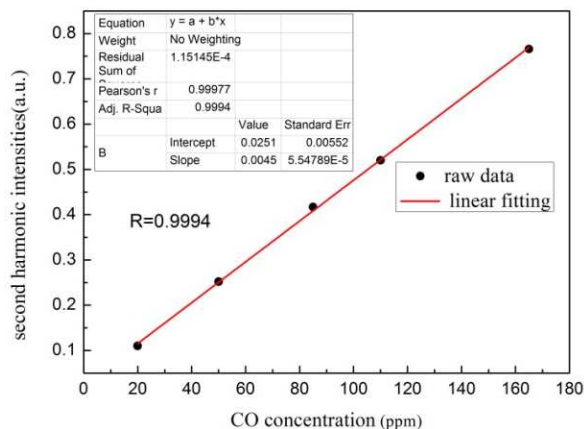


Figure 8: Relevance of CO concentration and second-harmonic spectrum intensity.

7. CONCLUDING REMARKS

For the trace gas detection, TDLAS technology has the advantages of high sensitivity, fast response speed, good selectivity and low detection limit, in several ppm levels. This will help to accurately detect the gas from the fire so as to realize the early detection of forest fires. It will be beneficial and meaningful to forest fire prevention and reduce the loss.

REFERENCES

1. Pyne, S. J., P. L. Andrews, and R. D. Laven, *Introduction to Wildland Fire*, Wiley, New York, 1996.
2. Brad, H., "Forest fire fuel type mapping using GIS and remotes sensing in British Columbia," *Ninth Annual Symposium on Geographic Information Systems*, Vancouver, British Columbia, Canada, 1995.
3. Bowman, D., J. K. Balch, P. Artaxo, et al., "Fire in the earth system," *Science*, Vol. 324, 481–484, 2009.
4. Zheng, Y., "Study on forest fire auto-inspecting system base on wireless sensor network," Dissertation of Master Degree of Nanjing Forest University, 2007.
5. Jackson, M. A. and I. Robins, "Gas sensing for fire detection: Measurements of CO, CO₂, H₂, O₂, and smoke density in European standard fire tests," *Fire Safety Journal*, Vol. 22, 181–205, 1994.
6. Daniel, T., J. Michelle, J. Richard, et al., "Advanced fire detection using multi-signature alarm algorithms," *Fire Safety Journal*, Vol. 37, 318–194, 2002.
7. Han, Z. G., D. L. Tianya, and G. Zhang, "Influences of climate on forest fire during the period from 2000 to 2009 in Hunan province," *CSEE 2011*, Part I, CCIS 214, 123–130, 2011.
8. Hagen, B. C. and J. A. Milke, "The use of gaseous fire signatures as a mean to detect fires," *Fire Safety Journal*, Vol. 34, No. 1, 55–67, 2000.
9. Huang, X. and R. Zhang, "The study of Early fire detection method based on process feature information," Dissertation of Master Degree of Hua Qiao University, 2006.
10. Du, J. and R. Zhang, "Research on process character information in early fire based on fourier transform infrared spectrum detection," *Spectroscopy and Spectral Analysis*, Vol. 28, No. 3, 559–563, 2008.
11. Chen, H., F. Zhou, et al., "An integrated control system for carbon monoxide detection, emission and recycling," *Laser Technology*, Vol. 35, No. 3, 360–363, 2011.
12. Werle, P., "A review of recent advances in semiconductor laser based gas monitors," *Spectrochimica Acta Part A*, Vol. 54, No. 2, 197–236, 1998,
13. Drasek, W. V., O. Charona, and K. Mulderinka, "Multi-functional industrial combustion process monitoring with tunable diode lasers," *SPIE*, Vol. 4201, 133–141, 2001.
14. Doussin, J. F., D. Ritz, and P. Carlier, "Multiple pass cell for very long-path infrared spectrometry," *Appl. Opt.*, Vol. 38, No. 19, 4145–4150, 1999.

15. Trutna, W. R. and R. L. Byer, “Multiple pass Raman gain cell,” *Appl. Opt.*, Vol. 19, No. 2, 301–312, 1980.
16. Rice, C. A. and G. Perram, “A tunable diode laser absorption system for long path atmospheric transmission and high energy laser applications,” *Atmospheric and Oceanic Propagation of Electromagnetic Waves V*, 7924, SPIE, San Francisco, California, USA, 2011.
17. Hendricks, A. G., U. Vandsburger, and W. R. Saunders, “The use of tunable diode laser absorption spectroscopy for the measurement of flame dynamics,” *Meas. Sci. Technol.*, Vol. 17, No. 1, 139–144, 2006.
18. Basu, S., D. E. Lambe, and R. Kumar, “Water vapor and carbon dioxide species measurements in narrow channels,” *Int. J. Heat Mass Transfer*, Vol. 53, No. 4, 703–714, 2010.
19. Krzempek, K., R. Lewicki, and L. Nahle, “Continuous wave, distributed feedback diode laser based sensor for trace-gas detection of ethane,” *Appl. Phys. B*, Vol. 106, No. 2, 251–255, 2012.

Forced Solitary Wave in Water Wave Basin under the Earth's Gravity Field

Shigehisa Nakamura
Kyoto University, Japan

Abstract— Monitoring of solitary wave on water surface is introduced. For this purpose, a water basin for a hydraulic modeling is used. Under a given boundary condition of a hydraulic model, a sinusoidal wave is propagates to pass a slit to diffract just like a case of Fresnel diffraction of optical ray. A specific linkage of boundary conditions, bathymetry, and a generated sinusoidal wave with a specific period is found for producing a solitary water wave in the basin. Some experiments are helpful for basic understanding of a process of solitary wave formation at a generated sinusoidal wave. Then, the author tends to consider whether this solitary wave might suggest that the strange peak observed during the monitoring tsunami waves accompanied by the 2011 earthquake in the northwest Pacific.

1. INTRODUCTION

This work is on monitoring of solitary wave on water surface. For this purpose, a water basin for a hydraulic modeling is used. Under a given boundary condition of a hydraulic model, a sinusoidal wave is propagates to pass a slit to diffract just like a case of Fresnel diffraction of optical ray. A specific linkage of boundary conditions, bathymetric condition, and a generated sinusoidal wave with a specific period is found for producing a solitary water wave in the basin. Some experiments are helpful for basic understanding solitary wave formation at a generated sinusoidal wave.

Then, the author tends to consider whether this solitary wave might suggest that the strange peak observed during the monitoring tsunami waves accompanied by the 2011 earthquake in the northwest Pacific.

2. SOLITARY WAVE

It is well known that a simple harmonic wave on the water surface can be described as a small amplitude sinusoidal wave.

On the basis of this understanding, a linear formulation can be given generally that the water waves found on the water surface can be described as an ensemble of the waves with various kinds of frequencies and of wave numbers. This means that the waves have a periodic property.

On the other hand, there are various kinds of aperiodic waves.

For example, Lamb [1] had introduced about a solitary wave which was named by Scott Russel in referring to “Report on Waves” appeared in British Association Report in 1844. The details are not introduced here in this work simply as solitary wave can be specified as an aperiodic single peaked wave in experiments Lamb, [1879; 1957].

McCowan [2] must be a reference in the early age of solitary wave’s description.

Assuming a reference water depth h , then, a solitary wave η can be described in a mathematical form, i.e., as following to Lamb,

$$\eta = a \operatorname{sech}^2 \left[(1/2)(3a/(h^3))^{1/2} x \right], \quad (1)$$

where, the notation x is the horizontal axis and, the notation a is found in trochoidal wave,

$$x = x_0 a \exp(kz_0) \sin(kx_0), \quad \text{and}, \quad z = z_0 + a \exp(kz_0) \cos(kx_0), \quad (2)$$

which is called as Gerstner wave in a consideration of historical background of its finding, as Gerstner reduced theoretically in 1802 though Rankin independently found it in 1863.

As for the small amplitude wave, formulation can be in a linear expression though this solitary wave has to be solved on the basis of nonlinear equation referring Lagrangean technique in consideration.

3. HYDRAULIC MODEL FOR SOLITARY WAVE

Nakamura [3] has found a specific condition can be produce a solitary wave in a sample water basin experimentally.

Nakamura [3] had first aimed to produce a resonant mode in a harbor model or in a bay model by using the water basin in a manner of hydraulics.

His model was 7 m wide and 10 m long. Both of the side part is bounded by a vertical wall made from flat mortar face. The one end is face to the wave generating system. This system was consisted by an actuator of piston type controlled by a hybrid system of analog system and digital system. A plunger floating this end was connected to the actuator, so that the vertical oscillatory motion of the plunger acts as a forced water wave generator.

The actuator is fixed a steel frame work to transfer the signal of the controller to the plunger. Following the signal, the piston and plunger were driven to generate the water waves to propagate into the basin.

The other end of the basin is closed though in his case the bed of the basin is well arranged by a mortar plane in a gentle slope from the plunger side to the other end side. The slope of the bed was 50 cm high to 10 cm long, that is to say, gradient is 1/50.

Inside of the basin, a model shoreline was set at a distance from the front of the plunger. At the distances of 2 meter (Barrier A) and 4 meter (Barrier B), a barrier with a slit of 0.8 meter wide, respectively.

4. LINEAR WAVE INPUT FUNCTION

A part of the recorded wave pattern is introduced as shown in Figure 1. To the details, it should be referred to Nakamura's work in 1975.

The illustration in Figure 1 demonstrates that the specific pattern of the response of water in the hydraulic model basin.

The linear sinusoidal input function for the water wave in the basin transfers the wave energy in the basin to induce the resonant mode in the basin though this resonant mode is not so simple.

One of the typical pattern of the wave at the Station 3 is interesting one.

At this station, it can be seen that a cyclic collision of the couple of two solitary waves induced in the basin though separate into a couple of solitary wave pattern without any change of each wave energy apparently.

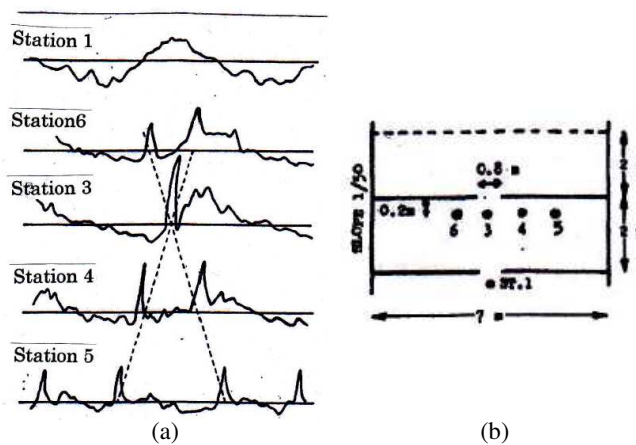


Figure 1: An evolution pattern of a couple of solitary water wave mode in a water basin. (a) (Station-1) An incident transferring passing a slit of barrier A. (Station-6) A transferring sinusoidal wave at the left of barrier B. (Station-3) A collision of the two young solitary waves at B center. (Station-4) A separation of the two growing solitary wave. (Station-5) A matured two solitary waves and a faint sinusoidal wave. (b) Plane of water basin profile. (1) Width is 7 m. (2) Length between two barriers A and B is 2 m. (3) Each slit of barriers A and B is 0.8 m, and, (4) positioning of Stations 1, 6, 3, 4, and 5, respectively.

5. INDUCED COUPLE OF NONLINEAR WAVES

The input function looks contributive to force at inducing a couple of the solitary waves in the water basin though it should be reminded that the water in the basin is a kind of the viscous liquids.

It should be reminded that the water is familiar to us, nevertheless nothing of the physical and dynamical properties are understood for us.

We have simply a basic table on the specific properties in physical and chemical phases.

6. A LEADING TSUNAMI WAVE WITH A SPIKE

Now, a recent seismic event in 2011 in the northwestern Pacific Ocean had given us a tsunami leading wave with a spike on the wave record at a location just neighbor the seismic epicenter (source of the earthquake).

Its wave form was apparently felt to be quite similar to the wave pattern as seen in the illustration in Figure 1 of this work.

Nevertheless, it should be aware of that the tsunami waves generated at the seismic fault formation on the sea floor is in a kind of transitional processes in a scope of hydrodynamics.

Then, the two waves in the basin and in the ocean could not be any of the same background in hydrodynamics even though those were obtained any advanced electronic recording systems respectively.

A common factor can be found that both of the two waves were produced by a forcedly. That is to say, the wave in the basin was induced by a forcing input function for an actuator and the wave in the ocean was generated at a sudden seismic displacement of the local sea floor.

There is left for a problem to be solved is that a linear input function can be in a position for any nonlinear wave, for example, a solitary wave in a model.

7. NUMERICAL MODELING

As far as the author concern, the author has never heard of any numerical modeling of the couple of solitary waves in a basin.

Almost all of the seismologists missed to pay any attention to the tsunami offshore in the ocean though noted the above section.

Then, the author takes it pity but he has to write that the scientists have to wait for a numerical modeling which gives a more reasonable solution in an advanced technique in a time not later than any hazardous event happens.

8. CONCLUSIONS

The author noted about monitoring of solitary wave on water surface in introduced. An induced resonant couple of solitary waves in a water surface wave in an open water basin for modeling was a trigger of the problem to see whether a linear input function can contributive for a nonlinear process in hydraulics and also in hydrodynamics.

There should be required for the purpose any one of some techniques, for example, a simple approximation, or, asymptotic concept for mathematical singularity, or relaxation for discontinuity, or, cut-off of high frequency band or high wave number constituents at digitizing the continuous functions.

REFERENCES

1. Lamb, H., *Hydro-Dynamics*, 6th Edition, Cambridge University Press, 1932 (1st Edition, 1879).
2. McCowan, J., "On the highest wave of permanent type," *Philosophical Magazine*, Ser. 5, Vol. 38, 351–358, 1894.
3. Nakamura, S., "Nonlinear lateral oscillation in a harbor model," *Proceedings of Symposium on Modelling Techniques*, 836–853, American Society of Civil Engineers, San Francisco, California, September 3–5, 1975.

Parameterized Dynamic Range Reduction for UWB SAR Image

Chao Li and Yue-Li Li

College of Electronic Science and Engineering
National University of Defense Technology, Changsha, China

Abstract— The visualization of ultra wide bandwidth synthetic aperture radar (UWB SAR) image data involves mapping from high dynamic range amplitude values to gray values of a lower dynamic range display device. In order to compress dynamic range of the UWB SAR image data appropriately, we examine several different dynamic range reduction techniques and come up to a new method with better visualization performance. This new arithmetical technique is analyzed based on the 3σ measurement and the amended mapping function. Compared with the original method, the new method has higher computational efficiency with the dark pixels are stretched appropriately and the bright details are well preserved.

1. INTRODUCTION

Low-frequency ultra-wide bandwidth synthetic aperture radar (UWB SAR) is a new domain, which combines the ultra-wideband technology with synthetic aperture radar imaging technology. However, it is more difficult for researchers to obtain useful information from the UWB SAR images due to their high dynamic range and great quantity of calculation [1]. Therefore, developing a fast visual method for the UWB SAR amplitude values is essentially important and necessary.

In the UWB SAR images, corner reflectors, which are used for calibration and geocoding purposes, generate a large dynamic range of amplitude values. Therefore the dynamic range compression is a crucial step in the processing. There are logarithmic transformation [2], linear mapping and many other traditional methods that are used in dealing with the data of UWB SAR images. Generally, the dynamic range of primary amplitude values is typically much wider than conventional display devices. The logarithmic transformation may map a great number of amplitude values in one same gray level. All information in similar amplitude values is lost when using this method. In order to reserve more information in images, some researchers have proposed partial linear mapping method for UWB SAR images. This method divides the gray values into different parts by previous experience. However, when the input date changed the original divided model may not available. So, if we want to process the UWB SAR data real-time, we need to explore a new visual method.

In this paper, we proposed a fast visualization method based on the idea that the 3σ measurement can reduce the impact of intense echo signal and has a good performance in dynamic range reduction.

This paper is developed as follows. The Section 2 introduces commonly used methods for the SAR image data visualization. The Section 3 analyzes the distribution of UWB SAR image data and presents a fast visualization method for UWB SAR images visualization. The Section 4 compares the performance of the traditional visual methods with the new method by simulation and then reaches a conclusion that the proposed method is adaptive, improve the visibility of local details, and suit for real-time visualization system.

2. TRADITIONAL VISUALIZATION METHODS

2.1. Logarithmic Mapping

Logarithmic mapping is often used with SAR data. It can be defined as:

$$L_d(x, y) = \frac{\log(1 + cA(x, y))}{\log(1 + c)} \quad (1)$$

where the parameter c controls the overall brightness of the result and $A(x, y)$ is amplitude values. Generally, the amplitude range is often partially mapped to gray levels, and the values outside this range are clipped to black or white. It is obvious this method may map a large number of amplitude values in one same gray level while the primary dynamic range of image data is much larger than display devices. Therefore, all information in similar amplitude values is lost when using this method.

2.2. Partial Linear Mapping

Linear mapping from amplitude image data to gray levels is only usable when a relatively range of the amplitude values has been determined and values outside of this range are clipped to black or white. To make better use of the available gray level range, the method divides the gray values into different parts by previous experience before mapping. It is dropped as follow.

$$L_d(x, y) = \begin{cases} k_1 A(x, y) + b_1 & 0 \leq A(x, y) \leq f_1 \\ k_2 A(x, y) + b_2 & f_1 \leq A(x, y) \leq f_2 \\ k_3 A(x, y) + b_3 & f_2 \leq A(x, y) \leq f_3 \end{cases} \quad (2)$$

where k_1 , k_2 and k_3 are parameters of different part of gray levels. The process of implementation is difficult because the original divided model may not available when the input date changed. Therefore we need to research a new real-time visualization method for UWB SAR data.

3. THE NEW VISUALIZATION METHOD FOR UWB SAR IMAGES

3.1. Statistical Property of UWB SAR Images

A notable feature of the low-frequency UWB SAR images is that the images have a large number of speckles due to the interaction of echo electromagnetic waves [3]. Goodman has proposed a statistical distribution model from researching the laser speckles [4]. With a similar theory, the statistical distribution model also demonstrates the statistical property of UWB SAR images. The reflectivity of each pixel in complicated UWB SAR image is defined as follows:

$$s = a + jb \quad (3)$$

Here, the real part and imaginary part both submit to zero-mean Gaussian distribution with equal variances and independent variables. The basic resolution unit of UWB SAR images can be viewed as a series of echo signals. According to the central limit theorem, the joint probability density function is defined as [5]:

$$p(a, b) = \frac{1}{2\pi\sigma^2} \exp \left[-\frac{(a^2 + b^2)}{2\sigma^2} \right] \quad (4)$$

So the magnitude of the low-frequency UWB SAR image data submits to

$$p(x) = \left(\frac{x}{\sigma_0^2} \right) \exp \left(-\frac{x^2}{2\sigma_0^2} \right) \quad (5)$$

this is the Rayleigh distribution, where the σ_0^2 is the variance of the UWB SAR image data.

3.2. Power Transformation Principles

From the above discussion we are able to find out that the distribution of UWB SAR image data submits to the Rayleigh distribution. In order to change the distribution, a modified method based on power transformation is proposed. The 3σ measurement, as we all know, is widely used in screening engineering data. When using the basic principle, the date which later will be screened must submit to Gaussian distribution.

In this case, the power transformation is [6]

$$Y = X^v, \quad 0 < v < 1, \quad (6)$$

where X is the original data, Y is the transformed data, and v is the coefficient of transformation. Assuming A is a vector; we can get the standard secondary matrix:

$$d^2 = (A - M)^T \Sigma^{-1} (A - M) = Z^T Z = \sum_{i=1}^n z_i^2 \quad (7)$$

where M and Σ are the mean and covariance matrix, respectively. $Z = B^T (A - M)^T \Sigma^{-1} (A - M)$, $B = \Sigma^{-1/2}$, $E\{z_i\} = 0$, $\text{var}\{z_i\} = 1$.

It is obvious that the d^2 submits to Chi-square distribution with n degrees of freedom.

$$\begin{aligned} E\{d^2\} &= n, \\ \text{var}\{d^2\} &= 2n. \end{aligned} \quad (8)$$

When $\{z_i\}$ is uncorrelated, the variance of d^2 is

$$\text{var} \{d^2\} = \gamma n \quad (9)$$

where $\gamma = E\{z_i^4\} - nE\{z_i^2\} = E\{z_i^4\} - n$.

Alternatively, we can calculate γ using this method [7]:

$$\gamma = \frac{E\{(y - \bar{y})^4\}}{E^2\{(y - \bar{y})^2\}} = \frac{E\{y^4\} + 6E\{y^2\}E^2\{y\} - 4E\{y^2\}E\{y\} - 3E^4\{y\}}{[E\{y^2\} - E^2\{y\}]^2} \quad (10)$$

where $E(y^n) = (\sqrt{2}\alpha)^{nv}\Gamma[nv/2 + 1]$.

As a result, we can get a value of 0.87 for v when $\gamma = 2$. Using this value, we are able to transform the distribution of the UWB SAR images data into Rayleigh distribution conveniently.

3.3. 3σ Measurement

The 3σ measurement is widely applied in screening engineering data. The basic principle is that the data must submit to Gaussian distribution when we use this method. In order to use the 3σ measurement in screening UWB SAR images data, we can utilize the power transformation, which has been discussed in the paper.

In the low-frequency UWB SAR images, the pixels with high intensity are in very limited amounts, yet the range of these pixels is extremely wide. The 3σ measurement regards some pixels with extremely high intensity as singular values. In this way, the high dynamic range of UWB SAR image data can be reduced adaptively.

Assume pixels in UWB SAR image' amplitude values are y_{ij} ($i \in [1, M], j \in [1, N]$). Therefore, the 3σ measurement can be written as below:

$$|y_{ij} - \bar{y}| \geq 3s \quad (11)$$

where \bar{y} is the mean and S is the variance. As a result, we can find the mapping boundary with this formula. A comparison between original amplitude values and new dates handled by 3σ measurement is shown in Fig. 1.

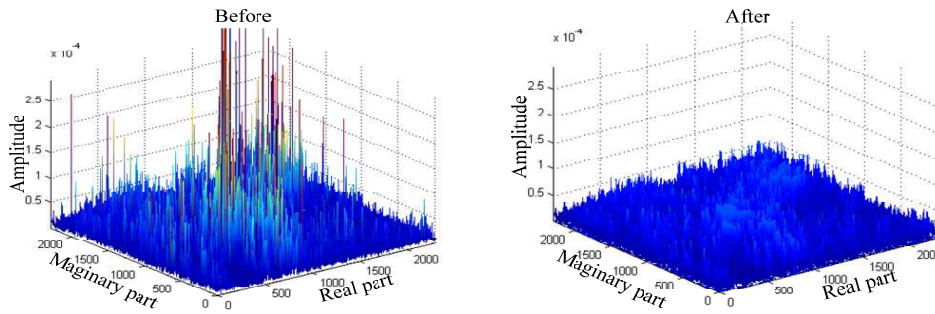


Figure 1: A comparison between different data.

Composed of low frequency UWB SAR image amplitude data, the Fig. 1 displays the range and tendency of the image amplitude. The influence of the strong echo signals is reduced while the small signals are well preserved using the 3σ measurement.

3.4. Amended Mapping Function

From the analysis discussed above, we know that the number of pixels with high intensity is limited when using the 3σ measurement. In a high contrastive visual image, the components of the histogram cover a wider range of the gray scale and extend further so that the PDF of the intensity levels is not too far from the log-normal distribution. Therefore, the lognormal distribution should be the target distribution of the transformed images. In this paper, we use the amended mapping function to achieve the transformation. It is defined as:

$$h = 255 \frac{\exp(z) - 1}{\exp(z_m) - 1} \quad (12)$$

where, z is the UWB SAR images data after the 3σ measurement is applied, and z_m is the maximum of z . This mapping function is monotonically increasing; hence it is known that the brighter pixels in the displayed result are caused by the larger amplitude values.

In the UWB SAR images, the major features of interest are the peaks in the data that have considerably greater amplitude than the surrounding region. We utilize the following method to reduce the dynamic accordingly:

- Change the distribution of original UWB SAR image data using power transformation principles.
- Decrease the dynamic range of UWB SAR amplitude values by the 3σ measurement.
- Map the amplitude values to gray levels by using formula 12.

With the use of the dynamic range reduction processing, the gray level of peaks in UWB SAR image data are still emphasized peaks in UWB SAR amplitude values, although this method decreases the amplitude of these peaks.

3.5. Quality of UWB SAR Images

Equivalent Noise Level (ENL) [8], as a variable to measure the relative intensity of SAR image speckle noise is defined as

$$ENL = \frac{E^2(R)}{\text{var}(R)} \quad (13)$$

where $E(R)$ and $\text{var}(R)$ are the mean and variance of UWB SAR gray images, respectively.

In the Human Visual System (HVS) [9], on one hand, the more central the position of pixel in UWB SAR images is, the more important it is. On the other hand, the HVS is also sensitive to contrast. Therefore, the indicator of HVS can be expressed as

$$Q = \frac{1}{N} \times \sum_{i=1}^N Q_f(i)Q_0(i) \quad (14)$$

where Q_f is the position of pixels, Q_0 is the contrast, and N is the number of block pictures.

4. RESULT

To demonstrate the effectiveness of the proposed method, we would use the echo data obtained from the airborne UWB SAR system.

Figure 2(a) shows the visualization result from the logarithmic transformation. Fig. 2(b) is the gray value histogram. Apparently, the result is not making the best use of gray scales.

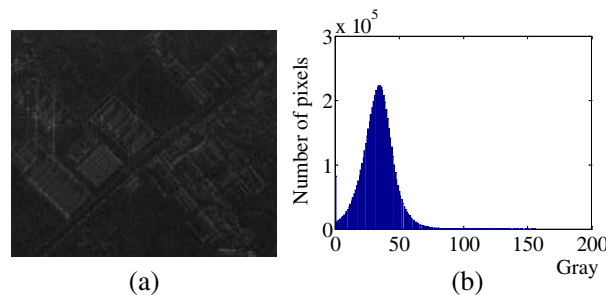


Figure 2: The UWB SAR data visualization result using logarithmic transform.

With the linear mapping method, the visualization result of UWB SAR amplitude values is shown in Fig. 3(a), which is different from Fig. 2(a). It is obvious that most of pixels in the image share the same gray values from the histogram in the Fig. 3(b). Therefore, some details of the image with similar amplitude values are disappeared.

The visualization result of UWB SAR data is based on the proposed method in this paper shown in Fig. 4(a), with the histogram being shown in Fig. 4(a). From the Fig. 4, we could see that the histogram covers a wider range of gray scale and details in the emphasized image. Therefore, it is relatively convenient for researchers to obtain useful information.

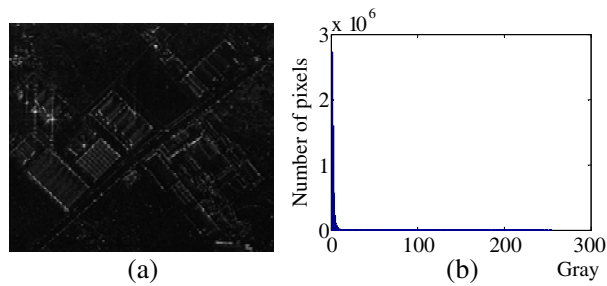


Figure 3: The UWB SAR data visualization result using linear mapping.

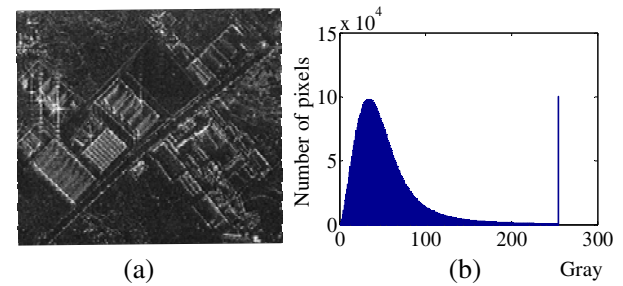


Figure 4: The UWB SAR data visualization result using proposed method.

Table 1: Quality of UWB SAR images.

		Mountains	Urban	Roads	Mean
logarithmic transform	time	10.1 s	12.2 s	11.5 s	11.267 s
	ENL	1.60	1.65	1.70	1.65
	HVS	0.5556	0.6445	0.4523	0.5508
linear mapping	time	8.3 s	8.9 s	9.5 s	8.3 s
	ENL	0.34	0.66	0.54	0.51
	HVS	0.6678	0.7022	0.6955	0.6885
proposed method	time	7.5 s	7.9 s	7.1 s	7.5 s
	ENL	1.97	2.33	2.13	2.14
	HVS	0.8889	0.9012	0.9123	0.9008

In order to measure the processing speed and image quality of the fast visualization algorithm proposed in this paper, mountains, urban, and roads are selected in the experiment. The result is shown in Table 1.

From the discussion above, it is obvious that the fast visualization algorithm is not only better than the ordinary methods, but also more suitable for real-time processing.

5. CONCLUSIONS

This paper presents a new fast visualization method for UWB SAR images based on 3σ measurement. Compared with the original method, this new method takes less time. In addition, the dark pixels are stretched appropriately, and the bright details are well preserved. The performance of the algorithm has been illustrated by the airborne UWB SAR data.

REFERENCES

1. An, D. X., Y. H. Li, X. T. Huang, X. Y. Li, and Z. M. Zhou, "Performance evaluation of frequency-domain algorithms for chirped low frequency UWB SAR data processing," *IEEE Journal of Selected Topics in Applied Earth Observations and Remote Sensing*, Vol. 7, No. 2, 678–690, Feb. 2014.
2. Lamber, M., H. Nies, and A. Kolb, "Interactive dynamic range reduction for SAR images," *Geoscience and Remote Sensing Letters*, Vol. 5, No. 3, 507, 2008.
3. Oliver, C. and S. Quegan, *Understanding Synthetic Aperture Radar Images*, [S.l.]: Sci Tech Publishing, 2004.
4. Goodman, J., *Statistical Properties of Laser Speckle Patterns Laser Speckle and Related Phenomena*, 9–75, Springer-Verlag, Berlin, 1975.
5. Zhou, G., W. An, J. Yang, and H. Zhong, "A visualization method for SAR images," *IGARSS*, 374, 2011.
6. Kukunage, K., *Introduction to Statistical Pattern Recognition*, 1990.
7. Jiao, L., X. Zhang, B. Hou, H. Wang, and F. Liu, *Intelligent SAR Image Processing and Interpretation*, Science Press, Beijing, 2008.
8. Wang, Z., L. G. Lu, and A. C. Bovik, "Foveation scalable video coding with automatic fixation selection," *IEEE Transactions on Image Processing*, Vol. 12, No. 2, 243–254, 2003.
9. Mannos, J. L. and D. J. Sakrison, "The effects of a visual fidelity criterion on the encoding of images," *IEEE Transactions on Information Theory*, Vol. 20, No. 4, 525, 1974.

The Mikaelian's Magnetic Lens for Static Magnetic Field Enhancement

Fei Sun^{1,2} and Sailing He^{1,2}

¹Centre for Optical and Electromagnetic Research

Zhejiang Provincial Key Laboratory for Sensing Technologies, JORCEP

East Building #5, Zijingang Campus, Zhejiang University, Hangzhou 310058, China

²Department of Electromagnetic Engineering, School of Electrical Engineering

Royal Institute of Technology (KTH), Stockholm S-100 44, Sweden

Abstract— Traditional lenses for static magnetic field concentration are often closed structures and the enhanced DC magnetic fields are inside these structures. The static magnetic flux diverges very quickly in the free space outside these closed lenses. In this paper, we extend the Mikaelian's lens which has been widely used for focusing the light wave to design a non-closed DC magnetic lens which can concentrate the DC magnetic field and give a good DC magnetic field enhancement in free space regions even after a certain distance from the back surface of the lens. Numerical simulations verify the performance of the device.

1. INTRODUCTION AND METHOD

Static magnetic field plays a significant role in many technologies and applications. Achieving an enhanced high DC magnetic field in free space region will lead a revolution in current technologies, e.g., improving the sensitivity of magnetic sensors, improving the medicinal technologies based on drug attached by magnetic nano-particles, and etc.. Magnetic lenses are passive devices which can focus/concentrate the static magnetic field. Many magnetic lenses have been proposed in recent years, e.g., based on the superconductor [1], various structures have been designed to achieve a static magnetic field enhancement in a closed free space region. Based on transformation optics (TO) and DC meta-materials, many novel magnetic lenses/concentrators have been designed within these two years [2–6]. Many of these (superconductor-based or most TO-based) lenses are closed structures, which mean they can only give a good magnetic field enhancement in the free space region inside the lenses. However in many other important applications, we need a non-closed structure/lens to achieve a static magnetic field enhancement in a region without magnetic materials far away from the lens. For example it requires a high strength and high gradient DC magnetic field achieved in a deeper human tissue to control magnetic nano-particles attached with drugs. As the static magnetic field strength falls off very rapidly with distance after the back surface of the active coil or magnet, conventional closed DC magnetic lenses cannot help to overcome this obstacle. A novel non-closed magnetic lens based on finite embedded transformation (FET) has been proposed very recently [3], which has been shown that it can give high DC magnetic field enhancement with high gradient even after a certain distance from the back surface of the lens. However this lens needs inhomogeneous anisotropic magnetic materials, which is very difficult to be fabricated. In this paper, we propose another kind of a non-closed magnetic lens for static magnetic field enhancement. An enhanced magnetic field can be achieved in a region without any magnetic materials after a certain distance (e.g., 5 cm) of the back surface of the lens. Compared with our former design based on FET, the magnetic lens proposed here is not anisotropic, which are easier to be realized.

Mikaelian's lens (ML) is one kind of self-focusing lens [7], which has been widely used in information optics. In this paper we use inhomogeneous magnetic materials of Mikaelian's profile (referred as a magnetic ML) to concentrate static magnetic field. Considering electric field and magnetic field are decoupled in static field's case, we only need permeability to describe the lens. For a two dimensional (2D) case, its geometrical shape is a rectangular with height H , thickness (length along the center axis direction) d and permeability of the lens can be given as:

$$\mu = \mu_c \operatorname{sech}(gy) \quad (1)$$

We have assumed that x axis is the magnetic ML's center axis in above expression. μ_c is the permeability in the center axis of the lens. g determines the speed of gradual changes in permeability of the lens in y direction. Larger g means permeability decreases faster from the center to the edge

of the lens. $\text{sech}(x)$ is the hyperbolic secant function. Next we will use finite element method (FEM) to study the performance of magnetic ML for static magnetic field enhancement. First we study a single 2D magnetic ML placed in a uniform background DC magnetic field with amplitude 1 T. As we can see from Figs. 1(a), (b) and (c), the magnetic flux is attracted to the center part of the magnetic ML due to the fact that permeability of the magnetic ML increases from the edge to its center. Compared with Figs. 1(a) and (b), we find that if other parameters keep the same, the higher height H of the magnetic lens, the larger field enhancement. We should note that if the height of the lens is larger, the permeability at the edge of the lens will approach infinitely small. Other studies have shown that it can achieve a DC magnetic field enhancement at the edge of materials with permeability $\mu \rightarrow 0$ [5], which is the reason why we can obtain a field enhancement at the edge of our lens. We can simply use a superconductor with ideal permeability $\mu = 0$ for DC magnetic field to achieve a good magnetic field enhancement. However for a single superconductor, the enhanced DC magnetic field is mainly at the geometrical singularity points or edges of the structure (similarly to the edges of our ML device). In many applications, we need an enhancement in the same direction of the background incident DC magnetic field and even after a certain distance from the back surface of the lens. Our magnetic ML can achieve this requirement: The enhancement field is in the same direction of the external incident magnetic field and the enhancement is still obvious even after a certain distance from the back surface of our lens (e.g., 5 cm after the back surface of the lens, the field enhancement on the center axis of the lens is about

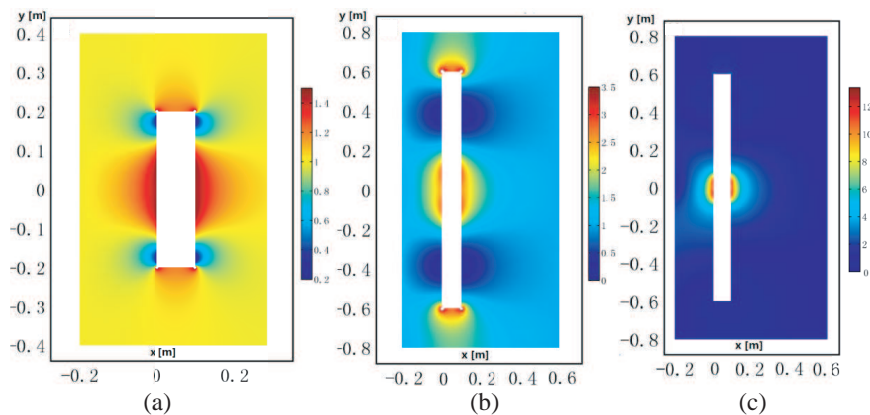


Figure 1: 2D FEM simulation results: The amplitude of total static magnetic field distribution when a uniform background DC magnetic field with amplitude 1 T is normally imposed onto the lens from $-x$ to $+x$ direction. The white rectangular region is the magnetic ML. The parameters of the magnetic ML: (a) $H = 0.4\text{ m}$, $d = 1\text{ cm}$, $\mu_c = 10$ and $g = 30\text{ m}^{-1}$. (b) $H = 1.2\text{ m}$, $d = 1\text{ cm}$, $\mu_c = 10$ and $g = 30\text{ m}^{-1}$. (c) $H = 1.2\text{ m}$, $d = 1\text{ cm}$, $\mu_c = 10$ and $g = 80\text{ m}^{-1}$.

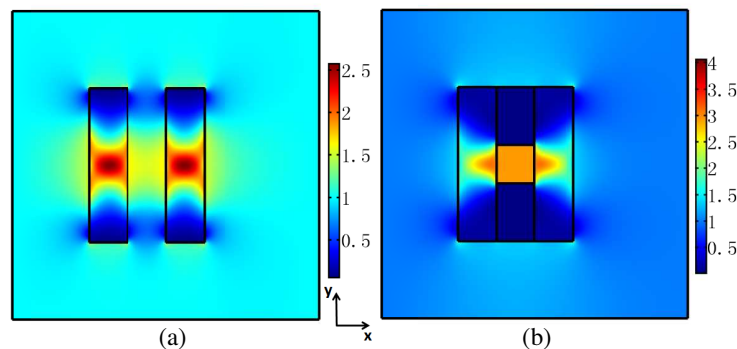


Figure 2: 2D FEM simulation results: The amplitude of total magnetic flux density distribution when a uniform background DC magnetic field of amplitude 1 T is normally imposed onto the structure from $-x$ to $+x$ direction. (a) The structure is two identical magnetic MLs with the same parameters of the one in Fig. 1(a) separated by 10 cm. (b) The structure is composed of two diamagnetic materials with height 15 cm in y direction, width 10 cm in x direction and permeability $\mu = 0.01$ placed between two identical MLs used in Fig. 2(a).

1.25, 1.98 and 5.15 in Figs. 1(a), (b) and (c) respectively). g determines the speed of gradual changes in permeability of the magnetic ML. Comparison between Figs. 1(b) and (c) shows if other parameters keep the same, the larger g the higher field enhancement.

If we add another identical magnetic ML after a certain distance from the first one, we can obtain a further degree of magnetic field enhancement. As shown in Fig. 2(a), two identical magnetic MLs with the same parameters of the one in Fig. 1(a) (separated by 10 cm) are placed in a uniform DC background magnetic field of amplitude 1 T. In this case the DC magnetic field enhancement on the center axis 5 cm after the back surface of the first lens is about 1.54 (one single lens can only achieve a 1.25 time field enhancement in Fig. 1(a)). We also study a case that if we add some additional structures to our double magnetic MLs in Fig. 2(a) to get a better magnetic field enhancement with a high uniformity. As shown in Fig. 2(b), we add two diamagnetic materials with permeability $\mu = 0.01$ in the middle of our two identical MLs, we get a nearly uniform 2.83 time of magnetic field enhancement in a 10 cm plus 10 cm rectangle air region.

2. SUMMARY

Based on Mikaelian's lens (ML) which has been widely used to focus the light wave, we proposed a magnetic ML for static magnetic field enhancement. The proposed magnetic ML has many special features: First the field enhancement factor can be tuned by changing parameters of the ML (e.g., g and μ_c). Second the enhancement is not only near the surface of the lens but also after a certain distance of from the lens (e.g., 1 cm to 5 cm). Third we can achieve higher enhancement degree with high uniformity by combining our magnetic ML with some other structures. Our magnetic ML will have many potential applications in magnetic sensors, wireless energy transmission and drug delivery by magnetic particles.

ACKNOWLEDGMENT

Fei Sun thanks the China Scholarship Council (CSC) for the support (No. 201206320083).

REFERENCES

1. Zhang, Z. Y., S. Choi, S. Matsumoto, R. Teranishi, G. Giunchi, A. F. Albisetti, and T. Kiyoshi, "Magnetic lenses using different MgB2 bulk superconductors," *Supercond. Sci. Technol.*, Vol. 25, 025009, 2012.
2. Sun, F. and S. He, "Create a uniform static magnetic field over 50 T in a large free space region," *Progress In Electromagnetic Research*, Vol. 137, 149–157, 2013.
3. Sun, F. and S. He, "Static magnetic field concentration and enhancement using magnetic materials with positive permeability," *Progress In Electromagnetic Research*, Vol. 142, 579–590, 2013.
4. Sun, F. and S. He, "DC magnetic concentrator and omni-directional cascaded cloak by using only one or two homogeneous anisotropic materials of positive permeability," *Progress In Electromagnetic Research*, Vol. 142, 683–699, 2013.
5. Navau, C., J. Prat-Camps, and A. Sanchez, "Magnetic energy harvesting and concentration at a distance by transformation optics," *Phys. Rev. Lett.*, Vol. 109, 263903, 2012.
6. Sun, F. and S. He, "Novel magnetic lens for static magnetic field enhancement," *PIERS Proceedings*, Stockholm, Sweden, 1689–1691, Aug. 12–15, 2013.
7. Sun, F., Y. G. Ma, X. C. Ge, and S. He, "Super-thin Mikaelian's lens of small index as a beam compressor with an extremely high compression ratio," *Optics Express*, Vol. 21, No. 6, 7328–7336, 2013.

Skin Color Measurements: Usefulness of the Metric Hue Angle of Uniform Color Spaces for Dermatological Treatment

Makio Akimoto¹, Yurika Koshiishi¹, Hikari Ikeda¹, Kazuhisa Maeda¹, and Mieko Hata²

¹Tokyo University of Technology, 1404-1, Katakura, Hachioji, Tokyo 192-0982, Japan

²Takano Medical Clinic, 6-4-23, Aoto, Katsushika-ku, Tokyo 125-0062, Japan

Abstract— Skin color is predominantly determined by pigments such as hemoglobin, melanin, carotene and bilirubin. The quantification of experimentally induced color changes is widely used method in dermatology and cosmetics since the color response can be used as an indicator of skin properties, drug properties and skin protection properties. The present study, we examined the usefulness of hue angle was calculated from the uniform color space. Metric hue angle is expected to correspond well to the appearance of skin color than the chromaticity coordinates or tristimulus values.

1. INTRODUCTION

Skin color and its variations are important in different fields such as cosmetics, dermatology, and medicine, as well as computer rendering [1, 2]. The diversity of skin colors among people, or according to different locations on the same person, at different times depends mostly on three main characteristic parameters. The concentration of melanosomes, the concentration of red blood cells, and the oxygen saturation of blood. The determination of these three parameters are of great interest. Previous studies to determine one or two of them have used the reflectance and absorbance spectra measured on real skin. For instance, the light propagation by the modified Beer-Lambert law and use a multiple regression analysis to determine the concentration of melanin and blood. Others use reflectance measurements at selected bands to estimate the melanin index and the erythema index, or the CIELAB coordinates to evaluate the individual typology angle that is related to the skin's pigmentation. How do the colours that we see on the surface arise? Light emitted by a source interacts with the surface and the interior of an object and through these interactions (mainly absorption and scatter) the spectral composition of the light is altered. The changes reflect the structure and optical properties of the materials constituting the object and in this sense the light remitted from the object encodes its properties. If this encoding is understood, it should be possible to deduce the structure and composition of the object from its color. Conventionally, Munsell color system and CIE color space have been used in the evaluation of skin color. However, these methods may not correspond to the subjective feeling has been pointed out. In this paper we examined the usefulness of metric hue angle was calculated from the uniform color space. Metric hue angle is expected to correspond well to the appearance of skin color than the chromaticity coordinates or tristimulus values. The focus areas of this work are as follows: a) examined the differences in the various color spaces using a standard skin color samples, and b) measuring the skin color such as cheeks and forehead of subjects by using a commercially available instruments.

2. STRUCTURE AND OPTICAL PROPERTIES OF THE SKIN

Skin has a definite layered structure as shown Figure 1. The epidermis is the outermost part of the skin and is subdivided into five layers (from superficial to the deepest) the stratum corneum, the stratum luecum, the stratum granulosum, the stratum spinosum, the stratum germinativum. The main substance concerning absorption and scattering of light are the melanin pigments [3, 4]. Stratum corneum outermost layer, also called the horny layer, is mostly comprised of polygonal flattened dead cells filled with mature keratinocyte that are pushed towards the surface and gradually die and break apart. It is covered with a layer of sebum, a oily-waxy material produced by the sebaceous glands, that keeps the layer flexible and waterresistant. Stratum lucidum also called the clear layer it represents a transition from the underlying stratum granulosum to the above stratum corneum. Stratum granulosum also called the granular layer. The granules accumulated in the keratinization process contain lipides whose role is to help prevent fluid loss from the body. Stratum spinosum also called the spiny layer, it consists of several layers of newly created cells from the stratum germinativum. The stratum germinativum consists of a single layer of cells necessary

in the regeneration process of the above layers. Mitotic processes in this layer create new cells that migrate upwards through the different layers in the progressive maturation process of keratinization. Melanin Pigments are the most important part of the epidermis considering optics. Melanin pigments are found in skin, hair and eyes. These pigments are produced in the stratum germinativum and are also present in the stratum spinosum, the upper layers contain no melanin. These pigments protect the material of the underlying mitotic cells from ultra violet rays. Therefore the absorption spectrum increases towards shorter wavelengths to act as a protective filter. There are two types of melanin: eumelanin and pheomelanin. The black to dark-brown eumelanin is found in skin, black hair and the retina of the eye. The yellow to reddish-brown pheomelanin is found in red hair. All individuals have varying content of eumelanin whereas the pheomelanin is only found in individuals with the corresponding genetic trait.

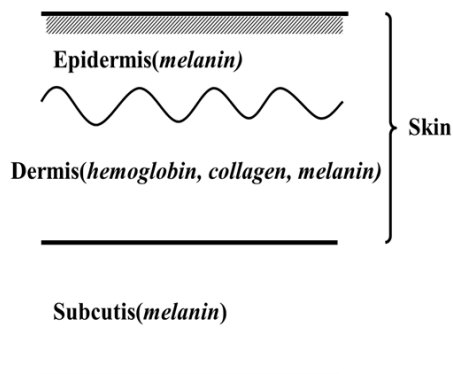


Figure 1: A cross section of human skin.

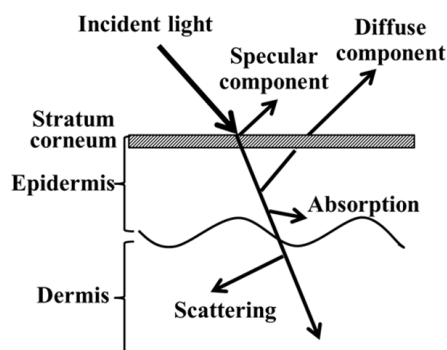


Figure 2: A schematic representation of the skin layers and their optical properties.

The skin consists of a number of layers with distinct function and distinct optical properties as shown Figure 2. White light shone onto the skin penetrates superficial skin layers and whilst some of it is absorbed, much is remitted back and can be registered by a camera. The stratum corneum is a protective layer consisting of keratin-impregnated cells and it varies considerably in thickness. Apart from scattering the light, it is optically neutral. The epidermis is largely composed of connective tissue. It also contains the melanin producing cells, the melanocytes, and their product, melanin. Melanin is a pigment which strongly absorbs light in the blue part of the visible spectrum and in the ultraviolet (see Figure 2). In this way it acts as a filter which protects the deeper layers of the skin from harmful effects of UV radiation. Within the epidermal layer there is very little scattering, with the small amount that occurs being forward directed. The result is that all light not absorbed by melanin can be considered to pass into the dermis. The dermis is made of collagen fibres and, in contrast to the epidermis, it contains sensors, receptors, blood vessels and nerve ends. Haemoglobin, present in blood vessels across the whole dermis, acts as a selective absorber of light. The dermis consists of two structurally different layers, papillary and reticular, which differ principally by the size of collagen fibres. The small size of the collagen fibres in the papillary dermis makes this layer highly back scattering; i.e., any incoming light is directed back towards the skin surface. The scatter is greatest at the red end of the spectrum and increases even further in near infrared. As absorption by melanin and blood is negligible in the infrared, this part of the spectrum is optimal for assessing the thickness of the thickened papillary dermis. Within the reticular dermis, the large size of collagen fibre bundles causes highly forward directed scattering. Thus any light which gets to this layer is passed on deeper into the skin and does not contribute to the spectrum remitted from the skin.

3. CALCULATION OF COLOR SPACE

The color and appearance of skin is more important in the field of medicine. During the diagnosis of skin diseases such as pigmented lesions, careful observation and visual assessment of the diseased area is always the first and most important step. In 1976, CIE suggested two uniform color spaces, the $CIE L^*a^*b^*$ (CIELAB) and $CIE L^*u^*v^*$ (CIELUV), based on XYZ tristimulus values [5]. The former was a nonlinear transformation of the tristimulus space and widely used in the colorant industry. These two spaces have opponent color axes representing redness-greenness

versus yellowness-blueness denoted as a^* against b^* , and u^* against v^* for CIELAB and CIELUV respectively. Both of them are three-dimensional space involving three attributes: lightness, hue and chroma. The lightness scale L^* shown in tristimulus values of color considered to Y_n of the reference white, expressed as (Y/Y_n)

$$L^* = 116 \left(\frac{Y}{Y_n} \right)^{\frac{1}{3}} - 16 \quad (1)$$

The hue and chroma of CIELAB and CIELUV are fomulated in Eq. (2) and Eq. (3) respectively.

$$a^* = 500 \left\{ \left(\frac{X}{X_n} \right)^{\frac{1}{3}} - \left(\frac{Y}{Y_n} \right)^{\frac{1}{3}} \right\} \quad (2)$$

$$b^* = 200 \left\{ \left(\frac{Y}{Y_n} \right)^{\frac{1}{3}} - \left(\frac{Z}{Z_n} \right)^{\frac{1}{3}} \right\} \quad (3)$$

$$h_{ab}^* = \tan^{-1} \left(\frac{b^*}{a^*} \right) \times \left(\frac{180}{\pi} \right) \quad (4)$$

$$C_{ab}^* = \sqrt{(a^*)^2 + (b^*)^2} \quad (5)$$

where X_n , Y_n and Z_n are the tristimulus values of the specific reference white, h_{ab}^* and C_{ab}^* are the metric hue angle and chroma component in CIELAB space. The term $180/\pi$ is necessary to convert the output of the inverse tan function from radians to degrees. The hue angle is measured in degrees starting with $h_{ab}^* = 0$ in the $+a^*$ axis direction and increasing counter clockwise.

$$u^* = 13L^* (u' - u'_n) \quad (6)$$

$$v^* = 13L^* (v' - v'_n) \quad (7)$$

$$h_{uv}^* = \tan^{-1} \left(\frac{v^*}{u^*} \right) \times \left(\frac{180}{\pi} \right) \quad (8)$$

$$C_{uv}^* = \sqrt{(u^*)^2 + (v^*)^2} \quad (9)$$

where $u' = 4X(X + 15Y + 3Z)$, $v' = 9X(X + 15Y + 3Z)$, u' , v' and u'_n , v'_n are the u' , v' coordinates of sample and reference white; h_{uv}^* and C_{uv}^* are the metric hue angle and chroma component

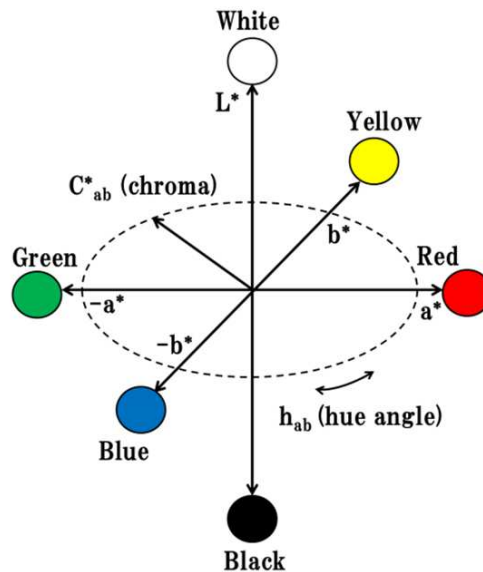


Figure 3: Diagrammatic representation of the CIELAB color space.

in CIELUV space. Both of the CIELAB and CIELUV define the hue and chroma by converting the rectangular axes into polar coordinates. Figure 3 shows a three dimensional representation of the CIELAB color space. The center of the color space is the neutral scale. The L^* values of 100 and 0 represent white and black respectively. The hue angle, h_{ab} , lies between 0° to 360° with the color arranged following the sequence of the rainbow colors. The C_{ab}^* scale is an open scale with a zero origin. The colors in the neutral scales have zero chroma value and do not exhibit hue. The CIELUV space has similar structure to the CIELAB space.

4. APPLICATION OF DERMATOLOGY TREATMENT

Reflectance spectroscopy is based on physical measurement of reflected light at specific wavelengths (400–700 nm), corresponding to the spectrum of visible light [6]. One tristimulus chromameter (Minolta Chromameter CR-200) and spectrophotometer (Minolta spectrophotometer CM-1000) were used in the study. With both instruments it is possible also to convert and display results as colorimetric values in the $L^*a^*b^*$ system where the CIELAB color space parameters are calculated from the spectral data. The aim of this study was to demonstrate that the colorimeter could measure a skin color and reproduce a rank order of the potency of the test formulations. For instrument measurement of skin color, basic studies on the 200 healthy female subjects have been chosen and divided into two groups; 100 young adults from 10 to 19 years old (average 16 years old) and 200 middle aged adults from 30 to 59 years old (average 35 years old and 54 years old). They were informed of the details of the experimental process and their consent was obtained prior to the measurements being made.

5. RESULTS AND DISCUSSION

The skin colors for the eighty male subjects in terms of the $CIEL^*a^*b^*$ color parameters L^* , hue angle, and chroma are shown in Figure 4 [7, 8]. The $CIEL^*a^*b^*$ parameters for any individual measure skin color as it would have been visually perceived. The skin of the lower forearm has characteristics determined by both hereditary skin color and environmentally induced melanin pigmentation. The ventral forearm, however, is relatively infrequently exposed to ultraviolet radiation and provided a readily accessible site to place over the viewing port of the spectrophotometers. The distribution of $CIEL^*a^*b^*$ parameters for the eighty male subjects represents objectively the ventral forearm skin color phenotype of the group. The range of each color space parameter within

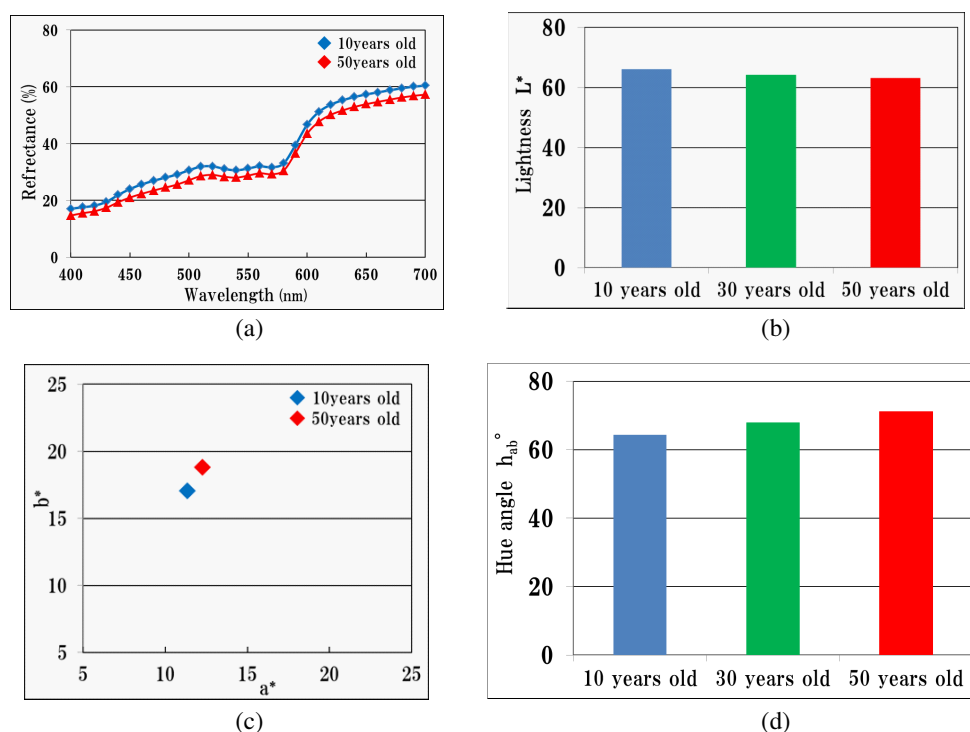


Figure 4: Distribution skin colors of 200 subjects expressed as the measured values of CIE- $L^*a^*b^*$ color space, reflectance spectra, L^* , $a^* - b^*$, metric hue angle h_{ab}° .

the group provides a numerical specification of the distribution of the corresponding color attribute as it would have been visually perceived. The L^* values ranged from 59.0 to 75.0. The apparent asymmetry of the distribution within the group was confirmed by a goodness of fit test showed that the hypothesis that the L^* values were normally distributed about a mean of 68.2 could be rejected at the 95% level of confidence. This meant that there were a few individuals whose skin was much lighter than would be expected from a normally distributed range of L^* values. The hue angles (h°) ranged from 54.0° to 78.0° . A difference in hue angle was noted between some subjects as the only color attribute that distinguished them because they were otherwise similar with respect to L^* and C^* . Differences in the skin color between individuals could be identified where both the L^* and h° values differed but the values for C^* were similar, or where the values for both the C^* and h° differed but the L^* values were similar. A further possibility was identified where differences in both L^* and C^* were evident but the hue angles were similar. For many randomly selected pairs of individuals all three $CIE L^*a^*b^*$ values were different. It was found to be suitable for representing skin color hue angle can be directly assessed the degree of red-yellow. For example, inflammatory skin lesions becomes stronger to red direction, normal skin becomes stronger yellow tone to reverse. Hue angle of normal skin color of Japanese is present in the range of 55 to 75 degrees.

6. CONCLUSION

Dermatologists or cosmetologists have long tried to quantify skin color and had few results until the advent of colorimetry. With the image colorimeter, quantification of skin color has become a simple matter: skin color can be measured rapidly, non-invasively, and reproducibly. The instrument, which can be used by paramedical staff, provides data that lend themselves for comparison, irrespective of where they are collected. The instrument has enabled definition of the range of physiologic values of skin color, and has revealed marked variations between exposed and non exposed skin. Constitutional skin color characterizes an individual's phenotype better than facultative skin color and is highly indicative of vulnerability to sunlight. On the practical level, colorimetric skin color values can be used to study pigmentation capacity, to program photo chemotherapy, and to predict the risk of, and prevent, actinic cancer. Colorimetry can be used to quantify the intensity of erythema of spontaneous and experimental lesions. Metric hue angle were found to correspond well to the appearance of skin color. However, the subjects are too few to make a general conclusion, and the authors would like to add additional observers in the not-too distant future.

REFERENCES

1. Everett, J. S., M. Budescu, and M. S. Sommers, "Making sense of skin color in clinical care," *Clin. Nurs. Res.*, Vol. 21, 495–516, 2012.
2. O'Donnell, A. T. and C. C. Kim, "Update and clinical use of imaging technologies for pigmented lesions of the skin," *Seminars in Cutaneous Medicine and Surgery*, Vol. 31, 38–44, 2012.
3. Bashkatov, A., E. A. Genina, V. I. Kochubey, and V. V. Tuchin, "Optical properties of human skin, subcutaneous and mucous tissues in the wavelength range from 400 to 2000 nm," *J. Phys. D: Appl. Phys.*, Vol. 38, 2543–2555, 2005.
4. Magnain, C., M. Elias, and J. M. Frigerio, "Skin color modeling using the radiative transfer equation solved by the auxiliary function method: Inverse problem," *J. Opt. Soc. Am. A*, Vol. 25, 1737–1743, 2008.
5. CIE Supplement No. 2 to Publication CIE No. 15, (E-1.3.1), *Colorimetry: Uniform Colour Spaces, Colour Difference Equations and Metric Colour Terms*, Central de la CIE, Paris, 1978.
6. Charys, P., K. Alewaeters, R. Lambrecht, and A. O. Bare, "Skin color measurements: Comparison between three instruments: The chromameter, the derma spectrometer and the mex-ometer," *Skin Res. Technol.*, Vol. 6, 230–238, 2000.
7. Yang, L., M. Egawa, M. Akimoto, and M. Miyakawa, "An imaging colorimeter for noncontact skin color measurement," *Optical Review*, Vol. 10, 554–561, 2003.
8. Akimoto, M., M. Miyazaki, H. H. Lee, T. Nishimura, M. Tamura, and M. Miyakawa, "Using fuzzy reasoning to support a system of diagnosis of skin disease," *Bioimages*, Vol. 17, 9–18, 2009.

New Method for Automated Disk Diffusion Test

Pavel Krepelka¹, Robert Kadlec³, Karel Bartusek², and Martin Jakubec³

¹Department of Theoretical and Experimental Electrical Engineering
Faculty of Electrical Engineering and Communication
Brno University of Technology, Technicka 12, Brno 616 00, Czech Republic

²Institute of Scientific Instruments of the ASCR v.v.i.
Kralovopolska, 147, Brno 612 00, Czech Republic

³Vyzkumny Ustav Mlekarensky s.r.o, Ke Dvoru 12a, Prague 160 00, Czech Republic

Abstract— Microbial resistance to antibiotics is a very important parameter in the selection of a proper therapy and in the control of resistance spreading. One of the most used methods for measuring microbial susceptibility is the disk diffusion test. The test is based on diffusion of concentrated antibiotics from paper disk into agar. Concentration of antibiotics in the agar is dependent on distance from the center of the disc. Near antibiotic disc is concentration much higher due difficult permeation of antibiotics in agar. The diffused antibiotics then inhibit growth of sensitive strains. The zones are usually measured manually or by electronic calipers. Several approaches for automatic inhibition zone detection have been introduced in recent years. Nevertheless, most of the algorithms are based on a similar radial profile analysis. We have designed a novel image-processing algorithm for measuring the size of inhibition zones of antibiotics based on an analysis of corrected image and rated this image with multicriterial algorithms (based on an observation of the radius profile). The algorithm was tested on 100 clinical isolates, resulting in calculation accuracy of 89% (ratio of success computed radii). If we include alternative radii (to be selected manually), the precision of the calculation rises to 98% (tolerance deviations between manual and automatic measurements were 2 mm). The achieved accuracy was independent of the culture medium (e.g., Muller-Hinton, blood agar, chocolate agar). The main advantage of the algorithm is the invariantness to the tested bacterial strain and culture medium. The new algorithm offers an alternative way to determine inhibition zones and evaluate antimicrobial susceptibility.

1. INTRODUCTION

The disk diffusion test is one of the most commonly used methods for microbial susceptibility testing which determined the size of inhibition zones of sensitive and resistant strains... The test is based on diffusion of concentrated antibiotics from paper disk into agar. Concentration of antibiotics in the agar is dependent on distance from the center of the disc. Near antibiotic disc is concentration much higher due difficult permeation of antibiotics in agar. The diffused antibiotics then inhibit growth of sensitive strains. The usual method for zone measurement is mostly based on manual reading of inhibition zones around the disk.

The presented algorithm eliminates effect of unwanted artifacts presented in scanned image (bacteria distributing residues, asymmetric inhibition zones etc.) and suggests the diffusion zones diameter (or alternatives) with comparable probability to any other presented system.

2. MATERIAL AND METHODS

Algorithms were developed and tested on clinical samples from St. Anne Faculty Hospital in Brno, Czech Republic. 100 clinical samples were used for measuring inhibition zones. Samples were cultivated on Muller-Hilton, blood or chocolate agar. Among analyzed samples was *Streptococcus spp.*, *Staphylococcus aureus*, *S. epidermidis*, *Pseudomonas aeruginosa*, *Enterococcus spp.*, *Escherichia coli* and some others unspecified clinical strains. All samples were cultivated 24 hours in 37°C. Standard petri dish with diameter 90 mm was used. Picture was taken by HP scanjet G3110 on 300DPI (bottom up).

Evaluation of the size of the diffusion zone consisted of the picture acquisition, image preprocessing, finding a dish and antibiotic disks, thresholding image, measurement of inhibition zones, confirmation or manual correction, processing output, and parameters extraction.

Image preprocessing consists of changing the image size (500px × 500px) to increase the computation speed. It is necessary to take a picture in high resolution (minimum 300DPI), so the speed of calculation will increase 10 times.

Furthermore, the image is converted to grayscale. It is important to select the correct RGB conversion coefficients. Improperly chosen values can minimize the contrast between the bacterial coating and the bacterial cultivating medium (agar) or highlight the unwanted artifacts and degrade the measurement.

It is necessary to correct the image before applying the thresholding operator. Areas (background plates, antibiotic targets) and parts which do not belong to the investigated area were corrected. These areas were replaced by a homogeneous field. To avoid histogram changes, brightness of the replaced area was chosen equal to the median (or average) of the brightness of the image. Figure 1 shows the histograms of raw and modified image.

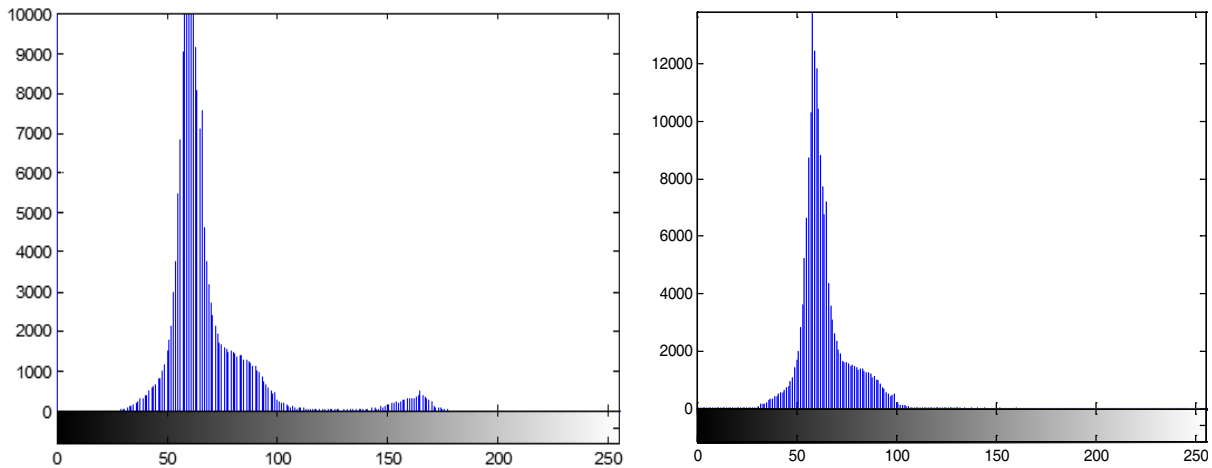


Figure 1: The histograms of raw and modified image.

Hough transform was applied to edge patterns. Result image was used to find a dish and antibiotic disks. First, the image was converted to grayscale, then Canny edge detector was applied (multi-step algorithm for finding the edges) and Hough transform was applied to this image. Hough transform is able to find a circle of known radii and calculate their coordinates — see [1].

Further, it is necessary to binarize the picture. Thresholding algorithm is applied to the modified image. The best results were achieved by using local thresholding (iterative thresholding, Otsu operator).

Otsu operator is described in [2]. To increase the efficiency, we have to equalize the image histogram. In the described procedure, both operators were applied (Otsu and Iterative). Combination of the results of both measurements is described below.

For the measurement of the size of these zones a unique algorithm is used which operates in the following steps:

- Initializing the radius to a value slightly greater than the radius of the disc. Do it for all investigated zones.
- Calculating the average brightness on the circle with the exclusion of conflict points.
- Conflicting points are those which belong to a different circle than the investigate.
- Circle points is evaluates by using Mid-point algorithm [3].
- If the calculated average brightness is greater than the specified threshold — end the circle calculation.
- Incrementing all radii of unfinished circles.
- For the unfinished circle — jump to point 2.

It is important to use an algorithm which reliably finds a circle whose circumference brightness is increased above a given brightness level. The algorithm is based on computing points, which do not belong to other circles. The problem is how to choose the optimum brightness level. Analytical deduction of the optimal luminance level is difficult and would require a complex description of the image. The described algorithm uses a different approach. Circles (the edges of the zone of inhibition) were detected using N different thresholds. For each investigated zone, we obtained N

potential radii of inhibition zones. The calculated radius probabilities are given by their frequencies in the measured set of size N . The radius with the biggest probability (most often measured) is considered to be final — other radii can be proposed as an alternative. The frequency calculation is supplemented by tolerance — this means that the measured radii are divided into groups that have similar radius size. The resulting value is given by the arithmetic mean in grouped values.

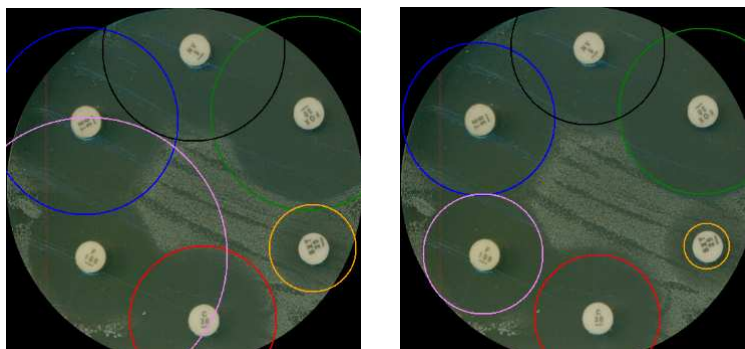


Figure 2: Incorrectly and correctly detected inhibition zones.

3. RESULTS AND CONCLUSION

In 98% of cases, the system measured zone correctly or the right size was in suggested alternative zones (user must choose the right zone — semi automate mode). Other testing would be necessary for chocolate agar and for yeasts.

The developed algorithm gives reliable and reproducible results even for damaged samples. If the border zone is not evident, the algorithm will calculate alternative zones. The user can then select the preferred one. The algorithm was tested on 100 dishes, resulting in calculation accuracy of 89%. If we include alternative radii (to be selected manually), the precision of the calculation rises to 98% (tolerance deviations between manual and automatic measurements were 2 mm). Figure 2 shows the output of the program. Abbas et al. [4] describe similar algorithm based on the analysis of the radial profile of the zone. This approach has achieved accuracy (the same tolerance of diversity) of 78%. The algorithm can be modified by time optimization and automatic labels reading.

ACKNOWLEDGMENT

The research described in the paper was financially supported by project from the Education for Competitiveness Operative Programme, No. CZ.1.07.2.3.00.20.0175 (Electro-researcher) and MVCR grant VG20102015023.

REFERENCES

1. Cuenca-Estrella, M., A. Gomez-Lopez, M. O. Gutierrez, M. J. Buitrago, and J. L. Rodriguez-Tudela, "Reliability of the WIDERYST susceptibility testing system for detection of in vitro antifungal resistance in yeasts," *Antimicrobial Agents and Chemotherapy*, Vol. 52, 1062–1065, 2008.
2. Zabidi, M. A., N. M. Yusoff, and Z. S. A. Kader, "Preliminary comparative analysis of antibacterial effects of activated and non-activated of expired platelet concentrate by disc diffusion method," *Indian Journal of Pathology and Microbiology*, Vol. 55, 47–51, 2014.
3. Sood, S. and R. Gupta, "Antibiotic resistance pattern of community acquired uropathogens at a tertiary care hospital in jaipur, rajasthan," *Indian J. Community Med.*, 39–44, India, 2012.
4. Abbas, S., H. Trabelsi, I. Amouri, H. Sallemi, S. Nej, C. Fatma, F. Makni, and A. Ayadi, "Methods for studying the in vitro susceptibility of *Candida* spp. to antifungals," *Annales De Biologie Clinique*, Vol. 70, 635–642, 2012.
5. Canton, R., M. Perez-Vazquez, A. Oliver, B. S. Del Saz, M. O. Gutierrez, M. Martinez-Ferrer, and F. Baquero, "Evaluation of the wider system, a new computer-assisted image-processing device for bacterial identification and susceptibility testing," *Journal of Clinical Microbiology*, Vol. 38, 1339–1346, 2000.

The Study of the Growth of Tissue Cultures under a Layer of Nanotextiles

M. Pokludova and P. Křepelka

Department of Theoretical and Experimental Electrical Engineering
Brno University of Technology, Technická 3082/12, Brno 612 00, Czech Republic

Abstract— Nowadays nanotextiles are very popular due to their unique properties (antibacterial, very light weight, thin, solid, high porosity, transparency, good mechanical properties, etc.). These characteristics bring new possibilities of classification in the various fields of human activity. For example, the filtration of air and water through the nanofiber membranes whose structure is similar to the construction of tissue that supports the growth of cells in their natural environment. Carbon nanofibers have their application in treating the effects of myocardial infarction. Nanotextiles consist of nanofibers with a diameter in the range from 50 to 500 nm. Production of such a fabric is much more complex than classical woven fabric. This material is not possible to hold by any device. Production is carried out using the electrospinning. The nanotextile produced by the spinning method was used on the samples of spruce embryos and concluded (with samples) in the plastic Petri's dishes. Spruce embryos were selected for their rapid growth, their biggest increase is till the fifteenth day then they are growth-stabilized. The aim of this paper is to determine the influence of the nanotextiles to the tissue cultures and whether the embryos will be able to grow under this structure. The samples were periodically removed from the magnetic field and moved in an isolated box throughout the outdoor environment into the room with NMR tomograph for obtaining the images of individual tissue cultures. After fifteen days the last measurement was carried out and the results of all measurements were evaluated using the programs Marevisi and Matlab. Observed parameters of individual samples were processed into graphs.

1. INTRODUCTION

Nanotextile is the collective name for textile fibers (nanofibers) their diameter is in the order of a few nanometers (50–500 nm). Nowadays nanotextiles are very popular due to their excellent mechanical properties in relation to their weight, in particular, are very thin with high porosity. The most important and most used property is an antibacterial character mainly used in health care. These characteristics bring new possibilities of application in the various fields of human activity. For example, the filtration of air and water through the nanofiber membranes whose structure is similar to the construction of tissue that supports the growth of cells in their natural environment. Carbon nanofibers have their application in treating the effects of myocardial infarction. In the construction industry are used for thermal and acoustic insulation [1].

Production of such a fabric is much more complex than classical woven fabric. This material is not possible to hold by any device. Production is carried out using the electrostatic spinning of polymer solutions in a strong magnetic field (electrospinning). The Nanospider technology uses two electrodes between which there is a strong electrostatic field. The first electrode has a cylindrical shape and by constant rotation creates a thin layer of polymer. By the electrostatic forces on the second electrode pull out a thin layer [2].

In measurements were used two materials: the Chitosan on matrix of polyethylene and the Polyamide on matrix of viscose. Chitosan is a polysaccharide occurring in shells of crustaceans, which is non-toxic and compatible with living tissue. It is used in a health care for faster healing of wounds or for production of artificial skin. Another use is in cosmetics, food industry, or for the treatment of wastewater. The second material Polyamide is made of petroleum. This material is very flexible and has high tensile strength. It is able to resist moisture very well but has little resistance to light and weather conditions [3]. Illustrative photography of nanotextiles made of polyamide is shown in Figure 1.

2. EXPERIMENTAL MEASUREMENTS

Nanotextiles made by Nanospider technology were inserted to the samples of tissue cultures of early spruce embryos, which were grown in the plastic Petri's dishes with the diameter of 50 mm. In each dish there was placed a cluster of plant tissue culture with a sample of nanotextile. The spruce embryos were selected for their rapid growth. The largest increase is till the fifteenth day

then the growth is stabilized. The dishes of samples were placed in a dark place without the action of external lighting, at a constant temperature and humidity. All samples in the plastic Petri's dishes were divided into two main groups. At the first group of samples were applied thin layer nanotextiles with a circular shape (different diameters). The second group served as the controls and comparative samples. Distributions of all dishes with the samples are listed in the Table 1.

Table 1: Distribution of all dishes with the samples.

Nanotextiles	Dishes with nanotextiles			Control dishes
	Dishes 1–3	Dishes 4–5	Dishes 6–7	Dishes 8–10
Size	Diameter 50 mm	Diameter 30 mm	Diameter 50 mm	-
Type	Chitosan S PEO		PA 612	
Fiber diameter	100–350 nm		100–250 nm	
Basis weight	0,89 gsm		0,86 gsm	

All dishes were periodically withdrawn from the constant environment and moved in an isolated box through the outside environment into the room with nuclear magnetic resonance tomograph (NMR) to obtain images of the tissue culture. The measurement of nuclear magnetic resonance is gentle for the tissue culture, by which the cuts of images plant are acquired, without any deformation or destruction of the plant tissue culture [4]. The images from the NMR tomograph were obtained by spin echo method with parameters: $T_E = 18,35$ ms, $T_R = 1$ s. Individuals times were chosen to achieve the best image contrast. The size of the resulting images are 128×128 pixels and the size of operating point is 30×30 mm. Individual slices have a width of 2 mm and are spaced 2 mm. After the fifteenth day the last measurement in the NMR tomograph was done and all acquired images were processed according to the following diagram. A more detailed description of the image processing is given in the article [4].

After loading the NMR cuts in the program Marevisi, the images were reconstructed using the inverse Fourier transform to the resulting image. In the picture there were executed selections of individual clusters and subsequently were obtained information about the sizes of clusters in pixels. In Table 2 are given the total sizes (in pixels) of clusters of tissue cultures from all measuring days obtained by NMR methods. All is plotted in Figure 2. To assessment of cluster growth are all sizes expressed as a percentage and sorted from the lowest value (Table 3). The control samples are

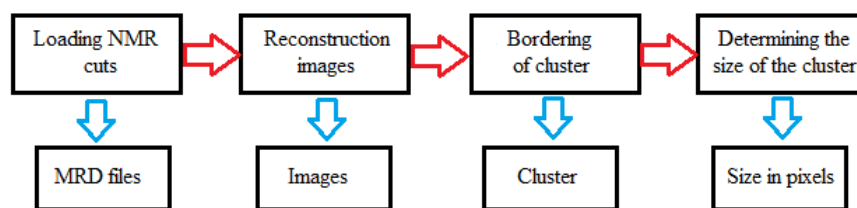


Figure 1: Diagram of evaluation of NMR images.

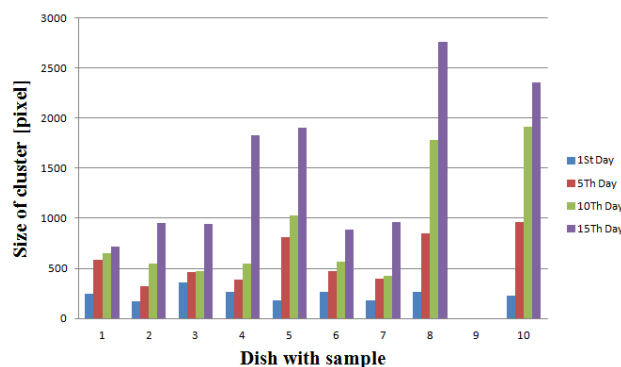


Figure 2: The comparison of the sizes of growth of all tissue cultures from all measurements.



Figure 3: Illustrative photography of nanotextiles.

Table 2: Data from measurements of tissue cultures.

Dish	1st day	5th day	10th day	15th day
	Size [pixel]	Size [pixel]	Size [pixel]	Size [pixel]
1	245	583	654	718
2	167	324	546	953
3	359	461	471	945
4	268	387	548	1831
5	184	810	1028	1908
6	263	475	569	889
7	184	396	423	965
8	263	853	1786	2765
9	154	0	0	0
10	229	958	1913	2358

Table 3: Cluster sizes sorted by percentage in two days.

5th day		10th day		15th day	
Dish	Size [%]	Dish	Size [%]	Dish	Size [%]
9	0	9	0	9	0
3	12,841	3	13,120	3	26,323
4	14,440	4	20,448	1	29,306
6	18,061	6	21,635	6	33,802
2	19,401	7	22,990	7	52,446
7	21,522	1	26,694	2	57,066
1	23,796	2	32,695	4	68,321
8	32,433	5	55,870	10	102,970
10	41,834	8	67,909	5	103,696
5	44,022	10	83,537	8	105,133

marked by red color. From Table 3 it can be seen that the majority of the control samples are in the lower part of the table, it means that the size has increased faster than for the other samples. Sample with No. 9 could not be further processed, due to necrosis of the sample. We can only assume that the dishes were poorly sealed and then an outdoor environment got to the inside.

During the last day of measurement the largest increase was recognized in samples No. 4 and No. 5, these are the samples in which nanotextiles made of the polysaccharide was placed. While in the samples No. 6 and No. 7, (with nanotextiles made of polyamide) the mold appeared during the growth the tissue culture. It is possible that during the samples transport through the outdoor environments to the area with NMR tomograph these were influenced by outside light and temperature, because nanotextiles of this type is susceptible to the surrounding environment.

3. CONCLUSIONS

The tissue culture grew along with the sample of nanotextiles Chitosan or Polyamide. The best rated on the end measurements were the samples with Chitosan, which had the fastest growth compared to other samples. In other samples grew a mold that could get in by bowls leakage, or the tissue culture respond to nanotextiles. Sample No. 9 was eliminated during the first few days due to necrosis of tissue culture plates inside. Based on this measurement was designed by additional measurements that will be deal by removing the mold that arise Petri's dishes during the growth of tissue cultures. Because insertion the nanotextiles at different intervals are needed to eliminate the effects of molds. The mold is highly undesirable and cause necrosis or destruction of samples.

ACKNOWLEDGMENT

The research described in the paper was financially supported by project of the BUT science fund, No. FEKT-S-14-2545, and a project from the Education for Competitiveness Operative Programme, No. CZ.1.07.2.3.00.20.0175 (Electro-researcher).

REFERENCES

1. Ulrich, C., “Nano-textiles are engineering a safer world,” *Human Ecology*, Vol. 34, No. 2, 2006.
2. Thandavamoorthy, S., G. S. Bhat, R. W. Tock, S. Parameswaran, and S. S. Ramkumar, “Electrospinning of nanofibers,” *Journal of Applied Polymer Science*, Vol. 96, No. 2, 2005.
3. Torres-Giner, S., M. J. Ocio, and J. M. Lagaron, “Development of active antimicrobial fiber-based chitosan polysaccharide nanostructures using electrospinning,” *Engineering in Life Sciences*, Vol. 8, No. 3, 2008.
4. Bartusek, K., E. Gescheidtová, R. Kízek, and Z. Dokoupil, “Zpracování dat pri studiu růstu raných smrkových embryí zobrazovacími MR technikami,” *Elektrorevue*, Vol. 43, ISSN 1213-1539, 2008 (in Czech).

Characterization of Ultrashort Pulse Laser by Using KNbO₃ Nanoneedles Based Frequency-resolved Optical Gating (FROG)

Jiaxin Yu and Fuhong Cai

Centre for Optical and Electromagnetic Research

Zhejiang Provincial Key Laboratory for Sensing Technologies

JORCEP [Joint Research Center of Photonics of the Royal Institute of Technology, Lund University and Zhejiang University], Zhejiang University, Zijingang Campus, Hangzhou 310058, China

Abstract— We demonstrate a measurement of Second Harmonic Generation (SHG) FROG using potassium niobate (KN) nanoneedle clusters, instead of bulk crystal, as nonlinear medium. Using this excellent nonlinear nano-material, we characterize the pulse time/frequency-dependent intensity of a 1040 nm picoseconds pulse laser. Due to the nanometer scale of this nonlinear medium, the phase matching constraints can be relaxed, and the measurement system is significantly simplified and thus more accessible for common users.

1. INTRODUCTION

Ultrafast pulse laser have been widely used in many areas because of their excellent properties, especially in nonlinear excitation. There are many methods to measure both the amplitude and the phase structure of an ultrafast pulse [1–3]. FROG is one of the most common approaches for this kind of characterization. With a piece of nonlinear crystal, a FROG system based on different nonlinear effects can be implemented, such as SHG-FROG and third-harmonic-generation (THG) FROG. However, being an essential element in FROG technique, the bulk nonlinear crystal always needs specially cutting for different wavelength band before usage. Moreover, when the pulse laser alters slightly, complicated modulations have to be operated to meet the altered phase matching condition.

Many efforts have been made to simplify the complexity of the conventional FROG system, and maintain the performance as well [3, 4]. Some research has reported using single nanoparticle instead of bulk crystal as nonlinear medium [5, 6], which avoid the complexity the of using bulk crystal and achieve a better spatial resolution than ever. However, since the signal generated from the single nanoparticle is weak, the acquisition time has to be extremely long. It will badly affect the measurement efficiency and signal to noise ratio (SNR) apparently.

In this work, we propose KN nanoneedle clusters based FROG approach to overcome the drawback of the low SNR in the previous literatures, without renouncing the performance of the FROG technique. By employing the nanoneedle clusters in a conventional noncollinear FROG system, the optical properties of a 1040 nm picoseconds pulse laser are characterized in both temporal and spectral domain.

2. METHODS

2.1. Experimental Set-up

As illustrated in Figure 1, a 2.5 ps Yb doped large-mode-area (LMA) photonic crystal fiber (PCF) laser is employed, with center wavelength at 1040 nm, ~ 50 nm width, and repetition rate of ~ 45 MHz. The output of the laser is split at beam splitter (BS) into the two arms of a homemade interferometer. A delay stage (DS) with 10 μm /step resolution, corresponding to 33.3 fs in time domain, is used to induce a difference between the optical paths. After being reflected by two retro-reflector (RR1 and RR2) respectively, the two beam are recombined at BS but with a separation. They are then non-collinearly focused on to the KN nanoneedles by a lens ($L1$). The signal is collected by another lens ($L2$) and detected by a spectrometer (Ocean optics, QE65000). No optical filter is required in this non-collinear system.

2.2. KN Nanoneedle

The KN nanoneedles used in this work are synthesized by a hydrothermal method [7]. The length of single KN nanoneedle varies around 1.6 μm , and the diameter decreases uniformly from 60 nm for bottom to 20 nm for top approximately [8]. The TEM image of individual KN nanoneedle and SEM images of nanoneedle clusters are provided in Figure 2. The clusters used for SHG are obtained by dropping suspension of nanoneedles in deionized water onto a coverslip and dried in the air. The

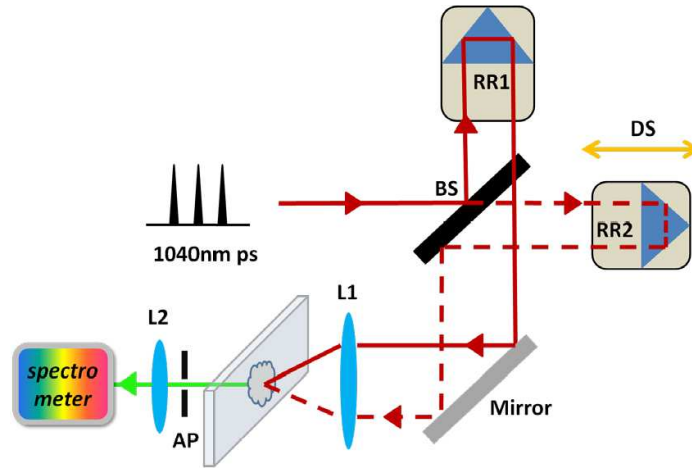


Figure 1: Schematic diagram of pump-probe system in the FROG measurement. BS: beam splitter; RR1 and RR2: retro-reflectors; DS: delay stage; L1 and L2: lens; AP: aperture.

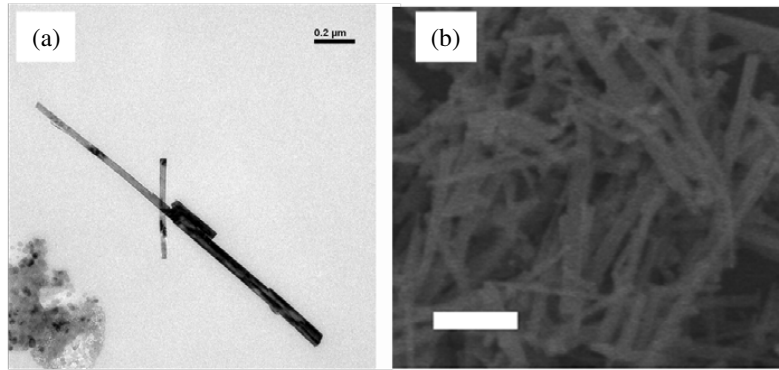


Figure 2: (a) TEM image of single KN nanoneedle. Scale bar: 200 nm. (b) SEM image of KN nanoneedle clusters. Scale bar: 500 nm.

randomly distributed clusters will not introduce disturbance into the pulse characterization as long as the same ensemble of clusters is excited in the process of pulse scanning.

As reported previously [9], the KN nanoneedles have the ability of wide-band frequency conversion, and the SHG efficiency is about 19.6 pm/V at 1004 nm, which is relative large among similar nano-materials [10].

2.3. Theory

Briefly, the FROG measurement can be described as follows. Define the complex electric fields of each pulse as

$$\hat{E}(t) = E(t) \exp(j2\pi f_0 t),$$

where the $E(t)$ is complex amplitude and f_0 is the carrier frequency.

The measured intensity of non-collinear FROG signal can then be written as

$$I_{\text{FROG}}^{\text{SHG}}(\tau, f) \propto \left| \int_{-\infty}^{\infty} \hat{E}(t) \hat{E}(t - \tau) \exp(-j2\pi f t) dt \right|^2,$$

with τ is the relative delay between the pulses, and $\hat{E}(t - \tau)$ is a variable-delay gate function. The spectrogram is the set of spectra of all gated chunks of $\hat{E}(t)$ as the delay is varied. Knowledge of the spectrogram of $E(t)$ is sufficient to completely determine $E(t)$ [11].

3. RESULTS AND DISCUSSION

Figure 3(a) shows the result of our measurement. The power of the LMA-PCF laser output was about 800 mW, and before the focused lens was about 10 mW for each arm. The non-collinear

FROG spectrogram can be obtained by measuring the spectrum of the SHG signal as the delay time between the two pump beams is scanned. The delay step of the FROG trace was fixed at $\Delta\tau = 33.3$ fs. The integration time of each spectrum was 100 ms, and the total acquisition time is 5 min, most of which is cost in the delay stage step motion.

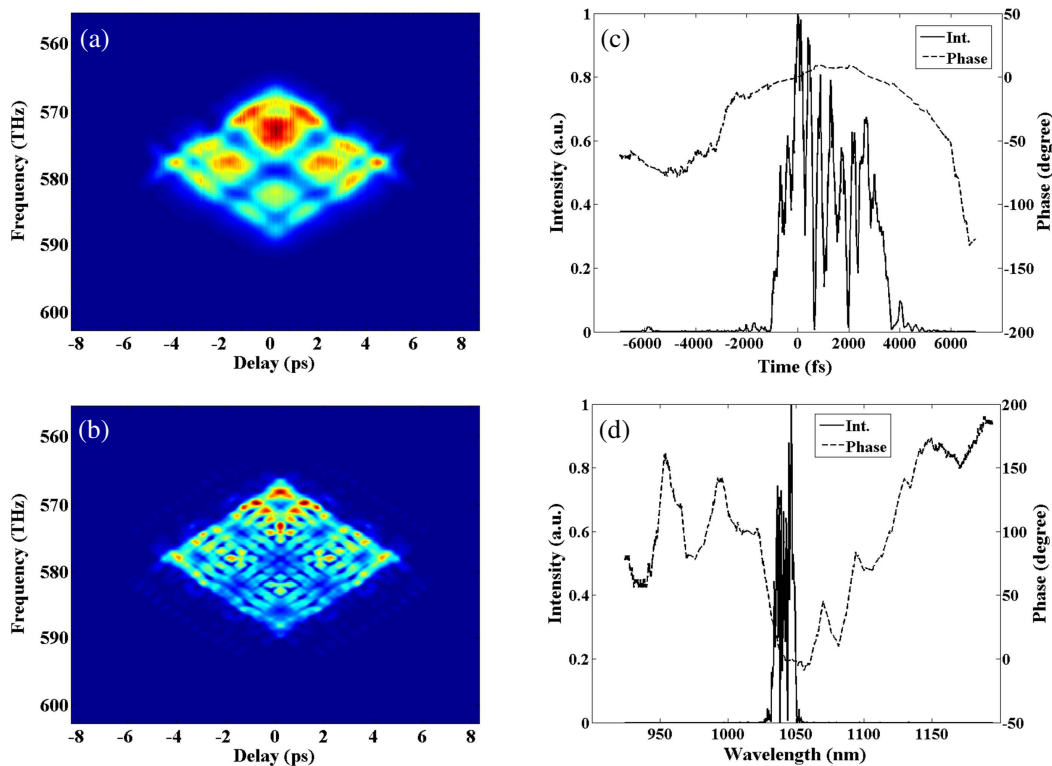


Figure 3: (a) Experimental FROG trace. (b) Retrieved FROG trace. Electric field intensity (solid line) and phase (dashed line) as a function (c) of time and (d) of wavelength.

The retrieval result shown in Figure 3(b) is obtained through a method given in Ref. [12]. Using the standard FROG algorithm, the complex pulse profile can be retrieved from the measured non-collinear SHG-FROG trace. The retrieved pulse intensity and phase profiles in temporal and spectral are also reported in Figures 3(c) and (d), respectively. The measurement can be further improved by employing a delay stage with finer step.

In our previous report, the KN nanoneedles can realize a wide-band second and third harmonic generation [9]. Combining the aforementioned ability to relax phase match constraints, they can be a potential replacement of bulk nonlinear crystal in ultrafast pulse characterization for SHG-FROG but THG-FROG. With respect to the bulk crystal, the nanoneedle clusters almost require no adjustment for different laser, which is more accessible for common users. Furthermore, by placing the nanocrystals on the focal plane, the pulse laser's properties on the sample can be reflected from the measurement, which is regarded as very valuable information for *in situ* bio-imaging.

ACKNOWLEDGMENT

This work was supported by the Science and Technology Department of Zhejiang Province (2010R-50007), the National Basic Research Program (973) of China (2011CB503700), and the “111” Project. We thank Dr. Dapeng Zhang for his assistances.

REFERENCES

1. Müller, M., J. Squier, and G. J. Brakenhoff, “Measurement of femtosecond pulses in the focal point of a high-numerical-aperture lens by two-photon absorption,” *Optics Letters*, Vol. 20, No. 9, 1038–1040, 1995.
2. Iaconis, C. and I. A. Walmsley, “Self-referencing spectral interferometry for measuring ultrashort optical pulses,” *IEEE Journal of Quantum Electronics*, Vol. 35, No. 4, 501–509, 1999.

3. Bowlan, P., et al., “Measuring the spatiotemporal electric field of ultrashort pulses with high spatial and spectral resolution,” *J. Opt. Soc. Am. B*, Vol. 25, No. 6, A81–A92, 2008.
4. Amat-Roldán, I., et al., “Starch-based second-harmonic-generated collinear frequency-resolved optical gating pulse characterization at the focal plane of a high-numerical-aperture lens,” *Optics Letters*, Vol. 29, No. 19, 2282–2284, 2004.
5. Li, H., et al., “Characterizing ultrashort optical pulses using second-order nonlinear nanoprobe,” *Applied Physics Letters*, Vol. 97, No. 26, 261108, 2010.
6. Extermann, J., et al., “Nano-FROG: Frequency resolved optical gating by a nanometric object,” *Optics Express*, Vol. 16, No. 14, 10405–10411, 2008.
7. Santos, I. C. M. S., et al., “Studies on the hydrothermal synthesis of niobium oxides,” *Polyhedron*, Vol. 21, No. 20, 2009–2015, 2002.
8. Wang, Y., et al., “Synthesis and second harmonic generation response of KNbO_3 nanoneedles,” *Journal of Crystal Growth*, Vol. 341, No. 1, 42–45, 2012.
9. Cai, F., et al., “Tunable SHG/THG from KNbO_3 nano-needles and their applications in finding optimal wavelength for deep-tissue NLO imaging,” unpublished.
10. Nakayama, Y., et al., “Tunable nanowire nonlinear optical probe,” *Nature*, Vol. 447, No. 7148, 1098–1101, 2007.
11. Trebino, R., et al., “Measuring ultrashort laser pulses in the time-frequency domain using frequency-resolved optical gating,” *Review of Scientific Instruments*, Vol. 68, No. 9, 3277–3295, 1997.
12. Trebino, R., *Frequency-resolved Optical Gating: The Measurement of Ultrashort Laser Pulses*, 1st Edition, Klumer Academic, Boston, MA, 2002.

FDTD-based CAD Simulator for Coaxial Applicator — Biomedical Application

C. W. Lee¹, K. Y. You¹, and C. Y. Lee²

¹Department Communication Engineering, Faculty of Electrical Engineering
Universiti Teknologi Malaysia, Skudai 81310, Malaysia

²Faculty of Bioscience and Medical Engineering
Universiti Teknologi Malaysia (UTM), Johor 81310, Malaysia

Abstract— This paper presents development of FDTD-based CAD simulator using MATLAB graphic user interface feature for solving the coaxial applicator problem. The capability of the CAD is to visualize the 2D and 3D electromagnetic field and bio-heat distribution. The CAD is competitive with commercial simulator in term of learning curve and simplicity in the program algorithm. In this paper, the creation steps of the CAD are described in detail. In addition, the comparison result between the CAD and commercial simulator are intensively discussed and analyzed. Some of the improvements of this CAD are also presented.

1. INTRODUCTION

Simulator is gaining importance nowadays for scientists and researchers to complete their research work. However, commercial simulator is costly. There exist few free open-source simulators [1] and those are not user friendly. Here, we attempt to develop simple graphical user interface (GUI) to overcome the above issue. In this paper, we only focused on Finite Difference Method (FDM) [2] and Finite Difference Time-Domain (FDTD) [3] which was applied to the coaxial type applicator in hyperthermia treatment. Coaxial applicator becomes popular due to its thin slot form and small cross section area which can realize minimal invasive treatment such as deep seated brain tumor.

2. THEORETICAL BACKGROUND

All the solutions to the problem of electromagnetic are always refer to the Maxwell's equation. Here, the FDTD is applied on coated monopole applicator to solve an electromagnetic (EM) fields using the Maxwell's equations in time, t domain and cylindrical coordinate (ρ , ϕ and z) [4]:

$$\frac{\partial E_\rho}{\partial z} - \frac{\partial E_z}{\partial \rho} = -\mu_o \frac{\partial H_\phi}{\partial t} + \sigma H_\phi \quad (1a)$$

$$-\frac{\partial H_\phi}{\partial z} = -\varepsilon_o \varepsilon_r \frac{\partial E_\rho}{\partial t} + \sigma E_\rho \quad (1b)$$

$$\frac{1}{\rho} \frac{\partial(\rho H_\phi)}{\partial \rho} = -\varepsilon_o \varepsilon_r \frac{\partial E_z}{\partial t} + \sigma E_z \quad (1c)$$

where E_ρ , E_z and H_ϕ are the radial, axial electric fields (V/m) and azimuth magnetic field (A/m), respectively. Symbols μ_o and ε_o are the permeability (H/m) and permittivity (F/m) of free space, while, ε_r and σ are the relative permittivity and conductivity (S/m) of ambient medium. While, the scatter heat distribution due to EM energy along the length of coated monopole driven from coaxial line, was solved by FDM. The governing Pennes' bioheat transfer equation [5] was used and given as:

$$pC_p \frac{\partial T}{\partial t} = K \left(\frac{\partial^2 T}{\partial \rho^2} + \frac{1}{\rho} \frac{\partial T}{\partial \rho} + \frac{\partial^2 T}{\partial z^2} \right) - \omega_b C_b p_b (T - T_a) + Q_{met} + Q_{ext} \quad (2)$$

where T is the final temperature ($^\circ\text{C}$) in biological medium; T_a is the arterial temperature ($^\circ\text{C}$). Symbols p , C_p and K are the density (kg/m^3), specific heat capacity ($\text{J}/(\text{kg}^\circ\text{C})$) and thermal conductivity ($\text{W}/(\text{m}^\circ\text{C})$) of the biological medium, respectively; Symbols p_b and C_b are the density (kg/m^3) and specific heat capacity ($\text{J}/(\text{kg}^\circ\text{C})$) of blood, respectively; ω_b is the blood perfusion rate ($\text{m}^3/(\text{kg} \cdot \text{s})$), which is assumed to be constant; Q_{met} is the metabolic heat generation rate (ignored in this study) and Q_{ext} is the external heat sources which is related to electric field, E , as:

$$SAR = \frac{\sigma |E|^2}{2\rho} = \frac{Q_{ext}}{p} \quad (3)$$

where SAR is the specific absorption rate (W/kg) of biological medium. In FDTD routine, the (1) is required to convert into discrete form as:

$$H_{\phi}^{n+0.5}(i, j) = H_{\phi}^{n-0.5}(i, j) + \frac{\Delta t}{\mu_0} \left[\frac{E_{\rho}^n(i, j+0.5) - E_{\rho}^n(i, j-0.5)}{\Delta z} \right] - \frac{\Delta t}{\mu_0} \left[\frac{E_z^n(i+0.5, j) - E_z^n(i-0.5, j)}{\Delta \rho} \right] \quad (4a)$$

$$E_z^{n+1}(i+0.5, j) = \frac{\left(1 - \frac{\sigma \Delta t}{2\varepsilon_o \varepsilon_r}\right)}{\left(1 + \frac{\sigma \Delta t}{2\varepsilon_o \varepsilon_r}\right)} E_z^n(i+0.5, j) + \frac{\frac{\Delta t}{\varepsilon_o \varepsilon_r}}{\left(1 + \frac{\sigma \Delta t}{2\varepsilon_o \varepsilon_r}\right)} \left[\frac{\rho_{i+1} H_{\phi}^{n+0.5}(i+1, j) - \rho_i H_{\phi}^{n+0.5}(i, j)}{\rho_{i+0.5} \Delta \rho} \right] \quad (4b)$$

$$E_{\rho}^{n+1}(i, j-0.5) = \frac{\left(1 - \frac{\sigma \Delta t}{2\varepsilon_o \varepsilon_r}\right)}{\left(1 + \frac{\sigma \Delta t}{2\varepsilon_o \varepsilon_r}\right)} E_{\rho}^n(i, j-0.5) - \frac{\frac{\Delta t}{\varepsilon_o \varepsilon_r}}{\left(1 + \frac{\sigma \Delta t}{2\varepsilon_o \varepsilon_r}\right)} \left[\frac{H_{\phi}^{n+0.5}(i, j) - H_{\phi}^{n+0.5}(i, j-1)}{\Delta z} \right] \quad (4c)$$

Similarly, for FDM, the (2) is discretized as:

$$\frac{\partial T}{\partial t} = \frac{K}{pc} \left[\frac{T(i+1, j) - 2T(i, j) + T(i-1, j)}{\Delta \rho^2} + \frac{1}{\rho} \frac{T(i+1, j) - T(i, j)}{2\Delta \rho} + \frac{T(i+1, j) - 2T(i, j) + T(i-1, j)}{\Delta z^2} \right] - \frac{\omega_b c_b p_b}{pc} [T(i, j) - T_a] + \frac{SAR}{c} \quad (5)$$

The Equation (5) is further solved explicitly by available MATLAB ode45 solver [6].

3. RESULTS AND ANALYSIS

3.1. Simulated Configuration

This study simulator considers the coated monopole driven from coaxial line as axis symmetrical in order to reduce the computational resource and run time. Source is fed from the end of the coaxial line and it is assume to be TEM along the coaxial line. Soft source is used to allow reflected wave to be absorbed. Since FDTD operates in time domain, differentiated Gaussian pulse excitation is performed. When steady-state is reached, Fourier transform is used to obtain frequency response. The domain for the analysis is truncated with perfectly matched layer (PML) based on recursive convolution and the use of complex frequency shifted (CFS) parameters to absorb all outgoing electromagnetic waves. To ensure stability, time step set adhere to ‘‘Courant-Friedrichs-Lewy condition’’, which is described in detail in [4]. Grid cell, $\Delta \rho$ used is 0.25 mm equivalent to 75 points per wavelength to reduce numerical dispersion error. The type of applicator to be used in this study is a thin monopole used in hyperthermia treatment coated with catheter made of Teflon. There exist thin air gap between the catheter and the conductor as shown in Figure 1. The height of the monopole is set to $\beta_L h = \pi/4$ at $f = 915$ MHz. The values of initial parameters of the study simulation are given in Table 1. Up to 10 watt power is introduced through the coaxial line for three minutes to obtain the final temperature.

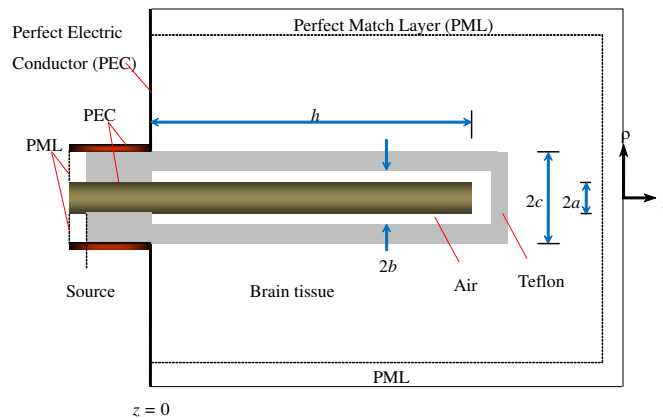


Figure 1: Geometry of coated monopole.

Table 1: Parameters in the FDTD simulation.

Dimensions of monopole	Dielectric Properties of Mediums	Thermal Properties of Mediums	
$a = 0.5 \text{ mm}$	Air: $\epsilon_r = 1$	Brain Tissue: $K = 0.497 \text{ W}/(\text{m}^\circ\text{C})$	Blood: $K = 0.45 \text{ W}/(\text{m}^\circ\text{C})$
$b = 0.75 \text{ mm}$	Teflon: $\epsilon_r = 2.06$	$p = 1030 \text{ kg}/\text{m}^3$	$p = 1058 \text{ kg}/\text{m}^3$
$c = 1.5 \text{ mm}$	Brain Tissue: $\epsilon_r = 42.5$	$C_p = 3600 \text{ J}/(\text{kg}^\circ\text{C})$	$C_p = 3960 \text{ J}/(\text{kg}^\circ\text{C})$
$h = 21.1 \text{ mm}$	$\sigma = 0.88 \text{ S}/\text{m}$		

3.2. GUI Features

GUI developed is simple and straight forward where it is made up of a graphic display, 6 function buttons and a display drop down list as shown in Figure 2. Comparison with COMSOL's GUI is shown in Figure 3.

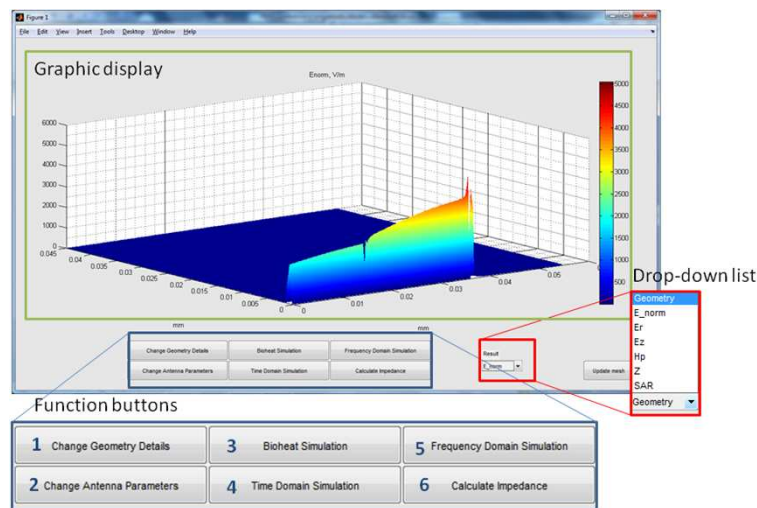


Figure 2: Developed simulator's GUI components.

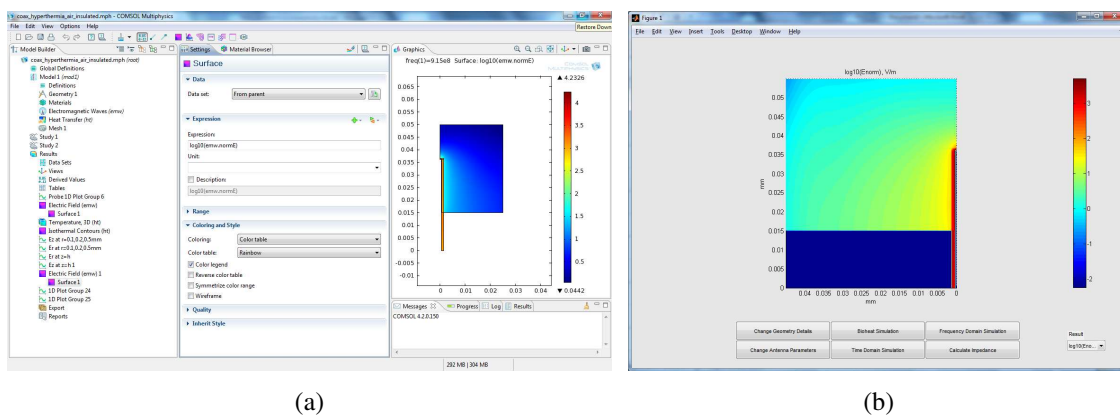


Figure 3: (a) COMSOL's GUI. (b) Developed simulator's GUI.

3.2.1. Graphic Display

Results and geometry model are plotted at a time on the graphic display base on the option selected in the drop-down list.

3.2.2. Drop-down List

There are 7 types of result to be selected from the drop down list which are geometry model, normalized electric field, axial and radial electric field, azimuth magnetic field, input impedance,

and *SAR* distribution.

3.2.3. Function Buttons

When function buttons are pressed, a dialog box is launched for assignment of respective parameters. To save the changes, press the OK button and respective simulation is performed.

1. “**Change Geometry Detail**” button is used to define the grid cell size, simulation domain size, number of PML layers, and biological medium properties.
2. “**Change Antenna Parameters**” button is used to define the antenna dimensions and material properties.
3. “**Bioheat Simulation**” button is used to solve bioheat equation and the final solution is interpreted in temperature distribution. Duration of the simulation and thermal properties of the biological and blood medium is defined in the dialog box.
4. “**Time Domain Simulation**” button will initiate real time animation of the electric field wave propagation. Type of source, frequency of interest, input voltage and maximum number of time steps can be defined in the dialog box.
5. “**Frequency Domain Simulation**” button is capable of calculating the electric and magnetic field distribution in frequency domain. Dialog box shown similar parameters as from button 4.
6. “**Calculate Impedance**” button is used to calculate variation of impedance with frequency. Parameters to be defined are range of frequencies, maximum number of time steps and type of source.

3.3. Results Discussion

In this section, the computed electric field, (E_ρ and E_z) and input impedance, Z_{in} at driving point are validated against analytical solution [7] and COMSOL simulation results. Electric field is compared at 6 different cross sections parallel to ρ -axis and z -axis. Due to differences excitation sources were respectively used by the three approaches, thus, the computed results are normalized to its maximum value for ease of comparison. The results of the radial and axial components of the electric field are plotted in Figure 4 and Figure 5, respectively.

Near the boundary of the domain, less efficient PML used will cause significantly small reflection back to the domain which can be seen in Figure 4(a). Analytical method is not susceptible to this problem, thus small difference is noticeable between analytical solution with COMSOL and FDTD near the end of $\rho = 10$ mm and. COMSOL method which shows more deviation than FDTD toward analytical method has less efficient PML. Secondly, Figure 5(a) shows that large difference between FDTD with analytical method at $z = 1.1$ mm, but good agreement with COMSOL simulation. The difference is due to the absence of fringing effect in analytical solution. Also in Figure 5(b), considerable difference with FEM and analytical is noticeable at $z = 21.1$ mm, mainly due to strong forces at the tip. Overall the agreement between simulator’s results with 2 other methods is good.

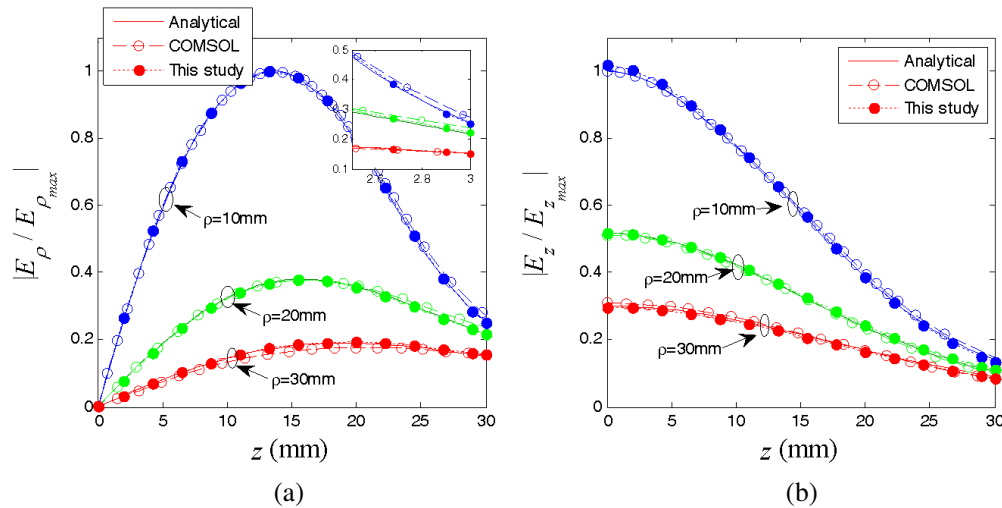


Figure 4: Electric field near insulated monopole normalized to maximum at cross section parallel to z -axis. (a) E_ρ and (b) E_z .

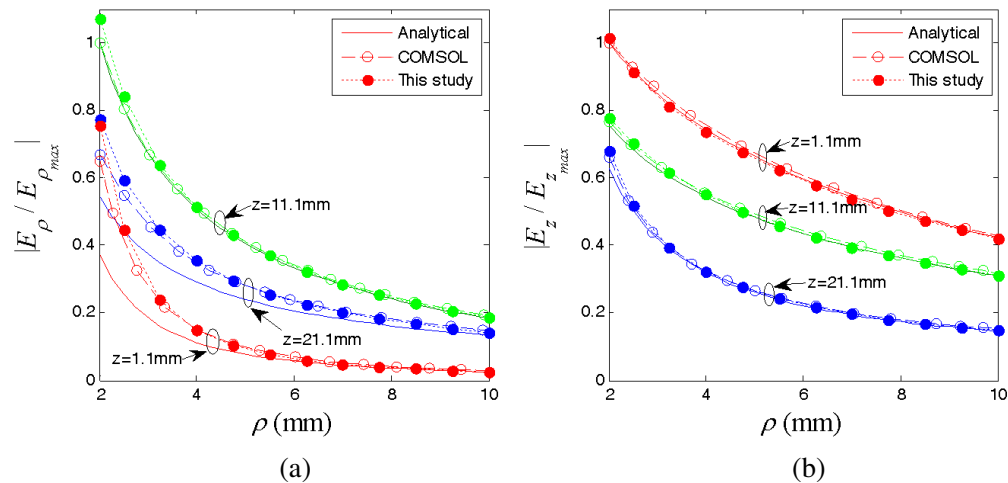


Figure 5: Electric field near insulated monopole normalized to maximum at cross section parallel to ρ -axis. (a) E_ρ and (b) E_z .

Input impedance, Z_{in} at driving point ($z = 0$) for analytical solution is obtained from characteristic impedance using the simple transmission line theory [7] and further corrected for its fringing effect. Comparison is made from 1 GHz to 8 GHz and plotted in Figure 6. Simulator's result agrees very well with FEM solution but deviate slightly in reactance, X_{in} at frequency higher than 5 GHz with analytical solution.

Comparison of temperature contour at 43°C surrounding monopole between the FDTD computed results and the COMSOL simulated results was shown in Figure 7. 43°C is the therapeutic temperature for effective hyperthermia treatment. From Figure 7, small difference is noticeable near the tip of the antenna. This is expected as rapid field growth is expected around that region.

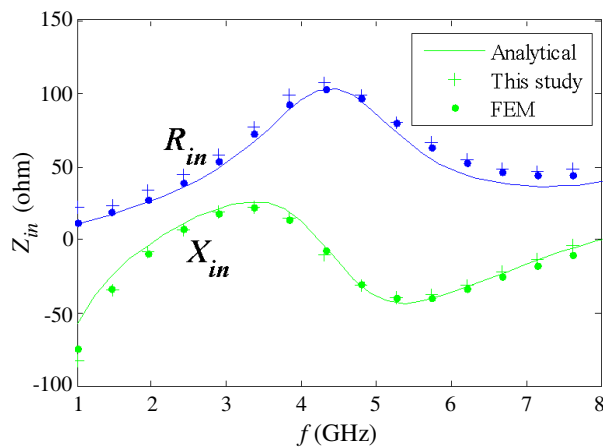


Figure 6: Comparison of simulator's result with analytical solution and FEM method.

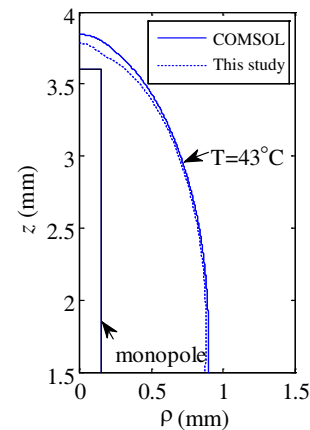


Figure 7: Comparison of temperature contour at 43°C with COMSOL simulation.

4. SIMULATOR'S LIMITATIONS

For the time being, simulator developed is not full-featured where it doesn't support anisotropic material, periodic boundary condition and other excitation mode such as transverse electric (TE) mode. Besides, only uniform grid size can be defined that further compromise the run time of simulation. For example in this study, fine mesh of 0.25 mm is used due to constraint of narrow air gap geometry between catheter and conductor. In fact, non uniform grid size will enable finer mesh defined at critical solution areas (area surrounding the tip and aperture of the monopole), while coarser mesh defined at other solution regions.

5. CONCLUSION

In this study, a FDTD-based simulator with simple GUI specifically caters for coaxial applicator was successfully developed. In future, the limitations above will be improved.

ACKNOWLEDGMENT

This study was supported by the Universiti Teknologi Malaysia and Ministry of Higher Education (MOHE) Malaysia under project number Q.J130000.2523.04H77.

REFERENCES

1. Liebig, T., et al., “OpenEMS — A free and open source equivalent-circuit (EC) FDTD simulation platform supporting cylindrical coordinates suitable for the analysis of traveling wave MRI applications,” *International Journal of Numerical Modelling: Electronic Networks, Devices and Fields*, Vol. 26, 680–696, 2013.
2. He, Z. Z., X. Xue, and J. Liu, “An effective finite difference method for simulation of bioheat transfer in irregular tissues,” *Journal of Heat Transfer-Transactions of the Asme*, Vol. 135, 2013.
3. Sullivan, D. M., *Electromagnetic Simulation Using the FDTD Method*, John Wiley & Sons, 2013.
4. Maloney, J. G., G. S. Smith, and W. R. Scott, “Accurate computation of the radiation from simple antennas using the finite-difference time-domain method,” *IEEE Transactions Antennas and Propagation*, Vol. 38, 1059–1068, 1990.
5. Wissler, E. H., “Pennes’ 1948 paper revisited,” *J. Appl. Physiol.*, Vol. 85, 35–41, 1998.
6. Schiesser, W. E. and G. W. Griffiths, *A Compendium of Partial Differential Equation Models: Method of Lines Analysis with Matlab*, Cambridge University Press, 2009.
7. King, R. W., B. Trembly, and J. Strohbehn, “The electromagnetic field of an insulated antenna in a conducting or dielectric medium,” *IEEE Trans. Microwave Theory Tech.*, Vol. 31, 574–583, 1983.

Shielding and Mutual Coupling Effect of Ground Penetrating Radar Antenna

M. N. A. Karim^{1,2}, M. F. A. Malek², M. F. Jamlos²,
F. S. Abdullah², H. A. Halim², and H. Nornikman³

¹School of Computer and Communications Engineering, Universiti Malaysia Perlis
Main Campus UniMAP, Pauh Putra, Arau 02600, Malaysia

²School of Electrical System Engineering, Universiti Malaysia Perlis
Main Campus UniMAP, Pauh Putra, Arau, Perlis 02600, Malaysia

³Department of Telecommunication Engineering

Faculty of Electronic and Computer Engineering, Universiti Teknikal Malaysia, Melaka, Malaysia

Abstract— This paper discusses the shielding and mutual coupling effect of ground penetrating radar (GPR) antenna for buried object detection. In this study, bi-static radar system is considered. The antenna used in this system is designed at wide operational frequency, 0.5 GHz to 3.0 GHz. To observe the shielding effect and mutual coupling between antennas, two antennas with the same operating frequency are placed in an individual shielded box. The study is accomplished using Computer Simulation Technology (CST) software. The antenna is designed using substrate Taconic TLY-5 with dielectric constant of 2.2 and thickness of 1.57 mm. The study and discussion includes the simulated results of radiation pattern, reflection coefficient and gain.

1. INTRODUCTION

Ground penetrating radar (GPR) is one of the non-destructive detection methods that have been tremendously explored mainly in the area of research and development. One of the important parts in the GPR system is the antenna itself. In a bi-static radar system, two antennas with the same specifications are used for transmitting and receiving the signal. When the transmitter sends the radio wave signal into the ground, the receiver will capture the reflected signal from the ground.

Generally, the antenna performance usually affected by mutual coupling and signal from other sources. As a result, the position or the distances between two antennas need to be considered [1–3].

Figure 1 shows the proposed GPR antenna. The antenna is shielded to minimize the coupling effect between antennas and isolate the antenna from undesired signals in the air.

As shown in Fig. 2, the signal is travelling from a transmitter to a receiver along a number of paths. The purpose of shielding is to selectively enhance some signals and suppress others. This study leads to the objectives of [2]:

- Maximize the energy on the path AA' to and from subsurface target (i.e.: focus on direct signal downward).

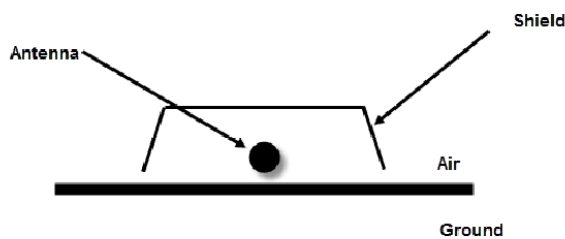


Figure 1: A shielded ground penetrating radar (GPR) antenna.

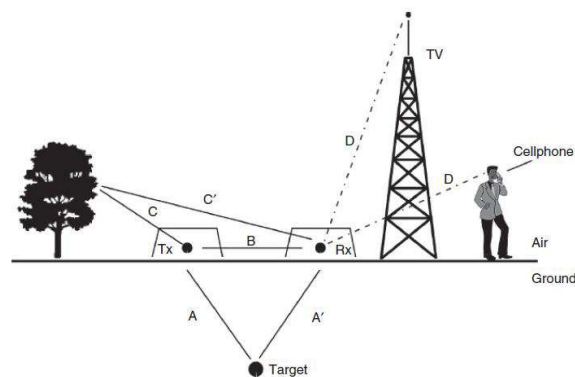


Figure 2: A Ground Penetrating Radar (GPR) system emits and detects radio wave signals. There are many possible signals and paths and the objective to maximize the target response and minimize others.

- b. Minimize the direct transmitter to receiver energy on path B.
- c. Minimize the energy that escape into the air as on path CC'.
- d. Minimize external EM noise as indicated by signal D.

2. DESIGN

The proposed GPR antenna is designed and simulated using Computer Simulation Technology software (CST). All the dimension of the proposed antenna with and without casing are shown in Table 1. The distance between antennas without casing, d_1 is 250 mm while distance between shielded antenna is 150 mm. The distance for both antennas is optimized to obtain a good results in term of return loss, gain and coupling effect and these antenna operates at 0.5 GHz until 3.0 GHz which is suitable for GPR applications. The formula for circular patch antenna was used to calculate the dimension of the antennas [4].

$$a = \frac{F}{\left\{1 + \frac{2h}{\pi\epsilon_r} \left[\ln\left(\frac{\pi F}{2h}\right) + 1.7726\right]\right\}^{1/2}} \quad h \text{ must be in cm} \quad (1)$$

where,

$$F = \frac{8.791 \times 10^9}{f_r \sqrt{\epsilon_r}} \quad (2)$$

Table 1: Dimension of dual separated GPR antenna.

Descriptions	Dimension (mm)
l_1	200
l_2	50
l_3	200
w_1	200
w_2	320
d_1	250
d_2	150
r_1	75

3. RESULT AND DISCUSSION

Figure 4 shows the reflection coefficient, S_{11} and transmission coefficient, S_{21} of the proposed antennas. The antennas with and without shielded box give a similar results across 0.5 GHz to 3.0 GHz. The optimization of the antenna parameters and gap for both antennas is depending on resonant frequency. The closer the antennas will give more directives but will introduce higher mutual coupling effect which will degrade the performance of the antennas.

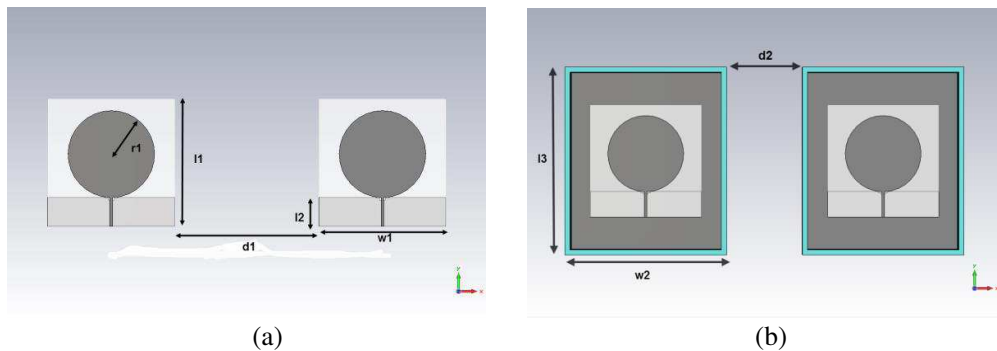


Figure 3: Dual separation antenna, (a) without casing, (b) with casing.

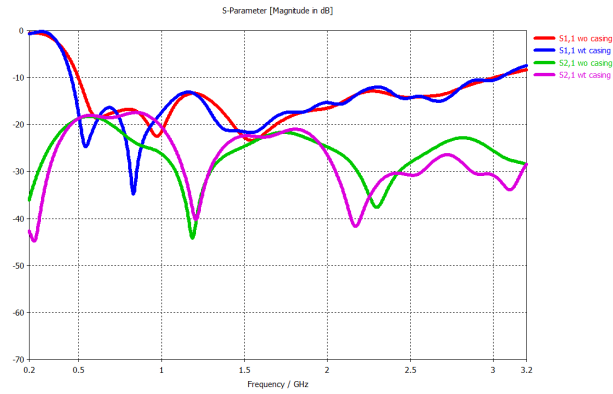


Figure 4: S-parameter for GPR antenna with and without casing.

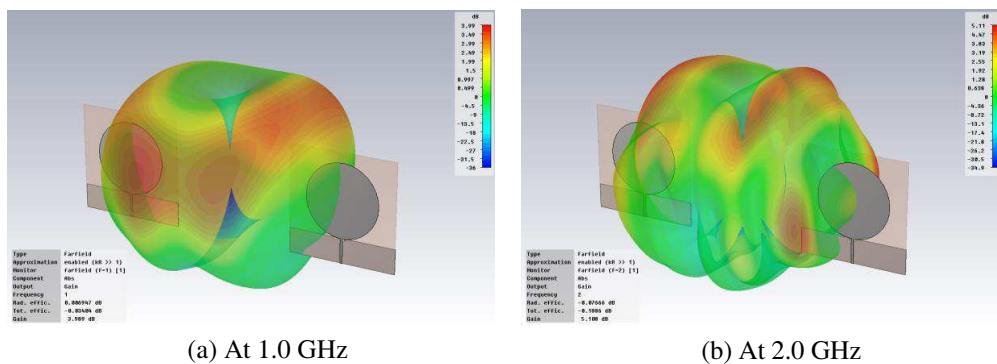


Figure 5: Radiation pattern of GPR antenna without casing at 1.0 GHz and 2.0 GHz.

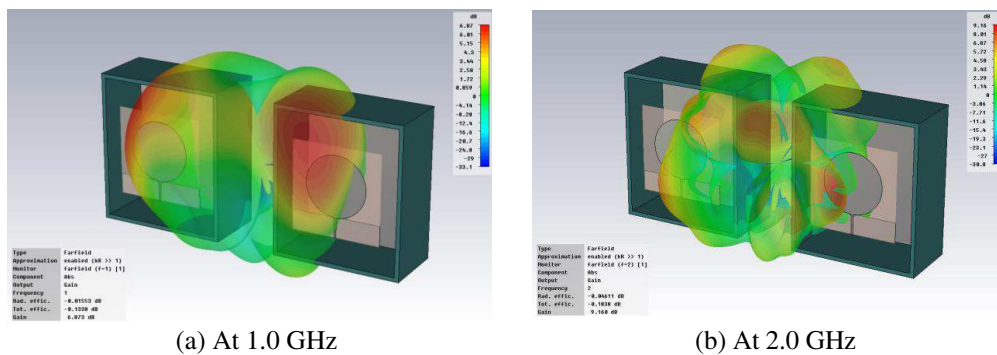


Figure 6: Radiation pattern of GPR antenna with casing at 1.0 GHz and 2.0 GHz.

Figures 5 and 6 show the simulated radiation pattern at 1.0 GHz and 2.0 GHz for shielded and unshielded GPR antennas. As can be seen, the gain of the antenna rise up to 6.68 dB and 9.17 dB at 1.0 GHz and 2.0 GHz compared to unshielded antenna respectively. This is due the reaction of the shielding effect which reflect the back lobe radiation to the front indirectly increase the gain of the antennas. So that, instead of eliminate the unwanted signal from various sources, the function of the shielded box also can increase the gain of the antennas.

4. CONCLUSION

Shielding and mutual coupling effect of Circular patch ground penetrating radar antenna which operates at 0.5 GHz until 3.0 GHz is discuss in this paper. The performance of the shielded antenna is better compared unshielded in term of radiation pattern and gain which increase 4 dB to 5 dB. Shielded antenna also can avoid antenna from receive undesired signal in the air.

REFERENCES

1. Daniels, D. J., *Ground Penetrating Radar*, 2nd Edition, D. N. Steward and P. H. Griffiths, Eds., The Institute of Electrical Engineers, 2004.
2. Annan, A. P., *Ground Penetrating Radar Principles, Procedures and Applications*, Sensor & Software Inc., 2003.
3. Jol, H. M., *Ground Penetrating Radar Theory and Applications*, Elsevier, 2009.
4. Balanis, C. A., *Antenna Theory Analysis and Design Book*, 2nd Edition, John Wiley, 1997.
5. Li, L., A. E. Choon Tan, K. Jhamb, and K. Rambabu, “Buried object characterization using ultra-wideband ground penetrating radar,” *IEEE Transaction on Microwave and Techniques*, Vol. 60, No. 8, Aug. 2012.
6. Cao, P., Y. Huang, and J. Zhang, “A UWB monopole antenna for GPR applications,” *6th European Conference on Antenna and Propagations, EuCAP*, 2012.
7. Agrawall, N. P., G. Kumar, and K. P. Ray, “Wideband planar monopole antennas,” *IEEE transaction Antenna and Propagation*, Vol. 46, 1998.
8. Atteia, G. E., A. A. Shaalan, and K. F. A. Hussein, “Wideband partially-covered Bowtie antenna for ground penetrating radar,” *Progress In Electromagnetics Research*, Vol. 71, 211–226, 2007.

Detection of Low-level Electromagnetic Signal of Partial Discharge by Means of Disturbed Acquisition Discrimination

P. Drexler¹, M. Cap¹, P. Fiala¹, M. Steinbauer¹, M. Kaska², and L. Kocis³

¹Brno University of Technology, Czech Republic

²TES, Trebic, Czech Republic

³EGU HV Laboratory, Praha, Czech Republic

Abstract— The article presents a new approach to the detection of a very weak electromagnetic (EM) signal, which is generated by partial discharge (PD) in a high-voltage, oil-filled power transformer. The new technique is based on the discrimination of signal acquisitions disturbed by interference; this procedure enables the desired weak signal to pass for further processing. The method was verified via an experiment, in which very short electrical pulses were injected in the transformer vessel by the antenna. The weak pulse signals were successfully detected in the presence of high level of interference.

1. INTRODUCTION

The electric energy is at the present (and in near future will be also) produced in central facilities, from which is transported after transformation into the place of consumption. The transition to the new decentralized energy sources will be rather consecutive [1]. The interface between the energetic facility and place of consumption plays an important role. Pivotal parts of these interfaces are high voltage power transformers. The security and reliability issues of energetic transformers have been intensively solved by research community [2, 3]. Critical transformer component is dielectric oil filling, which ensures isolation and cooling. The quality of oil filling is degraded due to activity of partial discharges (PD). Sudden failures in transformers isolation filling usually leads to energy delivery drop-out. It could lead to blackouts in severe cases of combined failures.

Various diagnostic methods for transformer condition determination have been developed. Each of these suffers from some disadvantages. The recent technology development and the availability of hi-tech instrumentation have opened new opportunities to employment of advanced diagnostic methods, as the radiofrequency (RF) method is [4]. RF method is based on the sensing, evaluation and source localization of the EM signal in UHF range. Therefore, it is frequently called the UHF method. Our group has developed an UHF method based diagnostic system for detection and localization of partial discharge activity, as described in [5].

One of the intensively solved aspects of UHF method is design and properties of suitable UHF sensors [10] for pulsed broadband signals and optimal design of high frequency signal processing chain [11]. The initial phase of PD activity is typical with a relatively low magnitude of its apparent charge, which could range from circa 100 pC. Such PD would generate relatively weak EM radiation. One of the often mentioned advantages of the UHF methods is that the PD radiated signals are sensed in metal transformer vessel. This will ensure efficient EM shielding and the weak PD signal could be therefore detected. However, experiments made by our group [6] have shown the presence of critical points on the vessels, which allows penetration of the outer EM disturbance [7]. One of the points was the connection of the sensing heads to the vessel. This has been solved by the installation of efficient EM shielding [8] (shown in Fig. 1(a)). It has allowed the suppression of the disturbance of remote sources. The second critical input point represents length compensative collars in the high voltage feedings encapsulation (bushing). However, more serious effect has been observed. Due to the imperfection of high voltage feedings installation on the inner isolators, a strong sparking activity is present in the bushings. Generated pulsed EM signal propagates into the vessel through the bushings and it is added to the weak PD EM signal. The above described shielding couldn't avoid this problem and the signal level of expected PD activity was still below the level of the interference.

2. DESCRIPTION OF NEW METHOD FOR LOW-LEVEL PD SIGNAL DETECTION

In order to overcome the above mentioned issue a new method for weak PD signal detection has been proposed and verified. The method exploits the multi-trigger ability of the diagnostic system (this means that the signal acquisition can be triggered by the signal threshold-crossing in any of

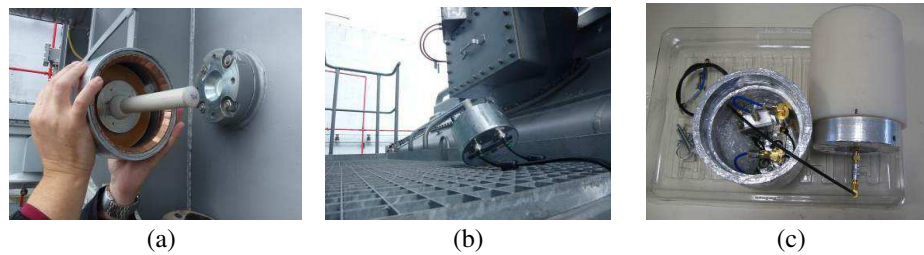


Figure 1: (a) Sensing head with EM gasket, (b) installed under the bushing collar, (c) disassembled external sensor.

the four channels simultaneously). One of the sensing head was removed from its vessel inlet and it was positioned near the place, where the interfering signal exits the feeding bushing (under the bushings collar, Fig. 1(b)). The signals acquisition procedure was initiated and the signal gain of sensing heads was set on suitable level. Now the acquisitions, which were recorded by the trigger from the outer head, were discriminated for further processing. Only acquisitions triggered from the vessel installed heads were stored and displayed. By this way, the outer disturbance was eliminated from the overall signal processing. Subsequently, the gain of the vessel installed heads was increased up to the level, where weak residual signals could be observed. In order to use high signal gain, the sensing heads have to be equipped with additional signal limiters, since residual strong interfering signal can occur.

After the method verification, a special purpose external sensor has been developed, which is shown in Fig. 1(c). The external sensor is based on the same components as the sensing heads. Within the transformer diagnostic procedure, the external antenna is installed in the vicinity of the transformer and senses the outer disturbing signal. In this case, only three vessel installed heads are used. Nevertheless, this is sufficient for the signal source localization. Following the successful verification, the method for PD signal detection by means of disturbed acquisition discrimination has been implemented into the control software of the system [9].

3. DETECTION OF ARTIFICIAL LOW-LEVEL SIGNAL

The diagnostic system development and detection method verification were conducted on the series of block transformer 15 kV/400 kV. The transformers have been recently put into operation and the quality of the oil filling was high. Therefore no PD activity was observed, despite of the new method utilization. In order to prove the ability of the low level EM signal detection, artificial pulses have been injected into the vessel by means of an antenna installed in the vacant inlet. The negative going pulse has been produced by avalanche transistor generator. The peak value of the pulse was -5.9 V, falling edge of the pulse was 300 ps and the FWHM (full width at the half of maximum) of the pulse was 700 ps. The pulse waveform is shown in Fig. 2(a). The radiated pulse has simulated the EM signal generated by PD in view of its waveform, time duration and spectral characteristic also. The calculated amplitude spectrum of the pulse is shown in Fig. 2(b). The

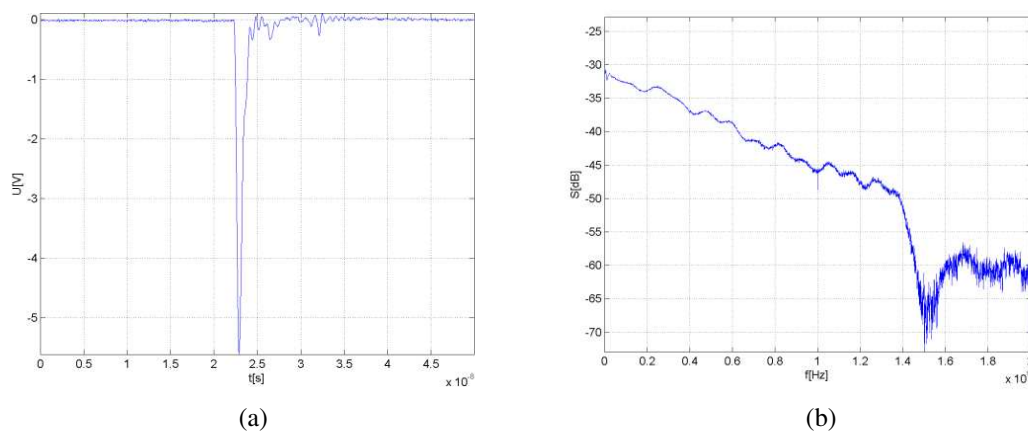


Figure 2: The waveform of (a) the artificial pulse signal and (b) its amplitude spectrum.

pulse generator has been built into the shielding cover and equipped with the same antenna as the sensing heads.

Following procedure of low level signal detection consist of two steps. In the first step, the all sensing heads (4) were installed into the inlets. The measurement and localization of the strong disturbing signal, which source is outside the vessel, was performed. The acquired waveforms of the disturbing signal are shown in Fig. 3(a) and the signal source localization is shown in Fig. 3(b). It is apparent that the signal comes from the first input feeding bushing. Therefore, the external antenna was installed close to the first input feeding bushing in the second step. The pulse transmitting head was installed into the third inlet in the transformer vessel and the diagnostic software has been switched over the mode of low-level signal detection by means of disturbed acquisition discrimination.

The transmitting head was switched on. Now the acquisitions interfered by the disturbing signal from the bushing were discriminated and only the acquisitions triggered by the signals from vessel installed heads were processed. The example of such acquisition is shown in Fig. 4(a). The third signal is missing, since this receiving channel is used for the external head signal, which is discriminated. The following signal source localization is shown in Fig. 4(b). It is obvious, that the result indicates the correct position of the transmitting head in the third inlet.

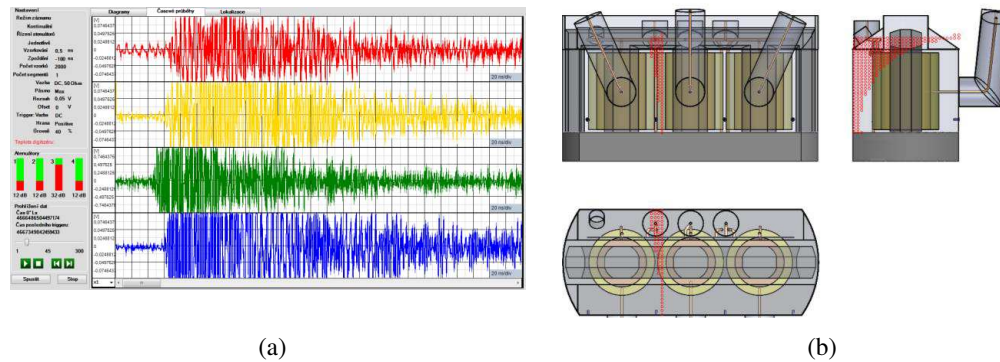


Figure 3: Acquired waveforms of (a) the disturbing signal and (b) its source localization.

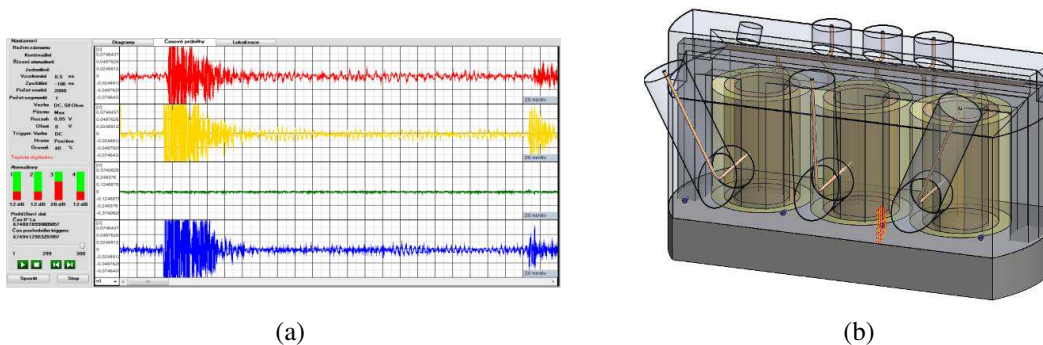


Figure 4: Acquired waveforms of (a) the artificial pulse signal and (b) its source localization.

In order to evaluate the sensitivity of the method in view of assumed apparent charge value of PDs a simple, straightforward consideration was proceeded. The consideration assumes, that the PD represents a charge transport through certain impedance. The similar case is the charge transport through the input impedance of pulse transmitting antenna. The difference is that the electromagnetic radiation effect will be more efficient in case of PD, since the antenna reflects some portion of the signal due to non-perfect matching. If we simply consider a real character of antenna's input impedance Z_i , then we can deduce the current waveform through this impedance $i(t) = u(t)/Z_i$. The waveform will be same as in Fig. 2(a). The current is defined as the transported charge during a time interval $i(t) = dQ(t)/dt$. It can be deduced from previous relations that the total charge transported through the antenna's input impedance is $Q = (1/Z_i) \int u(t)dt$. This rapidly transported charge causes an electromagnetic wave radiation as in case of PD. If we apply

the charge relation on the voltage waveform in Fig. 2(a), we find the charge value $Q = 94$ pC. It has to be noted, that for given pulse waveform the power of radiated wave will be proportional to 94 pC in the ideal case only, when antenna's input impedance will be real and perfectly matched. In real case, we obtain radiated wave, which power magnitude is lower and it is proportional to lower value of the charge than 94 pC. Therefore, we can estimate, that for the used antenna with known reflection coefficient, the equivalent apparent charge will be 30–50 pC. According to this result, we can conclude, that if we are able to detect above described artificial pulses in the environment with the presence of strong interference, we are able to detect the weak radiated signal of PD's with apparent charge in the order of tens pC also.

4. CONCLUSIONS

The UHF method is one of the most promising methods for transformer diagnostic in view of PD activity monitoring. Its advantage is the possibility of on-line PD detection and PD localization. However, several precautions have to be adopted. The EM signal of the PD is weak. Therefore the influence of outer, PD non-related pulse disturbance has to be taken into account. A great advantage in sensitivity improvement and interference immunity attainment is the developed method of disturbed acquisition discrimination. The method has been verified during an on-site measurement, where low-level pulsed signal, comparable to weak PD signal, has been detected and its source has been localized.

ACKNOWLEDGMENT

The research described in the paper was performed within the grant of Czech ministry of industry and trade No. FR-TI1/001, it was financially supported by project of the BUT Grant Agency FEKT-S-14-2545/2014 and by the project Education for Competitiveness Operative Programme CZ.1.07.2.3.00.20.0175.

REFERENCES

1. Fiala, P. and P. Drexler, "Power supply sources based on resonant energy harvesting," *Microsystem Technologies-Micro- and Nanosystems-Information Storage and Processing Systems*, Vol. 18, No. 7–8, 1181–1192, 2012.
2. Dalarsson, M. and M. Norgren, "First-order perturbation approach to elliptic winding deformations," *Proceedings of International Symposium on Electromagnetic Theory*, 13–16, Hiroshima, Japan, 2013.
3. Dalarsson, M., A. Motevasselian, and M. Norgren, "Using multiple modes to reconstruct conductor locations in a cylindrical model of a power transformer winding," *International Journal of Applied Electromagnetics and Mechanics*, Vol. 41, No. 3, 279–291, 2013.
4. Fiala, P., T. Jirku, P. Drexler, and P. Dohnal, "Detection of partial discharge inside of HV transformer, modeling, sensors and measurement," *PIERS Proceedings*, 1013–1016, Cambridge, USA, July 5–8, 2010.
5. Myška, R. and P. Drexler, "Simulation and verification of methods for partial discharge source localization," *PIERS Proceedings*, 704–708, Kuala Lumpur, Malaysia, March 27–30, 2012.
6. Drexler, P., M. Cap, R. Myška, P. Fiala, M. Steinbauer, and T. Kriz, "Proposal of technical measures for a partial discharge detection system based on real measurement," *PIERS Proceedings*, 1233–1236, Taipei, March 25–28, 2013.
7. Szabo, Z., J. Sedlacek, and M. Hadinec, "Optimization method of EMI power filters and its measurement," *PIERS Proceedings*, 1085–1088, Hangzhou, China, March 24–28, 2008.
8. Szabo, Z. and P. Fiala, "Characterisation and testing shielding fabrics," *PIERS Proceedings*, 1273–1276, Moscow, Russia, August 18–21, 2009.
9. Cap, M., P. Drexler, R. Myška, and P. Fiala, "Software for partial discharge and localization," *PIERS Proceedings*, 48–52, Taipei, March 25–28, 2013.
10. Lopez-Roldan, J., T. Tang, and M. Gaskin, "Optimisation of a sensor for onsite detection of partial," *IEEE Transactions on Dielectrics and Electrical Insulation*, Vol. 15, No. 6, 1634–1639, 2008.
11. Reid, A. K. and M. D. Judd, "Ultra-wide bandwidth measurement of partial discharge current pulses in SF₆," *Journal of Physics D — Applied Physics*, Vol. 45, No. 16, 2012.

A Novel Design of Ku Band Coaxial-waveguide Directional Coupler Used for the Measurement of the Short-circuited Line Method

Qijia Liu, Chao Wang, Binjie Tao, and En Li

University of Electronic Science and Technology of China, Chengdu, China

Abstract— An effective method was proposed to design a high power coaxial-waveguide directional coupler applied to the short-circuited line method. In this paper, the coupler designed using the proposing method has wide band, high directivity, flat coupling coefficient, lower SWR, and low requirement for machining accuracy. According to the required technology parameter, preliminary designed the aperture waveguide directional coupler and the adapter. In order to achieve the more excellent indices, we simulate and optimize the distance between the two hole and the two ends hole size of the coupler, the step size of the adapter. The VSWR of coaxial-waveguide transition designed in this paper is less than 1.06 in the 12.4–18 GHz octave bandwidth, and the high modulus produced is very small. Therefore, coaxial-waveguide directional coupler of the directivity and the coupling coefficient are improved.

1. INTRODUCTION

In the field of microwave measurement we need the coaxial-waveguide transitions which are playing an important role in microwave system and critical passive microwave components in Radar equipment, precision guidance and microwave testing circuit. Moreover, we need the Directional couplers in the measurement to sample the signal. In order to convenient our measurement we integrate the two components- the coaxial-waveguide transitions and the waveguide Directional couplers into one part. It has an excellent simulation result which VSWR is less than 1.05, the error between the simulation value of coupling and the required value -14 dB is less than 0.8 dB. It also has well performance in engineering application for Ku band measurement instrument of Terminal short-circuit.

2. THE BASIC THEORY AND ANALYSIS

We integrate the part in our design and the theory in each will be analysis in the following illustration.

In this paper, the design of coaxial-waveguide transitions is based on the utilization of a rectangular cavity and a cylinder probe with conical part, a 4-step Chebyshev-response impedance transformer was designed using the combination construction with single ridge waveguide and reduced size rectangular waveguide. Design formulas resulting in an equal ripple or Chebyshev-type response were given by Cohn, Collin [1], and Riblet, and were experimentally verified.

Figure 1 shows the designed structure of the coaxial-waveguide transitions. It has two critical parts that are stepped impedance transformer and mode converter. We know that the characteristic impedance of rectangular waveguide is more a function of frequency than a constant value in the traditional theory. Hence we need a multi-step matching transformer to satisfy such extreme high impedance ratio and the wide fractional bandwidth. There are 4 steps in the aforementioned structure. The first step is for the selection of the waveguide cross section on the basis of its characteristic impedance and guided wavelength. The combination construction with single-ridge waveguide (the first-step) and reduced size waveguide (the second-, third- and fourth-step) was employed to frame a 4-section Chebyshev response quarter-wave transformer [2]. The part of Single-ridge waveguide has been used to satisfy the compatibility between the conventional circular coaxial and the rectangular waveguide. The characteristic impedance of each step has been computed [3]. Calculation by HFSS, we can know wave impedance is $Z = 298$ Ohm which correspond the center frequency is $f_0 = 15.2$ GHz. The length l of each section in terms of the guide wavelengths in that section is defined by:

$$\begin{aligned}\Gamma(\theta) &= 2e^{-jN\theta} [\Gamma_0 \cos N\theta + \Gamma_1 \cos (N-2)\theta + \dots + \Gamma_n \cos (N-2n)\theta + \dots] \\ &= Ae^{-jN\theta} T_N(\sec \theta_m \cos \theta)\end{aligned}\quad (1)$$

As we know, $N = 4$. So we can obtain

$$\Gamma(\theta) = 2e^{-j4\theta} \left[\Gamma_0 \cos 4\theta + \Gamma_1 \cos 2\theta + \frac{1}{2}\Gamma_2 \right] = Ae^{-j4\theta} T_4(\sec \theta_m \cos \theta)\quad (2)$$

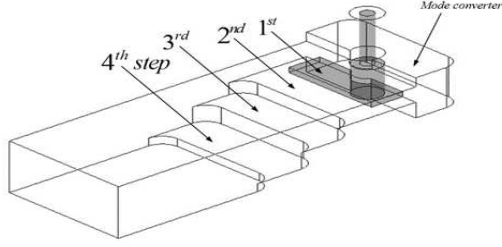


Figure 1: The structure of the coaxial-waveguide transitions.

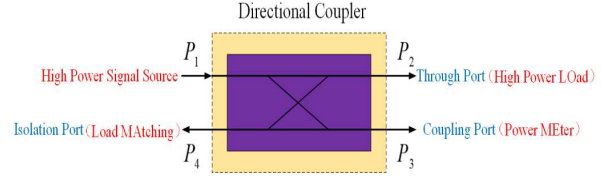


Figure 2: Structure of high power waveguide directional coupler.

As $A = \Gamma_m = 0.05$ and

$$\sec \theta_m = \cosh \left[\frac{1}{N} \operatorname{ar} \cosh \left(\frac{\ln Z_L/Z_0}{2\Gamma_m} \right) \right] = \cosh \left[\frac{1}{4} \operatorname{ar} \cosh \left(\frac{\ln 298/50}{2 \times 0.05} \right) \right] = 1.4251 \quad (3)$$

We can obtain

$$\begin{aligned} 2 \left[\Gamma_0 \cos 4\theta + \Gamma_1 \cos 2\theta + \frac{1}{2} \Gamma_2 \right] &= A \left[\sec^4 \theta_m (\cos 4\theta + 4 \cos 2\theta + 3) - 4 \sec^2 \theta_m (\cos 2\theta + 1) + 1 \right] \\ &= A \sec^4 \theta_m \cdot \cos 4\theta + (4A \sec^4 \theta_m - 4A \sec^2 \theta_m) \cdot \cos 2\theta + (3A \sec^4 \theta_m - 4A \sec^2 \theta_m + A) \end{aligned} \quad (4)$$

The corresponding coefficient equation can be obtained

$$\begin{aligned} 2\Gamma_0 &= A \sec^4 \theta_m \Rightarrow \Gamma_0 = \Gamma_4 = 0.1031 \\ 2\Gamma_1 &= 4A \sec^4 \theta_m - 4A \sec^2 \theta_m \Rightarrow \Gamma_1 = \Gamma_3 = 0.2094 \\ \Gamma_2 &= 3A \sec^4 \theta_m - 4A \sec^2 \theta_m + A \Rightarrow \Gamma_2 = 0.2625 \end{aligned} \quad (5)$$

So when $n = 0$, we can obtain

$$\begin{aligned} \ln Z_1 &= \ln Z_0 + 2\Gamma_0 = \ln 50 + 2 \times 0.1031 = 4.1182 \Rightarrow Z_1 = 61.4485 \text{HFSS} \Rightarrow l_1 = 1.63 \text{ mm} \\ n = 1, \ln Z_2 &= \ln Z_1 + 2\Gamma_1 = 4.537 \Rightarrow Z_2 = 93.4101 \Rightarrow l_2 = 2.48 \text{ mm} \\ n = 2, \ln Z_3 &= \ln Z_2 + 2\Gamma_2 = 5.062 \Rightarrow Z_3 = 157.906 \Rightarrow l_3 = 4.19 \text{ mm} \\ n = 3, \ln Z_4 &= \ln Z_3 + 2\Gamma_3 = 5.4808 \Rightarrow Z_4 = 240.038 \Rightarrow l_4 = 6.38 \text{ mm} \end{aligned} \quad (6)$$

where Γ is the reflection coefficient, and we can approximately compute the length of each section with formulas (1) to (6).

In this paper, we also referred to the waveguide directional couplers. As is shown in the Figure 2, the coupler is a network with 4 ports which are the input port, through port, coupling port and isolation port.

There are four main index-coupling, isolation, direction and bandwidth-to weigh the performance of the coupler. Here are the calculating method of the four parameter

(1) Coupling

$$C = 10 \cdot \lg \frac{P_3}{P_1} = 20 \cdot \lg |S_{31}| \text{ (dB)} \quad (7)$$

(2) Isolation

$$I = 10 \cdot \lg \frac{P_4}{P_1} = 20 \cdot \lg |S_{41}| \text{ (dB)} \quad (8)$$

(3) Direction

$$D = 10 \cdot \lg \frac{P_4}{P_3} = 20 \cdot \lg |S_{43}| \text{ (dB)} \quad (9)$$

(4) Bandwidth

Bandwidth refers to the frequency range design index of directional coupler are meet the requirements.

3. OPTIMIZATION AND RESULTS

In Figure 3, we provided the model designed and simulated by the HFSS. In our model, port 1 is the input port which the signal fed, and port 3 is the coupling port which used to connect our waveguide device.

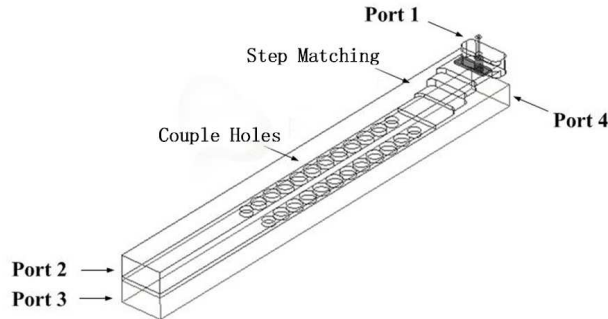


Figure 3: The model of the coaxial-waveguide we designed.

In Figures 4(a)–(c), we given the result of our simulation. In the Figure 4(a), the fluctuate of its couple coefficient is less than 1 dB (the couple coefficient we design is -13 dB). As is shown in Figure 4(b), the worst isolation of the coupler is -35 dB. In Figure 4(c), it is shown that the VSWR of the coupler is less than 1.1 which is better than 1.3 we needed in practice.

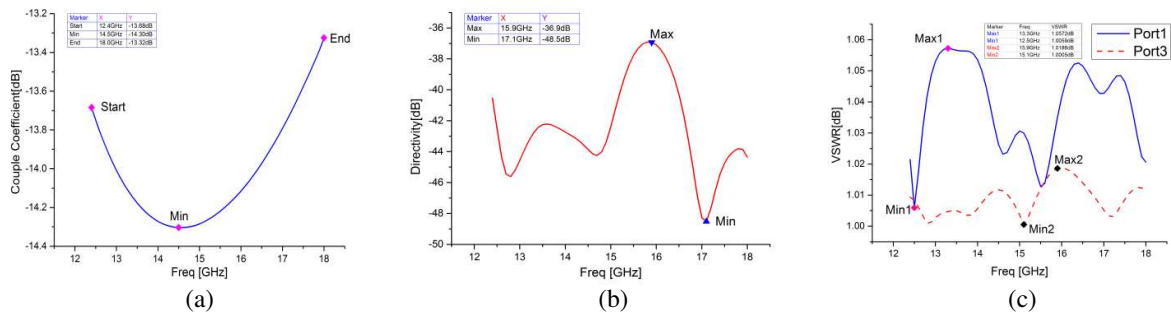


Figure 4: (a) The couple coefficient. (b) The directivity of the coupler. (c) The VSWR of the coupler.

As the result can satisfy our requirements, we processed the real product which is shown in Figure 5.

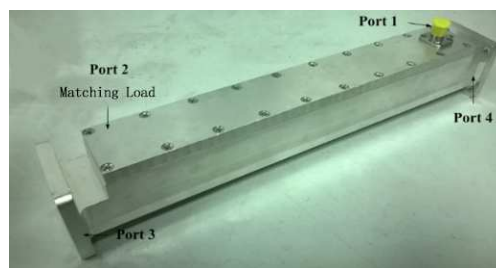


Figure 5: The real product of the coupler.

We measure our real product using Agilent E8363A and the result of the measurement of the coupler is shown in Figures 6(a)–(c). From the measurement, the range of the couple coefficient shown in Figure 6(a) is -12.4 dB \sim -13.4 dB which means that the fluctuate of the couple coefficient is less than 1 dB, the isolation coefficient shown in Figure 6(b) is less than -40 dB, the VSWR shown in Figure 6(c) is less than 1.20.

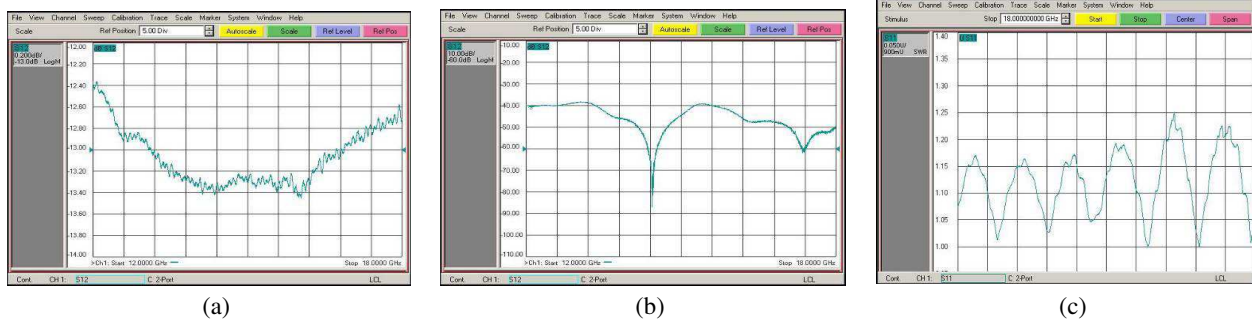


Figure 6: (a) The couple coefficient. (b) The isolation coefficient. (c) The VSWR of the coupler.

4. CONCLUSION

It is easy to discover that there are some difference when compare the result of simulation with the result of measurement. For instance, the curves have some difference when compare Figure 4(b) with Figure 6(b). In Figure 4(c), the VSWR is less than 1.05, while the VSWR in Figure 6(c) is less than 1.2. Here we put forward several reasons that may contribute to the difference. The first reason is machine error such as the inner wall smoothness of the waveguide, which could affect the performance of the device. At the same time, if the impedance transformer can not machine accurately, there must be some influence on the VSWR. The second reason is the connection between the adapter and the coupler. The performance may be worse if the adapter and the coupler cannot mate tightly when we using the VNA to measure the coupler.

REFERENCES

1. Collin, R. E., *Field Theory of Guided Wave*, 323–332, McGraw-Hill, New York, 1961.
2. Wang, Y., “An X-band coaxial-to-rectangular waveguide transition,” *Microwave Technology and Computational Electromagnetics*, 129–131, 2011.
3. Collin, R. E., “Theory and design of wide-band multisession quarter-wave transformers,” *Proc. IRE Trans. on Microwave Theory and Techniques*, Vol. 3, 16–21, Apr. 1955.
4. Xing, Z. N., “Optimal design of Ka waveband directional coupler,” *Electronic Test*, Vol. 6, 53–56, 2010.
5. Bethe, H. A., “Theory of diffraction by small holes,” *Phys. Rev.*, Vol. 66, 163–182, 1944.

Nanoscale Plasmonic Switch at Far Infrared Frequencies Using Graphene

Jieer Lao¹, Jin Tao^{2,3}, Qi Jie Wang^{2,3}, and Xu Guang Huang¹

¹Laboratory of Photonic Information Technology

South China Normal University, Guangzhou 510006, China

²OPTIMUS & NOVITAS, School of Electrical and Electronic Engineering

Nanyang Technological University, 50 Nanyang Avenue, Singapore 639798, Singapore

³CDPT, Centre for Disruptive Photonic Technology, School of Physical and Mathematical Sciences
Nanyang Technological University, Singapore 637371, China

Abstract— Nanoscale plasmonic switch based on graphene at far infrared frequencies are proposed and designed. Mode-guiding switching/mode-cutoff analyses are given for the modulation function. High modulation depth and bandwidth can be obtained. This plasmonic graphene-based switch can be used to promote the performance of current switches in the integrated optical field, providing another method for interconnect in ultrahighly integrated photonic circuits.

1. INTRODUCTION

Graphene, a single sheet of sp²-bonded carbon atoms, has attracted much attention due to its outstanding and intriguing properties [1]. The electro-optical switches using graphene have been the subject of much interest both theoretically and experimentally in the recent years [2, 3]. However, most of them are based on electro-absorption, which is relied on the modulation of the interband or intraband transition. Less work has been done in the electro-refraction with different Fermi level, which can also be employed in the modulation mechanism.

In this paper, we provide a different principle and method, the gate-voltage-controlled mode-guiding switching/mode-cutoff mechanism, to achieve the modulation function. The proposed structure has the advantages of large modulation depth and width bandwidth, which can be used to promote the performance of current switches in the integrated optical field, providing another method for interconnect in ultrahighly integrated photonic circuits.

2. MODELING AND NUMERICAL RESULTS

Electronic and optical characteristics of 2D graphene as a function of frequency, temperature, and carrier density have been analytically and experimentally studied in many papers [4–6]. The complex surface conductivity of graphene including intraband and interband transitions is estimated within the random-phase approximation [7] as:

$$\sigma(\omega) = \frac{2ie^2k_B T}{\pi\hbar^2(\omega + i\tau^{-1})} \ln \left[2 \cosh \left(\frac{E_f}{2k_B T} \right) \right] + \frac{e^2}{4\hbar} \left\{ \frac{1}{2} + \frac{1}{\pi} \arctan \left(\frac{\hbar\omega - 2E_f}{2k_B T} \right) - \frac{i}{2\pi} \ln \left[\frac{(\hbar\omega + 2E_f)^2}{(\hbar\omega - 2E_f)^2 + (2k_B T)^2} \right] \right\}. \quad (1)$$

Here \hbar is the reduced Planck's constant, ω is the angular frequency, τ is the carrier relaxation time, k_B is the Boltzmann constant, T is the temperature. Surface plasmon polariton (SPP) waves can be supported in a 1D slab waveguide constructed with an ideal graphene sheet sandwiched between dielectric mediums above and below. Under the condition of space wave vector $k_0 \ll k_{sp}$, the effective index N_{eff} of the 1D graphene waveguide can be approximately calculated as follows, based on Eq. (4) in Ref. [4]:

$$N_{eff} \equiv k_{sp}/k_0 = \varepsilon_0 \frac{\varepsilon_{r1} + \varepsilon_{r2}}{2} \frac{i2\omega}{\sigma(\omega)}, \quad (2)$$

where k_0 and k_{sp} are respectively vacuum and the plasmon wave vectors, and ε_{r1} and ε_{r2} are the dielectric constants of the mediums above and below the graphene, respectively. By applying different voltage patterns to the graphene strip, guiding or cut-off modes with low or high attenuation coefficient can be formed.

As can be seen in Figure 1, a monolayer graphene sheet is sandwiched between two aluminum oxide buffer layers forming a 1D field confinement in the y -direction. Three gold-plated silicon gating pads and an end layer are on top and bottom of the structure, respectively, providing another 1D field confinement along the x -direction and dividing the structure into the core and cladding sections. By altering the voltages applied to the graphene to form different Fermi level patterns, in the on state, the SPP waves will be confined within the core region due to higher effective index of the core than the surrounding cladding layers. In the off state, by decreasing the Fermi level in the cladding, the vast majority of energy will diffuse to the cladding, only small fraction of energy remains in the core.

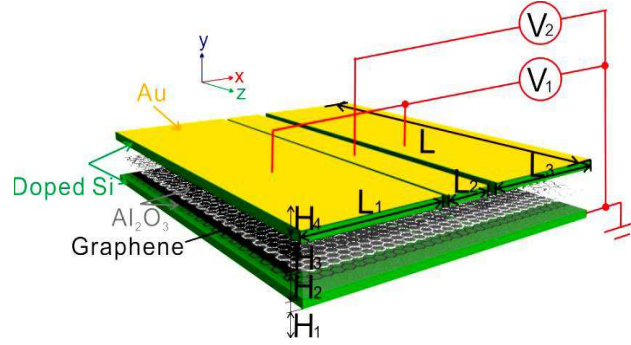


Figure 1: Schematic of the plasmonic switch configuration. The height of each layer is $H_1 = H_4 = 10$ nm, $H_2 = H_3 = 50$ nm. The width of the gating pads are $L_1 = L_3 = 650$ nm, $L_2 = 200$ nm and the length of the waveguide is $L = 500$ nm. This switch is fabricated on silicon substrate, which is not shown in the figure. The thickness of graphene is set to be $t_G = 0.6$ nm with the relaxation time of $\tau = 0.25$ ps, the working temperature is $T = 300$ K. Voltages will be applied to the silicon gating pads to adjust the Fermi level. Here V_1 stands for the voltage applied to the core and V_2 stands for the voltage applied to the cladding.

The finite-difference time-domain (FDTD) method is used to evaluate the optical performance with the working frequency $f = 37$ THz. Here the Fermi level in the core section is always kept at 0.6 eV while that in the cladding section are set to be 0.8 eV and 0.2 eV in the on and off states, respectively. Figure 2 shows the normalized light intensity profiles in the x - z plane. As N_{eff} is inversely proportional to the square of E_f , in the on state, the SPP waves are mainly confined in the core and the attenuation coefficient is $\alpha_{on} = 4.0$ dB/ μm (Fig. 2(a)). Inversely in the off state, the effective index discontinuity “pull” the energy from the core to the cladding and providing higher attenuation coefficient $\alpha_{off} = 25.4$ dB/ μm . As a result, up to 21.5 dB/ μm modulation depths can be achieved. 3-dB modulation depth can be satisfied as short as 139.8 nm.

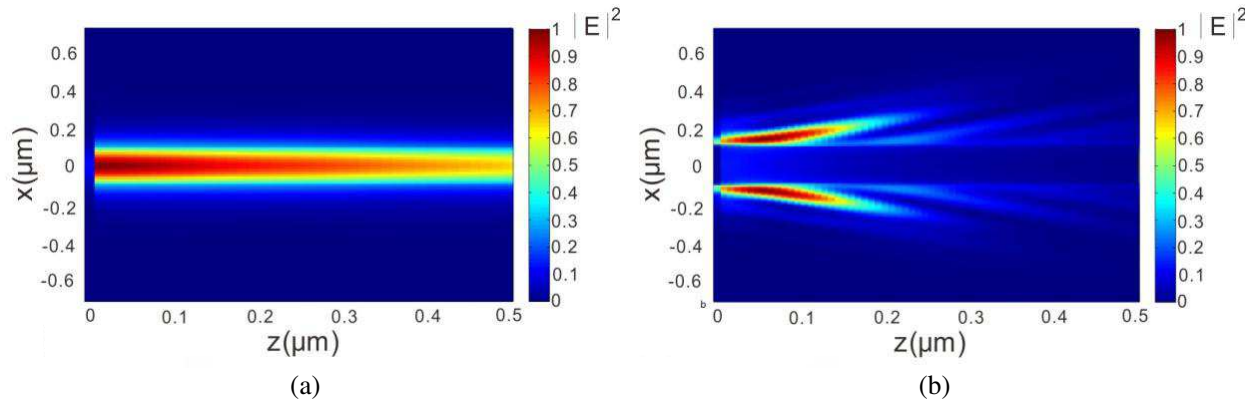


Figure 2: Normalized light intensity propagation profiles of the structure under different Fermi level in the cladding $E_{f,cladding}$: (a) $E_{f,cladding} = 0.8$ eV, (b) $E_{f,cladding} = 0.2$ eV. The Fermi level in the core is always kept at $E_{f,core} = 0.6$ eV. The working frequency is fixed at $f = 37$ THz.

Figure 3 shows the attenuations of the structure in the on and off states, respectively. The structure we propose was studied in the 35–50 THz range. It can be seen that the attenuation stays low in the on state for $E_{f,cladding} = 0.8$ eV while having large difference in the off state for

$E_{f,cladding} = 0.2 \text{ eV}$. More than 15 THz can be achieved, showing good performance in term of the bandwidth.

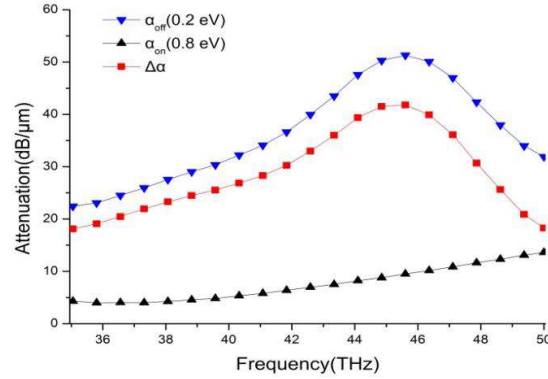


Figure 3: Attenuations of the structure as the function of frequency for $E_{f,cladding} = 0.2, 0.8 \text{ eV}$, respectively. The Fermi level of the core is fixed at $E_{f,core} = 0.6 \text{ eV}$.

3. CONCLUSION

We have proposed and designed the nanoscale plasmonic switch based on graphene at far infrared frequencies. By altering the voltages applied to the graphene to form different Fermi level patterns, guiding or cut-off modes with low or high attenuation can be formed. Our result shows that the switch has the large modulation depth and can be operated in a wide bandwidth, showing great potential in future integrated circuits.

REFERENCES

1. Geim, A. K. and K. S. Novoselov, *Nat. Mater.*, Vol. 6, 183–191, 2007.
2. Lu, Z. L. and W. S. Zhao, *J. Opt. Soc. Am. B*, Vol. 29, 1490–1496, 2012.
3. Gosciniak, J. and D. T. H. Tan, *Nanotechnology*, Vol. 24, 185202, 2013.
4. Jablan, M., H. Buljan, and M. Soljagic, *Phys. Rev. B*, Vol. 80, 245435, 2009.
5. Yao, Y., M. A. Kats, P. Genevet, N. Yu, Y. Song, J. Kong, and F. Capasso, *Nano Lett.*, Vol. 13, 1257–1264, 2013.
6. Tao, J., X. Yu, B. Hu, A. Dubrovkin, and Q. J. Wang, *Opt. Lett.*, Vol. 39, 271–274, 2014.
7. Falkovsky, L. A. and S. S. Pershoguba, *Phys. Rev. B*, Vol. 76, 153410, 2007.

Digital Multi-channel High Resolution Phase Locked Loop under Influence of Potential System Uncertainties

Mohamed Rizk, Shawky Shaaban, Usama Aboul-Nadar, and Alaa El-Din Sayed Hafez
Alexandria University, Alexandria, Egypt

Abstract— This paper is devoted to present a multi-channel, high resolution, fast lock phase locked loop (PLL) for surveillance radar applications under influence of system noise. Phase detector based PLLs are simple to design, suffer no systematic phase error, and can run at the highest speed. Reducing loop gain can proportionally improve jitter performance, but also reduces locking time and pull-in range. The system is studied under influence of system noise in the range from 5 to 30 dB to reflect the reliability of the system under these conditions. The results perform a comparison of noise power, VCO control input, Lock time, ISE and ITSE Performance indices for three selective channels among 38 channels operated in the desired frequency range. The results show superiority of the system in difficult operating conditions.

1. INTRODUCTION

Phase-locked loops (PLLs) are used in surveillance radar wave formers to implement a radar waveform synthesis. The major concerns in the design of PLLs are noise or jitter performance and the lock time. G. David [1], describe two simply implemented frequency detectors which, when added to the traditional phase detector, can improve acquisition even for very small loop bandwidths and large initial frequency offsets. Kurt M. Ware et al. [2] presents a numerical system simulation program that explores the time-domain behaviour of an idealized model based on the phase-locked loop design. Faster lock is attained while maintaining the PLL's gain/phase margin characteristics by B. David et al. [3]. Kent Kundert [4], presents a methodology for predicting the jitter performance of a PLL using simulation. Several researches introduce an improvement for the jitter and frequency lock time [5–11] but not consider multi-channel, high resolution PLLs Digital phase-locked loop (DPLL) design one of most active research topics in complex digital communication systems. It replaces traditional PLL designs, a charge-pump and voltage controlled oscillator (VCO) [12]. A new method for tracking narrowband signals acquired via compressive sensing is designed in Ref. [13]. This paper presents a multi-channel, high resolution PLL for surveillance radar systems based on developing the charge pump by a digital adaptive gain processor to achieve fast lock times while improving jitter performance in lock. Section 2 provides a theoretical analysis of the frequency synthesis and the phase locked loop. Section 3 briefly describes the proposed PLL architecture. Section 4 introduces a discussion about potential system uncertainties. Definition of the performance indices introduced in Section 5. Section 6 discusses the results and a summary is in Section 7.

2. THEORETICAL DESCRIPTION

The PLL is a well-established method for tracking the frequency and phase of a signal $s(t)$ using a feedback loop to continuously update an estimate of the signal. Figure 1 shows a general PLL architecture. In general, phase locking uses three component operations as generically depicted below,

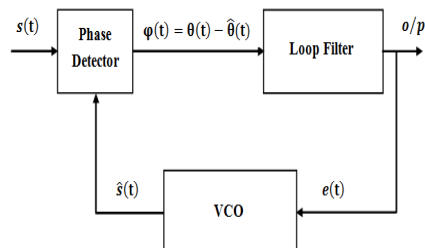


Figure 1: General phase locked loop architecture.

Phase-error generation — this operation, sometimes also called “phase detection,” derives a phase difference between the received signal’s phase $\theta(t)$ and the receiver estimate of this phase, $\hat{\theta}(t)$. The actual signals are [14],

$$s(t) = \cos(\omega_{to} + \theta(t)) \quad (1)$$

and

$$\hat{s}(t) = \cos(\omega_{to} + \hat{\theta}(t)) \quad (2)$$

but only their phase difference is of interest in synchronization. This difference is often called the phase error,

$$\square(t) = \theta(t) - \hat{\theta}(t) \quad (3)$$

3. THE PROPOSED PLL ARCHITECTURE

The proposed PLL synthesizes 51 frequency channels from 1.250 to 1350 MHz with frequency separation of 2 MHz. The general architecture of the proposed digital PLL is demonstrated in Figure 2. The synthesized frequency is divided by 625 to 675 corresponds to 51 frequency channel to produce 20 MHz signal compared with 20 MHz reference signal via XOR operation. The error signal from the comparator will be filtered with cut-off frequency of 100 kHz. The Butterworth filter is the best compromise between attenuation and phase response. It has no ripple in the pass band or the stop band, and because of this is sometimes called a maximally flat filter as shown in Figure 3. The output from the filter is converted to digital format in order to adaptively scale the error signal through adaptive digital multiplier. The block diagram of the designed digital compensator is shown in Figure 4. The digital multiplier scales the input signal according to the channel frequency code according to the following formula,

$$V(f) = U(f) * (\alpha N + \beta) \quad (4)$$

where $U(f)$ is the LPF output, α, β constants equal to 0.038, -17.75 respectively, N is the frequency division ratio of the selected operation frequency.

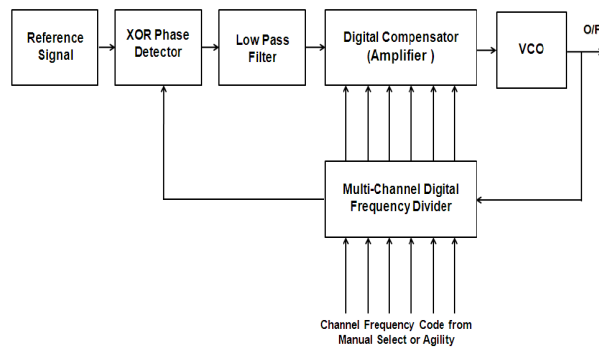


Figure 2: General architecture of the proposed PLL.

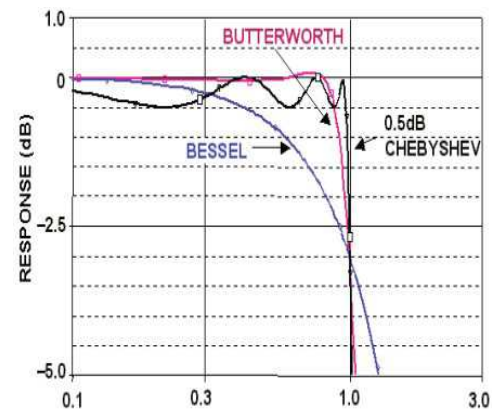


Figure 3: Comparison of amplitude response of Bessel, Butterworth, and Chebyshev filters.

4. POTENTIAL SYSTEM UNCERTAINTIES

A control system design assumes knowledge of the model of the plant and controller and constant parameters. The plant model will always be an inaccurate representation of the actual physical system because of parameter changes, unmodeled dynamics, sensor noise, and unpredicted disturbance inputs. The goal of robust systems design is to retain assurance of system performance in spite of model inaccuracies and changes. A system is robust when the system has acceptable changes in performance due to model changes or inaccuracies [16, 17]. The system structure that incorporates potential system uncertainties is shown in Figure (5). This model includes the sensor

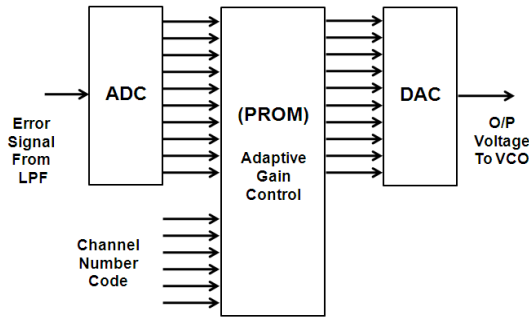


Figure 4: Digital compensator block diagram.

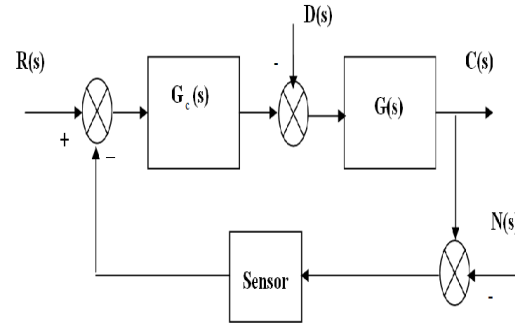


Figure 5: Closed-loop structural diagram.

noise $N(s)$, the unpredicted disturbance input $D(s)$, and a plant $G(s)$ with potentially unmodeled dynamics or parameter changes. The unmodeled dynamics and parameter changes may be significant or very large, and for these systems, the challenge is to design a system that retains the desired performance.

5. PERFORMANCE INDICES

Increasing emphasis on the mathematical formulation and measurement of control system performance can be found in the recent literature on automatic control. Modern control theory assumes that the systems engineer can specify quantitatively the required system performance. Then a performance index can be calculated or measured and used to evaluate the system's performance. A quantitative measure of performance of a system is necessary for automatic parameter optimization of a control system, and for the design of optimum systems [18, 19]. Whether the aim is to improve the design of a system or to design a control system, a performance index must be chosen and measured. A performance index is a quantitative measures of the performance of a system chosen so that emphases, is given to the important system specifications. A system is considered an optimum control system when the system parameters are adjusted so that the index reaches an extreme value, commonly a minimum value. A performance index, to be useful, must be a number that is always positive or zero. Then the best system is defined as the system that minimizes this index. A Suitable performance index is the integral of the square of the error, ISE, which is defined as:

$$\text{ISE} = \int_0^T e^2(t)dt \quad (5)$$

The upper limit T is the finite time chosen somewhat arbitrarily so that the integral approaches a steady-state value. It is usually convenient to choose T as the settling time, This performance index is designated the integral of the time multiplied by absolute error, ITAE. Another similar index is the integral of time multiplied by the squared error, ITSE:

$$\text{ITSE} = \int_0^T te^2(t)dt \quad (6)$$

A control system is optimum when the selected performance index is minimized. However, the optimum value of the parameters depends directly on the definition of optimum, that is, the performance index.

6. RESULTS

The proposed architecture is simulated using Matlab program Simulink. Next, we evaluate the effectiveness of the proposed technique. We assume that the frequency channels changes dynamically from Channel 1 to channel 51 with fixed and adaptive gain for comparison purpose. Figure 6 shows the transient time for the control signals which feed to the VCO in case of three selected channels for example. It is clear from the figure that it is no overshoot, all the channel are stable and reach the desired frequency value, and the lock times of the desired channels are between $7 \mu\text{sec}$

for the first channel and 11.5 μsec for the last channel. The simulation block diagram is shown in Figure 7. The system is studied under influence of system noise in the range from 5 to 30 dB to reflect the reliability of the system under these conditions. The system uncertainties are simulated as a Wight noise added to the control signal as shown in Figure 8. The noise power has considered

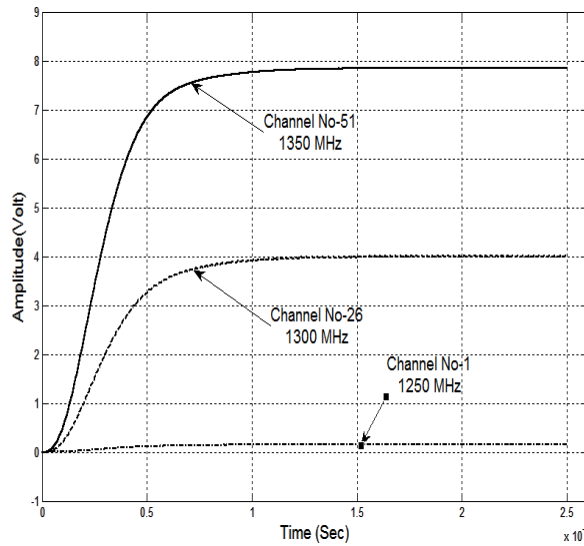


Figure 6: Control action transient.

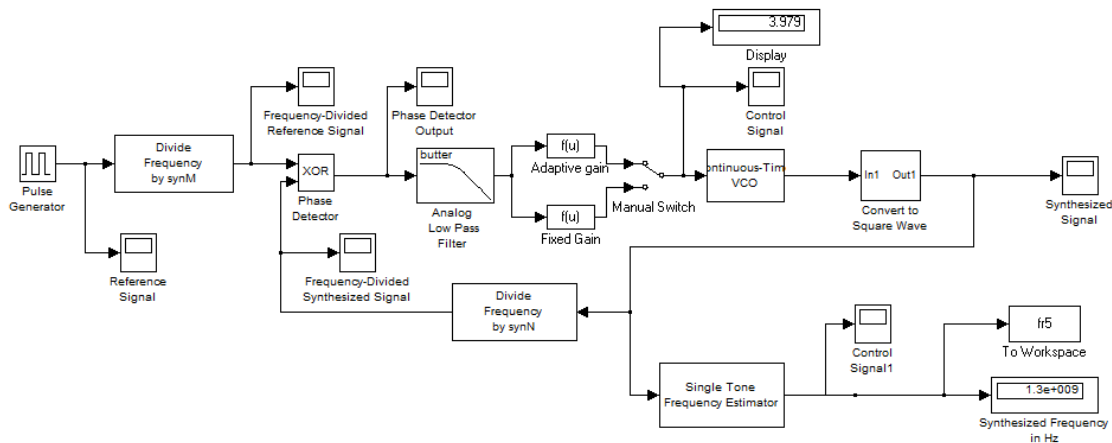


Figure 7: PLL Simulink block diagram.

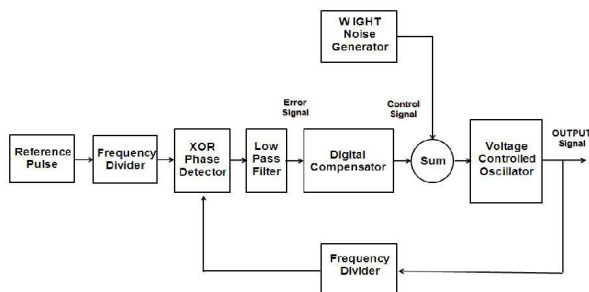


Figure 8: PLL with uncertainties.

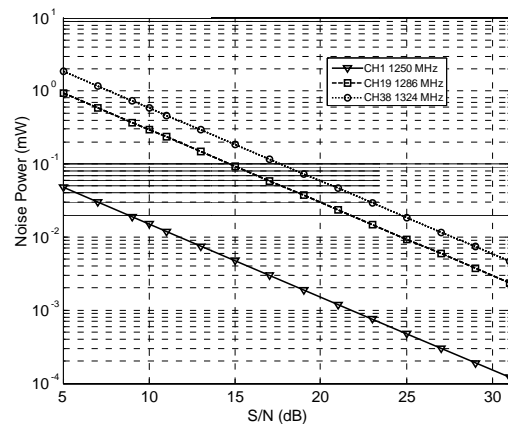


Figure 9: Noise Power versus S/N for three channels.

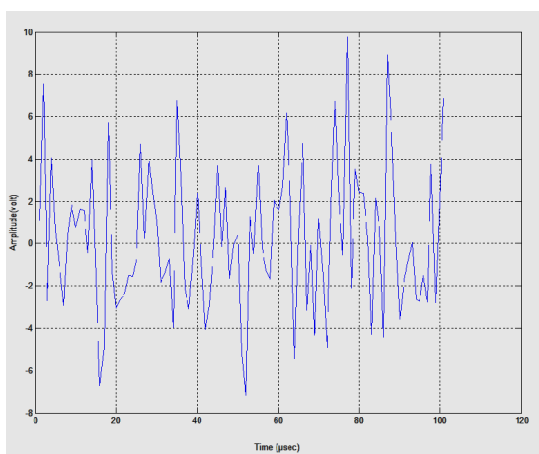


Figure 10: Shape of Wight noise.

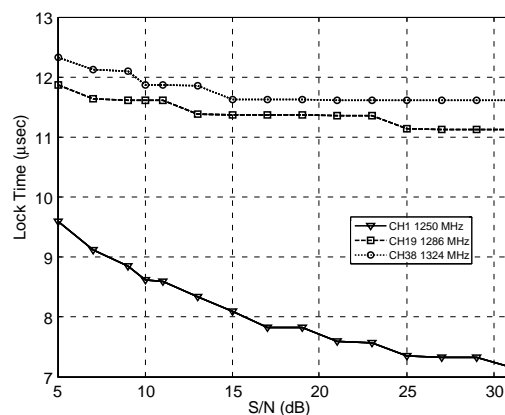


Figure 11: Lock time versus S/N for three channels.

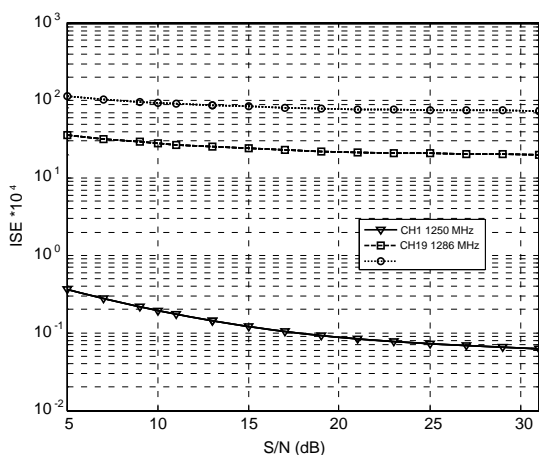


Figure 12: ISE index versus S/N for three channels.

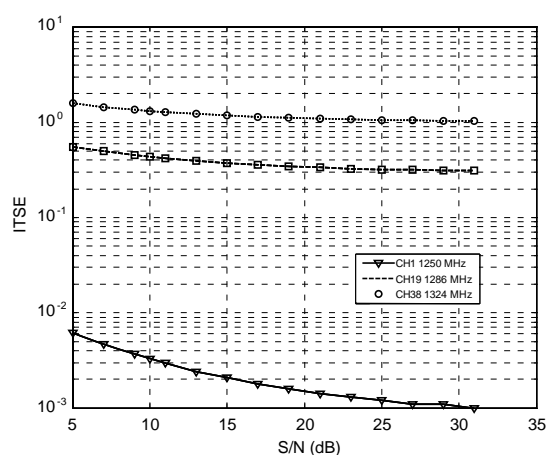


Figure 13: ITSE index versus S/N for three channels.

value corresponding to S/N ratio as shown in Figure 9 for three selected channels. When the noise showed in Figure 10 is added to the control signal, only the first 38 channels are completely stable and have a lock time $9.58 \mu\text{sec}$ for the first channel, and lock time $12.325 \mu\text{sec}$ for the last channel as shown in Figure 11. The proposed system is considered an optimum control system when the system parameters are adjusted so that the performance index reaches a minimum value. The two performance index ISE, and ITSE which discussed in Section 5, are used to test the optimality of the system under influence of system noise. Figures 12, 13 show that the performance indices is decreased when the S/N ratio increase.

7. CONCLUSION

This paper presents a multi-channel, high resolution PLL for surveillance radar systems based on developing the charge pump by a digital adaptive gain processor to achieve fast lock times while improving jitter performance in lock. The design also improves the frequency agility capability of the radar system. The results show a fast lock, high resolution PLL with transient time less than $12.325 \mu\text{sec}$ which is suitable for radar applications. The proposed system is tested under influence of system noise in the range from 5 to 30 dB. The results show superiority of the system in difficult operating conditions.

REFERENCES

1. David, G., "Frequency detectors for PLL acquisition in timing and carrier recovery," *IEEE Transaction on Communication*, Vol. 27, No. 9, 1979.
2. Ware, K. M., H.-S. Lee, and C. G. Sodini, "A 200-MHz CMOS phase-locked loop with dual phase detectors," *IEEE Journal of Solid State Circuits*, Vol. 24, No. 6, Dec. 1989.

3. Byrd, D., C. Davis, and W. O. Keese, “A fast locking scheme for PLL frequency synthesizers,” *National Semiconductor*, Jul. 1995.
4. Kundert, K., “Modeling and simulation of jitter in PLL frequency synthesizers,” *Cadence Design Systems*, 1998.
5. Perrott, M. H., “Behavioral simulation of fractional- N frequency synthesizers and other PLL circuits,” *11th International Biennial Baltic, Electronics Conference*, 2008.
6. Kong, C., “Delay locked loops — An overview,” *Phase Locking in High Performance Systems*, IEEE press, 2003.
7. Chan, M. J., A. Postula, Y. Ding, and L. Jozwiak, “A bang-bang PLL employing dynamic gain control for jitter and fast lock times,” *Journal of Analog Integrated Circuits and Signal processing*, Vol. 49, No. 2, Oct. 2006.
8. Zhou, G., S. Shetty, G. Simms, and M. Song, “PLL based time synchronization in wireless sensor networks,” *IEEE International Conference On Embedded And Real Time Computing Systems And Applications*, 2010.
9. Kuo, C.-C., M.-J. Lee, I.-C. Tsai, C.-N. J. Liu, and C.-J. Huang, “An accurate PLL behavioral model for fast Monte Carlo analysis under process variation,” *IEEE International Workshop on Behavioral Modeling and Simulation, BMAS 2007*, 2007.
10. Jung, H. and M. Pedram, “Continuous frequency adjustment technique based on dynamic workload prediction,” *21st International Conference on VLSI Design, VLSID 2008*, 2008.
11. Woo, K., Y. Liu, E. Nam, and D. Ham, “Fast-lock hybrid PLL combining fractional- N and integer- N modes of differing bandwidths,” *IEEE Journal of Solid-State Circuits*, Vol. 43, No. 2, Feb. 2008.
12. Kim, M. S., Y.-B. Kim, and K.-K. Kim, “All-digital phased-locked loop with local passive interpolation time-to-digital converter based on a tristate inverter,” *2012 IEEE 55th International Midwest Symposium on Circuits and Systems (MWSCAS)*, 2012.
13. Schnelle, S. R., J. P. Slavinsky, P. T. Boufounos, M. A. Davenport, and R. G. Baraniuk, “A compressive phase-locked loop,” *37th International Conference on Acoustics, Speech, and Signal Processing (ICASSP)*, 2012.
14. Skolnik, M. I., *Radar Handbook*, 2nd Edition, McGraw-Hill, 1990.
15. Mahafza, B. R., *Radar Systems Analysis and Design Using MATLAB*, CRC Press, USA, 2000.
16. Dorato, P., “Case studies in robust control design,” *IEEE Proceedings of the Decision and Control Conference*, 2030–2031, Dec. 1990.
17. Barmish, B. R., *New Tools for Robustness of Linear Systems*, Macmillan Publishing Company, 1994.
18. Dorf, R. C., R. H. Bishop, *Modern Control Systems*, Addison-Wesley Publishing Company, 1995.
19. Haykin, S., *Communication Systems*, John Wiley & Sons, 1978.

TM Wave Mode Analysis of Circular Dielectric Resonator with Anisotropic Permittivity

Hepi Ludiyati^{1,2}, Andriyan Bayu Suksmono¹, and Achmad Munir¹

¹Radio Telecommunication and Microwave Laboratory
School of Electrical Engineering and Informatics, Institut Teknologi Bandung, Indonesia

²Department of Electrical, Politeknik Negeri Bandung, Indonesia

Abstract— This paper presents the theoretical analysis of transverse magnetic (TM) wave mode for circular dielectric resonator with anisotropic permittivity. The analysis which is emphasized on its resonant frequency is required to investigate specific properties of resonator in TM wave mode which are useful for microwave application. By introducing the anisotropic permittivity, the resonator is expected to have the property with unique characteristic compared to the conventional one. To determine the resonant frequency of resonator for TM wave mode, Maxwell's equations with proper boundary condition are applied for circular waveguide that encapsulates an anisotropic circular dielectric resonator. The anisotropic permittivity is established by assuming the different values of relative permittivity in each axis of cylindrical coordinate, i.e., ϵ_ρ , ϵ_ϕ and ϵ_z . The analysis result shows that the circular dielectric resonator with anisotropic permittivity in z axis, i.e., propagation direction, has significantly changed the resonant frequencies of TM wave mode which can be applicable for resonance mode selection.

1. INTRODUCTION

Over 4 decades ago, after being first time introduced by Ritchmyer [1], dielectric resonators have been widely exploited for the implementation in numerous microwave applications including oscillators, filters and antennas [2–4]. One of the important milestones in the dielectric ceramic industry occurred in the mid nineteen seventies when the first temperature-stable, low-loss barium tetratitanate ceramics were developed [5]. Whilst the investigation of their properties in term of artificial dielectrics to explore the unique characteristics for microwave devices, e.g., anisotropic permittivities, has been conducted for a long time. In fact, more than a half century ago, one of the concepts has been expressed for the application of artificial dielectric when a dielectric lens was made by replacing the refractive material using a mixture of metal disks in a matrix [6]. From the concept, some applications based on artificial dielectrics have been proposed with the intention for a plane wave or TEM wave incidence, such as wave absorber, polarizer and phase shifter [7]. Moreover, by use of the artificial dielectric, a rectangular dielectric resonator has been successfully fabricated for the first time [8].

In principle, for various applications the performance of a dielectric resonator depends on its characteristics. This also applies for the dielectric resonator with anisotropic permittivity. In some specific application, it is sometimes required to implement dielectric resonators which have high relative permittivity as well as capability in resonance mode selectivity [9]. The kind of features, i.e., high relative permittivity, is rarely obtainable through simple chemical treatment such as natural dielectric. However, the capability of resonance mode selection needs another treatment which is required to yield dielectric resonators with anisotropic permittivity. One method to obtain the anisotropic permittivity which have been implemented experimentally is by configuring the orientation of constituent materials or particles [8]. In spite of implementation for a rectangular dielectric resonator, the method is also supposed to be applicable for a circular dielectric resonator. In order to have better understanding in the implementation for circular dielectric resonator, i.e., TM wave mode, in this paper, the theoretical analysis of resonance mode for circular dielectric resonator with anisotropic permittivity is investigated with emphasizing on its resonant frequency for the first 3 TM wave modes. Here, the resonant frequency is determined by applying Maxwells equations for a circular waveguide that encapsulates the circular dielectric resonator with different values of relative permittivity in each axis of cylindrical coordinate.

2. CALCULATION OF RESONANT FREQUENCY FOR TM WAVE MODE

In the analysis of resonator characteristics, one of the most essential properties is the resonant frequency which is determined by the value of relative permittivity. The proposed method to calculate the resonant frequency of circular dielectric resonator from its relative permittivity is by

use of a short-open termination [10]. Here, to obtain the resonant frequency of circular dielectric resonator with anisotropic permittivity for the TM wave mode, the resonator is assumed to be homogeneous and follows the standard analysis for an isotropic resonator.

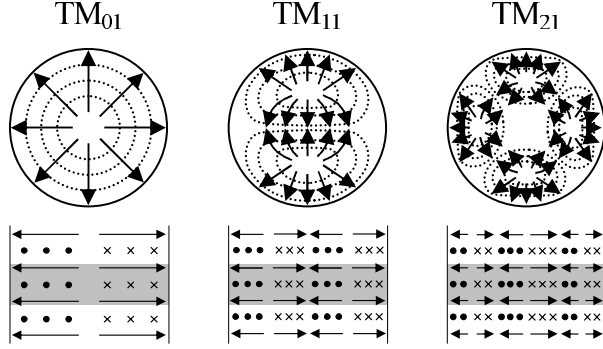


Figure 1: Field distribution of first 3 TM wave modes.

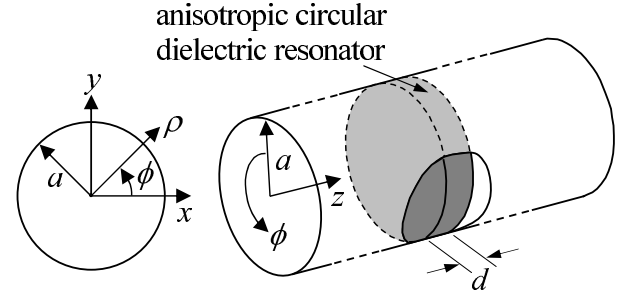


Figure 2: Illustration of resonant frequency calculation for anisotropic circular dielectric resonator.

As shown in Figure 1, field distribution of the first 3 TM wave modes, i.e., TM_{01} , TM_{11} , TM_{21} , are illustrated where the TM_{01} wave mode has a simple one since it has no variation of magnetic field in angular direction. While the depiction of resonant frequency calculation for anisotropic circular dielectric resonator with the radius of a and the thickness of d is indicated in Figure 2 in which the cylindrical coordinate system is the most appropriate one for its analysis in view of cylindrical geometry. The permittivity in term of tensor and the permeability of circular dielectric resonator are expressed in (1).

$$[\epsilon] = \epsilon_0 \begin{bmatrix} \epsilon_\rho & 0 & 0 \\ 0 & \epsilon_\phi & 0 \\ 0 & 0 & \epsilon_z \end{bmatrix}, \quad [\mu] = \mu_0 \quad (1)$$

where ϵ_ρ , ϵ_ϕ and ϵ_z are relative permittivity in the ρ , ϕ and z axes, respectively. Whilst, ϵ_0 and μ_0 are permittivity and permeability in free space, respectively. The field with time variation $e^{(j\omega t)}$ suppressed in the resonator is assumed to propagate in the $+z$ direction as $e^{-(j\beta z)}$. By substituting (1) into the Maxwell's equations with proper boundary condition and solving them with respect to E_z for the TM wave mode, the following equation can be obtained.

$$\frac{\partial^2 E_z}{\partial \rho^2} + \frac{1}{\rho} \frac{\partial E_z}{\partial \rho} + \left(\frac{k_\rho \sqrt{\epsilon_\phi}}{k_\phi \sqrt{\epsilon_\rho}} \right)^2 \frac{1}{\rho^2} \frac{\partial^2 E_z}{\partial \phi^2} + \frac{\epsilon_z}{\epsilon_\rho} k_\rho^2 E_z = 0 \quad (2)$$

where $k_\rho^2 = \omega^2 \mu_0 \epsilon_0 \epsilon_\rho - \beta^2$ and $k_\phi^2 = \omega^2 \mu_0 \epsilon_0 \epsilon_\phi - \beta^2$.

The general solution of (2) known as scalar Helmholtz equation for the electric field in cylindrical coordinate system is given by (3).

$$E_z = R(\rho)\Phi(\phi) \quad (3)$$

By substituting (3) into (2), the relation of $R(\rho)$ and $\Phi(\phi)$ can be obtained.

$$\frac{1}{\rho R} \frac{\partial}{\partial \rho} \left(\rho \frac{\partial R}{\partial \rho} \right) + \frac{1}{\rho^2 \Phi} \left(\frac{k_\rho \sqrt{\epsilon_\phi}}{k_\phi \sqrt{\epsilon_\rho}} \right)^2 \frac{\partial^2 \Phi}{\partial \phi^2} = -\frac{\epsilon_z}{\epsilon_\rho} k_\rho^2 \quad (4)$$

The solution of (4) can be taken from the method of variable splitting. Therefore, (4) can be split into 2 equations as function of ρ and ϕ which have the general solution as expressed in (5) and (6), respectively.

$$R(\rho) = A_1 J_n \left(\frac{\sqrt{\epsilon_z} k_\rho \rho}{\sqrt{\epsilon_\rho}} \right) + A_2 N_n \left(\frac{\sqrt{\epsilon_z} k_\rho \rho}{\sqrt{\epsilon_\rho}} \right) \quad (5)$$

$$\Phi(\phi) = A_3 \sin \left(\frac{k_\phi \sqrt{\epsilon_\rho}}{k_\rho \sqrt{\epsilon_\phi}} n \phi \right) + A_4 \cos \left(\frac{k_\phi \sqrt{\epsilon_\rho}}{k_\rho \sqrt{\epsilon_\phi}} n \phi \right) \quad (6)$$

where J_n and N_n are Bessel and Neumann functions, respectively. After substituting (5) and (6) into (3) and applying proper boundary condition in which the $R(\rho)$ is defined for $\rho < a$ and the value of $\Phi(\phi)$ is suitable for the defined value of $R(\rho)$, thence the solution of E_z in term of time domain which propagates in the $+z$ direction is revealed in (7).

$$E(z, t) = E_{z0} J_n \left(\frac{\sqrt{\epsilon_z}}{\sqrt{\epsilon_\rho}} k_\rho \rho \right) \cos \left(\frac{k_\phi \sqrt{\epsilon_\rho}}{k_\rho \sqrt{\epsilon_\phi}} n \phi \right) e^{j(\omega t - \beta z)} \quad (7)$$

From (7), the related fields in other axes can be calculated from Maxwell's equations. Furthermore, the evanescent fields, i.e., fields outside the resonator, can be obtained by replacing ϵ_ρ , ϵ_ϕ and ϵ_z in (1) with 1 and β with $-j\alpha$. Then, by using the method of short-open termination which is applied at the middle of resonator ($d/2$), the input impedances are calculated to attain the following relation (8).

$$Z_g \tan \left(\beta \frac{d}{2} - \frac{s\pi}{2} \right) = \frac{\alpha}{\omega \epsilon_0} \quad (8)$$

where s and Z_g are the integer number (1, 3, 5, ...) and the wave impedance of resonator for appropriate TM wave mode, respectively.

3. NUMERICAL RESULT AND ANALYSIS

In order to demonstrate the potentiality of anisotropic permittivity, the resonant frequencies of circular dielectric resonator property with for TM_{01} , TM_{11} , TM_{21} wave modes are calculated and compared to the natural circular dielectric resonator. In case of natural circular dielectric resonator, ϵ_ρ , ϵ_ϕ and ϵ_z are replaced by ϵ_r ; whilst k_ρ and k_ϕ are replaced by k_c where $k_c^2 = \omega^2 \mu_0 \epsilon_0 \epsilon_r - \beta^2$ and ϵ_r is the relative permittivity. The relative permittivity of circular dielectric resonator is taken as 5, 5 and 10 for ϵ_ρ , ϵ_ϕ and ϵ_z respectively; while for the natural one it is 5 being isotropic (ϵ_r). The resonator thickness (d) is set from 0.1 mm to 5 mm and the radius (a) is 16.27 mm. The cut-off frequency of hollow circular waveguide itself is 7.058 GHz, 11.246 GHz, and 15.069 GHz for TM_{01} , TM_{11} , and TM_{21} wave modes, respectively. The calculation results of resonant frequency as a function of resonator thickness (d) for TM_{01} , TM_{11} , TM_{21} wave modes are plotted in Figure 3. From the results, it can be seen that the resonant frequencies of circular dielectric resonator with anisotropic permittivity, i.e., ϵ_z higher than ϵ_ρ and ϵ_ϕ , are lower than of natural circular dielectric resonator for TM_{01} , TM_{11} , and TM_{21} wave modes. This means that the anisotropic permittivity in z direction has significant influences in lowering resonant frequency of circular dielectric resonator for TM wave modes.

Furthermore, if the relative permittivity of circular dielectric resonator is taken as 10, 5 and 5 for ϵ_ρ , ϵ_ϕ and ϵ_z respectively, in which ϵ_ρ is higher than others; and the natural one is 5 same as in the previous calculation, the resonant frequencies for first 3 TM wave modes have slightly lower than the natural one for the thickness of resonator thinner than 2 mm. The calculation result is

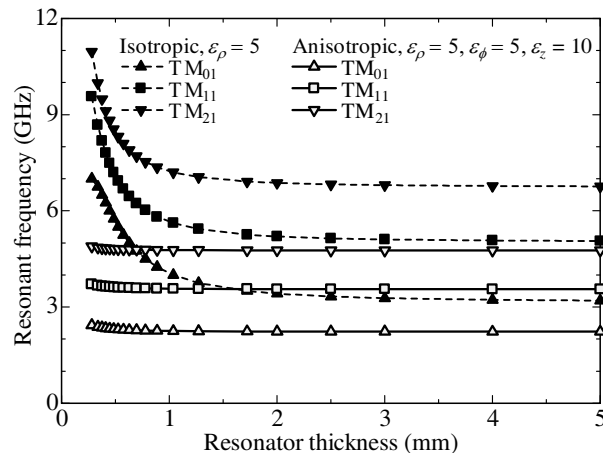


Figure 3: Resonant frequencies of first 3 TM wave modes ($\epsilon_r = 5$ for isotropic, while $\epsilon_\rho = 5$, $\epsilon_\phi = 5$ and $\epsilon_z = 10$ for anisotropic).

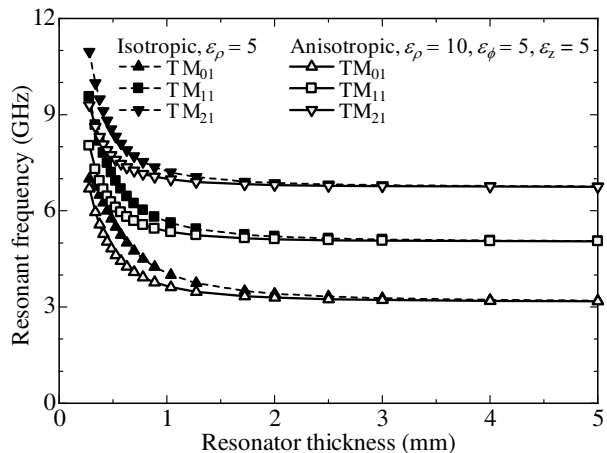


Figure 4: Resonant frequencies of first 3 TM wave modes ($\epsilon_r = 5$ for isotropic, while $\epsilon_\rho = 10$, $\epsilon_\phi = 5$ and $\epsilon_z = 5$ for anisotropic).

shown in Figure 4. From the result, it is noticeable that the anisotropic permittivity in ρ direction will have no effect if the thickness of resonator is more than 0.85 times of the radius. The results in Figures 3 and 4 are satisfied with (7) in which ϵ_z as the nominator plays an important role to the field. Although there is also k_ρ in (7) which covers ϵ_ρ , however its impact is lesser than ϵ_z . From (7), it can also be understood that ϵ_ϕ will have no effect in lowering the resonant frequency for TM wave modes.

4. CONCLUSION

The TM wave mode of circular dielectric resonator with anisotropic permittivity has been analyzed theoretically and compared to the natural one. The analysis result which was emphasized on its resonant frequency for the first 3 TM wave modes has indicated significant improvement for the resonant frequencies of resonator. This is beneficial in microwave application for a resonance mode selection and spurious property enhancement. It has been demonstrated that the anisotropic permittivity in z axis, i.e. propagation direction, has significantly changed the resonant frequencies of circular dielectric resonator. The similar impact was also shown for other anisotropic permittivity in ρ axis for the resonator thickness less than 0.15 times of radius. However, the anisotropic permittivity in z direction has had stronger impact in lowering the resonant frequency than in ρ direction. From the result, it can be concluded that the resonant frequencies of circular dielectric resonator for TM wave modes can be enhanced effectively by changing the relative permittivity in appropriate direction. In near future, FDTD-based computation method using cylindrical coordinate system is still underdevelopment for analyzing the property of circular dielectric resonator with anisotropic permittivity where the comparison results will be reported later.

REFERENCES

1. Richtmyer, R. D., "Dielectric resonators," *J. Appl. Phys.*, Vol. 10, 391–398, 1939.
2. Cohn, S. B., "Microwave bandpass filters containing high- Q dielectric resonators," *IEEE Trans. Microw. Theory Techn.*, Vol. 16, No. 4, 218–227, 1968.
3. O'Bryan, Jr, H. M., J. Thomson, Jr, and J. K. Plourde, "A new BaO-TiO₂ compound with temperature stable high permittivity and low microwave loss," *J. Am. Ceram. Soc.*, Vol. 57, No. 10, 450–453, 1974.
4. Fiedziuszko, S. J., "Microwave dielectric resonators," *Microwave Journal*, Vol. 29, 189–200, 1986.
5. Van Bladel, J., "On the resonances of a dielectric resonator of very high permittivity," *IEEE Trans. Microw. Theory Techn.*, Vol. 23, No. 2, 199–208, 1975.
6. Kock, W. E., "Metallic delay lenses," *Bell Syst. Tech. J.*, Vol. 27, 58–82, 1948.
7. Lindell, I. V., A. H. Sihvola, S. A. Tretyakov, and A. J. Vitanen, *Electromagnetic Waves in Chiral and Bi-isotropic Media*, Artech House, Inc., Norwood, 1994.
8. Munir, A., N. Hamanaga, H. Kubo, and I. Awai, "Artificial dielectric rectangular resonator with novel anisotropic permittivity and its TE_{10 δ} mode waveguide filter application," *IEICE Trans. Electron.*, Vol. E88-C, No. 1, 40–46, 2005.
9. Awai, I., H. Kubo, H. Kohno, T. Iribe, and A. Sanada, "Dielectric resonator based on artificial dielectrics and its application to a microwave BPF," *Proceeding of 32nd European Microwave Conference*, 1–4, Milan, Italy, Sep. 2002.
10. Ludyati, H., A. B. Suksmono, and A. Munir, "Basic theory of artificial circular resonator encapsulated in a circular waveguide and its theoretical analysis," *Proceeding of 3rd International Conference on Instrumentation, Communication, Information Technology and Biomedical Engineering (ICICI-BME)*, 392–395, Bandung, Indonesia, Nov. 2013.

Adaptive Optimal Polarization Detection of Target in Clutter Background Based on Generalized Rayleigh Quotient

S. Lei¹, Z. Zhao¹, Z. Nie¹, and Q. H. Liu²

¹School of Electronic Engineering, University of Electronic Science and Technology of China, China

²Department of Electrical and Computer Engineering, Duke University, USA

Abstract— Most current methods on polarization targets detection assume the target echoes to be ascertained in signal model during the detection period. But in fact, the target echo may obey a kind of distribution and the distribution relates with the polarizations. Aiming at improving the performance of polarization detection, an adaptive generalized likelihood ratio (AGLR) polarization detector is proposed. The detector assumes the target echo to be a non-zero mean Gaussian distribution with respect to the polarization states of transceiver. It adaptively adjusts the polarization states of transceiver according to the variation of the polarization characteristics of target and clutter to maximize signal to clutter and noise ratio (SCNR). The problem of maximizing the SCNR is converted to a problem of maximizing a generalized Rayleigh quotient (GRQ). Based on the GRQ, the AGLR detector is proposed. The performance of the AGLR detector is theoretically analyzed and numerically validated through some numerical experiments. Compared with two conventional GLR detectors, the AGLR detector achieves a 3 dB to 10 dB improvement.

1. INTRODUCTION

Detection of a target in clutter background is a challenging problem for target detection system when the target and the clutter are closely spaced in angle and Doppler domains. Polarization information has been widely used to improve the detection performance [1–3]. It has been demonstrated that polarization information is as important as amplitude, phase and frequency. Especially, when the polarization states of transceiver match target scattering characteristics well and mismatch clutter scattering characteristics, detection performance would be substantially improved.

The polarization information has been applied to improve detection performance since 1950s [4]. At the early stage, the researchers focused on the optimal polarization state selection, assuming the clutter and noise were given. A practicable polarization state selection method in an ideal environment was proposed by W. M. Boerner et al. [5]. L. M. Novak et al. extended this idea into a more realistic case where a target was embedded in a deterministic distributed noise background [6]. Gaussian distributed clutter model in [7] and non-Gaussian distributed clutter model [8, 9] were utilized to construct polarization detectors. For more generalized clutter and noise models, D. Pastina et al. used training data to estimate clutter [10]. A. Nehorai et al. applied compound-Gaussian distributed clutter models in different applications [11, 12].

In optimal polarization detection, the selection of a proper target model is also a critical issue. In recent years, a general framework for adaptive polarization waveform design was established in [13–17]. This framework obtained target information by estimating scattering parameters based on estimation theories. Methods based on the framework investigated the improvement of detection performance with fixed transceiver polarization states during every detection period. However, since the target echo obeys a kind of distribution that relates with the polarizations, receiver with a fixed polarization state may not receive the strongest echo.

Different from the condition of fixed transceiver polarization states [13–17], a variable transceiver polarization states in the detection period is studied to optimize the echo reception in this paper. The target echo is assumed to be a non-zero mean Gaussian distribution as in [18]. The clutter is estimated by training data. We propose an adaptive Generalized Likelihood Ratio (AGLR) detector by adaptively adjusting the polarization states of transceiver according to the variation of the polarization characteristics of the target, clutter and noise. In the design of the optimal detector, the optimization polarization detection problem is converted to a generalized Rayleigh quotient (GRQ) problem. Based on the GRQ, the detector achieves maximum signal to clutter and noise ratio (SCNR) and optimal polarization states of the transceiver. The detector is theoretically analyzed and numerically validated by several numerical experiments. Compared with two conventional generalized likelihood ratio (GLR) detectors, the proposed detector is always better in different clutter backgrounds.

The remainder of the paper is organized as follows. In Section 2, a measurement model is introduced. The optimization polarization detection problem is outlined. In Section 3, the optimization detection problem is induced to a GRQ problem. The AGLR detector is proposed by seeking of a maximum GRQ. Several numerical experiments are given in Section 4. Conclusions and remarks are drawn in the final section. Notations: the superscript “ H ” denotes the Hermitian transpose conjugate; “ $|\mathbf{A}|$ ” denotes the determinant of \mathbf{A} ; $\|x\|$ denotes the II-Norm of x . the brackets “ $\langle \cdot \rangle$ ” denotes ensemble averaging.

2. POLARIZATION DETECTION METHOD

In this paper, the clutter and the noise are assumed to be polarized and unpolarized, respectively. In this section, a measurement model will be described. The optimization detection problem is formulated based on the SCNR.

2.1. The Optimization Detection Problem

Considering a detection system, a transmitter emits polarization electromagnetic wave. The illuminated target may change the polarization state of the incident wave. As a result, the scattering waves propagate to different directions with different polarization states. Therefore, an ideal detection system should be the one which could adaptively adjust the polarization states of the transceiver with respect to the polarization scattering matrix (PSM) of the object.

Let \mathbf{S} represent the PSM, which is expressed as

$$\mathbf{S}(t) = \begin{bmatrix} s_{hh}(t), & s_{hv}(t) \\ s_{vh}(t), & s_{vv}(t) \end{bmatrix}, \quad (1)$$

where t denotes time, s_{ij} ($i, j = h, v$) stands for polarization scattering coefficient with transmitting in i state and receiving in j state. As in [3], the transmitter emits a polarized waveform which can be written as

$$\mathbf{s}(t) = \sqrt{P_0} \boldsymbol{\xi}(t) s(t), \quad (2)$$

where $P_0 \in R^+ P_0$ is transmitted power. $\boldsymbol{\xi}(t) = [\xi_h(t), \xi_v(t)]^T$ is transmitted polarization state vector and $\|\boldsymbol{\xi}(t)\| = 1$ ($\|\cdot\|$ denotes II-Norm). $s(t)$ is transmitted pulse waveform which has a complex envelope. The received signal is expressed as

$$x(t) = \sqrt{P_0} g [\boldsymbol{\eta}(t)]^T \mathbf{S}(t) \boldsymbol{\xi}(t) s(t - t_0) \exp(j2\pi f_d t) + n_0(t); \quad (3)$$

where g is a constant depending on wavelength, characteristic impedance of free space, distance between the target and the transceiver, gains, etc. $\boldsymbol{\eta}(t) = [\eta_h(t), \eta_v(t)]^T$ is received polarization state vector and $\|\boldsymbol{\eta}(t)\| = 1$. t_0 is delay time. f_d is target Doppler frequency and $n_0(t)$ is noise. Since parameters $s(t - t_0)$ and f_d would not affect the received power, filtering technology is utilized to normalize (3) for simplicity

$$x(t) = \sqrt{P} g [\boldsymbol{\eta}(t)]^T \mathbf{S}(t) \boldsymbol{\xi}(t) + n(t); \quad (4)$$

where $\sqrt{P} = \sqrt{P_0} s(t - t_0) \exp(j2\pi f_d t)$ is normalized received power, and, $n(t) = \sqrt{P_0/P} n_0(t)$ denotes normalized noise. When transmitted beam and received beam illuminate target and clutter at the same time, the \mathbf{S} consists of the \mathbf{S}_t of target and the \mathbf{S}_c of clutter; hence, (4) is rewritten as

$$x(t) = \sqrt{P} g [\boldsymbol{\eta}(t)]^T \mathbf{S}_t(t) \boldsymbol{\xi}(t) + \sqrt{P} g [\boldsymbol{\eta}(t)]^T \mathbf{S}_c(t) \boldsymbol{\xi}(t) + n(t), \quad (5)$$

We rearrange the scattering matrix and the antenna polarization states as

$$\begin{aligned} \mathbf{A} &= \boldsymbol{\eta}(t) \otimes \boldsymbol{\xi}(t) = [\eta_h(t) \xi_h(t), \eta_h(t) \xi_v(t), \eta_v(t) \xi_h(t), \eta_v(t) \xi_v(t)]^T, \\ \mathbf{S} &= [s_{hh}(t), s_{hv}(t), s_{vh}(t), s_{vv}(t)]^T, \end{aligned} \quad (6)$$

where \mathbf{A} is a compound coherent vector of the polarization states of transceiver. \otimes is the Kronecker product. Omitting the time index for notational simplicity, (5) is rewritten as

$$x = \sqrt{P} \mathbf{A}^T (\mathbf{S}_t + \mathbf{S}_c) + n = \sqrt{P} \mathbf{A}^T \mathbf{S}_t + \sqrt{P} \mathbf{A}^T \mathbf{S}_c + n \quad (7)$$

Hence, the signal to clutter and noise ratio (SCNR) can be defined as

$$\text{SCNR} = \frac{\left\| \sqrt{P} \mathbf{A} \mathbf{S}_t \right\|^2}{\left\| \sqrt{P} \mathbf{A} \mathbf{S}_c \right\|^2 + \|n\|^2} = \frac{P \mathbf{A}^H [\mathbf{C}_t] \mathbf{A}}{P \mathbf{A}^H [\mathbf{C}_c] \mathbf{A} + [\mathbf{C}_n]}, \quad (8)$$

where $[\mathbf{C}] = \|\mathbf{S}\|^2$. Let $\sigma_n^2 \mathbf{I}_4 = [\mathbf{C}_n]/P$, the SCNR is rewritten as

$$\text{SCNR} = \frac{\mathbf{A}^T [\mathbf{C}_t] \mathbf{A}}{\mathbf{A}^T [\mathbf{C}_c] \mathbf{A} + \sigma_n^2 \mathbf{I}_4}. \quad (9)$$

The objective of target detection is to maximize the SCNR. Therefore, the optimization problem is formulated as

$$\arg \max_{\|\mathbf{A}\|=1} \text{SCNR} = \frac{\mathbf{A}^T [\mathbf{C}_t] \mathbf{A}}{\mathbf{A}^T [\mathbf{C}_c] \mathbf{A} + \sigma_n^2 \mathbf{I}_4}, \quad (10)$$

2.2. Adaptive Optimal Polarimetric Detector

We define a matrix function $f(\mathbf{A})$ as

$$f(\mathbf{A}) = \frac{\mathbf{A}^T [\mathbf{C}_t] \mathbf{A}}{\mathbf{A}^T [\mathbf{C}_c] \mathbf{A} + \sigma_n^2 \mathbf{I}_4}, \quad (11)$$

Since matrices $[\mathbf{C}_t]$, $[\mathbf{C}_c]$ and $\sigma_n^2 \mathbf{I}_4$ are all positive semi-definite ones, is bigger or at least equal to zero. Compared (11) with (8), the optimization problem in (10) is equivalence to a problem of maximizing $\sigma_n^2 \mathbf{I}_4$. Since $\sigma_n^2 \mathbf{I}_4 = \mathbf{A}^T (\sigma_n^2 \mathbf{I}_4) \mathbf{A}$, problem (10) can be rewritten as

$$\arg \max_{\|\mathbf{A}\|=1} f(\mathbf{A}) = \arg \max_{\|\mathbf{A}\|=1} \frac{\mathbf{A}^T [\mathbf{C}_t] \mathbf{A}}{\mathbf{A}^T ([\mathbf{C}_c] + \sigma_n^2 \mathbf{I}_4) \mathbf{A}}. \quad (12)$$

Since matrix $[\mathbf{C}_c]$ is a Hermitian positive semi-definite one and matrix $\sigma_n^2 \mathbf{I}_4$ is a Hermitian positive definite one, the summation of these two matrices is a Hermitian positive definite one. Let $[\mathbf{C}_{c+n}] = [\mathbf{C}_c] + \sigma_n^2 \mathbf{I}_4$. The optimization problem is simplified as

$$\arg \max_{\|\mathbf{A}\|=1} f(\mathbf{A}) = \arg \max_{\|\mathbf{A}\|=1} \frac{\mathbf{A}^T [\mathbf{C}_t] \mathbf{A}}{\mathbf{A}^T [\mathbf{C}_{c+n}] \mathbf{A}}. \quad (13)$$

Hence, (13) is converted to a problem of maximizing a general Rayleigh quotient (GRQ). Let \mathbf{P} be a non-singular matrix, such that $[\mathbf{C}_{c+n}] = \mathbf{P} \mathbf{P}^H$. Let $\mathbf{Z}^T = \mathbf{A}^T \mathbf{P}$ and $\mathbf{Q} = \mathbf{P}^{-1} [\mathbf{C}_t] \mathbf{P}^{-T}$, (13) is rewritten as

$$\arg \max_{\|\mathbf{Z}\|=\|[\mathbf{C}_{c+n}]\|} f(\mathbf{A}) = \arg \max_{\|\mathbf{Z}\|=1} \frac{\mathbf{Z}^T \mathbf{Q} \mathbf{Z}}{\mathbf{Z}^T [\mathbf{C}_{c+n}] \mathbf{Z}}. \quad (14)$$

Assuming λ_i ($i = 1, 2, \dots, n$) are the eigenvalues of matrix \mathbf{Q} and $\lambda_1 \geq \lambda_2 \geq \dots \geq \lambda_n$. Applying the results of [19], we obtain

$$\arg \max_{\|\mathbf{Z}\|=\|[\mathbf{C}_{c+n}]\|} f(\mathbf{A}) = \lambda_1. \quad (15)$$

Let \mathbf{Z}_1 represent the eigenvector corresponding to the maximum eigenvalue λ_1 of matrix \mathbf{Q} . The optimum polarization state of transceiver obeys the following condition,

$$\mathbf{A}_{opt} = \mathbf{P}^{-T} \mathbf{Z}_1. \quad (16)$$

3. NUMERICAL SIMULATIONS

In this section, several numerical experiments are exploited to validate the detection performance of the AGLR detector in comparison with two conventional detectors, i.e., HH-GLR detector and HV-GLR detector. The general form of covariance matrix is

$$[\mathbf{C}] = \beta \begin{bmatrix} 1 & 0 & 0 & \delta \\ 0 & \alpha_1 & \phi & 0 \\ 0 & \phi & \alpha_2 & 0 \\ \delta & 0 & 0 & 1 \end{bmatrix}, \quad (17)$$

where β is the scaling factor to fulfill the given SCNR. δ is the correlation factor between co-polarized channels. ϕ is the correlation factor between cross polarized channels. α_1 and α_2 are the power ratio of the two cross polarized channels to the HH channel.

For comparison purposes, the following two fixed polarization detectors, i.e., HH and HV, is computed. Their polarization states \mathbf{A} :

$$\begin{aligned}\mathbf{A}_{hh} &= [1, 0, 0, 0]^T, \\ \mathbf{A}_{hv} &= [0, 1, 0, 0]^T.\end{aligned}\quad (18)$$

The parameters of the target are assumed to be: $\delta_t = 0.99$, $\phi_t = 0.1$ and $\alpha_1 = \alpha_2 = 0.1$. The constant parameters of the clutter are $\delta_c = 0.9$ and $\phi_c = 0.1$. In the following experiments, we assume $\text{CNR} = 10$ dB, the number of adjacent cells and pulses in one scan period are both 15; i.e., $M = 10$ and $N = 10$. The signal has a dimension of $D = 1$.

Figures 1(a)–(c) show the detection probability P_d of three detectors, i.e., the AGLR detector, the HH-GLR detector and the HV-GLR detector, as functions of the signal to clutter ratio (SCR). Results shows: 1) The AGLR detector has the best performance in different clutter scenarios. 2) When the clutter is stronger in co-polarized channel, i.e., $\alpha_1 = \alpha_2 = 0.1$, the HH-GLR detector outperforms the HV-GLR detector. 3) When the clutter is the same, i.e., $\alpha_1 = \alpha_2 = 1$, the HH-GLR detector and the HV-GLR detector have the similar performance. 4) When the clutter is weaker in the co-polarized channel, i.e., $\alpha_1 = \alpha_2 = 10$, the HH-GLR detector is worse than the HV-GLR detector.

Figures 2(a)–(c) illustrate the detection probabilities of the AGLR detector, the HH-GLR detector and the HV-GLR detector as functions of the false alarm probability at different signal to clutter ratios (SCRs). The figures show that the AGLR detector always outperforms the two conventional GLR detectors. It means that the AGLR detector has the highest detection probability for the same false alarm probability or the AGLR detector has a lower false alarm probability for the same detection probability.

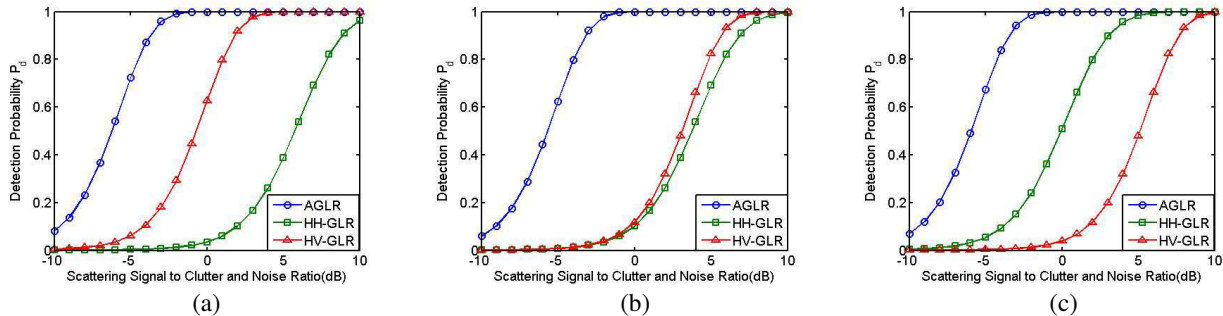


Figure 1: Detection probabilities of the 3 detectors as functions of SCNR with clutter to noise ratio (CNR) $\text{CNR} = 10$ dB, $P_{fa} = 10^{-4}$, $M = 10$, $N = 10$ and $D = 1$: (a) $\alpha_1 = \alpha_2 = 0.1$, (b) $\alpha_1 = \alpha_2 = 1$ and (c) $\alpha_1 = \alpha_2 = 10$.

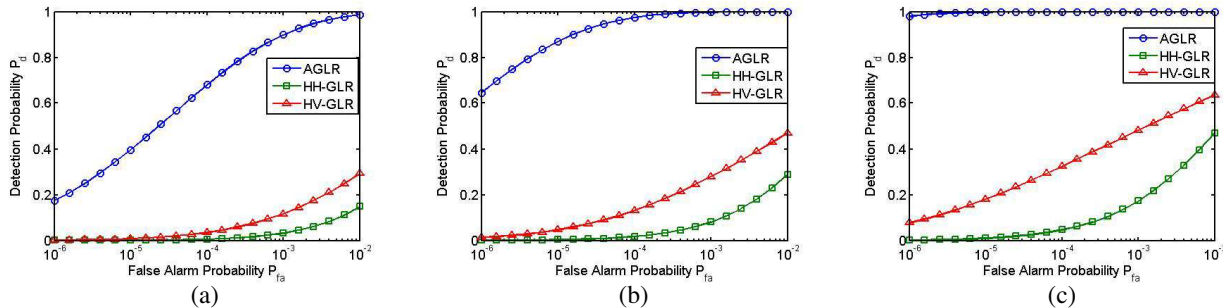


Figure 2: Detection probabilities of the 3 detectors as functions of false alarm probability for $\text{SCR} = 0$ dB, $\text{CNR} = 10$ dB, $M = 10$, $N = 10$ and $D = 1$: (a) $\alpha_1 = \alpha_2 = 0.1$, (b) $\alpha_1 = \alpha_2 = 1$ and (c) $\alpha_1 = \alpha_2 = 10$.

4. CONCLUSION

In this paper, the problem of detecting target in clutter background was addressed. Target was assumed to be a non-zero Gaussian distribution based on the fact that different transceiver polarization states would obtain different target echoes. We proposed an AGLR detector for adaptively adjusting the polarization states of transceiver so as to maximize the SCNR. Clutter and noise were not required to be known a priori. Training data were used to acquire the information of clutter and noise. Compared with two conventional GLR detectors, i.e., the HH-GLR detector and the HV-GLR detector, the AGLR detector always performs the best when dealing target detection in different clutter backgrounds.

REFERENCES

1. Maio, A. D. and G. Ricci, "A polarimetric adaptive matched filter," *Signal Processing*, Vol. 81, 2583–2589, 2001.
2. Hurtado, M. and A. Nehorai, "Polarimetric detection of targets in heavy inhomogeneous clutter," *IEEE Trans. Signal Process.*, Vol. 56, No. 4, 1349–1361, Apr. 2008.
3. Xiao, J. J. and A. Nehorai, "Joint transmitter and receiver polarization optimization for scattering estimation in clutter," *IEEE Trans. Signal Process.*, Vol. 57, No. 10, 4142–4147, Oct. 2009.
4. Giuli, D., "Polarization diversity in radars," *Proc. IEEE*, Vol. 74, No. 2, 245–269, Feb. 1986.
5. Kostinski, A. B. and W. M. Boerner, "On foundations of radar polarimetry," *IEEE Trans. Antennas Propag.*, Vol. 34, No. 12, 1395–1404, Dec. 1986.
6. Novak, L. M., M. B. Sechtin, et al., "Studies of target detection algorithms that use polarimetric radar data," *IEEE Trans. on Aerosp. Electron. Syst.*, Vol. 25, No. 2, 150–165, Mar. 1989.
7. Pastina, D., P. Lombardo, et al., "Adaptive polarimetric target detection with coherent radar Part I: Detection against Gaussian background," *IEEE Trans. on Aerosp. Electron. Syst.*, Vol. 37, No. 4, 1194–1206, Oct. 2001.
8. Maio, A. D. and G. Alfano, "A polarimetric adaptive detector in non-Gaussian noise," *Signal Processing*, Vol. 83, 297–306, Feb. 2003.
9. Pastina, D., P. Lombardo, et al., "Adaptive polarimetric target detection with coherent radar Part II: Detection against non-Gaussian background," *IEEE Trans. on Aerosp. Electron. Syst.*, Vol. 37, No. 4, 1207–1220, Oct. 2001.
10. Park, H. R. and H. Wang, "Adaptive polarization-space-time domain radar target detection in inhomogeneous clutter environments," *IEE Proc. Radar Sonar Navigation*, Vol. 153, No. 1, 35–43, Feb. 2006.
11. Wang, J. and A. Nehorai, "Adaptive polarimetry design for a target in compound-Gaussian clutter," *Signal Processing*, Vol. 89, 1061–1069, 2008.
12. De Maio, A., G. Alfano, and E. Conte, "Polarization diversity detection in compound-Gaussian clutter," *IEEE Trans. on Aerosp. Electron. Syst.*, Vol. 40, No. 1, 114–131, Jan. 2004.
13. Park, H. R., J. Li, et al., "Polarization-space-time domain generalized likelihood ratio detection of radar targets," *Signal Processing*, Vol. 41, 153–164, 1995.
14. Nehorai, A., F. Gini, M. S. Greco, A. P. Suppappola, and M. Rangaswami, "Introduction to the issue on 'Adaptive waveform design for agile sensing and communication'," *IEEE J. Sel. Topics Signal Process.*, Vol. 1, No. 1, 2–5, Jun. 2007.
15. Calderbank, R., S. D. Howard, and B. Moran, "Waveform diversity in radar signal processing," *IEEE Signal Process. Mag.*, 32–41, Jan. 2009.
16. Sira, S. P., Y. Li, A. P. Suppappola, D. Morrell, D. Cochran, and M. Rangaswami, "Waveform-agile sensing for tracking: A review perspective," *IEEE Signal Process. Mag.*, 53–64, Jan. 2009.
17. Sira, S. P., D. Cochran, et al., "Adaptive waveform design for improved detection of low-rs targets in heavy sea clutter," *IEEE J. Sel. Topics Signal Process.*, Vol. 1, No. 1, 56–66, Jun. 2007.
18. Touzi, R., W. M. Boerner, T. S. Lee, and E. Lueneburg, "A review of polarimetry in the context of synthetic aperture radar: Concepts and information extraction," *Can. J. for Remote Sens.*, Vol. 30, No. 3, 380–407, 2004.
19. Zhang, M. C., *Matrix Theory*, 126–130, Southeast University Press, China, 2002.

Calculation of Shielding Effectiveness of an Apertured Rectangular Cavity Against Planar Electromagnetic Pulses

Xiaoning Shi, Chongqing Jiao, and Shuai Niu

State Key Laboratory of Alternate Electrical Power System with Renewable Energy Sources
North China Electric Power University, Beijing 102206, China

Abstract— Based on the equivalent circuit method and the Fourier transform technique, an approximate analytical model for calculating the shielding effectiveness of an apertured rectangular cavity against planar electromagnetic pulse is presented. The validity of the theoretical model is verified by the comparison with the full-wave electromagnetic simulation software CST. The effects of the aperture's shape and size, and pulse width on the pulse shielding effectiveness are analyzed.

1. INTRODUCTION

Electromagnetic pulse is a kind of transient electromagnetic phenomenon characterizing wideband and high field intensity. Electromagnetic pulses, which usually are resulted from some transient processes like lightning, static discharge, high altitude nuclear burst, switching operation and circuit faults, may couple into electronic equipment and systems via antenna, hole, cable, etc., and then cause the performance degrade of the equipment and systems. With the development of wireless communication technology, high-speed circuit and extensive application of microelectronic device, the sensitivity of the electrical and electronic equipment to electromagnetic pulse is increasing continuously. The electromagnetic interference protection problem has received widespread attention [1–5].

Electromagnetic shielding is one of the most basic methods to suppress electromagnetic interference, and its common form is isolating the sensitive equipment using shielding shell made of metal materials to prevent the entry of external electromagnetic disturbance or the leakage of internal electromagnetic disturbance. Completely closed metal cavity has very high shielding effectiveness for electromagnetic fields except low frequency magnetic field. In practice, there exist a large number of holes on the shield for some indispensable functions like ventilation and heat dissipation. In general, the electromagnetic field penetrating directly through the metal wall of a shield can be neglected. Therefore, the hole on the shield is the dominant way for the coupling between the internal and external region of the shield, and hence is the key factor affecting the shielding effectiveness (SE) of a shield. So, lots of works focus their attention on the effect of apertures on shielding effectiveness, and some numerical [4–7], analytical [10–12] or experimental techniques [8–11] have been presented to solve the problem.

Although numerical method on this issue is widely applied, but its complexity, high computational cost [14–16] make the development of analytic method of easy implementation, quick calculation and clear physical meaning still necessary. For harmonic field, people have put forward the equivalent circuit method and analytical method based on the Bethe holes coupling theory and mode expansion theory [17–19]. For the non-harmonic field, relevant analytic theory model is rarely reported.

In this paper, a novel model is proposed to calculate the SE of an apertured cavity against electromagnetic pulses. The model is the combination of the frequency-domain equivalent circuit model reported in Ref. [8] and the Fourier transform technique. First, we transform the incident pulse signal in time domain into frequency domain. Second, equivalent circuit model is used to calculate the electromagnetic field in the cavity in frequency domain. Third, the waveform in time domain is obtained by using Fourier inverse transform. To test the validity of this model, the calculation results of the simulation software CST are also presented. The effects of the size and shape of the hole, and pulse width on the cavity shielding effectiveness are also analyzed.

2. THEORETICAL MODEL

Figure 1 shows an apertured rectangular enclosure under the illumination of planar electromagnetic pulses. The height, length and depth of the enclosure are denoted by a , b , and d , respectively. The wall of the enclosure is assumed to be perfect conducting and has a thickness of t . There is a rectangular aperture of length l and width w on the left wall of the enclosure. The point P_1 is

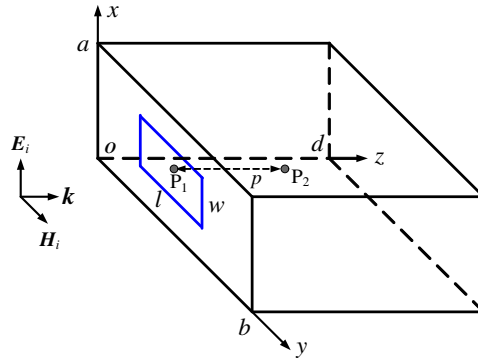


Figure 1: Apertured rectangular enclosure against planar electromagnetic pulses.

the center of the aperture and P_2 represents the point where the shielding effectiveness will be observed.

The electric shielding effectiveness S_E at a given point is defined as the ratio of the maximum electric field intensity of the time domain E_0 at the point with the enclosure removed to the maximum electric field intensity E_s at the same point with the shield applied.

$$S_E = 20 \log_{10} \left| \frac{E_0}{E_s} \right| \tag{1}$$

Similarly, the magnetic shielding effectiveness S_H is defined as

$$S_H = 20 \log_{10} \left| \frac{H_0}{H_s} \right| \tag{2}$$

The shielded field E_s and H_s can be calculated by the equivalent circuit in Fig. 2, Where the incident plane wave is represented by voltage V_0 and impedance $Z_0 = 377 \Omega$.

The aperture is treated as a coplanar strip transmission line with a length of l along the y axis, shorted at each end. Then, the effect of the aperture can be embodied by the shunt impedance Z_{ap} in the circuit model with [8].

$$Z_{ap} = \frac{j l}{2 a} 120 \pi^2 \left[\ln \left(\frac{2 \left(1 + \sqrt{1 - (w_e/b)^2} \right)}{1 - \sqrt{1 - (w_e/b)^2}} \right) \right]^{-1} \tan \frac{k_0 l}{2} \tag{3}$$

where $k_0 = 2\pi/\lambda$, and $w_e = w - (5t/4\pi) [1 + \ln(4\pi w/t)]$.

The enclosure is considered as a rectangular waveguide with a length of d along the z axis and shorted at the right end ($z = d$). When the wave frequency is lower than the cutoff frequency of the second lowest mode of the waveguide, we can assume there is only a single mode of propagation, that is, the TE_{10} mode. Then, the waveguide can be modeled very well by a transmission line with its characteristic impedance $z_g = \eta_0 / \sqrt{1 - (\lambda/2a)^2}$ and propagation constant $k_g = k \sqrt{1 - (\lambda/2a)^2}$.

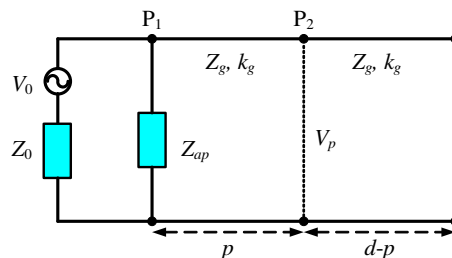


Figure 2: The equivalent circuit model for the apertured rectangular enclosure against planar electromagnetic pulses.

For the Gaussian excitation case, the time domain expression of plane wave electromagnetic pulse is $f_i(t)$. We can obtain its expression in frequency domain by Fourier transform.

$$F(\omega) = \int_{-\infty}^{+\infty} f_i(t) e^{-j\omega t} dt \quad (4)$$

This expression is used as the voltage source V_0 of equivalent circuit. By Thevenin's equivalent circuit theorem, combining V_0 , Z_0 and Z_{ap} gives an equivalent voltage V_1 and source impedance Z_1 .

$$V_1 = V_0 \frac{Z_{ap}}{Z_{ap} + Z_0} \quad (5)$$

$$Z_1 = \frac{Z_{ap} Z_0}{Z_{ap} + Z_0} \quad (6)$$

We now transform V_1 , Z_1 , and the short circuit at the end of the waveguide to P_2 , giving an equivalent voltage V_2 , source impedance Z_2 , and load impedance Z_3 .

$$V_2 = \frac{V_1}{\cos k_g p + j(Z_1/Z_g) \sin k_g p} \quad (7)$$

$$Z_2 = \frac{Z_1 + jZ_g \tan k_g p}{1 + j(Z_1/Z_g) \tan k_g p} \quad (8)$$

$$Z_3 = jZ_g \tan k_g (d - p) \quad (9)$$

The voltage and current at P_2 in frequency domain is now

$$V_p = V_2 \frac{Z_3}{Z_2 + Z_3} \quad (10)$$

$$I_p = \frac{V_2}{Z_2 + Z_3} \quad (11)$$

Then the unilateral Fourier inverse transform is used to get the time-domain expression of electric field and magnetic field in the cavity.

$$f_E(t) = \frac{1}{\pi} \int_0^{+\infty} \text{Re} [V_p(\omega) e^{j\omega t}] d\omega \quad (12)$$

$$f_H(t) = \frac{1}{\pi} \int_0^{+\infty} \text{Re} [I_p(\omega) e^{j\omega t}] d\omega \quad (13)$$

The maximum of $f_E(t)$ is E_S , and the maximum of $f_i(t)$ is E_0 . The maximum of $f_H(t)$ is H_S , and the ratio of the maximum of $f_i(t)$ and Z_0 is H_0 . All of the electric fields calculated are in the direction of x axis and the magnetic fields are in the direction. of y axis.

3. WAVEFORM OF ELECTRIC AND MAGNETIC FIELDS IN THE CAVITY

3.1. The Electric Field Waveform

The time domain expression of the incident plane wave electromagnetic pulse (Gaussian pulse) is

$$f_i(t) = e^{-u(t-t_0)^2} \quad (14)$$

The value of u are 1×10^{17} , 7×10^{17} , $1 \times 10^{18} \text{ s}^{-2}$, respectively. The spectrum of the incident Gaussian pulse is shown in Fig. 3. The dimensions of the enclosure employed for calculation are: $a = 30 \text{ cm}$, $b = 12 \text{ cm}$, $d = 30 \text{ cm}$, $t = 1.5 \text{ mm}$, $l = 5 \text{ mm}$ and $w = 5 \text{ mm}$. Figs. 4–6 plots the curves of the electric field waveform at the center of the cavity ($p = 15 \text{ cm}$) for the three different values of u .

Figure 4 shows that when u is $1 \times 10^{17} \text{ s}^{-2}$, the electric field strength is zero before $t = 5 \text{ ns}$. From about $t = 5 \text{ ns}$ to $t = 20 \text{ ns}$, the waveform is approximately a complete sine wave, and then goes to zero. The second half of the sine wave is actually the reflection of the first half of wave at

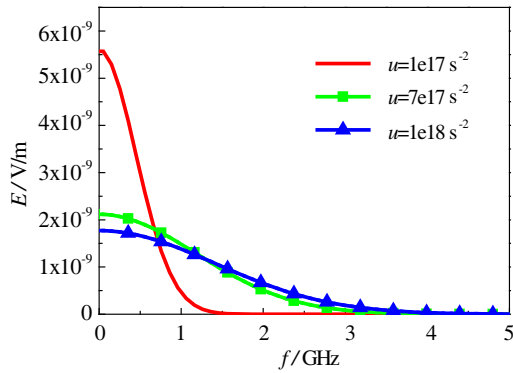
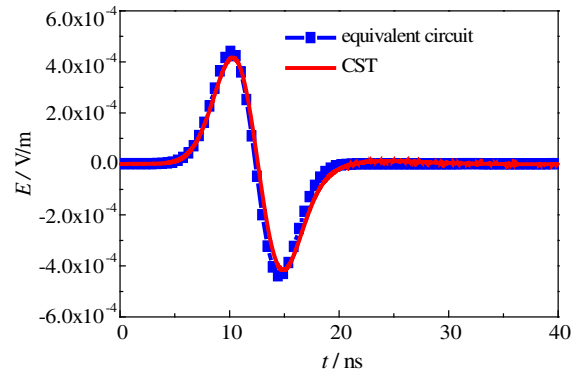
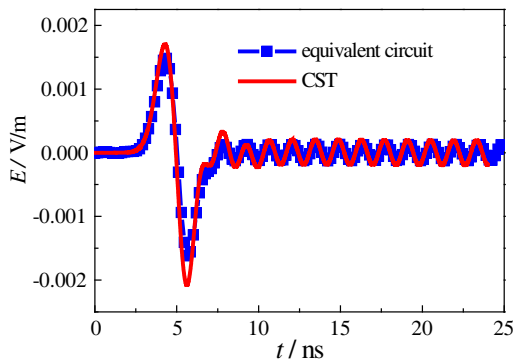
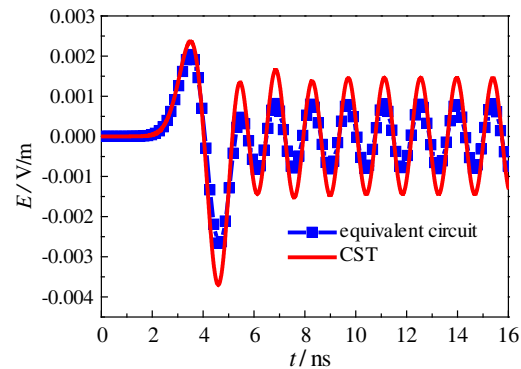


Figure 3: Frequency spectrum of Gaussian pulses.

Figure 4: Time domain waveform at the center of the enclosure against planar electromagnetic pulses ($u = 1 \times 10^{17} \text{ s}^{-2}$, $t_0 = 12 \text{ ns}$).Figure 5: Time domain waveform at the center of the enclosure against planar electromagnetic pulses ($u = 7 \times 10^{17} \text{ s}^{-2}$, $t_0 = 5 \text{ ns}$).Figure 6: Time domain waveform at the center of the enclosure against planar electromagnetic pulses ($u = 1 \times 10^{18} \text{ s}^{-2}$, $t_0 = 4 \text{ ns}$).

the back of the cavity wall. When u increases to $7 \times 10^{17} \text{ s}^{-2}$, the Fig. 5 shows that the waveform of electric field intensity contains not only a single period of the sine wave of high amplitude, but also a sinusoidal steady state response of low amplitude. The frequency of the steady state response is 0.7 GHz which is resulted from the resonance of the TE_{101} cavity mode. There are two aspects of the impact for the increase of the high frequency components caused by the increase of u . On the one hand, it makes the maximum value of the electric field inside the cavity increases, and the shielding effectiveness of the cavity reduces. On the other hand, it will also stimulate the resonance mode of the cavity forming the steady-state oscillation.

As is shown in Fig. 6, when u increases to $1 \times 10^{18} \text{ s}^{-2}$, the maximum of electric field strength increases further, and the amplitude of the steady-state response of increases as well. When u is small, our method has a good agreement with the computational result of CST software (Figs. 4 and 5). When u is bigger, the two results are in good agreement in the time synchronization, but there is a little difference in the amplitude. The reason is that the frequency component more than 1 GHz appears in great quantities, making higher order waveguide modes (such as TE_{20} mode whose cutoff frequency is 1 GHz) can't be ignored, while only the influence of the TE_{10} mode is considered in this paper. It should be noted that all of the TE_{10n} cavity modes are incorporated in the present model, since they can be regarded as the different spatial distribution forms of TE_{10} waveguide mode along the z axis.

3.2. The Magnetic Field Waveform

The Gaussian pulse parameter u is set to be $1 \times 10^{18} \text{ s}^{-2}$, and the magnetic field waveform at $p = 0.15 \text{ m}$ and $p = 0.25 \text{ m}$ are calculated respectively, as is shown in Fig. 7 and Fig. 8.

From Fig. 7 we can see that the magnetic field strength waveform at $p = 0.15 \text{ m}$ in the cavity has only a large positive pulse wave with neither a large negative pulse nor a periodic oscillation following up, which are very different from the electric field waveform in Fig. 6. The reason is that when reflecting after encountering the back wall of the cavity, the direction of the electric field

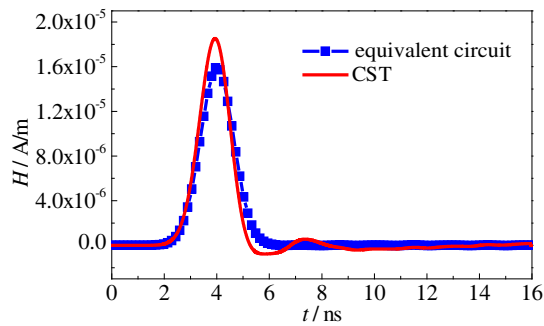


Figure 7: Time domain waveform of the magnetic field ($p = 0.15$ m).

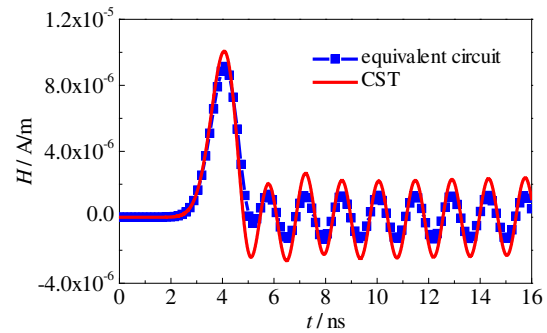


Figure 8: Time domain waveform of the magnetic field ($p = 0.25$ m).

will reverse, while the direction of the magnetic field will not. Thereby, for the electric field, the reflected wave and incident wave are superimposed in the same direction, and because of the lag in the former, the waveform with a positive pulse part and a negative pulse part is formed. As to the magnetic field, the reflected wave and incident wave are superimposed in the opposite direction, but there are not enough time intervals to form two separate parts of waveform. The reason why there is also no subsequent periodic oscillation is not that no TE_{101} resonance is formed, but the oscillation is in the standing wave form, and the center of cavity just is the node of the standing wave. For the point of $p = 0.25$ m, which is not the node of standing wave, the magnetic field waveform contains a periodic steady state response of 0.7 GHz as shown in Fig. 8.

4. CALCULATION OF SHIELDING EFFECTIVENESS

Take the parameter u of the Gaussian pulse plane wave for $1 \times 10^{18} \text{ s}^{-2}$, and shielding effectiveness at the center of the cavity with different apertures and pulse width is analyzed.

4.1. Different Size of the Aperture

Assume that the shape of the aperture is square. Shielding effectiveness at the center of the cavity with different size of the aperture is shown in Fig. 9. As you can see, SE decreases with the increasing the side length. Our calculated results and the simulation results match well when the side length of the aperture is about 23 mm. while the aperture is bigger or smaller, there is a little difference which is less than 10 dB.

4.2. Different Shape of the Aperture

Figure 10 shows the SE at the center of the cavity versus the length a when the area of the aperture is fixed at 16 cm^2 . We can see that the shape also affects the shielding effectiveness, which is decrease with the increasing of the length of the long side. Therefore, in order to get good shielding effectiveness, seam and slim aperture should be avoided. And the shape of the aperture should be square or circular. The calculation results of equivalent circuit are slightly larger than the simulation results, but the maximum difference is within 8 dB.

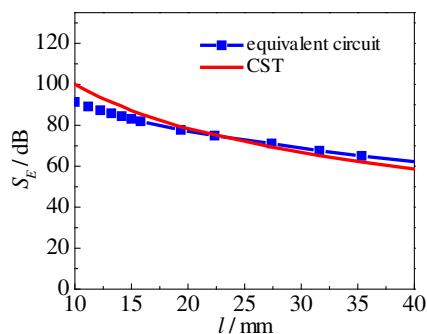


Figure 9: SE for different size of the square aperture.

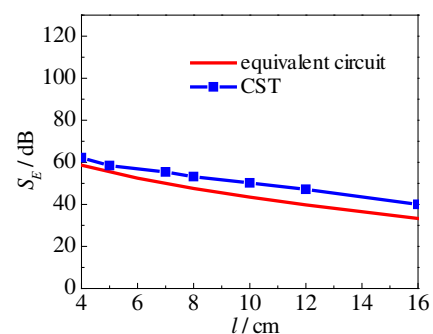


Figure 10: Dependence of the SE on the length of the aperture.

4.3. Different Pulse Width

Figure 11 shows the shielding effectiveness of the cavity with certain aperture parameters ($l = 0.1$ m, $w = 0.05$ m) while the parameter u changes.

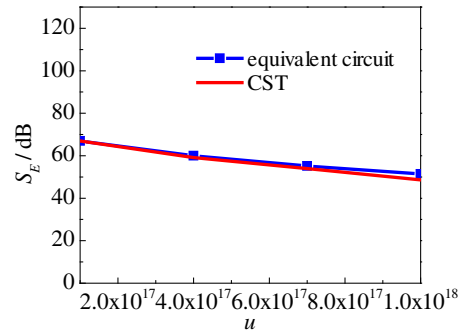


Figure 11: SE for the different values of u .

As can be seen from Fig. 11, shielding effectiveness is falling with the increase of u . It's because of the increasing of the high frequency components. And the calculation results of equivalent circuit method and CST match very well.

5. CONCLUSION

Based on the frequency domain equivalent circuit method, and combining the time-frequency domain conversion of the Fourier transform, an analytical model is established to calculate SE in an apertured rectangular cavity against planar electromagnetic pulses is established. This model is characterized by simple implementation, fast computing speed, and its calculation results are consistent with the calculation results of electromagnetic simulation software CST. Take Gaussian pulse as an example, the electric and magnetic field in the cavity in time domain is analyzed. Also, the influence of size and shape of the capture and pulse width on the shielding effectiveness is also revealed. It is shown that the electromagnetic response in the cavity contains transient part and steady part. The former is mainly composed of the incident wave and the reflected wave, and the latter is due to the resonance modes. When the width of Gaussian pulse spectrum is small, there is no steady-state response. With the increasing of the size and length of the aperture and width of Gaussian pulse spectrum, shielding effectiveness of the cavity will decrease. Higher order modes, transmission and polarization direction of incident wave are not consider in this model, the influence of these factors can be resolved by superposition of the modes and decomposition of the incident field in future work.

REFERENCES

1. Faghihi, F. and H. Heydari, "Reduction of leakage magnetic field in electromagnetic systems based on active shielding concept verified by eigenvalue analysis," *Progress In Electromagnetics Research*, Vol. 96, 217–236, 2009.
2. Wang, Y. J., W. J. Koh, C. K. Lee, and K. Y. See, "Electromagnetic coupling analysis of transient signal through slots or apertures perforated in a shielding metallic enclosure using FDTD methodology," *Progress In Electromagnetics Research*, Vol. 36, 247–264, 2002.
3. Xu, X. and X. Yang, "A hybrid formulation based on unimoment method for investigating the electromagnetic shielding of sources within a steel pipe," *Progress In Electromagnetics Research*, Vol. 12, 133–157, 1996.
4. Harrington, R. F. and J. R. Mautz, "Characteristic modes for aperture problems," *IEEE Trans. Microw. Theory.*, Vol. 33, No. 6, 500–505, Jun. 1985.
5. Audone, B. and M. Balma, "Shielding effectiveness of apertures in rectangular cavities," *IEEE Transactions on Electromagnetic Compatibility*, Vol. 31, No. 1, 102–106, Feb. 1989.
6. Wang, T., R. F. Harrington, and J. R. Mautz, "Electromagnetic scattering from and transmission through arbitrary apertures in conducting bodies," *IEEE Trans. Antennas Propag.*, Vol. 38, No. 11, 1805–1814, Nov. 1990.
7. Ma, K. P., M. Li, J. L. Drewniak, T. H. Hubing, and T. P. Van Doren, "Comparison of FDTD algorithms for subcellular modeling of slots in shielding enclosures," *IEEE Transactions on Electromagnetic Compatibility*, Vol. 39, No. 2, 147–155, May 1997.

8. Robinson, M. P., T. M. Benson, C. Christopoulos, J. F. Dawson, M. D. Ganley, A. C. Marvin, S. J. Porter, and D. W. P. Thomas, “Analytical formulation for the shielding effectiveness of enclosures with apertures,” *IEEE Transactions on Electromagnetic Compatibility*, Vol. 40, No. 3, 240–248, Aug. 1998.
9. Shim, J. J., D. G. Kam, J. H. Kwon, and J. Kim, “Circuit modeling and measurement of shielding effectiveness against oblique incident plane wave on apertures in multiple sides of rectangular enclosure,” *IEEE Transactions on Electromagnetic Compatibility*, Vol. 52, No. 3, 566–577, Aug. 2010.
10. Jiao, C. Q., “Shielding effectiveness improvement of metallic waveguide tube by using wall losses,” *IEEE Transactions on Electromagnetic Compatibility*, Vol. 54, No. 3, 696–699, Jun. 2012.
11. Dehkhoda, P., A. Tavakoli, and R. Moini, “An efficient and reliable shielding effectiveness evaluation of a rectangular enclosure with numerous apertures,” *IEEE Transactions on Electromagnetic Compatibility*, Vol. 50, No. 1, 208–212, Feb. 2008.
12. Solin, J. R., “Formula for the field excited in a rectangular cavity with a small aperture,” *IEEE Transactions on Electromagnetic Compatibility*, Vol. 53, No. 1, Feb. 2011.
13. Nie, B. L., P. A. Du, Y. T. Yu, and S. Zheng, “Study of the shielding properties of enclosures with apertures at higher frequencies using the transmission-line modeling method,” *IEEE Transactions on Electromagnetic Compatibility*, Vol. 53, No. 1, 73–81, 2011.
14. Chen, J. and J. G. Wang, “A three-dimensional semi-implicit FDTD scheme for calculation of shielding effectiveness of enclosure with thin slots,” *IEEE Transactions on Electromagnetic Compatibility*, Vol. 49, No. 2, 354–360, 2007.
15. Wallyn, W., D. D. Zutter, and H. Rogier, “Prediction of the shielding and resonant behavior of multi section enclosures based on magnetic current modeling,” *IEEE Transactions on Electromagnetic Compatibility*, Vol. 44, No. 1, 130–138, 2002.
16. Fan, Y. P., Z. W. Du, and K. Gong, “Analysis on shielding effectiveness of rectangular cavity perforated with a single slot,” *Journal of Electronics & Information Technology*, Vol. 27, No. 12, 2005.
17. Nitsch, J. B., S. V. Tkachenko, and S. Potthast, “Transient excitation of rectangular resonators through electrically small circular holes,” *IEEE Transactions on Electromagnetic Compatibility*, Vol. 54, No. 6, 1252–1259, 2012.
18. Jiao, C. Q. and L. Qi, “Electromagnetic coupling and shielding effectiveness of apertured rectangular cavity under plane wave illumination,” *Acta Physica Sinica*, Vol. 61, No. 13, 134104–134109, 2012.
19. Azaro, R., S. Caorsi, and M. Donelli, “Evaluation of the effects of an external incident electromagnetic wave on metallic enclosures with rectangular apertures,” *Microwave and Optical Tech.*, Vol. 28, No. 5, 289–293, 2001.

Parametric Inversion of 2-D Dielectric Rough Surface Based on SVM

Qiyuan Zou, Qinghe Zhang, and Fei Xu

School of Science, Three Gorges University, Yichang, Hubei 443002, China

Abstract— The inverse scattering of the geometric parameters with the 2-D rough surface is studied in this paper. Relative parameters are estimated by means of a regression technique based on the use of support vector machines (SVM). The Radar Cross-Section (RCS) is used as feature value, after a proper training procedure, the proposed method is able to reconstruct the parameters of the rough surface. Numerical results are provided for the validation of the approach.

1. INTRODUCTION

Inverse scattering is one of the most challenging problems in electromagnetic field due to its nonlinear and probabilistic characteristics. However, it is still gaining a considerable amount of attention because of its numerous applications in civil areas as well as military areas. In the past, the inversion techniques that have been proposed are mainly based on the numerical inversion of the integral scattering equations in the spatial domain or on iterative minimization technique. Unfortunately, these methods often require a great amount of computational resources and long CPU time. Recent years, techniques based on the use of Machine Learning Methods (MLM) such as neural networks (NNs) and support vector machines (SVM) have been proposed to solve inverse scattering problems.

SVM is based on the Structural Risk Minimization Principle (SRMP) and Statistical Learning Theory (SLT), the solution of which is global optimal. A lot of specialists have already performed inverse scattering researches to detect the buried target by the use of SVM. In this paper, numerical solution based on method of moment (MoM) is used to compute scattering field, then with the help of support vector regression (SVR), we establish the inverse scattering model to reconstruct the parameters of the rough surface.

2. INVERSE SCATTERING MODEL

Generally, research on inverse scattering problem usually measure the scattered field containing scatterer characteristic information such as geometric size, physical material at first. Then we obtain the estimated value of the scattered field by the SVR process. In this paper, we acquire the scatterer information (RCS in this passage) by MoM.

SVR theory can be simply stated as following. Given several training samples ($\{X_i, y_i\}; i = 1, 2, \dots, n; X_i \in R^n; y_i \in R$). X_i may be the RCS value while y_i may be the unknown properties of the surface or the target in this passage. By training the samples we can find a function that have a maximum fixed error ε for all the samples from the training set, at the same time, the function should be as smooth as possible in order to reduce the effects on the estimated values caused by the perturbation of the input data. This function as follow

$$\Phi(X) = \sum_{i=1}^N (\alpha_i - \alpha_i^*) K(X_i, X) + b \quad (1)$$

N is the number of support vector, while functional parameters (α_i, α_i^*, b) are unknown quantities and must be chosen in order to minimize the distance between the values predicated by the function and the samples. Besides, nonlinear transformation function k is a kernel function. Function (1) also contain structural parameters (ε, C, γ^2). Parameter C is called penalty factor which measures the trade-off between the training error rate and the model complexity. γ^2 is square of the standard deviation when Gaussian function serve as the kernel function. The ε is called insensitive loss function which is defined as

$$\varepsilon(X, y) = \begin{cases} 0 & \text{if } |y - \Phi| \leq \varepsilon \\ |y - \Phi| - \varepsilon & \text{others} \end{cases} \quad (2)$$

3. NUMERICAL RESULTS

In order to assess the effectiveness of the SVM approach, several numerical simulations have been performed.

We reconstruct the root-mean-square (rms) height δ and relevant length ℓ of the surface in this paper. The kernel function used for SVM here is a radial kernel, which is given by

$$K(X_i, X) = e^{-|X_i - X|^2 / \gamma^2} \quad (3)$$

Simplified model of the problem illustrated as Figure 1. A random rough surface (length $L = 10\lambda_0$) generated by Monte Carlo method divides the region into two parts (air-soil). A tapered wave with HH polarized uniform (frequency $f = 300$ MHz) illuminating the air-soil interface in the x - z plane (with incident angle $\theta = 30^\circ$). Region below the rough surface is filled by dielectric substance of known dielectric property ($\varepsilon_2 = 2 - 0.2j$, $\mu_2 = \mu_0$), while μ_0 is the magnetic permeability of the vacuum. Five observation points of different direction ($\theta_s = i\pi/6$; $i = 1, 2, 3, 4, 5$) are used to measure the scattered field.

The RCS of the target used as samples, RCS at the observation points are calculated by MoM. We calculate 50 different rough surfaces to avoid the randomness of the rough surface. Then we obtain 100 training samples ($\delta_i = 0.025\lambda_0 + (i-1)\Delta x$, $i = 1, 2, \dots, 10$, $\Delta x = 0.0075\lambda_0$; $\ell_i = 0.5\lambda_0 + (i-1)\Delta y$, $i = 1, 2, \dots, 10$, $\Delta y = 0.1\lambda_0$) and 81 test samples ($\delta_i = 0.0255\lambda_0 + (i-1)\Delta x$, $i = 1, 2, \dots, 9$, $\Delta x = 0.0075\lambda_0$; $\ell_i = 0.51\lambda_0 + (i-1)\Delta y$, $i = 1, 2, \dots, 9$, $\Delta y = 0.1\lambda_0$).

After the training phase, we acquire the structural parameters of the SVM regression. Then we use the test samples mentioned above to evaluate the precision of the SVM. The reconstruction of both the root-mean-square (rms) height δ and relevant length ℓ are shown in Figures 3 and 4

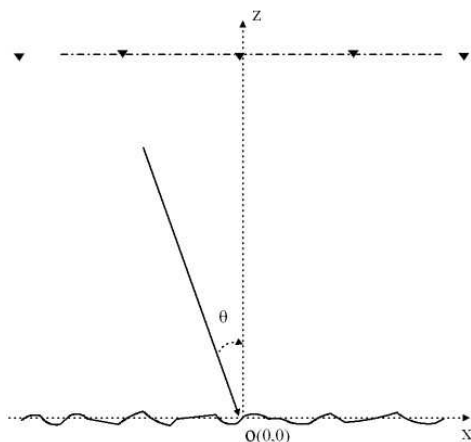


Figure 1: Cross section of the 2-D dielectric rough surface.

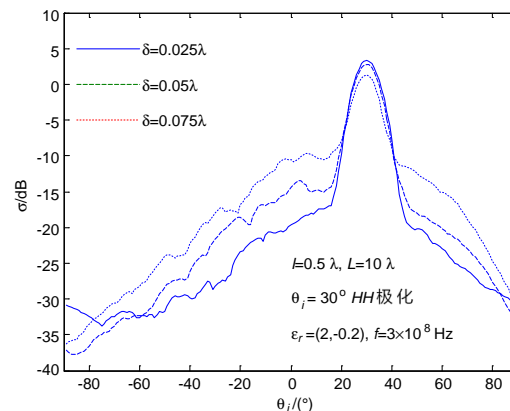


Figure 2: RCS with different δ .

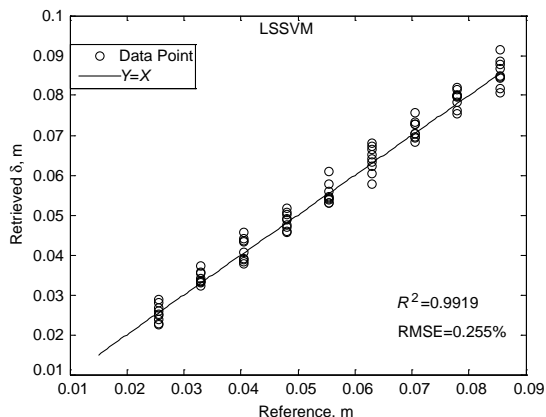


Figure 3: Estimation of the root-mean-square height δ .

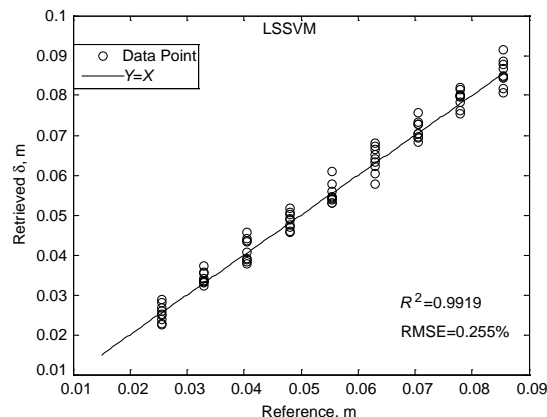


Figure 4: Estimation of the relevant length ℓ .

Table 1.

	δ	ℓ
R^2	0.9919	0.9959
RMSE	0.255%	2.376%

comparison with the reference, respectively. The correlation coefficient (R^2) between the retrieved and reference of the surface parameters and root-mean-square error (RMSE) are shown in the Table 1. Our retrieval result is very encourage.

We also found that the algorithm had multi solution problem for several references that produced large estimation errors. Figure 4 shows that the deviation will increase when the relevant length exceed within limits. This is probably because the RCS changes acute when ℓ get larger, but our sampling interval is not small enough.

4. CONCLUSION

In this paper, several observations points are set to acquire the scattered field, then we calculate the RCS at the points by MoM, finally, geometric parameters reconstruction of the random rough surface shallow buried cylinder is achieved with the help of SVM theory. The training of SVM requires the solution of a constrained quadratic optimization problem, this is a key point of the proposed approach which allows to overcome the typical drawbacks as overfitting or local minima (compared with NNs). Numerical results show the validity and veracity of SVM approach. Future work will be focused on the use of SVM to 3-D target buried beneath a rough surface.

REFERENCES

1. Tsang, L., C. H. Chan, K. Pak, and H. Sangani, "Monte-Carlo simulations of large-scale problems of random rough surface scattering and applications to grazing incidence with the BMIA/canonical grid method," *IEEE Trans. on Antennas and Propagation*, Vol. 43, No. 8, 851–859, Aug. 1995.
2. Lawrence, D. E. and K. Sarabandi, "Electromagnetic scattering from a dielectric cylinder buried beneath a slightly rough surface," *IEEE Trans. on Antennas and Propagation*, Vol. 50, No. 10, 1368–1376, Oct. 2002.
3. Rao, S. M., D. R. Wilton, and A. W. Glisson, "Electromagnetic scattering by surfaces of arbitrary shape," *IEEE Trans. on Antennas and propagation*, Vol. 30, No. 3, May 1982.
4. Toupikov, M., Y. Tretiakov, and G. Pan, "Numerical study of random surface scattering using wavelets," *2nd International Conference on Microwave and Millimeter Wave Technology, ICMMT 2000*, 399–402, 2000.
5. Cheng, Y., H. Zhou, and G. Zhang, "Study of solving two dimensional time domain electric field integral equation by the method of moments," *Nuclear Electronics & Detection Technology*, Vol. 20, No. 1, Jan. 2000.
6. Lawrence, D. E. and K. Sarabandi, "Acoustic and electromagnetic wave interaction analytical formulation for acousto-electromagnetic scattering behavior of a dielectric cylinder," *IEEE Trans. on Antennas and Propagation*, Vol. 49, No. 10, 1382–1392, Oct. 2001.
7. Xu, C.-W., F. Zhu, L.-N. Liu, and D.-P. Niu, "Unitary analysis of T -matrix method in 2D dielectric scattering by TE Wave incident," *2012 International Workshop on Microwave and Millimeter Wave Circuits and System Technology (MMWCST)*, 1–3, 2012.
8. Zhang, Q. H., B. X. Xiao, and G. Q. Zhu, "A new solution of real-time electromagnetic inverse scattering," *Chinese J. Geophys.*, Vol. 49, No. 5, 1546–1551, 2006 (in Chinese).
9. Zhang, Q. H., "Inverse scattering by dielectric circular cylinder based on BP neural networks," *Chinese Journal of Radio Science*, Vol. 25, 398–402, 2010.
10. Singh, D., "An efficient electromagnetic approach to train the SVM for depth estimation of shallow buried objects with microwave remote sensing data," *IEEE International Geoscience and Remote Sensing Symposium, IGARSS 2007*, 4961–4964, 2007.

Electromagnetic Field-focusing EBG Lens

G. A. Balykov¹, V. A. Kaloshin², A. N. Semenov¹, and A. P. Smirnov¹

¹Lomonosov Moscow State University, Moscow, Russia

²Kotelnikov Institute of Radio Engineering and Electronics, Moscow, Russia

Abstract— The electromagnetic field focusing capabilities of non-continuous periodic Mikaelian lens is considered. Theoretical continuous Mikaelian lens has the electromagnetic field focusing properties and concentrates incident wave field in one point on the border. Also this lens has sophisticated structure and cannot be implemented using current technologies. The alternative way to implement similar structure is by using periodic layers of constant permittivity which are separated by the periodic layers of air. The idea is to replace continuous lens with the another one, which structure could be easily implemented in practice. Continuous lens has permittivity reducing from 2.56 on the axis of symmetry to 1.0 at the borders. The new lens is a periodic structure, that does not have the same redundancy of permittivity as the continuous one. Such lens has layers containing both the non-conductor and the air, and the ratio of thickness of air to thickness of material increases in the direction from axis of symmetry towards the borders. Thickness ratio of air to thickness of material in each layer is calculated according to the permittivity in the continuous lens on the same distance from the axis of symmetry. Material and air create necessary permittivity in total. It is shown, that the ratio of wavelength to the one period length should be higher than specific value. FDTD method is used for the numerical simulation. The thickness of one layer expressed in the number of grid points is important numerical parameter. When this number is too small, structure of lens close to the axis of symmetry cannot be resolved, and this leads to loss of focusing capabilities. To avoid this, the number of grid points per layer should be at least equal to 10, but the higher this number is the better result would be achieved. The problem with increasing the number is that grid size should also be increased, and the amount of needed memory will also significantly rise. Number of computational experiments is performed and electromagnetic-field focusing capability of layered lens is obtained.

1. INTRODUCTION

A. L. Mikaelian found a solution of synthethis problem of gradient lens with index of refraction which depends on one cartesian coordinate [1]. Gradient Mikaelian lens focuses field of electromagnetic wave in focal point on its surface. There are different ways to implement them in reality, for example ion implantation. This way is used in optics. Another way is to approximate this gradient lens, and approximated one will have almost the same focusing features. EBG Mikaelian lens was proposed in [2]. In this work the focusing features of its special case are studied.

2. GRADIENT LENS

Three-dimensional structure with two metal surfaces is equal two-dimensional, when wave vector is parallel to metal surfaces and orthogonal to periods, and field vector E is orthogonal to surfaces. Figure 1 shows three-dimensional structure where two parallel bricks are metal surfaces and 6 parallel bricks are dielectric periods.

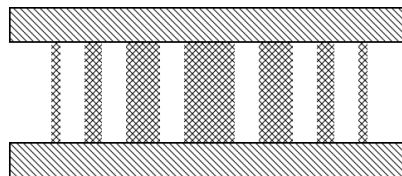


Figure 1: Three-dimensional structure.

A. L. Mikaelian has shown a solution for such gradient lenses. Structure, which has reflection index changing across only one axis proportional to the minus first power of hyperbolic cosine, is

a lens for electromagnetic waves. Let reflection index change across the O_y axis, and planar wave will propagate across the O_x axis. Lens width by O_x axis is \mathbf{L} . This lens has an axis of symmetry and the O_x axis is set to exactly match it, the axis of symmetry is parallel to the wave vector and orthogonal to the O_y axis. Axis of symmetry divides structure into two symmetrical parts. O_y axis is set to exactly match left border of the lens, i.e., the first border wave reaches during propagation.

Reflection index changes according to [1]:

$$n(y) = \frac{n_0}{ch\left(\frac{\pi|y|}{2L}\right)} \quad (1)$$

Note that permittivity is expressed like this using reflection index:

$$\varepsilon(y) = n^2(y) \quad (2)$$

Permittivity and reflection index reduce from the maximum value on the O_x axis (axis of symmetry) to the minimum value on upper and lower borders. \mathbf{R} is the thickness of both upper and lower symmetrical parts by O_y axis. Let the maximum value of reflection index be $n_0 = 1.6$, the minimum value equals 1.0, which is the same to the value of the vacuum, surrounding the structure. The maximum value of permittivity is $\varepsilon_0 = 2.56$. The thickness \mathbf{R} becomes determined after setting the width \mathbf{L} , because \mathbf{R} is retrieved from the next formula:

$$n(R) = \frac{n_0}{ch\left(\frac{\pi R}{2L}\right)} = 1.0 \quad (3)$$

3. LAYERED APPROXIMATION

Gradient lens is difficult to create because of continuous permittivity and refraction index change. But permittivity could be divided into parts, i.e., gradient change could be replaced with discrete change. New layered lens has discrete levels of permittivity, and permittivity also reduces from the axis of symmetry to upper and lower border, but not in a continuous way. Figure 2 shows difference in permittivity distribution between this layered lens and a gradient one.

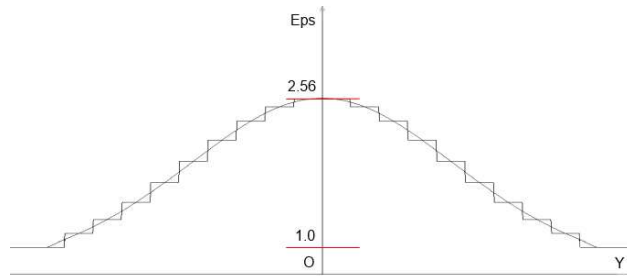


Figure 2: Permittivity distribution in gradient and layered lenses.

In layered lens permittivity in each layer is set according to permittivity in gradient lens at the same point on O_y axis as the middle point of the layer. N is the total number of layers, i is the number of current layer. For reflection index:

$$n(y) = n_i, \quad l_i - \frac{R}{2N} \leq y < l_i + \frac{R}{2N} \quad (4)$$

$$n_i = \frac{n_0}{ch\left(\frac{\pi l_i}{2L}\right)} \quad (5)$$

$$l_i = \left(i + \frac{1}{2}\right) \frac{R}{N} \quad (6)$$

$$0 \leq i < N - 1 \quad (7)$$

Such a layered lens is easier to implement in reality than a gradient one, but let's use another approximation.

4. EBG APPROXIMATION

There is another way to approximate gradient lens [2]. Each layer (period) will be divided into two internal layers of material and vacuum. In each period internal layer of material will be closer to the axis of symmetry, besides, material will be the same everywhere and will have permittivity equal to the permittivity on the axis of symmetry. This approximation is called Electromagnetic Bandgap (EBG). Figure 3 shows difference between layered and EBG approximations. This lens is easier to create in reality.

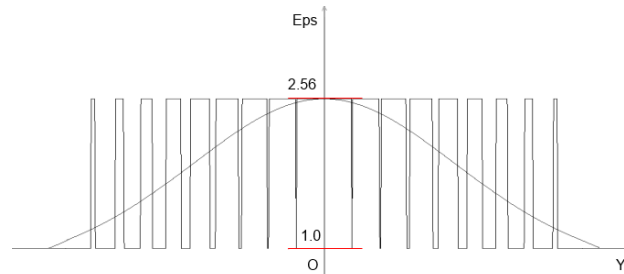


Figure 3: Permittivity distribution in gradient and EBG lenses.

The idea is that permittivity in each period in average will be equal to the permittivity in gradient lens at the same point on O_y axis as the middle point of the period. Average permittivity in period is

$$\varepsilon_{average_i} = \varepsilon_0 * \frac{l_{1_i}}{l_i} + \frac{l_{2_i}}{l_i} \quad (8)$$

$$l_{1_i} + l_{2_i} = l_i \quad (9)$$

l is the thickness of one period, l_1 is the thickness of material in period and l_2 is the thickness of vacuum. Period filling index is the ratio of material thickness to vacuum thickness [3]:

$$c_i = \frac{l_{1_i}}{l_{2_i}} = \frac{\varepsilon_{average_i} - 1}{\varepsilon_0 - 1} \quad (10)$$

Reflection index in EBG Mikaelian lens is calculated like this:

$$n(y) = \begin{cases} n_0, & l_i - \frac{R}{2N} \leq y \leq l_i - \frac{R}{2N} + c_i \\ 1, & l_i - \frac{R}{2N} + c_i < y < l_i + \frac{R}{2N} \end{cases} \quad (11)$$

$$\varepsilon_{average_i} = n_i^2 \quad (12)$$

Average refraction index in period n_i and coordinate of the middle point of the period l_i are retrieved from (5) and (6).

5. NUMERICAL MODELLING OF EBG MIKAELIAN LENSES

Numerical modelling was done using total field/scattering field method for wave excitation and perfectly matched layer for scattered wave cancelation [4]. TMz mode was simulated.

Permittivity of material and vacuum create necessary permittivity in total. That's why this lens does not work as a lens to all the incident waves, the ratio of wavelength to the thickness of one period should be higher than some value, then wave sees structure in total and not as separated pieces of material. This ratio is the first significant parameter. Numerical experiments show that it should be equal at least 2, but the higher it is, the better results would be achieved.

The second significant parameter is the thickness of one period expressed in number of grid points. When this number is too small, periods close to the axis of symmetry lose all differences between them. They become almost fully-filled with material except one line of grid points, because there are not enough points to fulfill needed permittivity accuracy. Numerical experiments show that to avoid this problem number of grid points per period should be at least 10, but the higher it is, the better results would be achieved. The problem with increasing both significant parameters is that large amounts of memory are required.

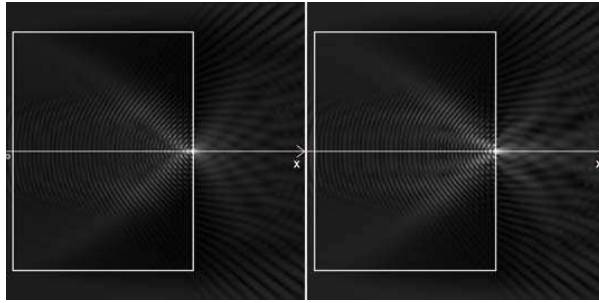


Figure 4: $|E_z|$ distribution for gradient and EBG lenses.

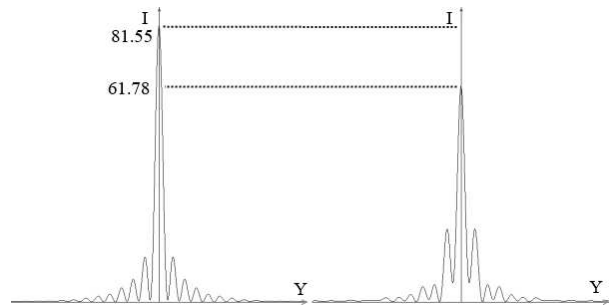


Figure 5: $|E_z|^2$ distribution for gradient and EBG lenses in focus plane.

Next results were achieved for lens with $\mathbf{L} = 100 * 10^{-3}$ m and wave with wavelength $\lambda = 6.7 * 10^{-3}$ m and amplitude 1.0. From previous formulas $\mathbf{R} = 67 * 10^{-3}$ m. Lens has 80 periods in every symmetrical part, thickness of one period is $l = 0.84 * 10^{-3}$ m. Ratio of wavelength to thickness of one period is 7.98 and the grid was set to have 20 points in each period. Figure 4 shows planar wave field amplitude E_z distribution for gradient lens on the left side and for EBG lens on the right side. The brighter the point is, the higher field value it has. White rectangle is a lens itself.

Focus point of EBG lens is moved $0.125 * 10^{-3}$ m forward by O_x axis from focus point of gradient lens, it is also blurred by O_x axis, i.e., EBG lens has a bit higher focus length. Focus intensity of EBG lens is 76 percent of focus intensity of gradient lens. Focus spots have the same diameter. Figure 5 shows intensity distribution in focus plane.

6. CONCLUSION

In this work EBG approximation of Mikaelian lens was studied. In order to simulate such structures, large amounts of memory are required, which will allow to set both significant parameters to acceptable values. First significant parameter is ratio of wavelength to the thickness of one period, which should be greater than 2 to get focusing of electromagnetic wave. Second significant parameter is number of grid points per period; it should be high enough to simulate all structure properties.

EBG Mikaelian lens definitely has focusing features, but lens has to have large amount of periods to get close to focusing capabilities of gradient lens. EBG Mikaelian lens field distribution will get closer to field distribution of gradient lens during increasing of number of periods, and it was shown that total 160-period lens has good focusing features.

ACKNOWLEDGMENT

This work is supported by Russian Foundation for Basic Research (RFFI grant 14-01-00337).

REFERENCES

1. Mikaelian, A. L., "About one solution method of geometric optics inverse problem," *DAN SSSR*, Vol. LXXXVI, No. 5, 1952.
2. Kaloshin, V. A., Doctor of Science Dissertation, 1959 (in Russian).
3. Kaloshin, V. A. and S. V. Stoyanov, *Soviet Journal of Communications Technology and Electronics*, Vol. 35, No. 5, 134–137, 1990.
4. Smirnov, A. P. and A. N. Semenov, "Full wave Maxwell's equations solver EMWSolver3D," *PIERS Proceedings*, 252–255, Moscow, Russia, Aug. 19–23, 2012.

Performance Analysis of Parallel FDTD Algorithm on IBM BlueGene Supercomputer Series

A. P. Smirnov¹, A. N. Semenov¹, and A. V. Pozdnev²

¹Lomonosov Moscow State University, Moscow, Russia

²IBM East Europe/Asia Ltd., Moscow, Russia

Abstract— The advances in high performance computing nowadays have increased the need of the computational resources to solve the large-scale problems. The large-scale electromagnetic and optical problems with the size of the order of 400 wavelengths in every dimension for a problem with arbitrary complex geometry structure can be solved. One of the most widespread numerical methods for Maxwell equations solving is Finite Difference Time Domain (FDTD) method. FDTD is based upon Yee lattice and Maxwell equations in integral form and differential relations from which finite difference approximation is obtained. In this paper, IBM BlueGene/P and BlueGene/Q performance is compared to calculate the large electromagnetic problem using parallel Finite Difference Time Domain method. Introduced early EMWSolver3D was implemented on Lomonosov Moscow State University IBM BlueGene/P supercomputer. Using 1D data decomposition for the highly elongated spatial domains together with the asynchronous transfer operations between nodes of supercomputer it is allows to solve problems up to 10^{10} computational cells on more than a thousand nodes. Parallel implementation of FDTD algorithm based on hybrid MPI/OpenMP approach is used in this paper. The scalability of the algorithm on both BlueGene/P and BlueGene/Q systems that runs in different parallel modes is considered. Parallel processing performance comparison of both systems shows that the IBM BlueGene/Q supercomputer gives near linear speedup and the great efficiency on FDTD algorithm.

1. INTRODUCTION

Nowadays the numerical modeling of electromagnetic wave propagation in microelectronics, nanooptics and biodiagnostics require full-wave solution of system of Maxwell equations on large spatial grids. The large-scale electromagnetic problems with the size of the order of 400 wavelengths in every dimension for a problem with arbitrary complex geometry structure require more than 1 terabyte of memory. Such large spatial grids are used to describe the complex geometry of the problem. One of the most widespread numerical methods for Maxwell equations solving is Finite Difference Time Domain (FDTD) method. FDTD is based upon Yee lattice and Maxwell equations in integral form and differential relations from which finite difference approximation is obtained. Nowadays the advances in the high performance computing have increased the need of the effective parallel implementations of the well known numerical methods. In this work the scalability of the parallel FDTD algorithm on both BlueGene/P and BlueGene/Q systems is considered.

2. PARALLEL FDTD ALGORITHM

Let's consider convolutional FDTD algorithm [1] based upon Yee algorithm [2] that uses material spatial averaging technique [3]. The Yee algorithm solves for both electric and magnetic fields in time and space using the coupled Maxwell's curl equations. With the systems of finite-difference expressions considered in [1], Chapter 3, the new value of an electromagnetic field vector component at any lattice point depends only on its previous value, the previous values of the components of the other field vector at adjacent points, and the known electric and magnetic current sources. Therefore, at any given time step, the computation of a field vector can proceed either one point at a time, or, if p parallel processors are employed concurrently, p points at a time [1]. The proper balance of performed computations and memory consumption is very significant for the efficient implementation of the algorithm. Because of BlueGene distributed memory architecture and strong computational power per gigabyte of memory, we chose to store in memory only data that is required for the next time step.

The parallel FDTD algorithm is based upon domain decomposition technique. For the sake of simplicity, we assume that the subdomains are partitioned along one z -direction and we use 1-D decomposition. The most important factor that influences the parallel efficiency is the load balancing. The amount of data to be exchanged is directly proportional to the cross-sectional area

of the subdomain interface. Hence, the optimal domain decomposition scheme goes hand in hand with the appropriate choice of the processor distribution [4].

3. HYBRID MPI/OPENMP PARALLEL PROGRAMMING TECHNIQUE

Hybrid MPI/OpenMP approach is an effective parallel programming technique [5], that can be applied to the parallel implementation of the FDTD algorithm. In case of the FDTD algorithm, inner node OpenMP parallelization is taken upon main loop of electric and magnetic field calculation and does not require complex atomic operations. There is no critical sections between MPI operations, so the algorithm can be effectively executed on high performance computational systems with large number of processor cores per computational node.

4. TARGET BLUEGENE SUPERCOMPUTER SPECIFICATIONS

In this work the computations are performed on the Lomonosov Moscow State University's IBM Blue Gene/P supercomputer [8] and on IBM Blue Gene/Q, installed in IBM Thomas J. Watson Research Center [7].

The BG/Q is the third generation of the IBM Blue Gene line of supercomputers targeted primarily at large-scale scientific applications. Each BG/Q node is based on a system-on-a-chip processor. Functionally, the chip contains 16 compute cores and 1 supplemental core to handle operating system tasks. Each core supports four-way simultaneous multithreading (SMT) and two-way concurrent instruction issue: one integer, branch, or load/store instruction and one floating-point instruction per clock cycle. Within a thread, dispatch, execution, and completion are in order. Four threads per core are sufficient to fully utilize the execution pipelines, prevent memory latency from adversely affecting performance, and avoid the necessity of out-of-order execution. Each core contains a quad SIMD double precision floating point unit (FPU) capable of 8 floating point operations (fused multiply add) per cycle. The 16 user processor cores at 1.6 GHz gives a BG/Q node a peak performance of 204.8 GFlop/s. The node main memory is 16 GByte of directly attached SDRAM-DDR3 providing 42.7 GB/s total bandwidth. A single BG/Q rack contains 1024 BG/Q nodes like its predecessors.

The BG/Q network has a 5-D torus topology; each compute node has 10 communication links with a peak total bandwidth of 40 GB/s. The internal BQC interconnect has a bisection bandwidth of 563 GB/s. An integrated five-dimensional torus serves as the principal node-to-node communication network and also handles collectives and fast interrupts. Compared to the 3D torus architecture of its predecessor BG/P, the 5D torus in BG/Q markedly decreases the number of hops required to reach the farthest node in the machine from any given node, and thereby both increases the bandwidth and reduces the latency of node-to-node communication.

5. ALGORITHM SCALABILITY

The strong and weak scalability are defined in work [6]. The strong scalability is defined as:

$$S_{strong} = \frac{T(N_{proc}^{ref}, M)}{T(N_{proc}, M)}, \quad (1)$$

where $T(N_{proc}^{ref}, M)$ — fixed size problem computation time with computational costs with N_{proc}^{ref} number of processors, which taken as reference time, and $T(N_{proc}, M)$ same size problem computation time with N_{proc} processors. For the weak scalability: $T(N_{proc}^{ref}, M^{ref})$ reference problem computation time with computation costs M^{ref} with reference number N_{proc}^{ref} of processors, than $T(N_{proc}, \frac{N_{proc}}{N_{proc}^{ref}} M^{ref})$ — problem computation time with $\frac{N_{proc}}{N_{proc}^{ref}}$ times more with N_{proc} processors. Measure of the weak scalability is defined as:

$$S_{weak} = \frac{T(N_{proc}^{ref}, M^{ref})}{T(N_{proc}, \frac{N_{proc}}{N_{proc}^{ref}} M^{ref})}. \quad (2)$$

In case of BG/P, FDTD solver is compiled by IBM XL compiler with keys “-o3-qarch=450d-qtune=450”. All tasks are run in SMP mode. For the first strong scalability measurement on BG/P, the spatial grid size is taken $128 \times 128 \times 1024$, so the problem can be fully computed on

the one computational node. The second strong scalability measurement on BG/P is performed with spatial grid size $1024 \times 1024 \times 4096$. Bigger problem can load every computational node more effectively. The result scalability plots are presented at Figure 1. As we can see from the plot, in the case of $128 \times 128 \times 1024$ grid, from 2 to 32 nodes the strong scalability is linear. From 64 nodes scalability factor starts to decrease, but still holds near linear. Strong scalability drop is caused by load lowness of each node because of small size of the reference problem. In fact, for the bigger task with spatial grid size $1024 \times 1024 \times 4096$, we have strong scalability drop from 128 to 256 computational nodes.

Let's consider the weak scalability of FDTD algorithm implementation on BG/P. The computation is performed for $1024 \times 1024 \times 16N_{proc}$ and $1024 \times 1024 \times 64N_{proc}$ spatial grids. Figure 2 illustrates the weak scalability plot for both sizes of the problem. In both cases it's fair enough. The weak scalability drop at 512 nodes is presumably caused by unbalancing of computational domain on each node and the size of the sent and received data to the nearby nodes. Also, in the case of the bigger task, the average weak scalability is better.

In case of BG/Q, FDTD solver is compiled by IBM XL compiler with keys “-o5-qhot”. All tasks are run in 16, 32 and 64 threads modes.

The strong scalability measurement on BG/Q with spatial grid size: $1024 \times 1024 \times 16384$ is illustrated in Figure 3. As we can see, strong scalability is linear, except 4096 computational nodes. The drop is probably caused by distinctive features of interconnection between two racks of the supercomputer.

The weak scalability measurement of FDTD algorithm on BG/Q is performed for $1024 \times 1024 \times 64N_{proc}$ spatial grid. Figure 4 illustrates the weak scalability plot for three multi-thread modes of

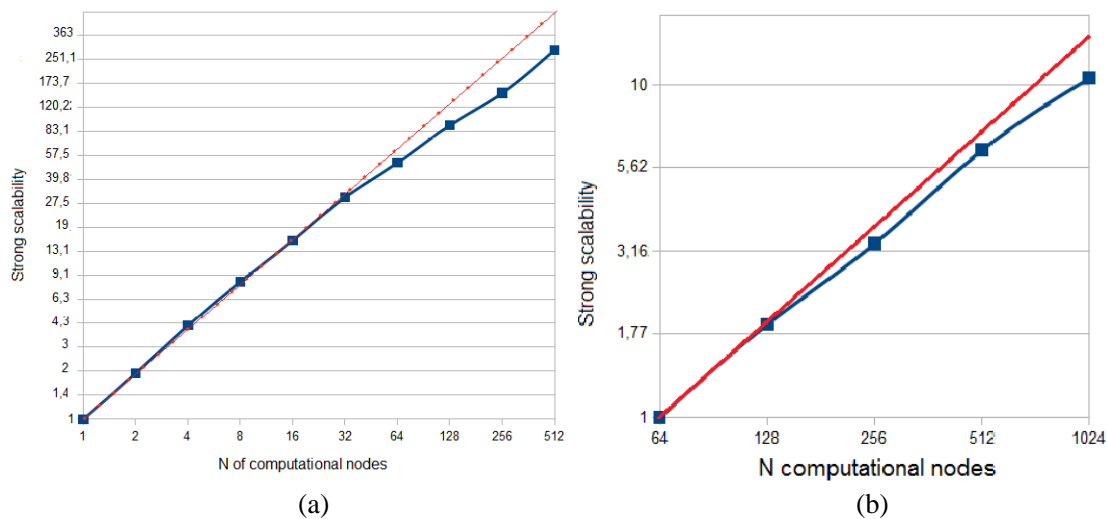


Figure 1: Strong scalability plot on BlueGene/Q with spatial grid size: (a) $128 \times 128 \times 1024$, (b) $1024 \times 1024 \times 4096$.

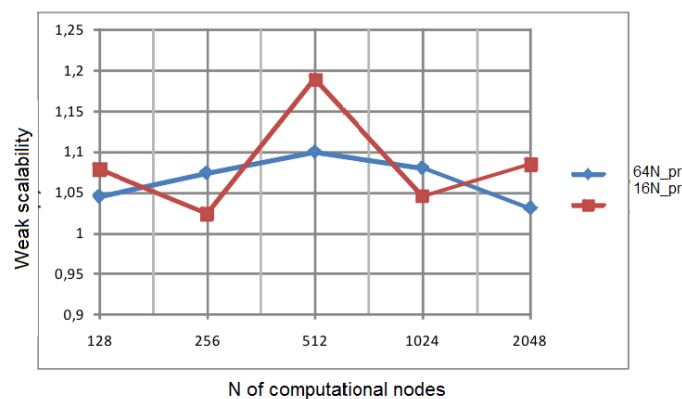


Figure 2: Weak scalability plot on BlueGene/P with spatial grid size: $1024 \times 1024 \times 16N_{proc}$ and $1024 \times 1024 \times 64N_{proc}$.

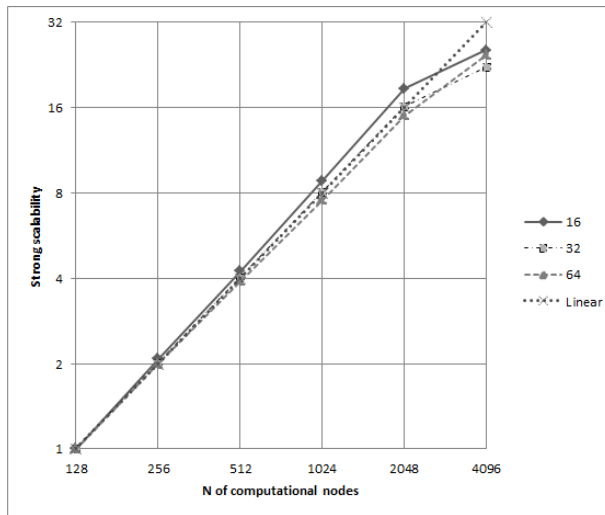


Figure 3: Strong scalability plot on BlueGene/Q with spatial grid size: $1024 \times 1024 \times 16384$.

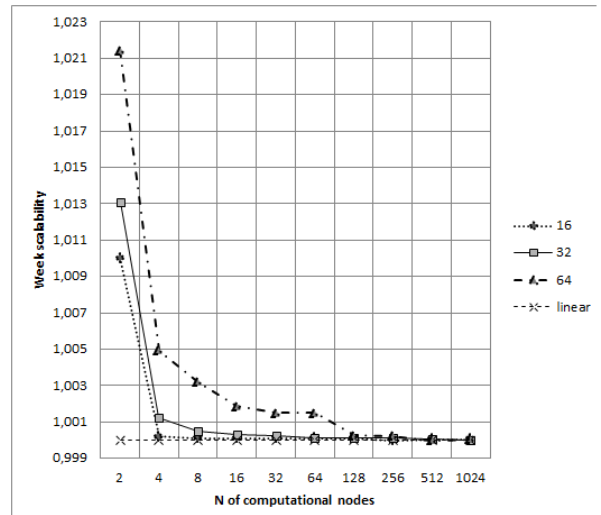


Figure 4: Weak scalability plot for three multi-thread modes of BlueGene/Q with spatial grid size: $1024 \times 1024 \times 64N_{proc}$.

supercomputer. In all three cases, the weak scalability is almost perfect.

6. CONCLUSION

Parallel implementation of FDTD algorithm based on hybrid MPI/OpenMP approach is used in this paper. The scalability of the algorithm on both BlueGene/P and BlueGene/Q systems that runs in different parallel modes is considered. Parallel processing performance comparison of both systems shows that the IBM BlueGene/Q supercomputer gives near linear speedup and the great efficiency on FDTD algorithm.

ACKNOWLEDGMENT

This work is supported by Russian Foundation for Basic Research (RFFI grant 14-01-00337).

REFERENCES

1. Taflov, A. and S. C. Hagness, *Computational Electrodynamics: The Finite-difference Time-domain Method*, Norwood, 2000.
2. Yee, K., "Numerical solution of initial boundary value problems involving Maxwell's equations in isotropic media," *IEEE Transactions on Antennas and Propagation*, Vol. 14, No. 3, 302–307, May 1966.
3. Semenov, A. N. and A. P. Smirnov, "Numerical modeling of Maxwell's equations with dispersive materials," *Matem. Mod.*, Vol. 25, No. 12, 1932, 2013.
4. Yu, W., R. Mittra, T. Su, Y. Liu, and X. Yang, *Parallel Finite-difference Time-domain Method*, 1st Edition, Artech House, 2006.
5. Rabenseifner, R., G. Hager, and G. Jost, "Hybrid MPI/OpenMP parallel programming on clusters of multi-core SMP nodes," *2009 17th Euromicro International Conference on Parallel, Distributed and Network-based Processing*, 427–436, Feb. 18–20, 2009.
6. Chatelain, P., et al., "Billion vortex particle direct numerical simulations of aircraft wakes," *Comput. Methods Appl. Mech. Engrg.*, Vol. 197, 1296–1304, 2008.
7. Haring, R. A., M. Ohmacht, T. W. Fox, M. K. Gschwind, D. L. Satterfield, K. Sugavanam, P. W. Coteus, P. Heidelberger, M. A. Blumrich, R. W. Wisniewski, A. Gara, G. L.-T. Chiu, P. A. Boyle, N. H. Chist, and C. Kim, "The IBM BlueGene/Q compute chip," *IEEE Micro.*, Vol. 32, No. 2, 48–60, Mar.–Apr. 2012.
8. "Overview of the IBM BlueGene/P project," *IBM Journal of Research and Development*, Vol. 52, No. 12, 199–220, Jan. 2008.
9. Smirnov, A. P. and A. N. Semenov, "Full wave Maxwell's equations solver EMWSolver3D," *PIERS Proceedings*, 252–255, Moscow, Russia, Aug. 19–23, 2012.

Analytical Formulation for Electromagnetic Leakage from an Apertured Rectangular Cavity

Y. Y. Li and C. Q. Jiao

State Key Laboratory of Alternate Electrical Power System with Renewable Energy Sources
North China Electric Power University, Beijing 102206, China

Abstract— An analytical formulation has been developed for the electromagnetic leakage from an apertured rectangular cavity excited internally by an electric dipole. The formulation consists of three parts: the interior problem of determining the field distribution within a closed cavity with the eigen-mode expansion method; the problem of characterizing the leakage mechanism of aperture by using the Bethe's small hole coupling theory; the exterior problem of determining the transmission field by using antenna theory. Theoretical values of shielding effectiveness are in good agreement with full-wave simulations. Analytic approaches, disregarding limited scope of application, are still of realistic interest in both science and engineering aspects due to clear physical meaning, high computation efficiency and easy to be programmed. In this paper, an analytic formulation is implemented to investigate the electromagnetic leakage from an aperture rectangular cavity. The formulation is based on the Bethe's small aperture coupling theory, which uses equivalent electric and magnetic dipoles to describe the relationship between the internal field of a closed cavity excited by an internal source and the leakage field from apertures. This Bethe's theory had been employed by some authors in earlier papers, and it is shown that the approach can work very well provided that the size of aperture is much smaller than one wavelength.

1. INTRODUCTION

With the rapid development of electronic technologies and the wide applications of wireless communication technologies, electromagnetic environment becomes more and more subtle and complex. So, various protection measures to prevent electromagnetic interference from both conducting and field coupling mechanisms have been studied and developed [1–4].

Electromagnetic shielding is the primary technology for suppressing electromagnetic interference via field coupling channel. It can be implemented by using a metallic enclosure to enclose an interference source to lower its field leakage, or to screen a sensitive object by reducing external field strength. Although a closed metallic enclosure generally has very high shielding effectiveness (SE) for electromagnetic waves, apertures that exist inevitably on the enclosure for some practical functions can result in dramatic reduction of SE. Thus, lots of work has given attention to the effect of apertures on shielding effectiveness, and some numerical, analytical [5] or experimental results have been reported.

Usually, in standard method for SE measurement, the SE of a shielding enclosure is defined as the ratio of the field strength at a given point with the enclosure removed to that at the same point with the enclosure applied. Where, the field source is required to be placed outside the enclosure. In other words, the field observation point is inside the enclosure, which has the advantage of reducing the potential influence of other unwanted interference source on the received field strength. As a result, in lots of literatures the SE of an enclosure is evaluated against an external field source.

However, the opposite case with source inside an enclosure is also in practical interest and deserves to be concerned. In principle, the two cases can be transformed into each other according to the reciprocity principle. However, since the “external source” cases have not been studied overall and thoroughly, we can not find appropriate “dual problem” for each of the “internal source” cases. For example, field distribution in near field zone is the primary concern for the latter case but for the former the exciting source (frequently, a plane wave is assumed) locates obviously in the far field zone [6, 7].

2. ANALYTICAL MODEL

Figure 1 shows an empty metallic rectangular cavity excited by an electric dipole placed inside it. The x , y , and z dimensions of the cavity are x_e , y_e , and z_e . A circular aperture is cut in the $x = x_e$ wall with its center at (x_e, y_0, z_0) . The z -directed electric dipole source is located at the point (x_s, y_s, z_s) . It is assumed that the cavity wall is perfectly conducting with a vanishing thickness.

According to the Bethe's theory, the aperture can be represented by equivalent aperture dipole moments \mathbf{p} and \mathbf{m} [8, 9]. The electric dipole moment is perpendicular to the aperture, and the

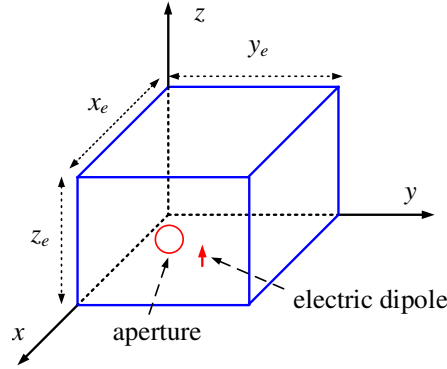


Figure 1: A rectangular cavity with a circular aperture and excited by an electric dipole placed inside the cavity.

magnetic dipole moment lies in the aperture plane. The strength of \mathbf{p} and \mathbf{m} are, respectively, proportional to the E and H fields existing on the inner wall with the aperture filled. Essentially, these fields are the “unperturbed” field of a closed cavity. Since the cavity walls are assumed to be perfectly conducting, the fields consist only of a normal E field and a tangential H field. The relationships between the dipole moments and the unperturbed fields are given through the aperture polarizability coefficients. Especially, for the configuration in Fig. 1, we have

$$\mathbf{p} = \alpha_e \varepsilon_0 E_x \mathbf{e}_x, \quad \mathbf{m} = -\alpha_{my} H_y \mathbf{e}_y - \alpha_{mz} H_z \mathbf{e}_z \quad (1)$$

Various expressions and curves of polarizability coefficients are available for some simple aperture shapes. Especially, for a circular aperture with a diameter of d , the coefficients are

$$\alpha_e \approx d^3/6, \quad \alpha_{my} = \alpha_{mz} = d^3/3 \quad (2)$$

Once the dipole moments are known, the field outside the cavity due to aperture leakage can be described by the free space field of the equivalent dipole antenna. Since the analytic formula of both electric and magnetic dipoles radiation can be found easily from textbooks, they are omitted here.

The remaining problem is the determining of unperturbed field distribution. Fortunately, the problem can be solved by using the eigen-mode expansion methods [9]. For the configuration displayed in Fig. 1, the expression for E -field is

$$\begin{aligned} \mathbf{E}(\mathbf{r}_0) &= \frac{j\omega\mu_0}{k^2} Idl \delta(\mathbf{r}_0 - \mathbf{r}_s) \mathbf{e}_z \\ &- \frac{j\omega\mu_0}{k^2} Idl \sum_{n=0}^{\infty} \sum_{m=0}^{\infty} \sum_{l=0}^{\infty} \frac{\varepsilon_{0n} \varepsilon_{0m} \varepsilon_{0l} \sin \frac{n\pi x_s}{x_e} \sin \frac{m\pi y_s}{y_e} \cos \frac{l\pi z_s}{z_e}}{x_e y_e z_e [k^2 - (n\pi/x_e)^2 - (m\pi/y_e)^2 - (l\pi/z_e)^2]} \\ &\times \left\{ \left[\left(\frac{n\pi}{x_e} \right)^2 + \left(\frac{m\pi}{y_e} \right)^2 \right] \sin \frac{n\pi x_0}{x_e} \sin \frac{m\pi y_0}{y_e} \cos \frac{l\pi z_0}{z_e} \mathbf{e}_z \right. \\ &- \frac{m\pi}{y_e} \left(\frac{l\pi}{z_e} \right) \sin \frac{n\pi x_0}{x_e} \cos \frac{m\pi y_0}{y_e} \sin \frac{l\pi z_0}{z_e} \mathbf{e}_y \\ &\left. - \frac{n\pi}{x_e} \left(\frac{l\pi}{z_e} \right) \cos \frac{n\pi x_0}{x_e} \sin \frac{m\pi y_0}{y_e} \sin \frac{l\pi z_0}{z_e} \mathbf{e}_x \right\} \quad (3) \end{aligned}$$

wherein, $\varepsilon_{0n} = 1$ for $n = 0$, $= 2$ for $n \neq 0$, and so on. The singularity resulted from the term containing the δ -function can be neglected since only the fields far away from the source are concerned.

In order to accelerate the convergence of the three-dimension series, the following formulas are

applied.

$$\sum_1^{\infty} \frac{\cos nx}{n^2 - a^2} = \frac{1}{2a^2} - \frac{\pi \cos(x - \pi) a}{2a \sin \pi a} \quad (0 \leq x \leq 2\pi) \quad (4)$$

$$\sum_1^{\infty} \frac{n \sin nx}{n^2 - a^2} = \frac{\pi \sin(x - \pi) a}{2 \sin \pi a} \quad (0 \leq x \leq 2\pi) \quad (5)$$

Substituting Eqs. (4) and (5) into Eq. (3) reduces the sums to a two-dimension series

$$E_z(x_0, y_0, z_0) = \frac{-j\omega\mu Idl}{k^2(x_e y_e z_e)} \sum_{n=0}^{\infty} \sum_{m=0}^{\infty} \Gamma_{nm} \left(\frac{z_e}{2k'} \right) \times \frac{\cos k'(z_0 + z_s - z_e) + \cos k'(|z_0 - z_s| - z_e)}{\sin k' z_e} \quad (6)$$

$$E_y(x_0, y_0, z_0) = \frac{-j\omega\mu Idl}{k^2(x_e y_e z_e)} \sum_{n=0}^{\infty} \sum_{m=0}^{\infty} \Gamma'_{nm} \left(\frac{z_e}{2} \right) \times \frac{\sin k'[z_e - (z_0 + z_s)] + \operatorname{sgn}(z_0 - z_s) \sin k'(z_e - |z_0 - z_s|)}{\sin k' z_e} \quad (7)$$

$$E_x(x_0, y_0, z_0) = \frac{-j\omega\mu Idl}{k^2(x_e y_e z_e)} \sum_{n=0}^{\infty} \sum_{m=0}^{\infty} \Gamma''_{nm} \left(\frac{z_e}{2} \right) \times \frac{\sin k'[z_e - (z_0 + z_s)] + \operatorname{sgn}(z_0 - z_s) \sin k'(z_e - |z_0 - z_s|)}{\sin k' z_e} \quad (8)$$

where, $\operatorname{sgn}(x)$ is the sign function, and

$$k' = \sqrt{k^2 - (n\pi/x_e)^2 - (m\pi/y_e)^2}, \quad (9)$$

$$\Gamma_{nm} = \varepsilon_{0n}\varepsilon_{0m} \left[\left(\frac{n\pi}{x_e} \right)^2 + \left(\frac{m\pi}{y_e} \right)^2 \right] \sin \frac{n\pi x_0}{x_e} \sin \frac{n\pi x_s}{x_e} \sin \frac{m\pi y_0}{y_e} \sin \frac{m\pi y_s}{y_e}, \quad (10)$$

$$\Gamma'_{nm} = \varepsilon_{0n}\varepsilon_{0m} \left(\frac{m\pi}{y_e} \right) \sin \frac{n\pi x_0}{x_e} \sin \frac{n\pi x_s}{x_e} \cos \frac{m\pi y_0}{y_e} \sin \frac{m\pi y_s}{y_e}, \quad (11)$$

$$\Gamma''_{nm} = \varepsilon_{0n}\varepsilon_{0m} \left(\frac{n\pi}{x_e} \right) \cos \frac{n\pi x_0}{x_e} \sin \frac{n\pi x_s}{x_e} \sin \frac{m\pi y_0}{y_e} \sin \frac{m\pi y_s}{y_e}. \quad (12)$$

The corresponding H field components can be obtained directly by using the Faraday's electromagnetic induction law:

$$H_x(x_0, y_0, z_0) = \frac{Idl}{(x_e y_e z_e)} \sum_{n=0}^{\infty} \sum_{m=0}^{\infty} \Gamma'_{nm} \frac{z_e \cos k'[z_e - (z_0 + z_s)] + \cos k'(z_e - |z_0 - z_s|)}{2k' \sin k' z_e}, \quad (13)$$

$$H_y(x_0, y_0, z_0) = -\frac{Idl}{(x_e y_e z_e)} \sum_{n=0}^{\infty} \sum_{m=0}^{\infty} \Gamma''_{mn} \frac{z_e \cos k'(z_0 + z_s - z_e) + \cos k'(|z_0 - z_s| - z_e)}{2k' \sin k' z_e}, \quad (14)$$

By coordinate transform, the above model is also feasible for x -directed or y -directed source. Then, by using superposition principle, the model can be expanded further to account for any direction-directed electric dipole source. With the increase of n and m , k' will become an imaginary number, the sine terms in the denominator position will lead to an exponential attenuation, and the series begins to converge rapidly. However, for the field point having the same z -coordinator with the source, the convergence becomes slow due to the denominator and the numerator having close exponential growth rates. In this case, the value of n and m must be increased further to achieve stable results.

3. RESULTS AND DISCUSSIONS

In the following contents, it is assumed that $x_e = 300$ mm, $y_e = 300$ mm, $z_e = 120$ mm, and the aperture is circular with a radius of 5 mm. Since the z component is dominate among the three electric field components, the electric shielding effectiveness S_E is define as $S_E = 20 \log_{10}(E_{z0}/E_{zs})$, where E_{z0} and E_{zs} are, respectively, the z -directed E -field with the shielding absent and present. Similarly, the magnetic shielding effectiveness S_H is referred to the y component H field.

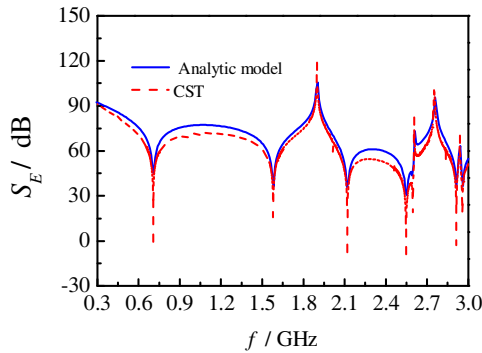


Figure 2: Dependence of the electric field shielding effectiveness S_E on frequency with $r = 0.4$ m.

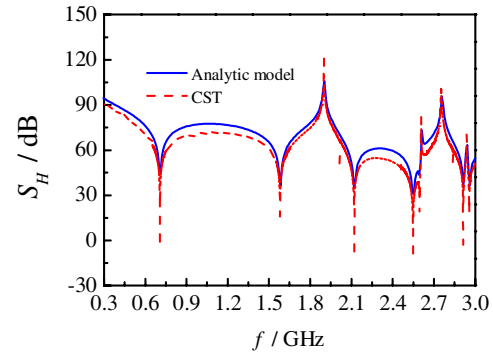


Figure 3: Dependence of the magnetic field shielding effectiveness S_H on frequency with $r = 0.4$ m.

The S_E and S_H are shown in Fig. 2 and Fig. 3, respectively, as the function of frequency with $x_s = 150$ mm, $y_s = 150$ mm, $z_s = 20$ mm, and the aperture located at the center of the $x = x_e$ wall. The observation point of shielding effectiveness is chosen at the position (700 mm, 150 mm, 60 mm). In other words, the observation point is at the right ahead of the aperture and the distance between the aperture and the point is $r = 0.4$ m. It can be seen that the results obtained by using the present analytic model are in good agreement with those acquired by employing the frequency domain algorithm of the full-wave simulation software CST. Also, the electric shielding effectiveness S_E is approximately equal to the magnetic shielding effectiveness S_H . The underlying reason is that the field point is already within the far-field zone for both the exciting source and the equivalent dipole, and hence the wave impedance at the field point keeps unchanged no matter the shielding applied or removed. Sharp reduction of SE around several frequencies like 0.71 GHz, 1.58 GHz, 2.12 GHz and 2.55 GHz are attributed to, respectively, the resonance effect of the modes TM_{110} , TM_{310} , TM_{330} , and TM_{510} . Where, a mode is classified as a TM (transverse magnetic) mode if it has no the magnetic field component along the z direction. The three subscripts correspond to the values of the three mode index n , m , and l , respectively. It is interesting to note that the resonance effects from some modes are not found. For example, the z -component of the electric field of the TM_{210} mode has a zero point at the position of the source, so this mode can not be stimulated by the source. In addition, sharp increase of SE is also observed near several frequencies. This phenomenon is usually explained as the result of the position of the source or the aperture coincides with the position of the wave node of the standing-wave field within the cavity.

4. CONCLUSIONS

An analytic formulation had been implemented to analyze the electromagnetic leakage from an apertured rectangular cavity. The leakage fields are represented by equivalent electric and magnetic dipoles at the aperture center with their dipole moments expressed by the “closed cavity” field according to the Bethe’s small aperture coupling theory. Comparison with the full wave simulation software CST had verified the reliability of the formulation over a broad frequency bandwidth.

REFERENCES

1. Henry, W. O., *Electromagnetic Compatibility Engineering*, 1st Edition, Wiley Interscience, New York, 2009.
2. Zhou, B. H., *EMP and EMP Protection*, 1st Edition, National Defense Industry Press, Beijing, 2003.
3. He, J. L., *Introduction to Electromagnetic Compatibility*, Science Press, Beijing, 2010.
4. Gomory, F., M. Solovyov, J. Souc, C. Navau, J. Prat-Camps, and A. Sanchez, “Experimental realization of a magnetic cloak,” *Science*, Vol. 335, 1466–1468, 2012.

5. Jiao, C. Q. and L. Qi, “Electromagnetic coupling and shielding effectiveness of apertured rectangular cavity under plane wave illumination,” *Acta Phys. Sin.*, Vol. 61, No. 13, 134104, 2012.
6. Bethe, H. A., “Theory of diffraction by small holes,” *Phys. Rev.*, Vol. 66, No. 7, 163–182, 1944.
7. Jiao, C. Q. and S. Niu, “Shielding effectiveness of an apertured rectangular cavity against the near-field electromagnetic waves,” *Acta Phys. Sin.*, Vol. 62, No. 11, 114102, 2013.
8. Rahmat, S. Y., “On the question of computation of the dyadic Green’s function at the source region in waveguides and cavities,” *IEEE Trans. Microw. Theory Techn.*, Vol. 23, No. 9, 762–765, 1975.
9. Robert, E. C., *Field Theory of Guided Waves*, 2nd Edition, Wiley-IEEE Press, New York, 1990.

Transient Electromagnetic Topology Method for Complex Wiring Consisting of Random and Nonuniform Transmission Lines

Haiyan Xie¹, Yong Li¹, Hongfu Xia¹, Chun Xuan¹, and Jianguo Wang²

¹Northwest Institute of Nuclear Technology, P. O. Box 69-12, Xi'an, Shaanxi 710024, China

²Northwest Institute of Nuclear Technology, P. O. Box 69-1, Xi'an, Shaanxi 710024, China

Abstract— The transient electromagnetic topology (TEMT) method is improved to include random and nonuniform transmission lines first and then is applied for the analysis of a car with complex wiring, which is composed by two random and a nonuniform transmission lines, under an electromagnetic pulse (EMP). In the TEMT method, the SPICE model for the nonuniform transmission line is composed by cascading the SPICE models for the segments of uniform lines, which compose the nonuniform transmission line. For the random transmission line, the average parameters are computed first and then the SPICE model is developed as the usual transmission line. The study on the car with complex wiring show that the improved TEMT method can deal well with the nonuniform and random transmission lines and the induced voltages of the devices generated by the EMP can be up to 100 V, which may cause upsets or damages to the devices.

1. INTRODUCTION

External high power electromagnetic pulse (EMP) interaction with electronic systems has attracted extensive attentions due to the development of the EMP sources [1] and the wide usage of electronic systems. External EMP can couple with systems through many paths (such as antennas, cables, and apertures) into interior subsystems or circuits and generates interferences and damages to them. The problem is complicated due to it relates to electromagnetic coupling, where the cable is hard to fix and can be random or nonuniform, and circuit or device effects.

The electromagnetic topology (EMT) method has been applied to analyze this problem since it was proposed. A car with complex wiring under EMP has been analyzed by using the EMT method in 2002 [2]. Kirawanich et al. have applied it to study EMP coupling with cables of communication systems [3]. In these researches, the Baum-Liu-Tesche (BLT) equation was employed to obtain voltages or currents generated by EMP at the terminals of transmission lines and it can not be used for transmission lines with nonlinear loads. In order to allow for the analysis of the nonlinear loads, the transient electromagnetic topology (TEMT) method was proposed [4]. The TEMT method applies the SPICE models of transmission lines and has been applied in EMP interaction with nonlinear systems [5]. However, the TEMT method has only considered uniform transmission lines. In reality, the transmission lines of systems are hard to fix and can be random or nonuniform.

In this paper, the TEMT method is extended to include random and nonuniform transmission lines and then is applied for the analysis of a car with complex wiring, which is composed by random and nonuniform transmission lines, under an EMP.

2. TEMT METHOD INCLUDING RANDOM AND NONUNIFORM TRANSMISSION LINES

2.1. Concept of TEMT Method

External EMP interaction with electronic system is a complex problem due to that: 1) the pulse width is short and the interaction is a transient process; 2) there are many coupling paths, including “front-door” and “back-door” couplings; 3) the configuration of electronic system is complex, including not only electromagnetic structures (cavities, apertures) but also wires, PCB, integrated circuits, and semiconductor devices; and 4) the nonlinear effect should be considered due to the high intensity of EMP. Due to the complexity, It is nearly impossible to solve this problem with only one numerical or experimental method.

Electronic systems include electromagnetic structures (cavities, antennas, and apertures, et al.), transmission line structures (such as wires and cables), and circuit structures (such as integrated circuits and semiconductor devices). The governing equations of these structures are different and their dimensions differs a lot. As a result, different methods and techniques are needed for different structures. This is the main reason that the interaction of EMP with electronic systems is difficult

to solve. As a result, how to decompose the whole problem into the analyses of electromagnetic structures, line structures, and circuit structures apart and combine them effectively is the key.

The TEMT method assumes that the effect of transmission lines on the incident wave can be ignored [6] and transforms the problem of electromagnetic field coupling with transmission line structures into the problem of circuit analysis. This realizes the effective decomposition and combination of the analyses of different structures. In order to transform the problem of electromagnetic field coupling with transmission lines into the problem of circuit analysis, the SPICE models for several types of uniform transmission lines have been developed [7, 8].

2.2. Including Random and Nonuniform Transmission lines

For transmission line with weak nonuniformity, the coupling with external fields can be described by

$$\begin{aligned} \frac{\partial}{\partial z} \mathbf{V}(z, t) + \mathbf{L}(z) \frac{\partial}{\partial t} \mathbf{I}(z, t) &= \mathbf{V}_F(z, t) \\ \frac{\partial}{\partial z} \mathbf{I}(z, t) + \mathbf{C}(z) \frac{\partial}{\partial t} \mathbf{V}(z, t) &= \mathbf{I}_F(z, t) \end{aligned}, \quad (1)$$

where $\mathbf{V}(z)$ and $\mathbf{I}(z)$ are the line voltage and current vectors, respectively. $\mathbf{L}(z)$ and $\mathbf{C}(z)$ are the per-unit-length (p.u.l.) inductance and capacitance matrices of the line, which are not constant but the functions of the z axis. \mathbf{V}_F and \mathbf{I}_F are distributed voltage and current source vectors which denote the effects of the external fields. Due to the inductance and capacitance matrices are the functions of the z axis, (1) can not be decoupled by similarity transformation for general configurations of nonuniform transmission line. However, they can be approximated by cascaded series of segments of uniform lines [9]. Thus nonuniform transmission line is divided into segments of uniform lines first, then the SPICE model for each segment of uniform line is developed according to [7, 8], and at last the SPICE model for the nonuniform transmission line is composed by connecting the SPICE model of each segment.

Random transmission lines may be nonuniform ones. Because nonuniform transmission lines can be approximated as cascaded series of many short sections of uniform lines, random uniform transmission lines are the basis. The equation for field coupling with random uniform transmission lines can be written as

$$\begin{aligned} \frac{\partial}{\partial z} \mathbf{V}(x, y, z) + \mathbf{L}(x, y) \frac{\partial}{\partial t} \mathbf{I}(z) &= \mathbf{V}_F(x, y, z) \\ \frac{\partial}{\partial z} \mathbf{I}(x, y, z) + \mathbf{C}(x, y) \frac{\partial}{\partial t} \mathbf{V}(z) &= \mathbf{I}_F(x, y, z) \end{aligned}. \quad (2)$$

Where the coordinates x and y are random. [10] and [2] point out that the average voltage can be approximated by the voltage when the average parameters (inductance, capacitance, et al.) are applied, that is, the average voltage and current satisfy the equation approximately as

$$\begin{aligned} \frac{\partial}{\partial z} \bar{\mathbf{V}}(z) + \bar{\mathbf{L}} \frac{\partial}{\partial t} \bar{\mathbf{I}}(z) &= \bar{\mathbf{V}}_F(z) \\ \frac{\partial}{\partial z} \bar{\mathbf{I}}(z) + \bar{\mathbf{C}} \frac{\partial}{\partial t} \bar{\mathbf{V}}(z) &= \bar{\mathbf{I}}_F(z) \end{aligned}. \quad (3)$$

Here $\bar{\mathbf{L}}$ and $\bar{\mathbf{C}}$ are the average inductance and capacitance. $\bar{\mathbf{V}}_F$ and $\bar{\mathbf{I}}_F$ can be computed from the electromagnetic fields at the average position. As a result, with the average parameters and the excitation fields at the average position, the SPICE model for the random line can be developed from [7, 8].

3. NUMERICAL SIMULATION

Figure 1 shows a car with complex wiring inside under an EMP. The wiring consists of a three-wire transmission line, a two-wire transmission line, and single-wire transmission line, with the radius of 0.75 mm and the lengths of 0.4 m, 0.6 m, and 0.5 m, respectively. The average height of these lines to the bottom of the car are 30 mm and all the terminal loads are 50Ω . The load R_{11} connects with R_{21} , R_{12} connects with R_{22} , and R_{13} connects with R_3 . The EMP is a biexponential pulse defined by $E(t) = kE_0[\exp(-\beta t) - \exp(-\alpha t)]$, where $k = 1.3$, $E_0 = 50 \text{ kV/m}$, $\alpha = 6.0e8 \text{ s}^{-1}$, and $\beta = 4.0e7 \text{ s}^{-1}$.

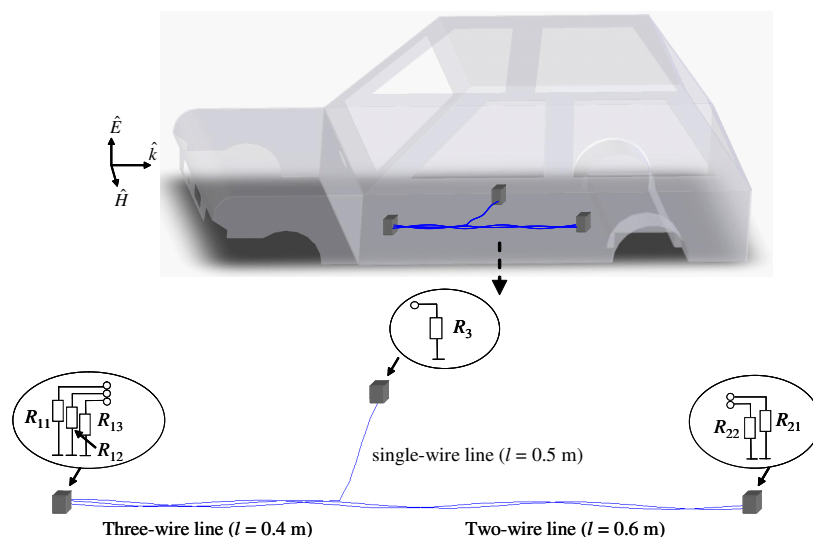


Figure 1: Car with complex wiring under an EMP.

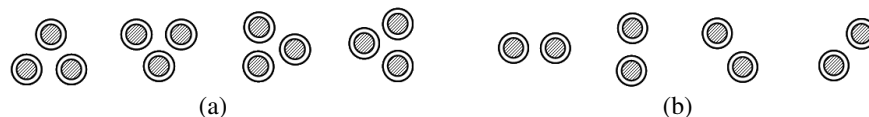


Figure 2: Different appearances of the transmission line cross section. (a) Three-wire transmission line. (b) Two-wire transmission line.



Figure 3: (a) Single-wire transmission line is approximated by cascaded series of sections of (b) uniform lines.

Due to that the wires are hard to fix exactly, the three-wire and two-wire transmission lines are random and their cross sections may have several different appearances, as shown in Figure 2, and the single wire is a nonuniform transmission line, as shown in Figure 3.

For this problem, the three-dimensional (3D) finite-difference time-domain (FDTD) method is applied to obtain the excitation fields along the lines at the average height. Then the inductance and capacitance matrices for the three-wire and two-wire transmission lines are computed according to the method described in Section 2, which are

$$\mathbf{L}_1 = \begin{bmatrix} 0.876 & 0.571 & 0.571 \\ 0.571 & 0.876 & 0.571 \\ 0.571 & 0.571 & 0.876 \end{bmatrix} \mu\mathbf{H}, \quad \mathbf{C}_1 = \begin{bmatrix} 26.11 & -10.29 & -10.29 \\ -10.29 & 26.11 & -10.29 \\ -10.29 & -10.29 & 26.11 \end{bmatrix} \mathbf{pF} \quad (4)$$

and

$$\mathbf{L}_2 = \begin{bmatrix} 0.876 & 0.571 \\ 0.571 & 0.876 \end{bmatrix} \mu\mathbf{H}, \quad \mathbf{C}_2 = \begin{bmatrix} 26.11 & -10.29 \\ -10.29 & 26.11 \end{bmatrix} \mathbf{pF}, \quad (5)$$

respectively. The single-wire transmission line is approximated by six segments of uniform lines, as shown in Figure 3, and the inductance and capacitance of each section is computed. For the three-wire and two-wire transmission lines, the excitation fields are the fields at the average height of the lines, but for the single-wire transmission line, linear interpolation is applied to get the excitation fields of each segment from the fields at the average height. With the per-unit-length parameters and excitations fields, the SPICE models for these transmission lines can be developed according to [7]. Then a SPICE software can be employed to obtain the voltages induced at the loads.

Figure 4 shows the average voltages at the loads of the near and far ends of the wiring induced by external fields. The results show that the loads R_{11} and R_{12} have the same average voltages with the loads R_{21} , R_{22} , respectively. This is because the lines connecting them have the same statistical property. The magnitudes of these induced voltages can up to 100 V, which implies that the external EMP can generate interferences on the car's system.

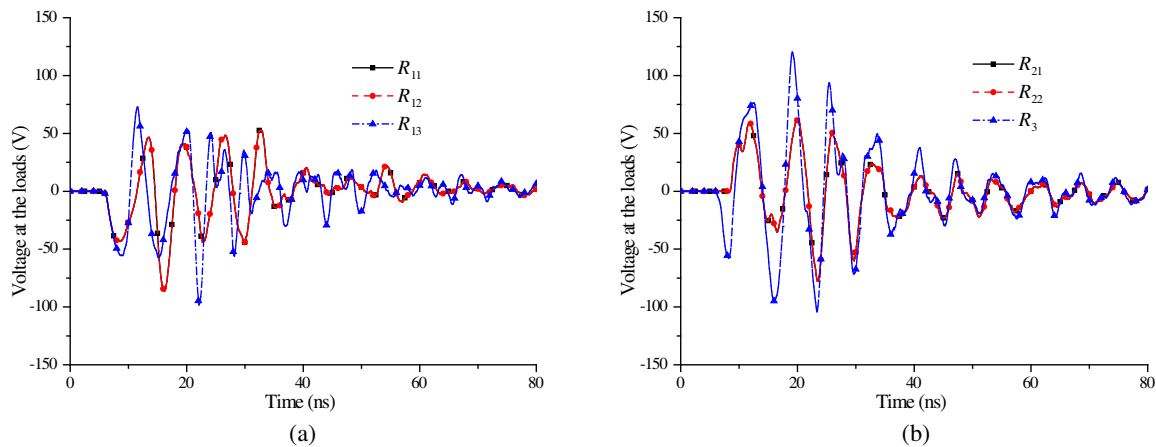


Figure 4: Voltages induced at the loads of (a) the near end (b) the far end.

4. SUMMARY AND CONCLUSION

The TEMT method has been improved to include random and nonuniform transmission lines in this paper. Then the improved TEMT method is applied for the analysis of a car with complex wiring, which is composed by two random and a nonuniform transmission lines, under an EMP. The results show that the improved TEMT method can deal well with the nonuniform and random transmission lines and the induced voltages at the inside devices of the car generated by the EMP can be up to 100 V, which may cause upset or damage to the devices.

ACKNOWLEDGMENT

Acknowledgement is made to National Natural Science Foundation of China for the support of this research through Grant No. 61231003 and No. 61201090.

REFERENCES

1. Baum, C. E., "From the electromagnetic pulse to high-power electromagnetics," *Proceedings of the IEEE*, Vol. 80, No. 6, 789–817, 1992.
2. Paletta, L., J. P. Parmantier, F. Issac, et al., "Susceptibility analysis of wiring in a complex system combining a 3-D solver and a transmission-line network simulation," *IEEE Trans. Electromagn. Compati.*, Vol. 44, No. 2, 309–317, 2002.
3. Kirwanich, P., N. Kranthi, N. E. Islam, et al., "Electromagnetic topology-based analysis of coupling through small apertures on cables on communications systems," *Electromagnetics*, Vol. 25, Nos. 7–8, 589–602, 2005.
4. Xie, H., J. Wang, D. Sun, R. Fan, and Y. Liu, "Analysis of EMP coupling to a device from a wire penetrating a cavity aperture using transient electromagnetic topology," *Journal of Electromagnetic Waves and Applications*, Vol. 23, Nos. 17–18, 2313–2322, 2009.
5. Xie, H., J. Wang, D. Sun, R. Fan, and Y. Liu, "SPICE simulation and experimental study of transmission lines with TVSs excited by EMP," *Journal of Electromagnetic Waves and Applications*, Vol. 24, Nos. 2–3, 401–411, 2010.
6. Parmantier, J. P. and P. Degaugue, "Topology based modeling of very large systems," *J. Hamelin. Modern Radio Science*, 151–177, Oxford Univ. Press, Oxford, UK, 1996.
7. Xie, H., J. Wang, R. Fan, et al., "A hybrid FDTD-SPICE method for transmission lines excited by a nonuniform incident wave," *IEEE Trans. Electromagn. Compati.*, Vol. 51, No. 3, 811–817, 2009.
8. Xie, H., J. Wang, R. Fan, et al., "SPICE models to analyze radiated and conducted susceptibilities of shielded coaxial cables," *IEEE Trans. Electromagn. Compati.*, Vol. 52, No. 1, 215–222, 2010.
9. Omid, M., Y. Kami, and M. Hayakawa, "Field coupling to nonuniform and uniform transmission lines," *IEEE Trans. Electromagn. Compati.*, Vol. 39, No. 3, 1997.
10. Xie, H., J. Wang, Y. Li, and C. Xuan, "Influence analysis of stochastic translation of transmission lines over ground," *Progress In Electromagnetics Research Letters*, Vol. 44, 53–61, 2014.

Influence of the Socket on Chip-level ESD Testing

Yu Xiao¹, Jiancheng Li², Jianfei Wu², Yunzhi Kang³, and Jianwei Su¹

¹P. O. Box 9010, Xiangtan University, Xiangtan, Hunan 411105, China

²National University of Defense Technology, Changsha, Hunan 410073, China

³Freescale Semiconductor Inc., TEDA, TianJin 300457, China

Abstract— This paper introduces a method of IC-level Electrostatic Discharge (ESD) testing and discusses the influence of the socket on Chip-Level ESD testing. During the powered ESD (PESD) testing, welding the chip to the PCB is a necessary process which can be a repetitive process and time consuming. In order to solve this problem, a ball grid array (BGA) test socket is used during the test. The socket is built from copper-clad pogo pin and is pinned in an 8×8 mm array with 121 pins on a 0.65-mm pitch. As the test results suggest, there is little difference between testing with the socket and without. So in this study we take such factors into account as the pan angle range between ESD gun and PCB, the ESD gun, etc.. It is found in this study that the difference value (D-value) percentage between socketed ESD testing and non-socketed ESD testing is within 6.4%, the D-value percentage that the pan angle range of the ESD gun produces is within 5.8%, and the D-value percentage that the ESD GUN produces is within 5.8%. Based on these findings, it is concluded that work efficiency can be greatly improved by using the socket in PESD testing.

1. INTRODUCTION

The existing system level ESD test methods and their application field have been discussed in great detail. It is noted that IEC 61000-4 is a set of EMC test standards which includes the system level ESD test method, IEC 61000-4-2 [1]. It specifies calibration waveforms, procedures and stress points for executing ESD tests on systems.

In most of the electronic modules and systems, the signal and power have to travel through few levels of interconnections, and the signal path is crossing few discontinuities from the board level up to the MCU die [2]. The BGA socket is an electromechanical system that provides a separable electrical and mechanical connection between BGA component and a test-fixture. The basic structures of a BGA type socket consist of plastic housing and metal pogo contacts. The functions of plastic housing are to electrically insulate the pogo contact members, and mechanically support, and maintain them in the original position. The pogo pin provides a stable electrical connection to the pad. The socket is built from copper-clad pogo pin and pinned in an 8×8 mm array with 121 pins on a 0.65-mm pitch. The BGA type socket is shown in Figure 1. Figure 2 shows the structure of spring probe.

During the PESD test, welding the chip to the PCB is a necessary process which can be a repetitive process and time consuming. The BGA socket is used to fix the problem. The final aim of this paper is to investigate the influence of the socket on Chip-level ESD testing.

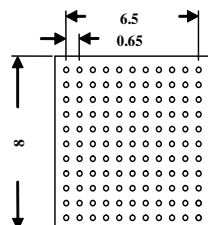


Figure 1: BGA socket for 8×8 mm matrix array.

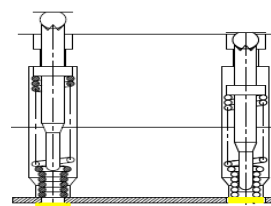


Figure 2: 0.4 mm pitch spring probe.

2. APPROCH AND TEST STRUCTURES

The existing system level ESD test methods are introduced in IEC 61000-4-2. The IEC standard defines typical discharge current waveforms, range of test levels, test equipment, test configuration, and test procedure. The characteristic of the waveform according to the system test standard IEC61000-4-2 is with a raise time of $0.85 + / - 0.15$ ns and a hold time of approximately 60 ns. The

waveform parameters are shown in Table 1 and the typical waveform of output current is shown in Figure 3 [3, 4].

Table 1: Waveform parameters.

Level	Indicated voltage kV	First peak current of discharge $\pm 10\%$ (A)	Rise time t_r with discharge switch ns
1	2	7.5	0.7 to 1
2	4	15	0.7 to 1
3	6	22.5	0.7 to 1
4	8	30	0.7 to 1

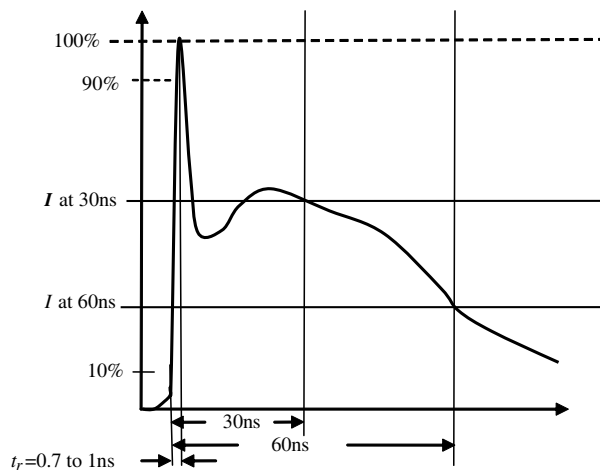


Figure 3: Typical waveform of the output current of the ESD generator.

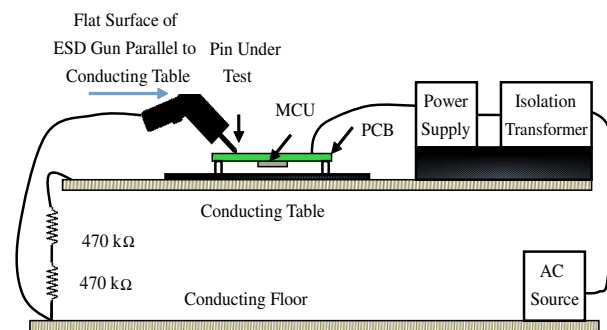


Figure 4: Powered direct contact pin ESD test table setup.

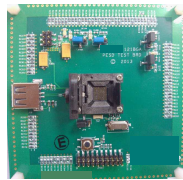


Figure 5: Bottom view of the test board (socketed).

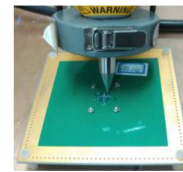


Figure 6: Measurement set up.

Powered direct contact pin ESD test platform is shown in Figure 4. The ESD gun is built in compliance with specification defined in IEC 61000-4-2, using the ESD gun model proposed and validated in [5]. The socket is used to fix the MCU on the PCB board, which is shown in Figure 5. RF current probe (Figure 6) connected to the oscilloscope is used to monitor the output voltage of the ESD generator.

3. RESULTS AND DISCUSSIONS

3.1. Analysis of the ESD GUN

To estimate the influence of the socket on the test results, we have to know how much influence the ESD gun itself may produce. The current of ESD has three paths to discharge [6].

1. Discharge from the capacitor between PCB and conducting table.
2. Discharge from the capacitor in power supply.
3. Discharge from the power supply wire.

Firstly, we measured the waveform at five different configurations:

- 1) Normal configuration (shown as Figure 4), ESD gun is configured at 1 kv.
- 2) Turning off the power supply, ESD gun is configured at 1 kv.
- 3) Cutting off the power line of the power supply, ESD gun is configured at 1 kv.
- 4) Cutting off the power line of the PCB, ESD gun is configured at 1 kv.
- 5) Cutting off both power line of power supply and PCB, ESD gun is configured at 1 kv.

During the test, the ESD gun was contacted to the GND layers of the PCB. Each configuration was tested three times and the average value was plotted in Figure 7:

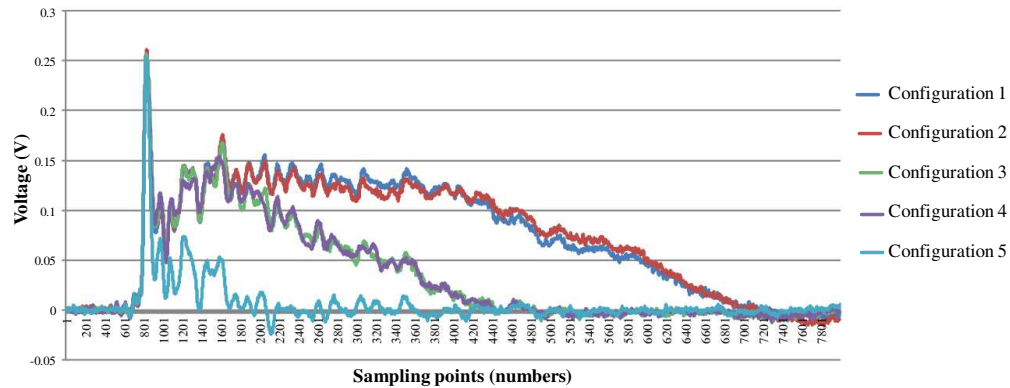


Figure 7: The test results of five different configurations.

The vertical axis represents the voltage (measured by RF current probe) of discharge as the horizontal axis demonstrates the sampling points which are extracted from the oscilloscope (8000 sampling points are extracted). From Figure 7, it can be learned that the results of configuration 1 and configuration 2 are nearly the same. Besides, the results of configuration 3 and 4 are also nearly the same. All the first peak values of the waveforms don't show much difference.

To avoid the effect of the changing test environment, we did another 1002 times of test (configuration 5). During the test the first peak values was measured. From Figure 8, it can be found that 90% of peak values are between 0.243V and 0.258V. So, the biggest D-value percentage is equal to $(0.258 - 0.243)/0.258 = 5.81\%$. Figure 9 shows the statistics of the test results.

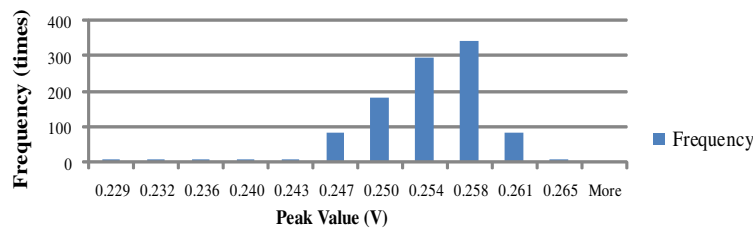


Figure 8: Percentage of the peak value.

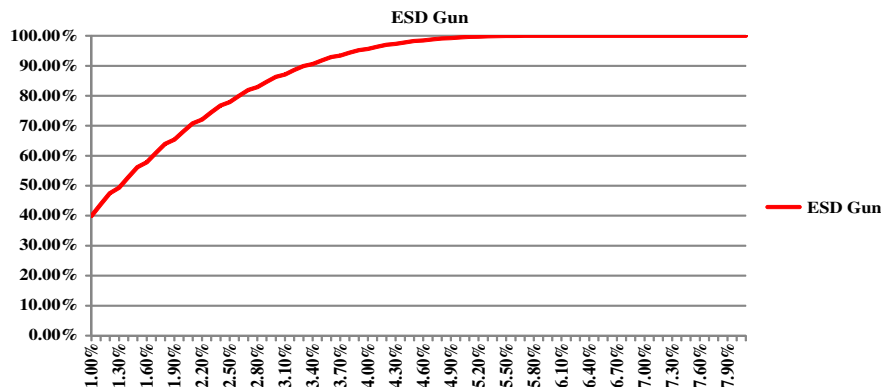


Figure 9: D-value percentage produced by ESD gun.

3.2. Alterations in the Test Results Resulted from the Pan Angle Range of the Printed Circuit Board

In the non-socketed ESD test, the printed circuit board was respectively revolved 0, 45, 90, 135, 180 degree horizontally. It was tested three times for each angle and the voltage is changed from 1 kV to 8 kV (step: 1 kV). 1440 sets of D-value percentage data are obtained from the test. Figure 8 shows the statistics on these test results:

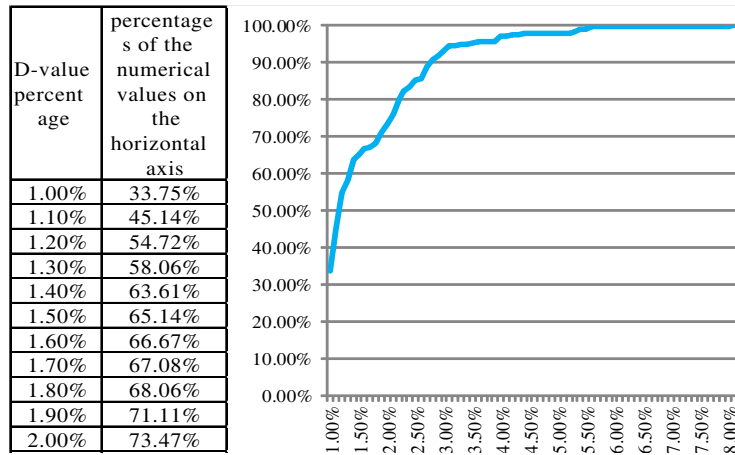


Figure 10: D-value percentage between different angles.

From the raw data and Figure 10 we can see that the D-value percentage is within 5.8%, which is less than 10% (shown in Table 1).

3.3. D-value Percentage between Using with and without Socket

Because we care about the voltage on the pad, the voltage instead of current was measured by the oscilloscope. The first discharge peak voltage was measured and three pins were tested (VSS, VDD and VDD2). Each pin was tested three times at the same voltage level ranging from ± 1 kV to ± 8 kV (step: 1 kV).

After the test, 432 sets of D-value percentage data are obtained. The statistics are shown in Figure 11. The horizontal axis presents D-value percentages ranging from 1.0% to 8.1% as the vertical axis showcases percentages of the numerical values on the horizontal axis (e.g., There are 102 sets of data which are lower than 1.0% in numerical values. So, the numerical value on the vertical axis would be $102/432 = 23.61\%$). “non-socketed” represents “without socket”.

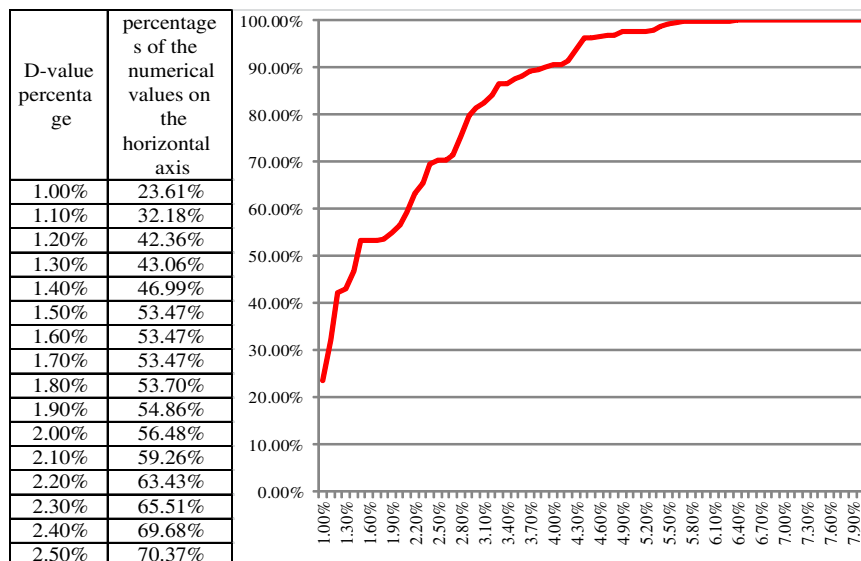


Figure 11: D-value percentage between socketed & non-socketed.

The first peak current of discharge is one of the main reasons that causes the MCU failure and damage. From the Raw data and Figure 11, it can be concluded that the D-value percentage between socketed and non-socketed is within 6.4%. It is less than 10% (shown in Table 1).

3.4. Comparison between Testing with and without Socket

In order to compare all the results above and describe the results more intuitively, Figure 12 is presented as follows. The test results of D-value percentage between 3 tests without using the socket and D-value percentage between 3 tests using the socket is added in this figure, which are not discussed above.

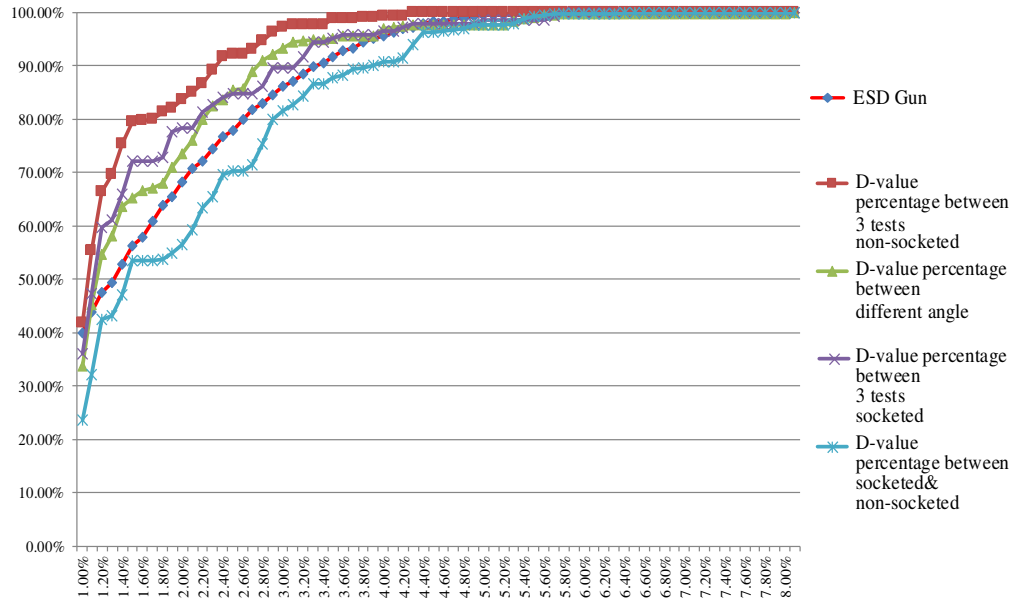


Figure 12: D-value percentage of all the test results.

From Figure 12, it can be seen that D-value percentage between socketed & non-socketed is the worst case. The curve related to ESD Gun is between the worst case and others. It means that the D-value produced by the test itself is inevitable. Statistically speaking, this test result is acceptable.

4. CONCLUSION

From the test results, it can be found that the D-value percentage which the ESD GUN produces is within 5.8%, 3 tests non-socketed is within 4.2%, different angles is within 5.8%, 3 tests by using the socket is within 5.7% and D-value percentage between socketed and non-socketed is within 6.4%. All the results are less than 10%. The test results show a good performance of the socket. Therefore, the socket can be used during the PESD test with little influence on the test results.

REFERENCES

1. IEC 61000-4-2 Standard, EMC, "Testing and measurement techniques, electrostatic discharge immunity test," Part 4-2, IEC, 2008.
2. Rotaru, M. D. and W. W. Weng, "Electrical characterization of a high performance microprocessor socket for system level simulation," *EPTC*, 415–420, 2003.
3. Wang, K., D. Pommerenke, and R. Chundru, "Numerical modeling of electrostatic discharge generators," *IEEE Trans. Electromagn. Compat.*, Vol. 45, No. 2, May 2003.
4. JEDEC Standard JESD22-A114-B, "Electrostatic discharge (ESD) sensitivity testing human body model," JEDEC, 2000.
5. Caniggia, S. and F. Maradei. "Analytical and numerical simulation models for calculating EMI into circuits due to ESD radiated fields," *IEEE International Symposium on Electromagnetic Compatibility*, 602–606, 2011.
6. System Level ESD Part II, "Implementation of effective ESD robust designs," 2012.

Solitary Wave Induced in a Sinusoidal Water Surface Wave Field of Hydrodynamics

Shigehisa Nakamura
Kyoto University, Japan

Abstract— Monitoring for nonlinear processes of water surface waves is introduced in brief. It was found a kind of nonlinear water surface waves which had a single crest wave with an infinitely long wave in a water tank. This wave was named as solitary wave on water surface in an experiment first. Then, a solitary wave had been led in a mathematical formulation. Another nonlinear wave known as a cnoidal wave was found in a form of cn function mathematically. An extensive experiment in an water tank has led to see a process in which an input function of linear sinusoidal wave induced a nonlinear wave quite similar to the solitary wave.

1. INTRODUCTION

This work is concerning to a problem on monitoring of solitary wave on water surface. For this purpose, a historical review is introduced about an experiment of a single crested wave in brief. It was found a kind of nonlinear water surface waves which had a single crest wave with an infinitely long wave in a water tank. This wave was named as solitary wave on the water surface in an experiment first. Then, a solitary wave had been led in a mathematical formulating procedure. Another nonlinear wave known as a cnoidal wave was found in a form of cn function mathematically. An extensive experiment had been led to see a process in which an input function of linear sinusoidal wave induced a nonlinear wave quite similar to the solitary wave.

2. LINEAR MODEL OF WATER SURFACE WAVE

At starting to introduce some specific features of nonlinear water surface wave, a brief note is given some note to water waves for a convenience in an hydrodynamic understanding of the present interesting nonlinear waves.

First, assume that water is isotropic for a linear water surface wave model.

This assumption has been introduced even in the publication by Lamb in 1879 [1].

What is essential is the problems on a sinusoidal water surface wave under assuming of a small amplitude as a linear problem of water waves in hydrodynamics.

3. NONLINEAR PROCESS OF SOLITARY WAVE

On the other hand, there are various kinds of aperiodic waves.

For example, Lamb in 1879 had introduced about a solitary wave which was called by Scott Russel as seen in “Report on Waves” appeared in British Association Report in 1844 [1]. Following what noted Lamb had noted in 1879, the author could introduce the work undertaken by Scott Russel as follow.

Scott Russell, in his interesting experimental investigations, was led to pay great attention to a particular type which he called the ‘solitary wave’. This is a wave consisting of a single elevation, of height not necessarily small compared with the depth of the fluid, which, if properly started, may travel for a considerable distance along a uniform canal, with little or no change of type. Waves of depression, of similar relative amplitude, were found not to possess the same character of performance, but to break up into series of shorter waves.

What noted above was given independently by Bousinesquq [2] and Rayleigh (as noted in his publication [3]).

The above note can specify the solitary wave. Then, some note in relation to one of the water waves reduced by a mathematical procedure as what is noted by Lamb in 1879 can be seen as follow.

Russel’s solitary type which may be regarded as an extreme case of Russel’s solitary type may be regarded as an extreme case of Stokes’ oscillatory waves of permanent type, the wave length being great compared with the depth of the canal, so that the widely separated elevations are particularly independent of one another. Now, the methods of approximation employed by Stokes become, however, unsuitable when the wave-length much exceeds the depth; and subsequent investigations of solitary waves of permanent type have proceeded on different lines.

3.1. What Lamb Noted

Lamb notes that Rayleigh, treating the problem as one of steady motion, starts virtually the formula

$$\phi + i\psi = F(x + iy) = \exp[iy(d/dx)]F(x), \quad (1)$$

where $F(x)$ is real. The notations ϕ and ψ are for stream function and potential velocity.

Lamb's solution of the above differential equation can be written as following, i.e.,

$$\eta = a \operatorname{sech}^2[(1/2)(x/b)], \quad (2)$$

where,

$$y - h = \eta, \text{ and, } b^2 = [h^2(h + a)/(3a)], \quad (3)$$

if the origin of x be taken beneath the summit. The approximations consist in neglecting the fourth power of the ratio $(h + a)/(2b)$. The theory of the solitary waves has been treated by Weinstein in 1926 [1]. Then, it can be seen that

$$c^2 = g(h + a), \quad (4)$$

in the field of the earth's gravity field.

The motion at the outskirts of the solitary wave can be represented by a very simple formula. Lamb in 1987 had communicated from Stokes that McCowan investigated to reduce,

$$c^2 = (g/m) \tan(mh), \quad (5)$$

$$\text{where, } m\alpha = (2/3) \sin^2[m(h + (2/3)a)], \text{ and, } a = \alpha \tan[(1/2)m(h + a)], \quad (6)$$

and, the notations a and α are the maximum elevation above the mean level and a subsidiary constant.

Then, Lamb notes what are specific in the solitary wave. That is to say, the extreme form of the wave when the crest has sharp angle of 120 degree was examined. Adding to that, the limiting value of the ratio a/h was found to be 0.78, in which case the wave-velocity is given by $c^2 = 1.56gh$.

Lamb states as that by a slight modification the investigation of Rayleigh and Boussinesq can be made to give the theory of a system of oscillatory waves of finite height in a canal of limited depth [4].

3.2. McCowan and Solitary Wave

McCowan [5] must be a reference in the early age of solitary wave's description.

Assuming a reference water depth h , then, a solitary wave η can be described in a mathematical form, i.e., as following to Lamb,

$$\eta = a \operatorname{sech}^2 \left[(1/2) (3a / (h^3))^{1/2} x \right], \quad (7)$$

where, the notation x is the horizontal axis and, the notation a is found in trochoidal wave,

$$x = x_0 a \exp(kz_0) \sin(kx_0), \text{ and, } z = z_0 + a \exp(kz_0) \cos(kx_0), \quad (8)$$

which is called as Gerstner wave in a consideration of historical background of its finding, as Gerstner reduced theoretically in 1802 though Rankin independently found it in 1863.

As for the small amplitude wave, formulation can be in a linear expression though this solitary wave has to be solved on the basis of nonlinear equation referring Lagrangean technique in consideration.

4. RESONANT COUPLING OF SOLITARY WAVE

Nakamura [6] has found a specific condition can produce a solitary wave in a simple water basin experimentally though a cnoidal wave with cn function was in his interest.

In Nakamura's work [6], he expected a uni-nodal lateral oscillation can be seen first.

The two solitary waves translated to meet at the center of the barrier to increase the maximum height of the water level was about twice of those at the two side comers.

At the center of the barrier, a couple of the solitary wave meets to make a collision each other. After that, a couple of the solitary wave continue the cross motion as if the two waves have never distorted at the collision.

The collision cycle was to coincide to the cycle of the incident sinusoidal wave as an input function of energy.

So that, a center slit of the barrier must be acted as an energy supply for the two solitary waves to maintain their cross motion between the two side walls during the input function of the sinusoidal wave is repeatedly generated.

When the input function acts only for one cycle of the sinusoidal wave, the couple of the solitary wave becomes to be faint and repeat reflection on the wall of both side up to decay out and disappear the couple of the wave.

This process was seen at the frequency of the input function is satisfying a resonant mode under a certain combination when the boundary condition, bathymetric condition, and energy supply at the center of the barrier are satisfied the resonant mode of the couple of solitary wave in the water basin.

An illustration for various waves found on the water surface is shown by a dot as in Figure 1 [6]. Then, the couple of the solitary wave observed in the water basin fit to the McCowan limit extending an asymptotic line to the case of solitary wave of the water wave theory (a dot in Figure 1).

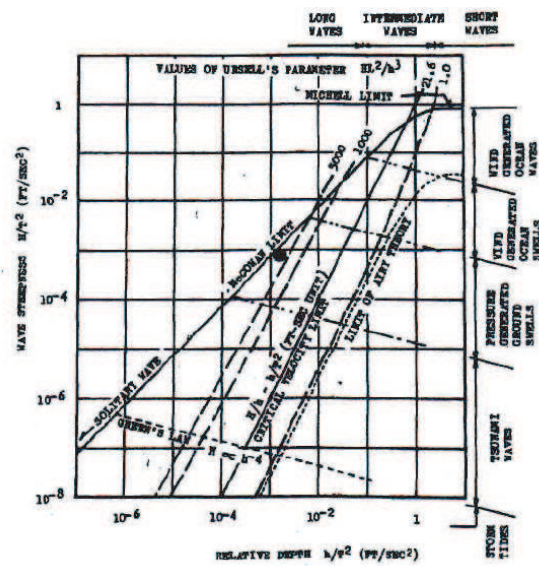


Figure 1: Characteristics of the couple of solitary waves. (1) A dot is for the experimental result. (2) McCowan's limit of breaking wave is demonstrated. (3) McCowan's limit extending to solitary wave is noticed. [courtesy of ASCE].

This result supports that the cross motion of the couple of solitary wave along the bathymetric line of the specific constant waterdepth crossing to the direction of the input function of sinusoidal wave.

REFERENCES

1. Lamb, H., *Hydro-Dynamic*, 6th Edition 1932 (1st Edition, 1879), Cambridge University Press, 1932.
2. Bousinesquq, J., *Comptes Rendus*, June 19, 1871.
3. Rayleigh, L., "On waves," *Philosophical Magazine*, Vol. 5, 1, 251, 257, 1876,
4. Korteweg, D. L. and G. de Vries, "On the change of form of long waves advancing in a rectangular canal and on a new type of long stationary waves," *Philosophical Magazine*, Series 5, Vol. 39, 422–443, 1895.
5. McCowan, J., "On the highest wave of permanent type," *Philosophical Magazine*, Series 5, Vol. 38, 351–358, 1894.
6. Nakamura, S., "Nonlinear lateral oscillation in a harbor model," *Proceedings of Symposium on Modelling Techniques*, 836–853, American Society of Civil Engineers, San Fransisco, California, September 3–5, 1975.

The Casimir Force and Heat Conduction Viewed as Exclusion of Natural Spatial Energy and Lateral EM Coupling between the Walls of a Waveguide

Michael J. Underhill

Underhill Research Ltd., Lingfield, UK

Abstract— This is a deliberately different view of the Casimir Force and Casimir Heat Conduction. It is based on and supports the newly discovered physics of ‘Lateral Electromagnetic (EM) Coupling (LEC)’ which underpins the philosophy that in the final analysis “everything is, or can be shown to be, electromagnetic” [1–10]. It is not a quantum mechanical view.

Both Casimir effects are viewed electromagnetically as processes that take place between surfaces that form the walls of a (micro-strip) waveguide cavity.

The Casimir force is first considered as an imbalance of radiation pressure from ‘Natural spatial energy’. ‘Natural spatial energy’ is excluded from the waveguide gap d up to a cut-off frequency $f_c = c/2d$. Natural spatial energy consists of thermal noise and Zero-Point-Energy, both of which have a white noise spectrum. Natural spatial energy is electromagnetic energy that exists in and is transported by the ‘fabric of space’, the ‘ether’ and it complies with the existence of free-space permeability μ_0 permittivity ε_0 and impedance $Z_0 = \sqrt{(\mu_0/\varepsilon_0)}$. A useful but novel view and model of antenna thermal noise is put forward based on existing antenna and new [11] noise measurements. ZPE is assumed to behave the same way as spatial thermal noise.

This simple ‘radiation pressure’ theory (like the virtual photon theory) predicts attraction and heat transport that is inversely proportional to the waveguide gap and both are much smaller than existing real measurements. Such radiation theories do not model any existing measurements with convincing accuracy.

When we introduce the properties of ‘Lateral Electromagnetic Coupling’ (LEM) coupling to the surfaces of the waveguide walls we find that we can apply a novel EM coupling formula [2]. This coupling formula saturates to unity at defined short distances and then any desired negative of distance may be selected. We can also define layered combination of higher inverse powers of distances at which the attraction and heat conduction saturates. In each layer (or region) a single distance power law dominates with on account of the newly discovered and universally applicable RSS (Root-Sum-of-the-Squares) process combination law [1–10].

It has been shown [2] that at room temperature photons below about 300 THz or longer in wavelength than about $1\ \mu\text{m}$ are not stable particles and evaporate into plane waves that are not quantised [2]. Thus the model and theory used here is not quantum-mechanical. It does not use the concept of ‘virtual photons’. The theory is consonant with and supports ‘The Physical EM Model of Everything’ [1].

1. INTRODUCTION

EM coupling is an essential concept for the Physical EM Model proposed as the basis for an Electromagnetic Theory of Everything (EMToE) [1, 8, 9]. It establishes the cut-off frequency of the waveguide cavity formed between two parallel surfaces, how much natural spatial energy is excluded between the surfaces and therefore the Casimir force between them. EM coupling also can explain heat conduction between the surfaces as discussed below in Section 4. The new part of EM coupling is better named as ‘Lateral Electromagnetic Coupling’ (LEM) as done for the first time here.

‘Natural spatial energy’ is taken to have two components both with a white noise (flat) spectrum. One is spatial thermal noise the other is the noise fluctuations of what can be called Zero-Point-Energy (ZPE). The relative magnitude of these is a function of temperature.

For reasons given below the ZPE process is preferred rather than the ‘virtual photon’ quantum process as the explanation for the Casimir force.

A previous paper showed that photons in free-space at room temperature are unstable below about 300 THz or one micron wavelength [10]). The stability frequency decreases as the square root of absolute temperature (\sqrt{T}) down to an expected ZPE fluctuation limit that remains to be established, in principle by measurements of the two Casimir effects?

A waveguide with conducting walls has an effective high-pass cut-off frequency. Any noise or fluctuation energy below this frequency is therefore excluded from exerting an outward pressure between the plates. There is thus a nett attractive force between the plates. The excluded energy per unit area is proportional to the distance d and inversely proportional to the TE waveguide cut-off frequency. The reasons why this is not found in practice are discussed in Sections 5 and 6.

An initial assumption is that EM coupling impedance is the primary cause of excess heat conduction over radiant energy coupling. But the square of the EM coupling is found to vary with distance in the same way as the energy is distributed in an evanescent wave traveling on a surface. The same distribution, density with distance, formula can be assumed to apply. See Section 5.

2. ENERGY EXCLUSION MODEL

Figure 1 shows the natural energy exclusion process that occurs in the waveguide formed between two parallel surfaces.

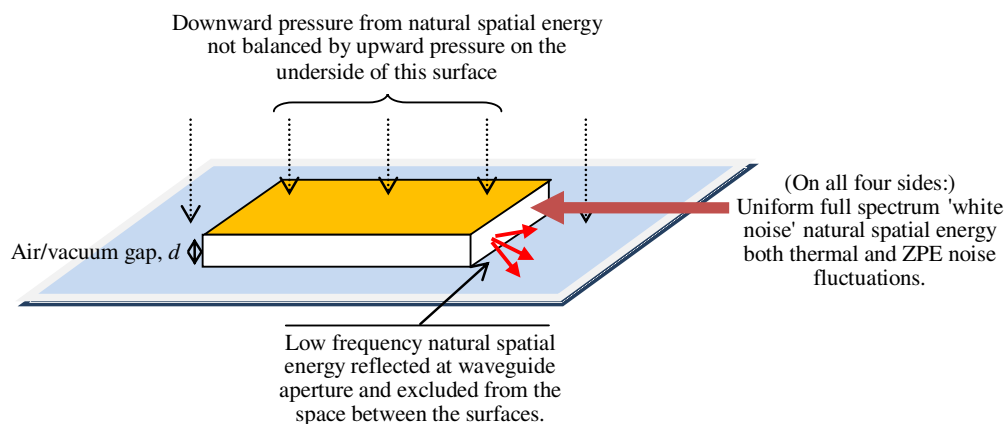


Figure 1: Casimir Force Model. A small (thin) surface on a large surface at uniform height d are the two walls of a waveguide. Low frequency components of natural spatial energy noise spectrum are excluded from the waveguide by reflection at the small surface boundaries.

Transverse Electric (TE) or Transverse Magnetic (TM) waves can travel between two uniformly spaced finite parallel plane conducting plates in any direction in the plane. If energy is supplied uniformly into the gap d between the two planes from all directions energy is stored between the planes in the form of standing wave modes. All waveguide modes have a cut-off frequencies f_c below which energy does not propagate. This high-pass cut off frequency depends primarily on the spacing d between the waveguide walls. In general we have $f_c = c/2d$ where $c = 3 \times 10^8$ m/s is the free-space wave velocity.

The resistivity, permeability, conductivity and permittivity of the wall surfaces can cause small variations in the mode cut-off frequencies. Also edge effects depending on the size of the surfaces under investigation can be expected also to be detectable and measurable in the future. For the time being such second order effects can be neglected until sufficient measurements have been made for their measurement and detection.

The 'natural spatial energy' available for exclusion is assumed to be a combination of heat energy and 'Zero-Point-Energy' ZPE. Both forms of energy are assumed to have a uniform 'white noise' spectrum over the frequency range of interest. The origin and characteristics of these two types of energy are discussed further in the next Section 3.

The Casimir force is now assumed to be proportional to the reduction of radiation pressure between the surfaces by the exclusion of the low frequency part of the natural spatial energy spectrum. The force is proportional to the area of the upper plate surface if edge effects are neglected. The excluded white spectrum energy is proportional to the cut-off frequency $f_c = c/2d$. Thus on this basis the main component of the Casimir force is predicted to be inversely proportional to the spacing d . Significant deviations from this law at very close spacing are discussed in the next section.

3. NATURAL ENERGY IN THE SPATIAL ETHER

The ‘natural spatial energy’ available for exclusion is assumed to be a combination of heat energy and ‘Zero-Point-Energy’ ZPE. Both can be considered as being carried by of the electromagnetic ether. Here the ether is considered to be real and substantive. A good reason for positing the existence of a real ether is the fact that the velocity of light and EM waves is found to be the same anywhere in the universe, and as a consequence the permittivity ϵ_0 , permeability μ_0 and impedance $Z_0 = \sqrt{(\mu_0/\epsilon_0)}$ of free space have to be constant everywhere. Thus ϵ_0 and μ_0 are the main defining parameters of a real and substantive ether.

Heat energy (radiance) in space has a flat ‘white noise’ spectrum of spectral density per unit area of kT watts/Hz/m⁻² (where k is Boltzmann’s constant). This useful, and perhaps novel, statement has been derived from antenna noise theory and confirmed by measurements.

To avoid ‘the ultra-violet catastrophe’ thermal white noise has to have a high frequency noise cut-off frequency proportional to temperature. What this cut-off frequency is in practice has not yet been established.

ZPE white noise is also assumed to be white noise with a constant spectral envelope but one that is independent of temperature. In practice it is best to find the magnitude of ZPE white noise fluctuations empirically, for example by Casimir effect measurements. As yet there is no reliable theoretical prediction of its value.

4. CASIMIR HEAT CONDUCTION MODEL

Figure 2 shows inductive and capacitive coupling between two parallel surfaces. In both cases the coupling impedance varies proportional to the frequency and inversely proportional to gap distance d . Neglecting edge ‘fringing’ effects and assuming that heat can be represented by white noise we can argue that on this basis for a single frequency ω heat conduction distance law of ω/d and a full spectrum distance law of d^{-2} . But neither of these agrees with reported results or predictions. Higher order EM coupling mechanisms therefore have to be considered.

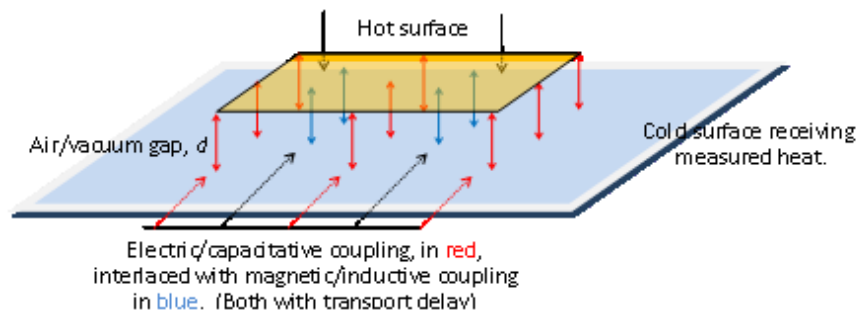


Figure 2: Casimir Heat Conduction Model. A small (thin) surface patch at uniform height d is coupled capacitatively and inductively (with a transport delay) to a lower larger surface. Significant coupling is predominantly at frequencies lower than the waveguide cut-off-frequency $f_c = c/2d$ but higher than the lowest resonant frequency of the patch.

5. ATOMIC LATTICE MATERIAL SURFACE MODEL

Figure 3 shows an idealised atomic lattice of the surface materials. The atoms are assumed to have a simple spherically symmetric structure consisting of an EM string loop ‘substance’ core surrounded by a ‘potential’ evanescent wave (non-radiating) atmosphere [9, 10]. Actually this model supports the existence of several concentric atmospheric layers of progressively less energy densities, larger radii and lower dominant EM spectrum line frequencies.

This EM particle model presumes that the core and its evanescent wave atmospheres has a dominant spectral line with frequency $f \sim mc^2/h$, where h is Planck’s constant and m is the mass of the protons or neutrons of the surface atoms. For protons $f \sim 2.27 \times 10^{23}$ Hz or $\lambda \sim 1.32 \times 10^{-6}$ nm. For electrons $f \sim 1.24 \times 10^{20}$ Hz or $\lambda \sim 5.88 \times 10^{-3}$ nm. The electron orbital resonance frequency of a hydrogen atom is 2.88×10^{20} Hz corresponding to an orbit circumference of 1.04×10^{-3} nm. These wavelength distances appear to be much too small and the frequencies are much too high to have any significant effects for the distances over which the Casimir effects are operative.

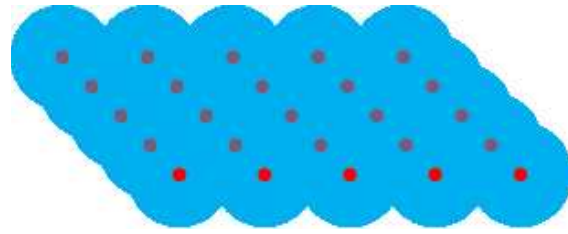


Figure 3: Lattice of surface atoms each consisting of (layered) core with surrounding atmosphere. The atmospheres of the atoms are regions where ‘potential’ dominates and so can be considered as ‘dark matter’. Dark matter is not quantised, by definition. The potential regions overlap, coalesce and combine according to the Root-Sum-of-the-Squares (RSS) process combination rule that applies to non-coherent potentials.

However the ‘lateral EM coupling distance’ for these frequencies is within the region of interest and is therefore a candidate for further investigation.

6. LATERAL ELECTROMAGNETIC COUPLING DISTANCE AND PROFILE

Evanescent waves are non-radiating travelling waves on wires and surfaces. The wave energy is trapped and confined within a boundary distance that has been found to be inversely proportional to the square root of wave frequency as in Equation (1) below. The process that confines the wave energy is ‘lateral’ electromagnetic coupling. This is a concept that was first introduced in reference [2] and is a cornerstone of “The Physical Model of Electro-magnetism for a Theory of Everything” [1] and subsequent theory and developments from this model [3–11].

In [2] the ‘Goubau distance’ r_h was defined as the mean distance within which the coupling energy is confined. Here we equate r_h to the boundary distance d_0 to give

$$r_h = d_0 = (f_0/f)^{1/2} = (14 \text{ MHz}/f)^{1/2} (\pm 10\%) \quad (1)$$

For the electron frequency of 1.24×10^{20} Hz we find $d_0 = 0.336$ nm. This is comparable with the silicon atomic lattice constant or atom spacing of 0.543 nm.

The profile with distance of lateral electromagnetic coupling κ_{11} for a given d_0 found from Equation (1), in reference [2] has been found to be

$$\left(\frac{\kappa_{11}}{\kappa_0} \right)^2 = 1 - e^{-\frac{d_0^n}{nr d^n}} \quad (2)$$

where the coupling in [2] has here been squared to become a representation *energy* distribution.

Figure 4 gives plots of $(\kappa_{11}/\kappa_0)^2$ as in (2) for three different negative powers of distance $n = 1, 2$ and 3. For convenience and by inspection the limit of the saturation region where $\kappa_{11} = 1$ is taken as $d/d_0 = 0.5$. Mathematical justification for this is under investigation.

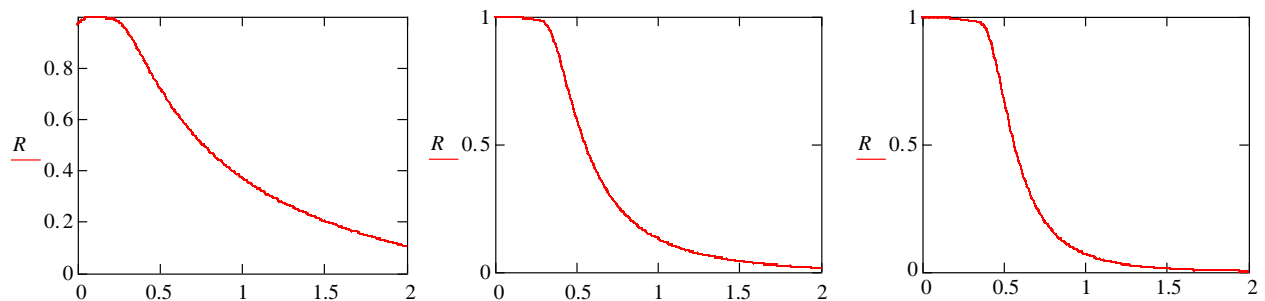


Figure 4: Plots of lateral EM coupling functions $(\kappa_{11}/\kappa_0)^2$ (vertical axis) against distance d (horizontal axis) using Equation (1) with negative powers of distance d with values n of 1, 2 and 3 going from left to right. Note saturation at small distances changing to a power law of $1/d^n$.

To obtain the *total* coupling it is necessary to integrate (2) with respect to frequency after inserting the frequency dependent $(1/\sqrt{f})$ value of d_0 together with the condition that a white noise spectrum is applied. The first term integral is simply f .

However the integration of the second term in (2) creates problems. No analytical solution in terms of known integral or transcendental functions has yet been found. On the other hand numerical integration is possible and it reveals that the second term integral only provides a small step addition to the first term integral.

The first term integral may thus be used on its own. Essentially it provides a $1/d$ additional slope to one of the distance laws shown in Figure 4. Which asymptotic power law should be chosen should be decided on the basis of best fit to measurements, when more accurate measurements become available. The measurements also should provide validation or not of the newly discovered physics process of ‘electromagnetic coupling’.

7. CONCLUSIONS

Radiation pressure by either ‘virtual photons’ or ‘natural spatial energy’ is too small to be the primary explanation of the Casimir force. Also exclusion of energy in the waveguide formed by the gap between two parallel surfaces does not itself give a sufficiently high negative order polynomial for the distance law to represent what has been measured in practice.

The classical coupling between waveguide walls is likewise too small to account for Casimir Heat Conduction.

‘Lateral Electromagnetic Coupling’ is a cornerstone of “The Physical Model of Electro-magnetism for a Theory of Everything” [1]. Initial examination shows that Lateral Electromagnetic Coupling (LEC) between two surfaces can possibly explain both the Casimir force and Casimir heat conduction.

In fact more accurate measurements of these two Casimir effects could in the future be used to calibrate and validate the parameters of LEC over most of the accessible range of electromagnetic spectrum frequencies to strengthen its claim of being a necessary addition to Electromagnetic Theory.

The theory put forward here is not per se quantum-mechanical.

REFERENCES

1. Underhill, M. J., “A physical model of electro-magnetism for a theory of everything,” *PIERS Online*, Vol. 7, No. 2, 196–200, 2011.
2. Underhill, M. J., “The phase noise spectrum and structure of photons?,” *Proc. 16th EFTF-2010*, 8 pages, Noordwijk, Netherlands, Apr. 13–16, 2010.
3. Underhill, M. J., “Maxwell’s transfer functions,” *PIERS Proceedings*, 1766–1770, Kuala Lumpur, Malaysia, Mar. 27–30, 2012.
4. Underhill, M. J., “A local ether lens path integral model of electromagnetic wave reception by wires,” *PIERS Proceedings*, 1005–1008, Moscow, Russia, Aug. 19–23, 2012.
5. Underhill, M. J., “Novel analytic EM modelling of antennas and fields,” *PIERS Proceedings*, 1771–1775, Kuala Lumpur, Malaysia, Mar. 27–30, 2012.
6. Underhill, M. J., “Antenna pattern formation in the near field local ether,” *PIERS Proceedings*, 1009–1012, Moscow, Russia, Aug. 19–23, 2012.
7. Underhill, M. J., “Wideband small loop-monopole HF transmitting antenna with implications for Maxwell’s equations and the Chu criterion,” *PIERS Proceedings*, 764–768, Taipei, Mar. 25–28, 2013.
8. Underhill, M. J., “Coupled electromagnetic wave propagation in space and around surfaces and interfaces,” *PIERS Proceedings*, 394–398, Stockholm, Aug. 12–15, 2013.
9. Underhill, M. J., “Electromagnetic structures and inertias of particles including the higgs boson,” *PIERS Proceedings*, 401–405, Taipei, Mar. 25–28, 2013.
10. Underhill, M. J., “The stability of EM particles and predicted mass ratios,” *PIERS Proceedings*, 399–404, Stockholm, Aug. 12–15, 2013.
11. Underhill, M. J., “Discovery and theory of small antenna near-field dissipation and frequency conversion with implications for antenna efficiency, beverage antenna noise reduction, Maxwell’s equations and the Chu criterion,” *PIERS Proceedings*, Guangzhou, 2014.

The Beam-wave Interaction for Different Modes in Three-gap Coupled Cavity Output Circuit

Jian Cui¹, Jirun Luo², Wenkai Liu¹, Haiyan Sun¹, Zhi Liu¹, and Ming Huang¹

¹North China University of Technology, Beijing 100144, China

²Institute of Electronics, Chinese Academy of Sciences, Beijing 100190, China

Abstract— An analytic theory describing the conversion efficiency of the electron beam in multi-gap coupled cavity is developed. Through calculating the electronic conversion efficiencies in three-gap coupled cavity for modes 2π , π and $\pi/2$ respectively, the mechanism of the beam-wave interaction in output circuit is discussed in this paper.

1. INTRODUCTION

Extended-interaction klystron (EIK) is invented to achieve a large power, wide frequency bandwidth and high gain in the millimeter/sub-millimeter wave length range [1–3]. Multi-gap coupled cavity in it is a key technique for enhancing the gain-bandwidth product and power capability.

Based on kinematics theory, by calculating the conversion efficiency of the electron beam in single gap, the beam-wave interaction was analyzed in paper [4]. On this basis, the effects of the distance of gap-gap, R.F. gap voltage on the conversion efficiency were discussed in paper [5]. But the analysis was carried out under the assumption of narrow gaps separated by drift tubes and neglected the beam-wave interaction of other modes in the multi-gap cavity. Because of strong electromagnetic coupling between the adjacent cavities, there are multiple resonant modes which have a very great difference of the electric field intensity on the gap. The mechanism of the beam-wave synchronization and coupling for these modes is the key technology investigation of multi-gap coupled cavity chain. Based on kinematics theory, this paper will present the simulation results of the conversion efficiencies in three-gap coupled cavity and discuss the effect of drift tube length on beam-wave interaction for modes 2π , π and $\pi/2$.

2. MODEL AND FORMULA

Assume that the model is one-dimensional and the effect of space charge is neglected. Hence, the equation of motion an electron moving under the assumption is given by

$$\frac{d^2z}{dt^2} = - \left| \frac{e}{m} \right| E_c(z) \sin(\omega t + \varphi_0) \quad (1)$$

where z is the axial distance, e and m are the electronic charge and mass respectively, $E_c(z)$ denotes the axial electric field intensity at a distance z , ω denotes the angular frequency, φ_0 specifies the electron entrance phase.

An electron entering the interaction region with a velocity u_0 at the phase φ_0 leaves the region with a velocity u which is obtained by successive use of Equation (1). With a pulse width θ_e of the electron beam, the conversion efficiency η is then given by

$$\eta = 1 - \frac{1}{\theta_e} \int_{\varphi_0}^{\varphi_0 + \theta_e} \left(\frac{u}{u_0} \right)^2 d\theta \quad (2)$$

If a resulting efficiency is positive, the kinetic energy of the electron beam will be converted to electromagnetic energy.

Taking three-gap coupled cavity as the output circuit, there are three eigen modes with different field distributions. Assume that the axial RF standing electric fields are constant on the gaps and vanish on the drift tubes as shown in Figure 1. Where $E_c = \alpha V_0/d$, $\theta_d = \omega d/v_0$, $\theta_{12} = \omega l_{12}/v_0$, $\theta_{23} = \omega l_{23}/v_0$, α is the modulation index of the gap voltage, v_0 is the longitudinal velocity of the electron under the accelerating voltage V_0 , ω is the angular frequency of the mode, d is the width of the gap, l_{12} and l_{23} are the lengths of the first and the second drift tube respectively. For 2π mode, the RF fields on gaps are the same both in amplitude and direction; For π mode, the adjacent RF fields on gaps are the same in amplitude and the opposite in direction; For $\pi/2$ mode, the RF fields vanish in middle gap and exist on the other two gaps with the same amplitude and the opposite direction.

3. RESULTS AND DISCUSSION

Taking for example $\theta_e = 0.5\pi$, $\theta_d = 0.5\pi$, $|\alpha| = 0.4$, $\varphi_0 = 0$ and $v_0 = u_0$, the efficiencies as function of θ_{12} and θ_{23} for 2π mode, π mode and $\pi/2$ mode are displayed in Figure 2.

The analytic result of 2π mode shows that the high efficiency region appears on the right of the bisector and the maximum efficiency $\eta = 80\%$ is obtained upon selecting the parameters $\theta_{12} = 1.26\pi$ and $\theta_{23} = 0.66\pi$. This can be explained that average speed of the electronic beam is reduced ceaselessly after passing a gap, and in view of transit time effect, the corresponding θ_{12} and θ_{23} decrease in order to make the electronic beam at the optimal phase in next gap.

Compared with 2π mode, there are four high efficiency regions with different distribution for π mode. However, when the efficiency η is over 80%, the corresponding parameter θ_{23} is too small to realize in structure. Therefore, it is practical to choose $\theta_{12} = 0.42\pi$ and $\theta_{23} = 1.32\pi$ in the upper left region with maximum efficiency $\eta = 78.48\%$.

Because the beam-wave interaction occurs on the two gaps, $\pi/2$ mode can be regarded as a kind of special π mode of double-gap cavity with a longer drift distance (Figure 1). In this case, the maximum efficiency η is only 60% with a fixed value of $\theta_{12} + \theta_{23} = 1.47\pi$.

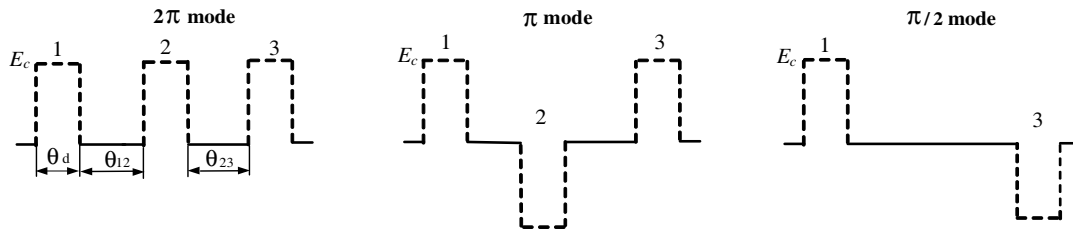


Figure 1: The electric field distribution for modes 2π , π and $\pi/2$.

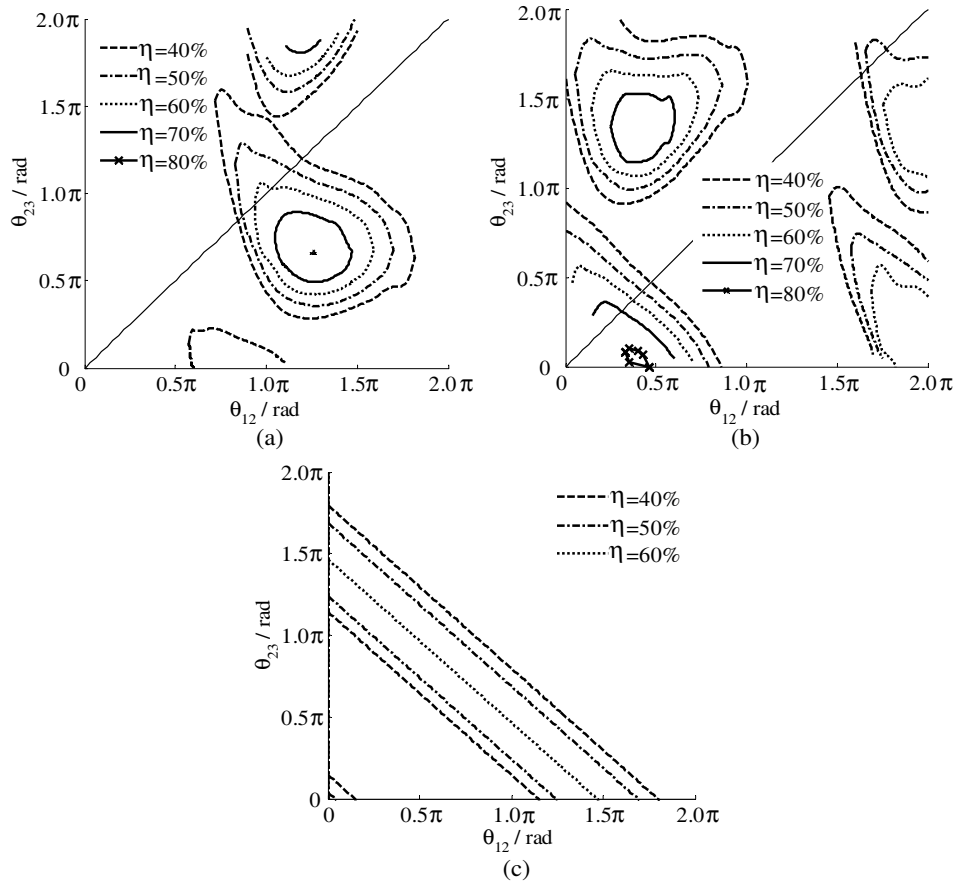


Figure 2: The electronic conversion efficiencies for (a) 2π mode, (b) π mode, (c) $\pi/2$ mode.

4. CONCLUSION

In this paper, an analytic theory describing the conversion efficiency of the electron beam in Multi-gap coupled cavity with different mode is developed. The conversion efficiencies of the electron beam in three-gap coupled cavity for modes 2π , π and $\pi/2$ have been obtained. The results show that the maximum efficiency depends on the optimal combination of θ_{12} and θ_{23} , which have a great difference for these modes. Considering the beam-wave interaction on two gaps for $\pi/2$ mode, the maximum efficiency η is only 60% less than that of 2π mode and π mode.

ACKNOWLEDGMENT

This work is supported by Beijing Natural Science Foundation (1144010) in project of investigation of the key techniques in an extended interaction klystron using multi-gap and modes overlapping coupled cavity chain.

REFERENCES

1. Roitman, A., P. Horoyski, M. Hyttinen, and B. Steer, "Wide bandwidth, high average power EIK's drive new radar concepts," *The First IEEE International Vacuum Electronics Conference*, 3–5, Monterey, May 2–4, 2000.
2. Roitman, A., D. Berry, and B. Steer, "State-of-the art W-band extended interaction klystron for the cloudsat program," *IEEE Trans. on Electron Devices*, Vol. 52, No. 5, 895–898, May 2005.
3. Dobbs, R., M. Hyttinen, B. Steer, and A. Soukhov, "Rugged and efficient Ka-band extended interaction klystrons for satellite communication systems," *The Eighth IEEE International Vacuum Electronics Conference*, 107–108, Kitakyushu, Japan, May 15–17, 2007.
4. Marder, B. M., M. C. Clark, L. D. Bacon, J. M. Hoffman, R. W. Lemke, and P. D. Coleman, "The split-cavity oscillator: A high-power E-beam modulator and microwave source," *IEEE Trans. Plasma Sci.*, Vol. 20, No. 3, 312–331, January 1992.
5. Blotekjer, K., "Optimization of R.F. voltage amplitudes and gap spacing of the generalized floating drift-tube oscillators," *Journal of Electronics and Control*, Vol. 12, No. 6, 461–499, February 1962.

Efficient Electromagnetic Scattering Simulation Approach of the Rotating Moving Complex Targets

Guoqing Zhu¹, Chunzhu Dong^{1,2}, Kainan Qi¹, Jing Huang¹, and Hongcheng Yin^{1,2}

¹Science and Technology on Electromagnetic Scattering Laboratory, Beijing 100854, China

²Information Engineering School, Communication University of China, Beijing 100024, China

Abstract— The detection and recognition of moving target is focused by lots of research scholars greatly. However, the algorithms for detection and recognition have to be tested and verified by a great deal of radar echo data. Efficient electromagnetic scattering simulation becomes an effective and economic method for achieving it. The design of appropriate moving target electromagnetic scattering simulation for computer-generated bots poses serious challenges as they have to satisfy stringent requirements that include computation and execution efficiency. This paper discusses a novel efficient high-frequency electromagnetic scattering simulation approach of the rotating moving complex targets. Based on the wide-adopted high-frequency asymptotic methods, such as Physical Optics (PO), Equivalent Edge Current (EEC) and Shooting Bouncing Ray (SBR), a novel efficient approach is proposed by employing the adaptable NVIDIA OptiX ray-tracing engine to solve scattering problems of rotating moving complex targets. High accuracy and efficiency of the hidden-surface-removal (HSR) in PO/EEC and the ray-tracing in SBR are realized at the same time with the state-of-art GPU computation technology. The precise scattering modulation effects of rotating moving target are therefore achieved. Experiments show the effectiveness of the approach.

1. INTRODUCTION

With the development of radar technology, the information of observation target is expanded. Various moving styles such as translation, spin, roll, precession and so on exist in realistic situations. Signatures result from those moving styles are focused by research scholars who are interested in radar detection and recognition, including moving target detection (MTD), moving target indication (MTI), synthetic aperture radar (SAR) imaging and SAR identification, etc.. Above all things, obtaining radar echo data is the most important procedure.

Electromagnetic simulation and electromagnetic measurement are two major approaches for obtaining radar echo data. Compared to the second one, Electromagnetic simulation has more advantage in aspect of cost and convenient. In high frequency, quasi-static electromagnetic simulation which based on high-frequency asymptotic theory is an effective method for obtaining wide band electromagnetic scattering echo data of moving targets. When the targets' rotational frequency is far smaller than the frequency of incidence electromagnetic wave, and the maximum linear velocity of moving targets is far smaller than light speed. It assumes that scattered field generating from moving targets at a moment is similar to the ones that generating from the motionless targets which dwell at its trajectory. Therefore, the simulation radar echo generating from moving targets is equal with a series of the same motionless targets which dwell at its trajectory.

In practically, radar band becomes wider continuously, the modulation action of electromagnetic wave which produced from moving targets turn out to be more conspicuous. In order to obtain radar echo simulation data accurately and efficiently, this paper discusses a novel efficient high-frequency electromagnetic scattering simulation approach of the rotating moving complex targets. Based on the wide-adopted high-frequency asymptotic methods, such as Physical Optics (PO) [2], Equivalent Edge Current (EEC) [1] and Shooting Bouncing Ray (SBR) [6], the approach is proposed by employing the adaptable NVIDIA OptiX ray-tracing engine to solve scattering problems of rotating moving complex targets.

2. SIMULATION PROGRAM

The approach proposed in this paper possesses three main steps. Firstly, moving complex targets model building; secondly, utilize NVIDIA OptiX for ray tracing and shading; thirdly, high-frequency electromagnetic scattering calculation.

2.1. Step 1: Moving Complex Targets Model Building

A complex target consists of several components; each component has its motion style. In order to describe target's motion, transformation matrix T is introduced, the T has the forms as follow:

$$\mathbf{T} = \begin{bmatrix} a_{11} & a_{12} & a_{13} & a_{14} \\ a_{21} & a_{22} & a_{23} & a_{24} \\ a_{31} & a_{32} & a_{33} & a_{34} \\ a_{41} & a_{42} & a_{43} & a_{44} \end{bmatrix} \quad (1)$$

where, $\begin{bmatrix} a_{11} & a_{12} & a_{13} \\ a_{21} & a_{22} & a_{23} \\ a_{31} & a_{32} & a_{33} \end{bmatrix}$ represented the transformation of scaling, rotating and dislocation; $\begin{bmatrix} a_{14} \\ a_{24} \\ a_{34} \end{bmatrix}$ represented the transformation of translation; $[a_{41} \ a_{42} \ a_{43}]$ represented the transformation of projection; $[a_{44}]$ represented the transformation of entire scaling.

2.2. Step 2: Utilize NVIDIA OptiX for Ray Tracing and Shading

The NVIDIA OptiX ray tracing engine is a programmable system designed for NVIDIA GPUs and other highly parallel architectures. The OptiX engine builds on the key observation that most ray tracing algorithms can be implemented using a small set of programmable operations. Consequently, the core of OptiX is a domain-specific just-in-time compiler that generates custom ray tracing kernels by combining user-supplied programs for ray generation, material shading, object intersection, and scene traversal. This enables the implementation of a highly diverse set of ray tracing-based algorithms and applications, including interactive rendering, offline rendering, collision detection systems, artificial intelligence queries, and scientific simulations such as sound propagation. OptiX achieves high performance through a compact object model and application of several ray tracing-specific compiler optimizations.

There are seven different types of programs in OptiX, each of which operates on a single ray at a time. In addition, a bounding box program operates on geometry to determine primitive bounds for acceleration structure construction. The combination of user programs and hardcoded OptiX kernel code forms the ray tracing pipeline which is outlined in Figure 1. For more information please refer to [8].

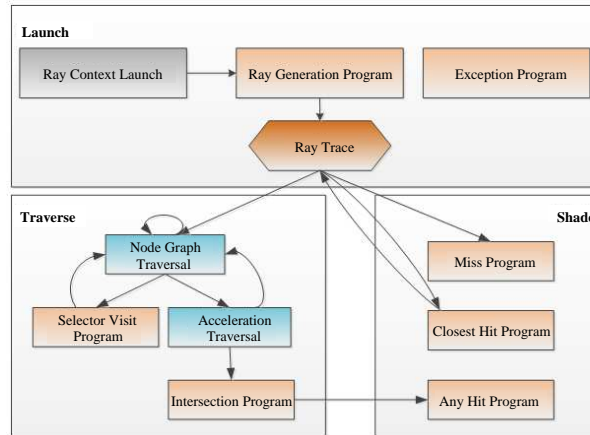


Figure 1: A flow chart of the ray tracing pipeline which based on NVIDIA OptiX.

2.3. Step 3: High-frequency Electromagnetic Scattering Calculation

In the situation of plane wave incidence and ignore time-harmonic factor $e^{j\omega t}$, according to Stratton-Chu equation, the surface scattered far-field could be written as follow [3]:

$$\mathbf{E}_s(\mathbf{r}) = \frac{jk}{4\pi} \frac{e^{-jkr}}{r} \int_S \hat{\mathbf{s}} \times (\mathbf{M}_s(\mathbf{r}') + Z_0 \hat{\mathbf{s}} \times \mathbf{J}_s(\mathbf{r}')) \exp(jk\mathbf{r}' \cdot \hat{\mathbf{s}}) ds' \quad (2)$$

The above formula can only calculate the targets' surface far-region radiation field, it's not suit for calculating the edge diffraction. Usually, the edge diffraction is often calculated by the method

of EEC. According to the concept of EEC which raised by Michaeli, the edge diffraction far-field could be written as follow [4]:

$$\mathbf{E}^d = \frac{jk}{4\pi} \frac{e^{-jkr}}{r} \int_C \{Z_0 \hat{\mathbf{s}} \times [\hat{\mathbf{s}} \times \mathbf{J}(\mathbf{r}')] + \hat{\mathbf{s}} \times \mathbf{M}(\mathbf{r}')\} e^{jk\hat{\mathbf{s}} \cdot \mathbf{r}'} dl \quad (3)$$

For more calculation details, please refer to interrelated literature.

3. SIMULATION RESULTS

3.1. Sample 1: Accuracy Analysis

In order to test and verify the correctness and accuracy of proposed method, a propeller model is introduced as show in Figure 2. Because the motion style of propeller is simple, namely propeller blades rotate around its symmetry axis. Under these circumstances, the RCS data generated from motionless propeller while incidence of electromagnetic wave rotating one cycle corresponds with the RCS data generated from rotating propeller while incidence of electromagnetic wave changeless. Under this precondition, two RCS data simulated by proposed method and Method of Moment (MoM) respectively are show in Figure 3. The simulation condition of MoM is listed as follow: *HH* polarization, radar frequency $f = 10$ GHz, pitch angle $\theta = 45^\circ$, azimuth angle $\phi = 0 \sim 360^\circ$ and step is 0.2° . The simulation condition of proposed method is list as follow: *HH* polarization, radar frequency $f = 10$ GHz, pitch angle $\theta = 45^\circ$, azimuth angle $\phi = 0^\circ$, rotating velocity $\omega = 333.33$ r/s, time sampling rate is 400 Hz.

From Figure 4, the consistency of simulation results is quite obvious while some differences still exist. These differences are caused by high-order scattering mechanism on analysis. In order to analyze moving targets have modulation effect on electromagnetic wave, the propeller model is utilized once more. The simulation condition is listed as follow: *HH* polarization, radar frequency $f = 10$ GHz, pitch angle $\theta = 45^\circ$, azimuth angle $\phi = 0^\circ$, rotating velocity $\omega = 20$ r/s, time sampling rate is 4 kHz. Analysis of Simulation RCS data are show in Figure 4 and Figure 5.

From Figure 5, we could know that the space of modulation spectrum Δf is 60 Hz, and the width of modulation spectrum ΔB is 3.96 kHz. We also could get the theoretical result by calculate the

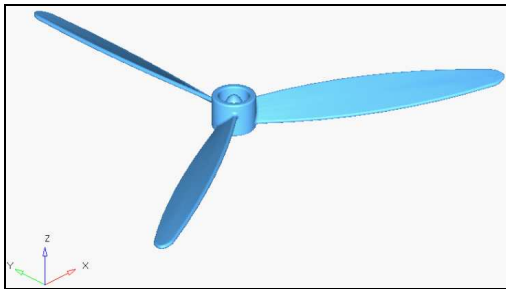


Figure 2: The propeller model.

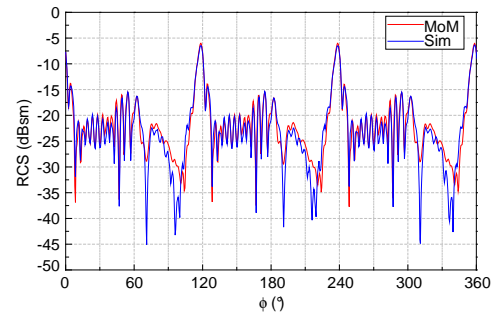


Figure 3: Simulation results comparison between MoM and proposed method.

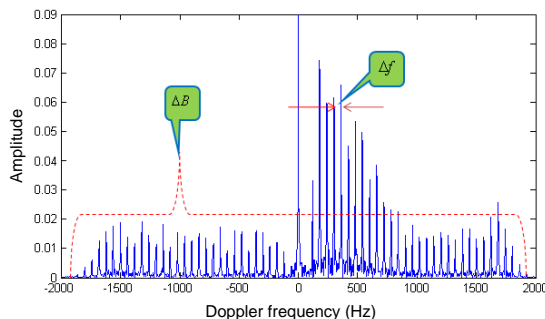


Figure 4: Doppler frequency characteristics of dynamic propeller model.

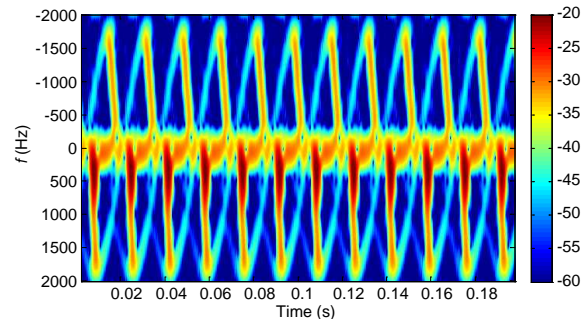


Figure 5: Time-frequency graph of dynamic propeller model.

simulation parameters, where

$$\begin{aligned}\Delta f &= N f_T = 3 \times 20 = 60 \text{ Hz} \\ \Delta B &= \frac{8\pi f_T L \cos \theta}{\lambda} = \frac{8\pi \times 20 \times 0.34 \times \cos 45^\circ}{0.03} = 4.02 \text{ kHz}\end{aligned}$$

From Figure 6, we could get the time-frequency repetition period is about 0.0167 s, while the propeller owns three blades. Therefore, the rotating period of propeller is 0.0501 s, which agrees with the simulation parameters.

3.2. Sample 2: Efficiency Analysis

In order to test the efficiency of proposed method whether NVIDIA OptiX is utilized, a well-known complex target namely Apache-64 model is introduced. Apache-64 model is meshed in different element size, and the geometry is dispersed by triangular element in different numbers. We set ten as the maximum ray tracing times, and the simulation platform is GTX 560 Ti. As a result, statistical results are show in Table 1.

Table 1: Statistical results of dynamic ray tracing for Apache-64 model.

Element size (mm)	Element number	Memory (MB)	Tree-building time (ms)	Ray-tracing time (ms)	Total time (ms)	Total time without NVIDIA OptiX (ms)
100	75 K	5	109	206	315	2803
35	251 K	18	125	257	382	2875
25	530 K	38	125	292	417	2904
15	1.02 M	74	171	312	483	2975
10	2.06 M	149	219	328	547	3108

From Table 1, the efficiency of ray tracing that utilizing NVIDIA OptiX is improved greatly. It's nearly ten times speed than the one without utilizing NVIDIA OptiX in present simulation platform. What's more, the efficiency of ray tracing is subject to the number of flow-processor in GPU. There are 384 flow-processors in GTX 560 Ti merely. With the development of GPU hardware technology, the number of flow-processor is growing in geometric progression. Take GTX 680 for example, there are 1536 flow-processors. Therefore, ray tracing time will be reduced greatly in the offing.

4. CONCLUSIONS

A novel efficient high-frequency electromagnetic scattering simulation approach of the rotating moving complex targets is proposed in this paper. It utilizes transformation matrix to describe the moving attributes of the complex target, and NVIDIA OptiX ray tracing engine is introduced to accelerate ray tracing in high-frequency electromagnetic scattering simulation. Simulation results and theoretical analysis indicate the feasibility of the approach.

REFERENCES

1. Michaeli, A., "Equivalent edge currents for arbitrary aspects of observation," *IEEE Transactions on Antennas and Propagation*, Vol. 32, No. 3, 252–258, 1984; Vol. 33, No. 2, 227, 1985.
2. Klement, D., J. Preissner, and V. Stein, "Special problems in applying the physical optics method for backscatter computations of complicated objects," *IEEE Transactions on Antennas and Propagation*, Vol. 36, No. 2, 228–237, 1988.
3. Gordon, W. B., "High frequency approximations to the physical optics scattering integral," *IEEE Transactions on Antennas and Propagation*, Vol. 42, No. 3, 427–432, 1994.
4. Michaeli, A., "Elimination of infinities in equivalent edge currents — Part I: Fringe current components," *IEEE Transaction on Antennas and Propagation*, Vol. 34, No. 7, 912–918, Jul. 1986.
5. Michaeli, A., "Elimination of infinities in equivalent edge currents — Part II: Physical optics components," *IEEE Transactions on Antennas and Propagation*, Vol. 34, No. 8, 1034–1037, Aug. 1986.

6. Lee, S. W., “Ray-tube integration in shooting and bouncing ray method,” *Microwave Optical Tech. Letter*, Vol. 1, No. 8, 286–289, 1988.
7. Weinmann, F., “Ray tracing with PO/PTD for RCS modeling of large complex objects,” *IEEE Transactions on Antennas and Propagation*, Vol. 54, No. 6, 1797–1806, Jun. 2006.
8. Parker, S. G., J. Bigler, et al., “OptiX: A general purpose ray tracing engine,” *ACM Transactions on Graphics*, Vol. 29, No. 4, Article 66, Jul. 2010.

The Research of Methods Based on Traveling Wave Suppression

Yongfeng Wang^{1,2}, Xiaonan Zhang², and Kainan Qi^{1,2}

¹College of Information Engineering, Communication University of China, China

²Science and Technology on Electromagnetic Scattering Laboratory, Beijing 100854, China

Abstract— The theory of traveling-wave scattering and two kinds of methods for restraining the traveling-wave scattering are represented in the paper. The traveling-wave scattering could be declined by shaping and radar absorbing material (RAM). The experimental results prove that inhibition effect of traveling-wave scattering using the above methods is prominent. A traveling-wave current comes into being, when a long, thin body is illuminated by grazing incident electromagnetic wave. The flowing traveling-wave current is reflected when it encounters the end of the truncation, and the traveling-wave scattering contributes a lot to the radar cross section (RCS) of the target. The traveling-wave scattering can be researched by making use of the existed concepts of antenna theory. In this paper, a sample of traveling-wave broad was manufactured. Firstly, we restrained the traveling-wave scattering by shaping. The end edge of traveling-wave broad was transformed into saw-tooth or circular arc shape, and measured results proved the shaping method could reduce the RCS of the traveling-wave broad by 10 dB at X-band. Moreover, we restrained the traveling-wave scattering by coating radar absorbing material on the surface of the broad. And the measured results showed that the method of radar absorbing material could reduce the RCS of the traveling-wave broad by more than 10 dB at X-band.

1. INTRODUCTION

Reducing target RCS by depressing strong scattering centers, i.e., air inlet, radar cabin, cockpit, etc., is the most primary approach to target stealth. Secondly, taking measures to prevent sub scattering centers caused by edge and surface travelling wave also plays important roles in RCS reduction. There exist a large number of components and parts with edges in target, which would result in strong radial diffraction in a wide angle, therefore, RCS contributed by target edges have great impact on target radar signature. Moreover, after strong scattering sources are suppressed, scattering from surface travelling wave would dominate the target signature, which is more difficult to reduce for stealth.

Travelling wave is a kind of surface current propagating along the direction of target length, the distinctive feature of which is to continuously radiate electromagnetic wave to the space during propagation. The source that emits travelling wave current can be RF generator and incident electromagnetic wave, and the latter leads to the travelling wave scattering.

2. PRINCIPLE OF TRAVELLING WAVE SCATTERING

Suppose an elongated conductor is excited by plane wave at a small angle. When the incident electric field has an axial component in the incident plane, the surface current induced by this component would flow along the axis, so the travelling wave current is produced. On the one hand, the travelling wave current will generate forward scattering similar to the radiation of travelling wave antenna, which would contribute to the bi-static scattering. On the other hand, if the elongated conductor is truncated at the terminal without load matching, the forward travelling wave would generate inverted secondary radiation due to the mismatch reflection once reaching the terminal. Consequently, the travelling wave contributes to the mono-static scattering as well. As for the travelling wave scattering, the illuminated target receives energy and guides it to transfer on the surface till the terminal, like the combination of antenna and transmission line, and then the energy will be reflected and reversely transform because of the load mismatch. The energy continually re-radiates during this process, which generates the so-called travelling wave scattering.

Generating traveling wave scattering must have two conditions: first the target is thin and long conductor, such as wire, cylinder, olive, strip plate, etc.; Second, the incident wave must have electric field component in the direction of propagation. For example, when the incident wave is vertical polarization, the wing and tail on target or missiles could generate strong wave traveling scattering. Using the radiation theory of traveling wave antenna can be well understood the travelling wave scattering. End-fire traveling wave antenna is used to analog traveling wave scattering by Peters et al., and the position of wave scattering peak of the long and thin conductor is well

estimated by this means, but it has certain difficulty when estimating the value of traveling wave scattering, in general, the greater the conductivity, slenderness ratio and distal reflectivity of the object, the bigger the wave scattering.

3. STANDARD MODEL

In this paper, we choose a long flat plate as the standard model for study. In Fig. 1, the plate (length = 500 mm, width = 50 mm, thickness = 2 mm) is laid up vertically, and the incident direction varied in different azimuth angles. According to traveling-wave scattering theory, the traveling -wave scattering is strong when incident wave is parallel polarization, and the traveling-wave scattering is weak when incident wave is vertical polarization. So we could research the parallel polarization only.

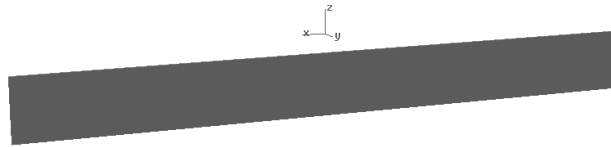


Figure 1: The long flat plate.

MOM [4, 5] is used to calculate the RCS of the long flat plate because of its high accuracy [6]. In this paper, the calculate parameters are: $f = 10$ GHz; Polarization: HH ; Azimuth angle: $-180^\circ \sim 180^\circ$; Angle of pitch: 0° ; Roll angle: 0° .

There are two ways of travelling wave suppression: one is by modifying the profile, the traveling wave electric current can generate the forward scattering as far as possible. The other is that the current traveling wave can be attenuated by adopting high performance absorbing materials. This article focuses on using shape method to suppress the traveling wave scattering.

There are two kinds of effective shape methods for suppression: First, the serrated modification in the tail; Second, the arc transition in the tail. Both methods can effectively restrain the traveling wave; the following are detailed analysis by taking the typical strip plate sample for example.

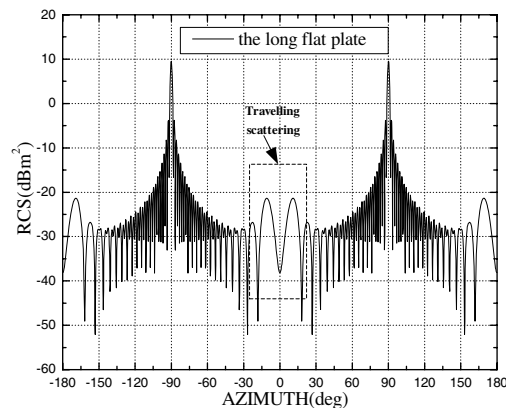


Figure 2: The scattering property of the long flat plate.

In Fig. 2, there are two high pioneers in the extent ($-20^\circ \sim 20^\circ$). The pioneer position is about $\pm 12^\circ$, and the amplitude is -21 dBm². This is a typical travelling-scattering contribution, and this kind of contribution must be repressed in the RCS reduction of target.

4. REPRESSING METHODS

4.1. Saw-Tooth Shape

According to the above analyze, the vertical edge at the end bring a powerful traveling-wave scattering. One improved measure is changing the straight edge into saw-tooth edge. From Fig. 3 to Fig. 5, one saw-tooth project is adopted, whose saw-tooth angle is 160° , 140° , 120° .

All of above models are simulated by MOM with the same emulational parameter as before, the result of simulation is shown in Fig. 6.

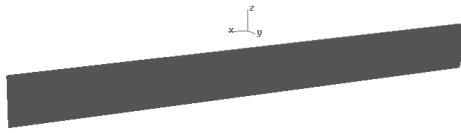
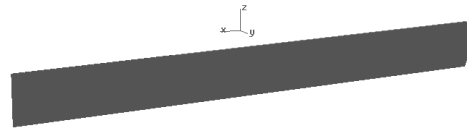
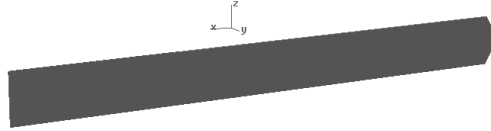
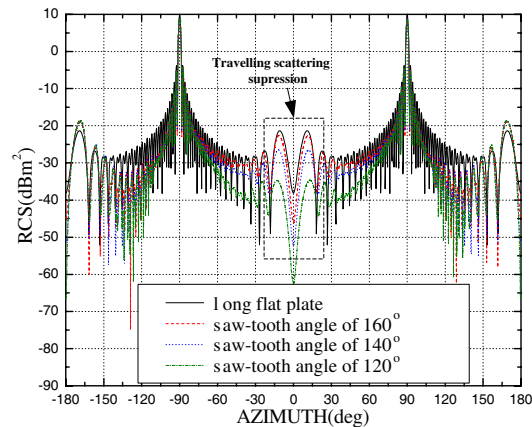

 Figure 3: Long flat plate with angle 160° .

 Figure 4: Long flat plate with angle 140° .

 Figure 5: Long flat plate with a saw-tooth angle of 120° .


Figure 6: The scattering property of the long flat plate with saw-tooth shape (obtuse angle).

In Fig. 6, the traveling-wave scattering of the traveling-wave scattering vary evidently when the end of the long plate was transformed into saw-tooth shape. The average value of all of the four models within azimuth angle range of $\pm 20^\circ$ at head direction is shown in Table 1.

 Table 1: The average value at the azimuth angle range of $0 \pm 20^\circ$ (dBm^2).

Long flat plate with vertical edge	Long flat plate with a saw-tooth angle of 160°	Long flat plate with a saw-tooth angle of 140°	Long flat plate with a saw-tooth angle of 120°
-25.74	-27.01	-30.69	-38.39

In Table 1, the traveling-wave scattering trail off gradually with the saw-tooth edge minishing. The average value of traveling-wave scattering for the long flat plate with a saw-tooth angle of 120° is -38.39 dBm^2 , which has more 12.65 dB attenuation than long flat plate with vertical edge. It is obvious that the traveling-wave scattering could be declined availably by transforming the edge into saw-tooth shape.

4.2. ARC Shape

According to the above analyze, the vertical edge at the end bring a powerful traveling-wave scattering, since he vertical edge can arose truncation effect. To trail off the truncation effect, the vertical edge at the end of the long flat plate should be transformed into circular arc shape. In Fig. 7 and Fig. 8, the circular arc radius is $\lambda/10$ (3 mm) and $\lambda/4$ (7.5 mm), respectively.

The two models are simulated by MOM with the same emulational parameter before, the result of simulation is shown in Fig. 9.

In Fig. 9, the traveling-wave scattering of the traveling-wave scattering weaken when the end of the long plate was transformed into arc shape. The average value of the two models within azimuth angle range of $\pm 20^\circ$ at head direction is shown in Table 2.

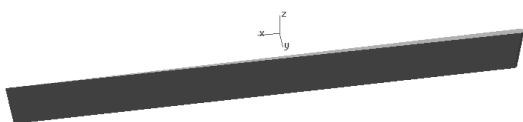


Figure 7: Long flat plate with a 3mm circular arc radius at the end.

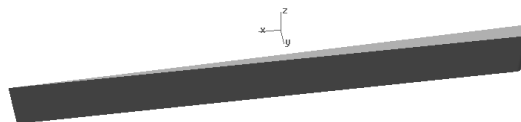


Figure 8: Long flat plate with a 3mm circular arc radius at the end.

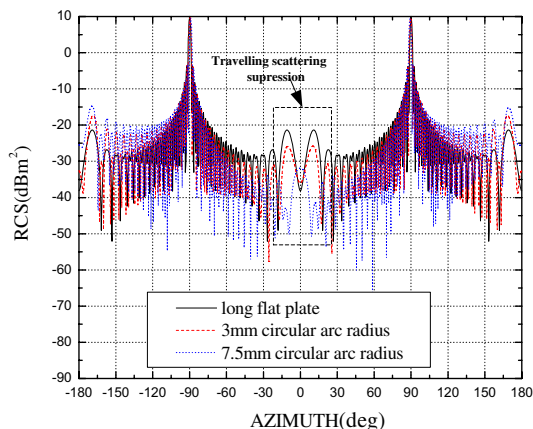


Figure 9: The scattering property of the long flat plate with circular arc radius at the end.

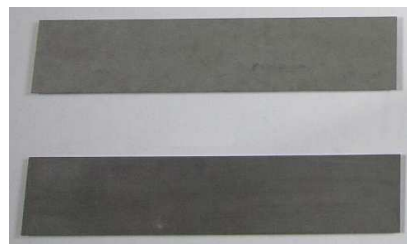


Figure 10: Long flat plate covering with radar absorbing material.

Table 2: The average value at the azimuth angle range of $0 \pm 20^\circ$ (dBm^2).

Long flat plate with vertical edge	Long flat plate with a 3 mm circular arc radius	Long flat plate with a 7.5 mm circular arc radius
-25.74	-29.82	-36.80

In Table 2, the traveling-wave scattering trail off gradually with the circular arc radius increasing. The average value of traveling-wave scattering for the long flat plate with a 3 mm circular arc radius is -36.80 dBm^2 , which has more 11.06 dB attenuation than long flat plate with vertical edge.

4.3. Radar Absorbing Coat

It is a common method for target stealth that coating radar absorbing material on the surface of the broad to restrain the traveling-wave scattering. According to the above analyze, because of long flat plate bring obvious traveling-wave scattering peak, it is a ideal model to checkout the effect of traveling-wave restraint. So we manufacture some templets, and select two kind radar absorbing materials which is coated on the templets(only for one side of templets). As shown in Fig. 10.

The RCS test standard is GJB 5022-2001document. To get the result of traveling-wave restraint of the templets covering with RAM, a metallic flat plate is also be tested for RCS at the same frequency. The test curve and data is shown in the following figure.

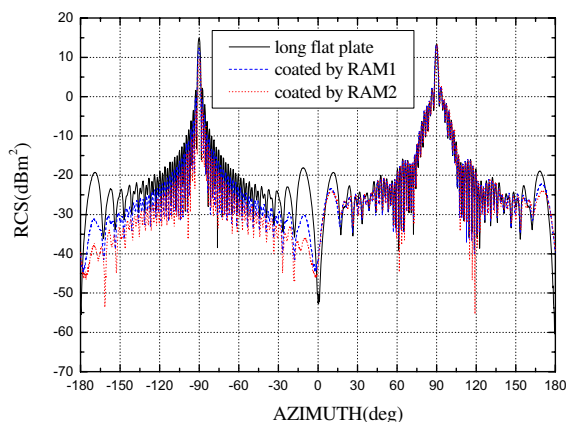


Table 3: The average value at the azimuth angle range between 0 and -20° (dBm²).

Long flat plate	circular arc radius is 15 mm	circular arc radius is 30 mm
-25.74	-41.43	-44.07

In Table 3, when the circular arc radius go on increasing, the traveling-wave scattering become more and more weak. The average value of traveling-wave scattering for the long flat plate with a 30 mm circular arc radius is -44.07 dBm², which has more 18.33 dB attenuation than long flat plate with vertical edge. Therefore, the traveling-wave scattering could be declined availably by transforming the edge into circular arc shape.

5. RESULT

After reducing the RCS of powerfull scattering source with effective measure in the design of high stealth target, traveling-wave scattering has became the chief threat in stealth design. Although traveling-wave scattering is a kind of low scattering, it can not be neglected, and must be restrained with effective measures. In this paper, traveling-wave scattering is restrained availably by using two kinds of methods in changing shape. Study on the representative model of long flat plate only be presented in the paper, but this method could be applied in the design of RCS reducing for some other complex object, and it has significant practical application value.

REFERENCES

1. Knott, E. F., J. F. Shaeffer, M. T. Tuley, *Radar Cross Section*, 2Rev. Edition, Artech House, Norwood, 1993.
2. Huang, P., *Radar Tatget Characteristic Signal*, Aero Flight Press, 1993.
3. Peters, L., "End-fire echo area of long, thin bodies," *TRE Trans. AP*, Vol. 6, No. 1, 138–139, 1958.
4. Amir, B. and M. Raj, "Complex multiple beam approach to electromagnetic scattering problems," *IEEE Antennas Propagation Symposium*, 856–859, 1993.
5. Shirman, Y. D., *Computer Simulation of Aerial Target Radar Scattering, Recognition, Detection, and Tracking*, Artech House, Boston, 2002.
6. Eric, D., "The fast multipole method: Numerical implementation," *Journal of Computational Physics*, Vol. 160, 195–240, 2000.
7. Frith, P. C., "Special issue on radar cross section," *Proc. IEEE*, Vol. 5, 1989.

Fan-shaped Patch Element Wideband Terahertz Metamaterial Perfect Absorber

Xiaodong Hao and Weiping Qin

School of Electronic Science and Engineering

Nanjing University of Posts and Telecommunications, Nanjing 210003, China

Abstract— The wide-band absorbance of the absorber made from the well-known metallic dipole patch has been realized by modifying geometrical shape of conventional rectangular bars in single periodic cell. The increase of relative bandwidth of this new absorptive structure with fan-shaped patch can reach and exceed 100% with respect to the centre frequency comparing with conventional dipole patch geometry. The new structure of absorber exciting a new broadband resonant modes results in the bandwidth expanding. The work presented here provides an efficient method to decrease the number of elements and layers of multi-layer metamaterial absorber compared to conventional element structures used previously.

1. INTRODUCTION

Recently, most studies of terahertz metamaterial absorber mainly focus on broadband realization in order to collect as more incident electromagnetic wave as possible. Many approaches such as single layer multiresonant elements composed of different single resonant frequency and multilayer self assembled elements based on electric dipole, LC or standing wave absorption resonance have been used to achieve broadband absorption [1–8].

One of the effective methods of wide-band operation is using multiple vertically stacked metallic and dielectric layers to realize multiband absorbencies, each absorption band corresponding to a specific layer. An alternative method is using single-layer dielectric structure with two or more resonators with self-similar patterns, the double square loop and double rings were reported in [9].

The structures of metamaterial perfect absorber proposed initially are based on using so called electric split-ring metamaterial resonators [10, 12] in the top metal layer and developed consequently by using dipole crossed dipole three-legged, square loop and concentric ring etc.. These element structures are all able to display electric resonance, however at narrow frequencies band range, usually called narrow-band structure. Crossed patch and three-legged patch based on dipole resonance consisted of simple straight metallic bars are well-known structures used in traditional frequency selective surface (FSS) as spatial filters of microwaves and millimeter waves in microwave engineering for many years and they have been successfully utilized in the design terahertz metamaterial perfect absorber as a basic element structure due to their many advantages, such as simple shape, polarized symmetric easy to fabricate and polarized stability. However, these traditional structures have a major drawback in wideband applications which is narrow bandwidth.

In this paper, a new wideband element structure was proposed which provides a possible method to develop simple single-layer absorber to obtain the performance of wide-band terahertz nearly perfect absorber. The work to investigate our idea was developed in two steps. In the first step, two of basic single-frequency element structure, crossed dipole and three-legged dipole were designed to obtain resonant frequencies at 3.0 THz. In the second step, these two elements were modified to achieve a wide-band response.

2. WIDEBAND FAN-SHAPED STRUCTURES FOR SINGLE-LAYERED ABSORBER

Configurations of the proposed element structure of wideband absorber, which are investigated here, are presented in Fig. 1(a). The geometric shape are fan-like and named here fan-shaped patch absorber, where the four leaf intersect at a right angle to form cross fan-shaped absorber, the three leaf intersect at a 120 degree angle to form three leaf fan-shaped patch absorber. The proposed element have a single metallic layer, and are printed on a dielectric of thickness d . The geometry of leaf is characterized by length L and width W and the unite cell periods are all taken $2L + 1.0$, where all the geometric parameters are in μm unit.

Absorber structure model is shown in Fig. 1(a), a TE mode plane wave with electric field E parallel to x axis direction and wave vector k perpendicular to the patch surface illuminates the patch at normal incidence. The domain of computation is truncated by defining the periodic boundary conditions on the sides that are perpendicular and parallel to the E -field, respectively.

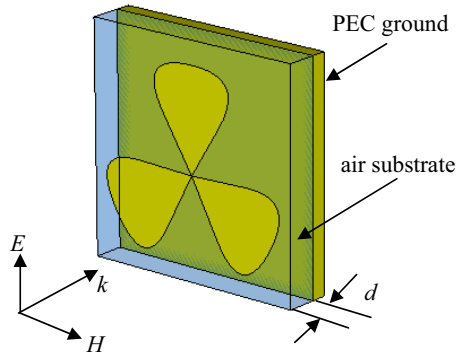


Figure 1: Schematic illustration of the electromagnetic wave incidence on proposed terahertz absorber.

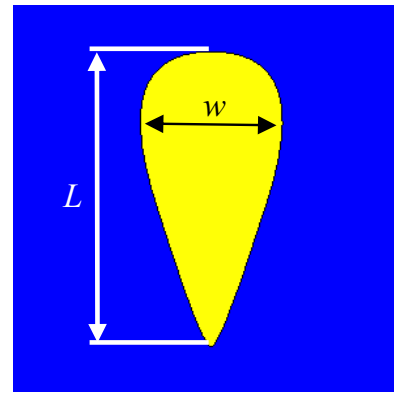


Figure 2: The geometry of investigated wideband absorber element.

The full-wave method of FDTD analysis software CST was used to design and analyze absorber. The metal ground plane with a $0.02 \text{ (}\mu\text{m)}$ thickness was adopted to make sure that the transmission is zero during the whole simulation. For simplification, each metallic patch was designed on air substrate (relative permittivity $\epsilon_r = 1.0$, permeability $\mu_r = 1.0$) to avoid the discussion of dielectric loss in design so that explanation of absorbing mechanism can be provided more clearly by resonance absorb theory. The geometric dimensions of the investigated elements are given in Table 1.

Table 1: Geometric dimensions of elements for investigation.

Element shape	$W \text{ (}\mu\text{m)}$	$L \text{ (}\mu\text{m)}$	$d \text{ (}\mu\text{m)}$
Traditional cross dipole	2.0	23.0	3.0
Traditional three-legged patch	2.0	26.0	3.0
Proposed cross fan-shaped	40.0	40.0	1.5
Proposed three leaf fan-shaped	30.0	43.0	1.5

3. RESULTS AND VERIFICATIONS

The calculated reflection coefficient and absorption coefficient for TE normal incidence were demonstrated. Fig. 3 and Fig. 4. The proposed structures exhibited a terahertz wideband response in Fig. 3(a) and Fig. 4(a). For comparison, the proposed structures and conventional structures are designed at the same resonant frequency. We see that the resonance point appears around 3.0 THz.

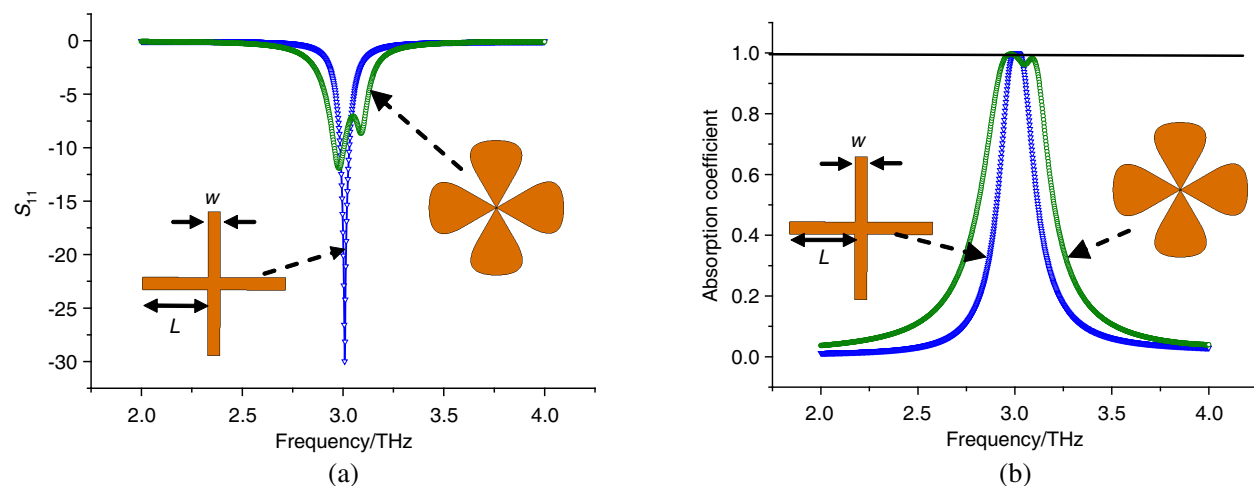


Figure 3: The comparison of reflection coefficients and absorption coefficients of cross patch and cross fan-shape patch.

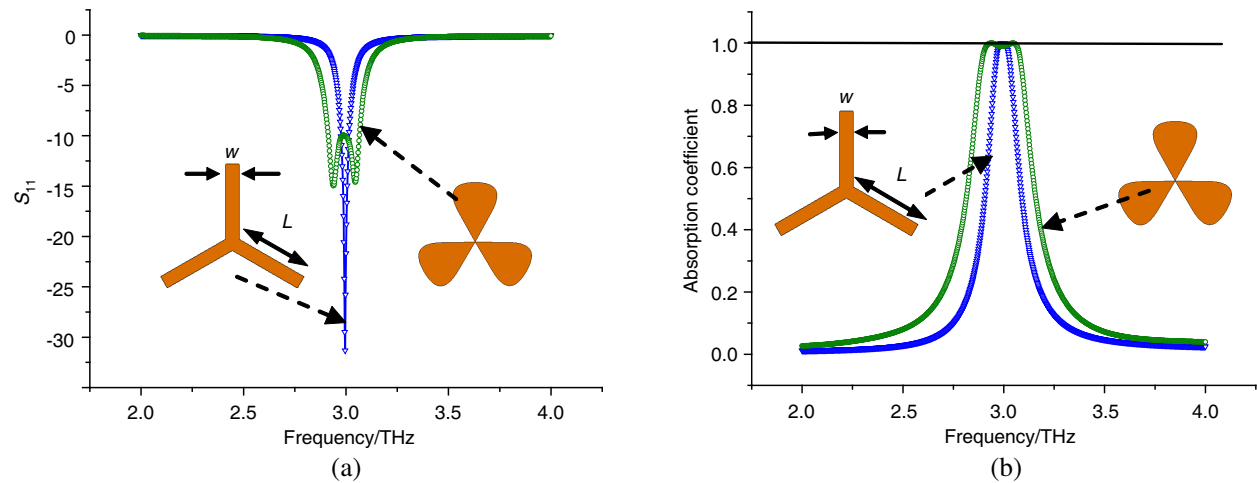


Figure 4: The comparison of reflection coefficients and absorption coefficients of three-leg patch and three-leaf fan-shape patch.

by a reflection below -8 dB. It should be pointed out that, practically, the resonant frequency can be controlled to appear at any frequency point by changing the geometric dimension of absorber.

The simulation results show obvious bandwidth improvement. In Fig. 3(a), the calculated -5 dB reflection coefficients bandwidth in the frequency range from 2.95 THz to 3.06 THz corresponding to a relative bandwidth of 3.67% for conventional cross cell, and the -5 dB relative bandwidth is calculated to be 7.67% for proposed cross fan-shaped cell, which indicating an expanding of relative bandwidth over 100%. In Fig. 4(a), the calculated -5 dB relative bandwidth of reflection coefficient is 2.67% for traditional three-legged cell, corresponded -5 dB bandwidth of proposed three leaf fan-shaped cell reaches 7.67%, which is more than 170% that of the traditional three-legged structure. The absorption coefficient A are depicted in Fig. 3(b) and Fig. 4(b) corresponds to cross fan-shaped and three leaf fan-shaped are also calculated out according to absorption formula $A = 1 - S_{11}^2$, which are all above 90% over the frequency range of interest.

4. CONCLUSIONS

Broadband THz absorption elements have been achieved by our proposed structure. Design and numerical investigations are presented for the new broadband nearly perfect absorbers with fan-shaped element structures in this article. An improvement of bandwidth by using proposed the structure resulted in the wide-band behaviour have been observed. Two examples of proposed structures of absorber are studied, and the results exhibit a high absorption peak over a wide range of resonant frequency. The work presented provides an efficient method to decrease the number of elements and layers of multiresonate wideband absorber compared to conventional element structure used previously.

REFERENCES

1. Gu, C., S. Qu, Z. Pei, H. Zhou, J. Wang, B.-Q. Lin, Z. Xu, P. Bai, and W.-D. Peng, "A wide-band, polarization-insensitive and wide-angle terahertz metamaterial absorber," *Progress In Electromagnetics Research Letters*, Vol. 17, 171–179, 2010.
2. Aydin, K., V. E. Ferry, R. M. Briggs, and H. A. Atwater, "Broadband polarization-independent resonant light absorption using ultrathin plasmonic super absorbers," *Nat. Commun.*, Vol. 2, 517, 2011.
3. Ye, Y. Q., Y. Jin, and S. He, "Omnidirectional, polarization-insensitive and broadband thin absorber in the terahertz regime," *J. Opt. Soc. Am. B*, Vol. 27, No. 3, 498–504, 2010.
4. Gu, S., J. Barrett, T. Hand, B.-I. Popa, and S. Cummer, "A broadband low-reflection metamaterial absorber," *J. Appl. Phys.*, Vol. 108, 064913, 2010.
5. Grant, J., Y. Ma, S. Saha, A. Khalid, and D. R. Cumming, "Polarization insensitive, broadband terahertz metamaterial absorber," *Opt. Lett.*, Vol. 36, No. 17, 3476–3478, 2011.
6. Huang, L., D. R. Chowdhury, S. Ramani, M. T. Reiten, and H.-T. Chen, "Experimental demonstration of terahertz metamaterial absorbers with a broad and flat high absorption band," *Opt. Lett.*, Vol. 37, No. 2, 154–156, 2012.

7. Hendrickson, J., J. Guo, B. Zhang, W. Buchwald, and R. Soref, “Wideband perfect light absorber at midwave infrared using multiplexed metal structures,” *Opt. Lett.*, Vol. 37, No. 3, 371–373, 2012.
8. Hendrickson, J., J. Guo, B. Zhang, W. Buchwald, and R. Soref, “Wideband perfect light absorber at midwaveinfrared using multiplexed metal structures,” *Opt. Lett.*, Vol. 37, No. 3, 371–373, 2012.
9. Huang, L. and H.-T. Chen, “A brief review on terahertz metamaterial perfect absorbers,” *Terahertz Science and Technology*, Vol. 6, No. 1, Mar. 2013.
10. Landy, N. I., S. Sajuyigbe, J. J. Sajuyigbe, M. D. R. Smith, and W. J. Padilla, “A perfect metamaterial absorber,” *Phys. Rev. Lett.*, Vol. 100, 207402, 2008.
11. Tao, H., N. I. Landy, C. M. Bingham, X. Zhang, R. D. Averitt, and W. J. Padilla, “A metamaterial absorber for the terahertz regime: Design, fabrication and characterization,” *Opt. Express*, Vol. 16, 7181–7188, 2008.
12. Lici, K. B., F. Bilotti, L. Vegni, and E. Ozbay, “Experimental verification of metamaterial based subwavelength microwave absorbers,” *J. of App. Phys.*, Vol. 108, 083113, 2010.

A Novel Tunable Dual-band Microwave Metamaterial Absorber Based on Split Ring Resonant

Jialin Yuan¹, Shaobin Liu¹, Borui Bian¹, Xiangkun Kong^{1,2}, Haifeng Zhang¹,
Ben Ma¹, Zhiwen Mao¹, and Beiyin Wang¹

¹Key Laboratory of Radar Imaging and Microwave Photonics

Ministry of Education, College of Electronic and Information Engineering

Nanjing University of Aeronautics and Astronautics, Nanjing 210016, China

²Jiangsu Key Laboratory of Meteorological Observation and Information Processing

Nanjing University of Information Science and Technology, Nanjing 210044, China

Abstract— We present the design, simulation, fabrication, and measurement of a tunable metamaterial at microwave frequencies by embedding varactor diodes as an active elements inside metamaterial units. A pair of feed lines are used to control the reverse bias voltage on the diode. The proposed absorber can perform absorption peaks at two resonant frequencies. The lower resonant frequency can be tuned in a wide range by tuning the values of the diodes while the higher resonant frequency keeps unchangeable. In addition, the absorber with the thickness of $\lambda/74$ at the lowest fundamental resonant frequency is ultra-thin. We also find that the absorber is insensitive to the polarization of incident waves for a wide range of incidence angles for both TE and TM polarizations. The experimental results show excellent absorption rates under different bias voltage on the diode, which are in good accordance to the simulated results.

1. INTRODUCTION

In the last decade, the research on electromagnetic (EM) metamaterial has attracted a lot of attention, due to its peculiar behaviors, such as negative refraction, miniaturization. Owing to its unusual properties, potential applications of metamaterial have been studied in many ways, like antenna structure, perfect lens, concentrator, cloaking and so on.

Recently, the metamaterial absorber (MMA) has become a research focus, by designing proper resonant units, a perfect absorber has many wonderful properties like high absorptivity and ultra-thin thickness. In 2008, Landy [1] first reported the concept of perfect metamaterial absorber, which consists of artificial sub-wavelength composites and has high absorption with small-size. Recently, MMAs are available in the microwave region, terahertz region, infrared and visible regions [2–5]. Dual-band and multi-band MMAs has been successfully realized which are based on different electric resonators [6, 7]. Broadband MMAs have also been studied in various designed forms of units [8]. However, the traditional metamaterial absorbers have a common shortcoming that their absorption performance can not be changed if they have been fabricated. Therefore, the design of tunable MMAs has attracted more and more interests. Jie Zhao et al. [9] introduced a tunable metamaterial absorber using varactor diodes. Its absorption frequency can be tuned by changing the bias voltage at the both ends of the diodes. A microwave diode switchable metamaterial reflector/absorber has been investigated by Wangren Xu et al. [10].

In this paper, we propose a simple design of tunable absorber structure to achieve a tunable dual-band absorber in GHz frequency regime. The lower absorption frequency can be tuned continuously by changing the reverse bias voltage on the diode while the higher absorption frequency keeps unchangeable. The thickness of the dielectric material in our absorber in only $\lambda/76$ at the lowest fundamental resonant frequency. In addition, current and field distribution analysis are performed to better understand the resonant mechanism. The simulation and experiment results are in excellent agreement to verify the designs with high absorption rate of more than 90%.

2. DESIGN AND BASIC UNIT

The proposed MMA based on the novel resonant structure is presented in Fig. 1. Fig. 1(a) shows the perspective view of the proposed MMA, which is composed of two conductive layers with a single substrate (FR-4) between them. Fig. 1(b) shows the photograph of the fabricated MMA sample and the detailed patterns of the unit cells appearing in the top layer. There are a cut wire and a SRR on the top layer, where the bottom layer has a metallic ground plate without patterning. The varactor diode illustrated as the blue cube in Fig. 1(a) is embedded in the disconnection of the

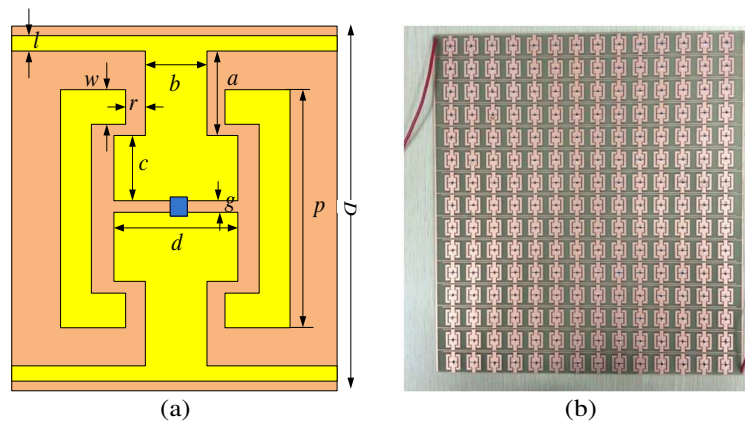


Figure 1: Structure of the unit cell of the proposed MMA. (a) Perspective view. (b) The photograph of the fabricated MMA sample.

cut wires. The chosen substrate is FR-4 with a relative permittivity $\epsilon_r = 4.4$ (loss tangent 0.025) and thickness $h = 1.5$ mm. The feeding lines of the diode are in the same plane with resonators. The dimensions of the resonator unit are shown in Fig. 2. All units are in millimeters: $D = 20$ mm, $a = 3$ mm, $b = 3.6$ mm, $c = 4.25$ mm, $d = 8$ mm, $g = 0.5$ mm, $l = 0.5$ mm, $w = 2$ mm, $p = 14$ mm, $r = 2.5$ mm.

3. SIMULATION RESULTS

Based on the previous dual-band absorber designed structure without varactor diode, the varactor diode is embedded between the gap in the middle of the surface. The absorption rates of the designed unit under different value of the diode are simulated in Fig. 4. Firstly, the two absorption frequencies are more close after added the varactor diode, then the ripple beside the lower absorption frequency disappears and the absorption rate becomes nearly 99%. Through tuning the bias voltage applied on the varactor, the junction capacitance of the varactor is changed, which results the shift of the resonance frequency. We found that there is a wide tuning frequency range from 2.69 GHz to 3.37 GHz by changing the diode's reverse bias voltage from -0 V to -15 V with the absorption rates closing to 99%.

At last, we will discuss the situations with large incident angles and instable polarization states. It is clear that the tunable MMA has a stable performance under both TE and TM polarizations, as shown in Fig. 3. The absorption rates is insensible to the incident angles (θ , defined as the angle between the wave vector and the normal). Fig. 4 shows the simulation results for the oblique incidence at different incident angles for TE [Fig. 4(a)] and TM [Fig. 4(b)] under the capacitance of 1.090 pF. From the figure, it can be concluded that the MMA unit has excellent performance even when the incident angle is up to 50° .

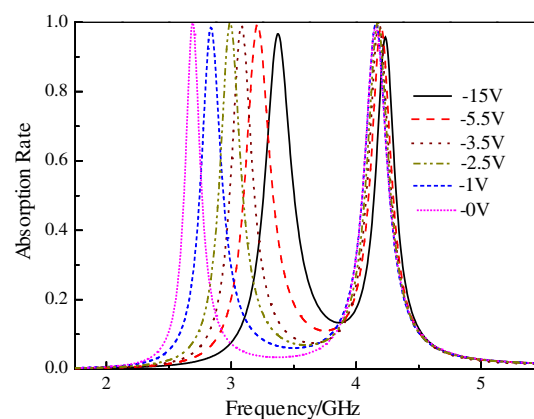


Figure 2: Simulation results of the absorption rates under different reverse bias voltages.

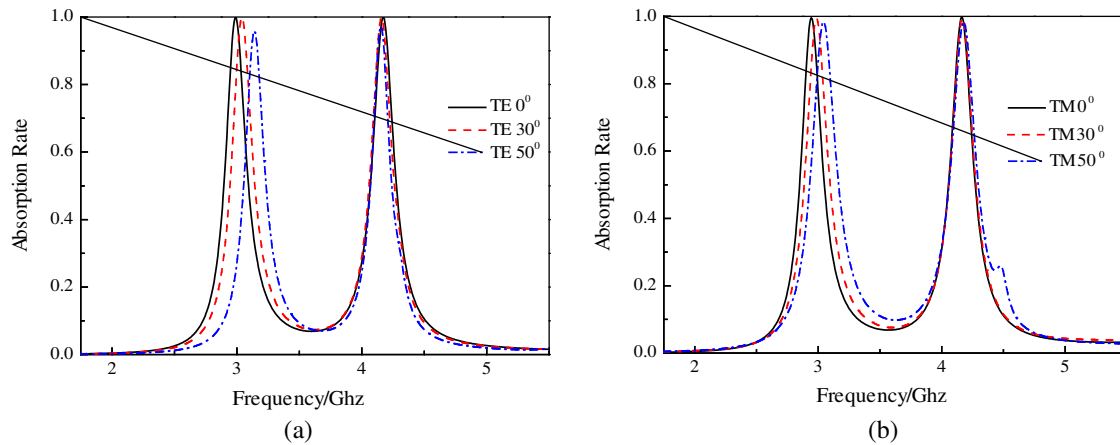


Figure 3: Simulation results of the absorption rates for oblique incidences at various incident angles for (a) TE and (b) TM polarizations under the capacitance 1.090 pF.

4. EXPERIMENTAL RESULTS

To experimentally verify the design procedure of the proposed tunable MMA, we have fabricated a MMA sample, as shown in Fig. 10(a). The unit cells are fabricated using the print circuit board technique on the FR4 substrate, with total footprint of $280\text{ mm} \times 300\text{ mm}$ consisting of 210 elements and the thickness of 1.5 mm as that used in numerical simulations. The fabricated tunable MMA is then measured by the free-space method, using two horn antennas in a controlled environment of an anechoic chamber. Fig. 10 illustrates the fabricated sample and the experimental simulation setup, in which two pairs of horn antennas connecting to the vector network analyzer (Agilent N5230C) by a low-loss coaxial cable. The incident wave's polarization is chosen to be along the vertical direction. The distance between the sample and the antenna is D^2/λ_0 , which is far enough to avoid the near-field effects of the antenna and the DFSS sample being tested. We also use pyramid absorbing materials to eliminate the electromagnetic (EM) scattering from the environment.

The experimental results of the reflection coefficient of the fabricated tunable MMA for TE polarizations under different reverse bias voltage are illustrated in Fig. 11. It is observed that the absorption rate is nearly 90% when the bias voltage changes from -1 V to -14 V . The slight frequency discrepancy may be due to the fabrication tolerance as well as the dielectric board material whose actual dielectric constant is slightly different from the value used in the simulations. In spite of these discrepancies, it is clearly that the experimental results agree with the simulation results that high can be obtained at the resonance frequency and validate the tunability of the tunable MMA and. In addition, the proposed MMA is relative thin, with a thickness nearly of $\lambda/74$ at the lowest fundamental resonant frequency of the working wavelength.

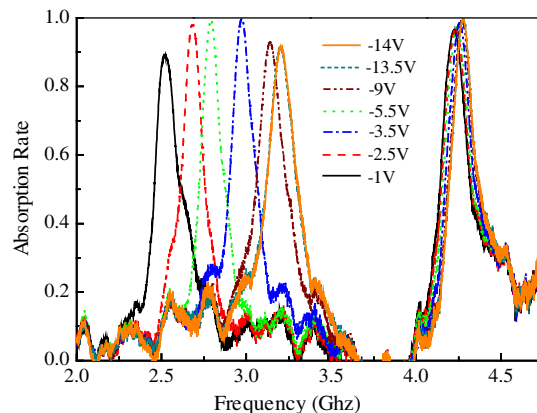


Figure 4: Experimental results of the absorption rates at different reverse bias voltage, ranging from -1 to -14 V .

5. CONCLUSIONS

In summary, we have proposed a tunable metamaterial absorber using cut wires embedded varactor diodes and SRR working in microwave region. The lower absorption frequency of the MMA can be tuned continuously by changing the bias voltage on the both ends of the varactor diode. While the higher absorption frequency keeps unchangeable. Both the absorption rates remain greater than 90% throughout the process of measurement. By placing the basic units orthogonally, we can achieve its property of polarization and large incident angles insensitivity. The detailed analysis of the surface current of the structure and E-field distributions have performed to better understand the resonant mechanism. The simulation and the experimental results are in good consistency, which verified the tunability of the dual-band MMA.

ACKNOWLEDGMENT

This work was supported by Funding of Jiangsu Innovation Program for Graduate Education (No. CXZZ13.0166), Youth Funding for Science & Technology Innovation in NUAA (NS2014039), Open Research Program in Jiangsu Key Laboratory of Meteorological Observation and Information Processing (Grant No. KDXS1207), the Chinese Specialized Research Fund for the Doctoral Program of Higher Education (No. 20123218110017), the Jiangsu Province Science Foundation (No. BK2011727), and the Foundation of Aeronautical Science (No. 20121852030). Chinese Natural Science Foundation (Grant No. 61307052)

REFERENCES

1. Landy, N. I., S. Sajuyigbe, J. J. Mock, et al., "Perfect metamaterial absorber," *Physical Review Letters*, Vol. 100, No. 10, 207–402, 2008.
2. Tao, H., N. I. Landy, C. M. Bingham, et al., "A metamaterial absorber for the terahertz regime: Design, fabrication and characterization," *Optics Express*, Vol. 16, No. 10, 7181–7188, 2008.
3. Shu, S., Z. Li, and Y. Y. Li, "Triple-layer Fabry-Perot absorber with near-perfect absorption in visible and near-infrared regime," *Optics Express*, Vol. 21, No. 21, 25307–25315, 2013.
4. Cai, W., U. K. Chettiar, A. V. Kildishev, et al. "Optical cloaking with metamaterials," *Nature Photonics*, Vol. 4, No. 1, 224–227, 2007.
5. Wang, H. and L. Wang, "Perfect selective metamaterial solar absorbers," *Optics Express*, Vol. 106, No. 21, A1078–A1093, 2013.
6. Ma, Y., Q. Chen, J. Grant, et al., "A terahertz polarization insensitive dual band metamaterial absorber," *Optics Letters*, Vol. 6, No. 36, 945–947, 2011.
7. Bian, B., S. Liu, S. Wang, et al., "Novel triple-band polarization-insensitive wide-angle ultra-thin microwave metamaterial absorber," *Journal of Applied Physics*, Vol. 19, No. 114, 194–511, 2013.
8. Wang, G. D., M. H. Liu, X. W. Hu, et al., "Broadband and ultra-thin terahertz metamaterial absorber based on multi-circular patches," *The European Physical Journal B*, Vol. 86, No. 7, 1–9, 2013.
9. Xu, W. and S. Sonkusale, "Microwave diode switchable metamaterial reflector/absorber," *Applied Physics Letters*, Vol. 103, No. 3, 031–902, 2013.
10. Zhao, J., Q. Cheng, J. Chen, et al., "A tunable metamaterial absorber using varactor diodes," *New Journal of Physics*, Vol. 15, No. 4, 043–049, 2013.

A Broadband Terahertz Metamaterial Absorber Based on Square Ring Resonators

Guo-Dong Wang, Jun-Feng Chen, Xi-Wei Hu, and Ming-Hai Liu

State Key Laboratory of Advanced Electromagnetic Engineering and Technology

School of Electrical and Electronic Engineering

Huazhong University of Science and Technology, Wuhan 430074, China

Abstract— A simple design of broadband metamaterial absorber (MA) is numerically investigated at terahertz frequencies in this paper. The unit cell of this absorber consists of two square rings with different geometric dimensions, a dielectric substrate and continuous metal film. A wide frequency band ranging from 2.95 THz to 3.71 THz with absorption rate of over 90% is obtained. Distributions of surface current density on the front and back metallic layers are illustrated. Finally, the loss contributions of metallic structures and dielectric substrate are also discussed. The proposed absorber is an ideal candidate as absorbing elements in many applications, such as thermal detectors, terahertz imaging, and stealth technology.

1. INTRODUCTION

Electromagnetic metamaterials (MM) have been attracting considerable attention during the past decade due to their ability to exhibit exceptional physical properties, which are not available in naturally occurring materials, such as negative refractive index [1, 2] superlensing [3], cloaking [4], and optical transformation [5]. Most of these proposed structures were mainly implemented at the microwave frequencies due to the simplicity in design and characterization. By adjusting proportionally geometric parameters of resonant components in MM unit, the response frequency can achieve the most part of the electromagnetic spectrum ranging from radio to the near optical regimes [6–9]. MMs can be widely used in many applications, including invisibility cloaks [4], perfect lens [3], and bandpass filters [10].

Recently, MMs are fashioned to create subwavelength resonant absorbers. In 2008, Landy et al. proposed the first configuration of MA. The MA is composed of electric resonator on the front side of FR-4 substrate and cut wire on the bottom and has an experimental absorption rate of 88% at 11.5 GHz [11]. Later, many novel MA designs were investigated to achieve polarization-insensitive absorption [12] or wide-angle absorption [13] at gigahertz and terahertz frequencies. The idea is to tune electric and magnetic response of absorber independently to make the effective impedance match to free space and to attain a large imaginary part of refraction index, the reflectance and transmission of the incident wave energy will be minimized simultaneously, the MA can completely absorb the incident electromagnetic wave. However, most of these designs are based on strong electromagnetic resonances to effectively absorb the incident wave. Consequently, the working bandwidth of these MAs is relatively narrow, typically no more than 10% with respect to the center frequency. At present, much attention has been paid to the design of multiband [14, 15] and broadband MAs [16], which are generally composed of multilayer metallic and dielectric components. These multilayer absorbers are usually difficult to design and fabricate. These above-mentioned defects impose many restrictions on future applications in the scientific and technological areas.

In this paper, we design a simple broadband terahertz MA using rectangular ring, dielectric substrate and continuous metal film. A wide frequency band ranging from 2.95 THz to 3.71 THz with absorption rate of over 90% is obtained. Simulated results show that the MA can achieve polarization-insensitive and wide-angle absorption for both TE and TM waves in this band.

2. DESIGN AND SIMULATION

The schematic diagram and geometric parameters of the proposed MA unit cell are depicted in Fig. 1. The outer and inner rings on the front side are shown in Figs. 1(a) and 1(b). The length and width of the outer and inner rings are equal to $b_1 = 11.2 \mu\text{m}$, $w_1 = 0.2 \mu\text{m}$ and $b_2 = 10.6 \mu\text{m}$, $w_2 = 2.5 \mu\text{m}$, respectively. Fig. 1(c) is the perspective view of the MA unit cell, the axes indicate that the polarization and propagation direction of the incident wave. The thickness of dielectric substrate is $t = 5 \mu\text{m}$. The lattice constants along the x and y directions are both $p = 14 \mu\text{m}$. The rectangular ring strongly couples to the electric component of the incident wave to provide an

electric response. The incident magnetic field couples to two metallic conducting layers on both sides of dielectric substrate, which exhibits a magnetic response. We can tune the geometric parameters of the unit cell to acquire tailored electric and magnetic response and achieve a perfect absorption.

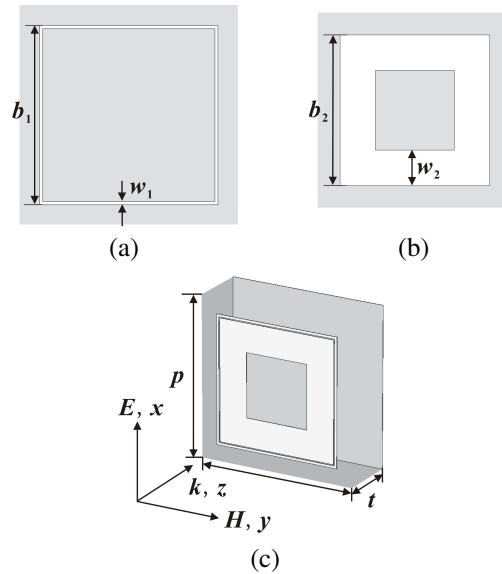


Figure 1: Schematic diagram and geometric parameters of the proposed MA unit cell. (a) The outer and (b) inner ring on the front side. (c) The perspective view with axes indicating the polarization and propagation direction of the incident wave.

The absorption rate is calculated by $A(w) = 1 - R(w) - T(w)$, where $R(w) = |S_{11}|^2$ and $T(w) = |S_{21}|^2$ are the reflectance and transmission, respectively. As the thickness of metal film in this paper is much larger than the penetration depth in the terahertz regime, the transmission is equal to zero in the whole frequencies of interest and the reflectance is the only factor determining the absorption. The absorption formula is simplified to $A(w) = 1 - R(w)$. To attain a perfect absorption, we can only minimize the reflectance.

The proposed MA is designed and optimized by the commercial finite difference time domain solver (CST Microwave Studio 2009). Unit cell boundary conditions are set along the lateral directions of the MA and open boundary condition is set along the direction. The substrate is modeled as FR-4 with relative dielectric constant = 4.9 and loss tangent $\tan = 0.025$. The simulated absorption spectra of the MA are shown in Fig. 2 (solid line). There is a wide frequency band ranging from 2.95 THz to 3.71 THz with absorption rate of over 90%. Therefore, the bandwidth of strong absorption is about 0.76 THz.

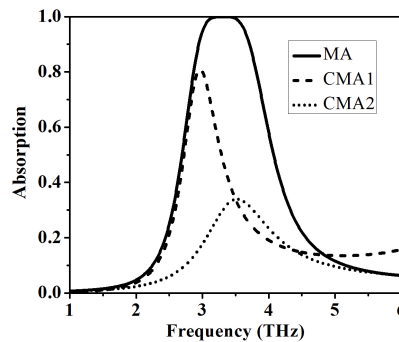


Figure 2: Simulated absorption spectra of the MA, CMA1 and CMA2 as a function of frequency.

For comparison, two designs of absorber (CMA1 and CMA2) are proposed. The only difference between CMA1 (or CMA2) and original MA is the front structure. The front structure of CMA1

and CMA2 are only composed of outer and inner ring, respectively, as shown in Figs. 1(a) and 1(b). The simulated absorption spectra of CMA1 (short dash line) and CMA2 (short dot line) are illustrated in Fig. 2. When the front structure is only composed of outer ring (CMA1), a distinct peak with absorption rate of 80.8% at 2.97 THz is obtained and the working bandwidth (more than 50%) is 0.56 THz. When the front structure is only composed of inner ring (CMA2), there is an absorption peak of only 34% at 3.53 THz. These results indicate that a wide absorption band is obtained by overlapping different resonances and a broadband MA could be achieved by integrating different resonant elements into a unit cell.

To get an insight into the intrinsic mechanism of high absorption, the distribution of surface current density on the front and back metallic layers at 3.33 THz is illustrated in Fig. 3. From Fig. 3(a), we can see that opposite current flows between the outer and inner rings are formed on the front structure of the MA. However, there are comparatively small opposite currents on the front and the back metallic layers as shown in Fig. 3(b). It is concluded that the rectangular rings can supply both electric and magnetic response.

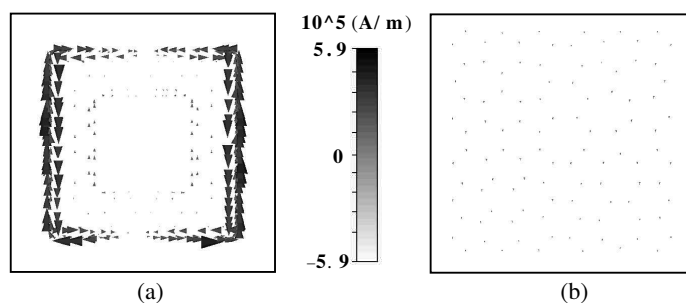


Figure 3: Distribution of surface current density on the (a) front and (b) back metallic layers at 3.33 THz.

3. POLARIZATION-INSENSITIVE AND WIDE-ANGLE ABSORPTION

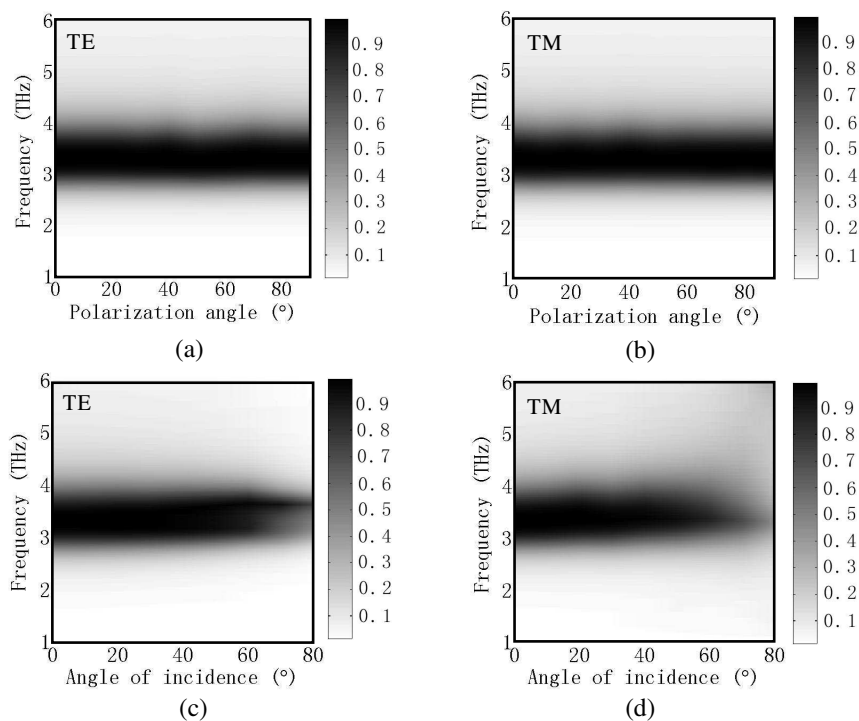


Figure 4: Absorption spectra as a function of frequency and polarization angle for (a) TE and (b) TM waves. Absorption spectra as a function of frequency and angle of incidence for (c) TE and (d) TM waves.

Figures 4(a) and 4(b) show the absorption spectra as a function of frequency and polarization

angle for TE and TM waves, respectively. As the polarization angle increases from 0 to 90, the absorption spectra for TE and TM waves almost remain the same. The absorption spectra as a function of frequency and angle of incidence for TE and TM waves are illustrated in Figs. 4(c) and 4(d), respectively. For the case of TE wave, the absorption spectra of the MA keep unchanged as the incident angle varies from 0 to 60. Beyond 60, the amplitude of the absorption peak decreases quickly and the absorption band becomes very narrow. For the TM wave, the absorption spectra are almost the same as the incident angle increases from 0 to 55. As the incident angle continues to increase, the amplitude of the absorption peak begins to decrease and the absorption band becomes narrower and narrower. These simulated results validate that the absorber can work at wide polarization angles and wide angles of incidence for both TE and TM waves.

4. THE LOSS CONTRIBUTIONS OF EACH PART OF THE MA

To understand how and where the absorption happens, the absorption spectra of the MA with different components are illustrated in Fig. 5. It is easily found that the front two absorption spectra are almost the same. There is a wide frequency band ranging from 2.95 THz to 3.71 THz with absorption rate of over 90% and the absorption bandwidth is 0.76 THz. When the metal is perfect electric conductor (PEC) and the substrate is lossy, there are two distinct peaks at 3.15 THz and 4.2 THz with corresponding absorption rate of 30.7% and 81.8%. These absorption spectra of different components suggest that high absorption of the MA mainly originates from the metallic absorption (Ohmic loss). This is different from the studies in previous works where Ohmic loss is minor compared with dielectric loss of the substrate. The MA has a great potential application in some fields where energy is needed to be absorbed by the metal structure.

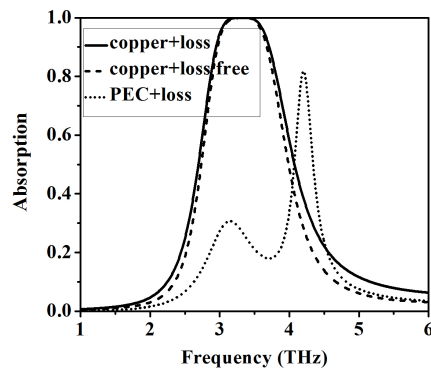


Figure 5: Absorption spectra as a function of frequency and polarization angle for (a) TE and (b) TM waves. Absorption spectra as a function of frequency and angle of incidence for (c) TE and (d) TM waves.

5. CONCLUSION

In summary, we have presented a polarization-insensitive and wide-angle broadband MA, which is composed of two rectangular rings with different geometric dimensions, dielectric substrate and continuous metal film. A wide frequency band ranging from 2.95 THz to 3.71 THz with absorption rate of over 90% is obtained. Distribution of surface current density is illustrated to indicate that the rectangular rings can supply both electric and magnetic response. Absorption spectra of the MA at different polarization angles and different angles of incidence validate that the MA can achieve polarization-insensitive and wide-angle absorption for both TE and TM waves. Absorption spectra of different components suggest that high absorption of the MA mainly originates from Ohmic loss and the dielectric loss of the substrate is minor compared with Ohmic loss. Importantly, the proposed MA is also geometrically scalable. Therefore, our results are not limited to terahertz frequencies and may be used in other parts of the electromagnetic spectrum. The MA has great promise for many applications ranging from the active element in a thermal detector to stealth technology.

ACKNOWLEDGMENT

This work was supported by Graduates' Innovation Fund of Huazhong University of Science Technology (Grant No. HF-11-15-2013) and the special funds of State Key Laboratory of Advanced Elec-

tromagnetic Engineering and Technology, Huazhong University of Science and Technology (Grant No. 2014ZZ001).

REFERENCES

1. Smith, D. R., W. J. Padilla, D. C. Vier, S. C. Nemat-Nasser, and S. Schultz, “Composite medium with simultaneously negative permeability and permittivity,” *Physical Review Letters*, Vol. 84, No. 18, 4814, 2000.
2. Shelby, R. A., D. R. Smith, and S. Schultz, “Experimental verification of a negative index of refraction,” *Science*, Vol. 292, 77-79, 2001.
3. Pendry, J. B., “Negative refraction makes a perfect lens,” *Physical Review Letters*, Vol. 85, No. 18, 3966, 2000.
4. Leonhardt, U., “Optical conformal mapping,” *Science*, Vol. 312, 1777-1780, 2006.
5. Pendry, J. B., D. Schurig, and D. R. Smith, “Controlling electromagnetic fields,” *Science*, Vol. 312, 1780-1782, 2006.
6. Huang, Y. J., H. L. Yang, X. W. Hou, Y. Tian, and D. Y. Hou, “Perfect metamaterial absorber with dual bands,” *Progress In Electromagnetic Research*, Vol. 108, 37–49, 2010.
7. He, X. J., Y. Wang, J. M. Wang, T. L. Gui, and Q. Wu, “Dual-band terahertz metamaterial absorber with polarization insensitivity and wide angle,” *Progress In Electromagnetic Research*, Vol. 115, 381–397, 2011.
8. Zhu, W. R. and X. P. Zhao, “Metamaterial absorber dendritic cells at infrared frequencies,” *J. Opt. Soc. Am. B*, Vol. 26, 2382–2385, 2009.
9. Zhu, W. R., X. P. Zhao, B. Y. Gong, L. H. Liu, and B. Su, “Optical metamaterial absorber based on leaf-shaped cells,” *Appl. Phys. A Mater.*, Vol. 102, 147–151, 2011.
10. Butt, H., Q. Dai, P. Farah, T. Butler, T. D. Wilkinson, J. J. Baumberg, and G. J. Amaratunga, “Perfect metamaterial absorber,” *Appl. Phys. Lett.*, Vol. 97, No. 77, 163102, 2010.
11. Landy, N. I., S. Sajuyigbe, J. J. Mock, D. R. Smith and W. J. Padilla, “Perfect metamaterial absorber,” *Physical Review Letters*, Vol. 100, No. 20, 207402, 2008.
12. Landy, N. I., C. M. Bingham, T. Tyler, N. Jokerst, D. R. Smith, and W. J. Padilla, “Design, theory, and measurement of a polarization-insensitive absorber for terahertz imaging,” *Physical Review B*, Vol. 79, No. 12, 125104, 2009.
13. Hu, T., C. M. Bingham, A. C. Strikwerda, D. Pilon, D. Shrekenhamer, N. I. Landy, K. Fan, X. Zhang, W. J. Padilla, and R. D. Averitt, “Highly flexible wide angle of incidence terahertz metamaterial absorber: Design, fabrication, and characterization,” *Physical Review B*, Vol. 78, No. 24, 241103(R), 2008.
14. Wang, G. D., M. H. Liu, X. W. Hu, L. H. Kong, L. L. Cheng, and Z. Q. Chen, “Multi-band microwave metamaterial absorber based on coplanar Jerusalem crosses,” *Chinese Physics B*, Vol. 23, No. 1, 017802, 2014.
15. Wang, G. D., J. F. Chen, X. W. Hu, Z. Q. Chen, and M. H. Liu, “Polarization-insensitive triple-band microwave metamaterial absorber based on rotated square rings,” *Progress In Electromagnetic Research*, Vol. 145, 175-183, 2014.
16. Wang, G. D., M. H. Liu, X. W. Hu, L. H. Kong, L. L. Cheng, and Z. Q. Chen, “Broadband and ultra-thin terahertz metamaterial absorber based on multi-circular patches,” *European Physical Journal B*, Vol. 86, No. 7, 304, 2013.

Ultrafast Photonic Differentiator and Integrator Employing Integrated Silicon Microring or MZI

Jianji Dong, Shasha Liao, Aoling Zheng, and Ting Yang

Wuhan National Laboratory for Optoelectronics, School of Optical and Electronic Information
Huazhong University of Science and Technology, Wuhan 430074, China

(Invited Paper)

Abstract— Integrated microwave photonics is becoming one of the most promising topics due to the compact size, light weight, and low power consumption. In this paper, we review several schemes of ultrafast photonic differentiator and integrator employing integrated silicon microring or MZI.

1. INTRODUCTION

Photonic integrated circuits for photonic computing open up the possibility for the realization of ultrahigh-speed and ultra wide-band signal processing with compact size and low power consumption. As we all known, the two important parts of photonic computing are differential and integral. Photonic differentiator (DIFF) has wide applications in numerous fields such as pulse characterization, ultra-fast signal generation, and ultra-high-speed coding. And one of the most important application of integral is solve the differential equations, which can be used in many field of science and engineering, such as temperature diffusion processes, physical problems of motion subject to acceleration inputs and frictional forces, and the response of different resistor-capacitor circuits, etc..

DIFFs can be achieved by nonlinear effects of semiconductor optical amplifiers (SOAs) [1, 2], incoherent photonic processors [3] and highly nonlinear fibers [4]. The typical schemes to solve the differential equation have focused on two routes toward solving first-order all-optical differential equations. The first one requires an optical feedback loop [5, 6], while the second one is based on a Fabry-Perot (FP) resonance cavity with properly designed temporal impulse response [7]. Nevertheless, the configurations of these schemes are bulky and complex, involving either redundant loop [5, 6] or additional optical pump [6, 7].

In this review, we report several schemes of ultrafast photonic differentiator and integrator. In Section 2, we demonstrate a high-order DIFF and fractional-order DIFF based on Mach-Zehnder Interferometer (MZI) structure and demonstrate linear ODE solver with constant-coefficient tunable based on a single microring.

2. HIGH-ORDER PHOTONIC DIFFERENTIATOR USING SILICON MACH-ZEHNDER INTERFEROMETERS [8]

An N th-order optical temporal differentiator provides the N th-time derivative of the complex envelope of an input optical signal. It has been proved that the MZI structure has a good linear frequency response near the MZI resonant notch, which can implement the first order DIFF. Therefore, to achieve N th-order differentiator, the MZI unit just needs to be cascaded by N times. We employ on-chip cascaded MZI structure for high-order DIFF. First we design and fabricate cascaded MZIs on commercial silicon-on-insulator (SOI) wafer. Fig. 1 shows the microscope image of our on-chip MZIs.

First, the laser wavelength is fixed at 1565.4 nm. And the BPG drives the two MZMs to generate a Gaussian pulse train with a pulsewidth of 18 ps, as shown in Fig. 2(a). When we employ the chips of MZI-1, MZI-2, and MZI-3, and fine tune the laser wavelength to align with the resonant notch, we measure the temporal waveforms of 1st order, 2nd order, and 3rd order DIFFs, respectively, which are shown in Figs. 2(b)–(d), respectively. It can be seen that the measured differentiated pulses fit well with the simulated pulses, except a small discrepancy in the pulse sidelobes, such as 2nd-order DIFF and 3rd-order DIFF. The deviation of the sidelobes may be caused by the finite bandwidth and the finite notch depth.

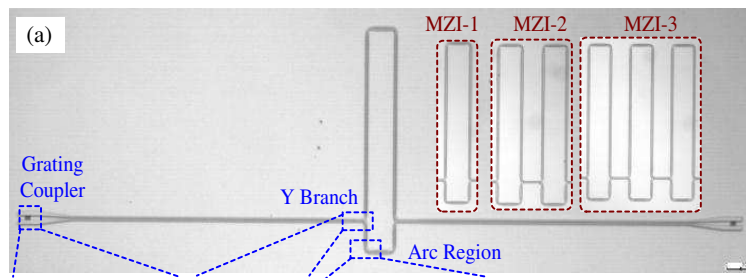


Figure 1: Microscope image of our on-chip MZIs, insets: photos of structures of MZI-1, MZI-2, and MZI-3.

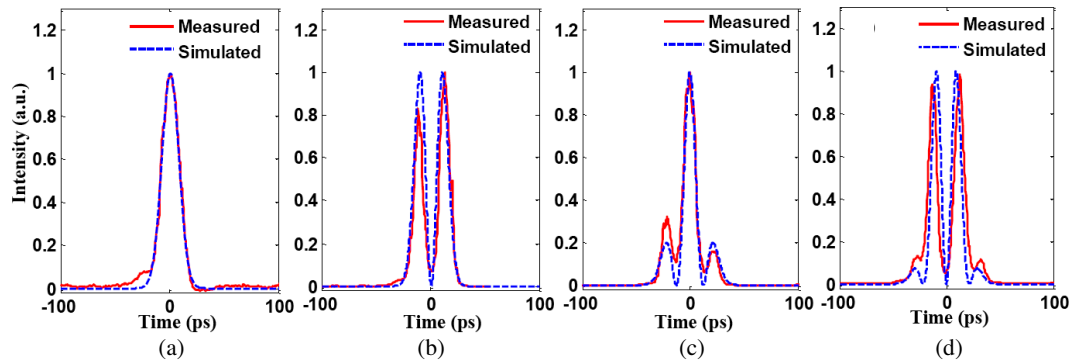


Figure 2: (a) input pulse, (b)–(d) temporal waveforms for 1st-, 2nd-, and 3rd-order DIFFs, respectively.

3. FRACTIONAL-ORDER DIFFERENTIATOR USING AN ELECTRICALLY TUNED SOI MACH-ZEHNDER INTERFEROMETER

From Eq. (2.1), we know that a MZI can play a role as a fractional-order differentiator if N is a fraction number and the power splitting ratio of two arms of MZI are not the same. So we fabricated an on-chip electrically tuned MZI to build a tunable fractional-order differentiator. Fig. 3 shows the micrographs of (a) total MZI structure, (b) coupling grating, (c) MMI, (d) p - i - n diode.

We change the voltage of the electrodes on the MZI, and fine tune the tunable laser diode wavelength to be aligned with the notch wavelength, the output differentiated waveforms are shown in Figs. 4(b)–(i). At the same time, the simulated waveforms of fractional-order differentiation are also shown, whose fractional orders are $N = 0.83, 0.85, 0.88, 0.93, 0.96, 0.98, 1.00, 1.03$, respectively. One can see there is a good agreement between the measured pulses and the ideal differentiators except a small discrepancy at the pulse notch.

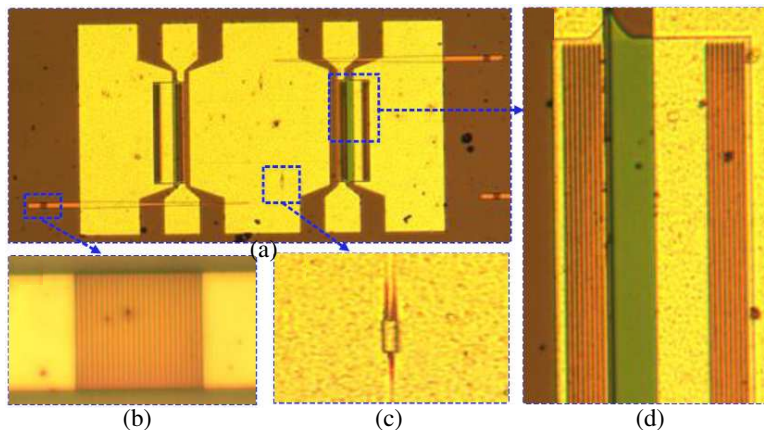


Figure 3: Micrographs of (a) MZI, (b) coupling grating, (c) MMI, (d) integrated p - i - n diode.

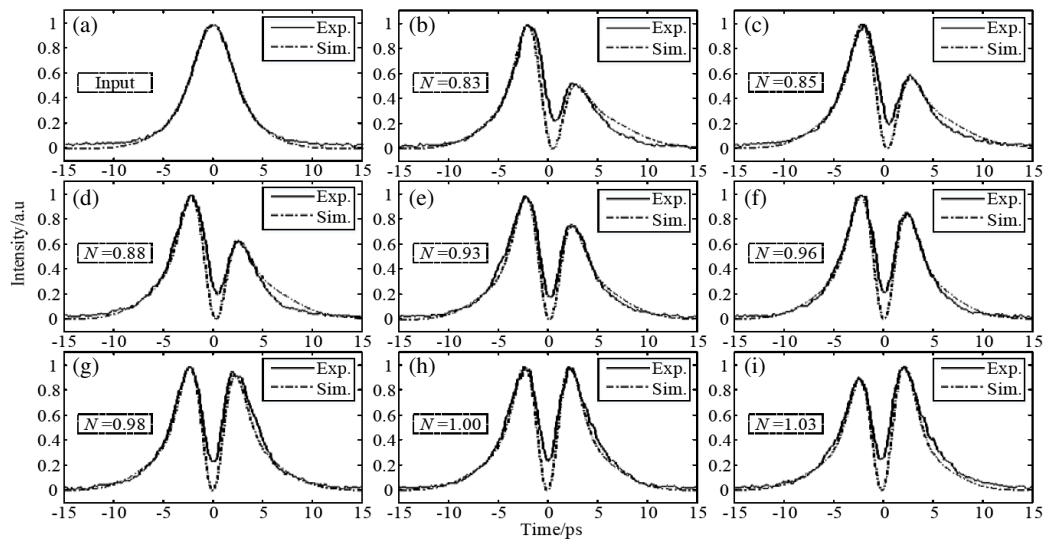


Figure 4: (a) An input Gaussian-like pulse with an FWHM of 5.4 ps, and the differentiated pulses at the different voltages corresponding to differentiation orders of (b) $N = 0.83$, (c) $N = 0.85$, (d) $N = 0.88$, (e) $N = 0.93$, (f) $N = 0.96$, (g) $N = 0.98$, (h) $N = 1.00$, (i) $N = 1.03$.

4. HIGH-ORDER ALL-OPTICAL DIFFERENTIAL EQUATION SOLVER BASED ON MICRORING RESONATORS

The common constant-coefficient first-order linear ODE can be expressed as:

$$\frac{dy(t)}{dt} + ky(t) = x(t) \quad (1)$$

where $x(t)$ represents the input signal, $y(t)$ is the equation solution (output signal) and k denotes a positive constant of an arbitrary value. We know that a silicon microring functions as a loss integrator, which has a similar transfer function to Eq. (1) at the drop port. Therefore, a single add-drop microring can be utilized to solve constant-coefficient first-order linear ODE. Similarly, cascading microrings can solve second-order linear ODE if two microring resonant peaks are matched.

The microrings we employed are two cascaded microrings fabricated on silicon-on-insulator (SOI) wafer with different radii ($R_1 = 100 \mu\text{m}$, $R_2 = 130 \mu\text{m}$) and Q factor ($Q_1 = 22038$, $Q_2 = 19045$), as illustrated in Fig. 5(a). The waveguide width and thickness of both straight and bending waveguide are 450 nm and 220 nm, respectively, while the gap between them is 200 nm (Fig. 5(b)). Employing

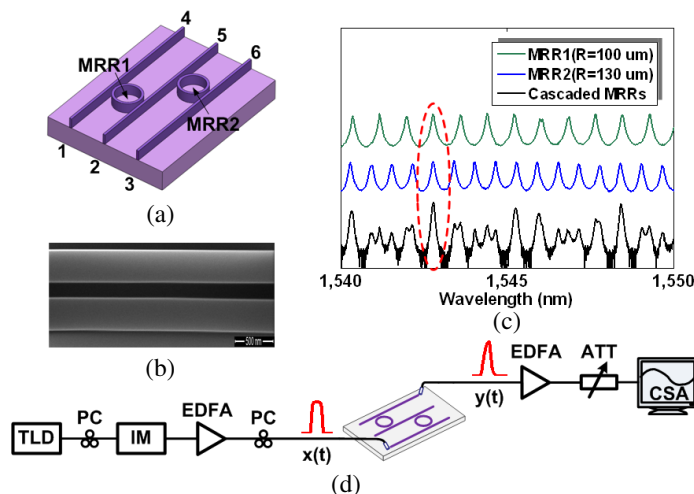


Figure 5: (a) Schematic of the cascaded microrings, (b) SEM picture of the coupling region between the ring and the straight waveguide, (c) measured spectra of each microring and the cascaded ones, (d) the experimental setup.

port 1 and 2, Microring 1 is used as a first-order all-optical ODE solver with the constant-coefficient $k_1 = 0.028/\text{ps}$; meanwhile Microring 2 can be treated as another first-order all-optical ODE solver with $k_2 = 0.032/\text{ps}$ when using port 5 and 6. Additionally, utilizing port 3 and 4, two cascaded microrings are working as a second-order all-optical ODE solver with the constant-coefficient given by: $a = k_1 + k_2 = 0.06/\text{ps}$, $b = k_1k_2 = 0.000896/\text{ps}^2$. The measured spectra of each microring and the cascaded ones are illustrated in Fig. 5(c).

The experimental setup is shown in Fig. 5(d). We choose super-Gaussian pulse as the input signal. As for Fig. 5(a), employing port 1 & 2 and port 5 & 6, respectively, Microring 1 and Microring 2 are used as a first-order all-optical ODE solver correspondingly. The measured spectra and the output waveforms are depicted in Figs. 6(a)–(d), along with the theoretical results achieved by ideal filters.

When launching the input signal at port 3, the solution of Eq. (4.4) for $a = k_1 + k_2 = 0.06/\text{ps}$ and $b = k_1k_2 = 0.000896/\text{ps}^2$ can be obtained at port 4 and vice versa. The measured spectrum and output waveform are demonstrated in Figs. 6(e), (f) along with the ideal ones, which confirm the feasibility of using cascaded microrings to solve high order all-optical ODE.

5. ALL-OPTICAL DIFFERENTIAL EQUATION SOLVER WITH CONSTANT-COEFFICIENT TUNABLE

From Section 3, we know that a microring can be a first-order ODE solver. And if we can change the Q value of the microring, we can build a constant-coefficient tunable ODE solver. So we fabricated an electrically tuned add-drop microring as shown in Fig. 7. Figs. 7(a) and (b) show the microscope

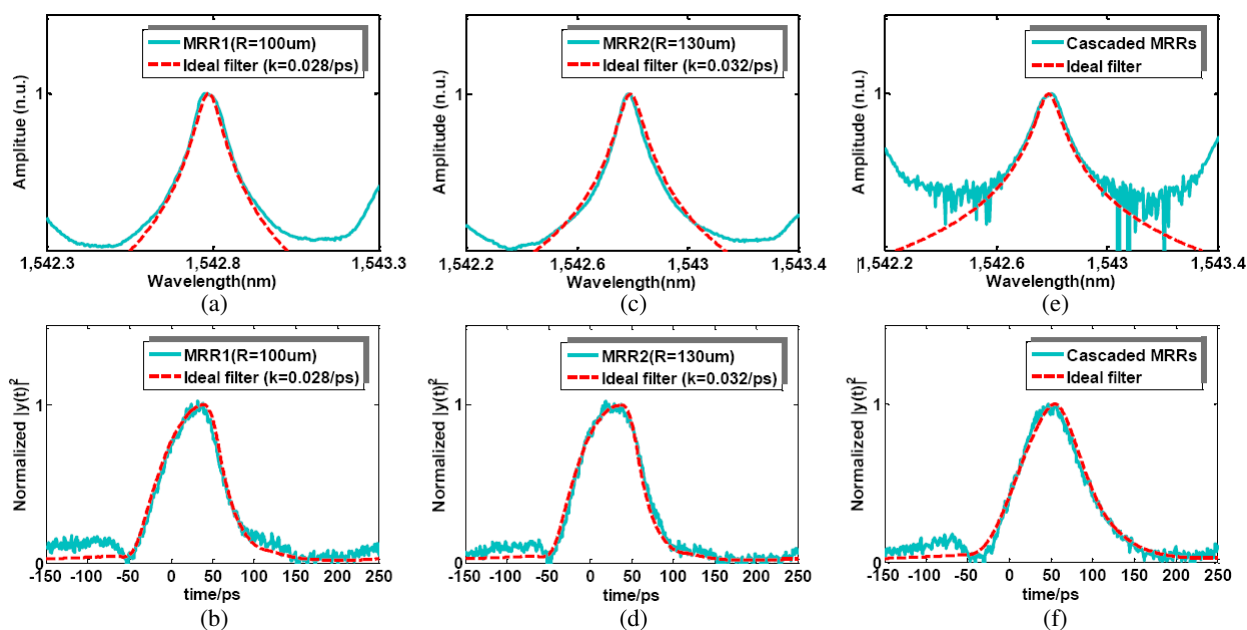


Figure 6: The plots represent both the measured experimental results (turquoise solid line) and the simulated theoretical results (red dotted line) of the spectra and temporal waveforms of the microring-based all-optical ODE solver: spectrum (a) and temporal waveform (b) for microring 1, spectrum (c) and temporal waveform (d) for microring 2, spectrum (e) and temporal waveform (f) for the cascaded microrings.

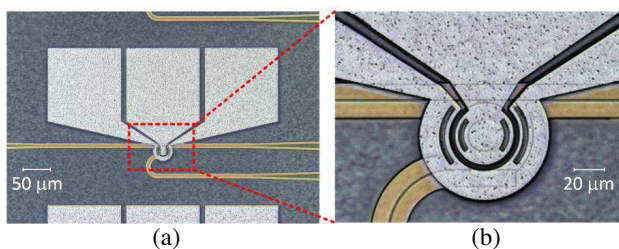


Figure 7: Microring design. (a) Microscope image of the fabricated microring, (b) microscope image of the zoom-in ring region.

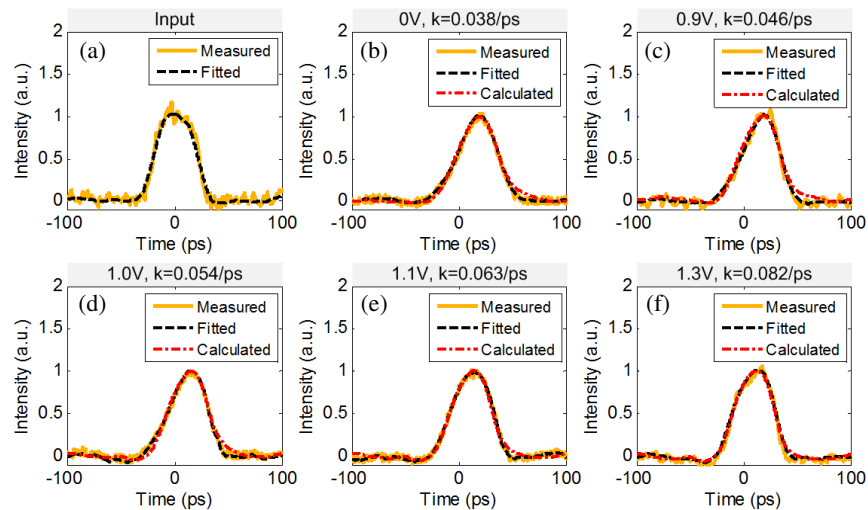


Figure 8: Experimental results for super-Gaussian input, (a) is the input waveform; yellow solid line: measured pulse, black dash line: fitted pulse, (b)–(f) are the outputs with different voltages applied on the MRR; yellow solid line: measured waveforms, black dash line: fitted waveforms and red attunement line: calculated ideal outputs.

images of the fabricated microring and the zoom-in ring region, respectively.

We choose super-Gaussian pulse as the input signal. And when the voltage applied on the microring is 0 V, corresponding to a constant-coefficient of about 0.038/ps, the output waveform (yellow solid line) is depicted in Fig. 8(b), and the calculated waveform (red attunement line) according to the ideal ODE solver is shown for comparison. When we change the voltages to 0.9 V, 1.0 V, 1.1 V and 1.3 V, corresponding to the constant-coefficient of 0.046/ps, 0.054/ps, 0.063/ps and 0.082/ps respectively, the measured output waveforms are depicted in Figs. 8(c)–(f). The fitted dash lines in Fig. 8 represent the smooth processes of measured waveforms.

6. CONCLUSION

Several schemes of ultrafast photonic differentiator and integrator was proposed and experimentally demonstrated in this paper. We demonstrated first-, second-, third-order DIFF, tunable fractional-order DIFF by on-chip MZI and first-, second-order linear ODE solver, first-order linear ODE with different values of constant-coefficient by microring. Our schemes show the advantages of compact footprint, flexible and versatile.

REFERENCES

1. Xu, J., X. L. Zhang, and J. J. Dong, "High speed all-optical differentiator based on cascading semiconductor optical amplifier and optical filter," *Opt. Lett.*, Vol. 32, No. 13, 1872–1874, 2007.
2. Xu, J., X. L. Zhang, J. J. Dong, and D. Huang, "All-optical differentiator based on cross-gain modulation in semiconductor optical amplifier," *Opt. Lett.*, Vol. 32, No. 20, 3029–3031, 2007.
3. Park, Y., M. H. Asghari, and R. Helsten, "Implementation of broadband microwave arbitrary-order time differential operators using a reconfigurable incoherent photonic processor," *IEEE Photonics Journal*, Vol. 2, No. 6, 1040–1050, 2010.
4. Velanas, P., A. Bogris, and A. Argyris, "High-speed all-optical first- and second-order differentiators based on cross-phase modulation in fibers," *Lightwave Technology*, Vol. 26, No. 18, 3269–3276, 2008.
5. Lu, L. Y., J. Y. Wu, and T. Wang, "Compact all-optical differential-equation solver based on silicon microring resonator," *Frontiers of Optoelectronics*, Vol. 5, No. 1, 99–106, 2012.
6. Tan, S. S., Z. Wu and L. Lei, "All-optical computation system for solving differential equations based on optical intensity differentiator," *Optics Express*, Vol. 21, No. 6, 7008–7013, 2013.
7. Slavík, R., Yongwoo Park, and N. Ayotte, "Photonic temporal integrator for all-optical computing," *Opt. Express*, Vol. 16, No. 22, 18202–18214, 2008.
8. Dong, J., A. Zheng, D. Gao, L. Lei, D. Huang, and X. Zhang, "Compact, flexible and versatile photonic differentiator using silicon Mach-Zehnder interferometers," *Opt. Express*, Vol. 21, No. 6, 7014–7024, 2013.

Wireless Millimeter-wave to Lightwave Signal Converters Using Simple Planar Antennas on LiNbO₃ Optical Crystal

Y. N. Wijayanto¹, A. Kanno¹, T. Kawanishi¹, H. Murata², and Y. Okamura²

¹National Institute of Information and Communication Technology, Japan

²Graduate School of Engineering Science, Osaka University, Japan

(Invited Paper)

Abstract— We propose wireless millimeter-wave (MMW) to lightwave (LW) signal converters using a simple planar antenna on LiNbO₃ optical crystal. The LiNbO₃ crystal is bonded with low- k dielectric material as the substrate. The simple planar antenna is formed with a rectangular patch antenna with a gap and inserted between the bonded structure. An optical waveguide are fabricated on the LiNbO₃ crystal and located between the gap. The LiNbO₃ crystal has relatively lower dielectric constant compared with a LiTaO₃ crystal. Larger antenna size can be obtained using the LiNbO₃ crystal. Additionally, an electro-optic coefficient of the LiNbO₃ crystal is larger than the LiTaO₃ crystal. Therefore, conversion efficiency enhancement can be achieved using the propose device.

1. INTRODUCTION

The wireless communication has attracted much interest in past decade, owing to its high mobility [1]. Since mobile devices are developed rapidly and high quality data are required, the wireless communication with high capacity should be developed furthermore. In order to enhance the capacity, the operational frequency of the microwave (MW) bands can be increased to millimeter-wave (MMW) bands. By increasing the operational frequency, the bandwidth becomes large. Now, 60 GHz MMW bands are one candidate for future wireless communication. However, the MMW bands have large transmission loss in the air and metal cables [2].

The large transmission loss in metal cable can be solved using optical fibers, where lightwave (LW) is used for carrying MMW signals. Several short coverage wireless links with pico/femto cells are required for solving large propagation loss of the MMW signal in the air. Therefore, optical fiber links are promising to contribute in the high capacity wireless communication. The important device is a converter from wireless MMW to LW signals [3].

We have studied and developed wireless MW/MMW to LW signal converters using patch antennas embedded with narrow gaps [4, 5]. The antennas were fabricated on an electro-optic (EO) crystal such as LiTaO₃ or LiNbO₃. The prototype devices were successfully fabricated on a LiTaO₃ crystal for MW and MMW bands. The LiTaO₃ crystal has relatively high dielectric constant of about 42. Since the dielectric constant of the LiTaO₃ crystal is high, antenna size and interaction length for MW/MMW-LW signal conversion is relatively small and short, respectively [6]. As a result the conversion efficiency is still low. In order to enhance it, a converter with large antenna size and long interaction length can be obtained using an optical crystal with lower dielectric constant. A LiNbO₃ crystal is promising, which has relative dielectric constant of about 28.

In this paper, we propose a wireless MMW to LW signal converters using a simple planar antenna fabricated on a LiNbO₃ crystal. The LiNbO₃ crystal with a thin thickness is bonded with a low- k dielectric material. The proposed device is composed of a straight optical waveguide and patch antenna with a gap. Large antenna size and long interaction length can be obtained. As a result, the conversion efficiency from wireless MMW to LW signals becomes larger. The proposed device has a simple and compact structure. It can be also operated with no external power supply.

2. DEVICE STRUCTURE

Figure 1 shows the proposed wireless MMW to LW signal converter. It is composed of simple planar antennas inserted between a thin LiNbO₃ crystal and low- k dielectric material. The planar antenna is formed using rectangular patch type. The antenna length, L , is set to a half wavelength of the designed MMW signal. The antenna width, W , is set to below one wavelength of the designed MMW signal to avoid unwanted higher order mode effects. A gap in μm -order, G , is introduced at the center of the patch, along y -axis. A straight optical waveguide is fabricated on the reversed side of the thin LiNbO₃ crystal and precisely aligned at the center of the gap. A ground electrode

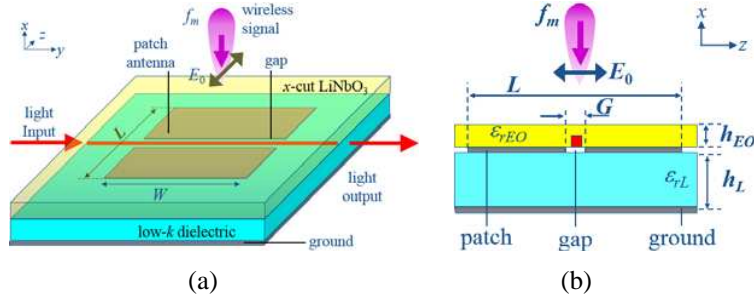


Figure 1: Proposed device structure: (a) whole-structure and (b) cross-section view in the xz -plane.

is covered on the reversed side of the low- k dielectric material. The thin LiNbO₃ crystal, h_{EO} , is required to eliminate the unwanted substrate mode effect in the MMW bands.

When a wireless MMW signal is irradiated to a standard patch antenna with no-gap, a standing-wave current is induced on the patch surface and becomes maximum at the center [7]. Then, a narrow gap is located at the center of the patch perpendicular to the surface current. Since the narrow gap width is used, the antenna characteristic in the proposed device are almost the same with standard patch antenna with no gap. By introducing the gap, a displacement current and strong electric field is induced across the gap for current flow continuity [8]. The strong electric field can be used for optical modulation through the Pockels effect of the LiNbO₃ crystal. A LW propagates into an optical waveguide located at the center of the gap is modulated by the wireless MMW signal. Therefore, wireless MMW signal can be received and converted directly to the LW signal using the proposed device.

Low effective dielectric constant can be achieved using the low- k dielectric substrate bonded with EO crystal. By using a LiNbO₃ crystal, lower effective dielectric constant can be obtained since the LiNbO₃ crystal has relatively low dielectric constant value compared to the LiTaO₃ crystal. Larger antenna size, longer interaction length, larger EO coefficient, and minimize substrate mode can be realized using the proposed device.

3. DEVICE ANALYSIS

An antenna size for receiving a wireless MMW signal can be calculated using the following equation by considering effective dielectric constant of the substrate of ϵ_{eff} ,

$$L = \frac{c}{2f_m \sqrt{\epsilon_{eff}}} \quad (1)$$

where c is the speed of light in vacuum and f_m is an operational frequency of MMW signal. The size of the antenna is inversely proportional to the square-root of the effective dielectric constant. By reducing the effective dielectric constant, the size of the antenna is enlarged. In order to reduce the effective dielectric constant of the substrate for the MMW-LW signal conveter, a new device structure using a thin LiNbO₃ crystal bonded with a low- k dielectric material is adopted as shown in Figure 1.

The effective dielectric constant of the proposed device using a LiNbO₃ bonded with low- k dielectric material is expressed as

$$\epsilon_{eff} = \frac{h_L + h_{EO}}{\left(\frac{h_L}{\epsilon_{rL}} + \frac{h_{EO}}{\epsilon_{rEO}}\right)} \quad (2)$$

where ϵ_{rL} and h_L are the dielectric constant and thickness of the low- k dielectric material, respectively, and ϵ_{rEO} and h_{EO} are the dielectric constant and thickness of the EO crystal, respectively. By using a bonded material structure with a thin EO crystal, the effective dielectric constant becomes low.

Analysis of the proposed device are discussed as follow. When a wireless MMW signal at an operational frequency of f_m is irradiated to the proposed device, the standing-wave MMW current is induced along the patch surface. Displacement current and strong electric field are induced across the gap. The induced electric field across the gap can be expressed as,

$$E(t) = E_0 \cos[2\pi f_m t] \quad (3)$$

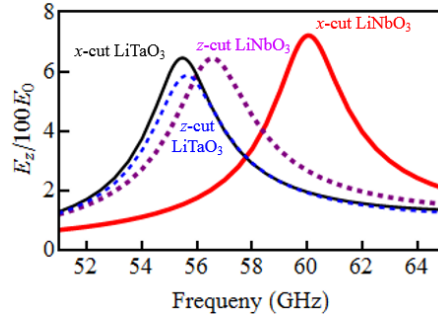


Figure 2: The calculated MMW electric field across the gap for several crystal types.

The induced MMW electric field across the gap can be utilized for optical modulation through the Pockels effect. Therefore, wireless MMW signals can be received and converted directly to LW signals.

The induced electric field across the gap was calculated using electromagnetic software analysis. The optical crystal thickness was set $80\ \mu\text{m}$ and low- k dielectric material thickness was set $130\ \mu\text{m}$ with dielectric constant of 4. The length and width of the patch antenna with aluminum metal were set $0.8\ \text{mm}$. A gap with $5\ \mu\text{m}$ -wide was located at the center of the patch antenna. Ultraviolet adhesive glue as a buffer layer was also inserted between the bonded structures. The calculated electric field across the gap as a function of MMW frequency are shown in Figure 2.

The MMW operational frequency is shifted depends on optical crystal types as shown in Figure 2. The shifted frequency is induced due to change the effective dielectric constant of the proposed device with bonded structure. As we know that the $\text{LiNbO}_3/\text{LiTaO}_3$ crystal are anisotropic crystal with different dielectric constant depends on crystal orientation. The proposed device using x -cut LiNbO_3 crystal has larger induced MMW electric field. Therefore, we expected that the proposed device using x -cut LiNbO_3 crystal has large conversion efficiency.

Since the proposed device is an optical phase modulator, we can take modulation efficiency for optical phase modulation as a measure of the efficiency of MMW-LW signal conversion. It can be calculated by considering the interaction of the MMW and LW electric fields. In order to calculate the modulation index, the transit time effect must be considered since the MMW electric field across the gap changes its phase during the time for the LW propagation. Therefore, the MMW electric field as would be observed by the LW propagating in the optical waveguide can be calculated. The modulation index can be calculated by the integration of the MMW electric field as would be observed by the LW along the gap, which is expressed as,

$$\Delta\phi = \frac{\pi r_{33} n_e^3}{\lambda} \Gamma \int_{\frac{w}{2}}^{\frac{w}{2}} E_0 \cos \left[2\pi f_m \frac{y}{v_g} + \varphi \right] dy \quad (4)$$

where v_g is the group velocity of the LW and φ is the initial phase of the LW, λ is the wavelength of the LW propagating in the optical waveguides, r_{33} is the EO coefficient, n_e is the extraordinary refractive index of the LiNbO_3 crystal, W is the width of the antenna as the interaction length between the MMW and LW signal and Γ is a factor expressing the overlap of the MMW and LW signals.

4. EXPERIMENT

In device fabrication, an optical waveguide was fabricated using the titanium diffusion method on a $500\ \mu\text{m}$ -thick x -cut LiNbO_3 crystal. The antenna with a gap was fabricated using aluminum metal on the LiNbO_3 crystal, where the optical waveguide was set between the gap. On the bottom surface of a low- k dielectric material was covered a ground electrode. For bonding process, an optical adhesive was layered on the top surface of the low- k dielectric material. Then, the LiNbO_3 crystal was flipped over and attached on the low- k dielectric material. Finally, the x -cut LiNbO_3 crystal was polished using diamond slurry to the designed thickness of $80\ \mu\text{m}$ -thick.

The fabricated device was measured experimentally. A MMW was irradiating to the fabricated device and a LW was coupled to the optical waveguide. The LW output was measured by an optical spectrum analyzer. An optical sidebands was obtained clearly as the converted LW signal. The conversion efficiency or modulation efficiency can be obtained by comparing optical powers

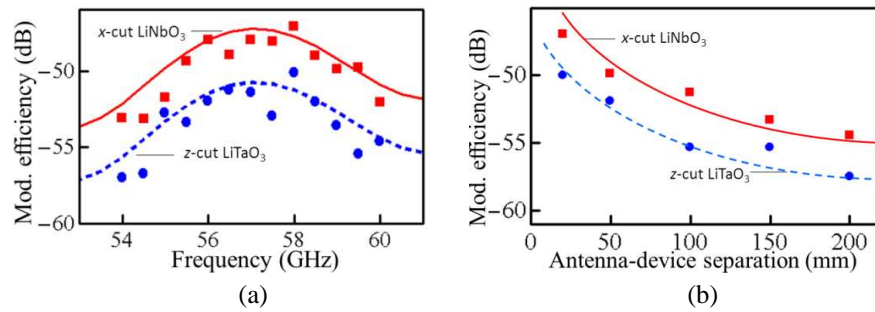


Figure 3: Measured modulation efficiency as functions of (a) MMW operational frequency and (b) separation of the fabricated device and antenna.

between the carrier and sidebands. The modulation efficiency as function of MMW operational frequency and separation between the fabricated device and antenna are shown in Figure 3. The measurement results of the proposed device have good agreements with the calculation results.

Based on the measurement results, the proposed device using the x -cut LiNbO_3 crystal has larger conversion efficiency about 3 dB compared with such device using a z -cut LiTaO_3 crystal. The device using the z -cut LiTaO_3 crystal was reported in detail [5]. Several factors might contribute for the enhancement of the conversion efficiency. First, the LiNbO_3 crystal has relatively larger EO coefficient than the LiTaO_3 crystal. Second, the LiNbO_3 crystal has relatively lower dielectric constant than the LiTaO_3 crystal. Larger antenna size are obtained for improving antenna gain and interaction length. Third, overlapping factor between MMW and LW electric fields might also contribute for conversion efficiency improvement.

5. CONCLUSION

The wireless MMW to LW signal converters using simple planar antennas was proposed. The proposed device was fabricated on a LiNbO_3 crystal bonded with a low- k dielectric material. Large antenna size and long interaction length can be obtained. The proposed device in 60 GHz-bands operational frequency was successfully fabricated and measured experimentally. The fabricated device with an x -cut LiNbO_3 crystal has 3 dB larger conversion efficiency compared with the z -cut LiTaO_3 device. Lower dielectric constant and large EO coefficient of the LiNbO_3 crystal might be contributed to the conversion efficiency enhancement. The conversion efficiency can be enhanced furthermore using low dielectric constant EO polymer with large EO coefficient [9].

ACKNOWLEDGMENT

Authors would like thanks to Dr. H. Shiomi and Dr. K. Kitatani from Osaka University Japan for their constructive comments in discussion and kind supports in experiment.

Y. N. Wijayanto, A. Kanno, and T. Kawanishi would like thank to the Ministry of Internal Affairs and Communications, Japan, for the financial support partly thru the project entitled “Research and Development of high-precision imaging technology using 90 GHz band linear cells” funded by the “Research and Development to Expand Radio Frequency Resources”.

REFERENCES

1. Pi, Z. and F. Khan, “An introduction to millimeter-wave mobile broadband systems,” *IEEE Communications Magazine*, Vol. 49, No. 6, 101–107, Jun. 2011.
2. Shi, J.-W., C.-B. Huang, and C.-L. Pan, “Millimeter-wave photonic wireless links for very high data rate communication,” *NPG Asia Materials*, Vol. 3, 41–48, 2011.
3. Chen, A. and E. Murphy, *Broadband Optical Modulators: Science, Technology, and Applications*, CRC Press, Taylor and Francis Group, North West, 2012.
4. Wijayanto, Y. N., H. Murata, and Y. Okamura, “Wireless microwave-optical signal conversion in quasi-phase-matching electro-optic modulators using gap-embedded patch-antennas,” *IEICE Transaction on Electronics*, Vol. E96-C, No. 2, 212–219, 2013.
5. Wijayanto, Y. N., H. Murata, and Y. Okamura, “Electro-optic millimeter-wave-lightwave signal converters suspended to gap-embedded patch antennas on low- k dielectric materials,” *IEEE Journal of Selected Topics in Quantum Electronics*, Vol. 19, No. 6, Nov./Dec. 2013.

6. Gupta, V. R. and N. Gupta, “Characteristics of a compact microstrip antenna,” *Microwave and Optical Technology Letters*, Vol. 40, No. 2, 158–160, 2004.
7. Lee, K. F. and K. M. Luk, *Microstrip Patch Antennas*, Imperial College Press, London, 2011.
8. Gupta, K. C., R. Garg, and I. Bahl, *Microstrip Lines and Slotlines*, Artech House, Inc., Norwood, 2001.
9. Zhang, X., B. Lee, C. Lin, A. X. Wang, A. Hosseini, and R. T. Chen, “Highly linear, broadband optical modulator based on electro-optic polymer,” *IEEE Photonics Journal*, Vol. 4, No. 6, 2214–2228, 2012.

Self-assembled Low Density Quantum Dot and Quantum Dot-in-nanowire Structures for Quantum Photonics

Guo-Wei Zha^{1,2}, Zhi-Chuan Niu^{1,2}, Ying Yu^{1,2}, Xiang-Jun Shang^{1,2},
Jian-Xing Xu^{1,2}, Si-Hang Wei^{1,2}, Li-Juan Wang^{1,2}, and Hai-Qiao Ni^{1,2}

¹State Key Laboratory of Superlattices and Microstructures
Institute of Semiconductors, Chinese Academy of Sciences, Beijing 100083, China

²Synergetic Innovation Center of Quantum Information and Quantum Physics
University of Science and Technology of China, Hefei, Anhui 230026, China

(Invited Paper)

Abstract— Self-assembled III-V quantum dots (QDs) are of particular attractive as solid quantum light emitters owing to their stability, narrow spectral linewidth, and short radiative lifetime. Meanwhile, semiconductor nanowires (NWs) have appeared as promising building blocks for future nanoscale electronic and photonic devices owing to their high crystalline quality and integration possibilities. To fully explore the potential of NW systems, many investigators have turned to the synthesis of artificial nanostructures in NW systems, such as quantum dots (QDs) and nanoclusters, to generate fascinating multifunctional properties. Single nanostructures embedded within NWs represent one of the most promising technologies for applications in quantum photonics. With NWs, a nanostructure can be constructed by inserting a slice of lower gap semiconductor along the growth direction such as CdSe/ZnSe, In(Ga)As/GaAs, GaAsP/GaAs, InAsP/InP and GaAs/AlGaAs systems, or via self-assembled epitaxy on the faceted NWs in the radial direction, utilizing the different surface energies, partly originating from different crystal lattices of hybrid materials, as a driving force. Herein, we report our latest work on self-assembled low density quantum dot and quantum dot-in-nanowire structures for quantum photonics, which might pave the way for the fabrication of highly efficient single-photon sources (SPSs) and novel quantum optics experiments.

NWs samples were grown on GaAs (001) substrates sputtered with 20 nm silicon dioxide or Si (111) with native thin silicon dioxide by a Veeco Mod Gen-II Molecular Beam Epitaxy (MBE) system in traditional VLS growth mode [1–4]. The substrates were dipped for 2 s by 10% HF aqueous solution, and degased at 620°C for 10 min prior to growth. Growth was initiated by the condensation of a nominal 1 nm Ga in the nanocraters of the SiO₂ layer. The GaAs backbones were grown at 560–600°C and an As₂/Ga flux ratio of 12.5–20. After depositing the GaAs backbones, the samples were exposed to a high As₂ ambient overpressure to consume their remaining gallium droplets on the top for preferential facet deposition. Self-assembled low density quantum dots were sandwiched between the GaAs core and GaAs/AlGaAs shell and coupled into the fundamental photonic mode of the hexagonal nanowire cavity.

During the epitaxial growth on the facet of NWs backbones, a strain-driven nucleation [1] of gallium-droplets (Figure 1) leads to formation of GaAs branches [2]. Particularly for the InAs QDs embedded branched NWs, the branches were found to preferentially nucleate on the very site of quantum dot as verified by STEM energy dispersive X-ray spectroscopy (EDS) line and spot scans as shown in Figure 2. Micro-PL spectra were measured at 77 K using a continuous wave He-Ne laser for above-band excitation, which is focused on a single NW with the help of white light imaging. An enhancement of ~ 20 times with single InAs QD signals from the branched NWs in comparison to those from the straight ones is observed (Figure 3). We attribute it to the combination of quantum confinement effect and QD-cavity interaction. For the higher band offset given by surrounding AlGaAs/GaAs thin film barriers, InAs QD exhibits a stronger confinement of excitons; while the branch helps light gathering together to the top and decreases the optical losses effectively due to its relatively large diameter, which is in consistent with numerical FDTD simulation. Sharp excitonic emission is observed at 4.2 K with a line width of 101 μeV and a vanishing two-photon emission probability of $g^2(0) = 0.031(2)$ (Figure 4). The branched GaAs nanowires turn out to be a better cavity to enhance the extraction efficiency of single InAs QDs emission.

As the most commonly used detectors in single photon characterization, silicon avalanche photodiodes present the best detection efficiency at ~ 700–800 nm. To accommodate this detecting

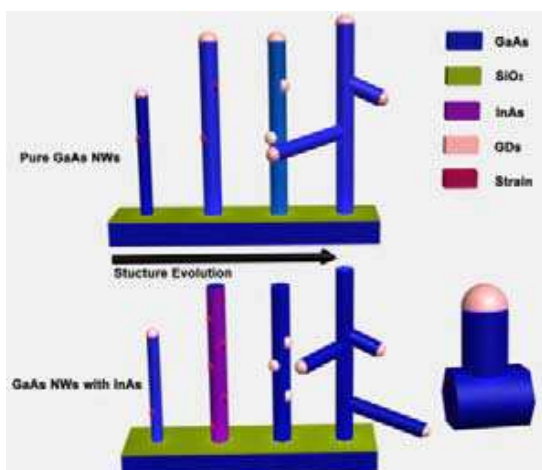


Figure 1: A schematic illustration of evolution mechanism for branched NWs.

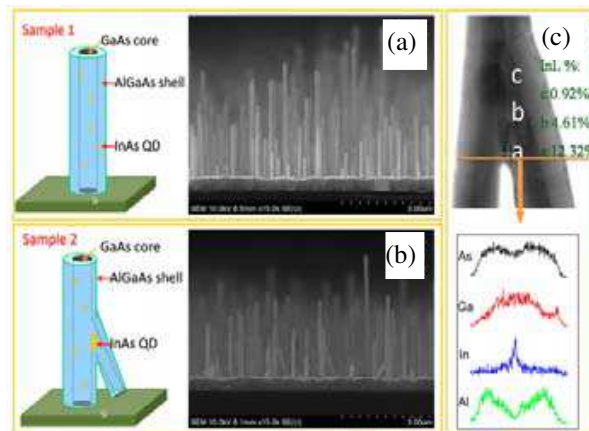


Figure 2: Typical SEM side-view images of both straight and branched NWs, (c) is the corresponding EDS measurement of branched NWs.

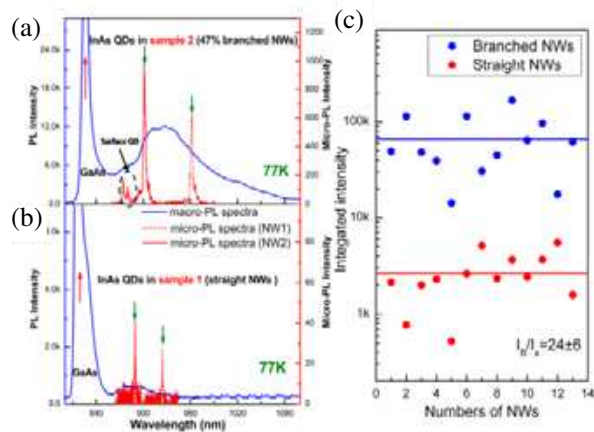


Figure 3: μ PL spectra measured at 77 K for both branched and straight NWs.

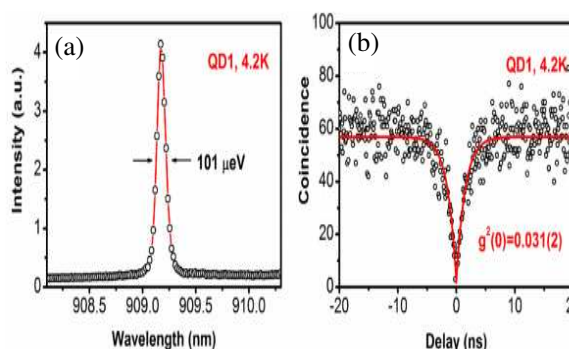


Figure 4: μ PL spectra and HBT measurements of a typical InAs QD measured at 4.2 K, respectively.

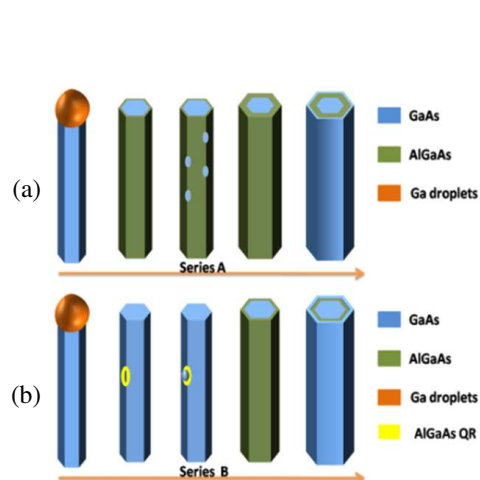


Figure 5: Schematics of the multiple-step fabrication process of GaAs QD-in-NWs.

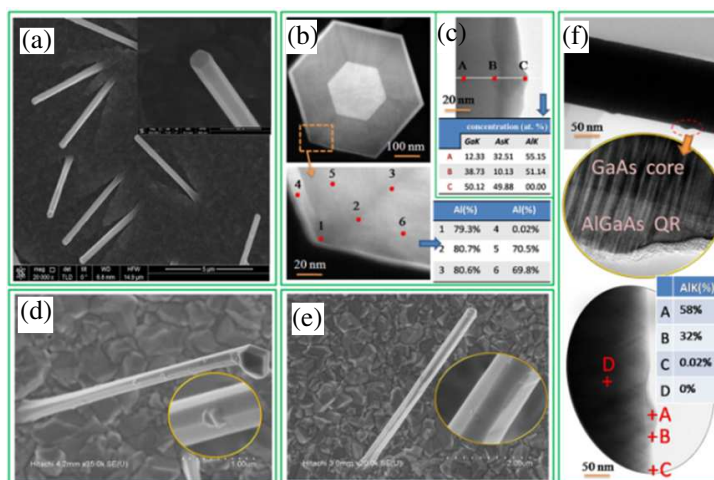


Figure 6: Typical SEM side-view and cross-section images of uncapped NWs, EDS analysis is given for the AlGaAs QR as shown in (d)–(f).

window and get the best resolved SPSs, we first present a promising self-assembled GaAs QD-in-NW [3] system as growth by the multiple-step process schematized in Figure 5. The structure consists of a GaAs core, which functions as the primary part of the optical cavity, and low density GaAs QDs sandwiched in two $\text{Al}_{0.7}\text{Ga}_{0.3}\text{As}$ barrier layers, which serves as single photon emission source. In addition, single separated GaAs QD can be achieved by using single $\text{Al}_{0.58}\text{Ga}_{0.42}\text{As}$ quantum ring (QR) on the facet of NWs as bottom surrounding barrier and $\text{Al}_{0.7}\text{Ga}_{0.3}\text{As}$ as

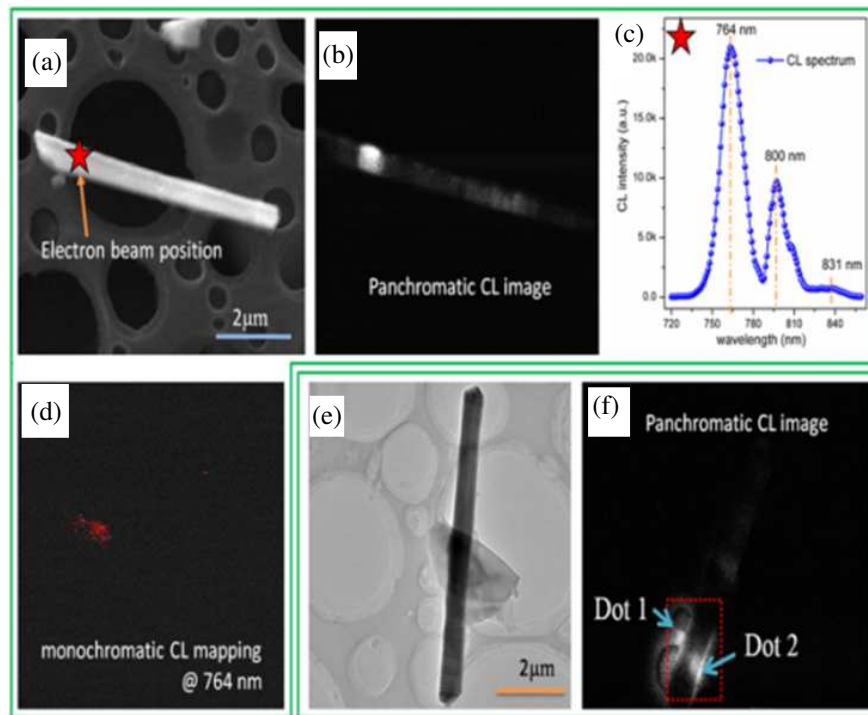


Figure 7: Cathodoluminescence of a single NW.

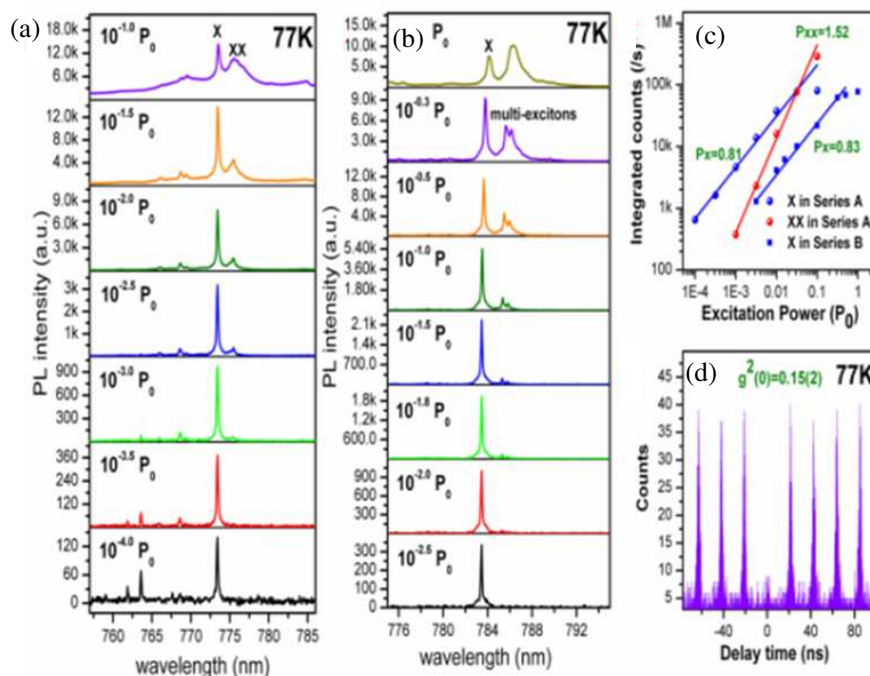


Figure 8: The excitation power dependent micro-photoluminescence spectra and HBT measurements of a typical GaAs QD.

top barrier. Cathodoluminescence measurements at 77 K (Figure 7) demonstrate spatially discrete spots ranging from 700 to 800 nm along the axial direction, indicative of the discrete distributed GaAs QDs. Sharp and enhanced excitonic emission is observed at liquid nitrogen temperature (77 K) with a emission rate of 8 MHz and a two-photon emission probability of $g_2(0) = 0.15(2)$ as shown in Figure 8. The smallest linewidth observed so far is $177 \mu\text{eV}$ while most QDs showing linewidths of sub- $200 \mu\text{eV}$, and the estimated count rate demonstrates an unprecedented bright SPS even at liquid nitrogen temperature.

As mentioned previously, self-assembly bottom-up approaches cannot avoid the difficulties of its stochastic nature and suffer the random position and density. We adopted a modified droplet-epitaxy for the self-assembly of nanostructure-decorated NWs, based on strain-driven, transport-dependent nucleation of gallium droplets at high temperature (Figure 9). By tuning the deposition temperature, arsenic overpressure and amount of gallium-droplets, we were able to control the density and morphology of the structure, yielding novel single quantum dots, QR, coupled QRs, and nano-antidots (Figure 10). We achieved a single-QR-in-NW structure as shown in Figure 11. The outer and inner side lengths of the QR are about 80–120 and 35–60 nm respectively, with heights of about 3–12 nm. The optical properties were analyzed using micro-photoluminescence

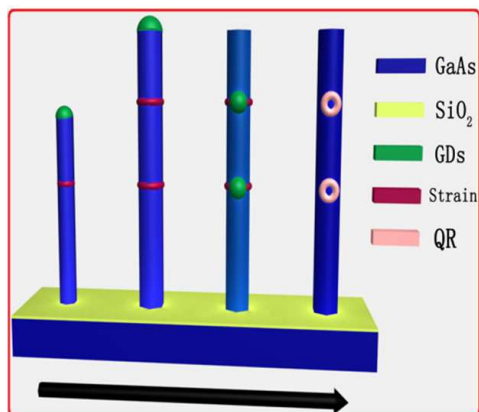


Figure 9: Schematic of the fabrication of the QR-decorated nanowires.

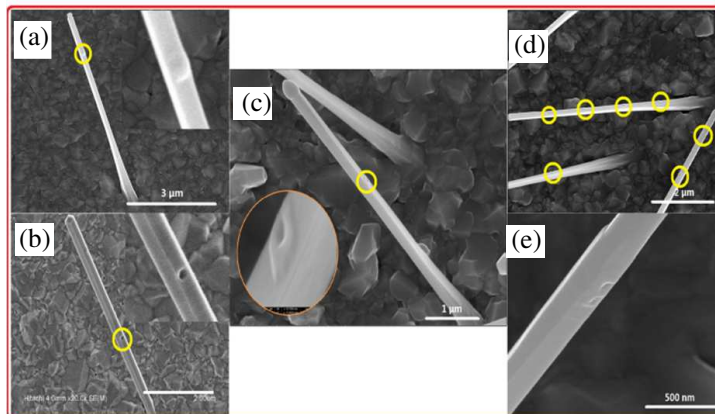


Figure 10: Representative SEM images of the obtained nanostructure-decorated nanowires.

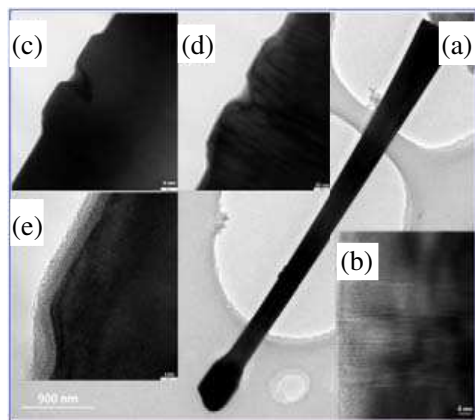


Figure 11: TEM image of a QR-decorated NW over its entire length.

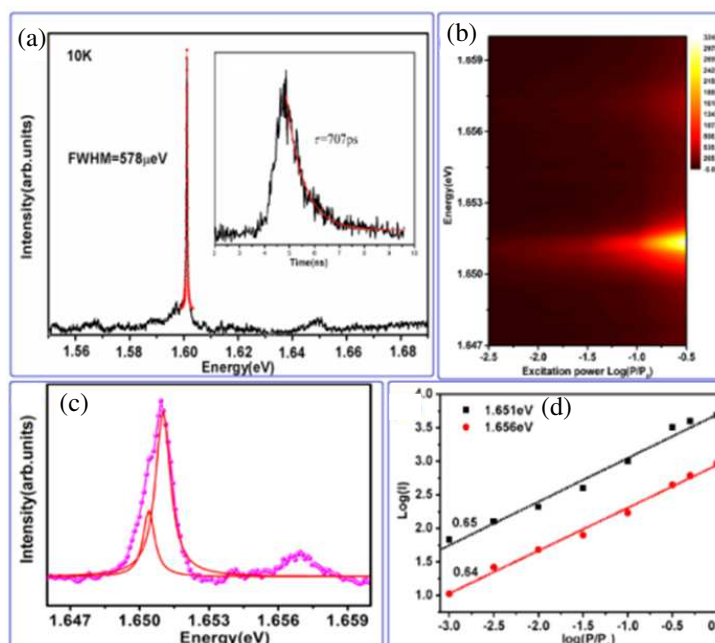


Figure 12: μPL spectroscopy for the single-QR-in-NW samples.

at 10 K (Figure 12) and the spectra show sharp discrete peaks; of these peaks, the narrowest linewidth (separation) was $578 \mu\text{eV}$ ($1\text{--}3 \text{meV}$), reflecting the quantized nature of the ring-type electronic states. This novel strain-driven formation mechanism can be extended to fascinatingly precisely controlling the site of nanostructures on the sidewalls of NWs, if the strain is intentionally introduced at certain sites (Figure 9), on the basis of structural phase control of NWs.

In conclusion, we have demonstrated a detailed investigation on the morphology and optical properties of self-assembled nanostructures decorated nanowires in different material systems and synthesis methods. These new nanostructures may open a new avenue to the fabrication of highly efficient single-photon sources, novel quantum optics experiments, as well as designing robust quantum optoelectronic devices operating at higher temperature required for practical applications.

REFERENCES

1. Zha, G., M. Li, Y. Yu, L. Wang, J. Xu, X. Shang, H. Ni, and Z. Niu, *Applied Physics Letters*, Vol. 102, 163115, 2013.
2. Yu, Y., M. F. Li, J. F. He, Y. M. He, Y. J. Wei, Y. He, G. W. Zha, X. J. Shang, J. Wang, L. J. Wang, G. W. Wang, H. Q. Ni, C. Y. Lu, and Z. C. Niu, *Nano Lett.*, Vol. 13, 1399–1404, 2013.
3. Yu, Y., X.-M. Dou, B. Wei, G.-W. Zha, X.-J. Shang, L. Wang, D. Su, J.-X. Xu, H.-Y. Wang, H.-Q. Ni, B.-Q. Sun, Y. Ji, X.-D. Han, and Z.-C. Niu, *Adv. Mater.*, 2014, DOI: 10.1002/adma.201304501.
4. Zha, G., X. Shang, D. Su, Y. Yu, B. Wei, L. Wang, M. Li, L. Wang, J. Xu, H. Ni, Y. Ji, B. Sun, and A. Z. Niu, *Nanoscale*, Vol. 6, 3190–3196, 2014.

Ultracompact On-chip Long-wave Photodetector Based on Hybrid Plasmonic Waveguides

Hao Wu, Xiaowei Guan, and Daoxin Dai

State Key Laboratory for Modern Optical Instrumentation
Centre for Optical and Electromagnetic Research
Zhejiang Provincial Key Laboratory for Sensing Technologies
Zhejiang University, Zijingang Campus, Hangzhou 310058, China

Abstract— An ultra-small on-chip long-wave photodetector by utilizing the thermal resistance effect of the metal strip on a hybrid plasmonic waveguide structure. When light propagates along a hybrid plasmonic waveguide, the metal strip is heated due to the light absorption. Accordingly, the resistance of the metal strip increases due to the thermal-resistance effect of metal and the resistance change can be measured accurately with a Wheatstone bridge so that the photodetector is with very high sensitivity. Owing to the nano-scale confinement of light in a hybrid plasmonic waveguide, the temperature increase of metal due to the metal absorption is enhanced in comparison with the conventional long-range plasmonic waveguide. A theoretical responsivity of as high as 74 mV/mW is obtained with a low bias voltage of 1 V. The photodetector also has a fast response ($< 1 \mu\text{s}$) and works in a very broad wavelength range (e.g., $1.5 \sim 7.5 \mu\text{m}$).

1. INTRODUCTION

Photodetection plays an important role in many applications, including optical interconnects [1] and optical sensing [2]. Particularly, photodetectors for long-wave (e.g., mid-infrared wavelength) are becoming increasingly attractive, regarding the significant applications of long-wave in temperature measurement, environment monitoring, human health, etc. [3–5]. Long-wave photodetector can be realized by utilizing the photo-electric effect of semiconductor materials [6]. However, the operation wavelength range of a photodetector based on the photo-electric effect is limited by the bandgap of the semiconductor [6, 7]. Although a mid-IR photodetector based on the quantum effect has a high responsivity, it has to be operated at a very low temperature ($< 100 \text{ K}$) [6–8] so that the thermal noise is depressed.

In recent years, silicon photonics for long-wave applications has been attracting lots of attention due to the great potentials in on-chip biochemical detections and environment monitoring [9]. Nevertheless, long-wave photodetection on silicon is still a big challenge since silicon is transparent for the wavelength larger than $1.1 \mu\text{m}$ [10]. To develop long-wave photodetectors on silicon, germanium has been utilized as the active material due to its favorable absorption coefficient [11–15]. However, the operation wavelength is still concentrated on the communication band around 1310 nm and 1550 nm. Furthermore, it is not easy to grow another semiconductor film with high quality on silicon due to the large lattice mismatch between them [16].

Long-wave photodetector can also be achieved based on the photo-thermal effect. When light is absorbed, the temperature will increase and the temperature variation can be measured with various techniques. For example, the resistance of a metal strip changes as the temperature increases according to the thermal resistance effect while the resistance can be measured in an electrical way. An integrated power monitor with a long-range surface plasmonic waveguide on silicon was reported [17], and the responsivity is about 0.15 mV/mW with an active length as long as 1 mm.

In this paper, we propose a long-wave photodetector with a silicon hybrid plasmonic waveguide (HPW), which consists of a metal strip, a silicon core and a sandwiched silica nano-layer [18]. The silicon HPW is with a nanoscale light confinement. The ultrasmall volume of the proposed photodetector helps improve the responsivity significantly. Furthermore, the silica nano-layer in such a structure also plays an important role as a thermal insulator, which can prevent the heat convection from the metal strip to the silicon region. In this way, heat generated due to the metal absorption is confined well in the metal region and consequently the responsivity is improved further. For example, the theoretical responsivity of the proposed photodetector with a footprint of $10 \mu\text{m} \times 300 \text{ nm}$ is as high as 74 mV/mW.

2. STRUCTURE AND DESIGN

Figure 1(a) shows the three-dimensional view of the proposed photodetector based on a silicon HPW, whose cross-section is illustrated by the inset. The silicon HPW consists of a metal strip,

a silicon core and a silica nanolayer sandwiched between them. The thickness of the silica layer is usually tens of nanometers to have a nanoscale light confinement. When light propagates in the silicon HPW, heat is generated due to the light absorption in the metal strip. As an example, a silicon-on-insulator (SOI) wafer with 340 nm-thick top-silicon is chosen. The SOI wafer is oxidized to produce a 20 nm-thick silica layer (i.e., 4 nm-thick silicon sacrificed), which not only helps to confine light tightly but also prevent the heat flow from the metal region to the silicon core. The waveguide width is chosen as $w = 300$ nm and a 20 nm-thick metal strip is covered on top of the waveguide. Here copper is chosen as the metal due to the COMS compatibility and high stability.

Figure 1(b) show the calculated field distribution of the silicon hybrid plasmonic waveguide in the proposed photodetector by using a finite-element method (FEM) mode solver. It can be seen that light is confined strongly in the silica nano-layer. Fig. 1(c) shows the calculated temperature profile of the silicon HPW when a power is applied in the metal strip. One sees that the metal strip has a peak temperature, which is attributed to the thermal isolation of the silica layer. In the present case, the applied power is actually the heat generated from light absorption. Since the resistivity of the metal is temperature dependent, one can figure out the temperature change by measuring the variation of the metal resistance by utilizing an electrical way with, e.g., the Wheatstone bridge circuit.

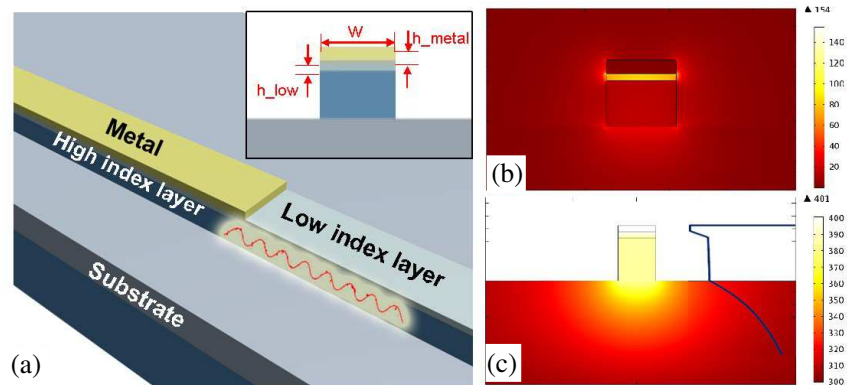


Figure 1: (a) The configuration of the proposed photodetector based on a silicon hybrid plasmonic waveguide (HPW). Inset shows the cross-section of the silicon HPW. (b) Field distribution of the silicon HPW with $w = 300$ nm @ $\lambda = 3.39$ μm . (c) The temperature distribution of the silicon HPW when 1 mW power is applied in the metal strip.

3. RESULT AND ANALYSIS

It is well known that both the light absorption [18] and the thermal response [19] of a hybrid plasmonic waveguide are dependent on the waveguide size. Since light is well confined in the low-index nanolayer, we focus on the dependence of the light absorption and the thermal response on the thickness of metal and the silica nanolayer, as well as the width of the waveguide.

Figure 2(a) show the maximum of the calculated temperature in the metal strip as the input power varies. Here the metal thickness $h_{\text{metal}} = 0.02$ μm , the silica-nanolayer thickness $h_{\text{low}} = 0.02$ μm , and the waveguide width $w = 0.3$ μm . With the optimized structure, the theoretical responsivity is as high as 91 K/mW. Fig. 2(b) shows the calculated temporal response and the rise time and the decay time are as short as 0.95 μs .

Figure 3 shows the wavelength dependence of the calculated propagation length and the 90% absorption length of the photodetector. It can be seen that the 90% absorption length of the photodetector is shorter than 10 μm in the wavelength range of [1.5, 7.5] μm , which indicates a ultracompact footprint of the photodetector. The operation can be broadened by choosing a longer absorption length.

In order to readout the temperature increase resulting from the input light, an electric circuit with the Wheatstone bridge is achieve an accurate measurement for the resistant change. Considering the calculated thermal responsivity 91 K/mW mentioned above, the responsivity of the Wheatstone bridge circuit is as high as 148 mV/mW for a bias voltage of 2 V, which is 1000 times larger than that reported in the previous work [17]. The dynamic range is about 6.5 mW due to the electrical current heating. The sensitivity, mainly limited by thermal fluctuation, is estimated as

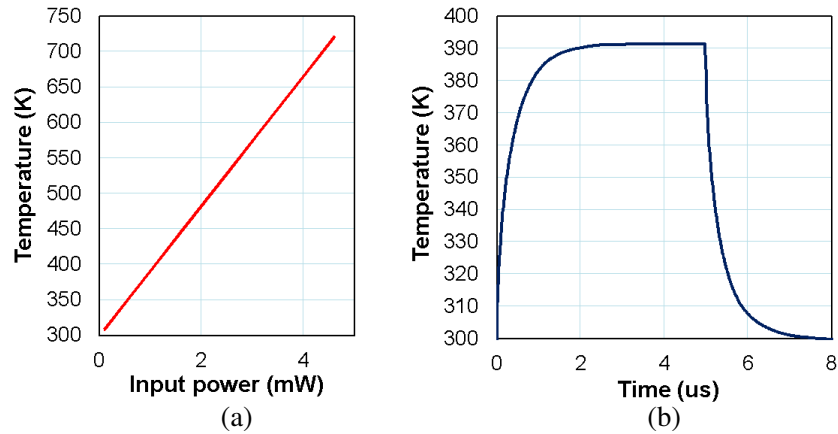


Figure 2: (a) The maximal temperature in the metal strip as the input power varies. Here, $h_{metal} = 0.02 \mu\text{m}$, $h_{low} = 0.02 \mu\text{m}$ and $w = 0.3 \mu\text{m}$. (b) The temporal response of the temperature of the metal strip with an applied power 1 mW.

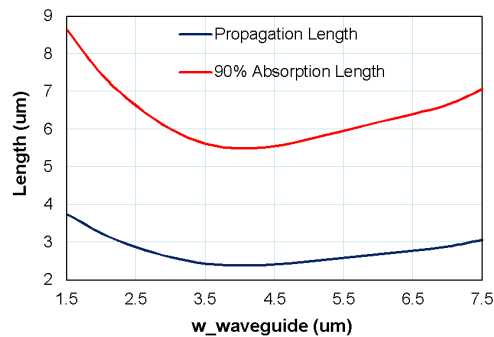


Figure 3: The wavelength dependence of the propagation length and the 90% absorption length. Here $h_{metal} = 0.02 \mu\text{m}$, $h_{low} = 0.02 \mu\text{m}$ and $w = 0.3 \mu\text{m}$.

low as 0.5 nW for a bias voltage of 1 V, which is four order of magnitudes smaller than the previous work [17].

4. CONCLUSION

In this paper, an ultra-small on-chip long-wave photodetector is proposed by utilizing thermal resistance effect of the metal strip on a hybrid plasmonic waveguide, which consists of a metal strip, a silicon core and a sandwiched low-index nanolayer. The metal strip is heated due to the light absorption and the resistance of the metal strip increases. An electric circuit with a Wheatstone bridge is used to measure the resistance change accurately so that the photodetector is with very high sensitivity. The designed long-wave photodetector has a theoretical responsivity of as high as 74 mV/mW when operating at 1 V. This photodetector also enables a sub- μs response due to a compact volume (e.g., 10 μm). Moreover, the present on-chip photodetector is available for an ultra-broad wavelength range (from 1.5 μm to 7.5 μm), which makes it useful for many optical sensing systems.

ACKNOWLEDGMENT

This project was partially supported by a 863 project (No. 2012AA012201), the Nature Science Foundation of China (No. 11374263), Zhejiang provincial grant (Z201121938), the Doctoral Fund of Ministry of Education of China (No. 20120101110094).

REFERENCES

1. Plant, D. V. and A. G. Kirk, "Optical interconnects at the chip and board level: Challenges and solutions," *Proceedings of the IEEE*, Vol. 88, No. 6, 806–818, 2000.

2. Luan, L., R. D. Evans, N. M. Jokerst, and R. B. Fair, “Integrated optical sensor in a digital microfluidic platform,” *IEEE Sensors Journal*, Vol. 8, No. 5, 628–635, 2008.
3. Godard, A., “Infrared (2–12 μm) solid-state laser sources: A review,” *Comptes Rendus Physique*, Vol. 8, No. 10, 1100–1128, 2007.
4. Werle, P., F. Slemr, K. Maurer, R. Kormann, R. Mücke, and B. J Nker, “Near- and mid-infrared laser-optical sensors for gas analysis,” *Opt. Laser Eng.*, Vol. 37, No. 2, 101–114, 2002.
5. Waynant, R. W., I. K. Ilev, and I. Gannot, “Mid-infrared laser applications in medicine and biology,” *Philosophical Transactions of the Royal Society A: Mathematical, Physical and Engineering Sciences*, Vol. 359, No. 1780, 635–644, 2001.
6. Rogalski, A., “Assessment of HgCdTe photodiodes and quantum well infrared photoconductors for long wavelength focal plane arrays,” *Infrared Physics and Technology*, Vol. 40, No. 4, 279–294, 1999.
7. Levine, B. F., “Quantum-well infrared photodetectors,” *J. Appl. Phys.*, Vol. 74, No. 8, R1–R81, 1993.
8. Phillips, J., “Evaluation of the fundamental properties of quantum dot infrared detectors,” *J. Appl. Phys.*, Vol. 91, No. 7, 4590, 2002.
9. Liu, X., R. M. Osgood, Y. A. Vlasov, and W. M. J. Green, “Mid-infrared optical parametric amplifier using silicon nanophotonic waveguides,” *Nature Photonics*, Vol. 4, No. 8, 557–560, 2010.
10. Edward, D. P. and I. Palik, *Handbook of Optical Constants of Solids*, Academic Press, Orlando, 1985.
11. Assefa, S., F. Xia, S. W. Bedell, Y. Zhang, T. Topuria, and P. M. Ü. Ä. Rice, “CMOS-integrated 40 GHz germanium waveguide photodetector for on-chip optical interconnects,” *Conference on Optical Fiber Communication*, 1–3, San Diego, California United States, Mar. 2009.
12. Ahn, D., C. Y. Hong, J. Liu, W. Giziewicz, M. Beals, L. C. Kimerling, J. Michel, J. Chen, and F. X. Kartner, “High performance, waveguide integrated Ge photodetectors,” *Opt. Express*, Vol. 15, No. 7, 3916–3921, 2007.
13. Assefa, S., F. Xia, and Y. A. Vlasov, “Reinventing germanium avalanche photodetector for nanophotonic on-chip optical interconnects,” *Nature*, Vol. 464, No. 7285, 80–84, 2010.
14. Luryi, S., T. P. Pearsall, H. Temkin, and J. C. Bean, “Waveguide infrared photodetectors on a silicon chip,” *IEEE Lectr. Device L.*, Vol. 7, No. 2, 104–107, 1986.
15. Chen, L. and M. Lipson, “Ultra-low capacitance and high speed germanium photodetectors on silicon,” *Opt. Express*, Vol. 17, No. 10, 7901–7906, 2009.
16. Luan, H., D. R. Lim, K. K. Lee, K. M. Chen, J. G. Sandland, K. Wada, and L. C. Kimerling, “High-quality Ge epilayers on Si with low threading-dislocation densities,” *Appl. Phys. Lett.*, Vol. 75, No. 19, 2909, 1999.
17. Bozhevolnyi, S. I., T. Nikolajsen, and K. Leosson, “Integrated power monitor for long-range surface plasmon polaritons,” *Opt. Commun.*, Vol. 255, Nos. 1–3, 51–56, 2005.
18. Dai, D. and S. He, “A silicon-based hybrid plasmonic waveguide with a metal cap for a nano-scale light confinement,” *Opt. Express*, Vol. 17, No. 19, 16646–16653, 2009.
19. Yang, L., D. Dai, and S. He, “Thermal analysis for a photonic Si ridge wire with a submicron metal heater,” *Opt. Commun.*, Vol. 281, No. 9, 2467–2471, 2008.

Four-wave Mixing Response of a Graphene Layer Covered on a Tapered Fiber

Jiamei Lu, Qiang Jin, Xibin Li, Qiang Yan, Qianyu Gao, and Shiming Gao

Centre for Optical and Electromagnetic Research
State Key Laboratory of Modern Optical Instrumentation
Zhejiang University, Hangzhou 310058, China

Abstract— The nonlinear optical response of four-wave mixing (FWM) in a graphene layer covered on a tapered fiber is numerically investigated. The required graphene length is optimized to realize the maximum conversion efficiency, which is both affected by the incident power and propagation loss. Analysis shows that the graphene length is very short due to the heavy absorption in graphene, and the structure exhibits ultrabroad bandwidth. A conversion bandwidth of more than 300 nm is achieved with a conversion efficiency of more than -30 dB in a wide wavelength range of 0.8–1.8 μm .

1. INTRODUCTION

Nonlinear optical materials are always expected to be of smaller size and higher nonlinear coefficient. Graphene, which is of a single atomic layer thickness and whose nonlinear coefficient is five orders higher than silicon [1], has the potential to be an ideal ultra-compact nonlinear material. Recent experiments have observed higher harmonics generation [2], nonlinear self-focusing [3], and four-wave mixing (FWM) [4, 5] phenomena in graphene. Since graphene is a very thin film, it is reasonable to be composed with other materials or devices, such as tapered fibers, to extend the interaction length with the optical field. When a graphene layer is covered on a tapered fiber, a large portion of light propagates outside the fiber via evanescent field if the core radius is small enough. Such a structure is expected to extend the interaction distance and enhance the nonlinear effect. Gorbach et al has tried to analyze the nonlinear property and loss in a graphene-clad tapered fiber [6], but the four-wave mixing response in such a structure is not studied yet. In this paper, we theoretically analyze the FWM effect in a graphene layer covered on a tapered fiber, whose structure is shown in Fig. 1. The structure length is optimized to obtain maximum conversion efficiency at different wavelengths. The bandwidth property is analyzed at a fixed waveguide length. At last, the nonlinear response of the graphene layer on a tapered fiber is compared to that of a pure tapered fiber.

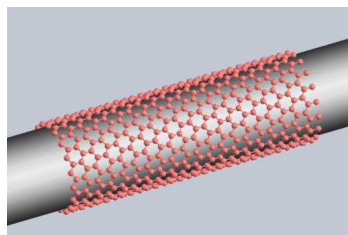


Figure 1: Schematic description of a graphene layer covered on a tapered fiber.

2. THEORETICAL ANALYSIS

When a pump ω_P and a signal ω_S are injected into a graphene layer covered on a tapered fiber, the total field is expressed as

$$E = \frac{1}{2} \sum_{j=P,S,I} E_j \exp[i(\beta_j z - \omega_j t)] + c \cdot c. \quad (1)$$

For the FWM process to generate the idler ω_I ($\omega_I = 2\omega_P - \omega_S$), the nonlinear response is

$$D(\omega_I) = \varepsilon_0 \varepsilon E(\omega_I) + \varepsilon_0 \chi^{(3)} : E(\omega_P) E^*(\omega_P) E(\omega_S) \quad (2)$$

where ε is the relative permittivity and $\chi^{(3)}$ is the third-order susceptibility tensor, which corresponds to graphene or silica for different locations on the transverse cross section. For the graphene layer, the relative permittivity ε ($= \varepsilon_g$) can be obtained from its dynamical conductivity using Kubo formula $\sigma_g = \sigma_{inter} + \sigma_{intra}$ [7], where the interband and intraband contributions are

$$\sigma_{intra}(\omega) = \frac{je^2\mu}{\pi\hbar^2(\omega + j\tau^{-1})} \quad (3)$$

$$\sigma_{inter}(\omega) = \frac{je^2}{4\pi\hbar} \ln \left(\frac{2|\mu| - (\omega + j\tau^{-1})\hbar}{2|\mu| + (\omega + j\tau^{-1})\hbar} \right) \quad (4)$$

where μ is chemical potential and τ is the relaxation time. Supposing that the thickness of graphene layer is Δ , one can obtain the relative permittivity:

$$\varepsilon_g \equiv \frac{i\sigma_g}{\varepsilon_0\omega\Delta} + 1 \quad (5)$$

According to the permittivity distribution of the composited structure, one can get the mode field distribution and the effective refractive index denoted as $n_{eff} = n(1 - iK)$. The linear phase mismatch can be got from the real part of the effective refractive, which is $\Delta\beta = 2\pi(n_S/\lambda_S + n_I/\lambda_I - 2n_P/\lambda_P)$ for the FWM process $\omega_I = 2\omega_P - \omega_S$. And the imaginary part represents the linear absorption of the structure. Considering the saturation absorption property and two-photon absorption (TPA) [8, 9] of graphene, the total propagation loss can be obtained as $\alpha = \alpha_0/(1 + I/I_S) + \beta_{TPA}I$, where I is the incident intensity, I_S is the saturation irradiance, $\alpha_0 = 2\omega(nK/c)$ represents the linear loss, and β_{TPA} is the TPA coefficient.

Substituting Eq. (2) to Maxwell's curl equations for the electric and the magnetic fields, one can get the coupled wave equations for degenerate FWM:

$$\begin{aligned} & \frac{\partial A_P}{\partial z} + \beta_{1P} \frac{\partial A_P}{\partial t} + \frac{i}{2} \beta_{2P} \frac{\partial^2 A_P}{\partial t^2} + \frac{1}{2} \alpha_P A_P \\ & = i\gamma_P \left(|A_P|^2 + 2|A_S|^2 + 2|A_I|^2 \right) A_P + 2i\gamma_P A_P^* A_S A_I \exp(i\Delta\beta z) \end{aligned} \quad (6)$$

$$\begin{aligned} & \frac{\partial A_S}{\partial z} + \beta_{1S} \frac{\partial A_S}{\partial t} + \frac{i}{2} \beta_{2S} \frac{\partial^2 A_S}{\partial t^2} + \frac{1}{2} \alpha_S A_S \\ & = i\gamma_S \left(|A_S|^2 + 2|A_P|^2 + 2|A_I|^2 \right) A_S + i\gamma_S A_I^* A_P^2 \exp(-i\Delta\beta z) \end{aligned} \quad (7)$$

$$\begin{aligned} & \frac{\partial A_I}{\partial z} + \beta_{1I} \frac{\partial A_I}{\partial t} + \frac{i}{2} \beta_{2I} \frac{\partial^2 A_I}{\partial t^2} + \frac{1}{2} \alpha_I A_I \\ & = i\gamma_I \left(|A_I|^2 + 2|A_P|^2 + 2|A_S|^2 \right) A_I + i\gamma_I A_S^* A_P^2 \exp(-i\Delta\beta z) \end{aligned} \quad (8)$$

In the graphene covered on a tapered fiber, the nonlinearities of graphene and silica are quite different. As a result, nonlinear parameters $\gamma_{P,S,I}$ should identify the local field corresponding to what kind of materials, which can be obtained by using a common expression [10]:

$$\gamma = \frac{3\omega}{4} \varepsilon_0 \frac{\iint \chi^{(3)}(x, y) |\vec{E}|^4 dx dy}{\left| \iint_{D_{total}} \text{Re} \left\{ \vec{E} \times \vec{H}^* \right\} \cdot \hat{e}_z dx dy \right|^2} \quad (9)$$

where E and H^* are the distribution of the electric field and the conjugate of magnetic field, and \hat{e}_z is the unit vector along the propagation direction. In Eq. (9), $\chi^{(3)}(x, y)$ represents the third-order susceptibility of graphene or silica due to the material that the micro area corresponds to.

To evaluate the FWM response in the graphene on a tapered fiber, the conversion efficiency can be defined as the ratio of the generated idler power with respect to the incident signal power:

$$\eta = |A_I(L)|^2 / |A_S(0)|^2 \quad (10)$$

By numerically solving Eqs. (6)–(8), the output idler $A_I(L)$ and hence the conversion efficiency can be obtained.

3. SIMULATION AND ANALYSIS

By setting $\mu = 0.02 \text{ eV}$ and $\tau = 5 \times 10^{-13} \text{ s}$ for graphene, and adopting the diameter of the tapered fiber as $0.7 \mu\text{m}$, the nonlinear parameter of the composite structure is calculated from the electric field distribution along with the linear absorption and the total loss involving both linear and TPA losses, as shown in Fig. 2(a). One can find that graphene greatly enhances the nonlinear parameter, but meanwhile a large loss is brought. In particular, the wavelengths for higher nonlinear parameters also suffer from higher losses because more electric field is restricted in the graphene layer. Fig. 2(b) shows the conversion efficiency as a function of graphene length using a pump whose pulse peak power is 10 W , pulse width is 100 ps , and wavelength is set to be 1.3 , 1.5 , or $1.7 \mu\text{m}$ (signal wavelength is approximately equal to the pump wavelength), respectively. From Fig. 2(b), one can find that different graphene lengths are needed to reach their maximum conversion efficiency for different pump wavelengths. The required graphene length and the corresponding maximum conversion efficiency are plotted in Fig. 2(c). Although the required graphene lengths are different for various wavelengths, they are all as short as few ten micrometers. The maximum conversion efficiency reaches -23.5 dB when the pump wavelength is $1 \mu\text{m}$. A short wavelength needs a short length to reach the maximum efficiency due to its high nonlinear parameter and heavy loss, and the peak efficiency is higher than that of longer wavelength.

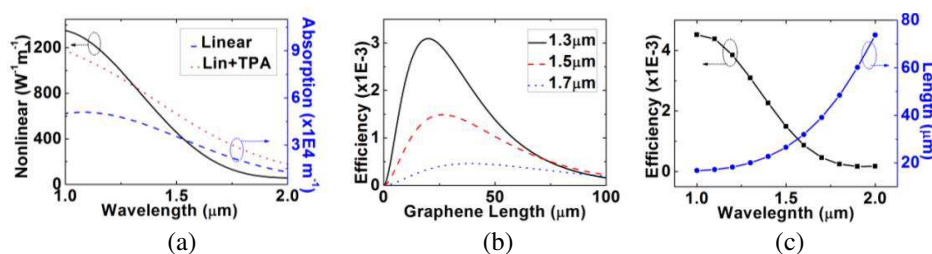


Figure 2: (a) Nonlinear parameter, linear absorption, and total absorption. (b) Conversion efficiency along the graphene length. (c) Optimized graphene length and the corresponding maximum conversion efficiency.

Since the required graphene layer is quite short, it is expected to have ultrabroad conversion bandwidth. Assuming the graphene length is $30 \mu\text{m}$, Figs. 3(a) and 3(b) show the nonlinear phase shift κL , where L is the graphene length and $\kappa = (\Delta\beta + 2\gamma P_P)$ is the total phase mismatch, and the corresponding conversion efficiency as the signal wavelength varies, pumped by 0.8 -, 1.3 -, and 1.8 - μm lights, respectively. The signal and converted idler wavelengths are set to be within $2.4 \mu\text{m}$ because the structure no longer constrains longer wavelength to form guide mode. As nonlinear parameter is rapidly enhanced as the wavelength shortens, which means a high efficiency for the conversion from long-wavelength signal to short-wavelength idler, the maximum conversion efficiency emerges at signal wavelength longer than pump wavelength. Fig. 3(c) shows the bandwidth and maximum efficiency at different pump wavelengths. It turns out that owing to graphene, the waveguide has an ultrabroad bandwidth about from 315 to 720 nm with maximum conversion efficiency about from -23.7 to -27.8 dB as the pump wavelength varies from 0.8 to $1.8 \mu\text{m}$. The bandwidth is related to the dispersion of the structure, as shown in Fig. 3(d). The zero dispersion wavelength (ZDW) emerges in $0.89 \mu\text{m}$, which corresponds the broadest bandwidth of 720 nm in Fig. 3(c).

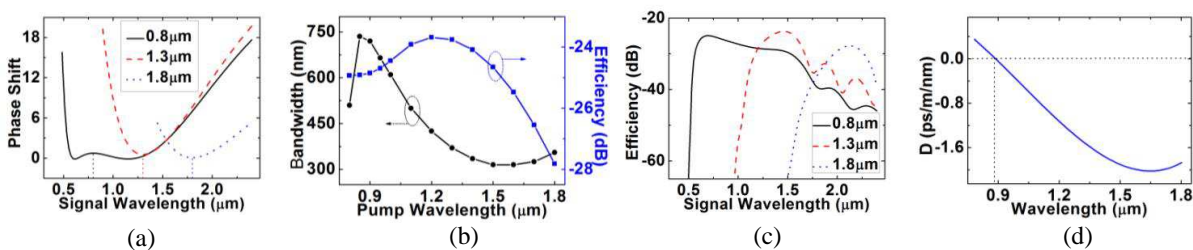


Figure 3: (a) Nonlinear phase shift and (b) conversion efficiency as the signal wavelength varies. (c) Bandwidth and the maximum conversion efficiency at different pump wavelengths. (d) Dispersion value of the structure as the wavelength varies.

For comparison, we also simulate the nonlinear optical response in a pure tapered fiber. The obtained nonlinear coefficient of the pure tapered fiber with the same dimensions is shown in Fig. 4(a), which is three orders smaller than graphene cover one. In order to reach the same conversion efficiency as graphene layer on the tapered fiber (-24.6 dB with a $1.5\text{-}\mu\text{m}$ pump), the pure tapered fiber length is set to be 10 cm. Figs. 4(b) and 4(c) show the nonlinear phase shift and the corresponding conversion efficiency for the pure tapered fiber pumped by a $1.5\text{-}\mu\text{m}$ light, whose pulse peak power is also 10 W and pulse width is 100 ps. The FWM bandwidth of the pure tapered fiber is calculated to be only 8.6 nm, which is much narrower than the graphene layer covered one since it needs to propagate much longer distance to attain the same conversion efficiency.

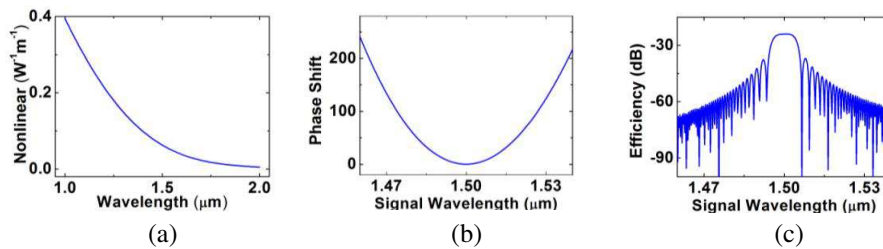


Figure 4: (a) Nonlinear parameter of pure tapered fiber. (b) Nonlinear phase shift and (c) conversion efficiency as the signal wavelength varies in the pure tapered fiber.

4. CONCLUSIONS

FWM are theoretically analyzed in a graphene layer covered on a tapered fiber considering the nonlinear parameter for composite structures. The graphene length is optimized to obtain maximum conversion efficiency at different pump wavelengths. Due to the ultrashort graphene length, such a composite structure shows the performance of ultrabroad bandwidth. A conversion bandwidth of more than 300 nm is achieved with a conversion efficiency of more than -30 dB in a wide wavelength range of $0.8\text{--}1.8\ \mu\text{m}$. By comparing with the pure tapered fiber without graphene, the composite structure shows much broader bandwidth to get the same conversion efficiency since much shorter interaction length is used.

ACKNOWLEDGMENT

This work was supported by the Specialized Research Fund for the Doctoral Program of Higher Education of China (Grant No. 20130101110089), the National Natural Science Foundation of China (Grant No. 61178001), and the Zhejiang Provincial Natural Science Foundation of China (Grant No. LY14F050006).

REFERENCES

1. Hendry, E., P. J. Hale, J. Moger, A. K. Savchenko, and S. A. Mikhailov, "Coherent nonlinear optical response of graphene," *Phys. Rev. Lett.*, Vol. 105, No. 9, 097401, 2010.
2. Dean, J. J. and H. M. van Driel, "Graphene and few-layer graphite probed by second-harmonic generation: Theory and experiment," *Phys. Rev. B*, Vol. 82, No. 12, 125411, 2010.
3. Gorbach, A. V., "Nonlinear graphene plasmonics: Amplitude equation for surface plasmons," *Phys. Rev. A*, Vol. 87, No. 1, 013830, 2013.
4. Gu, T., N. Petrone, J. F. McMillan, A. van der Zande, M. Yu, G. Q. Lo, D. L. Kwong, J. Hone, and C. W. Wong, "Regenerative oscillation and four-wave mixing in graphene optoelectronics," *Nat. Photonics*, Vol. 6, No. 8, 554–559, 2012.
5. Wu, Y., B. Yao, Y. Cheng, Y. Rao, Y. Gong, X. Zhou, B. Wu, and K. S. Chiang, "Four-wave mixing in a microfiber attached onto a graphene film," *IEEE Photon. Technol. Lett.*, Vol. 26, No. 3, 249–252, 2014.
6. Gorbach, A. V., A. Marini, and D. V. Skryabin, "Graphene-clad tapered fiber: Effective nonlinearity and propagation losses," *Opt. Lett.*, Vol. 38, No. 24, 5244–5247, 2013.
7. Vakil, A. and N. Engheta, "Transformation optics using graphene," *Science*, Vol. 332, No. 603m5, 1291–1294, 2011.
8. Yang, H., X. Feng, Q. Wang, H. Huang, W. Chen, A. T. S. Wee, and W. Ji, "Giant two-photon absorption in bilayer graphene," *Nano Lett.*, Vol. 11, No. 7, 2622–2627, 2011.

9. Li, W., B. Chen, C. Meng, W. Fang, Y. Xiao, X. Li, Z. Hu, Y. Xu, L. Tong, H. Wang, W. Liu, J. Bao, and Y. R. Shen, “Ultrafast all-optical graphene modulator,” *Nano Lett.*, Vol. 14, No. 2, 955–959, 2014.
10. Koos, C., L. Jacome, C. Poulton, J. Leuthold, and W. Freude, “Nonlinear silicon-on-insulator waveguides for all-optical signal processing,” *Opt. Express*, Vol. 15, No. 10, 5976–5990, 2007.

Semiconductor Plasmonic Nano-cavity Laser on Silicon: Simulation, Design and Fabrication

Qian Wang, Chee Wei Lee, and Kim Peng Lim

Agency for Science, Technology and Research, Data Storage Institute
5 Engineering Drive 1, 117608, Singapore

Abstract— Plasmonic nano-cavity laser based on a III-V semiconductor nano-ring on silicon can operate either in in-plane dipole mode or vertical coaxial mode. This paper gives the simulation, design and some fabrication discussions of this unique nano-cavity laser. Body-of-revolution finite-difference-time-domain (BOR-FDTD) is used for the modal analysis and design of cavity. The spatial and temporal lasing performance of this nano-cavity laser is simulated incorporating the BOR-FDTD with multilevel gain medium model. Comparison between these two lasing modes is presented and numerical analysis shows that the in-plane dipole mode can achieve the smallest mode volume reported so far. Fabrication of this semiconductor plasmonic nano-cavity laser is discussed. This semiconductor plasmonic nano-cavity laser has a deep sub-wavelength footprint and ultralow power consumption, which can act as an on-chip light source for intrachip data interconnect.

1. INTRODUCTION

On-chip light source with an ultra small footprint and ultralow power consumption is a key device enabling high-speed intra-chip data interconnect. Semiconductor plasmonic nano-cavity has the deep-wavelength light confining capability (overcoming the diffraction limit) and advantages of integration on silicon using heterogeneous III/V on silicon technology and electrically-pumping for practical applications. There are various semiconductor plasmonic laser demonstrated numerically and experimentally so far including Fabry-Perot, nanopatch, nanodisk and coaxial cavity [1–5]. In this paper, a plasmonic III-V semiconductor nano-ring integrated on silicon through an interlayer bonding is considered as shown in Fig. 1.

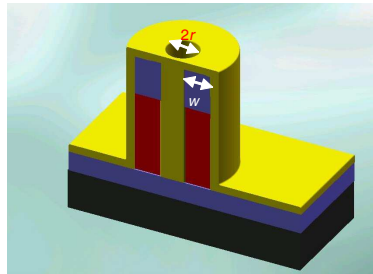


Figure 1: Semiconductor plasmonic nanoring laser.

This plasmonic nanoring cavity can operate at either in-plane dipole mode or vertical co-axial mode. To have a comprehensive analysis and comparison between these two modes, body-of-revolution finite-difference-time-domain is employed for modal analysis and cavity design. The spatial and temporal lasing performance is simulated incorporating the BOR-FDTD with multilevel gain medium model. Comparison between these two lasing modes is presented regarding the resonant wavelength, quality factor and mode profiles. Numerical analysis shows that the in-plane dipole mode laser can achieve the smallest mode volume reported so far. Fabrication of this semiconductor plasmonic nano-cavity laser is discussed and some results are presented. This semiconductor plasmonic nano-cavity laser with a deep sub-wavelength footprint and ultralow power consumption is promising as an on-chip light source for future intrachip data interconnect.

2. MODELING AND SIMULATION OF THE NANO-RING CAVITY LASER

The nanoring plasmonic laser schematically shown in Fig. 1 requires modeling and simulation in three aspects: 1) semiconductor gain medium; 2) Drude-Lorentz model for the metal and 3) spatial and temporal simulation of electromagnetic field of the nano-cavity using body-of-revolution FDTD.

The Maxwell equation in the format of body of revolution format

$$\left\{ \begin{array}{l} \frac{\partial H_{r,o}}{\partial t} = -\frac{1}{\mu} \left(-\frac{\partial E_{\phi,o}}{\partial z} - \frac{1}{r} m E_{z,e} \right) \\ \frac{\partial H_{\phi,e}}{\partial t} = -\frac{1}{\mu} \left(\frac{\partial E_{r,e}}{\partial z} - \frac{\partial E_{z,e}}{\partial r} \right) \\ \frac{\partial H_{z,o}}{\partial t} = -\frac{1}{\mu} \left(\frac{1}{r} \frac{\partial (r E_{\phi,o})}{\partial r} + \frac{1}{r} m E_{r,e} \right) \\ \frac{\partial D_{r,e}}{\partial t} = \left(\frac{1}{r} m H_{z,o} - \frac{\partial}{\partial z} H_{\phi,e} \right) \\ \left(\frac{\partial D_{\phi,o}}{\partial t} \right) = \left(\frac{\partial}{\partial z} H_{r,o} - \frac{\partial}{\partial r} H_{z,o} \right) \\ \frac{\partial}{\partial t} D_{z,e} = \left(-\frac{1}{r} m H_{r,o} + \frac{1}{r} \frac{\partial (r H_{\phi,e})}{\partial r} \right) \end{array} \right. \quad (1)$$

and $D_{j,e} = \frac{1}{\epsilon} \sum_{m=1}^M \frac{\partial P_m}{\partial t}$ ($j = r, z$) where P_m is the macroscopic polarization component that links the electromagnetic field with the dynamics of carrier densities for the active gain medium. Detailed formulation of the Drude-Lorentz model and multilevel gain medium model can be found in Ref. [5].

3. NANO-RING CAVITY LASER: IN-PLANE DIPOLE OR COAXIAL LASER?

The nano-ring cavity laser shown in Fig. 1 can operate as an in-plane laser, where the light is confined vertically and resonant cavity is the nano-ring in the horizontal plane. It can also lase

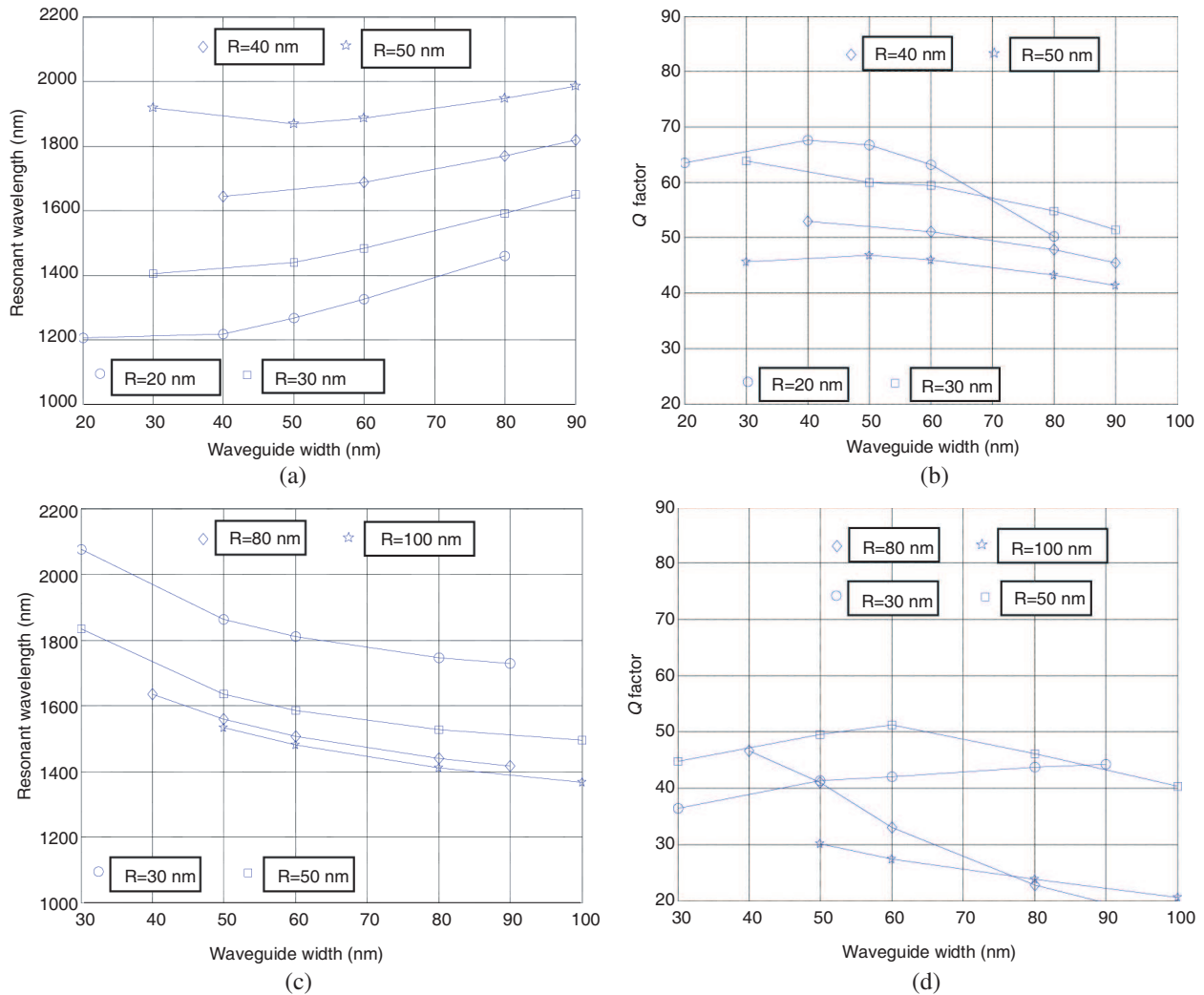


Figure 2: (a) and (b) are resonant wavelengths and Q -factors for nano-ring dipole laser cavity; (c) and (d) are resonant wavelengths and Q -factors for the coaxial laser cavity.

as a coaxial laser as demonstrated in Ref. [4], where the light is confined horizontally as a coaxial plasmonic mode and resonant cavity is formed in the vertical direction. With the above BOR-FDTD, the coaxial lasing mode corresponds to the case of $m = 0$. For the in-plane laser the corresponding $m > 0$ and in this paper $m = 1$ is specifically interested as it refers to in-plane nanoring dipole laser and it can achieve much smaller foot-print as compared to the cases $m > 1$.

As numerical examples, the height of the III-V semiconductor gain region is 200 nm with a refractive index of 3.5 and the material for the top-cladding and interlayer is silicon dioxide. The thickness for the interlayer is 200 nm preventing the leakage for in-plane ring laser and provides sufficient reflectance for coaxial laser. We vary the structure parameters and analyze the influence of these parameters on the device's performance. As representative results, resonant wavelength and quality factors for these two cases are presented in Figs. 2(a)–(d) when varying inner radius R and width of the waveguide W .

As a summary of analysis of both lasing modes: 1) the in-plane laser cavity has a relatively smaller foot print and relatively higher Q factors as compared to the case of coaxial mode when considering the InP material system and operating optical communication wavelength; 2) the coaxial laser cavity is strongly dependent on the thickness of top-cladding and material of interlayer due to the nature of resonant cavity; 3) the in-plane resonant mode has a much smaller mode volume as compared to the coaxial case. In our simulation examples, the in-plane dipole plasmonic laser has an inner radius of 30 nm and width of waveguide of 30 nm, the corresponding mode-volume is only $0.001(\lambda/2n)^3$. For coaxial lasing mode, a cavity with both inner radius and waveguide width of 80 nm gives a close lasing wavelength but the mode volume is $0.014(\lambda/2n)^3$.

Figure 3 shows the intensity profile of the dipole resonant mode (top view) and the corresponding L-L curve simulated with the previous FDTD program with gain medium model.

4. FABRICATION DISCUSSION

The whole device realization consists of three main modules: 1) bonding the InGaAsP gain medium onto silicon substrate through interlayer bonding with thermal SiO_2 , which is followed by removing

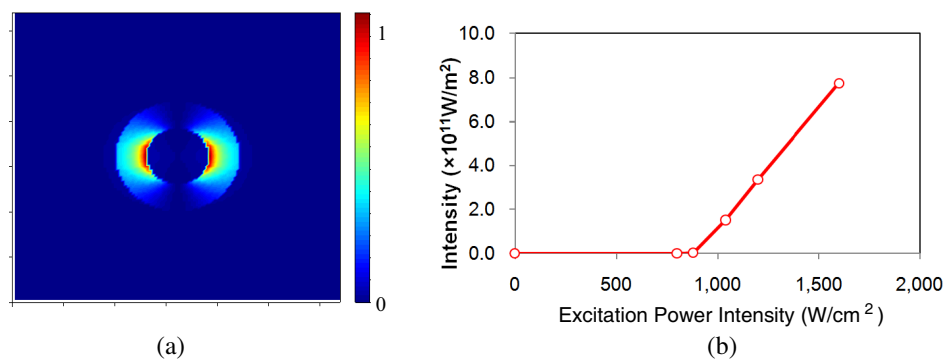


Figure 3: (a) Intensity profile of the dipole lasing mode; (b) L-L curve simulated by the FDTD program with gain medium model.

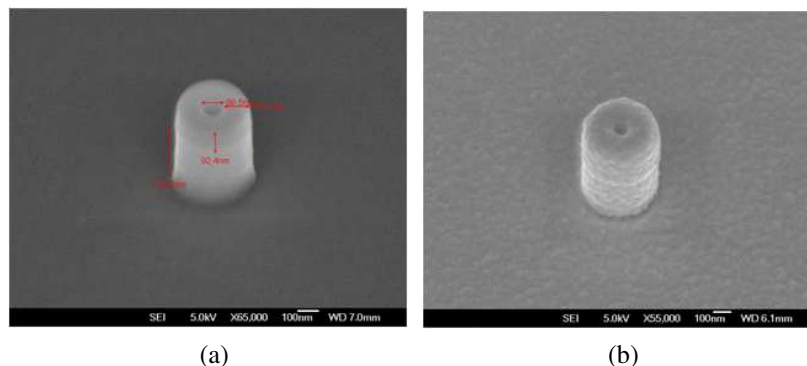


Figure 4: (a) SEM images of the etched III-V nano-ring cavity; (b) Nanoring cavity coated with silver film.

InP substrate in hydrochloric acid solution; 2) The submicron structures could be defined on the substrate via hydrogen silsesquioxane (HSQ) resist with electron beam lithography, and then directly etched down with chlorine recipe in an inductively coupled plasma reactive-ion-etching system (ICP-RIE) equipped with elevated temperature stage at 250°C; 3) metal film is deposited to form the plasmonic cavity and for the case of in-plane dipole laser, it should be etched back for optical pumping from the top. Figs. 4(a) and (b) are the scanning electronic microscopy images of our III-V etched devices bonded on silicon and coated with metal film. The device prototyping is undergoing.

5. CONCLUSION

This paper has presented the simulation, design analysis and some fabrication discussions of III-V on silicon plasmonic nano-cavity laser. Body-of-revolution finite-difference-time-domain has been used for the modal analysis and design of cavity, which has been also incorporated with the multilevel gain medium model for the spatial and temporal simulation of lasing performance. Comparison between the in-plane dipole laser and vertical coaxial laser has been presented and numerical analysis has shown that the in-plane dipole mode can achieve the smallest mode volume reported so far. Some key fabrication modules of this semiconductor plasmonic nano-cavity laser have been discussed.

REFERENCES

1. Hill, M. T., Y.-S. Oei, B. Smalbrugge, Y. Zhu, T. D. Vries, P. J. V. Veldhoven, F. W. M. V. Otten, T. J. Eijkemans, J. P. Turkiewicz, H. D. Waardt, E. J. Geluk, S.-H. Kwon, Y.-H. Lee, R. N. Tzel, M. K. Smit, “Lasing in metallic-coated nanocavities,” *Nature Photonics*, Vol. 1, 589–594, 2007.
2. Yu, K., A. Lakhani, and M. C. Wu, “Subwavelength metal-optic semiconductor nanopatch lasers,” *Optics Express*, Vol. 18, No. 9, 8790–8799, 2010.
3. Khajavikhan, M., A. Simic, M. Katz, J. H. Lee, B. Slutsky, A. Mizrahi, V. Lomakin, and Y. Fainman, “Thresholdlessnanoscale coaxial lasers,” *Nature*, Vol. 482, 204–207, 2012.
4. Ding, K., M. T. Hill, Z. C. Liu, L. J. Yin, P. J. van Veldhoven, and C. Z. Ning, “Record performance of electrical injection subwavelength metallic-cavity semiconductor lasers at room temperature,” *Optics Express*, Vol. 21, 4728–4733, 2013.
5. Wang, Q. and S.-T. Ho, “A numerical simulation of nanodisk semiconductor-plasmonic laser using BOR-FDTD with a multilevel gain medium model,” *IEEE Photonics Journal*, Vol. 4, 2346–2352, 2012.

Tunable V-cavity Semiconductor Laser and Modules

Jian-Jun He¹, Xiaohai Xiong¹, Jianjun Meng¹, Sen Zhang¹, Xiaolu Liao¹,
Hongli Zhu¹, Lin Wu¹, Li Zou², Lei Wang², and Guoping Li²

¹State Key Laboratory of Modern Optical Instrumentation
Centre for Integrated Optoelectronics, Department of Optical Engineering
Zhejiang University, Hangzhou 310027, China

²Lightip Technologies (Hangzhou) Co. Ltd.
11 Xiyuan Eighth Road, Suite D-502, Hangzhou 310030, China

(Invited Paper)

Abstract— We present the principle, design, packaging and measurement results of widely tunable V-cavity lasers. By using a novel half-wave coupler, single-mode lasing with high side-mode-suppression-ratio is achieved. Single-electrode controlled wide-band wavelength tuning with Vernier effect is realized. The full-band tuning of 50 channels with 100 GHz spacing is demonstrated by further employing temperature induced gain spectrum shift. The laser is packaged into a small-form-factor 9-pin TOSA, and the electronic driver has been developed for the wavelength tuning and direct modulation. The advantages of compactness, fabrication simplicity, and easy wavelength control offer great potential for the tunable laser to be used in low-cost access and data center networks, as well as in portable devices for spectroscopic analysis.

1. INTRODUCTION

Widely wavelength tunable semiconductor lasers are important components for next-generation optical networks, and for applications in spectroscopic measurements. Over the last two decades, high performance tunable lasers have been developed based on complex structures such as sampled grating distributed Bragg reflector (SGDBR) [1], superstructure grating DBR [2], digital super mode DBR [3], modulated grating Y-branch [4], and periodically etched slots [5]. In addition to fabrication complexity involving non-uniform gratings and multiple epitaxial growths, multiple electrodes with complex control algorithms are usually required for wavelength tuning. With the dense wavelength division multiplexing (DWDM) technology extending towards access and data center networks, and the emerging demands of portable devices for biomedical analyses, food safety and environmental monitoring etc., the cost reduction and operational simplicity become more and more important.

To reduce the fabrication complexity, widely tunable lasers using two ring resonators as intracavity Vernier filters have been developed [6]. This scheme eliminates the need of the complex grating fabrication. However, it still requires etch-and-regrowth for active-passive integration, and three electrodes for controlling the wavelength tuning. It also needs deeply etched ring resonators with small radius and coupling gaps which are difficult to fabricate without expensive tools such as ebeam lithography.

Simpler designs known as coupled-cavity lasers with an etched trench or cleaved-coupled-cavity (C^3) structure were investigated in the 1980's [7, 8]. However, they have not been widely used in practice because of their poor side mode suppression ratio (SMSR). Recently, a compact grating less V-coupled-cavity tunable laser was proposed [9] and single-electrode controlled wavelength tuning of 16 and 26 channels with 100 GHz spacing was demonstrated experimentally with an excellent SMSR of about 40 dB and 37 dB, respectively [10]. By combining temperature-induced gain spectrum shift with current controlled Vernier tuning mechanism, the tuning range was extended to 50 channels with a temperature variation of only 35°C [11]. It is an all-active device with no grating or ring resonators, and therefore does not require any epitaxial regrowth. The fabrication process is similar to simple Fabry-Perot lasers and the device size is only about $0.5 \times 0.3 \text{ mm}^2$.

2. DESIGN AND OPERATION PRINCIPLE

Figure 1 shows the top view of a V-cavity laser. It comprises a fixed gain cavity and a channel selector cavity with different optical path lengths, which form V-shaped branches with a reflective 2×2 half-wave coupler. The half-wave coupler, in which the cross-coupling coefficient has a π phase relative to the bar-coupling coefficient, is important for achieving high SMSR. A conventional

directional coupler or self-imaging multimode interference coupler, in which the cross-coupling coefficient has a relative phase of $\pi/2$ (quarter-wave) with respect to the bar-coupling coefficient, would produce no mode selectivity for the laser. In order to accurately control the coupler length for achieving optimal coupling coefficient, deeply etched facets are used to form the cavity mirrors. The length of the fixed gain cavity is designed so that its resonance frequency interval matches 100 GHz ITU grids. The length of the channel selector cavity is slightly longer so that the Vernier effect can be employed to realize wide tuning range. The whole device comprises the same quantum well structure without epitaxial regrowth or bandgap engineering.

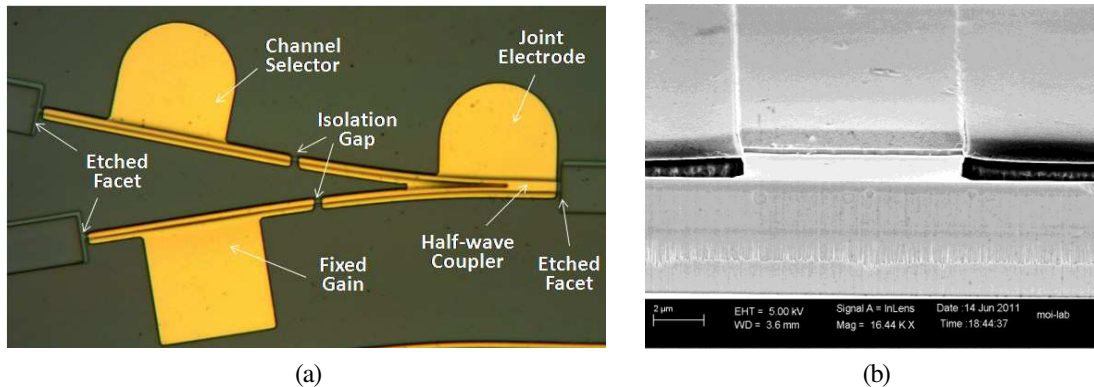


Figure 1: (a) Top view of an InGaAsP/InP based V-cavity laser with a chip size of $500 \mu\text{m} \times 300 \mu\text{m}$; (b) Deeply etched facet.

The principle of the wavelength tuning is based on the Vernier mechanism. Each of the two cavities has a series of resonant modes with slightly different frequency interval. The main lasing mode occurs at a common resonant frequency which can be switched to an adjacent mode of the fixed cavity by slightly shifting the resonant frequency comb of the channel selector cavity. Only a single electrode is required for the wavelength switching. Although the Vernier effect is also used in other widely tunable lasers such as SGDBR lasers, they typically have frequency interval larger than 600 GHz due to the limitation of the device length required for accommodating many sampling periods of the grating. For common dense wavelength division multiplexing applications with 50 GHz or 100 GHz channel spacing as defined by ITU, a multi-electrode control is necessary for accessing all operating channels. This complexity is removed with the V-cavity laser.

3. EXPERIMENTAL RESULTS

The fabrication process is similar to that of a Fabry-Perot laser with the addition of a deep etching step for the etched facets. Fig. 2 shows the overlapped spectra of 50 channels tuning in an InGaAsP/InP multiple-quantum well (MQW) V-cavity laser, obtained by varying the current injected into the channel selector cavity in combination with TEC temperature variation from 10°C to 45°C which extends the tuning range by shifting the MQW gain spectrum. The SMSR ranges

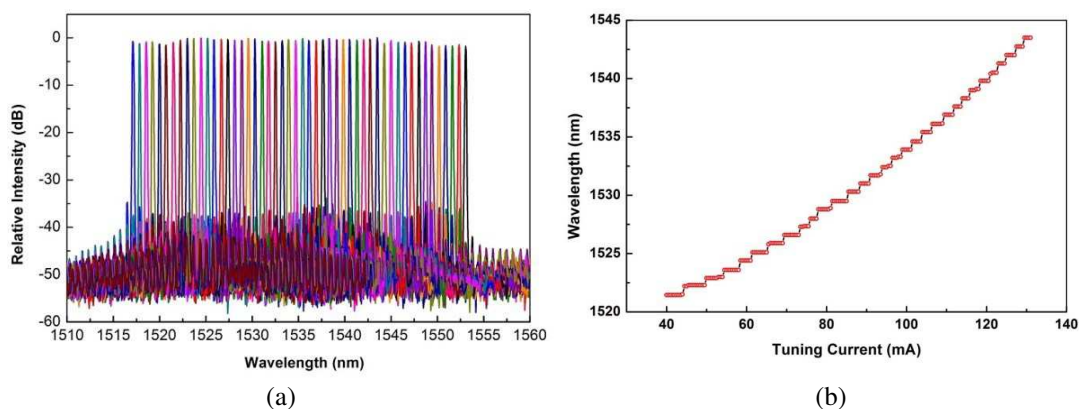


Figure 2: (a) Overlapped 50-channel laser spectra with 100 GHz spacing from an InGaAsP/InP MQW V-cavity laser; (b) Single-electrode controlled tuning curve when the TEC temperature is fixed at 20°C .

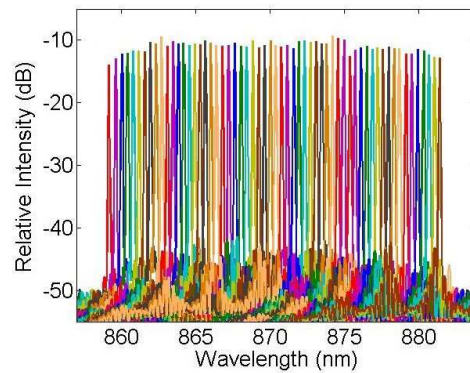


Figure 3: Overlapped 60-channel laser spectra with 150 GHz spacing from a GaAs/AlGaAs MQW V-cavity laser.

from 35 dB to 38 dB for most of the channels. The laser reaches the threshold when the three electrodes are biased at about 20 mA. When the electrodes are biased at 40 ~ 50 mA, the output power measured by collecting all the light from the coupler side using a broad area detector is about 8 mW. The wavelength tuning range of ~ 40 nm can potentially cover the full C- or L-band. Fig. 2(b) shows the wavelength tuning curve of the single-electrode controlled tuning of 31 channels when the TEC temperature is fixed at 20°C.

The grating less tunable V-cavity laser is even more advantageous for GaAs/AlGaAs based material system operating in the 850 nm window because it can overcome the two difficulties faced by grating based tunable lasers: the much smaller grating period (~ 120 nm versus 240 nm) that requires e-beam lithography and the oxidation of AlGaAs during the grating fabrication. Fig. 3 shows the measured spectra of a GaAs/AlGaAs MQWV-cavity laser, which cover 60 channels with ~ 150 GHz spacing. This wavelength band is within the transparent optical window of human tissue, and is therefore useful for wearable health monitoring devices.

4. PACKAGED MODULES

The V-cavity laser has been packaged into a small-form-factor 9-pin transmitter optical subassembly (TOSA). It contains a tunable laser diode chip-on-carrier, a monitoring photodiode, a TEC, a thermistor, an optical isolator, and optical lenses. The size of the housing box is only 7.4 mm × 5.8 mm × 5.3 mm, which is a small fraction of a conventional butterfly package, as shown in Fig. 4(a). An electronic driver has been developed for the wavelength tuning and direct modulation, as shown in Fig. 4(b). High speed modulation up to 5 Gbps has been achieved. The wavelength tuning can be controlled by computer software. Fig. 4(c) shows a compact module with an USB interface for computer control.



Figure 4: (a) Packaged TOSA module (lower) compared to a conventional butterfly package (upper); (b) An electronic driver circuit board for wavelength control and direct modulation; (c) An enclosed tunable laser module with a USB interface for computer control.

5. CONCLUSION

We have developed a simple and compact V-cavity tunable semiconductor laser which is capable of full-band wavelength tuning. By combining the current tuning on just one electrode and the TEC temperature control, > 5000 GHz frequency tuning is achieved in both InGaAsP/InP and GaAs/AlGaAs material systems. The laser structure does not involve any grating or epitaxial regrowth, and has a size of only $500 \mu\text{m} \times 300 \mu\text{m}$. Compact modules and electronic drivers have been developed for the wavelength tuning and direct modulation. The advantages of compactness, fabrication simplicity and easy wavelength control offer great potential for the tunable laser to be used in low-cost access and data center networks, and for portable medical and environmental monitoring devices.

ACKNOWLEDGMENT

This work was supported by the National High-Tech R&D Program of China (grant No. 2013AA014401).

REFERENCES

1. Coldren, L. A., "Monolithic tunable diode lasers," *IEEE J. Sel. Topics in Quantum Electron.*, Vol. 6, 988, 2000.
2. Tohmori, Y., Y. Yoshikuni, and H. Ishii, "Broad-range wavelength-tunable superstructure grating (SSG) DBR lasers," *IEEE J. Quantum Electron.*, Vol. 29, 1817–1823, 1993.
3. Ward, A. J., D. J. Robbins, G. Busico, E. Barton, L. Ponnampalam, J. P. Duck, N. D. Whitbread, P. J. Williams, D. C. J. Reid, A. C. Carter, and M. J. Wale, "Widely tunable DS-DBR laser with monolithically integrated SOA: Design and performance," *IEEE J. Select. Topics Quantum Electron.*, Vol. 11, 149–156, 2005.
4. Wesström, J.-O., G. Sarlet, S. Hammerfeldt, L. Lundqvist, P. Szabo, and P.-J. Rigole, "State of the art performance of widely tunable modulated grating Y-branch lasers," *Opt. Fiber Commun. Conf.*, paper TuE2, 2004.
5. Byrne, D., J. Engelstaedter, W. Guo, Q. Lu, B. Corbett, B. Roycroft, J. O'Callaghan, F. H. Peters, and J. Donegan, "Discretely tunable semiconductor lasers suitable for photonic integration," *IEEE J. Sel. Topics Quantum Electron.*, Vol. 15, 482–487, 2009.
6. Segawa, T., S. Matsuo, T. Kakitsuka, T. Sato, Y. Kondo, and H. Suzuki, "Full C-band tuning operation of semiconductor double ring resonator coupled laser with low tuning current," *IEEE Photon. Technol. Lett.*, Vol. 19, 1322–1324, 2007.
7. Coldren, L., K. Furuya, B. Miller, and J. Rentschler, "Etched mirror and groove-coupled GaInAsP/InP laser devices for integrated optics," *IEEE J. Quantum Electron.*, Vol. 18, 1679–1688, 1982.
8. Tsang, W. T., "The cleaved-coupled-cavity (C3) laser," *Semicond. Semimetals*, Vol. 22, 257, 1985.
9. He, J.-J. and D. Liu, "Wavelength switchable semiconductor laser using half-wave V-coupled cavities," *Opt. Express*, Vol. 16, 3896–3911, 2008.
10. Jin, J., L. Wang, Y. Wang, T. Yu, and J.-J. He, "Widely wavelength switchable V-coupled-cavity semiconductor laser with ~ 40 dB side-mode suppression ratio," *Opt. Lett.*, Vol. 36, 4230–4232, 2011.
11. Zhang, S., J. Meng, S. Guo, L. Wang, and J.-J. He, "Simple and compact V-cavity semiconductor laser with 50×100 GHz wavelength tuning," *Opt. Express*, Vol. 21, 13564, 2013.

The Proposal of Pulse Synchronous Laser Signal Source Based on Coupled-microdisk Photonic Molecules

Bo-Wen Liu, Yue-De Yang, Xiu-Wen Ma, and Yong-Zhen Huang

State Key Laboratory on Integrated Optoelectronics

Institute of Semiconductors, Chinese Academy of Sciences, Beijing 100083, China

Abstract— Here we propose a model to generate pulse synchronous laser signals based on waveguide coupled microdisk photonic molecules. Through the beating between the symmetric and anti-symmetric modes in the photonic molecules, dual pulse synchronous laser signals are coupled out from two waveguides. We simulate the light field distributions of the modes in the photonic molecules via finite difference time domain (FDTD) method, and compute the frequency differences between the symmetric mode and anti-symmetric transverse magnetic (TM) coupled modes. The frequency differences, which represent the pulse repetition frequency (PRF) of pulse synchronous laser signals, can reach from dozens of GHz to about 1 THz according to the simulation. The numerical results show that the proposed model can generate dual pulse synchronous laser signals with fixed pulse widths and complementary phase which can act as a pulse synchronous laser signal source.

1. INTRODUCTION

During the past twenty years, photonics molecules (PMs) which consist of clusters of electromagnetically coupled optical microcavities have been drawing a great attention for their distinctive optical properties [1]. Photonic molecules with different configurations or patterns are applied to realize variety kinds of photoelectronic devices, such as microlasers, sensors, and compact photonics information processing. On the other hand, in the radar system, transmitter utilize pulse synchronous signals to control different amplifier chains and modulation switch triggering time [2]. These pulse synchronous signals must keep a strict sequential relationship to make sure the transmitters operate properly. In addition, the synchronization between transmitter and indicator depends on pulse synchronous signals. With the determination range, especially the speed determination, being continuously expanded, pulse synchronous signals with higher PRF are needed.

In this paper, we analyze the operation of the waveguide coupled microdisk photonic molecules by the finite-difference time-domain (FDTD) method. The microdisk photonic molecules can generate dual pulse synchronous laser signals with fixed pulse widths and complementary phase from two coupled waveguide, through the beating between the symmetric and anti-symmetric coupled modes [3]. The PRF, which is equal to the frequency difference between the two beating modes, can be controlled by varying the gap between two microdisks. The results show the waveguide coupled microdisk photonic molecules can act as a pulse synchronous laser signal with PRF at microwave band.

2. MODEL FOUNDATION AND ANALYSIS

We study the waveguide coupled microdisk photonic molecules by the two-dimensional FDTD method and focus on the interaction between the symmetric and anti-symmetric coupled modes. In the following simulation, we only consider the transverse magnetic (TM) modes. Figure 1 shows the schematic diagram of the two-dimensional waveguide coupled microdisk photonic molecules. We set the radii of microdisk $R = 2 \mu\text{m}$, the width of waveguide $d = 0.4 \mu\text{m}$, the gap between the microdisk and corresponding coupled waveguide $s = 0.3 \mu\text{m}$, and the variable parameter w represent the gap between two microdisks. We set the refractive index of the two microdisks resonators and two waveguides to 3.2, and they are all surrounded by air with a refractive index of 1.0. The blue rectangular frame is a 10-cell perfectly matched layer (PML) to terminate the simulation window. The waveguides are inserted to the PML to confirm the lightwave coupled into the waveguides can be detected as output optical signal and eliminate the influence of waveguide port reflection. The dashed line between two microdisks is the symmetry axis, and the mode coupling between two microdisk will results in coupled modes with symmetric or anti-symmetric field distributions relative to the symmetry axis. To excite the symmetric mode and the anti-symmetric mode separately, we set two symmetric exciting sources relative to the symmetry axis near the adjacent boundaries of the two microdisks, which are the red points in the Figure 1. The exciting source used in the FDTD

simulation can be expressed as $P(t) = \exp[-(t - t_0)^2/t_w^2] \cos(2\pi ft)$, where t_0 and t_w are the times of the pulse center and the pulse half width respectively, and f is the center frequency of the pulse.

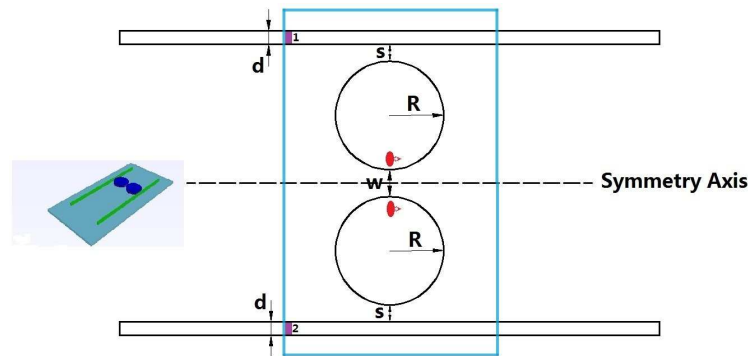


Figure 1: Schematic diagram of waveguide coupled microdisk photonic molecules for the FDTD simulation. (inset is 3D diagram).

At first, we using the symmetric and anti-symmetric sources to excite the symmetric and anti-symmetric modes respectively. The pulse sources covering a wide range of frequency are applied to excite all the considered TM modes, and then the Padé approximation method is used to calculate the intensity spectra from the time domain FDTD output. A 2.1×10^6 -step FDTD simulation is performed with the mesh cell size of 20 nm, $t_w = 2^8 \Delta t$, $t_0 = 2t_w$, $\Delta t = 4.67 \times 10^{-17}$ s and $f = 193.5$ THz. Through the simulation, we can get the intensity spectra of the waveguide coupled microdisk photonic molecules with different symmetry conditions. Figure 2(a) shows the intensity spectra from 203 THz to 210 THz when the gap between two microdisks $w = 0.3 \mu\text{m}$, from which we can find that there is obvious coupling induced mode splitting between the symmetric TM mode and the corresponding anti-symmetric TM mode. In fact, the mode splitting vary with w for different TM modes. This phenomenon has been observed by many study on common photonic molecules [4]. Thus, we can obtain the frequency difference between the symmetric mode and the corresponding anti-symmetric mode as a function of w . Figure 2(b) shows the frequency difference versus w for different TM modes. We can see that the frequency difference can reach from dozens of GHz to about 1 THz, but it decreases when w increases and would become zero when w is big enough for all the TM modes, at which time the coupling can be neglected. Nevertheless, for the forth-order mode $\text{TM}_{13,4}$, this trend is relatively flat because its evanescent field has a relatively large interaction area, especially when compared with that of the fundamental mode $\text{TM}_{23,1}$.

Utilizing the frequency difference produced by the coupling induced mode splitting, we can obtain optical microwave signal through the beating of the two nearly degenerate coupled modes. In

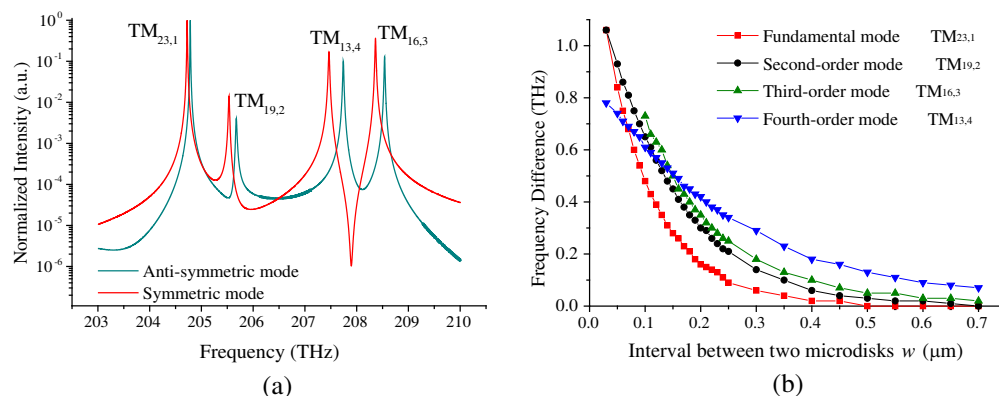


Figure 2: (a) Intensity spectra of the waveguide coupled microdisk photonic molecules with different symmetry conditions obtained by the FDTD simulation, where the radii of microdisk $R = 2 \mu\text{m}$, the width of waveguide $d = 0.4 \mu\text{m}$, the gap between microdisk and corresponding coupled waveguide $s = 0.3 \mu\text{m}$, and the gap between two microdisks $w = 0.3 \mu\text{m}$. (b) The variation of the frequency difference between the symmetric mode and the corresponding anti-symmetric mode with the gap between two microdisks w for different TM modes.

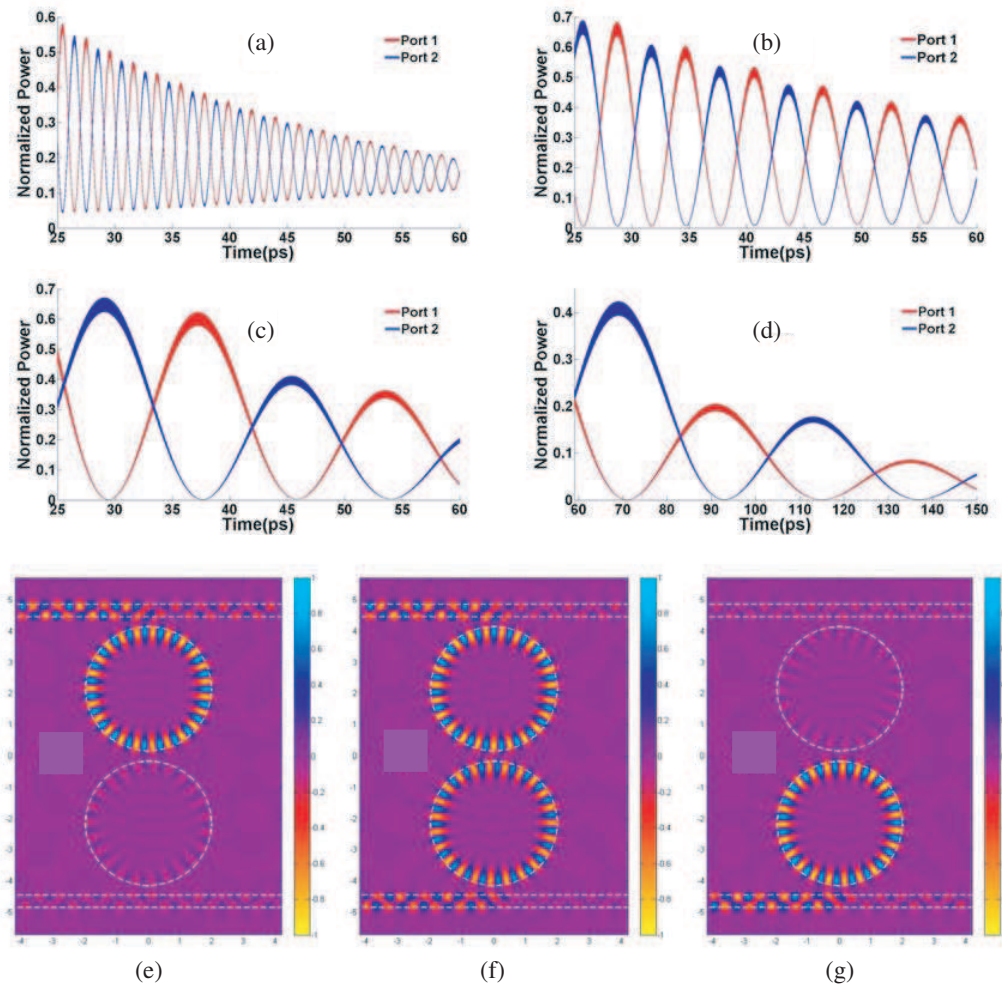


Figure 3: The oscillograms for the normalized power output at port 1 and port 2 with the gap between two microdisks w of (a) 0.1, (b) 0.2, (c) 0.3, (d) 0.4 μm , respectively; (e), (f), (g) the change of field distribution corresponding to the output converting between port 1 and port 2 with w of 0.3 μm .

either one of the two microdisks, when the symmetric mode and the corresponding anti-symmetric mode interact with each other, the time evolution of the produced light field has quasi-periodical character. If we assume that the symmetric mode frequency were f_1 and the corresponding anti-symmetric mode frequency were f_2 , the produced intensity would vary with sinusoidal function at the beating frequency $|f_1 - f_2|$, namely the frequency difference of the two nearly degenerate coupled modes. According to the property of the symmetric and anti-symmetric modes, when their phase difference in one of the two microdisks is zero, the phase difference in the other one should be π . This property lead to the oscillating intensity in the two microdisks has an additional phase difference of $\pi/2$. That is to say, the light field not only oscillates quasi-periodically in either one of the two microdisks, but also oscillates between the two microdisks alternately. On this basis, the produced quasi-periodically alternate oscillatory signals can be output through the two waveguides which couple with the two microdisks respectively. Then these two sets of output signals form dual pulse synchronous laser signals, and the pulse repetition frequencies are equal to the beating frequency $|f_1 - f_2|$. To obtain the quasi-periodically alternate oscillatory signals, we excite the symmetric mode and the corresponding anti-symmetric mode at the same time. We use the exciting source with the pulse half width of $t_w = 2^{18} \Delta t$, which covers a narrow frequency range centered at the obtained mode frequency above, and detect the output power signals of the two waveguides at port 1 and port 2 respectively, which are shown in Figure 1 as purple rectangles. The (a), (b), (c), (d) in Figure 3 are the oscillograms for the normalized power output at port 1 and port 2 when the gap between two microdisks w are 0.1, 0.2, 0.3, 0.4 μm , respectively, whose repetition frequencies are 0.4862, 0.1675, 0.0614, 0.0227 THz. They are equal to the frequency differences shown in Figure 2(b), which are 0.48, 0.16, 0.06, 0.02 THz, respectively. Meanwhile,

we can find that the phases of the output power at port 1 and port 2 are strictly complementary, namely, their phase difference remains $\pi/2$ as explained above. The Figures 3(e), (f), (g) show the change of E_y field distribution corresponding to the output converting between port 1 and port 2 when w is $0.3\ \mu\text{m}$, and the light field in the waveguides are amplified ten times for clearly. Obviously, the quasi-periodically alternate oscillatory output signals detected at port 1 and port 2 derive from the quasi-periodically alternate oscillation between the two microdisks.

On the other hand, we calculate the Q factors of these modes. Considering that the Q factor of the fundamental mode is much higher than that of the other modes, here we only give the Q factor of the fundamental mode versus w for the symmetric mode and the corresponding anti-symmetric mode, as shown in Figure 4. In the simulation, we set material absorption coefficient $\alpha = 10\ \text{cm}^{-1}$, and the mode group index $n_g = 3.6$. The anti-symmetric mode has a larger Q factor than the symmetric modes. This is due to that the optical leakage to the exterior domain of the anti-symmetric mode is reduced by destructive interference, and, on the contrary, the optical leakage to the exterior domain of the symmetric mode is enhanced by constructive interference [5]. We can find that the difference of Q factors between the symmetric mode and the corresponding anti-symmetric mode tapers off, when the gap between two microdisks w increases. The difference may result in, compared with the situation that w is small, it is easier to excite the two nearly degenerate modes at the same time when w is relatively larger. Namely, it is easier to produce dual pulse synchronous laser signals when w is relatively larger. However, the mode splitting would drop off as w increases, which correspond to a smaller PRF. Therefore, we should choose the gap between two microdisks properly in practice.

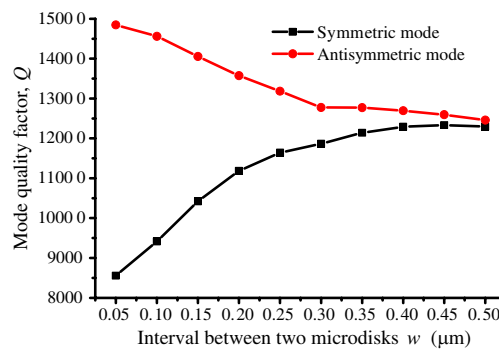


Figure 4: The Q factors of the fundamental mode $\text{TM}_{23,1}$ versus the gap between two microdisks w for the symmetric mode and the anti-symmetric mode.

3. CONCLUSION

This paper proposes a pulse synchronous laser signal source based on the waveguide coupled microdisk photonic molecules through the beating between the nearly degenerate symmetric mode and anti-symmetric coupled mode. We analyze the operation of the model by the finite difference time domain (FDTD) method. The pulse repetition frequency is equal to the beating frequency, that is the coupling induced frequency difference of the two nearly degenerate coupled modes, which could reach from dozens of GHz to about 1 THz and be controlled by the gap between two microdisks. Considering the influence of mode Q factor, we expect to optimize the model by replace the microdisk with microring in the follow-up study.

REFERENCES

1. Bayer, M., et al., "Optical modes in photonic molecules," *Physical Review Letters*, Vol. 81, No. 3, 2582–2585, 1998.
2. Liu, J., C. Guo, et al., "Design of a multiplex pulse synchronizer based on FPGA," *Electronic Engineer.*, Vol. 34, No. 7, 3–5, 2008.
3. Ryu, J.-W., et al., "Terahertz beat frequency generation from two-mode lasing operation of coupled microdisk laser," *Optics Letters*, Vol. 37, No. 15, 3210–3212, 2012.
4. Ishii, S., et al., "Modal characteristics and bistability in twin microdisk photonic molecule lasers," *IEEE Journal of Selected Topics in Quantum Electronics*, Vol. 12, No. 1, 71–77, 2006.
5. Benyoucef, M., et al., "Quality-factor enhancement of supermodes in coupled microdisks," *Optics Letters*, Vol. 36, No. 8, 1317–1319, 2011.

Simulation of Thermal Tuning in V-coupled Cavity Laser with an On-chip Thin-film Heater

Haoyu Deng, Jianjun Meng, and Jian-Jun He

State Key Laboratory of Modern Optical Instrumentation, Center for Integrated Optoelectronics
Department of Optical Engineering, Zhejiang University, China

Abstract— We present the design and simulation results of a thermally tuned V-coupled cavity laser (VCCL) with an on-chip heater. A thermal model based on finite-element method (FEM) is developed to calculate the transient and steady-state temperature distribution in the laser. The wavelength tuning behavior is simulated. The compact gratingless widely-tunable semiconductor laser is promising for reconfigurable optical networks as well for laser sensing.

1. INTRODUCTION

With the progress in reconfigurable optical communication network and laser sensing, tunable semiconductor lasers with high performances in terms of single-mode characteristics, wavelength-tuning as well as high reliability, low-cost and operational simplicity are highly desirable. V-coupled cavity laser (VCCL) is a compact, gratingless widely-tunable semiconductor [1] that does not require epitaxial regrowth, and can achieve single-electrode controlled wide wavelength with an excellent SMSR [2].

Adjusting the temperature of the whole laser including its carrier by thermo-electric cooler (TEC) can increase the tuning range of the VCCL [3, 4], but the tuning time and efficiency is not ideal for practical use because of the long distance between the light emitting region and the heat source. To solve that, we present a thermal tuning method using on-chip heaters [5] for VCCL. Simulation results of its tuning behavior are provided and discussed in this paper.

2. DEVICE DESCRIPTION AND TUNING MECHANISM

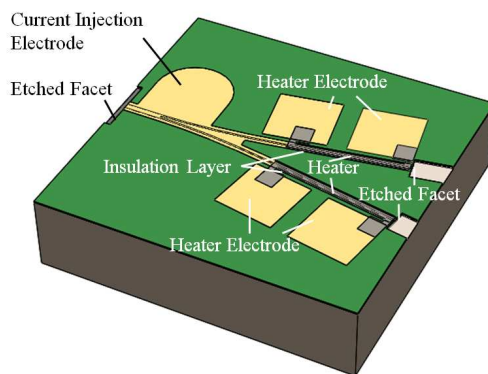


Figure 1: Schematic diagram of the VCCL with on-chip heater.

Figure 1 is the schematic structure of the VCCL with a thin-film heater. The laser is produced on an InP-based epitaxial wafer that includes 5 InGaAsP quantum-wells active region. The V-coupled cavity consists of two waveguides coupled through a reflective 2×2 half-wave coupler, forming a V-shaped geometry, bounded by etched facets. A layer of SiO_2 is patterned after the electrodes are fabricated, to insulate the p-electrodes from the heater. Finally, a NiCr film is deposited on the SiO_2 film to serve as the heater.

Thermal wavelength tuning can be accomplished by adjusting current injection into one of the heaters. The Joule-heat generated in the energized heater is conducted to the waveguide and changes its refractive index due to thermo-optic effect. Consequently, the resonant peaks of the cavity varies and the wavelength of output laser is tuned by employing the Vernier effect.

3. HEAT TRANSFER IN THE LASER

A heat-transfer model for an InP-based V-coupled cavity laser (VCCL) is first developed, where steady-state and time-dependent temperature distribution of the device is studied by using finite element method (FEM).

To simplify the model, we assume that the temperature variation along the waveguide is negligible. Therefore, the 2-dimensional temperature distribution in the cross-section perpendicular to the waveguide can represent the temperature distribution in the whole laser. Besides, an equivalent InGaAsP layer is used to represent the active region including 5 InGaAsP quantum-wells and the GRIN-SCH layers, thus enhancing the computing efficiency. Fig. 2 illustrates the 2-D model of the VCCL with top-heating structure. The heat sink and solder on which the laser chip is placed are included in the thermal model as well.

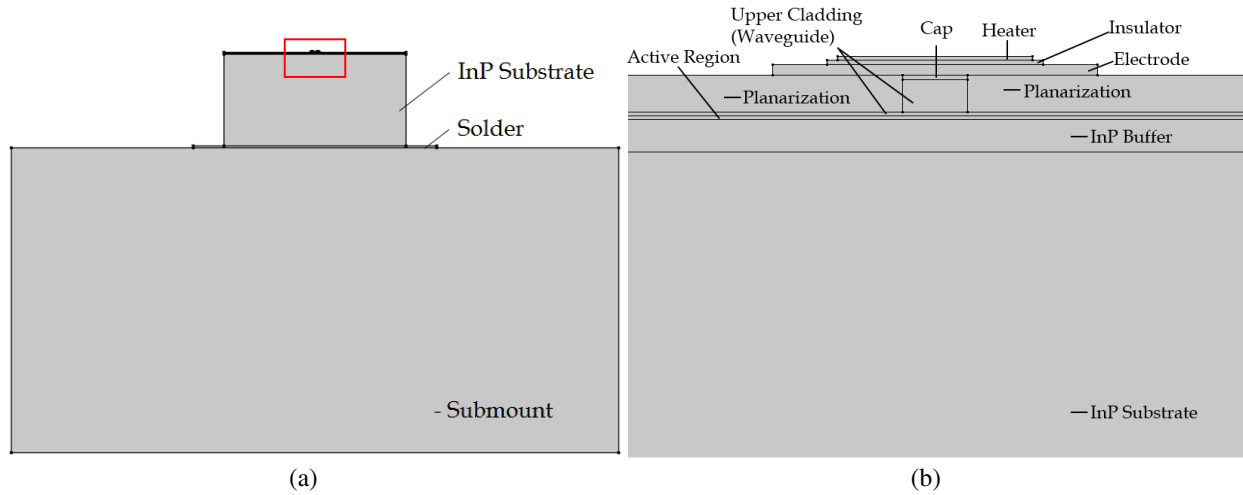


Figure 2: 2-D model of the VCCL with top-heating structure; (a) whole model including submount and solder and (b) magnified picture of the part in red box in (a).

The thermal model is constructed using the “Heat Transfer in Solids” module of COMSOL software. The structure and material parameters used in the model are defined in Table 1. We define the initial condition as 20°C in all domains in the model. The boundary condition is: 20°C for the bottom surface of the heat sink, and a heat exchange boundary of $h = 5 \text{ W}\cdot\text{m}^{-2}\cdot\text{K}^{-1}$ with temperature of 20°C in the adjacent environment for all other surfaces. With the heat generation rate of 100 mW in the heater, we can solve the transient heat-transfer equation [6] numerically using FEM.

Table 1: Material parameters used for thermal model.

Layer	Material	Density $\rho(\text{kg}\cdot\text{m}^3)$	Specific heat capacity $C_p(\text{J}\cdot\text{kg}^{-1}\cdot\text{K}^{-1})$	thermal conductivity $k(\text{W}\cdot\text{m}^{-1}\cdot\text{K}^{-1})$
Submount	AlN	3240	743	285
Solder	Au ₈₀ Se ₂₀	14500	137.88	57
Substrate, buffer, upper cladding	InP	4790	49.1	68
Active region	InGaAsP	5500	250	13.7
Cap	InGaAs	5500	350	5
Planarization	SU8	1214	1500	0.3
Electrode	Au	19300	129	327
Insulator	SiO ₂	2200	730	1.4
Thin-film heater	Nichrome	8529	12.6	11.2

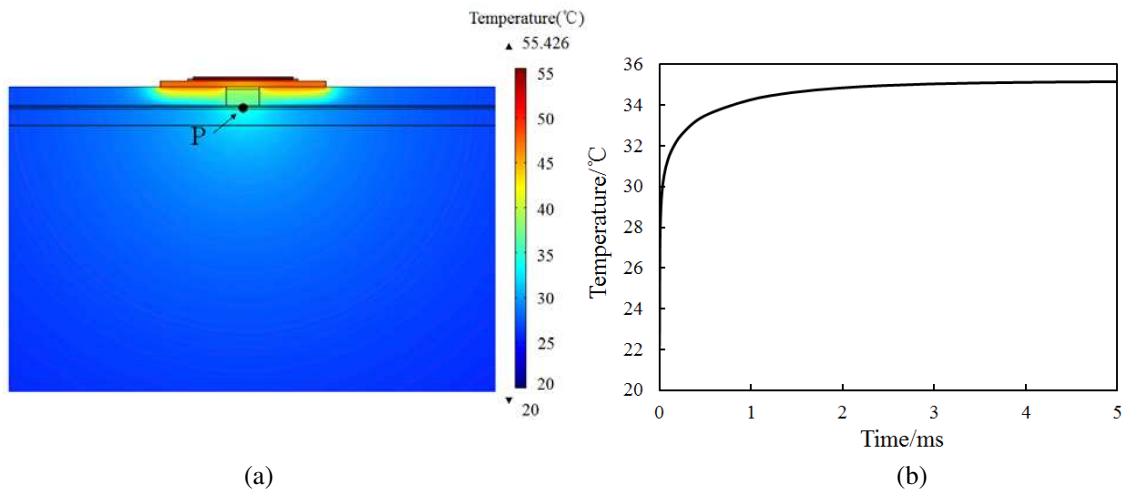


Figure 3: (a) 2-D temperature (degC) distribution at steady state of the laser with top-heating structure after 100mW heat provided in the heater; (b) temperature variation of probe P with time.

Figure 3(a) shows the model structure and the 2-D temperature distribution when the temperature reaches steady state. To observe the temperature variation in the active region over time, the center point P of the active region as shown in Fig. 3(a), is set as a probe. The temperature at the point P as a function of time is shown in Fig. 3(b), which indicates that the active region in the heated waveguide has a temperature increase of 15 K after 100 mW heating source power is provided on the heater. The time duration to reach a thermal balance is around 2 ms, which gives sufficiently high tuning speed for many applications.

4. THERMAL CROSSTALK AND TUNING RATE

During thermal tuning of the VCCL with heater, we change the temperature of the cavity supposed to be heated, while hoping the temperature in the other cavity to increase as weakly as possible. However, it is inevitable that heat spreads from the tuning cavity to the other one, which will reduce the thermal-tuning efficiency.

Heat spreading between the two waveguides of the VCCL was calculated using the 2-D finite element model. Considering that the space between the two cavities differs from $40\ \mu\text{m}$ to $110\ \mu\text{m}$ linearly, we assume the model of two parallel waveguides with a distance of $75\ \mu\text{m}$ and length of $200\ \mu\text{m}$ can approximately represent the heat transfer in VCCL. Fig. 4(a) shows the thermal model in the cross-section perpendicular to the center line of the VCCL and the calculated steady-state temperature distribution with 100 mW heat source provided in the heater on the left. Two temperature probes A and B are set at the center of the active region in the left and right cavities, respectively.

Figure 4(b) shows the temperature profile along the horizontal line in the center of the active region in Fig. 4(a). The thermal crosstalk is defined as the rate of temperature increase of probe B over that of probe A. In this example, probe A obtains a temperature rise of 15 K, while probe B obtains only 4 K, which gives the thermal crosstalk of 26.9%.

Considering the temperature induced wavelength tuning of about $0.1\ \text{nm/K}$ due to refractive index variation, the 11 K temperature distinction will cause 1.1 nm wavelength shift difference between the resonant peaks of the two cavities, and 22 nm wavelength shift of the output laser due to the Vernier effect of the VCCL with 5% difference in cavity lengths. This theoretical tuning rate of $0.22\ \text{nm/mW}$ is much more power-efficient than tuning by thermal-electric cooler (TEC).

5. ANALYSIS OF THERMAL INSULATING GROOVE

Etching a slot beside the heated waveguide to act as the thermal insulating groove is a convenient method to suppress thermal crosstalk and improve thermal tuning efficiency [7]. We evaluated the effect of the thermal insulating groove between the two cavities of VCCL, using the model as shown in Fig. 5(a).

The calculated thermal crosstalk as a function of the groove's depth scanned from $0\ \mu\text{m}$ to $50\ \mu\text{m}$ is as shown in Fig. 5(b). It is found that the crosstalk cannot be reduced to below 20% unless

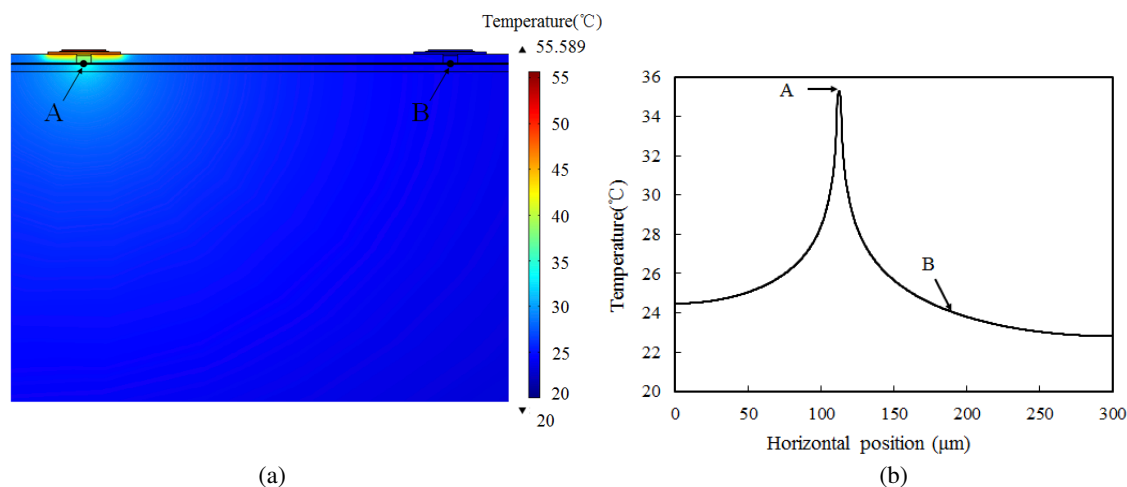


Figure 4: (a) 2-D steady state temperature (degC) distribution in the cross-section of VCCL with top-heating structure after 100mW heat source provided in the heater on the left; (b) temperature (degC) distribution along the horizontal line in (a) in the center of the active region.

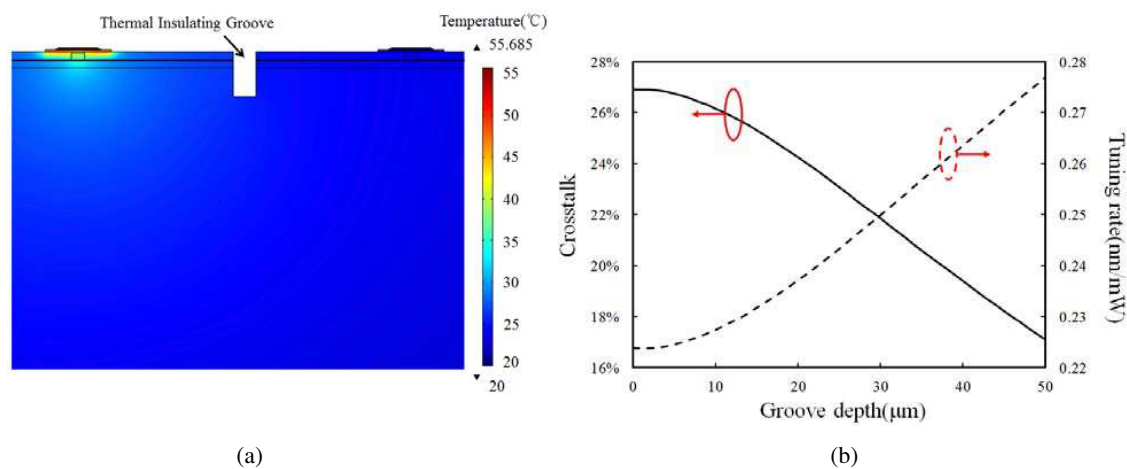


Figure 5: (a) 2-D thermal model with 10 μm deep thermal insulating groove and the steady-state temperature distribution; (b) thermal crosstalk (solid) and tuning range (dashed) as a function of depth of the thermal insulating groove.

the groove is deeper than 37 μm. With the etching depth of the groove increased to 50 μm, the crosstalk decreases to 17%, and the tuning rate increases to 0.28 nm/mW. Since such etching depth is usually unrealistic in monolithic devices, it is reasonable to conclude that the groove can hardly improve the thermal tuning efficiency.

6. CONCLUSION

We have developed a thermal model of the VCCL with on-chip thin-film heaters, using 2-D FEM. The calculation indicates that the heated waveguide obtains a balanced temperature increase of 15K in 2ms after 100mW heat generation rate is provided on the heater on top. The thermal crosstalk is 26.9% between the two cavities of the VCCL, which gives the theoretical thermal tuning rate of 0.22 nm/mW in a VCCL with 5% difference in cavity lengths. The thermal crosstalk cannot be obviously suppressed with thermal insulating groove. These results reveals that thermal tuning of VCCL using on-chip heater is a reliable and convenient wavelength tuning method, which provides sufficiently high tuning efficiency and tuning speed for many applications.

ACKNOWLEDGMENT

This work was supported by the National High-Tech R&D Program of China (grant No. 2013AA014 401).

REFERENCES

1. He, J.-J. and D. Liu, “Wavelength switchable semiconductor laser using half-wave V-coupled cavities,” *Optics Express*, Vol. 16, No. 6, 3896–3911, 2008.
2. Jin, J., L. Wang, T. Yu, Y. Wang, and J.-J. He, “Widely wavelength switchable V-coupled-cavity semiconductor laser with ~ 40 dB side-mode suppression ratio,” *Optics Letters*, Vol. 36, No. 21, 4230–4232, 2011.
3. Zhang, S., J. Meng, S. Guo, L. Wang, and J.-J. He, “Simple and compact V-cavity semiconductor laser with 50×100 GHz wavelength tuning,” *Optics Express*, Vol. 21, No. 11, 13564–13571, 2013.
4. Wei, W., H. Deng, and J.-J. He, “GaAs/AlGaAs based 870 nm-band widely tunable edge-emitting V-cavity laser,” *IEEE Photonics Journal*, Vol. 5, No. 5, 2013.
5. Sakano, S., T. Tsuchiya, M. Suzuki, S. Kitajima, and N. Chinone, “Tunable DFB laser with a striped thin-film heater,” *IEEE Photonics Technology Letters*, Vol. 4, No. 4, 321–323, 1992.
6. Wang, H. and Y. Yu, “New theoretical model to analyze temperature distribution and influence of thermal transients of an SG-DBR laser,” *IEEE Journal of Quantum Electronics*, Vol. 48, No. 2, 107–113, 2012.
7. Tanaka, S., A. Uetake, S. Yamazaki, M. Ekawa, and K. Morito, “Output level control of SOA using on-chip heater for high output power operation,” *IEEE Journal of Lightwave Technology*, Vol. 28, No. 17, 2477–2482, 2010.

Dynamical Characteristics for Semiconductor Microdisk Laser Subject to Optical Injection

Ling-Xiu Zou, Yong-Zhen Huang, Bo-Wen Liu, Xiao-Meng Lv,
Yue-De Yang, Jin-Long Xiao, and Yun Du

State Key Laboratory on Integrated Optoelectronics
Institute of Semiconductors, Chinese Academy of Sciences, Beijing 100083, China

Abstract— In this paper, the dynamic characteristics of four-wave mixing, period-one and period-two oscillations, and optical injection locking state are demonstrated for a 8- μm -radius directional-emission microdisk laser subject to optical injection. For the microdisk laser biased at 7 mA, the 3 dB bandwidth of the small signal modulation response is increased from 3.4 to 137 GHz due to the optical injection locking with an injected optical power of 0.5 mW.

The rapid development of computing systems, data centers, and other short reach datacom networks has driven the demand for optical output devices with higher bandwidth. One potential candidate to meet this requirement is the directly modulated semiconductor microlaser due to its compactness and low cost. However, the 3 dB modulation bandwidth is ultimately limited by its relaxation resonance frequency for a typical semiconductor laser. Optical injection-locking is an effective technique to enhance the modulation bandwidth.

In this paper, dynamical characteristics are investigated for an 8- μm -radius microdisk laser connected with a 2- μm -width output waveguide subject to optical injection. Dynamic states under optical injection including four-wave mixing, period double and optical injection locking are observed at different detuning wavelengths, and the enhancement of the 3 dB bandwidth due to optical injection are demonstrated.

Microdisk lasers are fabricated using an AlGaInAs/InP laser wafer grown by metal-organic chemical vapor deposition, with the technique process similar as in [1, 2].

The scanning electron microscope (SEM) cross-sectional-view for a cleaved waveguide which is directly connected to a microdisk resonator is shown in Fig. 1(a), while the microscopic picture of a fabricated microlaser laser is shown in Fig. 1(b). The microdisk cavity is laterally confined by BCB cladding layer, on which a pad patterned P-electrode is formed using lifting off technology.

After cleaving over the output waveguide, the microdisk laser is bonded p-side up on an AlN submount and mounted on a thermoelectric cooler (TEC).

The output powers coupled into a tapered multi-mode fiber (MMF) are measured as functions of the continuous-wave (CW) injection current and plotted in Fig. 2(a) together with the corresponding applied voltage. The maximum output powers obtained at 296, 290 and 288 K are 115.5, 163.3 and 176.2 μW , respectively. A series resistance of 28 Ω is estimated from the VI curve, and the threshold current is about 5.5 mA at 288 K. The laser spectra are measured by an optical spectrum analyzer (OSA) at the resolution of 0.1 nm. The spectrum measured at 288 K for the microdisk laser is plotted in Fig. 2(b) at an injection current of 10 mA, which shows single mode operation at 1540.1 nm with the side mode suppression ratio (SMSR) of 35.4 dB.

The optical injection locking provides an effective and promising method for generating microwave signals as well as enhancement of modulation bandwidth. Setting the output power of the tunable laser to 500 μW with the wavelength detuning $\Delta\lambda = \lambda_I - \lambda_C$ with λ_I and λ_C injection

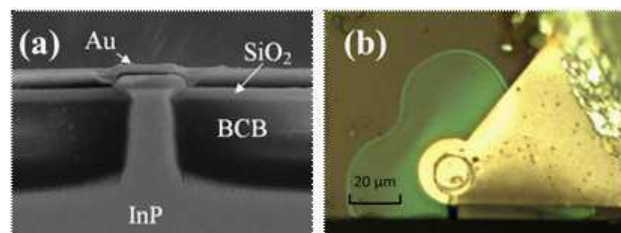


Figure 1: (a) SEM cross-sectional-view for a cleaved waveguide which is directly connected to a microdisk resonator, (b) the microscopic picture of a microdisk laser connected with an output waveguide.

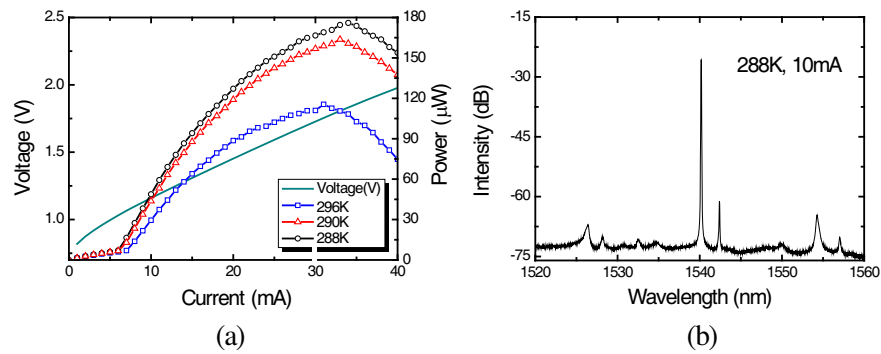


Figure 2: (a) MMF coupled power and the applied voltage versus CW injection current at 296, 290 and 288 K, and (b) laser spectra at the CW injection current of 10 mA for a 8- μm -radius microdisk laser at the temperature of 288 K.

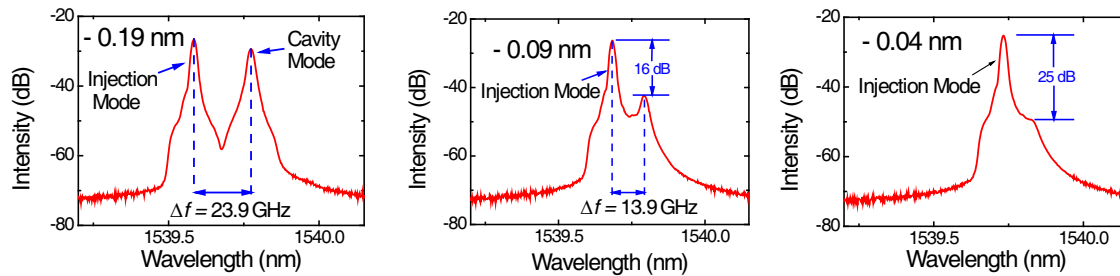


Figure 3: The measured lasing spectra at the wavelengths detuning $\Delta\lambda = -0.19$, -0.09 and -0.04 nm and injection power of 500 μW for the microdisk laser at the injection current of 7 mA.

light wavelength and the lasing mode wavelength, we firstly measure the impact of optical injection locking on the lasing spectra and dynamic performance for the microdisk laser biased slightly above threshold at 7 mA. The lasing spectra are plotted in Fig. 3 for the microdisk laser subject to optical injection at $\Delta\lambda = -0.19$, -0.09 and -0.04 nm. At $\Delta\lambda = -0.19$ nm, two clear peaks appear with the intensity difference of 2.7 dB, corresponding to the injecting mode and the lasing mode at the wavelengths of 1539.585 and 1539.775 nm, respectively. With the wavelength of the injection mode approaching the lasing mode, the intensity difference becomes 16 and 25 dB, respectively, at $\Delta\lambda = -0.09$ and -0.04 nm, and the optical injection locking is clearly observed at $\Delta\lambda = -0.04$ nm.

The small signal modulation response of the microlaser are measured by a 20-GHz-bandwidth network analyzer, at the free running state and subjection to optical injection. Using a high-frequency bias-T, the bias current together with the modulation is fed to the microdisk laser through a radio-frequency probe. The emitting light is coupled into a tapered single-mode fiber (SMF) and pass through an erbium-doped fiber amplifier (EDFA) followed by an optical band-pass filter, to suppress the amplified spontaneous emission noise. Afterwards, the output light is split into two waves by an optical fiber coupler. 1% of the output light is launched into an OSA, while 99% of the output is feeded into a high speed detector and then the converted high-frequency electrical signal is received by the network analyzer. Setting the TEC temperature of 288 K, small-signal modulation responses of the microdisk laser at biasing current of 7 mA are measured and plotted in Fig. 4 at the free running state and under optical injection locking at $\Delta\lambda = -0.04$ nm. At the free-running state, the microlaser has a 3 dB bandwidth of 3.4 GHz and a resonance frequency of 1.85 GHz. Under the optical injection locking with the optical power of 0.5 mW and $\Delta\lambda = -0.04$ nm, the 3 dB bandwidth is greatly enhanced by four times to 13.7 GHz for the microlaser under the injection locking.

The detail lasing spectra versus the detuning wavelength are measured and plotted in Figs. 5(a) and 5(b) at the injection optical power of 0.5 and 3 mW, respectively, for the microdisk laser at the injection current of 25 mA. As shown in Fig. 5(a), the optical injection locking is realized at the region I as -0.04 nm $< \Delta\lambda < 0.04$ nm, and multiple peaks of four-wave mixing are observed in the region II corresponding to a $\Delta\lambda$ ranged from -0.11 to -0.04 nm and 0.04 to 0.12 nm, respectively. In the region III, only one addition peak of four-wave mixing is observed. As the the injection optical power is 3 mW, the injection locking range is corresponding to the wavelength detuning

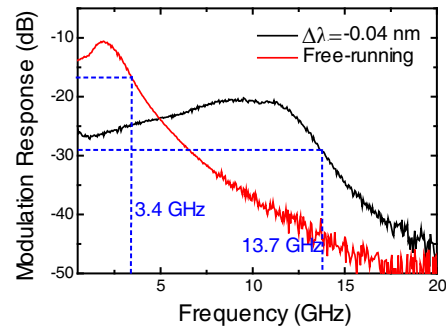


Figure 4: Small signal modulation response curves for the microdisk laser with the injection current of 7 mA at the free running state and subject to optical injection with $\Delta\lambda = -0.04$ nm and injection power of 0.5 mW.

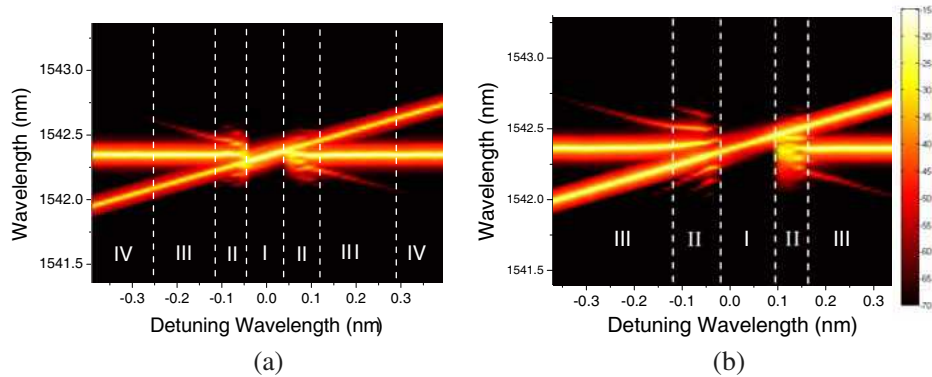


Figure 5: Lasing spectra versus wavelength detuning for the microdisk laser biased at 25 mA with the lasing wavelength of 1542.35 nm at the injection optical power of (a) 0.5 mW and (b) 3 mW, respectively.

from -0.02 to 0.09 nm, and clear four-wave mixing operation is observed for $\Delta\lambda$ ranged from -0.13 to -0.03 nm. Furthermore, period double states appear in the region II under the wavelength detuning from 0.09 to 0.16 nm.

In conclusion, optical injection locking, period double state, and the improvement of small signal modulation response have been demonstrated for an $8\text{-}\mu\text{m}$ -radius microdisk laser connected with a $2\text{-}\mu\text{m}$ -width output waveguide subject to optical injection. At the injection current of 7 mA, the optical injection locking enhances the 3 dB bandwidth from 3.4 to 13.7 GHz. The dynamic states under optical injection including four-wave mixing, period double and optical injection locking are demonstrated at different detuning wavelengths, and additional peaks appears at the halfway between the injection peak and the cavity peak similar to the period-doubling state is observed with the well-proportioned peak intensity in the central area.

ACKNOWLEDGMENT

This work was supported by the National Nature Science Foundation of China under Grants 61235004, 61021003, 61106048, and 61006042.

REFERENCES

1. Lv, X. M., Y. Z. Huang, L. X. Zou, H. Long, and Y. Du, "Optimization of direct modulation rate for circular microlasers by adjusting mode Q factor," *Laser & Photonics Reviews*, Vol. 7, 818–829 2013.
2. Lv, X. M., Y. Z. Huang, Y. D. Yang, L. X. Zou, H. Long, B. W. Liu, et al., "Influences of carrier diffusion and radial mode field pattern on high speed characteristics for microring lasers," *Appl. Phys. Lett.*, Vol. 104, 161101-161101-5, 2014.

Special Functions of Modified Optical Microfiber

Xueliang Zhang, Yang Yu, Zhangqi Song, Yuzhong Chen, and Zhou Meng

College of Optoelectronic Science and Engineering
National University of Defense Technology, Changsha 410073, China

Abstract— A common optical microfiber has usually been required to have very low loss so as to satisfy the research of optical microfiber based components. On the contrary, optical microfibers with special characteristics and a little higher loss are experimentally studied in this paper, just by modifying some of the parameters related to the optical microfiber fabrication system. Some optical microfibers have high backscattering characteristic, some have a little higher absorption loss. We have fabricated a kind of OM with high backscattering and no more than 5 mm waist region length, which can be evaluated as a reflector with low reflectance. The reflection function has been demonstrated by using the OM reflector as one of the two reflectors in a Fabry-Perot interferometer. We have also controlled the size and loss of OM to enhance its optical induced thermal effect. The OM is injected with intensity-modulated 980 nm light with average light power of about several milliwatts, the optical phase in the OM at 1550 nm wavelength is measured to be modulated while the OM is inserted into a Michelson interferometer. The result show that the OM acts as a kind of optical modulating material based on the optical induced thermal effect. In conclusion, OMs have been studied to evaluate reflection function and thermal modulation function, OM will become a kind of functional fiber and have potential value on research of new OM components.

1. INTRODUCTION

Optical microfiber (OM) has been paid much attention to for its special characteristics mainly due to its small diameter [1, 2]. Optical microfiber resonator (OMR) [3, 4] with very high quality is a typical application of OM, which requires the OM has very low loss. Corresponding works on researching low loss OM had been performed by improving the OM fabrication methods. On the contrary, we have set up an OM fabrication system and tried to research some other characteristics of OM by adjusting some fabrication parameters of the system. Modified OMs with high backscattering and a little loss are achieved and some special functions such as reflection function and light induced thermal modulation function are found in the modified OM.

2. IMPROVED OPTICAL MICROFIBER FABRICATION SYSTEM

An OM fabrication system has been set up according to the modified flame brushing method introduced by Reference [2]. The heater is an electronic heating wires embedded into special ceramic, which is driven by a DC source with digital current controlling function. The heater can heat the tapering fiber with different temperature. Meanwhile, we have built a monitoring system with a laser source and a photo-detector connected with a computer so as to monitor the transmitting light power variation during the fiber tapering process, and then we can get the ultimate loss of the fabricated OM sample. What's more, another photo-detector is used to detect the backscattering light of the tapering fiber by inserting a fiber circulator after the light source. The system with monitor function is shown in Figure 1.

It can be found that the heating temperature will have relation to the loss of the fabricated OM. We can control the heating temperature with high or low value to analyze the loss variation

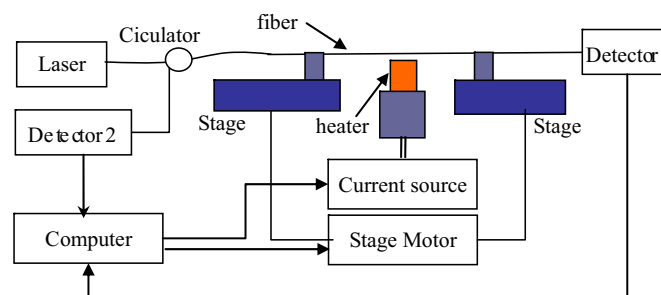


Figure 1: Schematic diagram of the OM fabrication setup with light monitoring.

rule of the OM. The heating temperature can also be designed and controlled in the computer, which means that a heating temperature function can be designed and applied by the system. Correspondingly, special OMs with not very low loss are achieved.

3. OPTICAL MICROFIBERS WITH HIGH BACKSCATTERING AND OPTICAL MICROFIBER REFLECTOR

A telecom fiber (outer diameter $\sim 125\ \mu\text{m}$, Numerical aperture ~ 0.12) is clamped onto two motorized precision translation stages and stretched under the microheater with temperature about 1200 Celsius degree. Usually, people will pay more attentions on the transmission loss. Here, we will care about the backscattering light from the drawn optical microfiber. According to experimental results, sharp cooling of the optical microfiber can produce additional loss of the microfiber. Meanwhile, we found that the backscattering light will be raised as the result of the sharp cooling of the optical microfiber. An optical microfiber with enhanced backscattering light is fabricated.

The fabrication process is described as following steps. One end of the 8 m drawn fiber is connected to a laser (Agilent 8148A, output power $\sim 10\ \text{dBm}$) through an optical circulator. The other end is angled to greatly decrease Fresnel reflection. Back reflected light is measured through a 3 dB optical fiber coupler with an Optical Power Meter (Lightwave 8210). Both stages and microheater shown in Figure 1 are connected to a computer. By accurately controlling the microheater's temperature, stretching speed and annealing time, we got a 10 mm waist length and $1\ \mu\text{m}$ diameter optical microfiber.

The inline monitoring light power data are plotted in Figure 2. The backscattering light power data are in Figure 2(a), the transmitting light power data are in Figure 2(b).

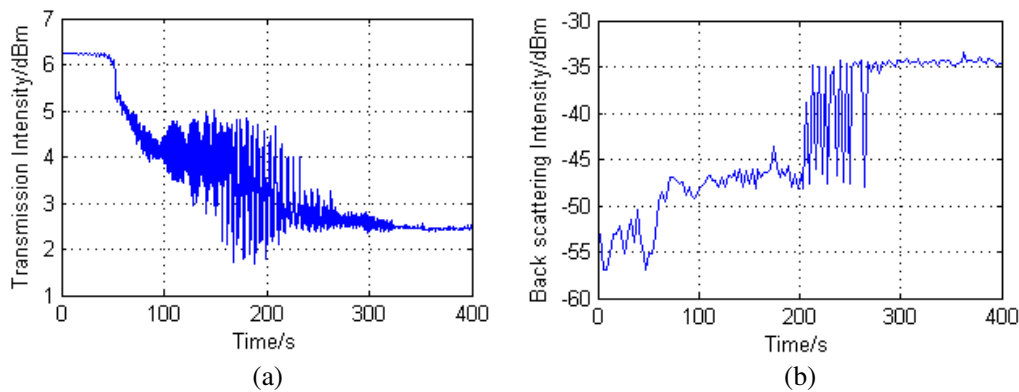


Figure 2: (a) The transmitting light power monitoring result, (b) the back reflecting light power monitoring result.

As shown in Figure 2(a), the transmitting light power is about 2.7 dBm, and the loss of the fabricated OM is about 3.7 dB, which is not a very low loss. In Figure 2(b), we can notice that at the last part of the tapering process, the backscattering increased, while we had specially shifted the heater away from the tapering fiber with a displacement about only no more than 1 mm, while still maintaining the tapering fiber in the heating region, but the heating temperature may decrease a little. The back-reflected light is measured to be about $-35\ \text{dBm}$, and has increased about 20 dB compared with the original back-reflected light of the fiber. In fact, the tapered OM has had backscattering function, and it is a reflector with low reflectance. The reflectance is about 41 dB, or 0.01%.

In order to identify the reflection is due to the modified special OM, we had the sample measured with a device called optical backscattering reflector (OBR), which can measure the distributed backscattering light of the fiber. We can measure the OM by just connecting the OM sample into the fiber connector of OBR. The measured result of the modified special OM is shown in Figure 3.

In Figure 3, the backscattering line at the displacement about 4200 mm is due to the OM sample. The peak at 0 mm and 7000 mm are separately due to the input fiber pigtail end and last fiber pigtail end. It can be got that the backscattering light power is about 15 dB higher than the fiber pigtail end. According to the result, we can conclude that the OM has obvious backscattering function, which is different with the common fiber.

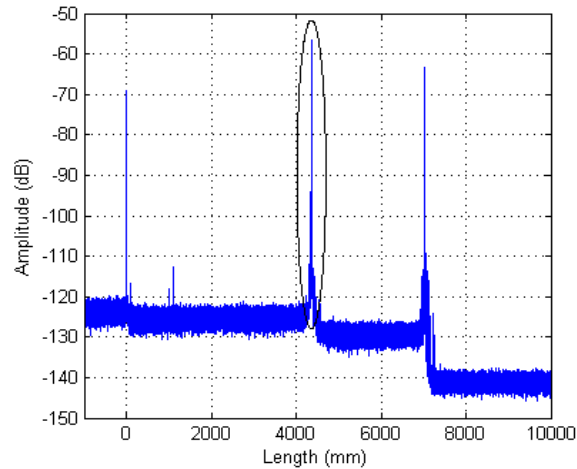


Figure 3: The distributed backscattering light of the OM sample measured with OBR.

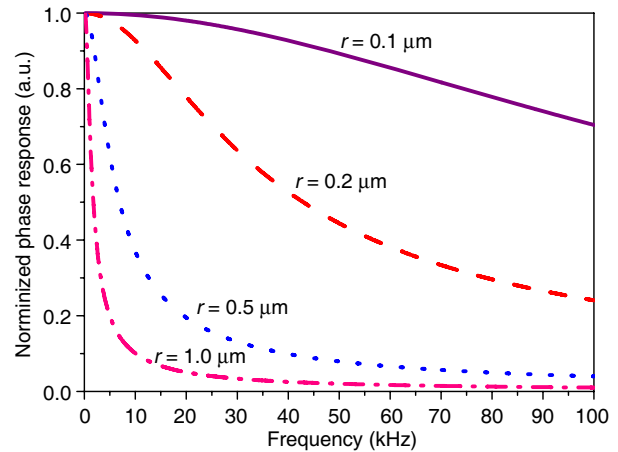


Figure 4: Calculated frequency responses of OM phase modulators with different OM radii.

We had also achieved another OM sample with stronger reflectance. The OM sample had been applied as a partial reflector in an interferometer, the work had been published by our group [5]. The result had demonstrated the OM as a real partial reflector.

4. OPTICAL INDUCED THERMAL EFFECT AND OPTICAL MICROFIBER PHASE MODULATOR WITH DIRECTLY LIGHT

We have been concerning the small diameter of the OM, only about $1 \sim 2$ micrometer for the usual OM. In Ref. [6], common fiber has been studied to produce phase modulation according to the light induced thermal effect. But the common fiber has bigger diameter so that the pump light must be very high to produce weak phase modulation. As the OM has small size, we want to produce a kind of OM to be useful on the light induced thermal modulation. We had simulated the OM phase modulation according to the fiber modulation driven by pump light. The modulation ability is shown in Figure 4 for different OM radii.

It can be seen that the smaller the radius of the OM is, the higher response the OM phase modulator will have.

Similar to the OM reflector, OM samples with a little loss have been experimentally studied for many times. OM phase modulator driven by intensity-modulated 980 nm light inserted into a phase demodulation system had been designed and experimentally studied. The setup is shown in Figure 5.

The measured phase modulation response amplitude (rad) of the OM phase modulator corre-

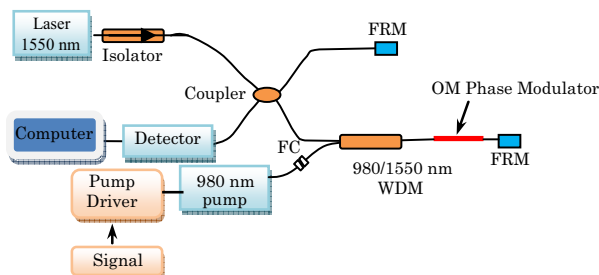


Figure 5: Schematic diagram of the OM phase modulator measurement system.

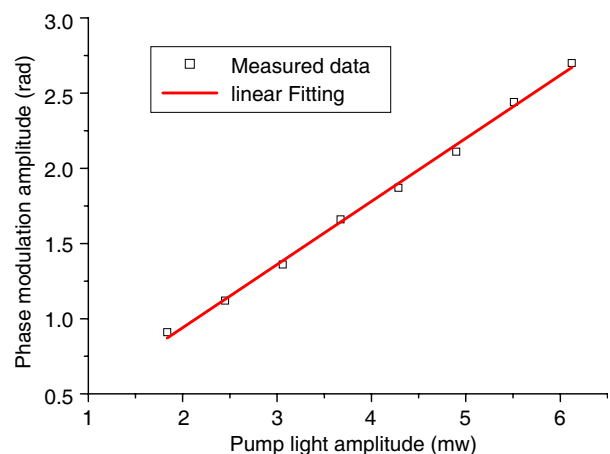


Figure 6: The phase response of the OM phase modulator with the changing pump light amplitude.

sponding to the changing average power of the intensity-modulated pump light with 1 kHz frequency are plotted in Figure 6. The linear fitting result is shown in Figure 6 in solid line. It can be seen that the OM has appeared phase modulation function and the OM modulator has good linearity for the average power of the pumped light. The detailed result of the OM phase modulator has been finished and will be published in the future by our group.

5. CONCLUSION

We have put forward to OM samples with two different special function: one is backscattering, which can be used to be partial reflector, the other is light induced thermal modulation function, which can be used as light modulator. The main property of the modified OMs is a little loss due to the thermal control during the OM fabrication process. However, the basic principle of the OMs has not been explained clearly, further works will be carried out to study the microstructure of the modified OMs.

REFERENCES

1. Tong, L., R. R. Gattass, J. B. Ashcom, S. He, J. Lou, M. Shen, I. Maxwell, and E. Mazur, "Subwavelength-diameter silica wires for low-loss optical wave guiding," *Nature*, 816–819, 2003.
2. Brambilla, G., F. Xu, and X. Feng, "Fabrication of optical fibre nanowires and their optical and mechanical characterisation," *Electronics Letters*, Vol. 42, No. 9, 2006.
3. Wu, Y., X. Zeng, C. L. Hou, J. Bai, and G. G. Yang, "A tunable all-fiber filter based on microfiber loop resonator," *Appl. Phys. Lett.*, Vol. 92, No. 19, 191112, 2008.
4. Guo, X., Y. H. Li, X. S. Jiang, and L. M. Tong, "Demonstration of critical coupling in microfiber loops wrapped around a copper rod," *Appl. Phys. Lett.*, Vol. 91, No. 7, 073512, 2007.
5. Yu, Y., X. Zhang, and Z. Song, "An investigation on optical microfiber reflector with low reflectance," *COL*, Vol. 12, No. 1, 012301, 2014.
6. Song, Z., Y. Yu, X. Zhang, Z. Wei, and Z. Meng, "Optical microfiber phase modulator directly driven with low power light," *COL*, Vol. 12, No. 9, 090606, 2014.

Miniaturized Fiber Interferometers and Their Applications as Fiber Sensors

Bo Dong, Banghong Zhang, Junhong Ng, and Yixin Wang
Institute for Infocomm Research (I2R), Singapore 138632, Singapore

Abstract— Recently, much attention has been focused on the miniaturized fiber interferometer devices due to their advantages of compact structure, small size and low cost. In this paper, we introduce two types of miniaturized fiber Mach-Zehnder interferometer (FMZI) and fiber Fabry-Perot interferometer (FFPI) and their applications as fiber sensors. An in line miniaturized FMZI could be fabricated by discharge or a point hydrogen flame. Here, we demonstrate its application as a fiber temperature sensor. A miniaturized FFPI could be fabricated by discharge when a hollow core photonic crystal fiber is spliced to a single mode fiber. Here, we demonstrate its application as a liquid refractive index sensor.

1. INTRODUCTION

Miniaturized fiber interferometers have attracted much attention due to their inherent advantages of small size, compact structure and low cost. Especially, they are more stable compared to the other common fiber interferometers and have been widely used in fiber sensing [1–9]. There are two main miniaturized fiber interferometers, fiber Mach-Zehnder interferometer (FMZI) and fiber Fabry-Perot interferometer (FFPI). Generally, miniaturized FMZI could be fabricated by discharge [1] or a point flame [2]. There is also the other method of just splicing a short-length multimode fiber [3] or photonic crystal fiber (PCF) between two sections of single mode fibers (SMFs) [4, 5]. Miniaturized FFPIs could be fabricated by discharge [6] or just splicing a short-length hollow core PCF between two sections of SMFs [7, 8]. To this day, miniaturized FMZIs have been widely used as fiber sensors for measuring force [3], strain [4, 5], displacement, temperature [4, 5, 9], vibration [2] and refractive index (RI), and miniaturized FFPIs have been applied to measure strain [7], pressure and RI [6].

In this paper, we demonstrate our recent research achievements in minimized FMZIs and FFPIs. An in line miniaturized FMZI could be fabricated in a short-length fiber with two abrupt-tapers by discharge or a point flame. Compared to the discharge method, a much smaller FMZI could be obtained by the point flame method. Here we demonstrate its application as fiber temperature sensor. An in line fiber miniaturized FFPI could be fabricated by discharge when splicing a hollow core PCF to an SMF. Here, we demonstrate its application as a liquid refractive index sensor.

2. MINIATURIZED FMZI AND ITS APPLICATION

To introduce a taper on the common fiber, two heating methods are generally applied, discharge and a point flame. The discharge method could fabricate the taper automatically by setting suitable splicing parameters of a splicer. The point flame could provide a higher heating temperature than the inner portion. To introduce the taper, one end of the fiber is fixed and the other end is pulled by a step motor or a suitable weight. Fig. 1(a) shows the schematic diagram of fabricating the taper. Figs. 1(b) and 1(c) show two typical types of tapers. Using the point flame method can not only get a longer, uniform and smooth fiber taper shown in Fig. 1(b) but also a much shorter abrupt taper shown in Fig. 1(c). However, using the discharge method can only get the abrupt taper, and the operation of this method is limited by the structure of the splicer.

Figure 2 shows the typical structure of an abrupt-tapered FMZI. The fundamental mode propagates in the untapered fiber, when it propagates to the left taper, corresponding core mode and high order cladding modes will be excited. When they meet at the right taper, corresponding interferences among them will occur. If the power is mainly distributed in the core mode and dominated cladding mode, the interference can approximatively be regarded as a two-beam Mach-Zehnder interference. To get an FMZI with a higher interference depth, a suitable taper waist diameter is required. Experiments show that to get the extinction ratio (ER) of more than 20-dB, generally $\sim 20\text{-}\mu\text{m}$ taper waist diameter of the common fiber is needed. However, for the Er/Yb co-doped fiber (EYF) based FMZI, only $\sim 50\text{-}\mu\text{m}$ waist diameter is needed. Fig. 3 shows the typical transmission spectrum of an EYF based FMZI and its corresponding spatial frequency spectrum. Its length is about 10.5 mm. The two tapers have waist lengths and diameters of 43.4 and 430 μm ,

and 56.1 and 470 μm , respectively. The distance between the two centers of the abrupt tapers is about 5 mm.

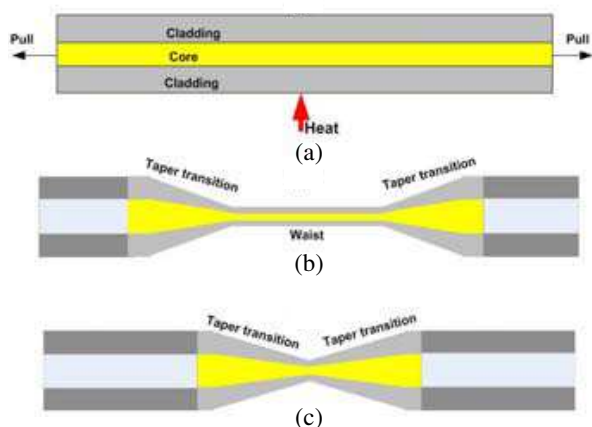


Figure 1: Schematic diagrams of two types of fiber tapers.

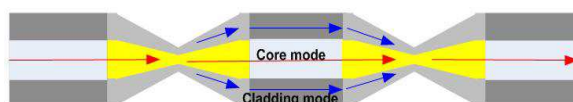


Figure 2: Schematic diagram of the FMZI.

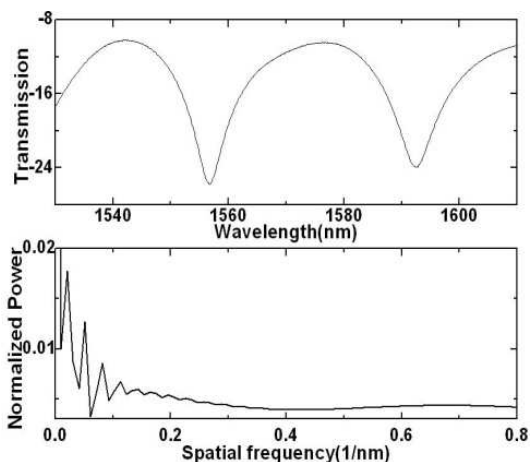


Figure 3: Typical transmission spectrum of the EYF based FMZI and its corresponding spatial frequency.

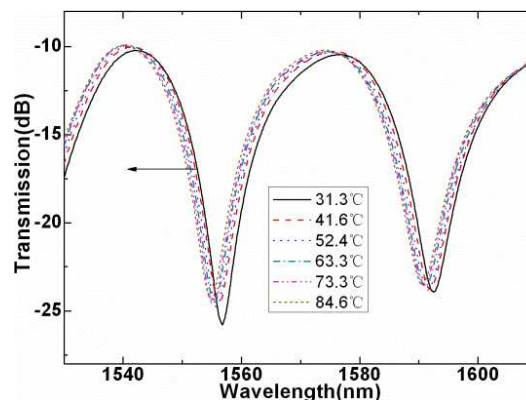


Figure 4: Transmission spectral response to temperature.

As can be seen more than three cladding modes are excited, and the power is mainly distributed in the core mode and dominated cladding mode. The other weak cladding modes have a modulation function on the interference pattern constructed by the core mode and dominated cladding mode. The phase φ of the FMZI at the output ($z = L$) can be expressed as,

$$\varphi \approx \frac{2\pi}{\lambda} \int_0^L [n_1 - n_2(z)] dz, \quad (1)$$

where n_1 and $n_2(z)$ are the effective refractive indexes (RIs) of the core mode and cladding mode, respectively, and $n_2(z)$ is position dependent. As the phase satisfies the condition of $\varphi = (2k + 1)\pi$, where k is the interference order, the resonance dip occurs. The wavelength shift $\Delta\lambda$ of the resonance dip due to temperature variation ΔT can be given by,

$$\Delta\lambda = \frac{2}{(2k + 1)} [\alpha(n_1 - \bar{n}_2) + (\xi_1 - \xi_2)L] \Delta T, \quad (2)$$

where $\int_0^L n_2(z) dz = \bar{n}_2 L$, \bar{n}_2 is the averagely effective RI of the cladding mode; $\alpha = \frac{1}{L} \frac{dL}{dT}$ is the

thermal-expansion coefficient of the FMZI, $\xi_1 = \frac{1}{n_1} \frac{dn_1}{dT}$, and $\xi_2 = \frac{1}{n_2} \frac{dn_2}{dT}$ are the thermal-optic coefficients of the core and cladding modes, respectively. Fig. 4 shows its transmission spectral response to temperature. The transmission spectrum experiences a blue-shift as the temperature increases. Fig. 5 shows the measured relationships between the temperature and wavelength shifts of the resonance dips. There are good linear relationships between the temperature and wavelength shifts. The sensitivities of the left and right resonance dips reach 33.8 and 35.2 pm/°C.

3. MINIATURIZED FFPI AND ITS APPLICATION

Miniaturized FFPI could be fabricated by discharge using a splicer when splicing a hollow core PCF to an SMF. Here, a commercial Fujikura FSM-40PM splicer was used to fabricate the FFPI. The PCF is from NKT Photonics company, with core, pitch and cladding diameters of $10 \mu\text{m} \pm 1 \mu\text{m}$, $3.8 \mu\text{m}$, and $120 \mu\text{m}$, respectively. The cleaning arc time was set to 40 ms to avoid collapsing the core of the HCPCF, and the discharge power and time of the splicer were set to 16.29 mA and 1090 ms, respectively. Fig. 6 shows the typical microscope image of the FFPI. A thin elliptical glass layer is at the end surface of the FFPI. The length of the FFPI is about $210 \mu\text{m}$. The maximum radial diameter of the sphere is about $180 \mu\text{m}$. Fig. 7 shows the typical reflection spectra of the FFPI under different RI values. When the FFPI was dipped in the liquid, there is a sharp insertion loss. The reflectivity of the inner surface between the SMF and the sphere is unchanged while that of the end surface between the sphere and ambient environment is influenced by the ambient RI. The reflectivity of the end surface can be given by $R = \left(\frac{n_e^- n_{amb}}{n_e^+ n_{amb}}\right)^2$, where n_e is the effective core RI of the FFPI at the end surface, and n_{amb} is the RI of the ambient environment. The nearer of n_{amb} to n_e , the smaller R becomes. then the total reflected intensity of the FFPI decreases accordingly. Hence, the insertion loss of the FFPI will be improved as the RI of the ambient environment

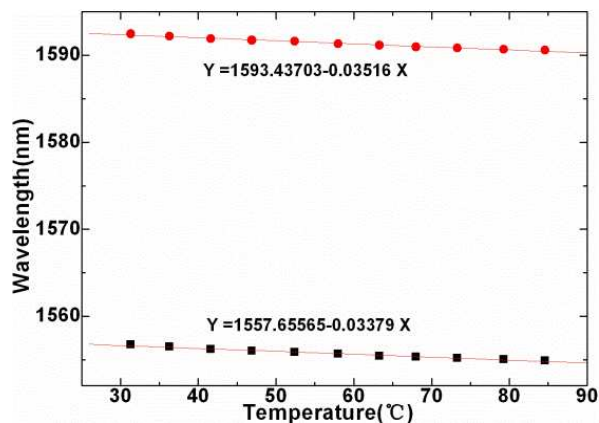


Figure 5: Relationships between the temperature and wavelength shifts of the resonance dips.

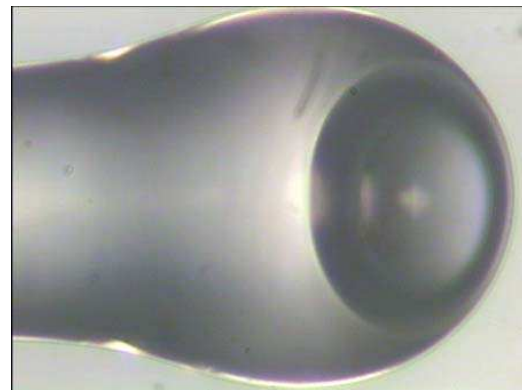


Figure 6: Typical microscope image of the FFPI.

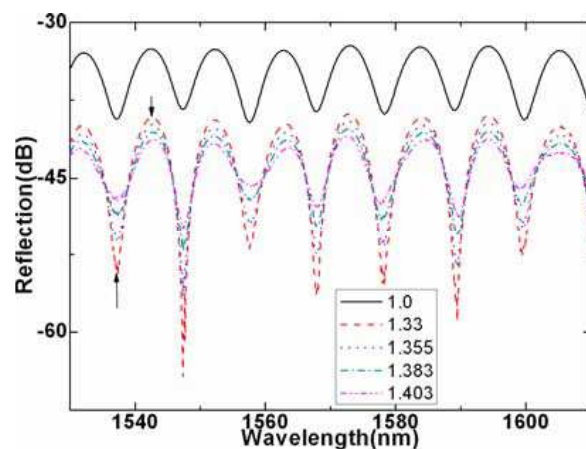


Figure 7: Typical reflection spectra of the FFPI under different RI value.

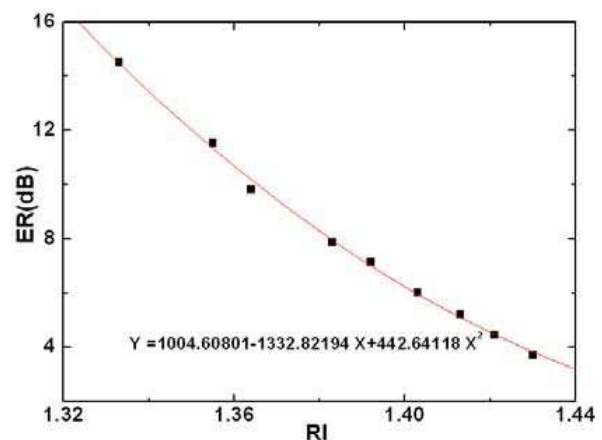


Figure 8: Reflection spectral response to RI.

increases.

Figure 8 shows the measured relationship between the RI and ER of the marked peak to dip in Fig. 7. There is a good quadratic relationship between the ER and RI. The ER changed 10.792 dB from 1.333 to 1.43. Within the RI range of 1.333 \sim 1.403, there is a quasi-linear relationship between the ER and RI. A RI sensitivity of \sim 120.9 dB/RI could be obtained. Under a 0.001 dB amplitude resolution, the RI resolution reaches \sim 8.3×10^{-6} . It should be noted that since the FFPI has the micro-size and hollow cavity structure, it has the advantages of temperature insensitiveness and high stability.

4. CONCLUSIONS

In conclusion, two types of fiber interferometers, FMZI and FFPI, and their applications as fiber sensors were demonstrated. The FMZI could be fabricated by discharge or a point flame. As a temperature sensor, its sensitivity reached 35.2 pm/°C. The FFPI could be fabricated by discharge. As a RI sensor, its RI sensitivity reached \sim 120.9 dB/RI. They are expected to have the other sensing applications, for example, the FMZI could also be used to measure the vibration, RI, strain, etc, while the FFPI could also be used to measure the pressure, vibration, etc.

ACKNOWLEDGMENT

This work is partially supported by the project of Singapore National Research Foundation with grant No. NRF2012EWT-EIRP002-044.

REFERENCES

1. Ni, K., X. Dong, C. C. Chan, T. Li, L. Hu, and W. Qian, "Miniature refractometer based on Mach-Zehnder interferometer with waist-enlarged fusion bitaper," *Opt. Commun.*, Vol. 292, 84–86, 2013.
2. Chen, N.-K., Y.-H. Hsieh, and Y.-K. Lee, "Tapered fiber Mach-Zehnder interferometers for vibration and elasticity sensing applications," *Opt. Exp.*, Vol. 21, 11209–11214, 2013.
3. Dong, B., D.-P. Zhou, L. Wei, W.-K. Liu, and J. W. Y. Lit, "Temperature and phase-independent lateral force sensor based on a core-offset multimode fiber interferometer," *Opt. Exp.*, Vol. 16, 19291–19296, 2008.
4. Qi, F., L. Hu, X. Dong, and Y. Xin, "A hollow core fiber-based intermodal interferometer for measurement of strain and temperature," *IEEE Sensors J.*, Vol. 13, 3468–3471, 2013.
5. Dong, B. and E. J. Hao, "Core-offset hollow core photonic bandgap fiber based inter-modal interferometer for strain and temperature measurements," *Applied Optics*, Vol. 50, 2949–2957, 2011.
6. Dong, B., J. Hao, T. Zhang, and J. Lim, "High sensitive fiber-optic liquid refractive index tip sensor based on a simple inline hollow glass micro-sphere," *Sensors and Actuators B*, Vols. 171–172, 405–408, 2012.
7. Shi, Q., F. Lv, Z. Wang, L. Jin, J. Hu, Z. Liu, G. Kai, and X. Dong, "Environmentally stable Fabry-PÉrot-type strain sensor based on hollow-core photonic bandgap fiber photonics," *IEEE Photon. Tech. Lett.*, Vol. 20, 237–239, 2008.
8. Dong, B., J. Hu, Z. Chen, and C. Yu, "Long distance fiber sensor system based on the second-order Raman pump and amplification," *Applied Physics B*, Vol. 108, 57–60, 2012.
9. Dong, B., N.-K. Chen, G.-L. Cheng, C. Yu, and Y. Gong, "Optical pump induced thermal sensitivity reduction in a minimized Er/Yb-codoped-fiber Mach-Zehnder interferometer," *IEEE/OSA Journal of Lightwave Technology*, Vol. 32, No. 5, 917–921, 2014.

A Universal Method for Constructing N -port Non-blocking Optical Router Based on 2×2 Optical Switch

Qiaoshan Chen, Fanfan Zhang, Ruiqiang Ji, Lei Zhang, and Lin Yang

State Key Laboratory on Integrated Optoelectronics
Institute of Semiconductors, Chinese Academy of Sciences, China

Abstract— We propose a universal method for constructing N -port non-blocking optical router fully based on 2×2 optical switches. The proposed optical router has fewer optical switches and lower power-consumption.

1. INTRODUCTION

With CMP continuously requiring more communication bandwidth, metallic-based electrical network-on-chip (NoC) gradually becomes the bottleneck for improving the performance of CMP due to its high power consumption, limited bandwidth and long latency [1]. Photonic NoC is considered as a potential solution to overcome the limitations of its electrical counterpart. Many topologies for photonic NoCs have been widely studied, such as Mesh, Torus, Crossbar, Fat-Tree and Clos. The optical router is located at each node of photonic NoC and connects the local processing core with other processing cores. Several nonblocking optical routers have been proposed or even demonstrated [2–5], which are not scalable. High-radix non-blocking optical routers have potential applications in the future on-chip optical interconnects, such as Cluster-Mesh and Clos photonic NoCs. We also propose a general guideline for designing the N -port non-blocking optical router based on MR optical switches [5]. Although MR optical switch or M-Z optical switch can manipulate two optical links simultaneously, most reported optical routers fully or partly utilize them as 1×2 optical switches. In this paper, we propose a universal method for constructing the N -port non-blocking optical router, in which all optical switches behave as 2×2 optical switches.

2. GUIDELINES FOR CONSTRUCTING N -PORT NON-BLOCKING OPTICAL ROUTER

Figure 1 shows the schematics of the M-Z optical switch, the MR optical switch with two parallel waveguides and the MR optical switch with two cross waveguides. Note that the MR optical switch with two parallel waveguides is rearranged so that two input ports are located at one side and two output ports are located at the other side. All three optical switches can be abstracted as a simplified 2×2 optical switch and the details in the dotted box do not affect our discussion on the construction method. One 2×2 optical switch can manipulate two optical links simultaneously.

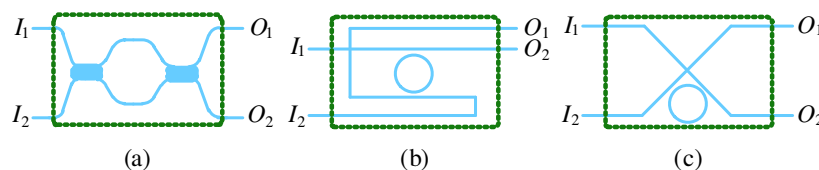


Figure 1: Schematic of (a) M-Z optical switches, (b) the MR optical switch with two parallel waveguides, (c) the MR optical switch with two cross waveguides.

Compared to 1×2 optical switch, 2×2 optical switch manipulate two optical links simultaneously. (see Fig. 2(b)). One 2×2 optical switch can realize the functions of two 1×2 optical switches. If the N -port non-blocking optical router is constructed by 2×2 optical switches, the number of the used optical switches can be reduced by half.

Any N -port non-blocking optical router for photonic NoC must obey the following rules, which have been adopted in the reported optical routers. (1) Communication from the input to the output for the same port is not required. (2) N -port optical router should be non-blocking in order to avoid link contentions. (3) For an N -port non-blocking optical router, light injected into the input of one port must be able to be guided to any output of the other $(N - 1)$ ports.

According to the guidelines mentioned above, if the N -port non-blocking optical router is constructed by 2×2 optical switches, $N(N - 2)/2$ optical switches are required if N is an even number

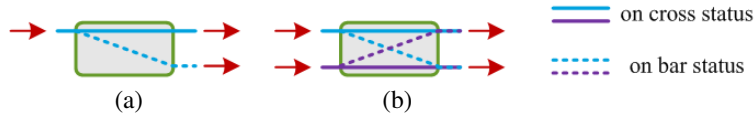


Figure 2: (a) 1×2 optical switch and (b) 2×2 optical switch.

and at least $(N - 1)^2/2$ optical switches are required if N is an odd number. N waveguides are required. Since the number of the used optical switches is dependent on the parity of N , we firstly introduce the simplest two optical routers when N is an odd and even number, respectively, and then introduce the expanding method from the $(N - 2)$ -port non-blocking optical router to the N -port non-blocking optical router. It should be noted that the expanding method for the N -port non-blocking optical router does not depend on the parity of N although the start point is different when N is an odd or even number.

Table 1 shows the schematics of the 3- and 4-port optical routers. The 3-port optical router has two routing states and the 4-port optical router has nine routing states. To demonstrate their non-blocking routing, all of the possible cases are listed in the Table 1. Clearly, the 3- and 4-port optical routers are non-blocking and their optical links obey the aforementioned rules.

Table 1: Schematics of the 3- and 4-port optical routers and their routing tables.

3-port optical router			4-port optical router																																																																										
<table border="1"> <thead> <tr> <th>State</th> <th>Optical links</th> <th>S_1</th> <th>S_2</th> </tr> </thead> <tbody> <tr> <td>1</td> <td>$I_1 \rightarrow O_2, I_2 \rightarrow O_3, I_3 \rightarrow O_1$</td> <td>Cross</td> <td>Bar</td> </tr> <tr> <td>2</td> <td>$I_1 \rightarrow O_3, I_2 \rightarrow O_1, I_3 \rightarrow O_2$</td> <td>Bar</td> <td>Cross</td> </tr> </tbody> </table>	State	Optical links	S_1	S_2	1	$I_1 \rightarrow O_2, I_2 \rightarrow O_3, I_3 \rightarrow O_1$	Cross	Bar	2	$I_1 \rightarrow O_3, I_2 \rightarrow O_1, I_3 \rightarrow O_2$	Bar	Cross	<table border="1"> <thead> <tr> <th>State</th> <th>Optical links</th> <th>S_1</th> <th>S_2</th> <th>S_3</th> <th>S_4</th> </tr> </thead> <tbody> <tr> <td>1</td> <td>$I_1 \rightarrow O_2, I_2 \rightarrow O_3, I_3 \rightarrow O_4, I_4 \rightarrow O_1$</td> <td>Cross</td> <td>Cross</td> <td>Bar</td> <td>Cross</td> </tr> <tr> <td>2</td> <td>$I_1 \rightarrow O_3, I_2 \rightarrow O_4, I_3 \rightarrow O_1, I_4 \rightarrow O_2$</td> <td>Bar</td> <td>Cross</td> <td>Cross</td> <td>Bar</td> </tr> <tr> <td>3</td> <td>$I_1 \rightarrow O_4, I_2 \rightarrow O_1, I_3 \rightarrow O_2, I_4 \rightarrow O_3$</td> <td>Cross</td> <td>Bar</td> <td>Cross</td> <td>Cross</td> </tr> <tr> <td>4</td> <td>$I_1 \rightarrow O_2, I_2 \rightarrow O_1, I_3 \rightarrow O_4, I_4 \rightarrow O_3$</td> <td>Cross</td> <td>Cross</td> <td>Cross</td> <td>Cross</td> </tr> <tr> <td>5</td> <td>$I_1 \rightarrow O_2, I_2 \rightarrow O_4, I_3 \rightarrow O_1, I_4 \rightarrow O_2$</td> <td>Bar</td> <td>Cross</td> <td>Cross</td> <td>Cross</td> </tr> <tr> <td>6</td> <td>$I_1 \rightarrow O_3, I_2 \rightarrow O_4, I_3 \rightarrow O_2, I_4 \rightarrow O_1$</td> <td>Bar</td> <td>Cross</td> <td>Bar</td> <td>Bar</td> </tr> <tr> <td>7</td> <td>$I_1 \rightarrow O_3, I_2 \rightarrow O_1, I_3 \rightarrow O_4, I_4 \rightarrow O_2$</td> <td>Cross</td> <td>Cross</td> <td>Cross</td> <td>Bar</td> </tr> <tr> <td>8</td> <td>$I_1 \rightarrow O_4, I_2 \rightarrow O_3, I_3 \rightarrow O_2, I_4 \rightarrow O_1$</td> <td>Bar</td> <td>Bar</td> <td>Bar</td> <td>Bar</td> </tr> <tr> <td>9</td> <td>$I_1 \rightarrow O_4, I_2 \rightarrow O_3, I_3 \rightarrow O_1, I_4 \rightarrow O_2$</td> <td>Bar</td> <td>Bar</td> <td>Cross</td> <td>Bar</td> </tr> </tbody> </table>					State	Optical links	S_1	S_2	S_3	S_4	1	$I_1 \rightarrow O_2, I_2 \rightarrow O_3, I_3 \rightarrow O_4, I_4 \rightarrow O_1$	Cross	Cross	Bar	Cross	2	$I_1 \rightarrow O_3, I_2 \rightarrow O_4, I_3 \rightarrow O_1, I_4 \rightarrow O_2$	Bar	Cross	Cross	Bar	3	$I_1 \rightarrow O_4, I_2 \rightarrow O_1, I_3 \rightarrow O_2, I_4 \rightarrow O_3$	Cross	Bar	Cross	Cross	4	$I_1 \rightarrow O_2, I_2 \rightarrow O_1, I_3 \rightarrow O_4, I_4 \rightarrow O_3$	Cross	Cross	Cross	Cross	5	$I_1 \rightarrow O_2, I_2 \rightarrow O_4, I_3 \rightarrow O_1, I_4 \rightarrow O_2$	Bar	Cross	Cross	Cross	6	$I_1 \rightarrow O_3, I_2 \rightarrow O_4, I_3 \rightarrow O_2, I_4 \rightarrow O_1$	Bar	Cross	Bar	Bar	7	$I_1 \rightarrow O_3, I_2 \rightarrow O_1, I_3 \rightarrow O_4, I_4 \rightarrow O_2$	Cross	Cross	Cross	Bar	8	$I_1 \rightarrow O_4, I_2 \rightarrow O_3, I_3 \rightarrow O_2, I_4 \rightarrow O_1$	Bar	Bar	Bar	Bar	9	$I_1 \rightarrow O_4, I_2 \rightarrow O_3, I_3 \rightarrow O_1, I_4 \rightarrow O_2$	Bar	Bar	Cross	Bar
State	Optical links	S_1	S_2																																																																										
1	$I_1 \rightarrow O_2, I_2 \rightarrow O_3, I_3 \rightarrow O_1$	Cross	Bar																																																																										
2	$I_1 \rightarrow O_3, I_2 \rightarrow O_1, I_3 \rightarrow O_2$	Bar	Cross																																																																										
State	Optical links	S_1	S_2	S_3	S_4																																																																								
1	$I_1 \rightarrow O_2, I_2 \rightarrow O_3, I_3 \rightarrow O_4, I_4 \rightarrow O_1$	Cross	Cross	Bar	Cross																																																																								
2	$I_1 \rightarrow O_3, I_2 \rightarrow O_4, I_3 \rightarrow O_1, I_4 \rightarrow O_2$	Bar	Cross	Cross	Bar																																																																								
3	$I_1 \rightarrow O_4, I_2 \rightarrow O_1, I_3 \rightarrow O_2, I_4 \rightarrow O_3$	Cross	Bar	Cross	Cross																																																																								
4	$I_1 \rightarrow O_2, I_2 \rightarrow O_1, I_3 \rightarrow O_4, I_4 \rightarrow O_3$	Cross	Cross	Cross	Cross																																																																								
5	$I_1 \rightarrow O_2, I_2 \rightarrow O_4, I_3 \rightarrow O_1, I_4 \rightarrow O_2$	Bar	Cross	Cross	Cross																																																																								
6	$I_1 \rightarrow O_3, I_2 \rightarrow O_4, I_3 \rightarrow O_2, I_4 \rightarrow O_1$	Bar	Cross	Bar	Bar																																																																								
7	$I_1 \rightarrow O_3, I_2 \rightarrow O_1, I_3 \rightarrow O_4, I_4 \rightarrow O_2$	Cross	Cross	Cross	Bar																																																																								
8	$I_1 \rightarrow O_4, I_2 \rightarrow O_3, I_3 \rightarrow O_2, I_4 \rightarrow O_1$	Bar	Bar	Bar	Bar																																																																								
9	$I_1 \rightarrow O_4, I_2 \rightarrow O_3, I_3 \rightarrow O_1, I_4 \rightarrow O_2$	Bar	Bar	Cross	Bar																																																																								

Figure 3 illustrates the expanding method from the $(N - 2)$ -port optical router to the N -port optical router. Two waveguides and $2(N - 2)$ optical switches are added to the $(N - 2)$ -port optical router. When N is an odd number, the 5-, 7-, ..., $(N - 2)$ - and N -port optical routers can be constructed successively based on the 3-port optical router by the expanding method. When N is an even number, 6-, 8-, ..., $(N-2)$ - and N -port optical routers can be constructed successively based on the 4-port optical router by the expanding method.

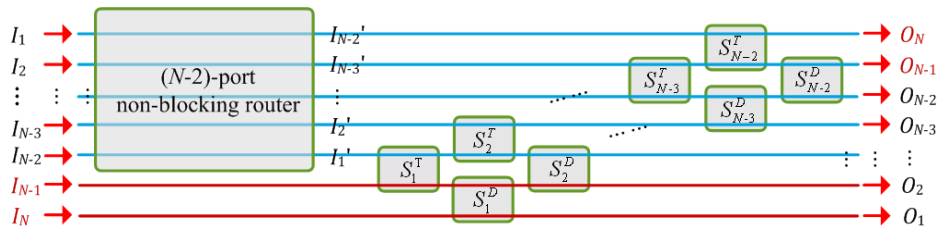


Figure 3: Expanding method from the $(N - 2)$ -port non-blocking optical router to the N -port non-blocking optical router.

Following the expanding method, the 5-port optical router can be constructed by adding two waveguides and six optical switches ($S_3, S_4, S_5, S_6, S_7, S_8$) to the 3-port optical router and the 6-port optical router can be constructed by adding two waveguides and eight optical switches ($S_5,$

$S_6, S_7, S_8, S_9, S_{10}, S_{11}, S_{12}$) to the 4-port optical router (see Figs. 4(a) and 4(b)). The 5-port optical router has 44 routing states and the 6-port optical router has 265 routing states. In order to check whether blocking occurs or not, we exhaust all optical links in each routing state and find that the 5- and 6-port optical routers are non-blocking. The 5- and 6-port optical routers have 8 and 12 optical switches respectively, which 50% less than the reported optical routers based on MR optical switches [28–32].

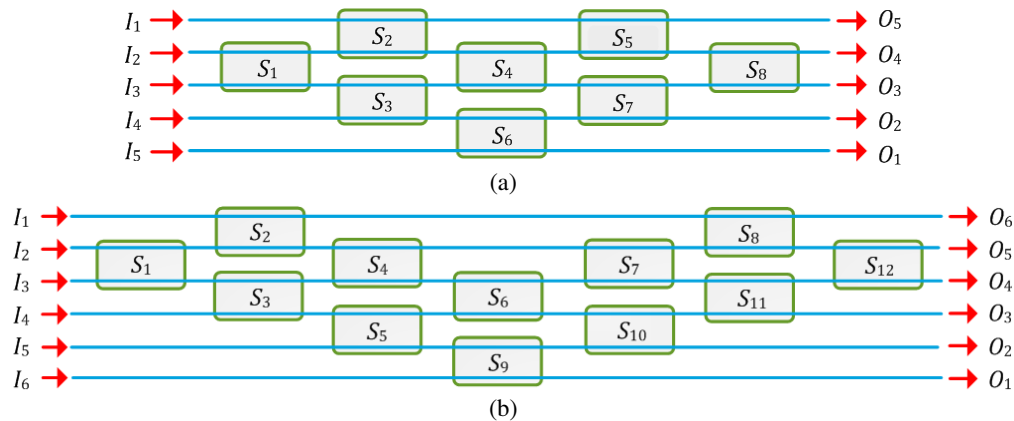


Figure 4: Schematics of the 5- and 6-port non-blocking optical routers.

Since all input ports are arranged on one side and all output ports are arranged on the other side for the reported optical router based on M-Z optical switch [24], we can compare the proposed optical router with it directly. Since the input and output for one specific port of the reported optical routers based on MR optical switches are arranged in the same physical address [25–31], we replace all 2×2 optical switches in the proposed optical routers by MR optical switches and arrange their input and output for one specific port in the same physical address. To facilitate expression, we define the propagation losses of the 2×2 optical switch on the “cross” and “bar” statuses as X_c and X_b respectively, the propagation loss of the waveguide cross as Y , the tuning power consumption of a 2×2 optical switch as P . The average power consumption of the proposed 5-port optical router is at least 28% less than the reported 5-port optical routers. All optical routers have small difference in average insertion loss and worst-case insertion loss. We can conclude that fully adopting 2×2 optical switches in the optical router can reduce its average power consumption and footprint without sacrificing its insertion loss. Tables 2 and 3 show the comparisons of the proposed 4- and 5-port optical routers with the reported 4- and 5-port optical routers.

Table 2: Comparison of the proposed 4-port optical router with the reported 4-port optical routers [6–9].

		Columbia [6]	HKUST [7]	ISCAS-Ji [8]	IBM [9]	This work
Switch		8	8	8	6	4
Average loss	MR	$\frac{24X_c + 8X_b + 40Y}{12}$	$\frac{24X_c + 8X_b + 32Y}{12}$	$\frac{24X_c + 8X_b + 24Y}{12}$		$\frac{16X_c + 8X_b + 36Y}{12}$
	M-Z				$\frac{21X_c + 7X_b + 32Y}{12}$	$\frac{16X_c + 8X_b}{12}$
Worst-case loss	MR	$2X_c + X_b + 4Y$	$2X_c + X_b + 4Y$	$2X_c + X_b + 2Y$		$2X_c + X_b + 4Y$
	M-Z				$2X_c + X_b + 4Y$	$2X_c + X_b$
Power /state		$24P/9$	$24P/9$	$24P/9$	$20P/9$	$16P/9$

The number of the optical switches used by an optical router decides its footprint. The 4- and

Table 3: Comparison of the proposed 5-port optical router with the reported 5-port optical routers [2–5].

	HKUST-Poon [2]	HKUST-Gu [3]	ISCAS-Ji [4]	ISCAS-Min [5]	This work
Switch	20	16	16	15	8
Average loss	$\frac{60X_c + 20X_b + 90Y}{20}$	$\frac{58X_c + 16X_b + 61Y}{20}$	$\frac{59X_c + 16X_b + 68Y}{20}$	$\frac{60X_c + 15X_b + 60Y}{20}$	$\frac{48X_c + 16X_b + 80Y}{20}$
Worst-case loss	$6X_c + X_b + 9Y$	$4X_c + X_b + 6Y$	$4X_c + X_b + 4Y$	$4X_c + X_b + 4Y$	$4X_c + X_b + 6Y$
Power /state	176P/44	176P/44	176P/44	165P/44	119P/44

5-port optical routers constructed by this method use 4 and 8 optical switches respectively, which is about 50% less than the reported optical routers based on MR optical switches and more than 30% less than the reported optical router based on M-Z optical switches.

Power consumption is one critical point for designing photonic NoC. To establish different optical links will require different power consumption for the optical routers. To characterize the power efficiency of the optical routers, we get the average power consumption per routing state by the statistics method. We assume that each routing state occurs with equal probability. 4-port optical router has 9 routing states, each of which comprises four independent links, and 5-port optical router has 44 routing states, each of which comprises five independent links. As shown in Tables 2 and 3, the average power consumption of the proposed 4-port optical router is at least 20% less than the reported 4-port optical routers and the average power consumption of the proposed 5-port optical router is at least 28% less than the reported 5-port optical routers.

Insertion loss is another critical point for designing photonic NoC. Different optical links of an optical router may have different insertion losses. The 4-port non-blocking optical router has 12 optical links and the 5-port non-blocking optical router has 20 optical links. Tables 2 and 3 show the comparisons in average insertion loss and worst-case insertion loss between the proposed 4- and 5-port optical routers and the reported 4- and 5-port optical routers. We find that all optical routers have small difference in average insertion loss and worst-case insertion loss.

Based on the above analysis, we can conclude that fully adopting 2×2 optical switches in the optical router can reduce its average power consumption and footprint without sacrificing its insertion loss.

3. CONCLUSION

We propose a universal method for constructing N -port non-blocking optical router for photonic networks-on-chip, in which all MR optical switches or M-Z optical switches behave as 2×2 optical switch. The optical router constructed by this method has the lowest average power consumption and requires the least theoretical optical switches, in which the number of the optical switches is reduced about 50% compared to the reported optical routers based on MR optical switches and more than 30% compared to the reported optical routers based on M-Z optical switches, and therefore is more compact in footprint.

REFERENCES

1. Briere, M., B. Girodias, Y. Bouchebaba, G. Nicolescu, F. Mieyeville, F. Gaffiot, and I. O. Connor, "System level assessment of an photonics NoC in an MPSoC platform," *Design, Automation & Test in Europe Conference & Exhibition*, 1–6, 2007.
2. Poon, A. W., X. Luo, F. Xu, and H. Chen, et al., "Cascaded microresonator-based matrix switch for silicon on-chip optical interconnection," *Proceedings of the IEEE*, Vol. 97, No. 7, July 2009.
3. Gu, H. X., K. H. Mo, J. Xu, et al., "A low-power low-cost optical router for optical networks-on-chip in multiprocessor systems-on-chip," *2009 IEEE Computer Society Annual Symposium on VLSI*, 19–24, 2009.
4. Ji, R., L. Yang, L. Zhang, et al., "Five-port optical router for photonic networks-on-chip," *Opt. Express*, Vol. 19, No. 21, 20258–20268, 2011.

5. Min, R., R. Ji, Q. Chen, L. Zhang, and L. Yang, “A universal method for constructing N-port nonblocking optical router for photonic networks-on-chip,” *J. Lightwave Technol.*, Vol. 30, No. 23, 3736–3741, 2012.
6. Sherwood-Droz, N., H. Wang, L. Chen, B. G. Lee, A. Biberman, K. Bergman, and M. Lipson, “Optical 4×4 hitless silicon router for optical networks-on-chip (NoC),” *Opt. Express*, Vol. 16, No. 20, 15915–15922, 2008.
7. Ye, Y., X. Wu, J. Xu, W. Zhang, M. Nikdast, and X. Wang, “Holistic Comparison of Optical Routers for Chip Multiprocessors,” *Anti-Counterfeiting, Security and Identification (ASID) International Conference*, 1–5, 2012.
8. Ji, R., L. Yang, L. Zhang, Y. Tian, J. Ding, H. Chen, Y. Lu, P. Zhou, and W. Zhu, “Microring-resonator-based four-port optical router for photonic network-on-chip,” *Opt. Express*, Vol. 19, No. 20, 18945–18955, 2011.
9. Yang, M., W. M. J. Green, S. Assefa, J. Van Campenhout, B. G. Lee, C. V. Jahnes, F. E. Doany, C. L. Schow, J. A. Kash, and Y. A. Vlasov, “Non-blocking 4×4 electro-optic silicon switch for on-chip photonic networks,” *Opt. Express*, Vol. 19, No. 1, 47–54, 2011.

Software Defined Networking (SDN) Enabled Optical as a Service (OaaS) with Dynamic Network Provisioning

Yongli Zhao and Jie Zhang

State Key Laboratory of Information Photonics and Optical Communications

Beijing University of Posts and Telecommunications, Beijing 100876, China

Abstract— Optical network has been deployed widely as one of the most important physical infrastructure because of the advantages of high capacity, long transmission distance, and low energy consumption. Then how to exploit the potentiality of optical networks gets more and more attention, especially in the current data center networks. Optical as a service (OaaS) is proposed and designed to provide the optical network resources directly for the data centers with considering both data center and network resources, which can be implemented with software defined networking (SDN). Under SDN enabled OaaS architecture, a new concept of network provisioning is proposed different from legacy connection (lightpath) provisioning, because the client's requests may include not only one end-to-end connection, but also several end-to-end connections, even a network. Also network with edge resources can be provided for the clients. A virtualization engine is designed in SDN enabled OaaS to efficiently complete the network provisioning. As a generalized optimization strategy in SDN enabled OaaS, the cross stratum optimization (CSO) strategy is described by considering both data center and network resource in the paper. Finally the SDN enabled OaaS testbed is demonstrated.

1. INTRODUCTION

With the advent of big data era, data center has become one of the most important application resources, and is necessary to be connected by high bitrate transport networks. Optical networks will be the inevitable choice because of the advantages of high capacity, long transmission distance, and low energy consumption. Then how to exploit the potentiality of optical networks in the current data center networks become more and more important. Because data centers are geographically distributed in different areas, long-haul transmission networks are necessary to delivery such high volume data center traffic. At the same time, with the exponential growth of burst Internet traffic between data centers, the traditional fixed grid optical networks are moving forward to flexi-grid optical networks because of its high spectrum-efficiency and flexibility [1], especially for the super-wavelength application beyond 100 Gbps. Data center interconnected by flexi-grid optical networks is a promising scenario to allocate spectral resources for applications in a dynamic, tunable and efficient control manner [2, 3], because flexi-grid optical networking is capable of ultra-high capacity, bit-rate transparency, distance adaption and low power density, and represent a potentially disruptive solution for overcoming emerging data center network bottlenecks. Inter-data center networking architecture, algorithm and control plane have been addressed in flexible bandwidth optical networks [4, 5].

On the other hand, in order to achieve the optimization of application and network resource, Cross Stratum Optimization (CSO) is proposed [6], which can enable a joint optimization of application and network resources and take the optical as a service (OaaS) [7]. Meanwhile, as centralized control architecture, the Software Defined Networking (SDN) enabled by OpenFlow protocol, has attracted much attention by supporting programmability of network functionalities and protocols [8, 9]. Extension of OpenFlow protocol is necessary to support CSO procedure for meeting the scalability and flexibility requirements, including resource customization and cooperation in dynamic multi-layer networks [10].

With the development of data center networks, the forms of client's requests are frequently changing. The current client's requests may include not only one end-to-end connection, but also several end-to-end connections, even a network in data center networks. Then, the network with edge resources can be provided for the clients together. Network provisioning will become an important request form relative to legacy lightpath provisioning. The dynamic anycast service [11] considering backup resource is one of the typical requests with network provisioning. In the process of network provisioning, no further detailed network information needs to be provided for the client, except the final virtualized network with edge data center resource. SDN will be the best choice of implementation technology because of its overview over heterogeneous network resources.

While resource virtualization is an effective solution to network provisioning. A lot of studies have focused on the mapping problem for resource virtualization [12]. At the same time, the control plane techniques with dynamic and intelligent virtual network provisioning have been coming into view [14]. The concept of network provisioning is proposed in the paper, which is implemented on the software defined networking (SDN) enabled optical as a service (OaaS) testbed.

2. SDN ENABLED OaaS ARCHITECTURE

We propose an OaaS architecture based on SDN as shown in Fig. 1. Two kinds of controllers are included in OaaS, which are network controller (NC) and application controller (AC). The former keeps the resources of multi-layer and multi-domain optical networks, and can provide the virtualized network from the underlying network by virtualization engine introduced in Section 4. While AC maintains the application resources in data centers, takes charge of data center resource scheduling, and triggers the related NC to complete the function of routing and resource allocation. According to the requirement, AC customizes appropriate virtual resources through related NC with extended OpenFlow protocol (OFP). OFP is deployed here as the interface protocol between south and north. Path Computation Element Protocol (PCEP) or OFP can be adopted here as the east and west interfaces in this architecture. For clients, SDN enabled OaaS architecture can be considered as an effective integration solution for resource provisioning, including network and data center resources. Optimal utilization of various resources can be achieved through the cooperation between AC and NC.

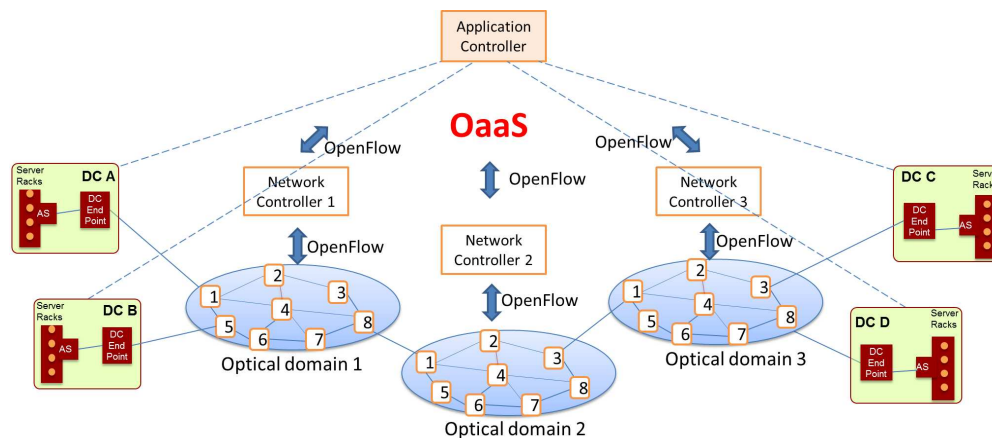


Figure 1: SDN enabled OaaS architecture.

3. NETWORK PROVISIONING

A new form of service request is emerging different from legacy lighpath provisioning, i.e., network provisioning, the meaning of which can be found in Fig. 2. The details are introduced as follows.

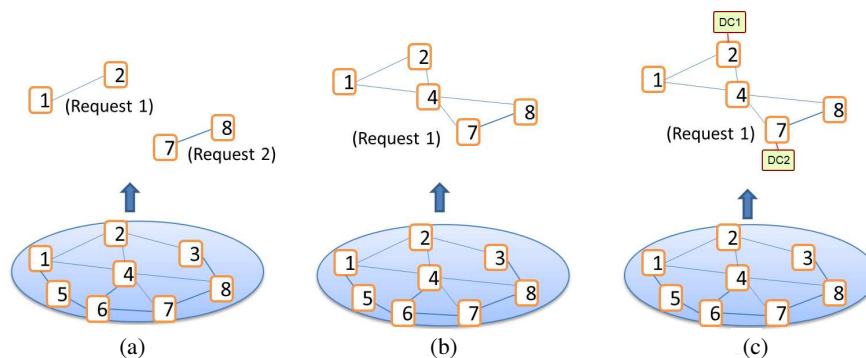


Figure 2: (a) lightpath provisioning, (b) network provisioning, (c) network provisioning with edge resource.

3.1. Lightpath Provisioning

In the traditional optical networks, what the client requests is point-to-point connection or point-to-multi-point connection as shown in Fig. 2(a). Different wavelength resources along different fiber links are provided for the clients. In the process of lightpath provisioning, routing function can choose the most suitable path from the source to the destination by some routing algorithms, such as Dijkstra algorithm and KSP algorithm. Of course, some parameters can be used as the weight value, such as the cost, path length, link delay and available resource. Then the wavelength resource is allocated for the request along the route by some wavelength assignment policies, such as First Fit (FF) and Random Fit (RF). Finally, an end-to-end lightpath is setup for the service request.

3.2. Network Provisioning

As a new form of dynamic service request, network provisioning requires a network with multiple nodes and links, just like Virtual Private Network (VPN). Also some network performance parameters may be proposed by the clients with the request, such as the latency, security, and robustness. A network with available resources and meeting the requirement above must be provided dynamically by the operator. No further detailed information about the network is necessary for the clients. But the operator must consider how to provide the network resource, not only meeting the client's requirement, but also considering the cost. Some routing algorithms can be deployed to finish the path computation between more than one node pairs. Then the wavelength resources are allocated for different connections on the network topology. Whether the wavelength continuity constraint is considered or not here depends on the network equipment. Resource mapping between the point-to-point request and physical topology must be considered in the process.

3.3. Network Provisioning with Edge Resource

For some requests, both the network resource and the application resource should be provided. This is a new request form, which we can name network provisioning with edge resource. Then, how to implement this function will be the main focus of the IT and network operator. Generally, the edge resource can be selected first according to some considerations, such as backup and traffic load balancing. And then a networking provisioning request emerges, which can be handled with the method mentioned in Subsection 3.2. Of course, some other methods can be used to meet this kind of request. For example, we can consider both application resource and network resource at the same time, and allocate the resource according to a comprehensive evaluation index, which is the key idea of Cross Stratum Optimization (CSO).

4. VIRTUALIZATION ENGINE EMBEDDED IN OaaS

In order to finish the network provisioning effectively, a virtualization engine is designed under SDN enabled OaaS architecture as shown in Fig. 3. The physical infrastructure in current data center networks consists of facilities in different network domains, e.g., optical transport networks, IP WAN, data centers, etc.. One or more Domain Virtualization Engines (DVE) can be deployed for each domain, and act as special network controllers to slice, partition or aggregate the controlled network or application resources. DVEs could be connected to controllers to provide virtual single-domain topologies, be cascaded recursively, or be aggregated to a high-level one called Infrastructure Virtualization Engine (IVE), which collects resource information of different domains from each DVE or directly from each domain, and can provide VIs to renter's controllers with various kinds of resource forms to meet different demands.

5. CROSS STRATUM OPTIMIZATION STRATEGY IN OaaS

The CSO of application and network resources can be realized under the unified control architecture based on SDN enabled OaaS as depicted in Fig. 4(a) by cross stratum virtualization (CSV) approach. According to the requirement, AC customizes appropriate virtual resources through related NC with extended OFP. In addition, dynamic global load balancing strategy (DGLB) can be implemented based on both application and network resources, while NC can trigger service-aware PCE algorithm (SA-PCE) based on the result of DGLB. NC interacts with each other for the security and virtual network information. OpenFlow enabled routers and optical transport nodes are realized by extending match domain in OFP. The responsibilities and interactions among entities are provided as shown in Fig. 4(b).

When OpenFlow parser (OP) receives a new flow, it will map it into request parameters and

forward it to server selection engine (SSE). The certified request is transmitted to application resource virtualization module (ARVM). ARVM provides SSE with the suitable application resource from data center network, while SSE customizes virtual network information from SC through secondary CSV. After completing DGLB, SSE chooses the most optimal server or virtual machine (VM) for users, allocates application resources and determines the location of application. According to the result, AC transmits application requirements to related SCs via OP. When data process (DP) in SCs receives the location of the server/VM and service type, it will translate this profile into connection and service parameters, such as bandwidth, delay and jitter, and forwards this profile to path computation element (PCE). Then extended OpenFlow module (EOM) assigns the wavelength resource in the optical networks.

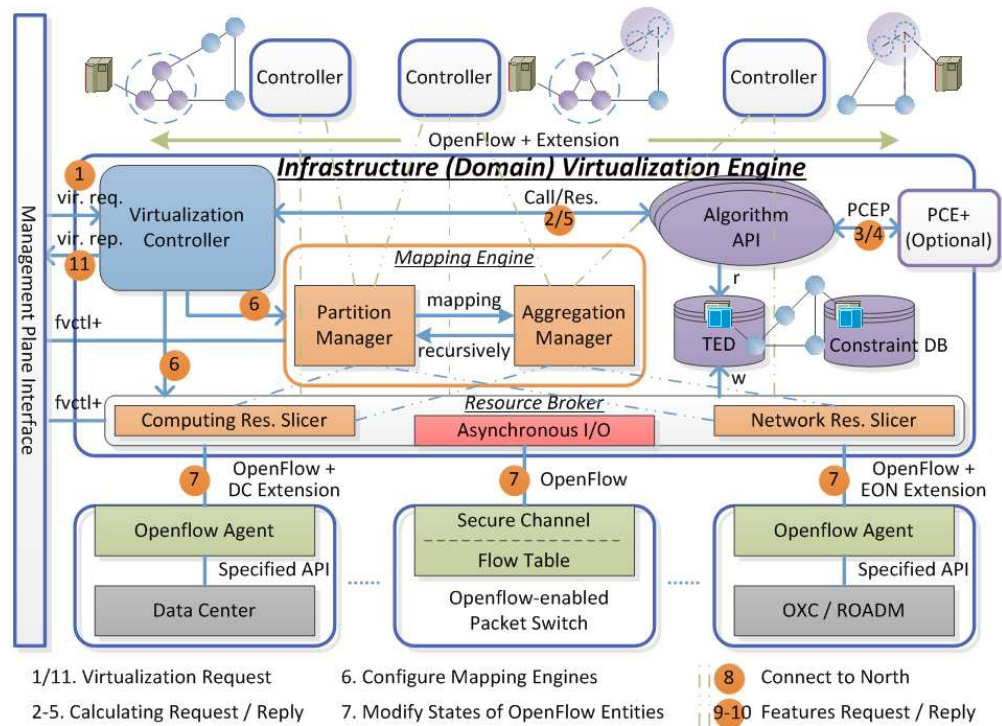


Figure 3: The composition block diagram of virtualization engine.

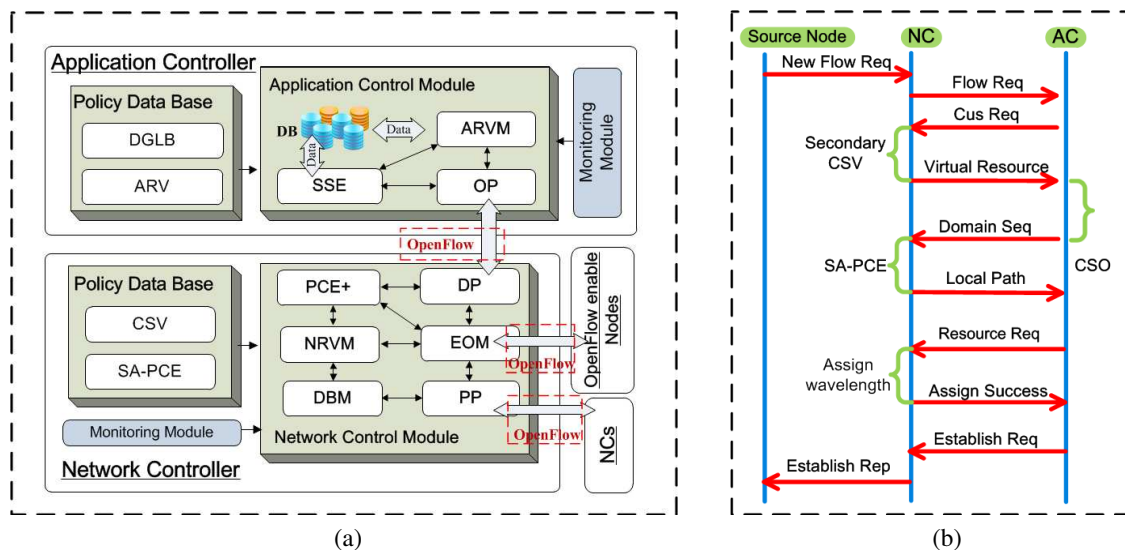


Figure 4: (a) Module diagram, (b) CSO procedure.

6. NETWORK PROVISIONING ON SDN ENABLED OaaS TESTBED

The OaaS architecture has been evaluated on the testbed [13]. Four OpenFlow-enabled Flexi-Grid optical nodes are equipped with OTN equipment, each of which comprises flex ROADM and ODU cards. DCs and the other nodes are realized on an array of virtual machines created by VMware software running on IBM X3650 servers. Since each virtual machine has the operation system and its own independent IP address, CPU and memory resource, it can be considered as a real node. The virtual OS technology makes it easy to set up experiment topology based on the backbone of US which comprises 14 nodes and 21 links. For OpenFlow-based SDN control plane, the NC is assigned to support the proposed architecture and deployed in three servers for spectrum control, physical layer parameter adjustment, PCE computation and resource abstraction, while the database server are responsible for maintaining traffic engineering database, management information base, connection status and the configuration of the database and transport resources.

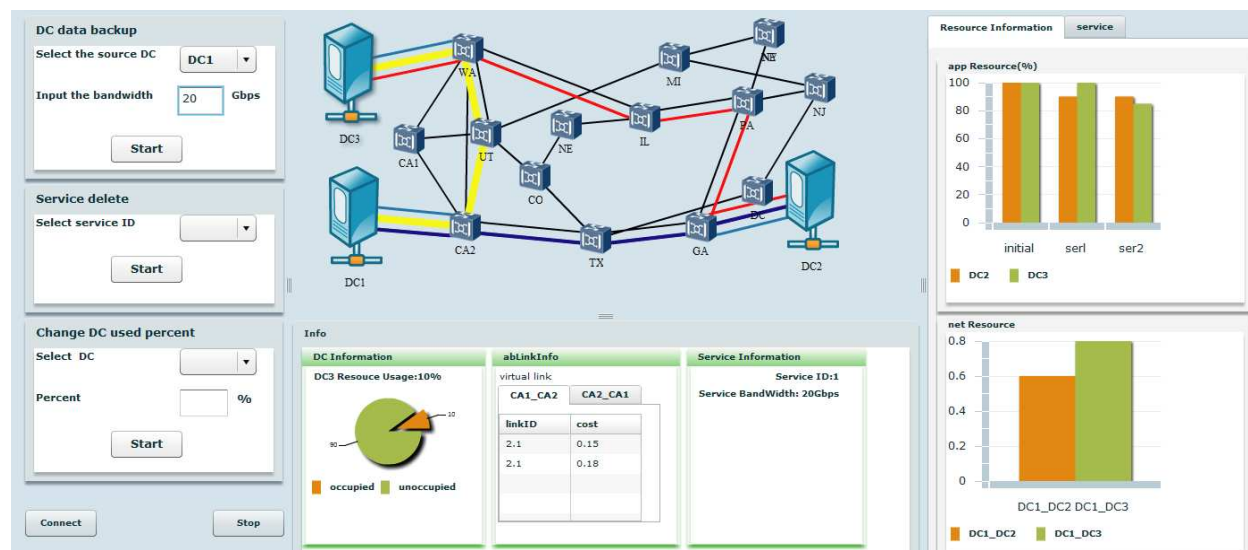


Figure 5: Application graphical user interface (GUI) of testbed.

We have designed and verified experimentally network provisioning in SDN over Flexi-Grid optical networks for Anycast service with backup consideration. The experimental results are shown in Fig. 5. The destination DC is determined by AC with CSO strategy based on various application utilizations among DCs and current network resource. The lightpath for the network provisioning is setup from source to destination node. Additionally, the spectrum bandwidth and corresponding modulation format can be tunable according to different lightpath distances. Fig. 5 verifies the status and destination node choice of data center and various bandwidths of lightpaths in application interface of SDN. The average mean time of network provisioning including three or four paths is about 200 ms, including the time of path computation, resource allocation, and lightpath establishment. The extended flow table modification message for network provisioning setup can be captured with some software tools like Wireshark.

7. CONCLUSIONS

SDN enabled OaaS architecture has been designed as an effective solution for data center networking, which can make full use of network resource and data center resource by considering them together through CSO strategy. Network provisioning is proposed compared with lightpath provisioning. As a new dynamic request form, network provisioning can provide the client with a complete network, which has enough bandwidth resource, required good performance, even enough edge resources. A virtualization engine is designed in this architecture to implement network provisioning with partition manager or aggregation manager. The cross stratum optimization (CSO) strategy is introduced in this architecture to optimize the utilization of network resource and data center resource, which is also implemented in SDN enabled OaaS Testbed as described.

ACKNOWLEDGMENT

This work has been supported in part by 973 program (2010CB328204), 863 program (2012AA0113-01), NSFC project (61201154, 60932004), Ministry of Education-China Mobile Research Foundation (MCM20130132), and Beijing Higher Education Young Elite Teacher Project

REFERENCES

1. Jinno, M., et al., "Spectrum-efficient and scalable elastic optical path network: Architecture, benefits, and enabling technologies," *IEEE Communications Magazine*, Vol. 47, 66–73, Nov. 2009.
2. Rofoee, B. R., et al., "Network-on-and-off-chip architecture on demand for flexible optical intra-datacenter networks," *ECOC 2012*, Amsterdam, The Netherlands, Sep. 2012.
3. Tatsumi, T., et al., "Disruption minimized spectrum defragmentation in elastic optical path networks that adopt distance adaptive modulation," *ECOC 2011*, Geneva, Switzerland, Sep. 2011.
4. Yoo, S. J. B., Y. Yin, and K. Wen, "Intra and inter datacenter networking: The role of optical packet switching and flexible bandwidth optical networking," *ONDM 2012*, Colchester, England, Apr. 2012.
5. Kachris, C. and I. Tomkos, "Energy-efficient bandwidth allocation in optical OFDM-based data center networks," *OFC 2012*, Los Angeles, USA, Mar. 2012.
6. H. Yang, Y. Zhao, et al., "Cross stratum optimization of application and network resource based on global load balancing strategy in dynamic optical networks," *OFC 2012*, Los Angeles, USA, Mar. 2012.
7. Zhao, Y., H. Yang, J. Zhang, J. Zhang, Y. Lin, and Y. Lee, "Experimental demonstration of optical as a service (OaaS) based on openflow," *OECC 2012*, Busan, Korea, Jul. 2012.
8. Liu, L., T. Tsuritani, et al., "Openflow-based wavelength path control in transparent optical networks: A proof-of-concept demonstration," *ECOC 2011*, Switzerland, Geneva, Sep. 2011.
9. Das, S., G. Parulkar, et al., "Packet and circuit network convergence with openflow," *OFC 2010*, San Diego, CA, USA, Mar. 2010.
10. Liu, L., R. Casellas, et al., "Interworking between openflow and PCE for dynamic wavelength path control in multi-domain WSON," *OFC 2012*, Los Angeles, USA, Mar. 2012.
11. She, Q., et al., "Survivable traffic grooming for anycasting in WDM mesh networks," *GlobeCom 2007*, Washington, DC, USA, Nov. 26–30, 2007.
12. Peng, S., R. Nejabati, and D. Simeonidou, "Impairment-aware optical network virtualization in single-line-rate and mixed-line-rate WDM networks," *IEEE/OSA Journal of Optical Communications and Networking*, Vol. 5, No. 4, 283–293, 2013.
13. Zhang, J., Y. Zhao, H. Yang, et al., "First demonstration of enhanced software defined networking (eSDN) over elastic grid (eGrid) optical networks for data center service migration," *OFC 2013*, Anaheim, USA, Mar. 2013.

Recent Progress in On-chip Multiplexing/Demultiplexing Silicon Photonic Devices and Technologies

Jian Wang

Wuhan National Laboratory for Optoelectronics, School of Optical and Electronic Information
Huazhong University of Science and Technology, Wuhan, Hubei 430074, China

Abstract— In this paper, we review our recent works in on-chip multiplexing/demultiplexing silicon photonic devices and technologies. On-chip demultiplexing of polarization and wavelength multiplexed OFDM/OQAM 64/128-QAM signals using silicon 2D grating coupler and microring resonators and on-chip two/three mode (de)multiplexing of OFDM 64/128/256-QAM signals using tapered silicon asymmetrical directional couplers are demonstrated in the experiments.

1. INTRODUCTION

The rapid growth of data traffic has driven the increasing demand for employing advanced modulation formats and multiplexing techniques both in optical fiber transmission and photonic signal processing. Various advanced multi-level modulation formats and multiplexing techniques have facilitated improved transmission capacity and processing throughput, including the use of m-ary phase-shift keying (m-PSK), m-ary quadrature amplitude modulation (m-QAM), orthogonal frequency-division multiplexing (OFDM), wavelength-division multiplexing (WDM), and polarization-division multiplexing (PDM) [1, 2]. Although separate bulky devices have been used to enable different (de)multiplexing functions, they cannot meet the demand for compactness, integration and multifunctionality. So one challenge would be to explore compact integrated photonic devices and technologies to enable on-chip multiplexing/demultiplexing.

Silicon-on-insulator (SOI) is an attractive low cost integration platform for fabricating photonic integrated circuits owing to its high index contrast and compatibility with complementary metal-oxide-semiconductor (CMOS) technology [3, 4]. In this scenario, a valuable goal would be to develop on-chip multiplexing/demultiplexing technologies using silicon photonic devices.

In this paper, we review our recent progress in on-chip multiplexing/demultiplexing silicon photonic devices and technologies, including: 1) on-chip polarization and wavelength demultiplexing of OFDM/OQAM m-QAM signals [5]; 2) on-chip two/three mode (de)multiplexing of OFDM m-QAM signals [6].

2. ON-CHIP POLARIZATION AND WAVELENGTH DEMULTIPLEXING OF OFDM/OQAM M-QAM SIGNALS [5]

Figure 1 illustrates the concept and principle of the proposed on-chip polarization and wavelength demultiplexer. As shown in Fig. 1(a), the polarization multiplexed signals are vertically fed into the silicon 2D grating coupler. By adjusting the input polarization state, the x -polarization (X-Pol.) and y -polarization (Y-Pol.) of the polarization multiplexed signal can be respectively coupled into the two waveguides (TE mode) which are connected to the 2D grating coupler, resulting in the polarization demultiplexing. Since each polarization after the polarization demultiplexing can still have multiple wavelength channels, wavelength demultiplexing is then followed. Shown in Fig. 1(b) is a simple scheme of two wavelength demultiplexing (S1: signal 1 at λ_{s1} , S2: signal 2 at λ_{s2}) using two silicon microring resonators with different resonance wavelengths which are equal to the two signal wavelengths (λ_{s1} , λ_{s2}). Those two microring resonators are respectively connected to the two output ports of the 2D grating coupler. The insets in Fig. 1(b) are schematic transmission spectra of through and drop ports of microring resonators. As shown in Fig. 1(b), the drop (through) port of the 1st microring and the through(drop) port of the 2nd microring can demultiplex wavelength λ_{s1} (λ_{s2}). Consequently, on-chip polarization and wavelength demultiplexer is applicable with integrated 2D grating coupler and microring resonators.

We fabricated the silicon photonic device by the electron beam lithography (EBL) and inductively coupled plasma (ICP) etching. An SOI wafer with top silicon layer of 220 nm and SiO₂ layer of 3 μ m was adopted. Fig. 2(a) shows the microscope image of the fabricated on-chip polarization and wavelength demultiplexer which is composed of a 2D grating coupler connected with two microring resonators. Figs. 2(b)–(e) show the scanning electron microscope (SEM) images of the 2D

grating coupler, coupling region between the bus waveguide and bending waveguide of microring resonator, and 1D grating coupler for easy fiber coupling.

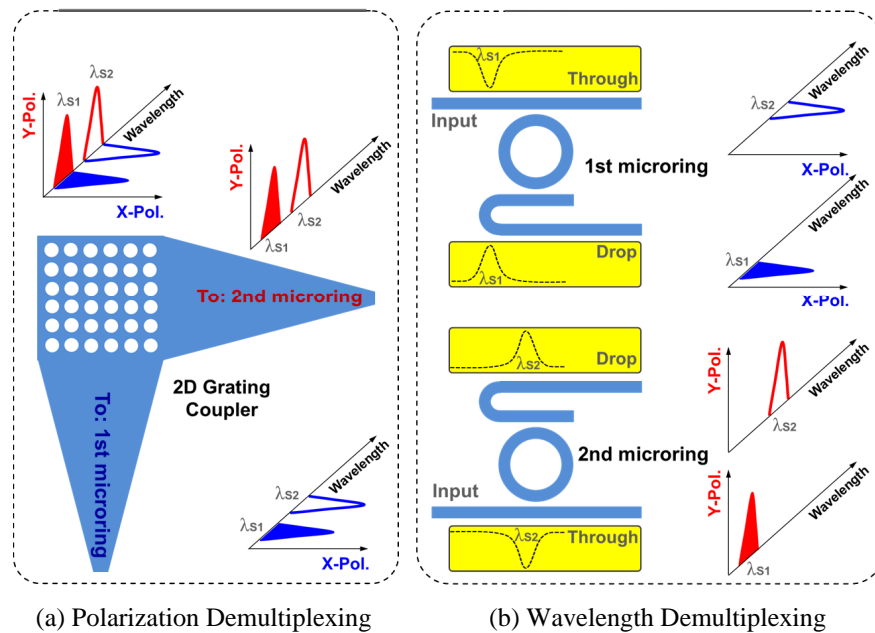


Figure 1: Concept and principle of on-chip demultiplexing of polarization and wavelength multiplexed signals. (a) Polarization demultiplexing using a silicon 2D grating coupler. (b) Wavelength demultiplexing using two silicon microring resonators [5].

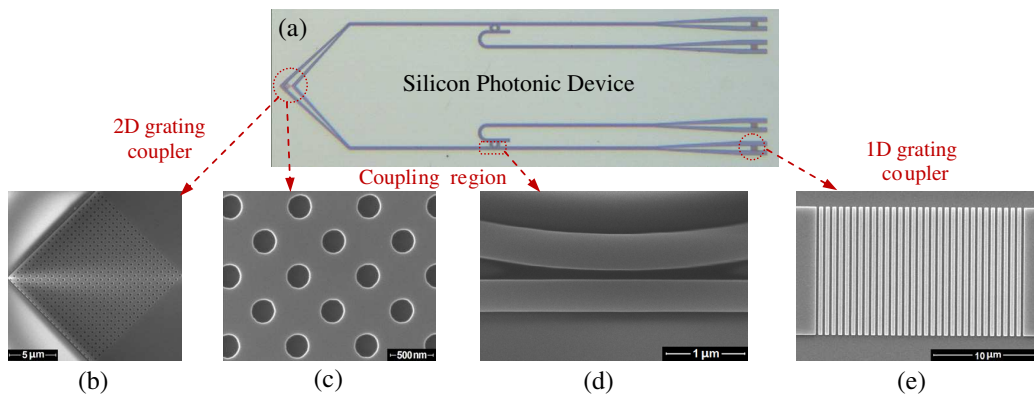


Figure 2: Fabricated silicon photonic device for on-chip simultaneous polarization and wavelength demultiplexing. (a) Microscope image and (b)–(e) SEM images of silicon photonic device. (b) 2D grating coupler. (c) Some of holes in the 2D grating coupler. (d) Coupling region between the bus waveguide and bending waveguide of microring resonator. (e) 1D grating coupler for easy fiber coupling [5].

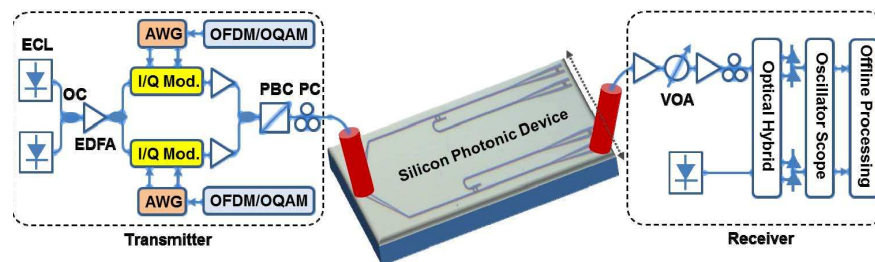


Figure 3: Experimental setup for on-chip demultiplexing of polarization and wavelength multiplexed OFDM/OQAM m-QAM signals. ECL: external cavity laser, EDFA: erbium-doped fiber amplifier, AWG: arbitrary waveform generator, I/Q Mod.: in-phase/quadrature modulator, PBC: polarization beam combiner, PC: polarization controller, VOA: variable optical attenuator [5].

Figure 3 shows the experimental setup for on-chip demultiplexing of polarization and wavelength multiplexed OFDM/OQAM m-QAM signals. At the transmitter, two external cavity lasers (ECL) at 1551.7 and 1554.1 nm are combined, amplified and then equally divided into two parts, each passing through an optical I/Q modulator (I/Q Mod.) to carry OFDM/OQAM signal. Two arbitrary waveform generators (AWGs) at 10 Gs/s are used to produce two single side band (SSB) electrical OFDM/OQAM m-QAM signals, which are respectively fed into the two I/Q modula-

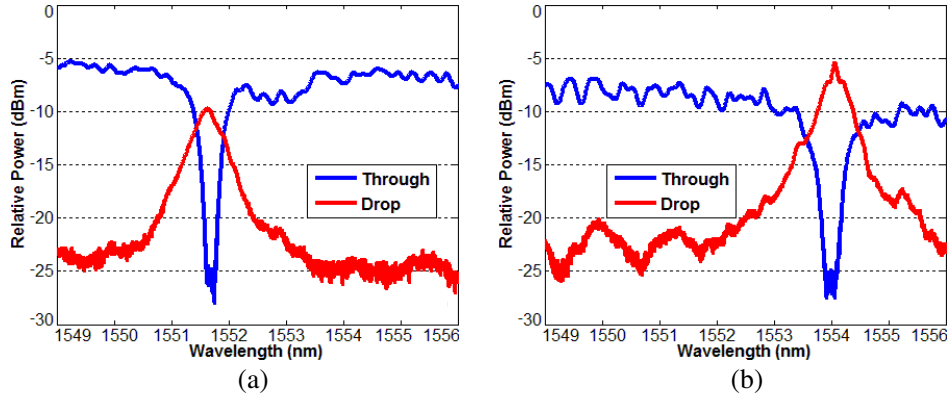


Figure 4: Measured spectra at through and drop ports of the (a) upper and (b) lower microring resonators [5].

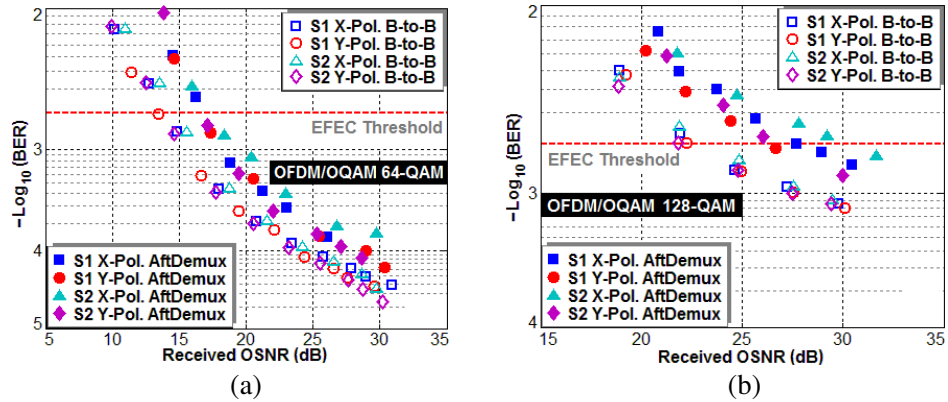


Figure 5: Measured BER performance. (a) OFDM/OQAM 64-QAM signals. (b) OFDM/OQAM 128-QAM signals [5].

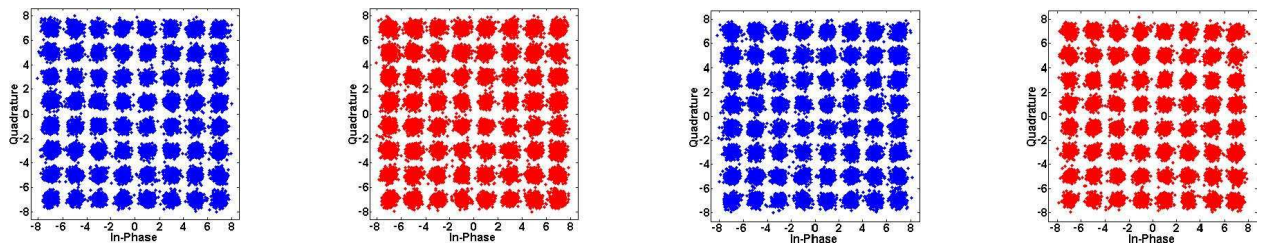


Figure 6: Measured constellations of demultiplexed OFDM/OQAM 64-QAM signals [5].

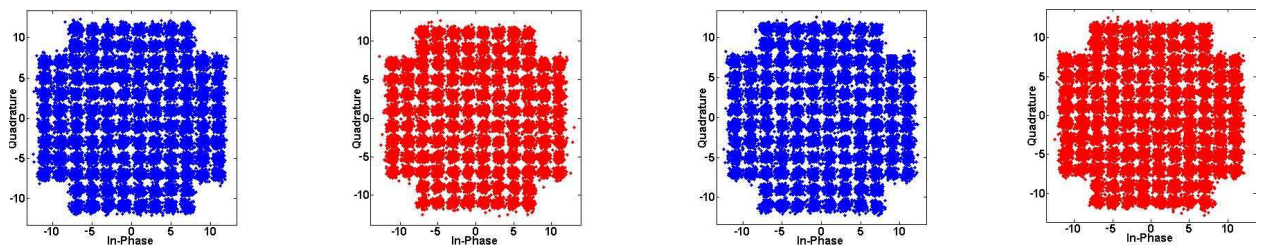


Figure 7: Measured constellations of demultiplexed OFDM/OQAM 128-QAM signals [5].

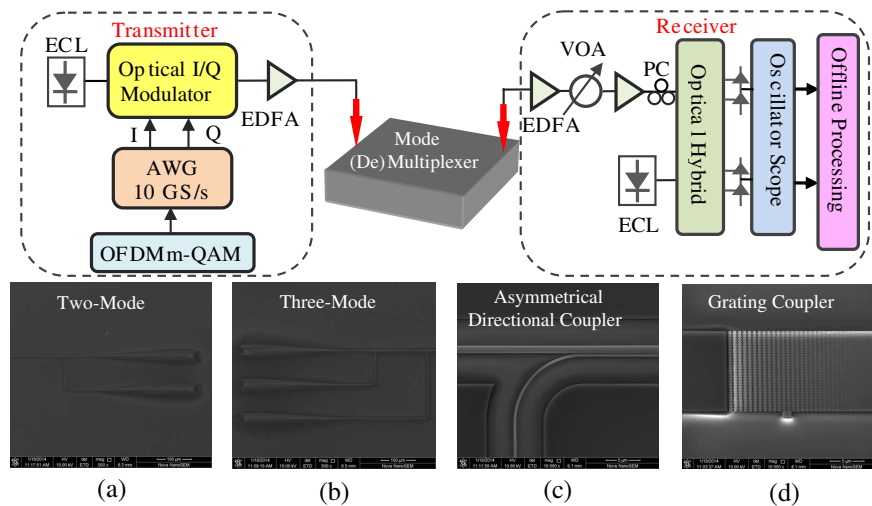


Figure 8: Experimental setup for on-chip two/three mode (de)multiplexing. ECL: external cavity laser, PC: polarization controller, AWG: arbitrary waveform generator, EDFA: erbium-doped fiber amplifier, VOA: variable optical attenuator. (a)–(d) SEM images of two-mode (de)multiplexer, three-mode (de)multiplexer, asymmetrical directional coupler, and apodized grating coupler [6].

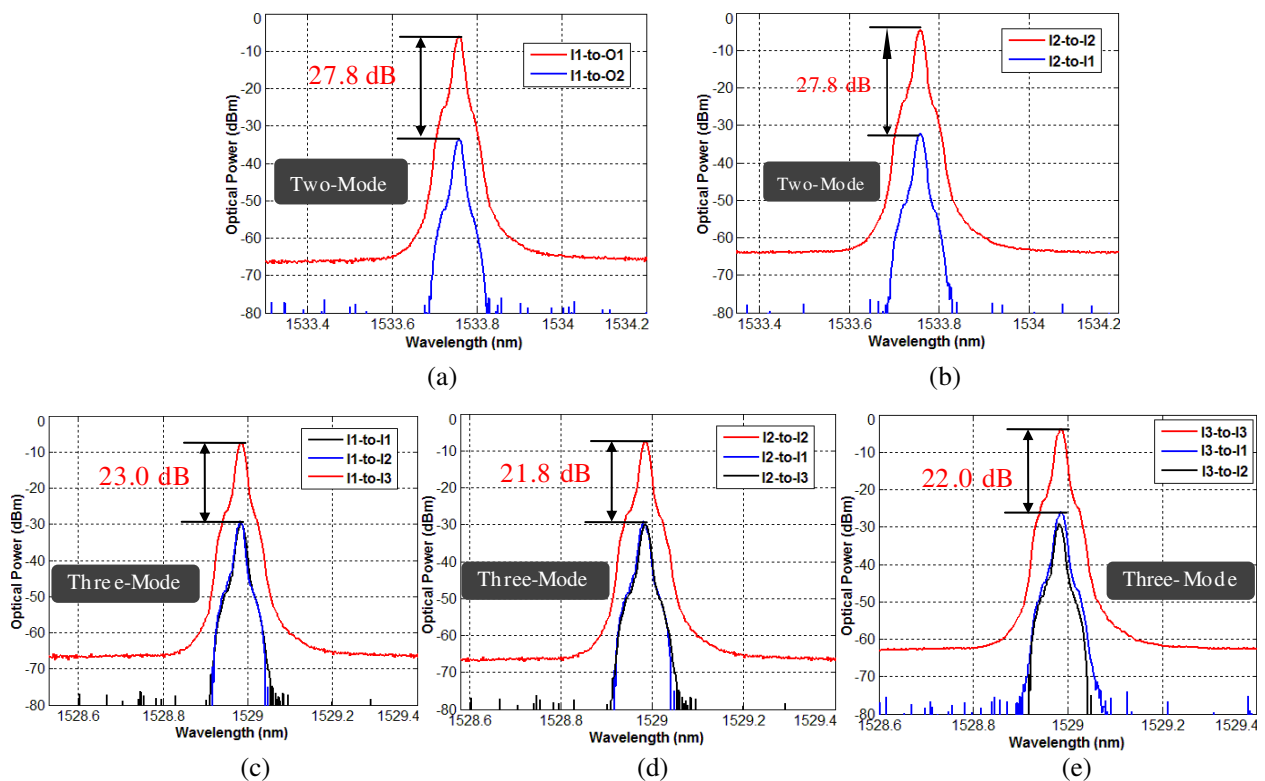


Figure 9: Measured spectra for (a), (b) two-mode (de)multiplexing and (c)–(e) three-mode (de)multiplexing [6].

tors. The OFDM/OQAM baseband signal is constructed with 82 OFDM subcarriers, in which 78 subcarriers are loaded with payloads using m-QAM modulation mapping while 4 subcarriers are selected as pilot subcarriers to estimate the phase noise. The two polarization parts from two I/Q modulators are combined with a polarization beam combiner (PBC) to output polarization and wavelength multiplexed OFDM/OQAM m-QAM signals. Note that all the devices before PBC are polarization maintained. We use vertical fiber coupling system to couple optical signal from fiber to silicon photonic device, and vice versa. A polarization controller (PC) is used to adjust the polarization state of polarization and wavelength multiplexed OFDM/OQAM m-QAM signals, so that two orthogonal polarizations are matched to the TE modes of two waveguides connected to

the 2D grating coupler. At the receiver, a variable optical attenuator (VOA) is applied to adjust the optical signal-to-noise ratio (OSNR). A local oscillator is fed into a coherent receiver to mix with the received signals. The two RF signals corresponding to I/Q components are fed into a Tektronix real-time scope and processed offline.

Figure 4 shows measured transmission spectra at through and drop ports of two microring resonators. One can clearly see that two wavelength demultiplexing (S1: 1551.7 nm, S2: 1554.1 nm) is achievable using these two microring resonators.

Figure 5 plots measured BER performance for on-chip polarization and wavelength demultiplexing. 35.8-Gbit/s OFDM/OQAM 64-QAM and 41.8-Gbit/s OFDM/OQAM 128-QAM signals are employed in the experiment. The observed OSNR penalties at a bit-error rate (BER) of $2e-3$ (enhanced FEC (EFEC) threshold) are less than 4 dB for 35.8-Gbit/s OFDM/OQAM 64-QAM and 6.8 dB for 41.8-Gbit/s OFDM/OQAM 128-QAM. Shown in Figs. 6 and 7 are measured constellations after polarization and wavelength demultiplexing (two polarizations, two wavelengths) for 35.8-Gbit/s OFDM/OQAM 64-QAM and 41.8-Gbit/s OFDM/OQAM 128-QAM signals.

Remarkably, the fabricated on-chip polarization and wavelength demultiplexer can also work in an opposite way, i.e., multiplexing four channels (two polarizations, two wavelengths) into polarization and wavelength multiplexed OFDM/OQAM m-QAM signals. Moreover, several future improvements could be considered as follows: 1) flexibly shifting the resonance of microring resonator by electrical control (carrier injection) or thermal control (thermo-optic effect); 2) integrating more number of microring resonators to enable multiple (> 2) wavelength demultiplexing; 3) incorporating mode-division multiplexing functionality to explore wider applications, e.g., on-chip polarization, wavelength and mode multiplexing/demultiplexing.

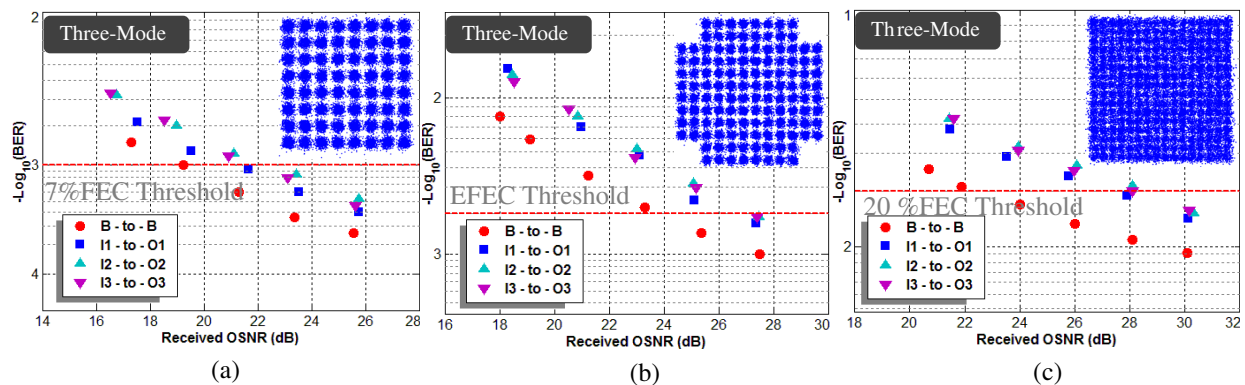


Figure 10: Measured BER curves for three-mode (de)multiplexing of OFDM (a) 64-QAM, (b) 128-QAM and (c) 256-QAM signals [6].

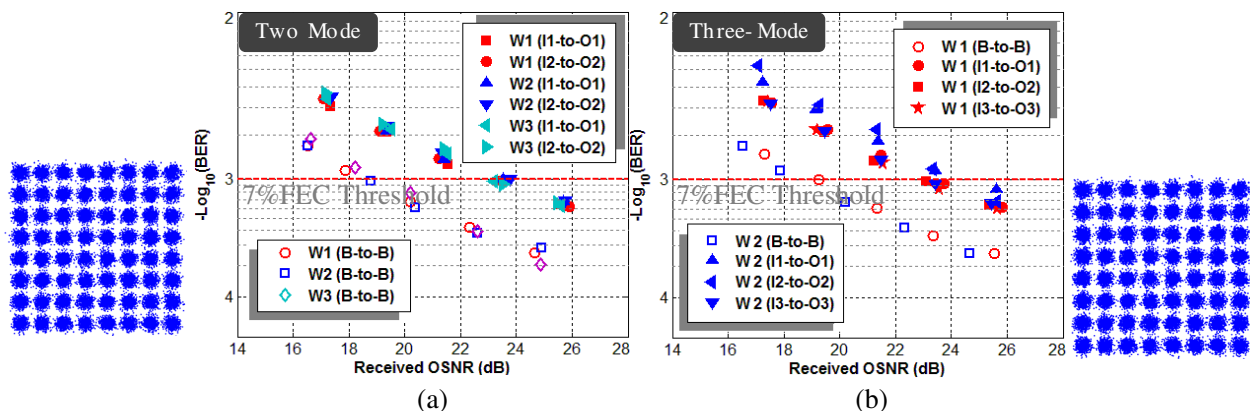


Figure 11: Measured BER curves for two-mode (de)multiplexing (three wavelengths) and three-mode (de)multiplexing (two wavelengths) with OFDM 64-QAM signals. Inserts are constellations [6].

3. ON-CHIP TWO/THREE MODE (DE)MULTIPLEXING OF OFDM M-QAM SIGNALS [6]

Shown in Fig. 8 is the experimental setup for on-chip two/three-mode (de)multiplexing. Fig. 9 shows the measured transmission spectra from inputs (I1, I2, I3) to the demultiplexed outputs (O1, O2, O3), respectively. For two-mode (de)multiplexer, the corresponding mode crosstalk from I1 and I2 to the demultiplexed O2 and O1 is -27.8 and -27.8 dB, respectively. For three-mode (de)multiplexer, the corresponding mode crosstalk from I1, I2 and I3 to the demultiplexed O2/O3, O1/O3 and O1/O2 is -23.0 , -21.8 and -22.0 dB, respectively. Fig. 10 shows measured BER performance of OFDM m-QAM data transmission as a function of received OSNR for three-mode (de)multiplexing. OSNR penalties of 2, 4 and 6 dB are obtained for three-mode (de)multiplexing of OFDM 64-, 128- and 256-QAM signals, respectively.

Additionally, we simultaneously transmit three wavelengths for two-mode (de)multiplexing and two wavelengths for three-mode (de)multiplexing with OFDM 64-QAM signals. The OSNR penalty is less than 4 dB as shown in Fig. 11.

ACKNOWLEDGMENT

This work was supported by the National Natural Science Foundation of China (NSFC) under grants 61222502, 11274131 and 61077051, the Program for New Century Excellent Talents in University (NCET-11-0182), the National Basic Research Program of China (973 Program) under grant 2014CB340004, the Wuhan Science and Technology Plan Project under grant 2014070404010201, the Fundamental Research Funds for the Central Universities (HUST) under grants 2012YQ008 and 2013ZZGH003, and the seed project of Wuhan National.

REFERENCES

1. Winzer, P. J., et al., *LEOS Newsletter*, 4–9, 2009.
2. Zhou, X., et al., *OFC2010*, Paper OMJ3, 2010.
3. Jalali, B., et al., *J. Lightwave Technol.*, Vol. 24, 4600–4615, 2006.
4. Leuthold, J., et al., *Nature Photon.*, Vol. 4, 535–544, 2010.
5. Wang, J., et al., *OFC2014*, paper Th2A.48, 2014.
6. Gui, C. C., et al., *CLEO2014*, paper JTU4A.105, 2014.

Higher-order Ring Resonators and Delayed Interferometers Based on 300-mm SOI Technology for WDM Applications

Seok-Hwan Jeong, Yu Tanaka, and Ken Morito

Photonics Electronics Technology Research Association (PETRA)
AIST West-7SCR, 16-1 Onogawa, Tsukuba, Ibaraki 305-8569, Japan

Abstract— We introduce high-performance Si-nanowire WDM devices based on higher-order coupled resonator optical waveguides (CROW) and multi-stage delayed Mach-Zehnder interferometers (DMZI) fabricated by 300-mm SOI wafer-scale ArF-immersion lithography process. For the two kinds of WDM devices, we experimentally demonstrate low insertion loss, spectral flatness and low crosstalk properties, together with high manufacturing tolerances.

1. INTRODUCTION

Recently, total bandwidth per central processing unit in high-performance servers reaches to a few Tbit/s, which requires advanced optical interconnect technologies based on Si photonics to surpass the limits of transmission bandwidth and power consumption by electric wirings [1]. Wavelength division multiplexing (WDM) would be one of promising technologies to enhance the aggregate bandwidth and to reduce the assembly cost for connecting to optical fibers [2]. WDM optical interconnect normally requires Si-nanowire optical multiplexers/demultiplexers (MUX/DeMUX), from the viewpoint of monolithic integration with compact and energy-efficient Si-nanowire optical modulators and photo-detectors [3]. In almost cases, WDM devices work with the help of the lightwave interference based on the splitting and remixing at multiple optical paths. Thus, their operational performances strongly depend on the controllability of the relative phase relation between all of the optical paths [4, 5]. The phase controllability is mainly determined by the sidewall roughness of Si-nanowire waveguides. 300-mm silicon-on-insulator (SOI) wafer-scale ArF-immersion lithography technologies could be attractive for markedly reducing the phase errors in Si-nanowire waveguides [6]. Here, we report high-performance Si-nanowire waveguide based WDM devices such as higher-order coupled resonator optical waveguides (CROW) and multi-stage delayed Mach-Zehnder interferometer (DMZI) demultiplexers fabricated by phase controllable and highly productive 300-mm silicon-on-insulator (SOI) wafer-scale ArF-immersion lithography process [7, 8]. For the two kinds of WDM devices, we experimentally demonstrate low insertion loss, spectral flatness and low crosstalk properties, together with high manufacturing tolerances.

2. FIFTH-ORDER MICRORING RESONATORS

As a feasibility study of ArF-immersion lithography technology, we designed and fabricated Si-nanowire 5th-order CROW and characterized their spectral characteristics and spectral uniformities on a 300-mm SOI wafer. We demonstrated flat-topped spectral response with an excess loss of only 0.4 ± 0.2 dB and a high out-of-band rejection ratio of > 40 dB. Additionally, good spectral uniformities in intra-dies and inter-dies were achieved.

The 5th-order CROWs were fabricated on a 300-mm SOI wafer with a 0.22- μ m-thick Si core layer and a 2- μ m-thick buried oxide layer through ArF-immersion lithography process in National Institute of Advanced Industrial Science and Technology. Fig. 1 shows the top views of the fabricated 5th-order CROW based on 440-nm-wide Si-nanowire channel waveguides. Total chip area was 50 μ m (width) \times 150 μ m (length).

Then, the fabricated 5th-order CROW devices were characterized with a linearly polarized TE-mode light. Fig. 2 shows the superimposed measured spectra in intra-dies uniformly spaced by 50- μ m (a) and in inter-dies spaced by ~ 3 cm on a 300-mm SOI wafer (b). For both cases, clear flat-topped box-like spectral response was obtained by virtue of good phase controllability based on ArF-immersion lithography process. In Fig. 2(a), the standard deviation of phase variation was analyzed to be $\sim 0.03\pi$ radian for the optical path length of each microring. In Fig. 2(b), the center wavelength deviation was less than 3.6 nm, although the tested dies were separated by ~ 18 cm (distance between D2 and D8).

Spectral superiority over the ArF-immersion lithography process was reconfirmed by evaluating the eye diagrams of 25 Gbps non-return to zero (NRZ) modulation signals [7]. Dynamic signal

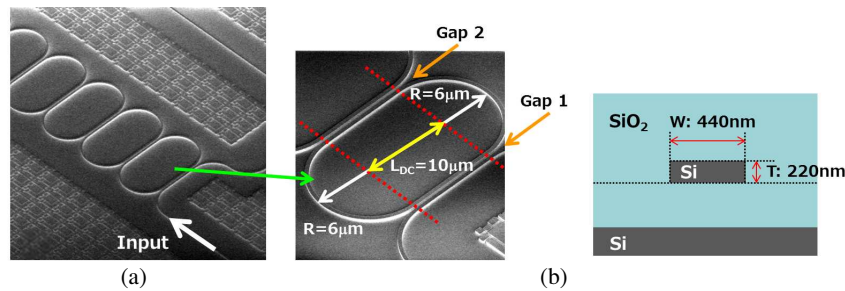


Figure 1: (a) Top views of the fabricated Si-nanowire based 5th-order CROW and (b) its schematic cross-sectional view of the waveguide with 440-nm-width and 220-nm-thickness.

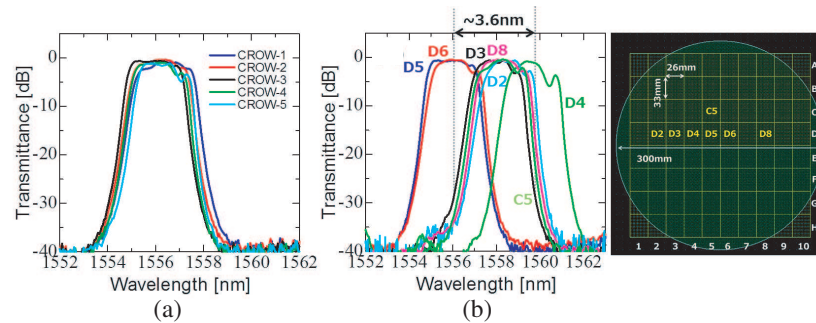


Figure 2: Measured spectra of the fabricated 5th-order CROWs, (a) intra-die distribution and (b) inter-die distribution.

waveforms were characterized by sending 25 Gbps NRZ modulation signals to the device. As a result, 25 Gbps modulation signal transmission was successfully implemented within almost passband wavelength range of the fabricated 5th-order CROW, which originated from the marked reduction of spectral ripple and low excess loss. This high-precision fabrication technology could also be applied to further advanced WDM DeMUX schemes. For example, by cascade-connecting such higher-order CROWs where filtering wavelengths for each microring are properly adjusted not to be overlapped with each other, optical DeMUX functionality could be achieved.

3. DELAYED-INTERFEROMETER-BASED OPTICAL MUX/DEMUX

Among several kinds of optical MUX/DeMUX, the DMZI-type devices [9–11] have a lot of advantages. Compared with higher-order CROW or arrayed waveguide grating (AWG), the DMZI-type device exhibits, in principle, much better spectral flatness that is one of important factors for relaxing the wavelength control accuracy of optical signal, without sacrificing insertion loss. Moreover, since the DMZI-type device can be formed with Si-nanowire channel waveguides only and does not need shallowly etched waveguide regions that are normally required to minimize scattering losses at around star couplers in AWG, fabrication process can be much simpler [10, 11]. Fig. 3 shows the device configuration of 1×4 Ch multistage DMZI-based optical DeMUX (a) and the measured spectra of the fabricated DMZI DeMUX with the channel spacing ($\Delta\nu$) of 10 nm (b) and 6.4 nm (c). As shown in Fig. 3(a), the fabricated device is composed of cascade-connected 21 delayed interferometers with different optical path lengths at each stage [8, 11].

In general, in order to spatially discriminate four different wavelength components, the device configuration can be much simpler. Cascade-connecting only 3 delayed interferometers can make 1×4 Ch optical DeMUX as already reported in [8, 9]. But, in that case, such device normally exhibits *sinc*-function-shaped spectra. Thus, its spectral performance becomes inferior in term of spectral flatness and low spectral crosstalk. These drawbacks can be overcome by introducing the device configuration shown in Fig. 3(a). Redundant delayed interferometers with different optical path lengths and optimized coupling ratios at each optical coupler make the optical DeMUX response spectrally flat and low crosstalk, maintaining low insertion loss. However, it should be noted that total phase errors becomes further higher than the case of the aforementioned simple device scheme, since the configuration shown in Fig. 3(a) inevitably needs much larger number of DMZIs with relatively longer interaction lengths even if we consider comparable phase errors at each DMZI

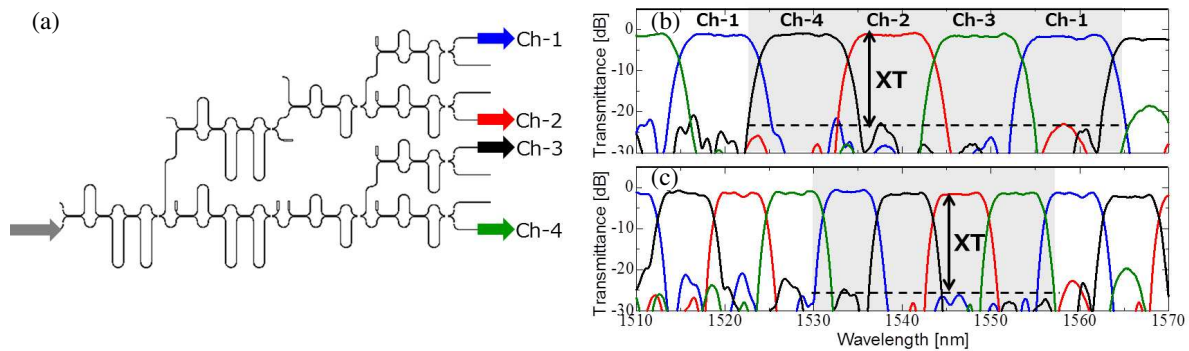


Figure 3: (a) Device configuration of 1×4 Ch multistage DMZI-based DeMUX, and measured spectra with (b) $\Delta\nu = 10$ nm and (c) $\Delta\nu = 6.4$ nm.

stage to the simple case. If the phase controllability of fabrication process far exceeds the degree of degradation by accumulated phase errors, we can count on spectral improvement in the device configuration shown in Fig. 3(a).

In this work, two kinds of $\Delta\nu$ were designed, fabricated and characterized. As shown in Figs. 3(b) and (c), irrespective of $\Delta\nu$, the DMZI-type device showed inter-channel-balanced flat-topped spectral response, together with low crosstalk of less than -22 dB for all output channels. These high performances resulted from good phase controllability enough to sustain desired spectral response within each DMZI by utilizing 300-mm wafer-scale ArF-immersion lithography process [8].

Finally, we experimentally evaluated spectral uniformity between inter-dies. In this experiment, the same multiple patterns equally spaced by ~ 3 cm were fabricated on a 300-mm SOI wafer. We characterized and compared DeMUX response of the devices located in the two nearest dies in the center of a 300-mm SOI wafer. As a result, the measured spectral characteristics including spectral shape, spectral flatness, insertion loss and crosstalk for the devices located in another die were almost the same as those shown in Figs. 4(b) and (c). Furthermore, the deviation of filtering wavelengths ($\delta\lambda$) was estimated to be < 0.65 nm for $\Delta\nu = 10$ nm and < 0.5 nm for $\Delta\nu = 6.4$ nm, in spite of the fabrication imperfections and Si-core layer non-uniformity of the SOI wafer. That is, $\delta\lambda$ was ~ 10 times smaller than the 0.5 dB flat-topped bandwidths of 6.7 nm ($\Delta\nu = 10$ nm) and 4.7 nm ($\Delta\nu = 6.4$ nm), which justifies 300-mm ArF-immersion lithography process would be a promising technique for realizing several kinds of WDM photonic integrated devices with good production yields.

4. CONCLUSION

We reported recent progress of higher-order CROW and delayed interferometer type optical DeMUX fabricated by 300-mm SOI technology for WDM applications. High precision fabrication technology based on 300-mm wafer-scale ArF-immersion lithography process was proven to be very promising to realize several kinds of WDM filter devices together with good production yields.

ACKNOWLEDGMENT

This research is partly supported by New Energy and Industrial Technology Development Organization (NEDO). The authors would like to thank TIA-Super Clean Room Management Office, AIST, and especially M. Seki, N. Yokoyama, M. Ohtsuka, and K. Koshino for technical support and device fabrication. The authors also thank PETRA staffs and particularly T. Mogami, T. Horikawa, D. Shimura, T. Simoyama, S. Tanaka, M. Okuno and S. Okumura for valuable discussions.

REFERENCES

1. Miller, D. A. B., "Device requirements for optical interconnects to silicon chips," *IEEE Proceedings*, Vol. 97, No. 7, 1166–1185, 2009.
2. Liu, A., L. Liao, Y. Chetrit, J. Basak, H. Nguyen, D. Rubin, and M. Paniccia, "Wavelength division multiplexing circuit on silicon-on-insulator platform," *IEEE J. Sel. Top. Quantum Electron.*, Vol. 16, No. 1, 23–32, 2010.
3. Feng, N., S. Liao, D. Feng, P. Dong, D. Zheng, H. Liang, R. Shafiiha, G. Li, J. E. Cunningham, A. V. Krishnamoorthy, and M. Asghari, "High speed carrier-depletion modulators with 1.4 V-

- cm $V_{\pi}L$ integrated on 0.25 μm silicon-on-insulator waveguides,” *Opt. Express*, Vol. 18, No. 8, 7994–7999, 2010.
4. Kim, D. J., J. M. Lee, J. H. Song, J. Pyo, and G. Kim, “Crosstalk reduction in a shallow-etched silicon nanowire AWG,” *IEEE Photon. Technol. Lett.*, Vol. 20, No. 19, 1615–1617, 2008.
 5. Jeong, S.-H., S. Tanaka, T. Akiyama, S. Sekiguchi, Y. Tanaka, and K. Morito, “Flat-topped and low loss silicon-nanowire-type optical MUX/DeMUX employing multi-stage microring resonator assisted delayed Mach-Zehnder interferometers,” *Opt. Express*, Vol. 20, No. 23, 26000–26011, 2012.
 6. Selvaraja, S. K., G. Murdoch, A. Milenin, C. Delvaux, C. Ong, S. Pathak, D. Vermeulen, G. Stercks, G. Winroth, P. Verheyen, G. Lepage, W. Bogaerts, R. Baets, J. V. Campenhout, and P. Absil, “Advanced 300-mm wafer scale patterning for silicon photonics devices with low record loss and phase error,” *Proc. OECC 2012*, PDP2-2, 2012.
 7. Jeong, S.-H., D. Shimura, T. Simoyama, M. Seki, N. Yokoyama, M. Ohtsuka, K. Koshino, T. Horikawa, Y. Tanaka, and K. Morito, “Low-loss, flat-topped and spectrally uniform silicon-nanowire-based 5th-order CROW fabricated by ArF-immersion lithography process on a 300-mm SOI wafer,” *Opt. Express*, Vol. 21, No. 25, 30163–30174, 2013.
 8. Jeong, S.-H., D. Shimura, T. Simoyama, T. Horikawa, Y. Tanaka, and K. Morito, “Delayed interferometer based Si-wire WDM demultiplexers fabricated by phase controllable and productive 300-mm wafer-scale ArF-immersion lithography technology,” *Proc. OFC 2014*, Th3F.5, 2014.
 9. Kim, D. W., A. Barkai, R. Jones, N. Elek, H. Nguyen, and A. Liu, “Silicon-on-insulator eight-channel optical multiplexer based on a cascade of asymmetric Mach-Zehnder interferometers,” *Opt. Lett.*, Vol. 33, No. 5, 530–532, 2008.
 10. Horst, F., W. M. J. Green, S. Assefa, S. M. Shank, Y. A. Vlasov, and B. J. Offrein, “Cascaded Mach-Zehnder wavelength filters in silicon photonics for low loss and flat pass-band WDM (de-)multiplexing,” *Opt. Express*, Vol. 21, No. 10, 11652–11658, 2013.
 11. Assefa, S., S. Shank, W. Green, M. Khater, E. Kiewra, C. Reinholm, S. Kamlapurkar, A. Rylyakov, C. Schow, F. Horst, H. Pan, T. Topuria, P. Rice, D. M. Gill, J. Rosenberg, T. Barwicz, M. Yang, J. Proesel, J. Hofrichter, B. Offrein, X. Gu, W. Haensch, J. Ellis-Monaghan, and Y. Vlasov, “A 90 nm CMOS integrated nano-photonics technology for 25 Gbps WDM optical communications applications,” *Proc. IEDM 2012*, 33.8, 2012.

Widely Tunable Inductors Utilizing Transmission-line with Variable Distributed Load Capacitor for Millimeter-wave Applications

Yixiao Wang, Xiucheng Hao, Le Ye, and Huailin Liao
Institute of Microelectronics, Peking University, Beijing 100871, China

Abstract— This paper proposes a widely tunable inductor realized by transmission lines (T-Line) for applications under 60 GHz. The inductor consists of several L-branch formed by short T-Line segments and variable distributed load capacitors. With changeable load capacitance, the equivalent inductance of whole T-Line would also be tunable. For conceptual demonstration, a prototype T-Line-C VCO is implemented for comparison to the conventional LC VCO. With the same $\pm 50\%$ capacitance variation rate, the traditional LC VCO with lumped inductors for comparison only achieves 11.6% frequency tuning range from 60.5 GHz to 67.6 GHz; However, the demonstrated VCO based on the proposed tunable T-Line inductors improve the frequency tuning range to 25.4% from 53.7 GHz to 68.4 GHz.

1. INTRODUCTION

With the development of high definition (HD) media and the demand of mobilized home entertainment, millimeter-wave (MMW) wireless systems are becoming more and more in demand. Compared to low frequency, MMW frequency bands provides larger bandwidth, faster transfer speed and therefore higher data rate. For example, the IEEE 802.11n wireless standards provides a data rate of 288.8 Mb/s which cost about 12 minutes to transfer a Blu-ray movie of a typical capacity 25 GB. In contrast, the recently approved IEEE 802.11ad standards support a data rate up to 7 Gb/s, which means there would be less than 30 seconds to transfer the same movie. In the meanwhile, in-room media-streaming applications, such as “Air Play”, also needs a large data rate which can only be provided by MMW systems. Figure 1 shows 60 GHz bands of different regions.



Figure 1: Unlicensed 60 GHz bands in different regions.

To fully cover 60 GHz bands in different regions, the MMW system is required to have a tuning range at least from 57 GHz to 66 GHz. It poses a great challenge to the MMW integrated-circuits, especially which have large PVT (Process, Voltage and Temperature) variations in modern deep-submicron processes. Unfortunately, design of the key building blocks, e.g., LNA, VCO, and filter, are suffering from lacking tuning elements, which leads to insufficient frequency tuning range for MMW systems. Recently, several VCOs have been developed for MMW applications [1–7]. Some of them focus on the phase noise, however, it has barely any frequency tuning range [1, 4]. Others pay attention to the tuning of varactors and negative resistance MOSFET pair [2, 3], which consumes large power and leads to poor phase noise.

In this paper, a widely tunable inductor realized by transmission-line (T-Line) segments and variable distributed load capacitor is proposed, which provides another dimension for frequency tuning in MMW systems. The T-Line structure performs as an inductor when choosing proper length at the resonant frequency. In our proposed tunable inductor, the T-Line is divided into several short segments. At the connection nodes of each two segments, a variable distributed load capacitor is shunt to ground. By changing the distributed load capacitance, the characteristics of the T-Line would change correspondingly, resulting in the effect of inductance tuning. In modern IC processes, the distributed capacitors in the proposed tunable T-Line inductor can be implemented by the varactors, or even the versus-biased Schottky diodes, which can give larger cutoff frequency

and higher Q factor. As a result, it gives us a possibility to realize widely frequency-tunable MMW circuits, such as VCO, LNA, PA and so on.

For conceptual demonstration, a prototype VCO consists of the proposed tunable T-Line inductors is presented. Based on the proposed tunable T-Line based inductor, the VCO is able to improve the frequency tuning range by simultaneously using the tunable inductors and lumped varactors. For comparison, another VCO consisted of lumped inductors is introduced. The simulation results show that the VCO with lumped inductors only has 11.6% frequency tuning range with the lumped tunable varactors, similar to recently published VCOs. In contrast, the demonstrated VCO consists of the proposed tunable inductors achieves a 25.4% frequency tuning range from 53.7 GHz to 68.4 GHz, by simultaneously tuning the variable distributed load capacitance and the lumped varactors. Thus, it is sufficient for MMW applications to cover worldwide 60 GHz bands.

This paper is organized as follows. Section 2 describes the theoretical analysis of the proposed inductor tuning method and architecture of the tunable T-Line inductor. The VCO demonstration for the proposed tunable T-Line inductor and simulation results are shown in Section 3, with comparison of the conventional LC VCO. Finally, conclusion is given in Section 4.

2. PROPOSED T-LINE INDUCTOR

2.1. Variable Distributed Load Capacitor

The equivalent RLGC model for conventional incremental T-Line is shown in Figure 2 excluding the C_L part. R_0 and L_0 are the series resistance and series inductance per unit length, while G_0 and C_0 are shunt conductance and capacitance per unit length, respectively. For an infinite transmission-line, the complex propagation constant and the characteristic impedance are given in (1) and (2). The distributed series inductance and shunt capacitance could be derived in (3) and (4).

$$\gamma = a + j\beta = \sqrt{(R_0 + j\omega L_0)(G_0 + j\omega C_0)} \quad (1)$$

$$Z_0 = \sqrt{(R_0 + j\omega L_0) / (G_0 + j\omega C_0)} \quad (2)$$

$$L_0 = \text{imag}(\gamma Z_0) / \omega \quad (3)$$

$$C_0 = \text{imag}(\gamma / Z_0) / \omega \quad (4)$$

For a T-Line of length Len , the input impedance of conventional T-Line could be written as (5). In practical applications, the T-Line is one-terminated short for providing DC bias voltage, so that the equivalent input impedance is bridged as (6).

$$Z_{in} = Z_0 \frac{Z_L + jZ_0 \tan(\beta Len)}{Z_0 + jZ_L \tan(\beta Len)} \quad (5)$$

$$Z_{in} = jZ_0 \tan(\beta Len) \quad (6)$$

In the proposed tunable T-Line, a variable distributed capacitor C_L is added into the conventional equivalent RLGC model as Figure 2 shows. Taking $R_0 = G_0 = 0$ to simplify the theoretical

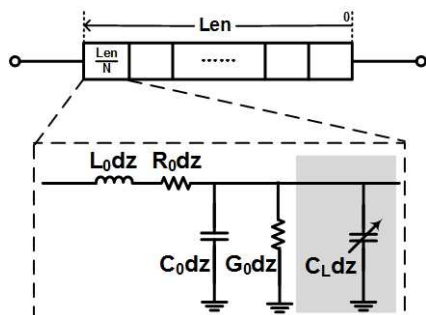


Figure 2: Equivalent RLGC model of the proposed T-Line inductor segment, $C_L dz$ is the variable distributed load capacitor.

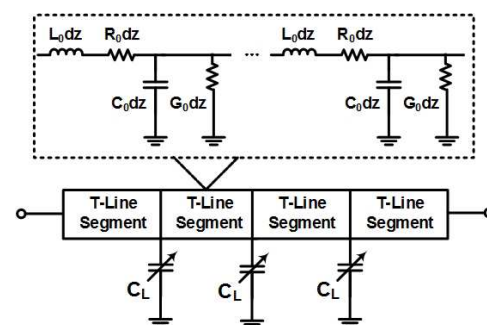


Figure 3: (a) T-Line cell and equivalent circuit; (b) T-Line inductor consisted of T-Line cells; (c) T-Line inductor.

analysis for lossless T-Line, we could get the tunable input impedance as (7).

$$Z_{in,tunabe} = j\sqrt{\frac{L_0}{C_0 + C_L}} \tan \left[\omega\sqrt{L_0(C_0 + C_L)} \cdot Len \right] \quad (7)$$

The positive imaginary part of the input impedance could be treated as the equivalent inductance of the T-Line. Thus, by tuning the variable distributed capacitor C_L , the equivalent inductance is configurable.

2.2. Practical Tunable T-line Inductor

However, in practical design, it would be impossible for adding real “distributed” load capacitor to T-Line segments of unity length. Then we make an approximation by limiting the segment length of the T-Line. The whole T-Line is divided into N parts, each segment is far smaller than the wavelength. At the connection node of each two segments, a shunt tunable load capacitor is introduced for tuning as Figure 3 shows. Apparently, while N is set larger tending to infinite, the approximation is more close to the real situation. The simulation results show the inductance approximation is quite match while $N \geq 4$. In this case, N is chosen of 4 in demonstration. The variable distributed load capacitor C_L can be realized by MOSFET varactors. It can also be realized by the versus-biased Schottky diodes, which shows much larger cutoff frequency and higher Q factor than conventional varactors.

For demonstration, four T-Line cells are connected serially to form the tunable T-Line inductor. Each T-Line segment is consisted of inductance about 16 pH with distributed load capacitor, which is manufacturable in modern CMOS processes. Figure 4 shows the simulated T-Line inductance with different distributed load capacitance C_L during 50 GHz and 70 GHz. With variable C_L values, the equivalent T-Line inductance shows a large variation range. As shown in Figure 4, the equivalent T-Line inductance changes from 80 pH to 275 pH at 70 GHz while C_L changes from 5 fF to 20 fF.

3. VCO DEMONSTRATION

To prove the effect of the proposed tunable T-Line inductor in MMW applications, we build a prototype VCO based on a standard 65 nm CMOS process. As Figure 5 shows, it consists of the tunable T-Line VCO and the output matching buffer. Figure 6(a) is the conventional LC VCO using fixed inductor for comparison, while Figure 6(b) is the VCO using the proposed tunable T-Line inductors. C_X is the varactor, while C_p is a constant capacitor coming from the parasitic capacitance in real circuits. The C_p is 20 fF which is reasonable assumption with careful layout design. The bias current is 6 mA for both VCOs, chosen as recently state-of-art works did. In the traditional VCO based on the lumped inductor for comparison as shown in Figure 6(a), the lumped inductor L_X is chosen as 80 pH, so that it can be resonant at around 60 GHz with $C_X = 20$ fF.

In the tunable T-Line inductor VCO as shown in Figure 6(b), the tunable T-Line inductor is consisted of 4 serial connected T-Line segments, in which a short T-Line and a load capacitor C_L are included. The tuning of the distributed capacitor C_L can be realized by varactors or versus-biased Schottky diodes in modern IC processes. As we mentioned before, we choose the segment

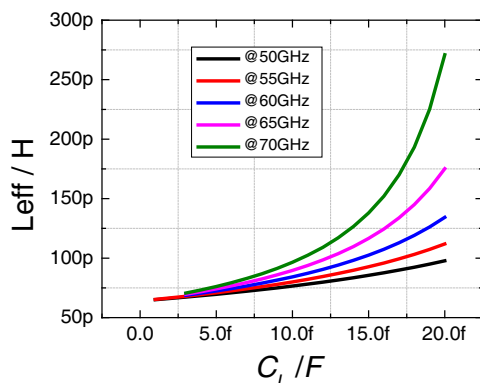


Figure 4: Simulation equivalent inductance of the tunable T-Line inductor with variable distributed capacitance C_L .

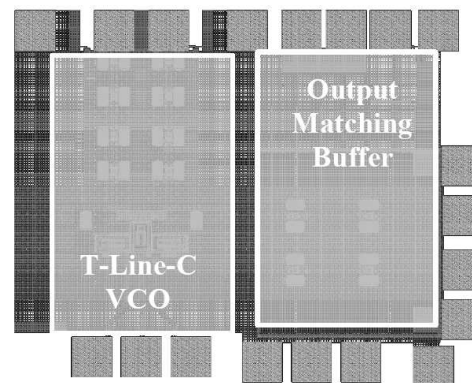


Figure 5: The Layout of the proposed T-Line-VCO and the output matching buffer.

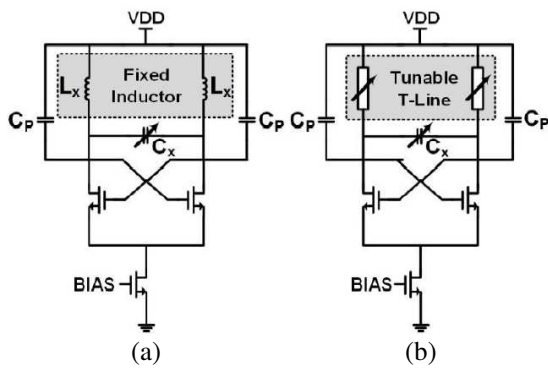


Figure 6: (a) Schematic of the LC VCO consists of fixed inductor L_X and varactor C_X ; (b) Schematic of the VCO consists of tunable T-Line inductor and varactor C_X .

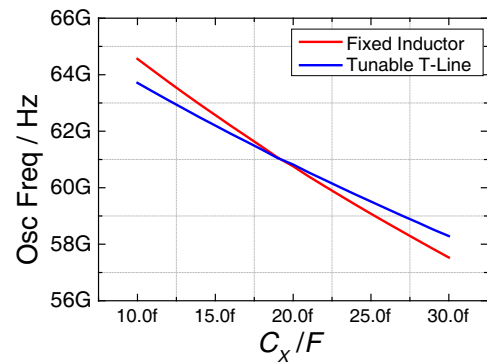


Figure 7: The frequency tuning range of both fixed L_X and tunable T-Line with changeable varactor C_X .

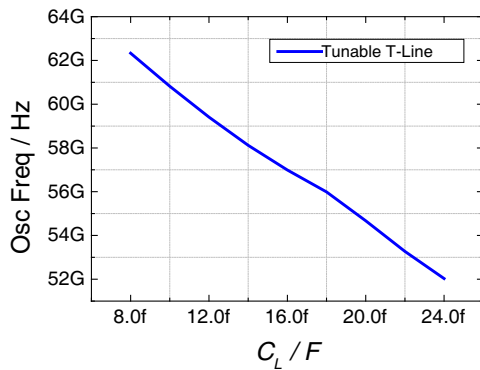


Figure 8: Oscillator frequency tuning range of tunable T-Line inductor VCO with variable load capacitance C_L (8 fF to 24 fF, 2 fF per step).

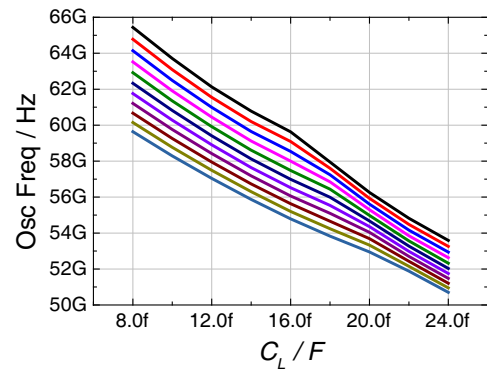


Figure 9: Oscillator frequency with both varactor C_X (10 fF to 30 fF, 2 fF per step) and distributed load capacitance C_L (8 fF to 24 fF, 2 fF per step).

Table 1: Comparison of recent state-of-art works.

	[1] JSSC 2009	[2] RFIC 2009	[3] MWCL 2010	[4] ISCAS 2010	[5] JSSC 2011	[6] MTT 2011	This work
Technology	90 nm CMOS	65 nm CMOS	0.18 μ m CMOS	65 nm CMOS	65 nm CMOS	65 nm CMOS	0.18 μ m CMOS
VDD (V)	0.43	1.2	2.5	1.5	1	1	1.8
Center Frequency (Hz)	60 G	56 G	69 G	77 G	58.2 G	-	
Frequency Range (Hz)	58.8 G–61.7 G	-	64.2 G–69.4 G	72.8 G–77.6 G	56 G–60.4 G	81 G–86 G	50.7 G ~65.44 G
Tuning Range	4.81%	17%	7.6%	6.27%	7.6%	-	25.4%
Output Power (dBm)	-19	-9.8	-18.5	-	-	-	-
Phase Noise (dBc/Hz)	-90@1 MHz	-99.4@1 MHz	-76@1 MHz	-109@10 MHz	-95/ -97 @1 MHz	-84@1 MHz	-
Power (W)	1.2 m	15 m	27.5 m	15.81 m	22 m	65 m	5 m~17.5 m

inductance of 8 pH, $C_L = 10$ fF to let the VCO also oscillate at about 60 GHz with $C_X = 20$ fF. The distributed load capacitor C_L can be changed to realize the tunable inductor to further enhance the frequency tuning range.

We fix the distributed load capacitor C_L of 10 fF in the tunable T-Line, then the two oscillate frequencies change from 60.5 GHz to 67.6 GHz and from 61.3 GHz to 66.7 GHz with varactor C_X from 10 fF to 30 fF, respectively as Figure 7 shows.

The VCO based on the tunable T-Line inductor is also able to realize frequency tuning by changing the distributed load capacitor C_L . Figure 8 shows the oscillator frequency tuning curves of the tunable T-Line inductor VCO with variable distributed capacitor C_L . As C_L changes from 8 fF to 24 fF, the oscillator frequency changes from 55.0 GHz to 65.3 GHz. Take frequency at $C_L = 16$ fF as the center frequency, the tuning range is about 18.1% with $\pm 50\%$ C_L variation.

In addition, the VCO based on the tunable T-Line inductor can further enhance the frequency tuning range by changing the distributed load capacitor C_0 and the lumped varactors C_L simultaneously. In Figure 9, the C_X varies from 10 fF to 30 fF, 2 fF as a step, and the C_L varies from 8 fF to 24 fF, 2 fF as a step. Take 58 GHz as the center frequency, the frequency tuning range is around 25.4% from 53.7 GHz to 68.4 GHz. The whole tuning range could cover worldwide 60 GHz bands, which is appropriate for MMW applications. Table 1 gives the comparison among recent state-of-art works.

4. CONCLUSION

In this paper, a widely tunable T-line inductor realized by variable distributed load capacitor is proposed. As the theoretical analysis, the T-Line could be realized as a tunable inductor by changing the distributed load capacitance of each short segment of the T-Line. For conceptual demonstration, a prototype VCO are demonstrated, consisted of tunable T-Line inductor and distributed load capacitors. With $\pm 50\%$ capacitance variation rate, the conventional VCO based on the fixed inductors for comparison only has 11.6% frequency tuning range, while the demonstrated VCO with the proposed tunable T-Line inductors has 25.4% tuning range from 53.7 GHz to 68.4 GHz with both varactors and distributed load capacitor tuning. It gives us another dimension to improve the frequency tuning range for MMW VCO. Furthermore, it also gives us a potential to achieve large frequency tuning range for other MMW modules, such as LNA, PA, which utilize T-Lines as the passive network.

ACKNOWLEDGMENT

This work was partly supported by National Science Foundation of China (NSFC), No. 60876020, and No. 61106023.

REFERENCES

1. Li, L., P. Reynaert, and M. Steyaert, "Design and analysis of a 90 nm mm-wave oscillator using inductive-division LC tank," *IEEE J. Solid-State Circuits*, Vol. 44, No. 7, 1950–1958, Jul. 2009.
2. Jimenez, J. L. G., F. Badets, B. Martineau, and D. Belot, "A 56 GHz LC-tank VCO with 17% tuning range in 65 nm bulk CMOS for wireless HDMI applications," *IEEE Radio Frequency Integrated Circuits Symp. Dig.*, 481–484, Jun. 7–9, 2009.
3. Chiu, H. C. and C. P. Kao, "A wide tuning range 69 GHz push-push VCO using 0.18 μ m CMOS technology," *IEEE Microw. Wireless Compon. Lett.*, Vol. 20, No. 2, 97–99, Feb. 2010.
4. Liu, G., R. Berenguer, A. Akhiyat, K. Kamtikar, and Y. Xu, "Configurable MCPW based inductor for mm-wave circuits and systems," *IEEE International Symposium on Circuits and Systems*, 1113–1116, May 30, 2010–Jun. 2, 2010.
5. Decanis, U., A. Ghilioni, E. Monaco, A. Mazzanti, and F. Svelto, "A low-noise quadrature VCO based on magnetically coupled resonators and a wideband frequency divider at millimeter waves," *IEEE J. Solid-State Circuits*, Vol. 46, No. 12, 2943–2955, Dec. 2011.
6. Xu, Z. W., Q. J. Gu, Y. C. Wu, H. Y. Jian, and M.-C. F. Chang, "A 7078-integrated CMOS frequency synthesizer for W-band satellite communications," *IEEE Trans. Microw. Theory Tech.*, Vol. 59, No. 12, 3206–3218, Dec. 2011.

Investigation of a Miniature and High Gain On-chip V Band Microstrip Antenna

Li-Yan Xie¹, Jia-Qi Liu^{1,2,3}, Yu-Bo Wang¹,
Chenghsin Chuang⁴, Albert Chin⁴, Joshua Le-Wei Li^{1,2,3}, and Kai Kang¹

¹Institute of Electromagnetics and School of Electronic Engineering
University of Electronic Science and Technology of China, Chengdu, China

²Advanced Engineering Platform and School of Electronic Engineering
Monash University, Selangor, Malaysia

³Advanced Engineering Platform and School of Electronic Engineering
Monash University, Victoria, Australia

⁴Department of Electronic Engineering
National Chiao Tung University, Hsinchu, Taiwan

Abstract— This paper presents a miniature and high gain on-chip V band microstrip antenna. A ground plane on the bottom metal layer M_1 has been approached to shield the wave from penetrating into the low-resistivity and high dielectric constant Si substrates to improve the antenna performance. Antenna parameters have been investigated to obtain an optimized antenna with $0.87\text{ mm} \times 1.16\text{ mm}$ occupation. The measured and simulated return loss results and simulated radiation pattern results of proposed antenna have been presented. The performance of the proposed antenna as compared to other published on-chip antennas has also been demonstrated.

1. INTRODUCTION

Recently, the increasing demands for high data rate over 100 MB/s wireless communications and compact volume with high performance [1] urge the developments of V band integrated circuits (IC). On-chip-antenna technology brings great chance to reduce the size of Complementary Metal-Oxide Semiconductor circuits (CMOS) for the less work in the impedance match with antenna. However, high dielectric constant, low-resistivity Si material and thin substrate make it difficult to design and fabricate high performance on-chip antenna in standard CMOS technology.

Different kinds of methods have been approached to solve the problem. Some authors [2] tried to solve the problem by adopting a silicon lens at the backside of the chip which changed the standard CMOS technology and cost a lot. Others improved the antenna performance by doing the research of antenna radiation mechanism. Different shapes of antenna such as dipole [3], inverted F [4], yagi [5] and slot [6] has been designed to fit with the circuits. However, the radiation efficiency and the gain still can't achieve a higher level.

In this paper, we approach the total bottom metal layer M_1 to work as a ground plane and shield the wave from penetrating into the low-resistivity and high dielectric constant Si substrates. The energy loss in the Si substrate has been reduced to improve the antenna performance. Considering the great occupation of the patch and thin substrate which is only $\lambda/500$ (around $10\ \mu\text{m}$), the investigation of patch radiation mechanism has to be done to obtain a miniature and high gain on-chip V band microstrip antenna. The process of design and simulation in the proposed antenna has been done through High Frequency Structure Simulator (HFSS) from Ansoft Corporation based on finite-element-method.

2. ANTENNA DESIGN

Figure 1 shows the geometry of the proposed on-chip patch antenna. This structure consists of a rectangular patch antenna on the top metal layer M_6 and a ground plane on the bottom metal layer M_1 . In order to make room for other circuit devices such as filters, the substrate height between the antenna and ground plane was designed to be $4\ \mu\text{m}$ and fabricated by ourselves. The dimension of main parameters are $Sub_h = 4\ \mu\text{m}$, $a = 2.2\text{ mm}$, $b = 1\text{ mm}$, $P_l = 1.16\text{ mm}$, $P_w = 0.87\text{ mm}$. The low-resistivity and high dielectric constant Si substrate is below the bottom metal layer M_1 . The patch size and the spacing between the patch and the edge were investigated to obtain the optimized miniature and high gain patch antenna. Other parameters such as the arguments of the feed-line are predetermined by demanded $50\ \Omega$ output impedance matching of the circuit and the chosen technology. The prototype of the designed patch antenna is shown in Figure 2.

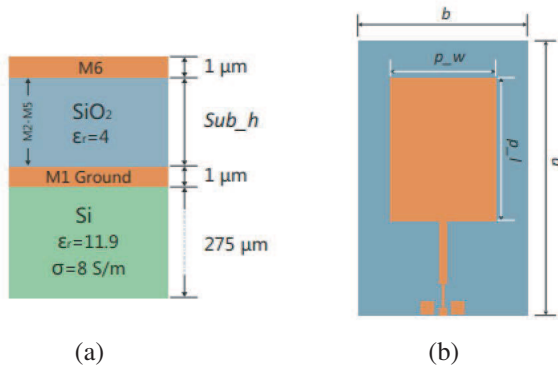


Figure 1: (a) The top-view and (b) cross-section of the designed on-chip antenna.



Figure 2: The prototype of the designed patch antenna.

3. RESULTS AND DISCUSSION

The simulated (blue line) and measured (red line) return loss results of the proposed antenna were shown in Figure 3. It can be seen that the resonance of the proposed antenna is around 62.85 GHz and the impedance bandwidth with $S_{11} < -10$ dB is from 62.25 GHz to 63.47 GHz. In comparison with the simulation results, the measured reflection coefficient offers a good match except for a 12.5% frequency shift. This may be due to the lower dielectric constant of the SiO_2 substrate and thinner epoxy glue layer on the antenna and the test board, thus leading to the lower resonant frequency.

The E -plane and H -plane radiation patterns of the designed antenna in the $4 \mu\text{m}$ SiO_2 substrate is displayed in Figure 4. The simulation results demonstrate the peak gain of the designed antenna is -10.3 dBi, which approached -2.69 dBi when the designed antenna is fabricated in the standard CMOS technology with $10 \mu\text{m}$. The performance of proposed antennas as compared to other published on-chip antennas is presented in Table 1.

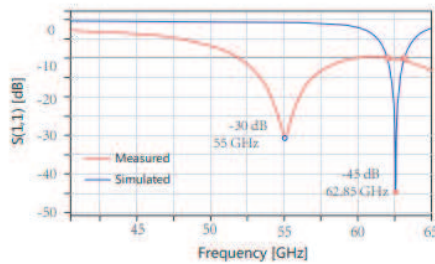


Figure 3: The simulated (blue line) and measured (red line) return loss results of the proposed antenna.

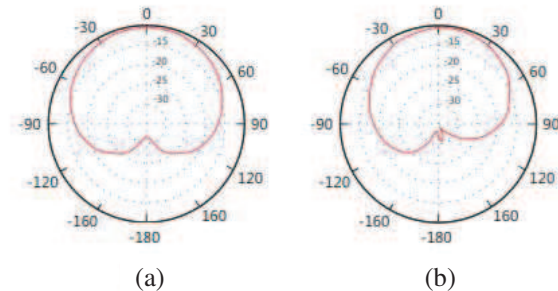


Figure 4: (a) The E -plane and (b) H -plane radiation pattern of the designed antenna.

Table 1: The performance of the proposed antennas as compared to other published on-chip antennas.

Ref.	Antenna Type	SiO_2 Substrate Height	Gain (dBi)	Area (mm^2)
[3]	Dipole	$9 \mu\text{m}$	-8 dBi@21 GHz	$3 \text{ mm} \times 0.5 \text{ mm}$
[4]	Inverted F	$22 \mu\text{m}$	-19 dBi@61 GHz	/
[5]	Yagi	/	-10 dBi@60 GHz	$1.1 \text{ mm} \times 1.34 \text{ mm}$
[6]	Slot	$12 \mu\text{m}$	-2 dBi@140 GHz	$1.2 \text{ mm} \times 0.6 \text{ mm}$
This work	Patch	$4 \mu\text{m}$	-10.3 dBi@60 GHz	$0.87 \text{ mm} \times 1.16 \text{ mm}$
This work	Patch	$10 \mu\text{m}$	-2.69 dBi@60 GHz	$0.87 \text{ mm} \times 1.16 \text{ mm}$

4. CONCLUSION

In this paper, a smaller occupation and higher gain antenna is designed by making detail analysis on the parameters of the on-chip microstrip antenna. The finally designed patch with $0.87\text{ mm} * 1.16\text{ mm}$ occupies half of the area of the same patch antenna in traditional design method.

REFERENCES

1. Liu, J.-Q., J.-Y. Jin, and J. L.-W. Li, "A miniature bandpass filter with split ring resonator and asymmetrical coupled lines," *2013 International Conference on Communications, Circuits and Systems (ICCCAS)*, Vol. 2, 425–427, 2013.
2. Babakhani, A., X. Guan, A. Komijani, A. Natarajan, and A. Hajimiri, "A 77-GHz phased-array transceiver with on-chip antennas in silicon: Receiver and antennas," *IEEE Journal of Solid-State Circuits*, Vol. 41, No. 12, 2795–2806, 2006.
3. Shamim, A., L. Roy, N. Fong, and N G. Tarr, "24 GHz on-chip antennas and balun on bulk Si for air transmission," *IEEE Transactions on Antennas and Propagation*, Vol. 56, No. 2, 303–311, 2008.
4. Zhang, Y. P., M. Sun, and L. H. Guo, "On-chip antennas for 60-GHz radios in silicon technology," *IEEE Transactions on Electron Devices*, Vol. 52, No. 7, 1664–1668, 2005.
5. Chuang, H.-R., L.-K. Yeh, P.-C. Kuo, K.-H. Tsai, and H.-L. Yue, "A 60-GHz millimeter-wave CMOS integrated on-chip antenna and bandpass filter," *IEEE Transactions on Electron Devices*, Vol. 58, No. 7, 1837–1845, 2011.
6. Pan, S. and F. Capolino, "Design of a CMOS on-chip slot antenna with extremely flat cavity at 140 GHz," *IEEE Antennas and Wireless Propagation Letters*, Vol. 10, 827–830, 2011.

An Ultra-wideband and Low Phase Noise LC-VCO Using NMOS Varactor with MOM Digital Capacitor Switching Arrays

Mohammed Aqeeli, Zhirun Hu, Xianjun Huang,
Abdullah Alburaikan, and Cahyo Muvianto

School of Electrical and Electronic Engineering
The University of Manchester, Manchester M13 9PL, UK

Abstract— This paper presents a novel low-phase-noise and ultra-bandwidth LC-tank voltage-controlled oscillator (VCO). The work fully-integrated 5.8 GHz VCO designed and simulated using 130-nm CMOS technology. Instead of using the conventional varactor in the tank design, a novel metal-oxidemetal (MOM) digital capacitor switching array (MOMDCSA) has been implemented with nMOS varactor is employed as an effective varactor bank. The proposed VCO-measured results at the centre frequency demonstrate a phase noise of -129.7 dBc/Hz and FOM of -198.38 dBc/Hz at 1 MHz frequency offset. The VCO shows approximately 33% tuning range under a power consumption of 2.8 mW.

1. INTRODUCTION

The recent exponential growth in higher integration and wireless communication has attracted tremendous effort to develop more channels in mobile communication applications [1]. VCOs are considered to be one of the important parameters in analogue and digital systems. Nowadays, the demand for high-performance, VCOs is increased; in turn, this demand has imposed more strict requirements on the phase noise of the VCO [2].

The phase noise of the VCO is used to describe phase fluctuations due to the random frequency fluctuations of a signal. Phase noise can be caused by a number of conditions, but is mostly affected by VCO frequency stability. It is one of the most important parameters for the quality and performance of information transfer, in turn affecting the reliability purposes in data communication. VCOs are a major design challenge and thus have received a lot of attention in recent years. Spectacular works considering switching capacitances inside the LC-tank have been conducted to extend the tuning range and improve the phase noise of VCO's [4–6]. However, these switches were implemented using stacked devices and a large size resistors to gain high impedance for RF signals and this occupied a larger die area. In addition, the dissipation power is relatively high and the measured and the simulated phase noise are still high.

This article, introduce a high performance 3-bit MOMDCSA using (MOM) digital switching capacitors for coarse tuning and body-grounded NMOS varactors for fine tuning in order to keep the VCO gain (K_{vco}) and variation low, to extend the bandwidth and minimize phase noise variance through the whole tuning range at the cost of chip size. The structure uses an adequate metal-oxide-metal (MOM) capacitors taking advantage of their high capacitance density, low parasitic capacitance and thinner dielectric. The proposed structure solves the conflict of high phase noise variation due to wider tuning range, minimize the sensitivity of the VCO noise by optimizing the gain and has an output frequency which varies linearly with control voltage. This paper is organized as follows: Section 2 explains the VCO's core design and the implementation process, while Section 3 presents the simulation results, followed by the conclusion in Section 4.

2. CIRCUIT DESIGN AND IMPLEMENTATION PROCESS

Cross-coupled NMOS differential VCO based on binary weighted switched capacitor bank and body-grounded nMOS varactor is depicted in Fig. 1. The LC tank is consists of a differentially tuned varactor a very small size symmetrical center-tapped inductor, the metal width and the lateral spacing between them were optimized to improve and to obtain an appropriate parasitic capacitance and a high Q , the measured quality factor Q was 16.50, for 460 pH inductors while the area was $16596 \mu\text{m}^2$. The cross connected differential pair provides the negative resistance to neutralize the tank losses with less current consumption and hence is more power efficient.

The wider varactors bandwidth the higher phase noise [3], RF VCO with sub-bands is the best choice for broadband implementation. The key contribution of this work is to design a broadband VCO employing the MOMDCSA to lower K_{VCO} and improve tuning linearity and obtains a minimum phase noise variation within all tuning ranges. The total tank capacitance is established

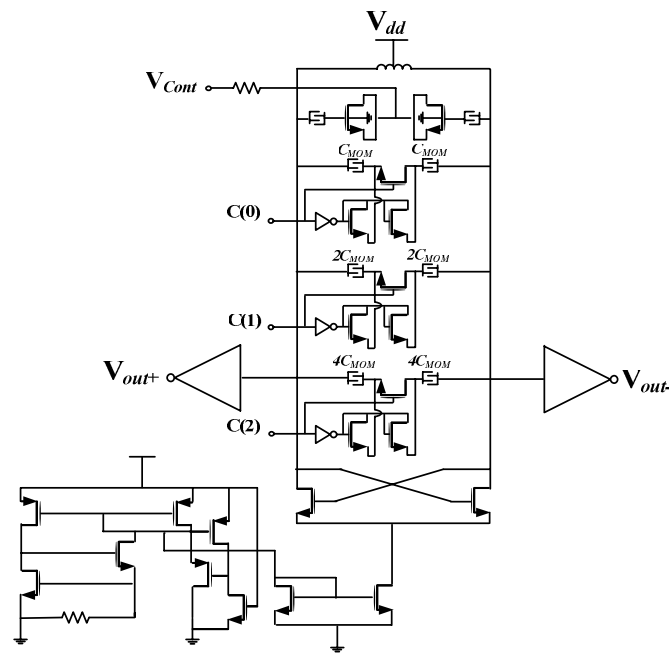


Figure 1: Schematic diagram of the designed 5.8 GHz 130 nm CMOS VCO.

by the nMOS varactor and the fixed MOM capacitance due to the parasitic and the switched MOM capacitance. MOS-based varactors are commonly used in VCOs due to their wider tuning range and higher Q factor [3], and lower phase noise. The nMOS varactors may have an advantages over pMOS varactors by its asymmetric characteristics effectiveness of area, which result less power consumption. In addition, the maximum capacitance per unit of area is approximately three times higher than that of a PN-junction varactor [1].

3. SIMULATION RESULTS

The proposed VCO was implemented using a commercially available UMC-130 nm, 6-metal, mixed mode CMOS process and simulated using Cadence Virtuoso Analogue Design Environment Tools. Simulation results indicate that the VCO exhibits wider tuning range from 4.84 GHz to 6.76 GHz and FoM varies from -201.7 dBc/Hz to -204.9 dBc/Hz as shown in Fig. 2.

The gain variation of the VCO has been reduced to 13.95%. As a result, the VCO immunity increases and the possibility of false locking for instant in PLL applications will decrease. In addition, the new varactor achieves steep transition for tuning voltages as depicted in Fig. 2. The circuit generates stable periodic signals with a harmonic index and measured output power of 3.73 dBm at the resonance frequency, as shown in Fig. 3, with tuning voltage varying from 0 to

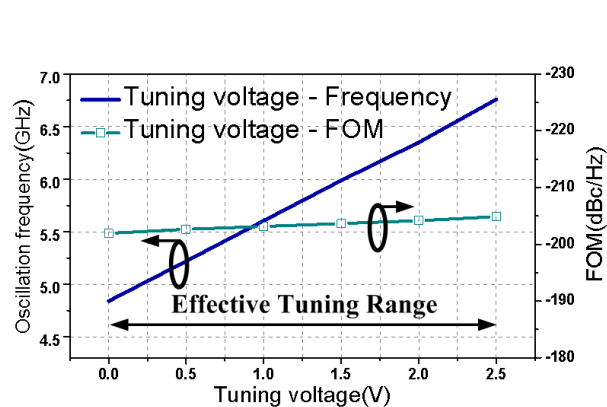


Figure 2: Tuning characteristics and FoM of the VCO.

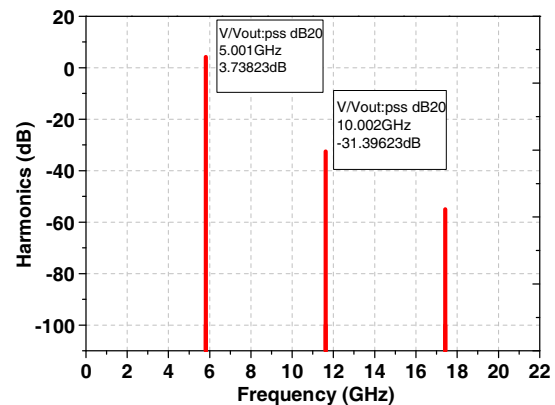


Figure 3: Simulated power output plot of a 5.8 GHz VCO.

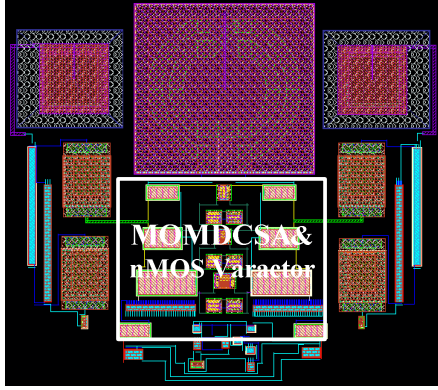


Figure 4: Layout of the designed CMOS VCO.

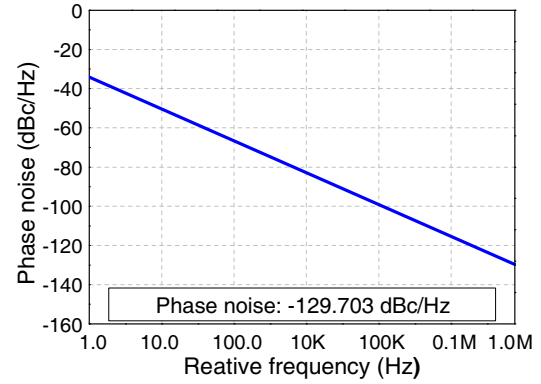


Figure 5: Simulated phase noise at 1 MHz offset.

3.0 V. The phase noise of an LCVCO is described, according to Leeson [3], as:

$$L(f_m) = 10 \log \left[\frac{1}{2} \left(\left(\frac{f_0}{2Q_l f_m} \right)^2 + 1 \right) \left(\frac{f_c}{f_m} + 1 \right) \left(\frac{FKT}{P_s} \right) \right] \quad (1)$$

Figure 4 shows the layout of the proposed VCO, the core circuit, and the output buffer occupies a silicon area of $862 \times 986 \mu\text{m}^2$ not including the bond pad. Circuit performance, which was simulated using cadence to show the transient analysis of the VCO, demonstrates clearly that steady-state oscillation starts at approximately 6.27 ns.

The results obtained from the simulation of the LC-VCO design show that the phase noise has been drastically reduced. A brief description of the performance summary is illustrated in Table 1. The phase noise is automatically decreased while the power consumption is reduced. Thus, there is a trade-off between the power consumption and phase noise [1]. The phase noise of -129.7 dBc/Hz at 1 MHz frequency offset as shown in Fig. 5.

Table 1: Performance comparison of CMOS VCOs.

Process	F (GHz)	P (mW)	PN (dBc/Hz)	Offset	TR (GHz)	FoM (dBc/Hz)	Ref.
0.18 μm CMOS	5.00	7.20	-90.20	1.0	4.10–5.00	-154.80	[4]
0.18 μm CMOS	4.20	4.50	-119.0	1.0	4.10–4.80	-184.47	[5] ^S
0.18 μm CMOS	5.00	13.00	-121.5	1.0	5.10–5.36	-192.10	[6] ^S
0.18 μm CMOS	5.20	9.70	-113.7	1.0	4.39–5.26	-180.00	[8]
0.18 μm CMOS	5.80	10.08	-117.0	1.0	5.27–6.41	-184.00	[9]
0.13 μm CMOS	5.80	2.88	-132.7	1.0	4.84–6.76	-198.38	This work ^S

F : Centre frequency, P : power, PN : Phase noise at 1 MHz, * at 10 MHz offset, TR : Tuning range, FoM: Figure of Merit, S : Simulation.

To compare the performance of previously published oscillators, and FOM, the one we have used was adopted by Ham and Hajimiri [7], and it normalizes the measured phase noise with respect to center frequency and power consumption. It is defined by Equation (2):

$$\text{FOM} = L\{\Delta f\} - 20 \log \left\{ \frac{f_0}{\Delta f} \right\} + 10 \log \left\{ \frac{Pd}{1 \text{ mW}} \right\} \quad (2)$$

A brief description of the performance summary and comparison with published work has been mentioned in Table 1, and shows that the design of the proposed VCO proved to be state of the art. The phase noise is considerably good where the FOM is found to be excellent.

4. CONCLUSION

We demonstrated a 5.80 GHz low-phase-noise and low-power LC-VCO based on cross-coupled topology using a 130 nm CMOS technology. We can conclude that the proposed MOMDCSA and the

nMOS varactor have better characterizations than other switches and a more significant effect on the reduction of phase noise. The feasibility of a high-performance, high-frequency VCO is demonstrated. The phase noise of the oscillator was optimized and the measured worst-case phase noise is -129.7 dBc/Hz at 1 MHz frequency offset. As a result, this CMOS VCO achieves the best FOM of -198.38 dB. The VCO shows approximately 33% tuning range and consumes 2.8 mW from a 3.3 V power supply.

REFERENCES

1. Tieboud, M., *Low Power VCO Design in CMOS*, Springer, Berlin, Heidelberg, Netherlands, 2006.
2. Aktas, A. and M. Ismail, *CMOS PLLs and VCOs for 4G Wireless*, Springer Science, Business Media Inc., USA, 2004.
3. Lesson, D. B., "A simple model of feedback oscillator noise spectrum," *Proceedings of the IEEE*, Vol. 54, No. 2, Feb. 1966.
4. Jin, J., X. Yu, X. Liu, W. Lim, and J. Zhou, "A wideband voltage-controlled oscillator with gain linearized varactor bank," *IEEE Transactions on Components, Packaging, and Manufacturing Technology*, 1–6, 2014.
5. Yin, X., C. Ma, T. Ye, S. Xiao, and Y. Jin, "A low-phase-noise LC-VCO with an enhanced- Q varactor for use in a high-sensitivity GNSS receiver," *Journal of Semiconductors*, Vol. 33, No. 5, 2012.
6. Tang, X., F. Huang, M. Shao, and Y. Zhang, "A wideband 0.13 μm CMOS LC-VCO for IMT-advanced and UWB applications," *IEEE MTT-S International Microwave Workshop Series on Millimeter Wave Wireless Technology and Applications*, 2012.
7. Hajimiri, A. and T. Lee, *The Design of Low Noise Oscillators*, Springer, USA, 1999.
8. Kuo, K. and C. Wu, "A low phase noise VCO for 5-GHz WiMAX/WLAN frequency synthesizer," *IEEE International Conference of Electron Devices and Solid-State Circuits (EDSSC)*, 2013.
9. Guo, C., J. Hu, S. Zhu, H. Sun, and X. Lv, "A 5-GHz low-phase-noise CMOS LC-VCO for China ETC applications," *2011 IEEE International Conference on Microwave Technology & Computational Electromagnetics (ICMTCE)*, 267–269, 2011.

Dual-band Bandpass Filter Based on GaN MMIC

Zhi Xia Du¹, Xiu Yin Zhang¹, and Hsuan-Ling Kao²

¹School of Electronic and Information Engineering, South China University of Technology
Guangzhou 510640, China

²Department of Electronic Engineering, Chang Gung University, Taoyuan, Taiwan

Abstract— Dual-band bandpass filter using stub-loaded resonators (SLR) based on GaN MMIC is presented in this paper. The proposed circuit consists of two symmetric stub-loaded resonators, which are folded and coupled to each other. The two passband frequencies can be easily controlled by tuning the length of the half-wavelength resonators and the open stubs shunted at the midpoint of the microstrip lines. Moreover, the ports are directly tapped at the resonators. And additional open stubs are added to the 50-ohm feed lines for better performance. Benefiting from the integrated circuit technology, the filter can be designed on GaN MMIC that only occupies a small size. For demonstration, a filter, centered at 40 GHz and 60 GHz, is designed and the simulated result shows good performance.

1. INTRODUCTION

In the recently years, the rapid developments of modern wireless communication systems attract great demand of multi-band (especially dual-band) bandpass filters. To meet this demand, much research has been carried out [1–11]. The most intuitive method to implement a dual-band bandpass filter is to simply combine two bandpass filters with two distinctive central frequencies [1] in parallel, at the cost of enlarged circuit size and complicated matching network. In [2–5], stepped-impedance resonators (SIRs) are very popular and have been widely adopted in dual-band bandpass filter designs. However, the SIRs are relatively large in size and can hardly provide sufficient flexibility for improving frequency ratios, coupling properties and harmonic responses. Moreover, the resonant frequencies of SIRs are dependent, complicating the filter design. In [6], by a cascade connection of a BPF and a bandstop filter, a dual-band bandpass filter (BPF) was achieved with the drawback of a large circuit size. Dual-band filters can also be realized by embedding a bandstop filter inside a wideband bandpass filter in [7] or combining two sets of resonators with common input and output in [8, 9].

What's more, a dual-band transformer is introduced to realize 90 phase shift at two frequencies and applied to dual-band branch-line coupler design in [10]. But the operating frequencies of the transformer are still dependent. So a resonator which has easily controlled resonant frequencies is proposed in [11]. Its resonant frequencies of even-mode can be conveniently tuned, while those of the odd-mode remain almost the same. Using the proposed SLR, a dual-band BPF is designed with three transmission zeros in [11]. But we can find that none of this filter is designed on MMIC and most of them are work at low frequencies.

Nowadays, the development of IC is fast. The electronic components on IC can be smaller, low power consumption, intelligent and high reliability. In addition, the dual-band filter based on MMIC can not only realize a small size, but also achieve a high operating frequency. Therefore, much research has been made for filters to work at high frequencies based on MMIC. For examples, A low-insertion-loss V-band CMOS bandpass filter whose center frequency is 63.5 GHz is demonstrated in [12]. A miniaturized and low-insertion-loss V-band bandpass filter implemented on the integrated passive device (IPD) is demonstrated in [13], which is centered at 55.85 GHz. In [14], a new 60 GHz fourth-order cross-coupled bandpass filter using a step-impedance-resonator (SIR) miniaturised open-loop resonator and the miniaturised-hairpin (MH) resonator was designed and fabricated on 0.13 mm bulk CMOS. In [15], a 77-GHz millimeter-wave on-chip bandpass filter with balanced output that was fabricated using a TSMC 0.18- μm standard CMOS process. However, none of this filters working at high frequencies is integrated on the substrate of GaN.

In this paper, a dual-band bandpass filter using stub-loaded resonators based on GaN MMIC is designed. The dual-band filter comprises two symmetric stub-loaded resonators, which are folded and coupled to each other. Every stub-loaded resonator is composed of a conventional microstrip half-wavelength resonator and an open stub. According to the even- and odd-mode analysis, the second passband can be controlled by the stubs while the first passband is fixed. The ports are directly tapped at the resonators. Moreover, additional open stubs are added to the 50-ohm feed

lines, which are used to couple with the resonators that can improve the performance of the filter. A dual-band bandpass filter, with center frequencies of 40 and 60 GHz, is shown in this paper. Benefitting from the integrated circuit technology, the filter can be designed on GaN MMIC that only occupies a small size, but good performance. The design will be shown in the following sections.

2. DUAL-BAND FILTER DESIGNED ON MMIC

Figure 1 in [11] shows a stub-loaded resonator (SLR) consists of a conventional microstrip half-wavelength resonator and an open stub shunted at the midpoint of the microstrip line. Odd- and even-mode analysis can be adopted to characterize it since the SLR is symmetrical in structure.

The odd-mode resonant frequencies of the stub-loaded resonator is

$$f_{odd} = \frac{(2n-1)c}{2L'_1\sqrt{\varepsilon_{eff}}} \quad (1)$$

where $n = 1, 2, 3, \dots$, c is the speed of light in free space, ε_{eff} denotes the effective dielectric constant of the substrate. It can be observed that the odd-mode resonant frequencies are not affected by the open stub.

For even-mode excitation, the even-mode resonant frequencies can be attained as

$$f_{even} = \frac{nc}{(L'_1 + 2L'_2)\sqrt{\varepsilon_{eff}}} \quad (2)$$

From the Equations (1), (2) we can find that by changing the stub length L'_2 , the fundamental even-mode resonant frequency can be shifted, whereas the fundamental odd-mode resonant frequency is preserved.

Based on the proposed SLR, A dual-band filter which consists of two folded SLRs is designed. Compared with the conventional open-loop resonator [12], this one has an extra open stub loaded inside the open loop. The passband frequencies are mainly determined by the entire length of the open loop and the length of the open stub.

As we know, the dual-band filter designed above works at low frequencies, which means that the open stubs of the filter can be put inside the open loops to get a small circuit size. However, when the dual-band filter works at high frequencies, the mutual coupling between the two open stubs is very serious, which can significantly inhibit performance of the filter. In addition, the space inside the filter may be not big enough for the open stubs if we want an appropriate rate of f_2/f_1 (f_1 presents the center frequency of the first passband while f_2 presents the second) since the lower of f_2 , the longer of the open stubs. And the limited space in each resonator may cause unwanted coupling between the open loop and the open stub. In order to reduce the interference, the open stubs are arranged at outside of the open loops while are still located at the midpoint of the main microstrip lines. Moreover, the passband bandwidths of this filter depend on the external quality factors and the coupling coefficients between the two resonators. Accordingly, the gap between two folded SLRs and the position of the feed lines determine the bandwidths. Furthermore, additional open stubs are added to the 50-ohm feed lines, which are used to couple with the resonators that can improve the performance of the filter. The length and the position of the open stubs can be tuned by analyzing the simulated results. The layout of the proposed dual-band filter based on MMIC is shown in Fig. 1(a).

Therefore, the dual-band filter based on GaN MMIC can be designed as follows. Firstly, the desired two passband frequencies can be obtained by tuning the length of half-wavelength resonators and the open stubs according to Equations (1) and (2). Secondly, the gap of the two resonators and the position of the feed lines are tuned to obtain a bandpass response with given specifications. Finally, the couple strength between the open stubs added to the 50-ohm feed lines and the open-stub resonators can be tuned to get a better performance. The couple strength depends on the distance between the added open stub and the half-wavelength resonator as well as the distance between the added open stub and the open stub shunted at the midpoint of the microstrip line.

Figure 1(b) shows the side of the filter on MMIC. There are three layers of substrates in this design. They are SiN, GaN and Silicon with relative dielectric constants of 6.5, 9, 11.9 and dielectric loss tangents of 0.09, 0.09, 0.01 from top to bottom. Respectively, their thicknesses are 0.15 μm , 6.28 μm and 93.57 μm . The material of the microstrip lines we used is gold, with a relative dielectric constant of 1, and its thickness is 2.15 μm .

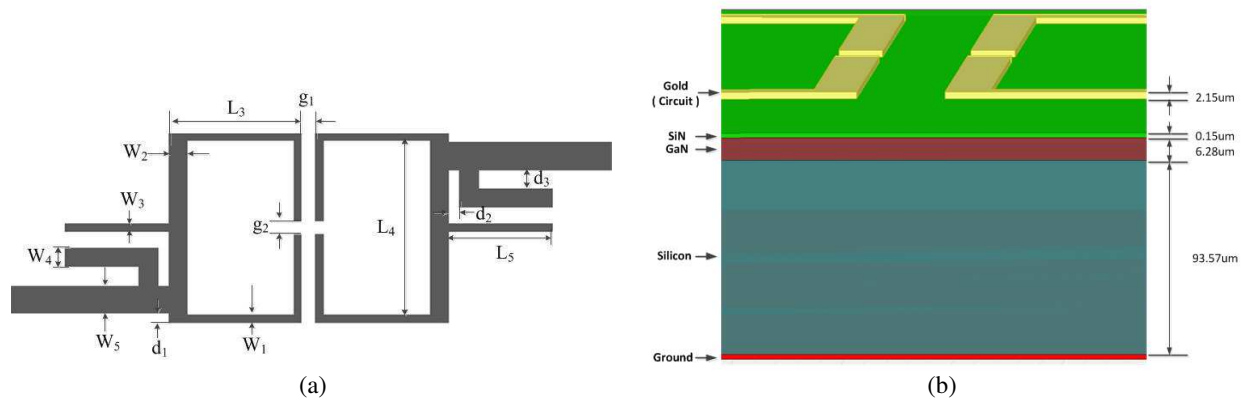


Figure 1: Proposed dual-band filter configuration. (a) Schematic diagram. (b) Partly 3-D view on IC.

3. EXPERIMENTAL RESULTS

To verify our proposal, a dual-band bandpass filter based on GaN MMIC is designed and implemented. According to the three design steps above, the design parameters of the proposed dual-band filter in Fig. 1(a) are $W_1 = 20 \mu\text{m}$, $W_2 = 50 \mu\text{m}$, $W_3 = 20 \mu\text{m}$, $W_4 = 50 \mu\text{m}$, $W_5 = 78 \mu\text{m}$, $L_3 = 360 \mu\text{m}$, $L_4 = 500 \mu\text{m}$, $L_5 = 280 \mu\text{m}$, $d_1 = 10 \mu\text{m}$, $d_2 = 30 \mu\text{m}$, $d_3 = 72 \mu\text{m}$, $g_1 = 40 \mu\text{m}$, $g_2 = 40 \mu\text{m}$.

Figure 2 shows the simulation result of the dual-band filter on MMIC which without open stubs added to the 50-ohm feed lines. The center frequencies of the passbands are located at 40 and 60 GHz, and their insertion losses are 4.1 and 5.1 dB at the lower and upper passbands. For improving the performance of the filter, additional open stubs are added to the 50-ohm feed lines. Fig. 3 shows the simulation result of the proposed dual-band filter on MMIC. The center frequencies of the passbands are located at 40 and 60 GHz, with 3 dB bandwidths of 15% (37 to 43 GHz) and 13.3% (56 to 64 GHz). The insertion losses are 3.4 and 4.0 dB at the lower and upper passbands and the return losses within the two passbands are better than 17 dB, which means better performance than the simulation result shown in Fig. 2. If the relative dielectric constant of GaN is 10, the center frequencies of the filter will be a little lower by Equations (1) and (2). So we have to decrease the length of the SLRs, making sure that the center frequencies of the dual-band are 40 GHz and 60 GHz. Let $L_3 = 350 \mu\text{m}$, we get the frequency responses that the insertion losses are 3.3 and 3.8 dB at the lower and upper passbands with almost the same bandwidths, which shows that the performance is better.

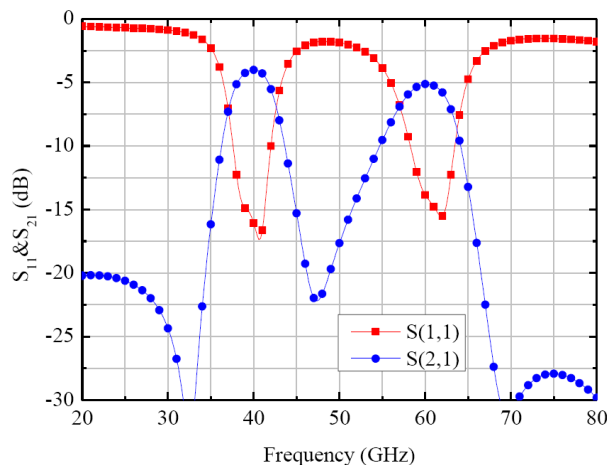


Figure 2: Frequency responses of the filter on IC without open stubs added to the 50-ohm feed lines.

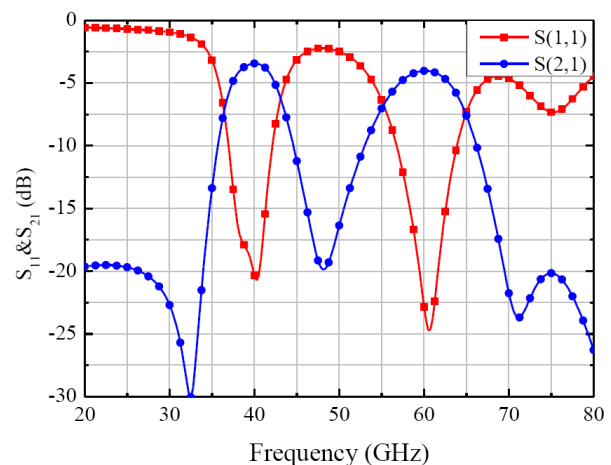


Figure 3: Frequency responses of the proposed filter on IC.

4. CONCLUSION

In this paper, a proposed dual-band bandpass filter based on GaN MMIC is demonstrated. The two passband frequencies can be easily controlled by tuning the length of the half-wavelength resonators and the open stubs shunted at the midpoint of the microstrip lines. In each SLR, the open stub is arranged at outside of the open loop to reduce interference. Furthermore, another open stub is added to the 50-ohm feed line respectively, which can be used to improve the performance of the filter. Benefitting from the integrated circuit technology, the design only occupies a small size. For verification, a dual-band filter whose center frequencies are 40 GHz and 60 GHz is given.

REFERENCES

1. Miyake, H., S. Kitazawa, T. Ishizaki, T. Yamada, and Y. Nagatomi, "A miniaturized monolithic dual band filter using ceramic lamination technique for dual mode portable telephones," *IEEE MTT-S Int. Microw. Symp. Dig.*, Vol. 2, 789–792, 1997.
2. Kuo, J.-T., T.-H. Yeh, and C.-C. Yeh, "Design of microstrip bandpass filters with a dual-passband response," *IEEE Trans. Microw. Theory Tech.*, Vol. 53, 1331–1337S, 2005.
3. Sun and L. Zhu, "Compact dual-band microstrip bandpass filter without external feeds," *IEEE Microw. Wireless Compon. Lett.*, Vol. 15, No. 10, 644–646, Oct. 2005.
4. Chang, S.-F., Y.-H. Jeng, and J.-L. Chen, "Dual-band step-impedance bandpass filter for multimode wireless LANs," *Electron. Lett.*, Vol. 40, No. 1, 38–39, Jan. 2004.
5. Wang, J., Y.-X. Guo, B.-Z. Wang, L. C. Ong, and S. Xiao, "High-selectivity dual-band stepped-impedance bandpass filter," *Electron. Lett.*, Vol. 42, No. 7, 538–539, Apr. 2006.
6. Tsai, L.-C. and C.-W. Huse, "Dual-band bandpass filters using equal-length coupled-serial-shunted lines and Z -transform techniques," *IEEE Trans. Microw. Theory Tech.*, Vol. 52, No. 4, 1111–1117, Apr. 2004.
7. Tsai, L. C. and C. W. Hsue, "Dual-band bandpass filters using equallength coupled-serial-shunted lines and Z -transform technique," *IEEE Trans. Microw. Theory Techn.*, Vol. 52, No. 4, 1111–1117, Apr. 2004.
8. Chen, C.-Y. and C.-Y. Hsu, "A simple and effective method for microstrip dual-band filters design," *IEEE Microw. Wireless Compon. Lett.*, Vol. 16, No. 3, 246–248, May 2006.
9. Chen, J.-X., T. Y. Yum, J.-L. Li, and Q. Xue, "Dual-mode dual-band bandpass filter using stacked-loop structure," *IEEE Microw. Wireless Compon. Lett.*, Vol. 16, No. 9, 502–504, Sep. 2006.
10. Zhang, H. and K. J. Chen, "A stub tapped branch-line coupler for dual-band operations," *IEEE Microw. Wireless Compon. Lett.*, Vol. 17, No. 2, 106–108, Feb. 2007.
11. Zhang, X. Y. and Q. Xue, "Dual-band bandpass filters using stub-loaded resonators," *IEEE Microw. Wireless Compon. Lett.*, Vol. 17, No. 8, 583–585, Aug. 2007.
12. Chang, J.-F., Y.-S. Lin, P.-L. Huang, and S.-S. Lu, "A micromachined V-band CMOS bandpass filter with 2-dB insertion-loss," *Electronic Components and Technology Conference*, 2009.
13. Lin, W.-C., T.-M. Shen, C.-F. Chen, T.-Y. Huang, and R.-B. Wu, "A miniaturized V-band bandpass filter using integrated passive devices technology," *Proceedings of Asia-Pacific Microwave Conference*, 2010.
14. Yang, B., E. Skafidas, and R. J. Evans, "60 GHz compact integrated cross-coupled SIR-MH bandpass filter on bulk CMOS," *Electronics Letters*, Vol. 44, No. 12, Jun. 5th, 2008.
15. Hsu, C.-Y., C.-Y. Chen, and H.-R. Chuang, "A 77-GHz CMOS on-chip bandpass filter with balanced and unbalanced outputs," *IEEE Electron Device Letters*, Vol. 31, No. 11, Nov. 2010.

Study of Response of PIN Diode to Electromagnetic Pulse

Yong Li¹, Haiyan Xie¹, Chun Xuan¹, Hongfu Xia¹, and Jian-Guo Wang^{1,2}

¹Northwest Institute of Nuclear Technology, Xi'an 710024, China

²School of Electronic and Information Engineering, Xi'an Jiaotong University, Xi'an 710049, China

Abstract— Response of PIN diode is numerically simulated by a self-developed 2D semiconductor device simulation GSRES to study the response behavior of PIN diode limiter under electromagnetic pulse (EMP). Current overshoot phenomena of PIN diode during the rise time of EMP, which is validated to be due to the capacitive performance of PIN diode under high frequency, are analyzed. Shorter rise time of EMP causes higher current peak value. Overshoot current is affected by the impurity doping concentration of PIN diode. Higher doping concentration of impurity in the P layer and N layer causes higher peak of current and sooner attenuation of overshoot current. Doping concentration of the I layer affects the overshoot current too, but not as salient as concentration of the P and N layers. These results can be used in radiation hardening for PIN diode limiter.

Electronic systems are used more and more widely in industryeconomic and science research as key equipment. Semiconductor devices, as basic component, determines the performance of electronic system. Since the development of manufacturer techniques, operation power of device becomes much lower than before, and therefore, much more susceptible by electromagnetic pulse (EMP). For these reasons, study of the effects of semiconductor devices in electronic system under EMP is now becoming immediately demand not only for industrial application but also in informationize process. PIN diode, which is used as a component in communication and radar systems, is also the key component of PIN limiter, so the study of its effect under EMP is important in electronic equipment harding and shielding.

Comparing with experimental method, numerical simulation of semiconductor devices can reflect the physical phenomena and mechanisms of devices, and is important in effect study. It is proved to be efficient and accurate as many research results showed [1–3]. One-dimension numerical simulation result of PIN diode under step voltage pulses with risetime less than 0.1 ns is obtained [4] and overshoot current phenomenon appears. Characters of PIN diodes in EMP field are researched by equivalent circuit models [5, 6]. Also, abecedarian study of response of PIN diode under EMP is developed [7]. In this paper, relationship between overshoot current of PIN diode under EMP with the risetime of pulse and relationship between overshoot current of PIN diode under EMP with density of impurity of diode are studied numerically by a simulator GSRES (General Semiconductor Radiation Effect Simulator).

1. INTRODUCTION OF SIMULATION METHOD

GSRES is now widely used in numerical simulation radiated field (EMP, HPM) effect of semiconductor device, which is developed by our research group. This simulator is assembled by modelling modular, meshing modular, data-base of material parameters and graphic vision modular. The numerical simulation of carriers bases on Drift-Diffusion Model (DDM). Two-dimension semiconductor device and simple circuit can be simulation numerically by this simulator [7–10].

Drift-Diffusion model is used more and more widely in numerical simulation of semiconductor device since the first use by Gummel. With out the consideration of the change of temperature, Poisson equation in double-carrier semiconductor device is

$$\nabla \cdot \varepsilon \nabla \psi = -q (p - n + N_D^+ - N_A^-) - \rho_s \quad (1)$$

where ψ is electrostatic potential, and in GSRES it is equivalent to vacuum energy level of electron. N_D^+ is the concentration of effective ionic donors, N_A^- is the concentration of effective ionic acceptor, and ρ_s is the static charge and interphase charge. Energy level of valence band and conduction band can be written up with ψ as

$$E_c = -q\psi - \chi + V E_c \quad (2)$$

$$E_v = E_c - E_g + V E_v \quad (3)$$

In equation, χ is electron affinity, VE_c and VE_v is the offset of energy band caused by heavily doped or internal stress. Electrostatic potential ψ is

$$\psi = \psi_{\text{intrinsic}} - \frac{\chi}{q} - \frac{E_c}{2q} - \frac{k_b T}{2q} \ln \left(\frac{N_c}{N_v} \right) \quad (4)$$

where $\psi_{\text{intrinsic}}$ is intrinsic Fermi potential. k_b is Boltzmann constant. N_c and N_v is the electron density of conduction band and valence band. Continuity equation of carrier is

$$\begin{cases} \frac{\partial n}{\partial t} = \frac{1}{q} \nabla \cdot J_n - (U - G) \\ \frac{\partial p}{\partial t} = \frac{1}{q} \nabla \cdot J_p - (U - G) \end{cases} \quad (5)$$

In Equation (5), J_n is the current density of electron. J_p is the current density of hole. U is the recombination term of carrier. G is the generation term of carrier. The current equation of J_n and J_p is

$$\begin{cases} J_n = q\mu_n n E_n + qD_n \nabla n \\ J_p = q\mu_p p E_p - qD_p \nabla p \end{cases} \quad (6)$$

where μ_n is mobility of electron and μ_p is mobility of hole. $D_n = \frac{k_b T}{q} \mu_n$ is the diffusion coefficient of electron and $D_p = \frac{k_b T}{q} \mu_p$ is the diffusion coefficient of hole. E_n is the equivalent electric field intensity to electron and E_p is the equivalent electric field intensity to hole. They can be expressed as

$$E_n = \frac{1}{q} \nabla E_c - \frac{k_b T}{q} \nabla \left(\ln(N_c) - \ln(T^{3/2}) \right) \quad (7)$$

$$E_p = \frac{1}{q} \nabla E_v + \frac{k_b T}{q} \nabla \left(\ln(N_v) - \ln(T^{3/2}) \right) \quad (8)$$

E_c is the electron energy level of conduction band and E_v is the electron energy level of valence band. If the temperature of lattice uniformity and invariableness, gradient term of temperature is 0. Combining to Equations (1) and (5), the basic Drift-Diffusion model without temperature effect is

$$\begin{cases} \frac{\partial n}{\partial t} = \nabla \cdot \left(\mu_n n E_n + \mu_n \frac{k_b T}{q} \nabla n \right) - (U - G) \\ \frac{\partial p}{\partial t} = -\nabla \cdot \left(\mu_p p E_p - \mu_p \frac{k_b T}{q} \nabla p \right) - (U - G) \\ \nabla \cdot \varepsilon \nabla \psi = -q(p - n + N_D^+ - N_A^-) - \rho_s \end{cases} \quad (9)$$

Equation (9) is the basic and mostly used calculation model in GSRES. In our simulation, voltage amplitude loaded in diode is 0.9 V, and rise time is 100 ps, as showed in Fig. 2. The maximum current in the diode is 3.3336×10^{-4} A, which is normalized in Fig. 2. In this example, total Joule heat is about 1.23×10^{-15} J and the alteration of device's temperature is less than 0.01 K. So, although none thermal effect is contained in this model yet, the simulation result according with references and theoretical analysis quite well.

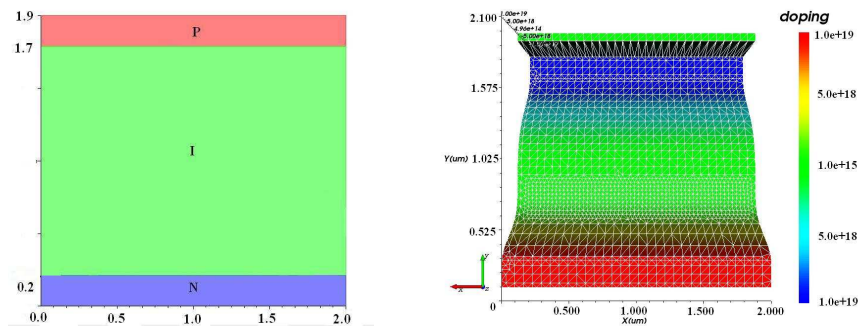


Figure 1: Two dimensional model of structure and doping density of PIN diode.

2. MODEL OF DEVICE

Figure 1 is a two dimensional model of a PIN diode, which is p^+nn^+ structure. The diode is uniformity in Z axis with a height of $1\ \mu\text{m}$. Width of this diode is $2\ \mu\text{m}$. Thickness of P layer and N layer are both $0.2\ \mu\text{m}$, with Gaussian doping both and peak density of impurity is $10^{19}\ \text{cm}^{-3}$. Diffusion width of P layer is $0.4\ \mu\text{m}$ and N layer is $0.2\ \mu\text{m}$. I layer is as thick as $1.5\ \mu\text{m}$ with a uniformity doping of $10^{15}\ \text{cm}^{-3}$ of acceptors.

3. SIMULATION RESULT AND DISCUSSION

3.1. Overshoot of Current under Electromagnetic Pulse

Effect of PIN diode under pulses with different risetime varying from $0.01\ \text{ns}$ to $0.5\ \text{ns}$ is studied using the numerical simulation method. The voltage pulse loaded in diode is step voltage with an amplitude of $0.9\ \text{V}$ as showed in Fig. 2 (In Fig. 2 the rise time of pulse is $100\ \text{ps}$). The maximum current in the diode is $3.3336 \times 10^{-4}\ \text{A}$ as referenced in part 1, and in Fig. 2 it is normalized.

As Fig. 2 shows, when voltage is rising, current in diode soon reaches to an great value; after risetime, voltage is steady and the current lows down to a small steady value. That is current overshoot phenomenon of PIN diode under EMP.

3.2. Relationship between Current Overshoot Phenomenon and Rise Time of Pulse

Current overshoot phenomenon appears because of the capacitance of PIN diode under the action from high frequency electromagnetic field of the pulse in risetime. Capacitive reactance relates with the frequency of the electromagnetic field which is induced by the rising edge of the pulse. Capacitive reactance becomes small when frequency increases. In this case, shorter the risetime of pulse is, higher the frequency is. So, Capacitive reactance of diode falls down when shorten the

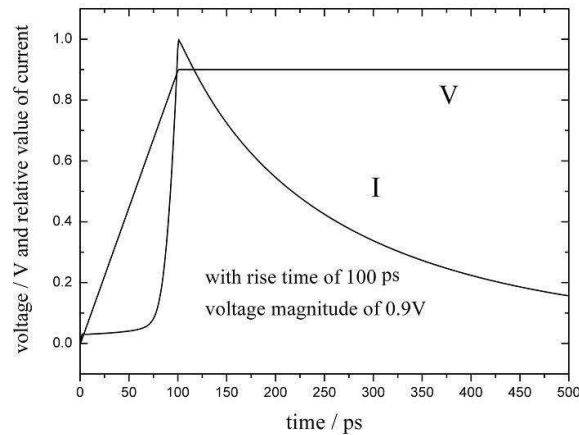


Figure 2: Behavior of current under EMP.

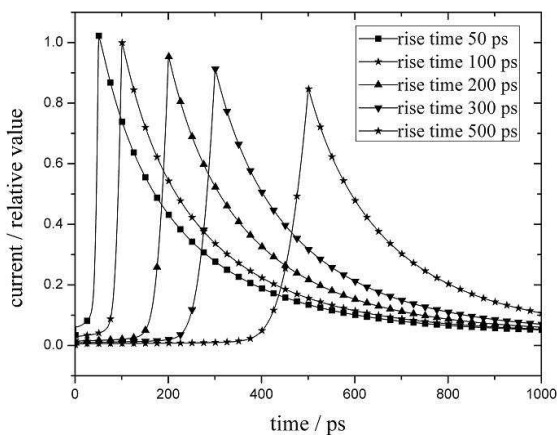


Figure 3: Behavior of current under EMP with varying rise time.

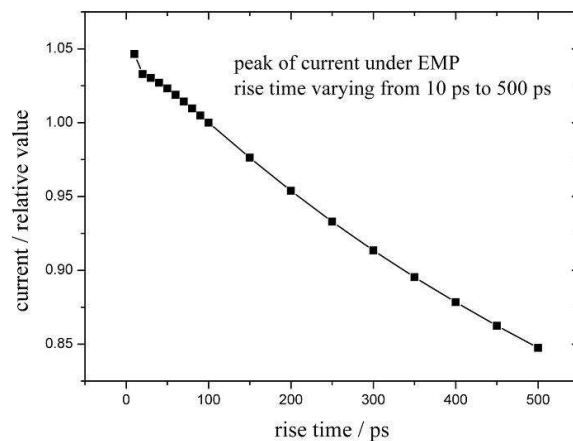


Figure 4: Peak of current under EMP with varying rise time.

risetime of pulse, and the peak value of overshoot current increases, as Fig. 3 showed. Pulse loaded in diode with amplitude of 0.9 V and risetime from 0.01 ns to 0.5 ns is showed in Fig. 3. Peak current of pulse with 0.01 ns risetime is higher than that of 0.5 ns and falls down faster than that of 0.5 ns too. Peak value of overshoot current in diode gives a nearly linearity relation with risetime as Fig. 4 shows.

3.3. Relationship between Current Overshoot Phenomenon and Density of Carriers

In this chapter, the density of impurity of the PIN diode is changed in order to analyse the response mechanism under EMP. The structure of diode is same as that in Fig. 1 but the doping densities of P layer and N layer are changed.

Current in different doping density PIN diodes loaded same pulse voltage with amplitude of 0.9 V and risetime of 0.1 ns is showed in Fig. 5 (In Fig. 5 current values are normalized). In each diode, the doping density of P layer is equal to that of N layer. Three diodes are simulated, the density of impurity of these diodes are $0.5 \times 10^{19}/\text{cm}^3$, $1.0 \times 10^{19}/\text{cm}^3$ and $2.0 \times 10^{19}/\text{cm}^3$. Peak value of current in the diode whose doping density is $2.0 \times 10^{19}/\text{cm}^3$ is greater than that in $0.5 \times 10^{19}/\text{cm}^3$ diode, and falls down more quickly than that in $0.5 \times 10^{19}/\text{cm}^3$ diode too. Behavior of current in $1.0 \times 10^{19}/\text{cm}^3$ diode is situated between that of the above two diodes. Peak value of overshoot current and falling down the speed are indicated to be related with the densities of carriers.

Peak values of overshoot current in these three diodes under voltage pulse with risetime from 0.01 ns to 0.1 ns are showed in Fig. 6(a) and risetime from 0.1 ns to 0.5 ns are showed in Fig. 6(b), the values are normalized in both two diagrams. Peak values of overshoot current are nearly linearly correlated with the periods of risetime according to Fig. 4. Slope of the linear fitting function of peak current values in the diode whose doping density is $2.0 \times 10^{19}/\text{cm}^3$ is greater than that in diode whose doping density is $0.5 \times 10^{19}/\text{cm}^3$ as Fig. 6 showed. This phenomenon suggests that the increase of doping density leads to not only the accretion of overshoot current but also the accretion of sensibility to the change of pulse waveform.

This phenomenon part I because the change of conductance induced by the varying of doping density. Current in the above three diodes under a 0.9 V stable voltage is showed in Table 1. Under stably voltage, while current is totally determined by conductance of diode, the variations between the three diodes are not the same comparing with that of pulse voltage. We suppose that the change of doping density inflects both conductance and capacitance of diode, thus influence the overshoot current.

Change of doping density in I layer inflects the current in diode too, but not as salient as that of P and N layers as Table 2 shows. Increase of doping density of I layer leads to the decrease of overshoot current. Discrepancy between current in diode with $0.1 \times 10^{19}/\text{cm}^3$ I layer doping density and current in $10 \times 10^{19}/\text{cm}^3$ diode is less than 3%. However, the change of doping densities of P and I layer from $1.0 \times 10^{19}/\text{cm}^3$ to $2.0 \times 10^{19}/\text{cm}^3$ cause an more than 40% change of current. Doping density of P layer and N layer influence the current in diode much more patently.

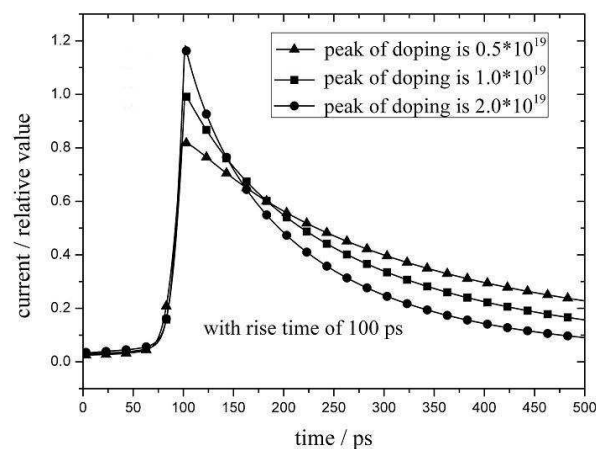


Figure 5: Behavior of current under EMP with varying doping concentration.

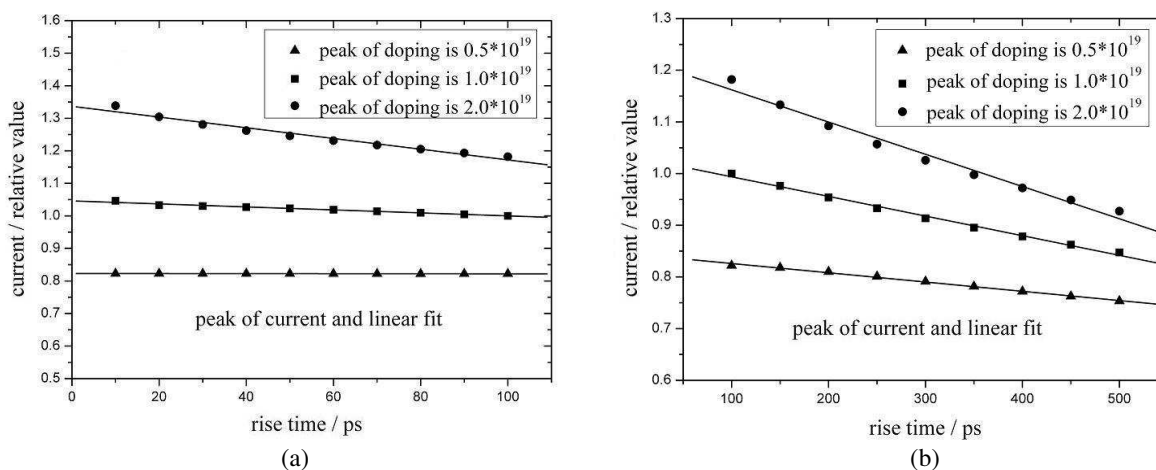


Figure 6: Peak of current under EMP with varying rise time in PIN diodes of different doping concentration, (a) with rise time varying from 10 ps to 100 ps, (b) with rise time varying from 100 ps to 500 ps.

Table 1: Current in PIN diode with varying doping concentration of P layer and N layer under 0.9 V stable voltage.

Doping density of P and N layer ($10^{19}/\text{cm}^3$)	Peak current under 0.9 V stable voltage (10^{-5} A)	Normalized peak current value under 0.1 ns risetime pulse	Normalized peak current value under 0.2 ns risetime pulse
0.5	1.1143	0.8145	0.8220
1.0	1.3680	1	1
2.0	2.0053	1.4658	1.1820

Table 2: Peak of current under EMP with varying doping concentration of I layer under EMP with risetime of 0.1 ns.

Doping density of I layer ($10^{15}/\text{cm}^3$)	Peak current under 0.9 V stable voltage (10^{-4} A)	Normalized value
0.1	3.3406	1.0021
0.5	3.3398	1.0019
1.0	3.3336	1
5.0	3.3035	0.9910
10	3.2675	0.9802

4. CONCLUSIONS

Current overshoot phenomenon appears in PIN diode because of the capacitance of diode under the action from high frequency electromagnetic field of the pulse in risetime. Capacitance of diode is influenced by doping density of P layer, N layer and I layer of diode and the frequency of loaded electromagnetic field. As simulation result shows, Peak value of overshoot current and the falling down speed are indicated to be negatively related with the densities of carriers in P layer and N layer almost linearly. Increase of doping densities in P and N layers leads to not only the accretion of overshoot current but also the accretion of sensibility to the change of pulse waveform. Doping density in I layer inflects the current in diode too, but not as salient as that of P and N layers.

Current overshoot phenomenon may causes a great transient current. If the risetime of pulse is short enough, transient current may interferes the signal in circuit or even leads to logical errors in circuits and causes the failure of electronic equipments. It is important in harding and shielding of electronic equipment. We plan to study the mechanism by analysing the causation of overshoot current using both numerical and experimental methods.

ACKNOWLEDGMENT

This work was supported in part by National Science Foundation of China (NFSC) under Grant 61201090 and 61231003.

REFERENCES

1. Gummel, H. K., "A self-consistent iterative scheme for one-dimensional steady state transistor calculations," *IEEE Trans. Electron Devices*, Vol. 9, No. 11, 455–465, 1964.
2. Yee, J. H., "Modeling of current and thermal mode second breakdown phenomena," *Electrical Overstress/Electrostatic Discharge Symposiums Proceedings*, 76–81, 1982.
3. Orvis, W. J., "Modeling and testing for second breakdown phenomena," *Electrical Overstress/Electrostatic Discharge Symposiums Proceedings*, 108–117, 1983.
4. Zhou, H., Z. Du, and K. Gong, "Overshoot phenomena in PIN diode under EMP with fast rise time," *High Power Laser and Particle Beams*, Vol. 17, No. 5, 783–787, 2005.
5. Wang, H., J. Li, Y. Zhou, H. Li, and X. Yu, "Experimental study and Pspice simulation of PIN diode limiter," *High Power Laser and Particle Beams*, Vol. 18, No. 1, 88–92, 2006.
6. Wang, B. and K. Huang, "Response of high power PIN diode limiter to electromagnetic pulse descending edge," *High Power Laser and Particle Beams*, Vol. 20, No. 7, 1177–1181, 2008.
7. Li, Y., C. Xuan, and J. Wang, "Study of response to electromagnetic pulse of PIN diode," *Proceedings of EME*, 280–283, 2012.
8. Gong, D., F. Han, and J. Wang, "2D hydrodynamic simulation of GaAs metal-semiconductor-field-effect-transistor," *High Power Laser and Particle Beams*, Vol. 18, No. 7, 1144–1148, 2006.
9. Gong, D., J. Wang, D. Zhang, et al., "A general purpose two-dimensional semiconductor simulator," *Chinese Journal of Computational Physics*, Vol. 24, No. 2, 247–252, 2007.
10. Xuan, C., D. Gong, H. Xie, et al., "Semiconductor device/circuit mixed-type simulation and its application in HPM effects," *Microelectronics*, Vol. 39, No. 3, 424–428, 2009.
11. Ji, L., *Calculate Microelectronics*, Science Press, Beijing, 1996.
12. Huang, K. and R. Han, *Solid Physics*, Higher Education Press, Beijing, 1988.

THz False-color Imaging with Flexible Tube-lattice Fiber Probe

Wenliang Lu^{1,2}, Shuqin Lou¹, Xin Wang¹, and Alexander Argyros²

¹School of Electronic and Information Engineering, Beijing Jiaotong University, Beijing 100044, China

²Institute of Photonic and Optical Science (IPOS), School of Physics

The University of Sydney, NSW 2006, Australia

Abstract— A flexible tube-lattice fiber is introduced into a THz-TDS system to implement a THz false-color imaging system. The fiber, which has three low-loss transmission windows in the frequency range of 0.1–1 THz, can lead THz radiation out of the system and lead back to the detector. It can be used as a probe to break the spatial limit of the THz-TDS system and widen the range of applications. A cuvette filled with two different kinds of white powder was used as a sample in the experiment. One end of the fiber was fixed and the other end near the sample was scanned by a 2D translation stage across the sample. THz radiation from the fiber passes through the sample and is reflected by a mirror at the back of the cuvette. The reflected THz radiation contains the sample's THz spectral information. Thus, the entire sample can be investigated by scanning the fiber. Three-primary colors (red, green and blue) are defined by spectral intensities of the fiber transmission windows. A 13×16 pixels false-color image was generated with the mix of values of the primary colors. In the false-color image, the two kinds of powder, the cuvette and the background present different colors and saturation which indicate different materials and the concentration, respectively. The resolution was also investigated by scanning slits in a metal sheet. The resolution of the imaging system is approximately 1 mm.

1. INTRODUCTION

Terahertz (THz) radiation can be transmitted through a wide variety of substances such as paper, cloth, plastics, wood, bone, fat, various powders, dried food, and so on [1]. THz radiation interacts with macromolecular materials, such as drugs, explosives, medicines and proteins [2, 3], allowing them to be identified through their unique fingerprint information, including absorption frequencies, amplitude and phase [4]. As such, THz imaging has great potential in security, forensic and medical applications. THz imaging is usually based on large THz time-domain spectroscopy (THz-TDS) systems, which is not suitable to move. The samples must be placed in the system, which is a limit for its applications. We demonstrate a low-loss flexible THz fiber [5] which can lead the THz radiation out and back to THz-TDS system to break the spatial limit. A false-color image has been generated to present frequency information in the THz domain.

2. LOW-LOSS FLEXIBLE TUBE-LATTICE FIBER

The structure of the low-loss flexible tube-lattice fiber is shown in Fig. 1. It has a hollow core with the diameter of 4 mm and a cladding composed of eight Zeonex tubes in a ring. The sample fiber length is 20 cm. The out diameter and thickness of cladding tubes are 2.4 mm and 0.378 mm, respectively. The cladding tubes are held in place by three short jackets at either end and in the center of the fiber. The outside is shrink tube which was used to enhance mechanical stability. Zeonex was used for its low absorption loss in the THz range [6]. Since the cladding tubes are not fused together and are free to slide against each other, the fiber is easy to bend.

Due to inhibited coupling, the energy can couple into cladding to cause high loss at only a few discrete frequencies, resulting in transmission windows for frequencies in between. A THz-TDS system (Fig. 3(a)) was used to measure the transmission spectrum of the fiber. The THz radiation passes through the fiber two times and couples back to the detector. The experimental result in Fig. 2 shows three transmission windows in the range of 0.1–1 THz, which are 0.1–0.35 THz, 0.35–0.7 THz and 0.7–1.0 THz.

3. FALSE-COLOR IMAGING SYSTEM

To visualize the THz image, the fake-color system was implemented with the integrated transmission over 0.23–0.32 THz corresponding to red, 0.45–0.65 THz to green, and 0.75–0.9 THz to blue, which are shown as color boxes on Fig. 2, and correspond the fiber's three transmission windows. Different materials have different absorption frequencies, and they will affect the integration value of each window, and hence the final color for the pixel of an image.

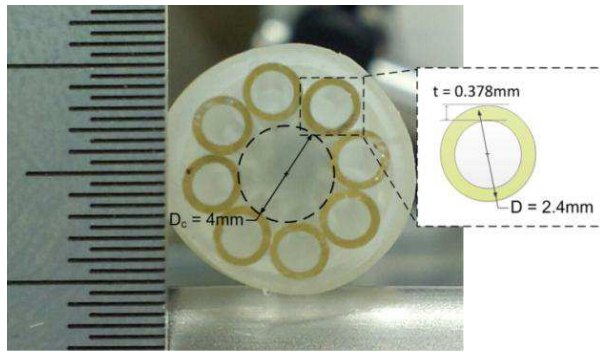


Figure 1: Fiber structure and structure parameters.

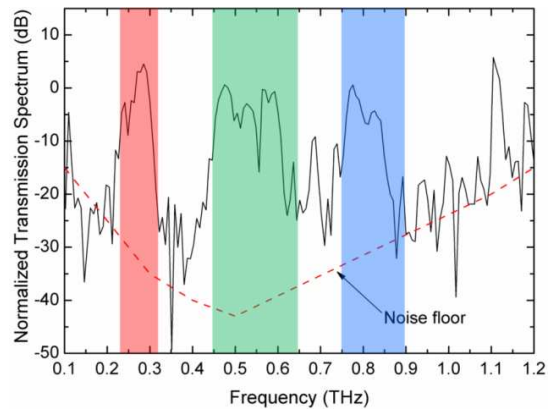


Figure 2: Normalized transmission spectrum.

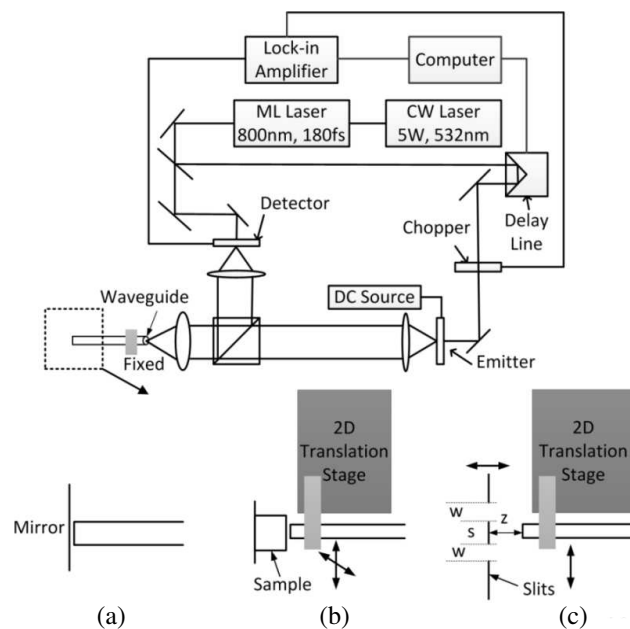


Figure 3: Experimental setups of THz-TDS. (a) is used to measure the fiber transmission spectrum, (b) is used to get the THz image of the sample, (c) is used to check the resolution of the imaging system.

A cuvette filled with two kinds of white powder, α -Lactose and 4-Aminobenzoic acid (PABA), was used. α -Lactose has one absorption frequency at 0.53 THz which is located in the second transmission window, and PABA has two absorption frequencies at 0.6 and 0.8 THz which are located in the second and third transmission windows.

The false-color imaging system is based on a THz-TDS system. One end of the flexible tube lattice fiber is fixed and the other end near the sample is scanned by a 2D translation stage (Fig. 3(b)). A 13×16 pixels image which is shown in Fig. 4(b), was obtained from the system. Compared to the optical image shown in Fig. 4(a), the background, cuvette, α -Lactose and PABA can be identified clearly due to their different colors and intensities. The α -Lactose absorbs only in the green windows, appearing magenta. PABA absorbs both in the blue and green windows, appearing red.

4. RESOLUTION

In order to explore the resolution of the imaging system, arrangement shown in Fig. 3(c) is used. The end face of the fiber was scanned across a pair of slits in a metal sheet. THz radiation incident on the metal would be reflected and some fraction would couple back into the waveguide for detection, whilst THz radiation passing through the slits would be lost. When two 1 mm slits, separated by 1 mm, are placed 1 mm away from the fiber ($w = s = z = 1$ mm), the two slits could

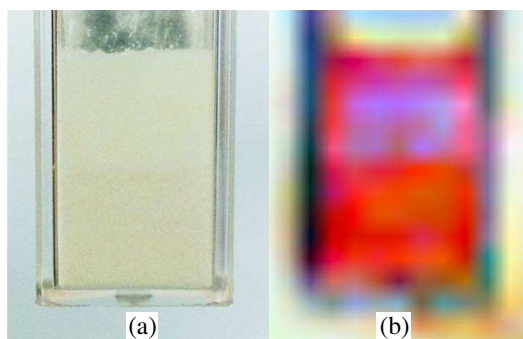


Figure 4: (a) Optical image and (b) THz fake-color image of the sample.

be clearly identified in the THz image, allowing the resolution to be estimated at 1 mm.

5. CONCLUSION

A low-loss, flexible tube lattice fiber was fabricated to have three transmission windows in the frequency range of 0.1–1 THz. The fiber was used to lead the THz radiation to a sample and lead it back to detector in the THz-TDS system. A false-color imaging system was set up with this fiber probe. A cuvette filled with α -Lactose and PABA is used as the imaging sample, and the different chemicals can be easily seen in through the false-color system. The resolution of the imaging system was estimated at 1 mm.

REFERENCES

1. Kawase, K., Y. Ogawa, Y. Watanabe, and H. Inoue, “Non-destructive terahertz imaging of illicit drugs using spectral fingerprints,” *Optics Express*, Vol. 11, 2549–2554, 2003.
2. Yasuda, T., Y. Kawada, H. Toyoda, and H. Takahashi, “Terahertz movie of internal transmission imaging,” *Optics Express*, Vol. 15, 15583–15588, 2007.
3. Melinger, J. S., N. Laman, and D. Grischkowsky, “The underlying terahertz vibrational spectrum of explosives solids,” *Applied Physics Letters*, Vol. 93, 011102, 2008.
4. Chan, W. L., J. Deibel, and D. M. Mittleman, “Imaging with terahertz radiation,” *Reports on Progress in Physics*, Vol. 70, 1325, 2007.
5. Setti, V., L. Vincetti, and A. Argyros, “Flexible tube lattice fibers for terahertz applications,” *Optics Express*, Vol. 21, 3388–3399, 2013.
6. Anthony, J., R. Leonhardt, A. Argyros, and M. C. J. Large, “Characterization of a microstructured Zeonex terahertz fiber,” *JOSA B*, Vol. 28, 1013–1018, 2011.

Simulation of Temperature Profile of Soot Preform during Sintering Process

Ramesh Behera and Sham Nagarkar
Sterlite Technologies Ltd, Aurangabad, India

Abstract— Sintering process in optical fiber manufacturing technology densifies the soot preform to glass preform which is used for drawing optical fiber. The analysis of temperature profile of the soot preform during sintering has been studied using Computational Fluid Dynamics (CFD) simulation software. The temperature profile inside the soot preform is discussed by changing the preform diameter during sintering process.

1. INTRODUCTION

Sintering is an important process to convert soot preform to glass preform by densification phenomena. There are many literature papers available to discuss on theoretical calculation during sintering process. Mathematical modeling is developed to quantify the heat conduction and helium gas diffusion inside the soot preform during sintering process [1]. The sintering rate of a soot body has been calculated using Frenkel approach [2]. The effect of temperature on fluorine dopant concentration profile is studied inside porous silica performs during sintering [3]. It has been understood from the literature survey that the temperature profile plays an important role in sintering process.

The quality of densification depends on the temperature profile of the preform which is controlled by furnace temperature and gas flow rate. The article presents a Computational Fluid Dynamics (CFD) calculation to find out the temperature of soot preform during sintering process. In this study, the temperature inside the soot preform has been discussed with varying the preform diameter following to a validation study.

2. THEORETICAL CALCULATION

ANSYS FLUENT [4] software is used to find out the temperature profile inside the soot preform by solving a set of the governing equations, which is a finite volume method (FVM) based CFD code. As part of the CFD calculation, the 3D geometry of the sintering apparatus is drawn including the soot preform as per Figure 1. The preform diameter in Figure 1(b) is 4 times more than that of Figure 1(a) keeping all others dimensions remaining unchanged. Another 3D geometry of sintering apparatus is constructed similar to Figure 1 without the soot preform for the validation study. A good quality mesh is generated in 3D geometry and the governing equations of mass conservation, Navier-Stokes, turbulence and species transport, energy conservation and radiation are solved.

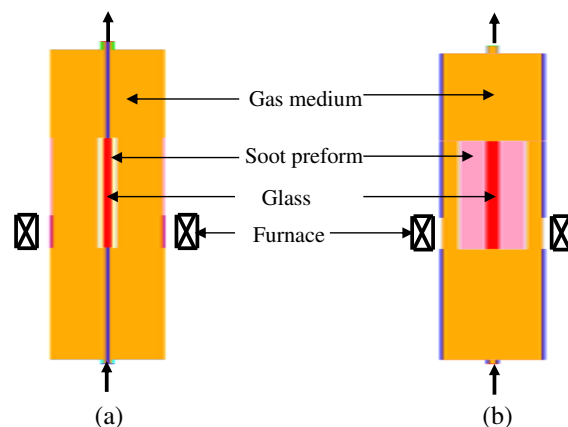


Figure 1: Sinter machine including soot preform: (a) smaller diameter preform and (b) higher diameter preform.

3. RESULTS

The validation study was carried out inside the sintering apparatus in stand by condition before discussing the soot temperature profile calculated using CFD software. The simulation result depicts that the temperature is maximum in furnace region as compared to other part of the apparatus (Figure 2(a)). The simulated temperature profile matches with the typical experimental (Figure 2(b)).

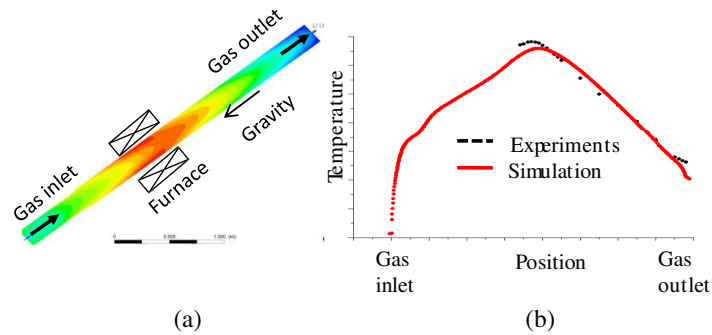


Figure 2: (a) Temperature field inside the sintering device in standby condition and (b) temperature comparison.

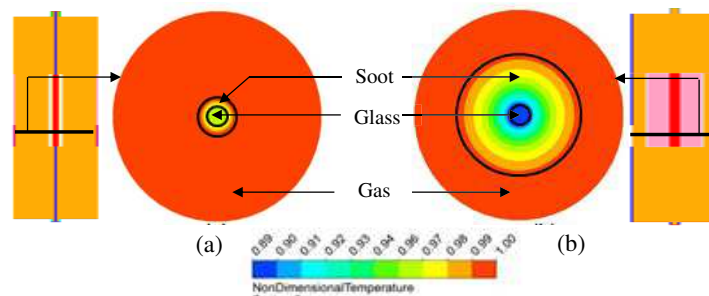


Figure 3: Temperature field in a cross section positioned at center of furnace in sintering apparatus: (a) smaller diameter preform and (b) higher diameter preform.

The temperature profile is calculated using CFD of soot preforms with two different diameters as shown in Figure 1. Temperatures are calculated using the conduction, convection and radiation equations in between the furnace muffle tube and soot preform & the conduction equation inside the soot preform respectively. The densification and gas diffusion inside the soot has not been considered in the calculation. It has been reported that the heat transfer through conduction inside the soot is faster than the gas diffusion [1].

Simulation results suggest that the temperature drop in between the furnace muffle tube and soot surface is negligible in both sizes of soot preforms (Figure 3). The heat is conducted from the muffle tube to soot surface through the radiation dominantly. However, the temperature drop inside the higher diameter preform (Figure 3(b)) is 3 times more than the smaller diameter preform (Figure 3(a)) which should be considered in the process parameter settings. The heat is conducted through conduction dominantly inside the soot preform and the temperature drop increases as the soot diameter increases.

4. CONCLUSIONS

A theoretical calculation was done using Computational Fluid Dynamics (CFD) simulation software to determine temperature profile of a soot preform during sintering process. A validation study was carried out to compare the calculated temperature profile with the typical experimental data in the sintering apparatus. Simulated results suggest that the temperature drop inside the higher diameter soot preform is 3 times more than the smaller diameter preform.

REFERENCES

1. Doorwar, S., S. Chakraborty, and S. Neogi, “A multiscale model for quantifying helium diffusion in porous unsintered glass,” *The Canadian Journal of Chemical Engineering*, Vol. 88, April 2010.
2. Scherer, G. W., “Sintering of low-density glasses: 1, Theory,” *Journal of the American Ceramic Society*, Vol. 60, Nos. 5–6, May–June 1977.
3. Tandon, P., “Doping of silica during sintering,” *Journal of Non-Crystalline Solids*, Vol. 351, 1466–1472, 2005.
4. FLUENT v13.0, *Theory Guide and User’s Manual*, ANSYS Inc..

Yield Improvement of Optical Fiber Manufacturing through Redesign of ACVD Burner

Ramesh Behera and Datta Pasare
Sterlite Technologies Ltd., Aurangabad, India

Abstract— A burner design has been proposed to improve the manufacturing yield of optical fiber. The burner is an important device to fabricate the soot preforms in ACVD process which leads to draw optical fiber in subsequent manufacturing process. The glass formation at the tip of burner fumes tube is a common defect which leads to scrap soot preform. The burner has been redesigned using Computational Fluid Dynamics (CFD) simulation software to understand the interaction of silica precursor, hydrogen and oxygen gas flow paths and to avoid glass formation.

1. INTRODUCTION

The ACVD is a well-known technology for manufacturing of glass preforms used for drawing optical fibers. A burner is an important device in ACVD manufacturing process and it is used for formation of silica particles from combustion of hydrogen, oxygen and silica precursors. Silica particles hence produced are deposited on a bait/glass rod in the form of soot preform. There are many technical papers published on theoretical calculation in ACVD technology and a couple of them have been discussed below. Fundamental understanding of soot deposition with process optimization has been discussed by Pushkar Tandon [1]. The variation of soot temperature with time is presented in the work. Modeling of the flame temperature with different steps of chemical reaction has been discussed by Hannebauer et al. [2]. It is also understood from the literature survey that the defects will generate during the soot preform fabrication if the burner is not designed correctly.

There are many defects such as glass formation at burner tip, wart on soot preform and bad interface on soot preform in the ACVD process which leads to scrap soot preform. The overall manufacturing cost of optical fiber increases if the soot preform is scrapped. It has been a challenging task to decrease the optical fiber manufacturing cost due to current competitive market. To understand and remove the defects, engineers explore to use of smart engineering tools which is a cost effective solution. The Computational Fluid Dynamics (CFD) simulation software has been used to understand the defect, known as glass formation at the tip of burner.

The article presents a CFD calculation of interaction of gas flow paths of silica precursor, hydrogen and oxygen in the generic and redesigned burners. In this study, the gas velocities resulted from CFD calculation have been discussed.



Figure 1: 3D drawing of generic burner.

2. THEORETICAL CALCULATION

ANSYS FLUENT [3] software is used to solve the governing equations, which is a finite volume method (FVM) based CFD code. As part of the CFD calculation, the 3D engineering drawings of the both generic and redesigned burners are prepared (as shown in Figure 1). A good quality mesh is generated in the 3D drawings (as shown in Figure 2). The governing equations of mass conservation, Navier-Stokes, turbulence and species transport are solved to find out the velocity profile of gases at the burner tip.

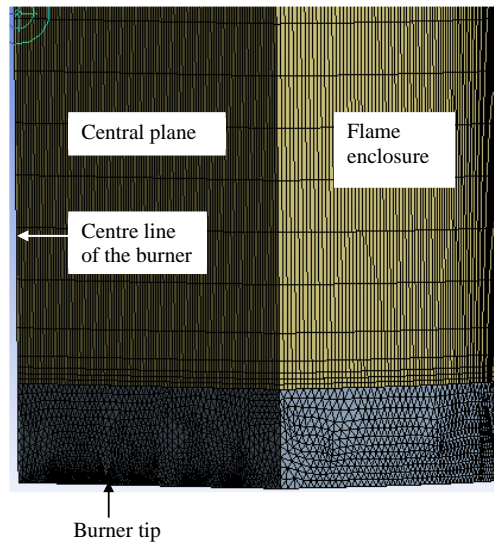


Figure 2: Mesh in a section of the generic burner.

3. RESULTS

The velocity vectors are shown in Figure 3 for both burners as part of CFD results. Figures 3(a) and 3(b) represent for generic and redesigned burners respectively.

The axis shown in Figure 3 represents for fumes tube of burners. The pitch circle diameters of redesigned burner are decreased by 4 units as compared to the generic burner keeping all other inputs constant. The gas injection locations are marked in arrow.

The velocity field causes for glass formation at the tip of fumes tube in the generic burner due to less gas flow between first and second injections and a recirculation zone between second and third injections (Figure 3(a)). Whereas the velocity field generated in the redesigned burner doesn't allow for glass formation as the gas flows are directed towards the first and second injections from the second and third injections respectively (Figure 3(b)).

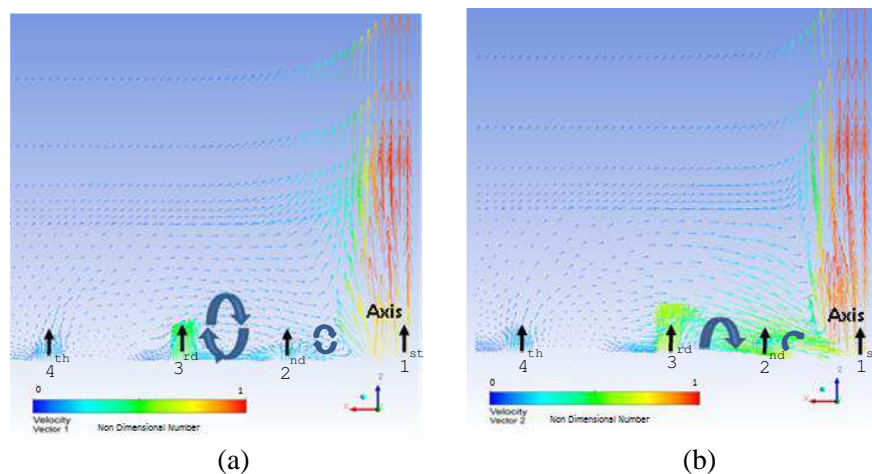


Figure 3: Non-dimensional velocity vectors: (a) generic burner, (b) redesigned burner.

4. CONCLUSIONS

A burner of the ACVD based optical fiber manufacturing technology has been redesigned to lower the scrap of soot preform. Computational Fluid Dynamics (CFD) simulation software was used to compare the gas flow interaction at the tip of generic and redesigned burners. The governing equations of mass conservation, Navier-Stokes, turbulence and species transport are solved in the CFD calculation. It is understood from the gas velocity field that the recirculation zone is observed in the general burner and the glass formation is found at the burner tip. The recirculation zone is not observed in the redesigned burner.

REFERENCES

1. Tandon, P., “Fundamental understanding of processes involved in optical fiber manufacturing using outside vapor deposition method,” *Int. J. Appl. Ceram. Technol.*, Vol. 2, No. 6, 504–513, 2005.
2. Hannebauer, B. and F. Menzel, “The combustion of SiCl_4 in hot O_2/H_2 flames,” *Z. Anorg. Allg. Chem.*, Vol. 629, 1485–1490, 2003.
3. FLUENT v14.0, *Theory Guide and User’s Manual*, ANSYS Inc., 2011.

Core Profile Based Dispersion Optimization in Trench Assisted Bend-insensitive Optical Fibers

Pramod R. Watekar, Archi Bhattacharya, and Nagaraju Bezawada
Sterlite Technologies Ltd., Aurangabad 431016, India

Abstract— We present a new design method to optimize the performance of bend insensitive optical fibers based on the core profile optimization. Validity of this method has been verified by experimentally fabricating ultra-bend insensitive optical fibers.

1. INTRODUCTION

Recently, with increasing deployment of FTTx applications, bend insensitive optical fibers are gaining much attention due to their capability to handle sharp bends by offering very low bending attenuation in premises, thus aiding in the tight power budget of deployment. This has resulted in commercial availability of a range of bend insensitive optical fibers (G.657.A1, A2, B2, B3) [1–3]. However, optical fiber manufacturers often face difficulty in experimental realization of ultra low bending loss fibers due to critical balancing of various optical parameters, such as the chromatic dispersion and the bending loss. It is well known that decrease in the bending loss causes the cable cutoff wavelength as well as the dispersion at 1550 nm to increase beyond recommended values suggested by ITU-T for G.657 category fibers [4]. Thus, a tradeoff between the high bend insensitivity and the dispersion limit at 1550 nm has to be well understood and addressed to obtain optimized parameters.

In the current communication, we present a design method based on the core profile optimization, which gives required balance between the bending loss and the dispersion. We also present experimental results obtained after adopting this method for designing G.657.B3 fibers.

2. THEORY

The trench assisted profile under consideration is shown in Fig. 1. It can be seen that the core is surrounded by inner silica cladding and the low-index trench, which are surrounded by the outer silica cladding.

In Fig. 1, the core of optical fiber has been shown in different shapes, which are defined by *alpha* parameter in the following equation:

$$n(x) = n_{\max} \sqrt{1 - 2\Delta \left(\frac{x}{w}\right)^\alpha} \quad (1)$$

where n is the refractive index at radial parameter x , n_{\max} is the maximum value of refractive index, w is the radius of core and Δ is the normalized index difference defined as:

$$\Delta = \frac{(n_{\max}^2 - n_{\min}^2)}{2n_{\max}^2} \quad (2)$$

Optical parameters of this profile can be obtained by solving the wave equation to get the spectral variation of propagation constant, which can be then used to obtain radial distribution of the mode field, values of chromatic dispersion, a cutoff wavelength, and the bending loss [5–7].

3. ANALYSIS

We select a typical profile of bend insensitive fiber as shown in Fig. 1 with parameters listed in Table 1. Parameter *Delta* used in the description of figures is the normalized refractive index in % (Eq. (2)) where n_{\min} is the minimum value of refractive index in the core. Illustrations of profiles at *alpha* = 1 and *Delta* = 0.2 and 0.4 are shown in Fig. 2.

Effects of *alpha* on the bending loss of bend-insensitive fiber are shown in Fig. 3. It is seen that the bending loss reduces with increasing *alpha*, while the bending loss increases with increasing *Delta*. This happens because increase in the value of *Delta* lowers the cutoff wavelength.

As we discussed earlier, choosing the minimum value of bending loss may affect other optical parameters of the bend insensitive fiber. For example, selecting the value of *alpha* to be 10 gives

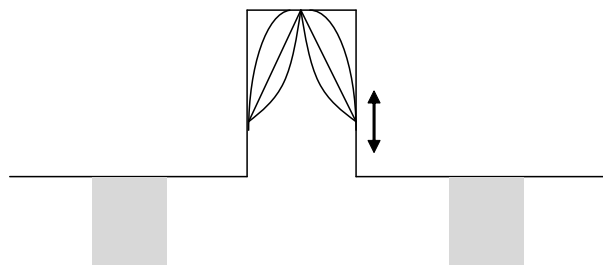


Figure 1: Trench assisted bend insensitive fiber at different α values.

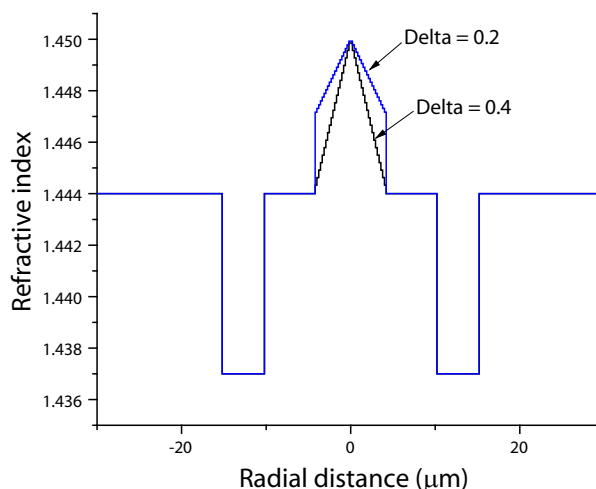


Figure 2: Refractive index profiles at $\alpha = 1$, $\Delta = 0.2$ and 0.4 and wavelength = 1550 nm.

Table 1: Typical parameters of the bend-insensitive fiber under consideration.

Parameter	Value
Maximum refractive index of core at 1550 nm	1.45
Minimum index difference of trench at 1550 nm	1.437
Core diameter (d)	$8.4 \mu\text{m}$
Separation of trench from the edge of core	$0.72d$
Trench width	$0.6d$

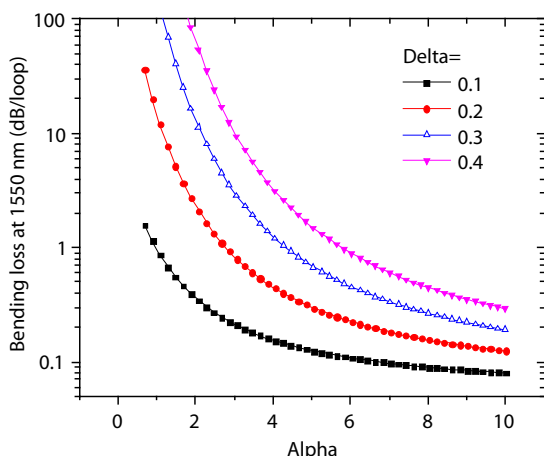


Figure 3: Effects of α on the bending loss at 5 mm bending radius.

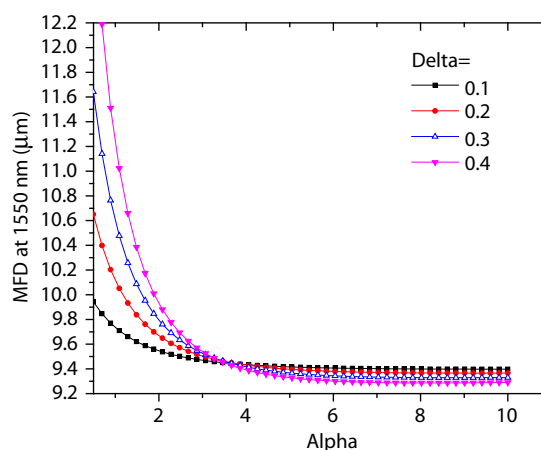


Figure 4: Effects of α on the mode field diameter at 1550 nm.

low bending loss, however, at the same time reduces the mode field diameter (MFD) at 1550 nm as shown in Fig. 4. It is also interesting to note that at $\alpha > 3.5$, the MFD value is the highest for $\Delta = 0.4$, while at $\alpha < 3.5$, the MFD value is the lowest for $\Delta = 0.4$. Reason for this behavior is the effective index, which reduces with reduction in α .

Finally, the effect of α on the dispersion is illustrated in Fig. 5. It can be observed that the dispersion has U-shape with respect to α and there exists minimum value of dispersion at 1550 nm for each Δ . This result is very useful to select optimum values of α and Δ so that optical parameters of the bend-insensitive fiber are within the ITU-T specified limits. In Fig. 5, $\Delta = 0.4$ gives minimum dispersion values, which is synonym saying that the bending loss will be high as shown in Fig. 3. Based on these results, a new method to design the bend insensitive optical fiber is proposed in the following section.

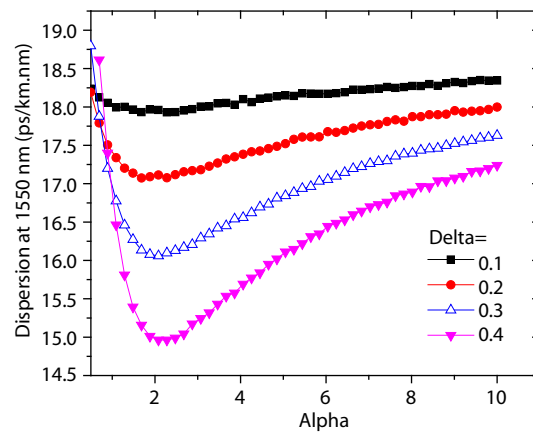


Figure 5: Effects of alpha on the dispersion at 1550 nm.

4. CORE PROFILE BASED OPTIMIZATION METHOD

The core profile based dispersion and bending loss optimization method is explained as follows. Firstly, an index profile similar to the well known single mode fiber is selected. A low-index trench is added to the profile at a distance from the core; we need to select trench index, width and its position from the core so that required macro-bending loss is obtained. It is noted that this may affect dispersion properties of the fiber, however, it is ignored at this stage.

Secondly, the shape of the core profile is changed by changing an α parameter as shown in Fig. 1. Optical parameters are calculated for this profile by solving the wave equation. Thus, we obtain a set of optical parameters for different α values. Typically, the curve representing variation in dispersion with respect to the α parameter is U-shaped and there exists α parameter value where the dispersion is minimum.

Finally, the optimum α profile is selected where all required optical parameters are obtained. If the dispersion value is still above the limit specified by ITU-T, then we need to start over from step one, where the trench position and dimensions are varied.

5. EXPERIMENT AND RESULTS

Various samples of the bend-insensitive fiber of G.657.B3 category were fabricated using the in-house facility. The design approach adopted for all these fibers was same as explained in Section 4. Measured optical parameters of these fibers are listed in Table 2, where it can be observed that dispersion values at 1550 nm are within the specification (i.e., < 18 ps/km-nm) with the bending loss has ultra low value. When the dispersion is < 17 ps/km-nm, the zero dispersion wavelength is near the higher limit of the specification (i.e., 1324 nm); this issue can be managed by targeting the dispersion to be 17–17.5 ps/km-nm. In all cases, the bending loss at 1550 nm was far below the specification (i.e., 0.15 dB/loop at 5 mm of bending radius).

Table 2: Measured optical parameters of the bend-insensitive optical fiber. BL is the bending loss at specified bending radius.

Sample No. G.657.B3	MFD (μm)	Cable cutoff (nm)	Dispersion at 1550 nm (ps/km-nm)	Zero dispersion wavelength (nm)	BL 5 mm (dB/loop)	BL 7.5 mm (dB/loop)
1	8.58	1238.5	16.68	1321.81	0.067	0.03
2	8.62	1231.5	17.29	1319.27	0.063	0.052
3	8.736	1259	17.15	1318.25	0.086	0.036
4	8.67	1239.5	16.77	1322.08	0.079	0.04
5	8.57	1247	17.2	1315.7	0.051	0.017
6	8.62	1238	17.49	1315.19	0.057	0.032
7	8.68	1229.07	16.92	1321.16	0.084	0.046

6. CONCLUSION

We presented a method to optimize the performance of bend insensitive optical fiber by using the core profile optimization, where dispersion and bending loss are optimized. Bend insensitive fibers of category G.657.B3 were fabricated and measured parameters were well below the limits suggested by ITU-T.

REFERENCES

1. www.sterlitetechnologies.com.
2. Matsuo, S., M. Ikeda, and K. Himeno, “Bend insensitive and low splice loss optical fiber for indoor wiring in FTTH,” *Proceedings of Optical Fiber Communication Conference (OFC)*, ThI3, Anaheim, USA, Feb. 23–27, 2004.
3. Li, M.-J., P. Tandon, D. C. Bookbinder, S. R. Bickham, M. A. McDermott, R. B. Desorcie, D. A. Nolan, J. J. Johnson, K. A. Lewis, and J. J. Englebert, “Ultra-low bending loss single-mode fiber for FTTH,” *Proceedings of OFC/NFOEC-2008*, PDP10, San Diego, USA, Feb. 24–28, 2008.
4. ITU-T recommendations for G.657.
5. Watekar, P. R., S. Ju, and W.-T. Han, “Single-mode optical fiber design with wide-band ultra low bending-loss for FTTH application,” *Opt. Express*, Vol. 16, 1180–1185, 2008.
6. Watekar, P. R., S. Ju, Y. S. Yoon, Y. S. Lee, and W.-T. Han, “Design of a trenched bend insensitive single mode optical fiber using spot size definitions,” *Opt. Express*, Vol. 16, No. 18, 13545–13551, 2008.
7. Snyder, A. W. and J. D. Love, *Optical Waveguide Theory*, Chapman and Hall, 1983.

Experimental Investigation of Modal Noise in Ultra Bend-insensitive Fibers

Nagaraju Bezawada, Manoj Gupta, and Pramod R. Watekar
Center of Excellence, Sterlite Technologies Limited, Aurangabad, India

Abstract— We experimentally investigate the modal noise characteristics of short length ultra bend-insensitive optical fibers with different splice conditions using broadband source/OSA technique.

1. INTRODUCTION

As the fiber penetrates indoor for FTTH, it needs to have very high bend resistance [1]. Harsh conditions like sharp turns, staples, and reduced storage space are very common in indoor applications. ITU has recommended a new fiber type called G.657 for these applications [2]. As the macro-bend loss of conventional matched clad fibers cannot be reduced beyond certain extent without disturbing mode field diameter (MFD) and dispersion, a trench in cladding design has been proposed. Fibers with trench in cladding design can achieve ultra low bend losses without compromising on MFD and dispersion. However, these fibers typically have higher cutoff wavelengths than matched clad fibers due to improved confinement of optical power [3]. Also, the existence of trench in the cladding of these fibers results in the existence of higher order mode (LP_{11} mode) beyond cutoff wavelength. The existence of this higher order mode can cause modal noise and needs to be investigated in short length bend insensitive fibers.

Because of the depressed index region in BIFs, the LP_{11} mode becomes leaky around cutoff wavelength and can interfere with fundamental mode due to superior bend resistance. Multipath interference (MPI) in a BIF is caused when signal in fundamental mode gets partially converted into higher order mode and reconverted back into fundamental mode after propagating certain distance. This can happen in a FTTH network due to closely spaced splices, staples, and bends.

In this paper, we present measurement results of modal noise in a 2 m length ultra bend-insensitive fiber (G.657B3 category) with different splice conditions. Modal noise is measured at both 1260 nm and 1310 nm with different splice losses.

2. EXPERIMENTAL SETUP

Our measurement method is based on wideband light source/OSA technique and monitors transmitted optical power through the short length fiber under test as a function of wavelength. The interference phenomenon between the fundamental and higher order mode is measured by capturing the maximum and minimum transmitted power over a range of wavelengths. Polarization variation of the input is used to ensure true power extremes are found. A schematic of the apparatus used for this test is shown in Fig. 1.

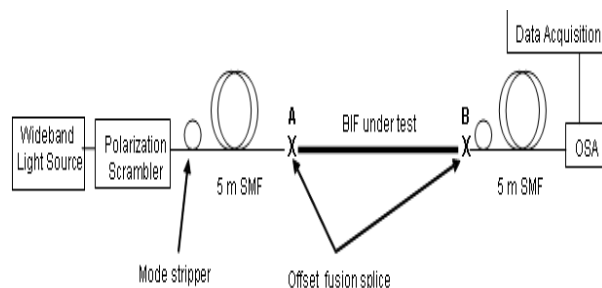


Figure 1: Experimental setup.

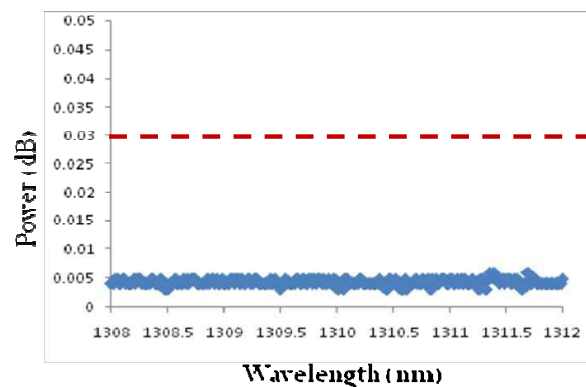


Figure 2: Source power drift with time over 15 mins.

3. RESULTS AND DISCUSSION

Spectral power stability of the source is very critical parameter and limits the baseline MPI. The fluctuations of the source power over measurement time are measured and found to be well within the requirement of ± 0.03 dB/15 minutes [4] as shown in Fig. 2.

The baseline MPI, which is the minimum MPI that can be measured with the system, is measured without sample with polarization scrambler switched on. Fig. 3 shows the Max and Min power curves without sample with polarization scrambler switched on. Baseline MPI is calculated using this Max and Min data and the formula given below [5].

$$\text{MPI (dB)} = 20 \log \left[\frac{10^{PR/20} - 1}{10^{PR/20} + 1} \right] \quad (1)$$

where PR is the difference between the maximum and minimum power levels detected (in dB). The baseline MPI is measured to be ~ -40.77 dB.

The fiber sample used for measuring multipath interference (MPI) is a G.657B3 category fiber with a macrobend loss of 0.07 dB/turn at a bend radius of 5 mm and cable cutoff wavelength of 1240 nm.

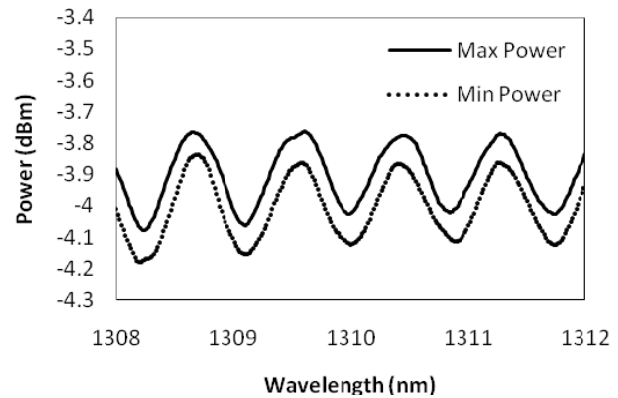
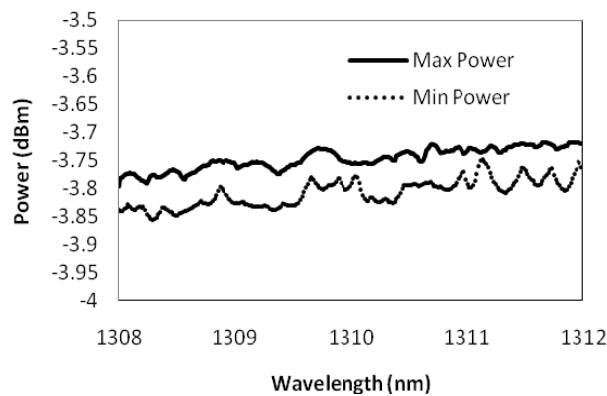


Figure 3: Max and Min power data for baseline MPI.

Figure 4: Measured Max and Min power curves at 1310 nm for an insertion loss of 1.49 dB.

MPI of the sample is measured at both 1260 and 1310 nm by inserting the sample and switching on the polarization scrambler. OSA was set into MAX and MIN hold mode and Max and Min power was measured for 15 minutes. This time was sufficient for the scrambler to explore all the polarization states on Poincare sphere. Fig. 4 shows measured Max and Min power curves at 1310 nm for an insertion loss of 1.49 dB.

MPI dependence on insertion loss is shown in Fig. 5. Required insertion loss is achieved through creating manually controlled offset splices. Measured MPI values as a function of insertion loss are

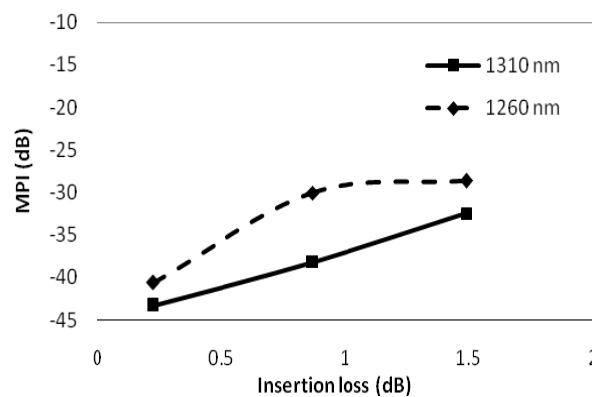


Figure 5: Dependence of MPI on insertion loss at 1260 nm and 1310 nm.

plotted at both 1260 nm and 1310 nm. As seen from this figure, MPI value increased with insertion loss. Also, as expected MPI value at 1260 nm is higher than that at 1310 nm.

4. CONCLUSION

We investigated modal noise in a 2 m length ultra bend-insensitive fiber with different splice conditions. It is found that MPI is negligible for fibers with worst case splice conditions at both 1260 nm and 1310 nm.

REFERENCES

1. Himeno, K., et al., “Low-bending-loss single-mode fibers for fiber-to-the-home,” *J. Lightwave Technol.*, Vol. 23, 3494–3499, 2005.
2. ITU-T Recommendation G.657, “Characteristics of a bending-loss insensitive single-mode optical fiber and cable for the access network,” 2009.
3. De Montmorillon, L.-A., et al., “Cutoff mechanisms in bend-insensitive single-mode fibers,” *OFC’11*, paper OTuA1, Los Angeles, CA, USA, 2011.
4. Recommendation G.650.1 (2010), Amendment 1, “Definitions and test methods for linear, deterministic attributes of single-mode fibre and cable,” 2012.
5. Ramachandran, S., et al., “Measurement of multipath interference in the coherent crosstalk regime,” *Photon. Technol. Lett.*, Vol. 15, 1171–1173, 2003.

Measurement of Nonlinear Coefficient of Ultra Bend-insensitive Optical Fiber

Manoj Gupta, Nagaraju Bezawada, and Pramod R. Watekar
Center of Excellence, Sterlite Technologies Limited, Aurangabad, India

Abstract— We present measurement results of nonlinear coefficient of bend insensitive fiber (G.657A2) at 1550 nm by direct continuous wave method. Measured nonlinear coefficient for G.657A2 fiber is 1.25 (W-km)^{-1} .

1. INTRODUCTION

Nowadays, the whole world is witnessing the fast and rapid optical communication based on dense wavelength division multiplexing (DWDM) networks. These networks carry high power densities and the rapid increase in the power put into an optical fiber gives rise to such phenomena as nonlinear optical effects. Nonlinear optical interaction will become prominent when optical power density is high and interaction between light signal and fiber medium takes place for longer distance. The intensity dependent refractive index (n_2) leads to variety of nonlinearity effects such as self-phase modulation (SPM), cross-phase modulation (XPM) and four wave mixing (FWM) in the optical fibers and is thus a critical parameter for long haul networks. Typically, G.652 D fibers are used in long haul networks. However, G.657 A fibers, which are designed for access networks, are expected to see applications outside access network in future. This is due to their improved microbending performance and compatibility with G.652 D. So, it is important to understand nonlinear characteristics of these fibers. There are various approaches proposed in the literature to measure the nonlinear coefficient of optical fibers [1–3]. We have used continuous wave-SPM (cw-SPM) method.

In this paper, we present a nonlinear coefficient measurement results based on self-phase modulation for Sterlite's Bowlite G.657 A2 optical fiber. At high electric fields induced due to high optical power density, fiber medium behaves as an anisotropic medium. In this medium, electric polarization can be written as

$$P = \varepsilon_0 \left(\chi E + \chi^{(2)} E^2 + \chi^{(3)} E^3 + \dots \right) \quad (1)$$

where $\chi^{(2)}$, $\chi^{(3)}$, \dots are higher order susceptibilities giving rise to nonlinear effect. For silica fiber, $\chi^{(2)}$ is zero and does not show any non linear effects. Third order nonlinear effects cause the various type of nonlinearity in the optical fibers. Cw-SPM method is based on measuring the nonlinear phase shift experienced by a dual-frequency beat signal and this beat signal is propagating along the fiber (neglecting dispersion) can be written as [4, 5]

$$E(t, L) = 2a \cos(\Delta\omega t) \exp(i\omega_0 t) \exp[i\varphi_{\text{SPM}} \cos^2(\Delta\omega t)] \quad \text{and} \quad n_2 = \frac{\lambda}{4\pi} \frac{A_{\text{eff}}}{L_{\text{eff}}} \left(\frac{\varphi_{\text{SPM}}}{P_{\text{in}}} \right) \quad (2)$$

where P_{in} is the input launch power of the signal into fiber, L_{eff} is the effective length of the fiber calculated by $L_{\text{eff}} = (1 - \exp(-\alpha L))/\alpha$, n_2 is the nonlinear refractive index and A_{eff} is the effective area which comes from averaging over the intensity profile of the mode in the fiber and is given by

$$A_{\text{eff}} = \frac{\left[2\pi \int_{-\infty}^{\infty} E^2 r dr \right]^2}{2\pi \int_{-\infty}^{\infty} E^4 r dr} \quad (3)$$

when beat signal is propagating in the fiber and interaction take place for longer distance, a typical spectrum is generated at the output as shown in Figure 1. I_0 and I_1 are the intensities of zero and first order harmonics respectively.

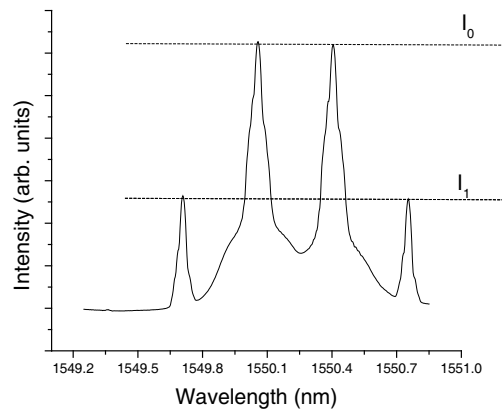


Figure 1: Typical spectrum generated by nonlinear effect.

2. EXPERIMENTAL SETUP

Two continuous signals centered at 1550.06 nm and 1550.23 nm were launched having power of 10 dBm each. The launch polarization of signals was adjusted using polarization controllers. These two signals are combined using a 50 : 50 splitters. The combined signal is amplified using a high power EDFA and launched into the fiber under test length of 1 km. A band pass filter (BW: 3.2 nm) is used to filter the noise. Output power spectrum was recorded by using optical spectrum analyzer (OSA). Resolution bandwidth of OSA was fixed to 0.02 nm. An attenuator of 20 dB loss was inserted before OSA for controlling power going to OSA input port.

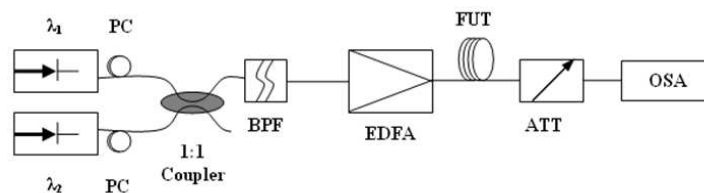


Figure 2: Experimental set for non linear coefficient measurement.

Table 1: Optical parameters for sterlite bowlite's G.657 A2.

Fiber Type	Cable Cutoff	MFD @1550 nm	Effective Area (A_{eff})	Dispersion at 1550 nm	Attenuation
G.657 A2	1251 nm	9.45 μm	67.1 μm^2	17.45 ps/nm-km	0.192 dB/km

3. RESULTS AND DISCUSSION

Total phase shift faced by signal while propagating (β_0 as propagation constant) inside the fiber of length L is given by

$$\varphi_{SPM} = \beta_0 L + \gamma L_{eff} P_{in} \quad (4)$$

γ is called nonlinear coefficient which is defined as $K_0 n_2 / A_{eff}$. When a continuous wave dual frequency beat signal used as a pump signal, the resultant spectrum is discrete (because electric field signal is continuous and periodic in time domain), consisting of harmonics of the beat frequency as shown in Figure 1. The nonlinear phase shift induced in the optical fiber by self phase modulation (SPM) effect and corresponding power are determined from the discrete shape of the spectrum, i.e., relative ratio of the spectral components given by [2, 3]

$$\frac{I_0}{I_1} = \frac{J_0^2\left(\frac{\varphi_{SPM}}{2}\right) + J_1^2\left(\frac{\varphi_{SPM}}{2}\right)}{J_2^2\left(\frac{\varphi_{SPM}}{2}\right) + J_1^2\left(\frac{\varphi_{SPM}}{2}\right)} \quad (5)$$

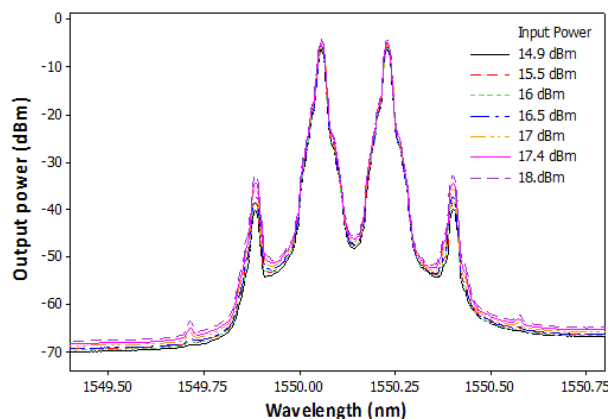


Figure 3: Output power spectrum at different input launched power level into fiber sample of G.657 A2.

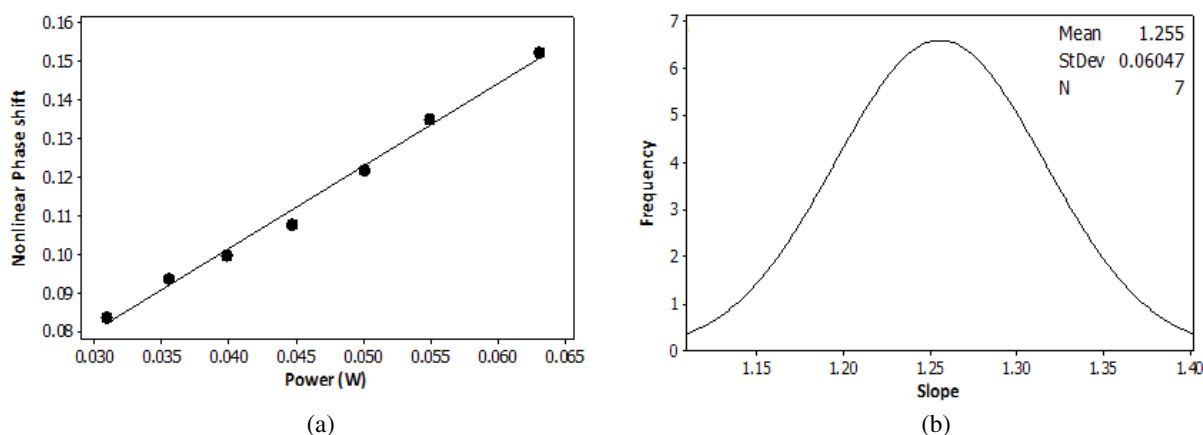


Figure 4: (a) Phase shift variation due to changing the input power (b) histogram of several measurement of nonlinear coefficient for G.657A2.

Multiple spectrums were plotted at different input power level as shown in Figure 3 to confirm that phase behavior should be linear as shown in Figure 4(a). The value of self-phase (φ_{SPM}) was calculated using the Equation (5) and by knowing the value of mode field diameter and attenuation in fiber it is then possible to measure the value of nonlinear refractive index (n_2) as well coefficient (γ). The value of nonlinear coefficient depends on state of polarization and this could generate the uncertainty in the result so we took repeatability of results and found the deviation from mean by the unit of 0.06 as shown in Figure 4(b).

4. CONCLUSION

In this paper, we measured the nonlinear coefficient of bend insensitive fiber (G.657 A2) and its average value was calculated 1.25 (W-km)^{-1} .

REFERENCES

1. Agrawal, G. P., *Application of Nonlinear Fiber Optics*, Academic Press, New York, 2001.
2. Namihira, Y., K. Miyagi, K. Kaneshima, M. Tadakuma, C. Vinegoni, G. Pietra, and K. Kawanami, "A comparison of six techniques for nonlinear coefficient measurements of various single mode optical fibers," *NIST*, 1–5, 2002.
3. Ju, S., P. R. Watekar, S. Jeong, Y. Kim, and W.-T. Han, "Nonlinear optical properties of Zinc doped germane-silicate glass optical fiber," *J. Nonlinear Optical Physics and Materials*, Vol. 19, No. 4, 791–799, 2010.
4. Boskovic, A., S. V. Chernikov, J. R. Taylor, L. Gruner-Nielsen, and O. A. Leving, "Direct continuous-wave measurement of n_2 in various types of telecommunication fiber at 1.55 μm ," *Optics Letters*, Vol. 21, No. 24, 1966–1968, 1996.
5. Kim, K. S., R. H. Stolen, W. A. Reed, and K. W. Quoi, "Measurement of the nonlinear index of silica-core and dispersion-shifted fibers," *Optics Letters*, Vol. 19, No. 4, 1994.

Bandwidth Limitations and Trade-off Relations for Wide- and Multi-band Array Antennas over a Ground Plane

B. L. G. Jonsson

School of Electrical Engineering, KTH Royal Institute of Technology, Stockholm, Sweden
(Invited Paper)

Abstract— There has been a recent drive to find fundamental limitations of bandwidth performance. Such results include Rozanovs (2000) bandwidth performance of absorbers, and Gustafssons (2007) limitation for single port antennas, similar bounds on transmission coefficients through a frequency selective screen and high-impedance surfaces are also known. In the present work we show a related bound for array antennas over a ground plane. We illustrate how this bound can be formulated as an array figure of merit, weighting impedance bandwidth, return loss, scan range and material and size information against each other.

The derivation of the array figure of merit is based on Bode-Fano theory for a scattering passive object, and is related to the Rozanov bound of absorbers. This result is essentially a sum-rule result that only requires that the array element is scattering passive, time-invariant and linear. The bound is derived for linearly polarized periodic arrays over an infinite planar ground-plane.

The array figure of merit can both be used to evaluate existing antennas. It can also be used as a prediction tool and hence as an a-priori assessment of impedance bandwidth limitations for a given antenna element. The array figure of merit contains return-loss, impedance bandwidth, scan range, and element specific information. We show how to use the array figure of merit to investigate trade-off between, e.g., return-loss and bandwidth or bandwidth versus thickness. We note that the array figure of merit easily extend to multi-band antennas.

1. INTRODUCTION

Physical limitations on impedance bandwidth for array antennas is a fairly recent research area. Initial investigation based on an antenna Q approach are known in [1, 2]. A sum-rule approach to these limitations are derived and analyzed in [3–5]. On the other hand, small single port antennas bandwidth limitations are known starting from [6, 7] for spherical regions, using a spherical mode approach. Antenna Q for small antennas analyzed through the input impedance are given in [8]. Arbitrary shaped small antenna limitations were first derived in [9] through a sum-rule for partial directivity over antenna Q , D/Q . Antenna Q , and D/Q through a current-density approach has been studied in [10–14]. Other approaches to bandwidth through stored energy can be found in [13, 15–18].

The present result is based on sum-rules for array antennas. Such sum-rules follow directly from that a unit-cell array antenna can be seen as a passive system [19–21], see also [22]. This approach is similar to scattering of layered homogeneous absorbers [23]. It was extended to periodic structures above a ground-plane in [24, 25] and applied to arrays over a ground-plane in [3]. In [4] we showed that these bounds are valid for linearly polarized multi-band array antennas. Here we also defined *the array figure of merit*. For a comparison of performance of recent array antennas see [4]. Extension to circular polarization can be found in [5].

In the present paper we illustrate how the array figure of merit can be used as a trade-off tool between scan-range, bandwidth at a particular return loss level and thickness for an array antenna. This enables us to predict what the fundamental limitations of an array are. Furthermore, it can also be used as a thumb-rule based on existing arrays as an a-priori figure of merit for a particular design-specification. The figure of merit is here limited to planar unit-cell arrays over a ground-plane. It is derived under the assumption that the array is passive, loss-less, reciprocal and time-invariant.

The paper is organized as follows, in Section 2 we introduce the array figure of merit. In Section 3 we illustrate how the array figure of merit can be used as a trade-off tool for arrays. We end with a conclusion.

2. ARRAY FIGURE OF MERIT

Consider a planar array antenna over a ground plane, see Fig. 1. We simplify the array to a model with a single unit cell with periodic boundary condition over a ground-plane. The antenna is feed

below the ground-plane, and matching is done within the unit-cell above the ground-plane. The unit-cell extend from the ground-plane a distance d upwards and with area A to include one element of the periodic array.

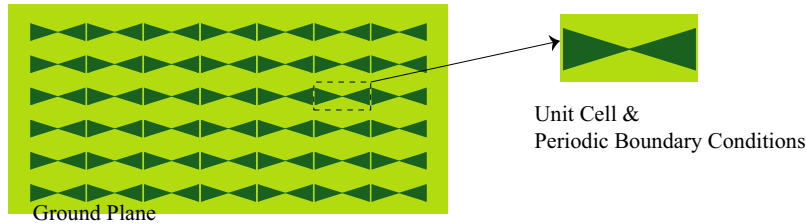


Figure 1: Schematic picture from above of a finite array with a ground-plane. The enlargement shows a unit-cell of the array.

The key parameter for the figure of merit is the array feed reflection coefficient Γ_Z . It is a function of angular frequency ω , note that $|\Gamma_Z| \leq 1$, and that it is analytic in $s = \sigma + j\omega$, $\text{Res} > 0$ [19, 26]. It also depend on the scan-angle θ . For the TE-radiating case we have the following relation [4]:

$$I(\theta) = \int_0^{\omega_G} \omega^{-2} \ln \left(|\Gamma_Z^{\text{TE}}(\omega, \theta)|^{-1} \right) d\omega \leq q_{\text{TE}}(\theta), \quad (1)$$

where ω_G is the angular frequency anzats of the grating-lobes and

$$q_{\text{TE}} = \frac{\pi d}{c} \left(1 + \frac{\tilde{\gamma}}{2dA} \right) \cos \theta \leq \frac{\pi d \mu_s}{c} \cos \theta. \quad (2)$$

Here c is the speed of light, μ_s is the maximal static relative permeability, d is the unit-cell thickness, A is the unit-cell area and $\tilde{\gamma}$ is a function of the magnetic polarizability tensor, see [25]. The array figure of merit is derived out (1) through the idea of measuring the maximal value of $I(\theta)/q(\theta)$. Let $\lambda = 2\pi c/\omega$, the we maximize I/q over one or several working bands $[\lambda_{-,m}, \lambda_{+,m}]$, $m = 1, \dots, M$ below ω_G and over the scan-range $R = [\theta_0, \theta_1]$. Given a maximal reflection coefficient Γ_m over working band m and for all angles in R , we find that the array figure of merit is defined as

$$\eta_M^{\text{TE}} = \frac{\sum_{m=1}^M \ln (|\Gamma_m|^{-1}) (\lambda_{+,m} - \lambda_{-,m})}{2\pi c \tilde{q}} \leq 1. \quad (3)$$

We obtain the highest value of the array figure of merit η_M^{TM} , if we know detailed structure information $\tilde{\gamma}$ about the unit cell, and insert $\tilde{q} = \min_{\theta \in R} q^{\text{TE}}(\theta)$ above. For most cases we only know the array thickness and maximal static permeability μ_s , in this case we use $\tilde{q} = \pi d \mu_s (\cos \theta)/c$. This imply that we get a slightly conservative measure of η^{TE} of the performance corresponding to making full use of the available volume. Note that the above calculation assumes a perfect ground-plane to determine $\tilde{\gamma}$ through a mirroring approach. Possible holes in the ground-plane could improve the possible performance limit.

The simplest case, with scan-range region $[0, \theta_1]$, and one working band $[\lambda_-, \lambda_+]$, assuming no information about the unit-cell structure we find the array figure of merit as:

$$\eta = \eta_1^{\text{TE}} = \frac{\ln (|\Gamma_m|^{-1}) (\lambda_{+,m} - \lambda_{-,m})}{2\pi^2 d \mu_s \cos \theta_1} \leq 1. \quad (4)$$

The highest known value of a wide-band and wide-scan array using (4) is $\eta^{\text{TE}} = 0.64$, see [4] and where also the TM-case is discussed. Given a measured or simulated array, it is fairly easy to estimate its array-figure of merit see [4]. Below we illustrate through an example how to use (4) as a tool for trade-off.

3. TRADE-OFF USING THE ARRAY FIGURE OF MERIT

The main point in this paper is to investigate how to use the array figure of merit as a trade-off tool and to evaluate different a-priori design-criteria. To do this, consider an array with a high

performance requirement. The desired array specification is:

$$\text{bandwidth ratio: } \frac{\lambda_+}{\lambda_-} = 6 \text{ at } RL = 15 \text{ dB or } RL = 10 \text{ dB} \quad (5)$$

$$\text{scan range: } [0, 60^\circ] \text{ or } [0, 45^\circ] \quad (6)$$

$$\text{thickness ratio: } \frac{d}{\lambda_-} = 0.5 \text{ or } \frac{d}{\lambda_-} = 1. \quad (7)$$

Here, $RL = 20 \log_{10}(|\Gamma|^{-1})$ is the return-loss. The smaller scan-range might be possible, but the larger is preferred. Similarly the higher return loss is desired, but if trade-off requires it the lower one is acceptable over the working band. Similarly, an array should clearly be as thin as possible and the 0.5 thickness ratio is the goal. Given such a specification it is often hard to know if its realizable and how it compares with existing arrays. Let's check the hardest requirements with the array figure of merit, $RL = 15 \text{ dB}$, $\theta_1 = 60^\circ$, $d/\lambda_- = 0.5$ and $\lambda_+/\lambda_- = 6$ we find that $\eta = 1.75 > 1$ and thus it is beyond the physically realistic case.

With one or several of the lower requirements we can enter into the physically possible range. Here it is interesting to compare performance with existing top performing arrays to understand how these requirements has to be modified in order for the design to be a reasonable input for an array design. We will show how the different parameters can be trade-against each other.

Given the specification of the array, to compare it with existing high-performing arrays we choose the figure of merit as $\eta \in [0.57, 0.63, 0.70]$. This corresponds to slightly below 0.57, at 0.64 and beyond 0.70 the best known array element today. We see that Eq. (4) for the scan-range depend only on θ_1 , thus we fix the two different maximal ranges 45° and 60° for our illustration. Similarly we also consider the two cases of return loss 10 dB and 15 dB. Sweeping thicknesses, we find the corresponding bandwidth ratio λ_+/λ_- in Fig. 2.

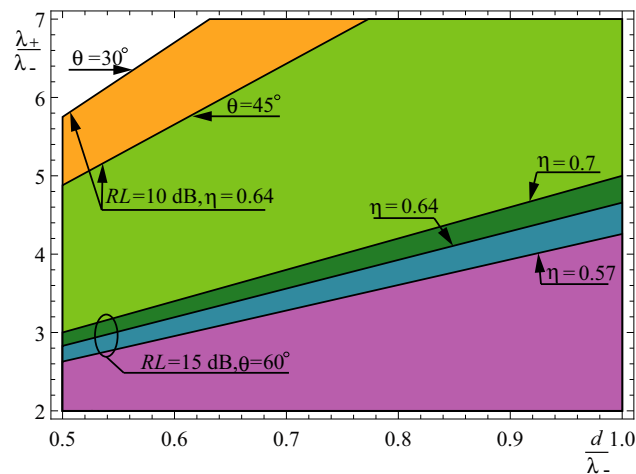


Figure 2: Bandwidth versus relative thickness. We consider two ranges of return loss 10 dB and 15 dB and compare with today's best arrays $\eta \in [0.57, 0.64, 0.70]$ for $[0, \theta_1]$ where $\theta_1 \in [30, 45, 60^\circ]$.

From this figure we see that with present day state-of-the art $\eta = 0.64$, a 6 : 1 bandwidth ratio with 10 dB return loss and 45° is possible only if the relative thickness satisfy $d/\lambda_- > 0.64$. If we desire 15 dB in return loss and $\theta_1 = 60^\circ$ we need a relative thickness ~ 1.4 . One can also verify that if we for $RL = 15 \text{ dB}$ lower the max scan-range to $\theta_1 = 45^\circ$, then a 6 : 1 bandwidth and relative thickness 1 correspond to the array figure of merit $\eta = 0.64$, which is the best figure-of-merit performing wideband array. Thus a fixed array figure of merit gives us a performance surfaces on which the antenna parameters trade-off at the same performance level. It unfortunately does not tell us how to realize these arrays, only that they are physically possible, and that there exists other arrays for a particular combination parameters of this performance level.

We can further illustrate how to trade the parameters, by sweeping return loss and scan-range against bandwidth ratio see Fig. 3. Fix the relative thickness of d/λ_- to 0.5 or 1, for a range of array figure of merit performances. It is clear from Fig. 3(a) that for a relative thickness of 0.5, we have the choice of a lower return loss of $\sim 7.7 \text{ dB}$ to obtain the desired 6 : 1 bandwidth ratio for

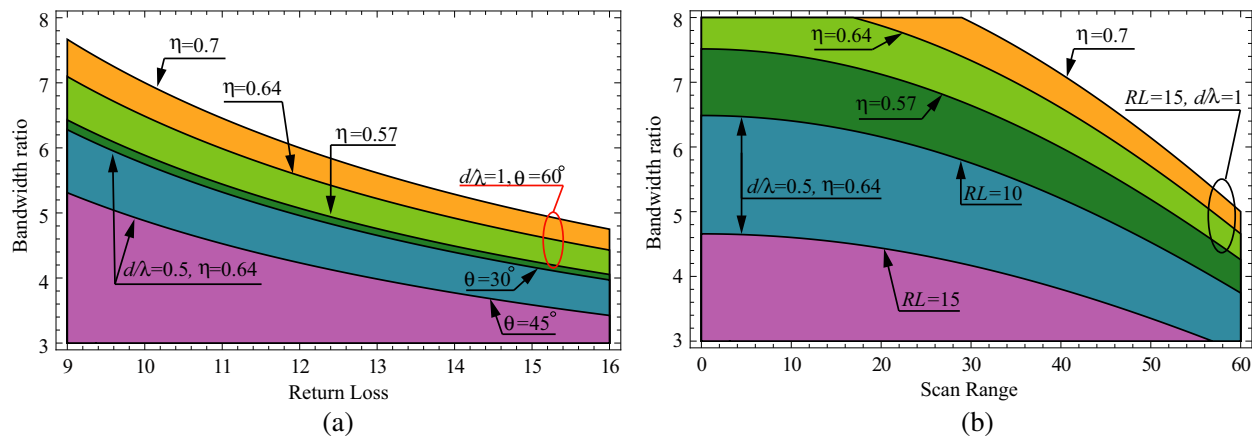


Figure 3: Bandwidth versus (a) return loss and (b) scan-range $[0, \theta_1]$.

45° or reducing the max scan-range to 30° and live with a return-loss of 9.4 dB. If we instead use, e.g., a WAIM layer and have a thick array with relative thickness 1, we see that a 6:1 bandwidth at 10 dB return-loss and maximal scan-range 60° , can be obtained for array figure of merits in $0.57 < \eta < 0.64$.

In Fig. 3(b) of trade-off is between bandwidth ratio and scan-range. Here we once again consider the two cases of $RL = 10$ dB and $RL = 15$ dB, and the two relative thicknesses 0.5 and 1. It is clear that the $RL = 10$ dB with relative thickness 0.5 reaches a 6:1 bandwidth if we accept a scan-range of $[0, 20^\circ]$ for $\eta = 0.64$. However $RL = 15$ and $d/\lambda = 1$ reaches 6:1 bandwidth ratio in the interval $[0, 40]$ degrees for $\eta = 0.57$, whereas if we can improve the design to beyond the state-of-the art $\eta = 0.7$, we can reach a scan-range of $[0, 52^\circ]$.

From the above considerations we see that there are several combination of the specified parameters that are in pair with today's state-of-the art array. With the above illustrations we have shown how return-loss, scan-range and thickness can be traded, in order to reach a good array specification. In the end, which of these parameters that should be weakened depend on the application.

Note that there are currently few known arrays with performance above $\eta > 0.45$, and unfortunately that the waist majority of arrays are below 0.30. A careful choice of antenna design and its technology is required to reaching towards $\eta = 0.64$. A survey of the best arrays in a desired array technology will easily yield a technology-specific figure of merit, which hence can be used as a design-tool and goal setting of such arrays.

4. CONCLUSION

In the present paper, we illustrate how the array figure of merit can be used to trade different array performance parameters against each other. We consider a high-performance array specification, and compare with the array figure of merit corresponding to a state-of-the art array of today. The array figure of merit enables us to realize how the array parameters depend on each-other. We can thus compare with the physical limitation $\eta = 1$, but also against top-performing published arrays. Through the array figure of merit, it is clear how the specification can be adjusted, in order to get an array that is comparable with existing arrays. Realizing a physical array design that have this performance remain an antenna engineering challenge, however we know that there exists realizations on this performance level.

ACKNOWLEDGMENT

We are grateful for the support from VINNOVA within the VINN Excellence Center Chase and the Swedish Research Council, and SSF and VR.

REFERENCES

1. Tomasic, B. and H. Steyskal, "Minimum Q of the element in an infinite phased array — TM^z case," *19th International Conference on Applied Electromagnetics and Communications, 2007, ICECom 2007*, 1–8, 2007.

2. Kwon, D. and D. Pozar, “Energy storage and radiation Q of infinite planar dipole phased arrays,” *IEEE Trans. Antennas Propagat.*, Vol. 62, No. 1, 2014.
3. Doane, J. P., K. Sertel, and J. L. Volakis, “Bandwidth limits for arrays backed by a conducting ground plane,” *IEEE Trans. Antennas Propagat.*, 2511–2518, 2013.
4. Jonsson, B. L. G., C. I. Kolitsidas, and N. Hussain, “Array antenna limitations,” *IEEE Antenn. Wireless Propag. Lett.*, Vol. 12, 1539–1542, 2013.
5. Doane, J., K. Sertel, and J. L. Volakis, “Bandwidth limits for lossless, reciprocal PEC-backed arrays of arbitrary polarization,” *IEEE Trans. Antennas Propagat.*, Vol. 62, No. 5, 2531–2542, 2014.
6. Chu, L. J., “Physical limitations of omni-directional antennas,” *J. Appl. Phys.*, Vol. 19, 1163–1175, 1948.
7. Collin, R. E. and S. Rothschild, “Evaluation of antenna Q ,” *IEEE Trans. Antennas Propagat.*, Vol. 12, 23–27, Jan. 1964.
8. Yaghjian, A. D. and S. R. Best, “Impedance, bandwidth, and Q of antennas,” *IEEE Trans. Antennas Propagat.*, Vol. 53, No. 4, 1298–1324, 2005.
9. Gustafsson, M., C. Sohl, and G. Kristensson, “Physical limitations on antennas of arbitrary shape,” *Proc. R. Soc. A*, Vol. 463, 2589–2607, 2007.
10. Vandenbosch, G. A. E., “Reactive energies, impedance, and Q factor of radiating structures,” *IEEE Trans. Antennas Propagat.*, Vol. 58, No. 4, 1112–1127, 2010.
11. Vandenbosch, G. A. E., “Simple procedure to derive lower bounds for radiation Q of electrically small devices of arbitrary topology,” *IEEE Trans. Antennas Propagat.*, Vol. 59, No. 6, 2217–2225, 2011.
12. Gustafsson, M., M. Cismasu, and B. L. G. Jonsson, “Physical bounds and optimal currents on antennas,” *IEEE Trans. Antennas Propagat.*, Vol. 60, No. 6, 2672–2681, 2012.
13. Capek, M., P. Hazdra, and J. Eichler, “A method for the evaluation of radiation Q based on modal approach,” *IEEE Trans. Antennas Propagat.*, Vol. 60, No. 10, 2012.
14. Gustafsson, M. and S. Nordebo, “Optimal antenna for Q , superdirectivity, and radiation patterns using convex optimization,” *IEEE Trans. Antennas Propagat.*, Vol. 61, No. 3, 1109–1118, 2013.
15. Mikki, S. M. and Y. M. Antar, “A theory of antenna electromagnetic near field — Part I & II,” *IEEE Trans. Antennas Propagat.*, Vol. 60, No. 12, 4691–4724, 2011.
16. Gustafsson, M. and B. L. G. Jonsson, “Stored electromagnetic energy and antenna Q ,” ArXiv Physics e-prints, arXiv:1211.5521, 2013.
17. Geyi, W., “On stored energies and radiation Q ,” ArXiv Physics e-prints, arXiv:1403.3129, 2014.
18. Yaghjian, A. D., M. Gustafsson, and B. L. G. Jonsson, “Minimum Q for lossy and lossless electrically small dipole antennas,” *Progress In Electromagnetic Research*, Vol. 143, 641–673, 2013.
19. Youla, D., L. Castriota, and H. Carlin, “Bounded real scattering matrices and the foundations of linear passive network theory,” *IRE Transactions on Circuit Theory*, Vol. 6, No. 1, 102–124, 1959.
20. Zemanian, A. H., “An n -port realizability theory based on the theory of distributions,” *IEEE Transactions on Circuit Theory*, Vol. 10, No. 2, 265–274, 1963.
21. Nussenzveig, H. M., *Causality and Dispersion Relations*, Academic Press, London, 1972.
22. Bernland, A., A. Luger, and M. Gustafsson, “Sum rules and constraints on passive systems,” *J. Phys. A: Math. Theor.*, Vol. 44, No. 14, 145205, 2011.
23. Rozanov, K. N., “Ultimate thickness to bandwidth ratio of radar absorbers,” *IEEE Trans. Antennas Propagat.*, Vol. 48, No. 8, 1230–1234, Aug. 2000.
24. Sjöberg, D., “Low frequency scattering by passive periodic structures for oblique incidence: Low pass case,” *J. Phys. A: Math. Theor.*, Vol. 42, 385402, 2009.
25. Gustafsson, M. and D. Sjöberg, “Physical bounds and sum rules for high-impedance surfaces,” *IEEE Trans. Antennas Propagat.*, Vol. 59, No. 6, 2196–2204, 2011.
26. Wohlers, M. and E. Beltrami, “Distribution theory as the basis of generalized passive-network analysis,” *IEEE Transactions on Circuit Theory*, Vol. 12, No. 2, 164–170, 1965.

A Simple Experimental Method to Analyze the Properties of Terahertz-wave Propagation in Complex Atmosphere

X. Q. Lin^{1,2}, P. Mei², X. F. Yang¹, J. W. Yu², Y. Jiang², and Y. Fan²

¹State Key Laboratory of Complex Electromagnetic Environment Effects on Electronic and Information System, Luoyang Electronic Equipment Center of China, Luoyang 471003, China

²EHF Key Laboratory of Science, School of Engineering University of Electronic Science and Technology of China, Chengdu 611731, China

Abstract— In this paper, a much simple experimental method is proposed to analyze the terahertz-wave propagation properties. The schematic diagram and process of parameters retrieval are presented in detail. Two terahertz-wave transmission paths are presented in one vacuum chamber but with different lengths. Two switches are required to select different transmission paths in a short time by which the system errors such as assembling error and instrumental error can be ignored. Different complex atmosphere can be injected into the vacuum chamber and its equivalent electromagnetic parameters such as propagation constant can be retrieved. Then the detailed propagation properties can be further calculated. The above method is certificated in full-wave simulation and the error is no more than 0.33% when isotropic material is used to simulate the atmosphere.

1. INTRODUCTION

Terahertz-wave has received considerable attention in both scientific and engineering communities for its higher communication speed, better imaging resolution and less harm medical care [1, 2]. More recently, satisfactory achievements are obtained in designing terahertz source and detector equipments [3, 4]. But the advancement of researches on terahertz-wave propagation properties is still poor. The main analysis method is given by ITU-R [5] which is only suitable for idea atmospheric as only the oxygen, nitrogen and water vapor are considerable. For real complex atmosphere, experimental method is preferred. However, the presented experimental systems are extremely complicated and expensive [6, 7]. They are difficult to be copied by common fabricated technology.

In this paper, a much simple experimental method is proposed to analyze the terahertz-wave propagation properties. Two terahertz-wave transmission paths are presented in one vacuum chamber but with different lengths. Two switches are required to select different transmission path in a short time by which the measurement errors such as assembling error and instrumental error can be ignored. Different complex atmosphere can be injected into the vacuum chamber and its equivalent electromagnetic parameters such as relative permittivity and permeability can be retrieved. The detailed retrieval process are listed and the method is certificated by full-wave simulation when isotropic material is used to simulate the atmosphere.

2. METHOD ANALYSIS

As for terahertz-wave propagation, the absolute results are easily affected by different kinds of errors, such as assembling error, instrumental error and environmental disturbance. Here, we suggest a comparison method to analyze the propagation properties of terahertz-waves. The schematic diagram are presented in Fig. 1, where two terahertz-wave transmission paths are presented in one closed vacuum chamber but with different lengths. Different complex atmosphere can be simulated in the closed chamber. Two switches are added to select different transmission path in a short time by which the measurement errors can be ignored. For path 1, the total scatter matrix $[S]_{P1}$ from port 1 to port 2 can be easily obtained by simulation or experiment. Then, the total transmission matrix $[T]_{P1}$ can be calculated by

$$[T]_{P1} = \begin{bmatrix} T_{11} & T_{12} \\ T_{21} & T_{22} \end{bmatrix}_{P1} = \begin{bmatrix} (-S_{11}S_{22} + S_{12}S_{21})/S_{21} & S_{11}/S_{21} \\ -S_{22}/S_{21} & 1/S_{21} \end{bmatrix}_{P1} = [T]_{P1-L}[T]_{P1-R}, \quad (1)$$

where

$$[T]_{P1-L} = \begin{bmatrix} T_{L11} & T_{L12} \\ T_{L21} & T_{L22} \end{bmatrix}_{P1}, \quad [T]_{P1-R} = \begin{bmatrix} T_{R11} & T_{R12} \\ T_{R21} & T_{R22} \end{bmatrix}_{P1} = \begin{bmatrix} T_{L11} & -T_{L21} \\ -T_{L12} & T_{L22} \end{bmatrix}_{P1}. \quad (2)$$

For path 2, the total scatter matrix $[S]_{P2}$ from port 1 to port 2 can be also easily obtained by simulation or experiment. Then, the total transmission matrix $[T]_{P2}$ can be calculated by

$$[T]_{P2} = \begin{bmatrix} T_{11} & T_{12} \\ T_{21} & T_{22} \end{bmatrix}_{P2} = \begin{bmatrix} (-S_{11}S_{22} + S_{12}S_{21})/S_{21} & S_{11}/S_{21} \\ -S_{22}/S_{21} & 1/S_{21} \end{bmatrix}_{P2} = [T]_{P2-L}[T]_{atm}[T]_{P2-R}, \quad (3)$$

where

$$[T]_{atm} = \begin{bmatrix} e^{\gamma\Delta l} & 0 \\ 0 & e^{-\gamma\Delta l} \end{bmatrix}. \quad (4)$$

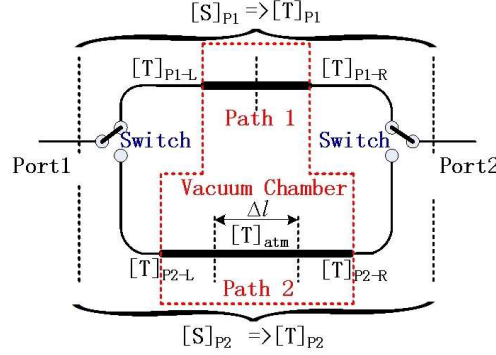


Figure 1: The schematic diagram of parameter retrieval.

Based on detailed optimization and design, $[T]_{P2-L} = [T]_{P1-L}$ and $[T]_{P2-R} = [T]_{P1-R}$ can be achieved. Then, the transmission matrix of complex atmosphere layer with propagation constant γ and length of l can be retrieved from Eqs. (1)–(3). For convenience, we assume that

$$[T]_{P1} = \begin{bmatrix} T_{11} & T_{12} \\ T_{21} & T_{22} \end{bmatrix}_{P1} = \begin{bmatrix} a_1 & b_1 \\ c_1 & d_1 \end{bmatrix}, \quad [T]_{P2} = \begin{bmatrix} T_{11} & T_{12} \\ T_{21} & T_{22} \end{bmatrix}_{P2} = \begin{bmatrix} a_2 & b_2 \\ c_2 & d_2 \end{bmatrix}. \quad (5)$$

We further obtain

$$S_{21-atm} = e^{\gamma\Delta l} = \frac{2b_1b_2 + a_2d_1 + a_1d_2 - \sqrt{T_0}}{2(a_2d_2 + b_2^2)}, \quad (6)$$

$$\gamma = \alpha + j\beta = \ln(S_{21})/\Delta l, \quad (7)$$

where

$$T_0 = 4b_1b_2a_2d_1 + 4b_1b_2a_1d_2 + a_2^2d_1^2 - 2a_2d_1a_1d_2 + a_1^2d_2^2 - 4a_2d_2b_1^2 - 4a_1d_1b_2^2. \quad (8)$$

Now, we summarize the retrieval process as follows:

- (1) Switch on path 1 and obtain the total scatter matrix $[S]_{P1}$;
- (2) Switch on path 2 and obtain the total scatter matrix $[S]_{P2}$;
- (3) Calculate the $[T]_{P1}$ and $[T]_{P2}$ by Eqs. (1) and (3);
- (4) Calculate the propagation constant γ by Eqs. (6)–(8);
- (5) Calculate the propagation properties with different lengths by $S_{21-atm} = e^{\gamma l}$.

3. SIMULATION VERIFICATION

In this section, we would like to verify the proposed retrieval method using full-wave simulation software of HFSS. The simulation models are presented in Fig. 2, where Figs. 2(a) and (b) refer to two terahertz-wave transmission paths with the same input/output transitions but different lengths of l_1 and l_2 . Fig. 2(c) refers to the continuous middle part which is used for the verification of our retrieval method. Two samples are detailed analyzed, where $l_1 = 1$ mm and $l_2 = 2$ mm are fixed. The isotropic material of $\epsilon_r = 1 - j0.1$ and $\epsilon_r = 3 - j0.45$ are filled in the chambers, respectively.

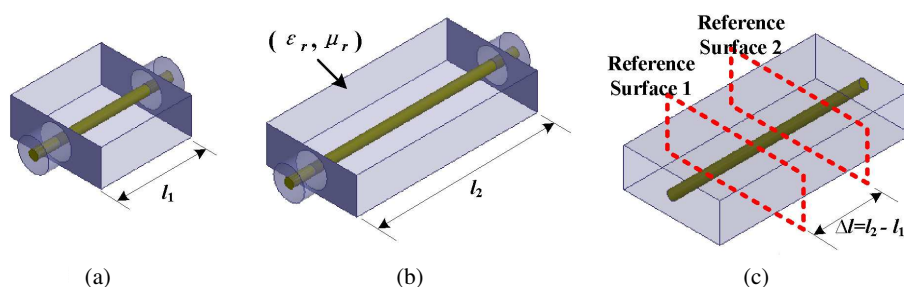


Figure 2: The simulation models. (a) Path 1. (b) Path 2. (c) Middle part.

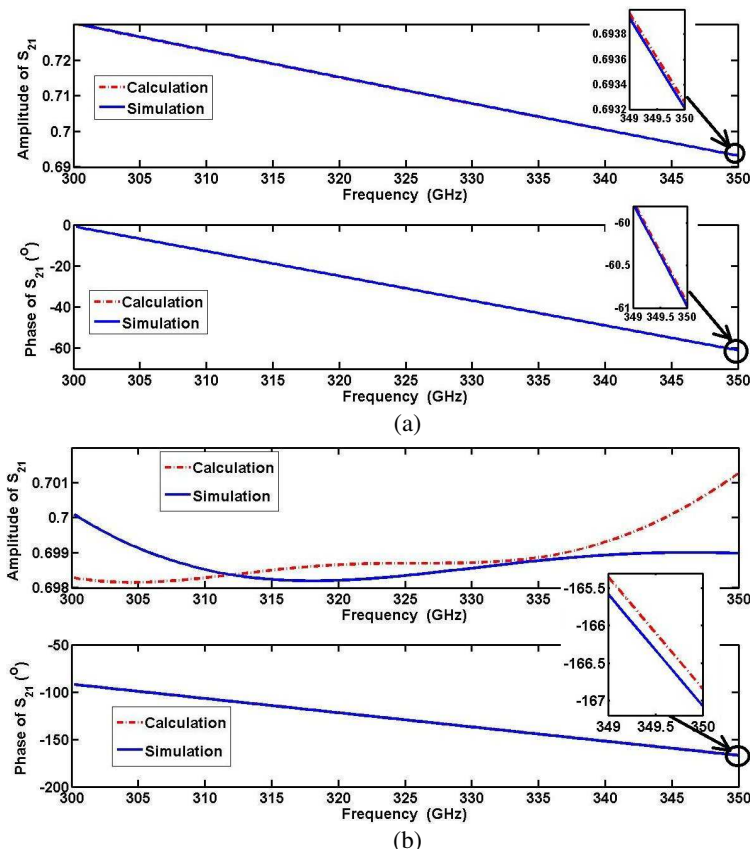


Figure 3: Retrieval results of two samples. (a) $\epsilon_r = 1 - j0.1$, $\mu_r = 1$. (b) $\epsilon_r = 3 - j0.45$, $\mu_r = 1$.

Relative amplitudes and phases of S_{21} retrieved by our proposed method are presented in Figs. 3(a) and (b), which are also compared to the simulated results by HFSS. From Fig. 3, we can see that the maximum relative errors of amplitude and phase are only 0.33% and 0.2%, respectively, which are presented at 350 GHz in sample 2. Compared Fig. 3(a) to Fig. 3(b), we further know if better matching through both paths are achieved, higher retrieval precision is hoped to be obtained.

We clarify that the coaxial waveguide is just used for input and output the signal in simulation. Other waveguide structures such as metallic rectangular waveguide or microstrip line should be replaced in real fabrication. What's more, the PEC-cylinder in closed rectangular chambers can also be replaced by two antennas with much larger chambers, by which better matching through both paths are easily finished.

4. CONCLUSION

We propose an experimental method to analyze the terahertz-wave propagation properties in this paper. A comparison method is suggested in the detailed retrieval process, by which the errors can be reduced greatly. Compared to those TDS (time-domain spectroscopy)-based experimental methods, our proposed method is much simpler and easier to be fabricated. Different propagation

modes such as wire transmission by PEC cylinder or wireless radiation by antennas can be used in such an experimental system. The core technology is just to be sure the identical transition and high isolation of path 1 and 2.

ACKNOWLEDGMENT

This work was supported in part by the State Key Laboratory of CEMEE Foundation under Grant No. CEMEE2014Z0201A, in part by the Fundamental Research Funds for the Central Universities under Grant Nos. ZYGX2010J021 and ZYGX2012YB002, in part by the Program for New Century Excellent Talents in University under Grant No. NCET-13-****.

REFERENCES

1. Song, H. J. and T. Nagatsuma, “Present and future of terahertz communications,” *IEEE Transactions on Terahertz Science and Technology*, Vol. 1, No. 1, 256–263, 2011.
2. Akyildiz, I. F., J. M. Jornet, and C. Han, “Terahertz band: Next frontier for wireless communications,” *Physical Communication*, Vol. 12, 16–32, 2014.
3. Bulgarevich, D. S., M. Watanabe, M. Shiwa, et al., “A polarization-sensitive 4-contact detector for terahertz time-domain spectroscopy,” *Optics Express*, Vol. 22, No. 9, 10332–10340, 2014.
4. Ollmann, Z., J. A. Fülöp, J. Hebling, et al., “Design of a high-energy terahertz pulse source based on ZnTe contact grating,” *Optics Communications*, Vol. 315, 159–163, 2014.
5. International Telecommunications Union, Radiocommunications Bureau, “Attenuation by atmospheric gases,” *Recommendation ITU-R P.676-9*, February 2012.
6. Meshkov, A. I. and C. D. L. Frank, “Laboratory measurements of dry air atmospheric absorption with a millimeter wave cavity ringdown spectrometer,” *Journal of Quantitative Spectroscopy and Radiative Transfer*, Vol. 108, No. 2, 256–276, 2007.
7. Yang, Y., M. Mandehgar, and D. Grischkowsky, “Determination of the water vapor continuum absorption by THz-TDS and Molecular Response Theory,” *Optics Express*, Vol. 22, No. 3, 4388–4403, 2014.

A General and Effective Clutter Filtering Strategy for Quiet Zone Evaluation in Tri-reflector Compact Range

Jingjuan Wang¹, Cheng Yang¹, Yuan Yao¹, Xiaoming Liu¹,
Junsheng Yu¹, and Xiaodong Chen²

¹School of Electronic Engineering
Beijing University of Posts and Telecommunications, Beijing, China
²School of Electronic Engineering and Computer Science
Queen Mary University of London, London, UK

Abstract— A clutter filtering strategy is presented to evaluate the performance of the quiet zone of a tri-reflector compact range. The method is based on the band limitation properties of the scattered fields to filter the noise in quiet zone. Prior information on the source, such as its size, geometry, and location, are required in this approach. By exploiting a simple low-pass filter, this filtering strategy can partially filter out the environmental clutter. Numerical results are presented to confirm the effectiveness of the method.

1. INTRODUCTION

Nowadays, millimeter and sub-millimeter wave technique is widely applied in fields such as remote sensing, radio astronomy. In order to verify the performance of millimeter and sub-millimeter system, accurate measurement should be performed. Compact range (CR) is a promising method for electrically large antenna measurement where a pseudo-plane wave region can be generated for the accurate measurement.

The performance of CR mainly depends on the amplitude and phase ripple in the quiet zone. Environment clutter is one of those interference sources that affect the performance of the quiet zone, especially in millimeter and sub-millimeter band. Method of moment (MoM) is famous for its simple principle and has been widely used to reduce clutter noise [1]. However, in the case of CR, MoM has to simulate all the processes such as wave packet generation, diffraction, and absorption, which causes complexity and large calculating quantity. Besides, for each new project all the properties have to be simulated all over again. It is highly desirable to develop a fast and simple method independent of these processes. The aim of this paper is to provide a brief and general method to diminish quiet zone clutter noise in CR system, exploiting the concept of effective bandwidth of scattered field and the theory of digital signal processing.

2. TRI-REFLECTOR COMPACT RANGE

The basic principle of CR is to collimate the radiated field from a horn feed and to transform it into a pseudo plane wave by lens or reflectors. The design of a tri-reflector CR is based on the theory of GO ray tracing. The proposed CR consists of a spherical main reflector, two shaped sub-reflectors and a Gaussian beam horn. Figure 1 shows the diagram of the designed tri-reflector CR. Usually the aperture of the main reflector is defined as its projection on $x-y$ plane. However, considering the diffraction effect the actual aperture should be larger [1]. It is acceptable to represent the actual aperture by $r_e = r + 5\lambda$ since the length of the serrated edge of CR is usually 5λ .

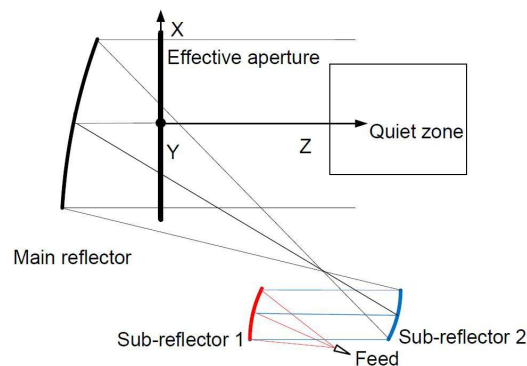


Figure 1: Diagram of the designed tri-reflector CR.

3. FILTERING STRATEGY APPLIED ON CR

This filter strategy is a supplementary solution for sophisticated measurement facility and requires prior information of the AUT, such as electrical size, geometry, location, etc.. The clutter noise can be filtered out since the prior information confines the electric field that the main reflector can generate.

The filter strategy is implemented by applying a filtering algorithm to a reduced field multiplying the measured field by a proper phase factor can get the reduced field. And due to Bucci's research [2,3], the reduced field can be precisely represented by a band-limited function whose bandwidth depends on AUT's electrical size, geometry, and location. Figure 2 gives a brief demonstration of this filtering problem.

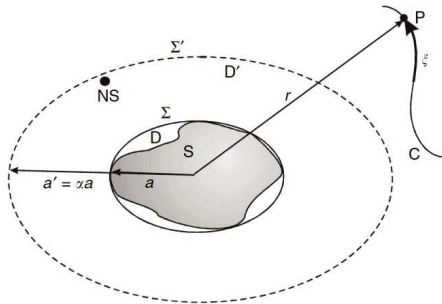


Figure 2: Geometry of filtering problem.

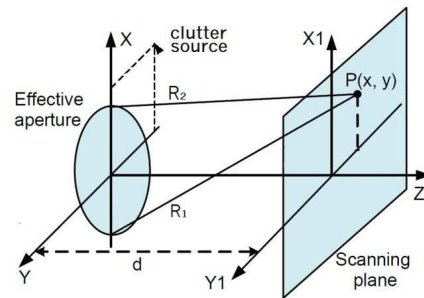


Figure 3: Geometry relevant to CR filter strategy.

Assuming S is the signal source contained in the D domain within a surface Σ , and NS is the clutter noise contained in D' domain within a surface Σ' , ξ is the curvilinear abscissa along C . Since bandwidth W is proportional to dimension, by projecting the reduced field on the band-limited function of the main reflector, clutter noise can be filtered out with a simple low-pass filter.

In the case of CR, the AUT is the main spherical reflector, and the field is simulated on a scanning plane. Figure 3 shows the geometry of the scanning system and Figure 4 gives the flow chart of the filtering algorithm in the case of CR.

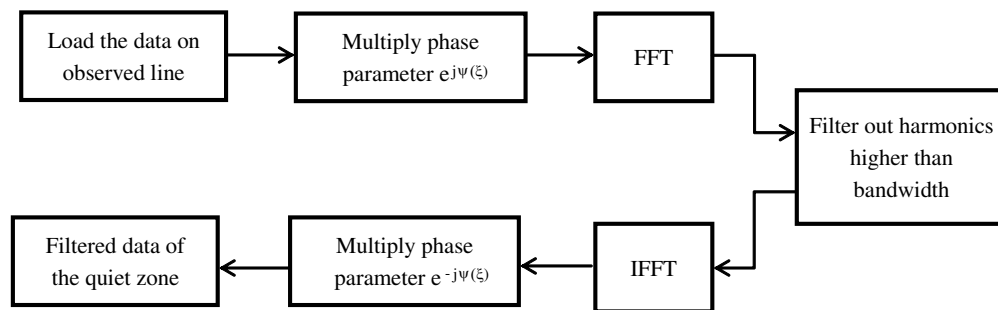


Figure 4: The flowchart of the filtering algorithm in case of CR.

Firstly, phase function is constructed as [4]

$$\psi = \beta\alpha v - \beta\alpha \quad (1)$$

where $v = R_1 + R_2$, α is the actual aperture of the reflector and β is the propagation constant. Thus, the reduced field can be represented by

$$F(\xi) = E(\xi) \exp[j\psi(\xi)] \quad (2)$$

The reduced field is an analytical function and can be approximated by a band-limited function whose bandwidth is

$$W = \beta\alpha/2\pi \quad (3)$$

To control the representation error of the field in quiet zone the enlargement bandwidth factor x_1 is introduced. The band-limited error decreased fast with x_1 and can be neglected when x_1 is a little

larger than one. Besides this, to get an optimal result, the oversampling factor x_2 is also required to be selected to prevent aliasing caused by sample deficiency. With x_1 and x_2 , effective bandwidth $w = x_1 * x_2 * W$ is constructed. The next step is to get the corresponding azimuth spectrum with an FFT algorithm and set harmonics higher than the effective bandwidth to zero with a simple sharp-window filter. Finally an IFFT algorithm is used to recover the quiet zone field.

4. NUMERICAL EXAMPLES AND DISCUSSIONS

To evaluate the process, the filtering strategy is applied to the quiet zone. The aperture of the main reflector is 1 m, and the diameter of the quiet zone is 0.7 m. The clutter caused by the reflector support can be simulated by a Gaussian beam horn placed 0.7 m away from the main reflector center, shown in Figure 3. The whole CR system works at 340 GHz. Commercial simulation software GRASP-10.0 is used to obtain the required field in quiet zone.

First, the quiet zone field without the clutter noise is simulated at a half wave-length interval. Then the field data is collected again with the clutter noise. Enlargement bandwidth factor x_1 and oversampling factor x_2 are chosen as 1.65 and 1.2 respectively. After the collection of the required data, an FFT algorithm is used to get the corresponding spectrum, shown in Figure 5.

The dotted vertical line represents the effective bandwidth w . It can be seen in Figure 5 that a large part of the clutter noise energy falls outside the radiation field bandwidth of the main reflector which is $(-w, w)$. The performance of quiet zone with and without the effect of clutter is shown from Figure 6 to Figure 9. And the performance of the amplitude ripple, cross-polar isolation, and phase ripple with and without the proposed filtering strategy on the entire cut are shown in the Table 1.

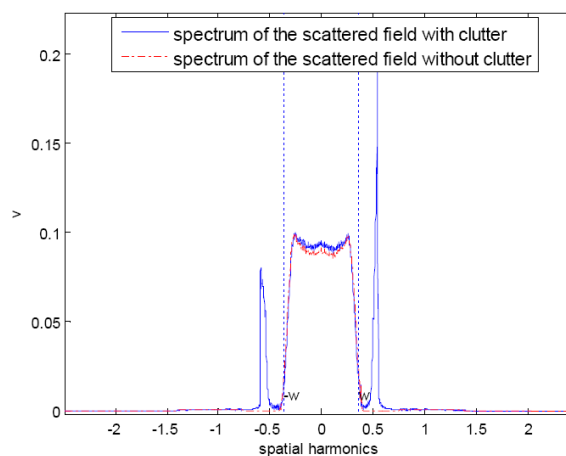


Figure 5: Amplitude of spectrum of reduced field.

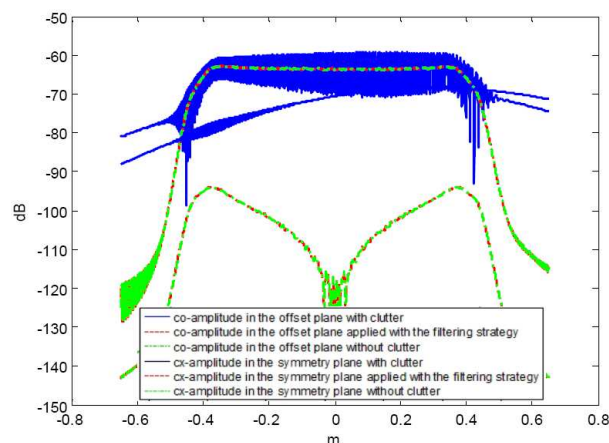


Figure 6: Amplitude of the quiet zone field in the offset plane.

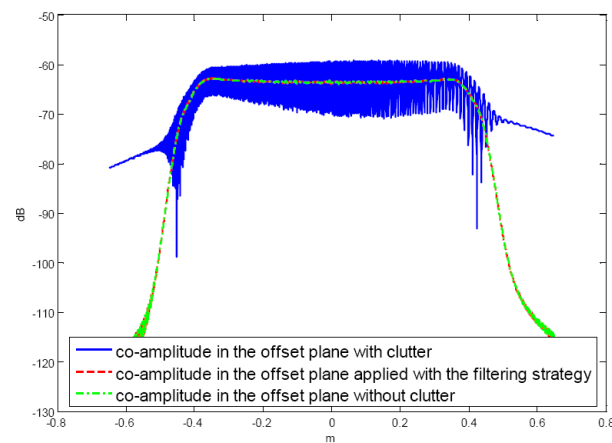


Figure 7: CO-amplitude of the quiet zone in the offset plane.

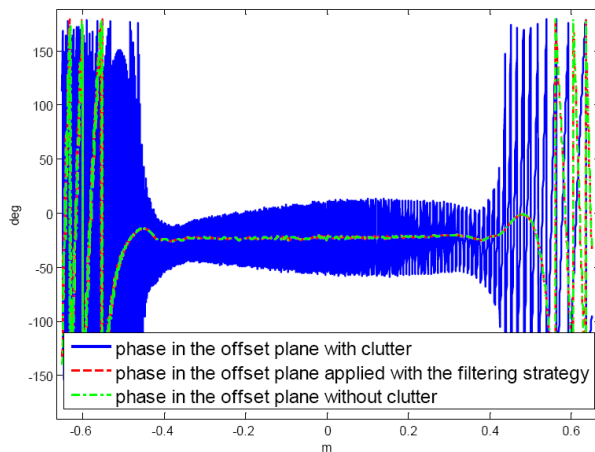


Figure 8: Phase of the quiet zone in the offset plane.

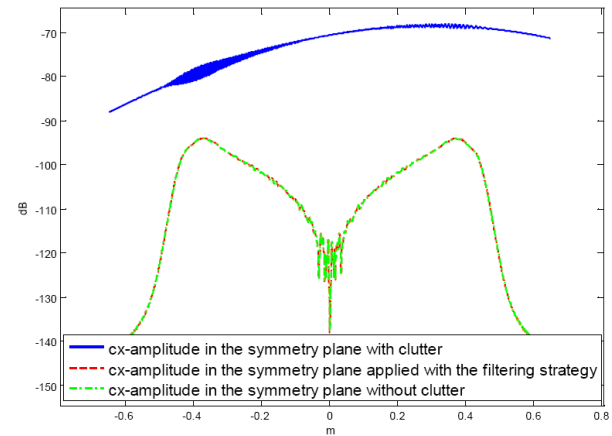


Figure 9: CX-amplitude of the quiet zone field in the offset plane.

Table 1: CR performance in different situation.

performance evaluation	amplitude ripple (dB)	cross-polar isolation (dB)	phase ripple (degree)
Without clutter	0.8435	33.0218	5.1096
With clutter	15.0974	-5.5150	89.8523
Filtered data	0.8529	33.0114	5.8712

5. CONCLUSION

The problem of diminishing the effect of clutter noise in the CR system has been investigated and solved. A clutter filtering strategy is presented to evaluate the performance of the quiet zone of a tri-reflector compact range with the clutter. The method is based on the band limitation properties of the scattered fields. By exploiting a simple low-pass filter, the noise in the quiet zone can be filtered. This filtering strategy can partially filter out the environmental clutter. Numerical results are presented to confirm the effectiveness of the method.

ACKNOWLEDGMENT

This work was supported by the CAEP THz Science and Technology Foundation under the Grant No. CAEP THZ201210 and the Scientific Research Foundation for the Returned Overseas Chinese Scholars, State Education Ministry.

REFERENCES

1. Yarovoy, A. G., "Monte-Carlo simulations of surface clutter in GPR scenarios," *Geoscience and Remote Sensing Symposium, IGARSS'03, Proceedings*, Vol. 1, 130–132, 2003.
2. Yang, C., J. Yu, and Y. Yao, "Quiet zone evaluation from nonredundant rectilinear data for tri-reflector compact antenna test range," *Microwave Conference Proceedings (APMC), Asia-Pacific*, 398–400, 2013.
3. Bucci, O. M. and G. Franceschetti, "On the spatial bandwidth of scattered fields," *IEEE Trans. Antennas Propag.*, 1445–1455, 1988.
4. Bucci, O. M., G. D'Elia, and M. D. Migliore, "A general and effective clutter filtering strategy in near-field antenna measurements," *IEE Proceedings Microwaves, Antennas and Propagation*, Vol. 151, No. 3, 227–235, 2004.
5. Bucci, O. M., C. Gennarelli, and C. Savarese, "Representation of electromagnetic fields over arbitrary surfaces by a finite and nonredundant number of samples," *IEEE Trans. Antennas Propag.*, Vol. 46, 351–359, 1998.

Implementation of Three-dimensional Diffractive Gaussian Beam Analysis Method

Fangyuan Cheng¹, Zejian Lu¹, Xiaoming Liu¹, Hai Wang¹, Junsheng Yu¹, and Xiaodong Chen²

¹School of Electronic Engineering, Beijing University of Posts and Telecommunications
279 Box, 10 Xi Tu Cheng Road, Haidian District, Beijing 100876, China

²School of Electronic Engineering and Computer Science, Queen Mary University of London
Mile End Road, London E1 4NS, UK

Abstract— This paper developed a 3-dimensional Diffractive Gaussian Beam Analysis (DGBA) method for the analysis of electrically large reflector antennas. Unlike a symmetrical 2-D structure, it adopts the approach of full plane expansion, where the illuminating field over the whole input plane is decomposed into a set of elementary Gaussian beams. These Gaussian beams are propagated to the reflector. Reflected beams are treated with Geometric Optics, while edge diffraction is modeled using the canonical problem of a 3D Gaussian beam incident upon an opaque Kirchhoff half-screen. The output beam is a superposition of all reflected and diffracted elementary beams. The proposed analysis method is verified against a GRASP Physical Optics.

1. INTRODUCTION

In millimeter wave and sub-millimeter wave radiometry and radio astronomy applications, analysis technology for quasi-optical (QO) system is the research focus for the analysis of electrically large systems [1, 2]. Many numerical calculation methods can be employed to predict the diffracted fields of reflector antennas such as Physical Optics (PO) and Geometrical Optics (GO). Unfortunately, GO does not account for the effects of boundary diffraction. PO is accurate but expensive in terms of computation time and storage for electrically large system. In this connection, a faster method, namely diffracted Gaussian beam analysis, combines the numerical efficiency of GO and the rigor of PO, has been developed. The current 2-Dimensional DGBA requires the incident wave and reflector to be symmetrical about a certain plane. To overcome this limitation, this paper introduces the approach of full plane expansion, where the field over the whole input plane is decomposed to a series of GBs. This proposed method can be applied to stereoscopic system in some practical applications.

2. THEORY

2.1. The Theory of DGBA

The process of DGBA method follows four steps [3]: (1) The incident fields that could be either the near field of a feed or the radiated field from a previous reflector are first expanded to Gaussian beams by windowed Fourier transform on the input plane; (2) These Gaussian beams will be propagated to the reflector to be analyzed according to Gaussian beam propagation theory; (3) The reflected Gaussian beams can be processed by Geometric Optic, and the diffraction coefficients of Gaussian beams can be modeled by an equivalent Kirchhoff half plane; (4) The reflected and diffracted Gaussian beams will be superposed on an output plane, which forms the input plane to the next reflector or other Quasi-Optical components. If this reflector is the last one in the system, far fields can be calculated by superposing the far field of each Gaussian beam.

2.2. Gaussian Beam Diffraction

2.2.1. Field Representation in the Forward-scattering Region

Diffraction of a Gaussian beam with a circular spot size normally incident upon an opaque Kirchhoff half-screen was investigated based on the boundary-diffraction wave (BDW) theory [4, 5]. The incident beam is assumed to propagate in z -direction and can be written as

$$U_i(x, y, z) = \frac{q(-z_0)}{q(z)} \exp(ik_0\phi(x, y, z)) \quad (1)$$

$P(x, y, z)$ is the observation point and $Q(x_0, y_0, z_0)$ is a source point of boundary-diffraction located on the boundary of the half-screen. Following the BDW theory, we can represent the total diffracted

field $U_K(P)$ in the forward scattering region ($z > 0$) at the observation point P as

$$U_k(P) = \sum_j F_j(P) + U_B(P) \quad (2)$$

In the formula, $U_B(P)$ and $\sum_j F_j(P)$. Separately represent Geometrical Optics incident field and diffraction part.

$$U_B(P) = \int_{\Gamma} \vec{W}(P, Q) d\vec{l} = \int_{\Gamma} U_i(Q) \frac{\exp(jk_0 s)}{4\pi s} \frac{\hat{s} \times \nabla_Q \phi}{1 + \hat{s} \cdot \nabla_Q \phi} d\vec{l} \quad (3)$$

$$\sum_j F_j(P) = E(x_s - x) U_i(P) \quad (4)$$

The total diffracted field can be written as a superposition in terms of complementary error functions:

$$U(P) = \begin{cases} U_i(P) - \frac{q(0)}{2q(z)} \operatorname{erfc} \left(j [jk_0 (d(y_s) - d(y_p^1))]^{1/2} \right) & x \leq x_s \\ \exp(-jk_0(d(y_s) - d(y_p^1) - s(Q_d))) U_i(Q_d) & \\ \frac{q(0)}{2q(z)} \operatorname{erfc} \left(-j [jk_0 (d(y_s) - d(y_p^1))]^{1/2} \right) & x \geq x_s \\ \exp(-jk_0(d(y_s) - d(y_p^1) - s(Q_d))) U_i(Q_d) & \end{cases} \quad (5)$$

2.2.2. Field Representation in the Backward-scattering Region

We can find an equivalent geometry, as valid in the forward-scattering, to describe the diffracted in the backward-scattering region. A new coordinate system with the transformed (x, y, z) pointing in $(-x, y, -z)$ as shown in Fig. 2. The equivalent half-screen must be complementary to the true half-screen to generate a shadow region in the lower half space. The BDW does only depend on the location of the edge and not on the orientation of the half screen.

2.2.3. Generalization to Oblique Incidence

The transmitted beam-related co-ordinate system (x_t, y_t, z_t) , the reflected beam related co-ordinate system (x_r, y_r, z_r) , the half-screen based co-ordinate system (x, y, z) and the observation point is being described in the half-screen based (ρ, ϕ, y) . The co-ordinate systems are expressed in terms of the half-screen co-ordinate system by simple translation and rotation around the y -axis:

$$\begin{pmatrix} z_t \\ x_t \end{pmatrix} = \rho \begin{pmatrix} \cos(\varphi - (\pi + \varphi_0)) \\ \sin(\varphi - (\pi + \varphi_0)) \end{pmatrix} + \begin{pmatrix} z_e \cos(\varphi) \\ 0 \end{pmatrix} \quad (6)$$

$$\begin{pmatrix} z_r \\ x_r \end{pmatrix} = \rho \begin{pmatrix} \cos(\varphi - (\pi - \varphi_0)) \\ \sin(\varphi - (\pi - \varphi_0)) \end{pmatrix} + \begin{pmatrix} z_e \cos(\varphi_0) \\ 0 \end{pmatrix} \quad (7)$$

Since the BDW is obtained as a line integral along the edge and does not depend on the orientation of the half-screen, we are now in a position to apply the formulas for normal incidence. The

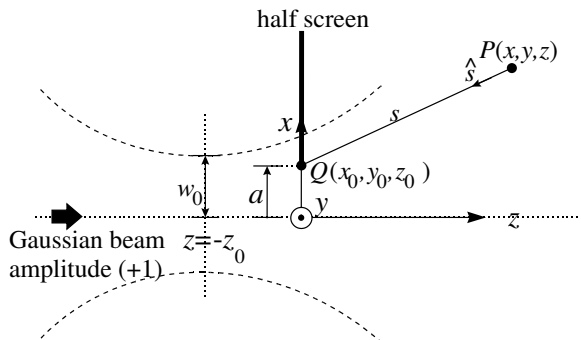


Figure 1: Geometry of the problem (forward-scattering region).

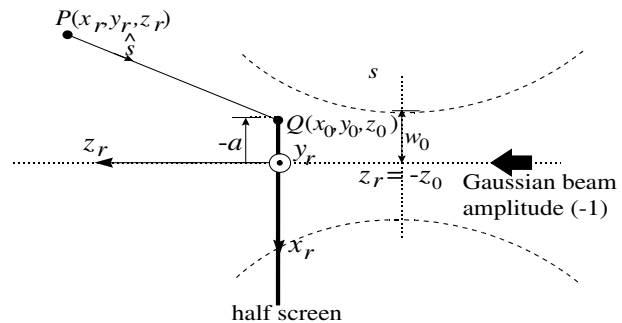


Figure 2: Mirror-symmetric geometry for determining the backward-scattered field.

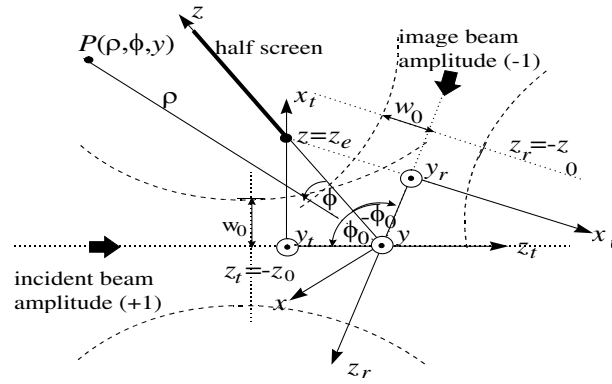


Figure 3: Equivalent geometry for determining the backward-scattered field at oblique incidence.

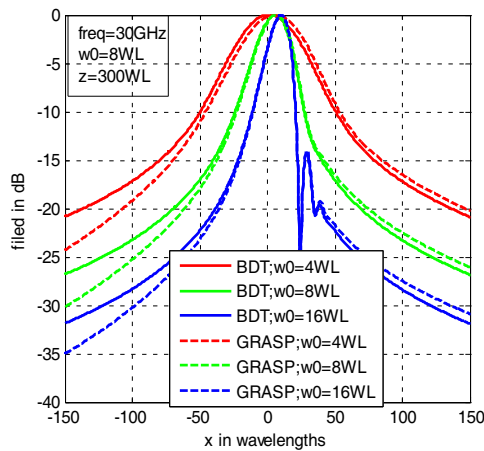


Figure 4: Comparison of the backscattered field with PO for various beam spot sizes.

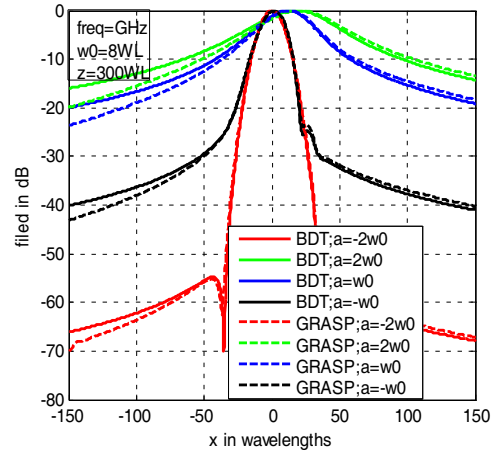


Figure 5: Comparison of the backscattered field with PO for various values of the parameter a .

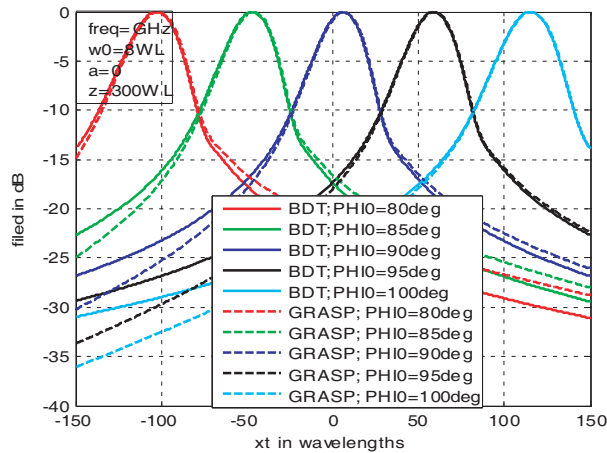


Figure 6: Comparison of the backscattered field with PO for various orientations of the half-screen.

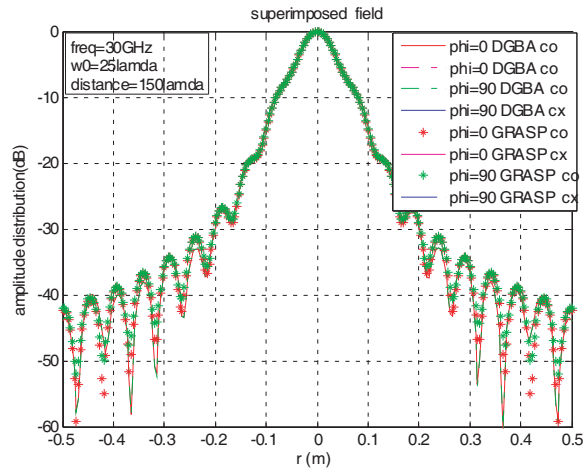


Figure 7: Comparison of the near field from main reflector with PO at 30 GHz.

offset distance a from the edge is related to the axial position z_e of the edge in the half-screen by $a = z_e \sin(\phi_0)$.

We consider the case of azimuthally normal incidence, but oblique incidence with respect to the polar angle. For incidence angles close to 90, the formulas (5) can still be applied. The beam direction of the transmitted and reflected beam changes, however according to GO and the transmitted and reflected related co-ordinate system are rotated by $(\pi/2 - \theta)$ around the x -axis compared to the case with normal incidence.

2.2.4. Simulation and Numerical Verification

To check the accuracy of the asymptotic method, the problem of an incident Gaussian beam upon a Kirchhoff half-screen has been analyzed with the commercial reflector analysis tool GRASP [6], using Physical Optics.

3. NUMERICAL RESULTS

The Gaussian beams normally incident upon the the paraboloidal reflector operate at 30 GHz. There are the following geometrical characteristics: the beam waist is 0.25 m, reflector diameter is 0.5 m, reflector focal length is 4 m, the distance from the feed to the reflector edge is 0.1 m and the output expansion plane is at $z = 1.5$ m. The results to be shown is of comparative field plots between GRASP and the DGBA.

4. CONCLUSION

The proposed 3-Dimensional DGBA procedure with the approach of full plane expansion has been presented. This method can be applied to 3D system, where the optical centers of the feed and all of the reflectors can lie on the different planes. The field in the result section demonstrates the effectiveness of the DGBA in comparison to GRASP.

ACKNOWLEDGMENT

This work was supported by the Scientific Research Foundation for the Returned Overseas Chinese Scholars, State Education Ministry.

REFERENCES

1. Martin, R. J. and D. H. Martin, "Quasi-optical antennas for radiometric remote-sensing," *Electronics & Communication Engineering Journal*, Vol. 8, No. 1, 37–48, Feb. 1996.
2. Jorgesen, R., G. Padovan, P. de Maagt, D. Lamarre, and L. Costes, "A 5-frequency millimeter waveantenna for a spaceborne limb sounding instrument," *IEEE Transactions on Antennas and Propagation*, Vol. 49, No. 5, 703–714, May 2001.
3. Yu, J., S. Liu, and Q. Wei, "A 3D design software for quasi-optical systems based on integrated methods," *Microwave Technology and Computation Electromagnetics, ICMTCE (2009)*, 2009.
4. Takenaka, T. and O. Fukumitsu, "Asymptotic representation of the boundary-diffraction wave for a three-dimensional Gaussian beam incident upon a Kirchhoff half-screen," *J. Opt. Soc. Am.*, Vol. 72, No. 3, 331–336, 1982.
5. O'sullivan, C., E. Atad-Ettedgui, W. Dunca, et al., "Far-infrared optics design & verification," *International Journal of Infrared and Millimeter Waves*, Vol. 23, No. 7, Jul. 2002.
6. GRASP8, "Reflector analysis code user manual," TICRA, Copenhagen, Denmark.

A Fast Gaussian Beam Tracing Method for Quasi-optical System Analysis Based on Gabor Frame Expansion

Hai Wang¹, Zejian Lu¹, Fangyuan Cheng¹, Junsheng Yu¹, Xiaodong Chen²,
Xiaoming Liu¹, and Yuan Yao¹

¹School of Electronic Engineering
Beijing University of Posts and Telecommunications, Beijing 100876, China

²School of Electronic Engineering and Computer Science
Queen Mary University of London, E1 4NS, UK

Abstract— Quasi-optical systems and techniques have been the topic of research in the past decades. The field of feed is expanded into a set of sub-GBs based on Gabor frame expansion method and field tracing is through astigmatic Gaussian beam (GB) techniques. Single astigmatic GB reflection under arbitrary curved surface is successfully analyzed. Near-field scanning result of quasi-optical systems having two parabolic mirrors matching up to -50 dB below peak value has been verified. Numerical and experimental comparison reveal a good trade-off between the accuracy and the computational effort.

1. INTRODUCTION

With the increase of frequency, GB analysis method is more accurate and practical especially in analyzing unsymmetrical and large electrically reflector antenna, with respect to Physical Optics (PO) [1] or Geometrical Optics (GO). Uniform geometrical theory of diffraction (UTD) is suitable to study curved edges illuminated by electromagnetic. In engineering applications, there is an urgent hope that quickly analyzing and obtaining emergent field of reflection mirror of millimeter wave on the premise of guaranteeing certain accuracy requirement.

The conventional modeling approaches in multi-reflector quasi-optical system analysis [2] are constituted by two aspects: expansion techniques and tracking techniques [3–5]. In that theory, electromagnetic field is first expanded into Gaussian beams (GBs), with different direction and energy, then they are traced into a reflector where reflection or diffraction occur and emergent beam field can be obtained via superimposing all GBs [6]. However, there is no doubt that GBs are often considered as paraxial transmission wave equation, which can be regarded as focused pure GB, and the energy of electromagnetic emergent from the feed is mainly up to the number of GBs in the center of optical axis, which also means that around the mirror the number and energy of GBs are very small.

Based on this conclusion, a fast quasi-optical analysis method is proposed on the assumption that the diffraction on the reflector edge is rare thus can be neglected if the reflector size is four times larger than the beam width on the surface. In this method, the field pattern of feed is expanded into sets of sub-GBs using Gabor frame expansion method [7–9], and near area of specular reflection point is approximated as parabolic model. Furthermore, introducing the astigmatic GB [10] as elementary beam wave equation to find out every emergent beam field so multi-reflection mirrors system can be continuous analyzed.

Feed is expanded into a series of sub-GBs based on Gabor frame expansion technique and the characters of astigmatic GB are viewed in Section 2. A quasi-optical system having two parabolic mirrors is discussed in Section 3, and in Section 3, we summarize all of the work.

2. METHOD

2.1. Gabor Frame Expansion Technique

In digital signal processing, according to the sampling theorem, the sampling values can restore the original signal. The field that incident upon the input plane in quasi-optical system may not possess an exact GB profile, which mean that decomposing into a sum of GBs. Gabor frame expansion is based on the fact that any form of field distribution can be expanded into a set of GBs, which have own direction and coefficients that are frequency-dependent. Field incident from feed are expanded into sub-GBs are showed in Fig. 1(a) and the expansion formula is as follow

$$f(t) = \sum_{m,n} A_{mn} \omega_{mn}(t) = \sum_{m,n} A_{mn} \omega(t - mL_0) \exp(jn\Omega_0 t) \quad (1)$$

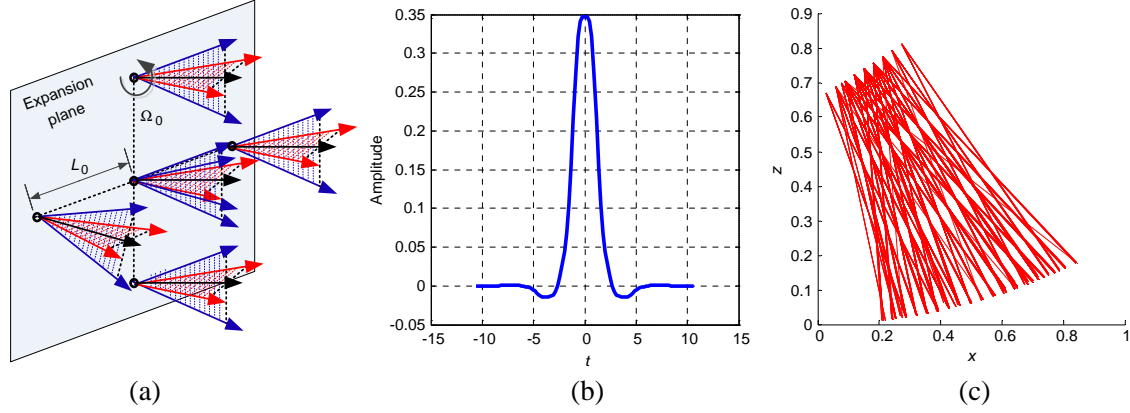


Figure 1: (a) Incident field is decomposed into a set of sub-GBs in the expansion plane. (b) Gabor frame window function. (c) The actual feed is expanded into sub-GBs projection in the xoz plane.

where A_{mn} is to be solved out coefficient of the GBs, $\omega(t) = \pi^{-1/4} \exp(-t^2/2)$ is the Gabor frame window function, which usually is the function of Gaussian shape and showed in Fig. 1(b). L_0 and Ω_0 is space spectrum and angle spectrum sampling interval respectively. The coefficient of formula is

$$A_{mn\mu\nu} = \iint f(x, y) \exp[-jK_0(nx + \nu y)] \tilde{\omega}(x - mL_0) \tilde{\omega}(y - \mu L_0) dx dy \quad (2)$$

where $|m|, |\mu| \leq M/2$, $|n|, |\nu| \leq N/2$, M and N is the number of space spectrum and angle spectrum sampling respectively.

2.2. Astigmatic GB Tracking Technique

Feed is expanded into a set of sub-GBs. It is necessary to find out the characters of a single astigmatic GB reflection under arbitrary curved surface. An astigmatic GB equation is as follows:

$$\vec{H}_i(x_i, y_i, z_i) = (\vec{x}_i H_1^i + \vec{y}_i H_2^i) \sqrt{\frac{\det(Q^i(z_i))}{\det(Q^i(0))}} \exp(-jkS^i) \quad (3)$$

where $S^i = z_i + \frac{1}{2} [x_i \ y_i] Q^i(z_i) [x_i \ y_i]'$, $Q^i(z_i) = \begin{bmatrix} \frac{1}{z_i + \rho_1^i} & 0 \\ 0 & \frac{1}{z_i + \rho_2^i} \end{bmatrix}$, ρ_1^i and ρ_2^i have relationship with

distance from the position of beam waist in x_i and y_i directions respectively to reflection point of mirror and the waist size of the input beam. Q matrix is wavefront curvature matrix and represents the actual propagation process of light path by function $[Q_i(z_i)]^{-1} = [Q_i(0)]^{-1} + z_i \cdot I$. Emergent field of astigmatic GB equation has

$$\vec{H}_r(x_r, y_r, z_r) = (\vec{x}_r H_1^r + \vec{y}_r H_2^r) \sqrt{\frac{\det(Q^r(z_r))}{\det(Q^r(0))}} \exp(-jkS^r) \quad (4)$$

where

$$Q^r(z_r) = \frac{1}{z_r + \rho_1^r} \frac{1}{z_r + \rho_2^r} \begin{bmatrix} \rho_1^r \rho_2^r Q_{11}^r + z_r & \rho_1^r \rho_2^r Q_{12}^r \\ \rho_1^r \rho_2^r Q_{21}^r & \rho_1^r \rho_2^r Q_{22}^r + z_r \end{bmatrix} \quad (5)$$

Tracking techniques need to solve out elementary GB intersection location in mirror on the basis of expansion start location and propagation direction. On the specular reflection points, three coordinate system, which are input, principal axes and output coordinate system as showed in Fig. 2(a), are established so that to obtain GB reflection field formula. A single GB reflection model of obliquely incidence and its reflection result comparing with PO having same surface are showed in Fig. 2(b).

3. DOUBLE REFLECTORS QUASI-OPTICAL SYSTEM

3.1. System Design

We set up a set of quasi-optical reflector system made up of two parabolic surfaces, working at the frequency of 30 GHz. The geometry model of the double reflectors system is showed in Fig. 3.

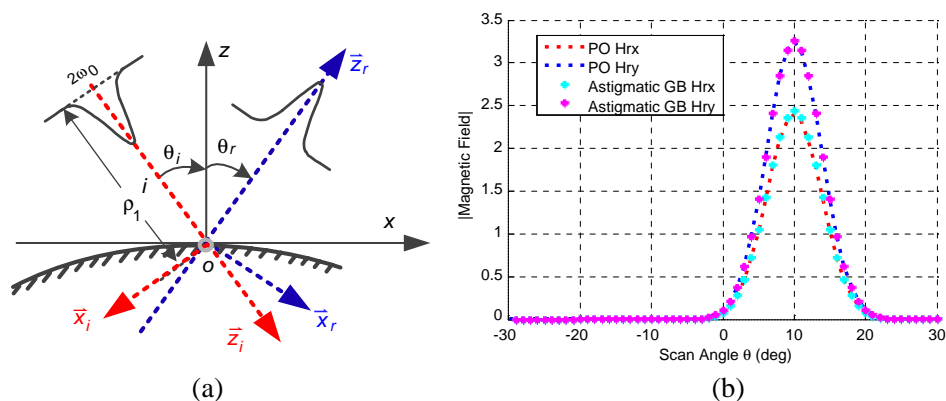


Figure 2: (a) The model of GB reflection from a curved surface, which will decide Q matrix. (b) A single astigmatic GB obliquely incident angle equal to 10 degree on the reflector point, and reflected field is scanned comparing between PO and astigmatic GB method.

The feed is placed on the focus of the first reflection mirror. The size of two parabolic mirrors is equal to 2 times of surface parameters Rim_1 and Rim_2 respectively. The field from feed is defined through the near-field pattern and is expanded at a plane with the distance D from phase center of feed. Two origins of output-field observation coordinate system are placed at specular reflection point where center beam intersects with the mirror respectively. In this coordinate system, the positive z -direction is created along the propagation direction of the reflected beam and the near-field scanning distance of two surfaces is ND_1 and ND_2 respectively.

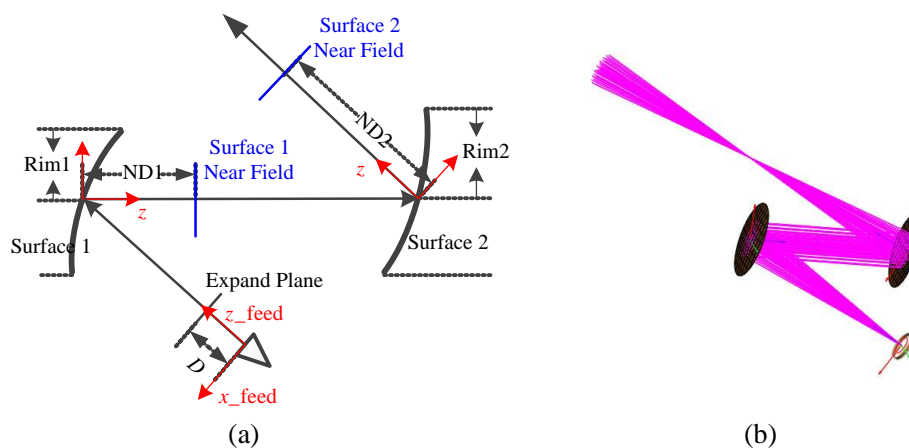


Figure 3: (a) Geometry of the double quasi-optical reflectors system. (b) 3D view of geometric model of double quasi-optical reflectors system is set up in the GRASP simulation software.

3.2. Simulation Validation

The Gaussian feed is radiating from the focus of first parabolic mirror, which is same of two being quite equal to 1 meters, working at 30 GHz along the feed positive z -axis. The expanded GB field consecutively goes through two parabolic mirrors. Location and mirror parameters are as follows:

- A. The rotation angle of feed around the y axis of global coordinate system is 150 degree and the distance from expand plane to phase center of feed is $D = 0.29$ m. Near-field pattern of feed being expanded into sets of sub-GBs using Gabor frame expansion method and its recovered field pattern after propagation distance 0.5 m are showed in Fig. 4(a). There are 3897 GBs in total counted in expanded plane.
- B. The radius of reflector surface 1 is $Rim_1 = 4 * \omega = 0.338$ m and near-field scanning distance $ND_1 = 0.5$ m. This ω is waist size of center beam on the mirror reflection point of surface 1, and the initial GB waist size is $\omega_0 = 0.05$ m. The near-field scanning result of surface 1 is showed in Fig. 4(b). There are 1137 GBs counted on reflector 1.

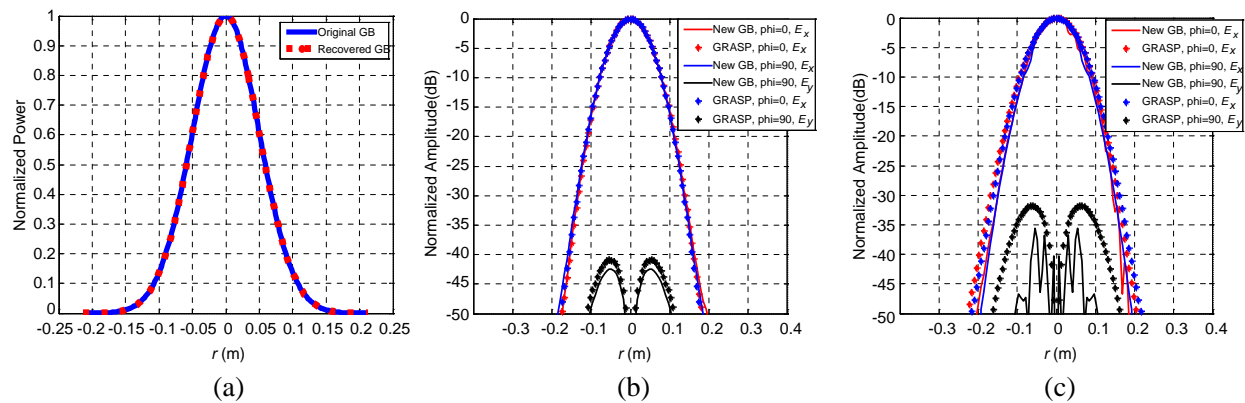


Figure 4: (a) Near-field pattern of feed (solid line) and its recovered field pattern (dotted line) after propagation distance 0.5 m. (b) Near-field scanning reflected after surface 1. (c) Near-field scanning reflected after surface 2.

C. The radius of reflector surface 2 is $Rim_2 = 0.338$ m and near-field scanning distance $ND_2 = 1.5$ m. The distance from center of surface 1 to surface 2 is 1.874 m. The near-field scanning result of surface 2 is showed in Fig. 4(c). There are 839 GBs counted on reflector 2.

4. CONCLUSION

A fast GB tracing method for quasi-optical system of two parabolic surfaces based on Gabor frame expansion technique at the frequency of 30 GHz has been presented.

Two reflection mirrors having different number of GBs respectively, meanwhile contrasting near-field scanning, reveal that GBs are paraxial transmission wave equation and energy of emergent is mainly up to the number of GBs in the center of optical axis. Gabor frame expansion coefficients are time-dependent, which result in calculating separately for each frequency. Astigmatic GB equation can characterize the transformation of the GB reflection, and obtaining reflection field formula only calculates Q matrix according to the incident field.

Near-field scanning results of main polarization and cross polarization in $\phi = 0$ degree and $\phi = 90$ degree are also matched up to -50 dB below peak value, which demonstrate the correctness of the algorithm, including Gabor frame expansion and tracking by astigmatic GB techniques. The accuracy of the method is connected with the distance of expanded plane and the number of GBs. Selecting parameters reasonably can achieve good trade-off between the accuracy and the computational effort.

ACKNOWLEDGMENT

This work was supported by the CAEP THz Science and Technology Foundation under the Grant No. CAEP THZ201210.

REFERENCES

- Hillairet, J., J. Sokoloff, et al., "Analytical physical optics scattering from a PEC finite plate illuminated by a vector gaussian beam," *Electromagnetics in Advanced Applications*, 283–286, Sep. 2007.
- Goldsmith, P. F., "Quasi-optical techniques," *IEE Proc.* Vol. 80, No. 11, 1729–1747, Nov. 1992.
- Hristos, T. A. and H. P. Prabhakar, "Closed form solution for three-dimensional reflection of an arbitrary Gaussian beam by a smooth surface," *Radio Science*, Vol. 37, No. 2, Apr. 2002.
- Casaletti, M., S. Skokic, S. Maci, and S. Sørensen, "Beam expansion in multi-reflector quasi-optical systems," *Antennas and Propagation of Fourth European Conference*, 1–4, Apr. 2010.
- Deschamps, G. A., "Ray techniques in electromagnetics," *IEE Proc.*, Vol. 60, No. 9, 1022–1035, Sep. 1972.
- Chou, H.-T. and H. P. Prabhakar, "Uniform asymptotic solution for electromagnetic reflection and diffraction of an arbitrary Gaussian beam by a smooth surface," *Radio Science*, Vol. 32, No. 4, 1319–1336, Jul. 1997.
- Lugara, D., C. Letrou, A. Shlivinski, E. Heyman, and A. Boag, "Frame-based Gaussian beam summation method: Theory and applications," *Radio Science*, Vol. 38, No. 2, Apr. 2003.

8. Bastiaans, M. J., “Gabor’s expansion of a signal into Gaussian elementary signals,” *IEE Proc.*, Vol. 68, No. 4, 538–539, Apr. 1980.
9. Feichtinger, H. G. and T. Strohmer, *Gabor Analysis and Algorithms: Theory and Applications*, Springer-Verlag, 1997.
10. Evgenia, K., W. Gudrun, S. Dennis, et al., “Modeling of the general astigmatic Gaussian beam and its propagation through 3D optical systems,” *Applied Optics*, Vol. 52, No. 24, 6030–6040, 2013.

Imaging Dielectric Objects by Limited Diversity of Scattering Data

C. X. Yang, R. P. Chen, Y. J. Zhang, C. N. Xu, S. C. Yan, and M. S. Tong

Department of Electronic Science and Technology, Tongji University
4800 Cao'an Road, Shanghai 201804, China

Abstract— In the reconstruction of dielectric objects by integral equation approach (IEA), the forward scattering integral equation (FSIE) and the inverse scattering integral equation (ISIE) are alternatively solved in the frame of distorted Born iterative method (DBIM) or its variations. In this work, we consider the reconstruction under a limited observation which is more practical. We use a DBIM-like Gauss-Newton minimization approach (GNMA) incorporated with a multiplicative regularization method (MRM) and a line search method (LSM) to solve the ISIE and the inversion quality of scattering data can be enhanced. The numerical example for reconstructing a two-dimensional (2D) dielectric object is presented to illustrate the inversion approach.

1. INTRODUCTION

Solving inverse scattering problems is challenging because the involved governing equations are nonlinear and the solutions are inherently nonunique [1]. This is particularly true when measuring conditions are unfavorable and diverse scattering data are not available. Usually, the inverse problems are solved by linearizing governing equations and gradually minimizing the mismatch between calculated data and measured data in an iterative scheme. In the integral equation approach (IEA) for reconstructing dielectric objects, there are forward scattering integral equation (FSIE) and inverse scattering integral equation (ISIE) and we need to alternatively solve them in the context of Born iterative method (BIM) [2] or distorted Born iterative method (DBIM) [3] although other methods can also be used [4]. The solution of permittivity from the ISIE can reveal the profile of unknown object in the imaging domain.

The ISIE is insolvable by direct inversion because the matrix equation is inherently ill-posed and the diversity of measured data with noise contamination is usually limited. One has to transform the inversion of measured data into an optimization problem and the best solution is chosen by minimizing a cost functional. The optimization problem can be solved by different approaches and we apply the DBIM-like Gauss-Newton minimization approach (GNMA) in this work [5] since it can be conveniently incorporated with the multiplicative regularization method (MRM) [6] and line search method (LSM) [7] to enhance the inversion quality. The MRM was proposed for gradient-type algorithms and was used for the inversion by the finite difference time domain (FDTD) approach [8], but we use it for the IEA in this work. The MRM can adaptively vary the regularization parameter as the iteration proceeds so it is unnecessary to perform a large number of numerical experiments for choosing the regularization parameter. We also incorporate the LSM which can optimize the search of step size in each iteration and accelerate the convergence of inversion process. The use of MRM and LSM is essential when we consider the reconstruction with a poor measurement condition which may be encountered in many applications [9]. A numerical example for reconstructing a two-dimensional (2D) dielectric object with a limited view is presented to illustrate the approach.

2. GOVERNING EQUATIONS

In the IEA, reconstructing an unknown dielectric object is to determine its profile and material property by solving the ISIE and FSIE alternatively in the context of the DBIM or its variations. We only consider the simplified 2D cases in this work and the generalized 3D cases will be addressed in our future work. The ISIE and FSIE in the 2D case with a TM_z incident wave can be written as [1]

$$E_z^{sca}(\boldsymbol{\rho}) = \int_S g(\boldsymbol{\rho}, \boldsymbol{\rho}'; k_b) \cdot \Delta k(\boldsymbol{\rho}') E_z(\boldsymbol{\rho}') dS' \quad (1)$$

$$E_z(\boldsymbol{\rho}) = E_z^{inc}(\boldsymbol{\rho}) + \int_S g(\boldsymbol{\rho}, \boldsymbol{\rho}'; k_b) \cdot \Delta k(\boldsymbol{\rho}') E_z(\boldsymbol{\rho}') dS' \quad (2)$$

respectively. In the above, $\boldsymbol{\rho}$ is the position vector of an observation point, $\boldsymbol{\rho}'$ is the position vector of a source point, E_z^{inc} is the incident electric field, E_z^{sca} is the scattered electric field obtained by

measurement, and E_z is the total electric field inside the imaging domain S . The imaging domain enclosing the unknown object is in the xy plane. Also,

$$\Delta k(\boldsymbol{\rho}') = k^2(\boldsymbol{\rho}') - k_b^2 = k_b^2[\varepsilon_r(\boldsymbol{\rho}') - 1] \quad (3)$$

is the contrast or difference between the squared wavenumber k^2 of the imaging domain and the squared wavenumber k_b^2 of the background. The contrast can determine the distribution of permittivity inside the imaging domain when its material is assumed to be nonmagnetic. In addition,

$$g(\boldsymbol{\rho}, \boldsymbol{\rho}'; k_b) = \frac{i}{4} H_0^{(1)}(k_b |\boldsymbol{\rho} - \boldsymbol{\rho}'|) \quad (4)$$

is the 2D Green's function in which $H_0^{(1)}$ is the first kind of Hankel function with the zeroth order. The above FSIE can be easily solved and we do not address it here.

3. GAUSS-NEWTON MINIMIZATION APPROACH FOR SOLVING THE ISIE

To solve the ISIE by the GNMA, we transform the inversion of model parameters into an optimization problem in which the following cost functional $F(\mathbf{x})$ is minimized [5]

$$F(\mathbf{x}) = \frac{1}{2} \left\{ \gamma \left[\|\bar{\mathbf{V}}_d \cdot \mathbf{e}(\mathbf{x})\|^2 - \delta^2 \right] + \|\bar{\mathbf{V}}_m \cdot (\mathbf{x} - \mathbf{x}_q)\|^2 \right\} \quad (5)$$

where \mathbf{x} is a vector describing the model parameters such as the distribution of permittivity in the imaging domain and $\mathbf{e}(\mathbf{x})$ is the error vector reflecting the mismatch between the predicted or calculated data (scattered electric field) and the measured data. Also, γ is a Lagrange multiplier whose inverse is the regularization parameter, δ is *a priori* estimate of noise in the measured data, $\bar{\mathbf{V}}_m^T \cdot \bar{\mathbf{V}}_m$ is the inverse of the model covariance matrix representing the degree of confidence in the prescribed model parameters \mathbf{x}_q , and $\bar{\mathbf{V}}_d^T \cdot \bar{\mathbf{V}}_d$ is the inverse of the data covariance matrix describing the estimated uncertainty due to the noise contamination in the measured data. The above cost functional can be minimized with the GNMA whose details can be found in [5]. In the GNMA, we have employed the MRM to select the regularization parameter which is the inverse of Lagrange multiplier γ . The MRM can adaptively vary γ as the iteration proceeds so that a large number of numerical experiments for selecting the parameter can be avoided. The MRM treats the regularization as a multiplicative factor in the cost functional and therefore the regularization parameter is set to be proportional to the original or non-regularized cost functional, i.e.,

$$\frac{1}{\gamma} = \frac{1}{2\eta^2} \|\bar{\mathbf{V}}_d \cdot \mathbf{e}(\mathbf{x})\|^2 \quad (6)$$

where η is a constant parameter determined by numerical experiments. Note that the reconstructed results are much more insensitive to η than to γ and η can be fixed in all simulations for one type of measured data [5]. To accelerate the reconstruction, we can use a line search method (LSM) [7] to optimize the step size. The LSM searches a real positive factor ζ_k along the search direction \mathbf{b}_k so that the new step is changed into $\mathbf{x}_{k+1} = \mathbf{x}_k + \zeta_k \mathbf{b}_k$ which can result in a sufficient reduction for the cost functional.

4. NUMERICAL EXAMPLE

To validate the inversion approach, we consider the reconstruction for two 2D dielectric circular cylinders which are contacting and identical in a $1.4\lambda \times 1.4\lambda$ imaging domain where λ is the wavelength in free space. Each cylinder has a radius $a = 0.3\lambda$ and a homogeneous relative permittivity $\varepsilon_r = 4.5$. Unlike the widely-adopted experimental setup of Institut Fresnel which allows a full view to the reconstructed object [10], we consider a limited view with less diverse measurement data in this work. We use 10 TM_z incident waves from the transmitter located along the line on a plane above the imaging domain to illuminate the object and the frequency is $f = 3.0$ GHz. The vertical distance between the line and the center of imaging domain is 20λ and the spacing between two neighboring transmitting positions is 0.5λ . We take 50 observation positions which are equally distributed along the same line to measure the scattered electric field (the measured data is replaced with the calculated data in simulations). Due to the lack of *a priori* information, we choose $\delta = 0$ and $\bar{\mathbf{V}}_d = \bar{\mathbf{V}}_m = \bar{\mathbf{I}}$. Figure 1(a) shows the reconstructed permittivity by the Born iterative method

(BIM) at the 40th step while Figure 1(b) and Figure 1(c) show the results by the GNMA at the 30th step and the 40th step, respectively. It can be seen that the GNMA images resemble the original distribution as shown in Figure 1(d) whereas the BIM cannot give a convergent result. Note that the discontinuity of the original distribution can only be reconstructed by using certain edge-preserving technique [5].

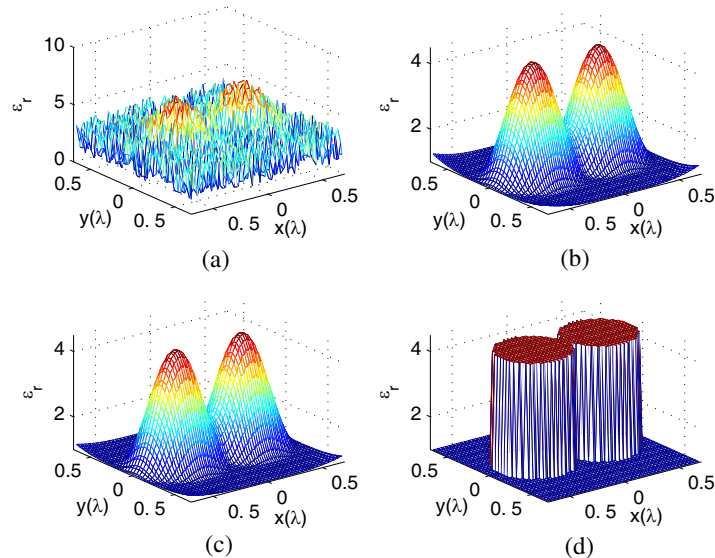


Figure 1: Reconstruction of permittivity for two 2D dielectric circular cylinders which are contacting and identical. Each cylinder has a radius $a = 0.3\lambda$ and a relative permittivity $\epsilon_r = 4.5$. (a) BIM at the 40th step. (b) GNMA at the 30th step. (c) GNMA at the 40th step. (d) Original distribution.

5. CONCLUSION

Obtaining diverse scattering data could be difficult due to unfavorable measurement conditions in practice. In this work, we consider the inversion of scattering data under a limited observation and employ the GNMA to minimize the cost functional by the IEA. The scheme incorporates the MRM to adaptively select the regularization parameter and the LSM to optimize the step size or search direction. The MRM can avoid a large number of numerical experiments in the selection of regularization parameter while the LSM can accelerate the convergence of inversion process. A numerical example for reconstructing 2D dielectric objects has been presented to demonstrate the inversion approach and good result can be observed.

ACKNOWLEDGMENT

This work was supported by the National Natural Science Foundation of China with the Project No. 61271097.

REFERENCES

1. Chew, W. C., *Waves and Fields in Inhomogeneous Media*, IEEE Press, New York, 1995.
2. Wang, Y. M. and W. C. Chew, "An iterative solution of two-dimensional electromagnetic inverse scattering problem," *Int. J. Imag. Syst. Technol.*, Vol. 1, No. 1, 100–108, 1989.
3. Chew, W. C. and Y. M. Wang, "Reconstruction of two-dimensional permittivity distribution using the distorted Born iterative method," *IEEE Trans. Med. Imag.*, Vol. 9, No. 2, 218–225, 1990.
4. Van den Berg, P. M. and R. E. Kleinman, "A contrast source inversion method," *Inverse Problems*, Vol. 13, 1607–1620, 1997.
5. Habashy, T. M. and A. Abubakar, "A general framework for constraint minimization for the inversion of electromagnetic measurements," *Progress In Electromagnetics Research*, Vol. 46, 265–312, 2004.

6. Van den Berg, P. M., A. Abubakar, and J. T. Fokkema, “Multiplicative regularization for contrast profile inversion,” *Radio Science*, Vol. 38, No. 2, 23.1–23.10, 2003.
7. Nocedal, J. and S. J. Wright, *Numerical Optimization*, Springer, New York, 1999.
8. Abubakar, A., P. M. van den Berg, and S. Y. Semenov, “Two- and three-dimensional algorithms for microwave imaging and inverse scattering,” *Journal of Electromagnetic Waves and Applications*, Vol. 17, No. 2, 209–231, 2003.
9. Steinberg, B. D. and H. M. Subbaram, *Microwave Imaging Technoques*, John Wiley & Sons, New York, 1991.
10. Geffrin, J. M. and P. Sabouroux, “Continuing with the Fresnel database: Experimental setup and improvements in 3D scattering measurements,” *Inverse Problems*, Vol. 25, 1–18, 2009.

Time Reversal Imaging Using Minimum Norm Iterative Type Partial Noise Subspace Method

Qiang Gao, Wei Gao, Xiao-Hua Wang, and Bing-Zhong Wang

School of Physical Electronics, University of Electronic Science and Technology of China
No. 4, Section 2, North Jianshe Road, Chengdu 610054, China

Abstract— Orthogonality between signal subspace and noise subspace is employed to time reversal (TR) imaging. Part of the noise subspaces are used to get a projection with the signal subspace to estimating the location of targets. The proposed method is similar to the minimum norm method in form. Several numerical simulations show that the proposed method can get the exact locations of the targets with less computing resources than the conventional multiple signal classification (MUSIC) method.

1. INTRODUCTION

Orthogonality between the signal subspace and noise subspace is the foundation of the time reversal operator (TRO) based imaging techniques. The decomposition of time reversal operator (DORT) method [1] and time reversal multiple signal classification (TR-MUSIC) method [2] are the well-known two types of TRO-based imaging algorithm which are widely used in optics and electromagnetics. The TRO-based methods have better performance than the traditional time reversal wave back propagation method, which benefits from the spatial and temporal focusing properties of the time reversal waves. Time reversal imaging techniques have many applications, such as detection for buried objects, ultrasonic nondestructive testing, medical imaging [3–6], etc.. In the direction-of-arrival (DOA) estimation, the whole noise subspaces are used in the well-known MUSIC method [7], while in the minimum norm method, only one vector is used to save the computing resource [8, 9]. By analyzing the mean square error of MUSIC method and minimum norm method, the results show that the relative performance of MUSIC method and the minimum norm method depends on the ratio of their parameter sensitivities [10].

In this paper, a minimum norm iterative type partial noise subspace imaging method is proposed to estimate the locations of targets in free space. Compared with the TR-MUSIC method by using all noise subspace vectors, the imaging precision of the minimum norm method has declined in a certain degree. To solve this problem, an iterative process is introduced. The proposed method avoids the difficulty of distinguishing the signal subspace with noise subspace while providing stable imaging of the targets. In multiple scattering case, the singular value decomposition of the MSR matrix is employed to generate the signal subspace vectors (signal vectors) and noise subspace vectors (noise vectors). Actually, the tow subspaces do not need to be divided. Finally, similar to the minimum norm type method, the single noise vector in noise-well case and the partial noise subspace (bottom noise vectors) in high-level noise case are used to compute the imaging pseudo-spectrum, respectively.

2. PARTIAL NOISE SUBSPACE METHOD

Assume an analytical imaging model consist of N acoustic or electromagnetic wave transceivers (located at α_n , $n = 1, 2, \dots, N$) and M point-like scatters (located at \mathbf{x}_m , $m = 1, 2, \dots, M$) in free space. While \mathbf{r} represents an arbitrary point in space, the total field Ψ_k , composed of the incident field Ψ_k^{in} and scatter field Ψ_k^{sca} , generated by the k th ($k \leq N$) transmitters at \mathbf{r} and \mathbf{x}_m can be expressed as follows:

$$\psi_k(\mathbf{r}, \omega) = \psi_k(\mathbf{r}, \omega)^{in} + \psi_k(\mathbf{r}, \omega)^{sca} \quad (1)$$

$$\psi_k(\mathbf{x}_m, \omega) = \psi_k(\mathbf{x}_m, \omega)^{in} + \psi_k(\mathbf{x}_m, \omega)^{sca} \quad (2)$$

Under the assumption of point scatters and receivers, the MSR matrix K under multiple scattering case can be given as:

$$K = G_0(\alpha_j, \mathbf{x}_m) \tau_m H^{-1} G_0(\mathbf{x}_m, \alpha_k) \quad (3)$$

where

$$H_{m,m'} = \delta_{m,m'} - (1 - \delta_{m,m'}) G_0(\mathbf{x}_m, \mathbf{x}'_m) \quad (4)$$

$G_0(\mathbf{r}, \mathbf{r}', \omega)$ is the free space Green function and δ is the Kronecker delta function. Considering the singular value decomposition (SVD) of K , the following equations can be gotten:

$$\mathbf{K} \cdot \mathbf{v}_j = \sigma_j \mathbf{u}_j \quad (5a)$$

$$\mathbf{K}^H \cdot \mathbf{u}_j = \sigma_j \mathbf{v}_j, \quad (5b)$$

where σ_j is the j th singular value, \mathbf{u}_j and \mathbf{v}_j denote the j th column singular vectors of the unitary matrices \mathbf{U} and \mathbf{V} , respectively. The detailed process of above is shown in [11]. In the processes of traditional TR-MUSIC method, the matrices \mathbf{U} and \mathbf{V} will be divided into signal subspace and noise subspace, which are spanned by the singular vectors corresponding to the nonzero and zero singular values. In the proposed method, the difficult dividing operation is omitted benefitting from the orthogonality between signal and noise subspaces. Obviously, the matrices \mathbf{U} and \mathbf{V} span the same space in echo-mode. For simplicity, echo-mode with matrix \mathbf{V} is illustrated in the rest of this paper.

For homogeneous and isotropic media, the signal subspace also spanned by the conjugation of Green function $g_0^*(\mathbf{x})$ vector, where

$$g_0(\mathbf{x}) = [G_0(\mathbf{x}, \alpha_1, \omega), G_0(\mathbf{x}, \alpha_2, \omega), \dots, G_0(\mathbf{x}, \alpha_N, \omega)]^T \quad (6)$$

is the background Green's function vector. Because of the existed orthogonality between signal subspace and noise subspace, the inner product of noise and signal vectors is zero in theory. The locations of the scatters can be determined by the pseudo-spectrum computed by any singular vector. In other words, the signal and noise subspaces do not need to be distinguished actually. The imaging pseudo-spectrum can be written as:

$$P_1(\mathbf{r}) = \frac{1}{|\langle v_{N-p+1}, g_0^*(\mathbf{r}) \rangle|^2}, \quad (7)$$

where p denotes the last p th singular vector. For more stable imaging in high-noise case, more bottom singular vectors can be used by an iterative strategy written as:

$$P_2(\mathbf{r}) = \frac{1}{\sum_{i=N-q+1}^N |\langle v_i, g_0^*(\mathbf{r}) \rangle|^2}, \quad (8)$$

where q denotes the bottom q th singular vectors. In the subsequent simulations, the proposed method is simulated in different level noise cases.

3. NUMERICAL VALIDATION AND EVALUATIONS

In this section, simulations of two targets ($M=2$) embedded in the free space in different SNRs are presented to show the performance of proposed method. The configuration of simulation model is set as Fig. 1(a). The targets are placed at $(1.5\lambda, 4.5\lambda, -6\lambda)$ and $(4.5\lambda, 1.5\lambda, -9\lambda)$ in the “ $6\lambda \times 6\lambda \times 6\lambda$ ” 3D cubic imaging domain. The operation frequency is set as 300 MHz and the imaging resolution is set as $\lambda/4$. All the imaging pseudo-spectrums are normalized as dB. The transmitters and receivers use the same array with the number $N = 32$ in echo-mode. The transceivers are distributed as a planar array located at the plane $z = 0$, the space between two adjacent transceivers is set as 1λ . The simulations are carried out on a PC with quad-core 3.5 GHz CPU and 4GB RAM, the programs are compiled by MATLAB 2012b.

When $SNR = 60$ dB, Fig. 1(b) shows the normalized singular values of the MSR matrix. Fig. 1(c) shows the imaging result in Eq. (13) with $p = 1$, which means that the last vector can get a good imaging of the targets. The proposed method employs only one noise vector while the conventional TR-MUSIC method employs N noise vectors (whole noise subspace). Thus, our method needs much less computing time and memory than TR-MUSIC method.

Figures 2(a)–(c) present the imaging results of Eq. (13) with $SNR = 35$ dB for $p = 1, 2, 3$, respectively. All the three vectors can get the accurate locations of the targets independently. Figs. 2(d)–(f) is the results with $SNR = 25$ dB while the vectors is the same as (a)–(c). In the high-level noise cases, a single noise vector is not enough to get a clear imaging. While the noise is getting high, the imaging performance is getting worse. Then Eq. (14) is employed to get a

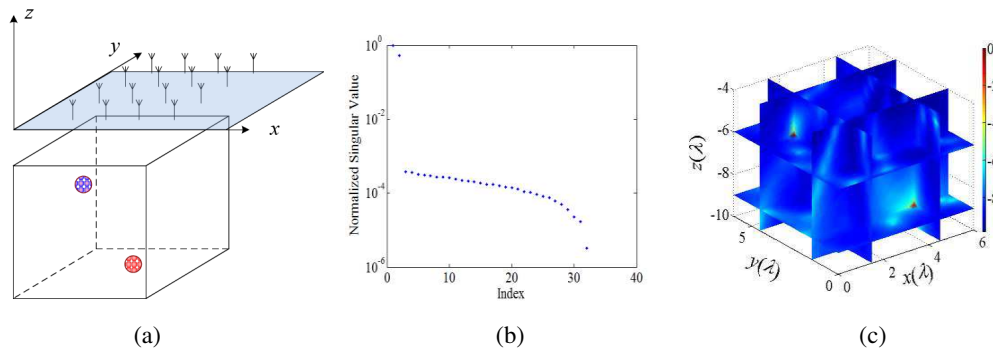


Figure 1: Three-Dimension imaging results with $SNR = 60$ dB. (a) Configuration of 3D imaging. (b) Normalized singular values of the MSR matrix K . (c) The imaging pseudo-spectrum of the proposed method with $p = 1$.

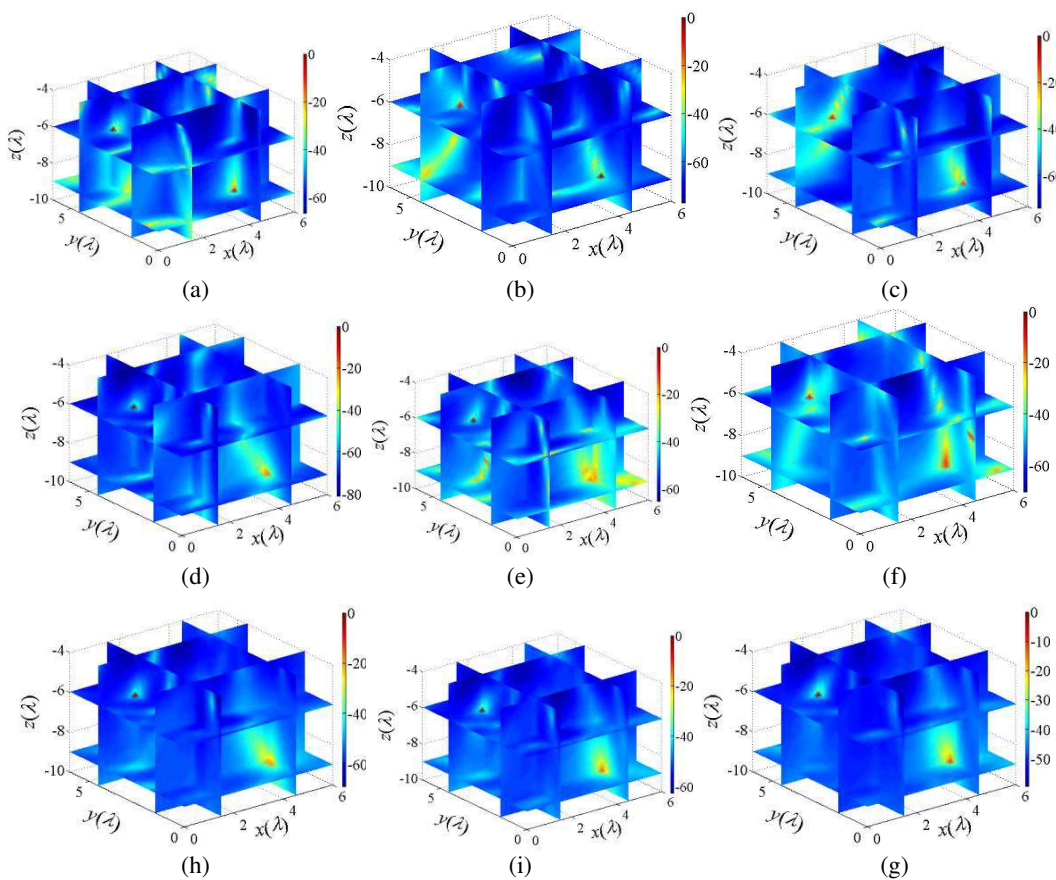


Figure 2: Images obtained using single vector method and partial noise subspace method. (a) The last noise vector ($p = 1$) with $SNR = 35$ dB. (b) The penultimate noise vector ($p = 2$) with $SNR = 35$ dB. (c) The 3rd last noise vector ($p = 3$) with $SNR = 35$ dB. (d) The last noise vector ($p = 1$) with $SNR = 25$ dB. (e) The penultimate noise vector ($p = 2$) with $SNR = 25$ dB. (f) The 3rd last noise vector ($p = 3$) with $SNR = 25$ dB. (g) The bottom two noise vector ($q = 2$) with $SNR = 25$ dB. (h) The bottom three noise vector ($q = 3$) with $SNR = 25$ dB. (i) The bottom four noise vector ($q = 4$) with $SNR = 25$ dB.

better imaging in such cases. Figs. 2 (g)–(i) show the results with $SNR = 25$ dB while $q = 2, 3, 4$, respectively. It is shown that while q is getting larger, the imaging performance is becoming better. Thus, in the noise-well case, Eq. (13) can be used as the imaging pseudo-spectrum to save computing resources. Whereas, in the high-level noise case, Eq. (14) can be an alternative method to get better imaging while costing relatively more computing resources than Eq. (13). Obviously, all these two methods employ less singular vectors than the TR-MUSIC method, so the proposed

method is suited for the fast target imaging and detection.

4. CONCLUSION

In multiple scattering case, the minimum norm iterative type partial noise subspace method is developed for target imaging. The proposed method provides stable imaging and reduces the computing resources than the TR-MUSIC method, while avoiding the cutoff between signal and noise subspaces without the loss of imaging precision. The partial noise subspace method can replace the TR-MUSIC method in many cases without any loss. It is a good method for fast detection and imaging of targets.

ACKNOWLEDGMENT

The author thanks the support by the National Natural Science Foundation of China (61301271), the Specialized Research Fund for the Doctoral Program of Higher Education of China under Grant 20120185130001, 20110185120008, and the Fundamental Research Funds for the Central Universities under Grant ZYGX2012J043.

REFERENCES

1. Prada, C. and M. Fink, "Eigenmodes of the time reversal operator: A solution to selective focusing in multiple-target media," *Wave Motion*, Vol. 20, No. 2, 151–163, Sept. 1994.
2. Devaney, A. J., E. A. Marengo, and F. K. Gruber, "Time-reversal-based imaging and inverse scattering of multiply scattering point targets," *Journal of the Acoustical Society of America*, Vol. 118, No. 5, 3129–3138, Nov. 2005.
3. Prada, C., S. Manneville, D. Spoliensky, and M. Fink, "Decomposition of the time reversal operator: Detection and selective focusing on two scatterers," *Journal of the Acoustical Society of America*, Vol. 99, No. 4, 2067–2076, Apr. 1996.
4. Micolau, G., M. Saillard, and P. Borderies, "DORT method as applied to ultrawideband signals for detection of buried objects," *IEEE Trans. Geosc. and Remote Sensing*, Vol. 41, No. 8, 1813–1820, Aug. 2003.
5. Kerbrat, E., C. Prada, D. Cassereau, and M. Fink, "Ultrasonic nondestructive testing of scattering media using the decomposition of the time-reversal operator," *IEEE Trans. Ultrasonics Ferroelectrics and Frequency Control*, Vol. 49, No. 8, 1103–1113, Aug. 2002.
6. Robert, J.-L. and M. Fink, "Green's function estimation in speckle using the decomposition of the time reversal operator: Application to aberration correction in medical imaging," *Journal of the Acoustical Society of America*, Vol. 123, No. 2, 866–877, Feb. 2008.
7. Schmidt, R., "Multiple emitter location and signal parameter estimation," *IEEE Trans. Antennas Propag.*, Vol. 34, No. 3, 276–280, Mar. 1986.
8. Kumaresan, R. and D. W. Tufts, "Estimating the angles of arrival of multiple plane waves," *IEEE Trans. Aerosp. and Electronic Syst.*, Vol. 19, No. 1, 134–139, Jan. 1983.
9. Rao, B. D. and K. V. S. Hari, "Statistical performance analysis of the minimum-norm method," *IEEE Pro.*, Pt. F, Vol. 136, 125–134, Jun. 1989
10. Ermolaev, V. T. and A. B. Gershman, "Fast algorithm for minimum-norm direction-of-arrival estimation," *IEEE Trans. Signal Processing*, Vol. 42, No. 9, 2389–2394, Sep. 1994.
11. Gao, W., X.-H. Wang, and B.-Z. Wang, "Time reversal ESPRIT method for the detection of single target," *Journal of Electromagnetic Waves and Applications*, Vol. 28, No. 5, 634–640, Mar. 2014.

A Microwave Radiation Interferometry Method Based on Adaptive Super-sparse Sampling

Suhua Chen, Lu Zhu, and Yuanyuan Liu

School of Information Engineering, East China Jiaotong University, Nanchang 330013, China

Abstract— The Interferometry Synthetic Aperture Imaging Radiometers (SAIRs) is to sample visibility function based on the Nyquist theory of space interferometry measurement, which do not need the mechanical scanning and can directly image. Due to the complex structure of the imaging system and low imaging resolution, the SAIRs practical application is limited seriously. According to the characteristic of the image is sparse or can be sparse representation in transform domain, the Compressed Sensing (CS) can project the high-dimensional signal to low-dimensional space, so the quantity of the projection measurement data is far less than that by the Nyquist sampling method. Also the microwave radiation interferometry conducted in the frequency domain, which has the characteristics of low frequency information less and high frequency information richer, and the distribution of them is centralized; at the same time, the microwave radiation image itself have the specialty of the gradient sparsity and the local smoothness, it can be sparse representation in differential domain. On the basis of the priori information about the observation and the sparse domain, we establish the incoherent optimization model between the observation matrix and the sparse matrix according to the principle of the two matrixes satisfying the irrelevant in the CS. Using the incoherent optimization model, we can adaptively obtain the spatial measurement with different probability, to realize super sparse interferometry. The adaptive super-sparse sampling method can overcome the disadvantage of equal probability of the Fourier random sampling methods. In order to reconstruct the microwave radiation image, we establish the imaging model based on total variation regularization constraint, and use the alternating iterative algorithm to realize the reconstruction. The simulation and experiment results show that it is fast to reconstruct microwave radiation image with the adaptive super-sparse sampling method, and it can greatly improve the quality of the microwave radiation image in the case of the same sampling rate.

1. INTRODUCTION

Synthetic Aperture Imaging Radiometers (SAIRs) [1] was suggested in the 1980s as an alternative to real aperture radiometry for the observation at low microwave frequencies with high spatial resolution. Instead of the traditional radiometer to directly measure in the spatial domain, SAIRs measurement does not need mechanical scanning, and can imaging by inverted the interference measurements. However, the practical application of microwave radiometric imaging system will be limited by the complexity and low resolution of the structure. The key to solve these disadvantages is reducing the data quantity of the measurement.

According to the principle of microwave radiation and synthetic aperture interferometry [2], the visibility function V and the modified brightness temperature T is related by a Fourier transform for an ideal interferometer:

$$V(u, v) \propto \iint_{\xi^2 + \eta^2 < 1} \frac{T(\xi, \eta)}{\sqrt{1 - \xi^2 - \eta^2}} F_k(\xi, \eta) F_j^*(\xi, \eta) R\left(-\frac{u\xi + v\eta}{f_0}\right) e^{-j2\pi(u\xi + v\eta)} d\xi d\eta \quad (1)$$

where $F_{k,j}$ is the normalized voltage antenna pattern, f_0 is the center frequency, R is the eliminated stripe function, (ξ, η) represents the direction cosine, and (u, v) is the baseline coordinates of the wavelength normalized. The space frequency can be discretization on the basis of (1), and then the microwave radiation interferometry model is represented by the following form:

$$V = F_{\wedge} T + e \quad (2)$$

Let $T \in R^{N \times N}$ is 2-D image, and $V \in R^{M \times 1}$ is the measurement vector. Where $F_{\wedge} \in R^{M \times N}$ is the sparse interferometry operator and e is the noise of receiver. In the ideal measurement condition, F_{\wedge} is the random sampling of Fourier frequency component. However in most cases, the number of salient features hidden in brightness temperature T is much fewer than its resolution according to the Compressed Sensing (CS) theory [3–5], so $M \ll N$. That means that the brightness

temperature distribution T is sparse or compressible under a suitable basis. Let $\Psi \in C^{N \times N}$ be an orthonormal basis, and then T can be represented by the following form:

$$T = \Psi x \quad (3)$$

The vector x contains k nonzero and T is K -sparse under Ψ . Due to the fact that the T possess the sparsity in wavelet domain and horizontal and vertical difference domain, so Ψ can be represent the wavelet basis, the vertical difference basis, or the horizontal difference basis. Then the (2) can be written as:

$$V = F_{\wedge} \Psi x + e \quad (4)$$

Let $F \in R^{N \times N}$ represent the 2-D discrete Fourier transform matrix and F_{\wedge} is the part Fourier transform matrix which select M rows from F . In most situations, the selection is simply random; it is rarely consider the structure information of measurement.

In order to reduce the data quantity, the variable density compressed image sampling method has been proposed [6, 7]. This approach is rely on the mutual coherence between sparse basis and sensing basis, the smaller the mutual coherence the less the required number of measurements for exact recovery. However this method is just for the theoretical analysis, it is suitable for the 1-D signal. Michael Lustig [8] pointed that the energy of magnetic resonance imaging (MRI) signals is usually concentrated at low spatial frequencies, thus they propose to select Fourier basis vectors according to a variable density sampling profile selecting more low frequencies than high frequencies. However in [8], the variable density sampling approach is only empirical.

On the basis of previous studies, and combined with the specialty of the distribution that low frequency and high frequency is centralized, we propose an adaptive super-sparse sampling (ASSp) method. It is based on the variable density sampling principle of 1-D signal, and transforms the 2-D image into two 1-D signal processing to realize the 2-D image sampling. According to this method, we give a optimal sampling profile based on the importance of the frequency for the whole image, that means that the sampling probability for the important information is larger than that for inconsequential information, and the data quantity for the reconstruction is much less than uniformly random sampling (URSp). Our method also gives a mathematical model which for the theoretical analysis.

2. THE ADAPTIVE SUPER-SPARSE SAMPLING

We know that if one want to sample more important frequency spectrums at the condition that the total sampling ratio is very low, the sampling probability of the vital spectrum needs to be high. The ASSp method will provide an optimal sampling profile according to the sampling probability of each spectrum, so as to realize adaptive sampling. In the following sections, we will focus on the introduction of ASSp.

Let $A = F\Psi \in R^{N \times N}$, and the 1-D signal $T \in R^N$ is S sparse on the basis Ψ . According to the (2), we need to select the sampling indices $\wedge = \{l_1, l_2, \dots, l_M\}$ randomly and independently according to a discrete probability measure P defined on $\{1, 2, \dots, N\}$. The incoherent optimization model can be defined as:

$$\mu(P) = \frac{1}{N^{1/2}} \max_{1 \leq i, j \leq N} \frac{|\langle F_i, \psi_j \rangle|}{P^{1/2}(i)} \quad (5)$$

where M needs to satisfy the following condition:

$$M \geq CN\mu^2(P)s \log^2(6N/\varepsilon) \quad (6)$$

In the (5), $\mu(P)$ is a function about P and stands for the mutual coherence between the measurement basis F and the sparse basis Ψ . The value depends on the probability measure P and satisfies $\mu(P) \geq N^{-1/2}$. Due to the fact that this model is just suitable for 1-D signal, we should transform the 2-D image into the form of 1-D signal in the setting of 2-D image sampling. Fortunately there is the following mathematical formula can achieve this transformation:

$$F(T) = WTW \quad (7)$$

where F is a 2-D discrete Fourier transform matrix, T is the original image and W is 1-D discrete Fourier transform matrix. So based on the mathematical formula, it is realizable to transform the 2-D Fourier transform into two 1-D Fourier transform, which are the horizontal direction transform

and the vertical direction transform. Then the image is sparse in these two directions respectively. For the wavelet basis, it is the same for these two direction sparsity. While for the difference basis, it is not in that case. Let Ψ_A be the vertical difference basis, and Ψ_B is the horizontal difference basis, the relationship of them is $\Psi_A = \Psi'_B$.

So for the 2-D image, the whole sampling can be seen as two sampling procedure, and it is need two functions about P based on (5), which one is $\mu(P_1)$, and the other is $\mu(P_2)$. Let $\mu(P_1)$ denote the vertical direction function about the vertical discrete probability measure P_1 , and $\mu(P_2)$ denote the horizontal direction function about the horizontal discrete probability measure P_2 . They can be denoted by the following form:

$$\mu(P_1) = \frac{1}{N^{1/2}} \max_{1 \leq i, j \leq N} \frac{|\langle W_i, \psi_{Aj} \rangle|}{P_2^{1/2}(i)} \quad (8)$$

$$\mu(P_2) = \frac{1}{N^{1/2}} \max_{1 \leq i, j \leq N} \frac{|\langle W_i, \psi_{Bj} \rangle|}{P_2^{1/2}(i)} \quad (9)$$

In practice, the choice of the optimized sampling profile P_1 and P_2 is difficult and should be adapted with the number of measurements M in order to obtain the best reconstruction qualities. In this paper, we try to solve this problem by convex optimization algorithms according to [7]. However, some frequencies are repeated sampled in the procedure. So in the final sampling profile, we need to modify the information and guarantee that every frequency is sampled once.

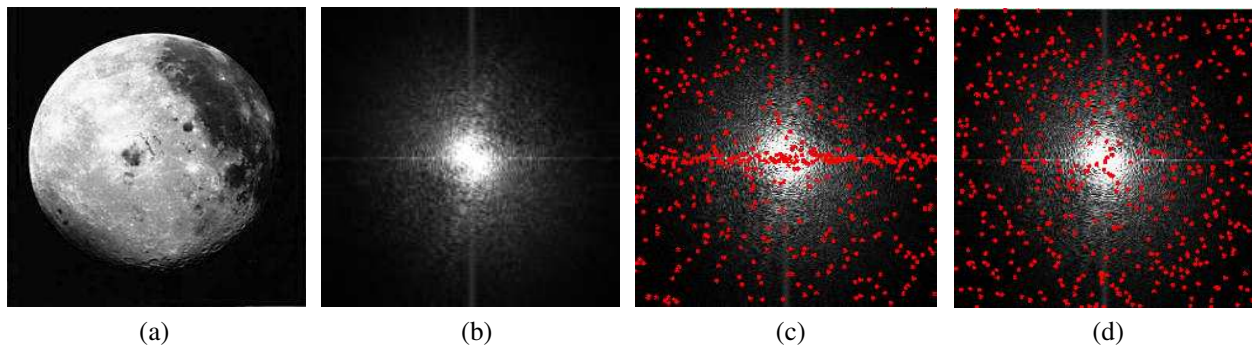


Figure 1: The spectrum analysis of the moon image. (a) The original image. (b) The frequency spectrum. (c) The sampling of ASSp. (d) The sampling of URSp.

For the ASSp, it can sample more important low frequencies than URSp effectively. An example of a moon image is shown in Figure 1(a). Figure 1(b) is the frequency spectrum of the moon. In order to exactly illustrate the comparison of these two sampling approaches, Figure 1 gives the sampling location in frequency domain at the sampling data is 512, and Figure 1(c) is the sampling of ASSp, Figure 1(d) is the sampling of URSp. We use the red point to denote the sampling location. Figure 1(c) shows that the ASSp can really sample more low information which located in the central position than URSp, and almost all the low frequencies could be got with the increase of sampling data. So in the ASSp, the sampling probability for low frequency is larger than that for high information, and our sampling method realize the adaptive sampling.

For the image reconstruction, considering the situations of microwave image itself is not only can be sparse in a wavelet base but also has the specialties of gradient sparsity and local smoothness, the use of difference base and wavelet base in regularization to exploit image sparsity and preserve edges. This paper refers the algorithm of RecPF in the [9], and adopts the Alternating Direction Algorithm (ADM) to achieve the correct result. By utilizing the separable structure of the variables, we gain the minimum value of the unknown parameters alternately at the each iteration, and then obtain the optimal reconstructed image after numerous iterations.

3. EXPERIMENTAL RESULTS

To test our proposed ASSp algorithm and compared it with URSp, a 256×256 moon temperature image is adopted, which is shown in the Figure 1(a). All experiments were performed under Windows XP and MATLAB R2008a running on a Acer laptop with an Intel Core i3 CPU at 2.4 GHz and 2 GB of memory. In the experiment, we simply set the maximum number of iterations

is 100, and the sampling rates (SR) are 10%, 20%, 40%, 50%, 60% and 80%. The specific parameters refer the [9]. All the results are the mean value of the code running 5 times.

The peak signal to noise ratio (PSNR) and the running time t are used to judge the quality of the reconstructed image. In our test, we adopt the Db1 wavelet basis and obtain the optimized sampling profile according to (8) and (9). The reconstructed images of two different sampling methods have been shown in the Figure 2.

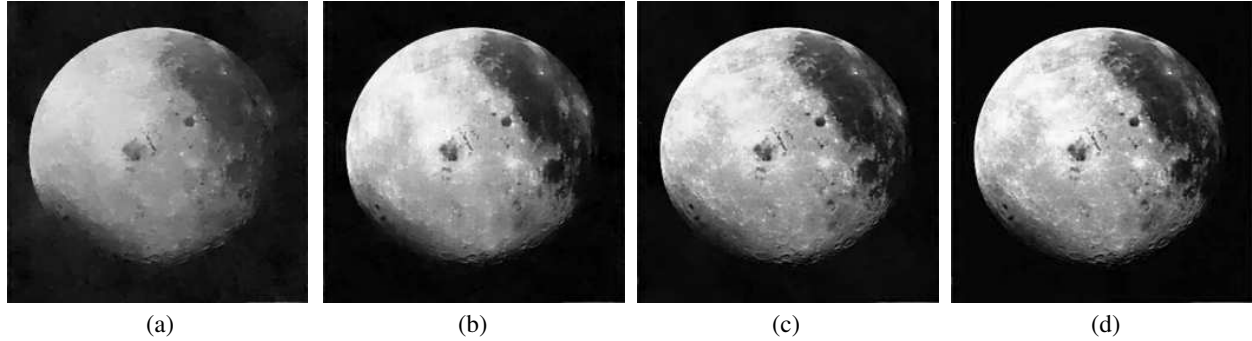


Figure 2: The reconstructed image of the two sampling method. (a) URSp SR = 20%. (b) ASSp SR = 20%. (c) URSp SR = 60%. (d) ASSp SR = 60%.

From the Figure 2, we can see from the visual perspective that the ASSp method could have better results than URSp at the same SR, whether it is 20% or 60%. That indicates the proposed ASSp method for the microwave radiation interferometry is effective. The superiority compared with URSp is obvious, and the reconstruction result become better and better with the SR increasing. In order to further illustrate the effectiveness, we analyze the comparison from the reconstructed parameter, and the reconstruction result of different radio is given in Table 1.

Table 1: Comparison between the two sampling methods.

SR(%)	PSNR/dB		t/s		SR(%)	PSNR/dB		t/s	
	URSp	ASSp	URSp	ASSp		URSp	ASSp	URSp	ASSp
10	26.65	28.74	2.4	22.8	50	28.94	47.31	2.3	14.7
20	27.20	36.23	2.4	19.3	60	37.44	50.85	2.3	14.0
40	28.28	42.98	2.3	15.4	80	42.97	53.30	1.4	13.1

As illustration, Table 1 shows that compared with the URSp, the ASSp can greatly improve the quality of reconstructed image. When the SR is very low, the superiority of ASSp is inconspicuous. However with the increase of SR, the advantage of ASSp become noticeable, the PSNR improves 13.41 dB when the SR is 60%. Simulation results illustrate that the ASSp is robust and effective for the microwave interferometry. While in the Table 1, we can see that the spending time of ASSp is much more than URSp. Therefore it is the focus of the next research and we will pay attention to the optimization problem in the future.

4. CONCLUSION

In this paper, we proposed a new sampling method on the basis of URSp. Compared with the traditional variable density sampling algorithm, the ASSp not only consider the prior information of the microwave image, but also introduce the theory of 1-D signal sampling into 2-D image. By computing the coherence between the sparsity and sensing bases, we can get the optimal sampling profile. The simulation results show that our sampling method can greatly reduce the sampling data and have good effect on the microwave image reconstruction.

ACKNOWLEDGMENT

This work was supported by National Science Foundation of China (No. 31101081, No. 61162015).

REFERENCES

1. Swift, C. T., D. M. Levine, and C. S. Ruf, “Aperture synthesis concepts in microwave remote sensing of the earth,” *IEEE Transactions on Microwave Theory and Techniques*, Vol. 39, No. 12, 1931–1935, 1991.
2. He, F., “Research on the statistical inversion approach for aperture synthesis microwave radiometric imaging,” Diss. Huazhong University of Science & Technology, 2010.
3. Candès, E., J. Romberg, and T. Tao, “Robust uncertainty principles: Exact signal reconstruction from highly incomplete frequency information,” *IEEE Transactions on Information Theory*, Vol. 52, No. 2, 2006.
4. Donoho, D., “Compressed sensing,” *IEEE Transactions on Information Theory*, Vol. 52, No. 4, 1289–1306, 2006.
5. Li, S., X. Zhou, B. Ren, et al., “A compressive sensing approach for synthetic aperture imaging radiometers,” *Progress In Electromagnetics Research*, Vol. 135, 583–599, 2013.
6. Wang, Z. and G. R. Arce, “Variable density compressed image sampling,” *IEEE Transactions on Image Processing*, Vol. 19, No. 1, 264–270, 2010.
7. Puy, G., P. Vandergheynst, and Y. Wiaux, “On variable density compressive sampling,” *IEEE Signal Processing Letters*, Vol. 18, No. 10, 595–598, 2011.
8. Lustig, M., D. Donoho, and J. Pauly, “Sparse MRI: The application of compressed sensing for rapid MR imaging,” *Magnetic Resonance in Medicine*, Vol. 58, No. 6, 1182–1195, 2007.
9. Yang, J., Y. Zhang, and W. Yin, “A fast alternating direction method for TVL1-L2 signal reconstruction from partial Fourier data,” *IEEE Journal of Signal Processing*, Vol. 4, No. 2, 288–297, 2010.

Introduction to the Researches on Radar Conducted in MIRSL/CAS

Yunhua Zhang, Xiaojin Shi, Xiang Gu, Wenshuai Zhai,

Xueyan Kang, Yuan Deng, Dong Li, Xiao Dong, Jiefang Yang,

Qilun Yang, Qingshan Yang, Yueying Tang, Xiangkun Zhang, and Jingshan Jiang

The Key Laboratory of Microwave Remote Sensing, Center for Space Science and Applied Research
Chinese Academy of Sciences, No. 1 Nanertiao, Zhongguancun, Haidian, Beijing 100190, China

Abstract— In this paper, we give an introduction to some of the research activities on radar for both the hardware development and signal processing algorithms conducted in recent years in the key lab of microwave remote sensing (MIRSL), Chinese Academy of Sciences (CAS). The works focus on the following aspects: (1) interferometric and wide-band radar system development; (2) radar signals and processing; (3) radar image registration; (4) polarimetric radar remote sensing; (5) radar compressive sensing. Some typical results are presented.

1. INTRODUCTION

The Key lab of microwave remote sensing (MIRSL), Chinese Academy of Sciences (CAS) is one of the major laboratories in china focusing on microwave remote sensing, especially on the development of both active and passive microwave sensors for both spaceborne and airborne applications, e.g., the scatterometers, altimeters and all kinds of radiometers. In recent ten years, we also put much efforts on the development of interferometric and wide-band radar systems, radar signal and radar image processing, polarimetric radar remote sensing, super-resolution algorithms and radar compressive sensing.

In the radar system development, we have developed Ku-band and Ka-band interferometric radar systems/subsystems with bandwidth up to 4 GHz, ground based and airborne experiments were carried out with these systems [1–9]. In signal model research, we designed high-performance chaotic radar signal, stepped-frequency chirp signal (SFCS), and stepped-frequency noise signal (SFNS), as well as high efficiency processing algorithms [10–12]. In signal and image processing [13–39], we proposed high efficiency compression algorithms for SFCS and SFNS [13, 14], developed algorithms for high-resolution imaging and super-resolution imaging [28–31], fast image registration [23], space-time adaptive processing (STAP) [15–18], ground moving target indication/imaging [19–21], circular-SAR imaging, etc.. In polarimetric SAR, we put our efforts on extending the Huynen dichotomy to the Huynen canonical dichotomy and further to the generalized Huynen dichotomy based on the wave dichotomy and N-target invariance, which can be applied to the scattering scenarios of irregularity and non-symmetry for unsupervised terrain classification [40–42]. In radar compressive sensing, we developed the 2D-double CS (chirp scaling and compressive sensing) algorithm for SAR imaging, as well as the Maximum a Posteriori Estimation (MAPE) algorithm based on multiplicative speckle model for SAR imaging of complex scenarios, we also developed compressive sensing based pulse compression algorithms for SFCS and SFNS [43–45].

The rest of the paper is organized as follows. Section 2 introduces the radar system development mainly on interferometric and wide-band radars; Section 3 introduces the developed high performance wide-band chaotic radar signals; Section 4 introduces the conducted works on signal and imaging processing; Section 5 introduces the work on extending Huynen’s decomposition for polarimetric SAR; Section 6 introduces the works on radar compressive sensing. Section 7 finally concludes the paper.

2. RADAR SYSTEMS/SUBSYSTEMS

2.1. Interferometric Radar Systems [1–5]

We have developed the first airborne interferometric radar experiment system (Figure 1(a)) in china and obtained the first single-pass airborne interferometric phase image (Figures 1(b), (c), (d)) in china in 2002 [1, 2]. In 2012, we conducted an airborne experiment for a newly developed interferometric radar altimeter and obtained interferometric echo waveforms over both lake and land [4, 5]. The altimeter system can work at multiple carrier frequencies. In this airborne experiment we also show that the interferometric phase of nadir echoes over smooth water can be used to infer the status information of the platform. This altimeter can work at SAR mode for high resolution imaging. We also conducted ground based interferometric imaging experiments during 2009–2012 [3]. Figure 2 and Figure 3 present the 2D and 3D imaging results, respectively.

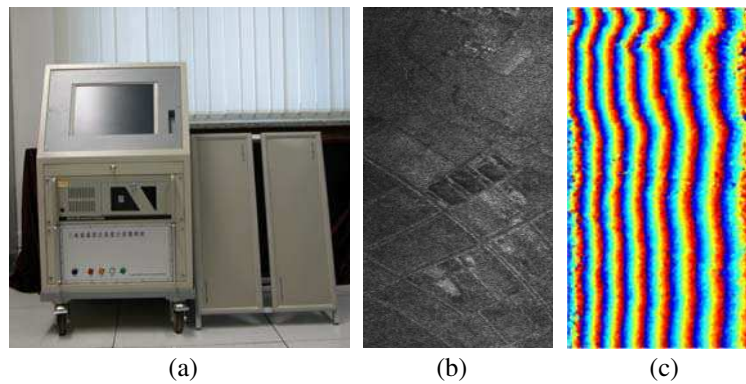


Figure 1: The airborne interferometric radar experiment system and airborne results. (a) The radar system, (b) amplitude image, (c) interferometric phase image.



Figure 2: The SAR image obtained by a newly developed multi-carrier-frequency radar system.

Figure 4 shows the obtained echo waveforms over lake for three carrier frequencies with both single channel waveforms and interferometric waveforms are presented, from which one can see that the interferometric waveforms are better for obtaining stable tracking center.

2.2. Wide-band Radar Systems [6, 7]

We have developed Ka and Ku wide-band radar systems with 2 GHz and 4 GHz bandwidth, respectively, and conducted ground moving target imaging experiment. In these radar systems, stepped-frequency technology is used for achieving the wide band. Figure 5 presents the imaging results by both Ku-band and Ka-band high-resolution radar systems. Figure 5(b) is the image by Ku-band system with 4 GHz bandwidth, Figure 5(c) is the image also by the same Ku-band system but with 2 GHz bandwidth, Figure 5(d) is the image by Ka-band system with 2 GHz bandwidth. It is clear that the Ka-band image reflects the ventilator structures very well. Along with the development of hardware, we also developed both software and hardware radar echo simulators used for testing signal processing algorithms [8, 9].

3. SIGNAL MODELS [10–12]

Wide-band chaotic noise signal model was proposed and practically realized by combining the stepped-frequency and the chaotic baseband signal. High performance chaotic radar signal has been designed and practically realized by combination of two chaotic maps, the realized chaotic signal has infinite repetition period as well as good randomness even with limited discretization length. The Modulating Group Delay Method was proposed to design ultra-low-sidelobe chaotic radar signal, which has been validated by experiment. Figure 6 presents the generated chaotic signals.

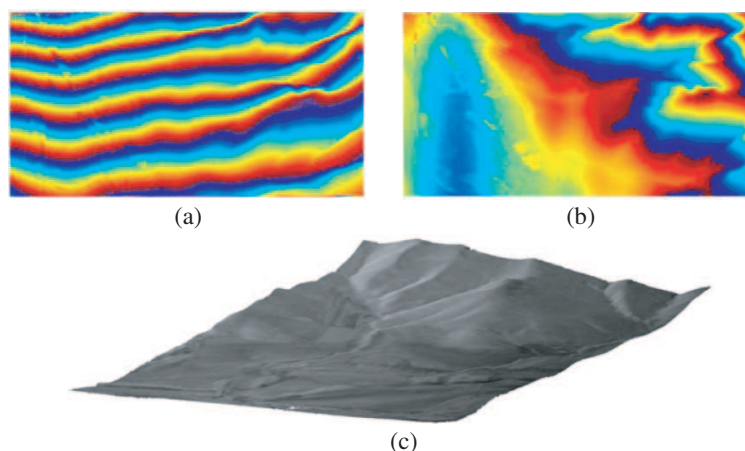


Figure 3: The DEM obtained by a newly developed multi-carrier-frequency interferometric radar system at Ku band. (a) Interferometric phase image, (b) interferometric phase image with flat earth effect removed, (c) the obtained DEM coated with scattering coefficient.

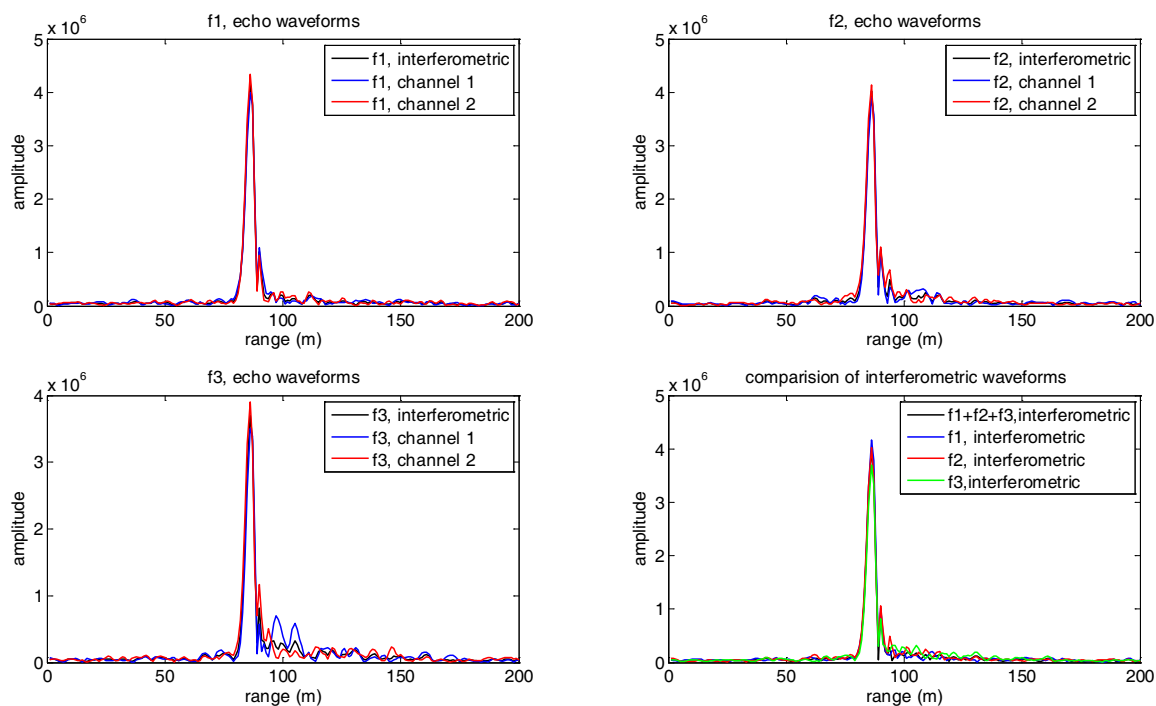


Figure 4: The echo waveforms obtained by a newly developed multi-carrier-frequency interferometric altimeter over a lake.

4. SIGNAL/IMAGE PROCESSING

4.1. Compression of SFCS/SFNS [13, 14]

High efficiency compressing algorithms for stepped-frequency chirp signal (SFCS) and stepped-frequency noise signal have been developed fitting for both matched-filtering and dechirping hardwares. Super-SVA and compressive sensing techniques have been applied to deal with the situation with some subpulses missed or the frequency step is larger than the bandwidth of subpulse.

4.2. Space-time Adaptive Processing [15–18]

We conducted researches on STAP algorithms based on sparse array as well as regular array. We developed a simulator for airborne STAP application. Multi-Carrier-Frequency STAP has been investigated. The STAP algorithm has been improved by applying APES [38]. Radial velocity ambiguity mitigation of moving target by dual-subband ATI approach with a Two-Channel SAR has been proposed.

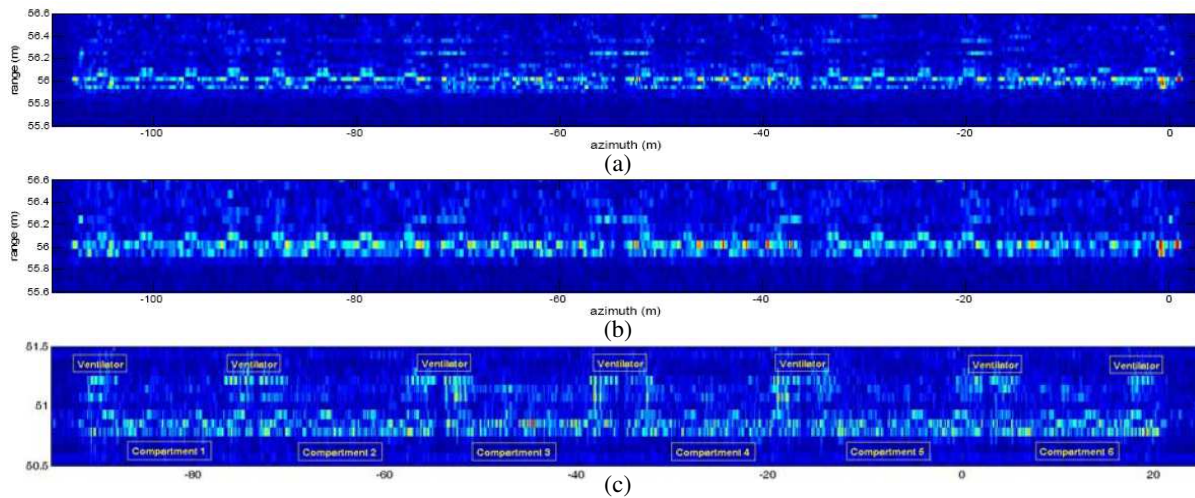


Figure 5: High-resolution radar images of a train by Ku and Ka radar systems. (a) Ku-band, bandwidth: 4 GHz. (b) Ku-band, bandwidth: 2 GHz. (c) Ka-band, bandwidth: 2 GHz.

4.3. Ground Moving Target Indication/Imaging [19–21]

A novel keystone-transform based algorithm with radon transform and fractional Fourier transform involved and a novel compressive sensing based dechirp-keystone algorithm have been investigated for ground moving target imaging.

4.4. InSAR and Image Registration [22–27]

Processing algorithms for InSAR, e.g., image pair registration, interferogram filtering, phase unwrapping, etc., were investigated. A fast registration algorithm has been proposed based on analytical formulae [23]. A rigorous SAR epipolar geometrical model was developed for accurate 3D target reconstruction [25].

4.5. Image Registration/Fusion [26, 27]

A novel approach for the registration of weak affine images has been proposed [26], some appropriate parameter retrieval algorithms for feature-based SAR image registration and the appropriate features for general SAR image registration have been investigated [27].

4.6. Super-resolution Algorithms [28–31]

Multiple Signal Classification (MUSIC), Estimation of Signal Parameters Via Rotational Invariance Techniques (ESPRIT), Auto Regressive (AR) and Super-SVA algorithms have been investigated. The effects of amplitude and phase errors on 2-D MUSIC and 2-D ESPRIT algorithms in ISAR imaging have been studied and the resolution threshold of MUSIC algorithm in radar range imaging was analyzed. Super-SVA has been used to fill the two-dimensional band gaps and satisfied results are obtained.

4.7. Other Algorithms [32–39]

We put a lot of efforts on developing algorithms for circular-SAR imaging [32, 33]. We derived concise formulae for ground-range-resolution improvement by InSAR and showed how the resolutions in both azimuthal and range directions can be improved with repeat-pass spaceborne SAR based on SFCS model [34]. Fractional Fourier Transform (FrFT), Time-Frequency analysis and Phase Gradient Autofocus (PGA) were applied to improve the imaging [36–38]. We recently proposed algorithms for estimating the motion parameters of high-speed target based on SFCS [39].

5. POLARIMETRIC SAR [40, 41]

We focus on extending the application of Huynen decomposition. Huynen decomposition was generalized to a unified Huynen dichotomy to cover full preferences for scattering symmetry and regularity, irregularity, non-symmetry, as well as their couplings. Scattering preference is identified as a key characteristic of target dichotomy and a novel description of which was developed to directly relate each dichotomy to a certain canonical scattering. Two representations of mixed radar target scattering were developed from the unified dichotomy in terms of scattering preference and statistical modeling, which then enable two classification schemes, i.e., the scattering preference-based classification and the Huynen scattering degree of preference (SDoP)/alpha classification.

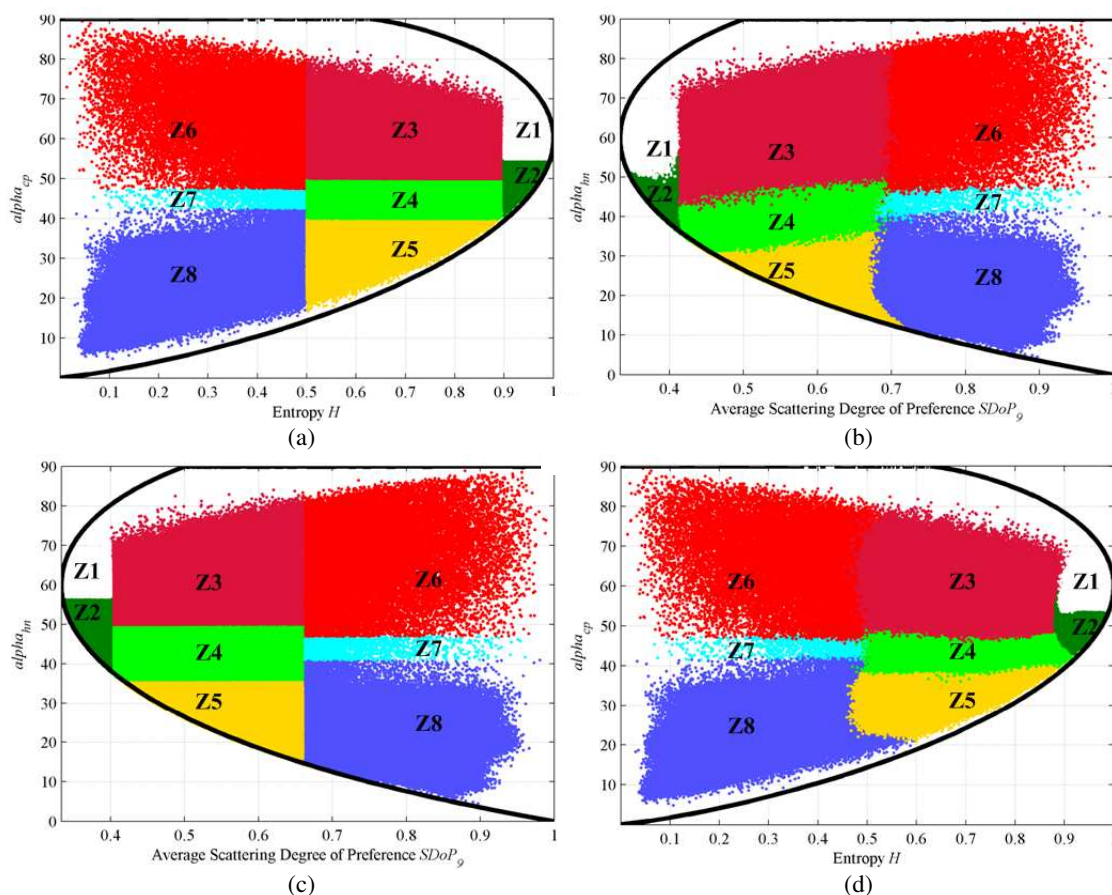


Figure 6: Consistency comparison of (a) Cloude-Pottier entropy/alpha classification plane and (c) Huynen SDoP/alpha plane on San Francisco scene. (b) is the equivalent presentation of (a) in SDoP/alpha space and (d) is the equivalent presentation of (c) in entropy/alpha space.

Fast PolSAR data visualization and classification based on Huynen canonical decomposition was also proposed. Figure 7 shows the Consistency comparison of Cloude-Pottier entropy/alpha classification plane and Huynen SDoP/alpha plane.

6. RADAR COMPRESSIVE SENSING (CS) [43–45]

We developed the 2D-double CS (chirp scaling and compressive sensing) algorithm for SAR imaging [86], as well as the Maximum a Posteriori Estimation (MAPE) algorithm based on multiplicative speckle model for SAR imaging of complex scenarios [87]. We applied CS to compress both SFCS and SFNS with much less data used. CS was also applied to GMTI by developing a novel compressive sensing based dechirping-Keystone algorithm [42].

7. CONCLUSION

This paper introduces the selected works on radar conducted in MIRSL/CAS over the past decades, which mainly focus on interferometric and wide-band radar system development, radar signals and processing algorithms, radar image registration/fusion, polarimetric radar remote sensing and radar compressive sensing. What we want to mention is that the introduced works in this paper cover just some but not the total activities on radar conducted in MIRSL.

REFERENCES

1. Zhang, Y., J. Jiang, et al., "Design and preliminary experiment of china imaging altimeter," *Proceedings of SPIE*, Vol. 4894, 190–198, 2003.
2. Zhang, Y., J. Jiang, et al., "Principle model and preliminary flight experiment of the three-dimensional imaging radar altimeter," *Acta Electronica Sinica*, Vol. 32, No. 6, 899–902, 2004 (in Chinese).

3. Zhang, Y., W. Zhai, et al., “Ground moving train imaging by ku-band radar with two receiving channels,” *Progress In Electromagnetics Research*, Vol. 130, 493–512, 2012.
4. Zhang, Y., W. Zhai, et al., “Experimental demonstration for the attitude measurement capability of interferometric radar altimeter,” *IRS*, Gdansk, Poland, June 14–20, 2014.
5. Zhang, Y., W. Zhai, et al., “Across-track interferometric SAR imaging experiment with multi-carrier frequencies,” *IRS*, Gdansk, Poland, June 14–20, 2014.
6. Xie, X. and Y. Zhang, “High-resolution imaging of a moving train by ground-based radar with compressive sensing,” *Electronic Letters*, Vol. 46, No. 7, 529–531, April 1st, 2010.
7. Zhang, Y., W. Zhai, et al., “Moving target imaging by both Ka-band and Ku-band high-resolution radars,” *Proceedings of SPIE*, Vol. 8179, 81790R-1~7, 2011.
8. He, Q., Y. Zhang, et al., “Fast electromagnetic modeling and imaging simulation of spacecraft by ground based ISAR,” *ISAPE*, 879–882, Guilin, October 27–30, 2006.
9. Chen, X.-W., Y.-H. Zhang, et al., “ISAR echo baseband simulation of high velocity moving-target,” *Journal of System Simulation*, Vol. 24, No. 2, 409–413, 2012 (in Chinese).
10. Yang, J. and Y. Zhang, “A novel sparse stepped chaotic signal and its compression based on compressive sensing,” *Progress In Electromagnetics Research*, Vol. 137, 335–357, 2013.
11. Yang, Q., Y. Zhang, et al., “A signal model based on combination chaotic map for noise radar,” *Progress In Electromagnetics Research M*, Vol. 28, 57–71, 2013.
12. Yang, Q., Y. Zhang, et al., “Design of ultra-low sidelobe chaotic radar signal by modulating group delay method,” *IEEE Trans. on Aerospace and Electronic Systems*, (1st revision).
13. Zhang, Y., J. Wu, et al., “Two simple and efficient approaches for compressing stepped chirp signals,” *AMPC*, Vol. 2, 690–693, Suzhou, China, December 4–7, 2005.
14. Zhang, Y.-H., H.-B. Li, et al., “Subaperture processing method for stepped-frequency Chirp signal,” *Systems Engineering and Electronics*, Vol. 28, No. 1, 1–6, 2006 (in Chinese).
15. Kang, X.-Y., B.-T. Jiang, et al., “GMTI study of STAP for spaceborne GMTI radar of sparse array,” *Systems Engineering and Electronics*, Vol. 29, No. 9, 1460–1463, 2007 (in Chinese).
16. Kang, X. and Y. Zhang, “Preliminary study on spaceborne sparse array millimeter wave radar for GMTI,” *Journal of the Korean Institute of Electromagnetic Engineering and Science*, Vol. 10, No. 4, 322–327, 2010.
17. Zhang, Y., Y. Zhang, et al., “Improved STAP algorithm based on APES,” *Journal of Systems Engineering and Electronics*, Vol. 22, No. 3, 387–392, 2011.
18. Zhang, Y. and Y.-H. Zhang, “Study of STAP system simulation for GMTI radar,” *Journal of System Simulation*, Vol. 24, No. 2, 493–503, 2012 (in Chinese).
19. Yang, J. and Y. Zhang, “A novel keystone-transform based algorithm for moving target imaging with radon transform and fractional fourier transform involved,” *PIERS Proceedings*, Guangzhou, China, August 26–28, 2014.
20. Yang, J. and Y. Zhang, “A novel compressive sensing based dechirp-keystone algorithm for SAR imaging of moving target,” (submitted).
21. Kang, X., J. Yang, et al., “Radial velocity ambiguity mitigation of moving target by dual-subband ATI approach with a two-channel SAR,” *Radar 2014*, Lille, France, October 13–17, 2014.
22. Shi, X. and Y. Zhang, “Quantitative comparison of phase unwrapping algorithms for SAR interferometry,” *APMC 2008*, Hong Kong, China, December 16–20, 2008.
23. Li, D. and Y. Zhang, “A fast offset estimation approach for InSAR image subpixel registration,” *IEEE Geoscience and Remote Sensing Letters*, Vol. 9, No. 2, 267–271, 2012.
24. Shi, X. and Y. Zhang, “Improving goldstein filter by image entropy for InSAR interferogram filtering,” *AP SAR 2011*, 411–414, Seoul, Korea, September 26–30, 2011.
25. Li, D. and Y. Zhang, “A rigorous SAR epipolar geometry modeling and application to 3D target reconstruction,” *IEEE Journal of Selected Topics in Applied Earth Observations & Remote Sensing (J-STARS)*, Vol. 6, No. 5, 2316–2323, October 2013.
26. Li, D. and Y. Zhang, “A novel approach for the registration of weak affine images,” *Pattern Recognition Letters*, Vol. 33, 1647–1655, 2012.
27. Li, D. and Y. Zhang, “On the appropriate feature for general SAR image registration,” *Proceedings of SPIE*, Vol. 8536, 85360Y R-1~R-7, 2012.
28. Gu, X. and Y. Zhang, “Effects of amplitude and phase errors on 2-D MUSIC and 2-D ESPRIT algorithms in ISAR imaging,” *AP SAR 2009*, 634–638, Xi’an, China, October 26–30, 2009.

29. Gu, X. and Y. Zhang, “Resolution threshold analysis of MUSIC algorithm in radar range imaging,” *Progress In Electromagnetics Research B*, Vol. 31, 297–321, 2011.
30. Yu, L. and Y. Zhang, “CSAR imaging with data extrapolation and approximate GLRT techniques,” *Progress In Electromagnetics Research M*, Vol. 19, 209–220, 2011.
31. Zhai, W.-S. and Y.-H. Zhang, “Apply super-SVA to processing stepped frequency Chirp signal with bandwidth gaps,” *Journal of Electronics & Information Technology*, Vol. 31, No. 12, 2848–2852, 2009 (in Chinese).
32. Zhang, X.-K., Y.-H. Zhang, et al., “Multi-aspect imaging of spotlight synthetic aperture radar,” *Chinese Journal of Radio Science*, Vol. 22, No. 4, 577–582, 2007 (in Chinese).
33. Yu, L. and Y. Zhang, “A 3D target imaging algorithm based on two-pass circular SAR observations,” *Progress In Electromagnetics Research*, Vol. 122, 341–360, 2012.
34. Zhang, Y., X. Shi, et al., “Resolution improvement in both azimuthal and range directions with repeat-pass spaceborne SAR,” *Proc. of SPIE*, Vol. 6746, 67460N-1~9, 2007.
35. Zhang, Y.-H., B.-T. Jiang, et al., “A concise formula derivation for ground-range-resolution improvement by InSAR,” *Chinese Journal of Radio Science*, Vol. 22, No. 4, 619–625, 2007 (in Chinese).
36. Yu, L. and Y. Zhang, “Application of the fractional fourier transform to moving train imaging,” *Progress In Electromagnetics Research M*, Vol. 19, 13–23, 2011.
37. Zhang, Y., Y. Deng, et al., “Time-frequency processing and analysis of radar imaging experiment data for a moving train,” *The IASTED ARP*, 43–48, Cambridge, Massachusetts, November 1–3, 2010.
38. Deng, Y. and Y. Zhang, “Improved PGA algorithm based on adaptive range bins selection,” *2nd International Conference on Image Analysis and Signal Processing*, Xiamen, Fujian, China, April 9–11, 2010.
39. Zhai, W. and Y. Zhang, “Velocity measurement and radar imaging of high high-speed target by using stepped-Chirp signal,” *Journal of Applied Remote Sensing*, (1st revision submitted).
40. Li, D. and Y. Zhang, “Huynen dichotomy-based unsupervised terrain classification,” *PIERS Proceedings*, 886–890, Stockholm, Sweden, August 11–15, 2013.
41. Li, D. and Y. Zhang, “Fast PolSAR data visualization and classification based on huynen canonical decomposition,” *EUSAR*, Berlin, June 3–5, 2014.
42. Li, D. and Y. Zhang, “Unified huynen phenomenological target dichotomy and application to unsupervised terrain classification,” *IEEE Trans. on Geoscience and Remote Sensing*, (submitted).
43. Dong, X. and Y. Zhang, “A novel compressive sensing algorithm for SAR imaging,” *IEEE Journal of Selected Topics in Applied Earth Observations & Remote Sensing (J-STARS)*, Vol. 7, No. 2, 708–720, February 2014.
44. Dong, X. and Y. Zhang, “SAR image reconstruction from undersampled data using maximum a posteriori estimation,” *IEEE Journal of Selected Topics in Applied Earth Observations & Remote Sensing (J-STARS)*, (submitted).
45. Xie, X.-C. and Y.-H. Zhang, “2D radar imaging scheme based on compressive sensing technique,” *Journal of Electronics & Information Technology*, Vol. 32, No. 5, 1234–1238, 2010 (in Chinese).

Comparison of the Time-reversal MUSIC and BP Algorithms in Multi-target Detection

Bing Li and Bin-Jie Hu

School of Electronic and Information Engineering
South China University of Technology, Guangzhou 510641, China

Abstract— Multi-target detection based on the time-reversal imaging with multiple signal classification (TR-MUSIC) and back-projection (BP) algorithms is presented in this paper. In the TR-MUSIC, firstly, the backscatter of a signal transmitted into a scattering environment is recorded. Secondly, the time reversal operator is obtained with the use of transfer matrix. Finally, the targets can be located through back-propagation of the eigenvectors of time reversal operator. In the BP, the imaging map is reconstructed by using the power of the electromagnetic wave corresponding to the travelling time from the transceivers to each pixel in imaging region. The imaging basic theories of TR-MUSIC and BP algorithms are outlined. In order to illustrate the performance of these two algorithms in detail, numerical simulations for three ideal point-like targets are conducted and analyzed. Here, we consider two versions of the simulation: targets detection with enough detection elements or not. Results show that the TR-MUSIC approach has a better performance than BP approach.

1. INTRODUCTION

Time-reversal imaging with multiple signal classification (TR-MUSIC) and back-projection (BP) algorithms are two well-developed imaging approaches dedicated to many applications, such as military, civil and biomedical imaging applications [1–5].

There are two stages in the time reversal process (TRP), namely, the time reversal forward propagation (TRFP) stage and the time reversal backward propagation (TRBP) stage. In the TRFP stage, the sources generate a signal, or the scatterers reflect a signal. A set of receivers record the signal. In the TRBP stage, these recorded signals are time reversed and rebroadcasted into the same scattering environment from the transmitters. The TRP is strictly within the framework of the wave equation [6]. In the contrast to the TR approach, the BP algorithm is a geometrical technique [7]. As a result, the imaging formulas adopted by these two algorithms are generally different. In this paper, these two algorithms are compared in multi-target detection.

The rest of this paper is organized as follows. In Section 2, the imaging methodologies and basic theories of TR-MUSIC and BP algorithms are introduced. Section 3 compares the two methods in multi-target detection by using the numerical experiment. The conclusion of this paper is presented in Section 4.

2. BASIC THEORY

We consider an array of N transceiver elements whose n th element is located at r_n ($1 \leq n \leq N$) and the backscattered signals are measured by all elements. Assume that the transceiver elements are all ideal that is the nonlinear of the transceivers can be neglected and targets are taken to be ideal point-like scatterers whose scattering only happens in first order, the receivers in the TRFP stage act as transmitters in the TRBP stage. The number of targets is L and the l th target is located at r_l ($1 \leq l \leq L$). The incident field at r excited by the emission signal of the n th transmitter denoted by $\varphi_n(r, \omega)$ is

$$\varphi_n(r, \omega) = G(r, r_n, \omega)S_n(\omega) \quad (1)$$

And receiving signal at the m th receiver located at r_m ($1 \leq m \leq N$) is

$$\psi_{mn}(r, \omega) = \varphi_n(r, \omega)A_r(\omega)G(r_m, r, \omega) = G(r, r_n, \omega)G(r_m, r, \omega)A_r(\omega)S_n(\omega) \quad (2)$$

where $S_n(\omega)$ is the transmission signal of n th transmitter, $A_r(\omega)$ is the scattering factor at r , $G(r_k, r_q, \omega)$ is background Green function that satisfies the reduced wave equation [6], representing the propagator from location r_q to r_k , because of the reciprocity of background Green function, that is $G(r_k, r_q, \omega) = G(r_q, r_k, \omega)$, the expression (2) can be presented as

$$\psi_{mn}(r, \omega) = G(r_n, r, \omega)G(r_m, r, \omega)A_r(\omega)S_n(\omega) \quad (3)$$

2.1. TR-MUSIC

Assume each transmitter individually is excited. So after scattered by L targets, the receiving signal of m th receiver is

$$\psi_m(r, \omega) = \sum_{n=1}^N \sum_{l=1}^L G(r_n, r_l, \omega) G(r_m, r_l, \omega) \tau_l(\omega) S_n(\omega) \quad (4)$$

where $\tau_l(\omega)$ is the scattering coefficient of l th scatterer.

The time reversal operator \bar{U} can be formed with the multi-static response transfer matrix \bar{K} that incorporates the scattering property of each target and the attenuation in the medium, \bar{U} is given by

$$\bar{U} = \bar{K}^* \bar{K} \quad (5)$$

where the “*” denotes the conjugation of a matrix or vector, the multi-static response transfer matrix \bar{K} is

$$\bar{K} = \sum_{l=1}^L \bar{G}_l(\omega) \bar{G}_l^T(\omega) \tau_l(\omega) \quad (6)$$

where the superscript “ T ” denotes the transpose of a vector or matrix, and $\bar{G}_l(\omega)$ is a N -dimensional column vector of Greens function, and can be represented as

$$\bar{G}_l(\omega) = [G(r_1, r_l, \omega), G(r_2, r_l, \omega), \dots, G(r_N, r_l, \omega)]^T \quad (7)$$

We can obtain the signal and noise sub-spaces by applying eigen decomposition on \bar{U} given by (5). The eigenvalues and eigenvectors of \bar{U} are denoted by $\{\lambda_l, \mu_l\}$ ($l = 1, 2, \dots, N$). The nonzero eigenvalues correspond to the signal sub-spaces, while the zero eigenvalues correspond to the noise sub-spaces which we use to construct the imaging function. The locations of the targets and their images can be determined by constructing the MUSIC pseudo spectrum from

$$I(r_p) = \frac{1}{\sum_{l_0=L+1}^N |\langle \mu_{l_0}^*, \bar{G}_p(\omega) \rangle|^2} \quad (8)$$

where $\mu_{l_0}^*$ is the conjugation of eigenvectors with zero eigenvalues and the inner product $\langle \mu_{l_0}^*, \bar{G}_p(\omega) \rangle$ is equal to zero whenever r_p corresponds to the location of one of the targets.

2.2. BP

To implement the numerical studies, supposing that the imaging region is divided into Q grids. If the n th transmitter is excited and the scatter signal is received by the m th receiver, the scatter field can be represented as

$$E^{scatter}(r_m, r_n, \omega) = \sum_{q=1}^Q \psi_{mn}(r_q, \omega) \quad (9)$$

If all transmitters are excited at the same time, the scattered field is given by

$$E^{scatter}(r_m, \omega) = \sum_{n=1}^N E^{scatter}(r_m, r_n, \omega) = \sum_{n=1}^N \sum_{q=1}^Q \psi_{mn}(r_q, \omega) \quad (10)$$

The imaging function of the BP method is

$$I^{BP}(r_p) = \sum_{m=1}^N E^{scatter}(r_m, t_{mp}) \quad (11)$$

where $t_{mp} = d_{mp}/c$, c is the light velocity in the free space, d_{mp} is the distance between the m th receiver and the p th grid in the imaging region. $E^{scatter}(r_m, t)$ is the inverse Fourier transform

of (10), that is

$$\begin{aligned}
 E^{scatter}(r_m, t) &= \frac{1}{2\pi} \int_{-\infty}^{+\infty} E^{scatter}(r_m, \omega) e^{j\omega t} d\omega = \frac{1}{2\pi} \sum_{n=1}^N \int_{-\infty}^{+\infty} E^{scatter}(r_m, r_n, \omega) e^{j\omega t} d\omega \\
 &= \frac{1}{2\pi} \sum_{n=1}^N \sum_{q=1}^Q \int_{-\infty}^{+\infty} \psi_{mn}(r_q, \omega) e^{j\omega t} d\omega \\
 &= \frac{1}{2\pi} \sum_{n=1}^N \sum_{q=1}^Q \int_{-\infty}^{+\infty} [G(r_n, r_q, \omega) G(r_m, r_q, \omega) A_{r_q}(\omega) S_n(\omega)] e^{j\omega t} d\omega
 \end{aligned} \quad (12)$$

The discretized version of (12) gives

$$E^{scatter}(r_m, t) = \frac{\Delta\omega}{2\pi} \sum_{k=1}^K \left\{ \sum_{n=1}^N \sum_{q=1}^Q [G(r_n, r_q, \omega_k) G(r_m, r_q, \omega_k) A_{r_q}(\omega_k) S_n(\omega_k)] e^{j\omega_k t} \right\} \quad (13)$$

Then, (11) can be written as

$$\begin{aligned}
 I^{BP}(r_p) &= \sum_{m=1}^N E^{scatter}(r_m, t_{mp}) \\
 &= \frac{\Delta\omega}{2\pi} \sum_{k=1}^K \left\{ \sum_{m=1}^N \sum_{n=1}^N \sum_{q=1}^Q [G(r_n, r_q, \omega_k) G(r_m, r_q, \omega_k) A_{r_q}(\omega_k) S_n(\omega_k)] e^{j\omega_k t_{mp}} \right\}
 \end{aligned} \quad (14)$$

Which can be formed as

$$\overline{I}^{BP} = \overline{I}_{Q \times K}^{BP} \cdot \overline{Z} \quad (15)$$

where $\overline{Z} = (\frac{\Delta\omega}{2\pi})[1, 1, \dots, 1]_{1 \times K}^T$. The k^{th} column of matrix $\overline{I}_{Q \times K}^{BP}$ is

$$\overline{I}_{\omega_k}^{BP} = \overline{G}e(\omega_k) \overline{G}A(\omega_k) \overline{S}(\omega_k) \quad (16)$$

where

$$\overline{G}e(\omega_k) = \begin{bmatrix} \langle \bar{e}_1(\omega_k), \bar{G}_1(\omega_k) \rangle & \langle \bar{e}_1(\omega_k), \bar{G}_2(\omega_k) \rangle & \dots & \langle \bar{e}_1(\omega_k), \bar{G}_Q(\omega_k) \rangle \\ \langle \bar{e}_2(\omega_k), \bar{G}_1(\omega_k) \rangle & \langle \bar{e}_2(\omega_k), \bar{G}_2(\omega_k) \rangle & \dots & \langle \bar{e}_2(\omega_k), \bar{G}_Q(\omega_k) \rangle \\ \vdots & \vdots & \dots & \vdots \\ \langle \bar{e}_Q(\omega_k), \bar{G}_1(\omega_k) \rangle & \langle \bar{e}_Q(\omega_k), \bar{G}_2(\omega_k) \rangle & \dots & \langle \bar{e}_Q(\omega_k), \bar{G}_Q(\omega_k) \rangle \end{bmatrix} \quad (17)$$

$$\overline{G}_q(\omega_k) = [G(r_1, r_q, \omega_k), G(r_2, r_q, \omega_k), \dots, G(r_N, r_q, \omega_k)]^T, \quad (1 \leq q \leq Q) \quad (18)$$

$$\bar{e}_q(\omega_k) = [e^{j\omega_k t_{1q}}, e^{j\omega_k t_{2q}}, \dots, e^{j\omega_k t_{Nq}}]^T, \quad (1 \leq q \leq Q) \quad (19)$$

$$\overline{G}A(\omega_k) = \begin{bmatrix} G(r_1, r_1, \omega_k) A_{r_1}(\omega_k) & G(r_2, r_1, \omega_k) A_{r_1}(\omega_k) & \dots & G(r_N, r_1, \omega_k) A_{r_1}(\omega_k) \\ G(r_1, r_2, \omega_k) A_{r_2}(\omega_k) & G(r_2, r_2, \omega_k) A_{r_2}(\omega_k) & \dots & G(r_N, r_2, \omega_k) A_{r_2}(\omega_k) \\ \vdots & \vdots & \dots & \vdots \\ G(r_1, r_Q, \omega_k) A_{r_Q}(\omega_k) & G(r_2, r_Q, \omega_k) A_{r_Q}(\omega_k) & \dots & G(r_N, r_Q, \omega_k) A_{r_Q}(\omega_k) \end{bmatrix} \quad (20)$$

$$\overline{S}(\omega_k) = [S_1(\omega_k), S_2(\omega_k), \dots, S_N(\omega_k)]^T \quad (21)$$

3. NUMERICAL SIMULATIONS

In order to illustrate the performance of these two algorithms in detail, the numerical experiment for three ideal point-like targets is constructed, and two situations are analyzed, that is, target detection with enough transceiver elements called situation I and target detection with few transceiver elements named situation II.

The setup of situation I is conducted as shown in Figure 1, and the setup of situation II is the same as that of situation I except the number of transceiver elements which are shown in the

bottom of imaging region in Figure 1. The “ \triangle ” represents the transceiver element and the “ \circ ” represents the target. The positions of these three targets are (1.5 m, 4 m) marked as S_1 , (3.75 m, 1.3 m) marked as S_2 and (2.9 m, 2.5 m) marked as S_3 . Fifteen transceiver elements are used to construct situation I which provide enough echo signals, for contrast, four transceiver elements are employed to achieve situation II.

The imaging results of TR-MUSIC and BP algorithms are shown in Figure 2 and Figure 3, respectively. In situation I, the targets based on both algorithms can be located accurately, while

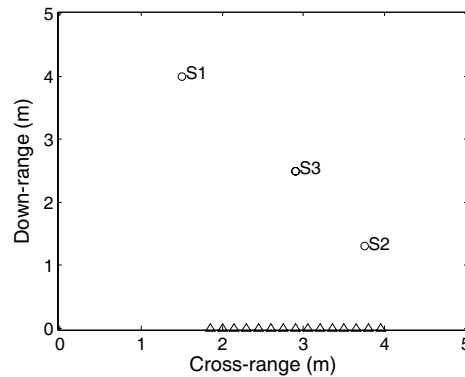


Figure 1: Setup of the numerical experiment.

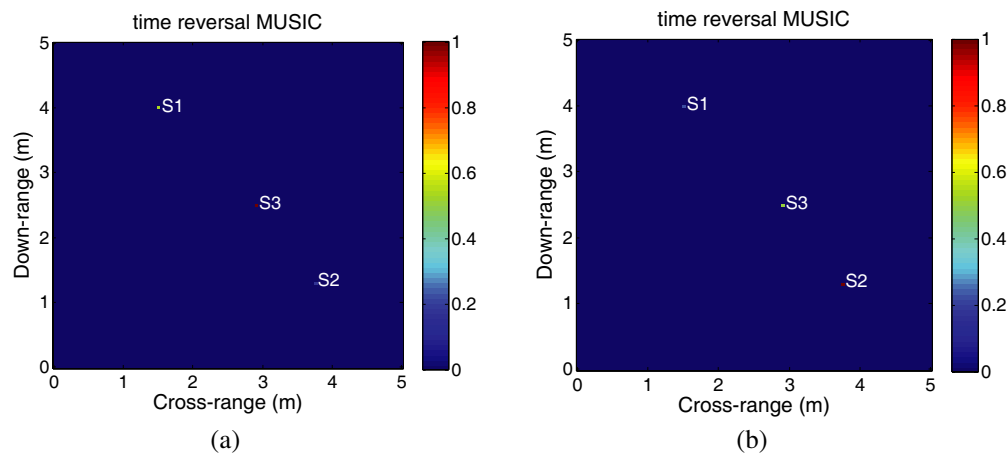


Figure 2: Imaging results based on TR-MUSIC algorithm: (a) 15 transceiver elements; and (b) 4 transceiver elements.

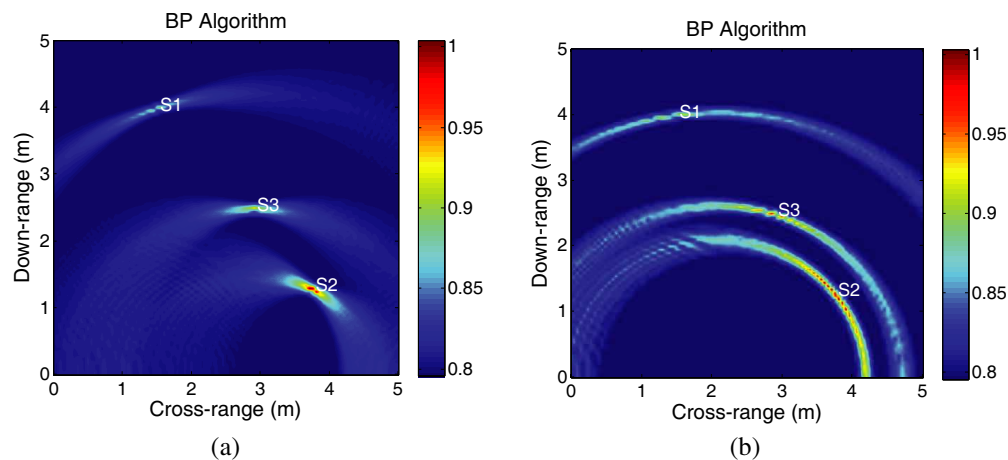


Figure 3: Imaging results based on BP algorithm: (a) 15 transceiver elements; and (b) 4 transceiver elements.

the imaging resolution based on TR-MUSIC algorithm is better than that based on BP algorithm in situation II. Thus, the TR-MUSIC approach outperforms BP approach in multi-target detection.

4. CONCLUSIONS

Two imaging methods, namely, TR-MUSIC and BP methods have been compared with numerical experiment in multi-target detection. From the analysis, in terms of imaging quality, the TR-MUSIC is superior to the BP method. In our future work, the limitations by using TR-MUSIC will be studied based on some current literature [8], the impact of noise and other impact factors of imaging resolution will be also investigated.

ACKNOWLEDGMENT

This work was supported by the NSFC-Guangdong under Grant No. U1035002, Guangdong-Hong Kong Key Project of Science and Technology under Grant Nos. 2011A011305001 and 2011A0113020 01, and University- Industry Key Project of Department of Education of Guangdong Province under Grant No. CGZHSD1102.

REFERENCES

1. Labyed, Y. and L. J. Huang, "TR-MUSIC inversion of the density and compressibility contrasts of point scatterers," *IEEE Transactions on Ultrasonics, Ferroelectrics and Frequency Control*, Vol. 61, No. 1, 16–24, 2014.
2. Zhang, L., H. L. Li, et al., "Integrating autofocus techniques with fast factorized back-projection for high-resolution spotlight SAR imaging," *IEEE Geoscience and Remote Sensing Letters*, Vol. 10, No. 6, 1394–1398, 2013.
3. Demirci, S., H. Cetinkaya, E. Yigit, C. Ozdemir, and A. A. Vertiy, "A study on millimeter-wave imaging of concealed objects: Application using back-projection algorithm," *Progress In Electromagnetics Research*, Vol. 128, 457–477, 2012.
4. Zhang, W., A. Hoorfar, and L. Li, "Through-the-wall target localization with time reversal MUSIC method," *Progress In Electromagnetics Research*, Vol. 106, 75–89, 2010.
5. Mohan, A. S., M. D. Hossain, and M. J. Abedin, "Beamspace based time reversal processing for breast cancer detection," *IEEE 2012 Antennas and Propagation Society International Symposium*, 1–2, 2012.
6. Brocea, I., G. Papanicolaou, and C. Tsogka, "Theory and applications of time reversal and interferometric imaging," *Inverse Problems*, Vol. 19, No. 6, S139–S164, 2003.
7. Anastasio, M. A., X. C. Pan, and E. Clarkson, "Comments on the filtered backprojection algorithm, range conditions, and the pseudoinverse solution," *IEEE Transactions on Medical Imaging*, Vol. 20, No. 6, 539–542, 2001.
8. Solimene, R. and A. Dell'Aversano, "Some remarks on time-reversal MUSIC for two-dimensional thin PEC scatterers," *IEEE Geoscience and Remote Sensing Letters*, Vol. 11, No. 6, 1163–1167, 2014.

A Novel Parallel Double Helix Loop Resonator for Magnetic Coupled Resonance Wireless Power Transfer

Cheng Yang and Koichi Tsunekawa
 Department of Computer Science Engineering
 Chubu University, Kasugai-shi, Aich, Japan

Abstract— A novel parallel double helix loop resonator for magnetic coupled resonance wireless power transfer (WPT) is proposed in this paper. The various characteristics are investigated by using simulation and experiment. Compare to a same geometry size traditional structure helix loop resonator, the proposed resonator could reduce the resistance loss about 48% and improve the maximum power transfer efficiency about 8% within the strong coupled region. On the other hand, the coupling efficiency of proposed resonator used WPT system is also increased. Finally, for increase the power transfer efficiency at the region of outside of the strong coupled, a pair of matching loops are used to match the transmitting and receiving resonator to the optimal port impedance at varying distance and the measurement results shows the maximum power transfer efficiency that the system could achievable by using traditional structure helix loop resonator and parallel double helix loop resonator are 34% and 57% at the distance of 20 cm, respectively.

1. INTRODUCTION

Magnetic coupled resonance WPT technology is expected to the next generation wireless power charging system, because of its advantage of mid-range power transfer distance and high efficiency [1]. There are two most important performances of this technology always be focus on which are: long power transfer distance and high power transfer efficiency. To achieve this, it is necessary to improve the resonator quality factor and the coupling efficiency. The quality factor of resonator is proportional to the resonance frequency and self-inductance of the resonator and inversely proportional to the resonator resistance loss. Therefore, it is necessary to reduce the resistance loss in order to improve the resonator quality factor.

2. RESONATOR DESIGN

A traditional structure helix loop resonator is widely used and researched for magnetic resonance WPT system as shown in Fig. 1. It can be represented in terms of a simplified LCR equivalent lumped circuit element [2]. The L and C are the resonator self-inductance and self-capacitance which could make it resonant at the operation frequency of ω_0 . R is the resistance loss including both radiation and conductivity loss.

From the fundamentals of an RLC circuit, when two inductors are connected so that the magnetic field of one affects the other which will occurs a mutual inductance L_m between them, and the mutual inductance increases or decreases the total inductance of circuit. When two inductors are connected in parallel with an aiding, the total inductance L_T becomes to (1). The mutual inductance can be calculated by using Equation (2) where k is the coupling efficiency between two inductors. From Equations (1) and (2), when the coupling efficiency between two parallel connected inductors is closely coupled where $k = 1$ and the inductance value of two inductors is the same

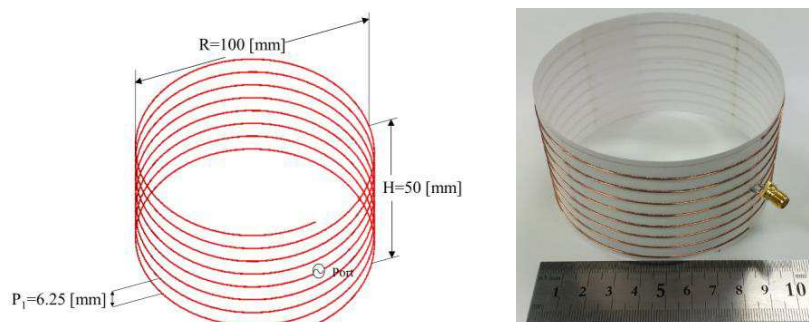


Figure 1: Traditional structure helix loop resonator configuration.

$L_1 = L_2 = L$, not only the mutual inductance between two inductors but also the circuit total inductance will equals to the value of inductor self-inductance. It means the circuit self-inductance will be not changed $L_T = L$. On the other hand, the total resistance loss of the circuit is reduced by a parallel connected resistance and it can be calculated by using Equation (3).

$$L_T = (L_1 + L_m)(L_2 + L_m)/(L_1 + L_m) + (L_2 + L_m) \quad (1)$$

$$L_m = k(L_1 L_2)^{(1/2)} \quad (2)$$

$$R_T = (R_1 R_2)/(R_1 + R_2) \quad (3)$$

Depend on this characteristic, a parallel double helix loop resonator is proposed as shown in Fig. 2, which has the same geometry size with the traditional structure helix loop that be proposed in this paper as shown in Fig. 1. Both of them are made by a 0.55 mm diameter copper wire. To maintain the resonator self-inductance, the currents on both helix loops of the parallel double helix resonator should be equal in magnitude. In this study, various structures have been analyzed and it is found out that when two same structure helix loops are coaxially parallel connected with 180 degree phase displacement in the same plane, the equal magnitude currents will be induced on each helix loop and occurs a highest mutual inductance between them.

At first, the input impedance of each resonator is calculated by using method of moment (MoM) and measured by a Vector Network Analyzer (VNA) under the condition that only one resonator exists. For the purpose of making the simulation and experiment results could have a great agreement with each other, the conductor conductivity loss should be considered in calculation, and it is assumed to $4e6$ S/m in this study Figs. 3(a) and (b) show the each resonator input impedance characteristic as a function of frequency, respectively. In the traditional structure helix loop resonator, the self-resonance frequency occurs at 44.24 MHz with 5.86Ω resistance loss and the parallel double helix loop is resonated at the frequency of 39.25 MHz with 3.07Ω resistance loss. It could confirm that, compare to the traditional structure the parallel double helix loop resonator decreases the resistance loss about 48%.

Table 1 lists the lumped parameters of traditional and parallel double helix loop structure

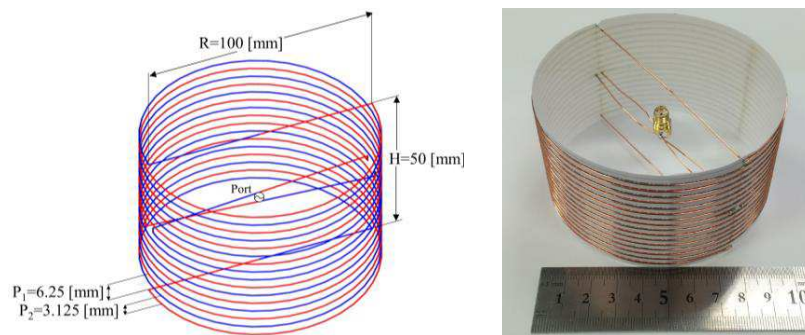


Figure 2: Parallel double helix loop resonator configuration.

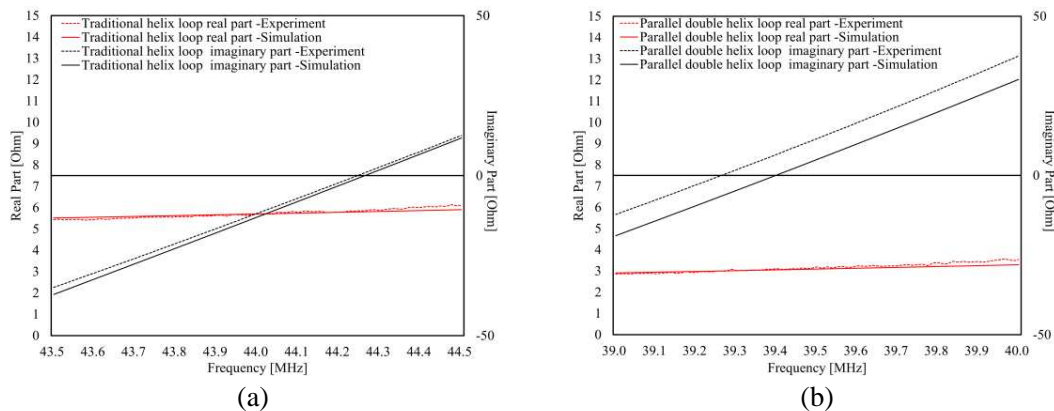


Figure 3: Resonator input impedance. (a) Traditional helix loop resonator. (b) Parallel double helix loop resonator.

Table 1: Lumped parameter of two resonators.

Parameter	Simulation		Experiment	
	Traditional helix loop	Parallel double helix loop	Traditional helix loop	Parallel double helix loop
Self-inductance [uH]	3.93	3.86	3.95	3.83
Self-capacitance [pF]	3.29	4.23	3.28	4.29
Resistance loss [Ω]	5.7	2.99	5.86	3.07
Resonance frequency [MHz]	44.26	39.39	44.24	39.25
Q	191	319.8	187.4	307.9

resonator, respectively. From experiment results, the proposed type resonator could maintain the self-inductance well. On the other hand, it should be noted that the resonator self-capacitance of parallel double helix loop also be increased and the reason can be assumed by the parallel connected self-capacitance of two helix loops. Nevertheless, because of the reduced resistance loss, compare to the traditional structure helix loop resonator the Q factor of proposed type resonator has been increased about 64.3%.

3. POWER TRANSFER CHARACTERISTICS

To analysis the power transfer characteristics of the system, the transmitting and receiving resonator are placed facing each other along their common axis as shown in Fig. 4 where a $\lambda/4$ sleeve balun is used for the network measurement and the port impedance is 50Ω . Fig. 5 shows the coupling efficiency calculation results comparison of traditional and parallel double helix loop used WPT system. From the result, the coupling efficiency of proposed resonator used condition is higher than the traditional type resonator used system at varying distance about 12% is confirmed. The reason can be considered by the stronger near magnetic field of parallel double helix loop resonator due to the alignment field by two helix loops and lower resistance loss.

The critical coupling $k_{critical}$ point is a very important factor for magnetic coupled resonance WPT system, which represents the maximum power transfer efficiency that the system could achievable at the furthest possible operation distance [2]. When the coupling efficiency k between transmitting and receiving resonator is greater than critical coupling point $k > k_{critical}$, the system is at the strong coupled region and the maximum power transfer efficiency resonance frequency is split at two points, the even mode ω_e and odd mode ω_o . Conversely, when $k < k_{critical}$, the system is sad to be under-coupled, the split two maximum efficiency resonance frequencies will converge to the resonator operation frequency point ω_0 and amount of power will dramatically fall off with the distance. Hence, if a frequency tracing system is used, which could automatically adjust to provide the maximum power transfer efficiency at varying distance, the power transfer efficiency characteristic as a function of distance will be shown in Fig. 6. The experimentally demonstrates that the maximum power transfer efficiency of parallel double helix loop resonator is 87% and traditional

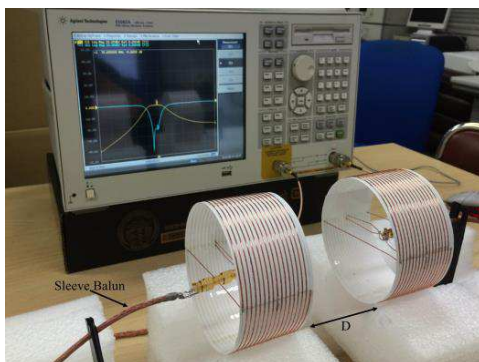


Figure 4: The wireless power transfer efficiency measurement setup.

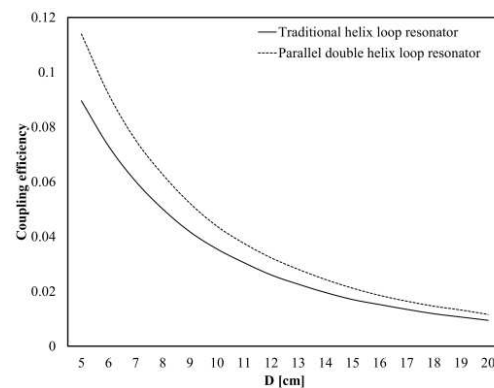


Figure 5: The coupling efficiency comparison of two type resonators used WPT system.

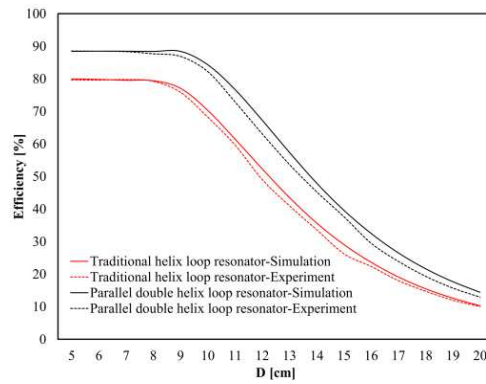


Figure 6: The power transfer efficiency comparison of two type resonators used WPT system when the system could automatically tuning the highest power transfer efficiency resonance frequency.

structure helix loop resonator is 79% within the strong coupled region, respectively.

4. IMPEDANCE MATCHING

In the magnetic coupled resonance WPT system, the optimal port impedance of resonator vary dramatically with the power transfer distance between transmitting and receiving resonator, because it is a function of the mutual inductance and is given by Equation (4) [3]. The L_m is the mutual inductance between transmitting and receiving resonator, R is the resistance loss of single resonator. From this equation, it is found out as the mutual inductance decreases, the optimal port impedance is closed to the resonator resistance loss. Equation (5) represents the maximum power transfer efficiency that the system could achievable when the resonator is matched to the optimal port impedance at varying power transfer distance.

$$Z_{opt} = \left\{ R^2 + (\omega_0 L_m)^2 \right\}^{(1/2)} \quad (4)$$

$$\eta_{opt}(\omega) = (\omega_0 L_m)^2 / (Z_{opt} + R)^2 \quad (5)$$

Thus for improve the power transfer efficiency at the region of under-coupled, match the resonator to optimal port impedance is a very efficiency method. Direct match the port impedance is very difficult to realize. Hence, a inductive coupling by using matching loop is chosen to match both of the transmitting and receiving resonator as shown in Fig. 7 [4]. The matching loop radius is 45 [mm] and the 50 Ohms feed port is directly connected to it.

After the matching loop size is fixed, the port impedance at the matching loop can be converted into the optimal impedance of the resonator by adjusting the separation between matching loop and resonator at different power transfer distance. Fig. 8 shows the power transfer efficiency comparison of two type resonators used WPT system after the resonator is matched by the matching loop.

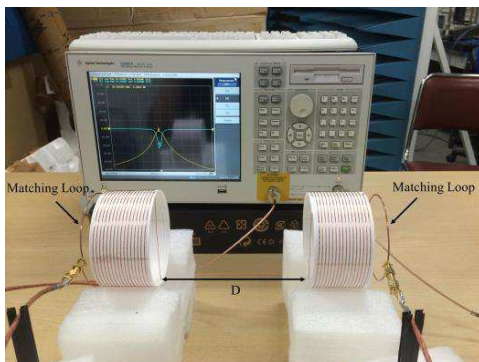


Figure 7: Power transfer efficiency measurement setup by using matching loop.

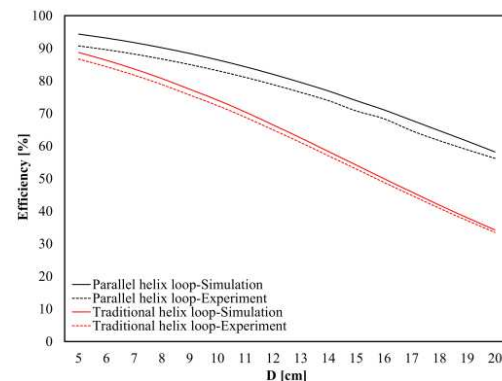


Figure 8: The power transfer efficiency comparison of two type resonators used system by using matching loop.

From the measurement result, the traditional structure helix loop resonator used system could only achieve to 34% but the parallel helix loop resonator could achieve to 57% at the transfer distance of 20 cm.

5. CONCLUSION

A novel parallel double helix loop resonator for magnetic coupled resonance WPT is proposed and investigated by using simulation and experiment in this paper. The experimentally demonstrates that the quality factor of proposed resonator is greater than a same geometry size traditional structure helix loop resonator about 64.3% and the maximum power transfer efficiency at the strong coupled region of parallel double helix loop resonator and traditional structure helix loop resonator used WPT system are 87% and 79%, respectively. On the other hand, due to the stronger near magnetic field and lower resistance loss, the coupling efficiency of parallel double helix loop resonator used WPT system is also increased. After a pair of matching loops are used to match the resonator to the optimal port impedance, the measurement results shows that the maximum power transfer efficiency of parallel double helix loop resonator used WPT system could achieve to 57% at the distance of 20 cm and compare to the traditional structure helix loop resonator used WPT system, the efficiency has been improved about 23% is confirmed.

REFERENCES

1. Kurs, A., A. Karalis, R. Moffatt, J. D. Joannopoulos, P. Fisher, and M. Soljacic, "Wireless power transfer via strongly coupled magnetic resonances," *Science*, Vol. 317, No. 5834, 83–86, 2007.
2. Sample, A. P., D. A. Meyer, and J. R. Smith, "Analysis, experimental results, and range adaptation of magnetically coupled resonators for wireless power transfer," *IEEE Transactions on Industrial Electronics*, Vol. 58, No. 2, 544–554, 2011.
3. Park, J., Y. Tak, Y. Kim, Y. Kim, and S. Nam, "Investigation of adaptive matching methods for near-field wireless power transfer," *IEEE Transactions on Antennas and Propagation*, Vol. 59, No. 5, 1769–1773, 2011.
4. Kim, J., W.-S. Choi, and J. Jeong, "Loop switching technique for wireless power transfer using magnetic resonance coupling," *Progress In Electromagnetics Research*, Vol. 138, 197–209, 2013.

Parabolic Strip Telescope

V. Kosejk, G. Chadzitaskos, and J. Červený

Department of Physics, Faculty of Nuclear Sciences and Physical Engineering
Czech Technical University, Břehová 7, Prague CZ-115 19, Czech Republic

Abstract— We present a proposal of a new telescope type using a rotating parabolic strip as the primary mirror. It is a principal modification of the design of telescopes from the times of Galileo and Newton. In order to demonstrate the basic idea, the image of an artificial constellation observed by this kind of telescope was reconstructed using the techniques described in this article. We present a working model of this new telescope, we have used an assembly of the primary mirror — a strip of acrylic glass parabolic mirror 30 cm long and 10 cm wide shaped as a parabolic cylinder of a focal length of 1 m — and an artificial constellation, a set of LED diodes in a distance of 15 m. In order to reconstruct the image, we made a series of snaps, each taken after the constellation had been rotated by 5 degrees. Using three different algorithms, we reconstructed the image of this artificial constellation. This contribution is based on [1] with new telescope designs and new experimental tests.

1. INTRODUCTION

The current telescopic systems are based on two basic principles: the Galileo-Kepler system uses optical lenses as the primary optic element (refractors) and the Newton-Cassegrain system has primary refracting surfaces shaped like a circle or n-gon. Their angular resolution is therefore identical in all directions. Images are acquired by means of photographic cameras, astronomic cameras or light-emission spectrometers. Images from CCDs and spectrometers are stored in a computer for further processing. In all the cases, images are taken in the same plane. The primary optical elements contained in both the reflectors and the refractors concentrate parallel light beams to a focal point. The other optical elements make use of different geometric configurations. For more details go to [2].

As a rule, the telescope is mounted on a support frame allowing to exactly adjust the position of the telescope and to carry out fine rectification of its movement. For this purpose, the azimuthal, parallactic or four-axis assemblies are used. In the case of azimuthal assembly, one axis is horizontal and the other vertical. A telescope rotates along the vertical axis in relation to the cardinal points; the height above the horizon is set in the horizontal axis. When observing celestial bodies, the positioning of a telescope around both axes must be changed smoothly; it is better-known as so called Dobson platform. The parallactic assembly has one axis parallel with the earth's axis pointing to the pole. The other axis is perpendicular to the first axis. When one object is tracked, a telescope rotates around the polar axis in a steady speed of 15 arc degrees per hour. The four-axis assembly is intended especially for the tracking of man-made satellites orbiting the Earth. Three of the axes are adjusted so that a telescope could track an object only by rotating around one axis.

An important parameter of the telescope is its angular resolution. It is determined by the smallest angle that enables us to distinguish two points. The smaller the angle, the better the angular resolution. If the diameter of an objective is D , then its plan area P is given by the following relation

$$P = \pi \frac{D^2}{4}, \quad \delta \approx 1.22 \frac{\lambda}{D}$$

for the monochromatic light of a wavelength of λ [3].

The main reason for the construction of telescopes of large diameters is that astronomers require a better angular resolution. As it follows from what was specified above, the disadvantage of these known solutions is that to achieve a better angular resolution, especially a large size of the primary optical element is required. The weight of these massive objectives is heavy, they are demanding in terms of their construction, and the technology and production is expensive.

1.1. Teleskop with a Rotating Objective Element

The principle of our new system was inspired by the fact that the angular resolution is inversely proportional to the length of an antenna, and by the technology of X-ray computer tomography (CT). An X-ray source is located on one side and an X-ray camera on the opposite side of an x-rayed sample. The integral absorptions of X-rays in different angles are measured step by step

during the rotation of the sample. The total absorption of all photons coming along different lines perpendicular to the camera are registered as points of a one-dimensional picture. Finally, the inverse Radon transform is used to reconstruct the image of absorption of X-rays in different points of the media.

Modern mathematical methods and software developed for CT involve the gathering of projection data from multiple directions and the feeding of the data into a tomographic reconstruction software algorithm processed by a computer [5]. Mathematical filters are used to improve the reconstructed image [6]. The idea and the image processing as performed by means of the technology of Single-Photon Emission Computer Tomography [7] is the same as in the case of our parabolic strip telescope. This technology is used in nuclear medicine where a patient is injected with a radiopharmaceutical which emits gamma rays. The emitted gamma rays are collected by a gamma camera and the emitted image is reconstructed [8].

The same approach can be used when a parabolic strip is the primary mirror [9, 10] of a telescope, following the scheme shown in Figure 2. The images of tracked objects are comprised of lines. Each line represents the integral intensity of light incoming from an object or objects perpendicular to the strip (parallel to the focal line) located inside the field of view, which is guaranteed by the geometry. When making a series of photos while rotating the telescope around its optical axis, the inverse Radon transformation can be used to reconstruct the image with the above mentioned angular resolution. It is also possible to use other tools, for example Matlab [8]. Secondary optical elements can be used to focus the lines from the focal plane into points.

The technological construction of the parabolic strip is simpler than the planar or paraboloid surface, because the stress of material helps to maintain the geometry. A precise parabolic bracket is required to support the parabolic strip made of elastic mirrors. It is also simpler to use adaptive optics for the correction of optical defects. One can control the surface by a laser pointer located on one side of the strip. By the detection of its reflected light on the other side of the strip during the scan, the whole surface can be controlled and corrected by corrective elements. Of course, secondary mirrors can be added, then we have a Newton — like or Cassegrain — like telescope. The area and the angular resolution of a parabolic strip telescope are

$$P = LW, \quad \delta_L = \frac{\lambda}{L},$$

where λ is the wavelength of light, L is the length of the projection of the strip on the tangent plane at the vertex line — in Figure 2 it is the length of the x -axis projection of the strip — and W is the width of the strip.

The proposed telescopic system involves preferably parallactic mounting and an instrument for image digitalization connected to a computer.

The mounting, however, has to perform one more rotation than the usual mounting: rotation of the primary element or of the whole system around the optical axis is necessary in order to reconstruct details of an object. The instrument for the digitalization of images has to be located in the image plane of a telescope.

2. PROCESSING IMAGES FROM A PARABOLIC STRIP TELESCOP

The basic mode of tracking by means of a rotational telescope will display various intensities for the parallel line segment corresponding to various tracked points. Line segments may correspond to more than one observed points on straight lines.

It is apparent that all the points correspond to the given line segments. On the edge, one line segment corresponds to five points while the middle three line segments correspond to two points. Changes in the intensities on the line segments correspond to the number of LEDs in the image. For the studied methods, it is necessary to pre-process every image and to use the set of images originating during the rotation of a telescope around the optical axis. For this processing, images of objects (line segments of various thickness values and various intensities) must be the same everywhere because they pertain to the same objects. Every image of an object will be displayed as a system of parallel line segments. The scanning device can be oriented so that all line segments would be parallel with one axis of an image.

To measure objects from the field of vision of a telescope, which is determined by the angle between the centre of an image and the edge of the parabolic strip, it is necessary to “trim” the line segments so that they would be reduced to the surroundings of the centre and then expand to the whole image. First, a number of images is scanned. Each of them is turned by an angle of θ . Then

the values from every image matrix are added up by columns, symmetrically around the centre $\pm n$ (multiplication of a matrix by vector \vec{e}) so that vector \vec{x}_k originates. Tensor multiplication of this vector by the all-ones matrix is executed so that we would obtain the final image \mathbf{Y}_k in the $m \times m$ form, where we have already achieved the desired shape. Image \mathbf{Q} results from the turning by an angle corresponding to the angle by which a telescope was turned. It is assigned a number and stored. The algorithm continues in this way until it reaches $\theta/360$ number of images, i.e., we have the images evenly spread.

2.1. Simulation Algorithm

To check the function, we first simulated images from a telescope corresponding to real pictures. We proceeded as follows: first, we produced a series of pictures of an object turned by multiples of angle θ and then we added up the intensities of the points of the images that are perpendicularly projected to the same point on individual straight lines turned by the angles passing through the centre. Thus, we obtained the vectors and by means of the tensor product of the vectors and all-ones matrix we will obtain a number of pictures corresponding to the simulated observations where points are displayed as segment lines. The model is first turned by the required angle of θ by means of interpolation in the MATLAB software. Then the image matrix is added up by columns so that vector \vec{x}_k results. Tensor multiplication of this vector by the all-ones matrix is executed. In this way, we obtain the final image \mathbf{Q} in the $m \times m$ form. The image is assigned a number and stored. The algorithm continues in this way until it reaches $\theta/360$ number of images.

$$\mathbf{X}_k \in \mathbf{R}^{m \times m} \quad (1)$$

$$\theta_1, \theta_2, \dots, \theta_N \in \langle 0, 2\pi \rangle \quad (2)$$

$$\mathbf{Y}_k = \text{rot}(\mathbf{X}_k, \theta_k) \quad (3)$$

$$\vec{x}_k = \vec{e}\mathbf{Y}_k, \quad \vec{e} = (1, \dots, 1) \in \mathbf{R}^m \quad (4)$$

$$\mathbf{Q} = \mathbf{Y}_k \quad (5)$$

2.2. Summation Algorithm

The summation algorithm is based on the principle of the reciprocal adding up of resulting projections. Intensities of the points that are covered by segment lines of individual images are accentuated by the summation of multiple images. The other points in lines can be removed by subtracting the matrix with constants in all the places. The value of the constants can be changed so that an image would become apparent.

$$\mathbf{X}_k \in \mathbf{R}^{m \times m} \quad (6)$$

$$\theta_1, \theta_2, \dots, \theta_N \in \langle 0, 2\pi \rangle \quad (7)$$

$$\vec{x}_k = \vec{e}\mathbf{X}_k, \quad \vec{e} = (0, \dots, 0, 1, \dots, 1, 0, \dots, 0) \in \mathbf{R}^m \quad (8)$$

$$\mathbf{Y}_k = f\vec{x}_k, \quad f = (1, \dots, 1)^T \in \mathbf{R}^m \quad (9)$$

$$\mathbf{Z}_k = \text{rot}(\mathbf{Y}_k, \theta_k) \quad (10)$$

$$\mathbf{Q} = \sum_{k=1}^N \mathbf{Z}_k \quad (11)$$

2.3. Radon Inverse Transform

The basic principle of a telescope is based on the Radon transform, however it is not possible to use the Radon inverse transform directly, especially because this algorithm does not always have a solution. Therefore its approximations are used. The process of reconstruction is hence based on the filtered back projection. This algorithm was originally designed for the reconstruction of an

image obtained from computed tomography

$$\mathbf{X}_k \in \mathbf{R}^{m \times m} \quad (12)$$

$$\theta_1, \theta_2, \dots, \theta_N \in \langle 0, 2\pi \rangle \quad (13)$$

$$\vec{x}_k = \vec{e}\mathbf{X}_k, \quad \vec{e} = (0, \dots, 0, 1, \dots, 1, 0, \dots, 0) \in \mathbf{R}^m \quad (14)$$

$$\mathbf{Y}_k = f\vec{x}_k, \quad f = (1, \dots, 1)^T \in \mathbf{R}^m \quad (15)$$

$$\mathbf{S}_k = \text{Ramplfilter} \mathbf{Y}_k \quad (16)$$

$$\mathbf{Z}_k = \text{rot}(\mathbf{S}_k, \theta_k) \quad (17)$$

$$\mathbf{Q} = \sum_{k=1}^N \mathbf{Z}_k \quad (18)$$

2.4. Multiplication Algorithm

The multiplication algorithm is an enhanced analogy to the summation algorithm. It is based on reciprocal multiplication of individual pre-processed matrices. The advantage is that if we have a zero (i.e., a dark point) in one matrix, the zero will remain in the resulting matrix when we execute the multiplication. High values in matrices and more complicated weighting of an image during the multiplication.

$$\mathbf{X}_k \in \mathbf{R}^{m \times m} \quad (19)$$

$$\theta_1, \theta_2, \dots, \theta_N \in \langle 0, 2\pi \rangle \quad (20)$$

$$\vec{x}_k = \vec{e}\mathbf{X}_k, \quad \vec{e} = (0, \dots, 0, 1, \dots, 1, 0, \dots, 0) \in \mathbf{R}^m \quad (21)$$

$$\mathbf{Y}_k = f\vec{x}_k, \quad f = (1, \dots, 1)^T \in \mathbf{R}^m \quad (22)$$

$$\mathbf{Z}_k = \text{rot}(\mathbf{Y}_k, \theta_k) \quad (23)$$

$$\mathbf{Q} = \prod_{k=1}^N \mathbf{Z}_k \quad (24)$$

2.5. Iteration Algorithm

The iteration algorithm is based on mutual multiplication of the final projections that proceeds in multiple steps. Images are decomposed to subsets. The subsets are multiplied and extracted until one image remains.

$$\mathbf{X}_k \in \mathbf{R}^{m \times m} \quad (25)$$

$$\theta_1, \theta_2, \dots, \theta_N \in \langle 0, 2\pi \rangle \quad (26)$$

$$\vec{x}_k = \vec{e}\mathbf{X}_k, \quad \vec{e} = (0, \dots, 0, 1, \dots, 1, 0, \dots, 0) \in \mathbf{R}^m \quad (27)$$

$$\mathbf{Y}_k = f\vec{x}_k, \quad f = (1, \dots, 1)^T \in \mathbf{R}^m \quad (28)$$

$$\mathbf{Z}_k = \text{rot}(\mathbf{Y}_k, \theta_k) \quad (29)$$

$$\mathbf{Q} = \prod_{k=1}^N \mathbf{Z}_k \quad (30)$$

2.6. Non Standard Observation Method

The telescope can be successfully used for the tracking that requires a good resolving ability in one direction. In this case it is not necessary to rotate the mirror around an axis and it is possible to use a standard parallactic assembly with the adjusting of an angle so that it would be possible to set the directions of the required resolving abilities. This type of tracking can be successfully used for example for some special observations executed to give accuracy to the movement of objects in one direction. The method is based on one of the properties of a mirror, i.e., that every point of light in the field of vision displays as a line segment the length of which equals to the width of a parabolic mirror. The centre of the line segment is shifted against the centre of an image by an angle which is the same as the angle by which a tracked object is shifted against the axis of a telescope. The line segments are perpendicular to the reflector plane. Ideally, each of the line segments has the same intensity in any point. If line segments of multiple points partially overlap or connect one to another, the position and luminance of individual points can be identified on the basis of an analysis of proportion of intensities of lines.

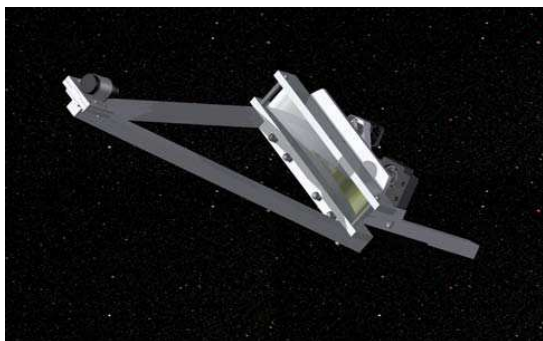


Figure 1: Parabolic strip telescope consists of a parabolic strip mirror, CCD camera in the image plane, supported by mounting.

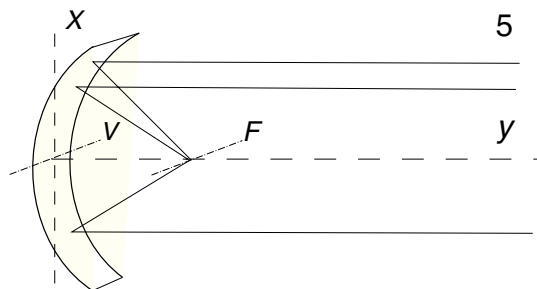


Figure 2: The paraxial beams 5 are reflected by strip on the focus line F , where V is the vertex line of the strip.

The intensities of the point sources along a line will jump grow at the beginning of a line segment and jump decrease at its end. Thanks to this, it is possible to reconstruct an image from the measurements of intensities. The ideal angular resolving ability in a point is lower in the direction of a line than in the direction perpendicular to it.

3. THE PROOF-OF-PRINCIPLE EXPERIMENT

In order to show that the principle works we have prepared a very basic experiment.

For the sake of simplification, the telescope was stationary. Figure 3 shows a parabolic strip telescope of a length of 30 cm. The artificial constellation was represented by means of a series of



Figure 3: The parabolic strips of length 30 cm, for the proof-of-principle experiment was used.

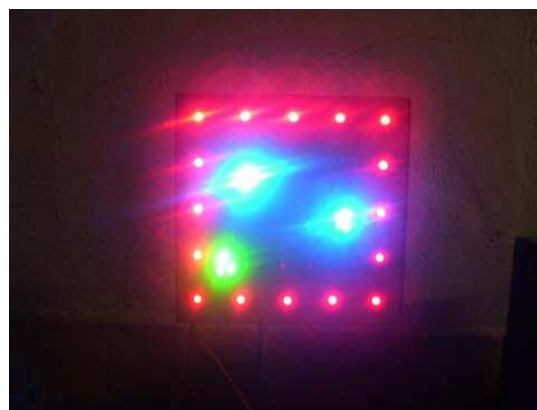


Figure 4: Two artificial constellations were used to demonstrate the principle.

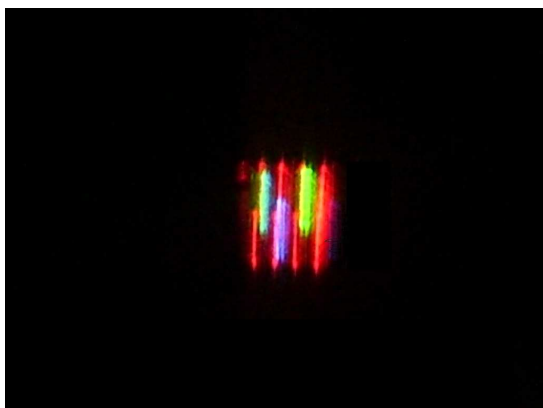


Figure 5: One of series of images from a camera.

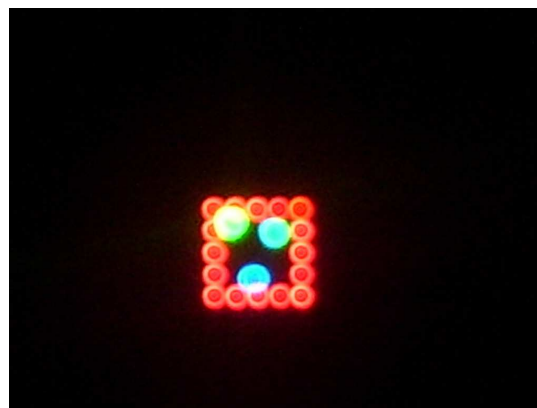


Figure 6: The image reconstructed from a series of pictures made with angular step of 5 degrees.

LED diodes. The artificial constellations used are shown in Figure 4.

The constellation was then rotated in steps by 5 degrees and the images were photographed by an ordinary digital camera. Figure 5 shows one of the photos. The reconstructed image is shown in Figure 6. For the image processing, Matlab was used.

The principle of the telescope was successfully tested. The resulting image can be compared with the reconstructed images in [8]. With higher quality components and more measurements at finer angle steps, the reconstructed image would be of better quality.

4. ADVANTAGES

- high mounting not being necessary,
- low wind influence,
- low gravitational influence.

5. CONCLUSIONS

The rotational telescope is a promising technology. It has a potential to supplement the existing types of telescopes used to observe the Universe. Although rotational telescopes are more complex in terms of their assembly and the processing of a final image, but contrary to standard reflectors, the mirror of this type of a telescope is much lighter and cheaper. This enables to construct telescopes with the primary optical element of a size of tens of meters, while the construction remains to be simple and production costs low. The ideal deployment of the telescope will be on an orbit where the size of mirrors could run to hundreds of meters and their resolving abilities will be sufficient for direct tracking of extra solar objects.

ACKNOWLEDGMENT

The support by the Ministry of Education of the Czech Republic pre-seed project has been acknowledged.

REFERENCES

1. Chadzitaskos, G., "Parabolic strip telescope," 2013, arXiv: astro-ph/1304.6530.
2. King, H. C., *The History of the Telescope*, Dover Publication, New York, 2003.
3. Crawford, Jr., F. S., *Berkeley Physics Course 3. Waves*, McGraw-Hill Book Co., New York, 1968.
4. ESO 2012, "The very large telescope," <https://www.eso.org/public/teles-instr/vlt.html>.
5. Herman, G. T., *Fundamentals of Computerized Tomography: Image Reconstruction from Projection*, 2nd Edition, Springer, 2009.
6. Jahne, B., *Digital Image Processing*, Springer-Verlag, 1995.
7. English, R. J., *Single-Photon Emission Computed Tomography: A Primer*, Publication of the Society of Nuclear Medicine, 1996.
8. Akram, W., et al., "Image processing using SPECT analysis," 1996, <http://www.clear.rice.edu/elec431/projects96/DSP/index.html>.
9. Chadzitaskos, G. and J. Tolar, CZ Patent 298313, 2007.
10. Chadzitaskos, G. and J. Tolar, *Proc. SPIE. 5487, Optical, Infrared, and Millimeter Space Telescopes*, 1137, 2004, doi: 10.1117/12.5546007, (arXiv: astro-ph/0310064).
11. Beylkin, G., *IEEE Transaction on Acoustics, Speech, and Signal Processing*, Vol. 35, No. 2, 162, 1987.

Frequency Tunable Antenna with Zeroth Order Resonator for UHF Near-field RFID Systems

Xiao-Dong Wei, Hong-Lin Zhang, and Bin-Jie Hu

School of Electronic and Information Engineering
South China University of Technology, Guangzhou, China

Abstract— This paper presents a frequency tunable antenna with epsilon negative (ENG) zeroth order resonator (ZOR) for ultra-high frequency (UHF) near-field radio frequency identification (RFID) systems. The ENG ZOR unit cell is composed of a toroidal inductor, a metal pin, a variable capacitor and an additional ground plane. The additional ground and the variable capacitor affect the shunt right-handed capacitance of the ENG ZOR unit cell. The measured resonant frequency of the antenna can be swept from 846 MHz to 1039 MHz by changing the capacitance of the variable capacitor. The measured maximum reading distance is 85 mm at 30 dBm input power. And the minimum input power for successful detecting of the near-field tag is -12 dBm, which is much lower than the conventional UHF near-field RFID reader antennas. The proposed antenna is suitable for UHF near-field RFID systems.

1. INTRODUCTION

The radio frequency identification (RFID) systems are widely used in tracking and detection objects in the past decades. Recently, ultra-high frequency (UHF) near-field RFID systems have gained much attention since they exhibit a better read rate for detecting objects surrounded by metals and/or liquids in their vicinity, such as drugs, bottles of water, clothes, and retail goods. The challenge to design a UHF near-field RFID antenna is to generate strong and uniform magnetic field in its interrogation zone.

Some UHF near-field loop antennas have been reported to generate strong and uniform magnetic field. A segmented loop antenna with lumped capacitor has been presented in [1] in order to generate strong and uniform magnetic field distribution. Some other techniques, such as distributed capacitor [2, 3], dash-line [4–6], dual-printed dipoles [7] and grid array antenna [8], are used to configure a UHF near-field loop antenna, the currents along the loop antennas are kept in-phase. Left-handed metamaterials (LHM) can be applied to designing UHF near-field RFID reader antenna [9]. Recently, zeroth order resonator (ZOR) antenna applications using artificial epsilon negative (ENG), mu negative (MNG), and double negative (DNG) composite right/left-handed transmission line (CRLH-TL) have been reported in [10–12]. But the impedance band width of those antennas are very narrow. So that the band width of the antenna designed using conventional ZOR technology cannot cover the entire UHF RFID frequency band.

In this letter, we present a frequency tunable UHF near-field RFID reader antenna using ENG ZOR for handheld devices. The ENG ZOR unit cell is composed of a toroidal inductor, a metal pin, a variable capacitor and an additional ground plane. By changing the capacitance of the variable capacitor, the shunt capacitance of the ENG ZOR unit cell can be changed, thus the resonant frequency of the antenna changed. The measured resonant frequency of the antenna can be swept from 846 MHz to 1039 MHz. And the maximum reading distance is 85 mm at 30 dBm input power. What's more, the maximum reading distance can still achieve 9 mm at -9 dBm input power. The antenna shows good performance in UHF near-field RFID systems.

2. ANTENNA STRUCTURE AND DESIGN

Figure 1 shows the configuration of the proposed antenna. The antenna is composed of a interdigital capacitor and an ENG ZOR unit cell. The ENG ZOR unit cell consists of a toroidal inductor, a metal pin, a variable capacitor and an additional ground plane. The additional ground plane is connected to the ground plane of the antenna through the variable capacitor. The antenna was fabricated on an FR4 substrate ($\epsilon_r = 4.7$, $\tan \delta = 0.2$, $h = 1$ mm). Figure 1(c) shows the equivalent circuit of the antenna. The capacitive effect between the top plane and the ground plane is modeled as C_G . The toroidal inductor provides the inductances of L_L . The interdigital capacitor is marked as C_0 . The capacitive effect between the toroidal inductor and the additional ground plane is marked as C_A . The capacitance of the variable capacitor is marked as C . The interdigital capacitor C_0 is used to match the antenna to 50Ω [12]. The parameters of the proposed antenna are as follows:

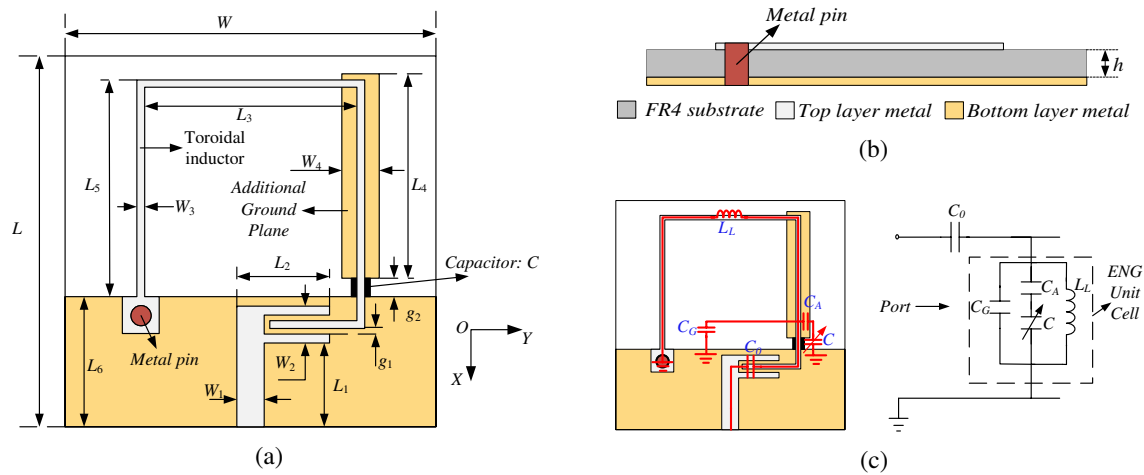


Figure 1: Configuration of the proposed antenna: (a) top view; (b) side view; and (c) equivalent circuit model.

$L = 20$ mm, $W = 20$ mm, $L_1 = 4.5$ mm, $W_1 = 1.5$ mm, $L_2 = 5$ mm, $W_2 = 2$ mm, $L_3 = 11.7$ mm, $W_3 = 0.4$ mm, $L_4 = 11$ mm, $W_4 = 2$ mm, $L_5 = 11.3$ mm, $L_6 = 7$ mm, $g_1 = 0.3$ mm, $g_2 = 1$ mm, $C = 1$ pF.

In order to better understand the performance of the proposed antenna and the effect of the parameters on the antenna performance, parametric studies are conducted. Only one parameter is varied at a time while the others are kept unchanged unless indicated.

Figure 2 plots the reflection coefficient of the proposed antenna at different values of L_5 . As can be seen, the resonant frequency of the antenna decreases from 0.98 GHz to 0.86 GHz while the value of L_5 increases from 9.7 mm to 12.7 mm. With the increasing of L_5 , the inductance of the toroidal inductor L_L increases, thus the resonant frequency decreases.

The capacitance of the variable capacitor (C) affects the shunt right-handed capacitance of the ENG ZOR unit cell. The shunt right-handed capacitance increases as C increases, thus the resonant frequency of the antenna decreases as can be seen from Figure 3. The simulated center frequency of the antenna can be tuned between 834 MHz to 1046 MHz.

Surface current distribution in the antenna plane is important for near-field analysis. Figure 4 shows the simulated current distribution of the proposed antenna at 904 MHz. It is observed that the current is in-phase along the toroidal inductor of the antenna. Such current distribution results in uniform and strong magnetic field distribution. Figure 5 shows a superposition of the simulated magnetic field distribution at the center frequency for different values of C . The input power is 30 dBm in the simulation. As can be observed, the magnetic field shape and strength are kept nearly constant over the tuning range. This means that the near-field performance of the antenna

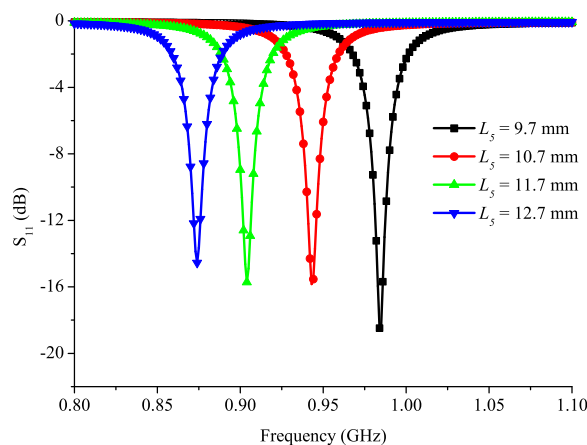


Figure 2: Simulated reflection coefficient of the proposed antenna for different values of L_5 .

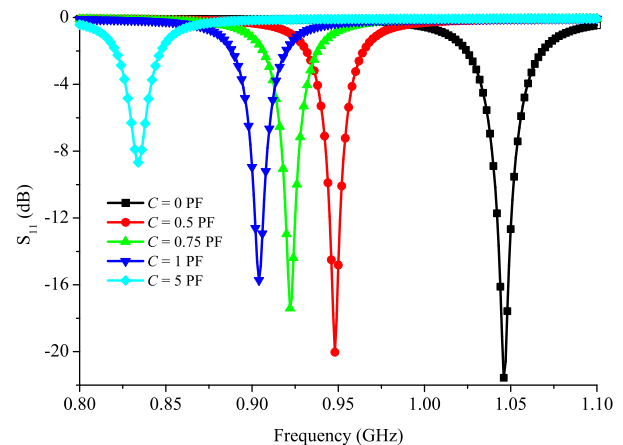


Figure 3: Simulated reflection coefficient of the proposed antenna for different values of C .

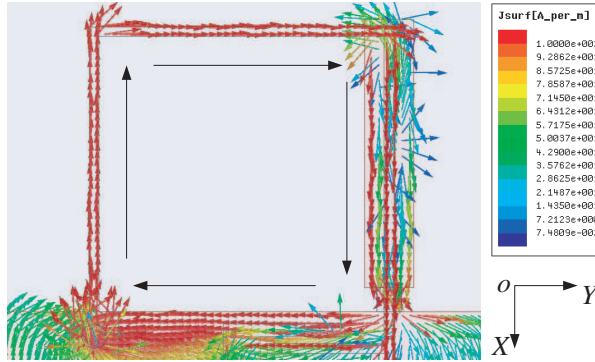


Figure 4: Simulated current distribution of the proposed antenna at 904 MHz.

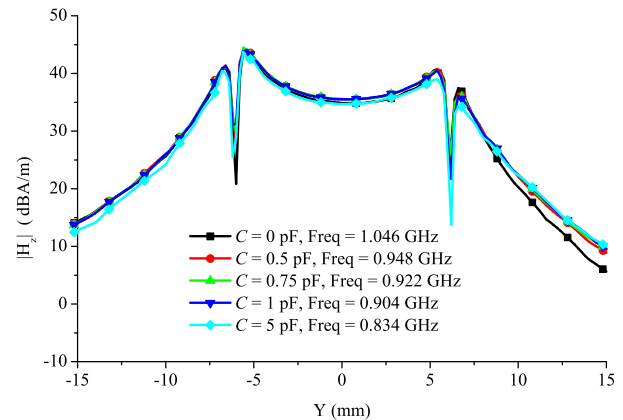


Figure 5: Simulated vertical magnetic field distribution of the proposed antenna along Y-axis.

is stable. The magnitude of the magnetic field in the center of the antenna is 35 dB(A/m) which is much stronger than the antennas in [5–8].

3. MEASUREMENTS AND RESULTS

The proposed antenna was fabricated and measured with the same dimensions as the simulated ones. The reflection coefficient ($|S_{11}|$) of the fabricated antenna was measured using Agilent E5071C network analyzer as shown in Figure 6. The measured resonant frequency can be varied from 846 MHz to 1039 MHz, which covers the entire UHF RFID frequency band. The measured results agree well with the simulated ones. The slight shift of $|S_{11}|$ is believed to be caused by the fabrication error and the accuracy error of the variable capacitor.

To further verify the near-field performance of the proposed antenna, the antenna was used as the reader antenna in a UHF near-field RFID system to detect near-field tags. The measurement configuration is shown in Figure 7. The antenna prototype was connected to the Impinj Speedway Revolution reader R220, with 30 dBm output power, to detect 25 Impinj button type tags (J41, 11 mm in diameter). The tags were positioned on an 80 mm \times 80 mm squar foam plate.

Figure 8 shows the measured reading rate of the antenna at different heights. As can be seen, the maximum reading distance is 85 mm which is about 48 mm higher than the antenna in [7]. And a 100% reading rate is achieved within the distance of 13 mm. The readable area is about 4 times larger than the area of the antenna.

Figure 9 shows the maximum reading distance at different input power for successful detecting of the tag. Because of the minimum out power of the reader is 10 dBm, an attenuator was used in the measurement. It is observed that the tag can be successfully detected while the input power is larger than -12 dBm. And the maximum reading distance can still achieve 9 mm at -9 dBm (0.126 mW) input power, which is very low input power. The antenna can be used in low-power

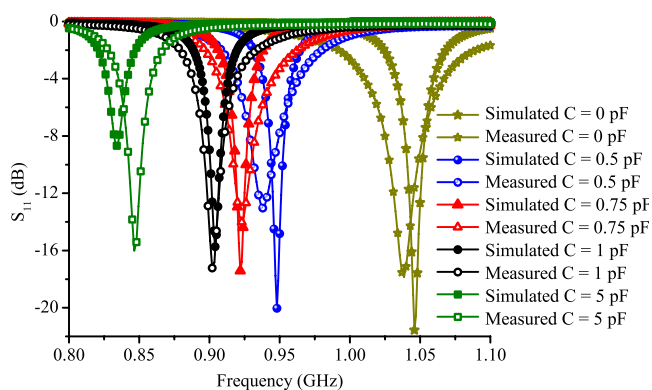


Figure 6: Simulated and measured reflection coefficient of the proposed antenna.

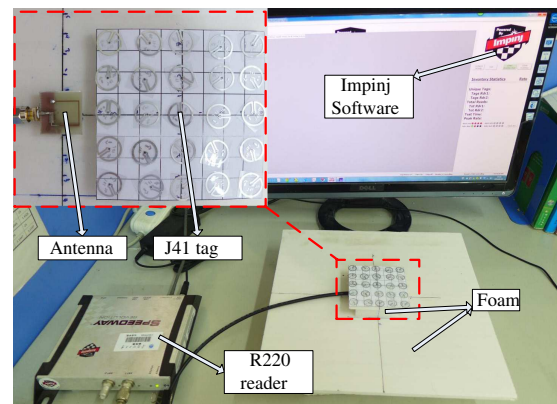


Figure 7: Near-field RFID measurement setup for the reading rang performance.

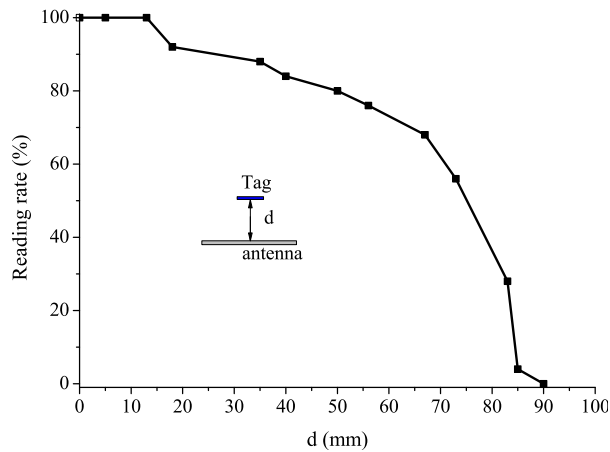


Figure 8: Measured reading rate of the proposed antenna at different heights.

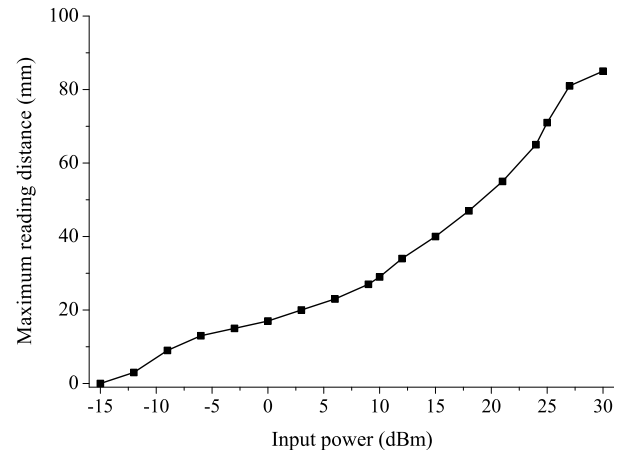


Figure 9: Maximum reading distance of the antenna at different input power.

consumption devices.

4. CONCLUSION

In this paper, a novel frequency tunable antenna with ENG ZOR for UHF near-field RFID systems is presented. The ENG ZOR unit cell is composed of a toroidal inductor, a metal pin, a variable capacitor and an additional ground plane. The variable capacitor is used to change the capacitance of the shunt capacitor of the ENG ZOR unit cell. The proposed antenna was fabricated and measured. By changing the capacitance of the variable capacitor, the measured resonant frequency of the antenna can be swept from 846 MHz to 1039 MHz. The measured results show that the maximum reading distance is 85 mm at 30 dBm input power. And the tag can still be successfully detected at very low input power. The antenna is suitable for UHF near-field RFID systems.

ACKNOWLEDGMENT

This work was supported by the NSFC-Guangdong under Grant No. U1035002, Guangdong-Hong Kong Key Project of Science and Technology under Grant Nos. 2011A011305001 and 2011A0113020 01, and University-Industry Key Project of Department of Education of Guangdong Province under Grant No. CGZHSD1102.

REFERENCES

1. Dobkin, D. M., S. A. Weigand, and N. Iyer, "Segmented magnetic, antennas for near-field UHF RFID," *Microw. J.*, Vol. 50, Jun. 2007.
2. Qing, X., Z. N. Chen, and C. K. Goh, "UHF near-field RFID reader antenna with capacitive couplers," *Electron. Lett.*, Vol. 46, 1591–1592, 2010.
3. Yong, S. O., X. Qing, C. K. Goh, et al., "A segmented loop antenna for UHF near-field RFID," *Antennas and Propagation Society International Symposium*, 1–4, Jul. 2010.
4. Qing, X., C. K. Goh, and Z. N. Chen, "A broadband UHF near-field RFID antenna," *IEEE Trans. Antennas Propag.*, Vol. 58, 3829–3838, 2010.
5. Li, X. and L. Cao, "Microstrip-based segmented coupling reader antenna for near-field UHF RFID applications," *Microw. Opt. Technol. Lett.*, Vol. 53, 1774–1777, Aug. 2011.
6. Jin, S., X. Qing, Z. N. Chen, et al., "Electrically large dual-loop antenna for UHF near-field RFID reader," *IEEE Trans. Antennas Propag.*, Vol. 61, 1019–1025, 2013.
7. Li, X. P. and Z. J. Yang, "Dual-printed-dipoles reader antenna for UHF near-field RFID applications," *IEEE Antennas Wireless Propag. Lett.*, Vol. 10, 239–242, 2011.
8. Shi, J., X. Qing, and Z. N. Chen, "Electrically large zero-phase-shift line grid-array UHF near-field RFID reader antenna," *IEEE Trans. Antennas Propag.*, Vol. 62, 2201–2208, Apr. 2014.
9. Borja, A. L., A. Belenguer, J. Cascon, et al., "A reconfigurable passive UHF reader loop antenna for near-field and far-field RFID applications," *IEEE Antennas Wireless Propag. Lett.*, Vol. 11, 580–583, 2012.
10. Lee, J. G. and J. H. Lee, "Zeroth order resonance loop antenna," *IEEE Trans. Antennas Propag.*, Vol. 55, 994–997, Mar. 2007.

11. Kim, J., G. Kim, W. Seong, et al., “A tunable internal antenna with an epsilon negative zeroth order resonator for DVB-H service,” *IEEE Trans. Antennas Propag.*, Vol. 57, 4014–4017, Dec. 2009.
12. Huang, J. Q. and Q. X. Chu, “Compact epsilon negative zeroth-order resonator antenna with higher radiation efficiency,” *Microw. Opt. Technol. Lett.*, Vol. 53, 897–900, Apr. 2011.

Electrical Lumped Model for Implemented RF-MEMS Capacitive Switch on Semi-suspended Coplanar-waveguide

Amin Khalili Moghaddam, Joon Huang Chuah, and Harikrishnan A/L Ramiah
 Department of Electrical Engineering, University of Malaya, Kuala Lumpur 50603, Malaysia

Abstract— A novel electrical lumped model for an RF MEMS capacitive switch which is implemented on a semi-suspended coplanar-waveguide is proposed and studied. The quality factor is mathematically studied taking the effects of air-gaps and substrate resistance into consideration. Results indicate that increasing the equivalent resistance of transmitting line and the switch, series resistance, in down-state has negative effect and can considerably decrease the quality factor. Increasing the capacitance of the switch also has a negative effect on the quality factor. Increasing the substrate resistance improves the quality factor. Lower capacitance can allow the switch to operate with a wider bandwidth of high quality factors and larger capacitance can make the bandwidth narrower.

1. INTRODUCTION

Micro-electro-mechanical systems (MEMS) are growing rapidly in the integrated and packaging device area especially for interfaces working with motion, light, thermic radiation, etc.. Furthermore, it offers incredible performance, high signal linearity, and low insertion loss for switches. Although they suffer from some minor drawbacks such as complexity, reliability issues, they operate with high quality factor with relatively small size [1]. PIN diodes, FETs switches cannot fulfil the expected performance for today's communication systems while MEMS switches can operate with great performance even with frequency above 100 GHz [2].

2. BACKGROUND REVIEW

In a MEMS switch an external effort is sometimes needed to stabilize the switch in “on” or “off” state. They can be used for many applications [3, 4]. Capacitive shunt switches are very suitable for wireless equipment since their power consumption and fabrication process are low and simple respectively. A capacitive shunt switch consists of a metal bridge (membrane) connected to RF ground moving in vertical direction. Without the electrical effort, the signal line is isolated from the metal bridge and it can pass through the switch. When the electrical effort is imposed, the metal bridge grounds the signal line. Figs. 1(a), (b), (c) depict the structure of a capacitive switch on a normal coplanar waveguide (CPW).

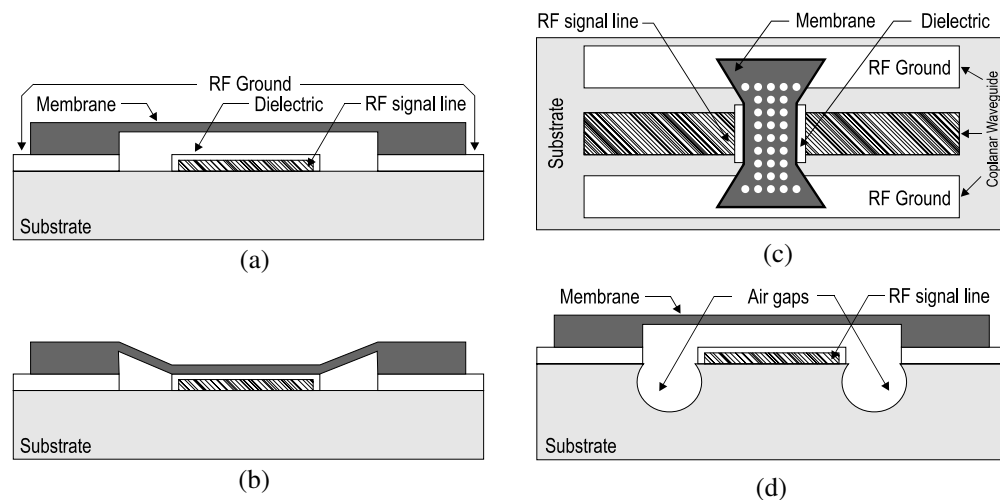


Figure 1: Structure of an RF-MEMS capacitive switch on normal CPW. (a) Up-state. (b) Down state. (c) Top plan view of the capacitive switch. (d) Structure of an implemented RF-MEMS capacitive switch on semi-suspended CPW [6].

3. MODELING AND METHODOLOGY

Normally, passive components degrade the efficiency but MEMS technology offers higher quality factor with less degradation. An electrical model is needed to for simulation with acceptable approximation. In [5] an electrical model was proposed and the study focused on quality factor including parasitic effects. A modified structure for RF-MEMS capacitive switch on semi-suspended CPW has been proposed in [6] (Fig. 1(d)). The switch had two air holes on two sides of the signal line. The study lacked proposing any electrical model for this structure. In this paper, the methodology of [5] is used to propose a novel electrical lumped model for the structure in [6].

According to the basic theory, the quality factor can be defined as [1]:

$$Q = \omega \frac{A_{es}}{L_{ss}} \quad (1)$$

where A_{es} is the average energy stored, L_{ss} is energy loss/second and ω is the operating frequency.

A physical discrete capacitor can be modeled with 3 basic electrical elements as L_s , C , R_s in series and L_s , C , R_p in parallel configuration which are depicted in Fig. 2. The impedance of the discrete capacitor is:

$$Z = R_s + j \left(\omega L_s - \frac{1}{\omega C} \right) \quad \text{for series} \quad Z = \frac{1}{\omega^2 C^2 R_p} + j \left(\omega L_s - \frac{1}{\omega C} \right) \quad \text{for parallel} \quad (2)$$

and the capacitor quality factor is $(1/\omega C R_s)$ and $\omega C R_p$ for series and parallel model respectively when $\omega L_s \ll 1/\omega C$.

The self-resonant f_0 occurs when $\text{Im}(Z) = 0$ and $f_0 = 1/(2\pi\sqrt{LC})$. Series inductance (L_s) has great effect on the capacitor impedance for higher frequency than f_0 [5].

An electrical model for a normal capacitive shunt switch is depicted in Fig. 2(c). This model is usually referred to as the T-model [1]. C , L , and R_s denote the effective variable capacitor, inductance of the switch, and series parasitic resistance of the suspended membrane respectively. The horizontal section of the T-model represents the 50Ω impedance matched of CPW (Z-line). The impedance of the line can be modelled by R_{sl} and L_{sl} [5]. Although this model is acceptable for predicting the quality factor, it fails to determine the quality factor for the frequencies lower than 10 GHz since the substrate effect of switch is not included.

Based on the T-model, the quality factor can be obtained [1]:

$$Q = -\frac{\text{Im}(Z_s)}{R_e(Z_s)} \quad (3)$$

where $Z_s = R_{sl} + j\omega L + (1/j\omega C) + R_s$. C can be in “up” or “down” state but in this paper down-state is studied. The resistance of the line and bridge are the culprits for the device loss [5] and the quality factor is a function of frequency causing the quality factor to rise to its peak and then drops to 0 [7].

Figure 3(a) shows an electrical lump model for the substrate of a normal capacitive shunt switch [5] but the physical description of the implemented switch on the semi-suspended CPW in Fig. 1(d) is slightly different. Fig. 3(b) is proposed to modify the electrical model for this switch since the effect of substrate and air-holes are included.

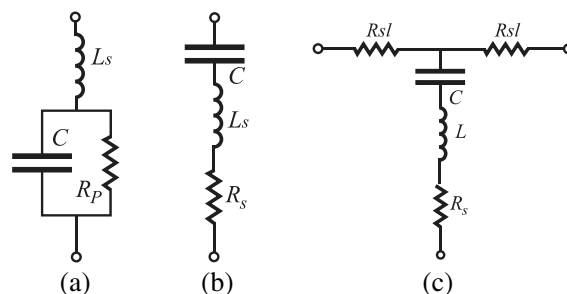


Figure 2: Electrical model for discrete capacitor in (a) parallel and (b) series configurations, (c) T-model for normal capacitive shunt switch [1].

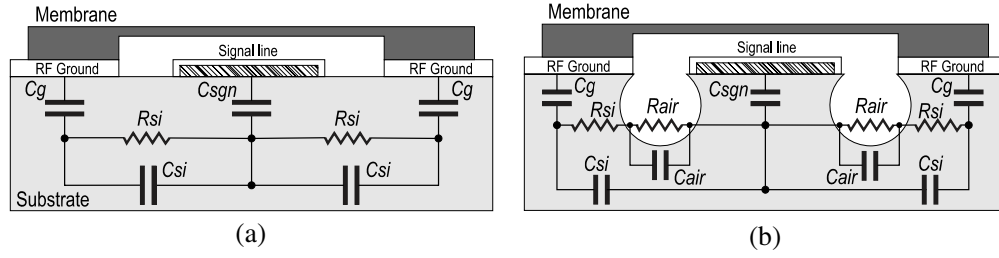


Figure 3: Electrical model for substrate of an implemented capacitive shunt switch on (a) normal CPW, (b) semi-suspended CPW.

A comparison between the normal structure and the new structure proposed in [6] shows that the only difference is the air gaps in the CPW which can be model as resistors (R_{air}) and capacitors (C_{air}) in parallel configuration. Therefore, the substrate has resistive and capacitive characteristics, and they are given by:

$$C_C = \frac{2C_g C_{sgn}}{2C_g + C_{sgn}} \quad (4)$$

where C_C is the equivalent capacitance of CPW. C_{sub} is $2C_{si}$ and represents the equivalent capacitance of substrate. R_{sa} is $(R_{air} + R_{si})/2$ and denotes the equivalent of both air and substrate resistances. Therefore, a complete lumped electrical model can be proposed and shown in Fig. 4. The highlighted section is equivalent circuit of the substrate effect. The two R_{air} are added to the circuit to model the two holes in the substrate while (C_{air}) is negligible.

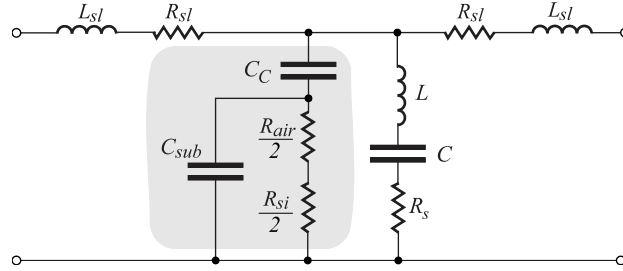


Figure 4: Proposed lumped electrical model for an RF-MEMS capacitive switch on semi-suspended CPW.

Characteristics of the added parallel section can be determined by $f_{zero} = 1/(2\pi(C_C + C_{sub})R_{sa})$ and $f_{pole} = 1/(2\pi C_C R_{sa})$.

In the frequency range $f_{zero} < f < f_{pole}$ the equivalent resistance of substrate (R_{sa}) shunts the MEMS capacitor. In this condition, the joint effect of series and shunt resistors cause the overall device loss, e.g. the quality factor is determined by shunt losses at low frequency but higher than f_{zero} while at higher frequency, it is determined by the effect of series parasitic resistance ($R_{series} = R_{sl} + R_s$). The inductive parasitic and the capacitive effects of substrate are negligible. The two sub-quality factors are $Q_{series}(\omega) = 1/(\omega C R_{series})$ and $Q_{shunt}(\omega) = \omega C R_{sa}$. Hence, the total device quality factor is:

$$Q_{SW}(\omega) = Q_{shunt}(\omega) || Q_{series}(\omega) \Rightarrow Q_{SW}(\omega) = \frac{\omega C R_{sa}}{1 + \omega^2 C^2 R_{sa} R_{series}} \quad (5)$$

and the maximum of quality factor in down-state happens when $\omega = \omega_P$:

$$Q_P = Q_{SW}(\omega_P) = \left(\frac{1}{2}\right)^{\frac{3}{2}} \sqrt{\frac{(R_{si} + R_{air})}{R_{series}}} \quad (6)$$

4. RESULT AND DISCUSSION

Figure 5 represents the performance of the switch over 1–50 GHz by assuming the physical parameters in [5] as $C = 1.8$ pF, $L = 170$ pH, $R_s = R_{sl} = 275$ m Ω and $R_{sa} = 1.4$ k Ω .

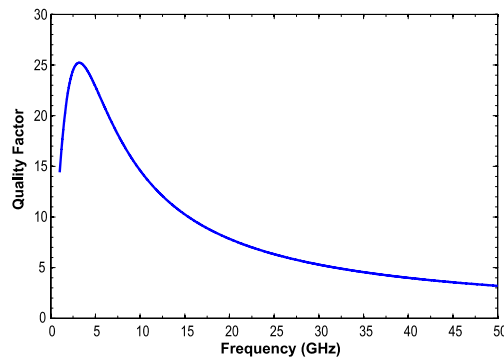


Figure 5: Fluctuation of the quality factor over frequency.

R_{series} is the main cause of power loss in the line [8]. Fig. 6 shows the effect of R_{series} on the quality factor. The effect is noticeable in the range of $0.2\text{--}0.8\ \Omega$. It also indicates that R_{series} is expected to be as small as possible for operating in high frequency region.

The equivalent resistance of substrate is $R_{sa} = (R_{air} + R_{si})/2$ where R_{si} is resistance of the high resistive silicon. Fig. 7 illustrates the effect of R_{sa} on the quality factor. Increasing the R_{sa} improves the quality factor especially in the lower operating frequency region. R_{sa} also determine the value of maximum quality factor but the frequency of maximum quality factor is independent of R_{sa} .

The value of the switch capacitance in the down-state plays a great role in the switch performance since it is one the influential factors in the isolation [9]. Fig. 8 shows the effect of down-state capacitance. Increasing the C can improve the quality factor in the lower frequency region. The value of the maximum quality factor is independent of C . In addition, the bandwidth of the switch is wider for smaller capacitance comparing to larger capacitance.

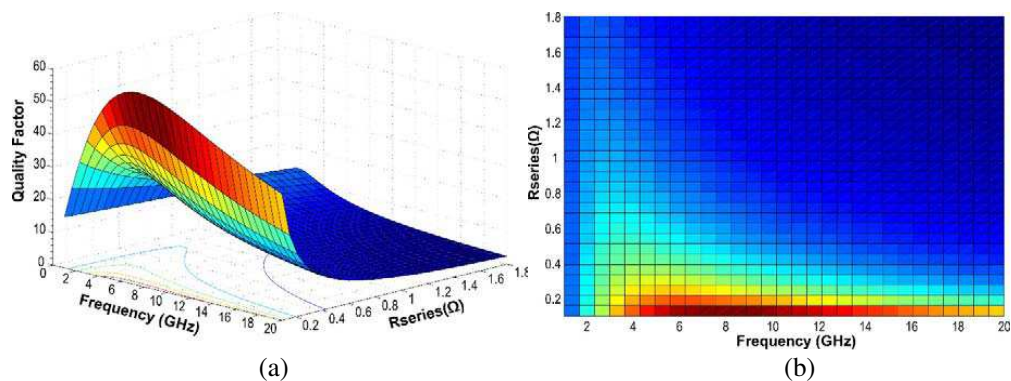


Figure 6: Effect of R_{series} on the quality factor over frequency.

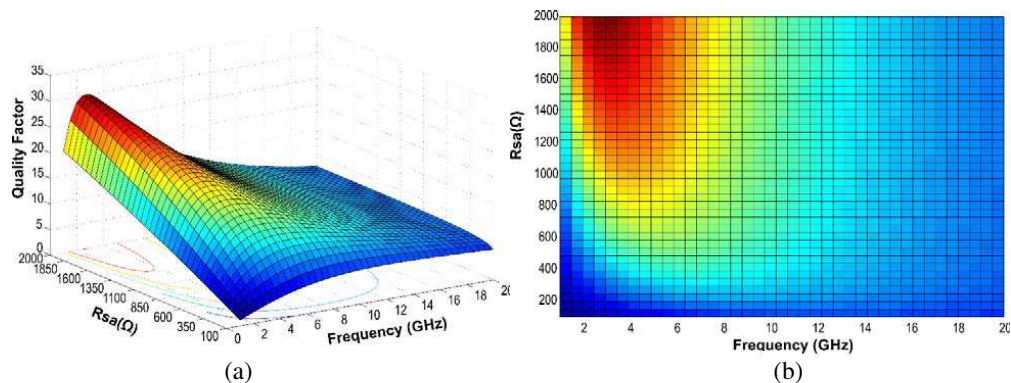


Figure 7: Effect of R_{sa} on the quality factor over frequency.

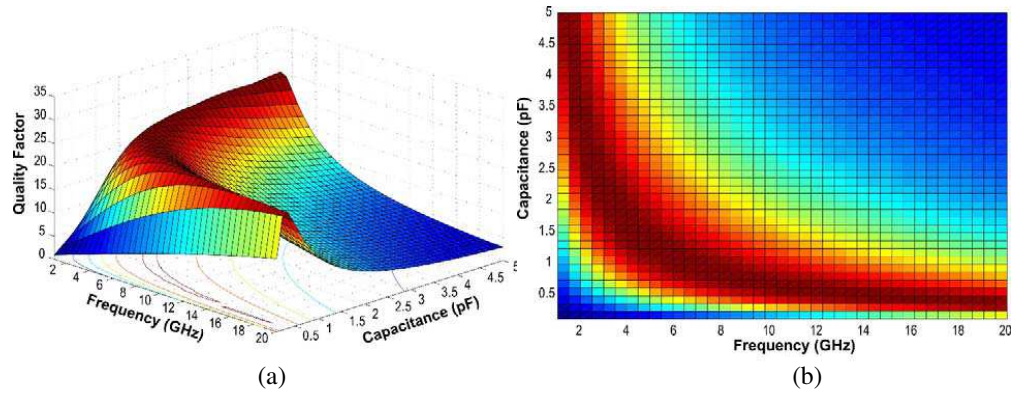


Figure 8: Effect of C on the quality factor over frequency.

5. CONCLUSION

A new lumped electrical model for RF-MEMS capacitive switch is presented for implemented switch on semi-suspended CPW. An equation for calculating the quality factor is derived. The resistance of T-line and bridge has negative effect on the quality factor while increasing the substrate resistance can improve the quality factor. The capacitance of the switch in down-state does not have any effect on the maximum quality factor amplitude while it has a great role in determining the maximum quality factor frequency. It also has noticeable effect on the bandwidth the switch.

ACKNOWLEDGMENT

This research is supported by the UM High Impact Research Grant UM.C/HIR/MOHE/ENG/51 from the Ministry of Higher Education Malaysia. Thanks are extended to Microelectronics Lab at the Department of Electrical Engineering, University of Malaya.

REFERENCES

1. Bao, M., *Analysis and Design Principles of MEMS Devices*, Elsevier, Amsterdam, 2005.
2. Rebeiz, G. M., *RF MEMS: Theory, Design, and Technology*, Wiley, 2004.
3. Mowler, M. and B. Lindmark, "Reconfigurable MEMS antenna for wireless applications," *First European Conference on Antennas and Propagation, 2006, EuCAP 2006*, 1–6, 2006.
4. Besoli, A. G. and F. De Flaviis, "A multifunctional reconfigurable pixelated antenna using MEMS technology on printed circuit board," *IEEE Transactions on Antennas and Propagation*, Vol. 59, 4413–4424, 2011.
5. Cusmai, G., et al., "A simple lumped electrical model for an RF MEMS switch considering lossy substrate effects," *Sensors and Actuators A: Physical*, Vol. 123–124, 515–521, 2005.
6. Fernández-Bolaños, M., et al., "RF MEMS capacitive switch on semi-suspended CPW using low-loss high-resistivity silicon substrate," *Microelectron. Eng.*, Vol. 85, 1039–1042, 2008.
7. Jansman, A. B. M., et al., "Elimination of accumulation charge effects for high-resistive silicon substrates," *33rd Conference on European Solid-State Device Research, 2003, ESSDERC'03*, 3–6, 2003.
8. Muldavin, J. B. and G. M. Rebeiz, "High-isolation CPW MEMS shunt switches. 1. Modeling," *IEEE Transactions on Microwave Theory and Techniques*, Vol. 48, 1045–1052, 2000.
9. Rebeiz, G. M. and J. B. Muldavin, "RF MEMS switches and switch circuits," *IEEE Microwave Magazine*, Vol. 2, 59–71, 2001.

Edge Effects in a Strongly Coupled Dipole Element Array in Triangular Lattice

C. I. Kolitsidas and B. L. G. Jonsson

Electromagnetic Engineering, School of Electrical Engineering

KTH Royal Institute of Technology, Sweden

(Invited Paper)

Abstract— In this work the focus is on the impact of edge effects in the equilateral triangular lattice of a strongly coupled dipole antenna array. A novel wideband strongly coupled, single polarized, dipole element is designed and studied in a triangular grid. The antenna element operates in 6 : 1 bandwidth ratio. Our analysis for the edge effects is based the finite \times infinite approach with multiple rows taken into account in order to capture the effects on the different edges that appear in triangular grids. The effects at the E-edge are studied as it is the plane where the currents are truncated. At the E-edge the variation on the behavior is mainly due to lack of closely coupling fields. Using the finite \times infinite approach the variations along the E-edge of the array are studied for both rectangular and triangular grid. Finally, periodic resistive loading was used on the dipoles to dissipate the waves produced from the edges and smooth the impedance behavior along the array row.

1. INTRODUCTION

Wideband antenna arrays for wireless communications is a topic that has attracted a lot of interest over the last few decades. Future wireless base stations are envisioned to support all commercially available bands. Furthermore, it is expected to offer advanced coverage characteristics, like dedicated user beams. It is the path towards implementing a multi-user multiple input multiple output (MU-MIMO) system for commercial applications. This generates the need for a wideband and wide-scan antenna array suitable for base station applications.

Over the last decade, a new class of wideband antenna array systems has been developed that is able to utilize strong inter-element coupling. Their ability to operate in such large bandwidth comes from the fact that the array allows almost continuous currents that results in greater operational bandwidths. It is the implementation of the Wheeler's concept of current sheet array [1], and it has developed into two major wideband antenna array technologies: The capacitively coupled dipoles [2], and connected dipoles/slots [3]. It was shown [2], that these elements are able to provide wideband (5 : 1) performance while keeping a relatively low profile ($d \approx \lambda_{high\ freq}/2.5 - \lambda_{high\ freq}/3$, d is the distance from the ground plane to the radiating structure). It is an attractive approach with the possibility for communication applications. In the case of base station application this type of array can be an ideal candidate and due to the limited space at the base station the mid-sized array is in need to be investigated.

An important factor that appears during the finite array design procedure is the performance variations of the elements with respect to their position in the array. These variations are mainly caused by the "edge effects" in the finite array. Thus it is expected that the outer elements in the finite array will have degraded performance when compared with the central array elements. Another important factor that impacts the scanning performance of the array is the array lattice selection. An eigen current approach was used in [4] to capture the edge effects on a finite array. A study for edge element evaluation at tapered slot antennas placed in triangular grid was conducted in [5]. Here, it is worth mentioning that tapered slot antennas also rely on strong interelement coupling to eliminate undesired structural resonances and achieve wideband performance. The size of the array needed in order to behave close to the unit cell analysis was the outcome of the study in [6].

In our previous studies, we have investigated the inter-element coupling [7], to enhance bandwidth performance and edge elements optimization [8], in order to compensate truncation effects at the edge elements. Recently, a general measure of the performance of planar arrays backed by a metallic reflector was derived: The array figure of merit [9]. It provides the possibility to connect physical and electrical characteristics that result in a measure of the arrays performance. In its simple form contains the distance (d) from the ground plane as the main physical characteristic which is the limiting factor of unidirectional planar arrays.

In the present work the edge effects at the E-edge of strongly coupled dipole with capacitive loading array will be studied. A comparison between the behavior in rectangular and triangular grids is made for low and high impedance loading on each element. The impedance loading is used to dissipate the waves from the edges and create a smooth active input impedance variation.

2. UNIT CELL DESIGN AND ARRAY CONFIGURATION

The geometry of the unit cell design of closely spaced dipoles is depicted in Fig. 1. The dipole has been capacitively loaded with a small inter-element gap $2 \cdot \delta$, where $\delta = 0.6$ mm, and an additional parasitic patch in the back of the dipole between the arms as can be seen in Fig. 1(c). The small gap in between the elements significantly increases the inter-element coupling between the adjacent dipole arms. The capacitive loading of the dipole is depicted as schematic in Fig. 1(d). The latter is required to counteract the inductive behavior of the ground plane as is indicated in [2, 7]. Furthermore the height between the dipoles and the ground plane is chosen to be $\lambda_{high\ freq}/2.5$ in order to avoid a zero in the broadside direction at the high end of the frequency band. Also, in order to increase the bandwidth towards the lower end of the frequency band we have loaded the dipole arms with a T-slot increasing the current path. The dipole is fed by a balanced co-planar strip line ($s = 0.3$ mm $C_l = 2$ mm) which is tapered to a wide microstrip line ($w = 11$ mm, $l = 9.52$ mm). For the T-slot the dimensions are: $w_{T1} = 2$ mm, $w_{T2} = 2$ mm and $T_l = 8$ mm. The unit cell dimensions are chosen $\lambda_{high\ freq}/2$ in order to be below at the grating lobe limit for the fundamental Floquet mode. The dipole is designed in Rogers RO4003 ($\epsilon_r = 3.55$, $\tan \delta = 0.0027$ & $h = 1.52$ mm) printed circuit board (PCB). Finally, the dipole is loaded with a WAIM (Wide Angle Impedance Matching) layer ($\epsilon_r = 2$) that improves bandwidth and scanning performance. The feeding of the array element will be completed with a commercial BalUn/4 : 1 impedance transformer from an unbalanced CPW (Co-Planar Waveguide) to a balanced CPS (Co-Planar Strips) line. The behavior of the VSWR of the array's unit cell is depicted in Fig. 2(a) where we can observe that the operational bandwidth of the array is 6 : 1 ratio. In Fig. 2(b) is depicted the computational domain used to evaluate the E-edge effects. We have applied periodic boundary conditions on two rows of the array to capture the E-edge effects. The analysis have been carried out on CST Microwave Studio [10].

The active reflection coefficient $\Gamma(\psi_x, \psi_y)$ of the unit cell takes into account all coupling phenomena that occur in the array. For a given planar rectangular lattice under Floquet excitation is given as in [11]:

$$\Gamma(\psi_x, \psi_y) = \sum_{n=-\infty}^{\infty} S_{mn} \exp \left[-j \left(\frac{d_x(m, n)\psi_x}{a} + \frac{d_y(m, n)\psi_y}{b} \right) \right] \quad (1)$$

where all scattering parameters S_{mn} contribute to the final active reflection coefficient. In detail, ψ_x and ψ_y are the phase differences between the adjacent elements, in our case $a = b = d$ and $d_x(m, n)$, $d_y(m, n)$ are the relative distances along the x and y direction between the m th and n th element. From the active reflection coefficient of each element in the array the active impedance can be extracted. This is used to evaluate the impedance variations along the E-edge.

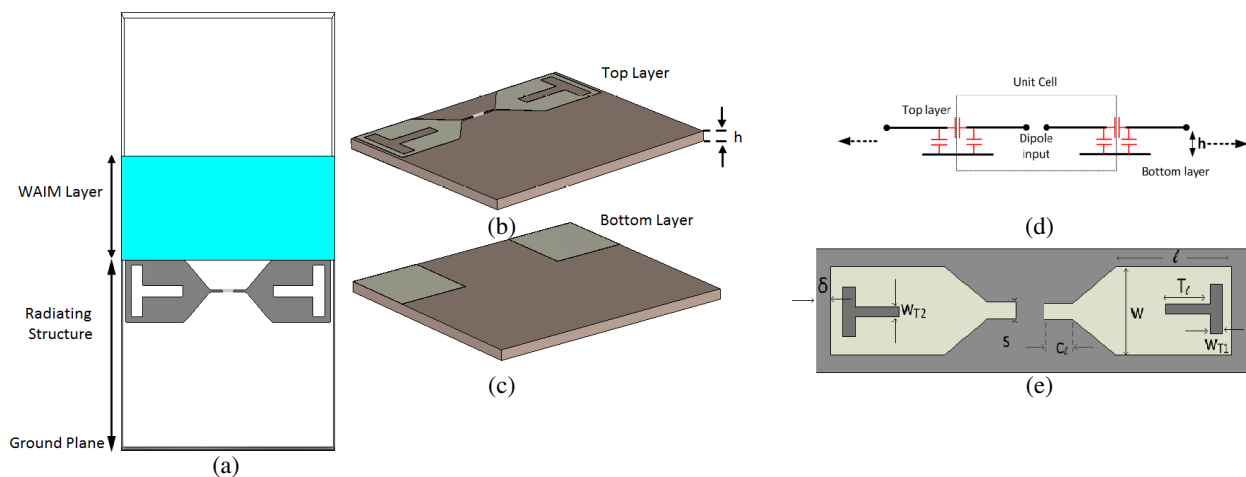


Figure 1: (a) Array unit cell with T-slot loaded dipole and WAIM. (b) Top layer. (c) Bottom Layer. (d) Capacitive dipole loading. (e) Element with corresponding dimensional variables.

3. ANALYSIS OF TRUNCATION AND PERIODIC RESISTIVE LOADING

The final current at each element on the finite array is the current from the unit cell analysis with a perturbation current that will be generated from the diffraction of the field at the edges. The edge effects have also been described with a heuristic Gibbsian model [12]. This perturbation on the current at each element will have an impact at the active input impedance of each element. Using the finite \times infinite approach it is possible to isolate the behavior of each edge separately. In this analysis we are focused on the E-edge behavior and the analysis is based on a 12 element linear array, electrical length of $6 \cdot \lambda_{high\ freq}$, that is placed on a rectangular and equilateral triangular lattice. In the case of the triangular grid two rows have been used of the linear array as the computational space (Fig. 2(b)). In order for the finite array to operate as the unit cell we must have as less impedance variations as possible. As part of the analysis two different load impedances have been used, one at 150 Ohms and one at 377 Ohms. The first load impedance offers maximum usable bandwidth on the array element and the second is chosen according to [13] which states that periodic high impedance loading of the array the waves that are produced from the edge effects can be dissipated. This concept is applied here for the first time in a triangular lattice and compared with the behavior of the rectangular lattice.

In Fig. 3(a), the results for the active input impedance with the 150 Ohm load are depicted for the frequency of 3 GHz, whereas at Fig. 3(b) are depicted the for the 377 Ohm active input impedance at the same frequency. It is observed that there is small difference between the two grids when the load is 150 Ohm but the triangular grid has smoother variation when the load

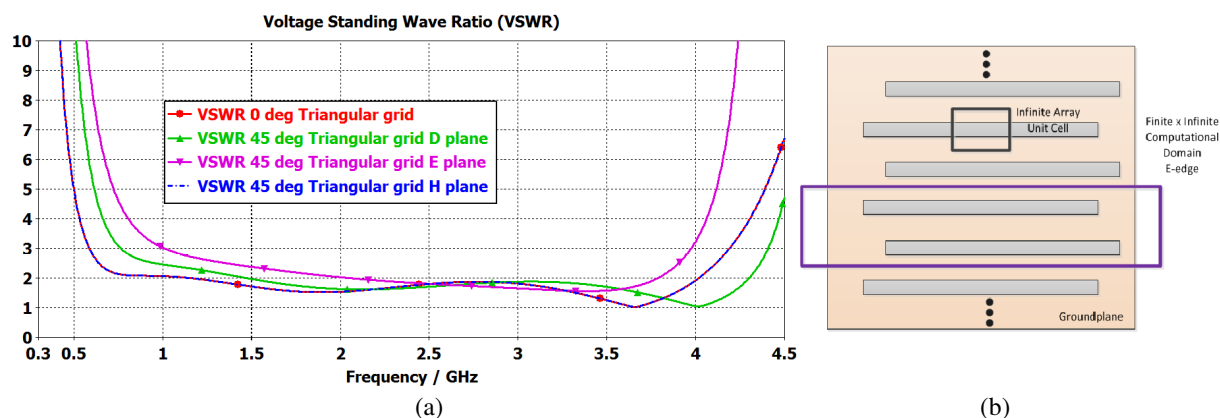


Figure 2: (a) Active VSWR for different scan angles of the array unit cell placed in a triangular lattice. (b) E-edge computational domain with finite \times infinite approach.

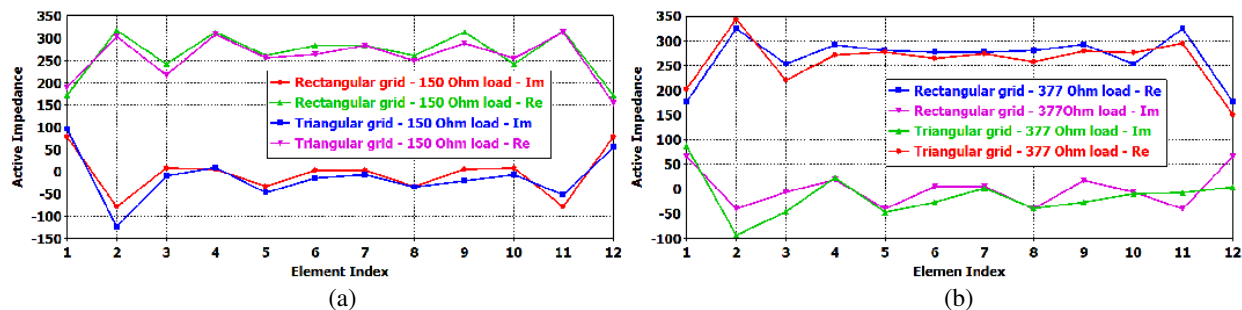


Figure 3: Active impedance of the elements at 3 GHz with finite \times infinite approach comparison of equilateral and rectangular lattice (a) with 150 Ohm loading and (b) 377 Ohm loading for periodic dissipation of edge effects.

Table 1: Root mean square error.

150 Ohm loading				377 Ohm loading			
Real		Imaginary		Real		Imaginary	
Rect.	Triang.	Rect.	Triang.	Rect.	Triang.	Rect.	Triang.
28.02%	26.28%	18.29%	16.55%	13.90%	18.11%	23.99%	23.71%

impedance changes to 377 Ohm. Also, if one compares the behavior of the two load impedances, it is clear that the high load impedance has better — more smooth behavior, especially at the 8 central dipoles. A summary with the root mean square error of the two configurations can be found on Table 1. The dissipation of edge generated waves with high impedance comes at the cost of the operational bandwidth shrinkage. This happens, as the matching impedance that is used is the peak of the real part of the strongly coupled dipole and not close to the mid point of 150 Ohms.

4. CONCLUSION

This work is focused on the impact of edge effects in the equilateral triangular lattice of a strongly coupled antenna array. A novel wideband strongly coupled, single polarized, dipole element is designed and studied in a triangular grid. The antenna element operates in 6 : 1 bandwidth ratio. Our analysis for the edge effects is based the finite \times infinite approach with multiple rows taken into account in order to capture the effects on the different edges that appear in triangular grids. The effects at the E-edge are studied for both rectangular and triangular grid and compared. A periodic resistive loading on the dipoles was used to dissipate the waves produced from the edges and smooth the impedance behavior along the array row. These results are compared with the case without resistive loading. This final approach produced improved results for the triangular grid but with the penalty of operational bandwidth shrinkage.

ACKNOWLEDGMENT

This work was financially supported by The Swedish Governmental Agency for Information Systems (VINNOVA) within the VINN Excellence center, Chase stage III through the research project Next Generation Antenna Arrays.

REFERENCES

1. Wheeler, H., "Simple relations derived from a phased array antenna made of an infinite current sheet," *IEEE Trans. on Antennas and Propag.*, Vol. 13, No. 4, 506–514, Jul. 1965.
2. Munk, B. A., *Finite Arrays and FSS*, Wiley-Inter-Science, New York, 2003.
3. Neto, A., D. Cavallo, G. Gerini, and G. Toso, "Scanning performances of wide band connected arrays in the presence of a backing reflector," *IEEE Trans. on Antennas and Propag.*, Vol. 57, No. 10, 3092–3102, Oct. 2009.
4. Bekers, D. J., J. L. Eijndhoven, and A. G. Tijhuis, "An eigencurrent approach of finite arrays of electromagnetically characterized elements," *Radio Sci.*, Vol. 44, RS2S90, 2009.
5. Ellgardt, A. and M. Norgren, "A study of edge effects in triangular grid tapered slot arrays using coupling coefficients," *Radio Sci.*, Vol. 4, RS2005, 2010.
6. Holter, H. and H. Steyskal, "On the size requirement for finite phased array models," *IEEE Trans. on Antennas and Propag.*, Vol. 50, No. 6, 836–840, Jun. 2002.
7. Kolitsidas, C. I. and B. L. G. Jonsson, "Investigation of compensating the ground plane effect through array's interelement coupling," *Proceedings of 7th European Conference on Antennas and Propagation (EuCAP)*, 1221–1224, Gothenburg, Sweden, Apr. 2013.
8. Kolitsidas, C. I. and B. L. G. Jonsson, "A study of partial resonance control for edge elements in a finite array," *PIERS Proceedings*, 253–256, Stockholm, Sweden, Aug. 12–15, 2013.
9. Jonsson B. L. G., C. I. Kolitsidas, and N. Hussain, "Array antenna limitations," *IEEE Antennas and Wireless Propagation Letters*, Vol. 12, 1539–1542, 2013.
10. CST *Microwave studio*[®], 2012.
11. Bhattacharyya, A. K., *Phased Array Antennas*, Wiley-Inter-Science, New York, 2005.
12. Hansen, R. C. and D. Gammon, "A Gibbsian model for finite scanned arrays," *IEEE Trans. on Antennas and Propag.*, Vol. 44, No. 2, 243–248, Feb. 1996.
13. Neto, A., D. Cavallo, and G. Gerini, "Edge-born waves in connected arrays: A finite \times infinite analytical representation," *IEEE Trans. on Antennas and Propag.*, Vol. 59, No. 10, 3646–3657, Oct. 2011.

The Multiple Periodic Structure Antenna Design

Z. L. Ma, L. J. Jiang, S. Gupta, and W. E. I. Sha

Department of Electrical and Electronic Engineering, The University of Hong Kong, Hong Kong, China

Abstract— In this paper, the generalized analysis and novel application of the multiple periodic (MP) structure are proposed. Both transmission and radiation performances of one dimensional MP structures are studied. The dispersion relations are analyzed from both layered media (distributive) and lumped circuits aspects. Regarding each aspect, both non-dispersive (conventional) and dispersive (composite right/left-handed (CRLH)) materials are discussed. It is found that with the increase of the periodicity, multiple stopbands are open up due to the reflections. Meanwhile the space harmonic modes' separation distance is reduced in the dispersion diagrams. It leads to simultaneously dualistic (right- and left-handed) radiation performance and multi-beam property, and more abundant radiation modes are excited at relatively lower frequencies comparing with conventional periodic structures. A general dispersion relation formula and a general Bragg condition for MP structures are derived. The dispersion relation is simply described by the former, and the latter helps to indicate the stopbands locations and engineer the dispersion relation consequently. Applications of MP structures to phase reversal (PR) antennas are also presented in this paper. They experimentally verifies both transmission and radiation characteristics of MP structures. In each analysis, single (SP), double (DP) and triple periodic (TP) structures are presented and compared. This work would also contribute to designs of multi-band devices.

1. INTRODUCTION

In past decades, periodic structures were widely applied in both optics and microwave areas. In optics, the characteristics of dielectric layered media are studied [1]. While, in microwave fields, a large number of studies are conducted on both dispersive (composite right/left-handed (CRLH)) and non-dispersive (conventional) materials. Their leaky-wave radiation properties are also investigated [2–4]. However, most research works are focused on the conventional single periodic structures.

In this paper, we generalize the multiple periodically (MP) loaded structure analysis. Unified characterization of both transmission and radiation performances for both non-dispersive (conventional) and dispersive (CRLH) MP structures are presented. This work aims to explore the general property variations due to increasing periodicities that could be arbitrary (multiple). MP phase reversal (PR) antennas are presented in this paper as one application of the proposed concept. The transmission and radiation properties are examined. It is found that MP PR antennas support simultaneous forward and backward radiations and multiple radiation beams. We know that the indoor wireless link has some intrinsic effects would affect the link quality, such as multipath and mutual interference effect. One effective solution from physical layer perspective for it is to adopt multi-beam directional antenna. Therefore, the MP PR antenna can be a candidate for indoor wireless system or other multi-beam required applications. On the other hand, this work reveals the increasing number of stopbands and passbands. Therefore it also gives a strong support for various multi-band component designs.

2. THEORY

Figure 1(a) is an illustration of a typical MP structure, where each supercell consists of several different unit cells (UCs). The supercell periodically repeats along one dimension. All UCs and supercells are connected in series. The physical length of each UC is p .

2.1. Non-dispersive and Dispersive Media

For non-dispersive layered media, each UC has different refractive indices, n_1, n_2, \dots, n_m . Based on the matrix theory, the transmission matrix can be written by the product of individual UCs' transmission matrices.

$$\begin{bmatrix} A & B \\ C & D \end{bmatrix} = \prod_{m=1}^M \begin{bmatrix} A_m & B_m \\ C_m & D_m \end{bmatrix} = \prod_{m=1}^M \frac{1}{2n_{m+1}} * \begin{bmatrix} (n_{m+1} + n_m)e^{-j\varphi_m} & (n_{m+1} - n_m)e^{j\varphi_m} \\ (n_{m+1} - n_m)e^{-j\varphi_m} & (n_{m+1} + n_m)e^{j\varphi_m} \end{bmatrix} \quad (1)$$

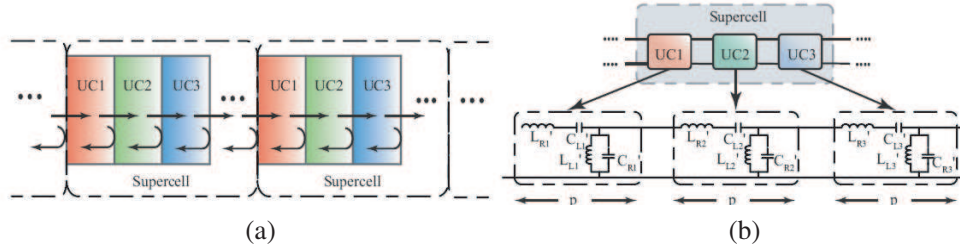


Figure 1: (a) MP structure illustration and (b) equivalent circuit model for CRLH (dispersive) layered media.

where M is the total number of UCs in each supercell, and the phase change in one UC is $\varphi_m = n_m k_0 p$. m denotes UC index. k_0 is the wave vector of free space. According to the Bloch-Floquet theorem, we can obtain the dispersion relation

$$\cos \phi = \frac{A + D}{2} \quad (2)$$

where $\phi = \beta M p$ is the phase change in one supercell. β is the phase constant of the supercell. Using derivations shown above, we derive the dispersion relation for an arbitrary MP structure in a general format,

$$\cos \phi = \frac{1}{2^{(M+1)} \prod_{i=1}^M n_i} \sum_{i=1}^{2^M} \left\{ \left(\prod_{j=1}^M S_i(j) \right) \left[\prod_{j=1}^M (n_j S_i(j) + n_{j+1} S_i(j+1)) \right] \cos(\bar{\varphi} \cdot \bar{S}_i) \right\} \quad (3)$$

where

$$\begin{cases} n_{j+1} = n_{j+1-M}, & \text{if } j+1 > M \\ \bar{S}_i^{1 \times M} = [\pm 1, \pm 1, \pm 1, \dots, \pm 1] \\ S_i(j+1) = S_i(j+1-M), & \text{if } j+1 > M \\ \bar{\varphi} = [\varphi_1, \varphi_2, \varphi_3, \dots, \varphi_M] \end{cases} \quad (4)$$

\bar{S}_i is a signs' vector with length of $1 \times M$. It has 2^M permutation types. For a given i , it stands for a kind of signs' permutation. According to the small reflection theorem, discontinuities on the MP structures cause multiple reflections and further lead to occurrence of stopbands. When reflected waves from UCs add in phase, the reflection will be the strongest, and the stopbands will be open up. As the Figure 1 shown, the round-trip phase in each UC is $2\varphi_1, 2\varphi_2, \dots, 2\varphi_m$. The strongest reflection condition is

$$2\varphi_1 + 2\varphi_2 + 2\varphi_3 + 2\varphi_4 + \dots + 2\varphi_m = 2\pi q \quad (5)$$

where q is integer. Thus, we can obtain a general Bragg condition for MP structure,

$$\sum_{i=1}^m \varphi_i = q\pi \quad (6)$$

According to the derived general dispersion formula, the dispersion relations of SP, DP and TP non-dispersive media are presented in Figures 2(a)–(c). We can see that the SP structure does not have stopband in the given frequency range, and the DP and TP structures have one and two stopbands, respectively. We can easily find out the quantity relation between the periodicity M and the maximum number of stopbands N_s , $N_s = M - 1$. Besides, since we keep the UCs' lengths same, the space harmonic modes' separation distance is correspondingly reduced. For SP, DP and TP structures, the separation distances are $2\pi/p$, $2\pi/2p = \pi/p$, $2\pi/3p$, respectively. In this figure, the general Bragg condition is also verified. The dash lines are $(\sum_{i=1}^m \varphi_i)/(mp)$. It is very obvious that the frequency points which satisfy general Bragg condition all fall into stopbands.

For the dispersive material, Figure 1(b) gives an illustration to the MP CRLH structure. The equivalent circuit model is shown. L'_R , C'_R , L'_L and C'_L are per-unit-length components. The refractive index of the CRLH structure can be represented by [4],

$$n(\omega) = c \left(\frac{1}{\omega'_R} - \frac{\omega'_L}{\omega^2} \right), \quad \text{and} \quad \omega'_L = \frac{1}{\sqrt{L'_L C'_L}}, \quad \omega'_R = \frac{1}{\sqrt{L'_R C'_R}} \quad (7)$$

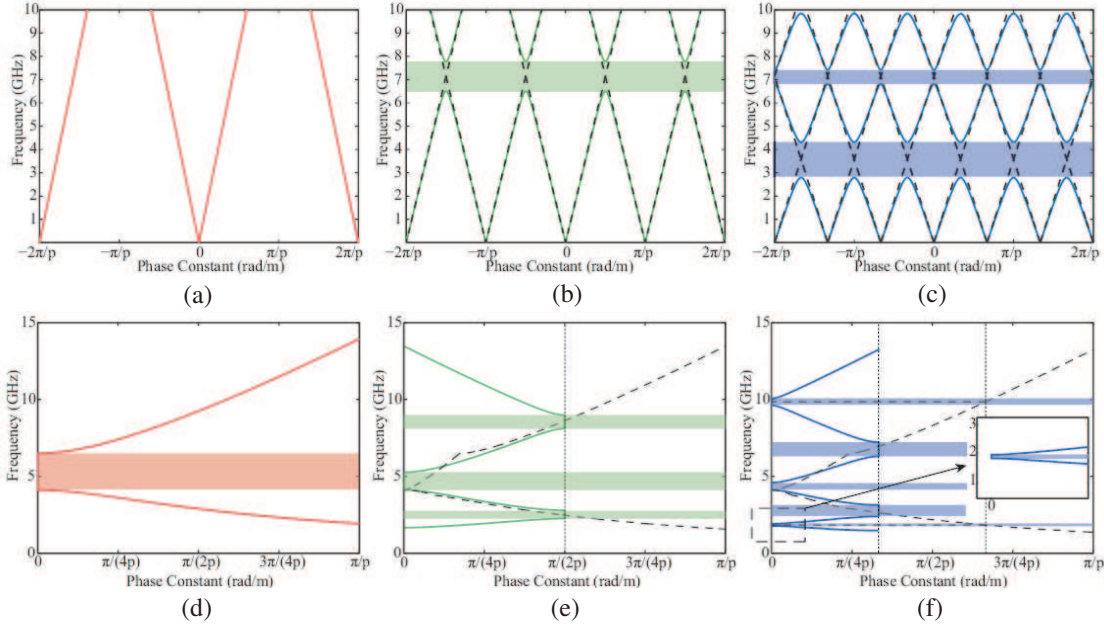


Figure 2: Dispersion Relations for (a)–(c) non-dispersive and (d)–(f) dispersive SP, DP and TP layered media. The solid lines are the dispersion curves. The dash lines stand for the general Bragg condition curves. The shadow regions refer to stopbands.

Here c is the light speed. w is the angular frequency. Substituting Equation (7) into (3), the dispersion relation for CRLH media can be obtained. Figures 2(d)–(f) present dispersion relations for SP, DP and TP CRLH structures. Similarly, the relation between the periodicity M and the maximum number of stopbands N_s can be summarized as $N_s = 2M - 1$. The space harmonic's period is also reduced correspondingly. The general Bragg condition is also verified in this figure. It shows that the general Bragg condition is also suitable for dispersive materials.

2.2. Non-dispersive and Dispersive Lumped Circuits

For the non-dispersive circuits, the transmission matrix can be represented as

$$\begin{bmatrix} A_m & B_m \\ C_m & D_m \end{bmatrix} = \begin{bmatrix} \cos \beta p j Z_{0m} & \sin \beta p \\ j Y_{0m} \sin \beta p & \cos \beta p \end{bmatrix} \quad (8)$$

where Z_{0m} is the m th UC's characteristic impedance. Following the same derivation shown in Section 2.1, the dispersion relation can be obtained. Figures 3(a)–(c) show dispersion relations of SP, DP and TP transmission lines (TLs). The results are consistent with previous analysis. In this analysis, the frequency interval from 0 GHz to 8 GHz covers two harmonic frequency ranges. Hence, we see two and four stopbands for DP and TP cases, respectively. Within one harmonic frequency range (0 GHz to 4 GHz), the number of stopbands also obeys the periodicity-stopbands number relation showed in Section 2.1. MP structures have more abundant radiation modes, simultaneously dualistic radiations and multi-beam properties. For instance, DP structure simultaneously has one right-handed (parallel phase and group velocities) and one left-handed (antiparallel phase and group velocities) radiation modes in the leaky-wave region at 6.5 GHz. Since two values of β are different, based on the leaky-wave theory, it also has two separated radiation beams. Similarly, for the TP case, it has more right/left-handed radiation modes at a specified frequency. In summary, MP structures can realize multi-beam performance.

For the dispersive (CRLH) TLs, the transmission matrix is [4]

$$\begin{bmatrix} A_m & B_m \\ C_m & D_m \end{bmatrix} = \begin{bmatrix} 1 + Z_m Y_m / 2 & Z_m (1 + Z_m Y_m / 4) \\ Y_m & 1 + Z_m Y_m / 2 \end{bmatrix} \quad (9)$$

where

$$Z_m = j \left(\omega L_{Rm} - \frac{1}{\omega C_{Lm}} \right), \quad Y_m = j \left(\omega C_{Rm} - \frac{1}{\omega L_{Lm}} \right) \quad (10)$$

Here L_{Rm} , L_{Lm} , C_{Rm} , and C_{Lm} are lumped inductances and capacitances, respectively. The equivalent circuit model is same with Figure 1(b). To examine the theory, we simulate Metal-

Insulation-Metal (MIM) CRLH structures in HFSS. Comparisons of theoretical and simulation results are presented in Figures 3(d)–(f). Conclusions are same with those of MP CRLH media. However, through our implementation, MP CRLH TLs' impedance matching is very challenging.

3. MULTIPLE PERIODIC PHASE REVERSAL ANTENNA

In this part, MP PR antennas are proposed. PR antenna is a periodically loaded antenna. It is introduced in [5]. The PR UC is presented in Figure 4(a). To realize the MP configuration, different UCs are set up by changing the characteristic impedances. Figure 4(b) shows the prototypes of SP, DP and TP PR antennas. We varied the dimensions of W from 30 to 70 mil (step is 20 mil) for SP, DP and TP cases. The PR antenna is a TEM type TL. We can characterize the dispersion relation

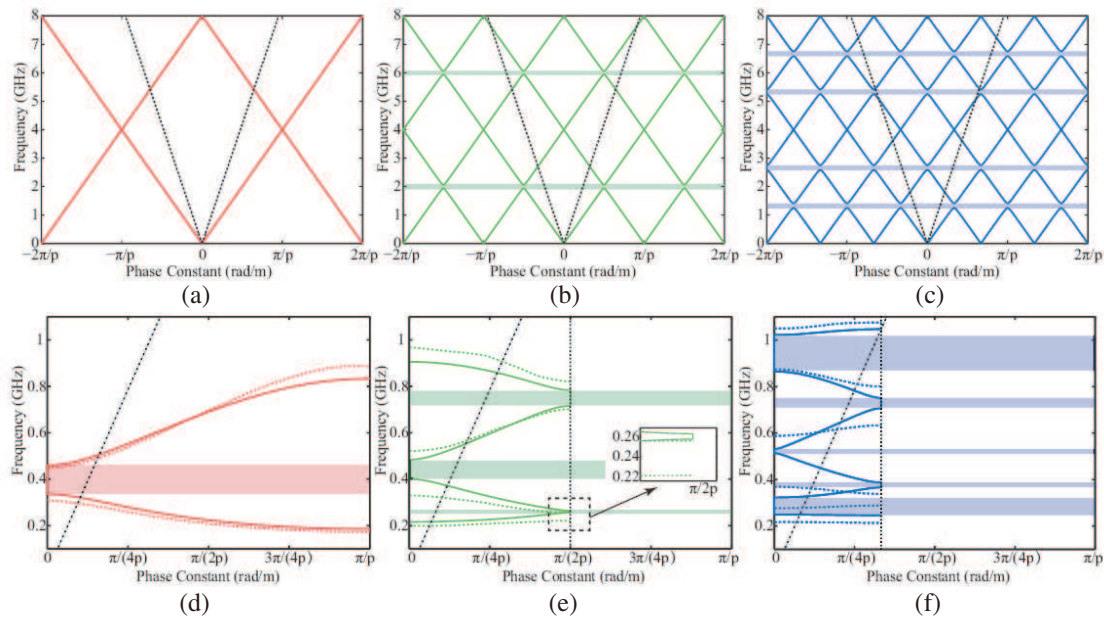


Figure 3: Dispersion relations for (a)–(c) non-dispersive and (d)–(f) dispersive SP, DP and TP circuits. The solid lines are the dispersion curves. The black and colored dash lines are the wave vectors in the free space (air lines) and full wave simulated CRLH dispersion curves. The shadow regions refer to stopbands.

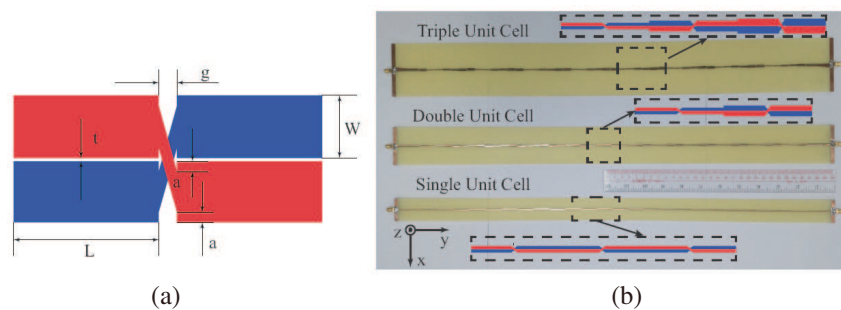


Figure 4: (a) UC of PR antenna and (b) prototypes of SP, DP and TP PR antennas.

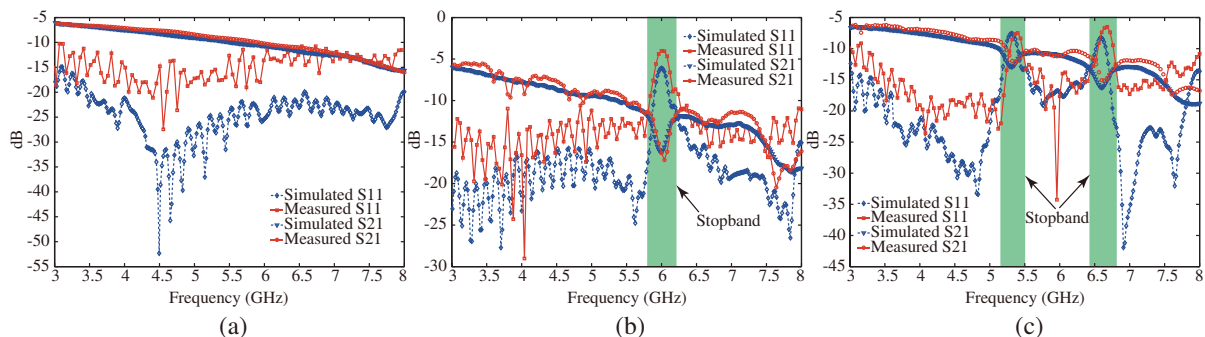


Figure 5: Simulated and measured S -parameters of (a) SP, (b) DP and (c) TP PR antennas.

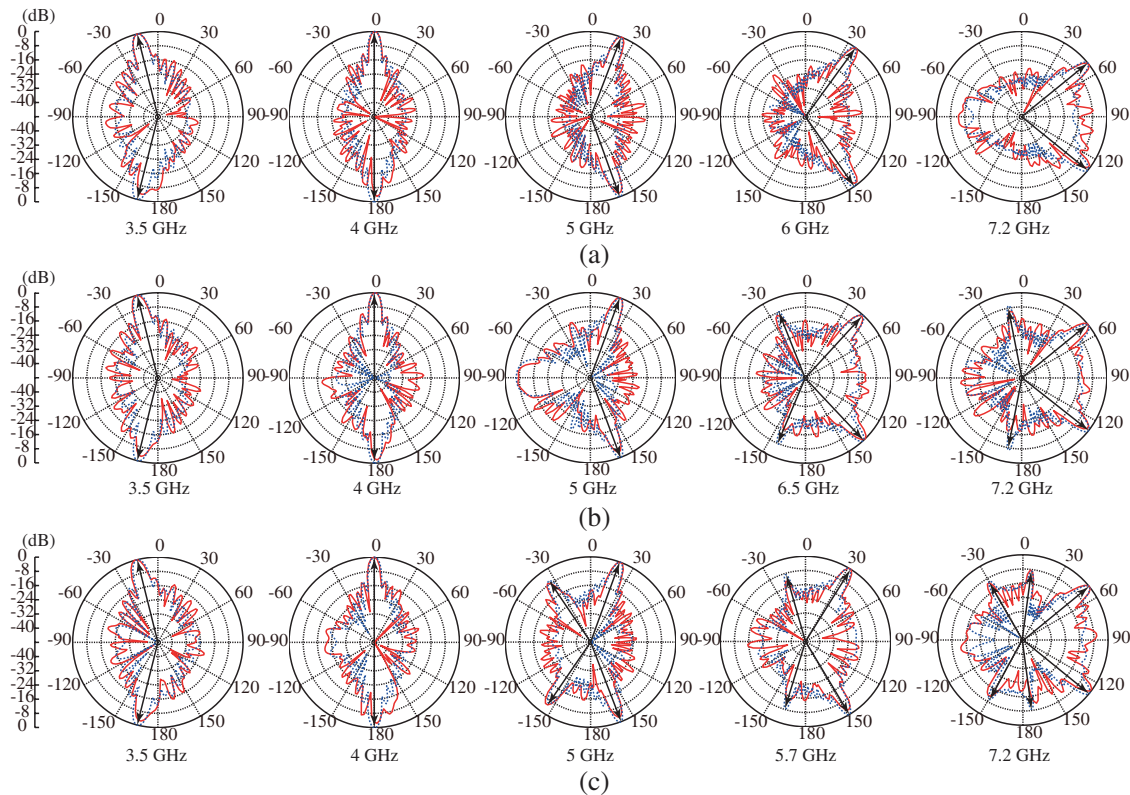


Figure 6: Simulated (red lines) and measured (blue lines) radiation patterns in y - z plane for (a) SP, (b) DP and (c) TP PR antennas.

of PR antennas based on the strip line TL model. But there is a difference, an extra frequency-independent π phase shift is generated per UC due to phase reversal. The dispersion relations of SP, DP, TP PR antennas can be obtained by simply shifting each space harmonic modes with π rad in dispersion diagrams of strip lines, as shown in Figures 3(a)–(c). Figures 5(d)–(f) present the simulated and measured S -parameters of SP, DP and TP PR antennas. Figure 6 shows the normalized simulated and measured radiation patterns of three antennas in y - z plane. It is very obvious that DP antenna at {6.5, 7.2} GHz and TP antenna at {5, 5.7} GHz all have two radiation modes. At these frequencies, both right- and left-handed radiations are excited. These beams scan with the frequency change. At 7.2 GHz, TP antenna has three radiation modes, and three beams are generated in each half plane. The radiation patterns show very good agreements with dispersion relations.

4. CONCLUSION

The dispersion relations of the general MP structure are analyzed theoretically for layered media and lumped circuits. Both non-dispersive and dispersive materials are discussed for each case. A unified dispersion relation formula and a general Bragg condition are presented. The transmission and radiation performances of MP structures are examined by MP PR antennas. The measurement results present very good agreements with the theories.

REFERENCES

1. Saleh, B. E. A. and M. C. Teich, *Fundamentals of Photonics*, 2nd Edition, Wiley, New York, 2007.
2. Ishimaru, A., *Electromagnetic Wave Propagation, Radiation, and Scattering*, Prentice-Hall, 1991.
3. Oliner, A. A. and D. R. Jackson, "Leaky-wave antennas," *Antenna Engineering Handbook*, 4th Edition, Ch. 10, J. Volakis, Ed., McGraw-Hill, New York, 2007.
4. Caloz, C. and T. Itoh, *Electromagnetic Metamaterials: Transmission Line Theory and Microwave Applications*, Wiley, New York, 2006.
5. Yang, N., C. Caloz, and K. Wu, "Full-space scanning periodic phase-reversal leaky-wave antenna," *IEEE Trans. Antennas Propag.*, Vol. 58, No. 10, 2619–2632, Oct. 2010.

A Dual-band Circularly Polarized Antenna with Novel Feeding Method for BDS, GPS and GLONASS Application

J. Zhang, X. Q. Lin, L. Y. Nie, F. Cheng, Z. Y. Kang, Y. Jiang, and J. W. Yu

EHF Key Lab of Fundamental Science, School of Electronic Engineering

University of Electronic Science and Technology of China, Chengdu 611731, China

Abstract— In this paper, a dual-band circularly polarized antenna is proposed. This antenna constructs with two layers, which provides two working frequency bands. One of the bands operates at the BDS B3 (1268.52 ± 10 MHz). The other band concludes the GPS L_1 (1575.42 ± 10 MHz) and GLONASS L_1 (1602 ± 8 MHz). By changing the length and width of four slots on each patch, its circular polarization performance and working bandwidth can be adjusted. The multistacked patches fed through two coaxial probes which provide two different input signal. To the probe feed on the lower patch it do not connect direct to the lower patch but solder to a small disc on the upper patch. By adjusting these parameters, we will obtain better impedance matching performance.

1. INTRODUCTION

Dual-band or tri-band circularly polarized antennas has been widely used in a compatible navigation systems. It has been reported that a multiband antenna can be realized by patches stacked [1] and cutting slots on the patch will achieve circularly polarization under the condition of single feed [2]. In [3], a S-shaped slotted patch antenna is proposed for dual-band operation of circularly polarization. The frequency ratio of this antenna is controlled by adjusting the S-shaped slot arm lengths. For other methods, [4] designed a circularly polarized cavity-backed annular slot antenna for GPS L_1 and L_2 bands. And [5] describes a multi-band circularly polarized printed slot antenna which covers 1.5 GHz for GPS, 2.4 GHz for Bluetooth, and 3.75 GHz for WiMAX. In this paper, we design a dual-band circularly polarized antenna using stacked patches. At the same time, we improve the method of feeding to the lower patch which avoids the problems of soldering and make very small impact on upper patch.

2. ANTENNA DESIGN

The proposed stacked patch antenna structure is shown in Fig. 1. This antenna is constructed of two round patches stacked on one another. Each layer fed by an individual coaxial probe. Both of the patches are etched on the FR4 substrate with relative permittivity $\epsilon_r = 4.6$ and $\tan \delta = 0.02$. The lower and upper patch has a thickness of 2.3 mm and 4 mm respectively. The ground plane size is 72 mm \times 72 mm. The radius is 29 mm for the lower patch and 23.1 mm for the upper patch. The antenna type in [7] is adopted in this paper. The common method for a single-fed patch antenna to activate circular polarization wave is to disturb the path of the current [6]. So the four slots etched on the patches are used to excite orthogonal resonant modes. The width of the slots is 1 mm. For the lower patch, the lengths of the slotted pair along the x - and y -direction are l_1 and l_2 respectively. For the upper patch, they are u_1 and u_2 along the x - and y -direction. A 50 Ω coaxial probe connected to the upper patch through the lower patch via a hole. The position of this feed point is as shown in Fig. 1. To the lower patch, the probe do not connect to it directly but solder to a small disc on the upper patch. The radius of the small disc is 1.5 mm. The width of the slot between the disc and upper patch is $d = 1$ mm. The location of the small disc is shown in Fig. 1.

The radius of each patch has been discussed in [7]. By changing the length and width of four slots on each patch, its circular polarization performance and working bandwidth can be adjusted. If the patch center is defined as the origin of the coordinate, feed at line $y = x$ will excite left hand circular polarization and $y = -x$ will excite right hand polarization. Actually, despite the structure of patch is symmetric, the two feed probes and small disc on the upper patch breaks the symmetry. So the best impedance matching point will deviate from the $y = x$ and $y = -x$ line. Fig. 2(a) shows the impedance when changing a only. The feed to lower patch is connected with the lower patch and the small disc. Because the dimension of the small disc is far less than the patch, this port can be considered as open and parallel with a capacitor (the slot between disc and upper patch). Therefore, the small disc dimension has little impact to lower patch, but the width of slot has a big impact to the upper patch as shown in Fig. 2(b).

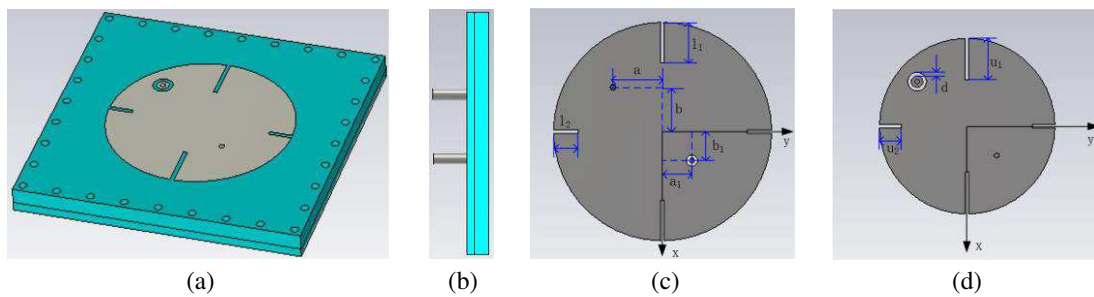


Figure 1. Structure of the proposed antenna. ($l_1 = 10.75$ mm, $l_2 = 6.5$ mm, $u_1 = 11$ mm, $u_2 = 5.85$ mm, $a = 13.2$ mm, $b = 11.7$ mm, $a_1 = 7.8$ mm, $b_1 = 7.7$ mm). (a) Perspective view. (b) Side view. (c) Lower patch. (d) Upper patch.

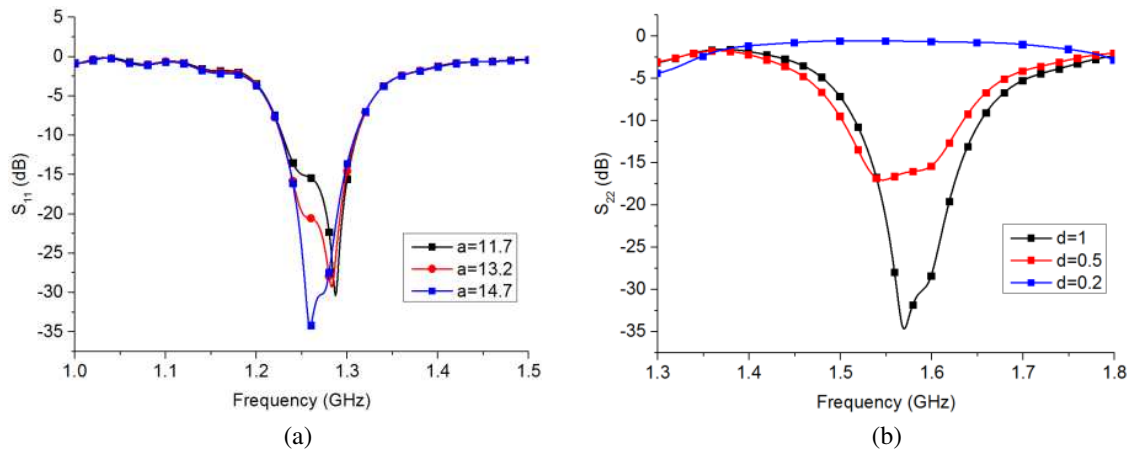


Figure 2. The influence of some parameters on the simulated return loss. (a) Simulated S_{11} for different feed position. (b) Simulated S_{22} for different gap width.

3. RESULTS AND DISCUSSION

In this paper, The radius of the disc and the gap width has small impact on the input impedance of two frequency band. By adjusting these parameters, we will obtain better impedance matching performance. The proposed antenna is optimized by the electromagnetic simulation package of computer simulation technology (CST) microwave studio. Fig. 3 shows the photograph of top and bottom view of this antenna. The simulation shows good agreement with the experimental results of the return loss for the proposed antenna in Fig. 4(a). The 10 dB impedance bandwidth of the measured return loss is from 1.227 GHz to 1.303 GHz and from 1.53 GHz to 1.654 GHz. Fig. 4(b) shows the simulated axial ratio for the two operating bands. The AR for 1.268 GHz (DBS B3), 1.575 GHz (GPS L_1) and 1.602 GHz (GLONASS L_1) is 1.86 dB, 1.67 dB and 3.25 dB respectively. Fig. 4(c) shows the radiation pattern for the three frequency. The comparisons are listed in Table 1. Compared to other multiband circularly polarized antenna, we can easily observe that the fabricated antenna exhibits better performances in bandwidth and size.



Figure 3. The photograph of the proposed antenna. (a) Top view. (b) Bottom view.

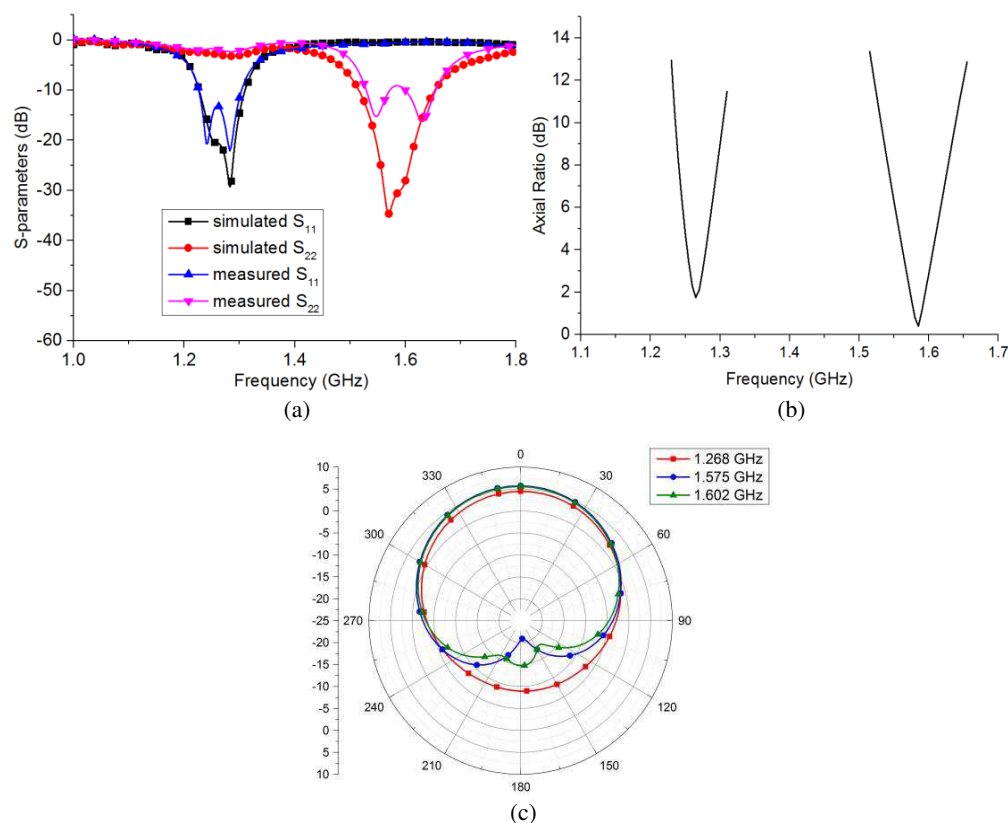


Figure 4. The simulated and measured results for the proposed antenna. (a) Simulated and measured return loss. (b) Simulated AR for the proposed antenna. (c) Simulated radiation pattern for the proposed antenna.

Table 1.

References	Center Frequency (GHz)	10 dB Return Loss BW (%)	3 dB AR BW (%)	Size (mm)
[1]	1.176, 1.227, 1.575	1.7, 2, 2.5	3.4, 0.81, 0.83	80 × 80 × 4.724
[3]	1.2, 1.54	16, 12.5	6.9, 0.6	115 × 115 × 21.5
[4]	1.2, 1.575	3.7, 1.2	0.9, 0.6	100 × 100 × 20
this work	1.268, 1.585	6.54, 8.7	1.34, 2.02	72 × 72 × 6.3

4. CONCLUSIONS

A dual-band circularly polarized antenna with a new feeding method is proposed in this paper. The stacked patches has been used to obtain dual-band operation. The thickness of the upper substrate is increased to broaden the bandwidth. A new feeding method is used in the lower patch, which make the assembly of the multistacked substrates easier and is conducive to error reduction. The simulated and measured results show that, this antenna can meet the requirements of using in DBS, GPS and GLONASS navigation system.

ACKNOWLEDGMENT

This work was supported in part by the State Key Laboratory of CEMEE Foundation under Grant No. CEMEE2014Z0201A, in part by the Fundamental Research Funds for the Central Universities under Grant Nos. ZYGX2010J021 and ZYGX2012YB002, in part by the Program for New Century Excellent Talents in University under Grant No. NCET-13-****.

REFERENCES

1. Falade, O. P., "Single feed stacked patch circular polarized antenna for triple band GPS receivers," *IEEE Transactions on Antennas and Propagation*, Vol. 60, No. 10, 4479–4484, 2012.
2. Agarwal, K., "RIS-based compact circularly polarized microstrip antennas," *IEEE Transactions on Antennas and Propagation*, Vol. 61, No. 2, 547–554, 2013.

3. Nasimuddin, Z., N. Chen, and X. Qing, “Dual-band circularly polarized S-shaped slotted patch antenna with a small frequency-ratio,” *IEEE Transactions on Antennas and Propagation*, Vol. 58, No. 6, 2112–2115, Jun. 2010.
4. Hsieh, W. T., T. H. Chang, and J. F. Kiang, “Dual-band circularly polarized cavity-backed annular slot antenna for GPS receiver,” *IEEE Transactions on Antennas and Propagation*, Vol. 60, No. 4, 2076–2080, April 2012.
5. Bod, M. and H. R. Hassani, “Multi-band circularly polarized slot antenna for GPS, bluetooth and wimax bands,” *Progress In Electromagnetics Research C*, Vol. 49, 171–178, 2014.
6. Gao, S., Q. Luo, and F. Zhu, *Circularly Polarized Antennas*, Wiley-Interscience, University of Kent, UK, 2014.
7. Tian, X. Q., S. B. Liu, Y. S. Wei, and X. Y. Zhang, “Circularly polarized microstrip antenna with slots for beidou (COMPASS) navigation system,” *International Symposium on Signals Systems and Electronics (ISSSE)*, Vol. 2, 1, 3, Sep. 17–20, 2010.

Broadband Circularly Polarized Loop Antenna Based on High-pass and Low-pass Filters for Handheld RFID Reader Applications

Bo Xu, Qi Liu, and Yusha Liu

Centre for Optical and Electromagnetic Research
Zhejiang University, China

Abstract— Recent researches on portable circularly polarized (CP) Radio Frequency Identification (RFID) reader antennas have 3-dB axial ratio bandwidth (ARBW) lower than 80 MHz. In order to cover all the Ultrahigh Frequency (UHF) RFID bands simultaneously, this paper presents a novel broadband handheld RFID CP reader antenna. The proposed antenna consists of a square-loop radiating element with 2 feed ports and a broadband feeding network in the same plane, measuring $95\text{ mm} \times 95\text{ mm} \times 1.6\text{ mm}$. The feeding network, which realizes broadband ARBW, is composed of a Wilkinson power divider, a high-pass filter (HPF) and a low-pass filter (LPF), connected to the radiating element, producing broadband right-hand circular polarization (RHCP) in z direction and left-hand circular polarization (LHCP) in $-z$ direction. The measured broad impedance bandwidth ($S_{11} < -10\text{ dB}$) is from 710 MHz to 1150 MHz. The measured 3-dB ARBW of the proposed antenna is from 800 MHz to 940 MHz. The peak gain in the maximum radiation direction is 1.3 dBi at 910 MHz.

1. INTRODUCTION

UHF RFID systems have been widely deployed in various areas including cold-chain, logistics, Electrical Toll Collection (ETC) and security systems. RFID systems are typically composed of two parts: tags and readers. RFID tags carrying information can be read or written by RFID readers through backscattering modulation in UHF band. Several UHF RFID band standards have been adopted, such as the band standards of U.S. (902–928 MHz), Europe (866–869 MHz) and China (840–844.5 MHz and 920.5–924.5 MHz).

Most tags in commercial applications are designed as dipole or patch antennas [1–4] with linear polarization (LP) because of low manufacturing cost and compact size. Therefore, reader antennas with circular polarization (CP) are preferred in order to avoid polarization mismatch between reader antennas and tag antennas. A lot of work has been done on handheld RFID CP reader antennas [5–8]. [5] proposed a single-layer, dual-fed CP square-ring via a Wilkinson power divider with 80 MHz ARBW. [6] proposed a compact X-shaped slotted square-patch antenna for CP application with 18 MHz ARBW. [7] presented a fractal-based coplanar waveguide CP antenna with 26 MHz ARBW. [8] proposed a dual-band CP antenna based on 4 dipoles with 90-degree difference, whose ARBW is about 20 MHz in UHF band. However, few works focused on broadening the ARBW of RFID CP reader antennas, for the purpose of covering all the mainstream band standards including the band standards of U.S., Europe and China (840–928 MHz).

In this paper, a UHF RFID reader antenna based on a feeding network, which consists of a HPF, LPF, and a Wilkinson power divider, is well designed and fabricated for handheld RFID reader applications. The proposed feeding network, based on [9], contributes to a broadband ARBW. The 3-dB ARBW of the proposed antenna is 140 MHz covering UHF RFID bands including the band standards of U.S., Europe and China.

The design of the proposed antenna is presented, followed by the simulated and measured results, discussions and conclusions.

2. ANTENNA CONFIGURATION AND DESIGN

For convenience, the geometry of the proposed antenna, which is depicted in Fig. 1, is similar to the one in [8]. It can be seen that in Fig. 1(a) the antenna consists of a $95\text{ mm} \times 95\text{ mm}$ square-ring loop, which works as a radiating element, and a feeding network based on a Wilkinson power divider. The left output of the Wilkinson power divider is connected to a pi-topology HPF, and the right output is connected to a T-topology LPF. The feed port of the power divider is connected to a $50\ \Omega$ SMA port. Lumped resistance $R = 100\ \Omega$ is used for isolation in Wilkinson Power divider. Impedance match can be acquired by selecting $W_1 = 3\text{ mm}$ and $W_2 = 1.6\text{ mm}$. By selecting appropriate values of lumped inductors and capacitors, and adjusting the resonant frequency of two filters to 910 MHz,

the HPF and the LPF working together as a broadband 90-degree phase shifter as [9, 10]:

$$L_1 = \frac{Z_0}{2\pi f \sin(\phi_1)} \tag{1}$$

$$L_2 = \frac{Z_0 \sin(-\phi_2)}{2\pi f} \tag{2}$$

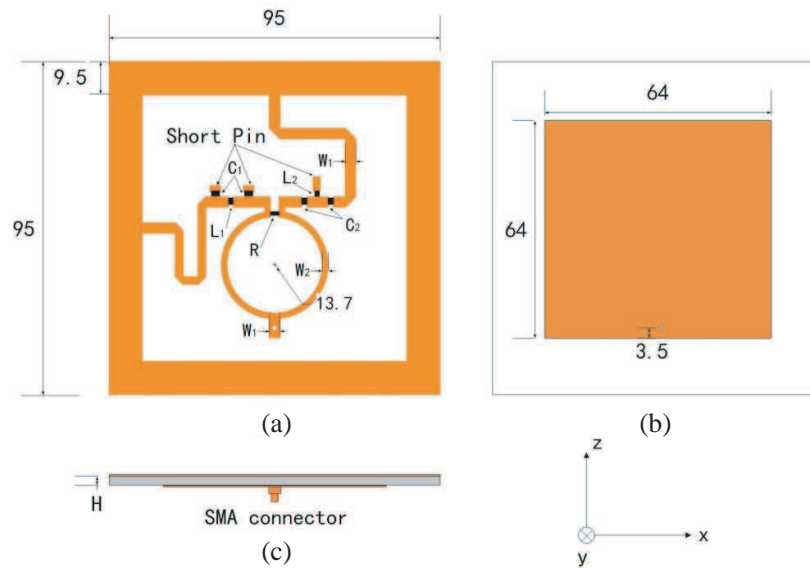


Figure 1: Geometry of the proposed RFID antenna. (a) Top view. (b) Bottom view. (c) Side view.

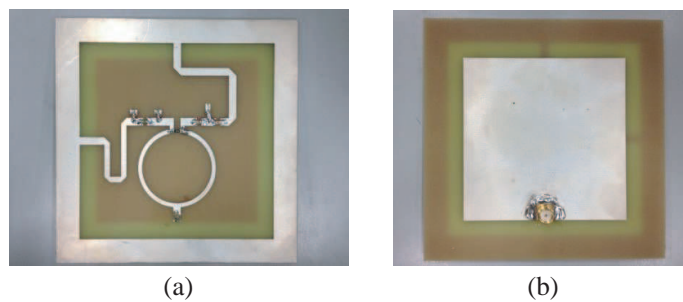


Figure 2: Fabricated antenna. (a) Top view. (b) Bottom view.

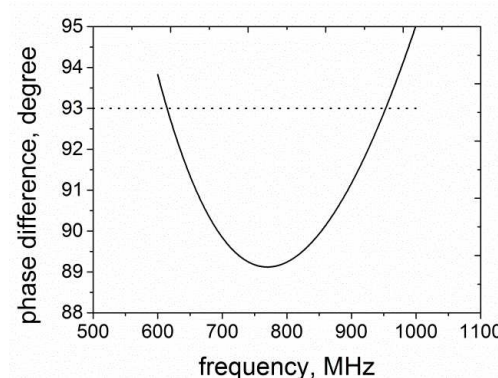


Figure 3: Simulated phase difference between two outputs corresponding to HPF and LPF.

$$C_1 = \frac{1}{2\pi f Z_0 \tan(\phi_1/2)} \quad (3)$$

$$C_2 = \frac{\tan(-\phi_2/2)}{2\pi f Z_0} \quad (4)$$

In this work, $f = 910$ MHz, $\phi_1 = 45^\circ$, $\phi_2 = -45^\circ$, $Z_0 = 50 \Omega$, thus, $L_1 = 6.2$ nH, $L_2 = 12$ nH, $C_1 = 1.4$ pF, and $C_2 = 8.5$ pF. The phase difference is $\Delta\phi = \phi_1 - \phi_2 = 90^\circ$. The length of the two microstrip lines connected to the Wilkinson power divider is equal, thus the microstrip lines contribute nothing to the phase shift. The HFSS simulated phase difference between the two outputs corresponding to the HPF and the LPF is $90^\circ \pm 3^\circ$ from 615 MHz to 952 MHz, as shown in Fig. 3.

The bottom view of the proposed antenna is shown in Fig. 1(b). By adjusting the size of ground plane, a good impedance match is achieved since the loop is inductive and the ground plane provide capacitive coupling. The proposed antenna is manufactured on a FR4 substrate with thickness $H = 1.6$ mm and relative permittivity $\epsilon_r = 4.4$. Fig. 2 shows the fabricated antenna.

3. RESULTES AND DISCUSSIONS

The antenna is designed to operate at the frequency of 910 MHz. The simulated and measured return loss is plotted in Fig. 4. It is shown that the proposed CP antenna has broad impedance bandwidth. The measured 10-dB return loss ranging from 710 MHz to 1150 MHz, agrees well with HFSS simulated results ranging from 645 MHz to 1050 MHz. The measured AR in the boresight direction is plotted in Fig. 5. The measured 3-dB ARBW is 800–940 MHz, covering UHF RFID bands including bands of U.S., Europe and China. Although the measured AR is 3.04 dB and 3.07 dB at 840 MHz and 850 MHz, respectively, we believe by adjusting the values of lumped inductors and capacitors, the AR at these frequencies can also be lower than 3 dB. Despite the flaws

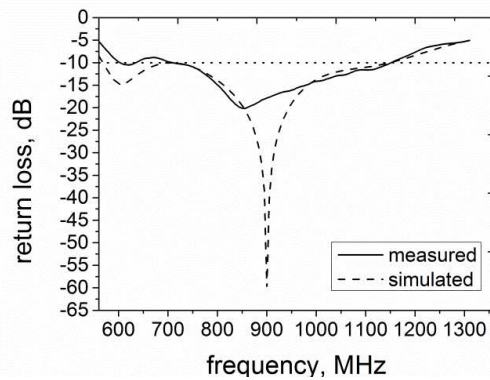


Figure 4: Simulated and measured return loss of the proposed antenna.

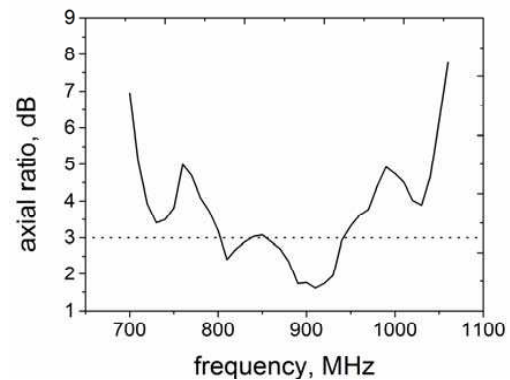


Figure 5: Measured axial ratio of the proposed antenna.

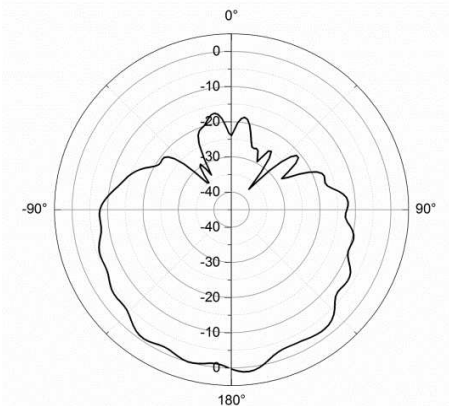


Figure 6: Measured LHCP radiation patterns at 910 MHz in x - z plane.

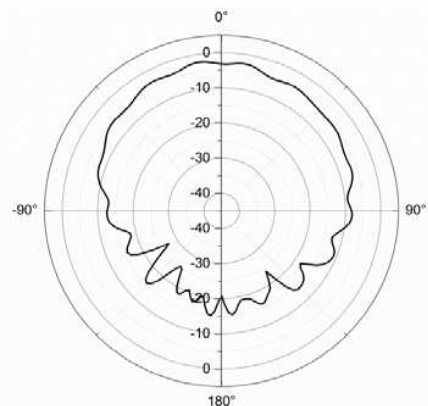


Figure 7: Measured RHCP radiation patterns at 910 MHz in x - z plane.

around 840 MHz, the measured 3-dB ARBW is much wider than [5–8]. Fig. 6 presents the measured left-hand circular polarization (LHCP) radiation patterns at 910 MHz. The measured 3-dB LHCP beamwidth is about 55° in x - z plane. The obtained peak gain is 1.3 dBic in $-z$ direction. Fig. 7 presents the measured right-hand circular polarization (RHCP) radiation patterns at 910 MHz. The measured 3-dB RHCP beamwidth is about 82° . The obtained peak gain is -2.21 dBic. Compared LHCP patterns with RHCP patterns, Fig. 6 and Fig. 7 show that the proposed antenna has better CP gain in $-z$ direction since the feeding network on the top severely affects the RHCP patterns.

4. CONCLUSIONS

In this paper, a RFID reader CP antenna has been proposed using a feeding network based on a Wilkinson power divider, a HPF, and a LPF. The proposed antenna can obtain 140 MHz ARBW with 1.3 dBic peak LHCP gain. Compared to other reader CP antennas [5–8] in similar size, it has a broader ARBW, which makes it a good choice for handheld RFID applications.

REFERENCES

1. Bjorninen, T., A. Z. Elsherbeni, and L. Ukkonen, "Low-profile conformal UHF RFID tag antenna for integration with water bottles," *IEEE Antennas and Wireless Propagation Letters*, Vol. 10, 1147–1150, 2011.
2. Tiovonon, M., T. Bjorninen, L. Sydanheimo, L. Ukkonen, and Y. Rahmat-Samii, "Impact of moisture and washing on the performance of embroidered UHF RFID tags," *IEEE Antennas and Wireless Propagation Letters*, Vol. 12, 1590–1593, 2013.
3. Du, G. H., T. Tang, and Y. Deng, "Dual-band metal skin UHF RFID tag antenna," *Electronics Letters*, Vol. 49, No. 14, Jul. 2013.
4. Choo, J. and J. Ryoo, "UHF RFID tag applicable to various objects," *IEEE Transactions on Antennas and Propagation*, Vol. 62, No. 2, 922–925, Feb. 2014.
5. Lin, Y.-F., H.-M. Chen, F.-H. Chu, and S.-C. Pan, "Bidirectional radiated circularly polarised square-ring antenna for portable RFID reader," *Electronics Letters*, Vol. 44, No. 24, 1383–1384, Nov. 24, 2008.
6. Lin, Y., C. Lee, S. Pan, and H. Chen, "Proximity-fed circularly polarized slotted patch antenna for RFID handheld reader," *IEEE Transactions on Antennas and Propagation*, Vol. 61, No. 10, 5283–5286, Oct. 2013.
7. Raviteja, C., C. Varadhan, M. Kanagasabai, A. K. Sarma, and S. Velan, "A fractal-based circular polarized UHF RFID reader antenna," *IEEE Antennas and Wireless Propagation Letters*, Vol. 13, 499–502, 2014.
8. Caso, R., A. Michel, M. Rodriguez-Pino, and P. Nepa, "Dual-band UHF-RFID/WLAN circular polarized antenna for portable RFID readers," *IEEE Transactions on Antennas and Propagation*, Vol. 62, No. 5, 2822–2826, May 2014.
9. Tang, X. and K. Mouthaan, "Design consideration for octave-band phase shifters using discrete components," *IEEE Transactions on Microwave Theory and Techniques*, Vol. 58, No. 12, 3459–3466, Dec. 2010.
10. Tang, X. and K. Mouthaan, "Large bandwidth digital phase shifters with all-pass, high-pass, and low-pass networks," *IEEE Transactions on Microwave Theory and Techniques*, Vol. 61, No. 6, 2325–2331, Jun. 2013.

Electromagnetic Heat-induced of Nanowire in Liquid: Computation of the Bubble Shape

A. Chaari, T. Grosjes, L. Giraud-Moreau, and D. Barchiesi

Project Group for Automatic Mesh Generation and Advanced Methods
Gamma3 Project (UTT-INRIA), University of Technology of Troyes, France

Abstract— The computation of the temperature with accuracy is essential to determine the shape of a bubble around a nanowire immersed in a liquid. The study of the physical phenomenon consists in solving a coupled photo-thermic system between light and nanowire. The numerical multiphysic model is developed to study and simulate the variations of the temperature and the shape of the induced bubble after the illumination of the nanowire. An optimized finite element method, including adaptive remeshing scheme, is developed and used to solve the problem. The evolution of the bubble is achieved by taking into account the physical and geometrical parameters of the nanowire. The feedback relation between the sizes and shapes of the bubble and nanowire is deduced.

1. INTRODUCTION

Many researchers are interested by the use of nanomaterials. Usually used materials in the chemical industry and in manufactures of nanotubes and nanowires are TiO_2 and ZnO [1–3]. The use of such nanomaterials (natural or artificial) increases and these are dispersed in air or in water [4]. The investigation on their impacts on the environment and health becomes a necessity (e.g., toxicity analysis) [5] and the detection of the presence of such nanomaterials in the environment becomes crucial. These detections of such a nanowire/nanotube can be achieved through two modes. The first mode consists in a direct detection of the nanowire by the measurement of the scattering of light emitted by the nanomaterial through optical microscopy. Such a detection mode must be difficult due to a weak signal/noise ratio. A second mode consists in an indirect method by studying the bubble created by the photo-thermal response of the illuminated nanowire immersed in the liquid. In that approach, the nanowire absorbs the electromagnetic radiation (energy), heats and induces the creation of a nanobubble [6, 7] for temperature exceeding the vaporization threshold of the liquid. The detection is achieved after the grow of the created bubble and the morphology of the nanowire is studied from the analysis of the shape and size of the bubble. Therefore, the problem consists in solving a photo-thermic coupled system (light, nanowire and heat) taking into account the physical parameters of the system (i.e., permittivity and conductivity of materials, wavelength and power of the laser).

In that context, a numerical multiphysic model is developed in order to analyse the behavior of the nanowires under illumination by a incident laser. The formation of the bubble, associated to the nanowire of TiO_2 immersed in water and illuminated by a laser pulse, is studied. An optimization process, including adaptive remeshing scheme, is used to detect the variations of the temperature, the bubble shape evolution and ensuring the convergence of the solution to the physical solution [8–10]. The paper is organized as follows: Section 2 describes the model and the numerical resolution method. In Section 3, the results of numerical simulations are presented before concluding.

2. MODEL AND FEM FORMULATION

Finite Element Method (FEM) has proved to be an efficient method for the computation of electromagnetic field around nanostructures [11]. The main advantages of the FEM are first its ability to treat any type of geometry and material inhomogeneity (with complex permittivity) [11], second the control of the accuracy of computation to evaluate accuracy of solutions, by using a non regular mesh of the domain of computation and remeshing process.

The PDE system is formed of the Helmholtz' for non-magnetic material with harmonic time dependence, and the Poisson's equations (the stationary heat equation, coupled by a source term in the second one [12]:

$$\left[\nabla \cdot \left(\frac{1}{\epsilon_r(x, y)} \nabla \right) + \frac{\omega^2}{c^2} \right] H_z(x, y) = 0 \quad (1)$$

$$[\nabla \cdot (\kappa(x, y) \nabla)] T(x, y) + \frac{\omega \epsilon_0 \text{Im}(\epsilon_r(x, y))}{2} |\mathbf{E}(x, y)|^2 = 0, \quad (2)$$

where ∇ is the differential vector operator, in cartesian coordinates, \cdot is the scalar product, c is the speed of light in vacuum, ω the angular frequency of the monochromatic wave, $\kappa(x, y)$ the thermal conductivity, $\epsilon_r(x, y)$ the relative permittivity of media and ϵ_0 , the permittivity of vacuum. The shape of the nanowire is defined in the (x, y) plane, as the electric field $\mathbf{E}(x, y)$ which is deduced from the magnetic field $H(x, y)$ along z direction, through the Maxwell-Ampere's equation. The boundary conditions result from the integration of the PDE and from the flux continuity [13]:

$$\mathbf{n}_{12} \cdot \left[\left(\frac{1}{\epsilon_2} \nabla H_2 \right) - \left(\frac{1}{\epsilon_1} \nabla H_1 \right) \right] = 0 \quad \text{and} \quad \mathbf{n}_{12} \cdot [(\kappa_2 \nabla T_2) - (\kappa_1 \nabla T_1)] = 0 \quad (3)$$

where \mathbf{n}_{12} is the normal to the boundary vector, ϵ_l ($l = 1, 2, 3$) are the complex permittivity and κ_l the thermal conductivity of the nanowire, vapor and water medium respectively. The electromagnetic boundary condition (Equation (3)) in 2D geometries, is formally equivalent to the continuity of the tangential component of the electric field. The boundary conditions on the fictitious external boundary of the domain of computation (water), corresponding to the free propagation of the diffracted field $H_3 - H_i$ [13] and the incoming illumination H_i , are defined by:

$$\mathbf{n}_{23} \cdot [(\nabla H_3)] = j[\mathbf{k} \cdot \mathbf{n}] \vec{H}_i + j \frac{\omega}{c} (H_3 - H_i) \quad \text{and} \quad T_3 = T_0, \quad (4)$$

where H_i is the illuminating monochromatic, lying along y , magnetic field: $H_i = H_i^0 \exp(j\omega t - j\mathbf{k} \cdot \mathbf{r})$, with $\mathbf{k} = (0, \omega/c, 0)$, the wave vector, and j the square root of -1 . The solution of this FEM formulation, including a improved remeshing procedure, has been checked and compared with rigorous Mie theory [10, 14, 15].

The resolution of the coupled electromagnetic and heat problems allows to extract the spatial distribution of the temperature in the computational domain. From the map of temperature and for a fixed threshold of vaporization α , the identification of the shape and size of the bubble around the nanowire can be achieved. Such informations on shape and size of the bubble would be used to construct a relation between the geometric characteristics of the bubble and the nanowire.

3. NUMERICAL RESULTS AND DISCUSSION

We consider a TiO_2 elliptical nanowire of semi-axes ($a = 45$ nm, $b = 10$ nm), with thermal conductivity $\kappa(\text{TiO}_2) = 11.7 \text{ Wm}^{-1}\text{K}^{-1}$ immersed in water ($\epsilon_r(\text{water}) = 1.79$, $\kappa(\text{water}) = 0.6 \text{ Wm}^{-1}\text{K}^{-1}$) at temperature $T_0 = 25^\circ\text{C}$ (298.15 K). The nanowire is illuminated by a TM-polarized laser pulse at wavelength $\lambda = 1050$ nm of complex permittivity $\epsilon_r(\text{TiO}_2)_{1050} = 5.4600 + j0.00148$ with a power density per area units $P_S = 1.75 \times 10^{12} \text{ W/m}^2$ [16, 17]. The materials of the system are considered isotropic and homogeneous.

The results of the adaptive process on mesh and on the temperature maps are illustrated on Figure 1. Figures 1(a), (d) show the initial mesh M_0 and the associated temperature. The adaptive process on the temperature field T produces the mesh M_T and the temperature map (see Figures 1(b), (e), respectively). The mesh is adapted on the outline of the nanowire that presents strong variations of the temperature. For a water vaporization threshold $\alpha = 100^\circ\text{C}$ (373.15 K), the detection of the new material (water vapor) is obtained from the temperature map computed on the mesh M_T . The Figure 1(c) presents the areas of the three materials: TiO_2 (red), vapor (green) and water (blue). The computation of the temperature on the domain that contains the water vapor requires to include the physical parameters of the vapor (permittivity $\epsilon_r(\text{vap}) = 1.79$ and thermal conductivity $\kappa(\text{vap}) = 0.05 \text{ Wm}^{-1}\text{K}^{-1}$). The spatial distribution of the temperature field T on the mesh M_{V_0} after detection of the bubble produced around the nanowire is shown on Figure 1(e). The final mesh M_F is obtained, after eight iterations, by applying the adaptive process on the field T taking into account the bubble. That mesh is adapted in the bubble especially on its outline where variations in the temperature occur and relaxed inside the nanowire where the temperature is almost constant (Figure 1(c)). The remeshing process takes into account the shape and size of the bubble. The Figure 1(f) shows the temperature map T on the mesh M_F after convergence to a stable solution. The level curves are smooth where a strong variation of the temperature is shown (in the vicinity of the boundary of the bubble and the nanowire). The map also shows an increase of the temperature in the nanowire due to the creation of the bubble. This increase is due to the diffusion of the temperature, produced by the nanowire after detection of the bubble (i.e., the water vapor has a smaller thermal conductivity than water).

To study the evolution of the shape and size of the bubble, we also consider the nanowire illuminated for various wavelengths ($\lambda = 950$ nm, $\lambda = 1000$ nm and $\lambda = 1050$ nm) with adapted physical

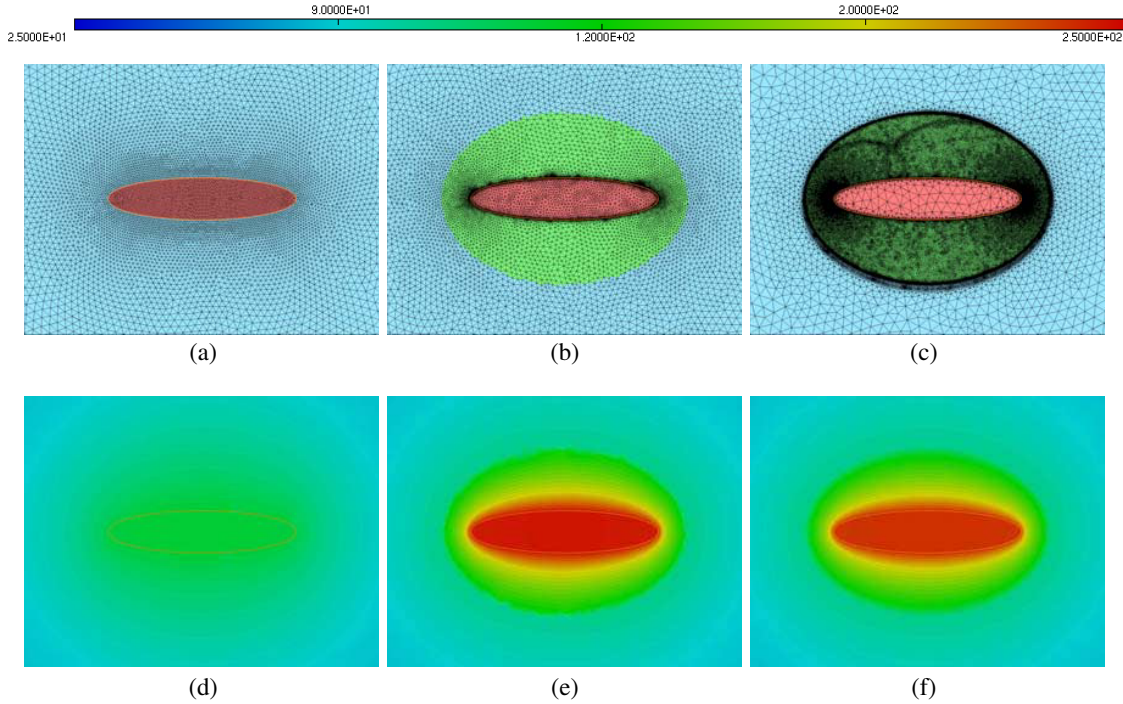


Figure 1: Meshes and temperature fields for nanowire illuminated at $\lambda = 1050$ nm: (a) Initial mesh M_0 , (c) adaptive mesh M_{V_0} , (e) M_F and the associated temperature maps on (b) M_0 , (d) M_{V_0} and (f) M_F .

parameters ($\epsilon_r(\text{TiO}_2)_{950} = 5.500 + j0.00164$, $\epsilon_r(\text{TiO}_2)_{1000} = 5.475 + j0.00154$ and $\epsilon_r(\text{TiO}_2)_{1050} = 5.460 + j0.00148$). For λ increasing, the imaginary part of the complex permittivity of the TiO_2 decreases, leading to a decrease of the energy absorbed by the nanowire. Therefore, the temperature also decreases and the shape and size of bubble are changing. The Figure 2(a) shows the evolution of the aspect ratio of the bubble $R_{\text{bubble}} = A/B$ (A and B being the semi-axes of the bubble) as function of the aspect ratio of the nanowire R_{nanowire} for the three wavelengths. From the computed data, a function F , satisfying $R_{\text{bubble}} = F(R_{\text{nanowire}})$, can be obtained through a nonlinear least-squares fit method (LLS) by the Marquardt-Levenberg algorithm [18, 19]. The method is used to find a set of the best parameters fitting the data. It is based on the sum of the squared differences or residuals (SSR) between the input data and the function evaluated at the data. The applied algorithm consists in minimizing the residual variance $\hat{\sigma}^2 = \text{SSR}/\text{NDF}$ with NDF the number of degrees of freedom (number of the data points (NDP) minus number of the estimated parameters) after a finite number of iterations (FNI). Therefore, the function can be written as follows:

$$R_{\text{bubble}} = F(R_{\text{nanowire}}) = c_0 + \frac{c_1}{(R_{\text{nanowire}} - c_2)^2}, \quad (5)$$

with c_0 , c_1 and c_2 are set of parameters varying as function of the wavelength. The parameter c_0 concerns the asymptote value which is related to the maximum ratio for a circular bubble, c_1 is the inverse of the decay rate of the function F which is related to the speed tending to the circular shape and c_2 is the initial ratio from which the bubble begins to form. Table 1 shows the fit parameters for each wavelength. The F function is continuous and strictly decreasing for R_{nanowire} in the interval $]c_2, +\infty[$, therefore the inverse function F^{-1} exists. The measurement of the aspect ratio of the bubble R_{bubble} allows to predict the aspect ratio of the nanowire R_{nanowire} through the relation: $R_{\text{nanowire}} = F^{-1}(R_{\text{bubble}})$. Figure 2(b) presents the evolution of the bubble volume (in 2D: $V_{\text{bubble}} = \pi AB$) as function of the volume of the nanowire (i.e., $V_{\text{nanowire}} = \pi ab$) for each wavelength. From the computed data (vapor bubble for each nanowire and for each wavelength) and by using the same method and the same algorithm a function G can be obtained through a fit. That function G allows to obtain the relation between the volumes ($\ln(V_{\text{bubble}}) = G(\ln(V_{\text{nanowire}}))$). The G function is continuous and strictly increasing, therefore the inverse function G^{-1} also exists. The measurement of the bubble volume V_{bubble} can be used to determine the volume of the nanowire V_{nanowire} through the relation $\ln(V_{\text{nanowire}}) = G^{-1}(\ln(V_{\text{bubble}}))$. With the two functions F^{-1} and

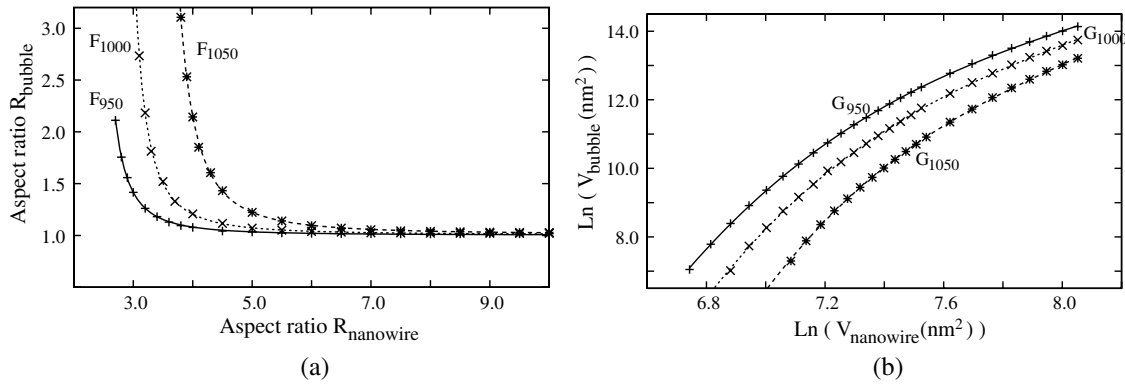


Figure 2: Evolution of (a) the aspect ratio of the bubble R_{bubble} as function of the aspect ratio of the nanowire R_{nanowire} for the three wavelengths and (b) evolution of the volume of the bubble V_{bubble} as function of the volume of the nanowire V_{nanowire} .

Table 1: Fit parameters of the F function.

λ	NDP	NDF	$\hat{\sigma}^2$	Set of parameters			FNI
				c_0	c_1	c_2	
950	42	39	1.8111e-5	1.0036	0.2418	2.2334	32
1000	38	35	5.5850e-5	1.0082	0.3659	2.6394	15
1050	31	28	1.1106e-4	1.0124	0.6529	3.2416	23

G^{-1} the size and shape of the nanowire can be obtained from the information on the bubble:

$$\ln(V_{\text{nanowire}}) = \ln(\pi b^2 F^{-1}(R_{\text{bubble}})) = G^{-1}(\ln(V_{\text{bubble}})), \quad (6)$$

consequently,

$$b = \left[\frac{\exp(G^{-1}(\ln(V_{\text{bubble}})))}{\pi F^{-1}(R_{\text{bubble}})} \right]^{1/2} \quad \text{and} \quad a = \left[\frac{F^{-1}(R_{\text{bubble}}) \exp(G^{-1}(\ln(V_{\text{bubble}})))}{\pi} \right]^{1/2}. \quad (7)$$

Therefore the measurement of the size and shape of the bubble can be used to obtain information on the geometry of the nanowire and to reconstruct the size and shape of the nanowire.

4. CONCLUSION

The paper focus on the forming and the evolution of the shape and size of the bubble through a photo-thermal process between a nanowire of TiO_2 immersed in water and an electromagnetic wave. The increase of temperature is related to the geometry of the nanowire which leads to an increase in the shape and size of the bubble. That solution is computed by developing an adaptive remeshing method to computed with accuracy the temperature and by adapting the mesh to the evolution of the bubble. The coupled problem light-matter and heat is solved through an adaptive loop process allowing to converge to a stable solution and to decrease the number of nodes. The influence of the laser source and the geometrical parameters (wavelength, size and shape of the nanowire) related to the size and shape of the bubble are presented and analyzed. The aspect ratio and the volume of the bubble can be expressed as function of the aspect ratio and the volume of the nanowire. By solving the inverse problem two functions are obtained enabling to find the size and shape of the nanowire from the size and shape of bubble.

ACKNOWLEDGMENT

The authors thank the ANR-2011-NANO-008 NANOMORPH for financial support.

REFERENCES

1. Boroski, M., A. C. Rodrigues, J. C. Garcia, L. C. Sampaio, J. Nozaki, and N. Hioka, "Combined electrocoagulation and TiO_2 photoassisted treatment applied to wastewater effluents from

- pharmaceutical and cosmetic industries original,” *J. Hazard. Mater.*, Vol. 162, No. 1, 448–454, 2009.
2. Chatterjee, D. and A. Mahata, “Demineralization of organic pollutants on the dye modified TiO₂ semiconductor particulate system using visible light original,” *Appl. Catal. B — Environ.*, Vol. 33, No. 2, 119–125, 2001.
 3. Karamanis, D., A. N. Okte, E. Vardoulakis, and T. Vaimakis, “Water vapor adsorption and photocatalytic pollutant degradation with TiO₂-sepiolite nanocomposites original,” *Appl. Clay Sci.*, Vol. 53, No. 2, 181–187, 2011.
 4. Bystrzejewska-Piotrowska, G., J. Golimowski, and P. L. Urban, “Nanoparticles: Their potential toxicity, waste and environmental management,” *Waste Manage.*, Vol. 29, No. 9, 2587–2595, 2009.
 5. Nowack, B., “The behavior and effects of nanoparticles in the environment,” *Environ. Pollut.*, Vol. 157, No. 4, 1063–1064, 2009.
 6. Lapotko, D. and E. Lukianova, “Laser-induced micro-bubbles in cells,” *Int. J. Heat Mass Transfer*, Vol. 48, No. 1, 227–234, 2005.
 7. Lapotko, D., E. Lukianova, and A. Shnip, “Photothermal responses of individual cells,” *J. Biomed. Opt.*, Vol. 10, No. 1, 014006, 2005.
 8. Barchiesi, D., T. Grosge, E. Kremer, and M. L. de la Chapelle, “Electromagnetic heat induced in meso-structures: Computation of temperature in metallic dimers,” *PIERS Online*, Vol. 7, No. 5, 406–410, 2011.
 9. Chaari, A., L. Giraud-Moreau, T. Grosge, and D. Barchiesi, “Numerical modeling of the photothermal processing for bubble forming around nanowire in a liquid,” *Sci. World J.*, Vol. 2014, No. 794630, 2014.
 10. Grosge, T., H. Borouchaki, and D. Barchiesi, “New adaptive mesh development for accurate near-field enhancement computation,” *J. Microsc.*, Vol. 229, No. 2, 293–301, 2008.
 11. Grosge, T., S. Petit, D. Barchiesi, and S. Hudlet, “Numerical modeling of the subwavelength phase-change recording using an apertureless scanning near-field optical microscope,” *Opt. Express*, Vol. 12, No. 24, 5987–5995, 2004.
 12. Baffou, G., C. Girard, and R. Quidant, “Mapping heat origin in plasmonic structures,” *Physical Review Letters*, Vol. 104, No. 13, 136805, 2010.
 13. Jin, J., *The Finite Element Method in Electromagnetics*, John Wiley and Sons, New York, 1993.
 14. Grosge, T., A. Vial, and D. Barchiesi, “Models of near field spectroscopic studies: Comparison between finite element and finite difference methods,” *Opt. Express*, Vol. 13, No. 21, 8483–8497, 2005.
 15. Grosge, T., H. Borouchaki, and D. Barchiesi, “Improved scheme for accurate computation of high electric near-field gradients,” *Opt. Express*, Vol. 15, No. 3, 1307–1321, 2007.
 16. Brown, T. L. and J. A. Rice, “The effect of laser wavelength and power density on the laser desorption mass spectrum of fulvic acid,” *Org. Geochem.*, Vol. 31, No. 7–8, 627–634, 2000.
 17. O’Connor, K., O. Morris, and E. Sokell, “Angular and energy distribution of Sn ion debris ejected from a laser-produced plasma source, for laser power densities in the range suitable for extreme ultraviolet lithography,” *J. Appl. Phys.*, Vol. 109, No. 7, 073301, 2011.
 18. Gill, P. E. and W. Murray, “Algorithms for the solution of the nonlinear least-squares problem,” *SIAM J. Numer. Anal.*, Vol. 15, No. 5, 977–992, 1978.
 19. Vasin, V. V. and G. Y. Perestoronina, “The Levenberg-Marquardt method and its modified versions for solving nonlinear equations with application to the inverse gravimetry problem,” *Proc. Steklov Inst. Math.*, Vol. 280, No. 1, 174–182, 2013.

Computation of the Field Enhancement by Small Facet Angles of Metallic Nanoparticles: Adaptive Remeshing for Finite Element Method

F. Mezghani, D. Barchiesi, A. Cherouat, T. Grosge, and H. Borouchaki

Project Group for Automatic Mesh Generation and Advanced Methods
Gamma3 Project (UTT-INRIA), University of Technology of Troyes, France

Abstract— The accurate calculation of the electromagnetic field enhancement around nanoparticles that exhibit facets with small angles is of interest to characterize their efficiency, given the experimental reproducibility of such structures. The finite element method is efficient to compute the enhancement of the field intensity at the surface of nanoparticles although the numerical results strongly depends on the mesh of the domain. An adaptive remeshing method is shown to be robust where the classical refinement method fails. The adaptive refinement method uses *a posteriori* error estimator with interpolation method of the physical field of interest, based on the residual method. The strategy of this method is to remesh the domain of calculation on the basis of the map of the physical and geometrical size that will ensure compliance with the initial geometry and the accuracy of the physical solution. The numerical application shows that the intensity enhancement computed near the vertex between facets with small angles (5°) can reach 23%.

1. INTRODUCTION

The outstanding optical properties of metal nanoparticles are used extensively in nanoscience [1]. As a matter of fact a huge local electric field is generated under excitation by an electromagnetic field (laser source). This field enhancement due to plasmon resonance in metallic nanoparticles produces a light source of nanometric size that is of interest among all in biology and nanotechnology applications, such as cancer therapy, drug delivery, fluorescence or spectroscopy enhancement. The optical response depends strongly on the size and on the shape of the nanoparticle [1, 2]. Therefore intense research activities occur on the synthesis of nanoparticles with control of their size and shape, and on related simulations of the field enhancement for their optimization. In some experimental cases, the shape of gold nanoparticles exhibits facets that are related to their mode of elaboration [3, 4]. Consequently an accurate method of calculation of the field around such nanostructures could help to their optimization.

The finite element method is suitable for the calculation of the electromagnetic field around complex geometries. It allows the control of the accuracy while ensuring the convergence of calculation through the adaptation of mesh. The adaptation of mesh can use various types of methods. These different techniques of adaptation lead to the refinement (or coarsening) of the mesh to meet the accuracy target deduced from a physical or geometrical estimator of error [5–7]. However the efficiency of the remeshing loop for the FEM depends on the error estimator and the adaptation strategy. In this study the remeshing process uses the interpolation of the physical solution of the problem obtained from the Finite Element Method at step t to calculate an approximation of the solution on the new mesh (step $t + 1$). An *a posteriori* error estimate enables the generation of a size map associated to the mesh elements. Then the construction of an adapted mesh conforming to this size map and the interpolation of the solution between the new and old meshes is repeated until the desired accuracy is obtained [8–11]. The application of this technique for electromagnetic modeling was shown to be efficient [8–11] but the calculation of the field enhancement near facets with small angles has never been investigated despite the fact that experimental shapes of crystalline structures exhibit such pattern. The purpose of this study is to evaluate accurately the field enhancement produced by the apex of the triangle constituted by two adjacent facets. The problem is hard, the angle between the considered facets being 5° . Indeed this problem cannot be solved with Finite Difference Time Domain (FDTD), Discrete Dipole Approximation (DDA) nor Green's tensor methods that are not able to give the field enhancement exactly on the surface of nanoparticles with accuracy and therefore to describe such small changes of slope in the shape of the nanoparticle.

The Section 2 is devoted to the description of the electromagnetic model used and its formulation for Finite Element Method. In Section 3 the refinement and the remeshing adaptive methods

are compared. The numerical simulation of the field intensity enhancement is proposed before concluding.

2. FORMULATION OF THE ELECTROMAGNETISM PROBLEM FOR FINITE ELEMENT METHOD

We consider a nanoparticle with an overall spherical but polygonal shape and center O . The metallic gold nanoparticle has complex relative permittivity ϵ_1 and is immersed in a dielectric medium with a relative permittivity ϵ_2 . Both media are linear, homogeneous and isotropic. This nanoparticle is illuminated by a monochromatic polarized plane wave $\mathbf{E}_i = \mathbf{E}_0 \exp(ik_0ct)$ with \mathbf{E}_0 the amplitude vector of the incident electric field, $k_0 = \frac{2\pi}{\lambda_0}$ the modulus of the wave vector of the illumination (λ_0 being the wavelength in vacuum), and c the speed of light in vacuum. The problem consists in solving the 3D vectorial Helmholtz equation (Partial Differential Equation of elliptic type, corresponding to time harmonic wave equation) in each non magnetic material, using the curl operator $\nabla \times$ [12]:

$$\nabla \times (\nabla \times \mathbf{E}) - k_0^2 \epsilon_i \mathbf{E} = \mathbf{0} \quad (1)$$

At the interface between two materials (n_{12} being the outgoing normal vector), the boundary conditions corresponds to the continuity of the tangential component of the electric field and at the external border of the domain of calculation Ω , the radiation condition corresponds to the free propagation of the scattered field and plane wave illumination [12]:

$$n_{12} \times (\mathbf{E}_2 - \mathbf{E}_1) = 0 \quad \text{and} \quad \nabla \times \mathbf{E}_2 = i[k_0 n_{12} \times (\mathbf{E}_2 - \mathbf{E}_i) + \mathbf{k}_0 \times \mathbf{E}_i] \quad (2)$$

The field intensity enhancement is the maximum of the square of the intensity ($I_{\mathbf{r}} = \|\mathbf{E}\|^2$) over the domain Ω .

Numerical data: we consider a metallic gold nanoparticle with complex relative permittivity $\epsilon_1 = -11 + 1.33i$ ($\lambda_0 = 632.8$) as in a previously published 2D study [14]. The amplitude of the illuminating field is $\mathbf{E}_0 = 8.10^6(1, 0, 0)$ V/m along the x axis. The mean radius of the spherical polygon shape particle is $r = 20$ nm. The radius of the domain of calculation is $R_{\Omega} = 1400$ nm.

3. ADAPTATION METHODOLOGIES AND NUMERICAL RESULTS

The accuracy of the FEM solutions depends on the quality of the mesh of domain [5–11]. The first step (#0) of any remeshing method is the meshing of the geometry of the domain. Nodes are put on surfaces between materials and in the volume Ω with respect to a geometrical map using quality of elements. The result of computation on this mesh is shown in Fig. 1. The small angle between facets is not “seen” by the numerical simulation: no field enhancement is observed near the vertex between two adjacent facets.

Therefore mesh adaption is necessary. Amongst the various methods, the r-method moves the nodes from the initial mesh. The hp-method is a combination of h- and p-methods that can change both the size of elements on the mesh (h-method) and the dimension of space of functions describing their shape (p-method) [5–7]. The refinement of mesh consists in adding nodes to the initial one that is based on geometry properties of objects. Therefore the adaption leads to an increase of the number of elements and then requires more memory and computational time to obtain the solution

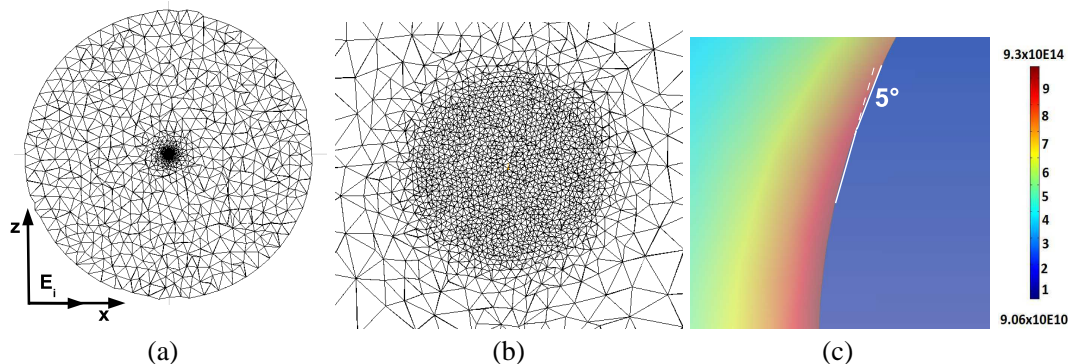


Figure 1: (a) Cut in the median plane $y = 0$ of the mesh at step #0 without remeshing, (b) zoom on the mesh around the nanoparticle and (c) the distribution of the intensity field.

at each step of the refinement loop. On the contrary, advanced methods of remeshing allow to improve the quality of the solutions by minimizing the overall error in the solutions obtained on the new mesh, with the possibility to increase or decrease locally the density of nodes. To reach this goal the error estimator indicates if the mesh density is too fine or too coarse. An efficient estimator of error must not be expensive in memory and CPU time. In this study we compare the refinement S_1 and the remeshing S_2 whose adaptation strategies are following. The first geometrical meshing (#0) is about the same for both methods. Then two methods S_1 (refinement) and S_2 (remeshing) are applied. The same solver for the finite element calculation of the electric field is used in both case.

- Refinement S_1 uses adaptation on the residual of the physical solution with h-adaptive mesh refinement (part of the software Comsol Multiphysics). The basic steps are:
 - Solve the problem on the mesh;
 - Evaluate the residual of the PDE on all mesh elements;
 - Refine a subset of the elements based on their size or of the local error indicators (the minimum and maximum element size are set automatically);
 - Repeat these steps until the requested number of refinements or the maximum number of elements are reached.
- Remeshing S_2 uses adaptation on the residual of the geometry and of the interpolation of the physical solution with h-adaptive mesh refinement and coarsening (OPTIFORM software). The basic steps are:
 - Solve the problem on the mesh;
 - Calculation of the interpolation error estimator to generate a unit metric on the physical map. It is based on the interpolation error depending on the Hessian of the finite element solution that is approximated by a local calculation of the solution.
 - Generation of an adapted meshing that meets the requirements of the metric physical card and the metric geometry for respecting the initial geometry (h_{\min} and h_{\max} are the minimum and maximum sizes of the elements respectively, ε is the maximum interpolation error that is tolerated in the solution);
 - Repeat these steps until the interpolation error is greater than ε .

The generation of an adapted meshing can be considered as an optimization problem which consists in minimizing a norm function (L2-norm or H1-norm) related to the distance between the new and the previous solutions.

The criteria of comparison between S_1 and S_2 are the accuracy of the solution, the memory (RAM) and the CPU time. Tables 1 and 2 gives the results of both methods S_1 and S_2 : for each refinement or remeshing steps: the number of nodes and elements, the parameters of the method and the maximum of the computed intensity ($\max \|E\|^2$) that corresponds to the field intensity enhancement.

Table 1: Number of nodes, tetrahedra, $\max \|E\|^2$, RAM, and computation time for the refinement strategy S_1 .

<i>Refinement</i> step	0	1
Nodes	49 285	208 934
Tetrahedra	289 609	1 148 123
$\max \ E\ ^2$ [V/m] ²	$9.3 \cdot 10^{14}$	$9.28 \cdot 10^{14}$
RAM [GB]	10.48	71
Time [s]	213	7 381

S_1 is efficient in the 2D case but we met difficulties when applied to 3D problem because of the calculation cost. In the investigated case of wide domain with small object (the ratio of the mean radius of particle to that of the whole domain of calculation is 1,4%) only one refinement is

Table 2: Number of nodes, elements (tetrahedra), h_{min} , ϵ , $\max \|E\|^2$, RAM, and computation time for the remeshing strategy S_2 .

Remeshing step	0	1	2	3	4	5
Nodes	48 781	51 851	76 796	317 642	377 681	404 107
Tetrahedra	289 605	308 333	459 179	1 922 512	2 277 531	2 432 568
h_{min}		0.35	0.35	0.35	0.35	0.35
ϵ		0.1	0.05	0.01	0.01	0.01
$\max \ E\ ^2$ [V/m] ²	$9.88 \cdot 10^{14}$	$1.06 \cdot 10^{15}$	$1.14 \cdot 10^{15}$	$1.22 \cdot 10^{15}$	$1.22 \cdot 10^{15}$	$1.22 \cdot 10^{15}$
RAM [GB]	8.72	9.57	12.89	54.53	65.95	66.14
Time [s]	214	208	292	1 568	1 942	1 932

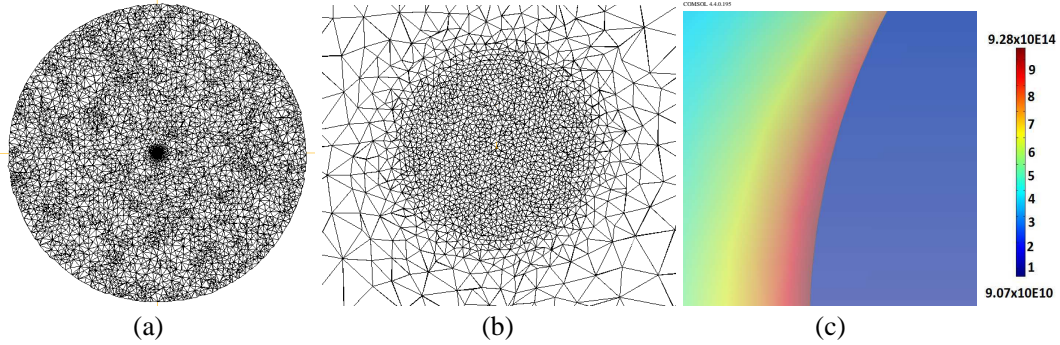


Figure 2: (a) Cut in the median plane $y = 0$ of the mesh at step 1 for the strategy S_1 , (b) zoom on the mesh around the nanoparticle, and (c) the distribution of the intensity field.

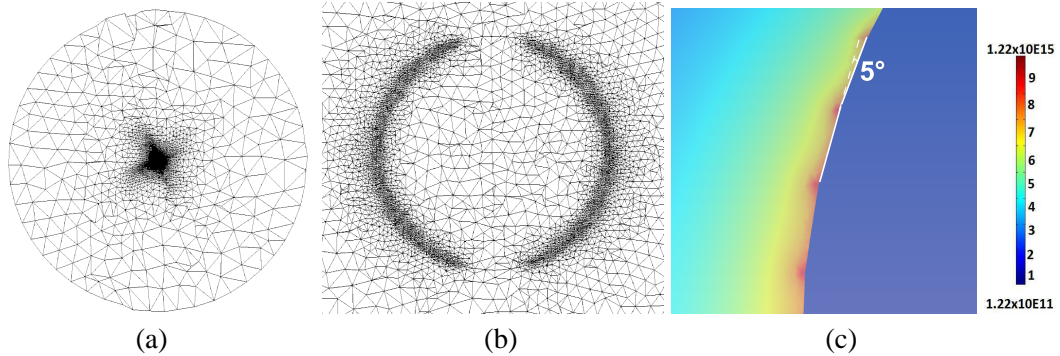


Figure 3: (a) Cut in median the plane $y = 0$ of the mesh at step 5 before remeshing for the strategy S_2 , (b) zoom on the mesh around the nanoparticle and (c) the distribution of the intensity field.

possible before divergence of calculation due to the huge increase of elements. The computational time at step #1 of S_1 is about four times that of each step of S_2 .

S_2 produces five new meshes to reach convergence toward the maximal error ϵ to 1%. The first iteration was performed to reach h_{min} . The computational time remains around half an hour and the number of nodes obtained from refinement (step #1 by S_1) is reached after two remeshing steps with S_2 . The value of the field intensity enhancement is stable from mesh #3 to #5. The corresponding increase of the number of elements is about 10%. The refinement S_1 guided by the physical error estimator of residual type increases the number of elements in the regions far from the particle where the field variation is smoother than in the vicinity of the particle (Fig. 2(a) compared to Fig. 1(a)). This explains the huge increase of nodes in the refinement method that prevent to reveal the field enhancement around the vertex. The performance of S_2 is illustrated in Fig. 3. The field enhancement appears in Fig. 3(c) using S_2 . Near vertex the size corresponding to the minimum element size h_{min} , it is about 0.35 nm and the error of the solution interpolated in each element is below the threshold of 0.01. The mesh is coarser far from the particle (Fig. 3(a)) and therefore the calculation requires less computational time and memory, the method giving a new mesh at each step, with optimized positions of nodes. Consequently, S_2 reveals that the

small angle at the junctions between two facets produces an increase in the value of the intensity enhancement around 23% for an angle of tilt between the two facets of 5° (Fig. 3).

4. CONCLUSION

This paper presents a remeshing method allowing to detect the effects of the small angles in the junction between two facets in nanostructures. A comparison between refinement and remeshing methods shows that remeshing gives accurate solution unlike the refinement that fails: angles of 5° between two adjacent facets can increase the value of the intensity of the electric field of 23% near the vertex. The adaptive remeshing allows to increase the accuracy and the convergence toward a solution having physical meaning. This method can be applied to any other shapes of nanostructures, which present facets with any angle and also roughnesses.

REFERENCES

1. Hu, M., J. Chen, Z.-Y. Li, L. Au, G. V. Hartland, X. Li, M. Marquez, and Y. Xia, "Gold nanostructures: engineering their plasmonic properties for biomedical applications," *Chem. Soc. Rev.*, Vol. 35, 10841094, 2006.
2. Kessentini, S. and D. Barchiesi, "Quantitative comparison of optimized nanorods, nanoshells and hollow nanospheres for photothermal therapy," *Biomed. Opt. Express*, Vol. 3, No. 3, 590–604, 2012.
3. Liu, B., J. Xie, J. Y. Lee, Y. P. Ting, and J.-P. Chen, "Optimization of high-yield biological synthesis of single-crystalline gold nanoplates," *J. Phys. Chem. B*, Vol. 109, 15256–15263, 2005.
4. Daniel, M.-C. and D. Astruc, "Gold nanoparticles: Assembly, supramolecular chemistry, quantum-size-related properties, and applications toward biology, catalysis, and nanotechnology," *Chem. Rev.*, Vol. 104, 293–346, 2004.
5. Verfürth, R., *A Review of A Posteriori Error Estimation and Adaptive Mesh-Refinement Techniques*, Wiley and Teubner, 1996.
6. Ainsworth, M. and J. T. Oden, "A posteriori error estimation in finite element analysis," *Comput. Methods Appl. Mech. Engrg.* Vol. 142, 1–88, 1997.
7. Borouchaki, H., D. Chapelle, P.-L. George, P. Laug and P. Frey, "Estimateurs d'erreur géométriques et adaptation de maillages," *Maillage et Adaptation*, sous la direction de P.-L. George, *Traité Mécanique et Ingénierie des Matériaux*, Hermès, France, 2001.
8. Grosgees, T., H. Borouchaki, and D. Barchiesi, "Improved scheme for accurate computation of high electric near-field gradients," *Opt. Express* Vol. 15, No. 3, 1307–1321, 2007.
9. Borouchaki, H., T. Grosgees, and D. Barchiesi, "Improved 3D adaptive remeshing scheme applied in high electromagnetic field gradient computation" *Finite Elements in Analysis and Design*, Vol. 44, Nos. 1–2, 84–95, 2010.
10. Grosgees, T., H. Borouchaki, and D. Barchiesi, "New adaptive mesh development for accurate near field enhancement computation," *J. Microsc.* Vol. 229, No. 2, 293–301, 2008.
11. Borouchaki, H., T. Grosgees, and D. Barchiesi, "Enhancement of the accuracy of numerical field computation using adaptive three dimensional remeshing scheme," *C. R. Meca.*, Vol. 338, No. 3, 127–131, 2010.
12. Jin, J., *The Finite Element Method in Electromagnetics.*, John Wiley and Sons, New York, 1993.
13. Barchiesi, D., E. Kremer, A. Cherouat, T. Grosgees, and H. Borouchaki, "Dilation of nanonantennas induced by an electromagnetic source," *Adv. Electromagn.*, Vol. 1, No. 2, 48–57, 2012.
14. Barchiesi, D., T. Grosgees, E. Kremer, and M. Lamy de la Chapelle, "Electromagnetic heat induced in meso-structures: Computation of temperature in metallic dimers," *PIERS Online*, Vol. 7, No. 5, 406–410, 2011.

A Unified Field Analysis Method for IR/MMW Beam Splitter

Yi Tian^{1,2,3}, Hui Yan^{1,3}, Xin Wang^{1,3}, Li Zhang², and Zhuo Li^{1,3}

¹School of Opto-Electronics, Beijing Institute of Technology, Beijing 100081, China

²Shanghai Institute of Electro-Mechanical Engineering, Shanghai 201109, China

³Beijing Key Lab for Precision Optoelectronic Measurement Instrument and Technology
Beijing 100081, China

Abstract— Aperture field integration method (AFIM) is proposed and utilized to efficiently compute the field distributions of infrared (IR)/millimeter wave (MMW) beam splitter including the MMW near field distribution and IR far field distribution. A single dielectric layer beam splitter is analyzed by AFIM. Compared to the multilevel fast multipole method (MLFMM), the memory requirement and CPU time consumption are reduced drastically from 4.6 GB and 2141 seconds to 1.2 MB and 58 seconds, respectively, when the MMW near field distribution is computed. In order to meet the far field condition a scale factor is proposed to transform the focal plane into a far field plane, when the IR far field in a focal plane is computed. The IR far field calculation accuracy is better than 97% compared to the analytical solutions. The simulation results show that the AFIM as a unified method can be applied to both beam splitters' MMW near field and IR far field engineering estimation.

1. INTRODUCTION

An IR/MMW dual-mode compound guidance system has both high-precision infrared imaging and all-weather-working millimeter wave imaging advantages at the same time. IR/MMW beam splitter is a key component of dual-mode compound guidance system. The beam splitter is tilted by 45° along the main axis and it transmits MMW signals and reflects IR signals at the same time as shown in Fig. 1. Its role is to spatially split the IR and MMW compound signal into a reflected IR signal received by an IR sensor in the vertical direction and a transmitted MMW signal received by a MMW sensor in the horizontal direction respectively [1].

Many types of beam splitters have been proposed, such as dielectric coated with an array of small conducting patches [2], holographic optical elements [3], frequency selective surface [4], conducting inductive meshes with periodic rectangle units [1] micro-mirror array [5], multilayered dielectric plate [6] and so forth.

No matter which kind of beam splitter is inserted in the dual-mode compound guidance system, the insertion of a beam splitter will affect the uniformity of the MMW field. Simultaneously, the insertion also affects the IR imaging quality. Moreover, the detecting and tracking precision will be limited by the distortion of the field received by MMW and IR sensors [5–7]. Therefore, it is necessary to build a theoretical model to analyze the MMW and IR field distribution. Generally, the calculation of electrical field in a MMW sensor aperture is a near field diffraction problem. However the calculation of optical field focused on an IR focal plane array through an IR lens is a far field diffraction problem. Nevertheless, both IR and MMW are electromagnetic wave and they can be described by Maxwell-Equations. So the MMW near field and IR far field problem can be solved by a unified method derived from integral formulation of Maxwell-Equations. Thus,

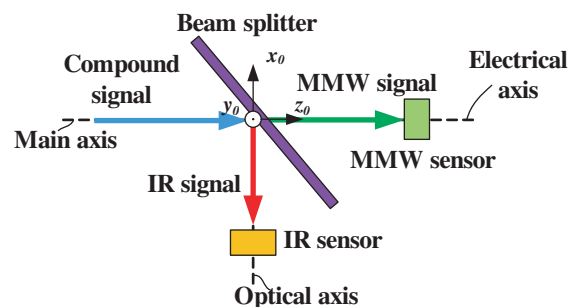


Figure 1: Working principle of beam splitter.

aperture field integration method (AFIM) is proposed to analyze both MMW near field and IR far field of beam splitters in this paper.

In Section 2 the basic theory and formulations about AFIM are introduced. In Section 3, the method is investigated through the calculation of a circular single layer beam splitter. The calculation results of MMW field are described and compared with MLFMM. The calculation results of IR field are also described and compared with the analytical solution. In the last section a brief conclusion is made.

2. METHODS AND FORMULATIONS

In order to obtain the diffracted field, the beam splitter is simplified to a 2D aperture as shown in Fig. 2. According to the equivalence principle, the field produced by the beam splitter current could be obtained by computing the field of the aperture equivalent source [8,9]. In this way, the analysis of the beam splitter can be converted to the analysis of the aperture.

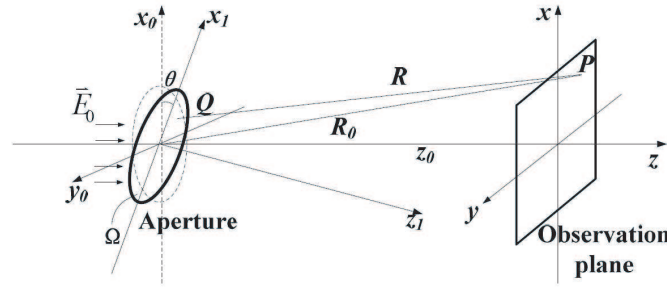


Figure 2: Principle of AFIM.

Assume that the aperture is tilted by an angle of θ along the main axis as shown in Fig. 2. The incident wave can be assumed as plane wave. The aperture field can be expressed as [1]

$$\vec{E}_A(x_1, y_0) = \vec{E}_0 \exp[-j(k_0 x_0 \tan \theta)] \quad (1)$$

where, k_0 is the wave number, \vec{E}_0 is the amplitude vector of polarized electrical field. According to the equivalence principle, the equivalent magnetic current is expressed as [9]

$$\vec{J}_m = -\hat{z} \times \vec{E}_A \quad (2)$$

The electrical vector potential is

$$\vec{A}_m = \frac{\varepsilon}{4\pi} \iint_{\Omega} \frac{\vec{J}_m e^{-jk_0 R}}{R} dx_1 dy_0 \quad (3)$$

The field at an arbitrary observation point P is [9]

$$\vec{E}(x, y) = -\frac{1}{\varepsilon} \nabla \times \vec{A}_m = -\frac{1}{4\pi} \iint_{\Omega} \left[R \times (\hat{z} \times \vec{E}_A) \right] \cdot (1 + jk_0 R) \frac{e^{-jk_0 R}}{R^3} dx_1 dy_0 \quad (4)$$

where R is the distance between the source point Q and field point P, which can be expressed as [1]

$$R = \sqrt{(x - x_0)^2 + (y - y_0)^2 + (z_0 - x_0 \tan \theta)^2} \quad (5)$$

where, z_0 is the distance between the aperture and the observation plane. The integration is over the aperture region Ω .

The near field and far field can be obtained by computing the Eq. (4). However, the far field distribution in a focal plane can't be obtained by directly solving the Eq. (4) because of the phase transformation by a lens with focal length of f . In order to calculate the far field distribution in a focal plane, a scale factor η is introduced to transform the focal plane to a far field plane. η should meet the far field condition [10]:

$$\eta \leq \frac{2r^2}{\lambda f} \quad (6)$$

where, r is the circumcircle radius of the aperture region Ω .

So the far field in a focal plane can be expressed as

$$\vec{E}_{far}(x', y') = -\frac{1}{4\pi} \iint_{\Omega} \left[R' \times (\hat{z} \times \vec{E}_A) \right] \cdot (1 + jk_0 R') \frac{e^{-jk_0 R'}}{R'^3} dx_1 dy_0 \quad (7)$$

where, $R' = \eta f$, $x' = \eta x$, $y' = \eta y$.

3. NUMERICAL EXAMPLE AND VALIDATION

3.1. Beam Splitter Example

In order to validate our computation method, a single layer circular beam splitter with IR film is analyzed. It is made of lossless material with relative dielectric constant of 3.8. Its thickness is 2 mm. The radius r of the beam splitter is 50 mm. The surface is coated with IR film proposed in [6]. The beam splitter is 45° tilted angles placed relative to the electrical axis of the MMW sensor. The distance between the MMW sensor and the beam splitter is 50 mm. It is designed for the MMW with 35 GHz frequency. The observation plane of the MMW sensor is assumed to be a square region with an edge length of 70 mm. The working center wavelength of IR is $4 \mu\text{m}$. The focal length of IR sensor objective lens is 120 mm. The observation plane of the IR sensor is assumed to be a square region with an edge length of $100 \mu\text{m}$.

3.2. MMW Near Field Validation

In order to validate the MMW near field computation ability of AFIM, the calculation results are compared with the results obtained by MLFMM, because MLFMM is considered to be a high precision computation [5, 7]. The computations made by AFIM and MLFMM are carried out on the same computer equipped with two 2.50 GHz Intel® Xeon® CPUs (12 cores) and 128 GB memories. Both of the MLFMM and AFIM codes support parallel computation.

In both of the computations the observation plane is discretized equally to 81 divisions along x -axis and y -axis. In MLFMM computation the edge of the triangle mesh is $\lambda/8$. So the mesh number and mesh edges are up to 43232 and 64848, respectively. As comparison, the edge of the mesh is $\lambda/22$ in AFIM computation, which brought to a mesh number of 65536. The computational efficiency comparison with two methods is shown in Table 1. MLFMM consumes 4.6 GB memories and more than 30 minutes. However, AFIM uses only several MB memories and less than 1 minute, even though the mesh size in AFIM is less than that in MLFMM. The comparison indicates that AFIM is much more efficient than MLFMM.

Table 1: Comparison of computational efficiency.

Method	Mesh size	Unknown field point	Memory	Time
MLFMM	$\lambda/8$	81×81	4.6 GB	2141s
AFIM	$\lambda/22$	81×81	1.2 MB	58s

In order to comparison, the amplitude and phase in observation plane are normalized by the value at $(x = 0 \text{ mm}, y = 0 \text{ mm})$. Figs. 3(a) and (b) are the amplitude distribution of MMW near field computed by AFIM and MLFMM, respectively. The maximum and minimum amplitudes computed by AFIM are 4.06 dB and -14.68 dB respectively as shown in Fig. 3(a). The maximum and minimum amplitudes computed by MLFMM are 2.94 dB and -12.56 dB respectively as shown in Fig. 3(b). However, the distributions of the amplitude obtained by the two methods match well. The maximum and minimum phases computed by AFIM are 43.68° and -61.87° as shown in Fig. 4(a). The maximum and minimum phases computed by MLFMM are 29° and -98.5° as shown in Fig. 4(b). Similarly, the patterns of the phase obtained by the two methods also match well. Compared with MLFMM, errors are introduced. One of reasons is that the beam splitter is equivalent to an aperture, and the detailed structure of the beam splitter is not considered in AFIM. However, compared to the commonly used MLFMM the memory requirement and CPU time consumption are reduced drastically. So AFIM can be used as an efficiency engineering approximation method.

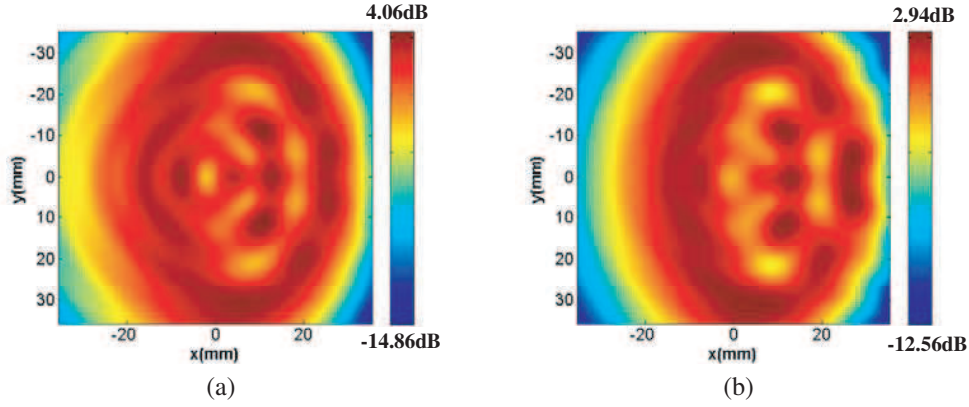


Figure 3: Amplitude distribution of MMW near field in observation plane computed by (a) AFIM; (b) MLFMM.

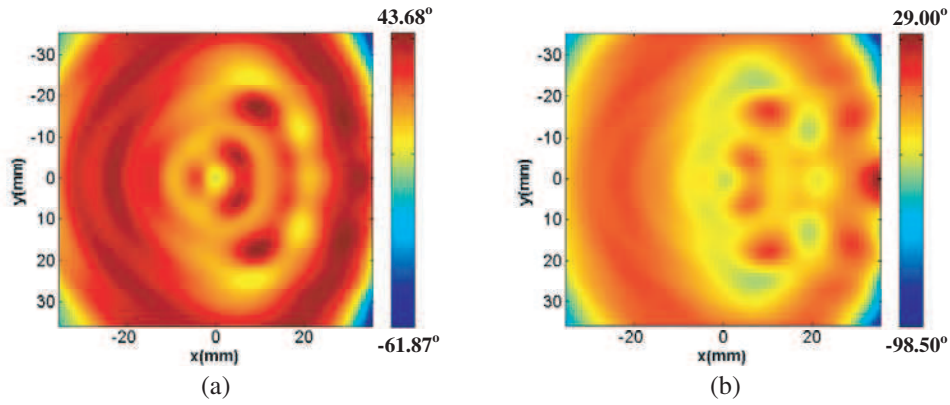


Figure 4: Phase distribution of MMW near field in observation plane computed by (a) AFIM; (b) MLFMM.

3.3. IR Far Field Validation

In order to validate the computation ability of IR far field by using AFIM, the calculation results are compared with the results obtained by analytical solution [10]. The analytical solution (AS) can be expressed as

$$\vec{E}_{far}(x, y) = Cr^2 \cos \theta \frac{2J_1(\alpha)}{\alpha} \quad (8)$$

where α , C can be expressed as

$$\alpha = \frac{2\pi r \sqrt{(\beta_1 \cos \theta)^2 + y^2}}{\lambda R_0} \quad (9)$$

$$C = \frac{\vec{E}_0 j k_0 e^{-jk_0 R_0}}{4\pi R_0} \quad (10)$$

where, β_1 and R_0 can be expressed as

$$\beta_1 = x + \tan \theta \sqrt{R_0^2 - x^2 - y^2} - R_0 \tan \theta \quad (11)$$

$$R_0 = \sqrt{x^2 + y^2 + z_0^2} \quad (12)$$

The focal plane is a square region with edge length of $100 \mu\text{m}$. It is 512×512 meshed. The aperture is 128×128 meshed for AFIM. In order to meet the far field condition, η should be larger than 1×10^4 , and let $\eta = 1 \times 10^6$ in this paper. In order to quantitatively compare the results, the relative error of far field intensity I_{AFIM} computed by AFIM is calculated according to [11]

$$\frac{\|I_{AFIM} - I_{AS}\|}{\|I_{AS}\|} \quad (13)$$

where $\| \cdot \|$ is the 2-norm and I_{AS} is the reference solution computed by AS with mesh number of 512×512 .

The normalized intensities of the IR far field computed by AFIM and AS are compared in Fig. 5. The error is only 0.14% as shown in Table 2. The relationship between the error, consumed time and mesh number of aperture is also listed in Table 2. The CPU time decreases drastically with the decrease of the mesh number. And the error increases with the decrease of mesh number. The right results can't be obtained when the mesh number of aperture is 8×8 . To keep an error lower than 3%, the mesh number more than 16×16 is required by AFIM.

Table 2: Error and CPU time versus mesh number of aperture.

Mesh number	Error	CPU time
128×128	0.14%	612.00 s
64×64	0.51%	162.08 s
32×32	1.35%	74.44 s
16×16	2.30%	21.56 s
8×8	288.92%	8.34 s

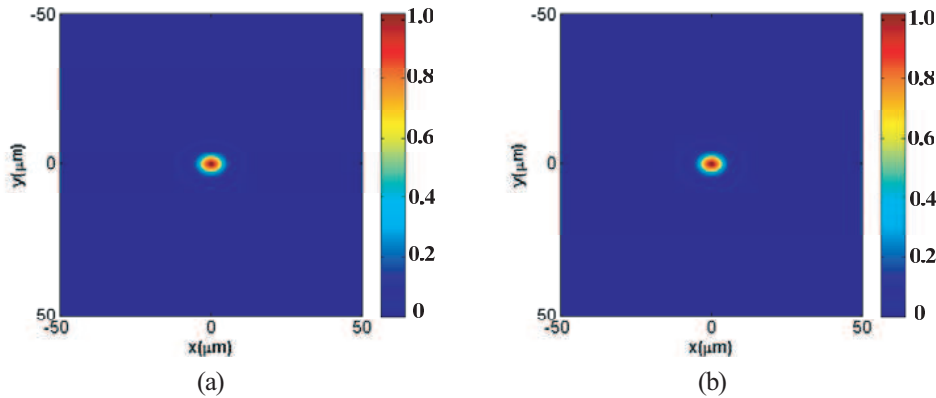


Figure 5: Normalized intensity distribution at focal plane computed by (a) AFIM; (b) AS.

The zero-order diffraction primary maximum widths along x -axis and y -axis acquired by AFIM are $16.56 \mu\text{m}$ and $11.86 \mu\text{m}$, respectively. If $\theta = 0^\circ$, the zero-order diffraction primary maximum diameter can be computed by $0.61\lambda f/r = 11.71 \mu\text{m}$. The simulation results show that the zero-order diffraction primary maximum width is stretched along x -axis while it remains unchanged along y -axis. The tilted angle will lead to increase the diffraction limit. Thus the resolution of the IR sensor will be decreased. It must be noted that the AFIM can also be used to analyze beam splitters with complex aperture shapes without analytical solution of far field.

4. CONCLUSIONS

According to equivalent principle, a unified method AFIM is proposed to compute field distribution of IR/MMW beam splitter including the MMW near field distribution and IR far field distribution. For a single layer beam combiner, the patterns of the MMW amplitude and phase obtained by the MLFMM and AFIM match well. An appreciable speedup on the order of 40 is achieved. In order to meet the far field condition, the scale factor is proposed and it should be larger than 1×10^4 in the numerical example. The calculation accuracy is better than 97% for IR far field computation when the mesh number of the equivalent aperture is more than 16×16 . The simulation results show that the AFIM can be used as an efficiency engineering approximation method in the design, analysis, and optimization of beam splitter.

REFERENCES

1. Liu, Y., J. Tan, and J. Ma, "Use of conducting inductive meshes with periodic rectangle units as an infrared/microwave dual-mode detecting beamsplitter," *J. Opt.*, Vol. 13, 035407, 6pp, 2011.
2. Mobley, S., J. Cole, J. Cooper, and J. Jarem, "U.S. Army Missile Command dual-mode millimeter wave/infrared simulator development," *Proc. SPIE*, Vol. 2741, 316–331, 1996.
3. Mobley, S. B. and J. Gareri, "Hardware-in-the-loop simulation (HWIL) facility for development, test, and evaluation of multi-spectral missile systems — Update," *Proc. SPIE*, Vol. 4027, 11–21, 2000.
4. Mobley, S. and J. Cole, "Dichroic beam combiner to support hardware-in-the-loop testing of dual-mode common aperture seekers," *Proc. SPIE*, Vol. 3368, 32–41, 1998.
5. Tian, Y., L. J. Lv, L. W. Jiang, X. Wang, Y. H. Li, H. M. Yu, X. C. Feng, Q. Li, L. Zhang, and Z. Li, "Infrared/microwave (IR/MW) micromirror array beam combiner design and analysis," *Appl. Opt.*, Vol. 52, 5411–5419, 2013.
6. Tian, Y., R. Xu, Rui. Shi, X. Wang, Q. Li, L. Zhang, and Z. Li, "IR/MW multilayered dielectric plate beam combiner design, optimization and evaluation," *Appl. Optics*, Vol. 52, 288–297, 2013.
7. Mobley, S., J. Cole, J. Cooper, and J. Jarem, "U.S. Army Missile Command dual-mode millimeter wave/infrared simulator development," *Proc. SPIE*, Vol. 2741, 316–331, 1996.
8. McKay, J. P. and R. S. Yahya, "Compact range reflector analysis using the plane wave spectrum approach with an adjustable sampling rate," *IEEE Trans. Antenna. Propag.*, Vol. 39, 746–753, 1991.
9. Quan, S., "Time domain analysis of the near-field radiation of shaped electrically large apertures," *IEEE Trans. Antenna. Propag.*, Vol. 58, 300–306, 2010.
10. Tan, J., Z. Lu, J. Liu, P. Jin, and Y. Wang, "Analysis of fraunhofer diffractive characteristics of a tilted metallic mesh for its effect on optical measurement," *Measurement Science and Technology*, Vol. 18, No. 6, 1703–1709, 2007.
11. Su, T., D. Ding, Z. Fan, and R. Chen, "Efficient analysis of EM scattering from bodies of revolution via the ACA," *IEEE Trans. Antenna. Propag.*, Vol. 62, No. 2, 983–985, Feb. 2014.

Conductor Modeling Based on Volume Integral Equations

J. Zhang and M. S. Tong

Department of Electronic Science and Technology
Tongji University, Shanghai, China

Abstract— The electromagnetic (EM) problems with conductive objects can be solved by surface integral equations (SIEs) with the method of moments (MoM) discretization in the integral equation approach. However, the solutions may not be valid for a wide range of frequency and conductivity. In this work, we use the volume integral equations (VIEs) to exactly formulate the problem and propose a point-matching scheme to solve it. The VIEs are usually well-conditioned because they are the second-kind of integral equation. The point-matching scheme can select current densities as unknowns so that the integral kernels are free of material parameters and the solutions can bear a significant change of frequency and conductivity. A numerical example for EM scattering by a conductive sphere with different parameters is presented to demonstrate the approach.

1. INTRODUCTION

Accurate solution of electromagnetic (EM) problems with lossy conductors requires to consider the finite conductivity of the conductors. The loss of the conductors may not be ignored when the frequency is low or the conductivity is small since the skin depth is large [1]. In the integral equation approach for solving the problem, one usually uses surface integral equation (SIE) approach with an approximate surface impedance when the skin depth is small [2]. For large skin depth caused by low frequency or small conductivity, one treats the conductors as dielectric-like objects and uses a two-region scheme to formulate the SIEs [3, 4]. The SIEs are solved by the method of moments (MoM) with the Rao-Wilton-Glisson (RWG) basis function [5]. However, the solutions may not be valid for a wide range of frequency and conductivity because the integral kernels include those parameters and the conditioning of SIEs is susceptible to the frequency [6].

In this work, we also treat the conductors as dielectric-like objects but use volume integral equations (VIEs) to exactly formulate the problem. The VIEs are the second-kind of integral equation, so they are well-conditioned in general [1]. Also, the VIEs only have one unknown function (electric current density) for dielectric (nonmagnetic) objects while two unknown functions appear in the SIEs. To solve the VIEs, we do not use the traditional MoM with the Schaubert-Wilton-Glisson (SWG) basis function [7] but propose a point-matching scheme which does not use any basis and testing functions and allows a geometric discretization of nonconforming meshes, resulting in much convenience in implementation [8]. Moreover, the scheme can choose current densities as unknowns so that the integral kernels are free of material parameters and the solutions can endure a wide change of frequency and conductivity. The scheme requires an accurate evaluation of hypersingular integrals resulting from the double gradient operation in the dyadic Green's function but we have developed a robust technique to handle them [9, 10]. We present a numerical example for EM scattering by a conductive sphere to illustrate the approach and good results can be observed.

2. VOLUME INTEGRAL EQUATIONS

Consider the EM scattering by a three-dimensional (3D) penetrable object in the free space with a permittivity ϵ_0 and a permeability μ_0 , the VIEs can be written as [1]

$$\vec{E}(\vec{r}) = \vec{E}^{inc}(\vec{r}) + i\omega\mu_0 \int_V \vec{\bar{G}}(\vec{r}, \vec{r}') \cdot \vec{J}_V(\vec{r}') d\vec{r}' - \nabla \times \int_V \vec{\bar{G}}(\vec{r}, \vec{r}') \cdot \vec{M}_V(\vec{r}') d\vec{r}', \quad \vec{r} \in V \quad (1)$$

$$\vec{H}(\vec{r}) = \vec{H}^{inc}(\vec{r}) + i\omega\epsilon_0 \int_V \vec{\bar{G}}(\vec{r}, \vec{r}') \cdot \vec{M}_V(\vec{r}') d\vec{r}' + \nabla \times \int_V \vec{\bar{G}}(\vec{r}, \vec{r}') \cdot \vec{J}_V(\vec{r}') d\vec{r}', \quad \vec{r} \in V \quad (2)$$

where $\vec{E}^{inc}(\vec{r})$ and $\vec{H}^{inc}(\vec{r})$ are the incident electric field and magnetic field, respectively, while $\vec{E}(\vec{r})$ and $\vec{H}(\vec{r})$ are the total electric field and magnetic field inside the object, respectively. The integral kernel is the dyadic Green's function given by

$$\vec{\bar{G}}(\vec{r}, \vec{r}') = \left(\vec{I} + \frac{\nabla\nabla}{k_0^2} \right) g(\vec{r}, \vec{r}') \quad (3)$$

where \vec{I} is the identity dyad, k_0 is the free-space wavenumber, and $g(\vec{r}, \vec{r}') = e^{ik_0 R}/(4\pi R)$ is the scalar Green's function in which $R = |\vec{r} - \vec{r}'|$ is the distance between an observation point \vec{r} and a source point \vec{r}' . The unknown functions to be solved are the volumetric electric current density and magnetic current density inside the object, which are related to the total electric field and magnetic field by

$$\vec{J}_V(\vec{r}') = i\omega[\epsilon_0 - \epsilon(\vec{r}')] \vec{E}(\vec{r}') \quad (4)$$

$$\vec{M}_V(\vec{r}') = i\omega[\mu_0 - \mu(\vec{r}')] \vec{H}(\vec{r}') \quad (5)$$

where $\epsilon(\vec{r}')$ and $\mu(\vec{r}')$ are the permittivity and permeability of the object, respectively. When the conductive objects are treated as dielectric-like objects, the above VIEs are also applicable. If we choose the current densities as the unknown functions to be solved, the above VIEs can be changed into

$$\frac{1}{i\omega[\epsilon_0 - \epsilon(\vec{r}')] } \vec{J}_V(\vec{r}) - i\omega\mu_0 \int_V \vec{G}(\vec{r}, \vec{r}') \cdot \vec{J}_V(\vec{r}') dV' + \int_V \nabla g(\vec{r}, \vec{r}') \times \vec{M}_V(\vec{r}') dV' = \vec{E}^{inc}(\vec{r}), \quad \vec{r} \in V \quad (6)$$

$$\frac{1}{i\omega[\mu_0 - \mu(\vec{r}')] } \vec{M}_V(\vec{r}) - i\omega\epsilon_0 \int_V \vec{G}(\vec{r}, \vec{r}') \cdot \vec{M}_V(\vec{r}') dV' - \int_V \nabla g(\vec{r}, \vec{r}') \times \vec{J}_V(\vec{r}') dV' = \vec{H}^{inc}(\vec{r}), \quad \vec{r} \in V \quad (7)$$

where $\epsilon(\vec{r}') = \epsilon_r' \epsilon_0 + i\frac{\sigma}{\omega} = \epsilon_c$ in which ϵ_r' is the real part of relative permittivity and σ is the conductivity while $\mu(\vec{r}')$ can be assumed to be a constant μ_c for conductive media. The conductive objects with a conductivity σ are usually nonmagnetic or $\mu(\vec{r}') = \mu_0$, the magnetic current density vanishes and the VIEs can be reduced to

$$\frac{1}{i\omega[\epsilon_0 - \epsilon(\vec{r}')] } \vec{J}_V(\vec{r}) - i\omega\mu_0 \int_V \vec{G}(\vec{r}, \vec{r}') \cdot \vec{J}_V(\vec{r}') d\vec{r}' = \vec{E}^{inc}(\vec{r}), \quad \vec{r} \in V. \quad (8)$$

3. POINT-MATCHING SCHEME

The above VIE for conductive objects can be solved with a point-matching or collocation scheme. Since the current density is chosen as the unknown function to be solved and the integral kernel, i.e., dyadic Green's function, does not include the material property of the objects, we can greatly facilitate the implementation. The VIEs are first expressed into a scalar form since we do not use any vector basis function. When we assume that the current densities are constant in a small tetrahedral element after discretization, the VIE can be changed into

$$\sum_{n=1}^N \int_{\Delta V_n} dV' \left\{ i\omega\mu_0 \vec{G}(\vec{r}_m^c, \vec{r}') \cdot \begin{bmatrix} J_V^x(\vec{r}_n^c) \\ J_V^y(\vec{r}_n^c) \\ J_V^z(\vec{r}_n^c) \end{bmatrix} - \begin{bmatrix} g_y(\vec{r}_m^c, \vec{r}') M_V^z(\vec{r}_n^c) - g_z(\vec{r}_m^c, \vec{r}') M_V^y(\vec{r}_n^c) \\ g_z(\vec{r}_m^c, \vec{r}') M_V^x(\vec{r}_n^c) - g_x(\vec{r}_m^c, \vec{r}') M_V^z(\vec{r}_n^c) \\ g_x(\vec{r}_m^c, \vec{r}') M_V^y(\vec{r}_n^c) - g_y(\vec{r}_m^c, \vec{r}') M_V^x(\vec{r}_n^c) \end{bmatrix} \right\} \\ - \frac{1}{i\omega(\epsilon_0 - \epsilon_c)} \begin{bmatrix} J_V^x(\vec{r}_m^c) \\ J_V^y(\vec{r}_m^c) \\ J_V^z(\vec{r}_m^c) \end{bmatrix} = - \begin{bmatrix} E_x^{inc}(\vec{r}_m^c) \\ E_y^{inc}(\vec{r}_m^c) \\ E_z^{inc}(\vec{r}_m^c) \end{bmatrix}, \quad m = 1, 2, \dots, N \quad (9)$$

$$\sum_{n=1}^N \int_{\Delta V_n} dV' \left\{ i\omega\epsilon_0 \vec{G}(\vec{r}_m^c, \vec{r}') \cdot \begin{bmatrix} M_V^x(\vec{r}_n^c) \\ M_V^y(\vec{r}_n^c) \\ M_V^z(\vec{r}_n^c) \end{bmatrix} + \begin{bmatrix} g_y(\vec{r}_m^c, \vec{r}') J_V^z(\vec{r}_n^c) - g_z(\vec{r}_m^c, \vec{r}') J_V^y(\vec{r}_n^c) \\ g_z(\vec{r}_m^c, \vec{r}') J_V^x(\vec{r}_n^c) - g_x(\vec{r}_m^c, \vec{r}') J_V^z(\vec{r}_n^c) \\ g_x(\vec{r}_m^c, \vec{r}') J_V^y(\vec{r}_n^c) - g_y(\vec{r}_m^c, \vec{r}') J_V^x(\vec{r}_n^c) \end{bmatrix} \right\} \\ - \frac{1}{i\omega(\mu_0 - \mu_c)} \begin{bmatrix} M_V^x(\vec{r}_m^c) \\ M_V^y(\vec{r}_m^c) \\ M_V^z(\vec{r}_m^c) \end{bmatrix} = - \begin{bmatrix} H_x^{inc}(\vec{r}_m^c) \\ H_y^{inc}(\vec{r}_m^c) \\ H_z^{inc}(\vec{r}_m^c) \end{bmatrix}, \quad m = 1, 2, \dots, N \quad (10)$$

where \vec{r}_m^c represents the center of the m th tetrahedron (observation element) and \vec{r}_n^c denotes the center of the n th tetrahedron (source element). Also, $\{g_x(\vec{r}, \vec{r}'), g_y(\vec{r}, \vec{r}'), g_z(\vec{r}, \vec{r}')\}$ are the three components of the gradient of scalar Green's function. The matrix elements in the above can be obtained by integrating the components of the dyadic Green's function or the gradient of scalar Green's function over each small tetrahedral element ΔV_n ($n = 1, 2, \dots, N$) for different observation

point \vec{r}_m^c ($m = 1, 2, \dots, N$). The dyadic Green's function has nine components but only six are independent due to its symmetry. If the media are nonmagnetic or $\vec{M}_V(\vec{r}') = 0$, then the above matrix equation can be reduced to

$$i\omega\mu_0 \sum_{n=1}^N \left\{ \left[\int_{\Delta V_n} \vec{G}(\vec{r}_m^c, \vec{r}') d\vec{r}' \right] \cdot \begin{bmatrix} J_V^x(\vec{r}'_n^c) \\ J_V^y(\vec{r}'_n^c) \\ J_V^z(\vec{r}'_n^c) \end{bmatrix} \right\} - \frac{1}{i\omega(\epsilon_0 - \epsilon_c)} \begin{bmatrix} J_V^x(\vec{r}_m^c) \\ J_V^y(\vec{r}_m^c) \\ J_V^z(\vec{r}_m^c) \end{bmatrix} = - \begin{bmatrix} E_x^{inc}(\vec{r}_m^c) \\ E_y^{inc}(\vec{r}_m^c) \\ E_z^{inc}(\vec{r}_m^c) \end{bmatrix},$$

$$m = 1, 2, \dots, N. \quad (11)$$

When $m \neq n$, the integral kernel is regular and we can use a numerical quadrature rule like the Gauss-Legendre quadrature rule to evaluate the matrix elements. When $m = n$, however, the integral kernel is hypersingular and we need to specially treat it. Since the integrand does not include the material parameters of the objects, we can use the singularity treatment technique developed for regular dielectric media to evaluate the relevant matrix elements [9, 10].

4. NUMERICAL EXAMPLES

We present two numerical examples to demonstrate the proposed approach. The first example considers the EM scattering by a conductive sphere which is embedded in a dielectric medium with a relative permittivity $\epsilon_r = 3.0$. The sphere has a radius $a = 5.0$ mm, a relative permeability $\mu_r = 20.0$, and a conductivity $\sigma = 2.0 \times 10^6$ S/m. The incident wave is excited by a z -polarized magnetic dipole with a unit moment and a frequency $f = 1.0$ KHz. The dipole is located at the $+z$ axis and is 50.0 mm away from the center of the sphere. We calculate the scattered electric field in a near zone, namely, the observation is taken along a line defined by $x = [-10, 10]$ mm, $y = 0$, and $z = 10$ mm. Figure 1 depicts the result when $x = [0, 10]$ mm (the field within $x = [-10, 0]$ mm is symmetric to the one within $x = [0, 10]$ mm) and we can see that it agrees well with the exact Mie-series solution.

The second example illustrates the EM scattering by a conductive sphere coated with a dielectric medium. The conductive sphere has a radius $a_1 = 0.3$ m and a conductivity $\sigma = 1.0$ S/m while the dielectric coating has an outer radius $a_2 = 0.4$ m and the relative permittivity $\epsilon_r = 4.0$. The incident wave is a plane wave propagating along the $+z$ direction and has a frequency $f = 300$ MHz. We calculate the bistatic radar cross section (RCS) observed along the principal cut ($\phi = 0^\circ$ and $\theta = 0^\circ$ – 180°) for the scatterer in both vertical polarization (VV) and horizontal polarization (HH). Figure 2 plots the solutions and it can be seen that they agree with the exact Mie-series solutions

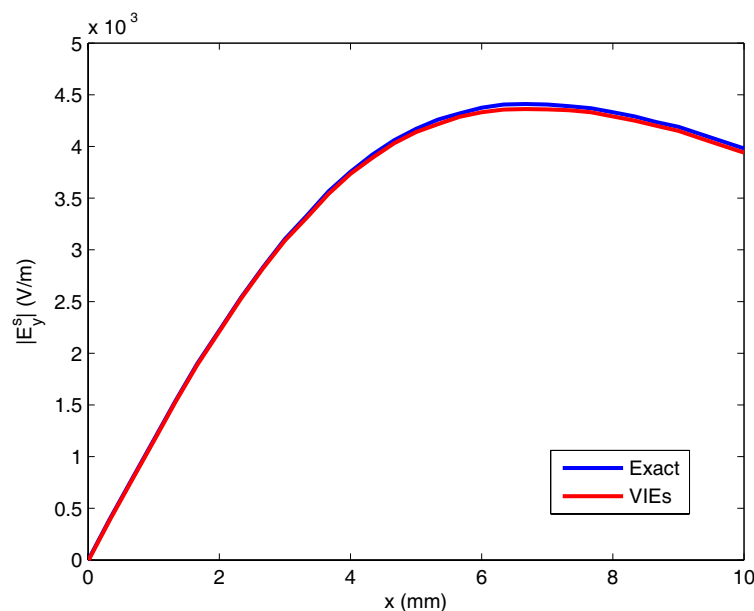


Figure 1: Scattered electric field (y -component) by a conductive sphere with a radius $a = 5.0$ mm and conductivity $\sigma = 2.0 \times 10^6$ S/m. The observation is taken along a line defined by $x = [0, 10.0]$ mm, $y = 0$, and $z = 10.0$ mm.

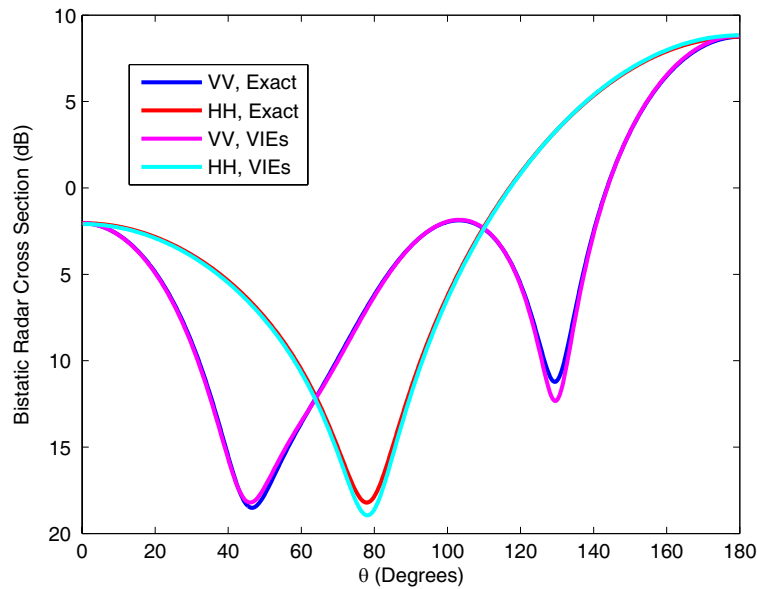


Figure 2: Bistatic RCS solutions for EM scattering by a conductive sphere coated with a dielectric medium. The conductive sphere has a radius $a_1 = 0.3$ m and a conductivity $\sigma = 1.0$ S/m while the dielectric coating has an outer radius $a_2 = 0.4$ m and the relative permittivity $\epsilon_r = 4.0$. The incident wave has a frequency $f = 300$ MHz.

very well. Note that the conductivities and frequencies in the two examples are very different, indicating that the approach can accommodate a wide change of conductivity and frequency. Also, the second example includes two very different materials, meaning that the object is very inhomogeneous, but the approach can also use the single VIEs to produce good solutions without a special treatment.

5. CONCLUSION

The EM scattering by conductive objects has been solved by the SIEs with the MoM discretization, but the solutions are susceptible to the choice of frequency and conductivity. In this work, we use the VIEs as governing equations and propose a point-matching scheme to solve the problem. The VIEs are usually well-conditioned and only has one unknown function to be solved for dielectric (nonmagnetic) objects. The point-matching scheme does not rely on any basis and testing functions and can use nonconforming meshes. Furthermore, the scheme can choose the current densities as unknowns and the integral kernels are free of the material parameters of objects so the solutions can be valid in a wide range of frequency and conductivity. A numerical example is presented to demonstrate the approach and its robustness has been seen.

ACKNOWLEDGMENT

This work was supported by the National Natural Science Foundation of China with the Project No. 61271097.

REFERENCES

1. Chew, W. C., M. S. Tong, and B. Hu, *Integral Equation Methods for Electromagnetic and Elastic Waves*, Morgan & Claypool, San Rafael, CA, 2008.
2. Glisson, A. W., "Electromagnetic scattering by arbitrarily shaped surfaces with impedance boundary conditions," *Radio Science*, Vol. 27, No. 6, 935–943, Dec. 1992.
3. Chu, Y. H. and W. C. Chew, "A robust surface-integral-equation formulation for conductive media," *Microwave Opt. Technol. Lett.*, Vol. 46, No. 2, 109–114, Jul. 2005.
4. Qian, Z. G. and W. C. Chew, "Generalized impedance boundary condition for conductor modeling in surface integral equation," *IEEE Trans. Antennas Propagat.*, Vol. 55, No. 11, 2354–2364, Nov. 2007.
5. Rao, S. M., D. R. Wilton, and A. W. Glisson, "Electromagnetic scattering by surfaces of arbitrary shape," *IEEE Trans. Antennas Propagat.*, Vol. 30, 409–418, 1982.

6. Coperich, K. M., A. E. Ruehli, and A. Cangellaris, “Enhanced skin effect for partial-element equivalent-circuit (PEEC) models,” *IEEE Trans. Microw. Theory Tech.*, Vol. 48, No. 9, 1435–1442, Sep. 2000.
7. Schaubert, D. H., D. R. Wilton, and A. W. Glisson, “A tetrahedral modeling method for electromagnetic scattering by arbitrary shaped inhomogeneous dielectric bodies,” *IEEE Trans. Antennas Propagat.*, Vol. AP-32, No. 1, 77–85, 1984.
8. Yang, K., J. C. Zhou, W. T. Sheng, Z. Y. Zhu, and M. S. Tong, “Efficient Nyström solutions of electromagnetic scattering by composite objects with inhomogeneous anisotropic media,” *IEEE Trans. Antennas Propagat.*, Vol. 61, No. 10, 5328–5332, Oct. 2013.
9. Tong, M. S. and W. C. Chew, “Super-hyper singularity treatment for solving 3D electric field integral equations,” *Microw. Opt. Technol. Lett.*, Vol. 49, 1383–1388, 2007.
10. Tong, M. S., Z. G. Qian, and W. C. Chew, “Nyström method solution of volume integral equations for electromagnetic scattering by 3D penetrable objects,” *IEEE Trans. Antennas Propagat.*, Vol. 58, No. 5, 1645–1652, May 2010.

Localisation of Motionless Persons in 3D Space by UWB Radar

P. Kazimir¹, D. Kocur¹, J. Fortes¹, and R. Zetik²

¹Technical University of Kosice, Park Komenskeho 13, Kosice 04210, Slovakia

²Ilmenau University of Technology, Ehrenbergstrasse 29, Ilmenau 98693, Germany

Abstract— In this paper, a new method of motionless person localization in 3-dimensional space (3D) by ultra wideband (UWB) radar will be introduced. The presented approach is based on the application of a multistatic UWB radar using one transmitting and four receiving antennas. The novel localization method is based on the approximation of 3D localization problem by solution of two 2D localization tasks. A proper lay-out of the radar antenna system will be introduced for the considered UWB radar applications. The performance properties of the outlined concept of 3D localization system have been evaluated by the experiments intent on indoor line-of-sight and through-the wall localization of motionless person.

1. INTRODUCTION

The current research in the field of human target positioning by radio frequency devices or sensor networks is focused on two types of tasks. The former is to localize persons in order to determine their position and/or navigate them in a known indoor environment. The solution of this task is represented by indoor positioning systems with a fixed infrastructure of sensors spread over the monitored area. Here, two basic approaches have been considered. In the first case, it is assumed that a person to be tracked (or to be navigated) carries an actively transmitting tag (e.g., [1–4]). In contrast to this approach, the second one consists in a tag-free localization of persons (e.g., [5]) using a sensor network with a fixed allocation of the particular sensors over a monitored area only. The comparison of the outlined approaches has shown that the method based on the active-tag employment can provide the higher accuracy of the target localization than that of tag-free approach.

The latter of the mentioned tasks is to provide a support for the emergency event solving by localization of persons of interest. By emergency events we understand either military, law enforcement and security operations or disasters such as earthquakes, fires or hurricanes. Persons of interest in such cases are, e.g., criminals, hostages or survivors. The nature of the described scenarios implies the use of mobile UWB systems. These systems should be able to detect and localize of human targets without any active tags. Several UWB radars that can potentially be used in such applications have been developed recently [6–9]. Usually, they provide a capability of short-range through-wall localization of human beings in 2-dimensional space (2D). A separate category of system able to localize a person in 3D has been presented by [10]. However, the development of this system is aimed towards applications such as gaming, remote control of household appliances, elderly people monitoring and fall detection.

According to security experts, person positioning under emergence events not only in 2D but also in 3D is needful. Following this demand, this paper is focused on a problem of motionless human being localization by a handheld UWB radar in 3D space.

The motionless target localization is a challenging task, especially in a realistic environment. In this paper, a new method of motionless person localization in 3D will be introduced. The presented approach is based on the application of a multistatic UWB radar using one transmitting and four properly distributed receiving antennas. The novel localization method is based on the approximation of 3D localization problem by solution of two 2-dimensional localization tasks. More precisely, the target localization by a multilateration method is substituted by a double application of a trilateration method.

The paper is organized as follows. In the Section 2, the problem of target localization in 3D based based on a multilateration method is set up. The Section 3 introduces a novel method of target localization in 3D based on time-of-arrival (TOA) estimates and a trilateration method. The performance of the novel approach for motionless human being localization in 3D by a short-range UWB radar is illustrated in the Section 4. Here, the results of person localization for indoor line-of-sight and through-the wall scenarios are presented. Section 5 contains concluding remarks.

2. PROBLEM STATEMENT

Let us assume a single multistatic UWB radar with 1 transmitting antenna Tx and N receiving antennas Rx_i ($i = 1, 2, \dots, N$) with known positions. The coordinates of the transmitting and receiving antennas will be labeled as $Tx = [x_t, y_t, z_t]$ and $Rx_i = (x_{r,i}, y_{r,i}, z_{r,i})$. The target coordinates, labeled as $T = [x, y, z]$, are unknown.

Let us consider the target localization by the multilateration method using TOA estimates. Let TOA_i be the measured propagation time of the UWB signal transmitted by Tx , reflected by the target T and received by Rx_i . Then, the distance between Tx , unknown target position T and Rx_i can be expressed as

$$d_i = c \cdot TOA_i \quad i = 1, 2, \dots, N \quad (1)$$

where c is the velocity of the propagation of the electromagnetic waves emitted by the radar. In our consideration, c is set to the electromagnetic wave propagation velocity in air, i.e., $c = 3 \times 10^8 \text{ ms}^{-1}$. The Euclidean distance between the points Tx , T and Rx_i can be expressed as

$$d_i = r_i + e_i = \|Tx, T\| + \|T, Rx_i\| + e_i \quad i = 1, 2, \dots, N \quad (2)$$

In this expression, the symbol e_i represents the additive noise component expressing the random errors of the TOA estimation.

The distance d_i can also be expressed by means of the antenna and target coordinates as follows:

$$d_i = \sqrt{(x - x_t)^2 + (y - y_t)^2 + (z - z_t)^2} + \sqrt{(x - x_{r,i})^2 + (y - y_{r,i})^2 + (z - z_{r,i})^2} \quad i = 1, 2, \dots, N \quad (3)$$

Then, the target localization problem can be defined as the estimation of the target coordinates, $T = (x, y, z)$, based on a solution of the set of nonlinear Equation (3). As it follows from this equation set, $N = 3$ represents the minimum number of equations and therefore the minimum number of receiving antennas necessary for target localization in 3D. The target localization based on the solution of (3) is usually referred to as the multilateration method.

From the mathematical point of view, each of the Equation (3) defines a rotational ellipsoid with foci placed in Tx and Rx_i positions. To obtain the target position, it is necessary to find an intersection at least of 3 ellipsoids. However, considering that distances d_i are estimated with the measurement errors e_i , such joint intersection does not always exist. Therefore, the TOA based multilateration method cannot be directly used in most real life scenarios.

3. A NOVEL 3D LOCALIZATION METHOD

The number of radar antennas and their lay-out are limited by the expected radar applications. In the scenarios described in this paper, we assume that the radar should be implemented as a small, lightweight device, proper for handheld usage. To be able to operate in real life situations, the radar should utilize small antenna array while providing reliable data about presence and position of persons.

Taking into account the mentioned requirements, we have proposed to use the radar antenna system according to Figs. 1–3. The proposed antenna system consists of one transmitting and four receiving antennas located in the same plane. The receiving antennas are located in the vertex of the square (rectangle), whereas the transmitting antenna is put in the intersection of the diagonals of the same square (rectangle). Such lay-out enables to approximate the 3D localization problem by two 2D localization tasks. This is achieved by processing the signals received by the pair of horizontally placed antennas separately (i.e., independently) from the signals received by the pair of vertically placed antennas. This will produce the estimate of target coordinates $[x, y_1]$ in the plane x - y parallel to the ground as well as the estimate of target coordinates $[y_2, z]$ in the plane y - z perpendicular to the ground.

Summarizing the obtained results, the target coordinates can be estimated as follows:

$$T(x, y, z) = T(x, (y_1 + y_2)/2, z) \quad (4)$$

4. EXPERIMENTAL RESULTS

The performance of the proposed approach for motionless person localization in 3D is demonstrated by processing of signals acquired by measurements with the multistatic UWB radar. The particular measurements were focused on line-of-sight and through-the-wall localization of tag-free

motionless persons. As the radar device, the 4-receiving channel M-sequence UWB radar has been used [7]. The clock frequency of the system is 6.95 GHz, which results in the operational bandwidth of approximately DC–3.5 GHz. The M-sequence order is 12, i.e., the impulse response covers 4095 samples regularly spread over 585 ns. This corresponds to an observation window of 585 ns leading to an unambiguous range of about 88 m in free space. In both measurements, horn-type antennas with vertical polarity were used, transmitting antenna placed in the center of “+”-shape.

The radar and target placement and measurement scenario for the line-of-sight measurement are shown in Fig. 1. Target was sitting motionlessly on the last of the series of stairs, in front of the transmitting antenna. The distance from the transmitting antenna to the edge of the stair was 3.75 m. The height of the transmitting antenna was 1.1 m above ground level. The height of the stair on which the target was located was 1.38 m above ground level.

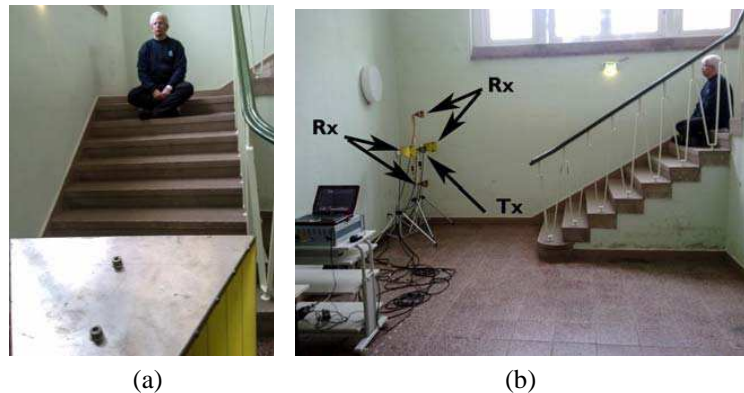


Figure 1: Line-of-sight scenario: (a) front view, (b) side view of a target and the antenna array setup.

Through-the-wall measurement setup shown in Fig. 2 was very similar to line-of-sight measurement. The radar was placed behind 18 cm thick wall of unknown material. Transmitting antenna was placed 0.77 m above ground level. The target was located in the 4.8 m distance (wall thickness included), shifted 1.5 m to the left side from the radar point of view.

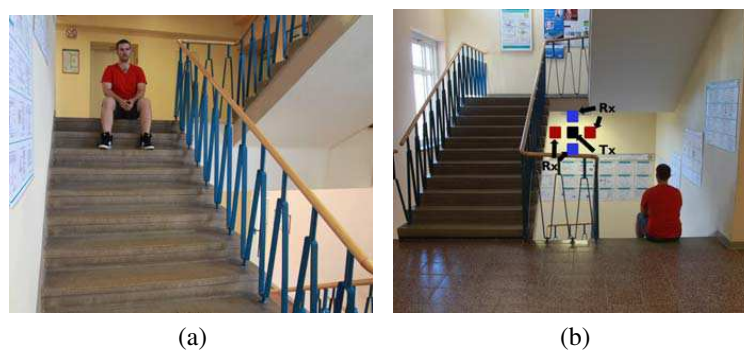


Figure 2: Through-the-wall scenario: (a) front view, (b) back view of a target and the antenna array setup.

For the TOA estimation corresponding to the particular pairs of $Tx - Rx_i$ ($i = 1, 2, 3, 4$), the procedure of raw radar signal processing consisting of the phases such as background subtraction (exponential averaging method [11]), estimation of the total energy of radar signals with the subtracted background in the frequency band 0.2–0.5 Hz corresponding to human beings breathing (integration method), target detection (CFAR detector application) and TOA estimation based on CFAR detector outputs [12] was used. Then, by using the estimated TOA_i for $i = 1, 2, 3, 4$, the target co-ordinates were finally estimated by the method described in the previous section.

The estimated positions of the target obtained for both scenarios are depicted in Fig. 3 as a red cross. The receiving antennas depicted by the red color were used to obtain the target position estimate in the x - y plane, which is outlined by the transparent red color. On the other hand, the antennas depicted by the blue color were used to compute the target position estimate in the y - z plane, outlined by the transparent blue color. In Fig. 3, the staircase borders and an appropriate

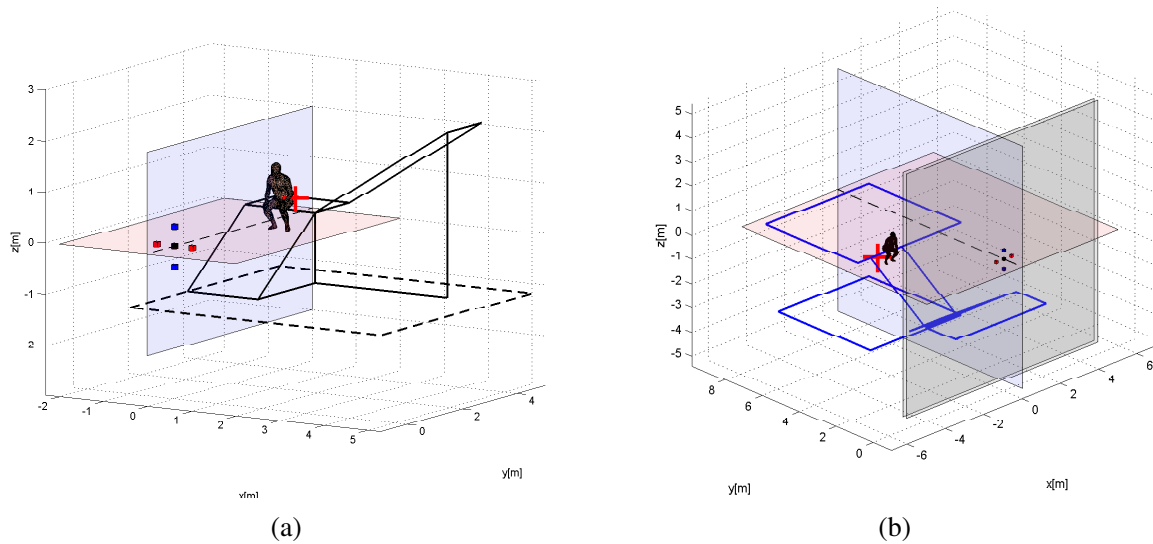


Figure 3: Experimental results: (a) indoor line-of-sight localization, (b) through-the-wall localization.

human body model are also drawn to create a model of measurement environment for the easier visual evaluation of the obtained results.

For the purpose of the evaluation of the localization error, we have defined the mid-point of the human thorax to be the true target position. Then, the difference between the estimated and true target position can be considered to be the target localization error. Taking into account this assumption, we have found that estimation error for the line-of-sight scenario and through-the-wall scenario was about 30 cm and 50 cm, respectively. Taking into consideration the true size of the target and the computational complexity of the novel localization method, it can be concluded that the new method of the motionless person localization in 3D can provide target position with an acceptable accuracy at low computational complexity.

5. CONCLUSION

In this paper, we have presented a simple method of the person localization by using short-range UWB radar in 3D, based on the approximation of 3D localization problem by the solution of two 2D localization tasks. The experiments intent on line-of-sight and through-the-wall localization of motionless persons have proved, that this method provides fairly good estimates of the target position while being of very low computational complexity. This localization method can be used as described, or as a part of more complex method (e.g., to calculate initial condition in localization based on Taylor series).

Although, the theoretical minimum number of receiving antennas for 3D localization is 3, we believe that using 4 receiving antennas can be of great advantage in harsh real life conditions and especially in search for motionless living persons. That is mainly because of the fact, that using a higher number of receiving antennas increases the probability of the true detection of the target. However, in the situations where radar system fails to detect the person presence in data acquired by one of the receiving channels, information from other 3 channels is still sufficient to obtain a rough estimate of the target position by TOA based multilateration method. In the case of failure of two receiving channels, the target position estimate can be still obtained in 2D space.

ACKNOWLEDGMENT

This work was supported by the Slovak Research and Development Agency under the contract No. APVV-0404-12.

REFERENCES

1. Zhang, C., M. Kuhn, B. Merkl, M. Mahfouz, and A. E. Fathy, "Development of an UWB indoor 3D positioning radar with millimeter accuracy," *IEEE MTT-S International Microwave Symposium Digest, 2006*, 106–109, 2006.
2. Irahauten, Z., H. Nikookar, and M. Klepper, "A joint TOA/DOA technique for 2D/3D UWB

- localization in indoor multipath environment,” *2012 IEEE International Conference on Communications (ICC)*, 4499–4503, Jun. 2012.
3. Goldoni, E., A. Savioli, M. Risi, and P. Gamba, “Experimental analysis of rssi-based indoor localization with IEEE 802.15.4,” *2010 European Wireless Conference (EW)*, 71–77, Apr. 2010.
 4. Kaemarungsi, K., R. Ranron, and P. Pongsoon, “Study of received signal strength indication in Zigbee location cluster for indoor localization,” *2013 10th International Conference on Electrical Engineering/Electronics, Computer, Telecommunications and Information Technology (ECTI-CON)*, 1–6, May 2013.
 5. Zhang, D., K. Lu, R. Mao, Y. Feng, Y. Liu, M. Zhong, and L. Ni, “Fine-grained localization for multiple transceiver-free objects by using RF-based technologies,” *IEEE Transactions on Parallel and Distributed Systems*, 2013.
 6. Taylor, J. D., *Ultra-wideband Radar Technology. Electrical Engineering*, Taylor & Francis, 2000.
 7. Sachs, J., M. Kmec, R. Herrmann, K. Schilling, R. Zetik, and P. Rauschenbach, “Ultra-wideband pseudo-noise radar: Principle of function, state of the art, applications,” *NATO Specialist Meeting, SET*, Vol. 120, 2008.
 8. Kocur, D., J. Gamec, M. Svecova, M. Gamcova, and J. Rovnakova, “Imaging method: A strong tool for moving target tracking by a multistatic UWB radar system,” *2010 IEEE 8th International Symposium on Applied Machine Intelligence and Informatics (SAMII)*, 11–19, Jan. 2010.
 9. Jovanoska, S. and R. Thoma, “Multiple target tracking by a distributed uwb sensor network based on the PHD filter,” *2012 15th International Conference on Information Fusion (FUSION)*, 1095–1102, Jul. 2012.
 10. Adib, F., Z. Kabelac, D. Katabi, and R. C. Miller, “3D tracking via body radio reflections,” *11th USENIX Symposium on Networked Systems Design and Implementation*, 2013.
 11. Rovnakova, J. and D. Kocur, “Weak signal enhancement in radar signal processing,” *2010 20th International Conference Radioelektronika (RADIOELEKTRONIKA)*, 1–4, Apr. 2010.
 12. Rovnakova, J., *Complete Signal Processing for Through Wall Tracking of Moving Targets*, LAP LAMBERT Academic Publishing, Sep. 2010.

Research of Composite Electromagnetic Scattering from Targets and Rough Surface Basing on the Efficient Numerical Algorithm

Yu Liang¹, Li-Xin Guo², Xiang-Hua Zeng¹, and Zhen-Sen Wu²

¹College of Physics Science and Technology, Yangzhou University, Yangzhou, Jiangsu, China

²School of Physics and Optoelectronic Engineering, Xidian University, Xi'an, Shaanxi, China

Abstract— Some studies of composite electromagnetic scattering from targets and rough surface are implemented by using the Propagation-Inside-Layer-Expansion (PILE) combined with the Forward-Backward Method (FBM) hybrid scheme. Multiply targets and rough surface case is considered. The composite scattering integral equations are built. The formation mechanisms of the EPILE+FBM scheme including the self- and mutual coupling inductions between targets and rough surface are analyzed. The accuracy and efficiency of the hybrid algorithm are verified. The applications of this scheme for the specific type of targets are carried out. The scattering results under different parameters, such as different target size, different roughness, etc., are investigated. The important scattering phenomena and characteristics are discussed and corresponding conclusions are obtained. The presented hybrid scheme will make sense to the domains of electromagnetics, remote sensing, radar surveillance, target recognition, optics, material science, etc..

1. INTRODUCTION

Electromagnetic scattering issues under land/sea environment has been concerned over past several years. Usually, the actual land/sea surfaces are not ideally flat, but are rough more or less, hence, the actual target and land/sea surface electromagnetic scattering are the target and rough surface electromagnetic scattering problem. For implementing the scattering analysis, significant contributions have been made and some important analytical, numerical, and hybrid algorithms have been presented, such as the SPM, the KA, the MOM [1], the FMM [2, 3], the FEM, the FDTD, the hybrid SPM+MOM technique [4], the hybrid KA+MOM technique. These methods are of respective advantages, some of them are computationally very fast, some of them are rather accurate in results, some of them are very efficient for single rough surface scattering, and some of them are rather suitable for the target and rough surface composite senses, etc., which have been widely applied and effectively promote the progress in electromagnetics research. Recently, owing to special academical and engineering demands, developing the numerical algorithms that are both efficient and accurate, and are compatible with more target and rough surface composite senses has becoming an important research subject, within which, one important contribution is the Propagation-Inside-Layer Expansion (PILE) and its hybrid scheme, that was firstly presented by N. Déchamps et al. [5]. This method, which shows high efficiency and accuracy, is able to handle problems configured with a huge number of unknowns. In this paper, the EPILE combined with FBM scheme is attempted to study more complex targets and rough surface composite scattering. The brief theory and formulations of this scheme are given, the accuracy and efficiency of it is confirmed, then, typical numerical results are exhibited and corresponding remarks are addressed.

2. BRIEF THEORY AND FORMULATIONS

Generally, electromagnetic scattering analysis should be implemented under the primary premise of reasonably modelling about the target or rough surface. Series of rough surface and targets composite senses have been aimed and modelled in our recent study. Taking the multiply targets both above and below the rough surface composite sense for example, and basing on the Ewald-Oseen' extinction theorem and electromagnetic boundary conditions for this composite sense, the scattering electric field integral equations (EFIE) (for TE case, HH polarization) and magnetic field integral equations (MFIE) (for TM case, VV polarization) can be obtained. The EFIE and MFIE can be further converted into the matrix equation, according to the inspiration of the matching technique and basis function schemes [1–3]. Usually, when the number of samples for the target, and the length of the rough surface increases, the computational cost of solving the matrix equation using the MOM with CGM [6], or the direct LU inversion becomes prohibitive, herein, the EPILE and FBM combined scheme is presented to speed up the scattering calculation. When

implementing the EPILE to study the composite electromagnetic scattering, the inverse matrix of global impedance matrix $\bar{\mathbf{Z}}$ [5, 6] can be partitioned into four blocks $\bar{\mathbf{Z}}1$, $\bar{\mathbf{Z}}2$, $\bar{\mathbf{Z}}3$, $\bar{\mathbf{Z}}4$ as follows,

$$\begin{aligned}\bar{\mathbf{Z}}1 &= \left[\bar{\mathfrak{R}}_1 - \bar{\mathfrak{R}}_2 \cdot (\bar{\mathfrak{R}}_3)^{-1} \cdot \bar{\mathfrak{R}}_4 \right]^{-1}, & \bar{\mathbf{Z}}2 &= - \left[\bar{\mathfrak{R}}_1 - \bar{\mathfrak{R}}_2 \cdot (\bar{\mathfrak{R}}_3)^{-1} \cdot \bar{\mathfrak{R}}_4 \right]^{-1} \cdot \bar{\mathfrak{R}}_2 \cdot (\bar{\mathfrak{R}}_3)^{-1} \\ \bar{\mathbf{Z}}3 &= - (\bar{\mathfrak{R}}_3)^{-1} \cdot \bar{\mathfrak{R}}_4 \cdot \left[\bar{\mathfrak{R}}_1 - \bar{\mathfrak{R}}_2 \cdot (\bar{\mathfrak{R}}_3)^{-1} \cdot \bar{\mathfrak{R}}_4 \right]^{-1}, \\ \bar{\mathbf{Z}}4 &= (\bar{\mathfrak{R}}_3)^{-1} - (\bar{\mathfrak{R}}_3)^{-1} \cdot \bar{\mathfrak{R}}_4 \cdot \left[\bar{\mathfrak{R}}_1 - \bar{\mathfrak{R}}_2 \cdot (\bar{\mathfrak{R}}_3)^{-1} \cdot \bar{\mathfrak{R}}_4 \right]^{-1} \cdot \bar{\mathfrak{R}}_2 \cdot (\bar{\mathfrak{R}}_3)^{-1}\end{aligned}$$

in which, the $(\bar{\mathfrak{R}}_1)^{-1}$ accounts for the local interactions on the targets, $(\bar{\mathfrak{R}}_3)^{-1}$ accounts for the local interactions on the rough surface, $\bar{\mathfrak{R}}_2$ propagates the resulting field on the rough surface toward the targets (surface-targets coupling), and $\bar{\mathfrak{R}}_4$ propagates the resulting field on the targets toward the rough surface (targets-surface coupling). To decrease the computing cost and speed up the calculation of term $(\bar{\mathfrak{R}}_3)^{-1}\xi_3$ (ξ_3 denotes the induced unknown vector on the rough surface), the fast iterative strategy-FBM [7, 8] can be sequentially applied. Then, the induced unknown vector ξ_3 and the impedance matrix $\bar{\mathfrak{R}}_3$ can be further decomposed as the following forms,

$$\xi_3 = \xi_3^f + \xi_3^b, \quad \bar{\mathfrak{R}}_3 = \bar{\mathfrak{R}}_3^f + \bar{\mathfrak{R}}_3^d + \bar{\mathfrak{R}}_3^b$$

Detailed description and operation of FBM can refer to [7, 8]. Substituting related reaction terms into composite scattering fields, the bistatic scattering coefficient (BSC) [1–8] can be obtained.

3. SELECTIVE NUMERICAL RESULTS AND DISCUSSIONS

Series of numerical results about the formational algorithm have been obtained. Considering the space limitation, herein, some selective numerical results are listed and corresponding discussions are given. The incident frequency is 3 GHz. Algorithm is tested on computer with 4 GB memory and Microsoft Windows operation system. All listed curves are expressed in decibel (dB) scale.

Figure 1 shows the comparison of BSC by the EPILE+FBM and MOM (CGM). The cylindrical targets above/below, and Gaussian spectrum rough surface are chosen. 100 surface realizations are statistic. The incident angle is set as 0° . For simplicity, some other parameters are not listed here (similarly hereinafter). It is obvious that, the scattering curves match well with each other for both HH and VV polarization, the Relative Residual Error (RRE) [5, 6] is far less than 10^{-3} . The average computational time by EPILE+FBM is about 45 seconds (S), by MOM (CGM) is 320 S. Similar time gap also can be found by other numerical computations, hence, comparing with the typical accurate numerical algorithm-MOM, the accuracy and efficiency of the EPILE+FBM is indicated.

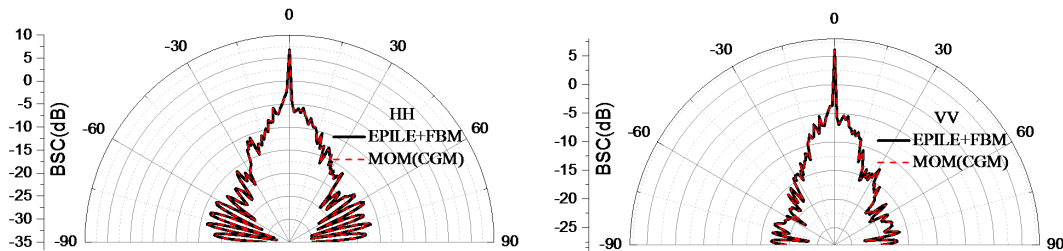


Figure 1: The BSC versus the scattering angle (EPILE+FBM and MOM (CGM)).

The BSC versus scattering angle with different radius size R_u of target above is exhibited in Fig. 2. It is shown that, with the increasing of R_u , the specular coherent scattering changes slightly, while the incoherent scattering at non-specular region increases evidently, due to the fact that, the coupling scattering between the ‘target above’ and the ‘rough surface’ is increased simultaneously.

The influence of different rough surface rms height δ on the BSC is investigated in Fig. 3. Obviously, with increasing of δ , in specular direction, the coherent scattering decreases, while at non-specular domain, the incoherent scattering increases evidently, especially at the backward direction. This phenomena can be explained in this way: the bigger rms height leads to the rougher surface, and results in the stronger coupling scattering intensity between target and rough surface.

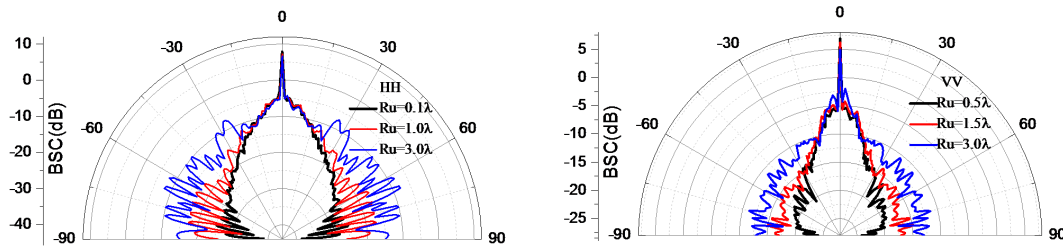


Figure 2: The BSC versus the scattering angle (different R_u).

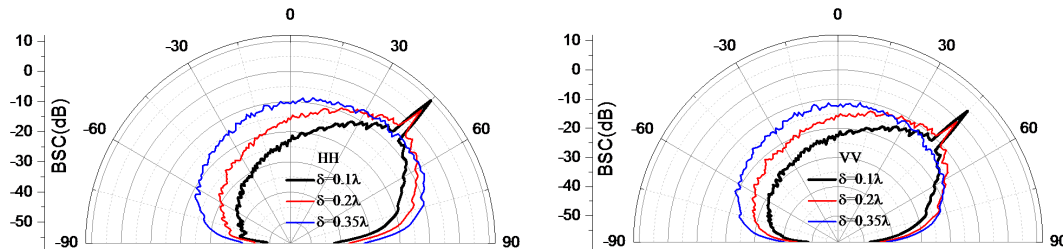


Figure 3: The BSC versus the scattering angle (different δ).

The influence of other more target and rough surface parameters, such as different height of target above, different depth of target below, different horizontal distance of target above/below, different size, correlation length and spectrum of rough surface, etc., have also been numerically investigated and analysed, considering the space limitation, they are temporarily not listed herein.

4. CONCLUSIONS

This paper discuss the implement of efficient numerical algorithm-the EPILE combined with FBM hybrid scheme in studying the rough surface and targets composite electromagnetic scattering. The formation mechanisms of this scheme is briefly introduced. The accuracy and efficiency of this algorithm is verified. Influence of typical targets and rough surface parameters in BSC is investigated by using the EPILE+FBM and corresponding scattering characteristics are analyzed.

ACKNOWLEDGMENT

This work was supported by the National Natural Science Foundation of China (Grant No. 11347182), by the University Science Research Project of Jiangsu Province (Grant No. 13KJB140020), by the National Natural Science Foundation for Distinguished Young Scholars of China (Grant No. 61225002) and by the Science Foundation of Yangzhou University (Grant No. 2012CXJ009). If any question, please contact with Yu Liang, et al. (e-mail: liangyu@yzu.edu.cn). The authors would like to thank the reviewers for their helpful and constructive suggestions.

REFERENCES

1. Tsang, L. and J. A. Kong, *Scattering of Electromagnetic Waves — Numerical Simulations*, 114–176, Wiley, New York, 2000.
2. Jandhyala, V., E. Michielssen, S. Balasubramaniam, and W. C. Chew, “A combined steepest descent-fast multipole algorithm for the fast analysis of three-dimensional scattering by rough surfaces,” *IEEE Trans. Geosci. Remote Sens.*, Vol. 36, No. 3, 738–748, 1998.
3. Liu, Q. H., L. Jiang, and W. C. Chew, “Large-scale electromagnetic computation for modeling and applications,” *Proc. IEEE*, Vol. 101, No. 2, 223–226, 2013.
4. Zhang, Y., Y. E. Yang, H. Braunisch, and J. A. Kong, “Electromagnetic wave interaction of conducting object with rough surface by hybrid SPM/MOM technique,” *Progress In Electromagnetics Research*, Vol. 22, 315–335, 1999.
5. Déchamps, N., N. De Beaucoudrey, C. Bourlier, and S. Toutain, “Fast numerical method for electromagnetic scattering by rough layered interfaces: Propagation-inside-layer expansion method,” *J. Opt. Soc. Amer. A*, Vol. 23, No. 2, 359–369, 2006.

6. Liang, Y., L. X. Guo, and Z. S. Wu, “The EPILE combined with the generalized-FBM for analyzing the scattering from targets above and on a rough surface,” *IEEE Antennas Wireless Propag. Lett.*, Vol. 9, 809–813, 2010.
7. Iodice, A., “Forward-backward method for scattering from dielectric rough surfaces,” *IEEE Trans. Antennas Propag.*, Vol. 50, No. 7, 901–911, 2002.
8. Liang, Y., L. X. Guo, and Z. S. Wu, “The fast EPILE combined with FBM for electromagnetic scattering from dielectric targets above and below the dielectric rough surface,” *IEEE Trans. on Geosci. Remote Sens.*, Vol. 49, No. 10, 3892–3905, 2011.

FPGA-based Real-time Generator of Combination Chaotic Frequency-modulated Signal for Noise Radar

Qilun Yang^{1,2}, Yunhua Zhang², and Bingjie Li^{1,2}

¹University of Chinese Academy of Sciences, Beijing 100049, China

²The Key Laboratory of Microwave Remote Sensing, Chinese Academy of Sciences, Beijing 100190, China

Abstract— This paper proposes a design scheme for generating the Combination chaotic frequency-modulated (CCFM) signal for noise radar in real-time based on FPGA. The CCFM signal is real-time generated by instant calculation in FPGA, and it keeps good chaotic property even with short quantization length. The experiment demonstrates that the generated CCFM signal has very low sidelobe of auto-correlation and excellent orthogonality.

1. INTRODUCTION

Noise radars use random waveforms, which are of thumbtack ambiguity and efficient spectrum utilization, so they can improve the electronic counter-countermeasure (ECCM) capability and low probability of detection and intercept (LPD/LPI) characteristics [1–3].

As a kind of pseudo-noise signal, chaotic signal is generated from deterministic system. Compared with general noise signal, chaotic signal is easy to produce and control, also the cost is small [4]. However, some chaotic signal has high peak sidelobe ratio (PSLR) of auto-correlation function, which may result in weak targets being masked by surrounding strong scatter targets [5, 6].

Some papers have proposed a few methods to reduce sidelobe [7, 8], but they do not consider the feasibility of digital realization. The short quantization length will destroy the chaotic property of chaotic signal. In order to keep good chaotic property with limited quantization length, we propose to adopt the combination chaotic map for frequency-modulation, so as to obtain the combination chaotic frequency-modulated (CCFM) signal [9]. In this paper, we further propose a scheme to generate the CCFM signal in real-time based on FPGA.

The rest of the paper is organized as follows. In Section 2, we introduce the CCFM signal model. In Section 3, we present the real-time generation of CCFM signal based on FPGA. In Section 4, we conduct experiment to demonstrate the performance of generated CCFM signal. Finally in Section 5, we conclude the paper.

2. CCFM SIGNAL MODEL

The maximum period of one-dimensional chaotic map is limited by the quantization length. If the quantization length is M , then their repetition periods will not exceed 2^M . In order to keep the chaotic characteristic in case of short quantization length, we propose the combination chaotic map by embedding the Logistic map into Bernoulli map, i.e., the Logistic map is used to produce the parameters for Bernoulli map, and then Bernoulli maps under diverse parameters are combined to obtain the combination map sequence [9]. The form of combination map is shown as follows:

$$\left\{ \begin{array}{l} x_{m+1} = u \cdot x_m \cdot (1 - x_m) \\ B_m = 1.4 + 0.6 \cdot x_m \\ y_{m,n+1} = g(y_{m,n}) = \begin{cases} B_m y_{m,n} + 0.5, & y_{m,n} < 0 \\ B_m y_{m,n} - 0.5, & y_{m,n} \geq 0 \end{cases} \\ \phi = \{\{y_{0,0}, y_{0,1}, \dots, y_{0,N}\}, \{y_{1,0}, y_{1,1}, \dots, y_{1,N}\}, \dots, \{y_{M,0}, y_{M,1}, \dots, y_{M,N}\}\} \end{array} \right. \quad \begin{array}{l} 0 < x_m < 1 \\ 0 \leq m \leq M \\ 0 \leq n \leq N \end{array} \quad (1)$$

where $\{x_n\}$ is the Logistic sequence and its parameter should satisfy $3.569945 < u \leq 4$. In view of the fact that the boundary of Logistic sequence is $0 < x_n < 1$, and the range of Bernoulli map parameter is $1.4 < B < 2$, one can let $B_m = 1.4 + 0.6 \cdot x_m$. Then the combination map is used for frequency-modulation to finally get the CCFM signal.

$$s(n) = A \exp \left\{ j 2\pi \sum_{i=0}^n \phi_i \right\} \quad (2)$$

3. DESIGN OF THE FPGA-BASED REAL-TIME GENERATOR OF CCFM SIGNAL

The hardware is composed of FPGA, digital-to-analog converter (DAC), low-pass filter (LPF) and intermediate-frequency (IF) modulator. The FPGA generates the digital inphase and quadrature (I/Q) components of the baseband CCFM signal, the DAC converts the digital signal into analog signal, and the IF modulator transforms the I/Q components of baseband signal into IF signal.

The FPGA software includes four functional modules: 1) Trigger module produces the trigger signal, which determines the duration and interval of each pulse. 2) The logistic map module generates the parameters for Bernoulli map. The Logistic map is realized by multiplexer and adder. 3) The Bernoulli map module generates the combination map sequence by combining Bernoulli map sequences under diverse parameters. The Bernoulli map is also realized by multiplexer and adder. 4) The chaotic FM module generates the I/Q components of the CCFM signal. In view of the Sine and Cosine function are complicated in FPGA calculation, we use two lookup tables instead of direct calculation, one is for Cosine function and the other is for Sine function. The lookup table is stored in the ROM.

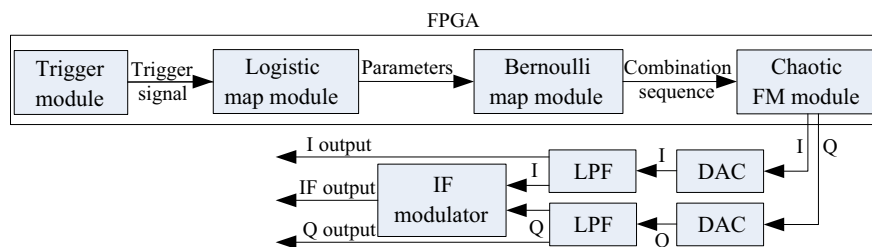


Figure 1: Block diagram of the FPGA-based real-time generator of CCFM signal.

4. EXPERIMENT RESULTS

In the experiment, we generate 20 pulses of CCFM signal corresponding to different initial values, and the signal parameters are listed in Table 1. Then the I/Q waveforms are sampled and restored by Tektronix MSO70404 oscilloscope with 8 bit sampling accuracy and 125 MHz sampling rate. The sampled waveforms are shown in Fig. 2.

Auto-correlation function (ACF) can describe the range resolution of a radar signal [10] and low sidelobe of ACF is preferred because it helps to avoid weak targets being masked by around strong targets. The ACF of sampled CCFM signal is shown in Fig. 3, where the peak-sidelobe-ratio (PSLR) is -22.72 dB.

When two or more radar systems operate at the same frequency band simultaneously, then mutual inference is usually unavoidable if without taking some specific measure. The orthogonality of signals is a good measure for anti-mutual inference capability [11], and better orthogonality means less mutual inference. The orthogonality can be described by the cross-correlation coefficient

Table 1: Parameters of generated CCFM signal.

Duration	Interval	Bandwidth	Quantization length
10 μ s	5 μ s	62.5 MHz	16 bit

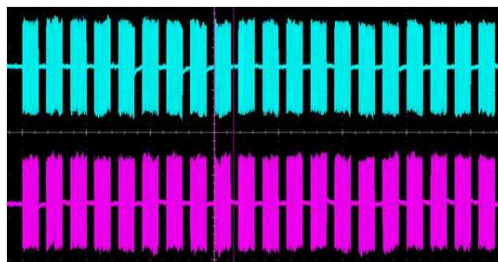


Figure 2: The I/Q components of sampled CCFM signal, where the upper is the inphase component, and the lower is the quadrature component.

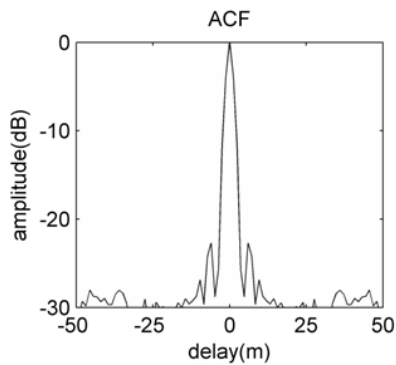


Figure 3: The ACF of sampled CCFM signal.

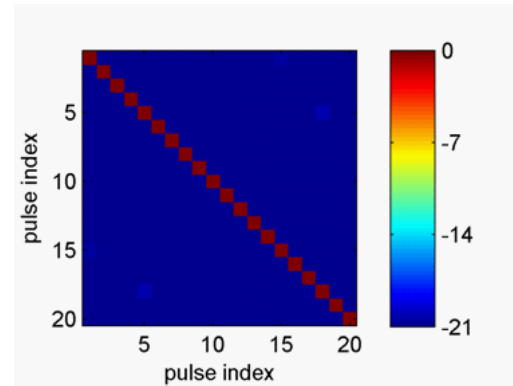


Figure 4: The cross-correlation coefficient of sampled CCFM signal.

between signals. The cross-correlation coefficients of sampled CCFM signals are presented in Fig. 4. The diagonal line is the auto-cross coefficients, which are normalized to 0 dB. The off diagonal line values are cross-correlation coefficients, and the maximum of them is -20.24 dB. The excellent orthogonality of the generated CCFM is demonstrated.

5. CONCLUSION

This paper proposes a design scheme for real-time generation of the CCFM signal for noise radar based on FPGA. The realized CCFM signals are of good chaotic property even with short quantization length. The combination map is generated by embedding the Logistic map into Bernoulli map, i.e., Logistic map produces the parameters for Bernoulli map, and then Bernoulli sequence under diverse parameters are combined to obtain the combination map sequence.

In the generator, the CCFM signal is generated by instant calculation iteratively in FPGA, so it does not need large memory space to store the whole waveform, and it is suit for generating long time signals. The experiment demonstrates that the generated CCFM signal has low sidelobe of auto-correlation and excellent orthogonality.

REFERENCES

1. Lukin, K. A., "Radar design using noise/random waveforms," *International Radar Symposium*, 1–4, 2006.
2. Soumekh, M., "SAR-ECCM using phase-perturbed LFM chirp signals and DRFM repeat jammer penalization," *IEEE International Radar Conference*, 507–512, 2005.
3. Garmatyuk, D. S. and R. M. Narayanan, "ECCM capabilities of an ultrawideband bandlimited random noise imaging radar," *IEEE Transactions on Aerospace and Electronic Systems*, Vol. 38, 1243–1255, 2002.
4. Flores, B. C., E. A. Solis, and G. Thomas, "Assessment of chaos-based FM signals for range-Doppler imaging," *IEE Proc. — Radar Sonar Navig*, Vol. 150, 313–22, 2003.
5. Yang, J., Z. K. Qiu, X. Li, and Z. W. Zhuang, "Uncertain chaotic behaviours of chaotic-based frequency- and phase-modulated signals," *IET Signal Processing*, Vol. 5, 748–756, 2011.
6. Ashtari, A., G. Thomas, H. Garces, and B. C. Flores, "Radar signal design using chaotic signals," *International Waveform Diversity and Design Conference*, 353–357, 2007.
7. Yunkai, D., H. Yinghui, and G. Xupu, "Hyper chaotic logistic phase coded signal and its sidelobe suppression," *IEEE Transactions on Aerospace and Electronic Systems*, Vol. 46, 672–686, 2010.
8. Yang, J., Z.-K. Qiu, L. Nie, and Z.-W. Zhuang, "Frequency modulated radar signals based on high dimensional chaotic maps," *10th IEEE International Conference on Signal Processing (ICSP)*, 1923–1926, 2010.
9. Yang, Q., Y. Zhang, and X. Gu, "A signal model based on combination chaotic map for noise radar," *Progress In Electromagnetics Research M*, Vol. 28, 57–71, 2013.
10. Park, J.-I. and K.-T. Kim, "A comparative study on ISAR imaging algorithms for radar target identification," *Progress In Electromagnetics Research*, Vol. 108, 155–175, 2010.
11. Wang, L., X. Fu, L. Shi, T. Li, and M. Gao, "Radar waveform design under the constraint of auto-correlation, orthogonality and Doppler tolerance," *IET International Radar Conference*, 1–4, 2013.

Uncertainty Estimation in Vector Wind Retrievals from Satellite-based Polarimetric Microwave Radiometer Measurements

Xiaolin Tong^{1,2,3}, Zhenzhan Wang², and Qingxia Li³

¹School of Physics and Electronics, Henan University, Kaifeng 475001, China

²Key Laboratory of Microwave Remote Sensing

National Space Science Center/Center for Space Science and Applied Research
Chinese Academy of Sciences, Beijing 100190, China

³Department of Electronics and Information Engineering

Huazhong University of Science and Technology, Wuhan 430074, China

Abstract— The main characteristic of wind vector is circularity in any reference direction, which creates problems when analyzing the data statistically. Due to this periodicity, standard statistical techniques cannot be used to analyze circular data. For example, (1) in the regions including upwind/downwind ambiguity, the STD obtained from the linear statistics approach is about 60–80°. However, we couldn't deduce that it is upwind/downwind ambiguity from the STD. (2) The Cramer-Rao bound (CRB) has been widely used as sensitivity estimation. The precondition of the CRB approach is the possibility distribution is normal one. Since the model of wind direction reverses is non-linear, the angel distribution is not normal. A problem appeared for wind-vector sensitivity estimation. The STD obtained from closest solution is lower than the sensitivity obtained from CRB. In this paper, we introduce the directional statistics approach for evaluating the uncertainty. The circular STD is always between zero and one inclusive, making it very different from its linear analog, which can have any positive value. It is indicative of the spread in a data set. If all samples point into the same direction, the circular STD will be small. If the samples are spread out evenly, the circular STD will be close to one. Importantly, however, a circular variance of 1 does not imply a uniform distribution around the circle. If all samples either point towards 0° or 180°, the circular variance is 1, yet the data is not distributed uniformly around the circle. The sensitivity is reassessed based on the directional statistics approach, and compared with CRB. The sensitivities of CRB are high where the derivatives of the brightness temperatures changing rapidly. The incorrect results come from the effect of nonlinearity. When the directional statistics approach is used, the peak disappeared where the derivatives of the brightness temperatures changing rapidly. In addition, the directional statistics approach can be used to estimate the characterization of uncertaintys in wind vector retrievals from Scatterometry.

1. INTRODUCTION

The uncertainty of the wind-vector estimator is critical for a variety of applications in Radiometer design [1], improving the accuracy of wind direction retrieval [2], and demonstration the capacity to obtain wind-direction over the global oceans from passive microwave measurements. The main characteristic of wind vector is circularity in any reference direction, which creates problems when analyzing the data statistically. Physical quantities referring to angles are called angular, directional, or circular data. Due to this periodicity, standard statistical techniques cannot be used to analyze circular data [3, 4]. For example, the samples mean of a data set on the circle is not the usual sample mean [5].

2. CIRCULAR DISTRIBUTIONS

The *sample mean direction* x_{mean} of observations $\theta_1, \theta_2, \dots, \theta_n$ is given by

$$\bar{x} = \arctan \frac{\sum_{i=1}^n \sin \theta_i}{\sum_{i=1}^n \cos \theta_i} \quad (1)$$

Circular variance is defined as

$$S_0 = 1 - \left[\left(\sum_{i=1}^n \cos \theta_i \right)^2 + \left(\sum_{i=1}^n \sin \theta_i \right)^2 \right] \quad (2)$$

It is important to note that the circular variance S_0 is always between zero and one inclusive, making it very different from its linear analog, which can have any positive value [3]. The circular variance S_0 thus indicates the dispersion of a sample. It is indicative of the spread in a data set. If all samples point into the same direction, the circular variance will be small. If the samples are spread out evenly, the circular variance will be close to maximal. Importantly, however, a circular variance of 1 does not imply a uniform distribution around the circle. If all samples either point towards 0° or 180° , the circular variance is 1, yet the data is not distributed uniformly around the circle.

3. POLARIMETRIC RADIOMETRY

Research in polarimetric radiometry modeling and measurements has demonstrated that usable wind direction information can be obtained by combining the vertical and horizontal polarizations with the cross correlation of those two polarizations [6, 7].

An empirical geophysical model function relating the amplitude of U and V to ocean-surface wind speed and direction has been derived from the Jet Propulsion Laboratory aircraft wind radiometer (WINDRAD) [8] as well as WindSat measurements. The directional dependence of the third and fourth Stokes parameters can be described [12] by

$$\begin{aligned} T_h &= T_{h0} + T_{h1} \cos \phi + T_{h2} \cos 2\phi \\ T_v &= T_{v0} + T_{v1} \cos \phi + T_{v2} \cos 2\phi \\ T_U &= T_{U1} \sin \phi + T_{U2} \sin 2\phi \\ T_V &= T_{V1} \sin \phi + T_{V2} \sin 2\phi \end{aligned} \quad (3)$$

where $\phi = \phi_0 - \phi_w$ is the relative angle between the observation azimuth angle ϕ_w and the wind direction ϕ_0 . The coefficients of the first harmonics account for upwind and downwind asymmetric surface features, while those of the second harmonics account for the upwind and crosswind asymmetry.

In order to analyze the dependence of ambiguous solutions on the true wind vector, we plot the errors associated with global cost function minima, along with the Monte Carlo simulation results.

The results of the uncertainty calculation are plotted in Fig. 1.

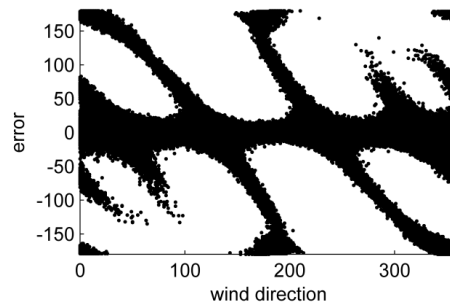


Figure 1: Black dots indicate errors associated with global cost function minima observed in Monte Carlo simulation results.

In the regions including upwind/downwind ambiguity, the STD obtained from the linear statistics approach is about $60\text{--}80^\circ$. It can not correctly indicate the dispersion of the wind vector. We can see from the Fig. 2(b) that the circular variance can produce the meaningful indication of the dispersion of the wind vector.

4. SENSITIVITY ANALYSIS

The sensitivity was used as an important parameter to character the capacity of wind-direction reverse. We use the directional statistics approach to calculate the sensitivity in wind vector inversions. The result was compared with the Cramer-Rao minimum variance bound and the closest cost function minimum to the true solution [9].

Generally linear statistics can be used with directional data only if the range of observations is small. Figure 3(a) displays the relationship of the wind direction STD versus the relative wind

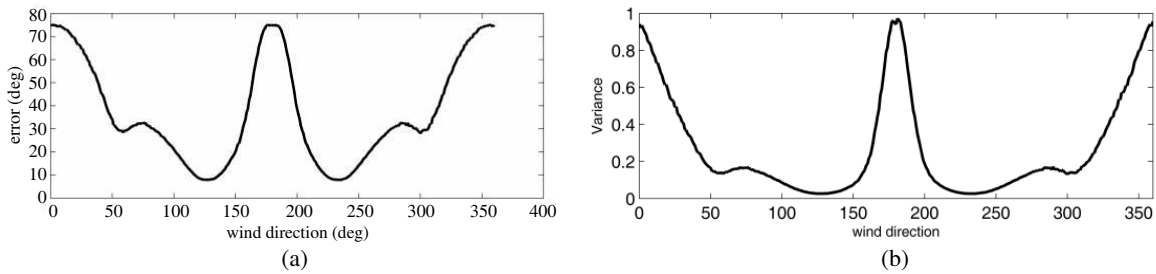


Figure 2: (a) The wind direction error obtained from the linear statistics approach, the solution corresponding to the global cost function minimum. (b) The wind direction variance obtained from the directional statistics approach, the solution corresponding to the global cost function minimum.

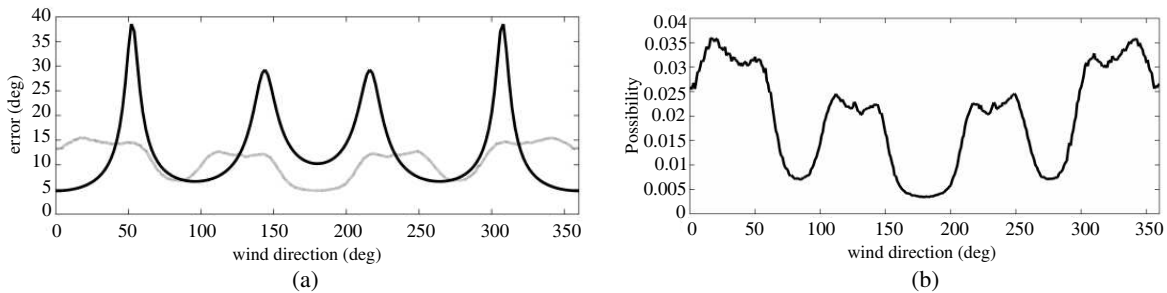


Figure 3: (a) The wind direction sensitivity obtained from the linear statistics approach. (b) The wind direction variance obtained from the directional statistics approach, the closest cost function minimum to the true solution was used.

direction angle. The regions agree well with each other, where the derivatives of the brightness temperatures changing slowly. The sensitivities of CRB are high where the derivatives of the brightness temperatures changing rapidly. The incorrect results come from the effect of nonlinearity. Fig. 3(b) displays the result of the directional statistics approach. The directional statistics approach is suitable to the nonlinear model. Compared to the sensitivities of CRM, the peak disappeared where the derivatives of the brightness temperatures changing rapidly.

Considering the distribution is not normal, the sensitivity described in this paper is more preferable than the one obtained from linear statistics approach.

5. CONCLUSION

In this paper, we introduced a method for evaluating the uncertainty of Vector Wind Retrievals from Satellite-Based Polarimetric Microwave Radiometer Measurements based on the Radiative Transfer Model. The Cramer-Rao bound (CRB) and MLE has been analyzed.

The sensitivity of Vector Wind Retrievals was computed used the new method, and compared with CRB and the closest solution of maximum-likelihood estimation (CS-MLE). The uncertainty method presented here can obtain minimum of sensitivity, according with the sensitivity conception, and can give a preferable explanation to the simulated result.

This paper also computed the different wind-vector ambiguous solutions and corresponding uncertainty, under the based Model method (BM) and maximum-likelihood estimation (MLE). A discrete representation for the wind-vector solutions has been obtained, which can predict the characteristics of errors in wind direction retrievals and their dependence on the true wind direction relative to the observation azimuth angle. It is anticipated that the techniques and strategies developed in this study, and prior related studies, to analyze wind direction uncertainty will be requisite for maximizing the information content of future instruments.

The method commutes over nonlinear operations, is potentially more reliable algorithm to assess radiometer system, Model Function and Retrieval Algorithm's performance.

REFERENCES

1. Racette, P. and R. H. Lang, "Radiometer design analysis based upon measurement uncertainty," *Radio Science*, Vol. 40, 2005.

2. Brown, S. T., C. S. Ruf, and D. R. Lyzenga, “An emissivity-based wind vector retrieval algorithm for the WindSat polarimetric radiometer,” *IEEE Transactions on Geoscience and Remote Sensing*, Vol. 44, 611–621, 2006.
3. Mardia, K. V. and P. E. Jupp, *Directional Statistics*, Vol. 494, Wiley, 2009.
4. Nikolaidis, N. and I. Pitas, “Nonlinear processing and analysis of angular signals,” *IEEE Transactions on Signal Processing*, Vol. 46, 3181–3194, 1998.
5. Ravindran, P. and S. K. Ghosh, “Bayesian analysis of circular data using wrapped distributions,” *Journal of Statistical Theory and Practice*, Vol. 5, 547–561, 2011.
6. Piepmeier, J. R. and A. J. Gasiewski, “High-resolution passive polarimetric microwave mapping of ocean surface wind vector fields,” *IEEE Transactions on Geoscience and Remote Sensing*, Vol. 39, 606–622, 2001.
7. Yueh, S. H., “Modeling of wind direction signals in polarimetric sea surface brightness temperatures,” *IEEE Transactions on Geoscience and Remote Sensing*, Vol. 35, 1400–1418, 1997.
8. Gaiser, P. W., K. M. St Germain, E. M. Twarog, G. A. Poe, W. Purdy, D. Richardson, et al., “The WindSat spaceborne polarimetric microwave radiometer: Sensor description and early orbit performance,” *IEEE Transactions on Geoscience and Remote Sensing*, Vol. 42, 2347–2361, 2004.
9. Laws, K. E., D. R. Lyzenga, D. M. Wiberg, and J. F. Vesecky, “Characterization of errors in vector wind retrievals from satellite-based polarimetric microwave radiometer measurements,” *IEEE Geoscience and Remote Sensing Letters*, Vol. 3, 45–48, 2006.

Multi-band Microwave Metamaterial Perfect Absorber Based on Mie Resonance Theory

Jun-Feng Chen¹, Guo-Dong Wang¹, Zhao-Quan Chen^{2,3}, Ming-Hai Liu¹, and Xi-Wei Hu¹

¹State Key Laboratory of Advanced Electromagnetic Engineering and Technology
School of Electrical and Electronic Engineering
Huazhong University of Science and Technology
Wuhan 430074, China

²University ITMO, Kronverkskiy pr. 49, St. Petersburg 197101, Russia

³College of Electrical and Information Engineering
Anhui University of Science and Technology
Huainan 232001, China

Abstract— A multi-band metamaterial absorber (MA) with near-unity absorption based on Mie resonance theory is proposed in the microwave region. It is composed of an array of dielectric cubes with different geometric parameters and a metallic ground plane. The simulated results show that four absorption peaks at 7.31 GHz, 7.58 GHz, 7.90 GHz and 8.19 GHz with the corresponding absorption rates of 99.05%, 99.37%, 99.65% and 99.16%, respectively. In addition, the composite MA is polarization-insensitive at the normal incidence and maintains high absorption rates at wide angles of incidence for both TE and TM wave. The influences of the permittivity and the side length of the dielectric cubes on its absorption characteristics are also investigated. This MA would be a promising candidate as absorbing elements in scientific and technical applications, such as cloaks, perfect lens and filters.

1. INTRODUCTION

Metamaterials (MMs) are artificial, effectively homogeneous electromagnetic (EM) structures consisting of dielectrics and highly conducting metals, which are periodically arranged. MMs research has always been popular because of its superior properties than natural materials. However, the metamaterials with perfect absorption have attracted plenty of attention from scientists over the past several years. Periodic dielectric or metallic structures have been a subject of continuing interest for applications to frequency selective or polarization selective devices in microwaves and optical waves. In 2008, Landy et al. [1] first demonstrated a perfect MM absorber (MA) in a narrow-band which was made of a sub-wavelength structure of electric ring resonators and metal cut wires separated by a dielectric substrate. The idea is that by adjusting the electric and magnetic resonances independently, it is possible to realize the impedance of the MM matching to the free space so as to minimize the reflection. Meanwhile, the transmission wave is completely consumed in the lossy substrate and two metallic layers. As a result, perfect absorption is achieved at the resonance frequency. Since then, the type of MAs excite a new wave of research such as fishnet structures [2], square Loops [3] and coplanar Jerusalem crosses [4].

Recently, an isotropic Mie resonance-based metamaterial perfect absorber with near unity absorbance at the microwave frequencies was reported by Liu et al. [5]. The metamaterial is constructed with an array of dielectric cubes and a metallic ground plane. The new type of absorber was fabricated successfully, which achieved a single band absorption at 9.96 GHz and the absorptivity was 98%. Indeed, Lewin [6] derived an expression based on Mie Resonance Theory [7] for the effective properties of an array of spherical particles embedded in a background matrix. A medium composed of periodically placed scatterers generates polarization and magnetization densities. The densities are related to the distribution of the scatterers and their polarizabilities. As a result, a wave propagating through an array of these scatterers will see the material as an effective medium. The problem of effective-medium theory and modeling the electromagnetic response of inclusions embedded in a host material has a long history going back to Maxwell and Rayleigh [8, 9]. Many other authors [6, 10] studied the properties and applications of the metamaterials in detail.

In this paper, we propose a four band polarization-insensitive MA based on a structure of periodic array of dielectric cubes with different geometric parameters and a metallic ground plane. The permittivity of the dielectric cube is $115 + 0.92i$, and the metallic ground plane is made of copper as reported in [5]. Simulation results show that the proposed MA has four distinct absorption peaks and their absorptivity is over 99%. Distributions of surface current density on

the dielectric cubes and back metallic layers are illustrated. The loss contributions of dielectric cubes and ground plane are also discussed. Moreover, the simulation results exhibit that the MA is polarization-insensitive and could operate well at different angles of incidence for both transverse electric (TE) and transverse magnetic (TM) waves, which is potential to be used in devices such as detection of explosives, stealth technology and bolometer.

2. EFFECTIVE DIELECTRIC AND MAGNETIC PROPERTIES OF A CUBICAL-PARTICLE COMPOSITE

As mentioned above, in 1947, Lewin [6] derived an expression based on Mie resonance theory for the effective permittivity and permeability of a composite material which was constituted of an array of lossless magneto dielectric spherical particles with the permittivity ε_2 and permeability μ_2 embedded in a background matrix with the permittivity ε_1 and permeability μ_1 . The effective permittivity ε_{re} and permeability μ_{re} of the composite shown in Fig. 1(a) are given by [6]

$$\varepsilon_{re} = \varepsilon_1 \left[1 + \frac{3f}{\frac{F(\theta)+2K_e}{F(\theta)-K_e} - v_f} \right] \quad (1)$$

and

$$\mu_{re} = \mu_1 \left[1 + \frac{3f}{\frac{F(\theta)+2K_m}{F(\theta)-K_m} - v_f} \right] \quad (2)$$

In these expressions,

$$K_e = \frac{\varepsilon_1}{\varepsilon_2} \quad K_m = \frac{\mu_1}{\mu_2} \quad (3)$$

The volume fraction v_f of the spherical inclusions is given by

$$v_f = \frac{4\pi r^3}{3p^3} \quad (4)$$

where r is the particle radius and p is the particle spacing. The function $F(\theta)$ is

$$F(\theta) = \frac{2(\sin \theta - \theta \cos \theta)}{(\theta^2 - 1)\sin \theta + \theta \cos \theta} \quad (5)$$

where $\theta = k_0 r \sqrt{\varepsilon_2 \mu_2}$, and the free-space wavenumber is $k_0 = \frac{2\pi}{\lambda}$, λ is the free-space wavelength. $F(\theta)$ is a resonant function and becomes infinite at some values of θ , which results in the magnetic and electric resonances. Among all the resonances, the first Mie resonance mode is the most intense and leads to the magnetic resonance of the spheres. We add a copper ground plane with the thickness of 0.1 mm under the dielectric particles to form a Mie resonance-based MA. Besides

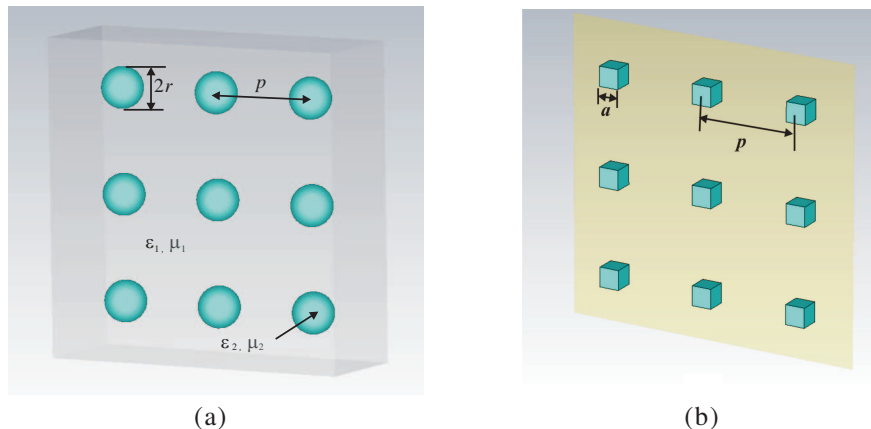


Figure 1: (a) Structure of the composite material in Lewins model. (b) Structure of the Mie resonance-based MA constituted of cubes and a metallic ground plane

spherical particles, other geometric shapes of particles have the same property [11]. For simplicity, we use cubes rather than spheres as the scattering objects shown in Fig. 1(b).

The cubes couple strongly to the incident magnetic field and the metallic ground plane couples to the incident electric field at the first Mie resonance mode [5]. It is possible to match the impedance of the MA to free space, thus minimizing the reflectance at the first Mie resonance mode. We design the MA structure of an array of dielectric cubes with different geometric parameters, which leads to a four-band MA with near unity absorbance based on the Mie resonance mode. Furthermore, from Eq. (5) we know that

$$f = \frac{\theta c}{2\pi r \sqrt{\varepsilon_2 \mu_2}} \quad (6)$$

and the lowest order resonant mode frequency, magnetic resonance, of a cubic dielectric resonator can be given by

$$f = \frac{\theta_1 c}{2\pi r \sqrt{\varepsilon_2 \mu_2}} = \frac{c}{2r \sqrt{\varepsilon_2}} \quad (7)$$

θ_1 is a constant which is approximately equal to π and μ is 1 for dielectric particles. Obviously, the first resonance frequency (f_1) of these dielectric particles is completely determined by ε_2 and r . As a result, the peak of the Mie resonance-based MA will change when we change the permittivity or size of the dielectric particles. By simply assembling four dielectric cubes with slightly different geometric parameters next to each other into a unit cell, a perfect four-band absorption can be effectively obtained.

3. DESIGN AND SIMULATION

The designed four-band MA is inspired by the narrow-band perfect absorber structure in Ref. [5] which is composed of an array of dielectric cubes and a continuous copper ground plane. The proposed MA is designed and optimized by CST Microwave Studio, which is based on the commercial finite difference time domain (FDTD) solver. The periodic boundary condition is set along the lateral directions of the MA and open boundary condition is set along the wave propagating direction. The unit cell of designed MA structure is displayed in Fig. 2(a). The metallic ground plane is copper with 0.1 mm in thickness and frequency independent conductivity $\sigma = 5.8 \times 10^7$ S/m. In order to achieve a four-band perfect absorption, four cubes with different geometrical parameters are positioned on the ground plane in a unit cell. The final optimized geometry of the unit cell is given by: $l = 17.6$ mm, $a_1 = 2.7$ mm, $a_2 = 2.6$ mm, $a_3 = 2.5$ mm, $a_4 = 2.4$ mm, and $t = 0.1$ mm. The absorption rate is calculated by $A(w) = 1 - R(w) = 1 - |S_{11}|^2$ in our design because the transmission of the MA is zero due to the metallic ground plane is thicker than the penetration depth of light in the microwave range.

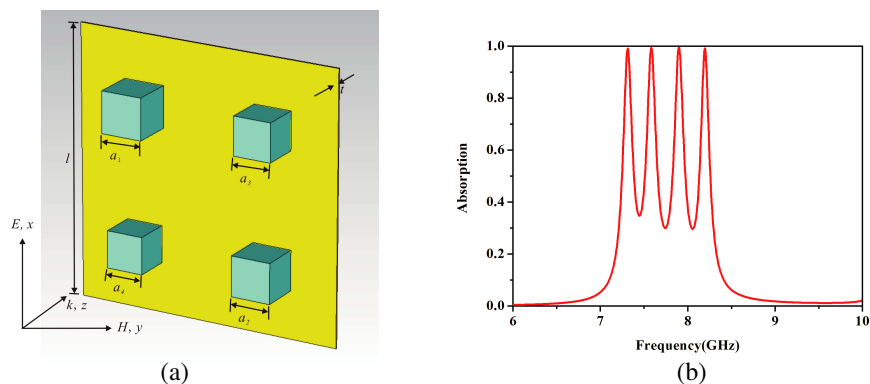


Figure 2: (a) The simulated unit cell. (b) The simulated absorption rate of the proposed MA.

4. RESULTS AND ANALYSES

The simulated absorption rate of the four-band MA is shown in Fig. 2(b). The results exhibit that there are four absorption peaks at 7.31 GHz, 7.58 GHz, 7.90 GHz and 8.19 GHz with the corresponding absorption rates of 99.05%, 99.37%, 99.65% and 99.16%, respectively. The proposed MA

is not geometrical symmetry owing to the four dielectric cubes with small differences in geometric parameters. So the polarization-insensitive feature is characterized by setting the polarization angles at 45° and 90° , as shown in Fig. 3. The result proves that the Mie resonance-based MA is polarization-insensitive at the normal incidence. The full width at half-maximum (FWHM) of each absorption peak is 0.14 GHz, 0.15 GHz, 0.15 GHz and 0.13 GHz, respectively.

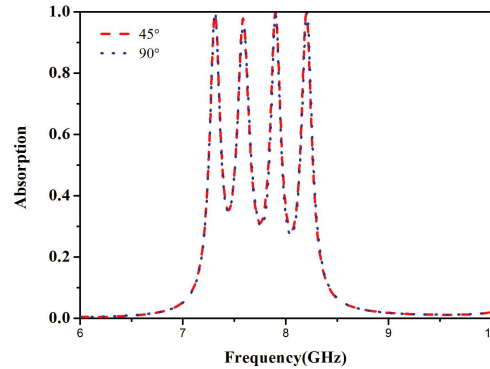


Figure 3: Simulated absorption rates of the four-band MA at an polarization angles of 45° and 90° under the normal incidence.

To get a better understand the intrinsic mechanism of the four bands MA, the surface current distributions and the power loss density distribution of the four resonances are monitored as shown in Fig. 4 and Fig. 5.

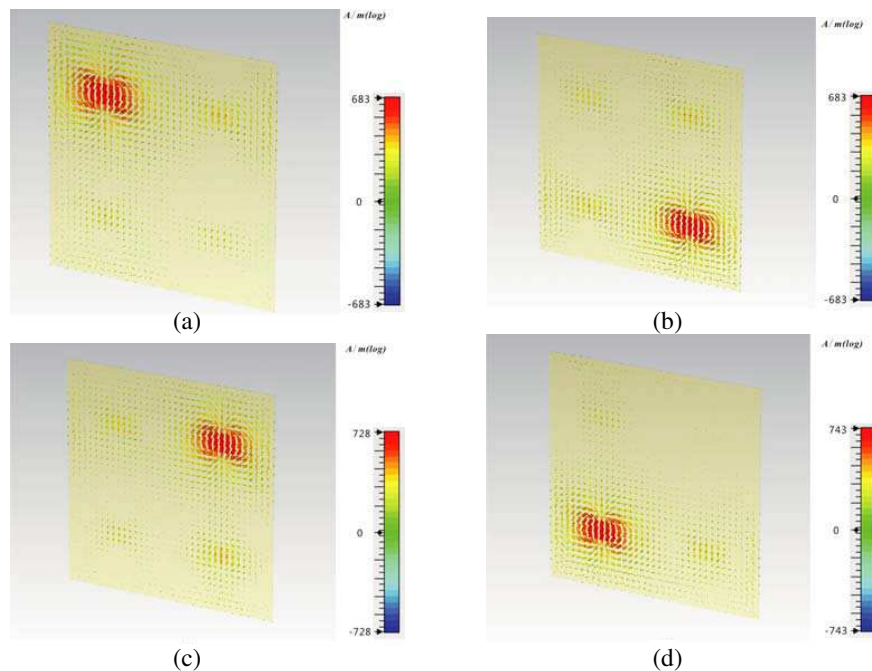


Figure 4: Surface current distributions of the MA at resonance frequencies corresponding to the four different geometrical parameters: (a) at 7.31 GHz, $a = 2.7$ mm; (b) at 7.58 GHz, $a = 2.6$ mm; (c) at 7.90 GHz, $a = 2.5$ mm; (d) at 8.19 GHz, $a = 2.4$ mm.

According to the previous study [12], the scattered field of dielectric particles can be decomposed into a multipole series. For the lowest resonant frequency, the cube particle is equivalent to a magnetic dipole resonance. It is observed from Figs. 4(a) ~ (d), the current flows on the copper plane along the incident electric field, which generates the absorption of the MA. It is observed that near the lowest resonant frequency, the cube is equivalent to a magnetic dipole. In general, the magnetic dipole response is usually weak. This can be driven into resonance, however, by using materials with a large permittivity. In addition, the cubes couple strongly to the incident magnetic

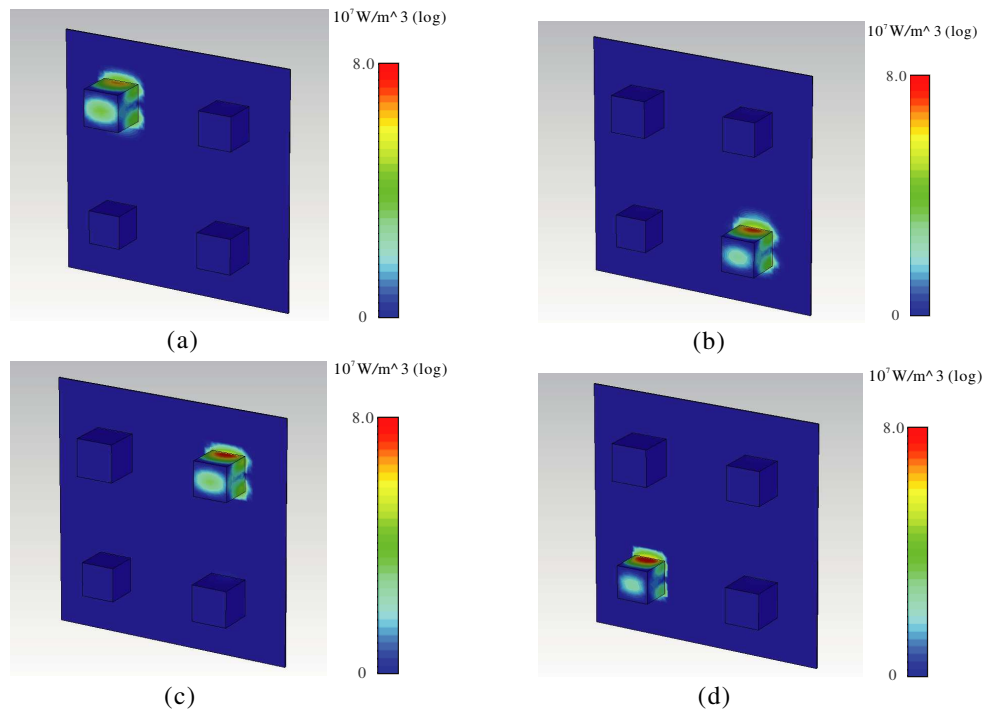


Figure 5: The distribution of the power loss density of the MA at resonance frequencies corresponding to the four different geometrical parameters: (a) at 7.31 GHz, $a = 2.7$ mm; (b) at 7.58 GHz, $a = 2.6$ mm; (c) at 7.90 GHz, $a = 2.5$ mm; (d) at 8.19 GHz, $a = 2.4$ mm.

field and the metallic ground plane couples to the incident electric field at the first Mie resonance mode. As shown in Fig. 5, the power loss densities distributions with the four different resonant frequencies are explored on the cubes and copper ground plane. It indicates that nearly all of the EM radiation is absorbed by the dielectric particles. In addition, we concluded that the MA can concentrate EM waves in some specified locations, where the energy is significantly reinforced and subsequently converted into thermal energy, leading to strong absorption [13].

The absorptivity of the MA at different angles of incidence for TE and TM waves are displayed in Fig. 6. For the case of TE wave (see Fig. 6(a)), the absorption peaks are all over 99% at normal incidence. With the increasing angle of incidence the four peaks monotonically decrease, but the lowest absorption still has a value of 85.87% at an incident angle of 60° . When the incident angle continues to increase, the peaks decrease quickly, as the x-component of the incident magnetic field drops rapidly to zero and no longer effectively induces a strong magnetic resonance.

For the TM case (see Fig. 6(b)), the absorption rates still remain more than 70% at the four resonance frequencies. This is because the direction of the incident magnetic field remains un-

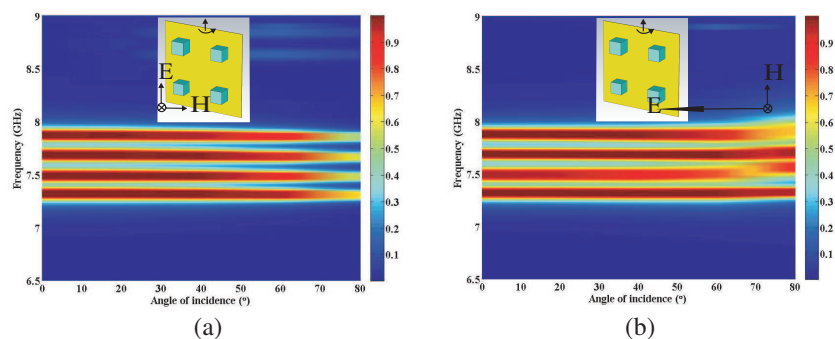


Figure 6: Simulated absorption rates of the four-band MA at different angles of incidence for (a) TE and (b) TM waves. The insets indicate the polarization and propagation directions of the incident wave.

changed at different angles of incidence and it can efficiently drive a strong magnetic resonance. It should be noted that the absorption peaks appear at the frequency of 7.31 GHz and 7.90 GHz are increased and the bandwidth are also slightly increased and frequency bands overlap in some degree. These results demonstrate that the Mie resonance-based MA could achieve high absorptivity at wide angles of incidence for both TE and TM waves.

According to Eq. (7), the absorption peak of the proposed MA will change if we change the permittivity or size of the dielectric particles. Fig. 7(a) showed that the simulated absorption peak frequency decreased from 8.60 GHz to 7.31 GHz as the side length (a) increased from 2.3 mm to 2.7 mm ($\varepsilon = 115$), and Fig. 7(b) indicated that the simulated absorption peak frequency decreased from 8.26 GHz to 7.58 GHz as the permittivity (ε) increased from 105 to 125 ($a = 2.5$ mm). We found good agreement between the theoretical and simulated results.

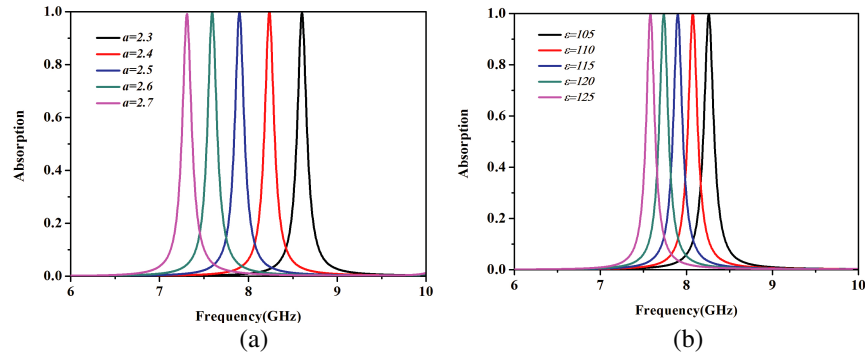


Figure 7: (a) The simulated absorption of the MA by different a (mm). (b) The simulated absorption of the MA by different ε .

5. CONCLUSION

In conclusion, we have presented a four-band metamaterial absorber (MA) with near-unity absorption based on Mie resonance theory in the microwave region. The MA is composed of periodic array of dielectric cubes with different geometric parameters and a metallic ground plane. The simulated results show that four absorption peaks at 7.31 GHz, 7.58 GHz, 7.90 GHz and 8.19 GHz with the corresponding absorption rates of 99.05%, 99.37%, 99.65% and 99.16%, respectively. The four-band MA is polarization-insensitive at the normal incidence. This absorber could operate well at different angles of incidence for both transverse electric (TE) and transverse magnetic (TM) waves. Finally, distributions of surface current density on the dielectric cubes and back metallic layers are illustrated. The loss contributions of dielectric cubes and ground plane are also discussed. Experiment of the Mie resonance-based MA will be conducted to validate the simulated results in the next work. The proposed multi-band MA has many potential applications such as the spectroscopic detection and phase imaging of hazardous materials and prohibited drugs which require distinct absorption features at multiple frequencies.

ACKNOWLEDGMENT

This work was supported by Graduates' Innovation Fund of Huazhong University of Science Technology (Grant No. HF-11-15-2013) and the special funds of State Key Laboratory of Advanced Electromagnetic Engineering and Technology, Huazhong University of Science and Technology (Grant No. 2014ZZ001).

REFERENCES

1. Landy, N. I., S. Sajuyigbe, J. J. Mock, D. R. Smith, and W. J. Padilla, "Perfect metamaterial absorber," *Physical Review Letters*, Vol. 100, No. 20, 207402, 2008.
2. Shchegolkov, D. Y., A. K. Azad, J. F. O'Hara, et al., "Perfect subwavelength fishnetlike metamaterial-based film terahertz absorbers," *Physical Review B*, Vol. 82, No. 20, 205117, 2010.
3. Shen, X. P., T. J. Cui, J. M. Zhao, H. F. Ma, W. X. Jiang, and H. Li, "Polarization-independent wide-angle triple-band metamaterial absorber," *Optics Express*, Vol. 19, No. 10, 9401–9407, 2011.

4. Wang, G. D., M. H. Liu, X. W. Hu, L. H. Kong, L. L. Cheng, and Z. Q. Chen, “Multi-band microwave metamaterial absorber based on coplanar Jerusalem crosses,” *Chinese Physics B*, Vol. 23, No. 1, 017802, 2014.
5. Liu, X. M., Q. Zhao, C. W. Lan, and J. Zhou, “Isotropic Mie resonance-based metamaterial perfect absorber,” *Applied Physics Letters*, Vol. 103, No. 3, 031910, 2013.
6. Lewin, L., “The electrical constants of a material loaded with spherical particles,” *Proceedings of the Institution of Electrical Engineers*, Vol. 94, No. 65, 65–68, 1947.
7. Mie, G., “Beiträge zur optik trüber medien, speziell kolloidaler metallösungen,” *Annalen der Physik*, Vol. 330, No. 3, 377–445, 1908.
8. Maxwell, J. C., *A Treatise on Electricity and Magnetism Unabridged*, Dover, 1954.
9. Rayleigh, L. L., “On the influence of obstacles arranged in rectangular order upon the properties of a medium,” *The London, Edinburgh, and Dublin Philosophical Magazine and Journal of Science*, Vol. 34, No. 211, 481–502, 1892.
10. Khizhniak, N. A., “Artificial anisotropic dielectrics: 2. Soviet physics-technical physics,” Vol. 2, No. 9, 1865–1876, 1957.
11. Holloway, C. L., E. F. Kuester, J. Baker-Jarvis, et al., “A double negative (DNG) composite medium composed of magnetodielectric spherical particles embedded in a matrix,” *IEEE Transactions on Antennas and Propagation*, Vol. 51, No. 10, 2596–2603, 2003.
12. Wheeler, M. S., J. S. Aitchison, and M. Mojahedi, “Three-dimensional array of dielectric spheres with an isotropic negative permeability at infrared frequencies,” *Physical Review B*, Vol. 72, No. 19, 193103, 2005.
13. Tuong, P. V., V. D. Lam, J. W. Park, E. H. Choi, S. A. Nikitov, and Y. P. Lee, “Perfect-absorber metamaterial based on flower-shaped structure,” *Photonics and Nanostructures-Fundamentals and Applications*, Vol. 11, No. 1, 89–94, 2013.

A Compact Plasmonic 4-way Wavelength Splitter for Planar Circuits

Yong Jin Zhou^{1,2} and Bao Jia Yang¹

¹Key Laboratory of Specialty Fiber Optics and Optical Access Networks

School of Communication and Information Engineering, Shanghai University, Shanghai 200072, China

²State Key Laboratory of Millimeter Waves, Southeast University, Nanjing 210096, China

Abstract— A compact plasmonic 4-way wavelength splitter with band-stop filters at microwave frequencies is proposed. The splitter is based on specially designed plasmonic structures and band-stop filters. The plasmonic structures are placed on the dielectric substrate and consist of two metal gratings with corrugated grooves in the inner surface, which are suitable for integration with planar circuits. The band-stop filters are constructed by composite-periodic grating structures with different groove depths, which can improve the isolations between different branches. The plasmonic 4-way splitter is investigated numerically based on full-wave simulations at microwave frequencies. Electromagnetic (EM) waves at the designed frequencies are confined and guided along different branches with good isolations.

1. INTRODUCTION

Plasmonics forms a major part of the fascinating field of nanophotonics, which explores how EM fields can be confined smaller than the wavelength. It is based on interaction processes between EM radiation and conduction electrons at metallic interfaces or in small metallic nanostructures, leading to an enhanced optical near field of sub-wavelength dimension [1]. Surface plasmon polaritons (SPPs) as one of the main ingredient of plasmonics which can propagate along the metal surfaces and can be tightly confined to sub-wavelength size beyond the diffraction limit at visible frequencies [2]. Recent researches have shown that structured metal surface drilled with arrays of sub-length holes or grooves at terahertz (THz) or microwave frequency can strongly support a kind of surface EM modes, whose behavior is similar to the SPPs and names as spoof SPPs (SSPPs) [3, 4]. The dispersion relation of SSPPs is determined by the shape and dimension of the subwavelength holes or grooves, so it provides an effective way to guide and manipulated EM surface waves.

In recent years, various geometries of structured surfaces have been proposed to guide the propagation of SSPPs. In Ref. [5], a back-side slit-illumination method that incorporates a periodic array of grooves carved into the front side of a thick metal film was proposed to generate a unique propagation direction for SPPs. A THz frequency splitter based on a bidirectional subwavelength slit resonating was proposed to guide the EM waves with different frequencies propagated along the opposite directions and then a theoretical discussion of the design of bidirectional wave couplers based on plasmonic Bragg gratings in the near infrared domain was presented [6, 7]. A surface wave splitter based on metallic gratings with sub-wavelength aperture can support surface waves with different frequencies at different sides [8]. Then a metal-film bidirectional surface wave splitter which can guide light at two visible wavelengths in opposite directions was demonstrated [9]. A bidirectional surface wave splitter excited by a cylindrical wire in the microwave frequency which has two grating branches with different depths was proposed [10]. Then a multidirectional surface wave splitter was presented in Ref. [11], but the isolation at low frequencies is bad. Recently, a multidirectional frequency splitter with band-stop plasmonic filters was proposed [12], and improved the problem of bad isolation at low frequencies appeared in Ref. [11].

In this paper, we proposed a novel 4-way wavelength splitter at microwave frequencies fed by coplanar waveguide (CPW). The 4-way splitter has a compact structure and suitable for planar circuits integration. The planar band-stop filters are introduced to improve the isolation between these four branches. The simulation results based on CST Microwave Studio (CST) show good performance of the special designed 4-way wavelength splitter.

2. DESIGNS AND SIMULATIONS

The 4-way splitter is composed of four branches and each branch consists of two symmetrical metal grating structures. The structure is shown in Fig. 1(a). Compared with the structures proposed in Refs. [10–12], the proposed plasmonic structure is placed at the surface of dielectric (FR4) whose thickness d is 0.5 mm and dielectric constant is 4.9. Obviously, this structure is suitable for planar integrated circuits. At the front of each branch is band-stop filter except *branch 4*. The thickness

t of the metal is $35\ \mu\text{m}$. The groove period and groove width are p and w , where $p = 5\ \text{mm}$, $w = 2\ \text{mm}$ and the depths of the grooves of four branches is h_1 , h_2 , h_3 and h_4 , where $h_1 = 3\ \text{mm}$, $h_2 = 5\ \text{mm}$, $h_3 = 8\ \text{mm}$ and $h_4 = 11\ \text{mm}$, respectively. The insulator between two graded metal grating structures is air and its width w_{air} is $2\ \text{mm}$. It is excited by CPW. The dispersion curves of such periodic structure can be calculated by using the eigenmode solver of CST. Fig. 1(b) shows the dispersion curves of the structures whose groove depths are $3\ \text{mm}$, $5\ \text{mm}$, $6\ \text{mm}$ and $10\ \text{mm}$, respectively.

From Fig. 1(b), we can see that the EM waves at $9\ \text{GHz}$, $7\ \text{GHz}$, $5\ \text{GHz}$ and $3\ \text{GHz}$ can well propagate on the branches whose groove depths are $3\ \text{mm}$, $5\ \text{mm}$, $7\ \text{mm}$ and $11\ \text{mm}$, respectively. But at low frequencies, the problem of bad isolation will appear as mentioned in Ref. [11]. So we designed the band-stop filters at the front of branches to apparently improve the isolation at low frequencies. For the *branch 4*, there is no need to design a filter, because the EM waves at other frequencies have been stopped and cannot propagate along this branch. The band-stop filters consist of double-periodic groove grating as shown in Fig. 2(a), the depths of shallow grooves and deep grooves is h_{f1} and h_{f2} , the period of composite structure P_f is $10\ \text{mm}$. The transmission spectra (S_{21}) of the band-stop filters with different h_{f1} and h_{f2} are given in Fig. 2(b). It shows that the performance of the band-stop filters can meet our design requirement.

The simulation results of the 4-way splitter are shown in Fig. 3. The two-dimension (2D) electric field distribution at the planar of $z = 1\ \text{mm}$ are observed. We can clearly see that the EM waves at

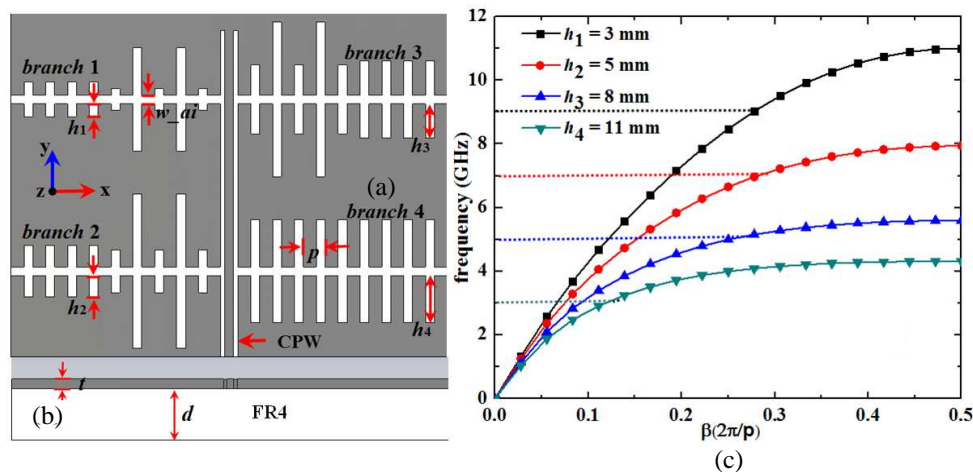


Figure 1: (a) Top view of 4-way wavelength splitter; (b) side view of the structure; (c) the dispersion curves of the four branches, corresponding to $h_1 = 3\ \text{mm}$, $h_2 = 5\ \text{mm}$, $h_3 = 8\ \text{mm}$ and $h_4 = 11\ \text{mm}$, respectively.

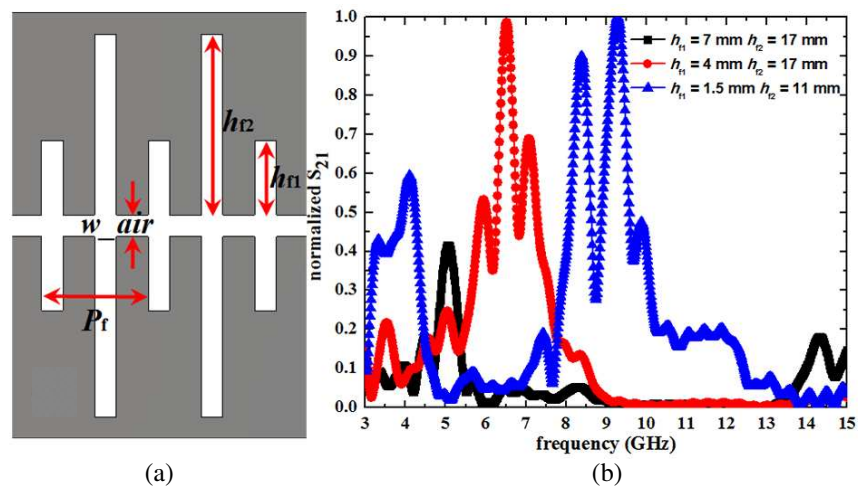


Figure 2: (a) The sketch of band-stop filter, $P_f = 10\ \text{mm}$, $w_{\text{air}} = 2\ \text{mm}$, h_{f1} and h_{f2} are variable; (b) transmission spectra (S_{21}) of the band-stop filters, black, red and blue lines are corresponding to $h_{f1} = 7\ \text{mm}$ and $h_{f2} = 17\ \text{mm}$, $h_{f1} = 4\ \text{mm}$ and $h_{f2} = 17\ \text{mm}$ and $h_{f1} = 1.5\ \text{mm}$ and $h_{f2} = 11\ \text{mm}$, respectively.

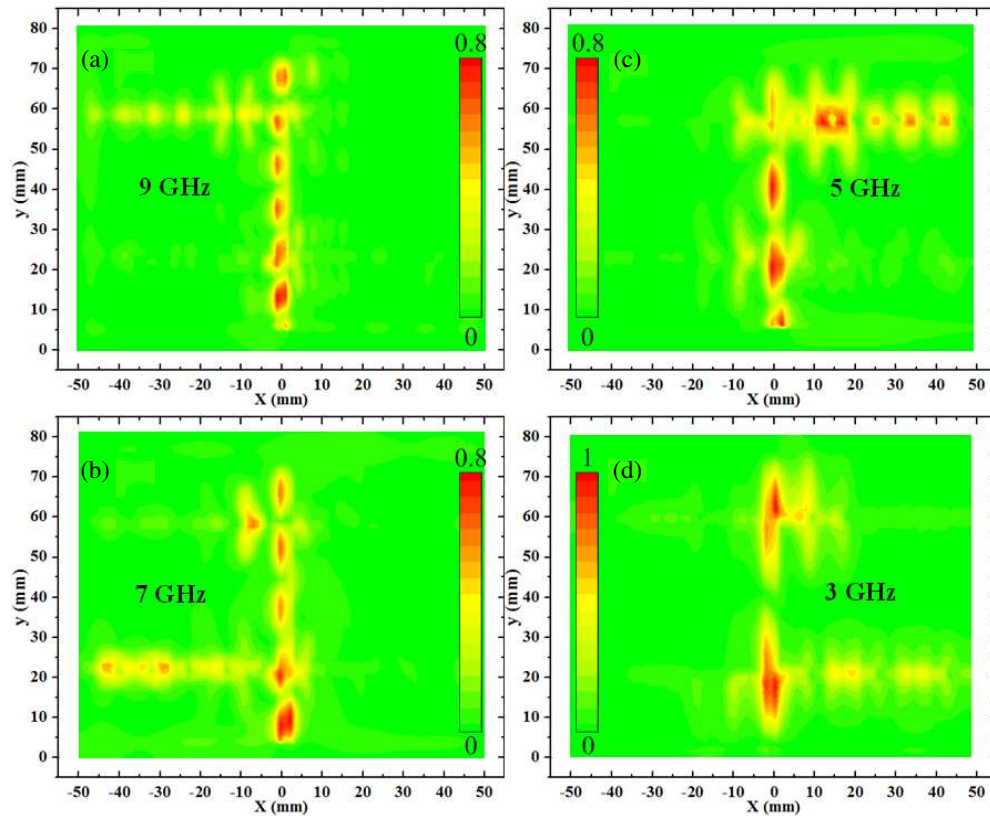


Figure 3: 2D E-field distribution of 4-way wavelength splitter; (a), (b), (c) and (d) corresponding to EM waves with the frequencies of 9 GHz, 7 GHz, 5 GHz and 3 GHz.

the frequencies of 3 GHz, 5 GHz, 7 GHz and 9 GHz are propagating along different branches with the depths of grooves of 11 mm, 8 mm, 5 mm and 3 mm, respectively. The isolation at low frequency is very well. It shows that the performance of this compact plasmonic 4-way wavelength splitter with band-stop filters is good.

3. CONCLUSION

We have proposed a compact plasmonic 4-way wavelength splitter at microwave frequency, which can make EM waves at different frequencies propagating along different branches. The introduction of band-stop filters improved the isolation between branches. The simulation results show that the performance of the designed 4-way frequency splitter is good. The whole structure can be easily manufactured by existing printed circuits board (PCB) technologies and it is suitable for the integration with planar circuits.

ACKNOWLEDGMENT

This work was supported in part by the National Natural Science Foundation of China under Grant No. 61307129, in part by the Shanghai Committee of Science and Technology under Grant No. 13ZR1454500, and in part by the Open Project Program of the State Key Laboratory of Millimeter Waves under Grant No. K201416.

REFERENCES

1. Stefan, A. M., *Plasmonics: Fundamentals and Applications*, Springer-Verlag, New York, 2007.
2. Barnes, W. L., A. Dereux, and T. W. Ebbesen, "Surface plasmon subwavelength optics," *Nature*, Vol. 424, No. 6950, 824–830, 2003.
3. Pendry, J. B., L. Martín-Moreno, and F. J. Garcia-Vidal, "Mimicking surface plasmons with structured surfaces," *Science*, Vol. 305, No. 5685, 847–848, 2004.
4. Alastair, P. H., R. E. Benjamin, and J. R. Sambles, "Experimental verification of designer surface plasmons," *Science*, Vol. 308, No. 5722, 670–672, 2005.

5. López-Tejiera, F., S. G. Rodrigo, L. Martín-Moreno, F. J. García-Vidal, E. Devaux, T. W. Ebbesen, J. R. Krenn, I. P. Radko, S. I. Bozhevolnyi, M. U. González, J. C. Weeber, and A. Dereux, “Efficient unidirectional nanoslit couplers for surface plasmons,” *Nature Physics*, Vol. 3, No. 7, 324–328, 2007.
6. Gan, Q. Q., F. Zhan, Y. J. Ding, and F. J. Bartoli, “Bidirectional subwavelength slit splitter for THz surface plasmons,” *Optics Express*, Vol. 15, No. 26, 18050–18055, 2007.
7. Zhan, F., Q. Q. Gan, K. L. Gao, Z. Q. Pan, and F. J. Bartoli, “Numerical investigation of a bidirectional wave coupler based on plasmonic bragg gratings in the near infrared domain,” *Journal of Lightwave Technology*, Vol. 26, No. 22, 2008.
8. Caglayan, H. and E. Ozbay, “Surface wave splitter based on metallic gratings with sub-wavelength aperture,” *Optics Express*, Vol. 16, No. 23, 19091–19096, 2008.
9. Gan, Q. Q. and F. J. Bartoli, “Bidirectional surface wave splitter at visible frequencies,” *Optics Letters*, Vol. 35, No. 24, 4181–4183, 2010.
10. Zhou, Y. J., Q. Jiang, and T. J. Cui, “Bidirectional surface wave splitters excited by a cylindrical wire,” *Optics Express*, Vol. 19, No. 6, 5260–5267, 2011.
11. Zhou, Y. J. and T. J. Cui, “Multidirectional surface-wave splitters,” *Applied Physics Letters*, Vol. 98, No. 22, 221901, 2011.
12. Zhou, Y. J., X. X. Yang, and T. J. Cui, “A multidirectional frequency splitter with band-stop plasmonic filters,” *Journal of Applied Physics*, Vol. 115, No. 12, 123105, 2014.

The Influence of Air-hole Filling Fraction of Photonics Crystal Fibers on Stimulated Brillouin Scattering Slow Light

Shanglin Hou, Ji Sun, Weiqing Ge, Yanjun Liu, Jingli Lei, and Xiaoxiao Li
School of Science, Lanzhou University of Technology, Lanzhou, Gansu 730050, China

Abstract— The influence of structural parameters of photonic crystal fiber (PCF) on the Stimulated Brillouin Scattering (SBS) slow light by the finite difference time domain method is investigated, the time delay and broadening factor of the pulse are studied for different air-hole filling fractions. The results indicate that time delay increases and broadening factor decreases with air-hole filling fraction increasing. Air-hole filling fraction has less effect on time delay and broadening factor for the same core diameter of PCF.

1. INTRODUCTION

Stimulated Brillouin Scattering (SBS) [1, 2] is a type of nonlinear optical phenomena in optical fiber. Because of the electrostrictive effect, it can lead to periodic modulation of refractive index of medium when the pump's power is greater than the Brillouin threshold power. The index grating generated by index modulation scatters the pump light. So Stokes wave is scattered by index grating and propagates in the opposite direction of the pump. SBS Slow light technology [3] has some advantages in comparison with the other slow light technologies in optical fibers, such as electromagnetic induction transparent (EIT), coherent population oscillation (CPO). Such as operating at room temperature, comparable with existing communication system, easy tailoring time delay and so on. The SBS slow light has great potential applications in fiber delay line, optical buffer and fiber optical sensor [4–6].

Photonics crystal fiber (PCF) is a new type of optical fiber with periodic arrangement of air hole on certain substrate materials. Due to the periodic cladding structures of PCF can be changed flexibly, the cladding-core refractive index difference of PCF is much larger than conventional doped fiber. It can improve the nonlinear property of PCF and enhance the SBS effect [7]. Dainese et al. [8] studied SBS in ultra core PCF, the results indicate that the Brillouin gain spectrum has multi-peak and Brillouin frequency shift is reduced to near 10 GHz as the diameter of PCF core is 70% of the incident light wavelength. This is due to a variety of acoustic mode couple in the PCF. J. Zhao et al. [9] observed SBS slow light in a high nonlinear PCF. They found that the high nonlinear PCF which compared with common fibers can effectively reduce its length and limit of pump power. Recently W. Wei et al. [10] used single pump and single-stage delay method to study SBS slow light in PCF which was generated by their own, they recorded the maximum of delay is 76 ns which is equivalent to 0.76 pulse width in length of 120 m high nonlinear microstructure fiber as pump power is 126.6 mW.

Based on previous research work [11] of our group, we used the finite difference method, and theoretically study the SBS process with the different structural parameters of PCF which influence on the delay time and broaden factor. We get the variation trend of delay time and broaden factor with the different air-hole filling fractions of PCF. The results shown that time delay increases and broadening factor decreases as the air-hole filling fraction increasing.

2. THEORETICAL ANALYSES

We stimulated the SBS process via solving the SBS three-wave coupled wave equations, which includes a forward pump wave, a backward Stokes wave and a forward acoustic wave. Under the slowly varying envelop approximation, the SBS three-wave coupled wave equations [12–14] is as follows

$$-\frac{\partial A_p}{\partial z} + \frac{1}{v_g} \frac{\partial A_p}{\partial t} = -\frac{\alpha}{2} + ig_2 A_s Q \quad (1)$$

$$\frac{\partial A_s}{\partial z} + \frac{1}{v_g} \frac{\partial A_s}{\partial t} = -\frac{\alpha}{2} + ig_2 A_p Q^* \quad (2)$$

$$\frac{\partial Q}{\partial t} + \left(\frac{\Gamma_B}{2} - i\Delta\omega \right) Q = ig_1 A_p A_s \quad (3)$$

where A_p is amplitude of pump wave, A_s is amplitude of Stokes wave, and Q is amplitude of acoustic wave. α is related to the loss coefficient of PCF. $\Gamma_B/2\pi = 40$ MHz is Brillouin gain bandwidth in silica. It is related to the lifetime of phonon. $\Delta\omega = (\omega_p - \omega_s) - \Omega_B$ is angular frequency which diverge from center of SBS gain spectrum. ω_p is angular frequency of pump wave, ω_s is angular frequency of stokes wave, and Ω_B is Brillouin frequency shift.

The actual gain is given by

$$G = \log(P_{out}/P_{in}) \quad (4)$$

where P_{in} is input stokes power and P_{out} is output stokes power.

Time delay T_d is defined as the time difference of stokes peak powers between in SBS and without SBS. Broaden factor B is defined as the ratio of FWHM of output stokes wave to FWHM of input stokes wave.

The cross section of PCF is shown in Fig. 1. The circles in the figure are tiny air hole. d represents the diameter of air hole, d_c is effective core diameter and Λ is pitch between two air holes. The air-hole filling fraction f related to d and Λ is defined as

$$f = d/\Lambda \quad (5)$$

The definition of PCF fiber core diameter is:

$$d_c = 2\Lambda - d \quad (6)$$

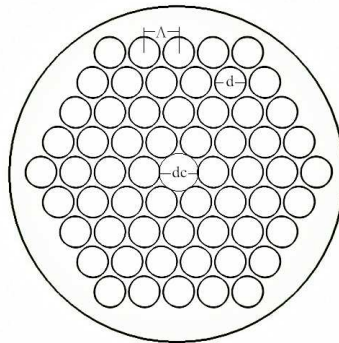


Figure 1: Cross section of PCF.

The variation of the air-hole filling fraction will affect the modal refractive index and area of core. These structure changes of PCF can influence on the SBS process. So we first achieve the results about the modal refractive index of core and calculate the area of the core by using the finite element method. Then we put the parameters into the Eqs. (1)–(3). The Stokes waveform can be solved by that set of equations. Finally we adopted the method [15], the required result can be obtained and be used to calculate the delay time and broaden factor.

3. NUMERICAL SIMULATIONS AND DISCUSSION

Setting PCF length L is 50 m. A 125 mW-power pump pulse with 1550 nm center wavelength and a full width at half maximum (FWHM) of 100 ns is injected in the fiber. Brillouin gain bandwidth is about 40 MHz, the gain coefficient is $g_0 = 5 \times 10^{-11}$ m/W.

Near the $G = 14$, the gain reaches saturation. The increase of delay becomes slower gradually as the gain continues to grown. Finally the time delay stops and slumps with pulse begin to compress. So we select $G = 10$, the delay increase steadily, and study the influence of the air-hole filling fraction on delay time and broaden factor.

3.1. The Diameter of Core Remains Unchanged

The influences of the air-hole filling fraction on delay time and broaden factor with $d = 1.7 \mu\text{m}$ and $G = 10$ are shown in Fig. 2 and Fig. 3. Fig. 2 shows time delay increases with the increase of air-hole filling fraction. The delay increases slowly under a small air-hole filling fraction. however, the delay increases quickly as $f > 0.5$. In Fig. 3, the broaden factor decreases when the air-hole filling fraction increases. The broaden factor decreases linearly as f from 0.4 to 0.6.

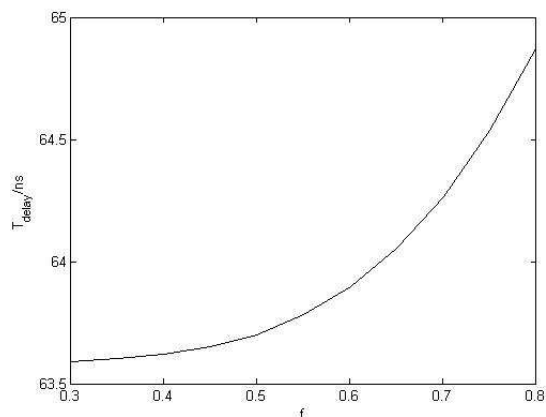


Figure 2: Variation of time delay and air-hole-fill fraction under the same air hole diameter.

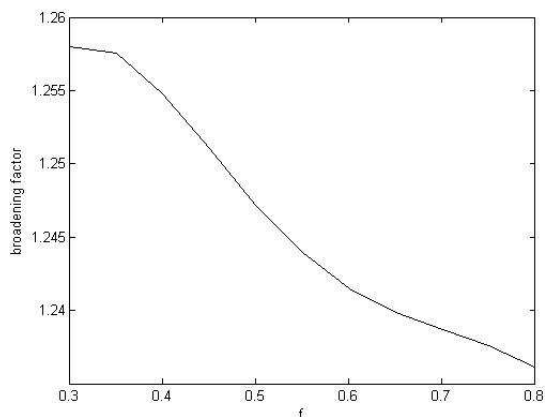


Figure 3: Variation of broadening factor and air-hole-fill fraction under the same air hole diameter.

3.2. The Pitch of the Air Hole Remains Unchanged

The influences of air-hole filling fraction on delay time and broaden factor with $\Lambda = 3 \mu\text{m}$ and $G = 10$ are shown in Fig. 4 and Fig. 5. It can be seen that the delay time increases and broaden factor decreases linearly with the increase of air-hole filling fraction. The curve in Fig. 4 is more closer to linear than Fig. 2. But the total delay time is smaller. The relation between broaden factor and the air-hole filling fraction shown in Fig. 5 is more close to linear. But the broaden factor in Fig. 5 reduce from 1.257 to 1.205.

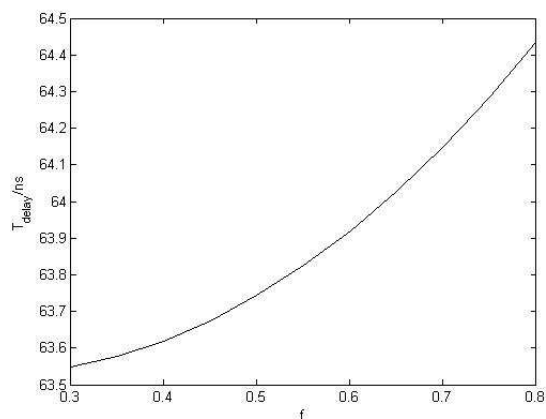


Figure 4: Variation of time delay and air-hole-fill fraction under the same air hole pitch.

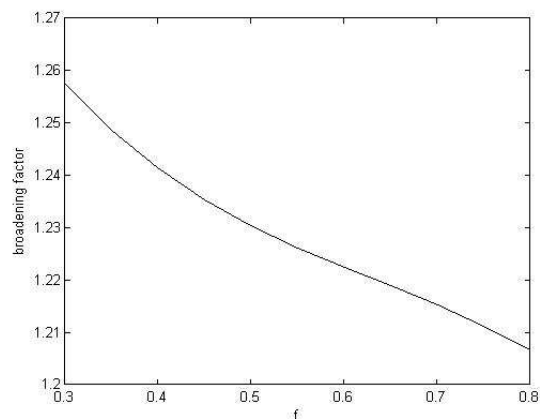


Figure 5: Variation of broadening factor and air-hole-fill fraction under the same air hole pitch.

4. CONCLUSION

The influence of the SBS slow light for the different structural parameters of PCF is theoretically studied by using the finite difference time domain method. We discuss the influence of the air-hole filling fraction on the delay time and broaden factor. The results show that the delay time increases and the broaden factor decreases with increase of the air-hole filling fraction. They have linear change as the pitch of PCF is fixed. When the diameter of core is fixed the change of air-hole filling fraction has little effect on delay time and broaden factor.

ACKNOWLEDGMENT

This paper was supported by: the National Natural Science Foundation of China (Grant No. 61167005). And The Natural Science Foundation of Gansu province of China (Grant No. 1112RJZA018).

REFERENCES

1. Agrawal, G. P., *Nonlinear Fiber Optics*, Academic Press, California, 1995.
2. Zhaoming, Z., D. J. Gauthier and R. W. Boyd, “Stored light in an optical fiber via stimulated Brillouin scattering,” *Science*, Vol. 318, 1748–1751, 2007.
3. Zadok, A., A. Eyal, and M. Tur., “Stimulated Brillouin scattering slow light in optical fibers,” *Applied Optics*, Vol. 50, No. 25, 38–49, 2011.
4. Song, K. Y., M. G. Herráez, and L. Thévenaz, “Observation of pulse delaying and advancement in optical fibers using stimulated Brillouin scattering,” *Opt. Express*, Vol. 13, No. 1, 82–88, 2005.
5. Wu, Y., L. Zhan, and Y. Wang, “Low distortion pulse delay using SBS slow-and fast-light propagation in cascaded optical fibers,” *Opt. Soc. Am. B*, Vol. 8, No. 11, 2605–2610, 2011.
6. Chin, S. and L. Thévenaz, “Tunable photonic delay lines in optical fibers,” *Laser Photonics Rev.*, Vol. 6, No. 6, 724–738, 2012.
7. McElhenny, J. E., R. K. Pattnaik, and J. Toulouse, “Unique characteristic features of stimulated Brillouin scattering in small-core photonic crystal fibers,” *Opt. Soc. Am. B*, Vol. 25, No. 4, 582–593, 2008.
8. Dainese, P., P. St. J. Russell, and N. Joly, “Stimulated Brillouin scattering from multi-GHz-guided acoustic phonons in nanostructured photonic crystal fibres,” *Nature Phys.*, Vol. 2, No. 6, 388–392, 2006.
9. Zhao, J., X. Yang, and Y. Li, “Stimulated Brillouin scattering slow light in photonic crystal fiber,” *Acta Optic Sinica*, Vol. 30, No. 8, 2437–2440, 2010.
10. Wei, W. and X. Zhang, “Slow light based on stimulated Brillouin scattering in microstructured fiber,” *Acta Physica Sinica*, Vol. 62, No. 18, 184208–184212, 2013.
11. Hou, S., H. Li, and S. Li, “Influence of Stokes pulse shapes on SBS slow light in fibers,” *Acta Optic Sinica*, Vol. 31, No. 6, 0606008–0606012, 2011.
12. Schneider, T., R. Henker, and K. Lauterbach, “Distortion reduction in slow light systems based on stimulated Brillouin scattering,” *Opt. Express*, Vol. 16, No. 11, 8280–8285, 2008.
13. Zhu, Z. and D. J. Gauthier, “Numerical study of all-optical slow-light delays via stimulated Brillouin scattering in an optical fiber,” *Opt. Soc. Am. B*, Vol. 22, No. 11, 2378–2384, 2005.
14. Winful, H. G., “Chirped Brillouin dynamic gratings for storing and compressing light,” *Opt. Express*, Vol. 21, No. 8, 10039–10047, 2013.
15. Cao, Y., P. Lu, and Z. Yang, “An efficient method of all-optical buffering with ultra-small core photonic crystal fiber,” *Opt. Express*, Vol. 16, No. 18, 14142–14150, 2008.

Investigation on Slow Light of Nonuniform Photonic Crystal Fiber Bragg Gratings

Shanglin Hou, Weiqing Ge, Yanjun Liu, Daobin Wang, Jingli Lei, and Xiaoxiao Li
School of Science, Lanzhou University of Technology, Lanzhou, Gansu 730050, China

Abstract— Based on the coupled-mode theory and transmission matrix method, the influences of Gaussian apodization coefficient and linear chirp coefficient on group velocity of photonic crystal fiber Bragg gratings are demonstrated. The results indicate that the minimum value of group velocity first decreases and then increases with the increase of apodization coefficient when the ‘dc’ index change value is big enough, which means that the minimum value of group velocity can be optimized at a certain apodization coefficient. But when the ‘dc’ index change value is very small, the minimum value of group velocity increases with the increase of apodization coefficient. A good linear area of the group velocity can be obtained by linear chirp and the linear area can be broadened by increasing the absolute value of chirp coefficient.

1. INTRODUCTION

In recent years, the researches on controllable slow light and its applications to optical memories, optical buffers and optical sensors have become the frontier and hot issue in optical field [1–4]. As fiber grating slow light technology has many advances, such as simple experiment conditions, easy modularization and distortionless transmission pulse [5], it has an promising future in practical applications. In 2005, a theoretical and experimental analysis of group velocity reduction in periodic superstructure Bragg gratings was presented by D. Janner [6] et al. Experimental demonstration of group velocity reduction of sub-nanosecond pulses at the 1.5 μm wavelength of optical communications for the first time was reported using a moiré fiber grating. And in 2012, He Wen [7] et al. showed theoretically for the first time that an FBG with a large index modulation and an optimized length and apodization can support light with a much lower group velocity than previously anticipated. But they did not show how does the apodization influence the group velocity of photonic crystal fiber Bragg gratings (PCFBGs).

Compared with ordinary fiber gratings, PCFGs have many advances [8–11], such as larger design freedom, endless single-mode transmission and adjustable dispersion characteristics. Therefore, PCFGs have wide potential applications in Optical fiber communication, optical fiber sensing and optical information processing field. In 2012, Bi Weihong et al. [12] theoretically analyzed the reflection spectrum characteristics of grapefruit-type photonic crystal fiber chirped grating by finite element method and transfer matrix method. The results indicated that both chirped parameters and photonic crystal fiber (PCF) parameters had influences on the reflection spectrum characteristics. The emergence of PCFG provides a new research direction for fiber grating slow light technology.

In this paper, the influences of gaussian apodization coefficient and linear chirp coefficient on slow light for PCFBGs are numerically simulated by improved full-vectorial effective index method and transfer matrix method. The paper is organized as follows: In Section 2, we show the convergence of two theoretical frameworks, the improved full-vectorial effective index method and transfer matrix method. In Section 3, detailed simulation results are presented; in Section 4, we discuss their merits and demerits.

2. THEORY MODEL

2.1. Improved Full-vectorial Effective Index Method

Improved full-vectorial effective index method can be used to simply, rapidly and accurately analyze the mode characteristics of PCF [13–15]. Its fundamental principle is as follows: first, suppose the cladding region of PCF as hexagon two-dimensional photonic crystal structure with numerous periodically spaced airholes and without central defects. Next, substitute hexagon unit cells with circular unit that has the equal area as the former. Then, obtain the effective index of the cladding fundamental mode by the vector theory of electromagnetic propagation. At last, PCF is equivalent to conventional step fiber with an effective core radius.

2.2. Transfer Matrix Method

Gaussian apodization function can be expressed as

$$\Delta n(z) = \Delta n \exp[-G(z/L)^2] \quad (1)$$

where Δn is the peak value of the ‘dc’ effective index change, G is the apodization coefficient and L is the length of fiber Bragg grating.

Chirped fiber Bragg grating is a kind of fiber grating with inhomogeneous period that changes with the position z . The periods of linear chirped fiber gratings can be expressed as

$$\Lambda(z) = \frac{\Lambda_0}{1 + Cz} \quad (2)$$

where Λ_0 is the period at the centre of fiber Bragg grating and F is the linear chirp coefficient.

The transfer matrix method to model nonuniform gratings is based on identifying 2×2 matrices for each uniform section of the grating. And then multiplying all of these together to obtain a single 2×2 matrix that describes the whole grating [16]. We divide the grating into M uniform sections and define R_i and S_i to be the field amplitudes after traversing the section i . The propagation through each uniform section i is described by a matrix F_i defined such that

$$\begin{bmatrix} R_i \\ S_i \end{bmatrix} = F_i \begin{bmatrix} R_{i-1} \\ S_{i-1} \end{bmatrix} \quad (3)$$

F_i is the transmission matrix of i th section and can be expressed as

$$F_i = \begin{bmatrix} \cosh(\gamma_B \Delta z) - i \frac{\sigma}{\gamma_B} \sinh(\gamma_B \Delta z) & -i \frac{\kappa}{\gamma_B} \sinh(\gamma_B \Delta z) \\ i \frac{\kappa}{\gamma_B} \sinh(\gamma_B \Delta z) & \cosh(\gamma_B \Delta z) + i \frac{\sigma}{\gamma_B} \sinh(\gamma_B \Delta z) \end{bmatrix} \quad (4)$$

where Δz is the length of i th section fiber grating, the ‘ac’ coupling coefficient κ and ‘dc’ self-coupling coefficient σ are the local values in the i th section and $\gamma_B = \sqrt{(\kappa^2 - \sigma^2)}$. Once all of the matrices for the individual sections are known, we find the output amplitudes from

$$\begin{bmatrix} R_M \\ S_M \end{bmatrix} = F_M F_{M-1} \cdots F_1 \begin{bmatrix} R_0 \\ S_0 \end{bmatrix} \quad (5)$$

For Bragg gratings we start with the boundary conditions $R_0 = R(L/2) = 1$ and $S_0 = S(L/2) = 0$, and the amplitude reflection coefficient $\rho = S_M/R_M$ can be obtained. Then the group delay can be shown as

$$\tau = \frac{d\theta}{d\omega} = -\frac{\lambda^2}{2\pi c} \frac{d\theta}{d\lambda} \quad (6)$$

where $\theta = \arctan(\rho)$ is the phase of reflection coefficient ρ .

So we can derive the relationship between the group velocity and the group delay

$$v_g = \frac{c}{n_g} = \frac{L}{\tau} \quad (7)$$

From the above equation we can conclude that adding the group delay can decrease the group velocity when the length of fiber grating is constant.

3. NUMERICAL SIMULATION AND RESULT DISCUSSION

3.1. Influences of Gaussian Apodization on PCFBG Slow Light

In the simulation, the cladding of PCFBG is composed of hexagonal arrangement airholes and germanium is doped in fiber core. We assume that germanium-doped fiber core does not affect the characteristics of the waveguide and PCF meets the single-mode transmission conditions [9, 13] (air filling rate $d/A < 0.4$). The refractive index of air $n_0 = 1$ and the refractive index of silica can be computed by Sellmeier equation [17].

The parameters are chosen as: diameter of airholes $d = 0.616 \mu\text{m}$, the pitch of airholes $A = 2.2 \mu\text{m}$, the length of grating $L = 1 \text{ cm}$, the period of grating $\Lambda = 0.5426 \mu\text{m}$, the fringe of the visibility of the index change $\nu = 1$, the ‘dc’ index change $\Delta n = 0.0006$ and the apodization

coefficient $G = 8$. The simulation result is shown in Fig. 1. Compared with the group velocity spectra of the uniform fiber gratings, apodization can efficiently restrain the side lobes in the long wavelength area, which means that the minimum values of group velocity can only appear in the short wavelength area. In Fig. 1, V represents the ratio of the minimum value of group velocity V_g and the vacuum speed of light c . In the following simulations, we replace the minimum value of group velocity with V . To demonstrate the effects of apodization coefficient G on the minimum value of group velocity.

The influences of gaussian apodization coefficient G on the minimum value of group velocity are detailedly described in Fig. 2. Parameters for Fig. 2 are same to that for Fig. 1 except apodization coefficient G . In Fig. 2, the three selected apodization coefficients are all in the range that the minimum value of group velocity decreases with the increase of apodization coefficient. From Fig. 2, the minimum value of group velocity not only decreases but also moves to smaller wavelength with the increase of apodization coefficient. The wavelength where the minimum value of group velocity appears becomes smaller with the increase of apodization coefficient G . At the same time, the full width at half maximum of the minimum group velocity peak increases with the decrease of minimum value of group velocity.

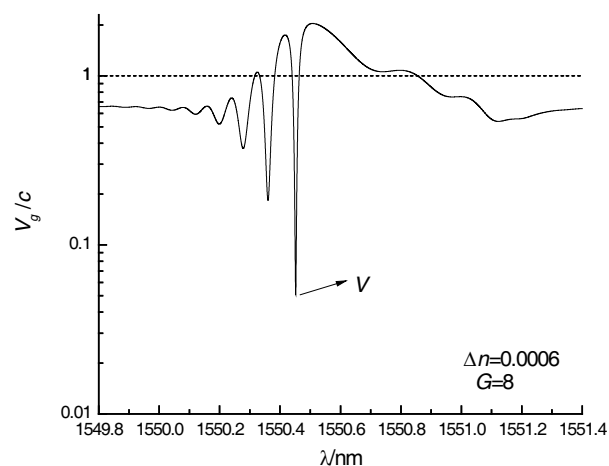


Figure 1: Group velocity spectra for PCF apodized grating.

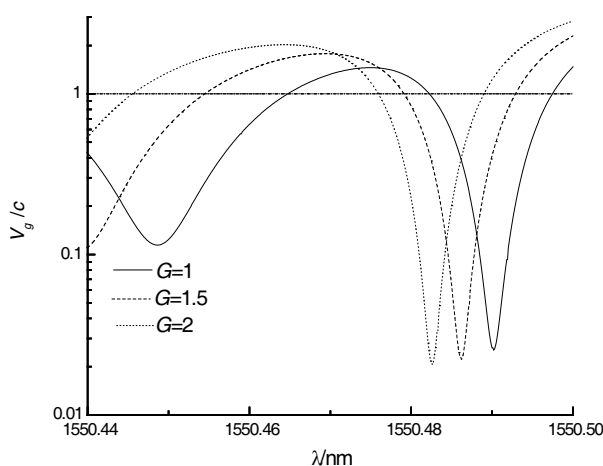


Figure 2: Group velocity spectra for PCF apodized gratings when G is 1, 1.5 respectively.

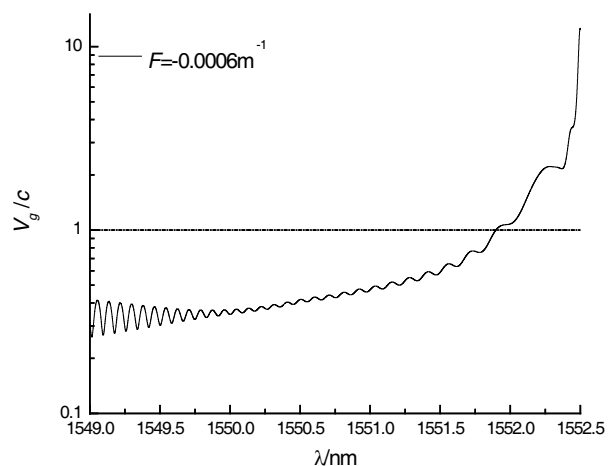


Figure 3: Group velocity spectra for PCF chirped gratings for $F = -0.0006 \text{ m}^{-1}$.

3.2. Influences of Linear Chirp on PCFBG Slow Light

To demonstrate the effects of linear chirp on slow light, Fig. 3 shows the group velocity spectra for PCFBGs similar to that described in Fig. 1, only here PCFBGs have linear chirp coefficients F as described by Eq. (2) and have not apodization coefficient G . In Fig. 3, the linear chirp coefficient is

chosen as $F = -0.0006 \text{ m}^{-1}$. Compared with Fig. 1, the minimum value of group velocity is much bigger, but the group velocity increases linearly with the increase of wavelength. And there is a band that has good linear characteristics.

4. CONCLUSION

For PCFBG, parameters of PCF, apodization and chirp have different influences on its characteristics of slow light. Appropriate gaussian apodization can not only decrease the minimum value of group velocity but also can adjust the full width at half height of the minimum group velocity peak; although chirp can not make the minimum value of group velocity smaller, it generates a good linear area in the group velocity spectra. On this basis, the influences of different apodization functions and nonlinear chirp on slow light for PCFBGs can be discussed under this method.

ACKNOWLEDGMENT

This work was supported in part by the National Natural Science Foundation of China (Nos. 61367007, 61167005), in part by the Natural Science Fund of Gansu Province of China (Nos. 1112RJZA017, 1112RJZA018) and in part by the Research Fund for the Doctoral Program of Lanzhou University of Technology.

REFERENCES

1. Boyd, R. W., "Slow and fast light: Fundamentals and applications," *Journal of Modern Optics*, Vol. 56, Nos. 18–19, 1908–1915, 2009.
2. Khurgin, J. B., "Slow light in various media: A tutorial," *Advances in Optics and Photonics*, Vol. 2, No. 3, 287–318, 2010.
3. Boyd, R. W., "Material slow light and structural slow light: Similarities and differences for nonlinear optics [Invited]," *JOSA B*, Vol. 28, No. 12, A38–A44, 2012.
4. Qu, L., Y. Meng, Z. H. Zhuo, et al., "Study on delay and dispersion characteristics of the fiber Bragg grating Fabry-perot cavity," *Acta Optica Sinica*, Vol. 33, No. 8, 0806001, 2013.
5. Mok, J. T., C. Martijn de Sterke, I. C. M. Littler, et al., "Dispersionless slow light using gap solitons," *Nature Physics*, Vol. 2, No. 11, 775–780, 2006.
6. Janner, D., G. Gakzerano, G. Della Valle, et al., "Slow light in periodic superstructure Bragg gratings," *Physical Review E*, Vol. 72, No. 5, 056605, 2005.
7. Wen, H., M. Terrel, S. H. Fan, et al., "Sensing with slow light in fiber Bragg gratings," *Sensors Journal*, Vol. 12, No. 1, 156–163, 2012.
8. Zhang, Y. N., "Design and optimization of low-loss low-nonlinear high negative dispersion photonic crystal fiber," *Acta Physica Sinica*, Vol. 61, No. 8, 084213, 2012.
9. Ademgil, H. and S. Haxha, "Endlessly single mode photonic crystal fiber with improved effective mode area," *Optics Communications*, Vol. 285, No. 6, 514–518, 2012.
10. Huang, C. L. and Y. L. Huang, "Research on resonance properties of photonic crystal fiber Bragg grating," *Laser & Optoelectronics Progress*, Vol. 49, 040601, 2012.
11. Liu, R., R. H. Qu, H. W. Cai, et al., "Analysis of the transmission spectral characteristics of fiber Bragg grating in photonic crystal fibers," *Acta Optica Sinica*, Vol. 26, No. 7, 1007–1012, 2006.
12. Bi, W. H., J. P. Li, and Y. F. Qi, "Reflection spectra characteristics of the grapefruit-type photonic crystal fiber chirped grating," *Acta Optica Sinica*, Vol. 32, No. 6, 0606001, 2012.
13. Park, K. N. and S. L. Kyung, "Improved effective-index method for analysis of photonic crystal fibers," *Optics Letters*, Vol. 30, No. 9, 958–960, 2005.
14. Song, M. Q., S. L. Hou, B. X. Zhang, et al., "Investigation on slow light of photonic crystal fiber Bragg gratings," *Infrared and Laser Engineering*, Vol. 42, No. 6, 1547–1552, 2013.
15. Kishor, K., R. K. Sinha, and D. V. Anshu, "Experimental verification of improved effective index method for endlessly single mode photonic crystal fiber," *Optics and Lasers in Engineering*, Vol. 50, No. 2, 182–186, 2012.
16. Erdogan, T., "Fiber grating spectra," *Journal of Lightwave Technology*, Vol. 15, No. 8, 1277–1294, 1997.
17. Li, Y. Q. and M. Cui, *Optical Waveguide Theory and Technology*, Posts & Telecom Press, Beijing, 2002.

Research on the Controllable Frequency Octupling Technology for Generating Optical Millimeter-wave by External Modulator

Jianming Shang, Yanjun Liu, Daobin Wang, Weiqing Ge, Jingli Lei,
Xiaoxiao Li, and Shanglin Hou

School of Science, Lanzhou University of Technology, Lanzhou, Gansu 730050, China

Abstract— A novel scheme is proposed for frequency octupling mm-wave generation based on an integrated triple-parallel MZM without filter. Two kinds of redundant sidebands are well eliminated by adopting 90 degrees of the electric phase-difference about two sub Mach-Zehnder modulators (sub-MZMs), driven by radio frequency (RF) signal. Then bias of the third sub-MZM is tailored to get best signal. The results indicate that the radio frequency spurious suppression ratio (RFSSR) is as high as 38.3315 dB under the condition of conventional extinction ratio (30 dB). Moreover, optical sideband suppression ratio (OSSR) can reach as high as 61.22878 dB at ideal extinction ratio (100 dB). Compared with previous schemes, it not only optimizes the method but get high RFSSR in the conventional condition.

1. INTRODUCTION

With rapid development in information construction all over the world, mm-wave radio-over-fiber (RoF) has been the general trend in the development of wireless communication, owing to its portability, wireless, datamation and broadband [1]. The key technology about optical mm-wave generation is to simplify the base station and reduce system cost [2]. It is mm-wave communication [3–8] that is also one of the academic focuses, which has important application in the future communication, military and other fields. Schemes for generating mm-wave [9–16], based on the nonlinear of Mach-Zehnder modulator (MZM), have a very wide range of applications and have been extensively studied. Due to this, several mm-wave solutions have been put forward.

Schemes mainly can be divided into two types according to whether using optical or electrical filter [13–16], while these without filter [13–15] will become the dominant. However, the filter is necessary to remove the undesired sidebands which are not well suppressed. Therefore, the high quality generation of mm-wave signal without filter is of great interest for the frequency octupling scheme. Recently, it still has the problem of low redundant sideband suppression efficiency [13], complex system [14, 15], high cost [14] and so on. In [13], optical sideband suppression ratio (OSSR) decreased seriously under the condition of conventional extinction ratio (ER), while it leads to low radio frequency spurious suppression ratio (RFSSR) without filter.

In this letter, a novel scheme is proposed for generating frequency octupling mm-wave without any filter, which can be used in mm-wave RoF system. Two sub Mach-Zehnder modulators (sub-MZMs) is driven by radio frequency (RF) signal and the third sub-MZM is driven by bias voltage. It can be integrated into a device and has great application foreground.

2. PRINCIPLE

The schematic diagram of the proposed scheme for frequency octupling is shown in Figure 1. The light-wave emitted from a continuous wave (CW) laser is modulated by an integrated triple-parallel MZM. The output of integrated MZM is amplified by erbium-doped fiber amplifier (EDFA). Then the optical signal is converted into electric signal by wide-band photo-detector (PD).

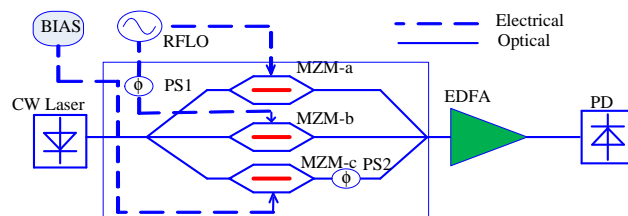


Figure 1: The scheme for the frequency octupling mm-wave signal.

The integrated MZM is a structure which consists of triple-parallel sub-MZMs and two phase shifts. MZM-a and MZM-b are driven by the RF signal to operated at the maximum transmission

point (MATP), while the MZM-c is driven by bias voltage with no RF signal applied. PS1 and PS2 are electrical and optical phase shift, respectively.

Assume the optical field of input to the integrated MZM is $E_{in}(t) = E_0 e^{j\omega_0 t}$. Where E_0 and ω_0 are the amplitude and angular frequency of the optical carrier, respectively.

Since MZM-a and MZM-b are biased at MATP the output optical field can be expressed respectively as

$$E_{out-a}(t) = \frac{1}{3} E_0 e^{j\omega_0 t} \cos [m \sin(\omega_{RF} t + \varphi_0)], \quad E_{out-b}(t) = \frac{1}{3} E_0 e^{j\omega_0 t} \cos [m \sin(\omega_{RF} t + \varphi_0 + \Delta\varphi)] \quad (1)$$

where m is the modulation-depth, which is defined as $\pi V_{RF}/2V_{\pi,1}$, while $V_{\pi,1}$ is the half-wave voltage of MZM-a as well as MZM-b. V_{RF} and ω_{RF} are the amplitude and angular frequency of the electrical driving signal, respectively. φ_0 and $\varphi_0 + \Delta\varphi$ are the phase of MZM-a and MZM-b respectively.

With no RF driving signal added onto MZM-c, the optical field at output of the MZM-c can be expressed as

$$E_{out-c}(t) = \frac{1}{3} E_0 e^{j\omega_0 t} \cos(\varphi_c) \quad (2)$$

where $\varphi_c = \frac{\pi V_{bias-c}}{2V_{\pi,2}}$, while V_{bias-c} and $V_{\pi,2}$ are the bias and half-wave voltage of the MZM-c, respectively.

On the arm of MZM-c, the angle of PS2 is φ . The output optical field of the integrated MZM can be expressed as

$$E_{out}(t) = \frac{1}{3} E_0 e^{j\omega_0 t} \left\{ \cos(\varphi_c) e^{j\varphi} + \sum_{-\infty}^{+\infty} J_{2n}(m) e^{j(2n)\omega_{RF} t} \cdot e^{j(2n)\varphi_0} \times [1 + e^{j(2n)\Delta\varphi}] \right\} \quad (3)$$

where $J_{2n}(m)$ is the first kind Bessel function of $2n$ order.

In order to implement the high quality frequency octupling with high RFSSR, the two fourth-order optical sidebands should be kept and maximized, and other optical sidebands should be suppressed. Therefore, it is crucial to eliminate the second and sixth-order optical sidebands for high quality frequency octupling mm-wave signal generation. It can be found from Eq. (3) that the undesired optical sidebands vanish when the following conditions are satisfied

$$1 + e^{2j\Delta\varphi} = 0, \quad 1 + e^{6j\Delta\varphi} = 0 \quad (4)$$

From Eq. (4), we can obtain $\Delta\varphi = \pi/2$. Take $m = 3.3379$ and $\varphi = 0$. Because $J_4(3.3379)/J_8(3.3379) \approx 165.0281$, the optical sidebands higher than eighth-order can be ignored. By adjusting V_{bias-c} to remove $J_0(m)$, the optical field can be written as

$$E_{out}(t) \approx \frac{2}{3} E_0 e^{j\omega_0 t} \{ J_4(m) e^{4j\omega_{RF} t} \cdot e^{4j\varphi_0} \times [1 + e^{4j\Delta\varphi}] \} \quad (5)$$

Therefore, the undesired optical sidebands are well suppressed. When following detection using a PD with responsivity of R , the desired frequency octupling signal is produced with its power being approximately expressed as

$$P_{8th} \propto R^2 \cdot E_0^4 \cdot J_4(m)^4 \quad (6)$$

3. SIMULATION RESULTS AND DISCUSSION

3.1. The Frequency Octupling mm-wave Signal Generation

The simulation system is set up as shown in Figure 1. The light wave with central wavelength of 1550 nm is emitted from a CW laser and modulated by the integrated MZM. MZM-a and MZM-b are driven by the RF of 10 GHz. The half-wave voltage of MZM-a and MZM-b is assumed as $V_{\pi,1} = 4$ V. After the integrated MZM, an EDFA with a noise figure of 4 dB is located. The responsivity of the PD is $R = 0.6$ A/W.

Figure 2 shows the output optical spectrum from the integrated MZM and the generated RF spectrum before transmission over fiber at ideal ER (100 dB). It can be seen from Figure 2(a) that the undesired optical sidebands are well suppressed and the OSSR is 43.9014 dB. For the

generated RF spectrum, the power of the desired 80 GHz mm-wave signal is obvious higher than other undesired RF component and the RFSSR is 38.3292 dB, as shown in Figure 2(b).

Figure 3 shows the output optical spectrum from the integrated MZM and the generated RF spectrum before transmission over fiber under the condition of conventional ER (30 dB). Compared with the ideal case, while the OSSR is decreased to 23.8873 dB, the RFSSR is still as high as 38.3315 dB.

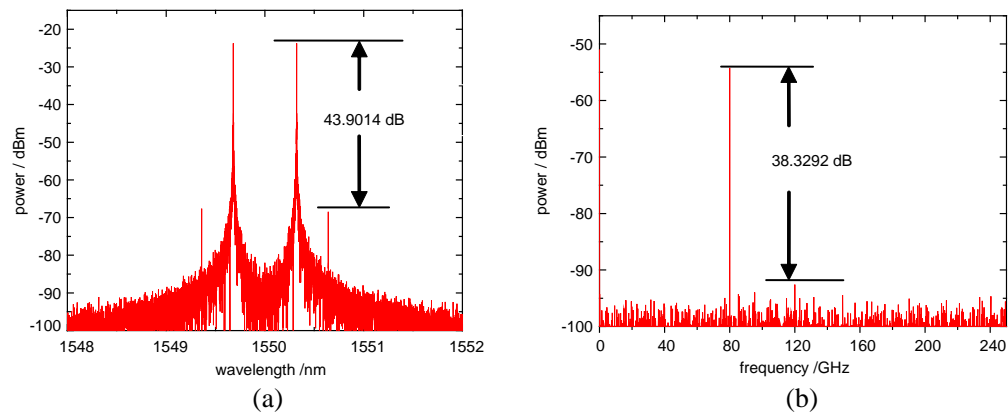


Figure 2: The simulated 80 GHz mm-wave signal generation for ER = 100 dB. (a) The output optical spectrum of the integrated MZM; (b) the generated RF spectrum.

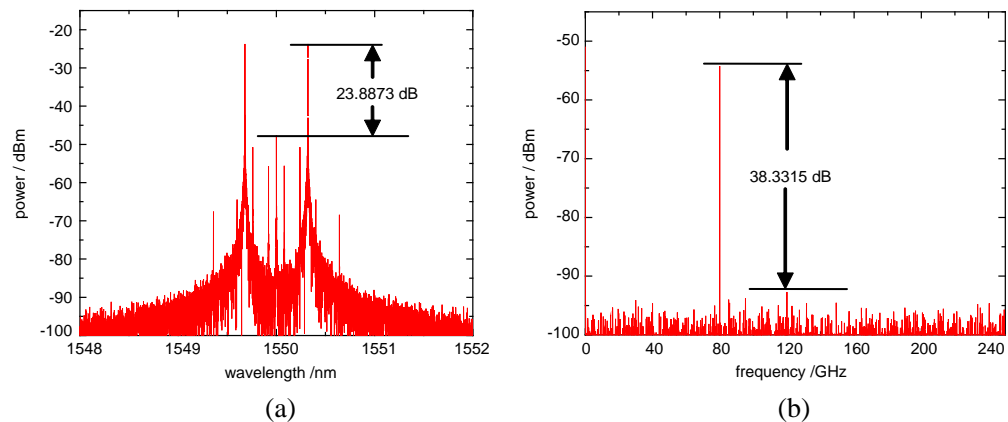


Figure 3: The simulated 80 GHz mm-wave signal generation for ER = 30 dB. (a) The output optical spectrum of the integrated MZM; and (b) the generated RF spectrum.

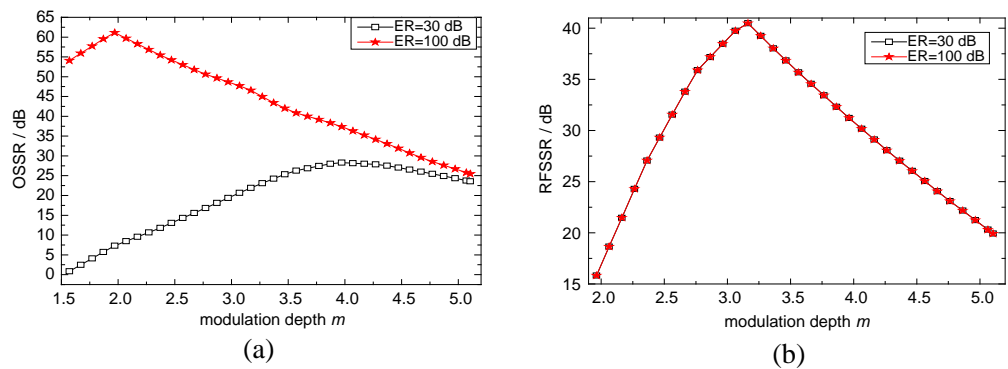


Figure 4: (a) OSSR against different modulation depths m ; (b) RFSSR against different modulation depths m .

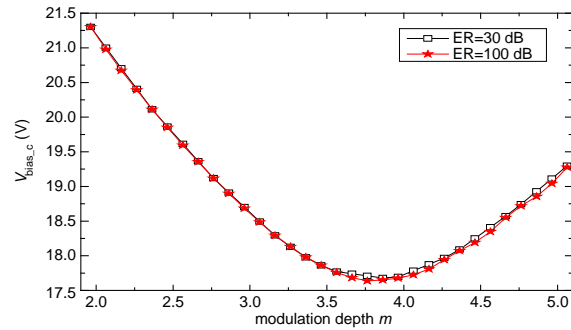


Figure 5: The best $V_{\text{bias},c}$ of MZM-c versus different modulation depths m .

3.2. Analysis of the Output Signal

The generated 80 GHz mm-wave signal quality is measured by OSSR and RFSSR. Figures 4(a) and (b) show OSSR and RFSSR against different modulation depths m , respectively. The dynamic optimum value is introduced to the bias voltage of MZM-c. The OSSR can reach as high as 61.22878 dB at ideal extinction ratio, while it is better than that under conventional case. However, RFSSR basically coincide in two cases. Therefore, RF spectrum is little affected by variations of ER.

Best bias voltage of MZM-c versus difference modulation depths m , as shown in Figure 5. The curve is a parabolic with upward opening.

4. CONCLUSIONS

A novel frequency octupling scheme is proposed for the optical mm-wave signal generation. The theoretical analysis and stimulation verification are both presented. Simulation results show the high quality frequency octupling mm-wave signal can be generated without any optical or electrical filters. Compared with the previous frequency octupling schemes, the proposed scheme can improve RFSSR to 38.3315 dB without filter and simplify the configuration. Generally speaking, the better performance is demonstrated. In order to obtain frequency octupling mm-wave signal, adjustment of RF and bias voltage is particularly critical. At the same time, it shows that the generation is controllable. In the practical application, the feedback can be taken to adjust RF and bias voltage dynamically. It is significant for practicability of high frequency mm-wave communication.

ACKNOWLEDGMENT

This work was supported in part by the National Natural Science Foundation of China (Nos. 613670-07, 61167005), in part by the Natural Science Fund of Gansu Province of China (Nos. 1112RJZA017, 1112RJZA018) and in part by the Research Fund for the Doctoral Program of Lanzhou University of Technology.

REFERENCES

1. Wei, Z. H., R. Wang, and T. Pu, "A wideband tunable phase shifter based on orthogonal optical single-sideband," *Chinese Optics Letters*, Vol. 11, No. S2, S20601, 2013.
2. Fang, Z. J., Q. Ye, and F. Liu, "Progress of millimeter wave subcarrier optical fiber communication technologies," *Chinese J. Lasers*, Vol. 33, No. 3, 481–488, 2006.
3. Ma, J. X., Y. Zhan, and M. Zhou, "Full-Duplex radio over fiber with a centralized optical source for a 60 GHz millimeter-wave system with a 10 Gb/s 16-QAM downstream signal based on frequency quadrupling," *J. Opt. Commun. Netw.*, Vol. 4, No. 7, 557–564, 2012.
4. Liu, L. M., Z. Dong, and Y. Z. Pi, "Radio-over-fiber system for frequency-quadrupled millimeter-wave generation by external modulator," *Chinese J. Lasers*, Vol. 36, No. 1, 148–153, 2009.
5. Zhen, Z. W., Y. Li, and J. G. Xiao, "A radio-over-fiber system with a novel scheme for optical local oscillator and mm-wave distribution," *Inform. Technol. J.*, Vol. 12, No. 1, 229–233, 2013.
6. Gong, Z. S., K. Xu, and X. J. Meng, "Effect of optical losses on the transmission performance of a radio-over-fiber distributed antenna system," *Chinese Optics Letters*, Vol. 11, No. 2, 020603, 2013.

7. Wang, Y. J., Y. F. Shao, and N. Chi, "Application of peak-to-average ratio reduction algorithm using precoding technique in 60 GHz orthogonal frequency-division multiplexing radio-over-fiber system," *Acta Optica Sinica*, Vol. 33, No. 7, 0706018, 2013.
8. Shen, D., Z. F. Hu, and J. Q. Wu, "Design and realization of a radio-over-fiber system based on self-homodyned 60 GHz receiver," *Acta Optica Sinica*, Vol. 33, No. 5, 0506005, 2013.
9. Shi, P. M., S. Yu, and Z. K. Li, "A novel frequency sextupling scheme for optical mm-wave generation utilizing an integrated dual-parallel Mach-Zehnder modulator," *Opt. Commun.*, Vol. 283, No. 19, 3667–3672, 2010.
10. Shi, P. M., S. Yu, and Z. K. Li, "A frequency sextupling scheme for high-quality optical millimeter-wave signal generation without optical filter," *Opt. Fiber Technol.*, Vol. 17, No. 3, 236–241, 2011.
11. Masella, B. G. and X. P. Zhang, "Linearized optical single-sideband mach-zehnder modulator for radio-over-fiber systems," *IEEE Photon. Technol. Lett.*, Vol. 19, No. 24, 2024–2026, 2007.
12. Ma, J. X., L. Chen, and X. J. Xin, "Transmission of a 40 GHz optical millimeter wave generated by quadrupling a 10 GHz local oscillator via a Mach-Zehnder modulator," *J. Opt. A: Pure Appl. Opt.*, Vol. 11, No. 6, 065406, 2009.
13. Ma, J. X., X. J. Xin, and J. Yu, "Optical millimeter wave generated by octupling the frequency of the local oscillator," *J. Opt. Netw.*, Vol. 7, No. 12, 837–845, 2008.
14. Lin, C. T., P. T. Shih, and W. J. Jiang, "A continuously tunable and filterless optical millimeter-wave generation via frequency octupling," *Opt. Exp.*, Vol. 17, No. 22, 19749–19756, 2009.
15. Shang, L., A. J. Wen, and B. Li, "A filterless optical millimeter-wave generation based on frequency octupling," *Optik*, Vol. 36, No. 13, 1183–1186, 2012.
16. Li, W. Z. and J. P. Yao, "Microwave generation based on optical domain microwave frequency octupling," *IEEE Photon. Technol. Lett.*, Vol. 22, No. 1, 24–26, 2010.

Temperature Dependence of Liquid Filled Photonic Crystal Fibers

Jingli Lei, Shanglin Hou, Yanjun Liu, and Xiaoxiao Li

School of Science, Lanzhou University of Technology, Lanzhou, Gansu 730050, China

Abstract— The effects of temperature on dispersion, effective area and nonlinearity of an index-guiding hexagon photonic crystal fiber filled by ethanol are described by using the vectorial beam propagation method, and a nearly zero ultra flattened dispersion fiber is optimized design with the dispersion coefficients of 0 ± 0.5 ps/(nm · km) at the wavelength of 1.46 μm to 1.65 μm . The results indicate that increasing temperature could lead to increase dispersion and nonlinearity, but decrease the dispersion slope so as to flatten the dispersion. The result provides theoretical base for designing continuously tailoring dispersion optical communication components or optical sensing devices.

1. INTRODUCTION

Photonic crystal fiber (PCF) [1], also called holey fiber (HF), has air holes arranging according to a certain rule in the cross section, and constant along the length of the fiber. Compared with the conventional fiber, photonic crystal fiber has many unique characteristics due to flexible design, for example, endless single mode transmission [2], Sensitive structure capable of dispersion characteristics [3, 4], Nonlinear controllability [5] etc..

Dispersion is one of the key factors affecting optical fiber transmission and transmission distance, near zero dispersion fiber and broadband ultra flattened dispersion characteristic have potential applications. The structural parameters and optimization of optical fiber can be tailored to achieve nearly zero ultra flattened dispersion, such as the ultra flattened dispersion of 0 ± 0.8 ps/(nm · km) at the wavelength of 1.515 μm to 1.622 μm designed by Chen Ming [6] et al., and 0 ± 0.65 ps/(nm · km) at the wavelength of 1.36 μm to 1.62 μm designed by Feroza Begum [7] et al.. In addition, liquid such as water, ethanol, polymer etc. is filled in the air holes to tailor its characteristics. Krishna Mohan Gundu [8] ever reported the realization of the broadband nearly zero flattened dispersion fiber by filling liquid in PCF, low dispersion is obtained within 0 ± 0.5 ps/(nm · km) in the 400 nm bandwidth, but for nonlinear and temperature dependence are not in-depth analysis.

In this letter, we simulate the transmission characteristics of liquid filled photonic crystal fiber by using the vectorial beam propagation method (VBPM) [9], and analyze the influence of temperature on the dispersion, effective area and nonlinearity. A nearly zero ultra flattened dispersion fiber is optimized design, which dispersion coefficients ranges from 0 ± 0.5 ps/(nm · km) at the wavelength of 1.46 μm to 1.65 μm . The result provides theoretical base for designing continuously tailoring dispersion optical communication components or optical sensing devices.

2. THEORY

Cross index profile of an index-guiding hexagon photonic crystal is shown in Fig. 1, d_1 to d_4 present air hole diameters of one to four layers from the core outward, Λ is hole pitch. Ethanol is filled into the air holes of all, because of the refractive index of ethanol is smaller than the quartz's, so optical fiber is based on total internal reflection. The total dispersion of photonic crystal fiber can be described as follow [10]

$$D(\lambda) = -\frac{\lambda}{c} \frac{d^2 n_{eff}}{d\lambda^2} + D_M(\lambda) \quad (1)$$

where λ is the vacuum wavelength, c is the speed of light in vacuum, n_{eff} is the effective refractive index, and $D_M(\lambda)$ as the material dispersion. The nonlinear coefficient of photonic crystal fiber is described as

$$\gamma = \frac{n_2 \omega_0}{c A_{eff}} = \frac{2\pi n_2}{\lambda A_{eff}} \quad (2)$$

here $n_2 = 2.76 \times 10^{-20}$ m²/W for nonlinear refraction rate of quartz, and ω_0 is the angular frequency. The fiber effective area of fundamental mode is defined as

$$A_{eff} = \left(\iint_s |E_t|^2 dx dy \right)^2 / \left(\iint_s |E_t|^4 dx dy \right) \quad (3)$$

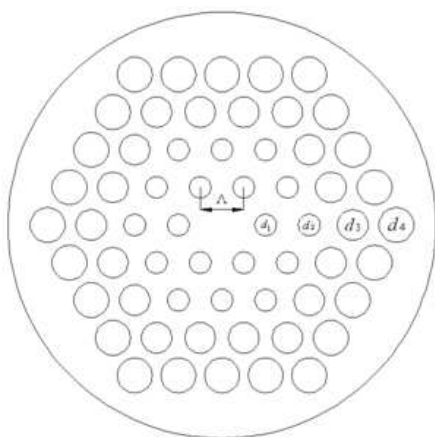


Figure 1: Cross profile of the ultra-flattened dispersion photonic crystal fiber.

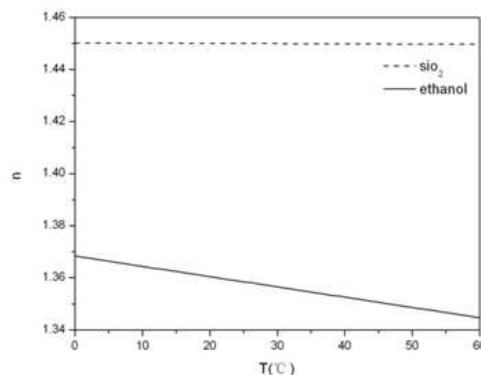


Figure 2: The refractive index of SiO_2 and ethanol at different temperatures.

where E_t is the horizontal electric field vector, s is the cross-section of the photonic crystal fiber. Material temperature coefficient of refractive index is defined as [11]:

$$\alpha = (n_0 - n)/(T - T_0) \quad (4)$$

where T is the operating temperature, T_0 is 20°C , n and n_0 are the refractive index at temperature of T and T_0 .

Ethanol is filled in the air holes, it is high temperature coefficient relevant with refractive index, the temperature coefficient of ethanol is $\alpha_{\text{ethanol}} = 3.94 \times 10^{-4}/\text{K}$, and the temperature coefficient of quartz is $\alpha_{\text{SiO}_2} = 8.6 \times 10^{-6}/\text{K}$, the temperature coefficient of quartz is two orders of magnitude lower than that of ethanol.

3. CALCULATED RESULTS AND ANALYSIS

Figure 2 is the refractive index curve of quartz and ethanol at different temperatures, compared with ethanol, the refractive index change of quartz can be ignored. When the temperature is 20°C , the parameters $d_1 = 0.53\Lambda$, $d_2 = 0.52\Lambda$, $d_3 = 0.7\Lambda$, $d_4 = 0.8\Lambda$, $\Lambda = 2.75 \mu\text{m}$, photonic crystal fiber dispersion curve is shown in Fig. 3, at the wavelength range of $1.46 \mu\text{m}$ to $1.65 \mu\text{m}$ the absolute value of dispersion is less than $0.5 \text{ ps}/(\text{nm} \cdot \text{km})$. Choosing this kind of fiber parameters can realize broadband near zero low dispersion transmission. On the basis of this, filling pore air with ethanol, the temperature effect on the dispersion is shown in Fig. 4, when temperature is 0°C , 20°C , 40°C , and 60°C , there has been a significant change in dispersion. In the short wavelength range, the higher the temperature, the greater the value of dispersion, and the smaller dispersion slope. At the $1.55 \mu\text{m}$ wavelength, the dispersion of 0°C is $1.9036 \text{ ps}/(\text{nm} \cdot \text{km})$ lower than 20°C , the dispersion

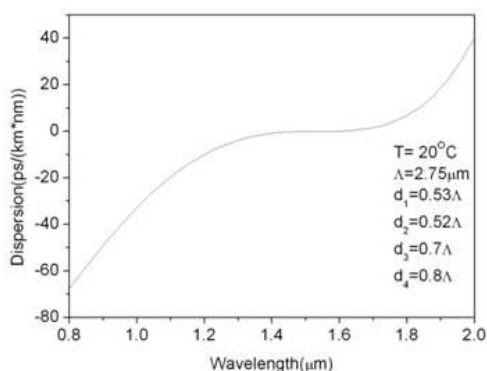


Figure 3: Dispersion curves of designed PCF.

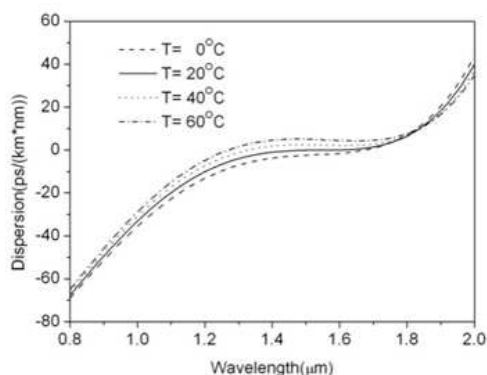


Figure 4: Dispersion curves at different temperatures.

of 20°C is 2.2895 ps/(nm · km) lower than 40°C, and the dispersion of 40°C is 2.4943 ps/(nm · km) lower than 60°C.

Figures 5 and 6 are the curves of the fiber mode field area and the effective nonlinear coefficient varies with temperature. The effective area increases with long wavelength, because the long wave optical field has better penetration ability into the pack layer hole than the short wave; at short wavelengths, the light energy is concentrated in the core, so the effective area is smaller. With the increase of temperature, ethanol refractive index is smaller, the effective refractive index of cladding reduces, so as to enhance the ability of local light, and thus area reduce effectively. At the 1.55 μm wavelength, the effective area of 0°C is 1.6868 μm^2 larger than 20°C, the effective area of 20°C is 1.1734 μm^2 larger than 40°C, and the effective area of 40°C is 0.8007 μm^2 larger than 60°C. With the increase of temperature and the temperature interval of the same, the difference of effective area is more and more small. This is because, with the increase of temperature, the refractive index of ethanol decreases, the cladding mode's effective refractive index decreases, the local capacity to light becomes strong, leading to the effective area is reduced, and the light field is more concentrated to the core and gradually away from the cladding layer, so the influence of liquid refractive index of the outer air hole on it is more and more small. In contrast, the nonlinear coefficient decreases with the increasing of wavelength, increases with the increasing of temperature, at the 1.55 μm wavelength, the nonlinear coefficient of -20°C is 0.2840 $\text{W}^{-1} \text{km}^{-1}$ smaller than 0°C, the nonlinear coefficient of 0°C is 0.2339 $\text{W}^{-1} \text{km}^{-1}$ smaller than 20°C, the nonlinear coefficient of 20°C is 0.1899 $\text{W}^{-1} \text{km}^{-1}$ smaller than 40°C, the nonlinear coefficient of 40°C is 0.1453 $\text{W}^{-1} \text{km}^{-1}$ smaller than 60°C.

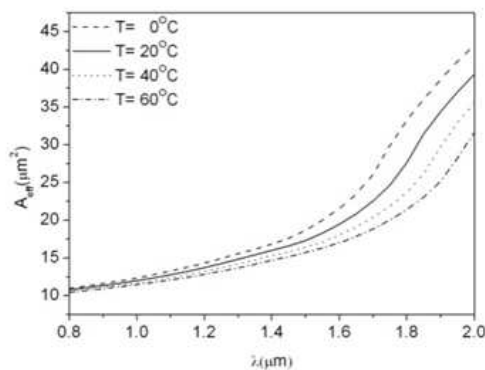


Figure 5: Effective area A_{eff} curves at different temperatures.

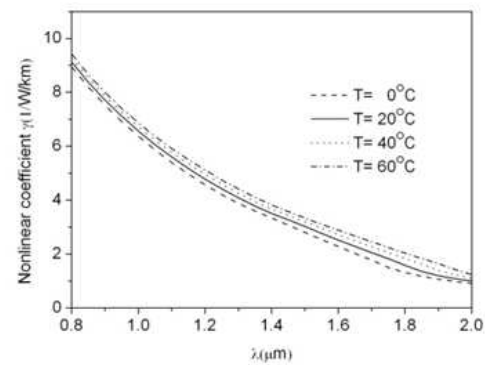


Figure 6: The nonlinearity curves at different temperatures.

4. CONCLUSIONS

The vectorial beam propagation method (VBPM) is used to simulate and analysis the characteristics of photonic crystal fiber. A nearly zero ultra flattened dispersion fiber with an index-guiding hexagon is optimized design, in the wavelength range of 1.46 μm to 1.65 μm , the dispersion coefficients ranges from 0 ± 0.5 ps/(nm · km), we fill the air hole with ethanol and study the temperature dependence of PCF. The results indicate that increasing temperature could lead to increase dispersion and nonlinearity, but decrease the dispersion slope so as to flatten the dispersion. These provide a theoretical reference for the use of optical fiber fabrication of continuous adjustable devices in optical communication and optical sensing transmission performance.

ACKNOWLEDGMENT

This work is financially supported by the Natural Science Foundation of China (Grant No. 61167005), the Natural Science Foundation of Gansu province of China (Grant No. 1112RJZA0-18).

REFERENCES

1. Knight, J. C., et al., "All-silica-single-mode optical fiberwith photonic crystal cladding," *Opt. Lett.*, Vol. 21, No. 19, 1547–1549, 1996.
2. Birks, T. A., J. C. Knight, and P. S. J. Russell, "Endlessly single-mode photonic crystal fiber," *Opt. Lett.*, Vol. 22, No. 13, 961–963, 1997.

3. Knight, J. C., J. Arriaga, T. A. Birks, et al., “Anomalous dispersion in photonic crystal fiber,” *Photonics Technology Letters*, Vol. 12, No. 7, 807–809, 2000.
4. Reeves, W., J. Knight, P. Russell, et al., “Demonstration of ultra-flattened dispersion in photonic crystal fibers,” *Opt. Express*, Vol. 10, No. 14, 609–613, 2002.
5. Hilligsøe, K. M., T. Andersen, H. Paulsen, et al., “Supercontinuum generation in a photonic crystal fiber with two zero dispersion wavelengths,” *Opt. Express*, Vol. 12, No. 6, 1045–1054, 2004.
6. Chen, M. and S. Xie, “New nonlinear and dispersion flattened photonic crystal fiber with low confinement loss,” *Optics Communications*, Vol. 281, 2073–2076, 2008.
7. Begum, F. and Y. Namihira, “Design and analysis of novel highly nonlinear photonic crystal fibers with ultra-flattened chromatic dispersion,” *Optics Communications*, Vol. 282, 1416–1421, 2009.
8. Gundu, K. M., M. Kolesik, J. V. Moloney, et al., “Ultra-flattened-dispersion selectively liquid-filled photonic crystal fibers,” *Opt. Express*, Vol. 14, No. 15, 6870–6878, 2006.
9. Saitoh, K. and M. Koshiba, “Full-vectorial imaginary-distance beam propagation method based on a finite element scheme: Application to photonic crystal fibers,” *Quant. Electron.*, Vol. 38, No. 7, 927–933, 2002.
10. Shen, L. P., W. P. Huang, G. X. Chen, et al., “Design and optimization of photonic crystal fibers for broad-band dispersion compensation,” *Photon. Tech. Lett.*, Vol. 15, No. 4, 540–542, 2003.
11. Barnes, N. P. and M. S. Piltch, “Temperature-dependent Sellmeier coefficient and coherent length for cadmium telluride,” *Opt. Soc. A.*, Vol. 67, No. 5, 628–629, 1977.

Dependence of Grating Length of Fiber Gragg Gratings on Slow Light

Chunlian Hu¹, Yanjun Liu², Jingli Lei², and Shanglin Hou²

¹Alloy Powder Co., Ltd, Lanzhou University of Science & Technology, Lanzhou 730050, China

²School of Science, Lanzhou University of Technology, Lanzhou 730050, China

Abstract— The influence of grating length of uniform fiber Bragg grating on delay is discussed by using numerical simulation method based on the coupled mode theory and slow light delay characteristics is studied by parameters optimization. The calculated result shows that grating length has a remarkable impact on the delay, when $L < 42.5008$ cm, the delay_{\max} increases with L increasing, when L tends to 42.5008 cm have a maximum delay_{\max} , the value increased to 3.797 ps, but when $L > 42.5008$ cm, delay_{\max} decreases with L increasing. This provides basis references for designing slow light components based on fiber Bragg gratings.

1. INTRODUCTION

Fiber Bragg grating has developed dramatically and performed an important role in fiber communications and optical fiber sensing in recent 30 years [1, 2]. Recently, the introduction of slow light with a wide range of novel properties results in unique spectral characteristics of fiber Bragg gratings [3], especially slow light delay of fiber Bragg grating is studied emphatically. K. B. Rochford and S. D. Dyer [4] reported reconstruction of minimum-phase group delay from fiber Bragg grating transmittance or reflectance measurements. The results indicate that phase reconstruction is compared to exact solutions using the reflectance from a uniform grating. An intermediate windowing process improves the recovery accuracy. J. T. Mok, ect. [5] observed 0.68 ns pulses delayed by 4.7 pulse widths in a 30 cm silica FBG without pulse broadening. Improved slow-light delay performance of a broadband SBS system using fiber Bragg grating was reported [6]. Tunable delay slow-light in an active fiber Bragg grating was also studied [7]. These studies provide a very simple approach to control the light group delay. However, this approach requires very high power signal, which limits its practical implications.

In this work, The influence of grating length of uniform fiber Bragg grating on delay is discussed by using numerical simulation method based on the coupled mode theory and slow light delay characteristics is studied by parameters optimization. The calculated result shows that grating length has a remarkable impact on the delay, when $L < 42.5008$ cm, the delay_{\max} increases with L increasing, when L tends to 42.5008 cm have a maximum delay_{\max} , the value increased to 3.797 ps, but when $L > 42.5008$ cm, delay_{\max} decreases with L increasing. This provides basis references for designing slow light components based on fiber Bragg gratings.

2. THEORY

Fiber Bragg gratings are produced by exposing an optical fiber to a spatially varying pattern of ultraviolet intensity. For sake of simplicity, we studied an unchirped uniform fiber Bragg grating whose refractive index can be described as follows [8]

$$\delta n_{eff}(z) = \overline{\delta n}_{eff} \left[1 + v \cos \left(\frac{2\pi}{\Lambda} z \right) \right] \quad (1)$$

where $\overline{\delta n}_{eff}$ is the “dc” index change spatially averaged over a grating period, v is the fringe visibility of the index change, Λ is the grating period and

$$\Lambda = \frac{L}{N} \quad (2)$$

where L is the grating length, N is the total number of the grating periods.

According to coupled mode theory, synchronous approximation and the boundary condition of the fiber Bragg grating [9–11]. The amplitude reflection coefficient can be expressed as

$$\rho = \frac{-\kappa \sinh \left(\sqrt{\kappa^2 - \hat{\sigma}^2} L \right)}{\hat{\sigma} \sinh \left(\sqrt{\kappa^2 - \sigma^2} L \right) + i \sqrt{\kappa^2 - \hat{\sigma}^2} \cosh \left(\sqrt{\kappa^2 - \hat{\sigma}^2} L \right)} \quad (3)$$

and the reflectivity

$$\gamma = |\rho^2| = \frac{\sinh^2\left(\sqrt{\kappa^2 - \hat{\sigma}^2}L\right)}{\cosh^2\left(\sqrt{\kappa^2 - \hat{\sigma}^2}L\right) - \hat{\sigma}^2/\kappa^2} \quad (4)$$

where $\kappa = \pi v \bar{\delta} n_{eff} / \lambda$ is the ‘‘ac’’ coupling coefficient, $\sigma = 2\pi \bar{\delta} n_{eff} / \lambda$ is the ‘‘dc’’ coupling coefficient, $\hat{\sigma}$ is a general ‘‘dc’’ self-coupling coefficient and $\hat{\sigma} = \delta + \sigma$. The detuning δ is defined as

$$\delta = \beta - \frac{\pi}{\Lambda} = 2\pi n_{eff} \left(\frac{1}{\lambda} - \frac{1}{\lambda_B} \right) \quad (5)$$

the Bragg wavelength λ_B is expressed as

$$\lambda_B \equiv 2n_{eff}\Lambda. \quad (6)$$

The delay of the reflected light induced by the fiber Bragg grating can be determined from Eq. (3). If we denote $\theta_\rho = \text{phase}(\rho)$, then at a local frequency ω_0 we may expand θ_ρ in a Taylor series about ω_0 . Since the first derivative $d\theta_\rho/d\omega$ is directly proportional to the frequency ω , this quantity can be identified as a time delay. Thus, the delay time τ_ρ for reflected light of a grating is expressed as [12]

$$\tau_\rho = \frac{d\theta}{d\omega} = -\frac{\lambda^2}{2\pi c} \frac{d\theta_\rho}{d\lambda} \quad (7)$$

3. CALCULATED RESULTS AND ANALYSIS

3.1. Influence of Grating Length on Delay

Setting $n_0 = 1.46$, $\Delta = 0.002$, $a = 5 \mu\text{m}$, $N = 20000$, $L = 42.5008 \text{ cm}$, $\bar{\delta} n_{eff} = 0.0001$ and $v = 1$ in Eq. (3), a delay-wavelength curve of a mode can be obtained, in order to studied the slow light delay of the uniform fiber Bragg grating, though not shown here. Let us first discuss the effects of grating length on the delay. When the grating length L is changed, the others were determined, the delay as functions of the wavelength λ can be obtained, so, the maximum value of delays are obtained from the various delays as functions of the wavelength λ . The influence of L on delay_{\max} is shown in Fig. 1. It can be seen that the delay_{\max} increases with L increasing, when L tends to 42.5008 cm have a maximum delay_{\max} , the value of delay_{\max} increased to 3.797 ps , but when $L > 42.5008 \text{ cm}$, delay_{\max} decreases with L increasing.

In order to further study influence of grating length on delay characteristics in uniform fiber Bragg grating, we calculated the delay_{\max} as a function of wavelength with $L = 42.5008 \text{ cm}$, shown in Fig. 2. It can be seen that the delay_{\max} curve becomes rectangle wave and the maximum value of delay is preceded right, which is 3.797 ps . Moreover, the bandwidth is 0.1 nm because of weak grating is to decide from the length.

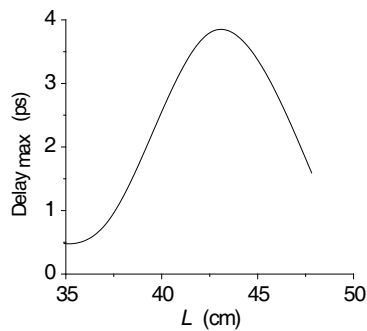


Figure 1: Influence of L on delay_{\max} .

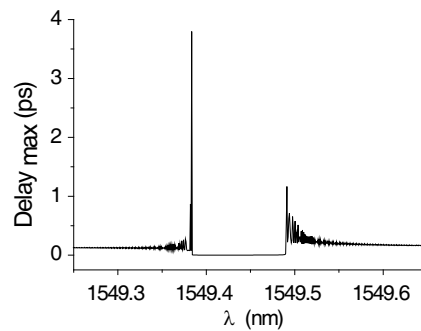


Figure 2: delay_{\max} as a function of wavelength with $L = 42.5008 \text{ cm}$.

4. CONCLUSIONS

The influence of grating length of uniform fiber Bragg grating on delay is discussed by using numerical simulation method based on the coupled mode theory and slow light delay characteristics

is studied by parameters optimization. The calculated result shows that grating length has a remarkable impact on the delay, when $L < 42.5008$ cm, the delay_{max} increases with L increasing, when L tends to 42.5008 cm have a maximum delay_{max}, the value increased to 3.797 ps, but when $L > 42.5008$ cm, delay_{max} decreases with L increasing. This provides basis references for designing slow light components based on fiber Bragg gratings.

ACKNOWLEDGMENT

This work was supported in part by the National Natural Science Foundation of China (Nos. 61367007, 61167005), in part by the Natural Science Fund of Gansu Province of China (Nos. 1112RJZA017, 1112RJZA018) and in part by the Research Fund for the Doctoral Program of Lanzhou University of Technology.

REFERENCES

- Hill, K. O. and G. Meltz, "Fiber Bragg grating technology fundamentals and overview," *J. Lightwave Technol.*, Vol. 15, No. 8, 1263–1264, 1997.
- Kersey, A. D., "A review of recent developments in fiber optic sensor technology," *Optic Fiber Technol.*, Vol. 2, No. 3, 219–317, 1996.
- Mok, J. T., M. Ibsen, C. Martijn de Sterke, and B. J. Eggleton, "Slow light generation using fiber Bragg grating," *OFC/NFOEC*, Vol. 10, 1109–1112, 2008.
- Rochford, K. B. and S. D. Dyer, "Reconstruction of minimum-phase group delay from fiber Bragg grating transmittance/reflectance measurements," *Electron. Lett.*, Vol. 35, No. 10, 838–839, 1999.
- Mok, J. T., M. Ibsen, C. M. de Sterke, and B. J. Eggleton, "Dispersionless slow light with 5-pulse-width delay in fiber Bragg grating," *Electronics Letters*, Vol. 43, No. 25, 1418–1419, 2007.
- Myungjun, L., P. Ravi, and N. A. Mark, "Improved slow-light delay performance of a broadband SBS system using fiber Bragg gratings," *Applied Optics*, Vol. 47, No. 34, 6404–6415, 2008.
- Qian, K., Z. Li, H. Li, X. Hu, J. Peng, L. Zhang, and Y. Xia, "Tunable delay slow-light in an active fiber Bragg grating," *Optics Express*, Vol. 17, No. 24, 22217–22219, 2009.
- Erdogan, T., "Fiber grating spectra," *J. Light Wave Technol.*, Vol. 15, No. 8, 1277–1294, 1997.
- Hou, S. L., C. Hu, X. M. Ren, Z. Xia, and Y. Q. Huang, "Influence of uniaxial crystal material cladding on reflectivity and dispersion of uniform fiber Bragg grating," *Optics Communications*, Vol. 271, No. 1, 109–115, 2007.
- Kogelnik, H. and C. V. Shank, "Coupled-wave theory of distributed feedback lasers," *J. Appl. Phys.*, Vol. 43, No. 5, 2327–2335, 1972.
- Kogelnik, H., "Theory of optical waveguides," *Guided-wave Optoelectronics*, T. Tamir, Ed., Springer-Verlag, New York, 1990.
- Ball, G. A., W. H. Glenn, and W. W. Morey, "Programmable fiber optical delay line," *IEEE Photon. Technol. Lett.*, Vol. 6, No. 6, 741–743, 1994.

A Low-cost CCD-based Imager for Mapping Venous Oxygenation

Jun Li and Xiao Zhang

Centre for Optical and Electromagnetic Research
South China Normal University, Guangzhou 510006, China

Abstract— A low-cost imaging system is developed for mapping skin venous oxygen saturation. The system consists of a black-and-white CCD camera and cheap LED light sources working at 660 nm and 800 nm wavelength. With the two wavelength sources alternately illuminating the skin, the CCD camera collects images carrying signals of diffuse reflectance before and after the venous occlusion induced by a low cuff pressure. Using the Monte Carlo method, the relationship between the venous saturation value and the diffuse reflectance is determined. Therefore images captured can be converted into the venous saturation map. Experiments on human fingers and palm show that the measured data is in line with previous published data, demonstrating the effectiveness of the system on monitoring blood oxygenation in local tissues.

1. INTRODUCTION

Diffuse reflectance spectroscopy with multi-wavelength can be used for measuring tissue oxygenation; however it generally works in a tissue-optode contact manner and provides point measurement. The need for non-contact mapping of skin tissue oxygenation in some clinical environments facilitates the development of a CCD-based imaging system [1–4].

Pulse oximetry measures the arterial oxygen saturation by monitoring the pulsatile alterations in light transmission of two or more wavelengths due to change in arterial blood volume induced by cardiac cycles. It provides arterial blood oxygen saturation S_aO_2 , a global parameter mainly reflecting cardiac information and lung function. Similarly, by varying the venous blood volume and recording changes in light transmission (or reflection), venous oxygen saturation S_vO_2 can also be obtained [5]. In contrast to arterial oxygen saturation, venous oxygen saturation provides information on local oxygen level after perfusion and tissue uptake, which is closely associated with the local tissue health. Thus venous oximetry can be applied in clinics to quantitatively monitor wounds, ulcers and oxygen metabolism in ischemic tissues.

The author reported earlier a CCD-based imaging system for non-contact mapping of venous oxygen saturation [3, 4]. The model used for converting the diffuse reflectance to S_vO_2 is a hybrid model combining the Beer-Lambert law and the photon diffusion theory. However, the diffusion approximation is not valid in the case where the optical path length is very short, for example, emitted light of a pixel coming from very adjacent region around the pixel. This may result in some unpredictable errors for the calculated S_vO_2 . Therefore, in this work, we use Monte Carlo simulation [6–8] to investigate the relationship between S_vO_2 and the diffuse reflectance. In addition to the theoretical model, hardware improvements are also made for the imaging system to achieve high quality of images. To demonstrate the effectiveness of the imaging system, time series of images were taken from fingers and palm of a human subject. The images recorded were converted into S_vO_2 , and two-dimensional (2-D) S_vO_2 maps are also presented.

2. METHODS

2.1. Imaging Setup

The system (as shown in Figure 1) is made up of a 14-bit black-and-white CCD camera (Pike F-032, Allied Vision Technologies GmbH, Stadtroda, Germany) and two high-power LED sources with one working at 660 nm and the other at 800 nm wavelength. The illuminating light is transmitted through a fiber optic ring light guide to insure a uniform illumination on the skin. To suppress direct surface reflection which carries useless information on tissue oxygenation, cross polarization detection is used. During image acquisition, the two LED sources illuminate alternately, which is controlled by a custom electronics and software developed with Labview. The CCD camera is set to work in a trigger mode, thus the onset of the illuminating light and the shutter of the camera is synchronized.

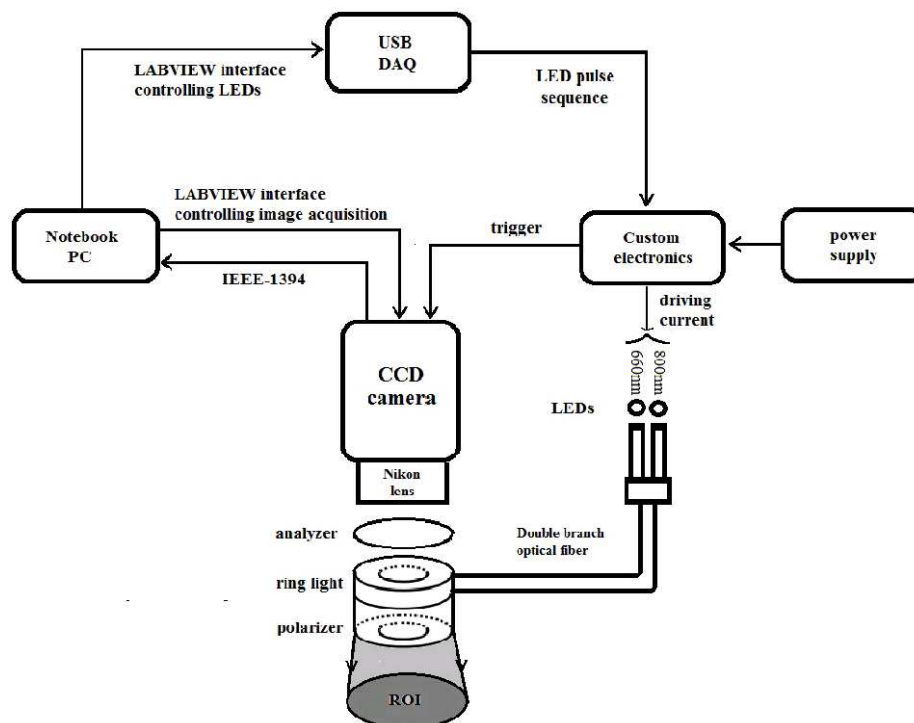


Figure 1: Block diagram for the imaging system.

2.2. Theoretical Model and Monte Carlo Simulation

Based on either the Beer-Lambert law or the hybrid model, there exists a linear relationship between $S_V O_2$ and the ratio-to-ratio R , $R = (\Delta I/I)_{\lambda_1} / (\Delta I/I)_{\lambda_2}$ is the ratio of the relative intensity change for the two wavelengths, a measurable quantity. However, the relationship derived previously, e.g., from the hybrid model, may not accurate enough for the back reflection geometry with the planar wave illumination, thus Monte Carlo simulation is used to investigate the relationship between $S_V O_2$ and R .

Monte Carlo simulation describes accurately light propagation in a turbid medium without any prior approximation [6–8]. To use the ratio-to-ratio method to calculate $S_V O_2$, two questions at least have to be addressed. First, with a certain $S_V O_2$, is the R a constant over a range of venous volume alteration? If the answer is yes, which implies there is a one-to-one relationship between R and $S_V O_2$, then the second question need to be answered, what is the exact relationship between R and $S_V O_2$. We use Monte Carlo simulation to investigate these issues.

Unlike the photon diffusion model, the Monte Carlo simulation can treat the tissue as a multi-layered medium without any restriction on either optical or geometric parameters. In our simulation, we used two skin models, one is a semi-infinite homogeneous model, and the other is a two-layered model. Assume the refractive index for skin tissue is approximately same for the two wavelengths, $n = 1.43$; thickness of epidermis, $d_{\text{epi}} = 50 \mu\text{m}$; volume fraction of melanin in epidermis, $f_{\text{mel}} = 2.0\%$; volume fraction of blood in dermis and tissue, $f_{\text{blood}} = 3\%$; average tissue blood oxygen saturation $S_t O_2 = 74\%$. The extinction coefficients of the oxygenated hemoglobin (HbO) and deoxygenated hemoglobin (Hb) for the two wavelengths are taken from the published data [9]. With the above data, the optical parameters used for the models can be estimated [10] and listed in Table 1.

Table 1: Optical parameters used for the Monte Carlo simulation.

Optical Parameters	μ_a [660 nm] (/cm)	μ_a [800 nm] (/cm)	μ'_s [660 nm] (/cm)	μ'_s [800 nm] (/cm)
Semi-infinite model				
	0.718	0.477	22.8	16.4
Two-layer model				
Epidermis	5.668	3.084	22.8	16.4
Dermis	0.459	0.377	22.8	16.4

Figure 2 gives the simulation result for R with respect to the alteration in venous volume. Clearly one can see for both models, the R is nearly constant over a wide range of venous volume alteration, e.g., from 6% to 50% volume change. This means R does not depend on the venous volume change as long as the venous volume change is within 6%–50%, implying the ratio-to-ratio method may work in this range for estimating S_vO_2 .

The second question was investigated by varying the venous blood volume (e.g., a 30% increase in volume) for different levels of S_vO_2 to induce changes in back reflectance for the two wavelengths. Therefore for each S_vO_2 a R value can be obtained. The simulation result is shown in Figure 3. By the polynomial fitting, the analytical relationship between the R and S_vO_2 can be identified for the two skin models. For the semi-infinite model, $S_vO_2 = -0.0304R^2 - 0.2031R + 0.9474$, while for the two-layered mode, $S_vO_2 = -0.0652R^2 - 0.1593R + 1.0084$. In contrast to the linear relationship between R and S_vO_2 derived from either Beer-Lambert law or the hybrid model, the relationship

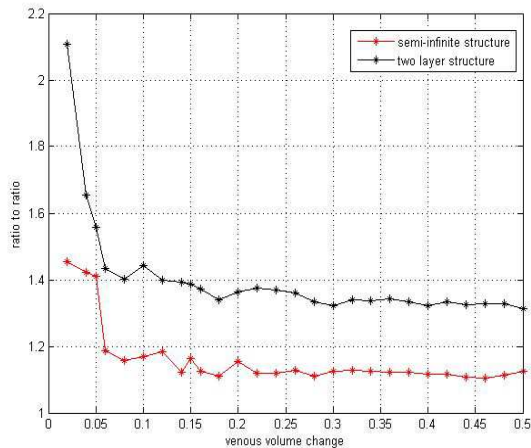


Figure 2: Ratio-to-ratio R with respect to changes on venous blood volume for the two skin models.

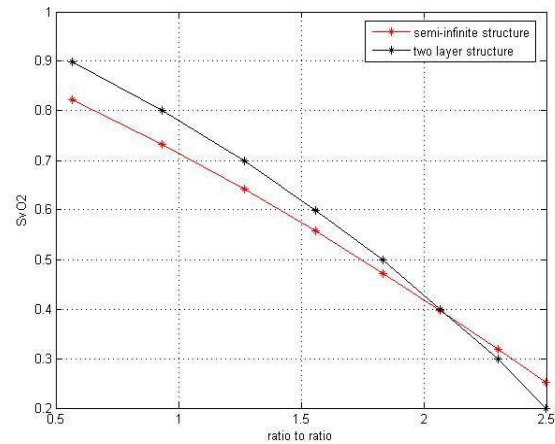
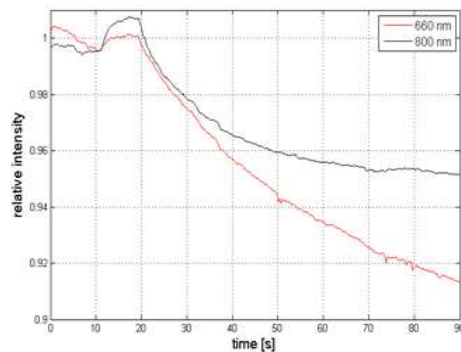
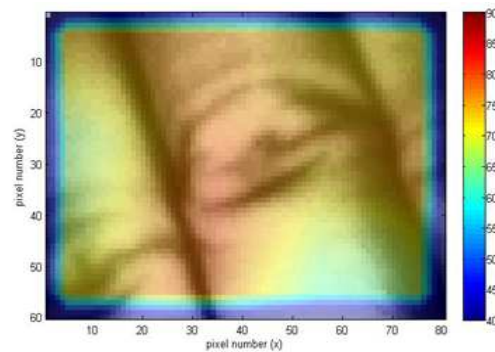


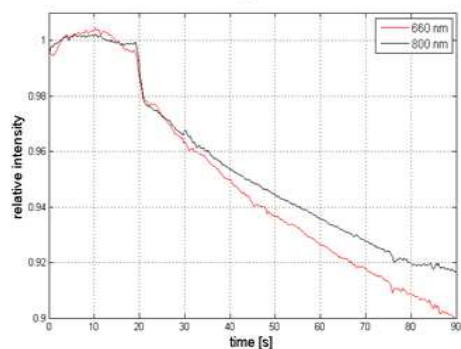
Figure 3: S_vO_2 with respect to R for the two skin models.



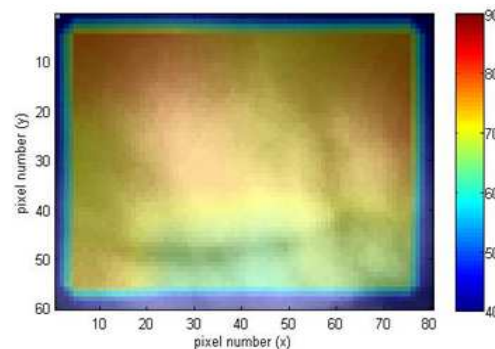
(a)



(b)



(c)



(d)

Figure 4: Relative intensity change over time for fingers (a) and palm (c), and S_vO_2 map for fingers (b) and palm (d). Venous occlusion occurs at time $t = 20$ s.

identified from the Monte Carlo simulation is no longer linear, especially for the two-layered model with higher non-linearity.

In comparison between the two skin models, the semi-infinite model gives smaller value as R is less than 2.1, slightly larger value as R is bigger than 2.1. However, within a wide reasonable range of S_vO_2 , e.g., 30%–85%, the maximum difference in the estimated S_vO_2 between these two models is only 5–6% in amplitude.

3. EXPERIMENTAL RESULT AND DISCUSSION

A preliminary experiment was performed with the developed imaging system. To induce venous volume change, a low cuff pressure (~ 50 mmHg) was applied on a subject wrist. This pressure is high enough to occlude the vein with less effect on the arterial flow. Dynamic images were collected from fingers and palm of the subject before and after the occlusion, separately.

Figure 4 shows the result of measurements on the fingers [Figures 4(a)–(b)] and the palm [Figures 4(c)–(d)]. The curves in Figure 4(a) give the average change in intensity for the red and IR light over the entire image area. The pressure cuff was quickly inflated to 50 mmHg at time $t = 20$ s to induce a rapid venous occlusion. Both 660 nm and 800 nm curves decrease rapidly due to the increase in light absorption caused by venous blood accumulation after the vein was occluded.

Using the two-layered model, images of diffuse reflectance are converted into the venous saturation map, as shown in Figure 4(b). It is a 2-D color map of S_vO_2 overlaid on the grayscale image of the fingers. The average S_vO_2 in the mapping region is $70.6 \pm 7.2\%$. The time window used for calculating palm S_vO_2 is 20–50 s.

Results for the palm are shown in Figures 4(c) and (d), the reflectance of 800 nm does not reach the saturation within the measurement period, possibly because it could be longer before the venous blood stops accumulating in the palm than in the fingers. The average S_vO_2 in the mapping region [Figure 4(d)] is $71.4 \pm 7.3\%$. The average values of S_vO_2 for the fingers and palm are in line with the published data [5].

4. CONCLUSION

We develop a low-cost imaging system based on a 14-bit black-and-white CCD camera and high power LED sources for mapping venous oxygen saturation S_vO_2 in skin tissue. Preliminary experiment results show the measured S_vO_2 is consistent with the published data, which demonstrates the effectiveness of the system.

ACKNOWLEDGMENT

This work was supported by Guangdong (China) Innovative Research Team Program (No. 201001D-0104799318).

REFERENCES

1. Wieringa, F. P., F. Mastik, and A. F. W. Van der Steen, "Contactless multiple wavelength photoplethysmographic imaging: A first step toward 'S_pO₂ camera' technology," *Ann. Biomed. Eng.*, Vol. 33, 1034–1041, 2005.
2. Moza, R., J. M. Dimaio, and J. Melendez, "Deep-tissue dynamic monitoring of decubitus ulcers: Wound care and assessment," *IEEE Eng. Med. Biol. Mag.*, Vol. 29, No. 2, 71–77, 2010.
3. Li, J., B. Dunmire, W. Beach, and F. Leotta, "A reflectance model for non-contact mapping of venous oxygen saturation using a CCD camera," *Opt. Commun.*, Vol. 308, 78–84, 2013.
4. Li, J., B. Dunmire, and D. Leotta, "Venous oxygenation mapping with a CCD camera," *2012 Asia Communications and Photonics Conference (ACP)*, 1–3, 2012.
5. Nitzan, M., A. Babchenko, B. Khanokh, and H. Taitelbaum, "Measurement of oxygen saturation in venous blood by dynamic near infrared spectroscopy," *J. Biomed. Opt.*, Vol. 5, 155–162, 2000.
6. Prah, S. A., M. Keijzer, S. L. Jacques, and A. J. Welch, "A Monte Carlo model of light propagation in tissue," *SPIE Proceedings of Dosimetry of Laser Radiation in Medicine and Biology*, Vol. 5, 102–111, 1989.
7. Wang, L. H., S. L. Jacques, and L. Zheng, "MCML—Monte Carlo modeling of light transport in multi-layered tissues," *Comput. Meth. Prog. Bio.*, Vol. 47, 131–146, 1995.
8. Wang, L. H., S. L. Jacques, and L. Zheng, "CONV — Convolution for responses to a finite diameter photon beam incident on multilayered tissues," *Comput. Meth. Prog. Bio.*, Vol. 54, 141–150, 1997.

9. Zijlstra, W. G. and A. Buursma, “Spectrophotometry of hemoglobin: Absorption spectra of bovine oxyhemoglobin, deoxyhemoglobin, carboxyhemoglobin, and methemoglobin,” *Comp. Biochem. Physiol.*, Vol. 118B, 743–749, 1997.
10. Yudovsky, D., A. Nouvong, K. Schomacker, et al., “Two-layer optical model of skin for early, non-invasive detection of wound development on the diabetic foot,” *Proc. of SPIE*, 755514-10, 2010.

A Novel Compact Tri-band Bandpass Filter with Good Selectivity

D.-H. Jia, Q.-Y. Feng, X.-G. Huang, and Q.-Y. Xiang

School of Information Science and Technology
Southwest Jiaotong University, Chengdu, Sichuan 610031, China

Abstract— A novel tri-band bandpass filter (BPF) based on multi-mode resonators is presented. The resonant modes of the resonators can be analyzed by the even- and odd-mode analysis method. The bandwidths of first and second passbands can be independently controlled. Furthermore, five transmission zeros (TZ) are introduced at the adjacent of the passbands in a narrow frequency range to improve the selectivity, resulting sharp skirts. Due to the small multi-mode resonator and tight coupling structure, the overall size of the proposed filter is really compact ($0.19\lambda_0 \times 0.18\lambda_0$). λ_0 is the wavelength of the center frequency of first passband in the substrate. Finally, a prototype to demonstrate the performance of the filter is designed and fabricated. The measured 3-dB fractional bandwidths for the three passbands (2.22, 2.98 and 3.5 GHz) are found to be 8.4%, 2.7% and 6.1%, respectively. The measurement shows good agreement with the simulation.

1. INTRODUCTION

In recent years, the filters, which are an indispensable part of RF front ends, have gained a lot of attention because of the rapid development of modern communication systems, such as wireless local area networks (WLAN), global system for mobile communications (GSM), the third generation (3G), the fourth generation (4G), and worldwide interoperability for microwave access (WiMAX), etc.. Due to the demands on working in multiband, the multiband bandpass filters, especially tri-band filters [1–13], have becoming a popular research issue.

Among these works, there are several typical design methods. One is to utilize multi-order of resonators [1–3]. With independent coupling paths, passbands can be easily controlled. However, the circuit sizes and insertion loss are always large. Another method is to use the hybrid microstrip/defect ground structure (DGS) technology [4, 5]. The dimensions of the device can be abated as the cost of increased design complexity. Also, it is a popular way to use multi-mode resonators to design tri-band BPFs by controlling the modes suitably [6–13]. In these reported works, shorted and open stubs are always connected to the main resonator for more modes and the circuit sizes are small. However, it is still hard to improve the selectivity of the filters, especially in a narrow frequency range.

In this paper, novel multi-mode resonators are introduced for designing tri-band filters. The formation of passbands can be analyzed by even-odd-mode method. Each passband can be controlled by tuning the corresponding parameters. Furthermore, five transmission zeros are generated to improve the sharp skirts of the BPF. The measured performance of the fabricated filter shows good agreement with the proposed theory.

2. FILTER DESIGN

Figure 1 shows the layout of the proposed compact tri-band bandpass filter. The tri-band bandpass filter consists of two multi-mode resonators and the coupling input/output. As the two resonators are only coupled with the in/out ports, the filter structure can be divided into two independent parts with the original parameters.

As depicted in Figure 2, the even-odd-mode analysis method can be adopted here since the Resonators a and b are symmetrical to the centre plane. The resonant conditions of Resonator a

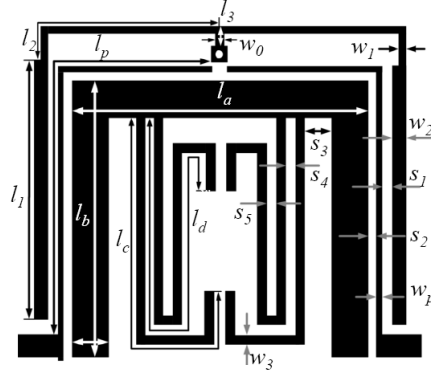
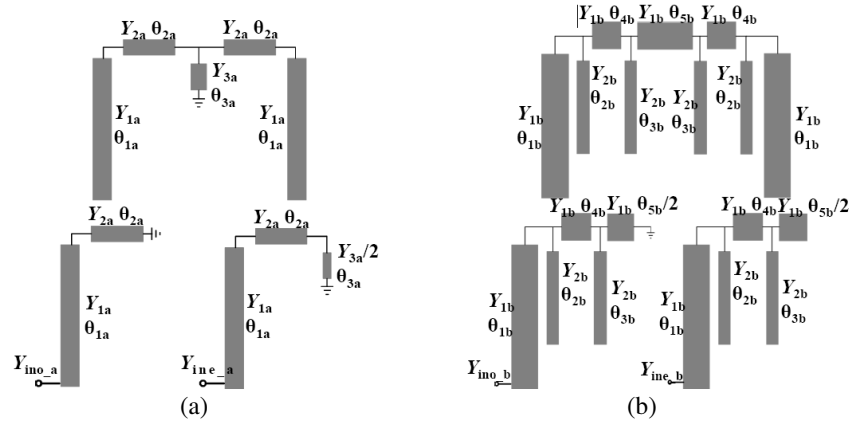


Figure 1: Layout of the proposed compact tri-band bandpass filter.

Figure 2: (a) Resonator a and its even- and odd-modes. (b) Resonator b and its even- and odd-modes.

and b can be achieved when $\text{Im}[Y_{ine}] = 0$, $\text{Im}[Y_{ino}] = 0$. The resonant modes can be expressed as

$$Y_{ino.a} = jY_{1a} \cdot \frac{Y_{1a} \tan \theta_{1a} - Y_{2a} \cot \theta_{2a}}{Y_{1a} + Y_{2a} \cot \theta_{2a} \tan \theta_{1a}} \quad (1)$$

$$Y_{ine.a} = jY_{1a} \cdot \frac{Y_{2a} \cdot \frac{2Y_{2a} \tan \theta_{2a} - Y_{3a} \cot \theta_{3a}}{2Y_{2a} + Y_{3a} \cot \theta_{3a} \tan \theta_{2a}} + Y_{1a} \tan \theta_{1a}}{Y_{1a} - Y_{2a} \cdot \frac{2Y_{2a} \tan \theta_{2a} - Y_{3a} \cot \theta_{3a}}{2Y_{2a} + Y_{3a} \cot \theta_{3a} \tan \theta_{2a}} \tan \theta_{1a}} \quad (2)$$

$$Y_{ino.b} = Y_{1b} \cdot \frac{Y_{load1} + jY_{1b} \tan \theta_{1b}}{Y_{1b} + jY_{load1} \tan \theta_{1b}}, \quad Y_{ine.b} = Y_{1b} \cdot \frac{Y_{load2} + jY_{1b} \tan \theta_{1b}}{Y_{1b} + jY_{load2} \tan \theta_{1b}} \quad (3)$$

$$Y_{load1} = jY_{1b} \cdot \frac{Y_{2b} \tan \theta_{3b} + Y_{1b} \tan \theta_{4b} - Y_{1b} \cot \frac{\theta_{5b}}{2}}{Y_{1b} - (Y_{2b} \tan \theta_{3b} - Y_{1b} \cot \frac{\theta_{5b}}{2}) \tan \theta_{4b}} + jY_{2b} \tan \theta_{2b} \quad (4)$$

$$Y_{load2} = jY_{1b} \cdot \frac{Y_{1b} \tan \frac{\theta_{5b}}{2} + Y_{2b} \tan \theta_{3b} + Y_{1b} \tan \theta_{4b}}{Y_{1b} - (Y_{1b} \tan \frac{\theta_{5b}}{2} + Y_{2b} \tan \theta_{3b}) \tan \theta_{4b}} + jY_{2b} \tan \theta_{2b} \quad (5)$$

It can be seen from formulas (1)–(5) that the resonant modes of Resonator a and b can be tuned by changing lengths of corresponding sections. The calculated results are shown in Figure 3. As depicted in Figure 3(a), the first even and odd mode of Resonator a are selected to design the passbands. While increasing the independent even-mode part l_3 , the $f_{even.a1}$ decreases and the $f_{odd.a1}$ keep constant. By the same method, the resonant modes of Resonator b can be confirmed, as depicted in Figures 3(b) and (c). There are four resonant frequencies during the range 2.7 GHz–4 GHz. It is notable that all the resonant modes are influenced by l_c except for $f_{odd.b1}$ and $f_{odd.b1}$ decrease while increasing l_d , meanwhile, $f_{even.b2}$ and $f_{odd.b2}$ almost keep constant.

Based on the modes analysis above, to confirm the generation of passbands ulteriorly, Figure 4 shows the filter coupling scheme. The first passband are independently generated by $f_{even.a1}$ and $f_{odd.a1}$ which are based on Resonator a . Meanwhile, the second and third passbands are mainly obtained by Resonator b . Resonant modes $f_{odd.b1}$ and $f_{even.b1}$ form the second passband, simultaneously, the third passband is made up by resonant modes $f_{odd.2}$ and $f_{even.b2}$.

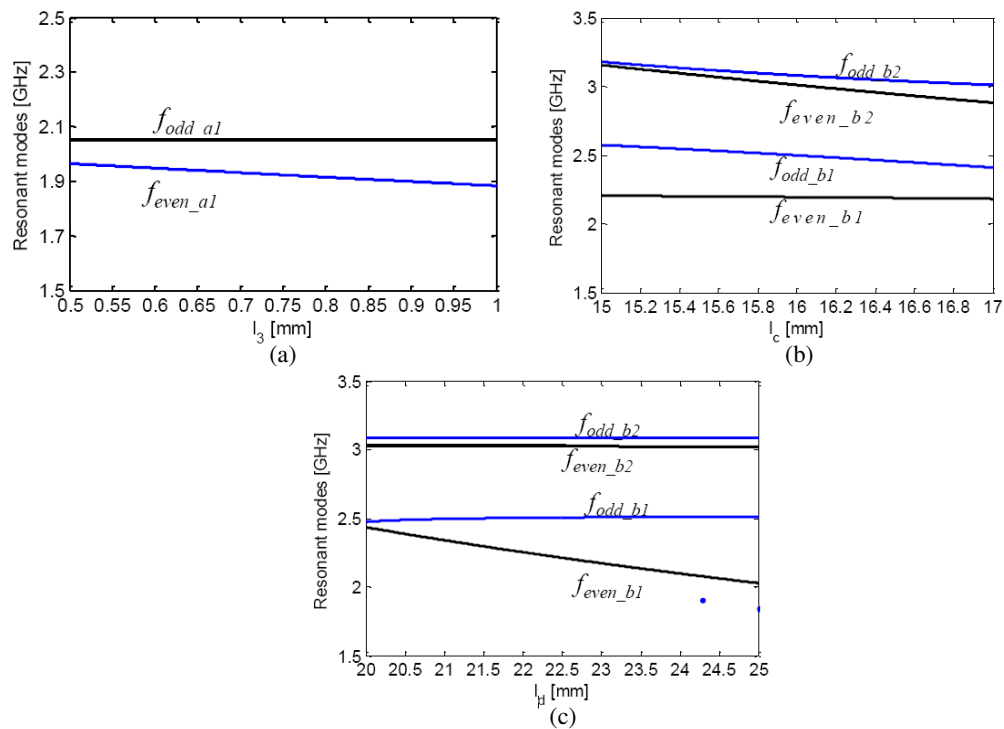


Figure 3: (a) Resonant-mode frequencies of Resonator *a* for different values of l_3 . Other parameters used in the calculated results: $Y_{1a} = 1/71$ s, $l_{1a} = 10.8$ mm, $Y_{2a} = 1/109$ s, $l_{2a} = 8.9$ mm, $Y_{3a} = 1/97$ s. l_{na} is the corresponding parameter of θ_{na} ($n = 1, 2,$ and 3). (b) Resonant-mode frequencies of Resonator *b* for different values of l_c . Other parameters used in the calculated results: $Y_{1b} = 1/38$ S, $l_{1b} = 13.6$ mm, $Y_{2b} = 1/97$ S, $l_{3b} = 22.7$ mm, $l_{4b} = 0.4$ mm, $l_{5b} = 5.1$ mm. l_{nb} is the corresponding parameter of θ_{nb} ($n = 1, 2, 3, 4,$ and 5). (c) Resonant-mode frequencies of Resonator *b* for different values of l_d . Other parameters used in the calculated results: $Y_{1b} = 1/38$ s, $l_{1b} = 13.6$ mm, $Y_{2b} = 1/97$ s, $l_{2b} = 15.9$ mm, $l_{4b} = 0.4$ mm, $l_{5b} = 5.1$ mm. l_{nb} is the corresponding parameter of θ_{nb} ($n = 1, 2, 3, 4,$ and 5).

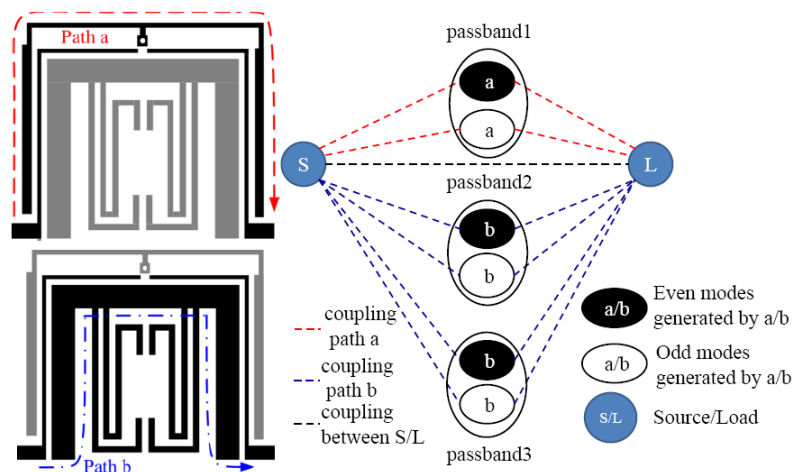


Figure 4: The coupling scheme of proposed tri-band bandpass filter.

3. VERIFICATION BY SIMULATION

To demonstrate the performance of the proposed filter, a compact tri-band filter is designed, fabricated and tested with an Agilent E5071C vector network analyzer, as shown in Figure 5. The dimensions for the filter are presented in Table 1 for $\epsilon_r = 2.65$, $h = 0.5$ mm. The overall size of proposed filter is only 15.8×14.7 mm² ($0.12\lambda_0 \times 0.11\lambda_0$). λ_0 is the wavelength of the centre frequency of first passband. The simulation and measurement are also shown in Figure 5. Clearly, The simulation and measurement show good agreement. The distinction between the simulation

and the measurement is mainly due to the mismachining tolerance. The measured 3-dB fractional bandwidths for the three passbands (2.22, 2.98 and 3.5 GHz) are found to be 8.4%, 2.7% and 6.1%, respectively. The measured minimum insertion losses including the loss from SMA connectors are 1.4, 3.5, and 1.5 dB, while the return losses are greater than 18.7, 27.6 and 40 dB, respectively. Five transmission zeros are created at 1.95, 2.75, 2.83, 3.14 and 3.66 GHz. These transmission zeros are generated near the passband edges, resulting in sharp roll-off in a narrow frequency range.

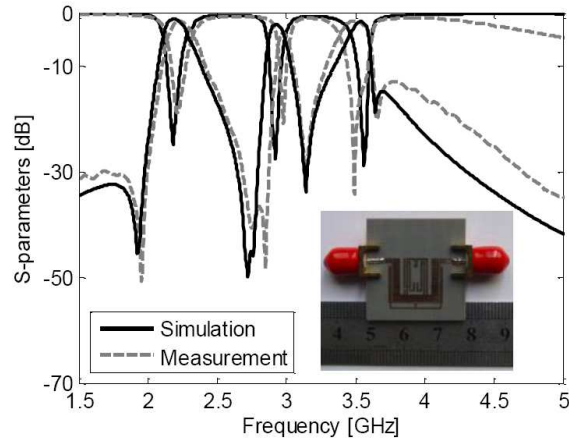


Figure 5: The photograph of fabricated filter and simulated, measured results.

Table 1: The parameters of proposed triple-band BPF (Unit: mm).

l_1	l_2	l_3	l_a	l_b	l_c	l_d	l_p	w_0	w_1	w_2	w_3	w_p	s_1	s_2	s_3	s_4	s_5
10.8	9.2	0.6	13.2	12.6	16.5	23.5	18.4	0.4	0.3	0.7	0.4	0.2	0.2	0.2	1.1	0.4	0.4

4. CONCLUSION

In this paper, a tri-band BPF based on multi-mode resonators is proposed. The passbands can be controlled according to even-odd-mode analysis, and five transmission zeros are introduced at the adjacent of passbands, resulting in high selectivity. Due to the tight resonators and coupling structure, the circuit size is really small. The compactness and high selectivity make the proposed filter attractive for multiband communication systems.

ACKNOWLEDGMENT

This work was supported by the National Natural Science Foundation of China (NSFC) under Grant 61271090, the National 863 Project of China under Grant 2012AA012305, the Fundamental Research Funds for the Central Universities under Grant 2682014RC24 and “2014 Doctoral Innovation Funds of Southwest Jiaotong University”.

REFERENCES

- Chen, J.-Z., N. Wang, Y. He, and C.-H. Liang, “Fourth-order tri-band bandpass filter using square ring loaded resonators,” *Electron. Lett.*, Vol. 47, 858–859, 2011.
- Chen, B.-J., T.-M. Shen, and R.-B. Wu, “Design of tri-band filters with improved band allocation,” *IEEE Trans. Microw. Theory Tech.*, Vol. 57, 1790–1797, 2009.
- Lai, X., B. Wu, T. Su, and C.-H. Liang, “A novel tri-band filter using stub-loaded open loop ring resonators,” *Micro. Opt. Technol. Lett.*, Vol. 52, 523–526, 2010.
- Ren, L.-Y., “Tri-band bandpass filters based on dual-plane microstrip/DGS slot structure,” *IEEE Microw. Wirel. Compon. Lett.*, Vol. 20, 429–431, 2010.
- Wang, L. and B.-R. Guan, “Compact and high selectivity tri-band BPF using nested DDGSRs,” *Electron. Lett.*, Vol. 48, 378–379, 2012.
- Zhang, X.-Y., Q. Xue, and B.-J. Hu, “Planar tri-band bandpass filter with compact size,” *IEEE Microw. Wirel. Compon. Lett.*, Vol. 20, 262–264, 2010.

7. Chen, W.-Y., M.-H. Weng, and S.-J. Chang, “A new tri-band bandpass filter based on stub-loaded step-impedance resonator,” *IEEE Microw. Wirel. Compon. Lett.*, Vol. 22, 179–181, 2012.
8. Chu, Q.-X., F.-C. Chen, Z.-Z. Tu, and H. Wang, “A novel crossed Resonator and its applications to bandpass filters,” *IEEE Trans. Microw. Theory Tech.*, Vol. 57, 1753–1759, 2009.
9. Deng, H.-W., Y.-J. Zhao, Y. Fu, X.-J. Zhou, and Y.-Y. Liu, “Design of tri-band microstrip BPF using SLR and quarter-wavelength SIR,” *Micro. Opt. Technol. Lett.*, Vol. 55, 212–215, 2013.
10. Liu, H.-W., “Design of tri-band microstrip bandpass filter using floded tri-section stepped-impedance resonator,” *Micro. Opt. Technol. Lett.*, Vol. 52, 895–898, 2010.
11. Liu, Y., Y.-J. Zhao, Y.-G. Zhou, and Z.-Y. Niu, “Integrated dual-band BPF and single-band BSF for tri-band filter design,” *Journal of Electromagnetic Waves and Applications*, Vol. 25, Nos. 17–18, 2420–2428, 2011.
12. Liu, S.-K. and F.-Z. Zheng, “A new compact tri-band bandpass filter using step impedance resonators with open stubs,” *Journal of Electromagnetic Waves and Applications*, Vol. 26, No. 1, 130–139, 2012.
13. Ye, C.-S., Y.-K. Su, and M.-H. Weng, “New compact tri-band bandpass filter with transmission zeros designed by using stub-loaded resonators,” *Journal of Electromagnetic Waves and Applications*, Vol. 26, Nos. 17–18, 2277–2283, 2012.

Dual-band Bandpass Filter with Good Selectivity and Stopband Rejection

Daotong Li¹, Yonghong Zhang¹, Kaida Xu¹, Kaijun Song¹, and Le-Wei Li²

¹EHF Key Lab of Science, University of Electronic Science and Technology of China, Chengdu, China

²Institute of Electromagnetics, University of Electronic Science and Technology of China, Chengdu, China

Abstract— Dual-band dual-mode bandpass filters with good selectivity and wide upper-stop-band performance based on circular ring resonator is presented. The two first-order degenerate modes are excited and split to form the first passband, while one of the third-order degenerate modes forms the second passband together with a second-order degenerate mode. After installing two parallel-coupled-line sections on a ring at the two ports with 90°-separation, five transmission zeroes are produced for the rejections between the two passbands and in the stopband. A dual-band filter with the two transmission poles in each passband is designed and measured, the measured filter shows good agreement with the simulated.

1. INTRODUCTION

As one of the essential microwave components, dual-band bandpass filters are highly desired in modern dual-band wireless communication systems [1, 2]. Therefore, various design approaches have been proposed. Microstrip ring resonators have been used to design various microwave circuits such as filters, mixer and oscillators and so on [3, 4]. By using the coexisting of the two degenerate orthogonal mode, a dual-band passband filter can be achieved [5]. Due to the characteristics of compact size, high- Q factors, and sharp rejection skirt, the ring resonators have been analyzed deeply and comprehensively in many reports [6–9]. In [6], the dual-band bandpass filter with adjustable first- and second-order resonator was presented by using stepped-impedance ring resonator. However, there is only a single transmission pole in the second passband for a single ring resonator filter. In [7], two dissimilar ring resonators with different resonant frequencies were utilized to achieve the desired dual-band passband performance, while the solutions need more design consideration and larger overall size. In [8], dual-band bandpass filter based on a signal ring resonator were designed. However, these structures need many perturbation elements to be installed along the ring. In [9], a dual-band bandpass filter was presented using a single rectangular ring resonator, but the out-of-band rejection and the selectivity are not good enough.

In this paper, a dual-band BPF using a single microstrip circular ring resonator has been presented. The two transmission poles are generated in each passband after installing two coupled-line sections at two excitation ports. A common two-port excitation angle of 90°-separation with the cooperation of the parallel-coupled feed line, five transmission zeroes are generated and controlled to provide a good isolation and wide upper stopband. A dual-band filter is designed and measured to demonstrate the good in-band matching and the good rejections outside the desired dual passbands.

2. FILTER DESIGN

2.1. Characteristic of Proposed Resonator

Figure 1 shows a configuration of the proposed quadruple-mode circular ring resonator. It consists of a circular ring resonator with two open ended stubs, where R , w and w_s are the radius and the widths of the square ring and open stubs, respectively. Because the resonator is an even symmetrical structure, its operating mechanism can be discussed by an even- and odd-mode analysis. Its equivalent circuits are depicted in Figs. 1(b), (c). Z_s and θ_s are the characteristic impedance and the electrical length of the loaded open-circuited stub on the ring. Z_l and Z_r respect the two oppositely oriented input impedances at the same position, the input impedances with superscript “e” and “o” are the even- and odd-mode impedances, respectively.

According to the Transmission line theory and odd-even mode analysis method, the resonant frequencies under the even- and odd-mode excitation satisfy [10]

$$Z_l^e + Z_r^e = 0 \quad (1)$$

$$Z_l^o + Z_r^o = 0 \quad (2)$$

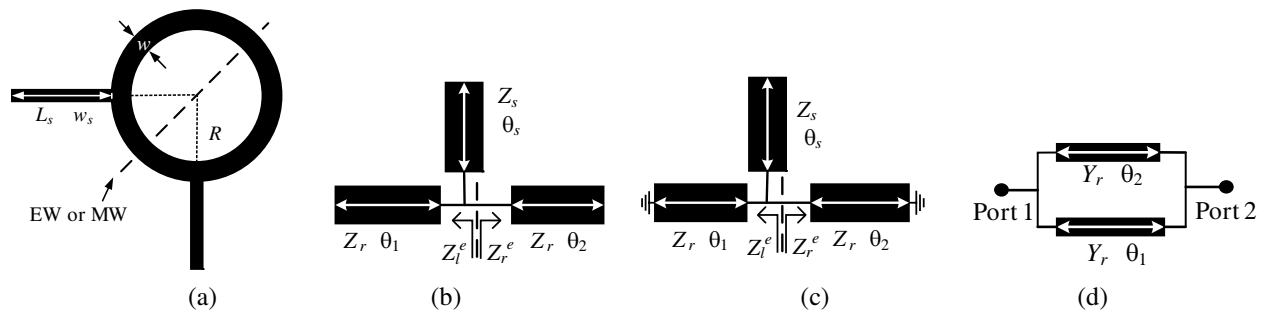


Figure 1: (a) Layout of proposed circular ring resonator; (b) Even-mode equivalent circuit; (c) Odd-mode equivalent circuit; (d) Circuit for obtaining transmission zero frequencies.

where $Z_l^e = -j \frac{Z_r}{\tan \theta_1 + \tan \theta_s}$, $Z_r^e = -\frac{j Z_r}{\tan \theta_2}$, $Z_l^o = -j Z_r \left(\frac{\tan \theta_1 \tan \theta_s}{\tan \theta_1 - \tan \theta_s} \right)$, $Z_r^o = j Z_r \tan \theta_2$.

Figure 1(d) is used for obtaining these transmission zeroes. The transmission zero frequencies are obtained when $Y_{21} = Y_{12} = 0$, where the admittance matrices are calculated by adding upper and lower Y -parameter of the two paths connected in shunt between port 1 and 2, and the calculated results are expressed by

$$\sin \theta_1 + \sin \theta_2 = 0 \quad (3)$$

where $\theta_2 = 3\theta_1$, so, the transmission zeros appear at $\theta_2 = (2n - 1) \times 90^\circ$, $n = 1, 2, 3, \dots$

Figure 2 shows the frequency responses of the circular ring resonator under a weak coupling. It can be seen that all the resonant frequencies become smaller as θ_s increase. The first two resonant frequencies f_1 and f_2 split from each other as θ_s increase, while the third and fourth resonances f_3 and f_4 further move close to each other and thus form a second passband. The fifth resonance f_5 becomes the first spurious frequency of this dual-band filter.

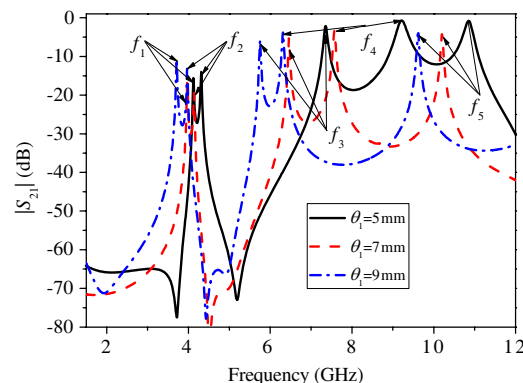


Figure 2: Simulation transmission response of the dual-band filter with weak coupling.

2.2. Characteristics of Parallel-coupled Feed Line

Figure 3(a) shows the layout of circular ring dual-band BPF which fed by the parallel-coupled feed lines. (L_1, w_1) and (L_2, w_2) are the electrical length and the width of the parallel-coupled feed line connecting with input/output port and the loaded open stub on the circular ring resonator, respectively.

To examine the characteristics of the parallel-coupled lines, only the parallel-coupled feed lines shown in Fig. 3(b) with three different length of L_1 are simulated. These three kinds of simulated results are shown in Fig. 4(a) when $L_1 = L_2$, $w_1 = w_2$, the transmission zeroes of the parallel-coupled lines are distributed in the stopband. According to the curves in Fig. 4(b), the transmission zero f'_{Tz2} can be changed widely by altering the length of parallel-coupled feed line of L_1 while the length of L_2 remain unchanged, and transmission zero f'_{Tz1} varies slightly. The effect of these overlaps can be displayed when the circular ring resonator and the parallel-coupled lines are used together. Fig. 5 shows the simulated results of the circular ring fed by the parallel-coupled lines shown in Fig. 3(b) with three different length of L_1 . The overlap of zeroes shown in Fig. 5 result in the fifth resonant frequency suppression in Fig. 2, cause sharper rejections at cutoff regions, and wider stopband.

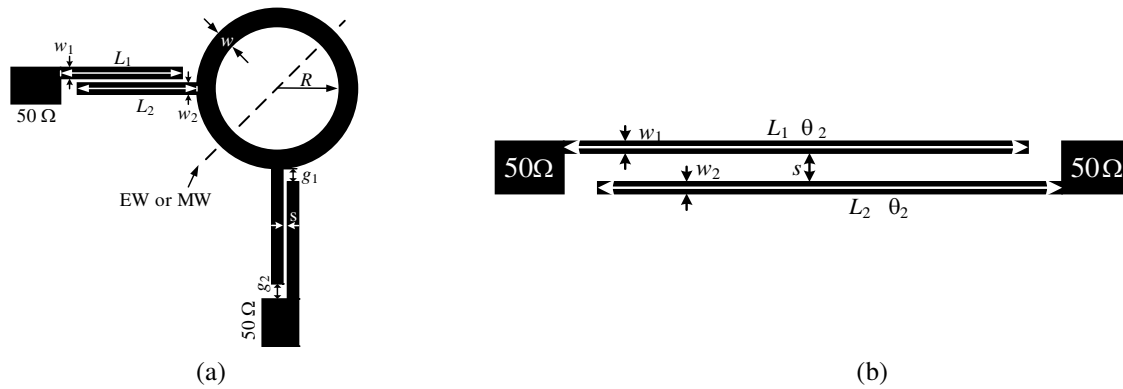


Figure 3: (a) Circular ring resonator fed by parallel-coupled lines; (b) Parallel-coupled feed line used in Fig. 3(a).

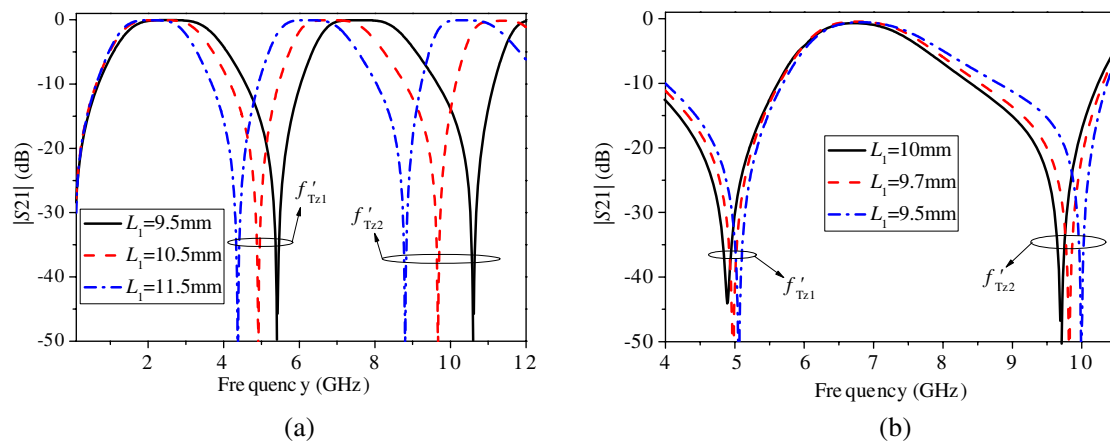


Figure 4: (a) Simulated results for the parallel-coupled feed line using three kinds of L_1 in the case of $L_1 = L_2$; (b) Variation of the transmission zeroes versus the length of L_1 .

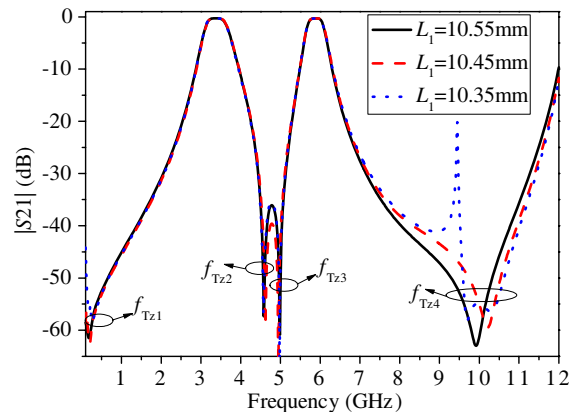


Figure 5: Simulated results of the circular ring resonator fed by the parallel feed line versus the length of L_1 .

3. EXPERIMENTAL RESULTS

Based on the circular ring quadruple-mode resonator, a dual-band BPF has been designed and fabricated on *Taconic* RF-35 substrate with relative dielectric constant of $\epsilon_r = 3.5$ and thickness of $h = 0.508$ mm. The geometry of the proposed filter is shown in Fig. 3(a). The dimensions are obtained as: $L_1 = 10.41$ mm, $L_2 = 10.55$ mm, $w_1 = 0.13$ mm, $w_2 = 0.16$ mm, $w = 0.6$ mm, $g_1 = 0.3$ mm, $g_2 = 0.44$ mm, $s = 0.21$ mm, $R = 6.5$ mm.

The photograph of the fabricated filter is presented in Fig. 6(a). The simulated and measured frequency responses are compared in Fig. 6(b). Dotted lines and solid lines indicate the simulated and measured results, respectively. A good agreement is achieved between the simulated and the measured results. The measured minimum insertion loss achieves 1.0 dB in the first passband and 1.6 dB in the second passband. The 3-dB fractional bandwidth of the proposed filter is 18% and 8%, respectively. Its passband return loss is larger than 15.6 dB. Three transmission zeroes are generated at 1.01, 4.62, 4.85, 9.85 and 10.32 GHz, respectively. With the help of an additional transmission zero provided by the coupled-line section, the fifth resonance which located in the upper stopband can be fully suppressed. In the measured upper-stopband responses, a 20 dB rejection in the frequency range of 6.78 to 12.25 GHz is obtained.

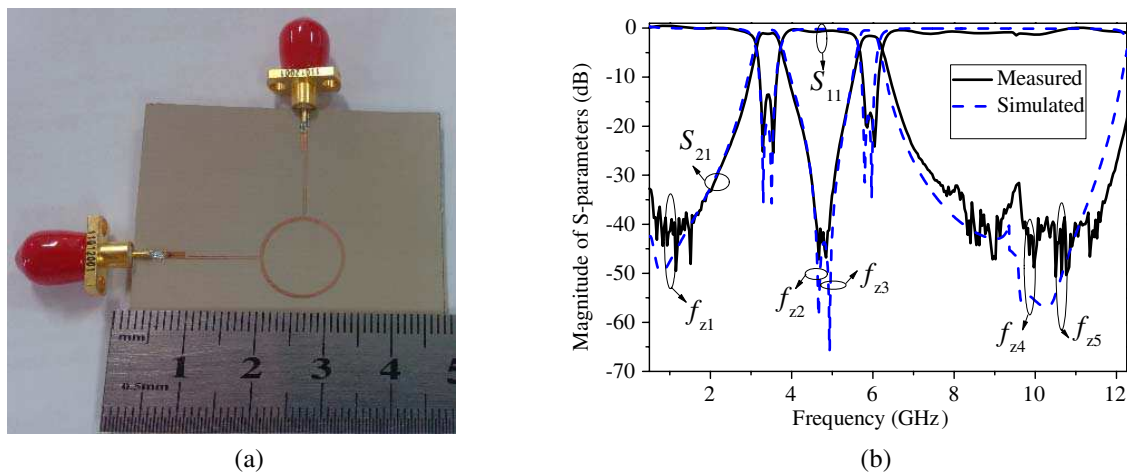


Figure 6: (a) Photograph of the fabricated dual-band bandpass filter; (b) Simulated and measured results of dual-band BPF.

4. CONCLUSION

A dual-band BPF using a single circular ring resonator has been presented. The two transmission poles are generated in each passband after installing two parallel-coupled-line sections at two excitation ports. Meanwhile, two transmission zeroes are placed between the two passbands and three transmission zeroes are created in the stopband which resulted in a good selectivity and wide upper stopband. The spurious frequency caused by the fifth resonance of the resonator has been suppressed by an additional zero brought by the parallel-coupled-line section, thus widening the upper stopband.

ACKNOWLEDGMENT

This work was supported by the National Key Scientific Instrument and Equipment Development Projects (Grant No. 2013YQ200503).

REFERENCES

1. Li, B., X. Wu, N. Yang, and W. Wu, "Dual-band equal/unequal Wilkinson power dividers based on coupled-line section with short circuited stub," *Progress In Electromagnetics Research*, Vol. 111, 163–178, 2011.
2. Xu, K. D., Y. H. Zhang, C. L. Zhuge, and Y. Fan, "Miniaturized dual-band bandpass filter using short stub-loaded dual-mode resonators," *Journal of Electromagnetic Waves and Applications*, Vol. 25, No. 16, 2264–2273, 2011.
3. Chang, K. and L. H. Hsieh, *Microwave Ring Circuits and Related Structures*, Wiley, New York, 2004.
4. Xu, K. D., Y. H. Zhang, Y. Fan, J. L. W. Li, W. T. Joines, and Q. H. Liu, "Planar dual- and tri-band bandpass filters using single improved ring resonator and simple feed scheme," *Microwave Opt. Technol. Lett.*, Vol. 56, No. 3, 574–577, 2014.
5. Sun, S., "A dual-band bandpass filter using a single dual-mode ring resonator," *IEEE Microw. Wireless Compon. Lett.*, Vol. 21, No. 6, 298–300, 2011.

6. Huang, T.-H., H.-J. Chen, C.-S. Chang, L.-S. Chen, Y.-H. Wang, and M.-P. Houn, “A novel compact ring dual-mode filter with adjustable second-passband for dual-band applications,” *IEEE Microw. Wireless Compon. Lett.*, Vol. 16, No. 6, 360–362, 2006.
7. Djoumessi, E. E. and K. Wu, “Multilayer dual-mode dual-bandpass filter,” *IEEE Microw. Wireless Compon. Lett.*, Vol. 19, No. 1, 21–23, 2009.
8. Chiou, Y.-C., C.-Y. Wu, and J.-T. Kuo, “New miniaturized dual-mode dual-band ring resonator bandpass filter with microwave C-sections,” *IEEE Microw. Wireless Compon. Lett.*, Vol. 20, No. 2, 67–69, 2010.
9. Sun, S., “A dual-band bandpass filter using a single dual-mode ring resonator,” *IEEE Microw. Wireless Compon. Lett.*, Vol. 21, No. 6, 298–300, 2011.
10. Sun, S. and L. Zhu, “Wideband microstrip ring resonator bandpass filters under multiple resonances,” *IEEE Trans. Microwave Theory Tech.*, Vol. 55, No. 10, 2176–2182, 2007.

New Design of Low Cost and Easy Tuning Compact GPS Microstrip Antenna

Chanjuan Li, Shiqiang Fu, Te Shao, and Hongmei Liu

School of Information Science and Technology, Dalian Maritime University, Dalian, Liaoning 116026, China

Abstract— A new low cost and easy tuning compact GPS microstrip antenna structure has been proposed. RHCP (right-hand circular polarized) radiation is realized with corner truncated on a square patch as the radiating element. The size of the antenna is reduced by cutting the central slot and marginal slits, which force the current to follow extra paths. Coaxial single-probe center feed loaded with microstrip stub is used to achieve impedance matching. The best operating frequency tuning can be achieved by varying the marginal slits. The design and tuning method is given. The final optimized antenna dimension has been obtained after a large of electromagnetic simulations. The simulated results show that the antenna has a good matching and CP radiation performance.

1. INTRODUCTION

In recent years, there has been an increase in demand for circularly polarized microwave antenna designs for civilian Global Positioning System (GPS) from small applications like in smart phones to complex applications found in marine operations. Microstrip antennas have several advantages compared to conventional microwave antennas such as low profile, small volume, light weight, low cost, compatibility with integrated circuit, ease of fabrication. Therefore, they are very useful for satellite and mobile communication applications [1].

The circular polarisation (CP) microstrip antennas are classified into single-feed type and dual-feed type. Single feed truncated corner square patch is the radiator largely used as a GPS receiver antenna because single-probe feeding makes the antenna a cost effective choice for mass production. The technique of truncating the patch corners of a square microstrip patch to obtain single-feed CP operation is well-known [2] and has been widely used in practical designs [3–8]. Characteristics of a novel design of single-feed, reduced-size CP square microstrip antenna with square-ring shaped patch [3] and slits cut in the patch [4] have been studied. Experimental results show that the proposed design has reduced antenna size as compared to the conventional CP square microstrip antenna with truncated corners at a given operating frequency. A feed method of placing the microstrip line at the inner patch boundary was demonstrated in [5]. It is possible to manufacture microstrip antennas with substrates having high loss tangent (like FR4) without severe degradation of their electrical performance was reported in [6]. Recently, a single-feed CP microstrip patch antenna with multi-frequency operation has been developed for GPS applications [7, 8].

In this paper, a new single probe feed CP microstrip antenna with low-cost FR4 as substrate for GPS applications has been designed. Variations in FR4 electrical permittivity can shift the operating frequency. So one microstrip stub is used to achieve impedance matching and two marginal slits are introduced for the best operating frequency tuning. The purpose is to get the best axial-ratio and the return loss at the fixed frequency. Design concepts and procedures are introduced, followed by simulations and discussions.

2. ANTENNA CONFIGURATION AND DESIGN

The configuration of the proposed antenna element is shown in Fig. 1. The square microstrip patch with a central slot, having an outer side length of L , and an inner side length of S , is printed on a substrate of thickness h and relative permittivity ϵ_r . The truncated corners are of equal side length ΔL . The feed position is located at the patch centre with a microstrip matching stub of width W_3 and length L_3 . Two narrow marginal slits are cut at two adjacent edges in the patch with the size of width W_1 , W_2 and length L_1 , L_2 . This antenna has a ground plane size of $G \times G$.

The main consideration is the cost of the substrate, when a low-cost radiator is required in antenna design for civilian GPS applications. FR4-epoxy substrate is a good choice. FR4-epoxy with $h = 2$ mm thick was selected because it is easily available in the market. The use of low-cost FR4 as substrate introduces some additional complexity on the antenna design. This additional complexity is due to the inaccuracy of the FR4 relative permittivity and its high loss tangent. Variations in FR4 electrical permittivity can shift the operating frequency.

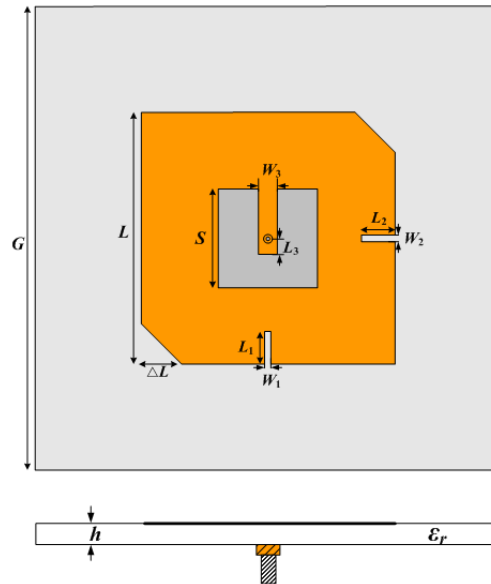


Figure 1: Configuration of the proposed antenna.

In order to minimize this effect, modifications are introduced in the antenna design. One microstrip open stub is used to achieve impedance matching and two marginal slits are introduced for the best operating frequency tuning. It should be mentioned that the side length ΔL of truncated corners dominates the axial ratio of CP and the microstrip matching stub determines the impedance matching of the antenna.

Throughout the studies, it is found that the real part of the antenna input impedance can be controlled by changing W_3 and L_3 , while the imaginary part of the antenna input impedance can be adjusted mainly by changing L_3 , which can be seen in Fig. 2. So we can first change L_3 to get a real input impedance (zero imaginary part), and then change W_3 to get the input resistance that we need. The impedance matching can be achieved without major modification of the radiator and the CP characteristic is also not so sensitive to the changing of the matching stub.

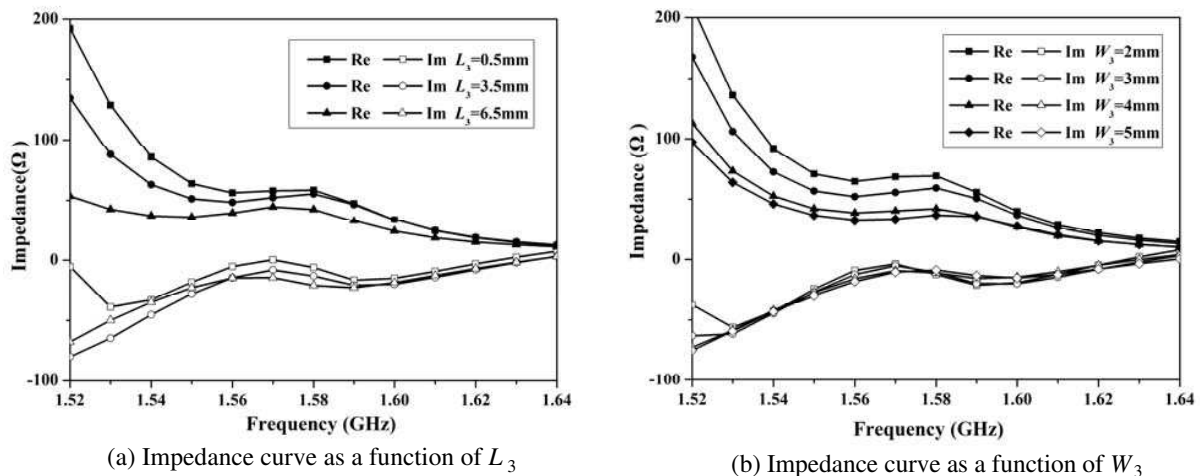


Figure 2: Input impedance as a function of matching stub length and width.

As mentioned before, the use of low-cost FR4 as substrate causes the frequency deviations due to the inaccuracy of its relative permittivity. The proposed antenna configuration to compensate this effect has two narrow slits, as shown in Fig. 1. Cutting properly the slits length, frequency deviations can be compensated. It is shown in Fig. 3 that by adjusting the inserted slit length L_1 (the slit width fixed to be $W_1 = 1$ mm), the CP axial ratio can be tuned. Meanwhile, the input reflection coefficient can be tuned by adjusting the inserted slit length L_2 (the slit width fixed to

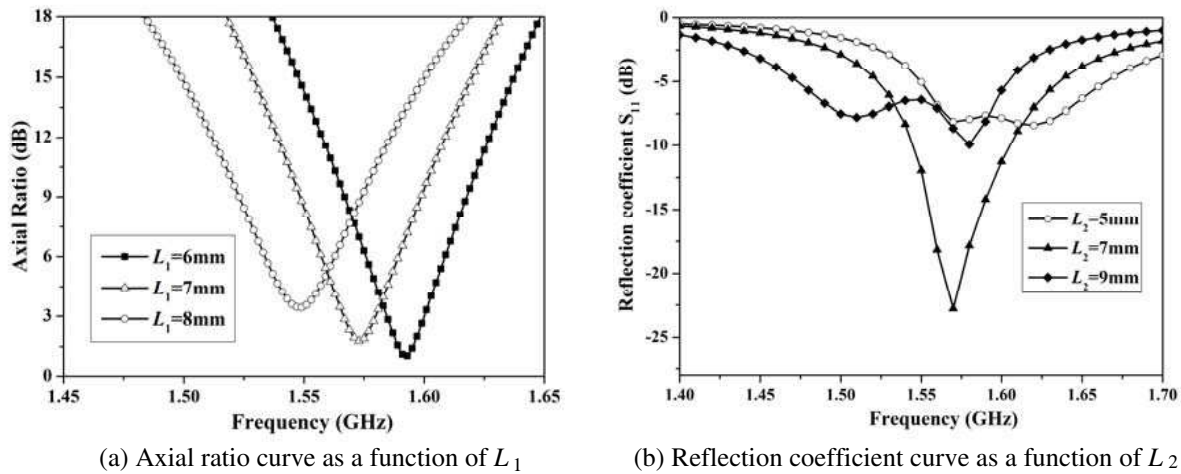


Figure 3: The operating frequency deviations by varying the slit length.

be $W_2 = 1$ mm). It gives a convenient tuning option for the best operating frequency by varying the slit length.

3. SIMULATION RESULTS AND DISCUSSIONS

The proposed antenna has been optimized for operation in the L_1 band with the centre frequency of 1575.42 MHz. The commercial simulation tool HFSS has been used in this study. After extensive simulations, the following values are selected: $L = 37$ mm, $\Delta L = 4.4$ mm, $S = 15$ mm, $L_1 = 7$ mm, $W_1 = 1$ mm, $L_2 = 7$ mm, $W_2 = 1$ mm, $L_3 = 2.5$ mm, $W_3 = 3$ mm, $h = 2$ mm, $\epsilon_r = 4.4$, $G = 70$ mm. The simulation results show that the final antenna displays good input impedance matching and excellent circular polarization radiation pattern.

Figure 4 shows the simulated input impedance match characteristics of the antenna. It is seen that the simulated $|S_{11}| < -15$ dB in the range from 1550 MHz to 1590 MHz, which is about 40 MHz bandwidth. Fig. 5 shows the simulated axial ratio and the power gain in the bore-sight direction. As can be seen from the figure, the simulated 3-dB axial ratio bandwidth is found to be from 1565 MHz to 1580 MHz and the lowest axial ratio is found to be 0.8 dB at 1576 MHz. In the 3-dB axial ratio bandwidth, the power gain is about 1 dB due to FR4 high loss tangent. The radiation patterns in two orthogonal planes of both right-hand circular-polarization (RHCP) and left-hand circular-polarization (LHCP) at the center frequency are shown in Fig. 6. It is clearly seen that this antenna can provide RHCP and very pure circular polarization radiation can be produced within a broad angular range.

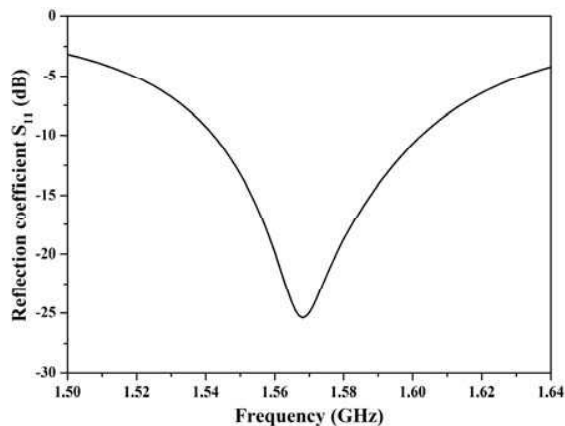


Figure 4: Simulated reflection characteristics versus frequency.

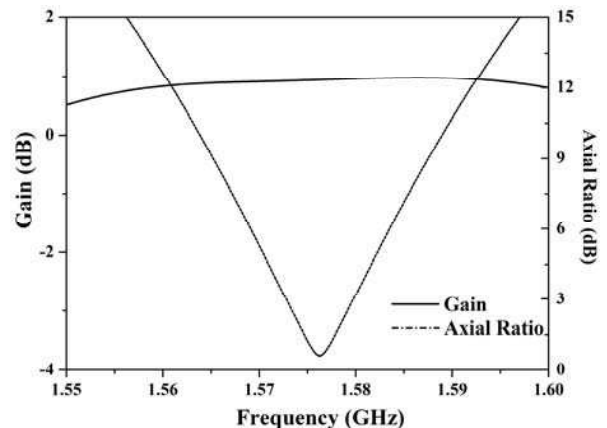


Figure 5: Gain and axial ratio characteristics of the antenna.

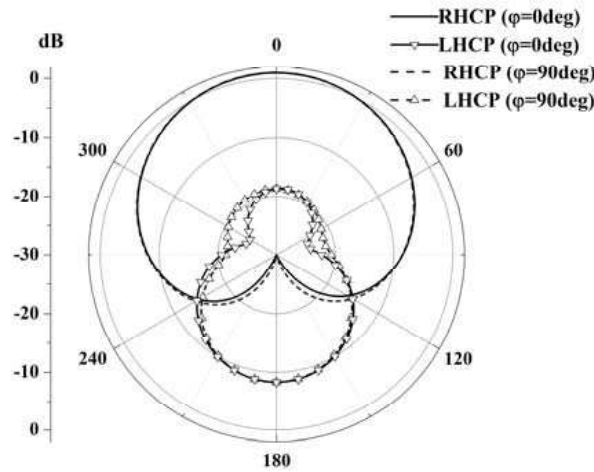


Figure 6: Simulated radiation pattern of antenna in two orthogonal planes at the center frequency.

4. CONCLUSION

A new compact GPS microstrip antenna with low-cost FR4 as substrate has been proposed. The size of the antenna is reduced by cutting the central slot and marginal slits. Coaxial single-probe center feed loaded with microstrip stub is used to achieve impedance matching. The best operating frequency tuning can be achieved by varying the marginal slits. Good antenna characteristics are achieved with a 3-dB axial ratio bandwidth of 15 MHz, and a $|S_{11}| < -15$ dB impedance bandwidth of 40 MHz. The results obtained for the proposed antenna meet the performance specifications for civilian GPS applications.

ACKNOWLEDGMENT

This work was supported by the scientific research project of the department of education of Liaoning province (No. L2012171) and the fundamental research funds for the central universities (No. 3132013052).

REFERENCES

1. Wong, K. L., *Compact and Broadband Microstrip Antenna*, John Wiley & Sons, Inc., New York, 2002.
2. Sharma, P. C. and K. C. Gupta, "Analysis and optimized design of single feed circularly polarized microstrip antennas," *IEEE Trans. Antennas Propag.*, Vol. 31, No. 6, 117–123, Nov. 1983.
3. Chen, W. S., C. K. Wu, and K. L. Wong, "Single-feed square-ring microstrip antenna with truncated corners for compact circular polarization operation," *Electronics Letters*, Vol. 34, No. 11, 1045–1047, May 1998.
4. Wong, K. L. and J. Y. Wu, "Single-feed small circularly polarised square microstrip antenna," *Electronics Letters*, Vol. 33, No. 22, 1833–1834, Oct. 1997.
5. Chen, H. M. and K. L. Wong, "On the circular polarization operation of annular-ring microstrip antennas," *IEEE Trans. Antennas Propagat.*, Vol. 47, No. 8, 1289–1292, Aug. 1999.
6. Nascimento, D. C., R. Schildberg, and J. C. S. Lacava, "Low-cost truncated corner microstrip antenna for GPS application," *Proc. of the 2006 IEEE AP-S International Symposium*, 1557–1560, Albuquerque, NM, USA, Jul. 2006.
7. Heidari, A. A., M. Heyrani, and M. Nakhkash, "A dual-band circularly polarized stub loaded microstrip patch antenna for GPS applications," *Progress In Electromagnetics Research*, Vol. 92, 195–208, 2009.
8. Falade, O., M. Rehman, Y. Gao, X. Chen, and C. Parini, "Single feed stacked patch circular polarized antenna for triple band GPS receivers," *IEEE Trans. Antennas Propag.*, Vol. 60, No. 10, 4479–4484, Oct. 2012.

Solitary Wave Induced in a Water Surface Wave Field

Shigehisa Nakamura
Kyoto University, Japan

Abstract— A problem on solitary wave induced in a water surface wave field, is introduced for obtaining an analytical solution in a manner of mathematics. By this time, it was recorded offshore at the case of the tsunamis generated by the earthquake in 2011 March 11 in the northwest Pacific. Adding to the above, a hydraulic experiment had been confirmed a couple of solitary waves induced in a field of water surface wave field artificially generated in a basin. Then, a problem is raised to solve in a manner of analytical mathematics for the solitary wave in a water surface wave field under the given conditions.

1. INTRODUCTION

This work concerns a certain problem on solitary wave in the water surface wave induced in a water field. This problem could be raised to solve in a manner of applied mathematics for physical science.

By this time, it was recorded offshore at the case of the tsunamis generated by the earthquake on 2011 March 11 in the northwest Pacific by a ocean wave recorder settled on the sea floor for monitoring the ocean water in order to realize the specific property of the ocean water surface waves which have been destructive for the super-tankers' navigation by chance. One of the professors had shown strongly interested in the record of a strange water surface wave at the earthquake under sea. Seismologists had pay a little attention to tsunamis energy in relation to any seismic mechanism.

Adding to the above, a hydraulic experiment had been confirmed a couple of solitary waves induced in a field of water surface wave field artificially generated in a basin.

Now, the problem should be raised to solve in a manner of analytical mathematics for the solitary waves in a water surface wave field under the given condition.

Some part of mechanism for inducing the solitary waves noted above could be realized after obtaining a solution reduced in a mathematical manner in brief.

2. SOLITARY WAVE

As for “solitary wave”, it can be seen what is the basic for seeing “solitary wave”, for example, in the publication by Lamb [1].

In the first edition of “Hydro-Dynamics” written by Lamb [1] must had included the papers presented by McCowan in 1894 [2] and by Korteweg and de-Vries in 1895 [3].

In the waves noted just above in this section, almost all of what are the essential and specific properties of the interested waves named as “solitary waves.”

This solitary wave advancing on a straight line in a canal apriori assumed.

The water in the canal is assumed to be isotropic and homogeneous.

Lamb [1] in 1879 started his publication to describe about the water as an idealized fluid for a linearized water motions.

A sinusoidal water surface wave was considered to be a small-amplitude wave first so that the problem was a linear problem.

Nevertheless, the wave discussed by McCowan [2] and Korteweg de-Vries [3] was not any one of the linear waves.

In this case, it was considered only “solitary wave” under a water depth was constant and a width of the canal was uniform.

Lamb [1] had noted about a decay of “solitary wave” though the viscosity was out of his consideration, though he noted about viscosity of fluid in the other chapter later separately.

3. TSUNAMI WAVE OBSERVED IN OCEAN

The author has to note that a strange case of the water surface variations observed offshore at the earthquake undersea on 2011 March 11 in the northwest Pacific.

In fact, the strange wave was surely generated and propagating in the ocean. The body force to the water at the earthquake must force to be in motion of the water column rom the surface to the bottom.

The leading wave of tsunamis generated by the earthquake had a sharp spike.

The observed data of the tsunami waves was obtained at only one station settled offshore at that time so that no information was seen about any three-dimensional motion of the water surface patterns.

The sharp spike at the head of the leading tsunami waves forced the seismological scientists' wondering at its dynamical understanding because they had not any bit of proper understanding of water motions at the earthquake even after the seismic event was happened offshore. Then, seismologists had tended to adjust the seismic parameters for finding any reasonable understanding of the processes on the water surface undulations.

4. SOLITARY WAVE IN HYDRAULIC EXPERIMENT

Nakamura [4] had ever found "solitary wave" induced in the cyclic water surface wave field.

4.1. Monitoring Water Surface Waves

He used a water basin in an arbitrary scaling to see long water wave transform process in the basin after generating a forced cyclic water surface waves.

What was point to see was box-shape block with a slits.

A barrier with a centered slit was arranged to block the incident water waves, so that his intension was to see the wave crest line should be orthogonally cross the barrier.

The barrier width was limited by the wall on both sides of the barrier ends to form a couple of rectangular corners.

The expected incident water wave with a cyclic period was sinusoidal just in front of the wave generator, nevertheless the water wave passed a centered slit for propagating the wave to the barrier just a waves affected to show a Fresnel diffraction at the first slit just in front of the wave generator.

Then, a couple of solitary waves was induced and established at the two corners.

The couple of the solitary waves at the corners moves to maintain each wave form.

Each one of the solitary waves moves between the corner in front of the barrier.

The two solitary waves meet at the center to pass without any wave form change.

Nakamura [4] had tried to confirm whether the couple of the induced waves could be taken as a kind of "solitary wave". Then, he had confirmed the two waves were under some conditions for fitting to McCowan's limit for the solitary wave (refer to [4]).

These two waves moving simply in a cyclic motion along the barrier.

Then, the barrier acted a part of the canal for the solitary wave (for example, [3]).

The energy loss of the couple of the solitary waves was supported by the part of the incident wave energy, even though the decay must be mainly caused energy dissipation after the viscous effect of the water and by the friction on the boundaries as the floor and as the barrier face. Height of the solitary waves decayed out when the incident wave was cut.

The solitary wave in the cyclic waves generated in the water basin was quite similar to the wave form observed at the earthquake noted above section.

It is pity that there was no information to the conditions around the wave gauge settled on the sea floor at the earthquake. Hence, it is hard here to take the observed leading wave with a spike as a solitary wave in a water surface wave field though its wave form pattern is quite similar to that of the couple of the solitary waves induced in a hydraulic base for water surface waves in the field of hydraulics.

4.2. Instrumentation

The above solitary wave in the water surface waves in the basin was monitored by an electric and electronic signal transfer system with a mechanical actuator which transfer a designed input function of the signal for generating a water wave in the basin through a metallic pipe in a form of a corresponding oil-pressure signal to force and drive a plunger.

4.3. Plunger

The plunger is designed to float in the water basin. Any size and shape could be for a designer's choice, though Nakamura [4] had designed a box-type float made by steel members. It was 7 meters wide, 2 meters long and 0.5 meter high. In order to a stable response to the actuator's forcing oil-pressure under the actuator fixed a cantilever frame work system in a truss structure following the manner in structural engineering standard.

4.4. Actuator

The actuator's forcing along its vertical axis transfer its designed forcing to the floating plunger tied to the actuator.

The final target of this system was to generate the expected design water wave in the basin after a transferred output forcing of the oil-pressure controlled by the actuator as they had done for their operations in the field of mechanical engineering.

What was important to drive the system successfully at a water wave generation in the basin, was the expected response of the plunger to be well following to the signal of the output function in a stable manner in motion.

4.5. Input Function

The most important part for designing this system was to design the input function for transfer the signal to the actuator generate the expected water waves in the basin.

4.6. Feedback

It is usual to control any output signal when an input function is designed. Nevertheless, in Nakamura's case [4], the time lag of the signal was very long so that its delay caused an disagreeable response of water motion in the basin in the early stage of his experiment. Then, the writer had to adjustment of the input function design at first on the bases of the mathematical and dynamical consideration in the fields of engineering technologies. The properly adjusted output function was completed in a finalized form on a disc of the transparent plate made by plastic after his skilled minor adjustment technique.

As for the input function, it was determined with consideration of a lubrication effect of the oil for the actuator and of a viscous effect of a water for experiment in the basin after some minor adjustments for energy balance maintaining during the experiment.

5. SOLITARY WAVE IN A WATER WAVE FIELD

Now, it is necessary to clearly describe what problem should be raised.

The spike in the leading wave of the tsunamis in the ocean and a couple of the solitary waves induced in a water surface wave field in a water basin are governed by the equation of motion for the theory in hydrodynamics.

Then, a problem to be raised could be described as that a solitary wave or a couple of the solitary waves should have a solution in a form of an applied mathematics under a certain boundary condition.

When the solution is obtained, it is clarified what mechanism is contributive for the induced solitary wave or waves.

6. CONCLUSIONS

A problem is raised for realizing a solitary wave or a couple of the solitary waves could be obtained in a form of a solution in a manner of applied mathematics.

Then, what is mechanism of inducing the solitary wave or a couple of the solitary waves in the water surface wave field.

REFERENCES

1. Lamb, H., *Hydro-Dynamics*, 6th Edition in 1932 (the First Edition in 1879), Cambridge University Press, 1932.
2. McCowan, J., "On the highest wave of permanent type," *Philosophical Magazine*, Ser. 5, Vol. 38, 351–358, 1894.
3. Korteweg, D. J. and G. de Vries, "On the change of form of long waves advancing in a rectangular canal and on a new type of long stationary waves," *Philosophical Magazine*, Ser. 5, Vol. 39, 422–443, 1895.
4. Nakamura, S., "Nonlinear lateral oscillation in a harbor model," *Proceedings of Symposium on Modeling techniques*, American Society of Civil Engineers, San Francisco, California, 836–853, 1975.

Chaotic FM Signals for Circular SAR Imaging

Lingjuan Yu¹, Xiaochun Xie², and Lingling Xiao¹

¹Jiangxi University of Science and Technology, Ganzhou 341000, China

²Gannan Normal University, Ganzhou 341000, China

Abstract— Noise radar has low probability of intercept and high resistance to electronic countermeasures, and has the ability of non-ambiguous measurement of range and velocity. Circular SAR (CSAR) has high two-dimensional (2D) ground range resolution and a certain three-dimensional (3D) imaging capability. The combination between noise radar and CSAR can achieve the complementary strengths, which has significance for target detection and high resolution imaging. In this paper, Ulam mapping chaotic frequency modulation (FM) signal is used as the transmitted signals for 2D and 3D CSAR imaging. All imaging results are compared with other imaging results when the transmitted signals are chirp and Ulam mapping chaotic amplitude modulation (AM) signals respectively. Simulation results of point-target show that when the transmitted signal is Ulam mapping chaotic FM signal, 2D and 3D resolution are higher and side-lobes except integral sidelobe ratio in height are lower than results of other two kinds of transmitted signals, because the effective bandwidth of Ulam mapping chaotic FM signal is wider than chirp and Ulam mapping chaotic AM signals. In addition, Ulam mapping chaotic AM and FM signals for CSAR imaging have stronger anti-interference ability than chirp signal.

1. INTRODUCTION

Noise radar has low probability of intercept and high resistance to electronic countermeasures, which improves the ability of radar to survive in a complex environment. The ambiguity function of ideal noise signal has an approximate thumbtack shape, which makes noise radar with the ability of non-ambiguous measurement of range and velocity. Because of these excellent features, noise radar has broad application prospects in the military and civilian areas. In circular synthetic aperture radar (CSAR) mode, both two-dimensional (2D) high resolution image and three-dimensional (3D) image of targets can be obtained because of the complete 360 degree synthetic aperture. The combination between noise radar and CSAR can achieve the complementary strengths, which has significance for target detection and high resolution imaging.

In this paper, Ulam mapping chaotic frequency modulation (FM) signal is used as the transmitted signals for CSAR imaging. All these 2D and 3D imaging results and anti-interference ability are compared with other results when the transmitted signals are chirp and Ulam mapping chaotic amplitude modulation (AM) signals respectively. The rest of this paper is organized as follows. In Section 2, the model of Ulam mapping chaotic FM signal is introduced. In Section 3, the echo model of CSAR is illustrated. In Section 4, analysis of anti-noise performance is introduced. Simulation results are shown in Section 5. Finally, Section 6 concludes the paper.

2. THE MODEL OF ULAM MAPPING CHAOTIC FM SIGNAL

The commonly used chaotic mappings are Bernoulli mapping, Tent mapping, Logistic mapping, and so on. Here, a special case of Logistic mapping, Ulam mapping, is considered. It can be expressed by,

$$x_{n+1} = 1 - 2x_n^2, \quad x_n \in (-1, 1) \quad (1)$$

Ulam mapping signal is called modulating signal, and the expression of frequency modulation is,

$$s(t) = \exp \left(j2\pi \Delta f \int_{-\infty}^t \xi(\tau) d\tau \right) \quad (2)$$

where Δf is frequency offset, and $\xi(t)$ is Ulam mapping chaotic AM signal, which can be written as,

$$\xi(t) = \sum_{n=0}^{N-1} x_n g(t - nT) \quad (3)$$

where x_n is the n th of Ulam mapping sequences of length N , and $g(t)$ is pulse signal of time width T . So, the time width of $\xi(t)$ is $T_N = NT$. When $t \in [nT, (n+1)T]$, the expression of Ulam mapping chaotic FM signal is,

$$s(t) = \exp \left[j2\pi\Delta f \left(T \sum_{i=0}^{n-1} x_i + x_n(t - nT) \right) \right] \quad (4)$$

The discrete model of (4) is,

$$s(nT) = \exp \left[j2\pi\Delta f T \left(\sum_{i=0}^n x_i \right) \right] \quad (5)$$

From (5), the instantaneous frequency is $f(n) = x_n \cdot \Delta f$. Because $x_n \in (-1, 1)$, the instantaneous frequency range is $-\Delta f \leq f \leq \Delta f$. According to Nyquist sampling theorem, $1/T \geq 2\Delta f$ is obtained. Suppose $1/T = 2\Delta f$, then Equation (5) is simplified as,

$$s(n) = \exp \left[j\pi \left(\sum_{i=0}^n x_i \right) \right] \quad (6)$$

3. THE ECHO MODEL OF CSAR

In CSAR mode, radar platform travels around targets in a circular trajectory, which is different from the traditional linear SAR mode. The CSAR system model for data acquisition is shown in Fig. 1(a). Its top view and side view are shown in Figs. 1(b) and (c), respectively.

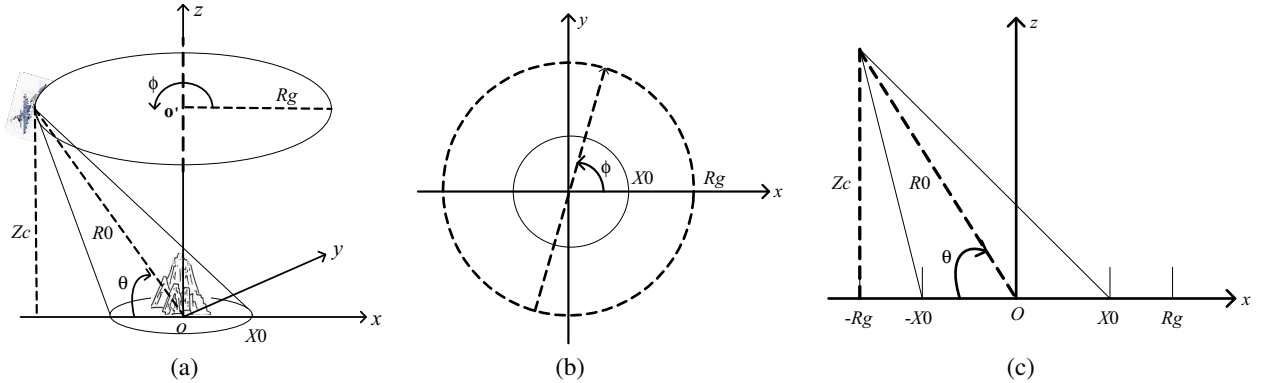


Figure 1: (a) Geometry of CSAR system. (b) Top view. (c) Side view.

From Fig. 1, the radar height is Z_c , and the flight radius is R_g . Denote radar azimuthal angle as $\phi \in [0, 2\pi)$, and denote the transmitted radar signal as $p(t)$. The reflectivity function of 3D target is defined as $f(x, y, z)$. Then the received echo signal can be given by,

$$s(t, \phi) = \int_z \int_y \int_x f(x, y, z) p \left[t - 2\sqrt{(x - R_g \cos \phi)^2 + (y - R_g \sin \phi)^2 + (z - Z_c)^2} / c \right] dx dy dz \quad (7)$$

where t is fast-time, and c is light speed. For 2D target, we only need to set $z = 0$ in Equation (7).

4. ANALYSIS OF ANTI-NOISE PERFORMANCE

In order to describe noise intensity, the input signal to noise ratio is defined as $\text{SNR}_{in} = 10 \log_{10}(P_{S_{in}}/P_{N_{in}})$, where $P_{S_{in}}$ is the power of echo signal, and $P_{N_{in}}$ is the power of noise. Noise interference belongs to barrage jamming. The equivalent number of looks (ENL) and correlation coefficient of SAR image are adopted in order to evaluate barrage jamming.

(1) ENL

$$\text{ENL} = \frac{\mu}{\sigma} \quad (8)$$

where μ is the statistical average value of a gray image, and σ is the standard deviation. ENL reflects contrast of a gray image, and large ENL means small image contrast and ambiguous image.

(2) Correlation coefficient

Denote a gray image without noise as $f(m, n)$, where m and n are respectively the numbers of row and column of the image. If it is interrupted by noise, then the image with noise is denoted as $g(m, n)$. The correlation coefficient ρ of these two images is,

$$\rho = \frac{\sum_m \sum_n f(m, n)g(m, n)}{\left[\sum_m \sum_n f^2(m, n) * \sum_m \sum_n g^2(m, n) \right]^{1/2}} \quad (9)$$

The correlation coefficient reflects the degree of deterioration of the image before and after interference. The large ρ means small noise interference. The value range of ρ is $0 \sim 1$.

5. SIMULATION

(1) 2D point target imaging

The CSAR system parameters are listed in Table 1. A 2D point target is located in the center of the scene. The back projection algorithm is used in imaging. When three kinds of signals including chirp, Ulam mapping chaotic AM, and Ulam mapping chaotic FM signals are transmitted, 2D imaging results are respectively shown in Figs. 2(a)–(c), and the x and y profiles of 2D imaging results are respectively shown in Figs. 3(a)–(b).

From Fig. 2 and Fig. 3, we can know that 2D imaging results are regular when the transmitted signal is chirp, while 2D imaging results are stochastic when the transmitted signal are Ulam mapping chaotic AM and FM. However, experiments can be repeated many times to obtain statistical values of resolution and sidelobes for Ulam mapping chaotic AM and FM signals. Imaging results show that when the transmitted signal is Ulam mapping chaotic FM, higher resolution and lower peak to sidelobe ratio (PSLR) and integrated sidelobe ratio (ISLR) in x and y profiles can be obtained than other two cases. The main reason is that the bandwidth of Ulam mapping chaotic FM signal is wider than other two kinds of signals.

Table 1: The CSAR system parameters.

Carrier frequency	10 GHz
Bandwidth of Chirp and chaos AM signal	4 GHz
Radius of the flight track	200 m
Height of the radar	200 m
Radius of imaging area	1 m

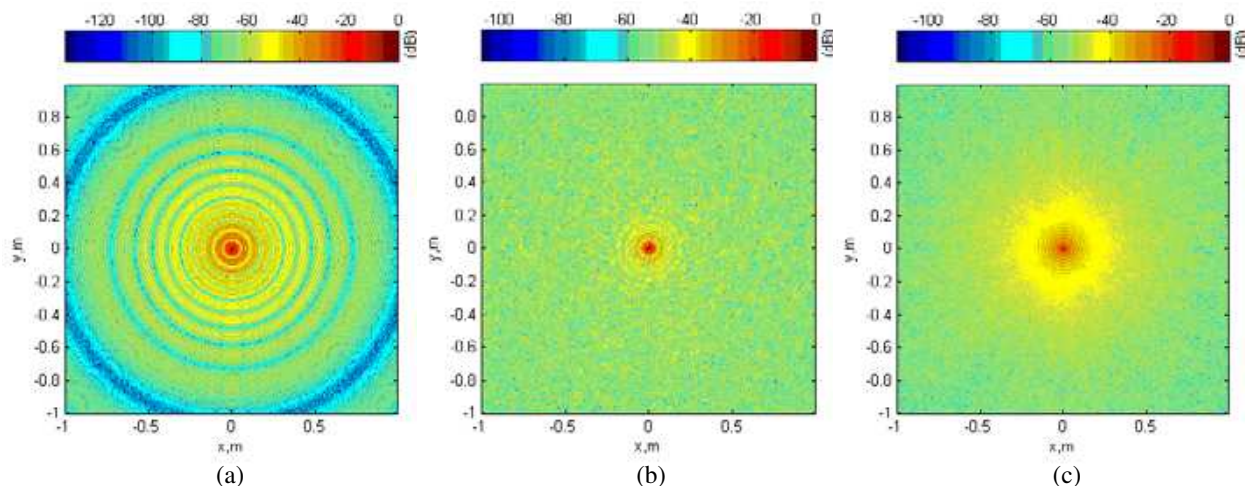


Figure 2: 2D imaging results of three kinds of transmitted signals. (a) Chirp. (b) Ulam mapping chaotic AM. (c) Ulam mapping chaotic FM.

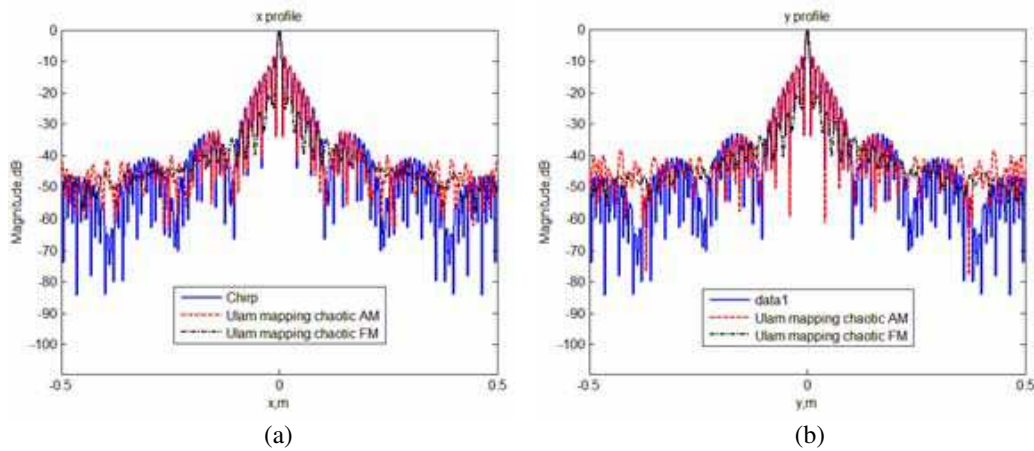


Figure 3: The x and y profiles of 2D imaging results of three kinds of transmitted signals. (a) x profile. (b) y profile.

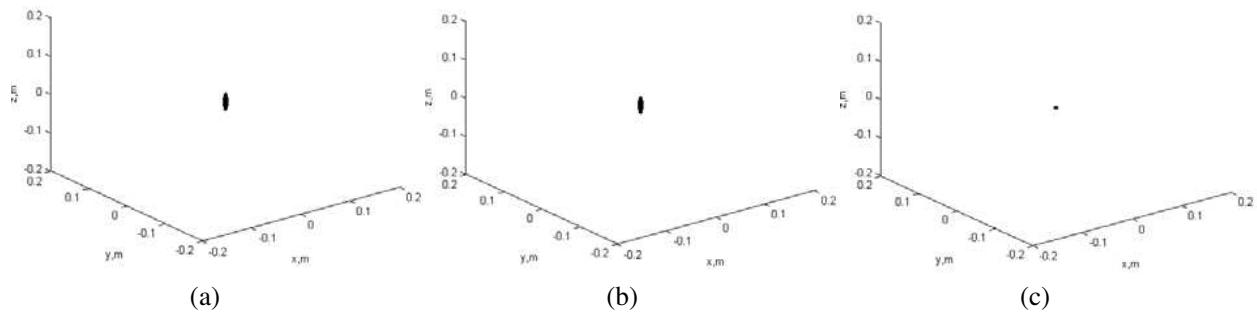


Figure 4: 3D imaging results of three kinds of transmitted signals. (a) Chirp. (b) Ulam mapping chaotic AM. (c) Ulam mapping chaotic FM.

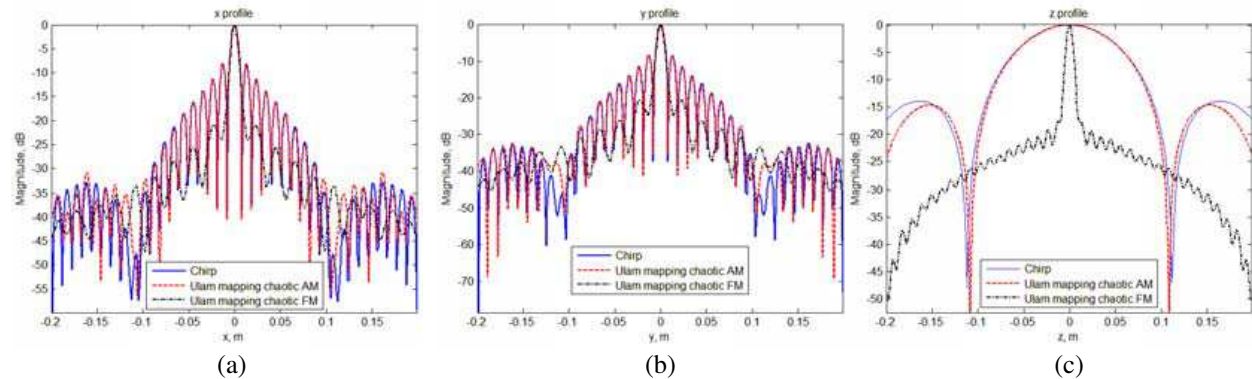


Figure 5: The x , y and z profiles of 3D imaging results of three kinds of transmitted signals. (a) x profile. (b) y profile. (c) z profile.

(2) 3D point target imaging

The CSAR system parameters are listed in Table 1. A 3D point target is located in the center of the scene. The back projection algorithm is used in imaging. When three kinds of signals including chirp, Ulam mapping chaotic AM, and Ulam mapping chaotic FM signals are transmitted, 3D imaging results are respectively shown in Figs. 4(a)–(c). The x , y and z profiles of 3D imaging results are respectively shown in Figs. 5(a)–(c).

The same as the 2D imaging, experiments are repeated many times to obtain statistical values of resolution and sidelobes for Ulam mapping chaotic AM and FM signals. Imaging results show that when the transmitted signal is Ulam mapping chaotic FM, higher resolution and lower PSLR and ISLR in x and y profiles can be obtained than other two cases. Higher resolution and lower

PSLR can also be obtained except higher ISLR than other two cases. The main reason is also the wide bandwidth of Ulam mapping chaotic FM signal.

(3) Analysis of anti-noise performance

Based on 2D point target imaging, Figs. 2(a)–(c) are changed into gray images, and the corresponding results are noiseless. If Gauss white noise is added to three kinds of echo signals, and the input signal to noise ratio SNR_{in} is equal to -40 dB, then 2D imaging results with this noise interference are obtained.

Repeat experiments 50 times. The statistical values of ENL and correlation coefficients for three kinds of echo signals without and with noise jamming are listed in Table 2. It is obvious that when the transmitted signals are Ulam mapping chaotic AM and FM, the change of ENL is smaller than the case of chirp signal. On the other side, when the transmitted signals are Ulam mapping chaotic AM and FM, the correlation coefficients are larger than the case of chirp signal. Small change of ENL and large correlation coefficients mean that when the transmitted signals are Ulam mapping chaotic AM and FM, the corresponding 2D imaging results are not sensitive to noise. It proves that noise radar has high resistance to noise jamming.

Table 2: The statistical values of ENL and correlation coefficients.

		Chirp	Ulam mapping chaotic AM	Ulam mapping chaotic FM
ENL	Without noise	0.201	0.538	0.615
	With noise	1.889	1.903	1.908
ρ		0.247	0.457	0.491

6. CONCLUSION

In this paper, Ulam mapping chaotic FM signal is presented for CSAR imaging. In order to illustrate the performance of this transmitted signal, Ulam mapping chaotic AM signal and chirp signal are used for comparison. Simulation results of point-target show that when the transmitted signal is Ulam mapping chaotic FM signal, 2D and 3D resolution are higher and side-lobes except integral sidelobe ratio in height are lower than results of other two kinds of transmitted signals, because of the wider effective bandwidth. In addition, Ulam mapping chaotic AM and FM signals for CSAR imaging have stronger anti-interference ability than the case of chirp signal.

REFERENCES

1. Soumekh, M., *Synthetic Aperture Radar Signal Processing with MATLAB Algorithms*, Wiley, New York, 1999.
2. Cantalloube, H. M. J., E. Colin-Koeniguer, and H. Oriot, "High resolution SAR imaging along circular trajectories," *IEEE International Geoscience and Remote Sensing Symposium*, 2007.
3. Axelsson, S. R. J., "Random noise radar/sodar with ultrawideband waveforms," *IEEE Transactions on Geoscience and Remote Sensing*, Vol. 5, 1099–1114, 2007.
4. Lukin, K. A. and R. M. Narayanan, "Historical overview and current research on noise radar," *IEEE International Asia-Pacific Conference on Synthetic Aperture Radar*, 2011.

Compact Microstrip Diplexer for 4G Wireless Communication

Fangqi Yang¹, Xuehui Guan¹, Lei Zhu², and Haiwen Liu¹

¹School of Information Engineering, East China Jiaotong University, Nanchang 330013, China

²Faculty of Science and Technology, University of Macau, Macau SAR, China

Abstract— A novel compact microstrip diplexer for 4G wireless communication system is proposed. The diplexer is composed of two stub-loaded dual-mode resonators (SLDMRs). The main advantage of stub-loaded dual-mode resonator is that a compact narrowband bandpass filter is easily realized and a transmission zero can be realized in the stopband of each channel, which improves the isolation between two channels. Two SLDMRs are then connected to a common port by the feed lines with two long fingers. Coupling scheme of the diplexer is given and analyzed. The diplexer is in final designed at 2.35 and 2.59 GHz for 4G wireless communication. The circuit is compact and occupies about $0.33\lambda_g \times 0.25\lambda_g$.

1. INTRODUCTION

Diplexer is an essential component in the RF front ends of communication system, which is used to transmit and receive signals by a single antenna in communication system. As a newly commercialized mobile communication system, 4G wireless mobile communication is a new emerge technique that can provide high-speed data service for subscribers. Researchers show great interests in developing high performance components for 4G wireless mobile communication systems, such as antennas, filters, and diplexers. A diplexer can be designed by combining two different bandpass filters with a matching network. In [1], a hairpin line diplexer is realized by using stepped-impedance coupled-line resonators. In [2], a diplexer for ultra-wideband systems is proposed using hairpin line wideband bandpass filters. An extra tapped open-stub is added to suppress the spurious responses of the first bandpass filter in the operating range of second filter. In [3] and [4], hybrid resonators and composite right/left-handed (CRLH) quarter-wave type resonators are used to design diplexers. However, the resonators require short-circuit through-holes that results in higher fabrication costs and errors. T-junction is usually used as matching network in a diplexer [3, 5]. Despite of the convenience of design, but the size of the diplexer is large. In [6] a diplexer for UMTS system using dual-mode stripline ring resonators is proposed.

In this paper, a novel diplexer for 4G communication systems is proposed based on two stub-loaded dual-mode resonators (SLDMR) with different sizes. Owing to the quarter-wavelength resonance of the loaded stub, each SLDMR will produce a transmission zero near the passband. Another transmission zero is produced by introducing the coupling between source and load, aiming to improve the isolation of the diplexer. Finally, a diplexer with a compact size operating in the 2.35/2.59 GHz band for 4G communication system is designed. The circuit size is about $0.33\lambda_g \times 0.25\lambda_g$. Simulated results show the isolation between two passband is -29 dB and -38 dB, respectively.

2. ANALYSIS OF THE STUB-LOADED DUAL-MODE RESONATOR

Figure 1 shows schematic of the proposed diplexer. The diplexer consists of two stub-loaded dual-mode resonators and three microstrip feed lines. SLDMR are folded to achieve a compact size. Two DMRs are interconnected by an appropriately designed microstrip junction with characteristic impedance of $50\ \Omega$, thus avoiding the conventional matching circuit of T-junction [2].

The basic configuration of a SLDMR in show in Fig. 2, where Y_1 , L_1 , Y_2 and L_2 denote the characteristic admittances and lengths of the microstrip line and open stub, respectively. Odd- and even-mode theory is used to analysis its resonant characteristics [7].

When the structure is excited by odd-modes, the symmetrical plane can be seen as short-circuited and the resonant frequencies can be expressed as

$$f_{odd} = \frac{(2n-1)c}{2L_1\sqrt{\epsilon_{eff}}} \quad (1)$$

where $n = 1, 2, 3, \dots$, c is the speed of light in the free space, and ϵ_{eff} is the effective dielectric constant of the microstrip line. Obviously, the odd-mode resonant frequencies are determined only by the open ring resonator.

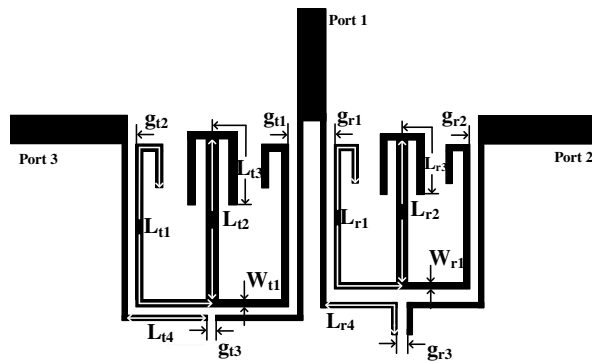


Figure 1: The schematic of the proposed diplexer.

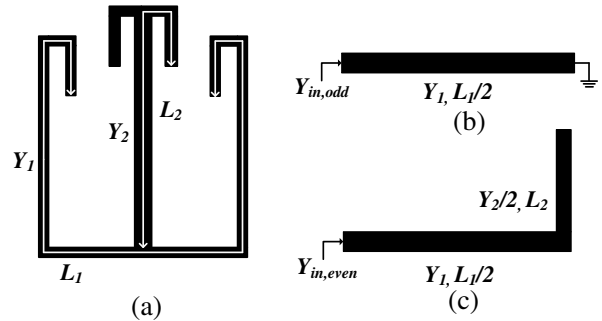


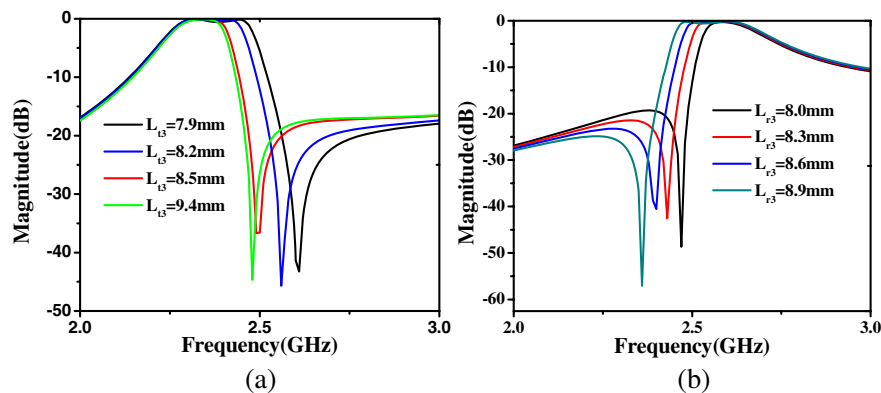
Figure 2: (a) Structure of the stub-loaded DMR, (b) odd-mode equivalent circuit, and (c) even-mode equivalent circuit.

When the structure is excited by even-modes, the symmetrical plane can be seen as open-circuited and the resonant frequencies can be determined by

$$f_{even} = \frac{nc}{(L_1 + 2L_2)\sqrt{\epsilon_{eff}}} \quad (2)$$

where $n = 1, 2, 3, \dots$. It is clearly observed that once L_1 is determined, the even-mode will vary with the length of the open stub.

Figure 3 shows transmission characteristics of the dual-mode resonators. A transmission zero can be achieved owing to quarter-wavelength resonance of the loaded stub. As to the resonator works at the lower passband, the transmission zero is set in the upper stopband, obtaining to decrease the interference with the upper passband. On the contrary, as to the dual-mode resonator works at upper passband, the transmission is set in the lower stopband, aiming to minimize the interference from the lower passband. Obviously, the position of the transmission zero can be tuned by changing the length of the loaded stub and the bandwidth of the circuit also change with the shift of the transmission zero.

Figure 3: Simulated responses of (a) SLDMR 1 versus L_{t3} when $L_{r3} = 8.9$ mm and (B) SLDMR 2 versus L_{r3} when $L_{t3} = 7.9$ mm.

3. ANALYSIS OF THE PROPOSED DIPLEXER

Figure 4 shows the coupling scheme of the proposed diplexer, where the solid lines indicate the main coupling and the dashed lines indicate the cross coupling, black dot and white dot represent resonant modes and source/load, respectively. Both modes of SLDMR are directly coupled to both source and load. Coupling between source and load is introduced in each channel by increasing the length of the feed lines. By use of source-load coupling, transmission zeroes can be introduced in the stopband, which improves the stopband characteristics while keep the transmission characteristics stable in the passband [8,9]. The length of the feed lines L_{t4} between port1 and port2, and L_{r4} between

port1 and port3 are extended, aiming to introduce direct source-load coupling. Meanwhile, isolation between the two channels of the diplexer is improved. Fig. 5 shows comparisons of transmission characteristics between the diplexer with and without source-load coupling. It is obviously seen that the attenuation of S_{21} improved about 8 dB in the stopband and the attenuation of S_{31} improved about 20 dB in the stopband when the coupling between source and load is introduced.

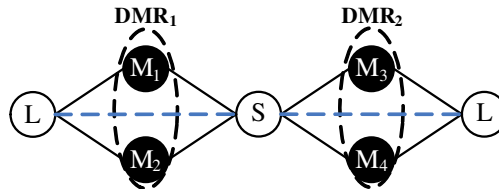


Figure 4: Coupling scheme of the proposed diplexer.

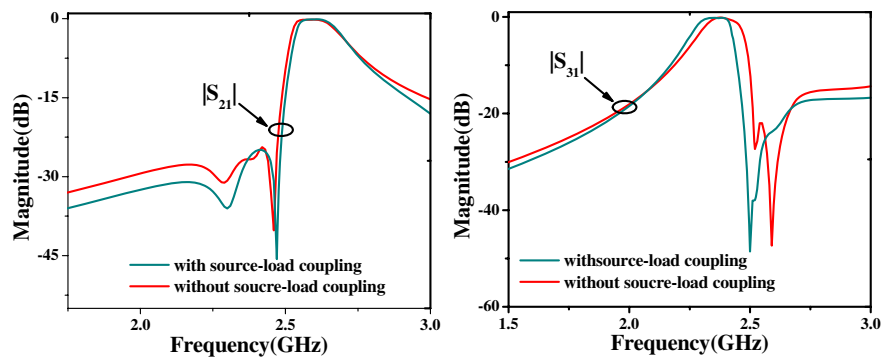


Figure 5: The frequency response of the proposed diplexer compared with the diplexer without source-load coupling.

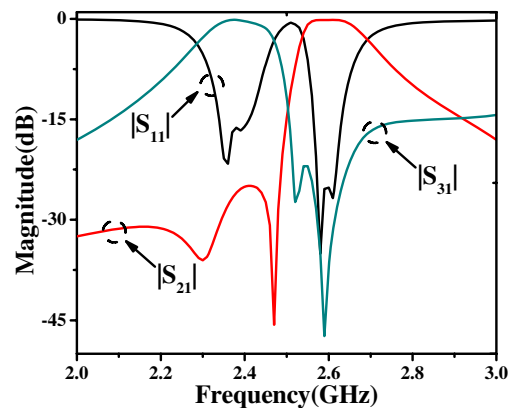


Figure 6: The frequency response of the proposed diplexer.

The simulated results of the proposed diplexer are shown in Fig. 6. A substrate with a dielectric constant of 3.5 and a thickness of 0.8 mm is used in the design. Associated dimensions are: $W_{t1} = W_{r1} = 0.4$ mm, $L_{t1} = 19.5$ mm, $L_{r1} = 21.3$ mm, $L_{t2} = 9.85$ mm, $L_{r2} = 10$ mm, $L_{t3} = 9$ mm, $L_{r3} = 8.2$ mm, $L_{t4} = 5.1$ mm, $L_{r4} = 6.9$ mm, $g_{t1} = g_{t2} = 0.4$ mm, $g_{r1} = g_{r2} = 0.35$ mm, $g_{t3} = 1.7$ mm and $g_{r3} = 1.75$ mm. The diplexer designed for 4G communication system operates in 2.35/2.59 GHz and the simulated 3-dB bandwidths of the two channels are 6.89% and 6.56%, respectively. The simulated isolations between port2 and port3 are below -30 dB. The circuit is very compact and it occupies about 23.5 mm \times 13.5 mm.

4. CONCLUSIONS

A compact microstrip diplexer using stub-loaded dual-mode resonators is proposed in this paper. The main advantage of the DMR is that a compact bandpass filter with an asymmetric frequency response is easily realized. The bandpass isolation is improved by introducing the source-load coupling. This property is utilized to design a compact high selectivity diplexer, for a system with two extremely close frequency bands. The proposed design offers a simple structure, which allows design flexibility and ease of fabrication.

REFERENCES

1. Srisathit, S., S. Patisang, R. Phromloungsri, S. Bunnjaweht, S. Kousulvit, and M. Chongcheawchamnan, "High isolation and compact size microstrip hairpin diplexer," *IEEE Microw. Wireless Compon. Lett.*, Vol. 15, No. 2, 101–103, Feb. 2005.
2. Weng, M. H., C. Y. Hung, and Y. K. Su, "A hairpin line diplexer for direct sequence ultra-wideband wireless communications," *IEEE Microw. Wireless Compon. Lett.*, Vol. 17, No. 7, 519–521, Jul. 2007.
3. Yang, T., P. L. Chi, and T. Itoh, "High isolation and compact diplexer using the hybrid resonators," *IEEE Microw. Wireless Compon. Lett.*, Vol. 20, No. 10, 551–553, Oct. 2010.
4. Yang, T., P. L. Chi, and T. Itoh, "Compact quarter-wave resonator and its application to miniaturized diplexer and triplexer," *IEEE Trans. Microw. Theory Tech.*, Vol. 59, No. 2, 260–269, Feb. 2011.
5. Djoumessi, E. E., "Compact packaged diplexer based on highly selective dual-mode bandpass filter," *IEEE Microw. Mag.*, Vol. 12, No. 1, 89–93, Feb. 2011.
6. Xu, W.-Q., M.-H. Ho and C.G. Hsu, "UMTS diplexer design using dual-mode stripline ring resonators," *IEEE Electronics Lett.*, Vol. 43, No. 13, 721–722, Jun. 2007.
7. Zhang, X. Y., J.-X. Chen, Q. Xue, and S.-M. Li, "Dual-band bandpass filters using stub-loaded resonators," *IEEE Microw. Compon. Lett.*, Vol. 17, No. 8, 583–585, Aug. 2007.
8. Zhou, M., X. Tang, and F. Xiao, "Compact dualband bandpass filter using novel E-type resonators with controllable bandwidths," *IEEE Microw. Wireless. Compon. Lett.*, Vol. 18, No. 12, Dec. 2008.
9. Mokhtaari, M., J. Bornemann, and S. Amari, "Quasi-elliptic dual-band filter design using stepped-impedance resonators and coupling topologies for narrow-towide band applications," *IET Microw. Antennas Propag.*, Vol. 2, No. 8, 863–870, Feb. 2008.

A High Gain Slot Antenna Based on Surface Plasmon Polaritons

Hongjuan Han, Huiping Guo, Xueguan Liu, and Ying Wang

School of Electronic Information Engineering, Soochow University, Suzhou, China

Abstract— Surface Plasmon Polaritons (SPPs) have been attracting the interest of microwave technology researchers recently because of the the property of near-field enhancement. In this paper, firstly, we discuss the existence of SPPs in the surface of metal in microwave regime. We also analysis the motivation of SPPs. Secondly, we introduce a high gain slot antenna with single-layer director briefly. Thirdly, a four-layered slot antenna with compact size and high gain is proposed. This antenna is based on the previous antenna. The difference between them is that a dielectric grid structure is added to the last one. The dielectric grid structure makes the incident electromagnetic wave scattered, which makes the wave vector of the incident electromagnetic matched with the surface plasmon polaritons in horizontal direction, so that the incident electromagnetic wave can couple with SPPs. The simulated gain of the previous antenna is 12.0 dBi at 5.6 GHz and measured gain is 10.4 dBi at 5.57 GHz. The simulated gain of the last antenna is 13.5 dBi at 5.6 GHz and measured gain is 11.4 dBi at 5.57 GHz. The 2 dBi dropped for the measured and simulated gain can be caused by the loss of dielectric. By motivating SPPs, the simulated and measured gain of the antenna enhances nearly 1.5 dBi and 1 dBi separately. The overall size of both the antenna is $100 \times 100 \times 19 \text{ mm}^3$.

1. INTRODUCTION

Antennas for wireless communications are required to exhibit characteristics such as high gain, compact size, high efficiency, low cost, wide bandwidth and so on. In the design processing, many methods can be used to improve the antenna gain. Among them, the typical high gain antenna is the traditional Yagi antenna and novel microstrip Yagi antenna. However, in order to realize a gain of 12 dBi, 10 directors are required in [1]. Several microstrip-Yagi or quasi-Yagi antenna structures have been reported in [2–5], which have high gain and high front-to-back (F/B) ratio. However, these antennas have narrow bandwidth and large size. Recently, the multilayer-stacked Yagi antenna is becoming hot research in the miniaturization and high gain antenna. A multilayer-stacked microstrip Yagi antenna is presented in [6], High gain of 11 dBi and 10.28 dBi can be achieved respectively with adopted four layers of directors for dipole and dual polarization applications. Obviously there is an increased demand of antennas with compact size, broad bandwidth and high gain. In this paper, firstly, a miniaturized high gain slot antenna with single-layer director is presented, which has the properties of wide bandwidth, high gain and compact size. Secondly, referred to the first one, a novel high gain slot antenna based on the SPPs theories and features is proposed.

The proposed antennas are designed at 5.6 GHz and detailed discussion is given in the following sections.

2. THE THEORY OF SPPS

The surface plasmon polaritons (SPPs) are transverse magnetic surface waves propagating along the interface between two materials whose dielectric constants are opposite, generally a metal and dielectric [7]. SPPs are attenuating exponentially in the direction perpendicular to the surface. This is the electromagnetic mode of SPPs. The dispersion relation can be obtained by Maxwell's Equation and boundary condition [8].

$$E = E_0^\pm \exp(i(k_x x \pm k_z z - \omega t)) \quad (1)$$

with “+” for $z > 0$, “−” for $z \leq 0$ and with imaginary k_z which causes the field E_z damping exponentially. Suppose electromagnetic wave has wave number k and it is incident to an interface between dielectric (permittivity ε_1) and metal (permittivity ε_2). The wave number k is

$$k = 2\pi/\lambda \quad (2)$$

where λ is the wavelength of electromagnetic wave. According to Maxwell's Equation and the boundary condition at the surface, the normal component of the wave vectors satisfy the following

relations,

$$\frac{k_{z1}}{\varepsilon_1} + \frac{k_{z2}}{\varepsilon_2} = 0 \quad (3)$$

$$\varepsilon_i \left(\frac{\omega}{c} \right)^2 = k_x^2 + k_{zi}^2 \quad i = 1, 2 \quad (4)$$

The wave vector k_x of surface plasmon is continuous through the interface. The dispersion relation can be written as

$$k_x = k_{spp} = \frac{\omega}{c} \left(\frac{\varepsilon_1 \varepsilon_2}{\varepsilon_1 + \varepsilon_2} \right)^{1/2} = k_0 \left(\frac{\varepsilon_1 \varepsilon_2}{\varepsilon_1 + \varepsilon_2} \right)^{1/2} \quad (5)$$

In the microwave regime, the permittivity of metal $\varepsilon_2 < 0$, $|\varepsilon_2| \gg 1$, $|\varepsilon_1 + \varepsilon_2| < |\varepsilon_2|$, thus, $k_{spp} > k_0$. Because of $k_{spp} > k_0$, the wave vector of the electromagnetic is not matched with the surface plasmons in horizontal direction, so that SPPs can't be excited. To excite surface plasmons, the wave vector of the electromagnetic must be matched with the surface plasmons in horizontal direction. In the visible and infrared frequency ranges, the typical method of realizing the coupling is using the diffraction of the metal or dielectric grid structures [9]. Comparing metal grid structures with dielectric grid structures, it is found that dielectric grid structures have better performance in enhancing the electromagnetic field and is more readily produced for industrial applications [10, 11].

In the microwave regime, SPPs do not exist in smooth metal surface. However, when there are periodic slits on the conductor, its Permittivity function is identified with SPPs in form by the equivalent medium processing [12].

3. PROPOSED SLOT ANTENNA WITH SINGLE LAYER DIRECTOR

The preliminary structure of the slot antenna with single-layer director as shown in Fig. 1 and Fig. 2, is named design 1, which contains a radiated slot on the metal plane called driver, a ground called reflector and a slot array in a metal plane called director. As noted in [6], three to four layers of directors are required to achieve high gain. Only one director layer is required to achieve a gain as high as shown in [6]. Dimensions of this structure are given in Table 1. The driver is designed on a 1.5 mm-thick FR4 substrate with dielectric constant (ε_{r1}) of 4.4 and the director is designed on the substrate with ε_{r2} of 2.55 and loss tangent of $\delta = 0.001$. The optimized distance between two slots is 13.75 mm, which is close to $\lambda/4$. The size of the director layer is $60(L) \times 60(L)$ mm² and the distance from the director to the driver is D_2 . All the parameters are listed in Table 1, where $D_1 = 11.5$ mm (0.205λ), $D_2 = 6$ mm (0.121λ), $L_2 = 38$ mm (0.709λ), $L_3 = 55$ mm (1.026λ) and $L_4 = 13.75$ mm (0.257λ). The overall height of the proposed antenna is 19 mm.

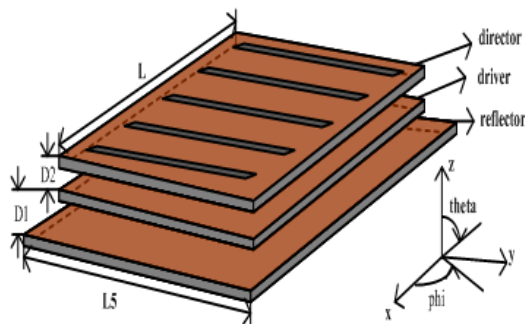


Figure 1: Structure of the proposed antenna (design 1).

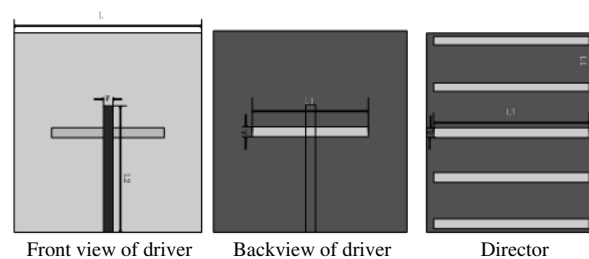


Figure 2: Structures of the proposed single layer director.

Performance of the proposed slot antenna with single-layer director is given in Fig. 3, Fig. 4 and Fig. 5. Photograph of the fabricated preliminary structure and the proposed slot antenna with single layer director is given in Fig. 3. Comparison between simulated and measured results is shown in Fig. 4 and Fig. 5. As shown in Fig. 4, the proposed slot antenna with five slots in the single-layer director has a simulated bandwidth of 21.1% and measured bandwidth of 19.6%, which exhibit wide band characteristics. Fig. 5 presents the simulated and measured xoy plane and $yo z$ plane radiation patterns of design 1. The main lobe focuses on the orthogonal direction of the director layer ($\theta = 0^\circ$). Good agreement between the measured and simulated radiation

Table 1: Parameters of antenna.

Symbol	Value	Unity
H	1.5	mm
L	60	mm
$L1$	36	mm
$L2$	38	mm
$L3$	55	mm
$L4$	13.75	mm
$L5$	100	mm
W	3	mm
$D1$	11.5	mm
$D2$	6.5	mm
ϵ_{r1}	4.4	/
ϵ_{r2}	2.5	/

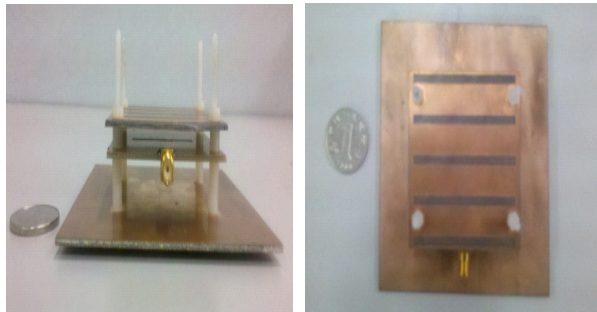
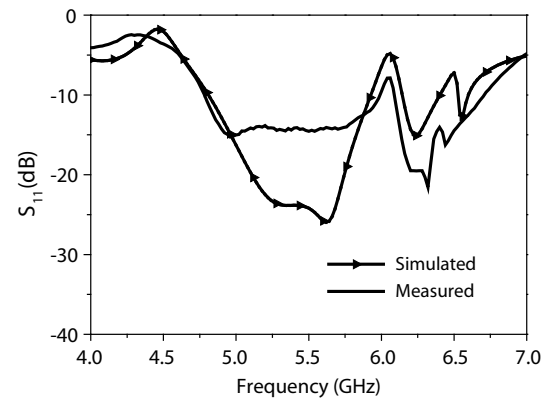
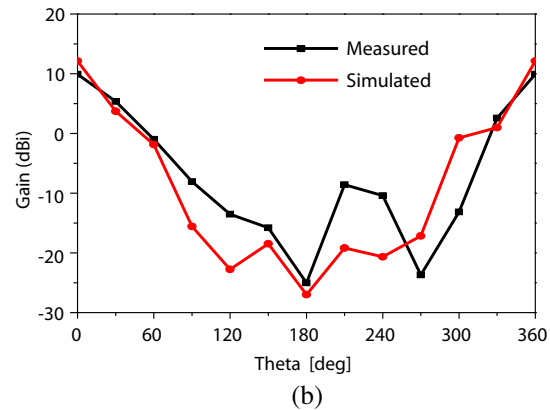
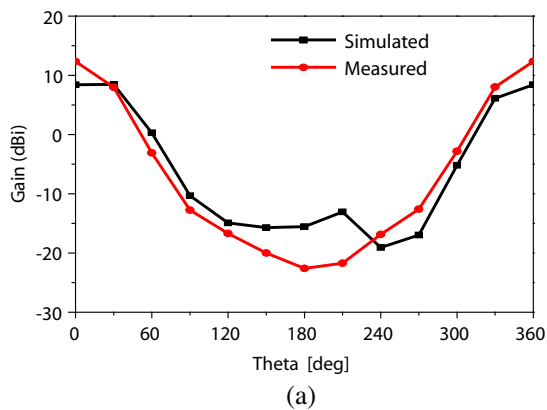


Figure 3: Photograph of the proposed slot antenna with single-layer director.


 Figure 4: Simulated and measured S_{11} design 1.

 Figure 5: (a) Measured and simulated radiation patterns of design 1 in xoz plane. (b) Measured and simulated radiation patterns of design 1 in $yo z$ plane.

patterns has been achieved. The maximum simulated and measured gains are 12 dBi at 5.6 GHz and 10.4 dBi at 5.57 GHz respectively.

4. THE NOVEL SLOT ANTENNA WITH GRID STRUCTURE

In this part, a novel antenna is designed, which is named design 2. The total size of design 2 is the same as design 1, while, the gain of design 2 is enhanced. In design 2, a special structure based on SPPs is added to the preliminary antenna. The structure between the driver and director is noted as dielectric grid structure, which is shown in Fig. 6. The permittivity of this dielectric

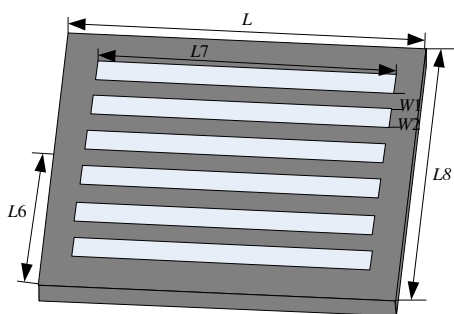


Figure 6: Structures of the proposed grid structure.

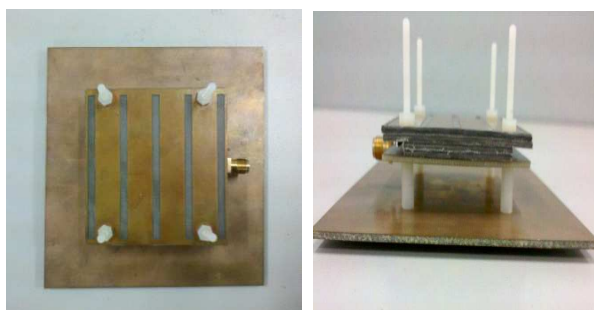
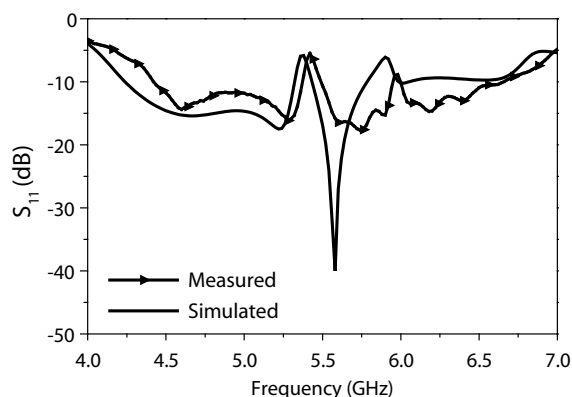
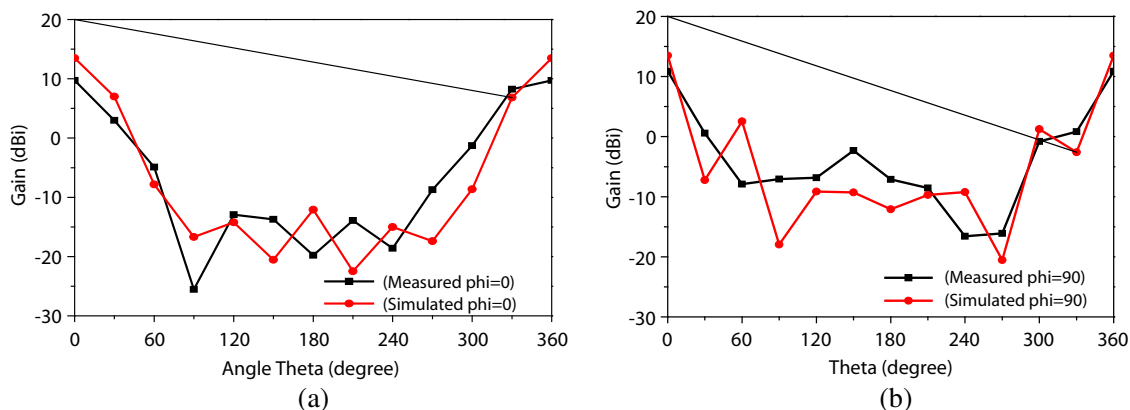


Figure 7: Photograph of design 2.

Figure 8: Simulated and measured S_{11} design 2.Figure 9: (a) Measured and simulated radiation patterns of design 2 in xoz plane. (b) Measured and simulated radiation patterns of design 2 in $yozy$ plane.

is $\epsilon_r 2$. According to the surface plasmons diffraction theory, the field of electromagnetic can be enhanced [11]. Therefore, the gain of antenna can be improved. Dimensions of this grid structure are as follows: $L6 = 20.15$ mm, $L7 = 50$ mm, $L8 = 40.3$ mm, $H2 = 3$ mm. The optimized distance between the two close slots is $W1 = 1.7$ mm and the width of the slots in the grid structure is $W2 = 3.6$ mm. In design 2, some parameters are different from design 1, such as $D2 = 6$ mm, $H = 3$ mm. Other parameters are listed in Table 1.

The fabricated prototype of design 2 is shown in Fig. 7. Comparison about S_{11} between simulated and measured is shown in Fig. 8. The simulated bandwidth is 6.1% and measured bandwidth is 8.0%, which shows good agreement generally. Fig. 9 presents the simulated and measured xoy plane and $yozy$ plane radiation patterns of design 2. The maximum simulated and measured gains are 13.5 dBi and 11.4 dBi respectively. The 2.1 dBi drop in measured gain may be caused by precision of production.

The comparison of simulated about design 1 and design 2 are discussed as following:

(a) As shown in Fig. 10, the bandwidth of design 1 and design 2 both cover frequencies from 5.49 GHz to 5.92 GHz.

(b) As shown in Fig. 11, the measured gain of design 2 is improved about 1 dBi than design 1, which is slightly lower than simulated. The measured gains of design 1 and design 2 have about 2 dBi dropped than simulated.

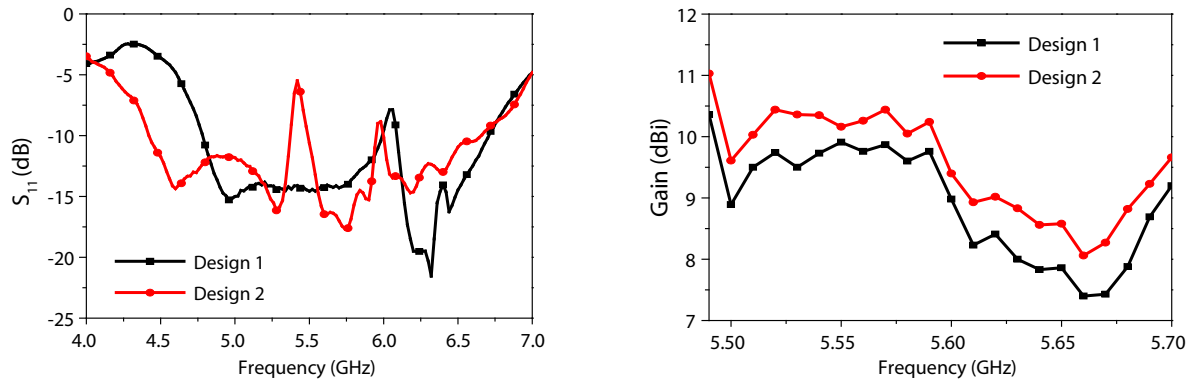


Figure 10: Measured S_{11} for design 1 and design 2. Figure 11: Measured gain for design 1 and design 2.

5. CONCLUSION

In this paper, a slot antenna with single-layer director and a novel high gain slot antenna with SPPs are proposed. By adding a substrate layer with grids structure between the driver and director of the design 1, the measured gain of the antenna is enhanced by 1 dBi. Good performance with gain of 11.4 dBi is achieved at 5.57 GHz. The overall optimum size of the proposed antenna is only $100 \times 100 \times 19 \text{ mm}^3$. Good agreement between simulated and measured results is achieved.

ACKNOWLEDGMENT

This project is supported by Natural Science Foundation of Jiangsu Province, China under Grant BK2010221 and also supported by Suzhou Key Laboratory for Radio and Microwave/Millimeter Wave under Grant SZS201110. The authors would like to thank Danpeng Xie and Dengkui Liu for making and measuring the antennas.

REFERENCES

1. Carvalho, R., R. R. Saldanha, B. N. Gomes, A. C. Lisboa, and A. X. Martins, "A multi-objective evolutionary algorithm based on decomposition for optimal design of Yagi-Uda antennas," *IEEE Transactions on Magnetics*, Vol. 48, No. 2, Feb. 2012.
2. Alsliety, M. and D. Aloï, "A low profile microstrip Yagi dipole antenna for wireless communications in the 5 GHz band," *Proc. Int. Conf. on Electrol/Information Technology*, 525–528, East Lansing, MI, May 2006.
3. De Jean, G. R., T. T. Thai, S. Nikolaou, and M. M. Tentzeris, "Design and analysis of microstrip bi-Yagi and quad-Yagi antenna arrays for WLAN applications," *Antennas Wireless Propag. Lett.*, Vol. 6, 244–248, Jun. 2007.
4. Lu, H.-D., L.-M. Si, and Y. Liu, "Compact planar microstrip-fed quasi-Yagi antenna," *Electronics Letters*, Vol. 48, No. 3, Feb. 2, 2012.
5. Deal, W. R., N. Kaneda, J. Sor, Y. Qian, and T. Itoh, "A new quasi-yagi antenna for planar active antenna arrays," *IEEE Transactions on Microwave Theory and Techniques*, Vol. 48, No. 6, Jun. 2000.
6. Kramer, O., T. Djerafi, and K. Wu, "Vertically multilayer-stacked Yagi antenna with single and dual polarizations," *IEEE Transactions on Antennas and Propagation*, Vol. 58, No. 4, Apr. 2010.
7. Clavero, C., K. Yang, J. R. Skuza, and R. A. Lukaszew, "Magnetic field modulation of intense surface plasmon polaritons," *Optics Express*, Vol. 18, No. 8, Apr. 2010.
8. Raether, H., *Surface Plasmons: On Smooth and Rough Surfaces and on Gratings*, Springer, Berlin, 1988.

9. Ritchie, R. H., E. T. Arakawa, J. J. Cowan, et al., “Surface plasmon resonance effect in grating diffraction,” *Physical Review Letters*, Vol. 21, No. 22, 1530–1533, 1968.
10. Li, Z.-B., J.-G. Tian, Z.-B. Liu, et al., “Enhanced light transmission through a single subwavelength aperture in layered film consisting of metal and dielectric,” *Optics Express*, Vol. 13, No. 22, 9071–9077, 2010.
11. Lin, D. Z., C. K. Chang, Y. C. Chen, et al., “Beaming light from a subwavelength metal slit surrounded by dielectric surface gratings,” *Optics Express*, Vol. 14, No. 8, 3503–3511, 2006.
12. Cao, Q., et al., “Negative role of surface plasmons in the transmission of metallic grating with very narrow slits,” *Physical Review Letters*, Vol. 88, 057403, 2002.

A Compact Circular Polarized Tag Antenna in UHF Band for Metallic Object Application

Yusha Liu, Qi Liu, Bo Xu, and Jun Hu

Centre for Opt. & EM Research, Zhejiang Provincial Key Lab for Sensing Technologies
Zhejiang University, Hangzhou, China

Abstract— In this article, a compact RFID tag antenna operated on UHF band with circular polarization is proposed. The antenna is comprised of a radiating square with two pairs of unequal crossed slots to produce a circularly polarized (CP) radiation and a simple quarter-wave microstrip line to feed the patch. A tag chip is embedded between the microstrip line and a short-circuited stub line. The simulated result for -3 -dB power reflection coefficient (PRC) is about 27 MHz (904–931 MHz) that covers the RFID bands of North and South America and Taiwan (920–928 MHz) and its corresponding simulated 3-dB axial-ratio (AR) bandwidth is about 7 MHz (910–917 MHz). The overall antenna size is 75 mm \times 75 mm \times 1.6 mm at 915 MHz. The results show a perfect circularly polarized radiation.

1. INTRODUCTION

In recent years, applications for radio frequency identification (RFID) systems in the ultra-high frequency (UHF) band has been received much interest in several service industries, such as, purchasing, distribution logistics, and animal tracking applications [1]. For a commercial RFID system, it usually consists of a reader and many tags. The reader antenna generally has a circular polarization radiation pattern to increase the orientation diversity. However, most of RFID tags are linear polarization (LP) in the UHF frequency band. Therefore, the polarization mismatch between them would result in that only half of the transmission power is received by tags. But, if the tag antenna is also circularly polarized, the power received by the CP tag antenna can be improved by 3 dB, and the maximum reading range can thus be increased by 41%, theoretically [2].

Currently a few antennas for RFID tag in UHF band with CP radiation are presented [3–5]. A compact circularly polarized tag antenna with a dimension of 80 mm \times 80 mm \times 1.6 mm at 915 MHz and a 3-dB AR bandwidth of 6 MHz is proposed in [3]. In [4], a circular microstrip RFID tag antenna for CP radiation has been presented. The antenna has a dimension of 74 mm \times 74 mm \times 1.6 mm at 915 MHz and a 3-dB AR bandwidth of 6 MHz. In [5], a circular polarization tag antenna with two diagonal dipoles is presented. The antenna has a dimension of 68 mm \times 68 mm \times 1 mm at 915 MHz and a wide 3-dB AR bandwidth of 31 MHz. But it is not used for metallic objects.

In this paper, a square-shaped CP tag antenna fed by a microstrip line is proposed in the UHF band. The proposed antenna exhibits a surface area of 75 mm \times 75 mm \times 1.6 mm at 915 MHz. And the antenna has a 3-dB AR bandwidth of 7 MHz, and its corresponding simulated -3 -dB power reflection coefficient is 27 MHz (904–931 MHz). The antenna presents a good performance when it mounts on a ground plane.

2. ANTENNA DESIGN PROCESS

The final structure and dimensions of the proposed compact circularly polarized tag antenna is shown in Fig. 1. The antenna is fabricated on a FR4 substrate ($\epsilon_r=4.4$, $\tan \delta = 0.02$) and has a thickness of H ($H = 1.6$ mm). The ground plane has a size of 75 mm \times 75 mm. While the radiating patch has a length of L ($L = 58$ mm), and the radiating patch is loaded with two pairs of crossed slots which have unequal lengths, and equal width W ($W = 4$ mm). The crossed slots embedded to the patch at corners along the direction of $\phi = \pm 45^\circ$ is used to produce a CP radiating pattern. The antenna is fed by a microstrip line at point of A. An IC chip is attached between the microstrip line and the short-circuited stub line, which is the red area as shown in Fig. 1.

In the proposed antenna, first, the radiating patch is loaded with four slits at the corners along the direction of $\phi = \pm 45^\circ$. In order to reduce the size of the antenna, other slits are added to lengthen the resonant length. Then the antenna with four cross-shaped slits is presented, and a better circular polarization radiation is achieved. Here, an Alien Higgs chip with an input impedance of $13 - j111\Omega$ and a threshold power sensitivity of -18.5 dBm at 915 MHz is provided. The conjugate impedance of the antenna is achieved by turning the parameters L_1 , L_2 , t_1 , and t_2 . The parameters S_1 , S_2 , b and d are used as variables to optimize the circular polarization.

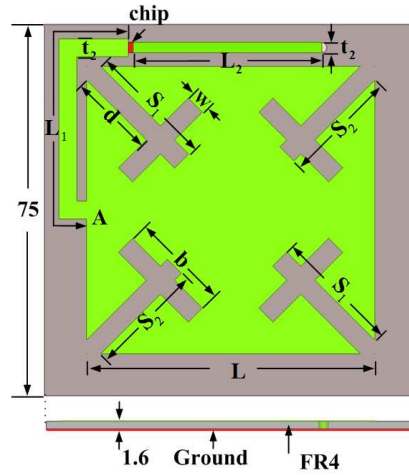


Figure 1: Geometry of the circularly polarized antenna.

3. RESULTS AND DISCUSSIONS

Note that the commercially available simulation software, Ansoft High Frequency Simulator Structure (HFSS) 14 is used for the simulated results. The simulated input impedance When $L_1 = 56$ mm, $L_2 = 38$ mm, $t_1 = 3.6$ mm and $t_2 = 2$ mm is presented in Fig. 2. The simulated input impedance is $13.2 + j112.4\Omega$ at approximately the center frequency 915 MHz. It is conjugately matched to the chip. The simulated power reflection coefficient of the proposed antenna is given in Fig. 3. The simulated -3 -dB PRC bandwidth of the tag antenna is about 27 MHz (904–931 MHz). It completely covers the North and South American UHF RFID band which ranges from 902 to 928 MHz. When $S_1 = 56$ mm, $S_2 = 38$ mm, $b = 24$ mm and $d = 16$ mm, the simulated CP bandwidth determined by the 3-dB axial ratio, is 7 MHz (910–917 MHz) and best at 913 MHz with $AR = 0.9$ dB. The maximum simulated gain for the proposed antenna is about -15 dB. The gain will be better when the antenna is mounted on a bigger metal plane.

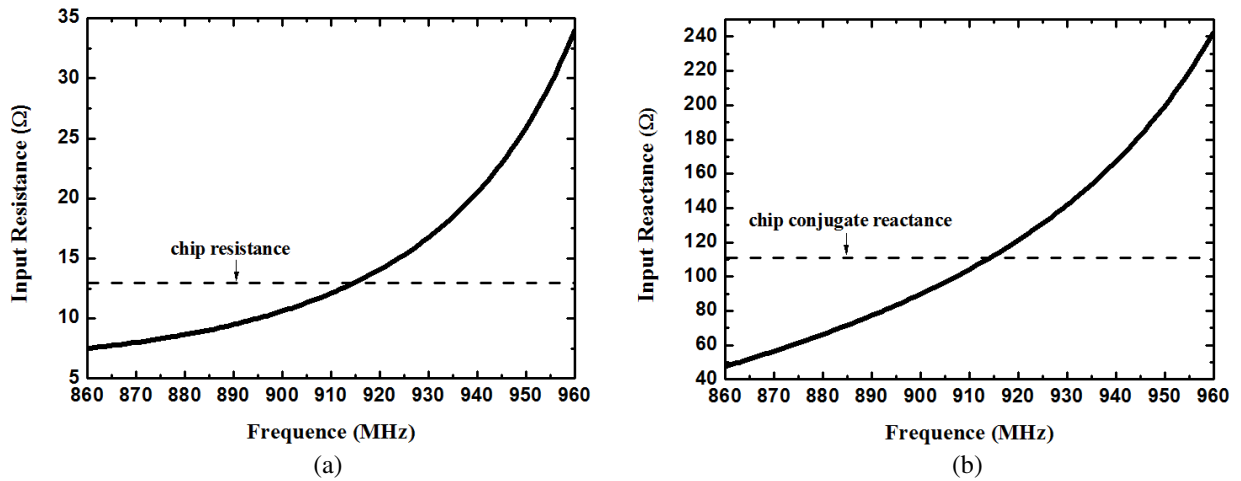


Figure 2: Simulated input impedance. (a) Input resistance. (b) Input reactance.

Here, a theoretical prediction for the reading range by considering the Friis transmission equation is presented as follow [6]:

$$r_{\max} = \frac{\lambda_0}{4\pi} \sqrt{\frac{P_t G_t G_r \rho (1 - |\Gamma|^2)}{P_{th}}} \quad (1)$$

where λ_0 is the wavelength, P_t is the transmit power of the reader, G_t is the gain of reader antenna, P_{th} is the minimum threshold power required by the tag chip to respond, G_r is the gain of tag antenna, ρ is the polarization factor, and Γ is the reflection coefficient of tag antenna. In this case,

both the reader antenna and the proposed antenna are circularly polarized, thus $\rho = 1$. The total transmitted power is 4.0 W effective isotropic radiated power (EIRP). The calculated reading range of the proposed tag antenna is about 2.4 m at 915 MHz.

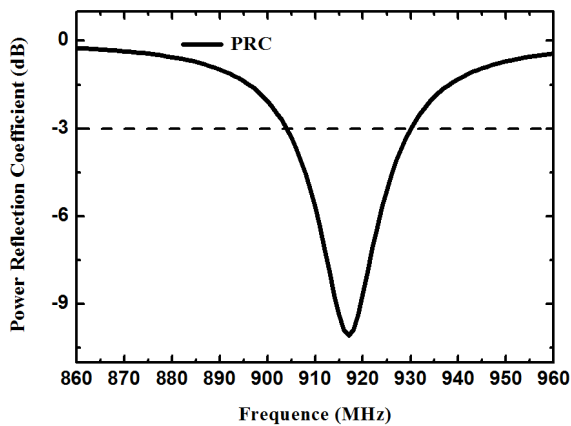


Figure 3: The simulated PRC of the proposed tag antenna.

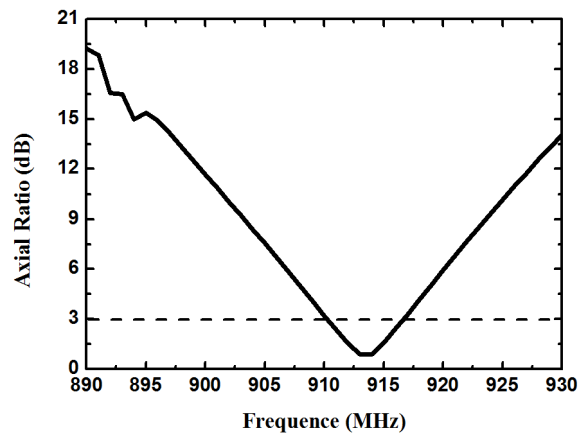


Figure 4: The simulated axial ratio.

4. CONCLUSION

A compact square-shaped tag antenna with excellent circular polarization has been designed. The circularly polarized bandwidth (910–917 MHz) obtained in this paper is determined by unequal crossed slots embed to the radiation patch. The complex impedance matching of the proposed tag antenna can be achieved by properly selecting the dimensions of the microstrip line and the short-circuited stub line. The power reflection coefficient is 27 MHz (904–931 MHz). The overall antenna size is $75 \text{ mm} \times 75 \text{ mm} \times 1.6 \text{ mm}$ at 915 MHz. The simulated results verified a good CP radiation when it mounts on a metal plane. With smaller size, lower weight, and lower cost, the proposed tag antenna is a good candidate for metallic object application in the UHF band.

REFERENCES

1. Finkenzeller, K., *RFID Handbook*, 2nd Edition, Wiley & Sons, New York, 2004.
2. Chen, H. D., S. H. Kuo, C. Y. D. Sim, and C. H. Tsai, "Coupling-feed circularly polarized RFID tag antenna mountable on metallic surface," *IEEE Trans. Antennas Propag.*, Vol. 60, No. 5, 2166–2174, 2012.
3. Chen, H. D., S. H. Kuo, and J. L. Jheng, "Design of compact circularly polarized radio frequency identification tag antenna for metallic object application," *Microwave and Optical Technology Letters*, Vol. 55, 1481–1485, 2013.
4. Tseng, Y. M., S. H. Kuo, H. D. Chen, and C. Y. D. Sim, "Circularly polarized circular microstrip RFID tag antenna," *Proceedings of APMC*, 1142–1144, 2012.
5. Liu, Y. S., Q. Liu, and J. Hu, "Novel circular polarization antenna for UHF RFID application," *International Symposium, Instrumentation and Measurement, Sensor Network and Automation*, 986–989, 2013.
6. Cho, C., I. Park, and H. Choo, "Design of a circularly polarized tag antenna for increased reading range," *IEEE Trans. Antennas Propagat.*, Vol. 57, No. 10, 3418–3422, 2009.

A Miniaturized Unidirectional Moxon Antenna for UHF RFID Tags

Q. Liu, S. Zhang, and B. Xu

Center for Optical and Electromagnetic Research, Zhejiang University, Hangzhou 310027, China

Abstract— A unidirectional moxon antenna for UHF RFID tags is proposed. Meander lines are applied in this structure for the size reduction. An inductively coupled feeding loop is used to match the impedance between the antenna and the chip. A gain of 4.48 dBi and an outstanding front-to-back ratio of 17.7 dB are achieved with a very broad frontal lobe (half power beamwidth is 70 degrees in the x - y plane and 150 degrees in y - z plane).

1. INTRODUCTION

RFID (Radio Frequency Identification) technology is a remote automatic identification technology, which enables target recognition and relevant data acquisition through radio frequency signals. The tag antenna is a vital part of the RFID system, and its performance greatly affects the performance of the RFID system. Most tag antennas have omnidirectional radiation patterns or quasi-isotropic radiation patterns. However, in some specific situations a unidirectional tag antenna is much more desired, as it gives a much longer reading range in the required direction than in other directions.

Two kinds of high gain Yagi-Uda UHF RFID tag antennas have been proposed in [1]. The first 5-element Yagi-Uda type UHF tag antenna has an overall size of $180\text{ mm} \times 140\text{ mm}$, a maximum gain of 6.6 dB, and a front-to-back ratio of 10 dB. In the second design, the overall size of the 5-element Yagi-Uda type UHF tag antenna has been reduced to $140\text{ mm} \times 80\text{ mm}$ with a maximum gain of 4.6 dB and a front-to-back ratio of 10.6 dB. The tag antenna size is reduced through a T-matching method.

In this letter, we propose a miniaturized unidirectional moxon antenna for UHF RFID tags. The moxon antenna is a parasitic dual-element array with the ends of each element folded back towards each other for additional coupling. The ends are separated to create a gap, which is mostly responsible for the unidirectional pattern [2]. Meander lines [3] and an inductively coupled feeding loop [4] are applied in this structure for the size reduction and the impedance match between the antenna and the chip, respectively. Our proposed antenna has an overall size of $80\text{ mm} \times 60\text{ mm}$, much smaller than the antennas in [1], while the maximum gain is 4.48 dB and the front-to-back ratio is 17.7 dB at 915 MHz. The measured maximum reading range is 18.5 m with a total transmitted power of 4.0 W EIRP at 915 MHz. In addition, the front-to-back ratios are all above 15 dB in FCC band.

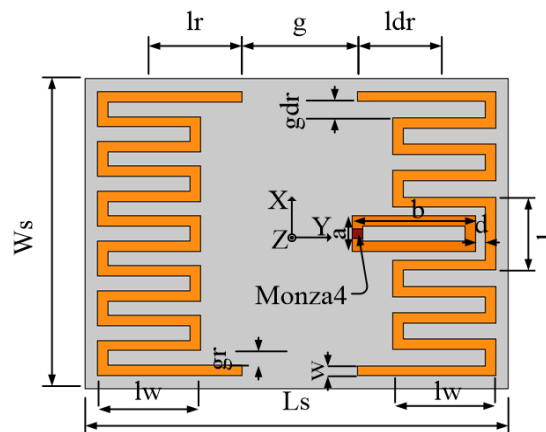


Figure 1: Geometry of the proposed RFID antenna.

2. ANTENNA STRUCTURE AND DESIGN

The configuration of the proposed antenna is illustrated in Figure 1. The antenna consists of a meander driven element and a meander reflector. Both of them are made of 0.01 mm aluminium and printed on a Polyethylene Terephthalate (PET) substrate with a thickness of 0.05 mm and relative

permittivity of 3.2. The ends of the driven element and reflector are bent inward. The front-to-back ratio of this antenna is highly affected by the lengths of inwardly bent lines (L_r , L_{dr}), as well as the spacing between the driven element and the reflector (g). An inductively coupled feeding loop, inserted in the middle of the driven element, is used instead of directly feeding into this structure. By adjusting the size of the feeding loop and the spacing between the loop and the radiating body of the driven element, the input impedance of the antenna can be conjugate-matched easily to the chip.

The actual overall size of the tag is $L_s \times W_s = 80 \times 60 \text{ mm}^2$. The optimal design parameters are as follows: $l_w = 20 \text{ mm}$, $l = 14.4 \text{ mm}$, $w = 2 \text{ mm}$, $g_r = 2.9 \text{ mm}$, $g_{dr} = 3.2 \text{ mm}$, $l_r = 19.2 \text{ mm}$, $g = 22.4 \text{ mm}$, $l_{dr} = 16 \text{ mm}$, $a = 7 \text{ mm}$, $b = 24 \text{ mm}$, and $d = 2 \text{ mm}$.

3. SIMULATED AND EXPERIMENTAL RESULTS

The prototype antenna is designed and optimised for the FCC band (902–928 MHz). The proposed tag antenna is fabricated in a roll to roll (R2R) process. A Monza 4 chip with an input impedance of $(11 - j143) \Omega$ and a threshold power sensitivity of -17.4 dBm at 915 MHz is used in the experiment.

A prototype of the proposed antenna is measured with Agilent E8358A VNA and NI-VISN-100 RFID tester. The tester has an EIRP (effective isotropic radiated power) of 4 W and consists of the RFID reader with a radiation power of 30 dBm and a reader antenna with a gain of 6 dBi.

Figure 2 gives the simulated and measured results of the input impedance, which agree well with each other. The simulated and measured results for the Power Reflection Coefficient (PRC) [5] are plotted in Figure 3. The -3 dB bandwidth is very wide because of the combined effect of the adjacent resonances of the feeding loop, the driven element and the reflector. The small deviation in frequency may be due to fabrication and chip bonding error.

The simulated gain pattern and measured reading range pattern are shown in Figure 4 for comparison. The outlines of the simulated and measured results are generally similar to each other, which indicates the agreement of the simulated and measured results.

The front-to-back ratio is obtained by:

$$\text{FBR (dB)} = 10 \log_{10} \frac{G_f}{G_b} = 20 \log_{10} \frac{R_f}{R_b} \quad (1)$$

where G_f and G_b are gains in the front and back directions, respectively, and R_f and R_b are reading ranges in the front and back directions, respectively.

With a simulated gain of 4.48 dB in the front direction and -15.6 dB in the back direction, the simulated front-to-back ratio is 20 dB at 915 MHz. The measured front-to-back ratio is 17.7 dB, and the measured reading range is 18.5 m in the front direction and 2.4 m in the back direction at 915 MHz. The measured half power beamwidth is 70° in the x - y plane and 150° in the y - z plane while the half power beamwidth of the dipole antenna is about 70° in usage plane.

The reading ranges in the front and back directions as a function of the frequency are shown in Figure 5. As in the grey zone, the front-to-back ratios in the FCC band are all above 15 dB. Good directivity can be achieved in the FCC band.

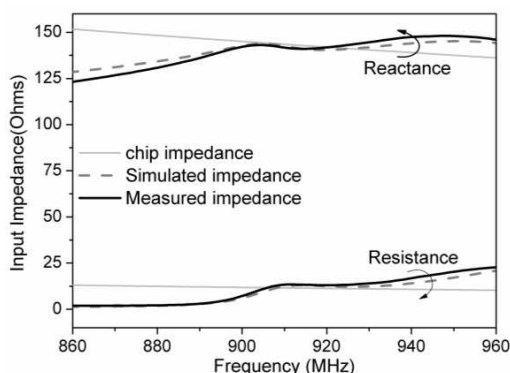


Figure 2: Simulated and measured input impedances of the proposed RFID antenna.

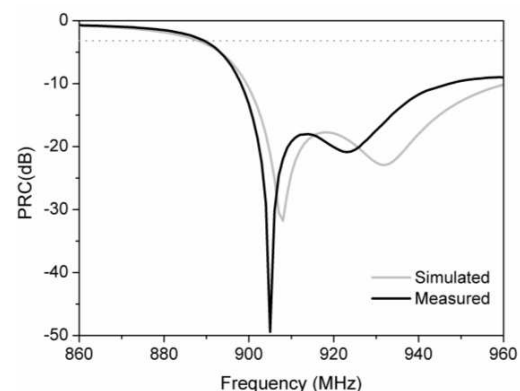


Figure 3: Simulated and measured results of PRC of the proposed RFID antenna.

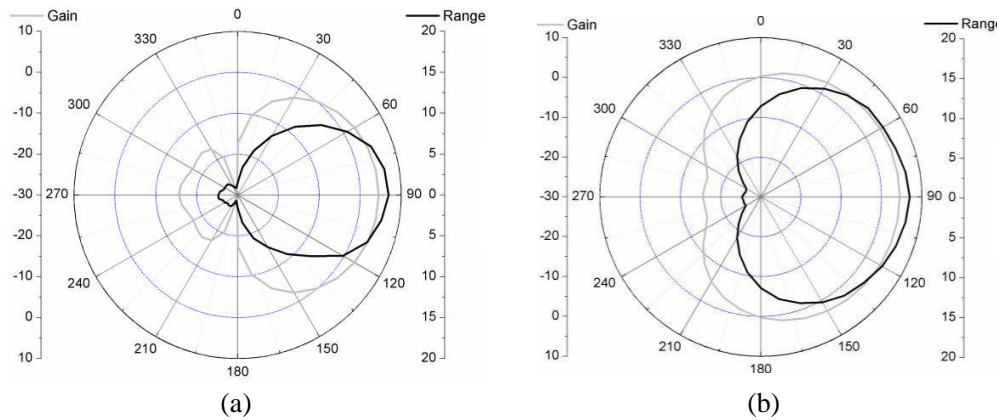


Figure 4: Simulated gain (dB) pattern and measured reading range (m) pattern at 915 MHz of the proposed RFID antenna. (a) Patterns in the x - y plane. (b) Patterns in the y - z plane

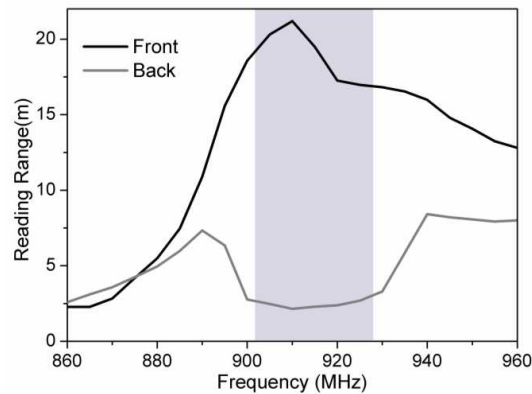


Figure 5: Measured reading ranges in front and back directions.

4. CONCLUSION

A unidirectional moxon RFID tag antenna has been proposed. The proposed antenna is very unidirectional with a long reading range, an outstanding front-to-back ratio, and a very broad frontal lobe in the FCC band. Meander lines and an inductively coupled feeding loop have been applied to make the antenna more compact and to match the impedance between the antenna and the chip.

ACKNOWLEDGMENT

This work is partially supported by the National High Technology Research and Development Program (863 Program) of China (No. 2012AA030402), the National Natural Science Foundation of China (Nos. 61178062 and 60990322), the Program of Zhejiang Leading Team of Science and Technology Innovation, Swedish VR grant (#v621-2011-4620), and AOARD.

REFERENCES

1. Kyoungwan, L. and C. C. You, "High gain Yagi-Uda UHF RFID tag antennas," *IEEE Antennas and Propagation Society International Symposium*, 1753–1756, Honolulu, HI, Jun. 9–15, 2007.
2. Cebik, L. B., W4RNL, "MOXON rectangle notes," <http://www.antennex.com/Sshack/moxon/moxon.html>.
3. Rashed, J. and C.-T. Tai, "A new class of resonant antennas," *IEEE Transactions on Antennas and Propagation*, Vol. 39, No. 9, 1428–1430, 1991.
4. Son, H.-W. and C.-S. Pyo, "Design of RFID tag antennas using an inductively coupled feed," *Electron. Lett.*, Vol. 41, No. 18, 994–996, 2005.

5. Nikitin, P. V., K. V. S. Rao, S. F. Lam, V. Pillai, R. Martinez, and H. Heinrich, “Power reflection coefficient analysis for complex impedances in RFID tag design,” *IEEE Trans. Microw. Theory Tech.*, Vol. 53, No. 9, 2715–2721, 2005.

Optimization of Machine Learning Parameters for Spectrum Survey Analysis

R. Urban and M. Steinbauer

Department of Theoretical and Experimental Electrical Engineering
Brno University of Technology, Technicka 12, Brno 612 00, Czech Republic

Abstract— This paper shows preliminary results of the optimization of machine learning parameters for cognitive radio application by brutal force calculations. We were analyzing frequency occupancy data of the huge measurement campaign of the spectrum background. For these data there are two possible states. Firstly, limited frequency band is occupied (detected signal level is above the threshold) by the other frequency signal — there will be an interference for our system for this frequency band. Secondly, the frequency band is free of any other wireless radiation. These true/false data are analyzed in a context of the cognitive radio by the reinforcement learning and simple learning. Each channel received a score from the learning algorithm given by weighting function. The quality of the output scores is discussed in this paper according to the learning algorithm parameters and optional learning time.

1. INTRODUCTION

In the modern wireless communication there is nearly no idle frequency spectrum capacity. The most suitable frequency bands are already allocated or sold out. The newly incoming wireless system has to be moved to higher frequency bands or to share spectrum with existing system. Nowadays two main approaches of spectrums sharing [1, 2] are discussed. The first one is called the underlay spectrum sharing which is using the limited radiation power to minimize interference with existing systems like UWB technology. The second one is called overlay spectrum which is sharing technique using utilization of the unused spectrum parts of the particular frequency band. All of these techniques are applied in cognitive radio system for spectrum allocation [2]. In this paper we are focusing mainly on the frequency spectrum data evaluation based on the real measurement [3], which is used predominantly for overlay spectrum sharing. Firstly, the occupied parts of the frequency spectrum need to be detected and the threshold level needs to be set up [4]. Afterwards, the measured frequency points are mapped into the channels of the particular examined service. This paper targets the machine learning algorithms for channel assignment in cognitive radio.

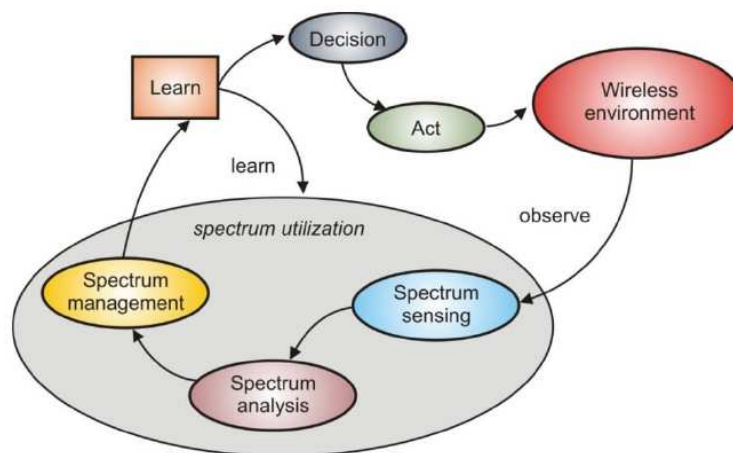


Figure 1: Cognitive cycle.

2. REASONS FOR MACHINE LEARNING

Generally, machine learning is the science how to get computers acting without being programmed. Machine learning influences our lives by many ways. It has given us by self-driving cars, effective web search and many other applications. Machine learning is so pervasive today that you probably

use it dozens of times a day without knowing it. For wireless communication learning starts to be popular to solve cognitive system problems, such as dynamic spectrum sharing. Cognitive radio systems are sensing its own surroundings and aware it. It needs to adapt to the environment with its system (modulation) and transmission (radiation frequency, radiation power) to the environment as it is given by cognitive cycle Fig. 1 [5, 6].

Machine learning is an innovative tool how to apply learning mechanism to cognitive radio [7, 8]. In our case, we are trying to learn, which channel is the best for transmission [4] based on real data. We passed huge measurement campaign to collect spectrum information from various scenarios (indoor and outdoor) and various time tom cover the differences in different wireless traffic over the day.

2.1. Reinforcement Learning

Reinforcement learning is type of the machine learning to maximize a numerical reward output. The agent is not told which actions to take, as in most forms of machine learning, but instead must discover which of his actions yield the most reward. In the most interesting and challenging cases, actions may affect not only the immediate reward but also the next situation and, through that, all subsequent rewards. These two characteristics Ctest and trial- search and delayed reward are the two most important distinguishing features of reinforcement learning. In our case, we will be evaluating the scores of the wireless channel of the particular system. The weighting function (1) is given by:

$$WR_{ch} = W_{ch,t-1} + RP, \quad (1)$$

where WR_{ch} stands for weight value of particular channel ch . $W_{ch,t-1}$ stands for the weight value for particular in previous learning step and RP symbolizes reward/punishment value for this step.

It is clear that RP function need to be carefully selected. The general form is presented as (2).

$$RP = \sum_{i=1}^{SW} P_i + R_i = \sum_{i=1}^{SW} \left(\sum_{y_i}^{n_i} C_P^m - \sum_{z_i}^{m_i} C_R^m \right), \quad (2)$$

where SW is size of the sliding window in data processing ($SW = 1$ when no sliding window used). C_P is constant values used as PUIHMENT and C_R stands for constant value for REWARD. All these values are discussed in results part of this paper. It is obvious that due to negative value of the reward WR can reach negative values. Indexes m_i , m , n_i , n will be discussed later.

For our purposes for cognitive radio we use negative logic — so we are counting punishment of each channel. The lowest score is the best channel from the frequency data perspective.

2.2. Simple Learning

On the one hand, reinforcement learning bring huge dynamic in the results, but on the other hand, there is also inconclusive results. From this reason we tried more basic learning mechanism. The most basic one is the counting the spectrum events occurrences (detected level over the threshold) for particular channel. As it is proved, this algorithm bring us simplification and surprisingly shortened learning times comparing to reinforcement learning. The weighting function is given by (3).

$$\begin{aligned} WI_{ch} &= W_{ch,t-1} + P \\ P &= 1, && \text{when interference detected,} \\ P &= 0, && \text{eslewhere} \end{aligned} \quad (3)$$

3. SIMULATION RESULTS

To compare results we firstly need to define comparable parameters. Firstly, we are focused on credibility of the simulations. The credibility it the comparison between the order of the channels based on the scores from the learning after the 5 minutes learning time (the lowest score the best channel) and the order of the channels by the scores given by the simple learning (interference count) over the whole data set. The same procedure was repeated 100 with the random starts of the learning sequence over the whole data set. The sufficient credibility performance is more than 80%. Getting significantly higher agreement is nearly impossible, because the difference between channel's scores should be very low. Secondly, the learning time is very important. The duration of the agent's successfully training is crucial for future application. The minimal learning time was found by changing the learning duration and comparing the channels order with total interference count channels order.

The simulations were performed for LTE system parameters, which is a modern cellular communication standard. Channel bandwidth we choose 3 MHz in LTE band #3, uplink (1710 MHz–1785 MHz).

The first set of results presented in Table 1 describing the average credibility for 100 random 5 minutes long parts of the measurement data (48 hours samples). The upper index N in last 3 rows in Table 1 presented the situation when are indexes m and n from (3). These indexes takes into account consecutive frequency samples in the same state (used frequency, free frequency point). We are counting the number of the same consecutive samples (y_i, z_i) resulting to the value m and n respectively. We assume that increasing number of the consecutive is representing quality of the channel. Single sparking interference is not such dangerous as continuous interference in particular channel. On the other hand, the frequency band without interference for long time is perspective

Table 1: The credibility results for different settings.

C_P [-]	C_R [-]	Credibility [%] without SW	Credibility [%] SW = 2	Credibility [%] SW = 5
1	1	50	51	51
2	5	78	79	79
5	10	75	75	74
10	10	55	56	57
2^N	5^N	81	83	87
5^N	10^N	74	78	79
10^N	10^N	71	72	74
1	0	85	-	-

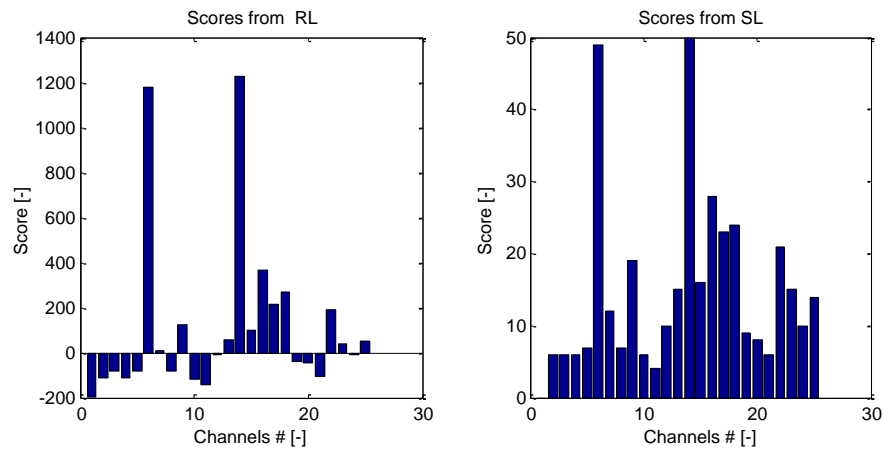


Figure 2: The output from the reinforcement learning (RL) and simple learning (SL) for 5 minutes learning tim.

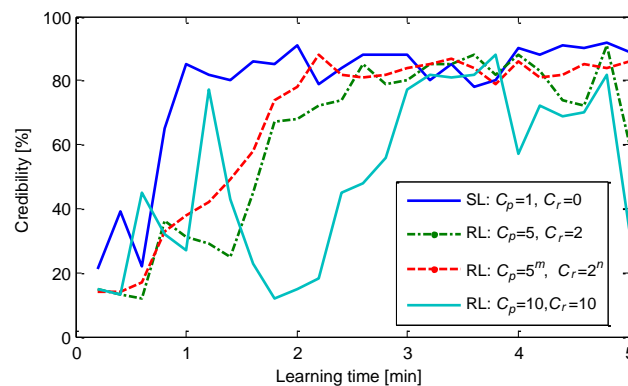


Figure 3: Learning time investigation for simple learning (SL) and reinforcement learning (RL).

for radio transmission — gain higher reward.

The last row in Table 1 is output from simple learning. It is obvious that it provides very high credibility with very low costs.

Finally, the learning time investigation is presented in Fig. 3. It is obvious that simple learning needed the shortest time to reach sufficient credibility (average of the 100 random starts for investigated time over the whole data file).

4. CONCLUSIONS

Recently, machine learning was proved as useful tool for representing learning part of the cognitive radio. It was presented, that reinforcement learning providing high dynamic results. The system using reinforcement learning needed longer learning times to provide credible results than simple learning. Simple learning provides sufficient result after 1 minute (6 time samples). Reinforcement learning provided results with same credibility after 2 minutes, but it is better for long-term channel sensing because of the reward feature — healing the channel. The wireless channel should improve its score after short-term interference. The optimal reward and punishment constants for presented learning algorithm were 5 for punishment and 2 for reward respectively. The further research should be divided into two groups. The best channel searching — based on the selected learning parameters we are able to find the best channel for transmission. Due to continuous spectrum sensing, we are able to update the channel scores. Secondly, rapid channel assignment should find its application for emergency networks. Our radio comes to the unknown environment and we need to choose interference less frequency band for communications.

ACKNOWLEDGMENT

This work was supported by the project CZ.1.07/2.3.00/30.0005 of Brno University of Technology.

REFERENCES

1. Yan, Z., “Dynamic spectrum access in cognitive radio wireless networks,” *IEEE International Conference on Communications (ICC’08)*, 4927–4932, 2008,
2. Berlemann, L. and S. Mangold, *Cognitive Radio and Dynamic Spectrum*, John Wiley & Sons, 2009, 9780470511671.
3. Urban, R., T. Korinek, and P. Pechac, “Broadband spectrum survey measurements for cognitive radio applications,” *Radioengineering*, Vol. 21, 2012, ISSN 1210-2512.
4. Urban, R. and E. Hutova, “Rapid channel assignment for intelligent indoor scenarios,” *European Conference on Antennas and Propagation, EUCAP 2014*, The Hague, 2014.
5. Maldonado, D., B. Le, A. Hugine, T. W. Rondeau, and C. W. Bostian, “Cognitive radio applications to dynamic spectrum allocation: A discussion and an illustrative example,” *First IEEE International Symposium on New Frontiers in Dynamic Spectrum Access Networks (DySPAN 2005)*, 597–600, 2005.
6. Mitola, J., “Cognitive radio architecture evolution,” *Proceedings of the IEEE*, Vol. 97, No. 4, 626–641, 2009.
7. Jiang, T., D. Grace, and P. D. Mitchell, “Efficient exploration in reinforcement learning-based cognitive radio spectrum sharing,” *IET Communications*, Vol. 5, No. 10, 1309–1317, 2011.
8. Urban, R., E. Hutova, and D. Nespov, “Enhanced spectrum planning in cognitive system based on reinforcement learning,” *PIERS Proceedings*, 759–762, Stockholm, Sweden, Aug. 12–15, 2013.

Novel Miniaturized Satellite Navigation Antennas Based on Substrate Integrated Waveguide

Shunyu Fang, Tailei Wang, and Shouzheng Zhu

Department of Communications Engineering, East China Normal University, Shanghai, China

Abstract— In this paper, two novel miniaturized satellite navigation antennas based on substrate integrated waveguide are proposed in this paper. A single-layer SIW annular slot antenna is studied and designed at first. Then through overlay a patch on top layer, a multi-layer SIW antenna is designed. The first antenna covers the Beidou satellite navigation system (BDS) B1I band with circular polarization (CP) and the second one covers the BDS B1I and B2I band with dual circular polarization. Performance has been proved to be better than microstrip navigation antennas in gain and front-to-back ratio (FBR) with the similar size. Both simulation and test results are given respectively.

1. INTRODUCTION

Antenna is one of the most important components in satellite navigation receiver. Patch antenna, which is small in size, easy to machining, and convenient to realize CP, is widely used in the navigation antenna. Patch navigation antenna using dual feed with multi-layers or slotting in single layer are given in [1] and [2]. These entire patch antennas have their shortcoming of big loss, and big back lobe, which is difficult to overcome.

Recently, the substrate integrated waveguide (SIW) causes a wide attention. Its application on antenna, has partly replaced patch antenna in millimeter wave. Etching quadrature slot on SIW cavity is the most popular method to realize CP and dual-band, which has a detailed application in [3]. However, because of its miniaturization is hard, related applications in satellite navigation antennas are rare.

In this paper, two novel miniaturized satellite navigation antennas based on SIW are proposed in this paper. By loading annular slot on the SIW cavity, the antenna can realize the radiation principle similar with patch antenna. Due the contribution of the SIW backed cavity, its gain and FBR is higher than patch antenna.

2. ANTENNA I: SINGLE LAYER STRUCTURE

This section gives the research on single layer structure at first, by loading annular slot on the top layer of SIW cavity and using the coupler to realize dual feed.

2.1. Antenna Configuration

The antenna configuration is shown in Figure 1 and Figure 2. Because the antenna has three layers structure, both configuration of each layer and 3-Dimension are given.

The principle of the proposed antenna is similar with patch antenna. In patch antenna, electromagnetic wave is driven through the slot between the patch and the ground then radiate power. The annular slot in the antenna uses field discontinuity on both sides of the slot to radiate, which is equivalent to move the slot onto the top layer of the SIW cavity. Consequently, circularly polarized radiation is produced when the radiations from the orthogonal slot pairs combine in the far field.

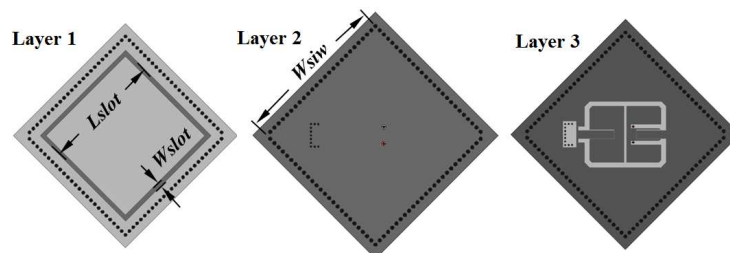


Figure 1: Configuration of Antenna I on each layer.

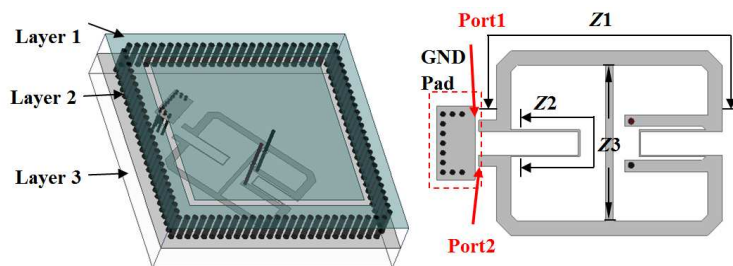


Figure 2: 3-D configuration of Antenna I and the coupler in details.

The resonant frequency is mainly determined by the length of the slot:

$$f = \frac{c}{2 \times L_{slot} \times \sqrt{\epsilon_r}} \quad (1)$$

where L_{slot} is the length of the slot, and ϵ_r is the relative permittivity. W_{slot} is the width of the annular slot, which affects the impedance match and the radiation efficiency.

The coupler on the bottom layer is a wideband device which is studied in [4]. It is composed of the main line and three branch lines, whose impedance are $Z1$, $Z2$ and $Z3$ respectively. Rogers 5880 with a thickness of 1.508 mm, a relative permittivity of 2.2 is used as the dielectric substrate. The dimensions of Antenna I are listed in Table 1 with Ansoft HFSS simulation and optimization.

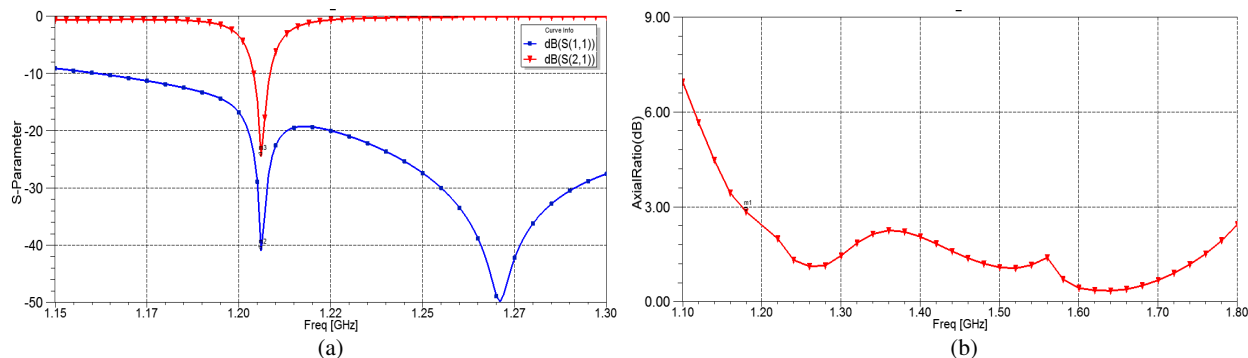
Table 1: Geometrical parameters of Antenna I (Units: mm).

Wsiw	Lslot	Wslot	l1	w1	l2	w2	l3	w3
44.00	41.50	1.10	51.25	2.26	27.40	0.24	26.40	1.15

2.2. Simulation Results and Analysis

Figure 3 shows the S parameter and axial ratio (AR) of the antenna with the 3-branch coupler in simulation. A resonant point of S_{11} can be viewed in BDS B2I band (1206 MHz), which also appears in S_{21} . That means the antenna is in radiation condition in this frequency, rather than straight-through from port 1 to port 2. This can also be proved by the following radiation pattern. A good axial ratio is shown in operation bandwidth, which is lower than 3 dB.

The simulated radiation patterns of the proposed antenna are shown in Figure 4. It is seen that the proposed antenna is a right hand circularly polarized (RHCP) antenna which can rightly receive the navigation signal. The antenna has a good RHCP gain in BDS B2I band which achieves 4.24 dB and a good FBR larger than 7 dB. The FBR is better than traditional patch navigation antennas due to the contribution of SIW backed cavity.


 Figure 3: S -parameters and AR of Antenna I with 3-branch coupler. (a) S -parameters, (b) AR.

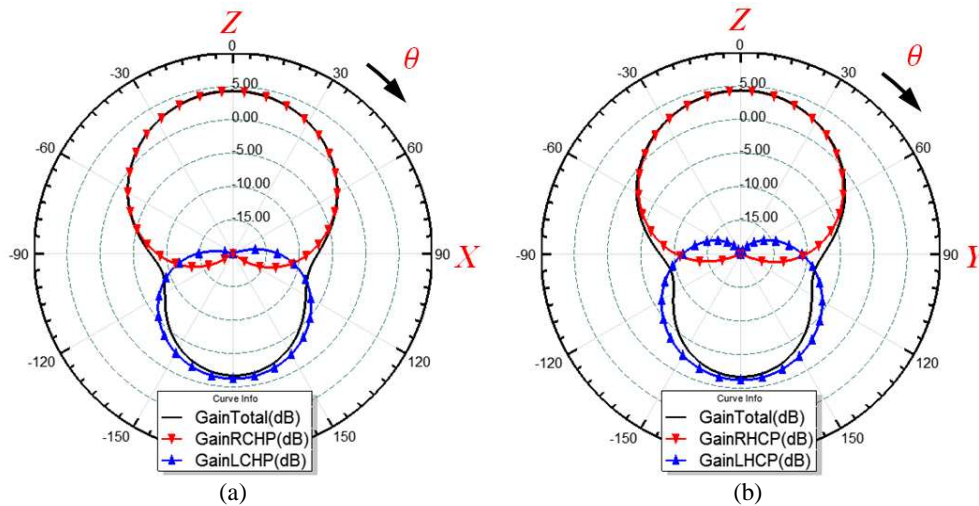


Figure 4: Radiation pattern of Antenna I at 1206 MHz. (a) X-Z plane, (b) Y-Z plane.

3. ANTENNA II: MULTILAYER STRUCTURE

From December, 2013, BDS has started to offer civilian dual-band service in B1I and B2I band, which demands antennas to have a capability of dual band operation. This section gives the design of a multilayer structure which can realize dual band radiation.

3.1. Antenna Configuration

The antenna configuration of 3-D view and top view is shown in Figure 5. The antenna has four metal layers in total. Because the same coupler on bottom layer serves as the feeder, detailed configuration on each layer is not given.

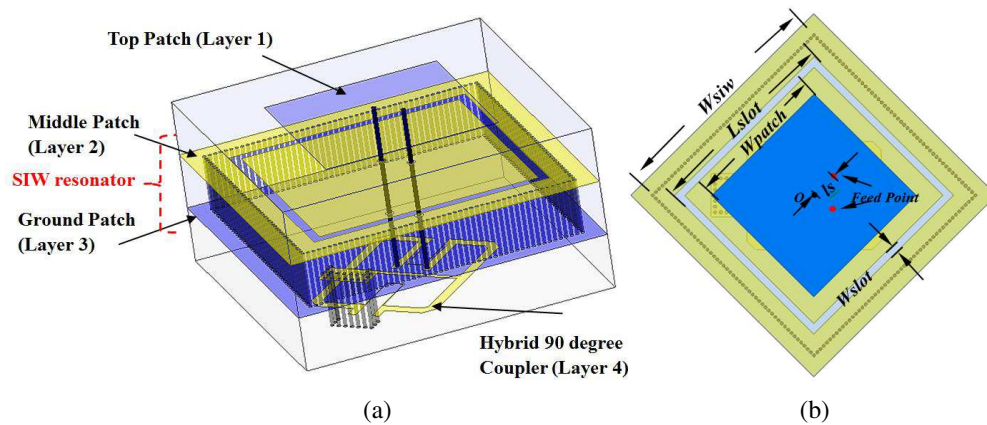


Figure 5: Configuration of Antenna II. (a) 3-D view, (b) top view.

In Antenna II, radiation on higher frequency is realized by the patch on top layer. The coupler feed the patch via the probe and coupling to the cavity through the aperture outside the probe. Antenna radiates power in lower frequency through the annular slot on SIW cavity, while through the top patch in higher frequency. The resonant frequency can be tuned by tuning the size of the patch and the annular slot, respectively. By using the same substrate in Antenna I, the dimensions of the Antenna II are listed in Table 2 with Ansoft HFSS simulation and optimization.

Table 2: Geometrical parameters of Antenna II (Units: mm).

Wsiw	Lslot	Wslot	Wpatch	ls	l1	w1	l2	w2	l3	w3
44.00	41.50	37.25	9.70	4.80	51.25	2.26	27.40	0.24	26.40	1.15

3.2. Simulation and Measurement Results with Analysis

The proposed antenna (Antenna II) has been fabricated on a multilayer PCB substrate and their photographs are shown in Figure 6, which has its top view and bottom view.

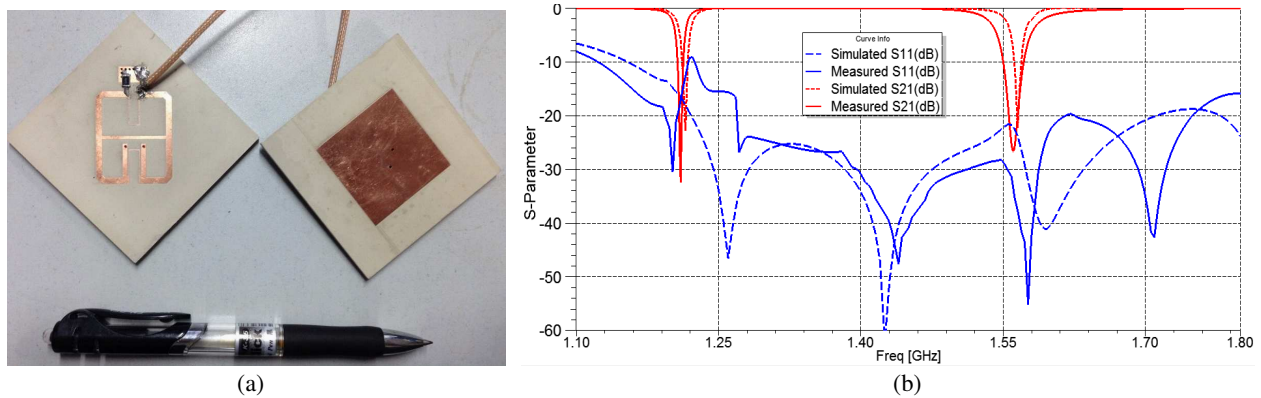


Figure 6: Antenna II. (a) Fabricated photo, (b) simulated and measured S -parameter.

The measured and simulated reflection coefficient is shown in Figure 7. From 1.1 GHz to 1.8 GHz, the S_{11} of the proposed antenna is below -10 dB. Furthermore, resonant frequency of S_{21} can be viewed in BDS B1I and B2I band (simulated in 1206 MHz and 1561 MHz). That means the antenna is in radiation condition in these two frequencies, rather than straight-through from port 1 to port 2. The center frequency shift between the measured and simulated results is only about 5 MHz in lower frequency and 7 MHz in higher frequency.

Table 3 shows the performance comparison for the simulated and measured results of Antenna II. The peak gain in both frequencies has all exceeded 3.5 dB, with the AR below 3 dB. Due to the contribution of SIW backed cavity, the lower frequency gain has remarkably increase, which is higher than traditional dual-mode satellite navigation antenna designed.

Table 3: Performance comparison for simulated and measured results of Antenna II.

Frequency (MHz)	1206	1561
Sim. Peak Gain (dB)	3.92	4.54
Meas. Peak Gain (dB)	3.25	4.03
Sim. Axial Ratio (dB)	1.71	1.87
Meas. Axial Ratio (dB)	2.33	2.41

4. CONCLUSION

Two novel miniaturized satellite navigation antennas based on SIW are proposed in this paper. The antennas have the advantages of small size, high gain and FBR, which is better than patch satellite navigation antenna. The measured results are satisfied at each operating band, and demonstrate good agreements with simulated results.

ACKNOWLEDGMENT

The authors gratefully acknowledge the Shanghai High-tech Special Fund and Shanghai VI Service Network company for their support.

REFERENCES

1. Maqsood, M., B. Bhandari, S. Gao, R. D. V. V. Steenwijk, and M. Unwin, "Dual-band circularly polarized antennas for GNSS remote sensing onboard small satellites," *Proceedings of International Symposium on Communication Systems Networks and Digital Signal Processing*, 86–90, Newcastle, UK, July 2010.
2. Liao, W., Q. X. Chu, and S. Du, "A small frequency ratio dual-band circularly polarized microstrip antenna," *Proceedings of Asia Pacific Microwave Conference*, 2798–2801, Singapore, December 2009.

3. Luo, G. Q. and Z. F. Hu, “Development of low profile cavity backed crossed slot antennas for planar integration,” *IEEE Trans. on Antennas and Propagation*, Vol. 57, No. 10, 2972–2979, 2009.
4. Muraguchi, M., T. Yukitake, and Y. Naito, “Optimum design of 3-dB branch-line coupler using microstrip lines,” *IEEE Trans. on Microwave Theory and Techniques*, Vol. 31, No. 8, 674–678, 1983.

A Novel Phase Measurement System Based on Six Port Reflectometer and LabVIEW

Tyler Wang, Jiajun Bian, and Shouzheng Zhu

School of Information Science and Technology, East China Normal University, 200241, China

Abstract— A novel six port reflectometer (SPR) measurement system based on LabVIEW and a simple calibration method used to reducing the drastic complication of the calibration algorithms is proposed in this paper. The efficiency of manual device measuring is improved by this novel measurement system. This new system can be operated easily. The amplitude and phase's experimental and theory results are provided to demonstrate the performance of the developed SPR.

1. INTRODUCTION

Six port technology was first used to microwave and millimeter wave measurement and network analyzer. During the 1970s, Engen and Hoer began to investigate the six-port technique as the heart of a simpler and less expensive network analyzer [1–3]. Since then, there has been considerable work in the analysis, design, and testing of six-port systems [4–7]. Generally speaking, the six-port reflectometer (SPR) is a passive linear circuit with one port connected to the signal source, one port to a device under test (DUT) and the remaining four ports connected to power detectors. DUT's signal amplitude and phase information can be computed by measuring the four power detectors ports' voltage amplitude or power [8]. Using the amplitude replace phase measuring, its measurement process was simple and hardware's imperfection would be made up by appropriate calibration procedure which reduced the cost of automatic network analyzer and microwave component's machining precision [9].

Six port measurement system's calibration was the core of six port technology. Among the calibration methods proposed, the Engen's six port to four-port reduction is the most popular. However, the iterations required by the W-plane calibration algorithm tend to be lengthy and may fail. To achieve an accurate calibration task, many ingenious techniques based on Engen's method have been proposed in the literature [10–15]. It has to be mentioned that most of these works result often in a drastic complication of the calibration algorithms. Furthermore, all the previous methods assume a linear response at the four arms of the SPR, while most of the power detection circuits are built with nonlinear diodes that require an additional calibration step to linearize the diodes over the dynamic range of interest.

With the development of computer communication and measurement and control technology, LabVIEW has been turned into main tool in automatic measurement development system. In this paper, a novel six port measurement system based on LabVIEW and a simple calibration methodology used to reducing the drastic complication of the calibration algorithms and is proposed. This novel measurement system will improve the efficiency of manual device measuring. In Section 2, we first highlight the SPR working theory, then we present our novel calibration method. In Section 3, the provided amplitude and phase's experimental results are corresponded to the theory results which demonstrate the performance of the developed SPR.

2. SYSTEM DESIGN AND OPERATING PRINCIPLE

2.1. Review of the SPR Theory

The architecture comprises a source S , a passive six-port network and four power detectors at P_i ($i = 3, 4, 5, 6$). Incident and emergent waves have been identified at the six ports and labeled a_i ($i = 1, \dots, 6$) and b_i ($i = 1, \dots, 6$), respectively. Γ is the complex reflection, and P_i ($i = 3, 4, 5, 6$) is the reading of the power meter. The incident and emergent waves are coupled through the parameters of the six-port network by the following forms:

$$b_i = \sum_{j=1}^6 S_{ij} a_j, \quad i = 1, \dots, 6 \quad (1)$$

$$a_i = b_i \Gamma_i, \quad i = 3, \dots, 6 \quad (2)$$

Consequently, there are only two degrees of freedom between these waves. Then, it is convenient to relate the emerging waves on the detectors as a linear superposition of the incident wave a_2 and the reflected wave b_2 .

One of the four detectors is usually taken as reference to normalize the other detected powers and should ideally depend only on the source power.

Before doing any measurement, the SPR has to be calibrated to obtain the 12 real calibration constants (four real terms C_i ($i = 3, \dots, 6$) and four complex terms q_i ($i = 3, \dots, 6$)). If a reference detector is used, then the number of calibration parameters is reduced to 11 [6].

2.2. Simple Calibration Method and Optimization

The calibration need one matched load and sliding short circuiter. The previous method had three steps, first step was using the matched load to calibrate q_i ; the second step was calibrating C_3 by using the sliding short circuiter; the third step was getting the other C_i value by calibrating 9 equations, this process was very complex owing to the equations' solving. In order to simplify equations' solving, three more equations are added to the calibration process by adding one more short position. So the twelve equations are paired and can easily be solved utilizing their symmetry.

3. MEASUREMENT SYSTEM AND EXPERIMENTAL RESULT

We manufactured a kind of waveguide six port reflectometer, this novel device is given in Fig. 1.

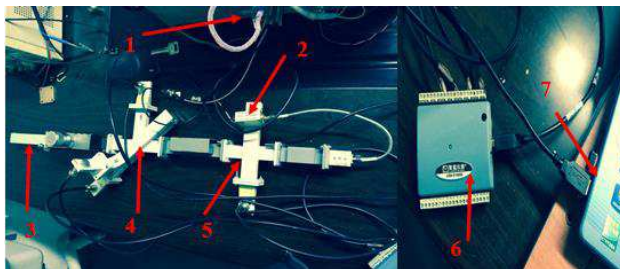


Figure 1: The system's hardware parts where part 1 is the power supply, part 2 is the 9375 MHz source, part 3 is the under test load, part 4 is the five port junction, part 5 is the directional coupler, part 6 is the DAQ board and part 7 is a computer that connected to the DAQ board by a USB line.

Figure 2 shows the LabVIEW working interface, it clearly indicates every step to get the reflection coefficient.



Figure 2: The LabVIEW working interface, the operating method is listed in detail.

To validate the proposed method and measurement system, the experimental and theory's amplitude and phase results in different sliding short circuiter position are compared in Table 1 and Table 2.

From these two tables, we can clearly say that experimental results are corresponded to the theory results both in amplitude and phase which means that the developed SPR owns a good precision.

Table 1: Amplitude results comparison.

Theory and experimental's amplitude results in different sliding short circuiter position (wavelength = 3.2 cm)					
Position (cm)	0	0.2	0.4	0.6	0.8
Theory	1.0	1.0	1.0	1.0	1.0
Experimental	1.03	1.05	1.07	1.02	1.09
Position (cm)	1.0	1.2	1.4	1.6	
Theory	1.0	1.0	1.0	1.0	
Experimental	1.03	1.02	1.08	1.01	

Table 2: Phase results comparison.

Theory and experimental's phase results in different sliding short circuiter position (wavelength = 3.2 cm)					
Position (cm)	0	0.2	0.4	0.6	0.8
Theory	0	45	90	135	180
Experimental	0	45.1	89.8	134.9	180.3
Position (cm)	1.0	1.2	1.4	1.6	
Theory	225	270	315	360	
Experimental	224.8	269.7	315.2	359.9	

4. CONCLUSION

With the development of computer communication and measurement and control technology, LabVIEW has been turned into main tool in automatic measurement development system. In this paper, a novel six port reflectometer (SPR) measurement system based on LabVIEW is proposed and a simple calibration method is used to reducing the drastic complication of the calibration algorithms. This novel measurement system improves the efficiency of manual device measuring and it is handled easily. Experimental results are provided to demonstrate the performance of the developed SPR both in amplitude and phase.

ACKNOWLEDGMENT

This work was sponsored by the Shanghai VI Service Network.

REFERENCES

- Engen, G. and C. Hoer, "Application of an arbitrary 6-port junction to power-measurement problems," *IEEE Trans. Instrum. Meas.*, Vol. 21, No. 4, 470–474, Nov. 1972.
- Hoer, C. A., "The six-port coupler: A new approach to measuring voltage, current, power, impedance, and phase," *IEEE Trans. Instrum. Meas.*, Vol. 21, No. 4, 466–470, Nov. 1972.
- Engen, G. F., "The six-port reflectometer: An alternative network analyzer," *IEEE Trans. Microw. Theory Tech.*, Vol. 25, 1075–1080, Dec. 1977.
- Engen, G. F., "A (historical) review of the six-port measurement technique," *IEEE Trans. Microw. Theory Tech.*, Vol. 45, No. 12, 2414–2417, Dec. 1997.
- Ghannouchi, F. M. and R. G. Bosisio, "A comparative worst-case error analysis of some proposed six-port designs," *IEEE Trans. Instrum. Meas.*, Vol. 37, No. 4, 552–556, Dec. 1988.
- Yeo, S. P. and K. H. Lee, "Improvements in design of six-port reflectometer comprising symmetrical five-port waveguide junction and directional coupler," *IEEE Trans. Instrum. Meas.*, Vol. 39, No. 1, 184–188, Feb. 1990.
- Haddadi, K., M. M. Wang, D. Glay, and T. Lasri, "Performance of a compact dual six-port millimeter-wave network analyzer," *IEEE Trans. Instrum. Meas.*, Vol. 60, No. 9, 3207–3213, Sep. 2011.
- Hoer, C. A., "The six-port coupler: A new approach to measuring voltage, current, power, impedance, and phase," *IEEE Trans. Instrum. Meas.*, Vol. 21, No. 4, 466–470, 1972.

9. Tang, S. X., *Microwave Measurement*, Beijing University of Science and Technology Press, Beijing, 1992.
10. Li, S. and R. G. Bosisio, “Calibration of multiport reflectometers by means of four open/short circuits,” *IEEE Trans. Microw. Theory Tech.*, Vol. 30, No. 7, 1085–1090, Jul. 1982.
11. Riblet, G. P. and E. R. B. Hansson, “Aspects of the calibration of a single six-port using a load and offset reflection standards,” *IEEE Trans. Microw. Theory Tech.*, Vol. 30, No. 12, 2120–2125, Dec. 1982.
12. Somlo, P. I. and J. D. Hunter, “A six-port reflectometer and its complete characterization by convenient calibration procedures,” *IEEE Trans. Microw. Theory Tech.*, Vol. 30, No. 2, 186–192, Feb. 1982.
13. Ghannouchi, F. M. and R. G. Bosisio, “A new six-port calibration method using four standards and avoiding singularities,” *IEEE Trans. Instrum. Meas.*, Vol. 36, No. 4, 1022–1027, Dec. 1987.
14. Stumper, U., “Finding initial estimates needed for the Engen method of calibrating a single six-port reflectometer,” *IEEE Trans. Microw. Theory Tech.*, Vol. 38, No. 7, 946–949, Jul. 1990.
15. Chahine, S. A., B. Huyart, E. Bergeault, and L. Jallet, “A six-port reflectometer calibration using Schottky diodes operating in AC detection mode,” *IEEE Trans. Instrum. Meas.*, Vol. 42, No. 2, 505–510, Apr. 1993.

TD-LTE Antenna Array Smart Cover Study

Feng Gao¹, Runhong Shan², Wentao Zhu¹, Kai He¹, and Zhiyuan Song¹

¹China Mobile Group Design Institute, Beijing 100080, China

²Copyright Protection Center of China, China

Abstract— This paper integrated the antenna array analysis with differential evolution algorithm to optimize weights of antenna ports efficiently based on the customers' expected pattern, which could form the special broadcast beam to cover weak coverage cell. The broadcast beams were optimized by this method coincide with expected pattern through antenna anechoic chamber test. The LTE network experiment shows that the RSRP (Reference Signal Receiving Power) of communication network are improved 5% averagely after optimized by this method.

1. INTRODUCTION

The Long Term Evolution (LTE) system has been specified by the Third Generation Partnership Project (3GPP) on the way towards fourth-generation (4G) mobile to ensure 3GPP keeping the dominance of the cellular communication technologies. Through the design and optimization of new radio access techniques and a further evolution of the LTE systems, the 3GPP is developing the future LTE-Advanced (LTE-A) wireless networks as the 4G standard of the 3GPP. With the increase of mobile users, communication network environment is more complex, especially in some special scenes broadcast coverage requires some special beams.

Smart antenna could realized the beamforming by each antenna array element excitation (also known as weights, including amplitude and phase), to make the antenna beam. The TD-SCDMA and TD-LTE systems include broadcast model and business model. The broadcast beam is 65 degree in general. For the special broadcast coverage, the current method is provided the table for some special beam weights, such as 90 degrees, 120 degrees and saddle shape beam.

At present the main achievement is the business beamforming, however the broadcast beamforming study is lack, and the existing broadcasting beamforming simulation software is mainly according to the manufacturers to provide the weights data to generate waveform simulation. These methods are lack of flexibility and accuracy. In addition, the system of TD-LTE, in the TM7 mode, using a single beamforming can also encounter this similar situation [1–3].

Based on the expected pattern, integrated the antenna array analysis with modern optimization algorithm, the weights of antenna ports can be optimized in the paper [4]. TDD antenna broadcast beam weights adaptive design is realized by this method and the optimized broadcast patterns coincide with expected pattern. Smart antenna broadcast shaped beam weights adaptive design technology is applied to improve the wireless network coverage. The antenna array weights can be deduced through the broadcasting beam. The simulated beam patterns match with cell's actual coverage. This technique can greatly reduce the workload of network optimization, and improve the coverage of the wireless network rate, success rate and handover success rate.

2. CONFIGURATION AND DESIGN

Figure 1 shows the antenna array, which is composed of uniform linear N unit antenna component, called the uniform linear array.

The pattern of uniform linear antenna array is [5]

$$f(u) = \sum W_n \exp [jkd(n-1)\sin\theta] f'_n(\theta) \quad (1)$$

where $f'_n(\theta)$ is the n th element pattern, and W_n is the n th element excitation. From the formula, the antenna pattern can be control through the weight W_n . The special patterns can achieve through the weights optimization.

2.1. Processing Analysis

Not only the beam width would change (usually become wider), but also maybe presents. When the beam of antenna array scans. The pattern mainly relates to mechanical parameters and frequency, shown in Figure 2.

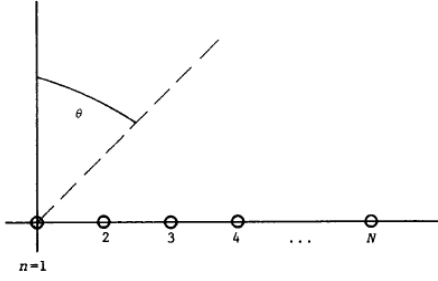


Figure 1: Uniform linear antenna array.

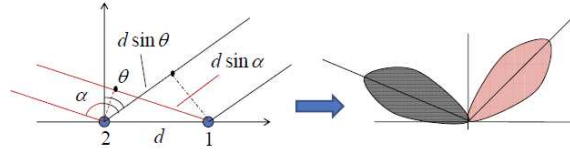


Figure 2: Grating lobe of antenna array.

Relationship of angle of antenna array with scanned angle is shown below [6]

$$\frac{d}{\lambda} = \frac{n}{\sin \theta_0 - \sin \theta_{GL}} \quad (2)$$

When the space of array element is less than or equal to $\lambda/2$, the beam would scan at $[-90^\circ, 90^\circ]$. During the scanning, array antenna pattern would not have grating lobes. The beam will have grating lobe pointing at 0 degree, given space d equal to λ .

Notably, the grating lobe cannot be cancelled by optimizing the array weight, therefore,

$$\theta_G = \arcsin\left(\frac{\lambda}{d} - 1\right) \quad (3)$$

According to the formula 3, we can get the 3 dB beam during scanning. So

$$\theta_{3\text{ dB}} = \arcsin\left(\sin \theta_0 + 0.4429 \frac{\lambda}{Nd}\right) - \arcsin\left(\sin \theta_0 - 0.4429 \frac{\lambda}{Nd}\right) \quad (4)$$

As a special case, the outer edge of the 3 dB beam reach $\pm 90^\circ$ degrees. For the directional antenna, such beams may no practical value in engineering application. Therefore in the process we give a angle (θ_{90}). θ_{90} satisfies with

$$\theta_{90} = \arcsin\left(1 - 0.4429 \frac{\lambda}{Nd}\right) \quad (5)$$

2.2. Optimized Algorithm for Smart Coverage

The optimization design of antenna array beamforming is looking for the best feed weight to obtain the desired pattern. From the mathematical view, it is a multi-variable, multiple targets, multi modal optimization problems.

The modern global optimization design methods for antenna array pattern include genetic algorithm (GA), the particle swarm is (PSO), differential evolution algorithm (Differential, Evolution, DE). Differential evolution algorithm has the advantages of simple operation, strong robustness, so the project using differential evolution algorithm as the main optimization method. Standard differential evolution algorithm flow diagram is shown in Figure 4, including the population initialization, mutation, crossover process, the selection process, the treatment of boundary conditions and termination conditions.

2.2.1. The Population Initialization

Differential evolution algorithm use real vector with a dimension D as each generation of the population, each individual is expressed as

$$\mathbf{X}_j = (x_{j1}, x_{j2}, \dots, x_{jD}), \quad 1 \leq j \leq N_P \quad (6)$$

where j is a sequence number for the individual in the population. N_p is the population size. The population size remains constant in the course of evolution. Before the optimized searching, population must be initialized. Usually the initialization of population was given in random within a boundary constraint. Give parameter variable boundaries $x_i^L \leq x_i \leq x_i^U$, there is

$$x_{ji} = \text{rand}[0, 1] \times (x_i^U - x_i^L) + x_i^L \quad i = 1, 2, \dots, D \quad j = 1, 2, \dots, N_P \quad (7)$$

where $\text{rand}[0, 1]$ is random number from 0 to 1.

2.2.2. Mutation Operation

Mutation refers to the parent between two random individual. Difference vector and the addition of a random vector superposition produce a variation vector, expression is as follows

$$v_j^{G+1} = x_{r_3}^G + F \times (x_{r_1}^G - x_{r_2}^G) \quad (8)$$

2.2.3. The Crossover Operation

In order to increase the diversity of individuals, the crossover operation implement between the target vector individual x_j^G and variable vector v_j^{G+1} . The test individual u_j^{G+1} is generated. The specific expression is shown below:

$$u_j^{G+1} = \begin{cases} v_j^{G+1} & \text{rand}[0, 1] \leq CR \quad \text{or} \quad i = \text{rand}n[i] \\ x_j^G & \text{rand}[0, 1] > CR \quad \text{and} \quad i \neq \text{rand}[i] \end{cases} \quad (9)$$

where $\text{rand}[i] \in (1, 2, \dots, D)$, the i expresses the i th variable. CR is crossover probability constant. Its value range is $[0, 1]$. Control of CR size could achieve a balance between global search and convergence speed.

2.2.4. Selection Operation

Differential evolution algorithm with “greedy” search strategy, the mutation and crossover operation is generated after the test individual and the current population of the target vector to compete. It will fit better vector selected for generation. To minimize the optimization selection operation, the equation is:

$$x_j^{G+1} = \begin{cases} u_j^{G+1} & f(u_j^{G+1}) < f(x_j^G) \\ x_j^G & f(u_j^{G+1}) \geq f(x_j^G) \end{cases} \quad (10)$$

2.2.5. Objective Function

Considering with the simple operation, good versatility and higher computational efficiency, the objective function is constructed below

$$E = \min \left\{ \alpha \frac{1}{N} \sum_1^N [f(i) - f_E(i)]^2 + \beta \{f(\theta_0) - \max[f(j)]\}^4 + \gamma E' + \tau E'' \right\}$$

where

$$E' = \frac{1}{M} \sum_{j=1}^M \begin{cases} [f(j) - 0.056]^2 & f(j) > 0.056 \\ 0 & f(j) < 0.056 \end{cases}$$

In formula (11), the first part is used to emphasize the main lobe area; the second part is used to constrain the maximum direction of the pattern. The third part is used to calculate the rear area of the pattern. The fourth part is used to constrain weight efficiency. α , β and γ are weighting factor for each part.

3. ANALYSIS AND TEST

The smart broadcast beamforming module structure is shown in Figure 5, including the input file, antenna element pattern, antenna optimization target pattern, optimized weight, actual optimized pattern and input file library.

The following example illustrates the process of simulation. Firstly, the element pattern and array pattern are shown in Figure 3. Input file is mainly pattern and target pattern, including the element number, frequency, amplitude, phase array spacing, and half power beam width.

Optimizing time is about a minute, and the optimized result is shown in Figure 4.

Figure 5 shows the target pattern and optimized pattern. The target pattern was constrained by 9 points. The optimized pattern coincides with the target pattern from the Figure 5.

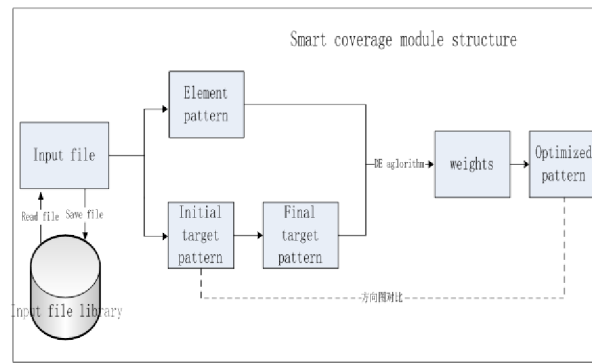


Figure 3: Optimized design of beamforming module structure.

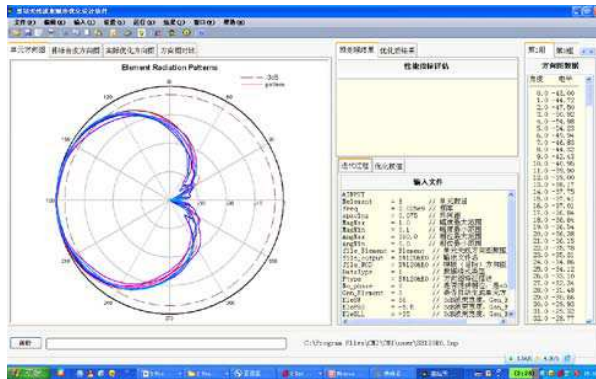


Figure 4: Simulation of interface of smart cover software.

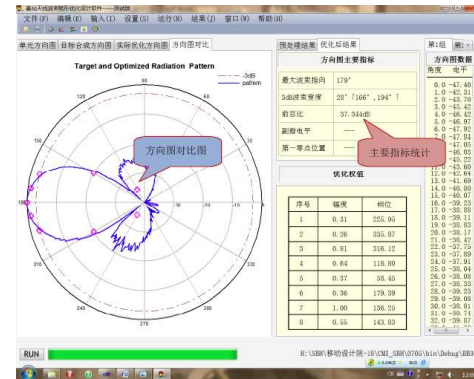


Figure 5: Optimized pattern with the target pattern.

4. CONCLUSIONS

This paper presented the smart coverage optimized algorithm for broadcast beam of smart antenna, based on the beamforming and global optimization algorithm. This method can implement adaptive broadcast beamforming weights adaptive signal processing of the TD-SCDMA or TD-LTE antenna. The application of this technology will greatly improve the network planning and optimization efficiency, and improve the quality of the coverage network.

REFERENCES

1. Martin, C. C., J. H. Winters, and N. R. Sollenberger, "MIMO radio channel measurements: Performance comparison of antenna configurations," *IEEE VTS 54th VTC, 2001 Fall*, Vol. 2, 1225–1229, Oct. 2001.
2. Li, H.-J. and C.-H. Yu, "Correlation properties and capacity of antenna polarization combinations for MIMO radio channel," *IEEE AP-S*, Vol. 2, 503–506, Jun. 22–27, 2003.
3. Michishita, N., H. Arai, K. Tsunekawa, and M. Karikomi, "FDTD analysis of dual frequency printed dipole antenna," *IEEE AP-S, 2002*, Vol. 2, 40–43, Jun. 2002.
4. Gao, F., J. He, W. Zhu, and X. Liu, "The dual polarized ceiling-mounted MIMO antenna analysis and its implementation," *International Conference on Green Communications and Networks*, 2011,
5. Liberti, J. C. and T. S. Rappaport, *Smart Antenna in Wireless Communication*, 81–210, Machinery Industry Press, (Translated by Ma Liang), 2002.
6. Kang, X., *Antenna Theory and Design*, 102–106, National Defense Industry Press, Beijing, 1995.

Investigation on Electromagnetic Scattering from Dielectric Soil Rough Surface with a PEC Object Embedded in It

Hongmei Miao¹ and Pengju Yang²

¹College of Physics and Electronic Information, Yanan University, Yan'an 71600, China

²School of Physics and Optoelectronic Engineering, Xidian University, Xi'an 710071, China

Abstract— In this paper, electromagnetic (EM) scattering from one-dimensional dielectric soil rough surface with a perfect electric conductor (PEC) embedded in it is investigated by method of moments (MoM) for HH polarization. The soil rough surfaces are modeled as realizations of a Gaussian random process with the exponential spectrum, while the tapered incident wave is chosen to reduce the truncation error. Several numerical results are presented to investigate the impact of rough surface parameters of rms height and correlation length on the bistatic scattering coefficient (BSC), while the influence of the size and position of the object on the BSC is discussed.

1. INTRODUCTION

Over the past several decades, a significant amount of research efforts has been spent toward developing viable buried object detection techniques, which is of great value in the detection of buried landmines, pipes and other buried objects of interest. The problem of detecting and imaging underground objects with electromagnetic sensors relies on accurate computational modeling which is challenging because of the complexity of the realistic ground surface. There are many difficulties associated with detecting objects beneath the ground due to the existence of clutter and low electromagnetic wave penetration into moist soil. The analytical algorithm has been applied to solve the problem of EM scattering from 2-D dielectric circular cylinder under beneath a slightly rough surface [1]. Although the analytical method is the computational simplicity and high efficiency, the disadvantage of the analytical method limited its applicability to canonical geometries, and to a small roughness rough surface. Consequently, one has to resort to numerical methods to deal with electromagnetic scattering from targets located below a dielectric rough surface [2–4].

Consequently, this paper is devoted to an investigation of EM scattering from soil rough surface with a perfect electric conductor (PEC) embedded in it.

2. THEORETICAL MODEL

2.1. Soil Surface Model

A rough surface is sampled at N points with spacing Δx over a simulated length $L = (N - 1)\Delta x$. The altitude of each point $x_m = (m - 1)\Delta x$ ($m = 1, \dots, N$) can be generated by (1)

$$f(x_m) = \frac{1}{L} \sum_{n=-N/2+1}^{N/2} F(k_n) \exp(ik_n x_m) \quad (1)$$

For $n \geq 0$

$$F(k_n) = \sqrt{2\pi LW(k_n)} \cdot \begin{cases} [N(0, 1) + iN(0, 1)]/\sqrt{2} & n \neq 0, \quad N/2 \\ N(0, 1) & n = 0, \quad N/2 \end{cases} \quad (2)$$

For $n < 0$, $F(k_n) = F^*(k_{-n})$, where the asterisk represents a complex conjugate. $N(0, 1)$ is a random variant with a Gaussian distribution of zero mean and unit variance. $k_n = \frac{2\pi n}{L}$.

Because land surfaces, including soil surfaces, have large slopes and fine-scale features and the exponential correlation surfaces have fine-scale features as depicted in Figure 1(b), it is reasonable to adopt exponential correlation spectrum in modeling randomly rough surface [6]. Furthermore, extensive soil rough surface profiles have been measured and the correlation functions were extracted from such profiles. It was concluded that the correlation functions were close to exponential correlation functions. Meanwhile, the results from exponential correlation functions are in much better agreement with radar measurements [6]. In this paper, randomly rough surfaces are modeled as realizations of a Gaussian random process with the exponential spectrum, and it can easily be generated by employing the spectrum method which has been widely used in the calculation of wave scattering.

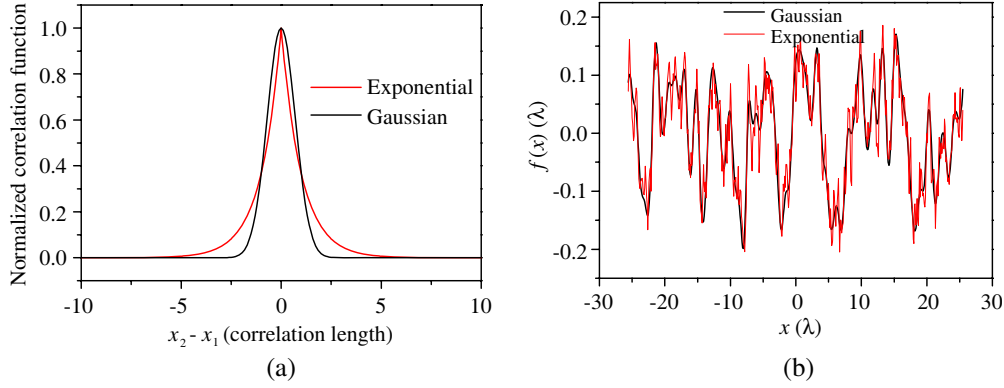


Figure 1: Comparison between surfaces with the Gaussian correlation function and exponential correlation function. (a) Normalized autocorrelation function; (b) 1-D rough surface profiles.

2.2. Composite Scattering Model

The basic geometry considered in this paper is that a PEC object is located below the dielectric rough surface with rms heights h and correlation length l . The height profile functions satisfy $\langle f_1(x) \rangle = 0$. The space is separated into two regions filled with different media by the rough interface: the upper medium denoted by $\Omega_0(\mu_0, \varepsilon_0)$ assumed to be free space, and the lower media represented by $\Omega_1(\mu_1, \varepsilon_1)$. The media involved in this study is supposed to be nonmagnetic, that is, $\mu_1 = \mu_0$. The time dependence of $\exp(-i\omega t)$ is assumed and omitted throughout this paper, where i denotes unit imaginary number. k_i and k_s are the incident and scattering wave vector, respectively. θ_i and θ_s are the incident and scattering angle, respectively. H represents the height of the object. Let ψ_0 and ψ_1 denote the fields in region 0 and region 1, respectively. Let $\bar{r}' = x'\hat{x} + z'\hat{z}$ and $\bar{r} = x\hat{x} + z\hat{z}$ represent source and field points, respectively.

Applying the Green's theorem to Ω_0 , and Ω_1 , respectively, one can obtain the surface integral equations for calculating EM scattering from the one-dimensional soil rough surfaces with a PEC object embedded in the lower media.

$$\frac{1}{2}\psi_0(\bar{r}) - PV \int_{S_r} ds' \hat{n}' \cdot [\psi_0(\bar{r}') \nabla' G_0(\bar{r}, \bar{r}') - G_0(\bar{r}, \bar{r}') \nabla' \psi_0(\bar{r}')] = \psi_{inc}(\bar{r}) \quad \bar{r} \in S_r \quad (3)$$

$$\begin{aligned} & \frac{1}{2}\psi_1(\bar{r}) + PV \int_{S_r} ds' \hat{n}' \cdot [\psi_1(\bar{r}') \nabla' G_1(\bar{r}, \bar{r}') - G_1(\bar{r}, \bar{r}') \nabla' \psi_1(\bar{r}')] \\ & - \int_{S_o} ds' \hat{n}' \cdot [\psi_1(\bar{r}') \nabla' G_1(\bar{r}, \bar{r}') - G_1(\bar{r}, \bar{r}') \nabla' \psi_1(\bar{r}')] = 0 \quad \bar{r} \in S_r \end{aligned} \quad (4)$$

$$\begin{aligned} & \frac{1}{2}\psi_1(\bar{r}) + \int_{S_r} ds' \hat{n}' \cdot [\psi_1(\bar{r}') \nabla' G_1(\bar{r}, \bar{r}') - G_1(\bar{r}, \bar{r}') \nabla' \psi_1(\bar{r}')] \\ & - PV \int_{S_o} ds' \hat{n}' \cdot [\psi_1(\bar{r}') \nabla' G_1(\bar{r}, \bar{r}') - G_1(\bar{r}, \bar{r}') \nabla' \psi_1(\bar{r}')] = 0 \quad \bar{r} \in S_o \end{aligned} \quad (5)$$

Note that in (3)–(5), the PV refers to the Cauchy principal value integral and $G_0(\bar{r}, \bar{r}') = (i/4)H_0^{(1)}(k_0|\bar{r} - \bar{r}'|)$, $G_1(\bar{r}, \bar{r}') = (i/4)H_0^{(1)}(k_1|\bar{r} - \bar{r}'|)$ are the Green's function in region Ω_0 and Ω_1 , respectively. $H_0^{(1)}(\cdot)$ is the zeroth-order Hankel function of the first kind. It should be pointed that the surface integral Equations (3)–(5), are applied to both TE and TM polarizations. The only differences between them is the integral term corresponding to object in surface integral Equation (5), and the surface integral (5) can readily be reduced to TE or TM case in terms of the boundary conditions.

In this paper, to avoid artificial edge diffraction resulting from the finite length of the simulated rough surface, the following Thorsos's tapered plane wave [7] rather than the generally used plane wave is chosen as the incident field.

$$\psi_{inc}(\bar{r}) = \exp[ik_0(x \sin \theta_i - z \cos \theta_i)(1 + w(\bar{r}))] \cdot \exp\left(-\frac{(x + z \tan \theta_i)^2}{g^2}\right) \quad (6)$$

where g is the tapering parameter controlling the tapering length of the incident wave. The additional factor in the phase term of the Thorsos's tapered plane wave is $w(\bar{r}) = [2(x + z \tan \theta_i)^2/g^2 - 1]/(k_0 g \cos \theta_i)^2$.

One applies the MoM with point matching and pulse basis functions. From boundary conditions of continuity of tangential electric and magnetic field the set of integral Equations (3)–(5), one obtain linear system corresponding to the scattering problem.

Upon solving the matrix equation by utilizing MoM algorithm, the surface fields and their normal derivatives can be obtained. When the point \bar{r} is located in the far field, the scattered field $\psi_s(\bar{r})$ in space Ω_0 is (7)

$$\psi_s(\bar{r}) = \frac{i}{4} \sqrt{\frac{2}{\pi k_0 r}} \exp\left(-i\frac{\pi}{4}\right) \exp(ik_0 r) \psi_s^{(N)}(\theta_s) \quad (7)$$

where

$$\psi_s^N(\theta_s) = \int_S ds [\psi(\bar{r})(-i\hat{n} \cdot \bar{k}_s) - \hat{n} \cdot \psi(\bar{r})] \exp(-i\bar{k}_s \cdot \bar{r}) \quad (8)$$

The normalized far-field bistatic scattering coefficient (BSC) with the Thorsos tapered plane wave incidence is defined as (9)

$$\sigma(\theta_s) = \frac{|\psi_s^N(\theta_s, \theta_i)|^2}{g\sqrt{\frac{\pi}{2}} \cos \theta_i \left(1 - \frac{1+2 \tan^2 \theta_i}{2k_0^2 g^2 \cos^2 \theta_i}\right)} \quad (9)$$

3. NUMERICAL RESULTS AND DISCUSSION

In this paper, the numerical simulations are conducted at a frequency $f = 1.2$ GHz. At $f = 1.2$ GHz, the relative permittivity of soil rough surface is taken as $\varepsilon_r = 9.77 + 0.48i$. Unless specified otherwise, the parameters of the rough surfaces are taken as $h = 0.1\lambda$, $l = 1.0\lambda$, respectively. The length of the soil rough surface is $L = 51.2\lambda$ with sampling step $\Delta x = \lambda/10$. Unless specified otherwise, the radius of the cylinder is $r = 1.0\lambda$. The results are presented here over 50 Monte Carlo realizations of rough surface for HH polarization.

Figure 2 presents the bistatic scattering coefficient (BSC) versus the scattering angle with different rough surface parameters of rms height and correlation length, respectively. One can observe that there exists an obvious peak in the specular direction for smaller rms height, which is attributed to the fact that a smaller rms height leads to a smaller roughness of the rough surface, giving rise to an obvious peak in the specular direction. The backscattering enhancement is also observed with rms height increasing, which is due to the fact that the roughness of the rough surface increases with rms height increasing. The influence of correlation length is also investigated in Figure 2. One can readily find backscattering enhancement with correlation length decreasing, which is attributed to the fact that roughness of the rough surface increases with correlation length decreasing.

In Figure 3, the dependency of the BSC on the size and the location of the cylinder are investigated. One can observe that, with the radius of the cylinder increasing, the BSC increases at non-specular region. It is readily found that the BSC almost unchanged in the specular direction, which is attributed to the fact that the total scattering strength depends mainly on the soil rough surface rather than the object due to the fact that the size of the object is really small compared to the soil rough surface. One can also observe that, the impact of the height of the cylinder is small with the height of the cylinder increasing due to the absorption of the lossy dielectric surface.

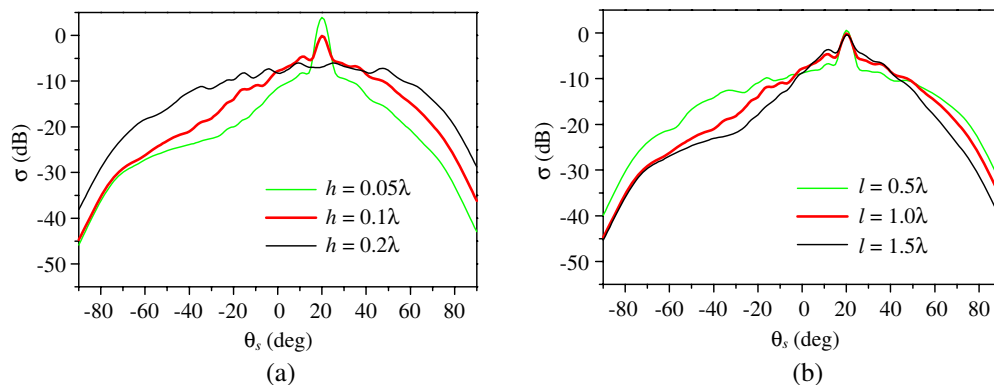


Figure 2: BSC versus the scattering angle with different rough surface parameters.

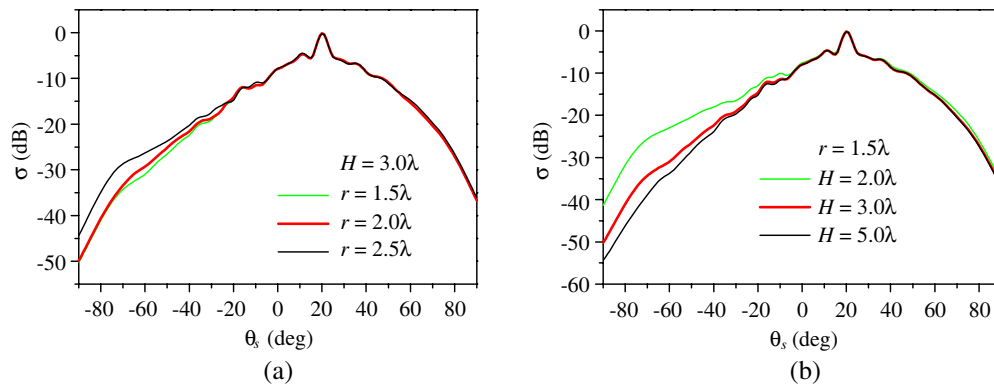


Figure 3: BSC versus the scattering angle with different object parameters.

4. CONCLUSION

In this paper, the influence of the rough surface parameters and the parameters of the size and the position of the cylinder on bistatic scattering coefficient is investigated by utilizing MoM. Numerical results have showed that the rms height and correlation length of the rough surface have significant influence on the angular distribution the BSC while the impact of the size and the position of the cylinder is relatively small under certain condition considered in this paper due to the fact that total scattering strength depends mainly on the soil rough surface rather than the object.

ACKNOWLEDGMENT

The authors would like to thank the anonymous reviewers for their helpful and constructive suggestions and Investigation on Electromagnetic Scattering from the Land Surface and the Land Parametric Inversion of Northern Shanxi Region, National Natural Science Foundation of China (Grant No. 61379026).

REFERENCES

1. Lawrence, D. E. and K. Sarabandi, "Electromagnetic scattering from a dielectric cylinder buried beneath a slightly rough surface," *IEEE Trans. Antennas Propag.*, Vol. 50, 1368–1376, 2002.
2. Wang, X., C.-F. Wang, Y.-B. Gan, and L.-W. Li, "Electromagnetic scattering from a circular target above or below rough surface," *Progress In Electromagnetics Research*, Vol. 40, 207–227, 2003.
3. Zhang, G. F., L. Tsang, and Y. Kuga, "Studies of the angular correlation function of scattering by random rough surfaces with and without a buried object," *IEEE Trans. Geosci. Remote Sensing*, Vol. 35, 444–453, 1997.
4. Bourlier, C., G. Kubické, and N. Déchamps, "Fast method to compute scattering by a buried object under a randomly rough surface: PILE combined with FB-SA," *J. Opt. Soc. Am. A*, Vol. 25, 891–902, 2008.
5. Tsang, L., J. A. Kong, K. H. Ding, and C. O. Ao, *Scattering of Electromagnetic Waves: Numerical Simulations*, Vol. 2, Wiley-Interscience, New York, 2001.
6. Tsang, L., K. H. Ding, S. W. Huang, and X. L. Xu, "Electromagnetic computation in scattering of electromagnetic waves by random rough surface and dense media in microwave remote sensing of land surfaces," *Proc. IEEE*, Vol. 101, 255–279, 2013.
7. Thorsos, E. I., "The validity of the Kirchhoff approximation for rough surface scattering using a Gaussian roughness spectrum," *J. Acoust. Soc. Am.*, Vol. 83, 78–92, 1988.

Study on the Characteristics of Long-wave Radiation over China Area

Y. T. Ma^{1,2}, L. S. Sun¹, and H. Ding¹

¹School of Civil Engineering, Shenyang Jianzhu University, Shenyang, China

²School of Resource & Civil Engineering, Northeastern University, Shenyang, China

Abstract— Long-wave radiation which escapes from Earth-atmosphere system often obviously changes before the occurrence of major natural hazards, therefore the research of OLR is necessary for the short-term forecast and early warning of disasters. This paper analyzed the long-wave radiation background field of Chinese mainland by using outgoing long-wave radiation (OLR) data from National Oceanic and Atmospheric Administration (NOAA), USA. The results showed that: the OLR value changed more obviously with the variation of latitude than that with longitude, and there are strongly seasonal and regional variations in outgoing long-wave radiation.

1. INTRODUCE

Long-wave radiation emitting from the earth-atmosphere system is observed from space by the Infrared channel of radiometer on Meteorological Satellite. It reflects convection strength of tropical regions and latent heat released by cloud cover, atmospheric vertical motion, divergence wind and convective condensation. Meanwhile, OLR contains information about sea surface temperature and air-sea interactions, which has a close relationship with rainfall of Tropical Ocean and continental monsoon. Before the outbreak of earthquakes, floods, volcanoes and other natural disasters, the radiation rises of OLR tend to be more obvious than that in the surrounding area, therefore, the research on OLR is becoming increasingly important. In the 1970s, people began to obtain OLR by satellite observations and apply it to atmospheric circulation, climate analysis and prediction [1–6]. Dongliang Li found the changes of OLR in El Niño years are quite different with those in Anti-El Niño years in mainland China, and investigated the connection between the OLR anomalies and the El Nino events [7]. Li Sun and others compared and analyzed the space-time distribution and the propagation characteristics of low-frequency oscillations of OLR field during the drought years in the Northeast, and the results showed that the drought of Northeast is closely related to the distribution and variation of OLR at low-latitude [8]. Since the significant meaning of studying OLR, the paper adopted global OLR data to investigate the spatial distribution and seasonal fluctuation characteristics of OLR.

2. DATA AND PROCESSING

2.1. Investigation Area

Higher west when compared to the East is one of the characteristics of China's terrain, and the mountains, plateaus are located in the west of Daxinganling — Taihang Mountains — Wushan — Xuefengshan line, while hills and plains are mainly in the east of the line. Yellow River, Yangtze River, Pearl River and other major rivers originate in the western highlands and mountains, tilting along terrain and flowing into the sea. Chinese climate has three characteristics: significant monsoon characteristics, distinct continental climate and various climate types.

2.2. Data

US National Oceanic and Atmospheric Administration (NOAA) provides $2.5^\circ \times 2.5^\circ$ and $1^\circ \times 1^\circ$ grid types of long-wave radiation data, where the data of $2.5^\circ \times 2.5^\circ$ grid type owns a long duration (from 1974 to date), which provides us with the data base to get more accurate spatial field characteristics of long-wave radiation. The study selected monthly average long-wave radiation data of $2.5^\circ \times 2.5^\circ$ grid type from January 1991 to December 2010 (20 years) as the original data of background field to analyze characteristics of OLR related to latitude and longitude, space and time.

2.3. Data Processing

First we combined monthly data from each year into quarterly data, and then synthesized the quarterly data into annual data; then we combined the 20 years' quarterly data into quarterly average data, and combined the 20 years' annual data into annual average data. Finally, based on the latitude, longitude, region and time, we analyzed the data.

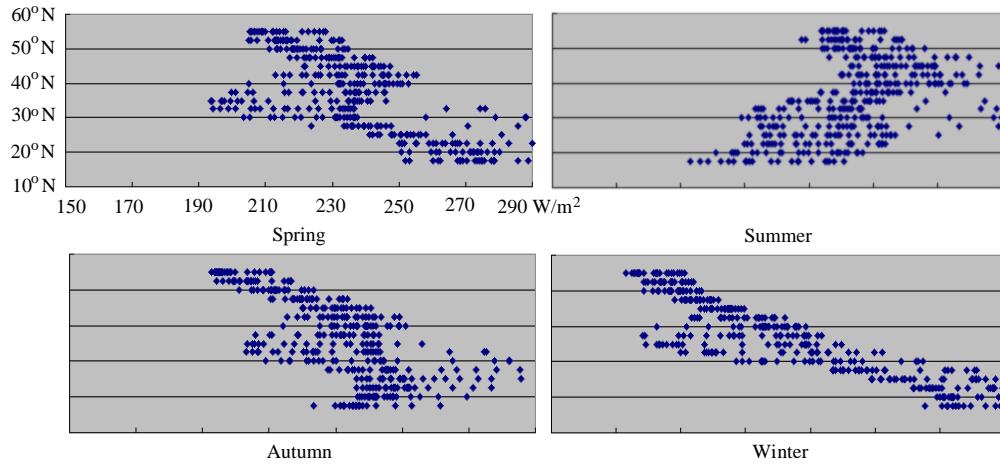


Figure 1: Characteristics of long-wave radiation along latitude.

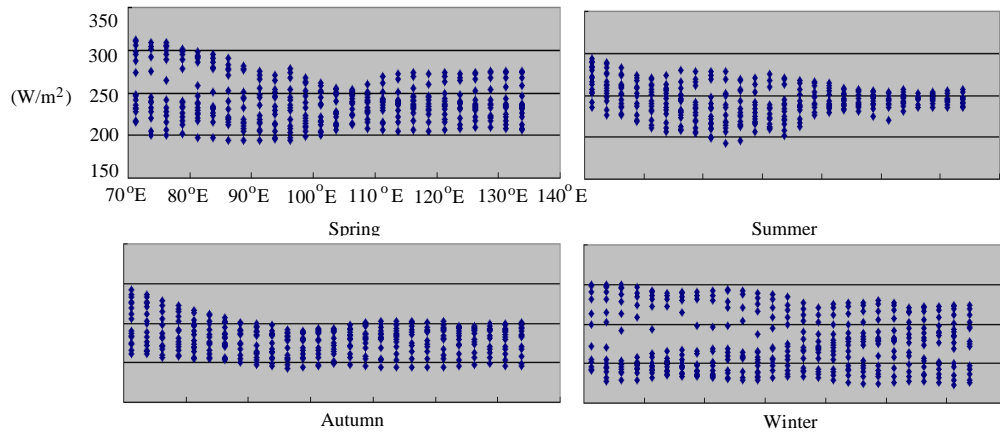


Figure 2: Characteristics of long-wave radiation along longitude.

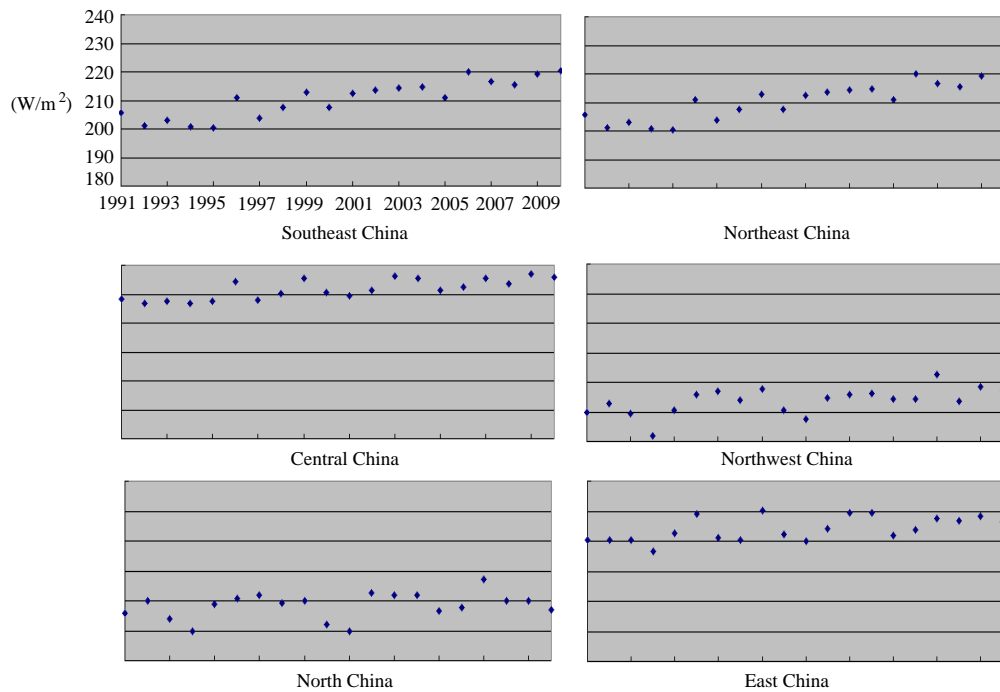


Figure 3: Characteristics of Chinese long-wave radiation data.

3. STUDY RESULTS

3.1. Characteristics of OLR along Latitude

The Figure 1 showed the variation of long-wave radiation data from 400 points in and around China where we could see that the OLR values with the variation of latitude had obvious seasonality. In spring, autumn and winter the long-wave radiation values had a decreasing trend with the increase of latitude, while the values had an increasing trend with the increase of latitude in summer. Generally speaking, the 35°N was feature latitude, where long-wave radiation changed obviously.

3.2. Characteristics of OLR along Longitude

Figure 2 showed the characteristics of long-wave radiation along longitude. Generally speaking, the changes of OLR along longitude were relatively gentle which were less obvious than those along latitude, and therefore it could be considered that the OLR values were mainly controlled by the latitude.

3.3. Spatial Distribution Characteristics of OLR

The Figure 4 showed that the OLR values were low in Northeast China and the Tibetan Plateau, and were high in Taiwan, Hainan, southern Yunnan province and northern Xinjiang province. The OLR values were higher relatively in Northwest China and East China than those in Tibetan plateau. The eastern of Xinjiang and the western of Inner Mongolia were two high value areas in Northwest China, especially in summer and autumn the values were abnormally obviously high.

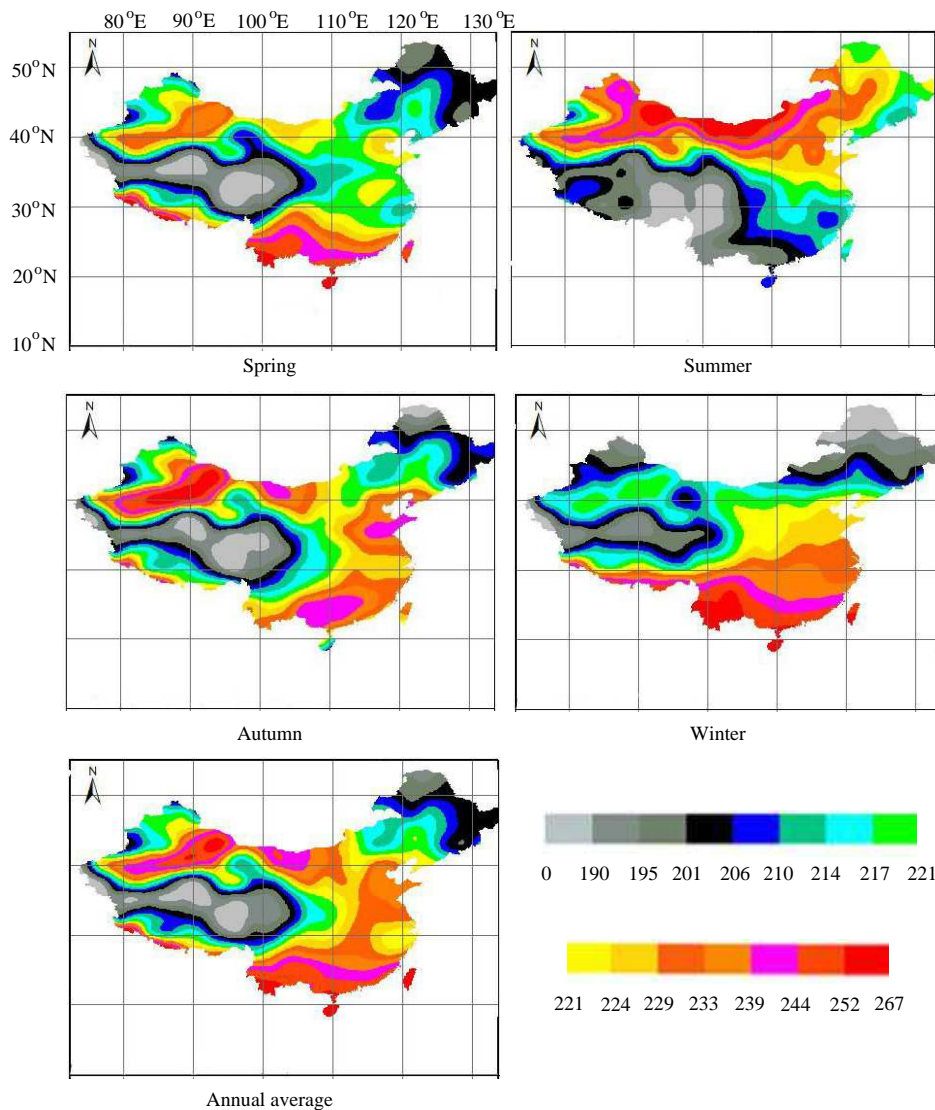


Figure 4: Characteristics of Chinese long-wave radiation data.

Similar to the Qinghai-Tibet Plateau blocks, the changes of OLR in the two high value areas were dramatic in spring and autumn and relatively slow in the summer and winter.

3.4. Time Distribution Characteristics of OLR

As could be seen from Figure 3, the OLR values had a overall increasing trend and were generally low in Northeast China and Northwest China, and were highest in Central China.

4. CONCLUSIONS

1. Long-wave radiation values changed significantly along latitude, and 35°N was feature latitude, where the long-wave radiation values changed significantly along latitude, but did not change significantly along longitude in the Chinese region.
2. The changes of long-wave radiation had seasonal and regional pattern. Being affected by topography, long-wave radiation of China's Qinghai-Tibet Plateau, Northwest, Southeast coastal region, Northeast and other had different characteristics. The regional characteristics were manifested as the low value of OLR in area of Qinghai-Tibet Plateau and northeast at all seasons, the relatively high value of OLR in Taiwan, Hainan, southern Yunnan and north Xinjiang in spring and winter, and the relatively high value of OLR in eastern Xinjiang and western part of Inner Mongolia in summer and autumn.
3. The time characteristics showed that in most parts of Chinese region the value of OLR advanced while in other regions, the value of OLR unchanged.

REFERENCES

1. Li, D. and S. C. Jiang, "On the prediction of tropical cyclone landfall and influence on southern china using monthly OLR anomalies for prime summer," *Journal of Tropical Meteorology*, Vol. 8, No. 2, 201–206, 2002.
2. Luo, Q. H., T. R. Li, and X. J. He, "The relationship between OLR and tropical cyclone development in the South China Sea," *Journal of Applied Meteorology*, Vol. 15, No. 1, 81–87, 2004.
3. Yu, Y. B. and X. P. Yao, "The relation between the characteristics of OLR and anomaly weather in the summer of 2003," *Meteorology*, Vol. 31, No. 7, 10–15, 2005.
4. Liu, D. F. and C. L. Kang, "The remote sensing of earth long-wave radiation (OLR) and the prediction of major natural disaster," *Earth Science Frontiers*, Vol. 10, No. 2, 427–435, 2003.
5. Li, D. F., Z. L. Luo, and K. Y. Peng, "The abnormal phenomenon of OLR before strong earthquakes," *Earthquake*, Vol. 17, No. 2, 126–132, 1997.
6. Qin, S. T. and H. B. Sun, "The analysis of satellite infrared long-wave radiation OLR before magnitude-6.6 earthquake in Delhi," *Plateau Earthquake*, Vol. 15, No. 3, 42–44, 2003.
7. Li, D. L., "OLR and El Niño in mainland China," *Plateau Meteorology*, Vol. 9, No. 4, 411–417, 1990.
8. Sun, L., G. An, and X. L. Tang, "Drought feature analysis of OLR in Northeast China," *Journal of Applied Meteorology*, Vol. 11, No. 2, 228–235, 2000.

The Study of the Generalized Stereopair Matching Method

L. S. Sun¹, Y. T. Ma^{1,*}, and H. Wang²

¹School of Civil Engineering, Shenyang Jianzhu University, China

²School of Resource & Civil Engineering, Northeastern University, China

Abstract— Traditional matching images method is required that remote sensing images must be obtained from same sensor in different times. If the region can't be covered by field view from one satellite sensor, images stereopair can't be acquired. It is necessary to match images from different satellites for getting the same overlap region. This method is called the generalized matching stereo pair. In this article, two images were selected for studying the generalized stereopair matching method, one was a QuickBird image, and other was a Spot image. Twenty six control points in same area in two images were selected for verifying the experimental results. The rate of success matching points was 88.5%. The result showed the generalized stereopair matching method was feasible and reliable.

1. INTRODUCE

The corresponding relationship between two or more points in the images is called image matching. The points set can be obtained from digitized images, maps, or GIS data et al.. Image matching method is widely used in the many fields, including navigation, aerial survey, satellite remote sensing, generation of DEM, three dimensional reconstruction, and military field et al. [1, 2].

The traditional method of images matching in the remote sensing field is researched for remote sensing images of the same sensor in different times. Although satellites can provide a lot of images on its flight path, the images in the region that sensor view angle can't be covered cannot be got. The images in some areas can't be got from satellite operator because of secrecy reasons. However the area without images may be interested, which is closely related national defense, economy, science and government major decisions and so on.

It is necessary to match images from different satellites for getting the same overlap region. This method is called the generalized matching stereo pair. This method has many advantages, such as enlarging the selection range of stereopair images, making full use of the existing data resources, saving costs, saving human and material resources.

2. CONSTRUCTION AND PROCESSING OF GENERALIZED STEREOPAIR

In photogrammetry and remote sensing, the stereopair is a pair of overlapping images taken from different stations. The stereo image points, lines and polygons constructed from any two images with overlapping areas is called generalized stereopair.

In this paper generalized stereopair was constructed from the multi-source images covering in the same area. The left and right images came from different sensors that their mechanisms were different. Therefore the spatial resolutions, colors and sizes of images were different. The left and right images should be normalized to facilitate automatic algorithm for matching the points with same position.

2.1. The Normalization of Spatial Resolutions

Before image automatic matching, left and right images spatial resolutions must be normalized. According to the spatial resolutions of the left and right images, the image resolution of high spatial resolution was lowered to low spatial resolution.

2.2. The Normalization of Colors

In this article, left image was a panchromatic image and right image was a color image, so left and right images should be unified into the same color space for matching images. The color image was transformed into gray image. The process of color image to gray image was calculated by each pixel by using the following formula:

$$Y = 0.3 * \text{Red} + 0.59 * \text{Green} + 0.11 * \text{Blue} \quad (1)$$

The standardized processing of image size was the last process. According to the small image size, the large image was subseted, the left and right images are coincident in size. Figure 1 was the standard image after processing.

*Corresponding author: Yuntao Ma (mayuntao7@163.com).

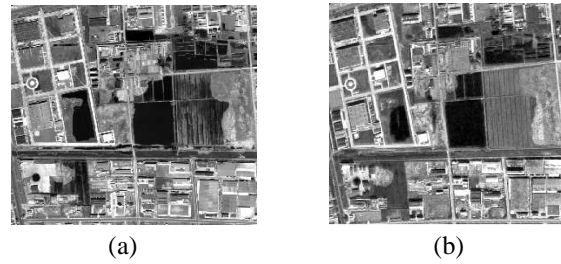


Figure 1: Generalized stereopair. (a) Left image. (b) Right Image.

3. MATCHING METHOD

3.1. Gray Scale Match

The correlation coefficient and the least squares matching algorithms are most often used. The least squares algorithm can make full use of information within the image window for adjustment calculation. Its image matching can achieve high accuracy in theory and practice. Correlation coefficient can reach one pixel precision, and even reach sub pixel level after simulation of correlation coefficient.

3.2. Determining Layers of Pyramid

Top image matching can be carried out smoothly if the levels of pyramid are reasonable. The number of pyramid levels should be small and image distortion is small. Pyramid levels were determined according to the image size, the change in disparity, the size of matching window and other factors [3–5]. In this article pyramid levels were determined by the priori parallax. Several points were measured by artificial, then the parallaxes of these points were calculated and the maximum parallax P_{\max} was estimated. If S pixels were searched on the top level matching, the pyramid levels N can be determined according to next formula:

$$p_{\max}/L^{N-1} = S * \Delta \quad (2)$$

Remark: The Δ in the formula is the size of pixel.

3.3. Theories of Correlation Coefficient and Least Squares Matching Algorithm

The commonly matching algorithms basing on gray scale are correlation function, covariance function, correlation coefficient, the absolute value sum and the mean variance of gray scale and so on. Among them correlation coefficient is the highest reliability, so this article adopted the correlation coefficient.

The correlation coefficient is defined as:

$$\rho(r, c) = \frac{\sigma(x, y)}{\sigma(x, x)\sigma(y, y)} = \max \geq T \quad (3)$$

In the formula, $\sigma(x, y)$ represents the covariance function of the target pixel gray and search area pixel gray, $\sigma(x, x)$ represents variance of pixel gray in the target area, ρ represents correlation coefficient. When ρ gets the maximum and (r, c) is the location of the same name point or the offset numerical, the threshold T is generally in the range of 0.6 to 0.8.

The correlation coefficient has good properties and can effectively eliminate the adverse effects of radiation on the matching results.

The geometric transformation parameters and radiation transformation parameters are introduced in the least Squares matching scheme. Geometric transformation parameters are used to compensate for the geometric difference between the two windows, and radiant transformation parameters are used to compensate radiate difference of pixel gray scale between the two windows.

Let the left and right images as f_1, f_2, g_1, g_2 is respectively corresponding to the matching window. For the size of the image matching window is very small, so higher distortion is ignored and linear distortion is left, the formula is followed:

$$\begin{cases} x_2 = a_0 + a_1x_1 + a_2y_1 \\ y_2 = b_0 + b_1x_1 + b_2y_1 \end{cases} \quad (4)$$

When taking the linear gray scale distortion into account between the right of the image and on the left image, the general model is followed:

$$g_1(x, y) + n_1(x, y) = h_0 + h_1g_2(a_0 + a_1x + a_2y, b_0 + b_1x + b_2y) + n_2(x, y) \quad (5)$$

The error equation individually is established, its matrix is followed:

$$V = AX - L \quad (6)$$

Method of least squares:

$$X = (A^T A)^{-1} AL \quad (7)$$

The purpose of matching is to get the homonymy points, and the central of the window is usually taken as the point to be matched. However, in the relevant high precision image, the center of the window must be taken into account whether it is the best matching point. The accuracy of matching theory LS shows that matching accuracy depends on the window gray gradient g'_x , g'_y . The square of the gradient can be taken as weight, and the sum of weighted average coordinates can be got in the left window:

$$\begin{cases} x_t = \sum xg'_x / \sum g'^2_x \\ y_t = \sum yg'_y / \sum g'^2_y \end{cases} \quad (8)$$

Taking it as the target point coordinates, coordinates of its homonymy point can be obtained by the geometric deformation parameters, which can be got from the least squares image matching algorithm:

$$\begin{cases} x_s = a_0 + a_1x_t + a_2y_t \\ y_s = b_0 + b_1x_t + b_2y_t \end{cases} \quad (9)$$

4. EXPERIMENTS AND ANALYSIS

In this article, the experimental data were a QuickBird image and a Spot image from same region. After standard processing, the spatial resolution of QuickBird image was transformed into 2.5 meters and the size was 800×716 pixels, and the spot image spatial resolution was transformed into 2.5 meters and the size was 907×789 pixels.

The technical route of this article was followed. First, left and right images in the selected experimental area were unified into the same standard. Then the image of the pyramid was built, the reasonable initial matching points of the top pyramid image were selected.

The least squares method was adopted in the bottom pyramid, and the correlation coefficient method was adopted in the others. Matching flowchart was showed in Figure 2.

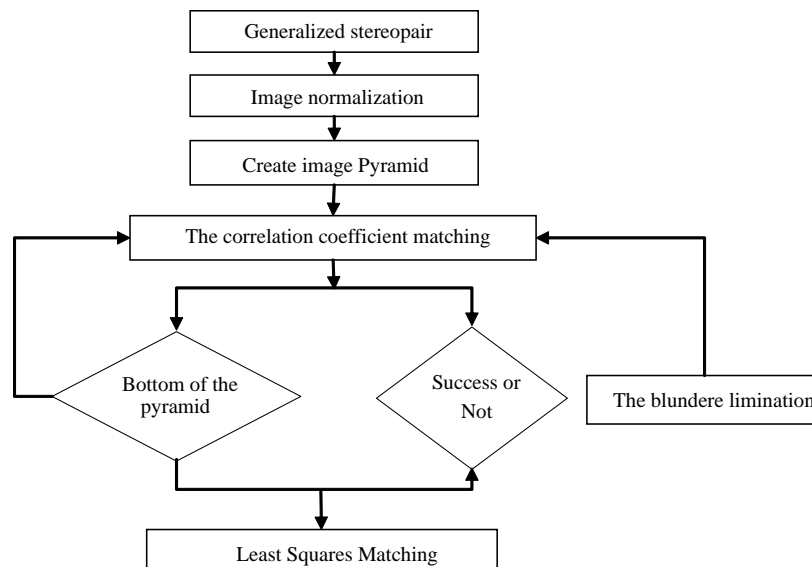


Figure 2: Matching flowchart.

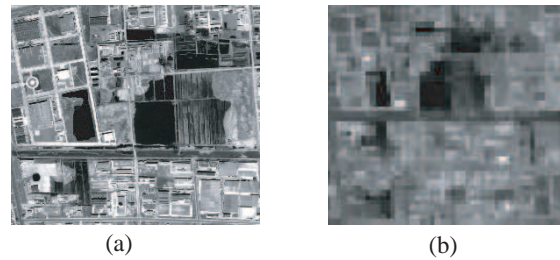


Figure 3: (a) Raw image. (b) Top of the pyramid image.

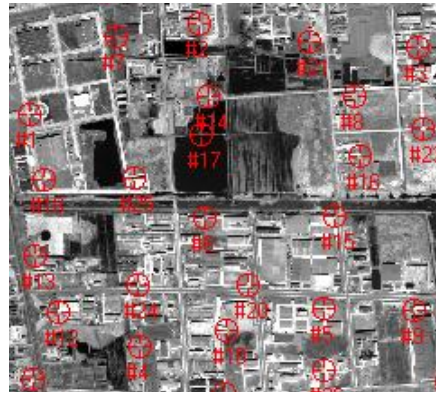


Figure 4: Matching points of verifying.

Pyramid image was created by using the Haar wavelet. It is shown in Figure 3, Figure 3(a) is a raw image, Figure 3(b) is the top of the image pyramid.

In this article, 1386 points were selected for image matching, matching window size is 5×5 , the search window size is 9×9 , the correlation coefficient threshold is 0.6, and the minimum is 0.4. In order to check up the accuracy of correlation matching hierarchical pyramid, 26 pairs of corresponding points were selected by artificial in the experiment; the points were shown in Figure 4. In normal circumstances, the parallax of matching points should be within 2 pixels. The result of the experiment showed that 23 matching points were correct; the correct rate was 88.5%.

5. CONCLUSIONS

In this article, the least squares and the generalized correlation coefficient methods were used in generalized stereopair. Haar wavelet was used in pyramid hierarchical. Twenty six control points with same places in two images were selected for verifying the experimental results. The success rate of matching points was 88.5%. The experiment has achieved better results. The experiment result showed the technical process of the generalized stereopair matching in this article was feasible and reliable.

REFERENCES

1. Li, F., "About stereo matching technology research," Ph.D. Thesis, Shanghai Jiao tong University, Shanghai, 1999.
2. Zhang, Z. X. and J. Q. Zhang, *Digital Photogrammetry*, Wuhan University Press, Wuhan, 2002.
3. Li, F. and Y. H. Zhou, "Least square matching algorithm using pyramid decomposing," *Journal of Shanghai Jiaotong University*, Vol. 33, No. 35, 513–515, 1999.
4. Wang, W. X., "The 3D reconstruction methods based on generalized stereopair," Ph.D. Thesis, Liaoning Technical University, Fuxin, 2007.
5. Fan, Y. H., "Stereoscopic image matching and DTM automatic generation of research and practice," Ph.D. Thesis, The PLA Information Engineering University, Zhengzhou, 2000.

Study on Surface Albedo of Different Land Cover Types in Liaoning Province

J. L. Wang¹, Y. T. Ma^{1,2,*}, and L. S. Sun¹

¹School of Civil Engineering, Shenyang Jianzhu University, Shenyang, China

²School of Resource & Civil Engineering, Northeastern University, Shenyang, China

Abstract— Using MODIS image, we analyzed the relationship between surface albedo and underlying surface in Liaoning Province. In this paper, we not only compared the magnitude of albedos of different surface coverage types in Liaoning, we also analyzed the relation between MODIS Surface Albedo of various surface coverage types and NDVI. It worked out that the sequence of surface albedos in different kinds of areas are shown in the following: grassland > urban area > cropland > wetlands > water. The surface albedos of water, wetland, urban area and cropland are linearly correlation with NDVI, and the surface albedos of grassland and woodland are negatively linearly correlation with NDVI.

1. INTRODUCE

The temperature of Earth has raised 0.7 degrees centigrade in the past 100 years. The changes of global warming already play a profound effect on the ecosystem and human society, as a result, the global warming problem is becoming one of the most hot issues in recent researches on earth science. We commonly believe that the main reason of the global warming is the so called ‘greenhouse effect’ which result from the high concentration of greenhouse gases in the air. However, with more researches on global climate changes, researchers gradually know that the surface albedo also affects the global climate significantly. In the last 100 years (1906–2005), the linear trend of global warming is an advance of 0.74 degrees centigrade (0.56–0.92), the temperature rises in high latitude area of the Northern Hemisphere is relatively more obvious. It is given that the areas with higher surface albedo can reflect more solar radiation into outer space, and as a result can relief temperature rise. With this reason, researchers care more about the influences and responses of climate changes which surface albedo result in. It is important to precisely obtain the parameters of surface albedo and to study its change and distribution characteristics since its significant meaning in study of regional climate change and its improvement and validation in land surface process. We know that the surface albedo is mainly affected by underlying surface regime, solar altitude, meteorological condition and other factors, and the underlying surface regime which includes land cover types and NDVI is the key factor that influences the surface albedo.

2. DATA AND PROCESSING

2.1. Research Area

In order to analyze the relationship between surface albedo from MODIS and underlying surface regime in Liaoning Province, in this paper, we choose 6 kinds of typical surface features which are water, wet land, urban area, glass land, farmland and forest land to process study. In each kind, we select 4 research regions to do the statistical analysis, the district distribution are shown in Table 1.

The Liaoning Province is located in east coast of Eurasia, belonging to temperate continental monsoon climate zone. It is showed that the area is characterized by nonuniform rainfall, abundant sunshine, rainy season which coincided with high temperature, high accumulated temperature, longer winter when compared to summer, wetter east when compared to west and shorter spring and autumn. The amount of precipitation in east hilly area is more than 1100 millimeters per year; and the amount of precipitation in west hilly area that connected with Inner Mongolia plateau is around 400 millimeters per year, which is the least precipitation area in the whole province; in its central plains, the amount of precipitation is relatively moderate, which is around 600 millimeters per year.

*Corresponding author: Yuntao Ma (mayuntao7@163.com).

Table 1: District distribution.

Plot name	Latitude (° ' ")	Longitude	Ecotype	Plot name	Latitude (° ' ")	Longitude	Ecotype
Baishi reservoir	N 41 42 02	E 120 59 17	water	Dalian grassland	N 39 37 48	E 122 33 00	grassland
Hun River	N 41 49 30	E 124 08 25	water	Fuxin grassland	N 41 15 00	E 121 40 48	grassland
Gedalou reservoir	N 40 58 04	E 122 08 47	water	Chaoyang grassland	N 41 30 00	E 119 38 24	grassland
Dahuofang reservoir	N 41 53 03	E 124 10 48	water	Huludao grassland	N 40 48 00	E 119 50 24	grassland
Shenyang wetland	N 41 16 12	E 122 13 48	wetland	Beisijiazi village	N 42 39 03	E 122 06 26	cropland
Dalian wetland	N 39 27 36	E 121 24 36	wetland	Beiwanzi village	N 41 26 25	E 119 49 26	cropland
Panjin wetland	N 40 53 24	E 121 58 12	wetland	Houliu village	N 40 46 50	E 122 21 54	cropland
Tieling wetland	N 43 06 36	E 124 52 12	wetland	Zhaojiawobao area	N 42 57 27	E 123 55 07	cropland
Shenyang	N 41 48 18	E 123 27 23	urban area	Qingshangou area	N 42 10 38	E 124 07 52	woodland
Liaoyang	N 41 15 40	E 123 11 17	urban area	Toudaogou area	N 42 10 38	E 124 51 27	woodland
Dalian	N 38 54 43	E 121 38 29	urban area	Daheishan area	N 40 52 07	E 123 33 45	woodland
Huludao	N 40 45 00	E 120 50 58	urban area	Bingyugou area	N 40 02 55	E 122 56 41	woodland

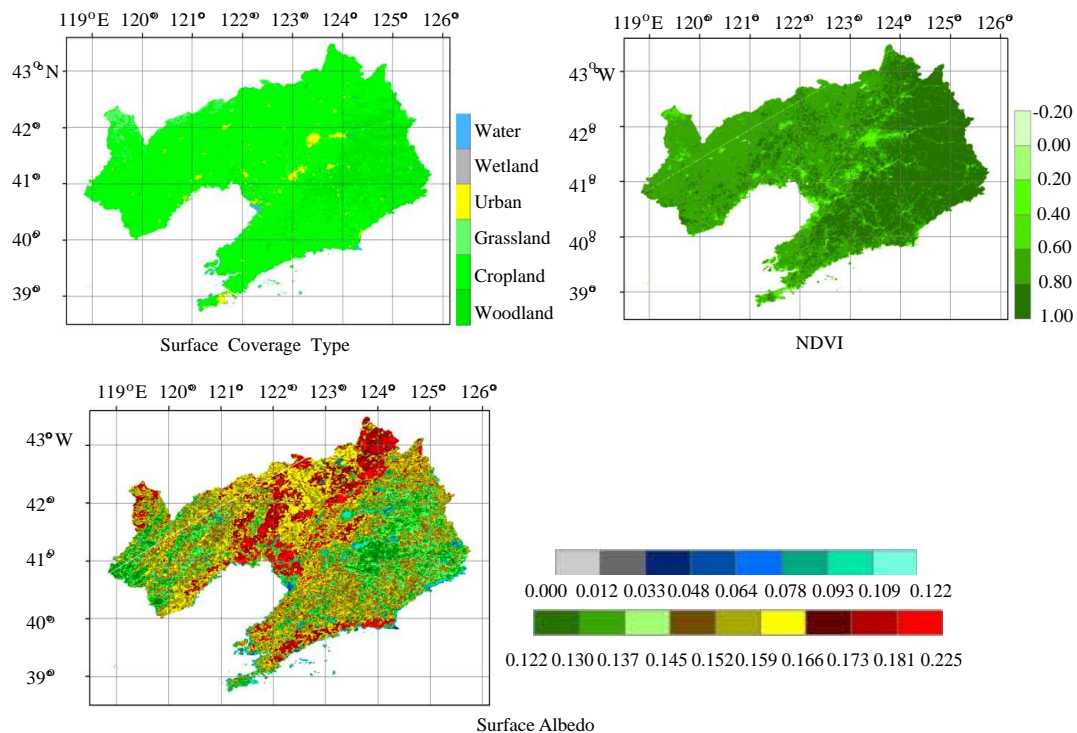


Figure 1: Maps of surface coverage type, NDVI and surface albedo.

2.2. Data Sources

In this paper, we adopted MOD43B3, MOD13A2, MOD12Q1 from MODIS data on August 12, 2012. The surface albedo image of Liaoning Province, NDVI image and the image of surface

coverage type which are after processing are shown in Figure 1.

2.3. Data Processing

In this paper, we overlaid the surface albedo image, NDVI image and the image of surface coverage type, all of which are after processing, and with the help of ENVI, we output its outcome to EXCEL to figure out the average value of surface albedo of different surface coverage type and the relationship of each surface coverage type and NDVI.

3. RESEARCH RESULTS

The relationships of different surface coverage types and statistics of surface albedo are shown in Table 2, and the relation of surface albedos and NDVI in different areas of Liaoning with different surface coverage are studied and only one of each kind (water, wetland, urban, grassland, cropland, woodland) is shown in Figure 2, in which y represents surface albedo WSA and x represents NDVI.

3.1. Comparison of Different Surface Coverage's Albedo

According to Table 2, we can figure out the sequence of features based on their values of NDVI was the following: woodland > cropland > grassland > urban area > wetlands > water, and the sequence of features based on their values of surface albedo was the following: urban area > grassland > cropland > woodland > wetlands > water. From this sequence, we can find that with

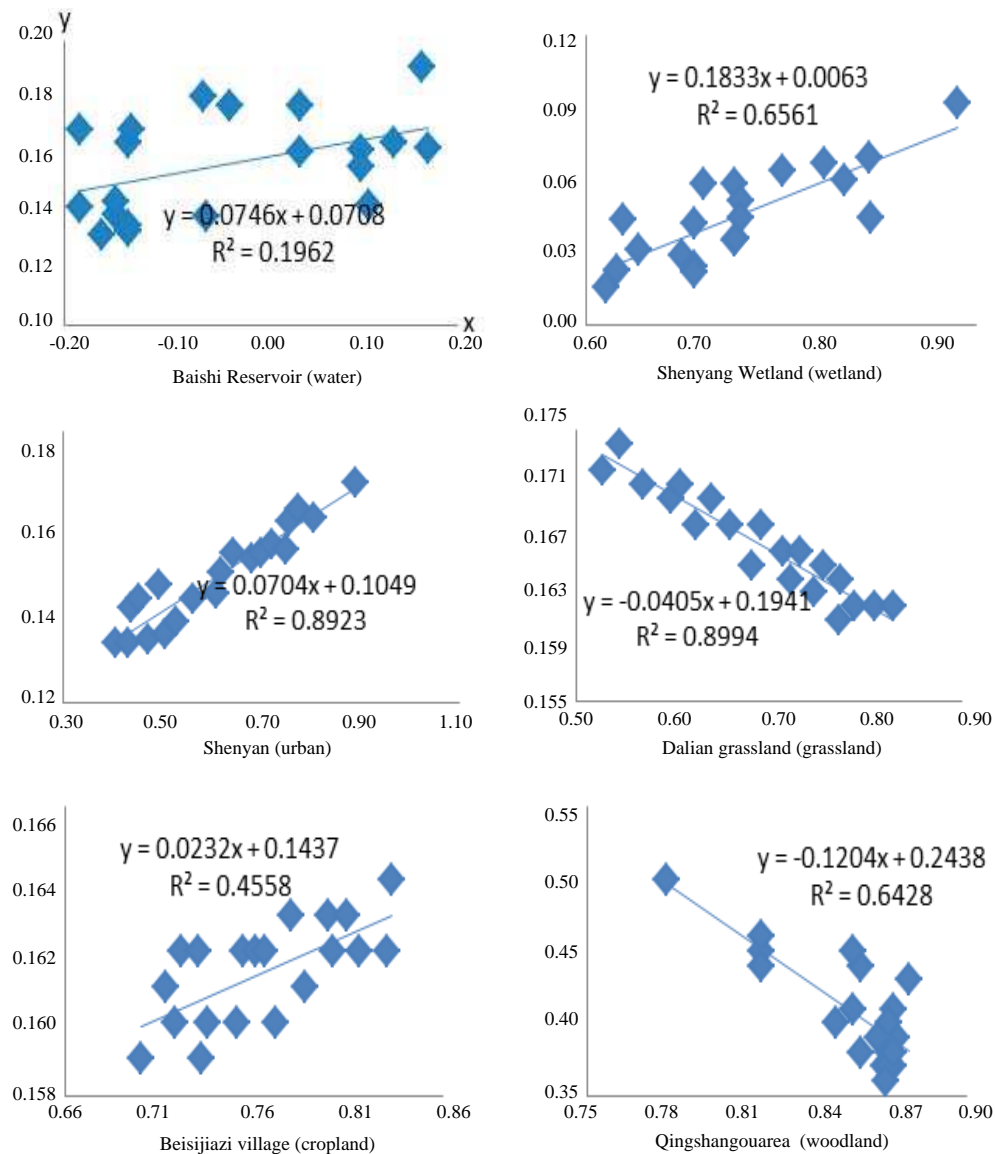


Figure 2: Relationship of MODIS Surface Albedo and NDVI in different Surface Coverage Types of Liaoning.

Table 2: The relationship between statistical value of surface coverage type and albedo.

surface coverage type	Mean of NDVI	Mean of albedo	Median of albedo	Mode of albedo
Water	0.0384	0.0484	0.0440	0.0400
Wetland	0.5757	0.1047	0.1070	0.1050
Urban area	0.6211	0.1503	0.1525	0.1510
Grassland	0.6999	0.1581	0.1590	0.1610
Cropland	0.7964	0.1482	0.1490	0.1490
Woodland	0.8583	0.1384	0.1390	0.1390

the increase of surface albedo, surface coverage type is gradually changed from woodland which is covered best (Since the specular reflection of water, the albedo of water and wetland are very low) to grassland which is covered worst (we speculate that the reason of higher albedo in urban area compared to albedo of grassland is that the specular reflection of building surface material).

3.2. Relationship of WSA and NDVI

3.2.1. Water

The WSA is linearly correlation with NDVI, and value of their correlation index is quite low, the value of R_2 is only around 0.2 (except the Gadalou reservoir which is 0.7956), the values of WSA mostly converge on 0.3 to 0.6, and the values of NDVI mainly concentrate on -0.2 to 0.2 , they are relevant most when the value of NDVI is between -0.2 to 0 .

3.2.2. Wetland

The WSA is linearly correlation with NDVI, and value of their correlation index is quite high, the value of R_2 is around 0.8 and even reaches 0.9625, the values of WSA mostly converge on 0.06 to 0.13, and the values of NDVI mainly concentrate on 0.6 to 0.8.

3.2.3. Urban Area

The WSA is linearly correlation with NDVI, and value of their correlation index is quite high, the value of R_2 is around 0.8 and even reaches 0.8923, the values of WSA mostly converge on 0.13 to 0.16, and the values of NDVI mainly concentrate on 0.5 to 0.8.

3.2.4. Grassland

The WSA is negatively linearly correlation with NDVI, and value of their correlation index is quite high, the value of R_2 is around 0.9 and even reaches 0.9071 the values of WSA mostly converge on 0.12 to 0.17, and the values of NDVI mainly concentrate on 0.6 to 0.8.

3.2.5. Cropland

The WSA is linearly correlation with NDVI, and value of their correlation index is not too high, the value of R_2 is around 0.5 (except the Houliu village which is 0.7956), the values of WSA mostly converge on 0.15 to 0.18, and the values of NDVI mainly concentrate on 0.7 to 0.8.

3.2.6. Woodland

The WSA is negatively linearly correlation with NDVI, and value of their correlation index is quite high, the value of R_2 is around 0.7 and even reaches 0.8137 the values of WSA mostly converge on 0.13 to 0.17, and the values of NDVI mainly concentrate on 0.7 to 0.9.

4. CONCLUSIONS

Above researches show that in Liaoning area the sequence of features based on their values of NDVI was the following: woodland > cropland > grassland > urban area > wetlands > water, the sequence of features based on their values of surface albedo was the following: urban area > grassland > cropland > woodland > wetlands > water. NDVI and surface albedo of the different land cover types (except wetlands and water bodies) showed a significant negative correlation.

In the same land cover types, the surface albedo and surface coverage type are obviously related (except water). NDVI and surface albedo of water, wetlands, urban and cropland were a positive linear correlation, NDVI and surface albedo of grassland and woodland were a negative linear correlation. This study provided a reference for feature extraction and regional climate change monitoring in Liaoning Province.

REFERENCES

1. Liu, S. J., J. H. Zhang, D. X. Cai, and G. H. Tian, “Study on relationship between vegetation index change and surface albedo,” *Journal of Anhui Agricultural Sciences*, Vol. 37, No. 30, 14852–14853, 2009.
2. Xiao, D. P., F. L. Tao, and P. Moiwo Juana, “Research progress on surface albedo under global change,” *Advances in Earth Sciences*, Vol. 26, No. 11, 1217–1224, 2011.
3. Li, R. P. and J. P. Zhang, “Study on the Remote Sensing of Surface Albedo in the Horqin Sandy,” *Journal of Anhui Agricultural Sciences*, Vol. 38, No. 9, 4671–4673, 2010.
4. Li, H. F., Z. L. Yuan, and T. Yu, “Surface albedo estimating based on HJ-1/CCD and relationship analysis between albedo and NDVI,” *Remote Sensing Information*, Vol. 27, No. 4, 16–21, 2012.
5. Zhang, Y. F., X. P. Wang, Y. X. Pan, Z. N. Wang, and R. Hu, “The dependence of surface albedo on soil moisture in an arid desert area,” *Journal of Desert Research*, Vol. 31, No. 5, 1141–1148, 2011.
6. Liu, H. Z., G. Tu, and W. J. Dong, “Surface albedo variations in semi-arid region,” *Chinese Science Bulletin*, Vol. 53, No. 10, 1220–1227, 2008.
7. Wang, G. and L. Han, “Progress in the research of surface albedo,” *Plateau and Mountain Meteorology Research*, Vol. 30, No. 2, 79–83, 2008.
8. Ma, J. F. and T. B. Yang, “The relationship between land surface albedo and land use type — A case study of Qaidam Basin,” *Journal of Northwest Normal University (Natural Science)*, Vol. 41, No. 3, 79–83, 2005.
9. Yang, J., H. B. Chen, and K. C. Wang, “Analysis of the surface albedo distribution and variation in Beijing region by using the modis data,” *Remote Sensing Technology and Application*, Vol. 21, No. 5, 403–406, 2006.
10. Yan, Y. and R. P. Shen, “The spatial and temporal variation characteristics of surface albedo in the middle yellow river based on remote sensing,” *Journal of Anhui Agricultural Sciences*, Vol. 40, No. 26, 13023–13025, 13137, 2006.

Study on the Variation of Vegetation in Shenyang City Based on MODIS Data

Y. T. Ma^{1,2}, J. L. Wang^{1,*}, and L. S. Sun¹

¹School of Civil Engineering, Shenyang Jianzhu University, Shenyang, China

²School of Resource & Civil Engineering, Northeastern University, Shenyang, China

Abstract—The distribution characteristics and interannual variation of vegetation in Shenyang city from 2001 to 2011 were analyzed according to vegetation index products MOD13A3 from MODIS. The results showed that the vegetation density increased gradually from the city center to the periphery, the overall trend of vegetation variation in whole city was degraded from 2001 to 2011, the vegetation around the outskirts of town were degraded slightly or seriously in different regions and at different periods, the vegetation in the town and in the periphery areas of Shenyang were gradually ameliorated more or less. The natural factors had certain influence on vegetation variation, but the main effect was still the influence of artificial factors including urban expansion and urban greening.

1. INTRODUCE

Vegetation is a natural bond which links soil and atmospheric and one of the important indicators for regional ecosystem environmental changes [1]. It is of great significance that the information and variation of vegetation be obtained accurately for analyzing the influence of human activities on the natural ecological environment. At present, vegetation index has played a very important role in many research fields such as the classification of vegetation, crop yield estimation, global and regional land using, land cover variation, and so on. Meanwhile, vegetation index has provided timely and effective information service for the environmental monitoring, agricultural, forestry, and other relevant departments. Foreign scholars has studied the vegetation information through the vegetation indices earlier and made many achievements [2–4]. Vegetations were classified by Nemani [5] according to seasonal variation characteristics of vegetation indices and the temperature of plant surfaces based on NOAA/AVHRR data [5]. Stow et al. found the trend of vegetation green in northern Alaska area by extracting SINDVI using AVHRR LAC data at a resolution of 1 km in 1990 and 1999 [6].

Civil Sheng Yongwei et al. used dynamic method to classify the vegetation in our country according to the characteristics of NDVI in time series, by using the NDVI data at 6 km spatial resolution from meteorological satellite [7]. The characteristics of vegetation distribution and vegetation interannual variation in Shenyang from 2001 to 2011 were studied by using MODIS-NDVI data in this paper.

2. DATA AND PROCESSING

2.1. Investigation Area

Shenyang city locates in the middle of Liaohe plain in Liaoning province, it is divided into five districts, Heping, Shenhe, Huanggu, Dadong, Tiexi, and five outskirts, Dongling, Hunnan, Yuhong, Sujiatun, Shenbei. Shenyang region is temperate continental monsoon climate with four distinct seasons. It's cold and dry in winter, wet and rainy in summer, rapidly changing temperature in spring and autumn, windy in spring, sunny in autumn.

Shenyang's midsummer is around the middle of August. In this time, vegetation grows the most densely, vegetation index achieves year-round maximum and is the most representative for vegetation growth information. So the maximum of NDVI in August was chosen to study the characteristics of vegetation distribution and variation in Shenyang from 2001 to 2011.

2.2. Data

The terrestrial vegetation index products (MOD13A3) come from NASA Earth Observation System (EOS) which contain two kinds of vegetation index: NDVI and EVI at a time resolution of the month and a space resolution of 1 km. According to the characteristics of NDVI which shows more sensitive in middle and lower vegetation coverage area and the relatively smaller vegetation

*Corresponding author: Jingli Wang (13898803180@163.com).

coverage [8], MODIS-NDVI was used to describe the information of vegetation in Shenyang in this study.

2.3. Data Processing

Through image projection conversion, subsetting, mosaicing, stacking and other steps, NDVI data in Shenyang were acquired. The vegetation coverage variations from 2002 to 2011 were acquired by NDVI data in August in 2001 respectively subtracting from the data in August from 2002 to 2011.

3. VARIATIONS AND DISTRIBUTION OF VEGETATION

3.1. Distribution Characteristics of Vegetation

NDVI data in 2002, 2005, 2008 and 2011 were chosen to analyze the distribution of the vegetation in Shenyang. Figure 1 showed the vegetation coverage increased from the vegetation density increased gradually from the city center to the periphery. The high vegetation density mainly distributed in farmland and woodland surrounding the town. The denser vegetation coverage area made up bigger proportion of city. Low vegetation coverage area, moderate vegetation coverage area and dense vegetation coverage area had smaller proportions. Low vegetation coverage area mainly distributed in the town.

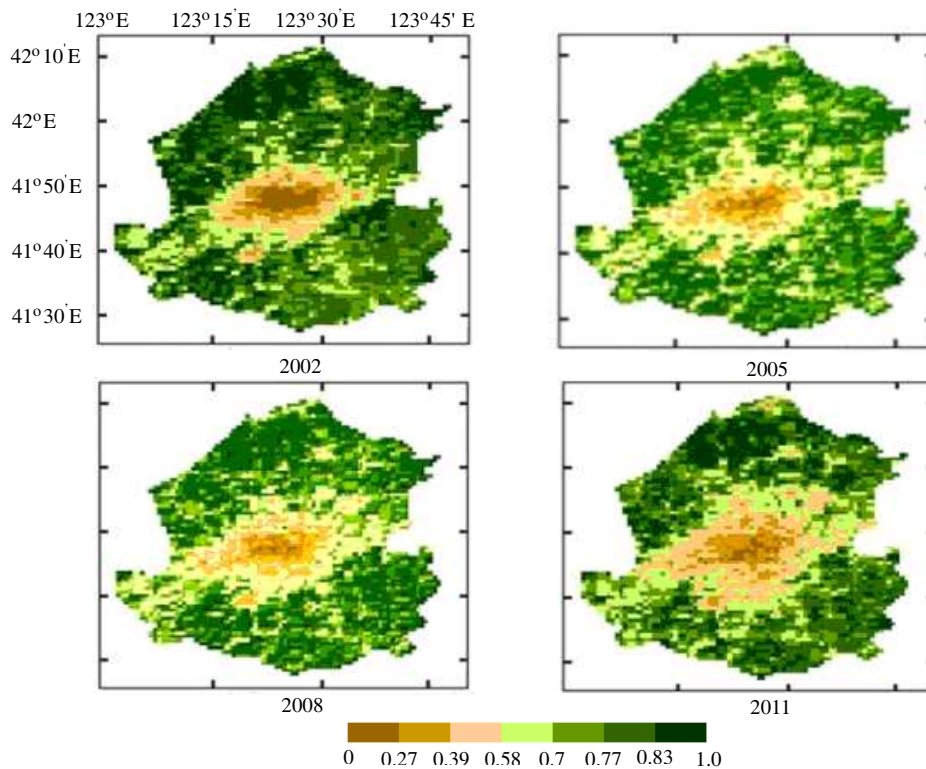


Figure 1: Maps of NDVI distribution in Shenyang from 2001 to 2011.

3.2. Statistics Characteristics of Vegetation Variation

Figure 2 was the line chart about the average of NDVI in August from 2001 to 2011 in Shenyang, it reflected the mean vegetation coverage and showed that vegetation coverage reduced gradually.

The vegetation coverage maintained at a high level in 2001 ~ 2004, the values of NDVI were between 0.73 and 0.74. The vegetation coverage obviously reduced in 2005 ~ 2007 (the values of NDVI were between 0.7 and 0.715) and reached the minimum in 2006. The vegetation coverage restored to the level before 2004 in 2008. The values of NDVI reached the minimum again as 2006 in 2009. The vegetation had a slight improvement in 2010 ~ 2011, the mean of NDVI maintained between 0.72 and 0.75.

The classification standard of vegetation coverage variation was shown in Table 1 [9]. According to the standard, vegetation coverage variation from 2001 to 2011 was classified into eight levels. The percentage of each classification was also counted in Figure 3.

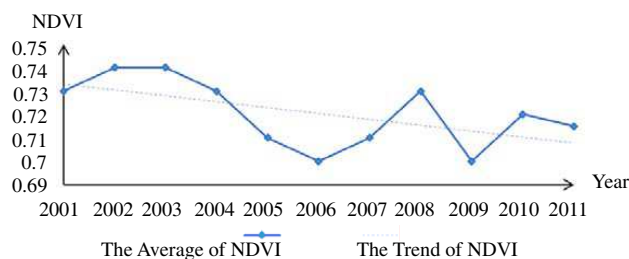


Figure 2: Average of NDVI in Shenyang in August from 2001 to 2011.

Table 1: Classification standards of vegetation variation.

NDVI variation range (X)	description	[legend]	NDVI variation range (X)	description	[legend]
$X < -0.3$	significant degradation	[red]	$0 \leq X < 0.1$	slight improvement	[light green]
$-0.3 \leq X < -0.2$	obvious degradation	[orange]	$0.1 \leq X < 0.2$	moderate improvement	[medium green]
$-0.2 \leq X < -0.1$	moderate degradation	[light orange]	$0.2 \leq X < 0.3$	obvious improvement	[dark green]
$-0.1 \leq X < 0$	slight degradation	[yellow]	$X \geq 0.3$	significant improvement	[dark green]

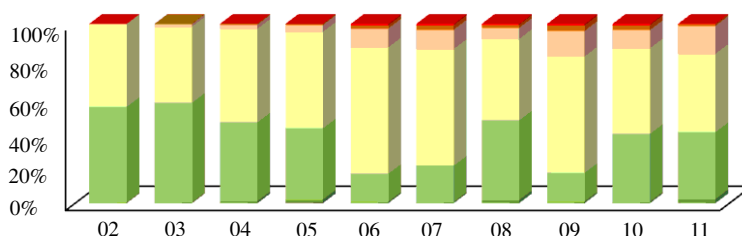


Figure 3: Percentage in column of vegetation variation relative to 2001 from 2002 to 2011 (legend in Table 1).

3.3. Regional Distribution Characteristics of Vegetation Variation

The classification maps of vegetation variation from 2002 to 2011 were made. For convenience, only the maps of vegetation variation in 2002, 2005, 2008 and 2011 were listed to explain the characteristics of the vegetation variation in Shenyang (Figure 4). The maps showed that: in 2002, the vegetation varied slightly, mainly concentrated in the outskirts of town in a mild and moderate degradation; in 2005, the vegetation variation around the outskirts of town was obvious in a moderate and obvious degradation. the vegetation degradation area in the west was larger and was in an obvious degradation; in 2008, the vegetation degeneration area around the outskirts of town and the vegetation degeneration area in the west continued to increase, the degradation was more serious; in 2011, the vegetation degradation in the west stopped, but the vegetation degradation developed fast in the north, the east and the south, and was in an obvious degradation; the vegetation in the town and in the south of the city had been improving from 2001 to 2011, and the improvement of the vegetation in 2011 was in an obvious improvement.

3.4. Causes of Vegetation Variation

3.4.1. Natural Factors

Vegetation growth is affected by natural conditions such as precipitation, temperature and so on. Only the effect of precipitation on vegetation was analyzed. The precipitation in Shenyang from 2001 to 2011 was provided by Shenyang Bureau of Meteorology and was shown as Figure 5 with the average of NDVI. It can be deduced from the line chart of precipitation and NDVI that precipitation and NDVI had little correlation which showed precipitation slightly impacted on vegetation.

3.4.2. Human Factors

The effects of human factors on vegetation were mainly artificial planting, cultivation, felling, etc. That the town has been expanding outwards is consistent with which vegetation has kept in degradation around the outskirts of town. That human habitat of Shenyang gathered to Tiexi

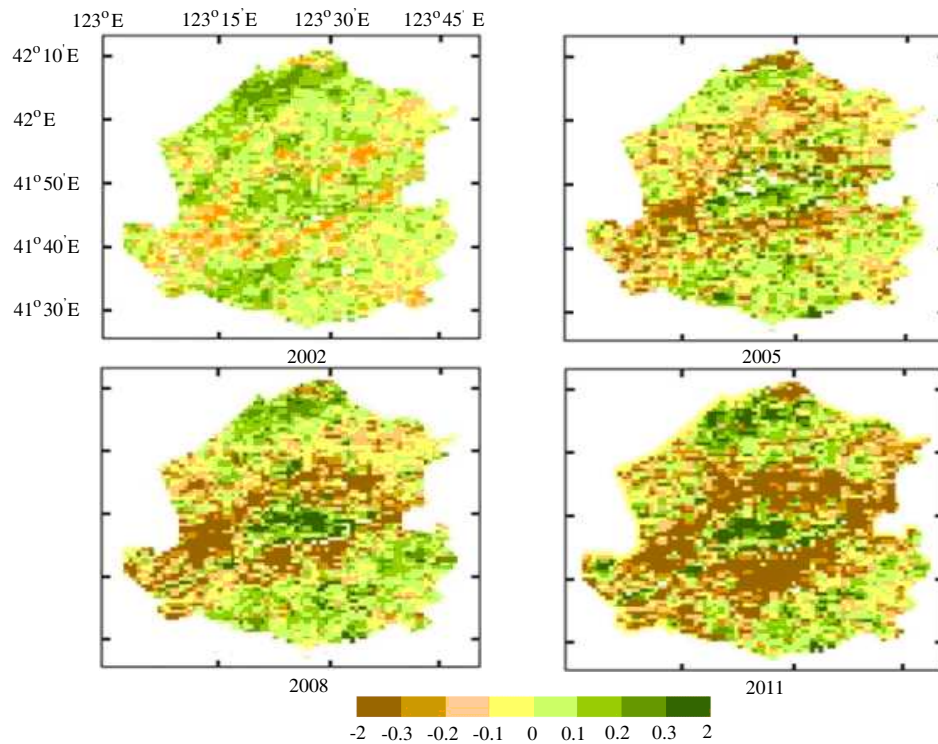


Figure 4: Maps of vegetation variation relative to 2001 from 2002 to 2011.

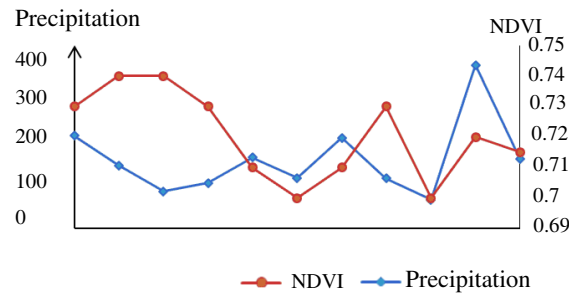


Figure 5: Precipitation and average of NDVI in Shenyang from 2001 to 2011.

District from 2000 and that Tiexi District had become living areas led to a continuous degradation of vegetation.

In 2008, the infrastructure of Tiexi District was basically finished and the urban construction developed to Hunnan District and Shenbei District, it was reflected that the vegetation in these regions began to decline.

4. CONCLUSIONS

The distribution and variation characteristics of vegetation in Shenyang city were analyzed by using NDVI data of MODIS sensor from Terra satellite. It was concluded that the vegetation density increased gradually from the city center to periphery; the overall vegetation in Shenyang showed a trend of deterioration from 2001 to 2011; Natural factors had slightly effect on vegetation variation, the main influence were human factors, the urban expansion led to the vegetation be destroyed around the outskirts of town, under the government’s initiative in recent years, vegetation coverage in town was increasing gradually, but the density was not high yet.

REFERENCES

1. Sun, H. Y., C. Y. Wang, and Z. Niu, “Analysis of the vegetation cover change and the relationship between NDVI and environmental factors by using NOAA time series data,” *Journal of Remote Sensing*, Vol. 2, No. 3, 204–210, 1998.
2. Lobell, D. B., S. M. Lesch, D. L. Corwin, et al., “Regional-scale assessment of soil salinity in

- the Red River Valley using multi-year MODIS EVI and NDVI,” *Journal of Environmental Quality* Vol. 39, No. 1, 35–41, 2010.
3. Li, H. I., L. Zheng, Y. P. Lei, et al., “Comparison of NDVI and EVI based on EOS/MODIS data” *Progress in Geography* Vol. 2, No. 1, 26–31, 2007.
 4. Wardlow, B. D. and S. L. Egbert, “A comparison of MODIS 250-m EVI and NDVI data for crop mapping: A case study for southwest Kansas,” *International Journal of Remote Sensing*, Vol. 31, No. 3, 805–830, 2010.
 5. Nemani, R. and S. Running, “Land cover characterization using multitemporal red, near-IR, and thermal-IR data from NOAA/AVHRR,” *Ecologation Applications*, Vol. 7, No. 1, 79–90, 1997.
 6. Stow, D., S. Daeschner, and A. Hope, “Variability of the seasonally integrated normalized difference vegetation index across the north slope of alaska in the 1990s,” *International Journal of Remote Sensing*, Vol. 24, No. 5, 1111–1117, 2003.
 7. Shen, Y. W., W. Y. Chen, and Q. G. Xiao, “China’s vegetation macro-classification based on meteorological satellite vegetation index,” *Chinese Science Bulletin*, Vol. 40, No. 1, 68–71, 1995.
 8. Carlson, T. N. and D. A. Ripley, “On the relation between NDVI, fractional vegetation cover, and leaf area index,” *Remote Sensing of Environment*, Vol. 162, No. 3, 241–252, 1997.
 9. Ma, B. D., S. J. Chen, and L. X. Wu, “Vegetation monitoring method in mining area based on SPOT-VGT NDVI,” *Geography and Geo-Information Science*, Vol. 25, No. 1, 84–87, 2009.

The Damping Model for Sea Waves Covered by Oil Films of Finite Thickness

Yunhua Wang¹ Yanmin Zhang², and Honglei Zheng²

¹Ocean Remote Sensing Institute
Ocean University of China, Qingdao 266100, China
²College of Information Science & Engineering
Ocean University of China, Qingdao 266100, China

Abstract— In combination with the wave action balance equation, the damping model for sea waves covered by oil film of finite thickness is presented. This damping model is not only related to physical parameters of oil film, but also related to marine environment parameters. Here, we conduct parametric analyzes to understand the sensitivity of the damping model to these parameters. Numerical simulations show that kinematic viscosity, surface/interfacial elasticity, thickness, and the fractional filling factor cause more significant effects on the damping ratio than the other physical parameters of oil film. On the other hand, the influences induced by wind speed and wind direction are also remarkable. In present work, fifteen ENVISAT ASAR images, which were acquired during Gulf of Mexico oil spill accident, are used to confirm the validity of the damping model.

1. INTRODUCTION

The hydrodynamic theory of wave damping by oil films of negligible thickness (e.g., monomolecular films) has been well established by Marangoni theory [1–4]. As a matter of fact, the thickness of mineral oil spill is generally much larger than that of monomolecular film, which results in different viscoelastic properties and, therefore, in different damping of the ocean surface waves. Thus, water wave damping by oil films of finite thickness is also of practical importance. However, the influence of the thickness of oil film on sea waves has not been widely investigated so far.

In present work, combining the wave action balance equation with the *Jenkins'* wave viscous damping function [5], a damping model for sea waves covered by oil films of finite thickness is proposed. Parametric analyses of the damping model indicate that kinematic viscosity, surface/interfacial elasticity, thickness, and the fractional filling factor cause significant effects on the damping ratio. Meanwhile, the influences induced by wind speed and wind direction are also remarkable.

2. THE DAMPING MODEL OF SEA SURFACE WAVES

The thickness of a mineral oil spill is generally much larger than that of monomolecular film, particularly, in the initial stages of an oil spill accident. Then, radar signal reduction by finite-thickness oil film has practical significance. In a system which consists of finite-thickness oil film covering on a Newtonian fluid of infinite depth, a viscous damping ratio model for gravity-capillary waves is theoretically derived by *Jenkins* [5]

$$y(k) = \frac{\text{Re}(\delta)}{2\nu} \quad (1)$$

with

$$\delta = \left\{ 2\nu + \frac{1}{2}v_T + j\Gamma^{-1/2}[\gamma(1 - \rho_+) - \gamma_-]D + \frac{1}{2\nu^{1/2}j^{1/2}}\rho_+D\Gamma^{1/4}v_T + \frac{1}{2\nu^{1/2}}j^{1/2}(\rho_+D)^2\Gamma^{3/4}(R^2 - 1) \right\} / \left\{ 1 + \frac{1}{\nu^{1/2}\Gamma^{1/4}}j^{1/2}v_T + \frac{1}{j^{1/2}\nu^{1/2}}\rho_+D\Gamma^{1/4} \right\} \quad (2)$$

and the other parameters are related to the film thickness, the kinematic viscosities of the underlying water and the floating oil film, the surface tension, and so on (for more details, please see Ref. [4]).

However, it should be pointed out that the damping ratio evaluated by Eq. (1) is only available for very gentle wind regimes because not only the viscous dissipation but also wind speed, nonlinear wave-wave interaction, and wave breaking dissipation would induce significant influences on the

damping behavior, too. In order to quantify these considerations, the evolution of surface wave spectrum can be described by the action balance equation [2, 3]

$$0 = \frac{dN^i}{dt} = S_{in}^i + S_{nl}^i - S_{vd}^i - S_{br}^i \quad (3)$$

where $i \in \{o; w\}$, and the superscripts (o) and (w) denote an oil-covered and an oil-free sea surface, respectively. The spectral action density $N^i = (\omega/k)\psi^i$, ω and ψ^i represent angle frequency and the full sea roughness spectrum. For oil-free sea surface, ψ^w is written as [6]

$$\psi^w = f(k, \varphi) \begin{cases} M_L(k) & k < k_{Lc} \\ M_M(k) & k_{Lc} \leq k < k_{Hc} \\ M_H(k) & k \geq k_{Hc} \end{cases} \quad (4)$$

where the isotropic part and the angle spread function of the spectrum are

$$M_L(k) = \frac{\alpha_g v_g F_g}{2k^4 v_{ph}} \kappa \exp\left[-\frac{(\sqrt{k/k_p}-1)^2}{2\delta^{7/2}}\right] \exp\left(-\frac{5k_p^2}{4k^2}\right) \quad (5)$$

$$M_H(k) = \frac{A(k)}{k^4} \left(\frac{u_f}{c}\right)^{a(k)} \quad (6)$$

$$M_M(k) = \frac{(k_{Hc} - k)}{(k_{Hc} - k_{Lc})} M_L(k) + \frac{(k - k_{Lc})}{(k_{Hc} - k_{Lc})} M_H(k) \quad (7)$$

$$f(k, \Phi) = \frac{1}{2\pi} [1 + \Delta_E \cos(2\phi)] \quad (8)$$

and the other parameters can be found in Ref. [6].

In the right-hand side of (3), S_{in}^i , S_{nl}^i , S_{vd}^i , and S_{br}^i , represent source functions describing the wind input, nonlinear wave-wave interactions, viscous dissipation, and wave breaking dissipation, respectively. In the present work, only the cases for low to medium wind speeds are in question, and the impact of S_{br}^i can be neglected. Here, the wind input term S_{in}^i can be expressed as [2]

$$S_{in}^i = \beta^i N^i \quad (9)$$

β^i is the wind wave growth rate as

$$\beta^i = 0.04 \cos \phi \left(\frac{u_*^i}{c_p}\right)^2 \omega \quad (10)$$

where c_p is the phase velocity of the considered wave. The angular frequency ω is defined by the dispersion relationship

$$\omega = \sqrt{gk + \frac{\tau k^3}{\rho_w}} \quad (11)$$

here, g is the acceleration of gravity, τ and ρ_w denote the surface tension and the sea water density, respectively. The frictional velocities u_*^i for oil-free and oil-covered areas are

$$u_*^o = \xi u_*^w \quad (12)$$

$$u_*^w = \sqrt{C_{10}} U_{10} \quad (13)$$

where, ξ is a coefficient due to the reduction of the friction velocity caused by surface film, and Gade et al. [7] suggested an average ξ value equal to 0.8. In our work, the experimental expression proposed by Wu [8] for the drag coefficient C_{10} is utilized and

$$C_{10} = (0.8 + 0.06U_{10}) \times 10^{-3} \quad (14)$$

where, U_{10} is the wind speed at a height of 10 m.

In (3), the viscous dissipation S_{vd}^i and the nonlinear wave-wave interaction terms S_{nl}^i can be written as [2]

$$S_{vd}^i = 2c_g \Delta^i N^i \quad (15)$$

and

$$S_{nl}^i = \alpha^i N^i \quad (16)$$

with $\Delta^w = \frac{4k^2\eta\omega}{\rho_w g + 3\tau k^2}$, $\alpha^w \approx -1.15\beta^i$, $\alpha^\circ = \alpha^w + \delta\alpha$, $\delta\alpha = 2c_g\Delta_{\max}^\circ (\frac{k}{k_M})^{3/2} (\frac{u^w}{u_{*c}})^2$. Here, c_g and Δ^i represent the wave group velocity and the viscous damping coefficient respectively. η and Δ_{\max}° denotes the dynamic viscosity and the maximal value of Δ° . k_M is the Marangoni resonance wave number. u_{*c} is the critical wind stress at which the nonlinear energy transfer has reached the level

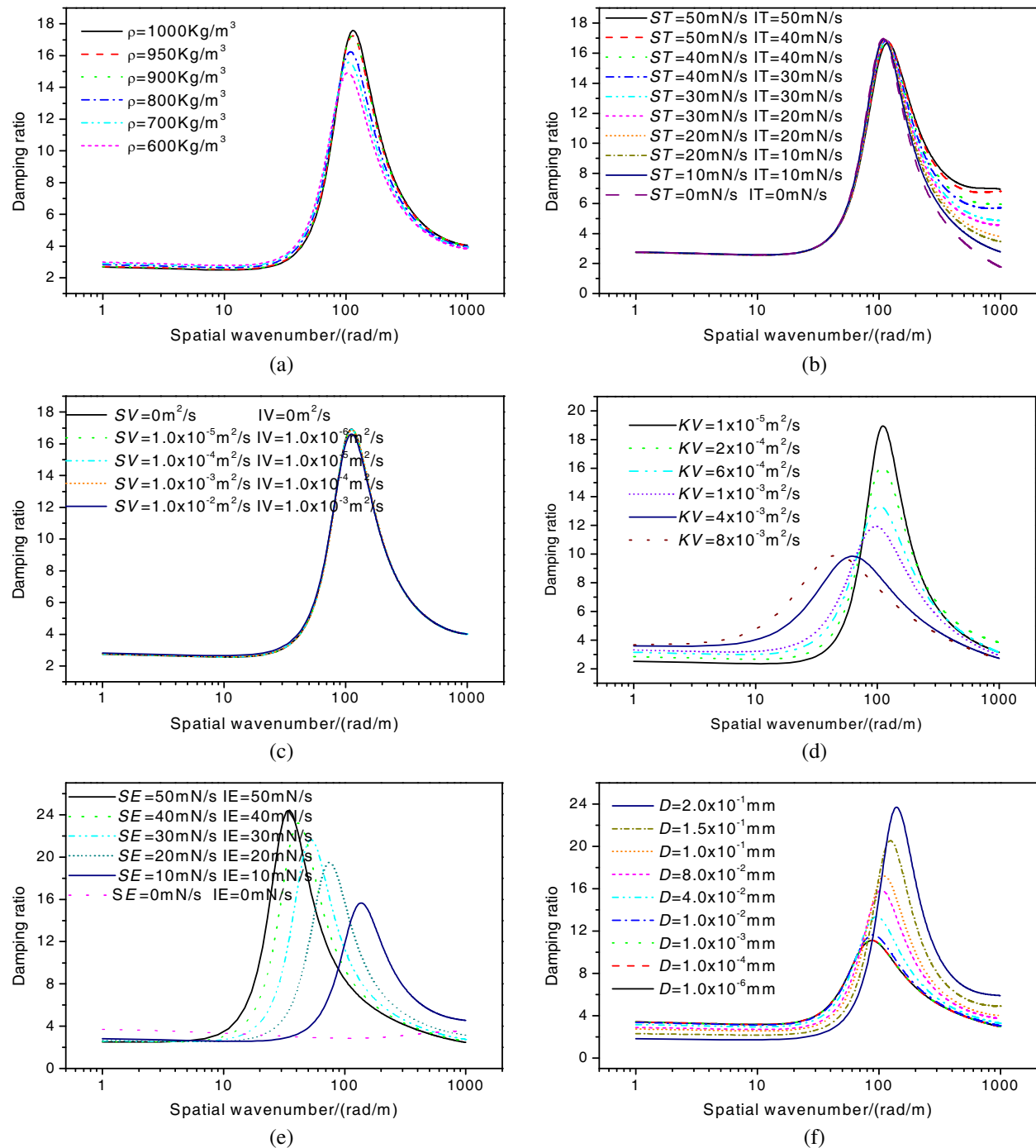


Figure 1: Damping ratio of sea wave spectrum for different physical parameters of oil film with wind speed $U_{10} = 5$ m/s, fractional filling factor $F = 1$, and wave spread azimuth angle $\phi = 0^\circ$ (a) for different oil density ρ ; (b) for different surface tension ST and interfacial tension IT ; (c) for different surface viscosity SV and interfacial viscosity IV ; (d) for different kinematic viscosity KV ; (e) for different surface elasticity SE and interfacial elasticity IE ; (f) for different film thickness D of the oil film.

where it just balances the oil damping. And u_{*c} is generally determined by experiment [2].

Substituting Eqs. (8), (14), and (16) into (6), we can obtain that

$$\frac{\psi^\circ(k, \phi)}{\psi^w(k, \phi)} = \frac{\beta^w - 2c_g\Delta^w + \alpha^w}{\beta^\circ - 2c_g\Delta^\circ + \alpha^\circ} \quad (17)$$

and the surface roughness spectrum for oil contaminated sea waves is

$$\psi^\circ(k, \phi) = \psi^w(k, \phi)/y'(k), \quad y'(k) = \frac{\beta^\circ - 2c_g\Delta^\circ + \alpha^\circ}{\beta^w - 2c_g\Delta^w + \alpha^w} \quad (18)$$

Generally, the oil film may be partially dispersed by wind and waves, so a fractional filling factor, F (i.e., the ratio of the area covered by film with respect to the total considered area) is introduced to modify the damping ratio. In this case, a modified damping ratio model $y'_m(k)$ can be written as [9]

$$y'_m(k) = \frac{1}{1 - F + F/y'(k)} \quad (19)$$

3. NUMERICAL RESULTS AND DISCUSSIONS

Figure 1 illustrates the damping ratios for different physical parameters of oil film. From Fig. 1, we can find that the damping ratio would be obviously affected by the kinematic viscosity, surface elasticity and thickness of oil film. As shown in Fig. 1(d), the damping ratio decreased with the increasing kinematic viscosity, and peaks of damping ratio move to lower spatial wavenumber.

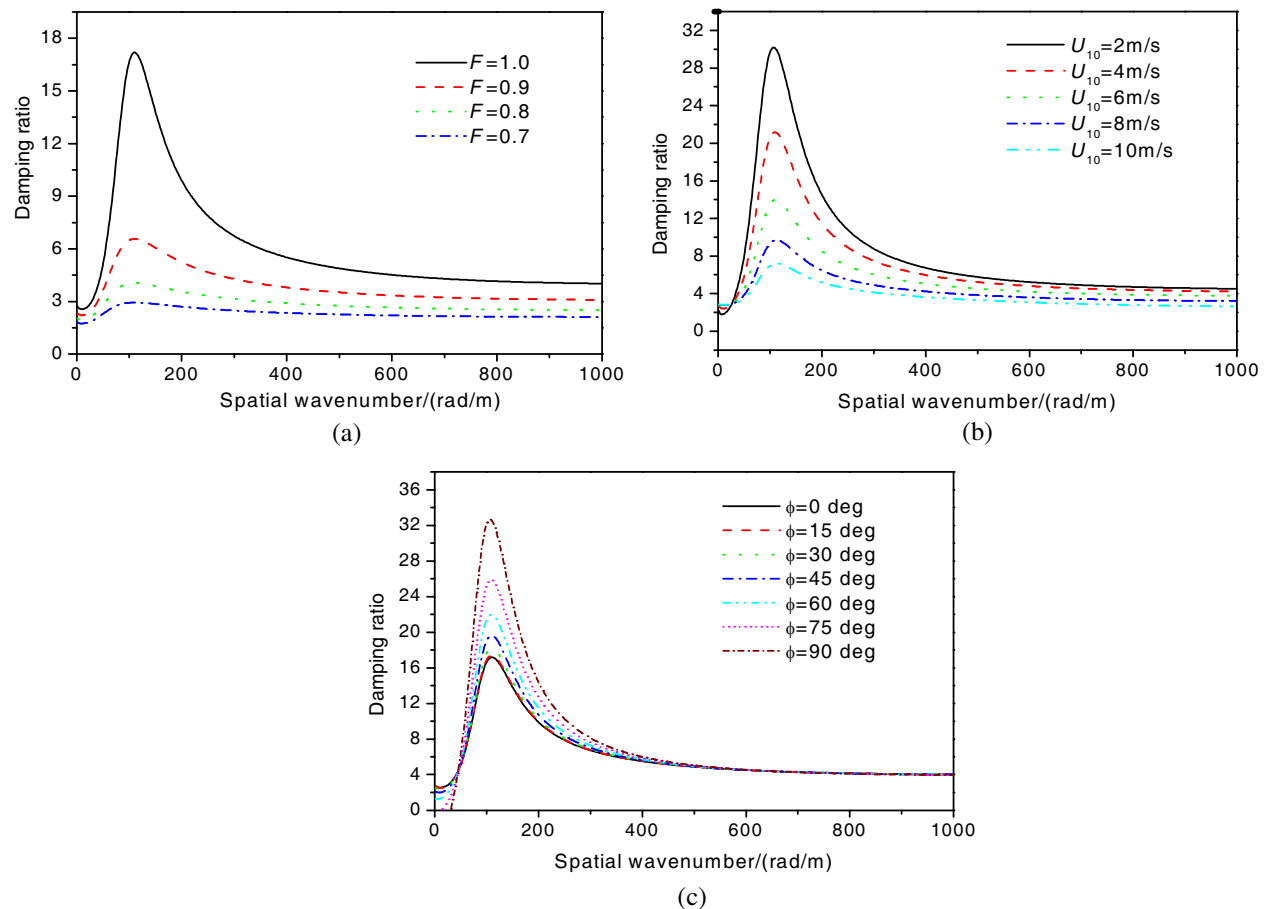


Figure 2: Theoretical damping ratio of sea wave spectrum evaluated by (19) for different environment parameters (a) for different fractional filling factors F with $U_{10} = 5$ m/s, $D = 0.1$ mm and $\phi = 0^\circ$; (b) for different wind speeds U_{10} with $D = 0.1$ mm, $F = 1$ and $\phi = 0^\circ$; (c) for different wave spread azimuth angles ϕ with $U_{10} = 5$ m/s, $D = 0.1$ mm and $F = 1$.

Fig. 1(e) shows that the damping ratio increases with the increase of the surface/interfacial elasticity, and peaks of the damping move to lower spatial wavenumber too. In Fig. 1(f), the damping ratio induced by oil film with thickness less than ~ 0.01 mm are only slightly different from that of a monomolecular film (a film of almost zero thickness); while the effect of the film thickness becomes noticeable if it is increased to ~ 0.01 mm, the damping ratio increases on the whole as the increasing thickness of the oil film, and peaks of damping ratio move to the higher spatial wavenumber.

From Fig. 2(a), we can find that the damping ratio is very sensitive to fractional filling factor F . It is found that the damping ratio for $F = 1$ is about twice larger than the value of the damping ratio for $F = 0.9$. The influences of wind speed and wind direction are illustrated in Figs. 2(b) and (c), respectively. And the figures show that the damping ratio decreases with increasing wind speed, and increases with the wave spread azimuth angle. One reason for this phenomenon is that the higher the wind speed, the higher the wind input energy, hence, the weaker the Marangoni damping effect. The other reason is that the wave-wave interaction becomes stronger when wave spread azimuth angle ϕ is small. And from (10), it is easy to find that the stronger the wave-wave interaction, the weaker the Marangoni damping effect.

Figure 3 shows the damping ratio versus wind speed. The solid squares correspond to the damping ratios evaluated by fifteen SAR images which are acquired in Gulf of Mexico during the 2010 BP oil spill accident, and the lines correspond to the theoretical damping ratios calculated by Eq. (19) with oil film thickness 0.01 mm. In Fig. 3, we can see that the evaluated data by SAR with lower wind speed agree the theoretical result with higher oil fractional filling factors better, meanwhile the evaluated data by SAR with higher wind speed agree the theoretical result with lower oil fractional filling factors better. And it seems reasonable that the fractional filling factor decreased with the increasing wind speed.

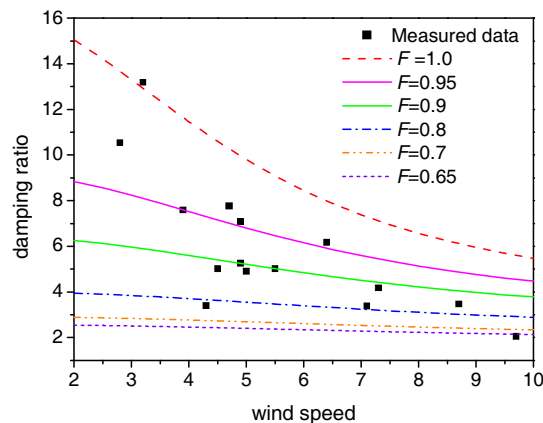


Figure 3: The damping ratio versus wind speed.

ACKNOWLEDGMENT

This research was supported by the Young Scientists Fund of the National Natural Science Foundation of China (No. 41106153), China Postdoctoral Science Foundation Funded project (No. 2012M52 1293). The ENVISAT ASAR data were provided by the European Space Agency.

REFERENCES

1. Huhnerfuss, H., W. Alpers, W. D. Garrett, P. A. Lange, and S. Stolte, "Attenuation of capillary and gravity waves at sea by monomolecular organic surface films," *J. Geophys. Res.*, Vol. 88, No. C14, 9809–9816, 1983.
2. Alpers, W. and H. Huhnerfuss, "The damping of ocean waves by surface films: A new look at an old problem," *J. Geophys. Res.*, Vol. 94, No. C5, 6251–6265, 1989.
3. Franceschetti, G., A. Iodice, D. Riccio, G. Ruello, and R. Siviero, "SAR raw signal simulation of oil slicks in ocean environments," *IEEE Trans. Geosci. Remote Sensing*, Vol. 40, No. 9, 1935–1949, 2002.

4. Pinel, N., N. Déchamps, and C. Bourlier, “Modeling of the bistatic electromagnetic scattering from sea surfaces covered in oil for microwave applications,” *IEEE Trans. Geosci. Remote Sensing*, Vol. 46, No. 2, 385–392, 2008.
5. Jenkins, A. D. and S. J. Jacobs, “Wave damping by a thin layer of viscous fluid,” *Phys. Fluids*, Vol. 9, No. 5, 1256–1264, 1997.
6. Wang, Y. H., Y. M. Zhang, H. H. Chen, and L. X. Guo, “Effects of atmospheric stability and wind fetch on Microwave sea echoes,” *IEEE Trans. Geosci. Remote Sensing*, Vol. 52, No. 2, 929–935, 2014.
7. Gade, M., W. Alpers, H. Huhnerfuss, V. R. Wismann, and P. A. Lange, “On the reduction of the radar backscatter by oceanic surface films: Scatterometer measurements and their theoretical interpretation,” *Remote Sens. Environ.*, Vol. 66, No. 1, 52–70, 1998.
8. Wu, J., “Wind-stress coefficients over sea surface near neutral conditions—a revisit,” *J. Phys. Oceanogr.*, Vol. 10, No. 5, 727–740, 1980.
9. Lombardini, P., B. Fiscella, P. Trivero, C. Cappa, and W. Garrett, “Modulation of the spectra of short gravity waves by sea surface films: Slick detection and characterization with a microwave probe,” *J. Atmos. Ocean. Technol.*, Vol. 6, No. 6, 882–890, 1989.

Microwave Radiation Image Reconstruction Method Based on Adaptive Multi-structural Dictionary Learning

Lu Zhu, Jiangfeng Liu, Yuanyuan Liu, and Suhua Chen

School of Information Engineering
East China Jiaotong University, Nanchang 330013, China

Abstract— Due to the complicated structure of microwave radiometric imaging system and the massive amount of data collection in one snapshot, it is difficult to achieve the high spatial resolution image by conventional microwave radiation imaging method based on the Nyquist sampling. In this paper, according to the priori information of the compressible multi-structural information of microwave radiation image, we adopt the Fourier random observation matrix to sparsely project the microwave radiation image, reducing the amount of data collection, and lowering the complexity of the system. Considering the multi-structural information of microwave radiation image, such as multi-sparsity in different domains, piecewise smoothness, etc, it is difficult to sparsely represent microwave radiation image in complex scene by the traditional orthogonal basis, but the piecewise smoothness ingredients of microwave radiation image meet the constraint condition of total variation, and the mixed orthogonal basis can sparsely represent the sparsity information of microwave radiation image. We make use of the sparse representation of the mixed orthogonal basis and the constraint condition of total variation regularization to construct the reconstruction model of microwave radiation image based on adaptive multi-structural sparsifying dictionary learning. We integrate dictionary learning technique to adaptively learn the multi-structural sparsifying dictionary, and the sparsifying dictionary is adapted to sparsely represent the microwave radiation image, and solve the convex programming problem of microwave radiation image reconstruction, and design the reconstruction method. The simulation results show that reconstructing microwave radiation image by the proposed algorithm achieves better reconstruction performance than that by the DLMRI algorithm.

1. INTRODUCTION

The characteristics obtained from soil microwave radiation image using microwave radiometers mainly depend on soil moisture. We can get precise soil moisture data by inverting the obtained microwave radiation image, and enhance the accuracy of weather forecasts by analyzing the soil moisture data, and effectively monitor geological disasters, such as drought, flood, etc.. Interferometric synthetic aperture microwave radiometry (ISAMR) [1] integrates the small-aperture array into large observation aperture, it doesn't need a mechanical scanning for imaging, and can solve the disadvantages of real aperture microwave radiometers. However, with the development of refinement and structuralization of the image, ISAMR has evolved into an enormous and complex system for the demand of high resolution, and it can easily reach tens of millions when collecting data in one snapshot. Taking example by the principle of the infrared and visible light, microwave radiation focal plane array imaging system adopts the stared working condition, and it improves the real-time performance of the system and reduces the complexity of the later image processing. However, in order to obtain high spatial image, we need to increase the complexity of the system [2]. So it is difficult to achieve the high spatial resolution image based on the conventional sampling and imaging method.

Compressed Sensing (CS) [3–5] changes the traditional concept of information acquisition. Combined with the sparse prior knowledge of signal for signal reconstruction, it utilizes the random sparse sampling to compress data, and adopts the nonlinear algorithm to achieve the signal, so as to effectively reduce the complexity of the sampling system. In the CS method, the sparse representation of the image is the key aspect for image reconstruction. Generally, the microwave radiation image contains additional structures, such as piecewise smoothness [6], and sparsity in transform domain, etc. [7]. Therefore, the single orthogonal basis is difficult to sparsely represent microwave radiation image in complex scene. Yang et al. [8] develop a reconstruction model of total variation (TV) l_1 - l_2 norm, using RecPF algorithm which only consider a single orthogonal basis to fast reconstruct magnetic resonance image (MRI). Ravishankar et al. [9] use a reconstruction model based on dictionary learning, adopt DLMRI algorithm and only consider dictionary learning in the pixel domain to reconstruct MRI. Liu et al. [10] adopt GradDLRec algorithm which just takes into account learning dictionary on TV domain to reconstruct MRI. On the basis of previous

studies, we integrate the TV and wavelet transform into the reconstruction model. According to the multi-structural characteristics of the microwave radiation image, we realize the sparsely sample by the Fourier random observation matrix, and sparsely represent the image by adaptive learning multi-structural dictionary, and solve the convex optimization problem of the image reconstruction to achieve high spatial resolution image.

2. MICROWAVE RADIATION IMAGING SCHEME BASED ON CS

2.1. The Basic Method of CS

CS reconstructs the unknown $x \in C^P$ from the measurements $y \in C^m$, or equivalently solves an underdetermined system of linear equations $F_u x = y$ by minimizing the quasi norm of the sparsified image Ψx , where $\Psi \in C^{T \times P}$ represents a global, typically orthonormal sparsifying transform for the image. For example, Ψ may be the wavelet transform, so that Ψx corresponds to the wavelet coefficients of x , assumed to be sparse (mostly zero). The corresponding optimization problem is given by

$$\min_x \|\Psi x\|_0 \quad s.t. \quad F_u x = y \quad (1)$$

$\|\cdot\|_0$ denotes the l_0 quasi-norm which counts the number of nonzero coefficients of the vector, $F_u \in C^{m \times P}$ represents the undersampled Fourier encoding matrix. This l_0 problem is NP-hard, there are greedy algorithms to solve this problem such as orthogonal matching pursuit (OMP). We can replace the l_0 quasi-norm with the l_1 relaxation, it can be solved via linear programming in this real case, or via second order cone programming in the complex case [9].

$$\min_x \|F_u x - y\|_2^2 + \lambda \|\Psi x\|_1 \quad (2)$$

2.2. Microwave Radiation Imaging Based on CS

According to the characteristics of complex structure and low imaging resolution for microwave radiometric imaging system, in this paper, we adopt the CS to realize microwave radiation imaging, and solve the above shortcomings. The specific method is to mine the priori information of the compressible multi-structural information of microwave radiation image, and adopt the Fourier random observation matrix to sparsely sample the image, reducing the amount of data collection and lowering the complexity of the system. We integrate the dictionary learning technique into adaptively learn the multi-structural sparsifying dictionary which is adopted to sparsely represent the image, and solve the convex programming problem of the image reconstruction model to achieve the high spatial resolution image.

3. PROPOSED IMAGE RECONSTRUCTION MODEL

Taking example by GradDLRec algorithm, we add the TV and wavelet transform to the reconstruction model which recovers more details, and use the Daubechies wavelet-4, and propose a new model based on adaptive multi-structural dictionary learning as follows:

$$\min_{u, D^{(i)}, \Gamma^{(i)}} \left\{ \sum_{i=1}^2 \sum_l \left\| D^{(i)} \alpha_l^{(i)} - R_l \left(\lambda_1 \nabla^{(i)} u + \lambda_2 \Psi u \right) \right\|_2^2 + \frac{v_1}{2} \|F_p u - f\|^2 \right\} \quad s.t. \quad \|\alpha_l^{(i)}\|_0 \leq T_0, \forall l, i. \quad (3)$$

where $(\nabla_x, \nabla_y) = (\nabla^{(1)}, \nabla^{(2)})$ denotes the difference operators in horizontal and vertical directions, Ψ denotes the wavelet transform, The first term in the cost function captures the sparse prior of the sparsified image patches with respect to dictionaries $\{D^{(i)} \mid i = 1, 2\}$, while the second term enforces data fidelity in k-space. The weight v_1 is set as $v_1 = (\lambda/\sigma)$ like the DLMRI algorithm does, where λ is a positive constant, λ_1 and λ_2 are positive scalars that balance the two sparse domain.

By introducing auxiliary variables $w^{(i)}$, $i = 1, 2$, the problem in (3) can be rewritten as follows:

$$\min_{u, w, D^{(i)}, \Gamma^{(i)}} \left\{ \sum_{i=1}^2 \sum_l \left\| D^{(i)} \alpha_l^{(i)} - R_l \left(w^{(i)} \right) \right\|_2^2 + v_1 \|F_p u - f\|^2 \right\} \quad s.t. \quad \|\alpha_l^{(i)}\|_0 \leq T_0, \forall l, i; w^{(i)} = \lambda_1 \nabla^{(i)} u + \lambda_2 \Psi u, \forall i. \quad (4)$$

Let $\nabla = [(\nabla^{(1)})^T, (\nabla^{(2)})^T]^T$, $b = [(b^{(1)})^T, (b^{(2)})^T]^T$ and $w = [(w^{(1)})^T, (w^{(2)})^T]^T$. Combined with the Bregman technique, we obtain a sequence of constrained subproblems as follows:

$$\left\{ u^{k+1}, \omega^{k+1}, \left(D^{(i)} \right)^{k+1}, \left(\alpha_l^{(i)} \right)^{k+1} \right\} \\ = \arg \min_{u, \omega, D, \Gamma} \left\{ \begin{array}{l} \sum_{i=1}^2 \sum_l \left\| D^{(i)} \alpha_l^{(i)} - R_l(\omega^{(i)}) \right\|_2^2 + v_1 \|F_p u - f\|_2^2 \\ + v_2 \|b^k + \lambda_1 \nabla u + \lambda_2 \Psi u - w\|_2^2 \quad s.t. \quad \left\| \alpha_l^{(i)} \right\|_0 \leq T_0, \forall l, i \end{array} \right\} \quad (5)$$

$$b^{k+1} = b^k + \lambda_1 \nabla u^{k+1} + \lambda_2 \Psi u^{k+1} - \omega^{k+1} \quad (6)$$

where v_2 denotes the positive penalty parameter. We use the alternating direction method (ADM) to solve the minimization of Eq. (5) with respect to u , w , D and α . This technique carries out approximation via alternating minimization with respect to one variable while keeping others fixed.

1) Updating the Solution u : At the k -th iteration, we assume w , $D^{(i)}$ and $\alpha^{(i)}$ to be fixed with their values denoted as w^k , $(D^{(i)})^k$, and $(\alpha^{(i)})^k$ respectively. After eliminating the constant variables, the objective function for updating u is given as

$$u^{k+1} = \arg \min_u \left\{ v_1 \|F_p u - f\|_2^2 + v_2 \left\| b^k + \lambda_1 \nabla u + \lambda_2 \Psi u - w^k \right\|_2^2 \right\} \quad (7)$$

Considering that Eq. (7) is a simple least squares problem, we can update u with its analytic solution:

$$u^{k+1} = F^{-1} \left(\frac{F [v_1 F_p^T f + v_2 (\lambda_1 \nabla^T + \lambda_2 \Psi^T) (\omega^k - b^k)]}{v_1 F F_p^T F_p F^T + v_2 F (\lambda_1 \nabla^T + \lambda_2 \Psi^T) F^T F (\lambda_1 \nabla + \lambda_2 \Psi) F^T} \right) \quad (8)$$

2) Updating the Sparsified Image Variables $w^{(i)}$, $i = 1, 2$: The minimization in Eq. (5) with respect to $w^{(1)}$ and $w^{(2)}$ is decoupled, and then it can be solved separately. It yields:

$$(\omega^{(i)})^{k+1} = \arg \min_{\omega^{(i)}} \left\{ \sum_l \left\| (D^{(i)})^k (\alpha_l^{(i)})^k - R_l(\omega^{(i)}) \right\|_2^2 + v_2 \left\| (b^{(i)})^k + \lambda_1 (\nabla^{(i)} u)^{k+1} + \lambda_2 (\Psi u)^{k+1} - w^{(i)} \right\|_2^2 \right\} \quad (9)$$

The least squares solution to (9) is written as:

$$(\omega^{(i)})^{k+1} = \frac{v_2 \left[(b^{(i)})^k + \lambda_1 (\nabla^{(i)} u)^{k+1} + \lambda_2 (\Psi u)^{k+1} \right] + \sum_l R_l^T (D^{(i)})^k (\alpha_l^{(i)})^k / \beta}{v_2 + 1} \quad (10)$$

3) Sparse Representation for Sparsified Patches with Respect to Variables $D^{(i)}$ and $\alpha_l^{(i)}$, $l=1, 2, \dots, L$: The minimization (5) with respect to dictionary and coefficient variables of the sparsified images is also decoupled, and thus can be solved separately. It yields:

$$\left\{ \left(D^{(i)} \right)^{k+1}, \left(\alpha_l^{(i)} \right)^{k+1} \right\} = \arg \min_{D^{(i)}, \Gamma^{(i)}} \left\{ \sum_l \left\| D^{(i)} \alpha_l^{(i)} - R_l(\omega^{(i)}) \right\|_2^2 \quad s.t. \quad \left\| \alpha_l^{(i)} \right\|_0 \leq T_0, \forall l, i = 1, 2 \right\} \quad (11)$$

The strategy to solve (11) is to alternatively update the dictionary $D^{(i)}$ and coefficient matrix $\alpha_l^{(i)}$, which is the same as that used in K-SVD [11]. The K-SVD algorithm has two steps: sparse coding and dictionary updating, the sparse coding is solved by the greedy algorithm-OMP algorithm, and the dictionary updating is solved by singular value decomposition (SVD) to minimize the approximation error.

Algorithm 1: The Proposed Algorithm**1: Initialization:**

$$(\Gamma^{(i)})^0 = 0, (D^{(i)})^0, (b^{(i)})^0 = 0, i = 1, 2; u^0 = F_p^T f;$$

2: For $k = 1, 2, \dots$ repeat until a stop-criterion is satisfied:

$$3: (\omega^{(i)})^{k+1} = \frac{v_2[(b^{(i)})^k + \lambda_1(\nabla^{(i)}u)^k + \lambda_2(\Psi u)^k] + \sum_l R_l^T (D^{(i)})^k (\alpha_l^{(i)})^k / \beta}{v_2 + 1}, i = 1, 2$$

4: Updating $\{(D^{(i)})^{k+1}, (G^{(i)})^{k+1}\}$ from sparse images $(w^{(i)})^{k+1}$ by Eq.(11), $i = 1, 2$

$$5: u^{k+1} = F^{-1} \left(\frac{F[v_1 F_p^T f + v_2(\lambda_1 \nabla^T + \lambda_2 \Psi^T)(\omega^{k+1} - b^k)]}{v_1 F F_p^T F_p F^T + v_2 F(\lambda_1 \nabla^T + \lambda_2 \Psi^T) F^T F(\lambda_1 \nabla + \lambda_2 \Psi) F^T} \right)$$

$$6: (b^{(i)})^{k+1} = (b^{(i)})^k + \lambda_1(\nabla^{(i)}u)^{k+1} + \lambda_2 \Psi u^{k+1} - (\omega^{(i)})^{k+1}, i = 1, 2$$

7: END

8: Output u^{k+1}

4. EXPERIMENT

In this section, we use CS to reconstruct the moon microwave radiation image, the size of image is 256×256 , we adopt the Fourier random observation matrix to sample the image. Our proposed algorithm is compared with the DLMRI algorithm. The parameters for DLMRI algorithm are set as the values: patch size $n^{1/2} = 6$, dictionary size $K = n = 36$, the patch overlap $r = 1$, $\beta = 36$, $\lambda = 140$, the learning stage (K-SVD) employed 10 iterations, $200 \cdot K$ patches, and a fixed sparsity $T_0 = 5$. The proposed algorithm followed the same setup, with additional choices of $\nu_2 = 3$, $\lambda_1 = 1$ and $\lambda_2 = 0.1$. We reconstructed the moon microwave radiation image using DLMRI algorithm and the proposed algorithm from reduced k-space data with the undersampling ratios of 30%–70%.

Table 1: The reconstruction PSNR (dB) values with different undersampling ratios.

Algorithm	Undersampling ratio				
	30%	40%	50%	60%	70%
DLMRI	42.4374	42.0343	41.0898	39.5656	37.3270
The proposed algorithm	45.6674	44.1393	42.2118	40.1677	37.6708

To evaluate the reconstruction performance under different sampling ratios at the same experimental setting, we adopt five undersampling ratios (0.3, 0.4, 0.50, 0.60 and 0.7) to acquire the partial

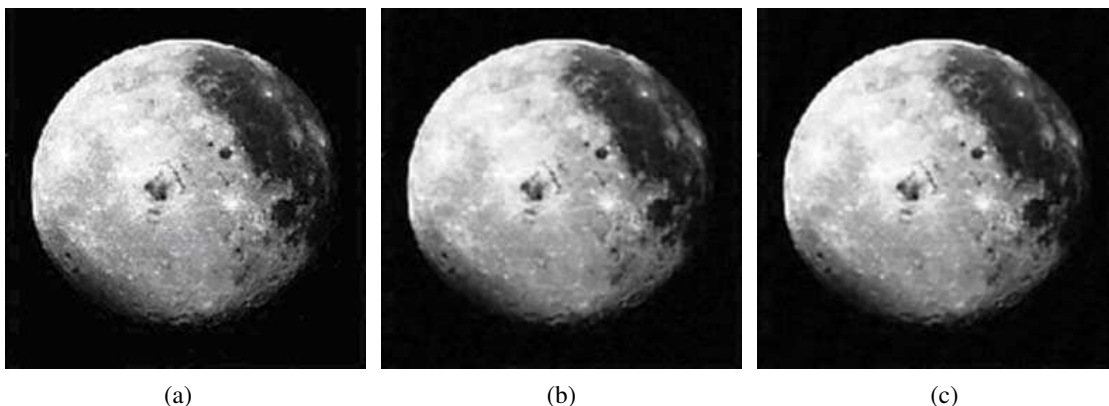


Figure 1: Visual comparison of image reconstructions using two methods with 70% undersampling. (a) The original image, (b) (c) Reconstructions using DLMRI and the proposed algorithm, respectively.

Fourier measurements respectively. The reconstruction PSNRs are given in Table 1. Figures 1(b) and (c) show the images reconstructed from 70% 2D undersampled measurements by DLMRI and the proposed algorithm. With the comparison of the PSNR values with different undersampling ratios, the results show that the proposed algorithm exhibits more accurate reconstruction with larger PSNR values than DLMRI for specified undersampling ratios.

5. CONCLUSION

In this paper, we propose a new CS reconstruction model based on adaptive multi-structural dictionary learning and an efficient algorithm to reconstruct the microwave radiation image. The model aims to learn multi-structural adaptive dictionary in the sparsified image for better reconstruction. We use a multi-structural adaptive learning dictionary from the sparsified image to reconstruct the image. The simulation results show that the proposed algorithm achieves better reconstruction performance than the DLMRI algorithm. Further studies will be conducted to improve the proposed algorithm, such as the parameter setting.

ACKNOWLEDGMENT

The work was supported by National Nature Science Foundation of China (No. 61162015, No. 31101081).

REFERENCES

1. Swift, C. T., D. M. L. Vine, and C. S. Ruf, "Aperture synthesis concepts in microwave remote sensing of the Earth," *IEEE Trans. on Microwave Theory and Tech.*, Vol. 39, No. 12, 1931–1935, 1991.
2. Li, H. F., "Passive millimeter wave focal plane array imaging system designing," Master thesis, Nanjing University of Science and Technology, 2013.
3. Donoho, D., "Compressed sensing," *IEEE Trans. Inform. Theory*, Vol. 52, No. 4, 1289–1306, 2006.
4. Candès, E., J. Romberg, and T. Tao, "Robust uncertainty principles: Exact signal reconstruction from highly incomplete frequency information," *IEEE Trans. Inform. Theory*, Vol. 52, No. 2, 489–509, 2006.
5. Baraniuk, R. G., "Compressive sensing," *IEEE Signal Processing Magazine*, Vol. 24, No. 4, 118–121, 2007.
6. Romberg, J., "Imaging via compressive sampling," *IEEE Signal Processing Magazine*, Vol. 25, No. 2, 14–20, 2008.
7. Liu, Y., M. D. Vos, I. Gligorijevic, V. Matic, Y. Li, and S. V. Huffel, "Multi-structural signal recovery for biomedical compressive sensing," *IEEE Transactions on Biomedical Engineering*, Vol. 60, No. 10, 2794–2805, 2013.
8. Yang, J., Y. Zhang, and W. Yin, "A fast alternating direction method for TVL1-L2 signal reconstruction from partial fourier data," *IEEE Journal of Selected Topics in Signal Processing*, Vol. 4, No. 2, 288–297, 2010.
9. Ravishankar, S. and Y. Bresler, "MR image reconstruction from highly undersampled k-space data by dictionary learning," *IEEE Trans. Med. Imaging*, Vol. 30, No. 5, 1028–1041, 2011.
10. Liu, Q., S. Wang, L. Ying, X. Peng, Y. Zhu, and D. Liang, "Adaptive dictionary learning in sparse gradient domain for image recovery," *IEEE Trans. on Image Processing*, Vol. 22, No. 12, 4652–4663, 2013.
11. Aharon, M., M. Elad, and A. Bruckstein, "K-SVD: An algorithm for designing overcomplete dictionaries for sparse representation," *IEEE Trans. Signal Process*, Vol. 54, No. 11, 4311–4322, 2006.

The EMC Impact due Household Appliances in Smart Grid Networks

Stefania Sousa¹, C. E. Capovilla², and H. X. Araujo¹

¹Universidade Federal de São João Del Rei — UFSJ, Brazil

²Universidade Federal do ABC — UFABC, Campus Alto Paraopeba
Rodovia MG 443, Km 7, Ouro Branco/MG, Brazil

Abstract— The Smart Grid technology has become a reality day by day due its clean proposal which can provide, for example, the link between wind and solar power with electric cars. However, the “smart” factor of the technology is obtained through electronic components, which are in general, the major responsible of unintentional emissions and coupling. Therefore, in this work, the EMC — Electromagnetic Compatibility of household appliances is deal with the use of a conducted emission technique. The obtained results are compared to the existing standards.

1. INTRODUCTION

Having as main goal improve the grid reliability, power quality and energy efficiency, the Smart Grid technology has become a subject of study nowadays [1]. However, the smartness of the grids is provided by electronics, which are in general the major responsible of unintentional emissions.

Due to the increase of the microelectronic and embedded electronic systems, every electronic device must be submitted to stricter EMC measurement, and their entries in the market are directly related to it responses on these test. However, only in the late 70s that the problems related to EMC — Electromagnetic Compatibility became of public knowledge, in general, due to the problems presented by TVs, communication devices, audio and video displays, among many other applications [2].

Basically, as far as the smart grid control is developed with microelectronic components, the conducted emission levels from the household appliance should be carefully observed, in order to guarantee the correct operation of the network. Moreover, the grid behavior must also be certified in order to ensure the correct operation of the devices connected to it in terms of electromagnetic compatibility. In this work, only the household devices will be investigated. This is extremely important because with no disturbances the voltage quality is perfect, otherwise not.

In order to analyze the conduct emission phenomena in some household appliance that are normally connected to the residential grid, the EMC Pre-Compliance Board — EPCB built in [3], and a LISN — Line Impedance Stabilization Network were employed.

The test setup, was performed in accordance to CISPR and FCC — Federal Communications Commission, agency in charge of standardization of radio communications and cable in the U.S. The preliminary results were compared to CISPR 14-1 [4] and CISPR 22 [5], depending on the class of the household appliance DUT.

In this work, the conducted emission levels from the household appliance are observed in order to ensure the correct operation of the devices connected to grid in terms of EMC. The obtained results were compared to the regulatory standard and it can be observed that most of the devices are out of it, thus compromising the performance of the grid as a whole.

2. SMART GRIDS NETWORK

The electrical power grids were developed using relatively few AC plants (50 or 60 Hz with very high-power), AC or DC interconnected, with many substations to attend residential or low-power industrial demands, as can be seen in Fig. 1. The Smart Grids (SG) are an evolution of the electrical power grids and are based on a more efficient employment of the generation, transmission, and distribution infrastructure. Its use is mandatory in order to manage the relationship between demand and power supply to avoid contingencies in the electrical system [6]. In this way, it is necessary to develop a whole telecommunications framework for a successful smart grid implementation. Inherently, its characteristic needs a strong interaction, composed by communication networks, real-time monitoring, and data management [7]. So, nowadays its integration is transforming the whole electrical energy scenario.

Therefore, the conducted emission levels from the household appliance are observed in order to ensure the correct operation of the devices connected to grid in terms of EMC.

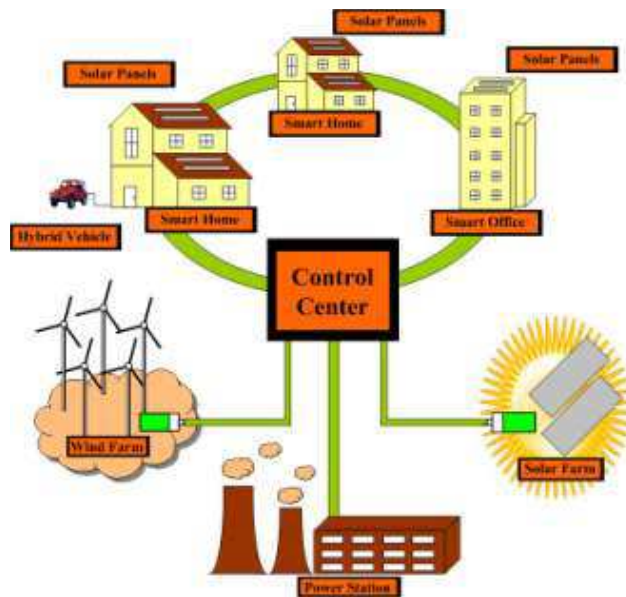


Figure 1: The smart grid network.

3. ELECTROMAGNETIC COMPATIBILITY

With the increase of the microelectronic and embedded electronic systems, every electronic device must be submitted to stricter EMC measurement, and their entries in the market are directly related to its responses on these tests. Although the challenges related to interference during the Second World War, only in the late 70s that the problems related to EMC — Electromagnetic Compatibility became of public knowledge, in general, due to the problems presented by TVs, communication devices, audio and video displays, among many other applications [4].

The Electromagnetic Interference — EMI is the process in which electromagnetic energy is transmitted from one electronic device to another via radiated or conducted emission, or both. On the other hand, the electromagnetic susceptibility — EMS deals with devices that are sensitive to interference from other devices. Thus, the EMC tests usually comprise both EMI and EMS measurement of the same electronic device.

The EMC setup tests, at the level of electronic systems are defined by the standards CISPR 25 /2002 for spurious emissions, and ISO-11452 for interference and susceptibility measurements. Thus, two major standards have been defined, with a first one for radiated and conducted emission and the second one for immunity RF test.

In general terms, the conducted interference is that in which occurs undesirable transfer of electromagnetic energy along a conductor through disturbances between the phase line and the ground power supply, and is governed by the standard IEC 61967-4. There are several tools and methodologies to perform conducted tests, and the frequency range normally used is 150 kHz–30 MHz, except in military applications that eventually require the extension band.

The most common method used for this type of analysis is the LISN, also known by AMN — Artificial Mains Network, which works through the AC power supply of the device to be analyzed. Another method widely used in performing conducted interferences measurements is the 1/150 Ω , where it is possible to measure the noise current in each driven pin of the DUT — device under test.

4. MEASUREMENTS

In order to analyze the conduct emission phenomena in some household appliance that are normally connected to the residential grid, the EMC Pre-Compliance Board — EPCB built in [3], and a LISN — Line Impedance Stabilization Network were employed.

The test setup, as shown in Fig. 2, was performed in accordance to CISPR and FCC — Federal Communications Commission, agency in charge of standardization of radio communications and cable in the US. The preliminary results were compared to CISPR 14-1 [4] and CISPR 22 [5], depending on the class of the household appliance DUT.

The obtained results for the electric heater, vacuum cleaner, blu-ray, satellite TV decoder, blender and hairdryer were compared to the CISPR 14-1 standard, Figs. 3 and 4(a), which refers

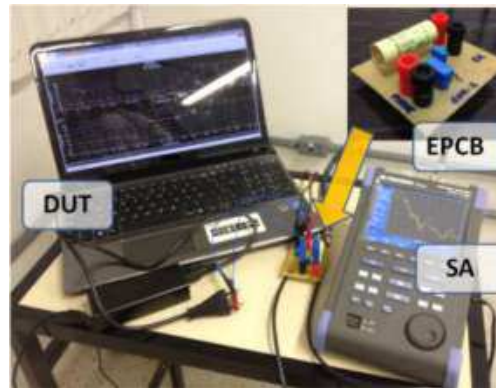


Figure 2: Conducted emission test setup using an EPCB.

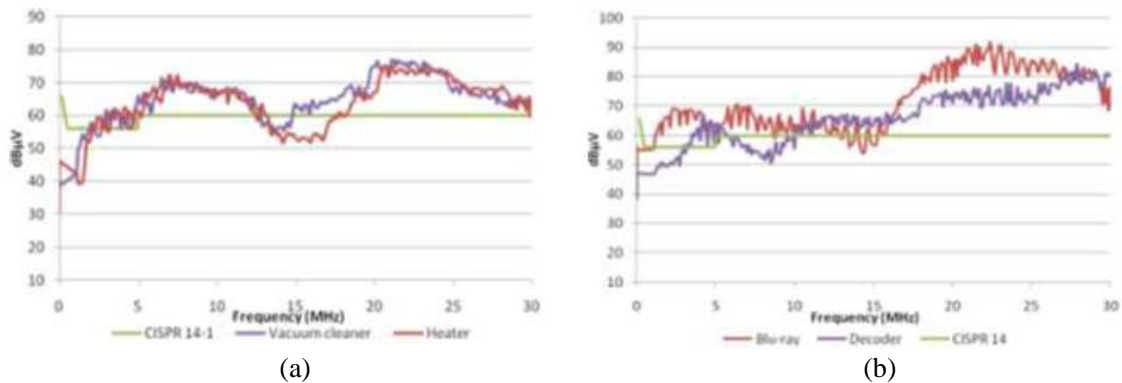


Figure 3: Measurement results of some household appliance. (a) Vacuum cleaner, heater. (b) Blu-ray and satellite TV decoder.

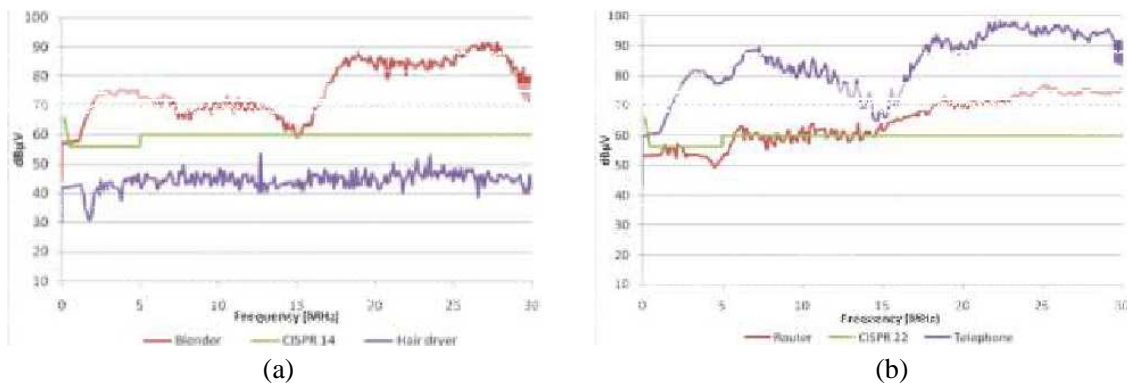


Figure 4: Measurement results of some household appliance. (a) Blender and hair dryer. (b) Router and wireless telephone.

to the conducted emissions allowed level, for household appliance devices. In the other hand, the router, wireless telephone, LED and tube TV, personal laptop and the printer were compared to the CISPR 22 standard, Figs. 4(b) and 5.

Basically, as far as the smart grid control is developed with microelectronic components, the conducted emission levels from the household appliance should be carefully observed, in order to guarantee the correct operation of the network.

It can be easily observed from the obtained results, most of the analyzed appliances are out of the standards. Therefore, without any solution to prevent the undesirable emissions, the grid performance will certainly be compromised.

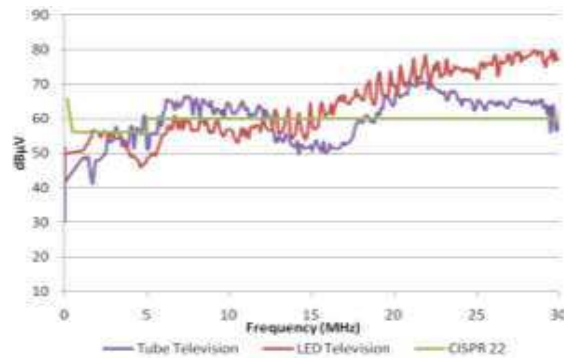


Figure 5: Measurement results of some household appliance: tube TV and LED TV.

5. CONCLUSIONS

In this work, the conducted emission levels from the household appliance are observed in order to ensure the correct operation of the devices connected to grid in terms of electromagnetic compatibility. In general terms, the conducted interference is that in which occurs undesirable transfer of electromagnetic energy along a conductor through disturbances between the phase line and the ground power supply. The obtained results were compared to the regulatory standard and it can be observed that most of the devices are out of it, thus compromising the performance of the grid as a whole.

ACKNOWLEDGMENT

The authors would like to thank CAPES for the partial financial support.

REFERENCES

1. Gunnar, A., K. Dursun, B. G. Hauge, and B. Bremdal, "Establishing sustainable and reliable smart grids," *2013 IEEE International Workshop on Applied Measurements for Power Systems (AMPS)*, 138–143, Aachen, Germany, 2013.
2. Montrose, M. I. and E. M. Nakauchi, *Testing for EMC Compliance: Approaches and Techniques*, New York, 2004.
3. Silva, F. R. L., L. R. Ribeiro, L. P. Dias, W. J. Santos, C. E. Capovilla, and H. X. Araujo, "The design and implementation of an EMC pre-compliance board," *PIERS Proceedings*, 1267–1270, Stockholm, Sweden, Aug. 12–15, 2013.
4. CISPR14-1 Ed. 5.1, "Electromagnetic compatibility — Requirements for household appliances, electric tools and similar apparatus — Part 1: Emission," International Electrotechnical Commission, 2009.
5. CISPR22 Ed. 6.0, "Information technology equipment — Radio disturbance characteristics — Limits and methods of measurement," International Electrotechnical Commission, 2008.
6. Gungor, V. C., D. Sahin, T. Kocak, S. Ergut, C. Buccella, C. Cecati, and G. P. Hancke, "A survey on smart grid potential applications and communication requirements," *IEEE Transactions on Industrial Informatics*, Vol. 9, No. 1, 28–42, Feb. 2013.
7. Yan, Y., Y. Qian, H. Sharif, and D. Tipper, "A survey on smart grid communication infrastructures: Motivations, requirements and challenges," *IEEE Commun. Surveys & Tutorials*, Vol. 15, No. 1, 5–20, 2013.

Determination of Microwave Conductivity of Electrolyte Solutions from Debye-Drude Model

Shuo Li, Sucheng Li, Shahzad Anwar, Fa Tian, Weixin Lu, and Bo Hou

School of Physical Science and Technology, Soochow University

1 Shizi Street, Suzhou 215006, China

Abstract— The solvation of ions in aqueous media is a fundamental process in biology and chemistry, and the characterization of dielectric constant of aqueous electrolyte solutions at microwave frequencies composes a powerful way to understand the dynamical process in aqueous media. In this work, we have combined the classical Debye and Drude models to determine the microwave conductivity of the salt (NaCl) solution by measuring its dielectric constant. We assume the permittivity of the electrolyte solution has a compound dielectric constant model which is the sum of the Debye model contributed by the water background and the Drude model accounting for the conductive ions in the solution. As a justification of the Drude model, the damping coefficient, γ , for the conductive ions need be far greater than the angular frequency, ω . From the DC conductivity measurement, we derive the damping coefficient of the conductive ions and prove the applicability of the Drude model in our experimental microwave regime from 0.1–20 GHz.

1. INTRODUCTION

The solvation of ions in aqueous media is a fundamental process in biology and chemistry [1]. The characterization of dielectric constant of aqueous electrolyte solutions at microwave frequencies composes a powerful way to understand the dynamical process in aqueous media [2–4]. In addition, it plays an important role in investigating the interaction between electromagnetic waves and the biological tissues that have high water content and a significant concentration of ions [5, 6]. Usually, conductivity and permittivity are the most fundamental parameters in the research of electromagnetic properties of the solutions. Compared with the direct current (DC) conductivity, it is interesting to ask if the microwave conductivity of the solutions could be measured and display some difference from the DC value.

In this work, we have combined the classical Debye and Drude models to determine the microwave conductivity of the salt (NaCl) solution by measuring its dielectric constant, i.e., permittivity, in the frequency range 0.1–20 GHz. As a typical example of Debye model, the relative permittivity of pure water obeys the dispersion relationship as following:

$$\varepsilon_r^{\text{water}}(\omega) = \varepsilon_r^{\text{water}'} + j\varepsilon_r^{\text{water}''} = \varepsilon_\infty + \frac{(\varepsilon_s - \varepsilon_\infty)}{1 + \omega^2\tau^2} + j\frac{(\varepsilon_s - \varepsilon_\infty)\omega\tau}{1 + \omega^2\tau^2}, \quad (1)$$

where ε_s is the static (DC) value of the dielectric constant, ε_∞ is the optical (infinite frequency) value of the dielectric constant, and τ is relaxation time which is the inverse of water molecules' collision frequency.

The Drude model of the relative permittivity for a metallic conductor could be written as

$$\varepsilon_r^{\text{Drude}} = \varepsilon_r^{\text{Drude}'} + j\varepsilon_r^{\text{Drude}''} = \left(1 - \frac{\omega_p^2}{\omega^2 + \gamma^2}\right) + j\frac{\omega_p^2}{\omega} \frac{\gamma}{\omega^2 + \gamma^2}, \quad (2)$$

$$\omega_p^2 = \frac{Ne^2}{\varepsilon_0 m}, \quad (3)$$

where ω_p is the plasma oscillation frequency, N is the particle number per unit volume, e is the electronic charge, ε_0 is the permittivity of vacuum, m is the mass of the conductive particle, and γ is the damping coefficient, representing the loss of the system. Within the approximation of $\omega \ll \gamma$, Eq. (2) can be simplified to be $\varepsilon_r^{\text{Drude}} \approx j\sigma/\varepsilon_0\omega$ where $\sigma = Ne^2/m\gamma$ is the conductivity [7].

Very similar to the free electrons in metals, the ions in the electrolyte solutions are considered as free carriers, responsible for the conductivity. The big difference is the background where the free carriers are moving is water for the electrolyte solutions and is atomic lattice for the metallic conductors. In order to exclude the influence of the background, we assume that the permittivity

of the electrolyte solution has a compound dielectric constant model which is the sum of the Debye model contributed by the water background and the Drude model accounting for the conductive ions in the solution.

2. EXPERIMENTS

The salt (NaCl) solutions of several mass concentrations are used in our experiments under ambient temperature. The measurement of the permittivity of the salt solution is performed by using a network analyzer (Agilent N5230C) which transmits and receives the microwave signals from 0.1 to 20 GHz and a coaxial probe (Agilent 85070E) which is a good choice to measure the permittivity for liquids. Figure 1 shows the real and imaginary parts of the relative permittivity for the pure water and the NaCl electrolyte of mass concentration 6.93%.

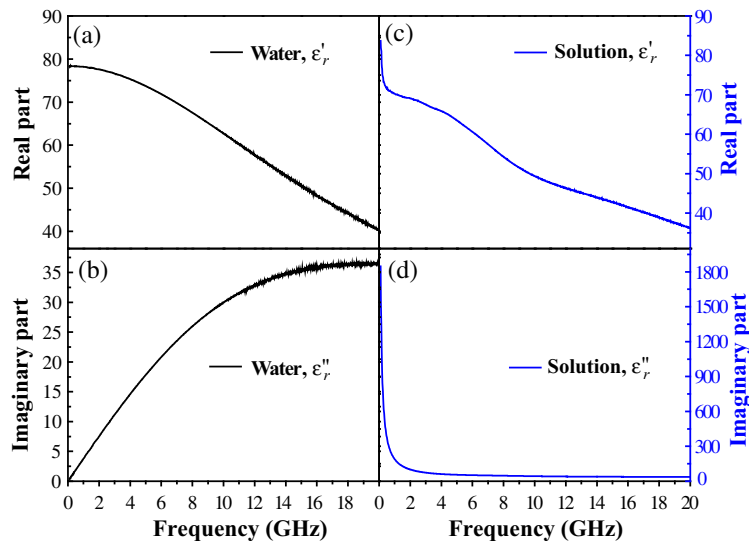


Figure 1: The measured relative permittivities of the pure water and the 6.93% salt solution. The permittivity values of the water are associated with the left axis, and those of the solution with the right axis.

3. RESULTS AND DISCUSSIONS

The contribution of Drude model from the conductive ions is calculated to be:

$$\varepsilon_r^{\text{Drude}} = \varepsilon_r^{\text{electrolyte}} - \varepsilon_r^{\text{water}} \quad (4)$$

From the simplified Drude model, we obtain the microwave conductivity $\sigma = \omega\varepsilon_0(\varepsilon_r^{\text{electrolyte}''} - \varepsilon_r^{\text{water}''})$. By this approach, we determine the microwave conductivity spectrum for various concentrated NaCl solutions, as depicted in Fig. 2. It is seen that the microwave conductivity is flat in the regime of lower frequencies and approaches to near zero at 20 GHz. This is not difficult to understand, taking into account that the conductive anions and cations in the electrolyte are much heavier than free electrons in the metal. At lower frequencies, the movement or relaxation of the ions can respond to the microwave electric field without obvious retard, resulting in a nearly constant conductivity. However, with the increase of frequency, the relaxation of the ion could not follow the oscillating external electric field, giving rise to the obvious decrease of the conductivity.

It is also interesting to compare the conductivity at lower frequencies with the DC value which is measured by using a conductivity meter (Mettler Toledo FE30). It should note the microwave conductivity with the lowest concentration at lower frequencies matches the DC value, but there is an increasing difference between these two values as increasing the salt concentration, which is attributed to the Debye-Falkenhagen effect [8].

In the above simplified Drude model, we require the damping coefficient, γ , is far greater than the angular frequency, ω . The DC conductivity can be utilized to evaluate γ , according to the following formula

$$\sigma_{\text{DC}} = Ne^2 \left(\frac{1}{m_{\text{Cl}^-}} + \frac{1}{m_{\text{Na}^+}} \right) \frac{1}{\gamma}, \quad (5)$$

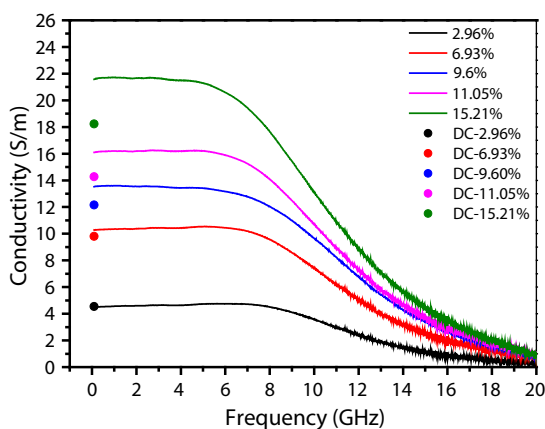


Figure 2: The microwave conductivities (solid lines) and the corresponding DC values (dots) for the five different mass concentrations of salt solution.

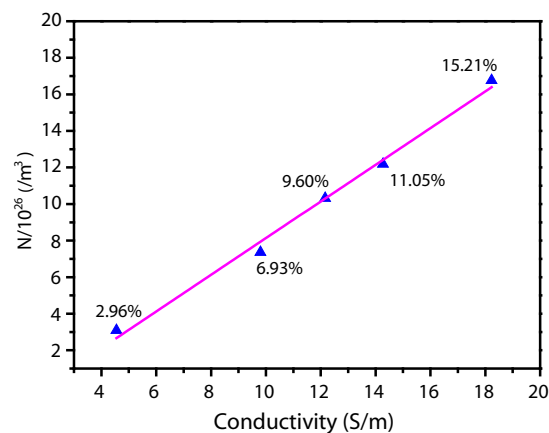


Figure 3: The N - σ_{DC} curve where the blue triangles denote the measurements and the red line is the linear fitting.

where the mass of Cl^- and Na^+ are 5.887×10^{-23} g and 3.818×10^{-23} g, respectively. Through the slope of the curve which describes the DC conductivity versus the particle number density N , we can calculate the value of damping coefficient. In Table 1, we list the unit volume particle number of ions in the solutions of different mass concentration.

Table 1: The number density of ions and the value of conductivity in the salt solutions with different mass concentration.

Sample number	Mass concentration	$N/10^{26}$ (number/ m^3)	DC Conductivity (S/m)
1	2.96%	3.09	4.55
2	6.93%	6.93	9.80
3	9.60%	10.31	12.16
4	11.05%	12.18	14.27
5	15.21%	16.77	18.23

As shown in Fig. 3, we have plotted the N - σ_{DC} curve, and done the linear fitting to obtain the slope and derived the damping coefficient $\gamma = 1.1 \times 10^{14}$ Hz. Compared with the angular frequency at microwave regime, the damping coefficient γ is seen to be much greater than ω , and it proves the applicability of the simplified Drude model in our experimental microwave regime.

4. CONCLUSION

In conclusion, we have regarded the compound dielectric constant of the salt (NaCl) solution as the sum of the free ions contribution (Drude model) and the water background (Debye model). In this way, the microwave conductivity can be determined from measuring the permittivities of the electrolyte and the water. We have obtained the microwave conductivity at different concentrations in the frequency range 0.1–20 GHz. Compared with the DC measurement, we observe the increasing difference between both at lower frequency with increasing the concentration. We also calculate the damping coefficient for the conductive ions and prove that in our experimental regime the damping coefficient, γ , is far greater than the angular frequency, ω , which means our assumption is valid.

REFERENCES

1. Kropman, M. F. and H. J. Bakker, "Dynamics of water molecules in aqueous solvation shells," *Science*, Vol. 291, No. 5511, 2118–2120, 2001.
2. Kaatz, U., "Microwave dielectric properties of liquids," *Radiation Physics and Chemistry*, Vol. 45, No. 4, 549–566, 1995.
3. Chandra, A. and B. Bagchi, "Frequency dependence of ionic conductivity of electrolyte solutions," *The Journal of Chemical Physics*, Vol. 112, No. 4, 1876–1886, 2000.
4. Chandra, A. and B. Bagchi, "Ion conductance in electrolyte solutions," *The Journal of Chemical Physics*, Vol. 110, No. 20, 10024–10034, 1999.

5. Gulich, R., et al., “Dielectric spectroscopy on aqueous electrolytic solutions,” *Radiation and Environmental Biophysics*, Vol. 48, No. 1, 107–114, 2009.
6. Peyman, A., C. Gabriel, and E. H. Grant, “Complex permittivity of sodium chloride solutions at microwave frequencies,” *Bioelectromagnetics*, Vol. 28, No. 4, 264–274, 2007.
7. Poo, Y., et al., “Measurement of ac conductivity of gold nanofilms at microwave frequencies,” *Review of Scientific Instruments*, Vol. 81, No. 6, 064701, 2010.
8. Anderson, J. E., “The Debye-Falkenhagen effect: Experimental fact of fiction?,” *Journal of Non-crystalline Solids*, Vol. 172, 1190–1194, 1994.

A Metamaterial-based Probe for EMC Measurements

M. F. P. Tartaglia¹, A. V. Cardoso¹, C. E. Capovilla², and H. X. Araujo¹

¹Universidade Federal de São João Del Rei — UFSJ, Brazil

²Universidade Federal do ABC — UFABC, Brazil

Abstract— In this work, planar probes for EMC — Electromagnetic Compatibility measurements are designed with metamaterials structures in order to improve its gain, bandwidth and resonance. Basically, three topologies are used (Jerusalem cross pair-JCP, fractal array and CSRR — complementary split ring resonator), in the square topology.

1. INTRODUCTION

The electrical circuit of any electronic device generates some kind of noise, which can reach levels of power that interfere in undesired ways on the operation of the equipment around and the environment as a whole. Each device generates a characteristic noise, due to its electrical circuit [1]. Depending on the electromagnetic emission of these noises, other electronic devices can then receive the interference by a path of radiation or, much less frequently a direct electrical connection.

The necessity to control the electromagnetic emissions and interference between circuits and electronic devices becomes a crucial point to assure its correct operation inside an electromagnetic environment. Some approaches were designed to support the pre-compliance tests (EMC/EMI/EMS) setups. In this work, is shown the design of low cost planar probes with metamaterial patterns for EMC measurements.

Actually, metamaterial is a macroscopic composite of periodic or non-periodic structure, whose function is due to both the cellular architecture and the chemical composition [2]. Therefore, the behavior of a material, in the presence of an electric field, is determined by the macroscopic parameters, permittivity ϵ and permeability μ . Several metamaterial structures have been investigated along the last years. In particular, ones those are capable to provide artificial magnetic responses and electric walls. The artificial magnetic conductors can be obtained when a plane wave focus on the capacitive gap, while the artificial electric conductor is obtained through the opposite way.

In fact, the metamaterial pattern is applied to physical devices aiming to obtain specific responses. In [3] a CSRR structure is employed to a UWB antenna in order to provide a rejection characteristic in a desired frequency. On the other hand, in [4] metamaterial structures are applied to an UHF antenna and a better gain is obtained, while in [5] the periodic is structures are applied to the septum of a GTEM — Gigahertz Transverse Electromagnetic chamber, expecting a shift on the resonance frequencies.

In this context, to improve the performance in terms of gain, bandwidth, resonance, and provide a rejected band, three different topologies are employed in planar probes.

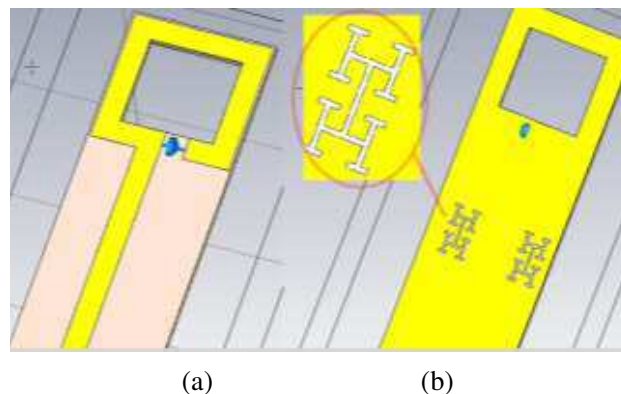


Figure 1: Square planar probe with fractal cells and 2 cm of diameter: (a) top; (b) bottom.

2. PLANAR PROBES

Generally, probes are designed in order to obtain low levels of disturbance in a wide range of applications. Thus, their shapes, balls or monopole and the variation of its diameter, are as a function of a frequency range, and if the field in question is electric or magnetic.

In this work, planar probes in square format are designed and improved in terms of bandwidth and gain with metamaterial technology. To minimize its impedance, a $50\ \Omega$ SMD resistor is used and the base of the probe has 6 cm of length. The diameter of the structures and the track width were varied in order to obtain the best response. The best combination consists of 5 mm of track width with $35\ \mu\text{m}$ of thickness on the o ROGERS R3003 substrate with 1.5 mm of thickness with a full ground plane.

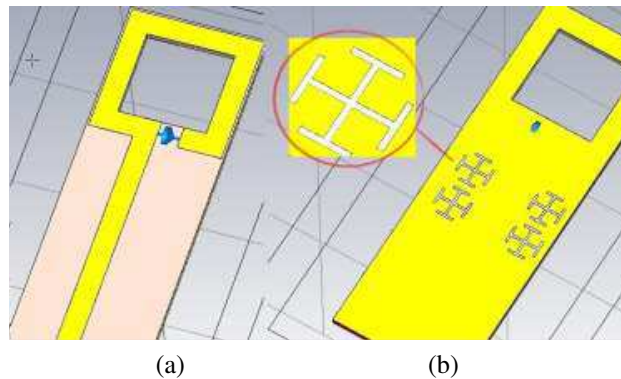


Figure 2: Square planar probe with JCP cells and 2 cm of diameter: (a) top view; (b) bottom view.

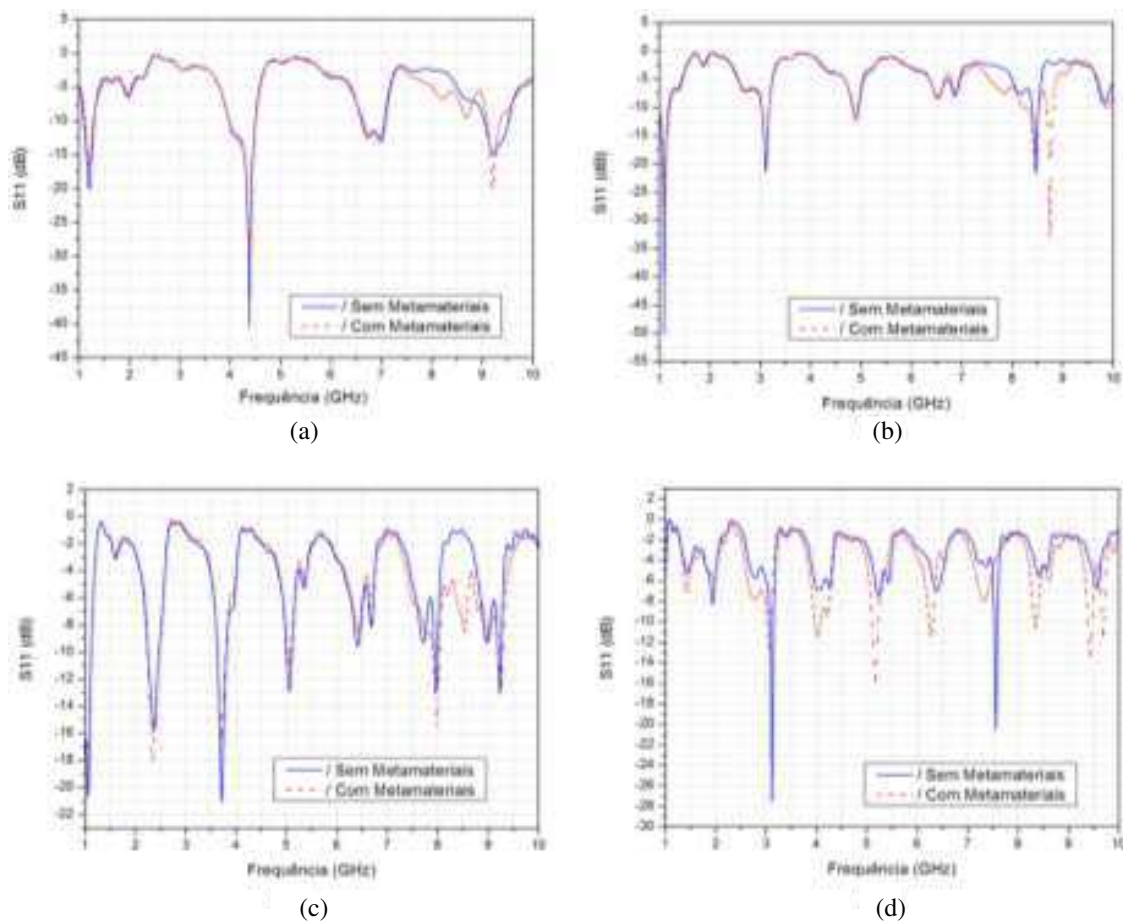


Figure 3: Comparison of S_{11} parameter between planar probe with and without JCP cells: (a) 2 cm of diameter; (b) 3 cm of diameter; (c) 4 cm of diameter; (d) 5 cm of diameter.

Therefore, metamaterial technology were applied to the planar probes as the Fractal and Jerusalem Cross Pair patterns. In the next section, they are carefully shown.

3. METAMATERIAL PATTERN APPLIED TO THE PROBES

Several metamaterial structures have been developed along the last years. In particular, it provides artificial magnetic responses, electric walls and barriers. The CLL -Capacitively Load Loop, allows the creation of artificial magnetic and electric conductor, AMC and AEC respectively.

On the other hand, the Fractal pattern allows the increasing of the electrical length of the structure, keeping the physical length. The versatility of applications and the effects of the sub-wavelength, are the two main advantages of the fractal model in H-shaped.

Through the sub-wavelength properties, the overall system is capable to present a size smaller than the wavelength along of all resonance directions, so the structure can operate as a compact reflector. Its similarity with FSS — *Frequency Selective Surfaces* structures and also its simple modeling, amplifies the use of H-shape fractal structures.

Therefore, several planar probes were design with the fractal pattern. Basically, the metamaterial structures were placed on the top and on the bottom of the probes. In Fig. 1 is shown a square size planar probe with fractals H-shape structures on the bottom. Besides the Fractal pattern show good responses in several applications, no significant variation was obtained when it was associated to the planar probe. Thereby, the JCP pattern were applied.

In Fig. 2, the proposed structure is the planar probe with JCP cells, which provide an isotropic response to any polarized incident wave. In fact, in any orientation, its perpendicular components are responsible to provide a loop current near to the displacement current on the external arms of the unitary cell.

In Fig. 3 is shown the S_{11} parameter of the planar probes with JCP cells as a function of its diameter. As expected, the efficiency of the metamaterial patterns are accentuated on the higher frequencies. Moreover, each configuration show a best resonance as a function of the diameter of the planar probe.

4. CONCLUSIONS

In this work, planar probes for EMC measurements were designed with metamaterials structures in order to improve its gain, bandwidth and resonance. Although it have been applied three different topologies in different strategic places on the planar probes, just the JCP cells showed efficiency, enhancing the resonance response in the high frequencies. Therefore, EMC measurements can be performed with this low cost planar probe.

ACKNOWLEDGMENT

The authors would like to thank CNPq, Capes and Rogers Corporation for the partial financial support.

REFERENCES

1. Cui, T. J., "Electromagnetic metamaterials: Recent advances on the theory, experiments, and applications," *IEEE Antennas Propag. Mag.*, 2008.
2. Capolino, F., *Metamaterials Handbook: Theory and Phenomena of Metamaterials*, 19-1–28, CRC Press, 2009.
3. Jo, N.-I, D.-O. Kim, and C.-Y. Kim, "A compact band notched UWB antenna for mobile applications" *PIERS Online*, Vol. 6, No. 2, 177–180, 2010.
4. Araujo, H. X., S. E. Barbin, and L. C. Kretly, "Metamaterial cell patterns applied to quasi-yagi antenna for RFID applications," *Radio and Wireless Symposium — RWS*, Santa Clara, USA, 2012.
5. De Araujo, H. X. and L. C. Kretly, "The effect of metamaterial patterning to improve the septum GTEM chamber performance," *PIERS Proceedings*, 1224–228, Marrakesh, Morocco, Mar. 20–23, 2011.

Design of Base Station Antenna for RF Energy Harvesting

Jung-Ick Moon, In-Kui Cho, Seong-Min Kim, Jae-Hun Yun, and Woo-Jin Byun

Radio Technology Research Department

Electronics and Telecommunications Research Institute (ETRI), Korea

Abstract— In this paper, a base station antenna changing the backward radiation energy into the renewable RF energy is proposed. The antenna is composed of the array radiator and RF harvesters using slots on the ground plane. The main radiator having a planar dipole type and several RF harvesters on the ground plane are used to renew the RF energy from the main radiators. The several harvesting ports are connected with the RF combiner by coaxial cables and the harvested energy is changed into the DC voltage through the rectifier circuit. Because the surface current on the ground plane flows into the RF harvesting port in the slot, the performance of the main radiator is little disturbed.

As a result, the amount of the harvested energy from this base station antenna is approximately 0.16% of the originally radiated power. The simulated radiation performances of the proposed antenna are almost same with that of the antenna without the harvester.

1. INTRODUCTION

Energy harvesting is the process of accumulating and storing ambient energy from various sources in surroundings to energy storage components. One of the energy harvesting is to use ambient RF energy. However, the RF harvested energy from the mobile communications is about from a 1,000 to 10,000 of other ambient energy sources [1]. Therefore more reasonable solution to harvest RF energy should be needed and developed.

Generally the base stations or repeaters are transmitted with very high power. However, some of the transmitted power is radiated backward and dissipated [2]. In this paper, a base station antenna changing the backward radiation energy into the renewable RF energy is proposed. The antenna is composed of the array radiator and RF harvesters using slots on the ground plane. From the surface currents on the slot, the coaxial ports connected with the rectifier circuit could harvest the RF energy.

2. THE DESIGN CONCEPT OF THE RF ENERGY HARVESTER

Figure 1 shows an element of the base station antenna with the rectangular ground plane and reflector. As shown in Figure 1, the antenna is composed of a dipole type patch and capacitive feeding to enhance the bandwidth characteristics [3]. The dipole antenna has a compact size of $79.2 \text{ mm} \times 70 \text{ mm} \times 34 \text{ mm}$ ($W_a \times L_a \times H_a$) to cover Korean LTE band (1.84~1.87 GHz).

Figure 2 shows the simulated comparison of the radiation patterns between the proposed rectenna and the antenna element shown in Figure 1. The reflector of the ground plane was a height of 12.5 mm (H_g) and used to reduce the back-lobe and increase the gain of antenna [4, 5]. The gain and FBR (Front Back Ratio) of antenna without harvesters are about 10.0 dBi and 23.0 dB, respectively. Even though the reflector such as the vertically side walls on the ground plane to reduce the back-lobe were already presented, the previous side reflector except our research [4] had

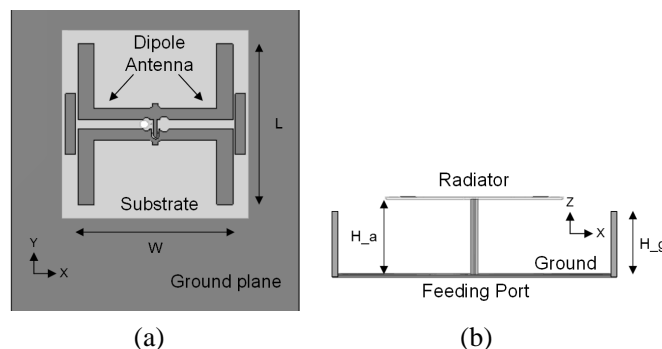


Figure 1: General dipole antenna above a rectangular ground plane. (a) Top view. (b) Side view.

no the harvesting function. To harvest the RF energy and compensate for the gain-loss of antenna, the height of reflector was increased from 12.5 mm to 25 mm.

As shown in Figure 2, the side reflector with slots and harvesting ports are able to suppress and harvest the back-lobe of antenna which has little effect on the forward radiation performance. The gain and lobe-suppression of the proposed model is much improved by 0.3 dBi and 10 dB,

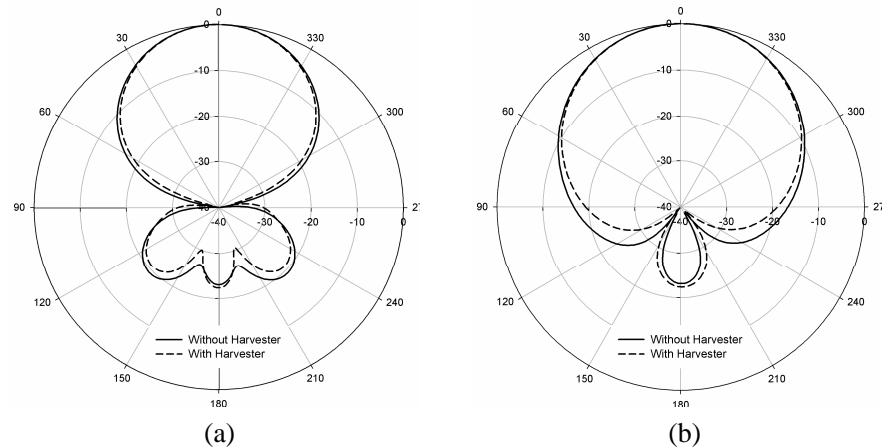


Figure 2: Comparison of the radiation patterns of the proposed array antenna on 1.87 GHz. (a) *E*-plane. (b) *H*-plane.

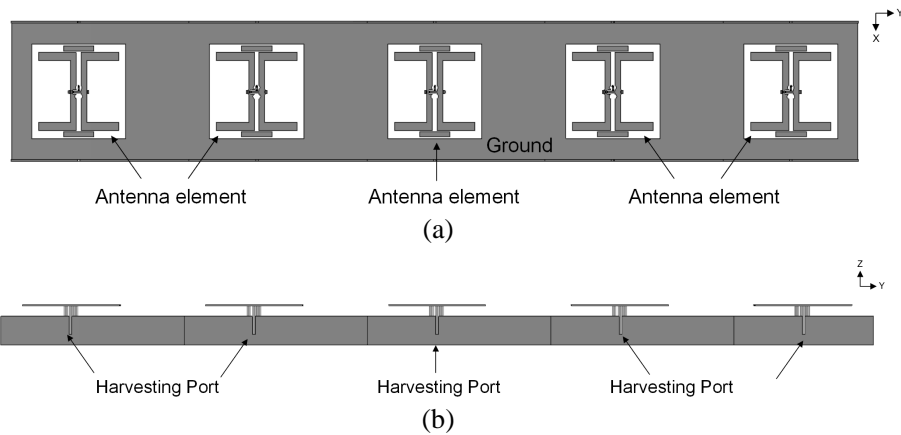


Figure 3: The array antenna with RF energy harvesters. (a) Top view. (b) Side view.

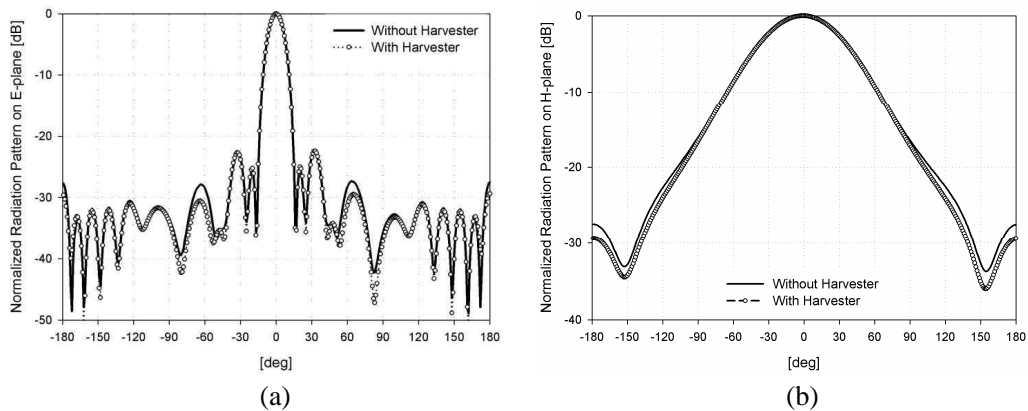


Figure 4: Comparison results of the radiation patterns of the proposed array antenna. (a) *E*-plane. (b) *H*-plane.

respectively. However, the height of the reflection should be increased. The coupling between the main radiator and the metallic wall can be controlled by the locations of the slot and walls.

3. THE DESIGN OF ARRAY ANTENNA WITH RF ENERGY HARVESTER

Figure 3 shows the proposed array antenna with RF energy harvesters. The main radiator is composed of five elements and has high gain with vertical polarized radiation performances. And several harvesting ports are arranged with the edge of ground plane shown in Figure 3(b). The coupling factor between the antenna element and the harvesting ports is about 30 dB in the operating band. From Figure 4, the back-lobe suppression on E and H -plane were 4.9 dB and 2.3 dB, respectively, for the absence of the harvesters. As a result, the amount of the harvested energy from this base station antenna is approximately 0.16% of the originally radiated power.

4. CONCLUSIONS

This paper presented the array antenna with RF energy harvesters. The slotted ground plane and harvesting ports were used to harvest the non-intentional radiation of the origin antenna. These results show that this proposed rectenna is useful for RF energy harvest applications. In addition, it would be very useful in practical and efficient antenna design.

ACKNOWLEDGMENT

This research was funded by the MSIP (Ministry of Science, ICT & Future Planning), Korea in the ICT R&D Program 2014.

REFERENCES

1. Fiorini, P., "Micropower energy scavenging," *Solid-State Circuits Conference*, 2008.
2. Siu, L. and K.-M. Luk, "Unidirectional antenna with loaded dielectric substrate," *IEEE Antenna and Wireless Propagation Letters*, Vol. 7, 2008.
3. Jeong, S. J., "Compact circularly polarized antenna with a capacitive feed for GPS/GLONASS applications," *ETRI Journal*, Vol. 34, Oct. 2012.
4. Moon, J. I., I. G. Cho, S. M. Kim, and Y. B. Jung, "Design of efficient rectenna with vertical ground-walls for RF energy harvesting," *Electronics Letters*, Vol. 49, 1050–1052, Aug. 2013.
5. Wong, T. P. and K. M. Luk, "A wide bandwidth and wide beamwidth CDMA/GSM base station antenna array with low backlobe radiation," *IEEE Trans. on Vehicular Technology*, Vol. 54, 903–909, May 2005.

Design of Compact Passive Tag Antenna for Practical RFID Applications

Zihan Chen¹, Sailing He^{1,2}, Dongdi Zhu³, and Chengcheng Du³

¹Department of Optical Engineering, Zhejiang University, Hangzhou 310027, China

²Department of Electromagnetic Engineering

School of Electrical Engineering, S-100 44 Stockholm, Sweden

³Department of Information Science & Electronic Engineering

Zhejiang University, Hangzhou 310027, China

Abstract— The communication quality between an RFID tag and a reader in a RFID network, especially the parameters of the passive tag antenna such as reading range, directivity and return loss, is affected by several factors from the environment. For practical RFID application, since the environment is complex and volatile, these factors include metallic surface of products, absorptions and impacts from neighbor tag antennas like scattering and mutual coupling. In this paper, it consists of the analysis of impacts caused by these factors and the design of passive tag antennas with resonant frequency 915 MHz able to be used in practical RFID applications against those impacts. Comparing with former ones, the proposed antenna reduces the size of the tag antenna to approximately commercial standard (18 mm × 48 mm × 3 mm) by using certain structures applied in the unit cell of metamaterial or HIS, while the properties including directivity, return loss and input impedance are still appropriate for RFID applications. Simulation results from HFSS indicates that at 915 MHz, the return loss can be about -21 dB, as most of the power can be radiated into the space towards the receiver. Meanwhile, the input impedance $Z_0 = 9.4738 + j143.9189 \Omega$, perfectly matching the impedance of the RFID chip placed on the top surface of the antenna. The above improved parameters play an important role in prolonging the reading range.

1. INTRODUCTION

Radio frequency identification (RFID) is a flourishing technology used for automatic object identification method for the efficient tracking, attracting more and more attention recently. In the last decade, with the development of the Internet of things, a considerable number of studies have been conducted on the design of RFID tag antenna for practical applications. When operated at higher frequency such as UHF band, RFID antenna has longer reading range, faster reading speed and lower collision [1]. However, as RFID tag is always directly attached to objects like metal containers or engineering plastics (ABS) boxes, parameters of tag antenna can be seriously deteriorate such as input impedance, radiation pattern, bandwidth, and return loss. These changes lead to bad performance as a result, especially for dipole antenna widely used in RFID applications [2].

Several solutions have been proposed to design UHF antennas operating at the surface of certain object. Since metallic objects are very common in transportation, and metallic surface has the most severe impact on UHF antenna, designing an anti-metallic UHF RFID tag antenna is the most crucial work to antenna engineers. Methods like planar inverted F antennas (PIFA) using a shorting plate [3] and printed inductor [4] have been proposed to improve the antenna performance against metallic boundary effect, while using the structure of HIS cell to design RFID antenna has been proved to be quite useful and efficient [5].

In this letter, a compact RFID passive tag antenna is proposed for metallic object application. And the impacts from the size of metallic object and the material of metalloid object are also analyzed. The antenna configuration will be explained in Section 2 while Sections 3, 4 demonstrate simulations and solutions to surface effect by metalloid material.

2. UHF ANTI-METALLIC PASSIVE RFID ANTENNA DESIGN

The proposed metallic RFID tag is comprised of two patches and several structures used for impedance match. Figure 1 shows the configuration of the antenna. The material used in substrate is FR4, whose relative permittivity is 4.4. And the RFID chip is Impinj Monza 4, whose input impedance is $(11 - j143) \Omega$ at 915 MHz (the operating frequency in North America).

The mechanism of the antenna can be approximately represented by an equivalent transmission line circuit. The simplified equivalent circuit model of assembled RFID tag antenna is shown in

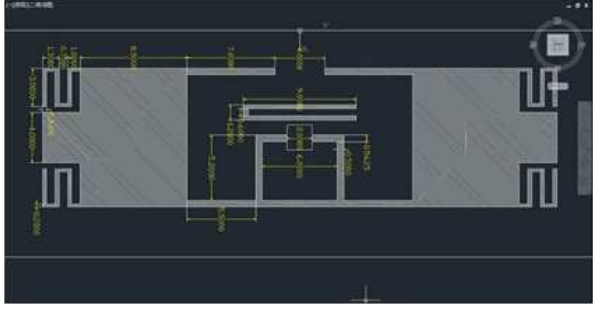


Figure 1: Configuration of the proposed RFID tag antenna.

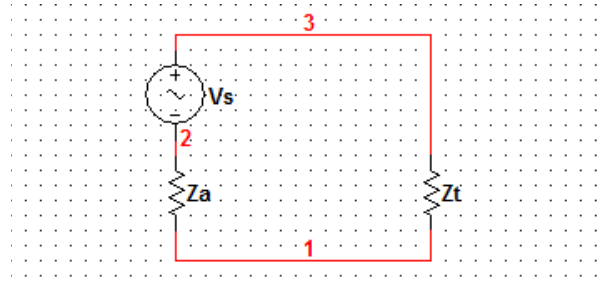


Figure 2: Simplified equivalent circuit model of tag antenna.

Figure 2. The V_s is the equivalent power source, $Z_a = R_a + jX_a$ is the impedance of the antenna, and $Z_c = R_c + jX_c$ is the impedance of the RFIC chip (here is Monza 4). From the transmission theory [6], for the maximum power transfer, the impedance of antenna and chip must meet condition of conjugating match

$$\begin{cases} R_a = R_c \\ X_a = -X_c \end{cases} \quad (1)$$

So the maximum power the chip can obtain from the antenna is

$$P_{\max} = \frac{|V_s|^2}{4R_a} \quad (2)$$

From the equivalent circuit, another important parameter is S_{11} which is defined as

$$\Gamma = \frac{Z_c - Z_a}{Z_c + Z_a} = 1 - \frac{4 \times R_c \times R_a}{(R_c + R_a)^2 + (X_c + X_a)^2} \quad (3)$$

Thus the return loss (RL) is defined as

$$\text{RL} = -S_{11} = 20 \log |\Gamma| = 20 \log \left| \frac{Z_c - Z_a}{Z_c + Z_a} \right| \quad (4)$$

Return loss represents how much power has been scattered back to the antenna instead of being absorbed by the chip.

When the radiated power delivered to the RFIC chip is larger than its threshold energy P_{th} , it will be activated, and the maximum reading range for a RFID tag antenna will be

$$r_{\max} = \frac{\lambda}{4\pi} \sqrt{\frac{P_t G_t G_r \tau}{P_{th}}} \quad (5)$$

where P_t is the power delivered from the RFID reader, G_t and G_r are the gain of reader and antenna. And τ is the power transmission coefficient, defined as $1 - \Gamma$, plays the most crucial role in prolonging the reading range.

To obtain a workable reading range, the most important work is impedance match. The impedance of the antenna can be influenced by the size and shape of the structures on the substrate. And some certain structures like T-match network are designed to adjust the impedance of the antenna, especially for reactance conjugating match.

3. RESULTS FROM MODELING AND SIMULATION

The antenna design is modeled and simulated using Ansoft high-frequency simulation software (HFSS). The metal sheet under the substrate is $0.5\lambda \times 0.5\lambda$ [5], as the surface of the metal to which tag antenna attaches. Figure 3 shows the impedance of the proposed antenna by HFSS simulation.

The impedance of the antenna operated at 915 MHz is $(9.4738 + j143.9189) \Omega$, and the impedance of the chip is $(11 - j143) \Omega$, respectively. From formula (4), the Return loss (in dB) can be calculated, and Figure 4 shows the curve of return loss with frequency 860–960 MHz.

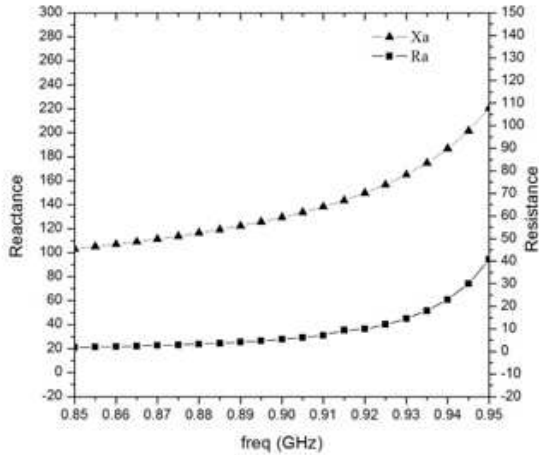


Figure 3: Impedance curve of the tag antenna.

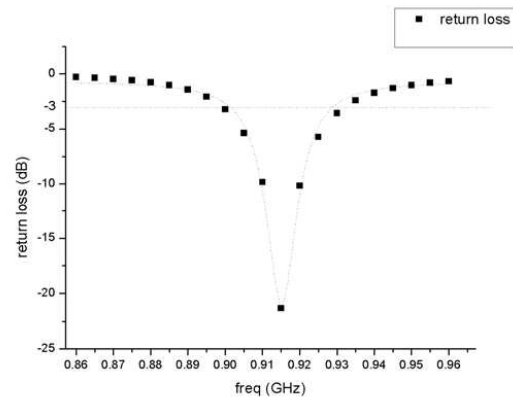
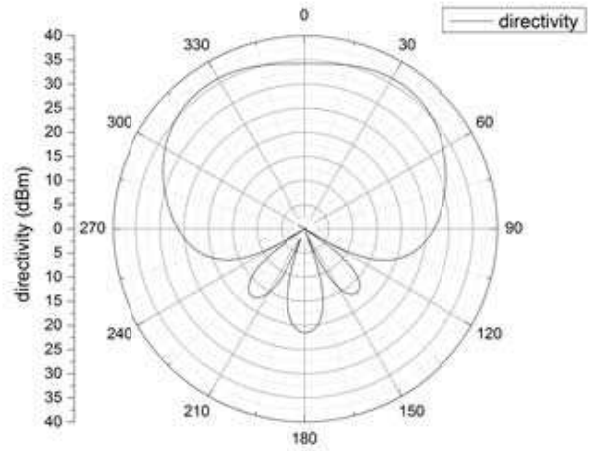
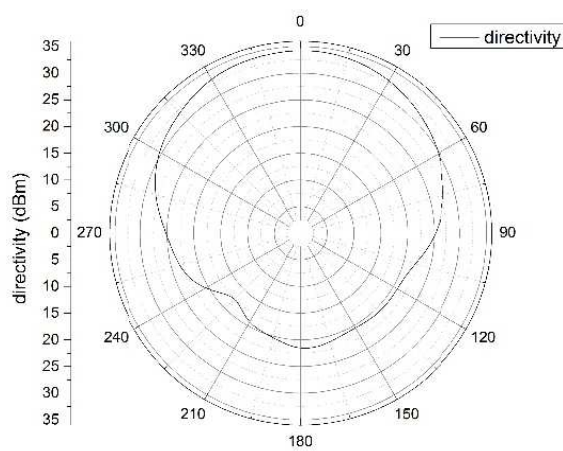


Figure 4: Return loss of the tag antenna.

Figure 5: Radiation pattern of XOZ plane and YOZ plane.

The simulated resonant frequency is $f = 915$ MHz, at which the return loss is -21.2 dB, and the -3 dB bandwidth is about 900–928 MHz (3.11%).

Furthermore, the radiation pattern of the proposed antenna are shown in Figure 5. The directivity of XOZ and YOZ plane is larger than 30 dBm, while the return loss at 915 MHz is -21.2 dB, there is enough energy to activate the chip.

4. IMPACT FROM THE GROUND PLANE ON TAG ANTENNA

For better use in practical RFID application, more researches about the performance of the proposed antenna in different conditions are conducted.

Firstly, the antenna is attached to metal objects of different surface size. Table 1 shows the sizes of the metallic objects and parameters such as impedance and return loss of the antenna at 915 MHz. And Figure 6 shows the impedance, return loss and radiation pattern of the antenna. When the size of the object becomes larger from 0.5λ to 2λ , the impedance and return loss change slightly. However, when the size is too much large ($1000\text{ mm} \times 1000\text{ mm}$), the resonant frequency shifts to 925 MHz, at which the return loss is almost equal to previous cases. This is from the fringing effect. So, for the best optimize, the size of the object surface should not be larger than $3\lambda \times 3\lambda$.

To verify the impact from attached object of different materials, the proposed antenna is put on the surfaces of objects made of ABS, Acrylic Slab, Cardboard and Pine Plywood. Table 2 indicates the properties of these materials. Figure 7 shows the impedance, return loss and radiation pattern by simulation.

Table 1: Impedance and return loss of the antenna in each cases at 915 MHz.

Size of the metallic object	Impedance/ Ω	Return loss/dB
200 mm \times 200 mm \times 15 mm	$9.16 + j142.10$	-19.87
500 mm \times 500 mm \times 15 mm	$9.33 + j141.69$	-19.68
1000 mm \times 1000 mm \times 15 mm	$8.11 + j133.11$	-6.36

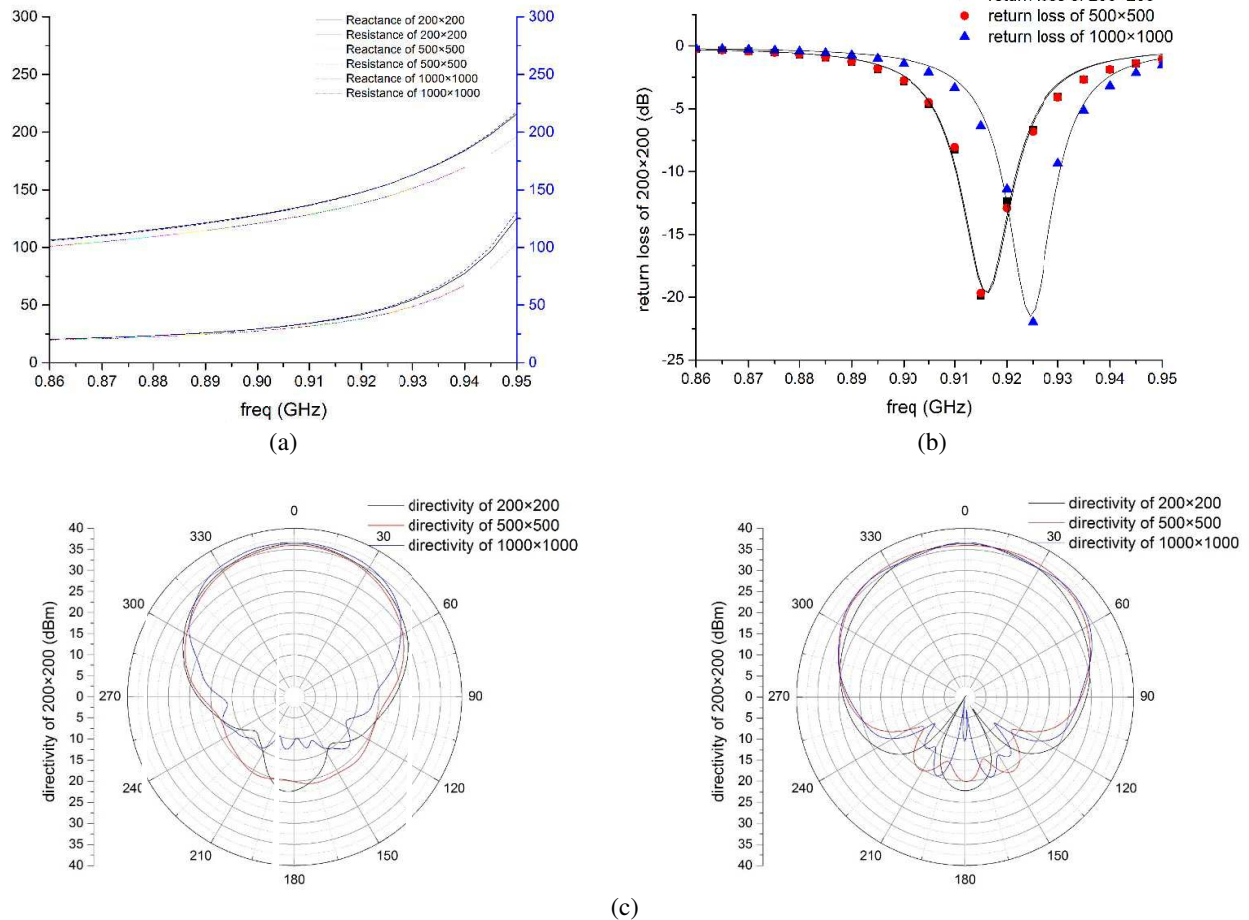

 Figure 6: (a) Impedance of the antenna in three cases. (b) Return loss of the antenna in 3 cases. (c) Radiation pattern of XOZ plane and YOZ plane.

Table 2: Properties of the materials.

material	Relative Permittivity	Dielectric Loss Tangent	Size of the object/ mm^3
ABS	2.8	0.01	$150 \times 150 \times 15$
Acrylic Slab	2.6	0.0061	$150 \times 150 \times 15$
Cardboard	1		$150 \times 150 \times 15$
Pine Plywood	1.7	0.036	$150 \times 150 \times 15$

The simulation results show that metalloid material has a negative impact on the proposed antenna, as the resonant frequency shifts to higher than 1.15 GHz. It is because as there is no metallic layer on the bottom of antenna, the effect capacity C became much smaller, which resulted in higher resonant frequency. It is not so difficult to optimize the frequency shift. One possible solution is adhering the proposed antenna to an optimized metal sheet, then put the sheet on the surface of these metalloid materials. Figure 8 shows the simulation result of the solution (taking ABS for example). At 915 MHz, the impedance is $(9.630 + j144543) \Omega$, and return loss is -20.0 dB, accordingly.

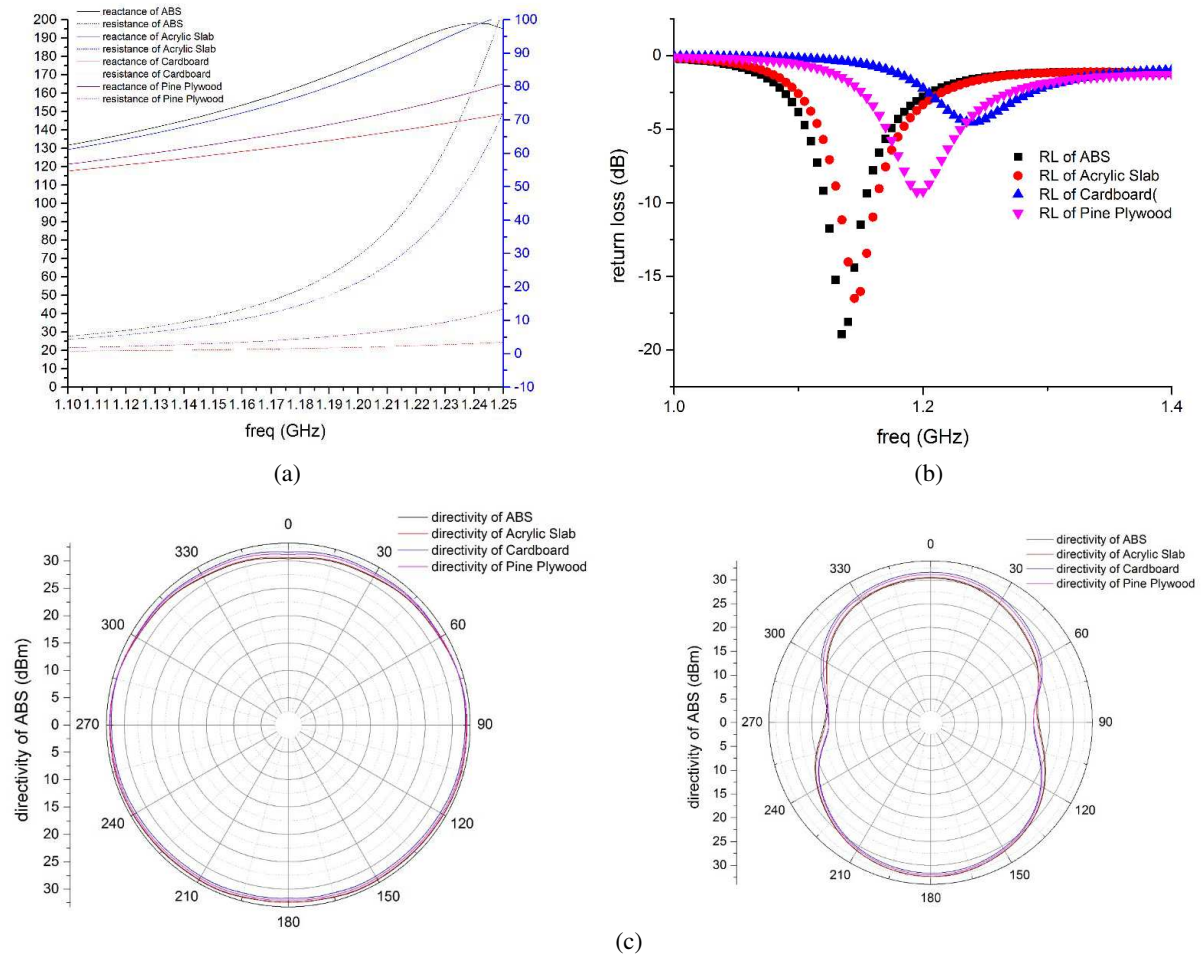


Figure 7: (a) Impedance of the antenna in these cases. (b) Return loss of the antenna in these cases. (c) Radiation pattern of XOZ plane and YOZ plane.

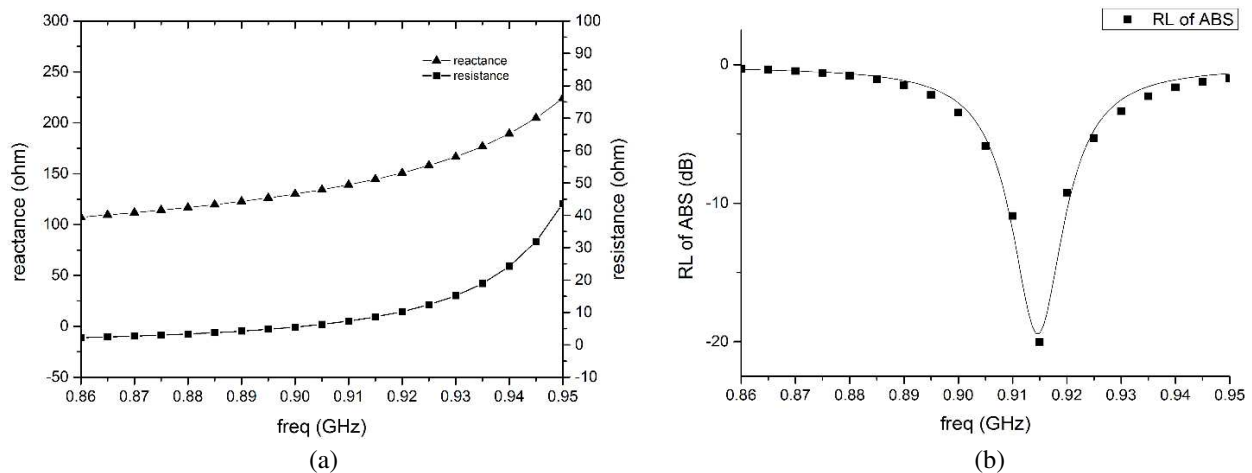


Figure 8: (a) Impedance of the antenna with metallic sheet. (b) Return loss of the antenna with metallic sheet.

5. CONCLUSION

In this letter, a compact and slim passive anti-metallic RFID tag antenna operated at 915 MHz is presented and implemented, and the impact caused by attached object has been investigated by simulation. Although the size of metal sheet and metalloid material will shift the resonant

frequency to a higher one, it can be solved by adding a metallic sheet with optimized size at the bottom of the antenna. All in all the proposed antenna can be used in practical RFID application.

REFERENCES

1. Rao, K. V. S., P. V. Nikitin, and S. F. Lam, “Antenna design for UHF RFID tags: A review and a practical application,” *IEEE Trans. Antennas Propag.*, Vol. 53, No. 12, 3870–3876, Dec. 2005.
2. Raunonen, P., L. Sydanheimo, L. Ukkonen, M. Keskilampi, and M. Kivikoski, “Folded dipole antenna near metal plate,” *Antennas Propag. Soc. Int. Symp.*, Vol. 1, 848–851, 2003.
3. Hirvonen, M., P. Pursula, K. Jaakkola, and K. Laukkanen, “Planar inverted-F antenna for radio frequency identification,” *Electron. Lett.*, Vol. 40, 848–850, 2004.
4. Son, H.-W., G.-Y. Choi, and C.-S. Pyo, “Design of wideband RFID tag antenna for metallic surfaces,” *Electron. Lett.*, Vol. 42, 263–264, 2006.
5. Chen, S.-L. and K.-H. Lin, “A slim RFID tag antenna design for metallic object applications,” *IEEE Antennas and Wireless Propagation Letters*, Vol. 7, 729–732, 2008.
6. Balanis, C. A., *Antenna Theory: Analysis and Design*, John Wiley & Sons, New York, 1997.

Statistical Characterization of Multiple Antennas Dynamic Body-to-body Radio Propagation Channel

H. A. Rahim¹, F. Malek¹, V. Ganesan¹, K. K. Goh¹,
F. A. A. Fuad¹, N. A. A. Talib², and F. S. Abdullah²

¹Embedded, Network and Advanced Computing Research Cluster (ENAC)
School of Computer and Communication Engineering, Universiti Malaysia Perlis
P. O. Box 77, d/a Pejabat Pos Besar, Kangar, Perlis 01000, Malaysia
²School of Electrical System Engineering, Universiti Malaysia Perlis
P. O. Box 77, d/a Pejabat Pos Besar, Kangar, Perlis 01000, Malaysia

Abstract— This paper presents the multiple antennas dynamic body-to-body channel in an indoor environment by utilizing quarter-wave planar textile monopole (TM) antennas at 2.45 GHz. The single input and multiple output (SIMO) measurement system uses a signal generator and two spectrum analyzers, to generate (transmit) continuous wave and measure (receive) the S_{21} parameters. During each measurement, two users are positioned at a 1 m distance where several body movements are performed, such as walking, sitting, running, jumping, bending and rotation of arms. The measured body-to-body path loss is evaluated and characterized by fitting to five well-known statistical distributions. The results exhibit that the Lognormal distribution provided the best fit for most of multiple antenna body-to-body dynamic link path loss in most of body movements performed in the experiment.

1. INTRODUCTION

Body-centric wireless communication systems (BCWC) are key components of future wireless communication systems, e.g., fourth generation (4G). A BCWC connects various devices around human bodies, such as body sensors, body monitors and wearable electronic devices. With respect to communication range, the BWCS are categorized as “off-body”, e.g., links between a person and a local access point (AP) or between two persons, and “on-body” systems, e.g., connections between devices mounted/worn on the same person [1, 2]. Body-to-body radio channel differs from the body-to-AP channels in antenna heights and types, communication range, device types and the device on-body locations which are not limited to belts or pockets. Knowledge on the body-to-body radio propagation channel is limited in the open literature, e.g., [1–3]. Thus, the aim of this study is to investigate the channel characteristics of dynamic body-to-body communications, highlighting on human body’s movement effects for SIMO system.

2. MEASUREMENT SETUP

The experiment is carried out in a strictly controlled indoor environment at Embedded, Computing Research Cluster, Universiti Malaysia Perlis to investigate effects of multipath propagation environment on body-to-body radio propagation channel. The dimension of the room is 7 m × 5 m. No other people are presented when the measurement is performed except two subjects and data collectors. Two light weight and simple structures of planar quarter wavelength textile monopole (TM) antenna (total dimension: 40 × 60 mm²) are utilized in the measurement (see Figure 2) [4]. A TM is placed on right upper arm and two TM receivers are spaced, ℓ at $\ell \gg \lambda/2$ in order to avoid mutual coupling. SIMO measurement system uses a Rohde & Schwarz signal generator (model SMBV100A) and two spectrum analyzers, Rohde & Schwarz (model FHS4 Handheld) and AdvanTest (model R1313A). Signal generator (SG) works in Continuous Wave at carrier frequency $f_o = 2.45$ GHz. The spectrum analyzers are set at span = 20 MHz, sweep time = 20 s, reference level = 10 dBm and attenuation = 40 dB. The average height and weight of a pair of gender subjects is 172 cm and 55 kg. The placement of transmitter (Tx) is fixed at the right side of upper arm on the Body 1 (SA) and the placement of receivers (Rx) are fixed on four pairs of second human body (SB); right chest-left upper arm (RC-LU), right chest-left waist (RC-LW), right chest-ankle (RC-A) and left upper arm-back (LU-B) (see Figure 1). Tx is connected to SG and the two Rxs are connected to the each port of Spectrum Analyzers. During each measurement, two users are positioned at a 1 m distance. The SA is static and SB is in dynamic movement where several body movements are performed, including walking, sitting, running, jumping bending and

rotation of arms. An antenna-body separation of 10 mm is applied by putting foam with $\epsilon_r \approx 1$. A 10 meter low loss semi-rigid and two 4 meter flexible (Multiflex-141) coaxial cables are used in the measurement campaign, manufactured by Huber-Suhner. Cables are wrapped with Eccosorb Flexible Broadband Urethane Absorber model: FGM-U-20-SA microwave absorbing foams. The SG is calibrated before the measurements to ensure that the RF input power supplied to textile monopole (TM) is 0 dBm by setting frequency offset = -7.8 dB. Both of the spectrum analyzers are also calibrated by measuring standing still position (static movement) and in walking movement. The S_{21} parameter is captured simultaneously using these two spectrum analyzers. The difference of S_{21} value (from both spectrum analyzers) is subtracted from S_{21} value of AdvanTest spectrum analyzer.

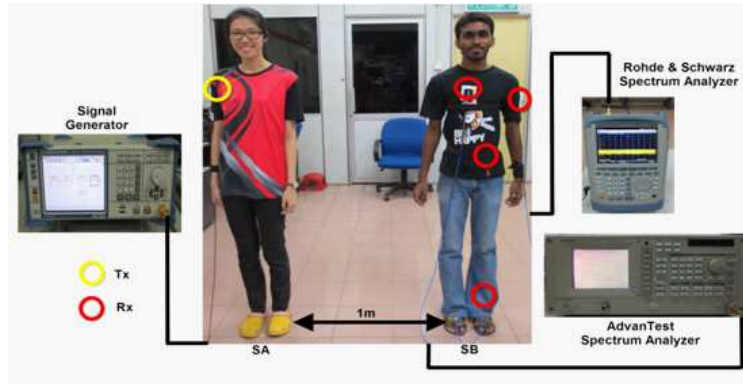


Figure 1: Body-to-body measurement setup in the laboratory environment.

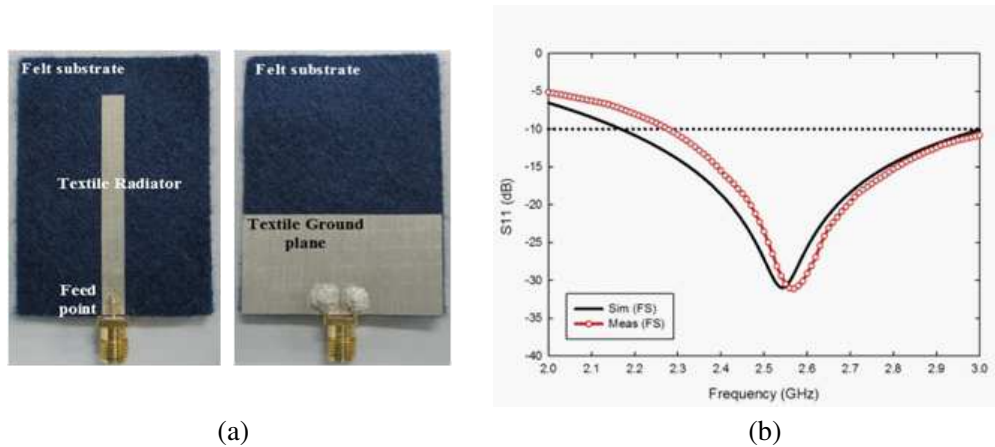


Figure 2: (a) Structure of planar TM and its fabrication prototype in front and back views. (b) Reflection coefficient of simulated and measured in free space (FS).

3. STATISTICAL ANALYSIS

To select the best model among several models of fading, Akaike Information Criterion (AIC) is used [8, 11]. The second order AIC, normally expressed as AIC_c , written as

$$AIC_c = -2 \log_e(L) + 2K + \frac{2K(K+1)}{n-K-1} \quad (1)$$

where L is the maximized log likelihood, model K is the number approximation parameters in the selected model and n is the sample size. The log likelihood is available in the Maximum Likelihood (ML) estimator and thus (1) can be directly computed. Meanwhile, the second part of (1) restricts additional parameters so as to guarantee that best fits the data with the least of parameters. In determining the models rank from the best to worst and to show strong proof that one model is better than another, the relative values of AIC_c is utilized. The expression for relative values of AIC_c is

$$\Delta i = AIC_{c,i} - \min(AIC_c) \quad (2)$$

where AIC_c is the AIC value for model index i . From (2), the best model among the set of models is determined when $\Delta i = 0$. In general, $\Delta i < 2$ refers to significant evidence for model and if values are between 3–7, it implies that the model has less satisfactory level. However, if values are greater than 10, it suggests that the model is impossible to happen.

4. RESULTS AND DISCUSSION

Table 1 presents the mean received power at Branch 1 (B1) and Branch 2 (B2) and power difference between two branches for four body-to-body channels at 2.45 GHz. The result shows that the maximum power difference between two branches is RC-A link for arm circulation movement. It is evident that the RC-A, with longer communication link, provides the maximum path loss variation between two branches of antennas. Meanwhile, the least power difference between two branches is seen on LU-B link for bending left motion. Although LU-B link is a non-line-of-sight (NLOS) scenario, it is observed that LU-B link obtains the minimum path loss variation of body-to-body channel in dynamic movement. This is due to the fact that bending left motion reduces the distance, and thus, more electromagnetic (EM) wave propagates in a direct path from Tx on SA to Rx(s) on SB. The measured data is statistically analyzed by applying the second-order AIC to determine the best fit model for all cases. The estimated parameters are computed based on 95% confidence interval utilizing dfittool in the Matlab statistical toolbox.

Table 1: Mean power difference for all body-to-body channels at 2.45 GHz.

Movement	LU-B			RC-A			RC-A			RC-LW		
	Mean Power (dB)		Power Difference (dB)	Mean Power (dB)		Power Difference (dB)	Mean Power (dB)		Power Difference (dB)	Mean Power (dB)		Power Difference (dB)
	B1	B2		B1	B2		B1	B2		B1	B2	
Walking	62.29	61.46	0.83	62.0	58.64	3.36	62.17	61.09	1.08	63.34	57.67	5.67
Sitting	63.54	61.58	1.96	62.61	62.06	0.55	60.45	62.03	1.58	62.54	59.93	2.61
Running	57.92	61.63	3.71	61.24	61.69	0.45	60.70	59.61	1.09	61.58	59.75	1.83
Jumping	62.38	60.81	1.57	61.76	60.29	1.47	61.05	59.01	2.04	59.37	58.6	0.77
Bending Left	60.86	61.07	0.21	55.64	60.63	4.99	60.97	60.83	0.14	61.7	61.04	0.66
Arm Circulation	61.21	59.72	1.49	56.64	64.04	7.40	60.65	61.24	0.59	59.07	60.76	1.69
Bending Backward	61.45	60.78	0.97	60.29	62.91	2.62	60.89	59.37	1.52	61.78	60.04	1.74

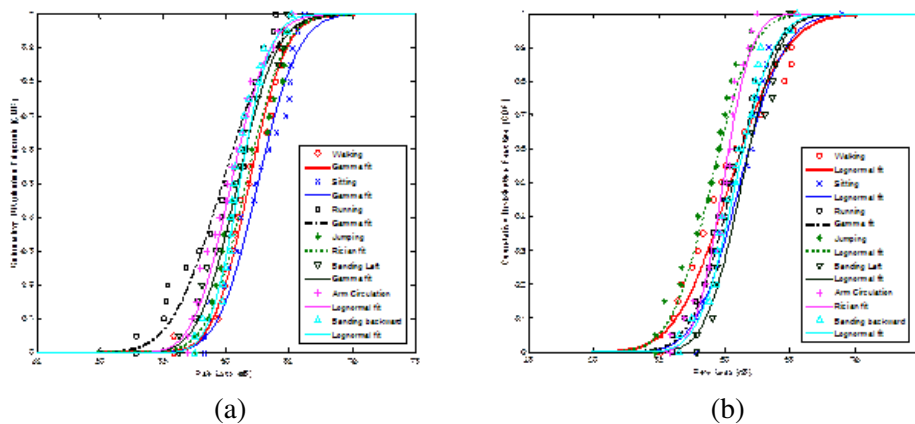


Figure 3: CDF for body-to-body channel (a) LU-B link and (b) RC-LW link.

Table 2 summarizes the best fit model for all body-to-body channels in different movements. In LU-B link case, Gamma provides the best fit for walking, sitting, running and bending left movements (see Figure 3(a)). Since B1 and B2 are located on the opposite side of each other, this introduces NLOS scenario. From this result, it is shown that Gamma distribution is best described for NLOS case in dynamic movement. For RC-A and RC-LW links, the channel fading follows Lognormal distribution for all movements, except for sitting and arm circulation (RC-A case) and running and arm circulation (RC-LW case) respectively. As Lognormal distribution usually models the shadowing effect [1], the reflection and diffraction of signal from the surrounding and arms (reflection and shadowing) affects the path loss of RC-A and RC-LW links (see Figure 3(b)). Although both Rxs are mounted on the front side of body, the shadowing from arms dominates the EM propagation, and thereby resulting in Lognormal fitting. However, for RC-LU link, Rician dominates the best fit for most of the movements (walking, sitting, bending left, and arm circulation).

Table 2: Best fit model for all body-to-body channels.

Rxs Location	Movement	Best Fit Model	Estimated Parameter	
LU-B	Walking	Gamma	$a = 743.56$	$b = 0.08$
	Sitting	Gamma	$a = 620.02$	$b = 0.10$
	Running	Gamma	$a = 348.65$	$b = 0.17$
	Jumping	Rician	$v = 0.29$	$\sigma = 0.14$
	Bending Left	Gamma	$a = 615.77$	$b = 0.10$
	Arm Circulation	Lognormal	$\mu = 4.10$	$\sigma = 0.04$
	Bending Backward	Lognormal	$\mu = 4.11$	$\sigma = 0.03$
RC-A	Walking	Lognormal	$\mu = 4.10$	$\sigma = 0.05$
	Sitting	Gamma	$a = 899.71$	$b = 0.07$
	Running	Lognormal	$\mu = 4.12$	$\sigma = 0.03$
	Jumping	Lognormal	$\mu = 4.11$	$\sigma = 0.04$
	Bending Left	Lognormal	$\mu = 4.06$	$\sigma = 0.06$
	Arm Circulation	Rician	$v = 0.80$	$\sigma = 0.40$
	Bending Backward	Lognormal	$\mu = 4.12$	$\sigma = 0.04$
RC-LU	Walking	Rician	$v = 0.19$	$\sigma = 0.10$
	Sitting	Rician	$v = 0.33$	$\sigma = 0.16$
	Running	Gamma	$a = 852.97$	$b = 0.07$
	Jumping	Lognormal	$\mu = 4.09$	$\sigma = 0.04$
	Bending Left	Rician	$v = 0.38$	$\sigma = 0.19$
	Arm Circulation	Rician	$v = 0.41$	$\sigma = 0.21$
	Bending Backward	Lognormal	$\mu = 4.11$	$\sigma = 0.05$
RC-LW	Walking	Lognormal	$\mu = 4.10$	$\sigma = 0.06$
	Sitting	Lognormal	$\mu = 4.11$	$\sigma = 0.04$
	Running	Gamma	$a = 580.73$	$b = 0.10$
	Jumping	Lognormal	$\mu = 4.08$	$\sigma = 0.04$
	Bending Left	Lognormal	$\mu = 4.12$	$\sigma = 0.04$
	Arm Circulation	Rician	$v = 0.14$	$\sigma = 0.07$
	Bending Backward	Lognormal	$\mu = 4.11$	$\sigma = 0.04$

5. CONCLUSIONS

In this work, we investigate the multiple antennas dynamic body-to-body channel modeling of radio propagation channel in an indoor environment at 2.45 GHz. Quarter-wave planar TM antennas are used in the measurement. The mean power difference between two Rxs for all pair locations is presented and analyzed. Besides, a statistical analysis is also performed to mean path loss of body-

to-body by fitting to well-known statistical distribution. The results show that most of dynamic body-to-body channel in most of body movements can be best described by Lognormal distribution due to reflection, diffraction and shadowing effects. Our analysis clearly shows that body movements and positioning between two receive

REFERENCES

1. Michalopoulou, A., A. A. Alexandridis, K. Peppas, T. Zervos, F. Lazarakis, K. Dangakis, and D. I. Kaklamani, "On-body channel modelling: Measurement and statistical analysis," *2010 Loughborough Antennas and Propagation Conference (LAPC)*, 201–204, Loughborough, UK, Nov. 8–9, 2010.
2. Abbasi, Q. H., M. M. Khan, S. Liaqat, M. Kamran, A. Alomainy, and Y. Hao, "Experimental investigation of ultra wideband diversity techniques for on-body radio communications," *Progress In Electromagnetics Research C*, Vol. 34, 165–181, 2013.
3. Rosini, R., R. Errico, D. Errico, and R. Verdone, "Body-to-body communications: A measurement-based channel at 2.45 GHz," 1763–1768, Sydney, Australia, Sept. 9–12, 2012.
4. Rahim, H. A., M. F. B. A. Malek, I. Adam, S. Ahmad, N. B. M. Hashim, and P. S. Hall, "Design and simulation of a wearable textile monopole antenna for body centric wireless communications," *PIERS Proceedings*, 1381–1384, Moscow, Russia, Aug. 19–23, 2012.

A Novel Idea of Evaluating Non-ionizing 2.45 GHz Wireless Body Area Network (WBAN) RF Radiation on Human Cognitive Performance Using Wearable Textile Monopole Antennas

H. A. Rahim¹, F. Malek¹, P. J. Soh¹, F. A. A. Fuad¹,
N. Hisham¹, N. A. A. Talib², and F. S. Abdullah²

¹Embedded, Network and Advanced Computing Research Cluster (ENAC)
School of Computer and Communication Engineering, Universiti Malaysia Perlis

P. O. Box 77, d/a Pejabat Pos Besar, Kangar, Perlis 01000, Malaysia

²School of Electrical System Engineering, Universiti Malaysia Perlis

P. O. Box 77, d/a Pejabat Pos Besar, Kangar, Perlis 01000, Malaysia

Abstract— This paper presents a novel idea of evaluating the non-ionizing 2.45 GHz Wireless Body Area Network (WBAN) radio frequency electromagnetic fields exposure effect on human cognitive performance. The study aims at determining whether exposure of non-ionizing 2.45 GHz WBAN radio electromagnetic fields (EMF) may affect the cognitive performance of human being. Twenty healthy and right-handed volunteers (10 males and 10 females) are involved in the test and exposed to 2.45 GHz WBAN, emitted by a pair of planar textile monopole antennas in 1-hr per-session, with two separate sessions; EMF exposure and sham exposure (no exposure). Paired Associates Learning (PAL) and Spatial Span Length (SSP) tasks using CANTAB eclipse version 4.0 cognitive software, are performed by each subject to assess the visual memory and working memory capacity during the exposure of on-body textile monopole (TM) antennas positioned on right-upper-arm-to-left-chest link. A total of two outcome measures are presented in measuring PAL which are PAL Total errors (adjusted) and PAL Mean errors to adjusted, measuring mean number of errors made before the stage is successfully completed. The result showed that both PAL outcome measures and SSP give no significant difference between exposure conditions (EMF and sham exposures), $p's > 0.05$. Thus, PAL and SSP performance (cognitive) is not affected by non-ionizing 2.45 GHz WBAN EMF exposure.

1. INTRODUCTION

A great concern has risen from public on the effects of radiation emitted by the communication devices due to numerous exposure of electromagnetic fields (EMF) in our daily life. It is debatable whether low-intensity EMF radiation can cause adverse health effects to human. In the open literature, many studies have been reported to examine whether radio frequency (RF) exposure emitted by mobile phone or base station may affect well-being, physiological parameters and other related human body parameters [1–6]. However, to date, the effect of non-ionizing 2.45 GHz WBAN emitted by wearable antennas on human cognitive performance has not been carried out. Thus, the main objective of the study is to investigate whether 2.45 GHz WBAN of non-ionizing exposure by wearable textile antennas in the vicinity of human body can affect human cognitive performance in terms of visual memory and working memory capacity. The study is conducted under high standard of experimental procedure, ensuring validity and important contribution to EMF effects on people's health.

2. MEASUREMENT SETUP

Twenty volunteers are involved in the study (ten are female and ten are male). Subjects are between 23 and 31 years of age (mean \pm standard deviation (SD), 25 ± 2.4), and have normal body weight (BMI 19–26 kg/m²). The volunteers are interviewed prior to the study. This is to identify whether they are healthy and free from neurological/psychiatric history problems. The participants receive small incentives at the end of experiment sessions.

The study is conducted in an RF shielded room, Electromagnetic Hyper Sensitivity (EHS) Laboratory, Jabatan Kejuruteraan Elektrik, Politeknik Tuanku Syed Sirajuddin, Arau, Perlis, Malaysia, between May and July 2013. The dimension of the RF-shielded room is $4 \times 3 \times 2.5$ m³. The room is furnished with one PC table with PC desktop, one sofa and a plastic armed chair. Subjects are seated on a comfortable armchair, with a distance of 40 cm from the subject's head to the PC desktop. The aim of the study is to investigate the effects of 2.45 GHz WBAN RF exposure on

human cognitive performance. The experiment consists of two sessions; RF and sham (no exposure) at 1-week intervals in a single-blinded, counterbalanced and crossover condition. CANTAB eclipse version 4.0 cognitive software by Cambridge Cognition Ltd, United Kingdom is utilized to perform the cognitive tests on subjects. Subjects spend 45–60 minutes to complete the cognitive tests (4 tasks) in each exposure session. Constant ambient light and room temperature conditions (average: 28.26 ± 0.32) are ensured throughout the whole campaign.

Two quarter-wave, omni-directional planar textile monopole antenna operating at 2.45 GHz are used as a source and receiving port, positioned parallel to the body surface (along z -direction). The total dimension of TM is $40 \text{ mm} \times 60 \text{ mm}$ with a substrate thickness of 1.7 mm. A patch length, $L_M = 0.25\lambda = 30.6 \text{ mm}$. The quarter-wavelength monopole has an excellent impedance matching and radiation performance in narrowband frequency [7]. A 2-port Vector Network Analyzer (VNA) (Agilent model number 5071C ENA) is used to transmit the continuous wave and receive the signal of on-body locations. RF input power supplied to TM is set to 0 dBm. Tx is fixed at the right side of upper arm while Rx is mounted on the left chest, mimicking the position of ECG sensor. Two low-loss semi-flexible Huber+Suhner coaxial cables, wrapped with microwave absorbing foam, are utilized to connect Tx with port 1 and Rx with port 2 (see Fig. 1). Antenna to body separation is 10 mm.

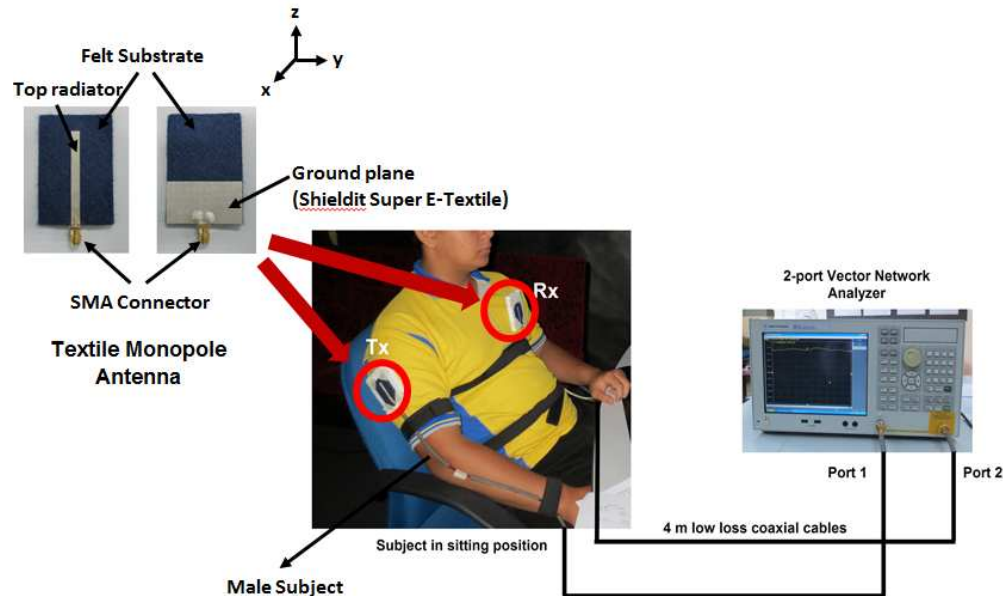


Figure 1: Measurement setup in the RF shielded room.

3. COGNITIVE TASK

We investigate the effects of wearable TM antenna RF radiation on visual memory PAL and SSP tasks using CANTAB eclipse version 4.0 cognitive software, performed by each subject to assess the visual memory and working memory capacity during the exposure of on-body textile monopole (TM). The CANTAB is a computerized neuropsychological battery that comprises 22 tests for accessing memory, attention test and executive function. A touchscreen computerized system that provides an accurate neuropsychological assessment and latency recording is used to test each subject. Subjects are required to memorize specific pattern locations with random assignment in the allocated boxes. If the subject makes an error, the pattern is re-presented to remind the subject of their locations. Three trials are allowable if error is made. In the clinical mode of battery test, the number of patterns increases from 1 to 8. 14 outcome measures for PAL are split into 4 groups; errors, trials, memory scores, stage completed. In this paper, two outcome measures are presented in measuring PAL in the study which are PAL Total errors (adjusted), measuring the total number of errors across all assessed problem and all stages, with an adjustment for each stage not attempted due to previous failure) and PAL Mean errors to adjusted, measuring mean number of errors made before the stage is successfully completed. Meanwhile, Spatial span (SSP) evaluates working memory capacity and the task is a visuospatial analogue of the Digit Span test. Nine

white squares are shown in the task where some of the squares abruptly changes colour in random sequence. Subjects have to touch the white boxes on PC screen according to same order after the sequenced colour boxes disappear (clinical mode). The number of boxes varies from 2 to 9.

4. RESULTS AND DISCUSSION

We use paired sample t -test (software: SPSS version 18.0) to analyze the human cognitive performance in terms of visual memory and working memory capacity (condition: RF and Sham). The paired sample t -test reveals that there is no significant difference between mean PAL total errors (adjusted) of subjects in both conditions on 2.45 GHz ISM band field exposures [$t(19) = 0.37$, $p > 0.05$]. In the PAL mean errors to success, error increases from Sham to RF exposure condition with no significant difference [$t(19) = 0.90$, $p > 0.05$]. In contrast, there is a decrease in SSP performance between Sham and RF exposure ($p = 0.353$; Table 1). Both conditions does not reach the maximum score 9 as the mean length, $M < 7$ in SSP. Thus, it can be concluded that PAL and SSP performances (Cognitive) are not affected by 2.45 GHz WBAN RF exposure.

Table 1: Results of cognitive performance.

Cognitive Test	Sham	RF	Sham vs RF
	Mean (SE)	Mean (SE)	p -value
PAL Total errors (adjusted)	5.75 (1.50)	6.40 (1.43)	0.36
PAL Mean errors to success	1.65 (0.44)	2.05 (0.51)	0.19
SSP Span length	6.80 (0.47)	6.65 (0.40)	0.35

PAL: Paired Associated Learning, SSP: Spatial Span, SE: Standard Error.

5. CONCLUSIONS

The paper presents a novel idea of evaluating the non-ionizing 2.45 GHz Wireless Body Area Network (WBAN) radio frequency electromagnetic fields exposure effect on human cognitive performance. In the study, it is found that brain physiology is not affected by RF radiation, particularly on visual memory and working memory capacity. Further work will be conducted to thoroughly analyze the effect of 2.45 GHz WBAN RF exposure on human cognitive performance in double-blinded condition.

ACKNOWLEDGMENT

The authors would like to thank all volunteers who involve in this measurement campaign. The authors also would like to thank Jabatan Kejuruteraan Elektrik, Politeknik Tuanku Syed Sirajuddin, Arau, Perlis, Malaysia for their collaboration in this project. This work is partially supported by the Knowledge Transfer Programme (KTP) grant by Ministry of Education (MOHE), Malaysia, under grant 9011-00016. The authors would like to express their highest gratitude to MOHE and Universiti Malaysia Perlis.

REFERENCES

1. Hamblin, D. L., A. W. Wood, R. J. Croft, and C. Stough, "Examining the effects of electromagnetic fields emitted by GSM mobile phones on human event-related potentials and performance during an auditory task," *Clinical Neurophysy.*, Vol. 115, 171–178, 2004.
2. Regel, S. J., S. Negovetic, M. Roosli, V. Berdinas, J. Schudere, A. Huss, U. Lot, N. Kuster, and P. Achermann, "UMTS base station-like exposure, well-being, and cognitive performance," *Environ. Health Persp.*, Vol. 114, 1270–1275, 2006.
3. Eltiti, S., D. Wallace, A. Ridgewell, K. Zougkou, R. Russo, F. Sepulveda, D. Mirshekar-Syahkal, P. Rasor, R. Deeble, and E. Fox, "Does short-term exposure to mobile phone base station signals increase symptoms in individuals who report sensitivity to electromagnetic fields? A double-blind randomized provocation study," *Environ. Health Persp.*, Vol. 115, 1603–1608, 2007.
4. Cinel, C., R. Russo, A. Boldini, and E. Fox, "Exposure to mobile phone electromagnetic fields and subjective symptoms: A double-blind study," *Psychomatic Medicine*, Vol. 70, 345–348, 2008.

5. Eltiti, S., D. Wallace, A. Ridgewell, K. Zougkou, R. Russo, F. Sepulveda, and E. Fox, “Short-term exposure to mobile phone base station signals does not affect cognitive functioning or physiological measures in individuals who report sensitivity to electromagnetic fields and control,” *Bioelectromagnetics*, Vol. 30, 556–563, 2009.
6. Trunk, A., G. Stefanics, N. Zentai, Z. Kovac-Balint, G. Thuroczy, and I. Hernadi, “No effects of single 3G UMTS mobile phone exposure on spontaneous EEG activity, ERP correlates, and automatic deviance detection,” *Bioelectromagnetics*, Vol. 34, 31–42, 2012.
7. Rahim, H. A., M. F. B. A. Malek, N. B. Hisham, and M. F. B. H. A. Malek, “Statistical analysis of on-body radio propagation channel for body-centric wireless communications,” *PIERS Proceedings*, 374–378, Stockholm, Aug. 12–15, 2013.

Fractal Etched Bow-tie Antenna Loading Zero-index Metamaterials

Kai Ma, Hui Feng Ma, Qiang Cheng, and Tie Jun Cui

State Key Laboratory of Millimeter Waves, Southeast University, Nanjing 210096, China

Abstract— Characterized by its wide impedance bandwidth and relatively stable radiation pattern, the bow-tie antenna has been widely utilized in the microwave as a suitable radiator. However, the comparatively limited radiation gain will constrain this type of antenna from more extensive applications when higher gain is required. In this paper, a bow-tie antenna etched with modified Sierpinski fractal patterns is proposed, which can enlarge the current path for radiation thus minimize the overall dimensions of the radiator to further increase its impedance bandwidth. Moreover, for the sake of gain-enhancement, an artificial structure consisting of zero-index metamaterials (ZIM) unit is carefully designed and adopted in the fractal pattern etched antenna.

1. INTRODUCTION

Bow-tie antenna is featured by its wide impedance bandwidth in the microwave band, thus can be versatile for various needs as an ideal radiator. Such type of antenna, which has been extensively used in the UWB system, is the planarization of bi-conical antenna. In consideration of the commercial aspects, the antenna should be compact, low-cost and easy to fabricate.

Miniature of antenna is always a hot-spot issue in modern antenna design. So as to further minimize the antenna dimension, Sierpinski fractal pattern has been adopted in bow-tie antenna [6, 7]. However, such fractal pattern will give rise to the current discontinuity thus inevitably narrow the impedance bandwidth.

Metamaterials are artificial composite materials that exhibit exotic electromagnetic properties, which will not be found in natural materials. With the development of metamaterials, a novel method is suitable for gain enhancement with the use of zero-index metamaterials (ZIM) [1]. Zero-index metamaterials are such unique artificial structure that one component of its permittivity or permeability tensor approaches to zero, which leads to a near zero refraction index [2, 3].

In this paper, a modified Sierpinski fractal pattern etched on the surface of bow-tie antenna structure is proposed. Our design will improve the current continuity to enlarge the electric current path floating across the two wings of the antenna compared with the previous work. Thus this pattern will have a wider working frequency band with a lower end. Furthermore, a ZIM structure is carefully designed and implemented with the antenna. The simulated results show that the use of ZIM will achieve a higher gain performance.

2. DESIGN OF BOW-TIE ANTENNA AND FRACTAL PATTERN

The bow-tie antenna is fed by a microstrip line, which transforms from a coaxial cable via a coaxial connector. The bow-tie antenna is a double-sided balanced antenna, so a balun [4, 5] is introduced as a transition between the balanced antenna and the unbalanced microstrip line.

The dielectric substrate is chosen as FR-4 with the permittivity of 4.3 and the loss tangent is 0.025. The length of the antenna (L_b) is 53 mm, and the angle of the wing of the antenna is 60° , as illustrated in Fig. 1(a). The balun structure shown in Fig. 1(b) provides a smooth transition from the microstrip line and the coplanar stripline (CPS).

Fractal pattern is a self-similarity pattern, which means the part of the structure is similar to the whole body. The fractal pattern usually used in the bow-tie antenna is the 3rd Sierpinski pattern [6, 7], which is easy to fabricate. The 2nd Sierpinski pattern is shown in Fig. 2(a).

The fractal pattern etched antenna is illustrated in Fig. 3(a). As can be seen, the fractal pattern slightly differs from the 2nd Sierpinski pattern, which is more similar to the picture exhibited in Fig. 2(b), with a little yellow triangle in the center of 2nd Sierpinski pattern. The current path is enlarged by the insertion of the triangle patch. Furthermore, we have modified the size of the 1st and 22nd triangles cutting from the original big triangle to form the fractal pattern shown in Fig. 3(b), which exhibits more continuity with respect to the pattern shown in Fig. 2(b).

From Fig. 4, the -10 dB return loss bandwidth ranges from 5.7 to 7.3 GHz for the original bow-tie antenna and from 4.5 GHz to 6.8 GHz for the fractal etched antenna, respectively. As can be seen, with the modified Sierpinski fractal pattern, the whole working frequency band extends

towards the lower frequency end. Thus a wider frequency band is obtained (from 24% of the original model to 41% of the model with fractal pattern).

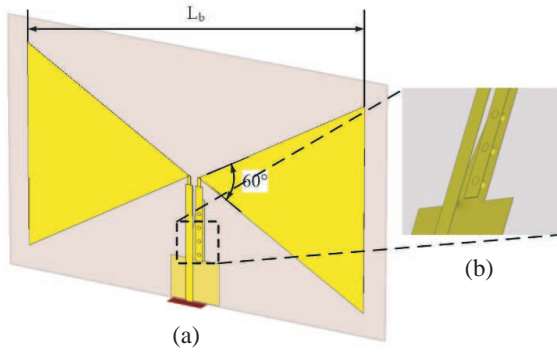


Figure 1: The original bow-tie antenna fed by a microstrip line with a balun as a transition.

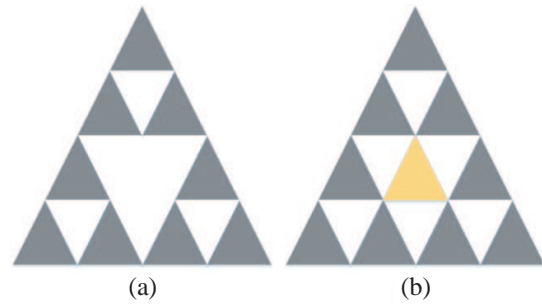


Figure 2: (a) The 2nd Sierpinski fractal pattern. (b) The 2nd Sierpinski fractal pattern with a 2nd triangle in center.

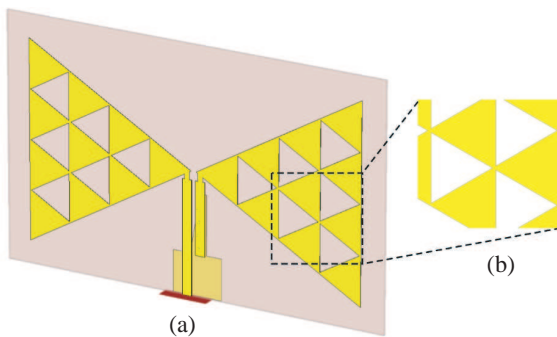


Figure 3: (a) The 2nd Sierpinski fractal etched bow-tie antenna. (b) The 2nd Sierpinski fractal pattern with a 2nd triangle in center.

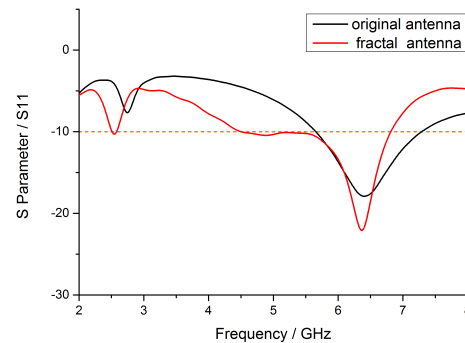


Figure 4: The S parameter of the original antenna and the fractal antenna around their working frequency.

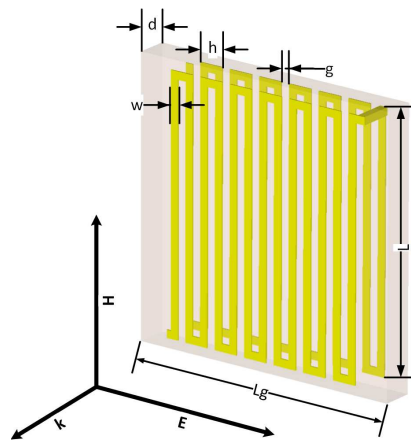


Figure 5: The designed ZIM unit cell structure is made of two meander lines which are on the front and back surface of the dielectric substrate. The parameters of the structure are: $L_g = 7$ mm, $L = 6.5$ mm, $w = 0.2$ mm, $d = 0.8$ mm, $h = 0.6$ mm, $g = 0.2$ mm. The substrate is chosen as Rogers RO4003 with the permittivity of 3.55 and the loss tangent is 0.0027.

3. DESIGN AND FABRICATION OF ZIM STRUCTURE

The zero-index metamaterials (ZIM) are such kinds of metamaterials whose value of permittivity or permeability approximates to zero. With such a unique property, ZIM can be used for gain enhancement of antennas [8,9]. As illustrated in the Fig. 5, the ZIM unit cell is a two-layer structure with meander lines etched on both sides of the dielectric substrate. Each tail of the two meander lines is connected by a metallic stick through the substrate, which enlarges the current loop thus minimizes the overall dimension of the unit cell.

The ZIM structure is carefully designed at the frequency of 5 gigahertz, with the unit length (denoted by L_g) of about 7mm. The unit cell is designed and simulated via the commercial microwave software CST MICROWAVE STUDIO.

As exhibited in the Fig. 6, the refractive index around 5 GHz is about 0.15 and enough for ZIM design [10]. We arrange the ZIM structure in front of the fractal etched antenna, as illustrated in

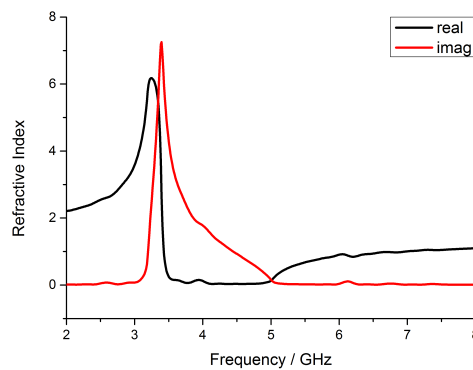


Figure 6: The real and imaginary part of refractive index of the ZIM structure, ranging from 2 to 8 GHz.

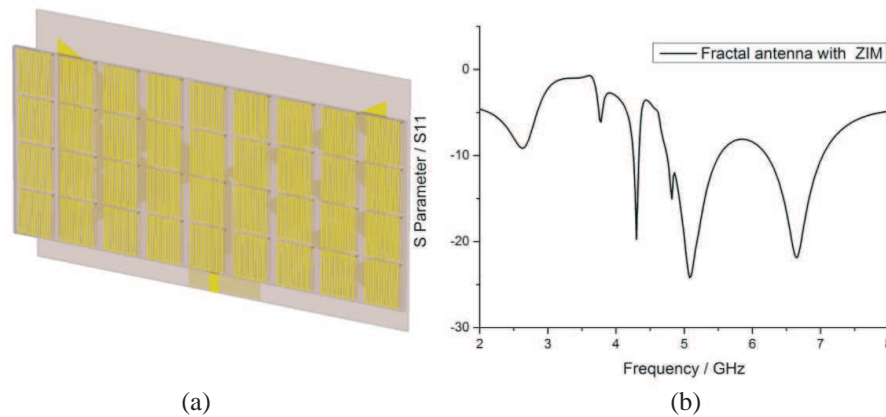


Figure 7: (a) The fractal etched antenna with ZIM structure. (b) The S parameter of the fractal antenna with ZIM.

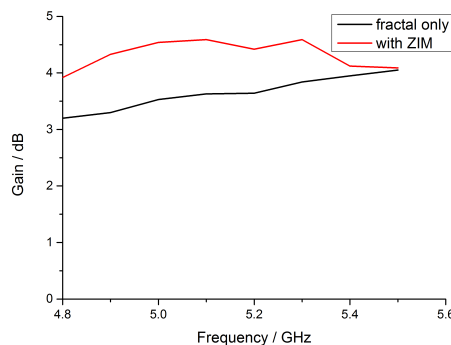


Figure 8: The gain versus frequency of the model with and without ZIM.

the Fig. 7(a).

The ZIM is a narrow band structure, as we can see from Fig. 6. The real part of refractive index increases as the frequency surpasses 5 GHz, which results to deterioration of the ZIM performance. While the frequency reaches to below 5 GHz, the imaginary part of refractive index increases, thus the loss will also degrade the performance. As Fig. 7(b) shows, when the antenna is implemented with the ZIM structure, the -10 dB return loss frequency band splits into two as can be seen from Fig. 4 and Fig. 7. Since the ZIM structure is designed at 5 GHz, the interested radiation gain versus frequency is plotted in Fig. 8. At 5 GHz, the gain of the model with ZIM is 1 dB higher than the model without ZIM.

4. CONCLUSION

In this paper, we proposed a bow-tie antenna etched with the modified Sierpinski fractal pattern. With this pattern, the working frequency bandwidth expands from 24% (5.7~7.3 GHz) to 41% (4.5~6.8 GHz) compared with the original model. To improve gain performance, a ZIM structure is implemented with the antenna, and the gain increases by about 1 dB at the interested frequency.

REFERENCES

1. Zhou, B., H. Li, X. Zou, and T.-J. Cui, "Broadband and high-gain planar vivaldi antennas based on inhomogeneous anisotropic zero-index metamaterials," *Progress In Electromagnetics Research*, Vol. 120, 235–247, 2011.
2. Ma, Y. G., et al., "Near-field plane-wave-like beam emitting antenna fabricated by anisotropic metamaterial," *Applied Physics Letters*, Vol. 94, No. 4, 044107, 2009.
3. Cheng, Q., W. X. Jiang, and T. J. Cui, "Radiation of planar electromagnetic waves by a line source in anisotropic metamaterials," *Journal of Physics D: Applied Physics*, Vol. 43, No. 33 335406, 2010.
4. Kim, Y.-G., et al., "Design of bow-tie-type UWB antennas using an ultra-wideband balun," *2007 IEEE Antennas and Propagation Society International Symposium*, 2007.
5. Chiu, C.-W., "Coplanar-waveguide-fed uniplanar antenna using a broadband balun," *Microwave and Optical Technology Letters*, Vol. 40, No. 1, 70–73, 2004.
6. Li, D. and J.-F. Mao, "A Koch-like sided fractal bow-tie dipole antenna," *IEEE Transactions on Antennas and Propagation*, Vol. 60, No. 5, 2242–2251, 2012.
7. Yamini, A. H. and M. Soleimani, "Multiband behavior of wideband sierpinski fractal bow-tie antenna," *The European Conference on Wireless Technology*, Vol. 3, 2005.
8. Lv, Y.-L., et al., "A zero index metamaterial lens for gain enhancement of patch antenna and H-plane horn antenna," *2013 IEEE International Wireless Symposium (IWS)*, 1–4, 2013.
9. Zhou, H., et al., "A novel high-directivity microstrip patch antenna based on zero-index metamaterial," *IEEE Antennas and Wireless Propagation Letters*, Vol. 8, 538–541, 2009.
10. Chung, K. L. and S. Chaimool, "Broadside gain and bandwidth enhancement of microstrip patch antenna using a MNZ-metasurface," *Microwave and Optical Technology Letters*, Vol. 54, No. 2, 529–532, 2012.

An Ultra-dense Optical Comb Based DWDM-OFDM-PON System

R. Lin¹, M. Tang¹, R. Wang¹, Z. Feng¹,
S. Fu¹, D. Liu¹, J. Chen², and P. Shum³

¹Next Generation Internet Access National Engineering Lab (NGIA)
School of Optical and Electronic Information

Huazhong University of Science and Technology, Wuhan, China

²School of ICT, The Royal Institute of Technology (KTH), Kista, Sweden

³School of EEE, Nanyang Technological University, Singapore

Abstract— We proposed and demonstrated an ultra-dense optical comb based DWDM-OFDM-PON scheme. At the optical line terminal (OLT), a cost-effective optical frequency comb generator (OFCG) is proposed and achieved as the multi-wavelength optical source. The OFCG is capable to provide multiple channels with reconfigurable wavelength spacing for ultra-dense WDM-PON based access network. In our scheme, OFDM signal with multi-level modulation will be encoded into the OFCG lines for the downstream transmission to enhance the spectral efficiency while the OFDM signal will be remodulated by OOK data for the upstream transmission due to its ease of implementation in optical network unit (ONU) side. In experiments, we demonstrated that 10 optical lines with 25 GHz channel spacing are generated and they were modulated by 2.5-GB/s QPSK-OFDM for the downlink signal transmission. We also demonstrated that the multiple wavelengths from the OFCG.

The demand bandwidth for end-to-end connectivity of broadband access services is expected to grow tremendous in the coming decades. Dense wavelength multiplexing-passive optical network (DWDM-PON) has been widely investigated for high data rate services [1–3]. In these paper, individual single wavelength laser was employed as continuous wave source providing carrier. The laser array in actual DWDM-PON is costly and unstable in maintaining coherence among multiple optical carriers. Optical frequency comb (OFC) [4–6] provides a alternative for the DWDM system lightwave source. Compared to the individual laser array, OFC generator based DWDM system simplifies the complexity of the system, lower the operation cost and promote the stability [7, 8]. OFC generated by cascading modulators is suitable for communication systems. Although in principle we can anticipate that more modulators can be used together to bring more comb lines, the complexity of the system, high operation cost and large power consumption will hinder the real applications of OFC in communication systems. On the other hand, orthogonal frequency-division multiplexing (OFDM) is considered as a strong candidate for future access network due to its contribution in high spectrum efficiency and resistance to dispersion effects and crosstalk, including inter-channel interference (ICI) and inter-symbol interference (ISI). It is also well known that of the OFDM technology is being widely applied in the fourth generation (4G) and the upcoming fifth generation (5G) mobile communication system thus it will be beneficial to investigate PON system employing OFDM infrastructure for the future seamless integration of wire-and-wireless communication system.

In this paper, we proposed an ultra-dense OFC based DWDM-OFDM-PON architecture, as illustrated in Figure 1. At the optical line terminal (OLT), an optical frequency comb generator (OFCG) is employed as the multi-wavelength optical source followed by a wavelength MUX where COMB lines can be divided into individual DWDM channels. Each channel is modulated by an intensity modulator (IM) respectively. In the downstream, quadrature phase shift keying OFDM (QPSK-OFDM) signal is converted to optical domain. An optical multiplexer (MUX) is employed to combine the DWDM channels with signal sent into the 25.6 km single mode fiber (SMF) for downstream transmission. At the optical network unit (ONU) side, direct detection (DD) receiver is adopted taking into account the cost of ONU. For upstream link transmission, the OFDM downstream signal is re-modulated by another intensity modulator at 2.5-Gbit/s OOK format at the ONU and transmitted back to the OLT.

In this paper, we proposed an ultra-dense OFC based DWDM-OFDM-PON architecture, as illustrated in Figure 1. At the optical line terminal (OLT), an optical frequency comb generator (OFCG) is employed as the multi-wavelength optical source followed by a wavelength MUX where COMB lines can be divided into individual DWDM channels. Each channel is modulated by an intensity modulator (IM) respectively. In the downstream, quadrature phase shift keying OFDM

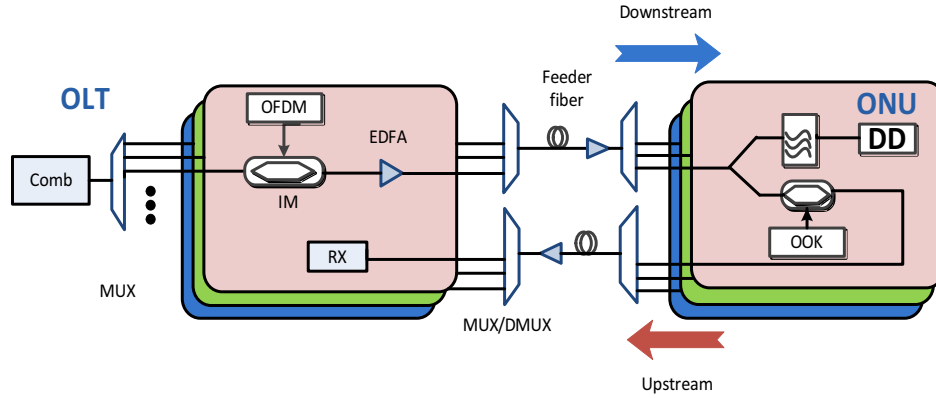


Figure 1: Illustration of the ultra-dense OFC based DWDM-OFDM-PON system. OLT: optical line termination, EDFA: Erbium-doped fiber amplifier, IM: intensity modulator, DD: direct detection, RX: receiver.

(QPSK-OFDM) signal is converted to optical domain. An optical multiplexer (MUX) is employed to combine the DWDM channels with signal sent into the 25.6 km single mode fiber (SMF) for downstream transmission. At the optical network unit (ONU) side, direct detection (DD) receiver is adopted taking into account the cost of ONU. For upstream link transmission, the OFDM downstream signal is re-modulated by another intensity modulator at 2.5-Gbit/s OOK format at the ONU and transmitted back to the OLT.

In our experiment, a comb generator using one IM and a DPMZM with only two microwave driving sources is firstly realized. This scheme is a relatively simple and low-power consumption solution for OFC generation in which high power RF signal sources and specially tailored waveforms are not used. The OFCG scheme is shown as Figure 2. A narrow linewidth continuous wave (CW) operated laser source is employed as the input signal. A dual-parallel Mach-Zehnder modulator (DPMZM) is used as the first stage OFC operated in Push-Pull configuration. 2 first order sidebands are generated by the upper arm biasing at null transmission point and the other three lines are excited by the lower arm operating at maximum point of the transmission curve. With the superposition of optical field of both arms, 5 comb lines are generated at point a in Figure 2. The DPMZM is followed by another MZM working as the second stage. The bias voltage of the second stage IM is adjusted at the point which leads to an equation of amplitude of carrier and first order sidebands. In that condition, the second order sidebands can be effectively suppressed. For any one wavelength from those 5 comb lines, the modulated output through IM can be expressed as:

$$E_{out3}(t) = E_{in3}(t) [\cos \Phi_{DC} J_0(m_3) \cos(\omega_0 t) + \sin \Phi_{DC} J_1(m_3) \sin(\omega_0 + \omega' t) - \sin \Phi_{DC} J_{-1}(m_3) \sin(\omega_0 - \omega' t)] \quad (1)$$

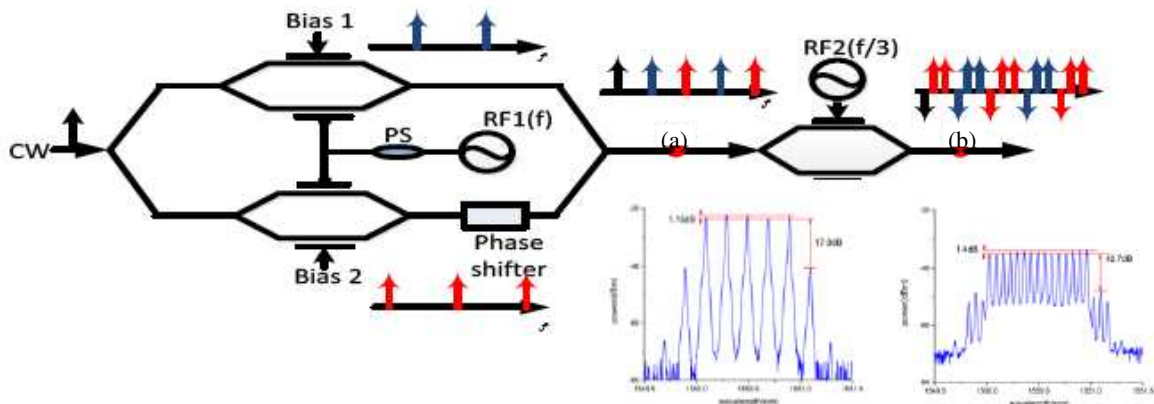


Figure 2: Experimental setup for the OFCG composed of one DPMZM and an MZM and the spectrum generated at point (a) and (b). (CW: continuous wave laser, RF: radio frequency, PS: 50 : 50 power splitter).

If we set $\omega' = \omega/3$ and let

$$\cos \Phi_{DC} J_0(m_3) = -\sin \Phi_{DC} J_1(m_3) \quad (2)$$

A single line will evolve into three with equivalent amplitude. Therefore, a spectrum of 15 comb lines with equal power can be generated with the spectral spacing as one-third frequency of the first stage comb.

With the proposed OFCG, 10 channels with 25 GHz spacing is provided at the transmitter. 10-Gb/s baseband QPSK signal is generated off-line with 64 subcarriers and a fast Fourier transform (FFT) size of 256 and a cyclic prefix (CP) of 0.1. The off-line signal was uploaded into arbitrary waveform generator (AWG, Tektronix AWG 7122), and a Mach-Zehnder modulator was employed to convert the OFDM signal to DSB optical signal. All the channels are modulated simultaneously. Optical distribution network was emulated with 25.6 km single mode fiber (SMF) and a variable optical attenuator. The downstream signal was photodetected using a PD, and sampled by a 50 GS/s Tektronix real-time scope. Demodulation and Bit Error Rate (BER) counting were implemented offline. Instantaneous multi-wavelength loading OFDM-QPSK signal is performed through direct modulation on the generated OFC. The constellation map shown in Figure 3(c) is acceptable in the case of simulating the PON transmission environment. And simultaneously multi-wavelength OOK modulation and transmission was also verified, the eye-diagram of the upstream with 2.5-Gb/s OOK after 25.6 km is displayed in Figure 3(d).

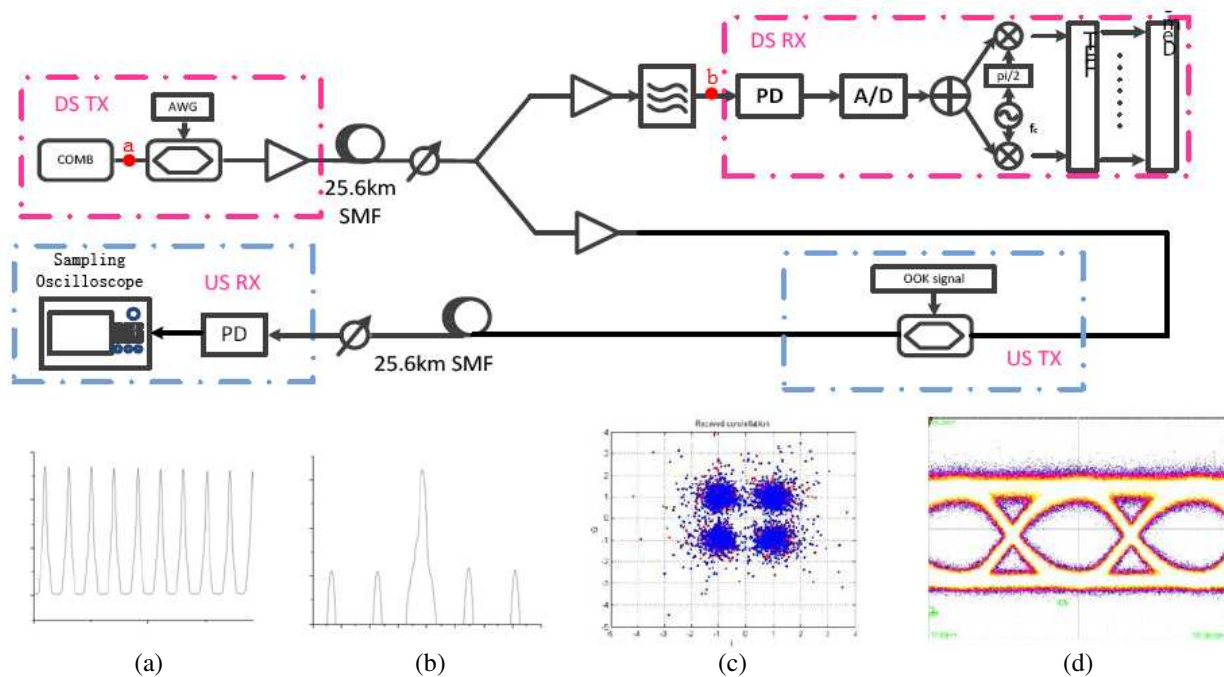


Figure 3: Experimental setup of the proposed DWDM-OFDM-PON system. The optical spectrum is measured at the corresponding point (a) and (b). Constellation map of downstream QPSK-OFDM signal in PON transmission environment (c) and eye-diagram of the 25.6 km transmitted upstream 2.5-Gb/s OOK signal with multi-carrier simultaneously modulation is displayed as (d). AWG: arbitrary waveform generator; A/D: analog to digital; PD: photo diode.

We proposed and demonstrated an ultra-dense optical comb based DWDM-OFDM-PON system. A simple and cost-effective OFCG consists of a DPMZM and an IM is posed for providing multiple channels with reconfigurable wavelength spacing for ultra-dense WDM-PON based access network. For the downstream, OFDM signal with multi-level modulation was encoded into OFC lines to enhance the spectral efficiency. And the OFDM signal would be remodulated by OOK data for uplink transmission for its ease implementation in ONU. We experimentally demonstrated the OFCG. 10 optical carriers with 25 GHz spacing were modulated by 2.5-Gb/s QPSK-OFDM for the downlink signal transmission. It is beneficial to investigate the OFDM-PON system for seamless integration of wired-and-wireless communication system.

ACKNOWLEDGMENT

This work is supported by the National High-tech R&D Program of China (863 Program) (Grant Nos. 022013AA013402), the National Natural Science Foundation of China (NSFS) under Grants 61331010 and 61107087). If any, including all funding information, should be gathered into a brief statement at the end.

REFERENCES

1. Yu, J. H. and N. Kim, “Remodulation schemes with reflective SOA for colorless DWDM PON,” *Journal of Optical Networking*, Vol. 6, No. 8, 1041–1054, 2007.
2. Lee, S. and M. King, “Demonstration of a bidirectional 80-km-reach DWDM-PON with 8-Gb/s capacity,” *Photonics Technology Letters*, Vol. 19, No. 6, 405–407, 2007.
3. Chow, C., “Wavelength remodulation using DPSK down-and-upstream with high extinction ratio for 10-Gb/s DWDM-passive optical networks,” *Photonics Technology Letters*, Vol. 20, No. 1, 12–14, 2008.
4. Takara, H. and T. Ohara, “More than 1000 channel optical frequency chain generation from single super continuum source with 12.5 GHz channel spacing,” *Electronics Letters*, Vol. 36, No. 25, 2089–2090, 2000.
5. Jiang, Z. and B. Huang, “Optical arbitrary waveform processing of more than 100 spectral comb lines,” *Nature Photonics*, Vol. 1, No. 8, 463–467, 2007.
6. Del’Haye, P. and A. Schliesser, “Optical frequency comb generation from a monolithic microresonator,” *Nature*, Vol. 450, No. 7173, 1214–1217, 2007.
7. Wu, R. and V. Supradeepa, “Generation of very flat optical frequency combs from continuous-wave lasers using cascaded intensity and phase modulators driven by tailored radio frequency waveforms,” *Optics Letters*, Vol. 35, No. 19, 3234–3236, 2010.
8. Healy, T. and G. Garcia, “Multi-wavelength source using low drive-voltage amplitude modulators for optical communications,” *Optics Express*, Vol. 15, No. 6, 2981–2986, 2007.